SiF 2008

Proceedings of the Fifth International Conference

Structures in Fire

Nanyang Technological University

Singapore

28 – 30 May, 2008

Kang Hai TAN
Nanyang Technological University
Singapore

Venkatesh K. R. KODUR
Michigan State University
USA

Teng Hooi TAN
Nanyang Technological University
Singapore

Organizer

Published by

Organising Committee
Fifth International Conference Structures in Fire (SiF'08)

Proceedings of the

Fifth International Conference Structures in Fire (SiF'08)

ISBN: 978-981-08-0767-2

Design & Printed by Research Publishing Services
E-mail: enquiries@rpsonline.com.sg

Preface

The idea of specialized "Structures in Fire" workshop series was conceived in late 1990's and bore fruit in 2000 when the "1^{st} International SiF workshop" was organized in Copenhagen, Denmark. This was followed by "2^{nd} International SiF workshop" that was held in Christchurch, New Zealand in 2002. Two years later, the "3^{rd} International SiF workshop" took place in Ottawa, Canada, followed by the "4th International SiF workshop" which was held in Aveiro, Portugal, in 2006. The objective of these specialized workshops was to provide an opportunity for researchers, practioners and engineers, specializing in *structural fire engineering* field, to share their research, technology and expertise with their peers at an international forum. The special features of SiF workshop series include high quality presentations, adequate time for presentation and discussion, single-track session, specific focus on "Structures in Fire" theme and affordable workshop costs for participants. The first four workshops were organized by various research groups under the "SiF" leadership headed by Dr. J. M. Franssen.

Over this period, the SiF forum and workshops have grown in size and stature, with increasing international awareness of its mission and vision. Taking note of this success, SiF members, at the "4^{th} International SiF workshop", endorsed the elevation of "SiF International workshop" series to "International Conference on SiF" series. In addition, to recognize the growing importance of this forum, a steering committee was formed to oversee the SiF activities and conferences. Under this new frame work Nanyang Technological University, Singapore, was selected to host the "5^{th} International Conference on SiF" in May 2008.

SiF steering committee received a total of 106 abstracts for this year's conference. Based on the review of each abstract by at least three reviewers, selected from the scientific committee, the steering committee finalized 68 papers for publication in the conference proceedings. Most of the submissions were of high quality and some of them could not be included in the program due to limited slots available over three days of the conference. The papers in the proceedings are grouped under:

- Steel, Stainless Steel and Aluminium Structures
- Connections in Steel and Composite Structures
- Structural Modelling and Analysis
- Concrete Structures
- Composite Structures
- Timber Structures
- Fire Safety Engineering and Fire Protection

The papers contained in the proceedings draw on the experience and special knowledge of academics and the practitioners, both in the public and private sectors, from 20 countries, namely Australia, Belgium, Canada, China, Czech Republic, Germany, Italy, Japan, Korea, Luxembourg,

New Zealand, Norway, Portugal, Romania, Singapore, Spain, Sweden, Switzerland, United Kingdom, United States of America.. The efforts of these authors are gratefully acknowledged.

It is hoped that the high quality of the work will enable researchers to develop greater insight of structural fire engineering, so that safer structures could be designed for fire conditions.

We would like to thank members of the "Scientific Committee" for reviewing the abstracts within an incredibly short period of time. Our sincere appreciation to the "SiF Steering Committee" for organizing the review process and for providing direction to the successful organization of this conference. Special acknowledgement to the "conference secretariat – CMA/NTU", for helping us with the nitty-gritty of organizing a conference. Thanks to generous sponsors for supporting the conference and supporting organizations for promoting the conference among the local fire safety engineers. Last but not the least, special thanks to all the authors and the participants of the conference for making the "5^{th} International Conference on SiF" a great success.

Kang Hai TAN
Co-Chairman
Organizing Committee

Venkatesh K. R. KODUR
Chairman
Scientific Committee

Teng Hooi TAN
Co-Chairman
Organizing Committee

Scientific Committee

Scientific Committee

Organising Committee

Associate Prof. Kang Hai TAN (Co-Chairman)
Nanyang Technological University, Singapore

Associate Prof. Teng Hooi TAN (Co-Chairman)
Nanyang Technological University, Singapore

Mr. Tian Chong TAN
Building & Construction Authority

Mr. Geok Kwang BOO
Singapore Civil Defence Force

Associate Prof. Richard J. Y. LIEW
National University of Singapore

Dr. Didier TALAMONA
The University of Newcastle, Australia, Singapore Campus

Steering Committee

Jean-Marc Franssen (Chairman)
University of Liege, Belgium

Andy Buchanan
University of Canterbury, New Zealand

Paulo Vila Real
University of Aveiro, Portugal

Venkatesh Kodur
Michigan State University, USA

Acknowledgements

The organizing committee gratefully acknowledges the following:

Sponsors

Corus South East Asia Pte Ltd

Defence Science and Technology Agency

Industrial Contracts Marketing (2001) Pte Ltd

LCP Building Products Pte Ltd

Singapore Structural Steel Society

University of Newcastle, Singapore

Supporting Organizations

Singapore Civil Defence Force

Building and Construction Authority

Contents

Session 5: Composite Structures

Session 6: Timber Structures

Steel, Stainless Steel and Aluminum Structures

ANALYTICAL MODEL FOR THE WEB POST BUCKLING IN CELLULAR BEAMS UNDER FIRE

O. VASSART[1], A. BOUCHAÏR, J.-P. MUZEAU[2] and A. NADJAI[3]

ABSTRACT

A finite element model using shell elements was developed in the software SAFIR considering both material and geometrical non-linearity. It was calibrated on the basis of experimental results. The comparison between the finite element prediction and actual experimental results showed a good agreement in terms of failure modes, load deflection relationship and ultimate loads[1]. During fire tests, failure arising by web post buckling, temperature measured during the fire tests indicated that this type of failure can not be simply estimated by applying temperature dependent reduction factors on stiffness, as given in codes. This paper describes an analytical model representing the web post buckling for cellular beams in case of fire. It is based on the ArcelorMittal web post buckling model developed by CTICM for cold conditions and some experimental results for full scale composite floor cellular steel beams at ambient and elevated temperatures.

1 INTRODUCTION

The fire resistance of cellular beams has been very controversial in recent years, with most of the debate being concerned with their requirements for intumescent protection. A rather conservative prescriptive "rule"[2], without mechanical basis, for beams with web openings, requiring 20% extra coating thickness compared with solid-web beams, has recently been much discussed on the basis of thermal tests using beams coated with specific intumescent products. This previously mentioned approach was followed by more recent publications[3,4,5] justifying the traditional prescriptive fire protection rules. They are based on some principles of structural mechanics applied to analyse the behaviour of cellular beams under fire.

[1] ArcelorMittal Belval&Differdange S.A.,Research Centre, Esch/Alzette, G.-D. of Luxemburg
olivier.vassart@arcelormittal.com
[2] CUST-LGC, Blaise Pascal University, Clermont 2, France
[3] University of Ulster, School Built Environment, FireSERT, Belfast BT37 OQB, UK

To date, the research into the fire resistance of cellular beams is very limited. Literature relating to the experimental or theoretical study of the behaviour of cellular beams in fire is virtually non-existent. Some experimental and numerical aspects[1] have the potential to provide essential data in several areas currently lacking systematic research results. It will underpin the current lead in expertise which is held by European fire engineering designers, and will assist European-based fabricators who have made cellular beams the most popular long-span system in current construction.

In this paper, a part of an analytical model representing the web post buckling for cellular beams in case of fire is described. It is based on the ArcelorMittal web post buckling model developed for cold conditions[6] and some experimental results for full scale composite floor cellular steel beams at ambient and elevated temperatures[1]. To check the validity of the analytical model, a finite element model using shell elements was developed considering both material and geometrical non-linearity.

2 FINITE ELEMENT MODEL DESCRIPTION

The finite element model was developed using the software SAFIR[7] in order to simulate the complete behaviour of cellular beams taking into account local instabilities. This model was calibrated on the basis of a large number of different cold tests performed over the past few years[6,8]. This model was then used to simulate the behaviour of cellular beams in case of fire.

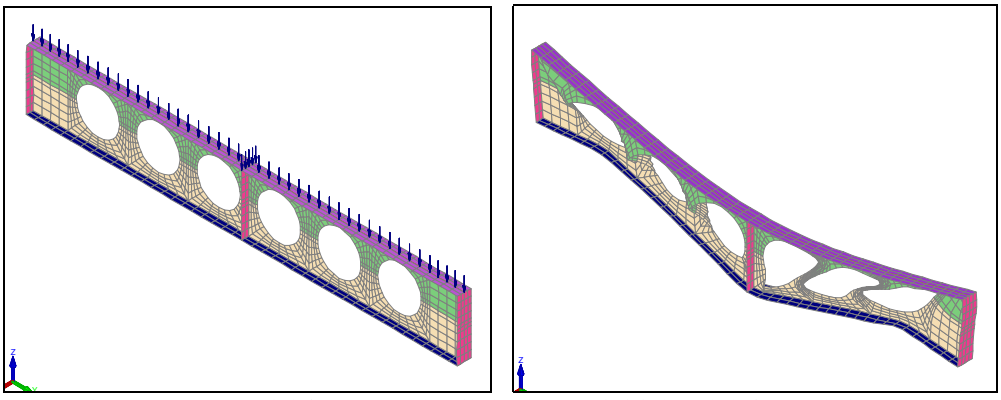

Fig. 1 - FEM model for a tested cellular beam (initial and deformed shapes).

The FEM model was calibrated on the basis of two tests of different geometrical configurations[1]. The different temperatures measured during the two tests at elevated temperature were directly introduced in the FEM model to simulate the behaviour of the cellular beams in high temperature conditions. These results[1] were concluding that the numerical model simulates well the mechanical behaviour of composite cellular beam sections in both cold and at elevated temperature conditions with a relatively high accuracy. An example of the numerical model results is given in Fig. 1. It shows that the model is well representing the common failure mode for steel cellular beams under high temperature which is the web post buckling.

3 WEB POST BUCKLING ANALYTICAL MODEL

The analytical method for the web post buckling in cold condition has been developed by CTICM on behalf of ArcelorMittal, as part of the ACB design optimisation study. It is described in many references[6,9,10,11].

This method was adapted for the cellular beam calculation in fire conditions. It is presented hereafter.

The criterion for resistance to buckling of an intermediate web post at elevated temperature is given by Equation 1. It is based on the calculation of $\sigma_{w.fi.Rd}$, the principal stress resistance in fire situation for the half post being studied and $\sigma_{w.fi.Ed}$, the principal compressive stress in fire situation in the half post being studied ($\sigma_{w.fi.Ed.up}$ for the upper half post and $\sigma_{w.fi.Ed.low}$ for the lower half post). These stresses are calculated for the critical section of the member being verified, adjacent to the opening where compression is at a maximum (Fig. 2).

$$\Gamma_b = \frac{|\sigma_{w.fi.Ed}|}{\kappa\, \sigma_{w.fi.Rd}} \tag{1}$$

Where κ is the factor for post critical reserve of strength, taking into account failure by a mechanism that occurs after the appearance of local buckling of the web post (see Equation 21).

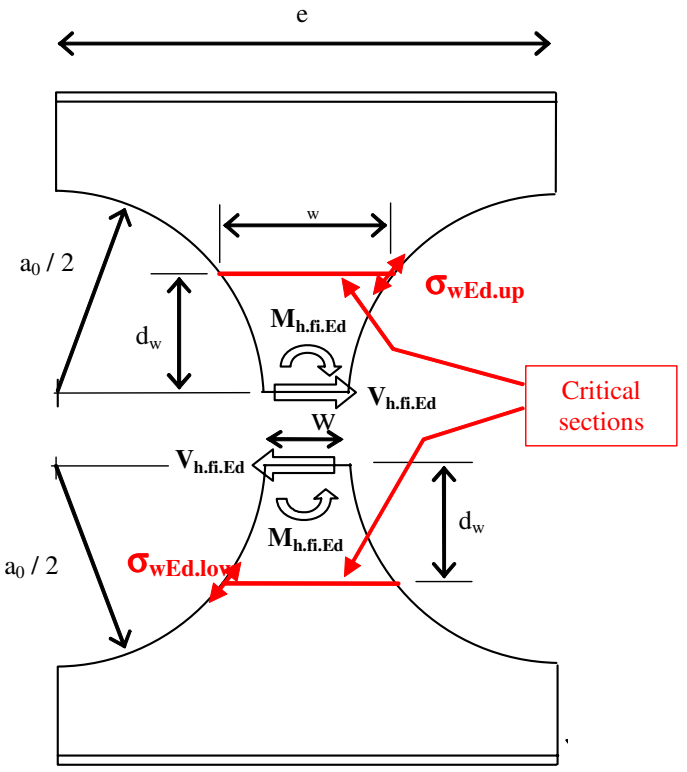

Fig. 2 - Definition of critical section for stability of an intermediate web post.

Throughout the following parts of this paper, the parameter α defines the width of the web post in terms of the following relationship:

$$\alpha = 1 + w / a_0 \tag{2}$$

The critical section of a half post is the section where the horizontal shear $V_{h.fi.Ed}$ gives the maximum bending stress in the plane of the web. This section is defined in terms of its distance dw from the joint between the two half posts, given by the Equation 3 based on geometrical considerations.

$$d_w = \frac{a_0}{2}\sqrt{\frac{\sqrt{\alpha^4 + 8\alpha^2} - 2 - \alpha^2}{2}} \tag{3}$$

The width $_w$ of the critical section is obtained by considering the following relationship (Equation 4).

$$_w = a_0\left(\alpha - \sqrt{1 - \left(\frac{2d_w}{a_0}\right)^2}\right) \tag{4}$$

The principal compressive stress in case of fire at the critical section due to local bending moment (Fig. 3) is given by Equation 5.

$$\sigma_{w.fi.Ed} = \frac{6M_{c.fi.Ed}}{^2_w t_w\left(1 - 4(d_w/a_0)^2\right)} \tag{5}$$

Where: $M_{c.fi.Ed}$ = Bending moment in the critical section in fire situation.

Upper member: $M_{c.fi.Ed.up} = V_{h.fi.Ed}\, d_w - M_{h.fi.Ed}$

Lower member: $M_{c.fi.Ed.low} = V_{h.fi.Ed}\, d_w + M_{h.fi.Ed}$ (6)

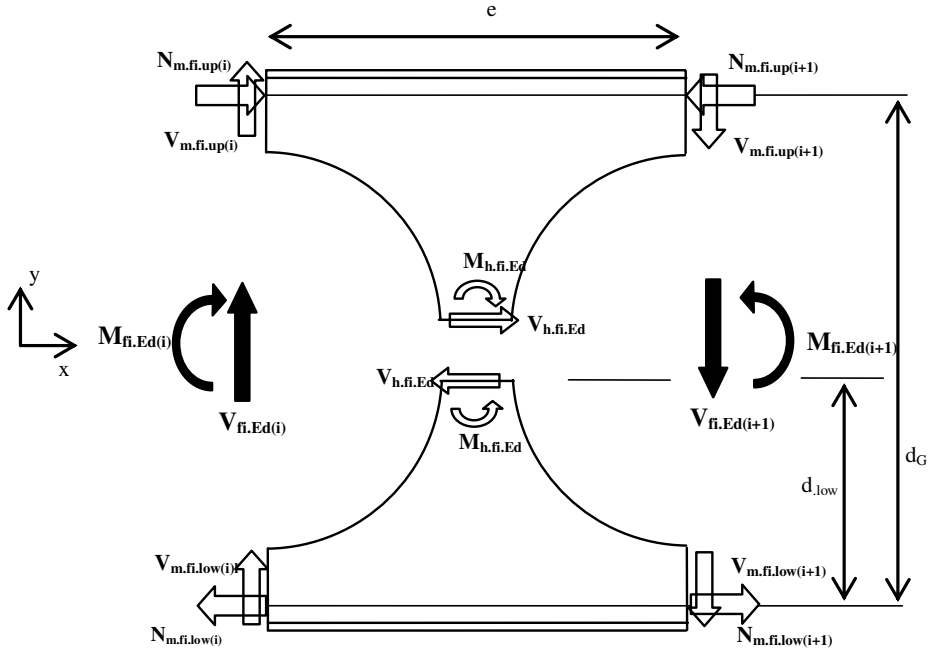

Fig. 3 - Forces acting on typical T sections

The shear area of a T is given by the following relationship:

$$A_{v.0} = \left(h_m - \frac{a_0}{2} - \frac{t_f}{2} \right) t_w + r_c t_f + \frac{4-\pi}{2} \cdot r_c^2$$

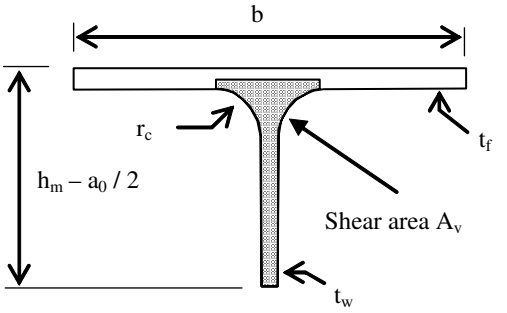

Fig. 4 - Shear area of a T at the location of an opening

The forces in the web post are given by :

$$V_{hm.fi} = N_{m.fi.up(i+1)} - N_{m.fi.up(i)}$$
$$= N_{m.fi.low(i+1)} - N_{m.fi.low(i)}$$

$$M_{hm.fi} = (V_{m.fi.low(i+1)} + V_{m.fi.low(i)})\, e / 2 - V_{hm.fi}\, d_{low}$$

Where:

d_{low} = Distance between the centre of gravity of the lower T (at the opening centre line) and the line of the joint between the half posts (Fig. 3).

The principal stress resistance is calculated using Equation 7 based on Eurocode 3 approach[12].

$$\sigma_{w.fi.Rd} = \frac{\chi_{fi} \cdot \xi \cdot k_{y,\theta} \cdot f_y}{\gamma_{M1}} \tag{7}$$

Where:

χ_{fi} = Reduction factor for out-of-plane buckling of the web post adapted for fire situation following the Eurocode 3[12], and calculated using the following formulae

$$\chi_{fi} = \frac{1}{\phi_\theta + \left(\phi_\theta^2 - \bar{\lambda}_\theta^2 \right)^{0,5}} \text{ and } \chi_{fi} \le 1,0 \tag{8}$$

$$\phi_\theta = 0,5\left(1 + \alpha_{EN} \bar{\lambda}_\theta + \bar{\lambda}_\theta^2\right) \tag{9}$$

$$\alpha_{EN} = 0,65\sqrt{\frac{235}{f_y}} \tag{10}$$

ξ : Shape factor for the critical section, given by

$$\xi = 1,5 + \frac{2 \cdot 10^{-5}}{(1-\alpha)^4} \tag{11}$$

The reduced slenderness $\bar{\lambda}_\theta$ of the web post being considered in case of fire is given by Equation 12.

$$\bar{\lambda}_\theta = \bar{\lambda}\sqrt{\frac{k_{y,\theta}}{k_{E,\theta}}} = \sqrt{\frac{\xi f_{yw}}{\sigma_{w.fi.Cr}}}\sqrt{\frac{k_{y,\theta}}{k_{E,\theta}}} \tag{12}$$

Where:

$k_{y,\theta}$ and $k_{E,\theta}$ are the reduction factors for steel strength limit and young modulus respectively, at elevated temperature.

The critical principal stress for instability $\sigma_{w.fi.Cr}$ in fire condition is given by Equations 13.

$$\begin{aligned} &\text{Upper half post : } \sigma_{w.fi.Cr.up} = \sigma_{cr.up}\,\sigma_{w.fi.up} \\ &\text{Lower half post : } \sigma_{w.fi.Cr.low} = \sigma_{cr.low}\,\sigma_{w.fi.low} \end{aligned} \tag{13}$$

Where:

$\sigma_{w.fi.up}$, $\sigma_{w.fi.low}$ = Principal stresses in fire situation in the upper and lower half posts respectively, due to the shear force $V_{hm.fi}$ alone and calculated using the formula given in the Equation 5.

$\alpha_{Cr.fi.up}$, $\alpha_{Cr.fi.low}$ = Critical coefficients for the upper and lower half posts respectively, taking into account interaction between the two members and given by Equations 14.

$$\begin{aligned} \alpha_{Cr.fi.up} &= \max\left(\beta_{Cr.fi.up}; \frac{2\,\beta_{Cr.fi.up}\,\beta_{Cr.fi.low}}{\beta_{Cr.fi.up}+\beta_{Cr.fi.low}}\right) \\ \alpha_{Cr.fi.low} &= \max\left(\beta_{Cr.fi.low}; \frac{2\,\beta_{Cr.fi.low}\,\beta_{Cr.fi.low}}{\beta_{Cr.fi.up}+\beta_{Cr.fi.low}}\right) \end{aligned} \tag{14}$$

Where:

$\beta_{Cr.fi.up}$, $\beta_{Cr.fi.low}$ = Critical coefficients for the upper and lower half posts respectively, taking into account only compression in the member and shear in the web post, given by Equations 15.

It is important to note that these coefficients are calculated assuming that the lower member is in tension and the upper member is in compression.

$$\begin{aligned} \beta_{Cr.fi.up} &= \frac{1}{\dfrac{V_{h.fi.Sd}}{V_{h.Cr.fi.up}} + \dfrac{N_{m.fi.up}}{N_{m.Cr.fi.up}}} \\ \beta_{Cr.fi.low} &= \frac{1}{\dfrac{V_{h.fi.Sd}}{V_{h.Cr.fi.low}} + \dfrac{1}{2}\dfrac{N_{m.fi.low}}{N_{m.Cr.fi.low}}} \end{aligned} \tag{15}$$

Where:

$V_{h.Cr.fi.up}$, $V_{h.Cr.fi.low}$ = Critical shear forces in fire condition for out-of-plane buckling of the upper and lower half posts respectively (see definition hereafter)

$N_{m.Cr.fi.up}$, $N_{m.Cr.fi.low}$ = Critical axial forces in fire condition for local buckling of the web of the upper and lower members respectively (see definition hereafter).

$N_{m.fi.up}$, $N_{m.fi.low}$ = Axial forces in fire condition in the webs of the upper and lower members respectively, given by Equations 16.

$$N_{m.fi.up} = \frac{A_{w.up}}{A_{0.up}} \min\left(N_{m.fi.up(i)}; N_{m.fi.up(i+1)}\right)$$

$$N_{m.fi.low} = \frac{A_{w.low}}{A_{0.low}} \min\left(N_{m.fi.low(i)}; N_{m.fi.low(i+1)}\right) \quad (16)$$

$A_{0.up}$, $A_{0.low}$ = Areas of the upper and lower T sections respectively, at the location of the openings.

$A_{w.up}$, $A_{w.low}$ = Areas of the webs of the upper and lower T sections respectively, at the location of the openings, given by

$$A_{w.up} = A_{0.up} - b_{up}\, t_{f.up}$$
$$A_{w.low} = A_{0.low} - b_{low}\, t_{f.low} \quad (17)$$

The critical forces, $V_{h.Cr.fi}$ for shear in the web post and $N_{m.Cr.fi}$ for compression in a member, are given by Equations 18 and 19.

$$V_{h.Cr.fi} = P_E\,(C_0 + C_1\, t_w) \quad (18)$$
$$N_{m.Cr.fi} = P_E\,(D_0 + D_1\, t_w) \quad (19)$$

Where:

P_E = Reference Euler buckling load, given by Equation 20.

$$P_E = \frac{\pi^2 E_a}{a_0^2}\, w\, t_w^3 \quad (20)$$

Expressions for the coefficients C_0, C_1, D_0 and D_1, based on experimental and numerical calibration, are given in reference[9].

The factor for post critical reserve of strength κ is given by Equation 21.

$$\kappa = 1 + 0{,}625\,(\psi - 0{,}3) \quad (21)$$

Where: ψ = Non-dimensional factor given by the following formulae.

Upper T : $\psi = M_{pl.Rd.up} / e\, V_{up}$

Lower T : $\psi = M_{pl.Rd.low} / e\, V_{low}$

where $M_{pl.Rd.up}$, $M_{pl.Rd.low}$ = Plastic moment resistances of the upper and lower T respectively, at the location of an opening.

and $V_{fi.up}$, $V_{fi.low}$ = Shear forces in the upper and lower members respectively. The lower of the values for ψ obtained to the right and left of the web post is used.

4 PARAMETRICAL STUDY USING FEM MODEL

A parametrical study was carried out in order to compare the critical temperature given by the calibrated FEM Model (SAFIR) and the simplified analytical model. The Fig. 5 shows the difference between the critical temperatures of the web post given by SAFIR and the analytical simplified model. All the results are on the safe side.

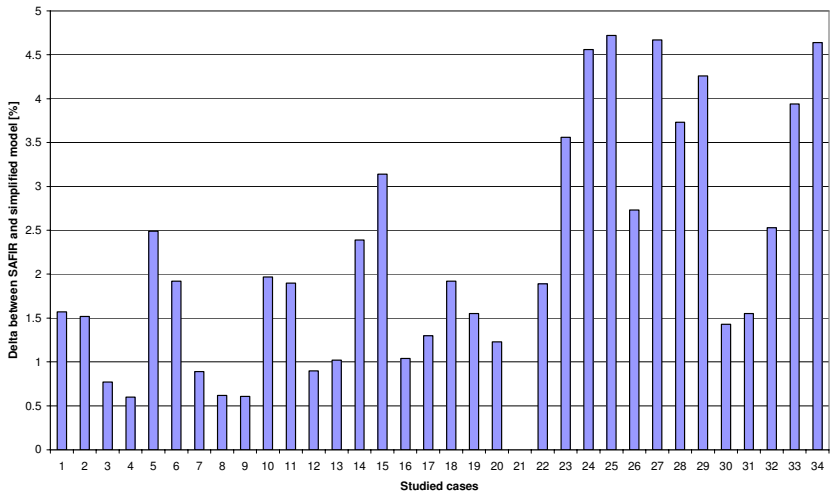

Fig. 5 - Difference of the critical temperature between the FEM and the analytical model

Analysing this graph, it can be seen that the simplified calculation model is always on the safe side and that the difference between the FEM model SAFIR and the simplified method is rather low.

This parametrical study was made varying the following parameters:

- steel profile
- geometry of the web-post
- steel strength limit
- loading intensity

The Fig. 6 shows the out-of-plane displacement of a web post versus the time of heating for a steel cellular beam heated using the ISO-curve.

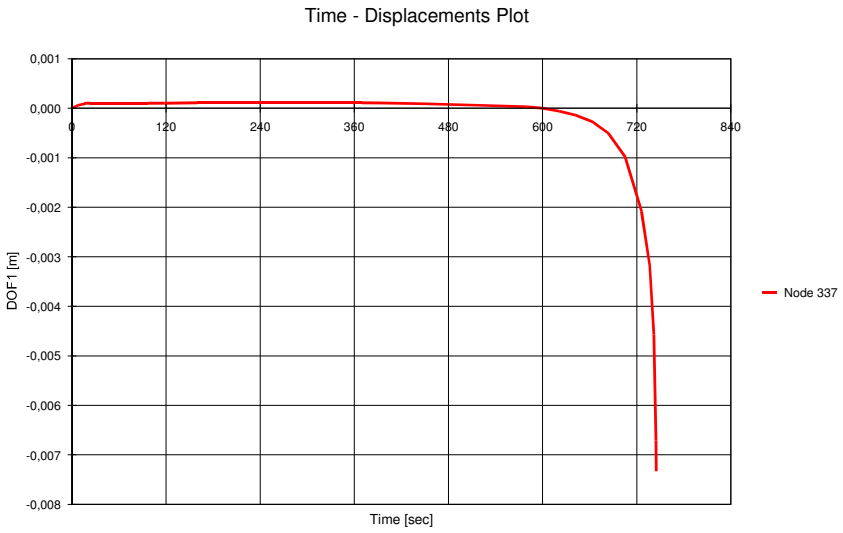

Fig. 6 - Evolution of the lateral displacement in a critical point versus time of exposure to fire

The web post buckling is a kind of instability. This instability is observed on the curve of the lateral displacement evolution versus time of heating. When this displacement becomes high, we consider that the beam reached its critical temperature (Fig. 6).

5 CONCLUSION

This paper describes an analytical model to calculate the web-post buckling resistance for cellular beams in case of fire conditions. The study suggests the following:

- The experimental results compared with the results from the Finite Element Modelling, showed a good agreement, giving confidence that the finite element modelling can be used for further parametric studies.
- The numerical model is able to simulate the mechanical behaviour of composite cellular beam sections in both cold and elevated temperature conditions with a relatively high accuracy.
- The simplified model developed for the evaluation of the critical temperature of the web post gives accurate and safe sided results compared to the experimental tests and FEM model.

Further improvement must be done in order to take into account the composite cellular beams in the analytical simplified model. The limits of application must also be defined considering a wide range of steel profiles.

6 REFERENCES

[1] Nadjai, A.; Vassart, O.; Faris, A.; Talamona, D.; Allam, A. & Hawes, M. 2006. Performance of cellular composite floor beams at elevated temperatures, Proc. SIF 2006, pp. 813-823.
[2] ASFP/SCI/FTSG, 1992. Fire Protection for Structural Steel in Buildings, Second Edition, (1992).
[3] Bailey, C.G. 2004. Indicative Fire Tests to Investigate the Behaviour of Cellular Beams Protected with Intumescent Coatings. Fire Safety Journal, Vol. 39, 2004, pp. 689-709.
[4] SCI, 2004. RT1006 Version 02 - Fire Design of Cellular beams with Slender Web Posts, SCI, Ascot, 2004.
[5] Newman, G.M.; Robinson, J.T. & Bailey, C.G., 2006. Fire Safe design - A New Approach to Multi-Storey Steel-Framed Buildings, Second Edition, SCI Publication, P288, The Steel Construction Institute, Ascot, 2006.
[6] Bitar, D.; Demarco, T.; Martin, P.O. 2005. Steel and non composite cellular beams – Novel approach for design based on experimental studies and numerical investigations, Proc. 4th Eurosteel Conference, Maastricht, june 2005.
[7] Franssen, J.M.; Kodur, V.R.K; Mason, J., 2005. User's manual for SAFIR 2004 a computer program for analysis of strutures subjected to fire, March 2005..
[8] ECSC, 2004. Large web Openings for service integration in composite floor, ECSC contract 7210-PR-315, 2004
[9] Martin, P.-O., 2003. ACB Design optimisation – web-post buckling, CTICM, Research report, November 2003 (in French).
[10] Galéa, Y. & Martin P.-O., 2003. ACB Design optimisation – displacement calculation, Research report, CTICM, Décembre 2003.
[11] Bitar, D. ; Martin, P.-O. ; Galéa, Y. & Demarco, T., 2006. Steel and composite cellular beams – Part 1 : proposal of a model for the web-post resistance, Revue Construction Métallique n°1-2006.
[12] CEN, 2004. Eurocode 3 – Design of steel structures - Part 1-2 : General rules – Structural fire design.

DEVELOPMENT OF A TRANSIENT HEAT TRANSFER MODEL ON EXTERNAL STEEL ELEMENTS BASED ON NUMERICAL MODELLING AND EXPERIMENTAL STUDIES

JESÚS DE LA QUINTANA[1] and FERNANDO MORENTE[2]

ABSTRACT

The Eurocodes provide limited information regarding the structural fire design of external steel structures. The Eurocode 1 provides the thermal action for the external member but only in steady-state conditions. On the other hand, the Eurocode 3 provides the methodology to determine the heat transfer to the external steelwork, but there is not distinction about cross section shapes and, in addition, the calculated temperature is assumed to be uniform in the cross section.

This paper presents the results of the research carried out to develop a new transient heat transfer model for external steel elements to improve the current approach of the Eurocodes.

1. INTRODUCTION

The Eurocode provides specific information for the fire design of external steel structures.

The Eurocode 1: "Actions on structures" - Part 1-2: "General actions - Actions on structures exposed to fire" provides in the Annex B a simplified calculation method to determine the thermal actions for external members.

With the information of the fire, floor area of the fire compartment and the design fire load density related to the floor area, and the geometrical information about total area of vertical openings on the façade walls, the Eurocode 1 provides:

[1] Head of Fire Safety Engineering, LABEIN-TECNALIA, Spain,
email: jq@labein.es
[2] Researcher, LABEIN-TECNALIA, Fire Safety Engineering, Spain,
email: fmorente@labein.es.

- the maximum temperatures of the compartment fire;
- the size and temperatures of the flame from openings;
- and the radiation and convection parameters.

But it is very important to underline that the Method of the Eurocode 1 considers steady-state conditions for the all the parameters.

Regarding to the "thermal response" of the external steel structures, the Eurocode 3: "Design of steel structures" Part 1.2 : "General rules Structural fire design", gathers a stationary model. This methodology it is presented in the Annex B "Heat Transfer to external steelwork".

The limitations of this method are:

- the calculated temperature is an uniform steel temperature, taken for the most heated cross section components of the external members,
- and the approach is the same for all type of cross sections, there is no consideration of the real shape to take into account in a detail way the shadow effect.

This paper provides the result of the research to improve the current Eurocodes methodology.

2. OBJETIVES OF THE NEW MODEL

To improve the Eurocodes approach to the fire safety design of external steel structures, LABEIN-TECNALIA carried out the needed research and development works, to obtain a new transient heat transfer model, within the RFCS project EXTFIRE, "Development of design rules for the fire behaviour of external steel structures".

The main aspects to be improved in the Eurocode's model are the following:

- Against the stationary model available currently, the new methodology deals with the transient effects related to a changing exposure to heat from flames and openings during the whole development of the fire.
- The Eurocode's model treats open and hollow sections in the same way, with a section factors based method. The new approach uses an improved definition of configuration factors to take into account the shadow effect. Shadow zones are established in a profile's section and the net heat flux that reaches different points in the section is computed, considering the radiation flux from other parts of the section at different temperatures.
- In open cross sections, due to the different exposure to heat from flames and openings, a thermal gradient is created through the section. Therefore, all the parts do not undergo the same temperature evolution and need to be dealt with separately. The temperatures of web and flanges are calculated for each step of time.

To improve the Eurocode´s model it is proposed the development of a new model: a "transient heat transfer model", the EXTFIRE model. The main objectives for the new transient heat transfer model are summarised in the Table 1.

The methodology for the development of the EXTFIRE model has been based on the following philosophy:

- The EXTFIRE model must be based on amendment to the Eurocode by using complementary and non contradictory information in other to make easier the upgrading of the Eurocodes with the EXTFIRE model.

- The validation of the model will be obtained by performing Computer Fluid Dynamics (CFD) simulations.

Tests performed by CTICM (France) (See Fig. 1) and TNO (The Netherlands) were used for the validation of the new models during the duration of the RFCS project EXTFIRE.

Table 1 – Summary of main objectives to be achieved by the new transient heat transfer model

Eurocode 1&·3.

Eurocode 1&3 Limitations	**EXTFIRE Objectives**
Stationary model Steady state conditions	Transient effect f(t)
Same approach for all type of cross sections	Real shape of the sections
Uniform temperature in cross section	Non uniform temperature in cross sections

Fig. 1 – Experimental external flaming (Efectis France).

The EXTFIRE methodology provides a performance based approach for the fire safety design in which structural fire resistance of the external members could be evaluated in function of time, helping the designer to calculate a more realistic time to collapse.

3. DESCRIPTION OF THE EXTFIRE MODEL

3.1 Assumptions for the EXTFIRE model

In addition to the general assumptions for the structural design and structural fire safety design of the Eurocodes, for the EXTFIRE model apply the following specific ones:

- The fire compartment is assumed to be confined to one storey only. All windows are assumed to be rectangular and with the same height.
- The temperature of the compartment and the parameters of the flames projecting from the openings (dimensions and temperatures) should be calculated apart.
- According to the Eurocode 3, a distinction is made between members not engulfed and engulfed in flame, depending on the size of the external flames and the position of the elements. A member that is not engulfed in flame is assumed to receive radiative heat transfer from all the openings and flames. An engulfed member is assumed to receive radiative and convective heat transfer from the engulfing flame and radiative transfer from the opening from which it projects.

- Flames and openings are considered like radiating surfaces with a fixed temperature. An emissivity of 1 is considered for openings and a specific emissivity depending on the thickness for the flames.
- No forced draught condition is assumed.

3.2 Thermal actions for external members

The simplified calculation method provide in the Annex B: "Thermal actions for external members – Simplified calculation method" of the Eurocode 1: "Actions on structures" - Part 1-2: "General actions - Actions on structures exposed to fire" considers steady-state conditions for the determination of the parameters relevant to define the thermal actions for external members.

The simplified calculation method of the Eurocode 1 provides the characteristics of the fire in the compartment for no forced draught conditions: rate of burning of the rate of heat release, Eq. (1), and temperature of the fire compartment, Eq. (2), and the flame dimensions, Eq (3).

$$Q = \min\left(\left(A_f \cdot q_{f,d}\right)/\tau_F ; 3{,}15 \cdot \left(1 - e^{\frac{-0{,}036}{O}}\right) \cdot A_V \cdot \left(\frac{h_{eq}}{D/W}\right)^{1/2} \right) \tag{1}$$

$$T_f = 6000 \cdot \left(1 - e^{-0.1/O}\right) \cdot O^{1/2} \cdot \left(1 - e^{-0.00286 \cdot \Omega}\right) + T_0 \tag{2}$$

$$L_L = \max\left(0 : h_{eq} \cdot \left(2.37 \left(\frac{Q}{A_V \cdot \rho_g \cdot \left(h_{eq} \cdot g\right)^{1/2}} \right)^{2/3} - 1 \right) \right) \tag{3}$$

In addition to the Eq. (3) the Eurocode 1 provides additional figures, Fig. 2, and equations to define the flame dimensions in a comprehensive way, Table 2.

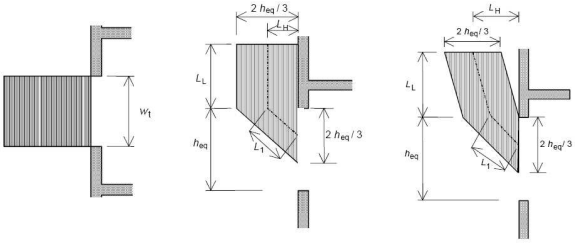

Fig. 2 – Dimensions: Horizontal, left, and vertical cross sections, middle and right, of the flame and compartment opening in the façade (Eurocode 1).

Table 2 – Flame dimensions for no forced draught conditions (Eurocode 1).

$h_{eq} < 1.25 \cdot w_t$	**Wall above**	**No wall above or** $h_{eq} > 1.25 \cdot w_t$
$L_L = h_{eq}/3$	$L_1 \approx h_{eq}/3$	$L_L \approx h_{eq}/2$
	$L_f = L_L + L_1$	$L_f = \sqrt{L_L{}^2 + \left(L_H - h_{eq}/3\right)^2} + L_1$

The improvement to this simplified approach of the Eurocode 1 proposed by the EXTFIRE model is the consideration of the transient effects of the fire. This is possible by using a rate of heat release depending on time according a realistic evolution of the fire in the compartment, instead of the Eq. (1), which considers steady-state conditions, "no-time-dependant" fire.

The approach used by the EXTFIRE model is based on the utilization of a zone model with a prescribed rate of heat release depending on the fire load, see Fig. 3.

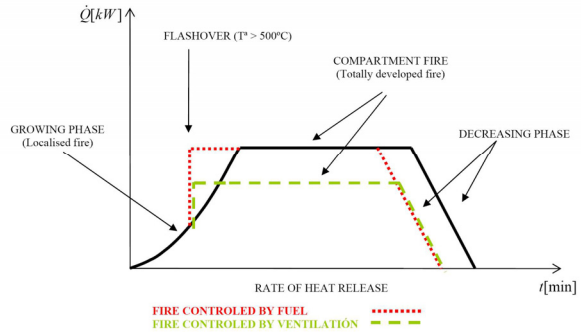

Fig. 3 – Consideration of the transient effects of the fire. Rate of heat release for all the fire duration stages.

The growing phase is modelled as a t^2 function, depending on the type of building, and it is supposed that the decay phase is reached when the 70% of the fire load is consumed.

The temperature of the upper layer is considered in the compartment before flashover conditions were reached. After that, the RHR reaches suddenly the plateau, bringing forward the decay phase.

The approach based on the zone model provides a realistic approach to analyze ventilation controlled fires, modifying the RHR taking into account the amount of oxygen available in the compartment.

The necessary input data to carry out the analysis of the fire conditions in the compartment are the following:

- Fire load, type, density and distribution.
- Combustion behaviour of the fire load.
- Compartment size and geometry.
- Ventilation conditions of the compartment.
- Thermal properties of the compartment boundaries.

Knowing the temperature evolution in the compartment, flame properties are calculated according to the equations (2) and (3).

3.3 Open cross section columns not engulfed in flames

In open cross sections, due to the transient effects related to different exposition to heat from flames and openings, a thermal gradient is created trough the section. Therefore, all the parts do not undergo the same temperature evolution and need to be dealt with separately (web and flanges). Other effects are also accounted for in this kind of sections, such as shadow effect and radiating from other parts of the section at different temperatures. The temperature of each part is calculated for each step of time.

The section is divided in three zones, the two flanges and the web. Each part of the section is going to receive different heat fluxes from openings and flames, so three different temperatures should be considered. Openings and flames are considered like radiating surfaces with a specific temperature and emissivity.

- The emmisivity of the radiating screen is 1 for windows, but for flames is calculated according to the EC:

$$\varepsilon = 1 - e^{-0.3 \cdot \lambda} \tag{4}$$

  where λ is the flame thickness at the top of the window (2h/3).
- The temperature of the radiating screen is the compartment temperature for windows. For flames, the temperature at a distance $\frac{h}{2}$ from the opening measured along the flame axis should be taken (calculated according to EC1).

The contributions of all flames and openings are summed to compute the whole radiative heat flux that arrives at each part of the element, considering that the absortivity of flames is taken as 0 for not engulfed members. The convective heat transfer is neglected for not engulfed elements.

Shadow effect is studied for each radiating screen, in all the surfaces of the section. First the zone in shadow is calculated for each surface. Then, a uniform heat flux is considered in the radiated zone, which value is calculated like the heat flux that arrives at the central point of this radiated zone (calculated according to EC1), considering the dimensions of the effective radiating surface for this point. Finally, the total heat flux that comes into contact with the radiated surface is assumed to be applied in the whole surface (flange or web, see Fig. 4 and Fig. 5).

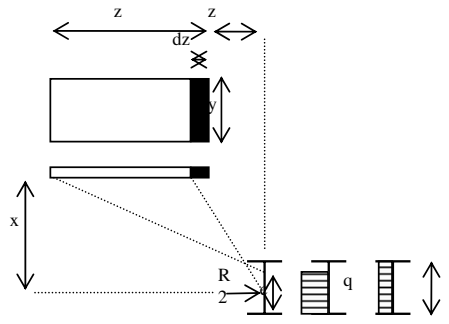

Fig. 4 – Calculation of the configuration factor for the web

$$\phi_{\perp}(x,y,z) = \frac{1}{2\pi}\left[\tan^{-1}\left(\frac{y}{x}\right) - \frac{1}{\sqrt{1+\left(\frac{z}{x}\right)^2}}\tan^{-1}\left(\frac{\frac{y}{x}}{\sqrt{1+\left(\frac{z}{x}\right)^2}}\right)\right] \tag{5}$$

$$\phi_2 = \phi_{\perp}(x,y,zo+z) - \phi_{\perp}(x,y,zo+dz) \tag{6}$$

$$R_2 = \phi_2 \cdot \varepsilon \cdot \sigma \cdot T^4 \cdot (1 - a_z) \tag{7}$$

$$q_2 = R_2 \cdot c / b \tag{8}$$

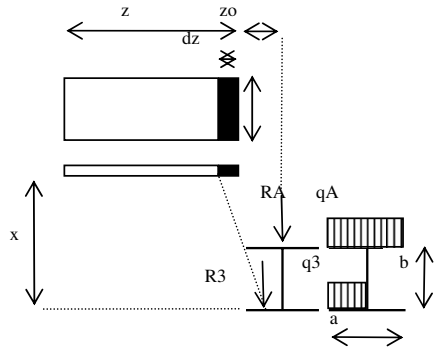

Fig. 5 – Calculation of the configuration factor for the flanges

$$\phi_{//}(x,y,z)=\frac{1}{2\pi}\left[\frac{\frac{y}{x}}{\sqrt{1+(\frac{y}{x})^2}}\tan^{-1}\left(\frac{\frac{z}{x}}{\sqrt{1+(\frac{y}{x})^2}}\right)+\frac{\frac{z}{x}}{\sqrt{1+(\frac{z}{x})^2}}\tan^{-1}\left(\frac{\frac{y}{x}}{\sqrt{1+(\frac{z}{x})^2}}\right)\right] \quad (9)$$

$$\phi_A=\phi_{//}(x-b,y,zo+z)-\phi_{//}(x-b,y,zo) \quad (10)$$

$$\phi_3=\phi_{//}(x,y,zo+z)-\phi_{//}(x,y,zo+dz) \quad (11)$$

$$R_A=\phi_A\cdot\varepsilon\cdot\sigma\cdot T^4\cdot(1-a_z) \quad (12)$$

$$R_3=\phi_3\cdot\varepsilon\cdot\sigma\cdot T^4\cdot(1-a_z) \quad (13)$$

$$q_A=R_A \quad (14)$$

$$q_3=R_3 \quad (15)$$

The interaction between surfaces is considered to compute the net radiative heat flux that each surface absorbs. The surfaces of the member are considered like gray surfaces (ε = α = 1- ρ). It is assumed that fictitious surfaces absorb all the radiation they receive (See Fig. 6).

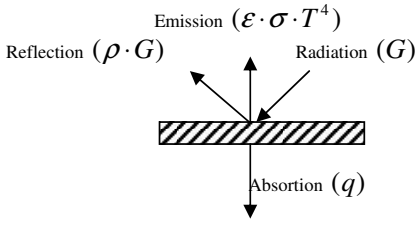

Fig. 6 - Interaction between surfaces

$$J=\varepsilon\cdot\sigma\cdot T^4+\rho\cdot G\rightarrow Radiossivity \quad (16)$$

$$q=G-J \quad (17)$$

The radiossivity of each part is the sum of the emission due to the temperature, the reflection of the radiation from the environment and the reflection of the radiation from the other parts of the section.

$$J_i = \varepsilon \cdot \sigma \cdot T^4 + \sigma \cdot T_o^{\,4} \cdot \rho + q_i \cdot \rho + J_j \cdot F_{j,i} \cdot \rho + J_k \cdot F_{k,i} \cdot \rho \tag{18}$$

The temperature of each part of the section used to compute the term of emission is delayed a step with the others ones, because this is just the wanted parameter.

The whole phenomenon of reflections, emissions… between all the parts of the section can be studied solving a linear equations system which collects all the heat balances.

$$J = [A]^{-1} \cdot v \tag{19}$$

After that it is possible to solve the heat balance to calculate the temperature in the different zones of the section (See Fig. 7).

$$Q_i = q_i + \sigma \cdot T_0^{\,4} - J_i + F_{j,i} \cdot J_j + F_{k,i} \cdot J_k \tag{20}$$

The increase of temperature in each step of time is computed according to EC3

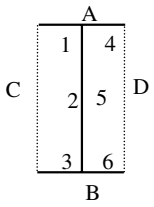

Fig. 7 - Surfaces in the section

$$h_{flange1} = \frac{a}{2} \cdot Q_1 + \frac{a}{2} \cdot Q_4 + a \cdot Q_A \tag{21}$$

$$h_{web} = b \cdot Q_2 + b \cdot Q_5 \tag{22}$$

$$h_{flange2} = \frac{a}{2} \cdot Q_3 + \frac{a}{2} \cdot Q_6 + a \cdot Q_B \tag{23}$$

$$\Delta\theta = \frac{h_s \cdot \Delta t}{\rho \cdot C_p \cdot l \cdot e} \tag{24}$$

When the column is between two openings, two radiating surfaces are considered in each side of the element. These surfaces have a specific temperature and emissivity.

- The emmisivity of the radiating screen is calculated for each side according to the EC

$$\varepsilon_m = 1 - e^{-0.3 \cdot \lambda m} \tag{25}$$

$$\lambda_m = \sum_{i=1}^{m} w_i \tag{26}$$

$$\varepsilon_n = 1 - e^{-0.3 \cdot \lambda n} \tag{27}$$

$$\lambda_n = \sum_{i=1}^{n} w_i \tag{28}$$

where w_i is the width of each opening, m is the number of openings on side m and n is the number of openings on side n.

- The temperature of the radiating screen is the temperature at a distance h/2 from the opening measured along the flame axis should be taken (calculated according to EC1).

The contributions of the two flames are summed to compute the whole radiative heat flux that arrives at each part of the element. The radiative heat transfer from the windows and the convective heat transfer are neglected.

Shadow effect is studied for each radiating screen in a similar way to the method presented in part 3.2. In this case there are not zones in shadow, but the effective screen dimensions for each zone must be calculated.

The interaction between surfaces and the calculation of heat fluxes and temperatures are calculated like it has been explained before.

3.4 Open cross section columns engulfed in flames

An engulfed member is assumed to receive radiative and convective heat transfer from the engulfing flame and radiative transfer from the opening from which it projects. Four fictitious radiating surfaces are considered enclosing the section in order to model the engulfing flame. The opening is considered like a radiating surface with a specific temperature and emissivity.

- The emmisivity of the radiating screen is 1 for windows, but for flames is calculated according to the EC (See Fig. 8):

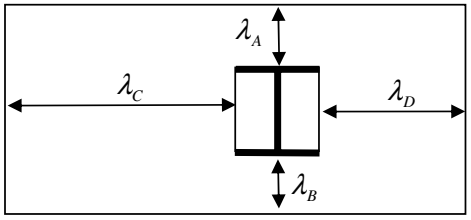

Fig. 8 - Surfaces in the section

$$\varepsilon = 1 - e^{-0.3 \cdot \lambda} \tag{29}$$

where λ is the flame thickness at the top of the window (2h/3).

- The temperature of the radiating screen is the compartment temperature for windows. For flames, the temperature at a distance $\frac{h}{2}$ from the opening measured along the flame axis should be taken (calculated according to EC1).

The absortivity of flames and the convective heat transfer are calculated according to Eurocode:

$$\alpha = 4.67 \cdot (\frac{1}{d_{eq}})^4 \cdot (\frac{Q}{A_v})^{0.6} \tag{31}$$

$$d_{eq} = \frac{a+b}{2} \tag{32}$$

where A_v is total area of vertical openings on all walls.

Shadow effect is only studied for the window radiating screen in a similar way to the method presented before.

The interaction between surfaces is considered to compute the net radiative heat flux that each surface absorbs. The surfaces of the member are considered like gray surfaces (ε = α = 1- ρ) (See Fig. 7).

The radiossivity of each part is the sum of the emission due to the temperature, the reflection of the radiation from the environment and the reflection of the radiation from the other parts of the section.

$$J_i = \varepsilon \cdot \sigma \cdot T^4 + \sigma \cdot T_o^4 \cdot \rho + q_i \cdot \rho + J_j \cdot F_{j,i} \cdot \rho + J_k \cdot F_{k,i} \cdot \rho + J_C \cdot F_{C,i} \cdot \rho \tag{33}$$

The temperature of each part of the section used to compute the term of emission is delayed a step with the others ones, because this is just the wanted parameter.

The whole phenomenon of reflections, emissions… between all the parts of the section can be studied solving a linear equations system which collects all the heat balances.

$$J = [A]^{-1} \cdot v \tag{34}$$

After that it is possible to solve the heat balance to calculate the temperature in the different zones of the section.

The increase of temperature in each step of time is computed according to EC3.

$$h_{flange1} = \frac{a}{2} \cdot Q_1 + \frac{a}{2} \cdot Q_4 + a \cdot Q_A + 2 \cdot a \cdot \alpha \cdot (T_{flame} - T_{flange1}) \tag{35}$$

$$h_{web} = b \cdot Q_2 + b \cdot Q_5 + 2 \cdot b \cdot \alpha \cdot (T_{flame} - T_{web}) \tag{36}$$

$$h_{flange2} = \frac{a}{2} \cdot Q_3 + \frac{a}{2} \cdot Q_6 + a \cdot Q_B + 2 \cdot a \cdot \alpha \cdot (T_{flame} - T_{flange2}) \tag{37}$$

$$\Delta\theta = \frac{h_s \cdot \Delta t}{\rho \cdot C_p \cdot l \cdot e} \tag{38}$$

3.5 Close cross section columns

Due to the shape of the section, neither shadow effect nor interactions between surfaces are taken into account. Heat flux boundary conditions are calculated to use them in other FEM programs to know the temperature distribution in the section.

4. VALIDATION

A fire compartment was built at the TNO Centre for Fire Safety for the purpose of carrying out full-scale experiments of external flaming acting on unloaded steel structures. Several tests were carried out for various compartment and opening dimensions, to study the effect of each parameter on the thermal action and thermal response of the steel structures.

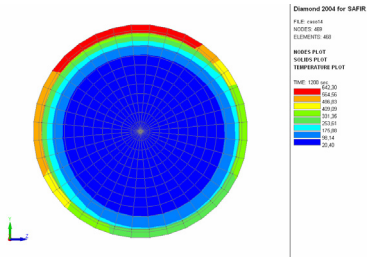

Fig. 9 - Thermal analysis of a concrete filled steel column

The size of the furnace is 4.4m of length, 4m of width and 2.6m of height. The fire compartment is constructed from cellular concrete blocks of thickness 150mm.

Two openings are placed symmetrically. A promatec panel of height 3m was attached to the top of the compartment in order to represent the façade of the upper floor of a typical multi-stored building.

Three columns are placed in front of the compartment as shown in figure 21, a HEA 200 and two rectangular concrete filled SHS columns (300mmx300mm) (See Fig.10).

The fire source is made up of 42 wooden Europallets stacked on a platform hanging about 0.1m above the floor of the compartment (1050Kg of wood). The fire load density is 60 Kg/m^2. The steel temperature is measured at 2.1m above floor level.

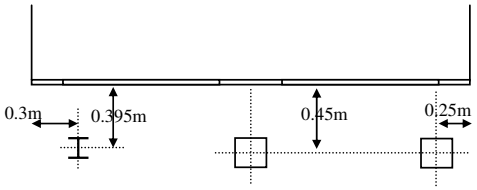

Fig. 10 - Columns in front of the fire compartment

Test data are used to simulate the compartment and flame properties:

- The highest measured values are taken for the opening and flames temperatures, and the mean value for the room temperature.
- The convection coefficient is calculated according to the Law model, so the heat release rate is not necessary for columns.
- External flaming occurs from 660 to 3000 sec, as shown in the test.
- The other flame properties not described in the report [2] are calculated according to the Law model.

5. CONCLUSIONS

There is a very good agreement between test and model results, discrepancies are due to how the thermal action is defined. (See Fig. 11)

The current model of the Eurocode could give results in the unsafe side, because peak temperatures are higher than the steady-state temperature predicted with the current model. For open sections, the results given by the model are quite close to tests results, lying in the safe side. Discrepancies are not quite large to render the model too conservative.

For composite sections, due to the low conductivity of concrete, large gradients occur, and a finite element calculation is addressed after calculation of heat fluxes on steel perimeter. A simplified 1D model has been checked, and in some cases it is a good estimate of heat

transfer within the section. If the peak temperature is the target of the calculation, this approach trends to overestimate the temperature of hottest point of the section because it neglects the conduction to colder parts of steel perimeter.

Otherwise, if a full description of temperature rise is targeted, it trends to underestimate temperature rise of coldest points. This result is an overestimation of thermal gradient within the section due to accidental actions. If the bending moment induced by this thermal gradient sums up to the initial bending moment this result is not unsafe, otherwise, in the first moments of the fire exposure it leads to a reduction of the actual bending moment acting on the member. This effect may be neglected once high temperatures within the section take the role in structural response and accidental induced actions do not play the main role in collapse mechanism.

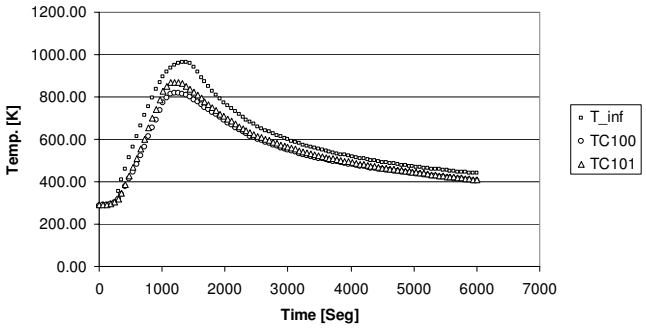

Fig. 11 – Comparison between EXFIRE model results and the measures of two thermocouples in the lower flange of a external column

The model has been implemented in a software (EXTFIRE) developed by LABEIN TECNALIA to make easier its application, and it has been validated with several fire tests carried out by CTICM and TNO during the development of the RFCS project mentioned before, being in a good agreement with test results.

6. ACKNOWLEDGEMENTS

The authors wish to thank the partners of the RFCS research project "Development of design rules for the fire behaviour of external steel structures (Contract No.: 7210-PR/380; 1/07/ 2002-21/06/2005)".

7. REFERENCES

[1] A. Blanguernon, "External steel structures research. Synthesis of fire test nº 94 – E – 158", CTICM, 2004.
[2] A D Lemaire et al., "Fire test with external flaming on unprotected steel columns included concrete filled columns (Version 1.0)", TNO, 2005.
[3] "Eurocode 1: Basis of design and actions on structures, Part 2.2: Actions on structures exposed to fire", 1994.
[4] "Eurocode 3: Design of steel structures, Part 1.2: General rules, Structural fire design", 1995.
[5] "Development of design rules for the fire behaviour of external steel structures" (Contract No.: 7210-PR/380; 1/07/ 2002-21/06/2005), 2002-2005.

COLUMN BEHAVIOUR DURING LOCALISED FIRE TEST

ZDENĚK SOKOL[1],, FRANTIŠEK WALD[1], PETRA KALLEROVÁ[1], NICOLAS BONNET[2],

ABSTRACT

The paper presents results of fire test performed on an industrial building before demolition. Two fire tests were performed; localised fire and compartment fire. The localised fire was focussed on heat transfer to steel column and temperature distribution in the surrounding structural elements. Analytical models for predicting beam temperature are in good agreement with the test for both the localised and the compartment fires. Numerical prediction using Ansys software used to predict the temperature distribution in the cross section and along the length of the column.

1. INTRODUTION

For determination of fire safety it is necessary to know the applied mechanical load and the maximum temperature achieved in the steel member. Both values have significant influence on mechanical properties and load-carrying capacity of the element. The temperature of the steel structure depends on fire development in the fire compartment, which is influenced by fire load, amount of oxygen necessary for burning, properties of flammable materials and area, shape and thermal properties of boundaries of the fire compartment. Based on these parameters it is possible to predict the gas temperature in the fire compartment by the use of methods of thermal analysis. The gas temperature is used for calculation of temperature of the steel structure.

[1] Czech Technical University in Prague, Department of Steel and Timber Structures, Prague, Czech Republic email: sokol@fsv.cvut.czt.
[2] Polytech Clermont-Ferrand, Département Génie Civil, Clermont-Ferrand, France .

2. CALCULATION OF TEMPERATURE OF STEEL STRUCTURES

The models for thermal analysis in a fire compartment and models for heat transfer into steel members can be used for design of a structure exposed to fire. The available models offer various precision of the solution and differ in complexity and in quantity of the input data. In practical design, parametric fire curve or zone models (e.g. program Ozone) can be used for the thermal analysis. Nominal fire curves are conservative because the cooling phase of the fire is not considered.

The heat transfer to the structure is solved by the use of step-by-step method. Finite element analysis can be used when there is non-uniform temperature of the cross-section. Simple model for determination of gas temperature can be applied for local fire and temperature of steel beams in ceiling above the fire can be evaluated. However, suitable model for determination of column temperature at local fire is not available. The column temperature is conservatively derived from the temperature of the steel beams attached to the column. Non-uniform heating of the cross section has significant influence on the behaviour of the column during local fire. The thermal gradient can lead to higher initial imperfection and therefore influence the buckling resistance of the column [1].

3. FIRE TEST IN OSTRAVA

Two fire tests were realized on a real building in Mittal Steel in Ostrava in Czech Republic in June 2006 [2]. The localized fire which is described in this article was performed 15th June, a day before the compartment fire. The results obtained from the localized fire were used for calibration of heat transfer model of a steel column exposed to localized fire. This experiment represent unique occasion for measuring gas temperature and temperature of steel column in a real structure exposed to localized fire.

A fire experiment was carried out in the second floor of the building. Dimensions of the fire compartment were 3,80 × 5,95 m, the height was 2,78 m. Three surrounding walls of the compartment were made from hollow ceramic bricks. The front wall with opening was made from lightweight concrete bricks. The opening was 2,4 m wide, 1,4 m high and the height of a windowsill was 1,07 m.

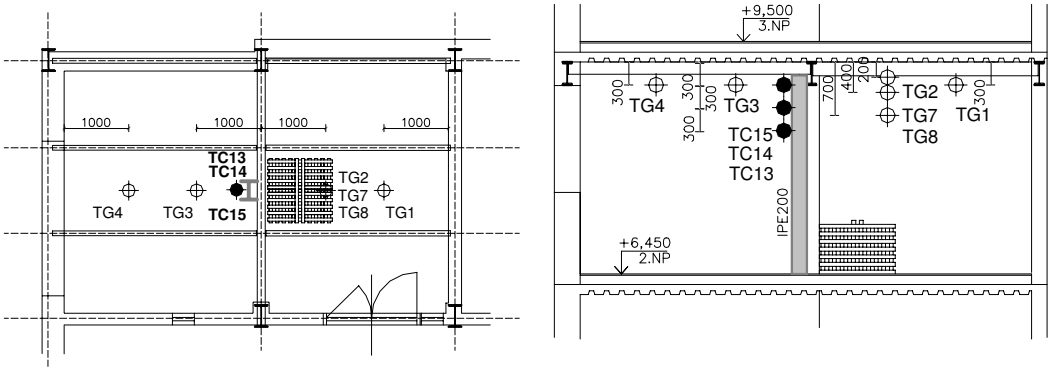

Fig. 1 – Fire compartment with location of thermocouples at the localised fire.

The localized fire experiment was performed in the centre of the fire compartment where a steel column IPE200 was situated. This column was not loaded; it was installed only for the temperature measurement. The temperature of the steel column was measured on the

web by thermocouples marked as TC13, TC14 and TC15, see Fig. 1. These thermocouples were located at 300 mm spacing from the ceiling above the fire compartment. Thermocouples were attached on the web side opposite to the fire.

Another six thermocouples were used to measure the gas temperature. All were located on a centre line of the fire compartment. The distance of the thermocouples from the front wall with the opening is on Fig. 1. The thermocouples TG1, TG3 and TG4 were 300 mm below the ceiling of the fire compartment, the thermocouples TG2, TG7 and TG8 were at distances 200 mm, 400 mm and 700 mm below the ceiling.

Fire load in the fire compartment ass represented by timber logs on floor area of 1 m^2. There were 13 rows of ten logs used, total of 130 logs. The softwood logs had length 1 m, cross-section 50 × 50 mm and moisture smaller than 13% [3]. The total fire load was 140 kg. The initiation of the localized fire was made by paraffin.

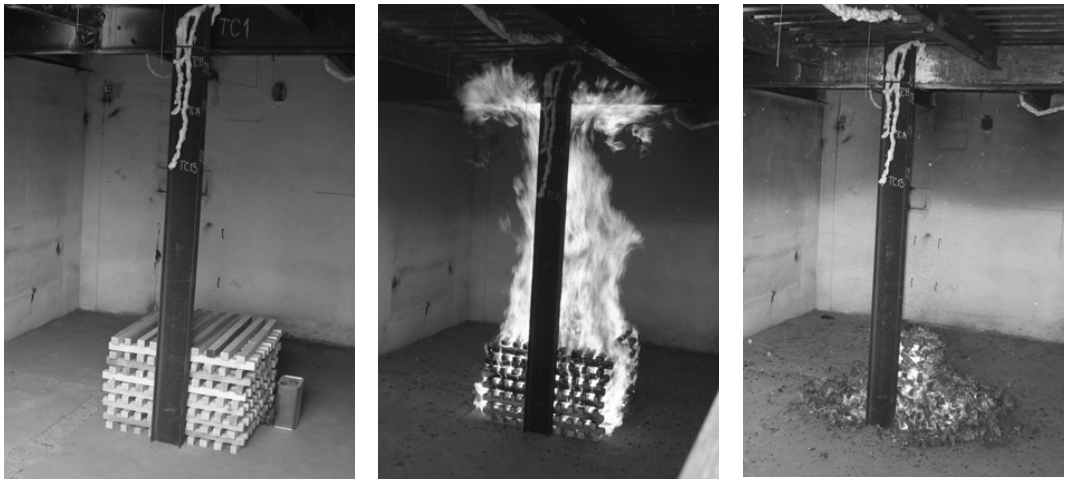

Fig. 2 – The localized fire in the fire compartment.

4. NUMERICAL ANALYSIS

4.1 Thermal analysis

There are two models available for the localised fire. These models are available for calculation of temperature of the steel beams. When the flame does not reach the ceiling of the fire compartment, the Heskestad model is used. This model determinates temperature along the vertical axis passing through the centre of the fire. Obtained temperatures are used for calculation of the heat transfer in the steel element. The Hasemi model is used in case when the fire reached the ceiling of the fire compartment. It gives the values of heat flux depending on the position of the steel member (its distance from the fire axis). The zone models (one-zone model, two-zone model) in program Ozone give another possibility for description of the fire behaviour. These models can be used to obtain the values needed for numerical analysis of heat transfer in the structure, which were not measured during the fire test.

The rate of heat release used in the calculation is plotted on Fig. 3. The rate of heat release is not influenced by ventilation conditions as there is enough of oxygen in the compartment during the fire. The RHR curve has three different phases. The first phase is the

fire development, which ends by reaching the maximum rate of heat release. The second phase is described as a period with steady state burning which is finished by releasing 70% of the gross thermal energy of fuel. Then the decay phase continues by linearly decreasing branch until all the fuel is burned. The fire compartment is horizontally divided into two parts. In the upper layer there are higher temperatures of gas while the lower layer is colder. The maximum temperature achieved in the upper layer was 462 °C. This occurs in the 19th min of the experiment. The upper layer has the biggest thickness at the time period from 9th to 19th min; see Fig. 4.

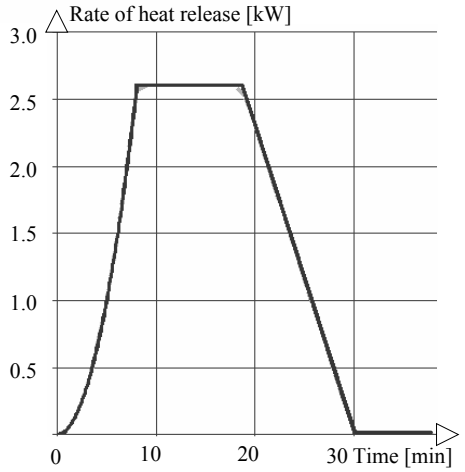

Fig. 3 – The rate of heat release (program Ozone).

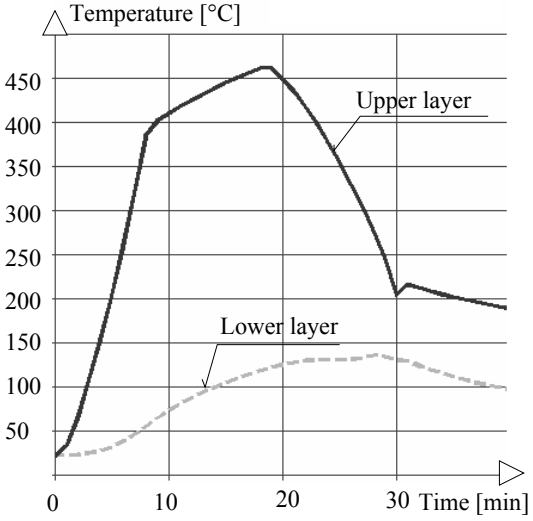

Fig. 4 – Temperatures of upper layer and lower layer (program Ozone).

Figures 5a) and 5b) show comparison of the measured temperature-time curves in the fire compartment during the localized fire and the temperature-time curve predicted by two-zone model in program Ozone. With regard to the fire development and the height of the flame, the thermocouples TG2, TG7 and TG8 were engulfed in to flame, see Fig. 2. The

measured temperature does not conform to the temperature of the upper layer but it corresponds to the temperature of the flames. Substitute temperature of the localized fire used as the flame temperature in numerical analysis is shown on Fig. 5a).

Comparison of temperatures measured by thermocouples TG1, TG3 and TG4 to temperature of the upper layer predicted by zone model is on Fig. 5b). The predicted temperature is in good agreement with the temperature measured by thermocouple TG1. The temperatures of thermocouples TG3 and TG4 are lower by about 80 to 100°C. It is probably caused by mixing of the hot gases with fresh air coming to the fire compartment through the opening in the front wall.

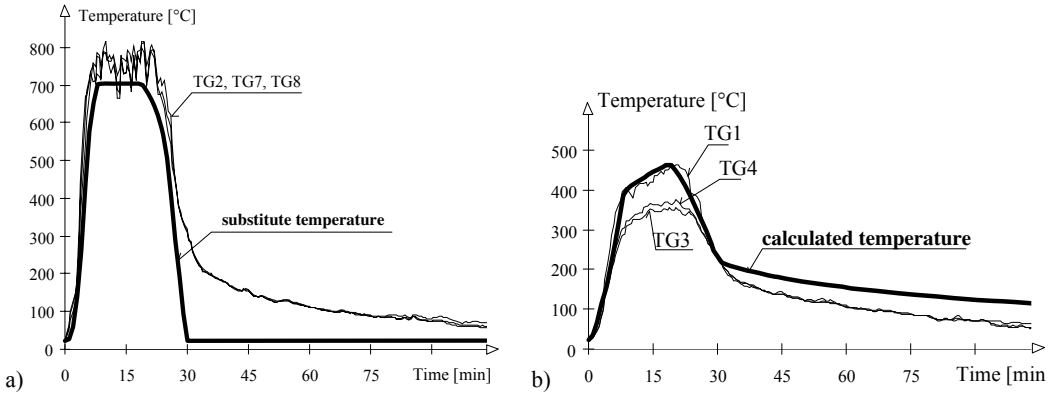

Fig. 5 – Comparison of measured temperature and calculated temperature.

4.2 Numerical analysis of column temperature

Heat transfer to the steel column exposed to the localized fire was simulated by program Ansys. The column with cross-section IPE 200 was modelled by elements SOLID 70. These are 3D elements with four nodes and one degree of freedom (temperature) at each node. Three layers of elements were used in column web and four layers were used in flanges of the cross-section. This model was loaded by heat effect of the localized fire.

Heat transfer from the hot gas surrounding the steel column was established as surface load applied to the free surfaces of the elements. The gas temperature is time variable and corresponds to the temperatures of the hot and cold zones as it were determined by Ozone.

The effect of radiation heat flux of the flames impacting the steel column was simulated by radiosity method. The flames were approximated as a cylindrical surface with diameter of the localized fire [4]. This surface was formed by shell elements SHELL 57.

The temperature of radiation cylindrical surface (flame) and the height of flame were variables in the course of the fire. The height of the flame depending on the rate of heat release was determined using Heskestad model. The substitute temperature of the localized fire was used as the flame temperature. The temperature of the remaining part of cylindrical surface above the flames was set to gas temperature of the hot layer.

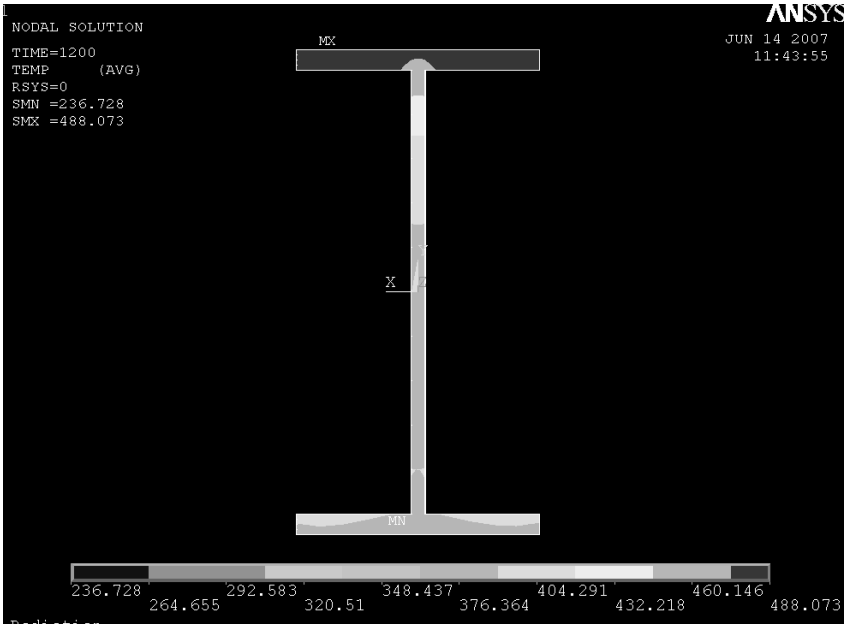

Fig. 6 – Temperature of the cross section, height 2,1 m, time 20 min, position 3.

4.3 Parametrical Study - Temperature-Time Curves for Variable Location of Localized Fire

Numerical model in Ansys was used to develop parametrical study focused on the influence of column temperature with regard to orientation and distance of the column to the localized fire. Four cases were examined in the parametrical study. The distance of the column to the edge of the fire was 200 mm or 1200 mm. These four positions of the column and the fire are shown on Fig. 7.

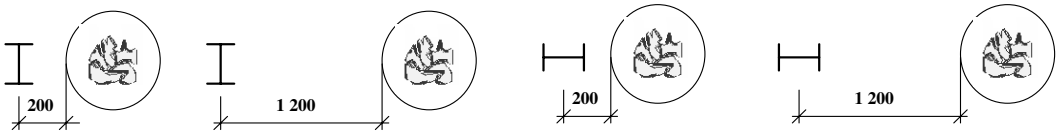

Fig. 7 – Column positions for the parametrical study.

The calculated temperature-time curves for these positions of steel column are shown on Fig. 8. The greater is the distance between the column and the fire smaller temperature is obtained. When the distance between the column and the fire is increased from 200 to 1200 mm the temperature decrease about 100°C. Orientation of the column cross-section does not have significant influence on the maximum temperature, see Fig. 8. The difference between maximum temperatures is only 10°C when position 1 to 3 or position 2 to 4 are compared. The time when the maximum temperature is reached is also similar.

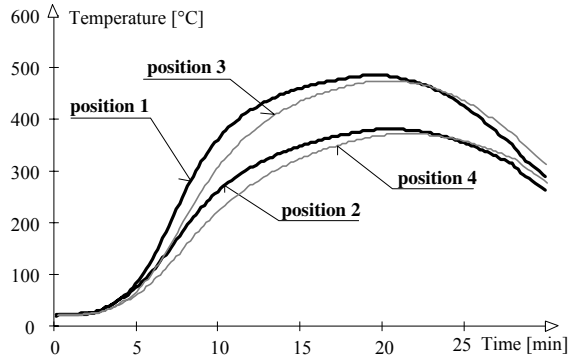

Fig. 8 – Temperature-time curves for different position of steel member and localized fire.

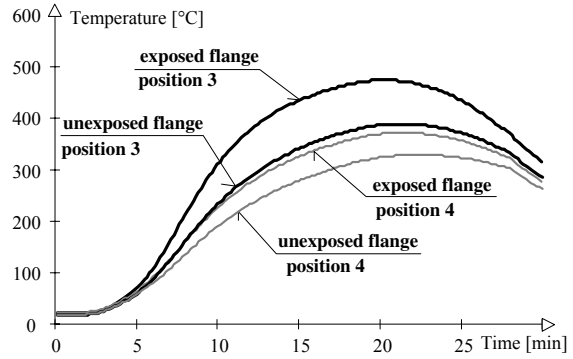

Fig. 9 – Temperature-time curves for exposed and unexposed flange of column cross-section.

The temperature-time curves for exposed and unexposed flanges of steel column are shown on Fig. 9. The higher temperature is achieved in the flange exposed to the fire. It is due to shadow effect of the exposed flange and different distance of flanges from heat source (influence of configuration factor on heat transfer by radiation). The temperature difference (temperature gradient) is getting smaller when the column is located at larger distance from the localized fire. The thermal gradient is shown on Fig. 10. Heat transfer by convection is the same in both cases because the same parts of the column are engulfed in the hot and cold layers. The column temperature along the length is almost constant, see Fig. 11.

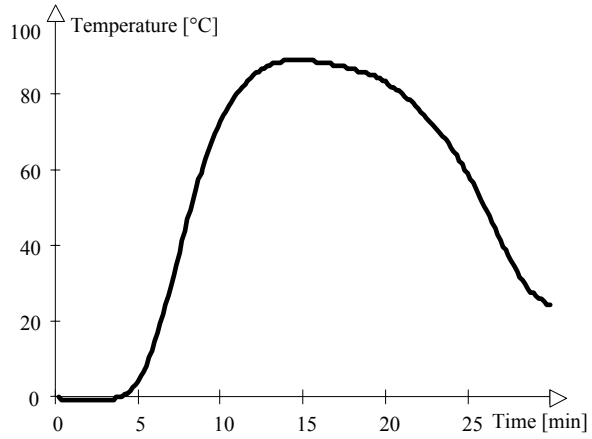

Fig. 10 – Thermal gradient at height 2,1 m, position 3.

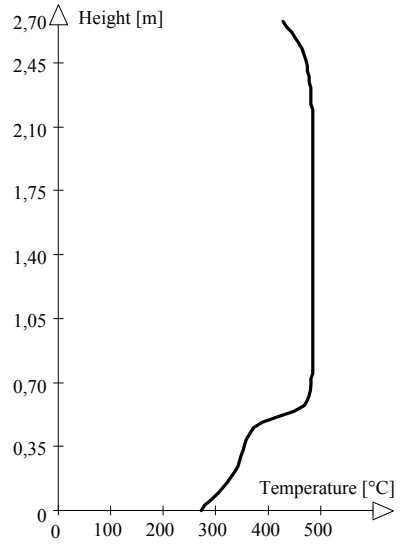

Fig. 11 – Temperature distribution along the column height, position 1, time 20 min.

5. CONCLUSION

The temperature in the column at localised fire can reach significant values. At 500°C, the effective yield strength is decreased to 80% and the modulus of elasticity to 60%. The effect of non-uniform temperature distribution along the length is not important for columns of length similar to the length of the flames of the localised fire. For tall columns the temperature distribution could vary significantly along the length with much lower value at the upper end.

The thermal gradient in the column cross section leads to increase of the initial imperfection of the column and influence the buckling resistance of the column.

ACKNOWLEDGEMENT

This outcome has been achieved with the financial support of the Ministry of Education, Youth and Sports, project No. 1M0579, within the activities of the CIDEAS research centre.

REFERENCES

[1] Kamikawa D., Hasemi Y., Yamada K., Nakamura M., Mechanical responses of a steel column exposed to a localized fire, In: P. Vila Real, J.M. Franssen, N. Lopes, Fourth International Workshop Stuctures in Fire, SiF'06, Volume 1, Aveiro, Portugal, 2006.

[2] Uhlíř T., Kallerová P., Wald F., Fire Test on Industrial Building. Proceedings of the Fifth International Conference on Advances in Steel Structures - Volume III, p. 757-762, Singapore, 2007.

[3] Wald F., Baierle T., Sokol Z., Předpověď teploty při lokalizovaném požáru. In Reakcia na oheň stavebných materiálov a požiarna bezpečnosť v stavbách.: Technická univerzita vo Zvolene, p. 8-14, Zvolen, 2007.

[4] Franssen J.M., Zaharia R., Design of Steel Structures Subjected to Fire, Background and Design Guide to Eurocode 3, University Liège, 2005.

FIRE-RESISTANT STEEL AT ELEVATED TEMPERATURES

JUERGEN KRAMPEN[1], PETER SCHAUMANN[2] and OLIVER BAHR[3]

ABSTRACT

Visible steel structures are interesting from architectural point of view. However, in case of fire it is in general necessary to protect the steel from elevated temperatures to provide sufficient fire resistance. This can be attributed to its high thermal conductivity leading to fast heating and hence rapid decline of elastic modulus and effective yield strength. For members with reasonable load-ratios, it is not possible to meet the requirements for fire resistance time of 30 minutes using carbon steel. This means that costly intumescent coating has to be applied. Nowadays, the advancement of metallurgy allows for producing fire-resistant steel with enhanced mechanical properties at elevated temperatures. Thus, it becomes a genuine alternative to traditional fire protection systems.

1. INTRODUCTION

There are different means to assure fire safety of steel constructions. Traditional fire protection systems, such as plasterboard, spray or intumescent coating, are proven and tested. Nevertheless they are linked with an additional working process and therefore extra costs. The latter are mainly labour costs, which are high in industrialized countries.

In contrast to this, fire-resistant steel comes with inherent fire protection achieved by modified alloy. Thus, the owner can save significant labour costs. More reasons can be cited in favour of fire-resistant steel. The steel structure remains visible and hence architecturally appealing. Fire-resistant steel allows for fast erection of buildings using standardized connections. Besides, usable space is increased as fire protection can be omitted. In the aftermath of the World Trade Center disaster further aspects as robustness of fire protection and its integrity were spotlighted. Whereas traditional fire protection can be removed and is prone to damage this is not the case for fire-resistant steel. Composite solutions are excluded from this consideration. Seeing these advantages the rare use of fire-resistant steel bewilders at first glance. On closer inspection the reasons become clear. Both normative regulations and material properties for fire-resistant steel are missing. Accurate prediction of the material properties of fire-resistant steel is crucial for determining the load-bearing capacity of fire-exposed structures.

Moreover, the scope of application for fire-resistant steel is not clear, e.g. if it is suitable for members in bending as well as members endangered by global instability.

For these reasons research work on fire-resistant steel performed by VALLOUREC & MANNESMANN TUBES addressed the arising questions. Research included both numerical and experimental investigations. On behalf of VALLOUREC & MANNESMANN TUBES, scientific support was provided by Leibniz Universitaet Hannover.

The project aimed at the algebraic formulation of the stress-strain relationship of newly developed fire-resistant steel, which is referred to as VM-FIRE in the following. Moreover, reasonable fields of application for the new product should be identified. Answer to the latter is dominated by the relative load-bearing behaviour of carbon steel. Thus, carbon steel is included in the following considerations.

2. STRESS-STRAIN RELATIONSHIP OF FIRE-RESISTANT STEEL VM-FIRE

2.1 Tests

Small-scale tests were performed by the research institute Salzgitter Mannesmann Forschung on behalf of VALLOUREC & MANNESMANN TUBES to establish the mathematical formulation of the stress-strain relationship of fire-resistant steel at elevated temperatures. A test series of small-scale transient state tests at high temperatures was conducted. The test set-up can be seen in Figure 1. On this basis, it was possible to establish the mathematical formulation of the fire-resistant steel. The material model is based on the formulation used in [1].

2.2 Determination of yield strength

Two tests at ambient temperature were performed in order to determine the yield strength. It is obvious that VM-FIRE does not have distinct yield strength. According to [2] yield strength is defined as $R_{p0.2}$, which is the stress at 0.2% residual strain. Yield strength of $R_{p0.2}$ = 458 MPa was determined. As this strength is clearly above the required nominal elastic limit, VM-FIRE can be classified as S355. The latter is characterized by its yield strength of 355 MPa.

Fig. 1 - Test set-up for small-scale tests.

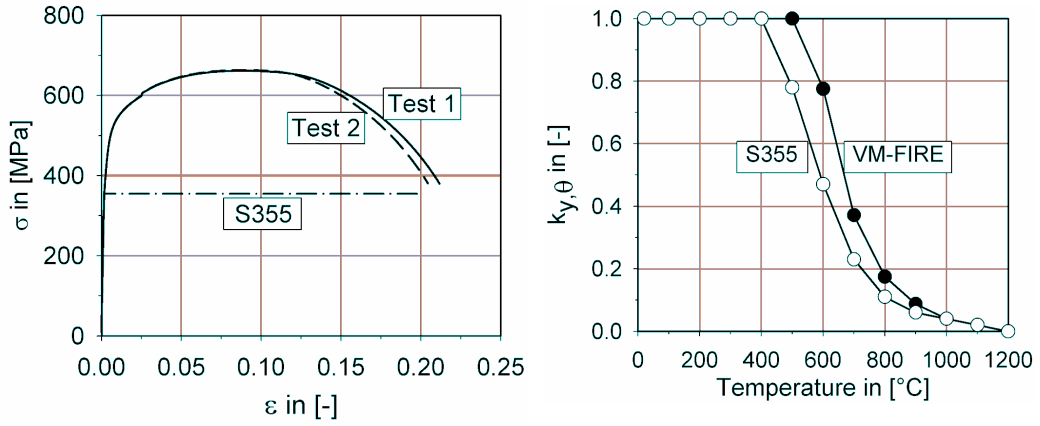

Fig. 2 - Results of tension tests at ambient temperature (left) and reduction factor $k_{y,\theta}$ of carbon and VM-FIRE steel for elevated temperatures (right).

On the left side of Figure 2, test results at room temperature are compared to the bilinear stress-strain curve of S355 steel according to [1]. Strains are noted nondimensionally, i.e. the proof limit $R_{p0.2}$ corresponds to $\varepsilon = 0.002$. Regarding Figure 2 it can be seen that the strength increase of VM-FIRE takes place for large strains. The elastic behaviour at small strains is very comparable to that of carbon steel. On the right side of Figure 2, improved strength retention can be noted for VM-FIRE at temperatures exceeding 400°C.

2.3 Transient state tests

Besides the tests at room temperature, transient state tests were performed by the research institute Salzgitter Mannesmann Forschung. It had been previously planned to perform tests at stress levels of 3, 10, 20, 40, 80, 120, 170, 355 and 466 MPa. Due to testing problems it was not possible to perform the tests with stresses less than 20 MPa. Test data is presented on the left side of Figure 3. Thermal strains were determined in a separate test with an unloaded specimen, which is not presented here.

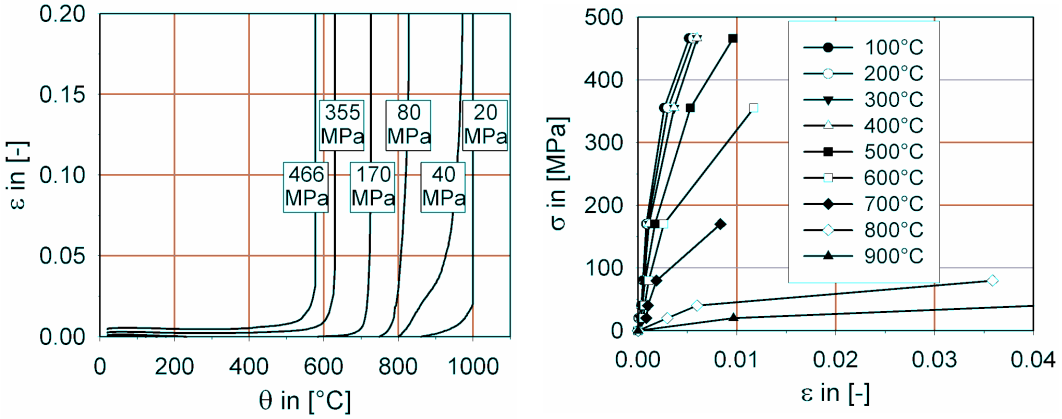

Fig. 3 - Results of transient state tests (left) and σ-ε-θ-curves for VM-FIRE steel (right).

Investigations aimed at the establishment of stress-strain formulae of VM-FIRE. Therefore the stress-strains curves for the different stress levels had to be cleared from thermal strains. These will be taken implicitly into account in the algebraic formulae.

3. EVALUATION OF SMALL-SCALE TESTS

Formulation of the newly developed fire-resistant steel VM-FIRE should lean to existing stress-strain relationships as defined for carbon steel in [1], which is based on [3]. The small-scale tests aimed at the identification of the different parameters defining this relationship, which are presented in Figure 8 in the Appendix. Detailed description of the mathematical formulation can be found in [1].

After reduction of the thermal strains it was possible to allocate mechanical strains to different stress levels. In accordance with [1] temperatures between 100°C and 900°C were considered with intermediate steps of 100°C. Higher temperatures could not be taken into account due to yielding of the specimens. The established σ-ε-θ-curves are shown on the right side of Figure 3.

This data was used to determine the necessary parameters describing the stress-strain relationship. Results of the latter are compared to test data in Figure 4 (left side). Each curve was established on the basis of six data points. Under these circumstances the agreement between experimental und numerical results can be regarded as acceptable. Additional tests would be required to amend the algebraic formulation in particular for small strains. However, it is not expected that this would result in major diversion in comparison to carbon steel.

3.1 Determination of the elastic range ($\varepsilon_{p,\theta}$, $f_{p,\theta}$ and $E_{a,\theta}$)

As a result of the limited number of test results, it was not possible to identify the elastic range. It would be necessary to perform further tests for stress levels less than 20 MPa in order to determine the transition from elastic to plastic behaviour. These tests could not be performed owing to immediate yielding of the steel.

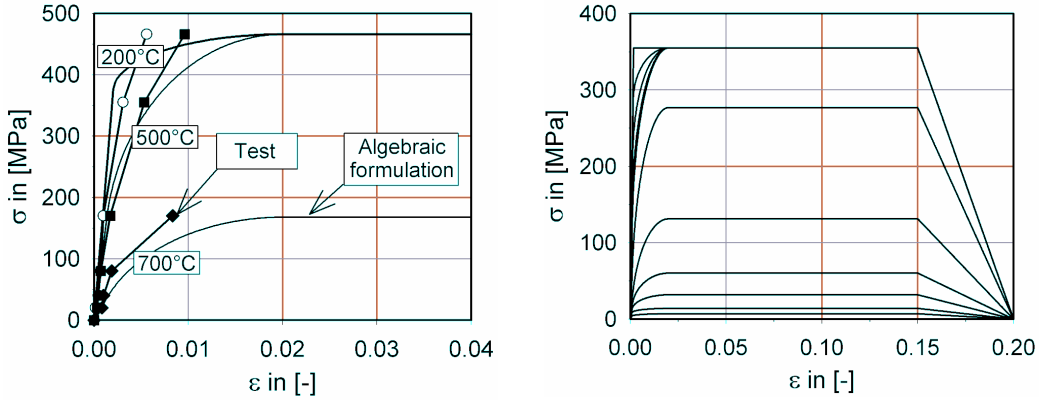

Fig. 4 - Comparison between test data and algebraic formulation of VM-FIRE steel for selected σ-ε-θ-curves (left); determination of σ-ε-θ-curves for VM-FIRE after transformation to nominal yield strength (right).

Thus, it was not possible to define all reduction factors for the fire-resistant steel VM-FIRE. As it is shown later-on, knowledge of these parameters is not compulsorily required. Therefore the corresponding parameters of carbon steel were taken for the VM-FIRE steel.

3.2 Determination of the yield point ($\varepsilon_{y,\theta}$ and $f_{y,\theta}$)

The effective yield strength $f_{y,\theta}$ could be identified on the basis of the carried out experimental work. Resulting values are shown on the left side of Figure 2. The yielding strain $\varepsilon_{y,\theta}$ was chosen as 0.02, which is in accordance with [1]. For temperatures exceeding 900°C, the corresponding values of carbon steel were assumed to be also valid for VM-FIRE steel as experimental data was not available.

3.3 Determination of the limiting strain for yield strength and ultimate strain ($\varepsilon_{t,\theta}$ and $\varepsilon_{u,\theta}$)

The transient state tests could not be performed until rupture of the test specimens. Therefore the according parameters of carbon steel were chosen for VM-FIRE steel. This results in a limiting strain for yield strength $\varepsilon_{t,\theta} = 0.15$ and ultimate strain $\varepsilon_{u,\theta} = 0.20$.

3.4 Transformation to nominal elastic limit

As previously shown, the actual yield strength of $R_{p0.2} = 458$ MPa was considerably higher than the nominal yield strength of 355 MPa. For a comparison between the stress-strain curves it was necessary to transform the actual to the nominal strength. The strains and stresses were hence transformed using the subsequent factor. Resulting stress-strain curves are shown on the right side of Figure 4.

$$\eta = \frac{f_{y,Nominal}}{f_{y,Actual}} = \frac{355\ MPa}{458\ MPa} = 0.775 \leq 1 \qquad (1)$$

With:

$f_{y,Nominal}$ Nominal strength;
$f_{y,Actual}$ Actual proof limit $R_{p0.2\%}$.

Knowledge of the material properties concerning the elastic range is crucial for the investigated columns that are prone to global instability. Because of the small number of stress levels it was not possible to establish all necessary parameters to describe the material model according to [1]. As it will be shown later-on, numerical validation of the established material model at test results showed nevertheless good agreement between computed and tested failure times of columns consisting out of VM-FIRE steel.

The reason for this is that there could not be expected significant divergence between the elastic modulus of VM-FIRE and carbon steel. Bleck and Muenstermann [4] investigated on the influence of different alloys on the elastic modulus. It is confirmed that modification of alloy has only minor influence. Therefore the elastic modulus of the newly developed fire-resistant steel VM-FIRE should approximately correspond to that of carbon steel.

For gaining a complete algebraic description of VM-FIRE steel, more load levels at stresses less than 20 MPa would be required to comprehend the elastic range. Furthermore it would be necessary to include temperatures up to 1,200°C and to continue the tests until fail-

ure occurs. Nevertheless the authors only expect faint differences to carbon steel so that there is no unconfined recommendation to resume the tests.

4. NUMERICAL SIMULATION OF FULL-SCALE FIRE TESTS

The development of the fire-resistant steel VM-FIRE was accompanied by full-scale fire tests. The test data was used to validate the established material model for fire-resistant steel with the computer program BoFIRE. This code is based on the Finite Element formulation and written by Schaumann [5]. Only the alloy of the last of the three tests (see section 4.1) is completely identical to the material of the small-scale tests presented in section 2. The steel alloy of the first two tests (see section 4.2 and 4.3) was slightly different. Nevertheless, the approach for the material properties was taken for the simulation of all tests.

4.1 Second full-scale fire test performed in Brunswick, Germany

At 11 July 2006 a full-scale fire test on a column consisting out of VM-FIRE steel was performed on behalf of VALLOUREC & MANNESMANN TUBES. It is first presented because the material formulation established in section 2 is based on the alloy used in this test. In comparison to a previous test (see section 4.2) proof load was reduced to N = 770 kN, resulting in a load-ratio of 47%. Moreover, the alloy of the VM-FIRE steel was improved compared to the alloy used in the first test. The static system and cross-section, which are shown on the left side of Figure 5, correspond to the previous test. Mechanical properties and loads are given in Table 3 in the Appendix, where the column is denoted as 'BS-2'. The column failed after 29 minutes exposure to ISO standard fire. The deformed column after test and cooling can be seen on the right side of Figure 5.

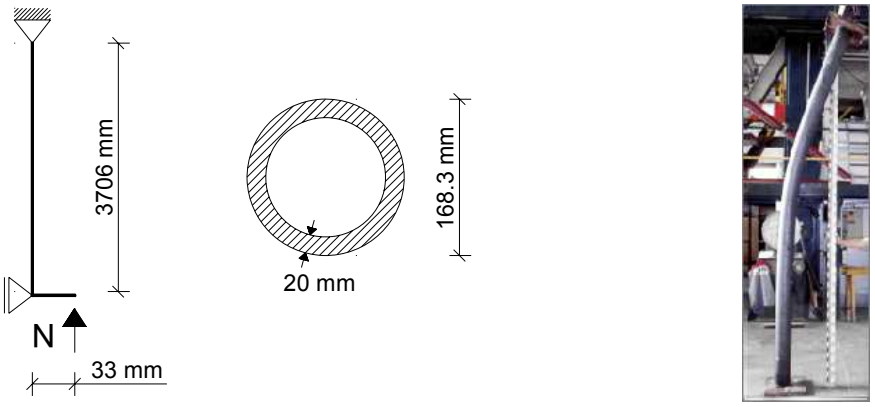

Fig. 5 - Static system and cross-section of the columns tested in 2005 and 2006 (left); column tested in 2006 after fire test (right).

The fire test was simulated using the Finite Element based computer program BoFIRE. Due to the moment resulting from the planned eccentricity at the column end, the imperfection of the test specimen was of secondary importance. Nevertheless its influence was investigated for the following assumed sinus-shaped imperfections, where the actual yield strength of VM-FIRE steel was used in the numerical simulations:

1) L/1,000 = 3,706 mm/1,000 = 3.706 mm
2) L/2,000 = 3,706 mm/2,000 = 1.853 mm
3) No imperfection

With:
L = Length of the column.

Results of the numerical study are summarized in Table 1. It is evident that the magnitude of the imperfection has only slight influence on the computed fire resistance. The actual fire resistance of 29 minutes was underestimated for all calculations, whereas the axial displacement was overestimated with a maximal divergence of 2.9 mm.

Tab. 1 - Results of the second full-scale test in Brunswick, Germany.

Test specimen	VM-FIRE Imperfection L/1,000	VM-FIRE Imperfection L/2,000	VM-FIRE without Imperfection
Measured max. cross-sectional temperature in [°C]	726		
Computed max. cross-sectional temperature in [°C]	*660*	*665*	*670*
Measured max. axial displacement in [mm]	28		
Computed max. axial displacement in [mm]	*30.6*	*30.8*	*30.9*
Tested fire resistance time in [min]	29		
Computed fire resistance time in [min]	*26.3*	*26.6*	*26.9*

4.2 First full-scale fire test performed in Brunswick, Germany

A previous full-scale test was performed at 31 August 2005 in Brunswick. An interim alloy of VM-FIRE steel was used, which was later-on improved for the second fire test in Brunswick. It should be noted that the algebraic formulation developed in section 3 bases on the alloy used in the second test (section 4.1). Apart from that both the static system and cross-section of the second test correspond to the first test (see Figure 5). Material properties and column load can be seen in Table 3. The column was subjected to ISO standard fire and loaded with 850 kN, which corresponds to a load ratio of 55%. It failed after 26 minutes.

The fire-test was simulated with the computer program BoFIRE. Numerical results are to be found in Table 3 in the Appendix (column 'BS-1'). It can be seen that the tested fire resistance of 26 minutes is accurately predicted using the established material properties. The axial displacement is overestimated with a maximum divergence of 4.6 mm. Compared to this, the computation for the same column out of S355 carbon steel led to a reduced fire resistance of only 18 minutes.

4.3 Full-scale fire tests performed in Berlin, Germany

In the year 1999 three unprotected steel columns were tested on behalf of the former German company Mannesmannroehren-Werke AG. Static system and cross-section are shown in Figure 6 along with the deformed columns after testing and cooling. One column consisted out of a preliminary alloy of the fire-resistant steel VM-FIRE (denoted as column 'K1' in the following). The two other columns were constructed out of carbon steel S355 (columns 'K2' and 'K3'). Material properties and loading are summarized in Table 3 in the Appendix.

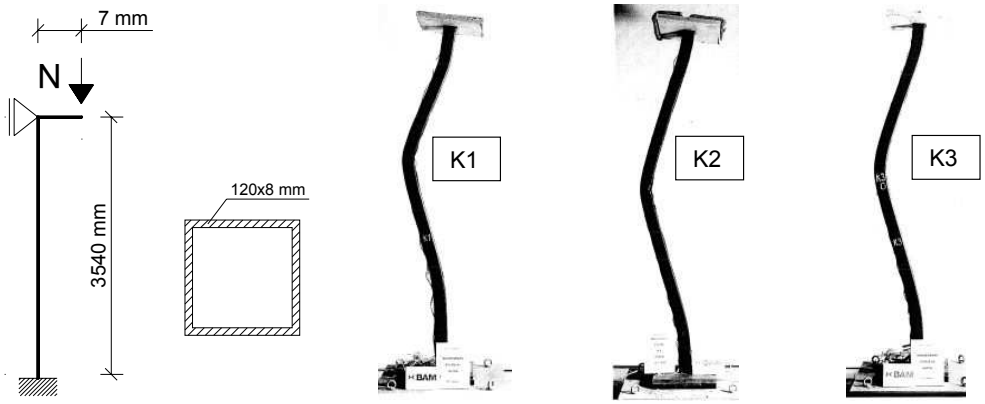

Fig. 6 - Static system and cross-section of the columns tested in Berlin (left); deformed columns K1 to K3 after test and cooling.

All columns were subjected to ISO standard fire until failure occurred. An imperfection of L/1,000 = 3,580 mm/1,000 = 3.58 mm was assumed. Selected results of the fire tests as well as numerical investigations can be found in Table 3 in the Appendix.

The measured cross-sectional temperatures, which are not presented here, exceed the calculated ones from 34°C (column K1) to 45°C (column K3) at most. However, a significant thermal gradient of about 400°C along the height of the column is documented in the test report [6].

This temperature gradient induces thermal bowing and complicates the comparison between experimental and numerical results. As the test data does only include information on axial displacement of the column head but not lateral displacement of the mid of the column, it is not reasonable to assess the effect of the temperature gradient.

Notwithstanding this fact the numerically and experimentally determined fire resistance times stand in excellent agreement with a maximum difference of one minute (column K3). Attention should though be paid to the fact that material properties used for the numerical simulation were established for the second test in Brunswick, Germany. This has to be ascribed to the missing material properties for the preliminary alloy of VM-FIRE steel used in this test in Berlin, Germany.

Altogether the good agreement between numerical simulation and fire tests is nevertheless striking. This can be explained by the fact that the material properties and namely the stress-strain relationship are comparable for small strains. Significant differences only occur for large strains. Since the tested columns were slender and therefore prone to global instability, which is linked with small strains, it becomes scarcely noticeable that the used stress-strain relationship was derived from another alloy of the fire-resistant steel. Therefore it can be concluded that the defined stress-strain relationship allows for sufficiently precise estimations considering column failure at small strains.

5. IDENTIFICATION OF OPTIMAL CROSS-SECTIONAL DIMENSIONS FOR CIRCULAR HOLLOW SECTIONS WITH 30 MINUTES FIRE RESISTANCE

It becomes evident from the previous investigations that columns consisting out of VM-FIRE steel showed considerably higher fire resistance times than similar columns out of

S355 carbon steel. The increased fire performance of VM-FIRE steel can be attributed to its superior strength retention. Referring to the right side of Figure 2, the use of the newly developed fire-resistant steel is in particular interesting for cross-sectional temperatures between 500°C and 700°C. In unprotected steel sections, these temperatures are typically attained after 30 minutes exposure to ISO standard fire. Thus, it was the aim to identify optimal cross-sectional dimensions for circular hollow sections constructed out of VM-FIRE steel with cross-sectional temperatures between 500°C and 700°C when exposed to 30 minutes ISO standard fire.

Five different circular hollow sections were numerically investigated. The heating was computed by means of simplified formulae according to [1]. The investigated hollow sections are summarized in Table 2.

Heating of fire-exposed cross-sections is significantly influenced by their section factor 'A/V'. This is the fire-exposed surface area of the member divided by its volume, both per unit length. High values indicate fast heating and vice versa. Circular profiles should in general be preferred from fire design point of view as their heating is delayed due to their small area of fire exposure [7,8].

Besides an often used cross-sections (line 2 in Table 2), two profiles with high (line 1) and low section factor A/V (line 3) were examined as upper and lower limit, respectively. In addition, two hollow sections were identified where the cross-sectional temperatures after 30 minutes exposure to ISO standard fire attained 543°C (line 5) and 702°C (line 4). For this reason, the latter examples show temperatures within the previously recommended temperature range from 500°C to 700°C. Profiles with cross-sectional temperatures of about 600°C are particularly interesting for the use of VM-FIRE steel and were hence also considered (line 6).

The right side of Figure 7 shows the heating of the different hollow sections exposed to ISO standard fire. It is obvious that the cross-sectional temperatures approximate the gas curve with increasing section factor.

Tab. 2 - Studies on different hollow sections regarding their heating under ISO standard fire.

Line	Circular hollow section	A/V in $[m^{-1}]$	Characterization
1	101.6 × 4.0 mm	260	Upper limit
2	323.9 × 8.0 mm	128	Standard profile
3	508.0 × 40.0 mm	27	Lower limit
4	323.9 × 20.0 mm	53	Interesting for VM-FIRE
5	323.9 × 40.0 mm	29	Interesting for VM-FIRE
6	323.9 × 30.0 mm	37	Ideal for VM-FIRE

By means of simplified formulae it was pointed out that a hollow section with dimensions of 323.9 × 30.0 mm is particularly reasonable for the use of VM-FIRE steel. This is confirmed by numerical investigation using the program BoFIRE. The static system is chosen according to Figure 5. Nominal yield strength of 355 MPa is assumed for VM-FIRE steel. The column is loaded with N = 3,500 kN with load eccentricity of 33 mm and imperfection of L/1,000. This results in a load ratio of $\eta = 59\%$.

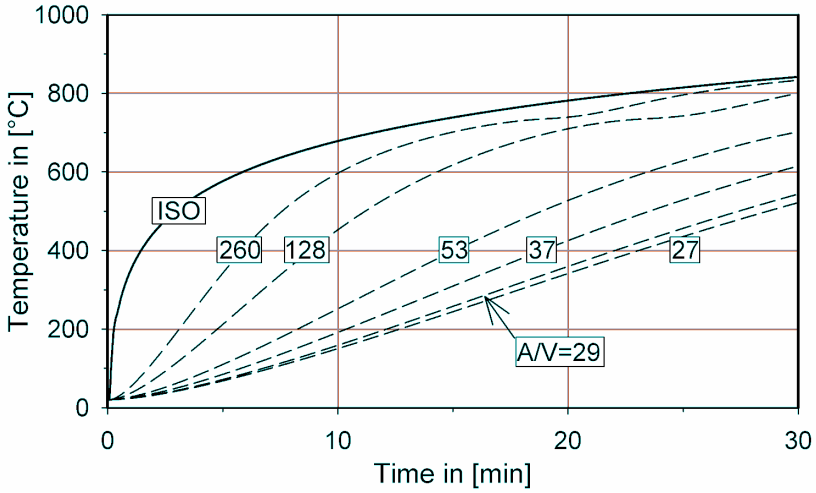

Fig. 7 - Cross-sectional temperatures for different section factors and exposure to 30 minutes ISO standard fire (right).

The member failed after 39 minutes so that it meets the requirements of fire resistance class R30. The calculation was repeated using the material properties of carbon steel S355. In this case, the column already failed after 26 minutes and thus did not meet the requirements. The investigated columns are characterized by a related slenderness of $\overline{\lambda} = 0.46$.

To study effects of slenderness, the column height was increased to 7 m, which in turn results in a greater related slenderness of $\overline{\lambda} = 0.88$. The other boundary conditions remained unchanged. As concerns the column consisting out of VM-FIRE steel, fire resistance time decreased from 39 to 26 minutes. Thus, requirements of the fire resistance class R30 could not be met. The same column out of carbon steel S355 already failed after 20 minutes. It becomes clear from this simple example that VM-FIRE steel is interesting for compact columns or beams that are not prone to global buckling.

The comparison between slender and non-slender columns underlines the importance of appropriate boundary conditions to benefit from fire-resistant steel. The higher initial costs can only be justified for members that are not prone to stability problems. At large strains, the fire-resistant steel gains high effective yield strength, which exceeds that of conventional steel by far in fire case.

In general VM-FIRE steel is ideal for members where stability problems can be excluded, e.g. compact columns or members in bending, such as beams. A significant increase of the elastic modulus by means of metallurgy can be excluded. Under the provision of large strains it is possible to benefit from the superior effective yield strength of VM-FIRE steel at elevated temperatures.

6. SUMMARY AND OUTLOOK

In this paper a report is presented on material investigations, five fire tests on steel tubular columns and numerical investigations in connection with new fire-resistant steel called VM-FIRE. The research work was carried out by VALLOUREC & MANNESMANN TUBES with scientific support of the Institute for Steel Construction, Leibniz Universitaet Hannover.

The constitutive law of VM-FIRE was derived from transient state tests and implemented in the computer program BoFIRE. Comparison between numerical results and results from five full-scale tests on columns showed that the established material formulation is appropriate to accurately predict the load-bearing behaviour of fire-exposed members constructed out of VM-FIRE steel. Moreover, reasonable range of application for columns with circular hollow sections and constructed out of VM-FIRE steel was identified to meet requirements for fire resistance class R30.

The future market trend for VM-FIRE or other fire-resistant steels does not depend so much on its price. Rough estimates yield in additional 10% to 20% costs compared to conventional mild steel. A short-term availability is decisive for the success. It is completely clear that the wide product range cannot be held up by steel merchants for steel beams and plates. It is therefore important to identify interesting application fields and cross-sectional dimensions. A first step towards this objective was made in this contribution.

REFERENCES

[1] European Committee for Standardization (CEN), EN 1993-1-2 (Eurocode 3), **"**Design of steel structures, Part 1-2: General rules - Structural fire design**"**, 2005.
[2] DIN EN 10002-1:2001-12, **"**Metallic materials, tensile testing, part 1: method of test at ambient temperature**"**, Berlin, 2001.
[3] Rubert, Achim and Schaumann, Peter, **"**Structural steel and plane frame assemblies under fire action**"**, Fire Safety Journal, Volume 10, Issue 3, pp. 173-184, 1986.
[4] Bleck, Wolfgang and Muenstermann, Sebastian, **"**Influences on the elastic modulus of steels used for vehicle manufacturing**"** (*published in German*: **"**Einflussgroeßen auf den Elastizitaetsmodul von Staehlen für den Fahrzeugbau**"**), Institut für Eisenhuettenkunde, RWTH Aachen, Schriften-Reihe Nr. 182, 2004.
[5] Schaumann, Peter, **"**Computation of steel members and frames exposed to fire**"** (*published in German*: **"**Zur Berechnung staehlerner Bauteile und Rahmentragwerke unter Brandbeanspruchung**"**), Technisch-wissenschaftliche Mitteilungen Nr. 84-4, Institut für konstruktiven Ingenieurbau, Ruhr-Universitaet Bochum, Germany, 1984.
[6] Schriever, Robert and Korzen, Manfred, **"**Testing of unprotected steel columns regarding the altered fire resistance time as an outcome of a newly developed steel grade with reference to DIN 4101-2**"** (*published in German*: **"**Pruefung von unbekleideten Stahlstuetzen auf Brandverhalten in Anlehnung an DIN 4101-2 im Hinblick auf die Veraenderung der Feuerwiderstandsdauer durch einen neuentwickelten Werkstoff**"**), Berlin, 2001 (*internal report*).
[7] Schaumann, Peter, Bahr, Oliver and Kodur, Venkatesh, **"**Numerical studies on HSC-filled steel columns exposed to fire**"**, Tubular Structures XI, Taylor & Francis Group, London, ISBN 0-415-40280-8, pp. 411-416, 2006.
[8] Schaumann, Peter, Bahr, Oliver and Kodur, Venkatesh, **"**Fire resistance of high strength concrete-filled steel columns**"**, SIF'06 - 4th International Workshop "Structures in Fire", Aveiro, Portugal, pp. 837-848, 2006.

APPENDIX

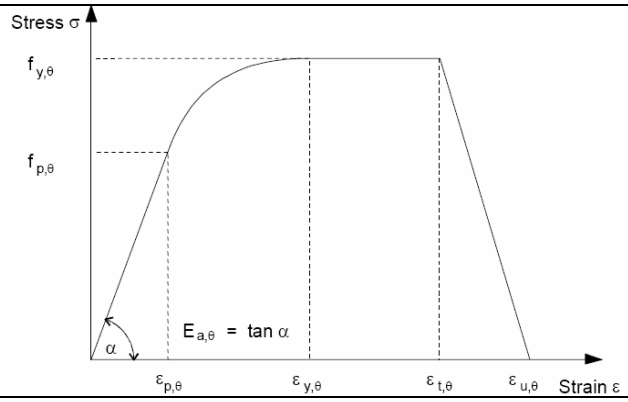

Key:		
	$f_{y,\theta}$	effective yield strength;
	$f_{p,\theta}$	proportional limit;
	$E_{a,\theta}$	slope of the linear elastic range;
	$\varepsilon_{p,\theta}$	strain at the proportional limit;
	$\varepsilon_{y,\theta}$	yield strain;
	$\varepsilon_{t,\theta}$	limiting strain for yield strength;
	$\varepsilon_{u,\theta}$	ultimate strain.

Fig. 8 - Stress-strain relationship for carbon steel at elevated temperatures acc. to [1].

Tab. 3 - Test data and numerical results for investigations on large-scale columns.

Test	**BS-2**	**BS-1**	**K-1**	**K-2**	**K-3**
Steel hollow section	Circular 168,3 × 20 mm		Square 120 x 8 mm		
Material	VM-Steel	VM-Steel*)	VM-Steel*)	S 355	S 355
Actual yield strength [MPa]	449	413	610	430	430
Compression load [kN]	770	850	638	638	450
Static system	both ends pin ended		pin ended / fixed		
Length [m]	3.706		3.540		
Eccentricity [mm]	33		7		
Actual load ratio	0.47	0.55	0.55	0.71	0.49
Fire resistance time [min]	29	26	16	12	16
Numerical Simulation					
Material model applied	New VM-FIRE approach			Eurocode approach	
Calculated fire resistance time [min]	27	26	16	12	15

*) *Intermediate alloy*

SLENDER STEEL COLUMNS EXPOSED TO LOCALISED FIRE

GRANT WANG[1] and DAVID BARBER[2]

ABSTRACT

The performance of steel columns in fire has not been fully studied due to the complexity of the non-linear behaviour in stress-strain relationship, thermal properties and large displacements at elevated temperatures.

There is no simplified method to predict buckling load capacity of a steel column exposed to localised fire that may result significant temperature difference along the length. In practice, buckling load capacity in fire is assessed by conservatively assuming the column to be a 'uniform element' and hence simplified methods assuming the constant section and uniform properties can be used.

To predict the buckling resistance of slender steel columns exposed to localised fire, a simplified method is established by introducing a concept of Equivalent Modulus that is applied to the Eurocode Approach and modified Rankine Approach.

The behaviour of slender steel columns exposed to localised fire is further investigated via numerical computer modelling using Strand 7 finite element analysis software by varying the heating regime and the load ratio.

The verticality and straightness of steel columns will not be constant at an elevated temperature and this introduces uncertainty in using simplified methods, such as adopted in EuroCode. The predictability of actions for steel columns is varied at high temperature due to the large deflections that may present at the support of the column, which will reduce the bucking resistance of columns and could result in global structure instability.

The results of the numerical modelling show that for a critical temperature less than 650°C, the Equivalent Modulus Approach gives a better prediction of buckling resistance of slender columns than that by assuming uniform columns.

For a critical temperature greater than 650°C, a simplified calculation method will not provide a reasonable prediction for slender steel columns exposed to localised fire.

[1] Fire Engineer, Arup Fire, Level 17, 1 Nicholson Street Melbourne VIC 3000, Australia, email: grant.wang@arup.com.au.
[2] Senior Associate, Arup Fire, Level 17, 1 Nicholson Street Melbourne VIC 3000, Australia, email: david.barber@arup.com.au.

Hence it is recommended that calculation results showing a critical temperature in excess of 650 °C using a simplified method will need to be verified via structural frame modelling to consider the global structural behaviour due to the localised fire exposure to the slender steel column.

1. INTRODUCTION

The behaviour of steel columns in fire has not been fully studied due to the complexity of non-linear stress-strain behaviour, thermal properties, geometry of the structure at elevated temperature, and uncertainty of fire exposure.

Steel columns are primarily required to resist vertical loads. Buckling load resistance is often critical to determine the capacity of steel columns. In the case of structural design of slender steel columns at ambient conditions, the vertical load capacity is governed by the buckling resistance, because buckling occurs typically before the squash load capacity of the steel section is reached.

A slender steel column is defined as a column with slenderness ratio greater than 150 (cf Slenderness Ratio = effective length of the column / radius of gyration). A short column is defined as a column with slenderness ratio less than 40 while an intermediate column is defined as a column with slenderness ratio between 40 and 150. At ambient conditions, short columns are dominated by the strength limit of the material and slender columns are governed by the elastic buckling limit. For intermediate columns buckling may occur after the axial load in the column exceeds the buckling limit but before the stress reaches the squash load capacity.

For slender columns at ambient temperature, the critical load that will cause buckling is derived from the elastic stability when out of plane deformation is small. Once the critical load is reached, multiple equilibrium positions are still possible. Hence the structure still has post-buckling capacity to carry load.

The straightness and verticality of steel columns will not be constant at an elevated temperature and this will increase the uncertainty of results when using simplified methods to predict the buckling resistance of steel columns in fire, such as adopted in EuroCode,. The predictability of actions for a steel column is limited at high temperature due to the large deflections that may be present at the supports, which will reduce the buckling resistance of the column.

Hence, the assessment of load capacity based on structural behaviour at ambient temperature is not applicable at elevated temperatures, especially for the slender steel columns exposed to a localised fire which will result non-uniform temperature distribution along the length of the column. Buckling load of the column is governed by the non-linear behaviour of the cross section and occurs after stress exceeds the proportional limit at the heated portion of the column. At an elevated temperature the deformation may well be large enough to cause stress re-distribution throughout the structure. Currently, there are no simple calculation methods that will provide a reasonable prediction of load capacity for steel columns under localised fire exposure.

Steel column behaviour in fire has been studied by a number of researchers [1, 2, 3, 4]. Typically steel columns uniformly heated in the cross section and along the length were studied. The major contribution of these studies was the investigation of the actual mechanical behaviours of steel columns in fire under certain conditions and provision of simplified solutions for design.

By considering the temperature gradient in the cross section of steel columns, the structural behaviour of partially fire-exposed slender steel columns was investigated [5]. It

shows that partially fire-exposed slender columns suffer considerably from a thermal gradient over the cross-section causing thermal bowing and increasing load eccentricity.

An overview of research on the beam-to-column joints [6] summarised that high tensile forces are predicted to occur at joints during the cooling phase of fire. The high tensile forces may increase the horizontal movement at the joints.

To simplify the assessment of buckling resistance for design purposes, Eurocode 3 [7] provides a simple method for uniform steel columns, assuming the temperature distribution in the cross section and along the length of the column are constant at a certain time of fire exposure. In all calculations the Eurocode method gave better fire resistance than results from finite element software based on the research by Anderberg [5], i.e. the Eurocode method has a level of conservatism.

A unified approach for fire resistance prediction of steel columns and frames was developed [8] based on the Rankine Approach which provides a linear interaction relationship between the plastic squash load and the elastic buckling load [9]. This method applies for the uniform steel columns.

The real fire exposure to the steel columns is more complicated than for uniform columns that will increase the level of uncertainty to predict the buckling resistance of columns, especially for slender steel columns.

A steel column exposed to a post-flashover fire (such as a fire in an office building) can be simplified to be a uniform column. The steel column can be considered to be heated uniformly along its length in this situation.

However, in some instances, a steel column exposed to a localised fire will result significant temperature difference along the length of column. For example, in a large space, such as the circulation mall in a shopping centre which has a high ceiling, a flashover fire is highly unlikely to occur in the mall area due to the limit amount of fuel load present in the mall area and significant heat loss to the surroundings.

Currently there are no simplified methods to predict the buckling load capacity of steel columns exposed to localised fire. Current practice either uses the available simplified methods conservatively assuming that the column is uniform or alternatively adopting a complex analysis by using finite element software, such as Safir [10], Abaqus [11] or Strand 7 [12].

The finite element (FE) Approach requires calculation of heat transfer in the cross section before undertaking the structural analysis. A non-linear static analysis and a non-linear transient dynamic analysis are both required to be carried out by varying the heating regime and the load ratio. The FE approach can give a numerical solution, with a number of assumptions applied.

To predict the buckling resistance of a slender steel column exposed to localised fire, a simplified method, i.e. Equivalent Modulus Approach is proposed. The equivalent modulus of the column is applied to the Eurocode Approach and the Modified Rankine Approach by considering the non-uniform temperature distribution along the length of the column. This method can be further refined in practice by using FE Approach.

The buckling resistance of the steel column with a significant thermal gradient over the cross-section can not be predicted using this simplified method.

2. STEEL COLUMNS EXPOSED TO LOCALISED FIRE

In the case that a flashover fire is not predicted to occur, a fire may still be able to result in buckling of a steel column which is engulfed in flame or exposed to high levels of radiated heat flux.

In practice, a compartment fire can be modelled using one zone or two zone models. Two zone models are suitable to predict the smoke layer temperature in the early stages of fire development while one zone models are more suitable for predicting fire conditions after flash-over has occurred.

The smoke layer temperature which is predicted in a two-zone fire situation is considered as the average smoke temperature in the hot smoke zone. A steel column located remote from fuel bed is heated by the heat flux from the hot smoke zone with minor radiative heat flux from the flame. In reality, thermal impact of a localised fire can be much more severe on a steel column located in the vicinity of flame. Hence the localised fire impact on the steel column is to be considered in order to investigate the structural stability in this case.

There are two types of localised fire exposure to consider in the analysis:

- The column is fully engulfed in fire flame or significant heat flux from a fire.
- A portion of the column is engulfed in the flame or significant heat flux from a fire.

In both cases the temperature may vary along the length of heated columns, especially for a column with only a portion engulfed in flame.

To simplify the analysis, the significant temperature gradient over the cross-section is not considered.

The thermal impact on a steel column can be predicted using either simplified methods, such as thermal actions for external members or a localised fire as detailed in Eurocode 1 [13], or alternatively by numerical fire modelling using computational fluid dynamics (CFD) model, such as Fire Dynamics Simulator (FDS) [14]. Hence the heated patterns on a steel column exposed to localised fire can be obtained prior to undertaking structural analysis using either simplified methods or numerical structural modelling.

3. BUCKLING RESISTANCE AT AMBIENT TEMPERATURE CONDITIONS

Failure of steel columns at ambient temperatures can be predicted using simplified methods based on the classification of steel columns. For short columns, the failure of a column occurs once the yield strength of material is reached. As columns become more slender, the stiffness and geometry of the column become more important and buckling occurs before yield strength is reached.

The critical buckling load for a slender column can be predicted using elastic stability limit for a simply-supported column is given by Euler's formula which can be found in any relevant text book:

$$N_{cr} = \frac{EI\pi^2}{L^2} \tag{1}$$

Where:

E - Modulus of elasticity (or Young's modulus) of steel at normal temperature
I - Second moment of area
L - Length of steel column

The Euler formula is the rationalised solution of the following governing equation, which can be solved more correctly by adopting a finite element approach (FE Approach):

$$\frac{d^2w}{dx^2} + \frac{N}{EI}w = 0 \tag{2}$$

Considering the boundary conditions, Equation (1) can be expressed in a simple unified form:

$$N_{cr} = \frac{EI\pi^2}{L_{eff}^{\ 2}} \tag{3}$$

Where

L_{eff} - Effective length (or buckling length)

Considering the eccentric axial load and imperfections of columns, buckling solutions also have a simple form. However, it is not possible to have a simple unified form of mathematical buckling solutions by considering the plastic-elastic behaviour of steel columns.

Based on Equation (3), an empirical solution for inelastic buckling was established by replacing the Young's modulus E with the tangent modulus E_t or reduced modulus E_r.

For a column with a rectangular cross section, the reduced modulus is defined as:

$$E_r = \frac{4EE_t}{(\sqrt{E} + \sqrt{E_t})^2} \tag{4}$$

Notwithstanding with the empirical solution above, Eurocode 3 [15] provides an applicable empirical solution for steel column design. A second-order plastic-elastic approach, Rankine Approach is also developed for steel members and frames [16].

4. BUCKLING RESISTANCE OF STEEL COLUMNS UNDER UNIFORM FIRE EXPOSURE

Two approaches, i.e. the Eurocode Approach, and the Modified Rankine Approach are established as practical solutions to predict the buckling resistance of uniform steel columns under fire exposure.

4.1 Eurocode Approach

The design bucking resistance for compression members in accordance with Eurocode 3 is as follows:

$$N_{b,fi,t,Rd} = \chi_{fi} A k_{y\theta} f_y / \gamma_{M,fi} \tag{5}$$

Or:

$$\frac{N_{b,fi,t,Rd}}{A f_y} = \chi_{fi} k_{y\theta} / \gamma_{M,fi} \tag{5a}$$

Where

A - The cross-section area

f_y - The yield strength at 20°C

χ_{fi} - The reduction factor for flexural buckling in the fire design situation

$k_{y\theta}$ - The reduction factor for the yield strength of steel at the steel temperature θ reached at time t

$\gamma_{M,fi}$ - The partial factor for the relevant material property, for the fire situation. The use of $\gamma_{M,fi} = 1.0$ is recommended.

The χ_{fi} is the function of $\overline{\lambda}, k_{y\theta}$, and $k_{E\theta}$ where $\overline{\lambda}$ is the non-dimensional slenderness and $k_{E\theta}$ is the reduction factor for the slope of the linear elastic range at the steel temperature θ reached at time *t*.

4.2 Modified Rankine Approach

The Rankine Approach considers the elastic bucking load and plastic collapse load within one formula [17] in an empirical way. The original formula is written as:

$$\frac{1}{\lambda_u} = \frac{1}{\lambda_p} + \frac{1}{\lambda_e} \tag{6}$$

Or:

$$\lambda_u = \frac{\lambda_p}{1 + \lambda_p / \lambda_e} \tag{6a}$$

Where:

λ_u - Ultimate collapse load factor

λ_p - Plastic collapse load factor

λ_e - Elastic critical load factor

The Modified Rankine Approach can be written as the following equation, given by [8].

$$\frac{P(T)}{P_p(20)} = \frac{k_y(T)}{1 + \frac{k_y(T)}{k_E(T)} \cdot \left[\frac{\lambda}{\lambda_E(20)}\right]^2} \tag{7}$$

Where

$P_p(20)$ - Plastic squashing load at a temperature of 20°C

$k_y(T)$ -Equals the reduction factor for the yield strength in the Eurocode Approach

$k_E(T)$ - Equals the reduction factor for the slope of the linear elastic range in the Eurocode Approach

$\lambda / \lambda_E(20)$ - Non-dimensional slenderness which can be expressed as:

$$\lambda / \lambda_E(20) = \frac{1}{93.9} \cdot \frac{L_{cr}}{i} \sqrt{\frac{f_y}{235}} \tag{8}$$

Where

L_{cr} - Buckling length in the buckling plane considered

i - The radius of gyration about the relevant axis, determined using the properties of the gross cross-section.

5. BUCKLING RESISTANCE OF STEEL COLUMNS EXPOSED TO LOCALISED FIRE – EQUIVALENT MODULUS METHOD

5.1 Equivalent Modulus

In order to estimate the buckling resistance of steel columns exposed to localised fire, an equivalent modulus E_{eq} at elevated temperature is introduced in an empirical way to consider the non-uniform temperature distribution along the steel column.

The equivalent modulus at time *t* of fire exposure is defined as:

$$E_{eq} = \frac{L}{\gamma_t \int_0^L \frac{1}{E_t(l)} dl} \tag{9}$$

Where:

$E_t(l)$ - Modulus at distance *l* from one end of the column at time *t* of fire exposure

γ_t - The partial factor at time *t* of fire exposure relevant to the heated patterns of steel columns. The use of $\gamma_t = 1.0$ is recommended for a simple heated pattern, such as the steel columns detailed in the Case Studies in this paper.

5.2 Equivalent Modulus Approach Based on the Modified Rankine Approach

To apply the E_{eq} to Equation (7), the Modified Rankine Approach can be re-written as follows:

$$\frac{P(T)}{P_p(20)} = \frac{k_y(T)}{1 + \frac{k_y(T)}{E_{eq}/E(20)} \cdot \left[\frac{\lambda}{\lambda_E(20)}\right]^2} \tag{10}$$

The highest temperature in the steel column at time *t* of fire exposure is used to determine the value of $k_y(T)$ for a steel column with simple heated patterns.

5.3 Equivalent Modulus Approach Based on the Eurocode Approach

Applying the equivalent modulus E_{eq} and selected value of $k_y(T)$ to Eurocode is similar to applying the equivalent modulus to the Modified Rankine Approach. The reduction factors for stress-strain relationship of steel at elevated temperatures provided in Eurocode are used to determine the equivalent modulus. It is expected that the Eurocode Approach can also be used to estimate the buckling resistance of a steel column under localised fire exposure.

6. CASE STUDIES

Three cases are investigated using the Equivalent Modulus Approach to predict buckling resistance of steel columns exposed to localised fire. The uniform steel column under fire conditions is also included in the analysis for comparison.

The heated portion from the bottom of the columns for Cases 1, 2 and 3 is 1/2, 1/3, and 2/3 of the length, respectively. The uniform steel column is to be uniformly heated on the full length.

The heated portion along the steel columns is assumed to have a uniform high temperature at time *t* of fire exposure while the un-heated portion along the steel columns is assumed to have a temperature less than 100°C at any time. The yield strength of steel at 20°C is taken as 235 N/mm^2 (or 235 MPa).

The reduction factor against non-dimensional slenderness based on the Modified Rankine Approach at temperatures of 100°C, 400°C, 500°C, 600°C, and 700°C is plotted in Fig. 1 in which the reduction factor = $P(T)/P_P(20)$.

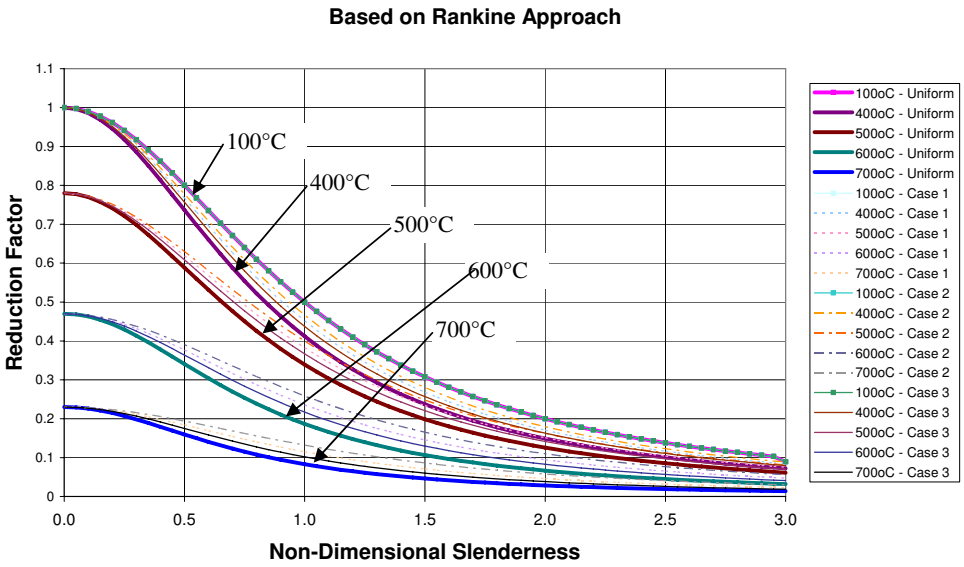

Fig. 1 – Equivalent Modulus Approach Based on the Modified Rankine Approach.

The reduction factor against non-dimensional slenderness based on the Eurocode Approach at temperatures of 100°C, 400°C, 500°C, 600°C, and 700°C is plotted in Fig. 2 in which the reduction factor = $N_{b,fi,t,Rd}/Af_y$.

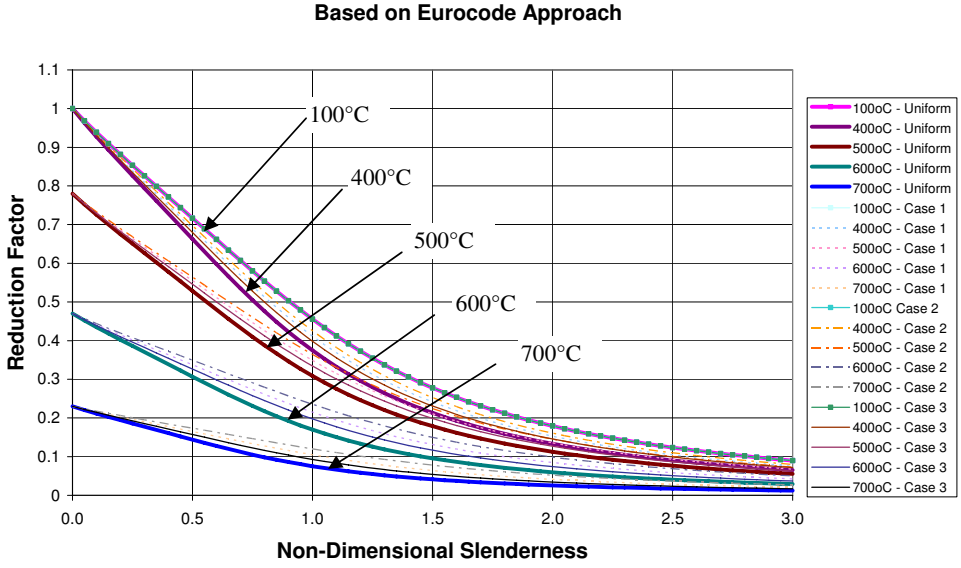

Fig. 2 – Equivalent Modulus Approach Based on the Eurocode Approach.

Fig. 1 and Fig. 2 show that the reduction factor curves have a similar trend for columns with a non-dimensional slenderness greater than 0.5. The larger the heated portion of steel columns, the smaller the reduction factor becomes.

The reduction factors based on the Modified Rankine and Eurocode approaches for the steel column with a non-dimensional slenderness of 1.6 (a slender steel column) and 0.5 (a short steel column) are also detailed in Tables 1 and 2, respectively.

Table 1 – Reduction factor for a slender steel column

$\bar{\lambda}$=1.6	Cases	100°C	200°C	300°C	400°C	500°C	600°C	700°C
Based on Rankine Approach	Uniform	0.281	0.260	0.238	0.215	0.180	0.096	0.042
	Case – 1	0.281	0.270	0.258	0.243	0.213	0.133	0.065
	Case – 2	0.281	0.274	0.265	0.255	0.227	0.152	0.079
	Case – 3	0.281	0.267	0.251	0.233	0.201	0.118	0.055
Based on Eurocode Approach	Uniform	0.253	0.234	0.214	0.192	0.162	0.086	0.037
	Case – 1	0.253	0.243	0.232	0.219	0.192	0.120	0.058
	Case - 2-	0.253	0.246	0.238	0.229	0.204	0.137	0.072
	Case - 3	0.253	0.240	0.225	0.209	0.181	0.106	0.049

Table 2 – Reduction factor for a short steel column

$\bar{\lambda}$=0.5	Cases	100°C	200°C	300°C	400°C	500°C	600°C	700°C
Based on Rankine Approach	Uniform	0.800	0.783	0.762	0.737	0.589	0.341	0.159
	Case – 1	0.800	0.791	0.780	0.767	0.619	0.377	0.184
	Case – 2	0.800	0.794	0.787	0.778	0.630	0.390	0.194
	Case – 3	0.800	0.788	0.774	0.757	0.609	0.364	0.175
Based on Eurocode Approach	Uniform	0.716	0.702	0.684	0.663	0.529	0.307	0.144
	Case – 1	0.716	0.709	0.700	0.688	0.555	0.337	0.165
	Case – 2	0.716	0.711	0.705	0.697	0.564	0.349	0.173
	Case – 3	0.716	0.706	0.694	0.680	0.546	0.326	0.157

Table 1 shows that for Case 1 (i.e. a slender steel column with a half length exposed to fire), based on the Eurocode Approach the reduction factor at 500°C, 600°C, 700°C is 0.192, 0.120, and 0.058 that is approximately 1.19, 1.40, and 1.57 times of that for an uniform steel column, respectively.

For a short steel column with a half length exposed to fire, as shown in Table 2, based on the Eurocode Approach the reduction factor at 500°C, 600°C, 700°C is 0.555, 0.337, and 0.165 that is approximately 1.05, 1.10, and 1.15 times of that for an uniform steel column, respectively.

Hence for a slender steel column, using the Equivalent Modulus Approach will give a higher critical temperature than that assuming a uniform steel column.

The reduction factor predicted based on the Rankine Approach is approximately 10% larger than that predicted based on the Eurocode Approach for a steel column with yield strength of 235 N/mm^2.

Given that the plastic squash load is greater than yield load at a temperature of 20°C, the Equivalent Modulus Approach based on Eurocode will have a greater level of conservatism than that based on the Modified Rankine Approach.

7. APPLICATION OF THE PROPOSED EQUIVALENT MODULUS APPROACH IN DESIGN

Equivalent Modulus Approach based on Eurocode was used in a real project at Concept Design Stage to determine a suitable level of fire protection. The buckling load resistance of a slender steel column exposed to localised fire was predicted. The heated patterns of the steel column were varied to consider the uncertainty due to the localised fire exposure.

The slender steel column in the building is shown in Fig. 3.

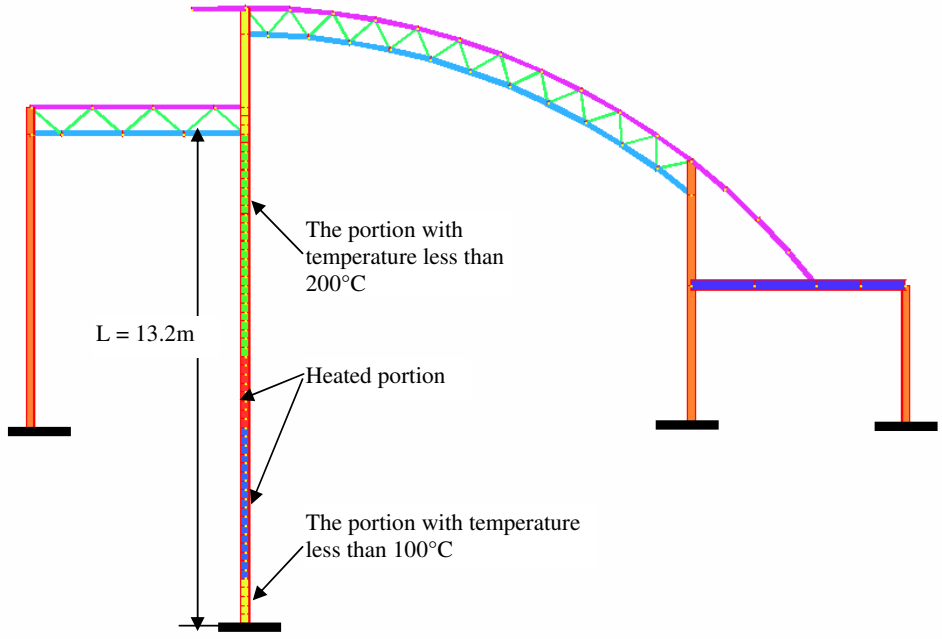

Fig. 3 – Slender steel column in a building.

The structural global behaviour due to the localised fire exposure to the slender steel column was investigated utilising an advanced numerical tool – Strand 7 finite element analysis software. The FE model is shown in Fig. 4. Heat transfer in the cross section of the steel column, non-linear static analysis, and non-linear transient dynamic analysis was carried out by varying the heating regime and the load ratio. The buckling resistance of the steel column was predicted. The results of the FE modelling were compared with those using the Equivalent Modulus Approach based on Eurocode. The results show that the Equivalent Modulus Approach gave a better buckling resistance prediction than that by assuming uniform steel columns compared with FE modelling results.

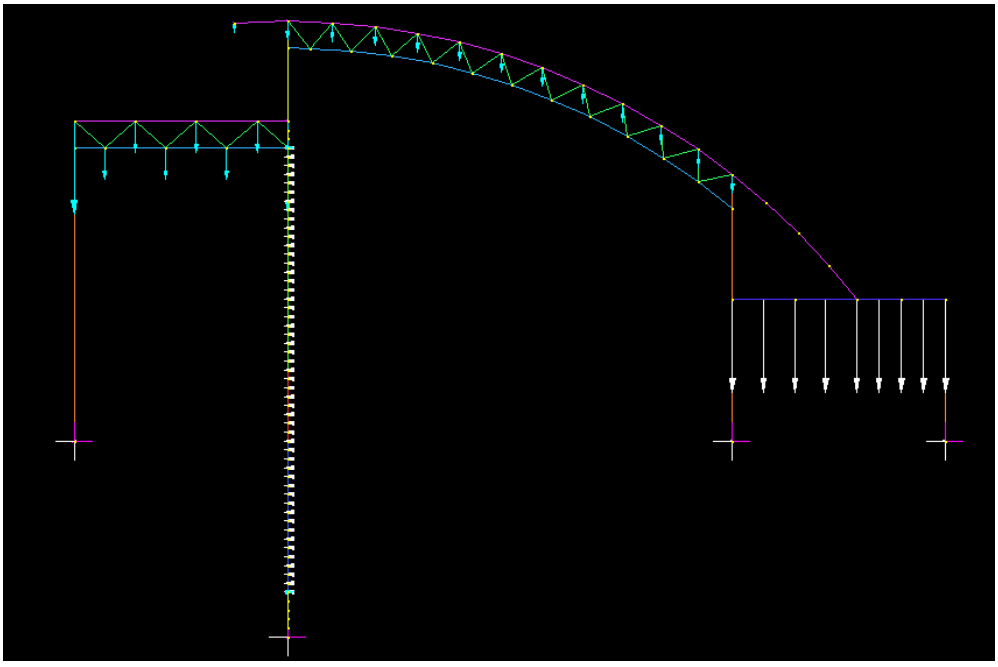

Fig. 4 –FE model using Strand 7.

However, for the cases that buckling was not predicted to occur at temperature greater than 650°C using the Equivalent Modulus Approach based on the Eurocode Approach, the FE modelling has shown that the failure of structures occurred due to the large horizontal and vertical deformations.

Once a very high temperature was reached in a slender steel column, the simplified calculation method did not provide a reasonable prediction for slender steel columns exposed to localised fire as the global structural stability is to concern in this case.

8. CONCLUSION

A concept of Equivalent Modulus is introduced for steel columns with simple heated patterns and based upon, a simplified method – Equivalent Modulus Approach is established derived from Eurocode to predict the buckling resistance of steel columns exposed to localised fire. The equivalent modulus is also employed in the Modified Rankine Approach.

The behaviour of slender steel columns exposed to localised fire was investigated via numerical computer modelling using Strand 7 finite element analysis software by varying the heating regime and the load ratio.

For a critical temperature less than 650°C, the Equivalent Modulus Approach gives a better prediction of buckling resistance of slender columns than that predicted by assuming a uniform column for a slender steel column exposed to a localised fire.

For a critical temperature greater than 650°C, simplified calculation methods will not provide a reasonable prediction for slender steel columns exposed to a localised fire.

It is recommended that calculation results showing a critical temperature in excess of 650 °C using a simplified method will need further to be verified using a numerical structural modelling to investigate global structural behaviour.

REFERENCES

[1] Burgess IW, Olawale AO, Plank RJ. Failure of steel columns in fire Fire Saf 1992; 18:183-201

[2] Talamona D, Franssen JM, Schleich JB, Kruppa J., Stability of steel columns in case of fire: numerical modelling. J Struct Eng (ASCE) 1997; 123(6): 713-20.

[3] Bailey C.G., Moore D.B., Lennon T., The structural behaviour of steel columns during a compartment fire in a multi-storey braced steel-frame, Journal of Construction Steel Research, Volumne 52, Number 2, November 1999 pp. 137-157 (21).

[4] Toh WSTan KH, Fung TC. Compressive resistance of steel columns in fire: Rankine approach. J Struct Eng(ASCE) 2000; 126(3):398-405.

[5] Yngve Anderberg, Structural behaviour and design of partially fire-exposed slender steel columns, Second International Workshop – Structures in Fire 18-19 march, 2002 at University of Canterbury, Christchurch, New Zealand.

[6] Khalifa S.A., Buick D., and Ian W. B., Performance of beam-to-column joints in fire – A review, Fire Safety Journal 43 (2008) 50-62.

[7] EC 3, European Committee for Standardization, Eurocode 3: Design of steel structures - Part 1-2: General rules — Structural fire design, BS EN 1993-1-2:2005

[8] Chu Yang Tang, A Unified approach for fire resistance prediction of steel column and frames, Second International Workshop – Structures in Fire 18-19 march, 2002 at University of Canterbury, Christchurch, New Zealand.

[9] Merchant, W., The Failure Loads of Rigid Jointed Frameworks as Influenced by Stability, The structural Engineer, 32, pp185-190, 1954.

[10] Franssen, J-M., Kodur, V.K.R., and Mason, J., 'User manual for SAFIR: a computer program for analysis of structures submitted to fire'. Internal Report SPEC/2000_03, 2000, University of Liege, Ponts et Charpentes, Belgium

[11] Hibbett, Karlsson & Sorenson Inc., 'ABAQUS v6.5 Manuals', ABAQUS Manual Set, 2004.

[12] Strand 7 Release 2.4, Strand 7 Pty Ltd, Sydney Australia, http://www.strand7.com/

[13] EC 1, European Committee for Standardization, Eurocode 1: Actions on structures – Part 1-2: General actions – Actions on structures exposed to fire, BS EN 1991-1-2:2002

[14] NIST, Fire Dynamics Simulator version 5 - User's Guide, National Institute of Standards and Technology, NIST Special Publication 1019-5, USA, 2008.

[15] EC 3, European Committee for Standardization, Eurocode 3: Design of steel structures – Part 1-1: General rules and rules for buildings, BS EN 1993-1-1:2005

[16] Maquoi, R. & Jaspart, J.P. A simple approach for the design of steel and composite frames accounting for effective overall stability, Pestschrift Prof Richard Greiner, Graz University, Austria, October 2001

[17] Home, M. R., 'The Rankine-Merchant Load and Its Application', Summation Theorems in Structural Stability, Edited by T Tarnai, Springer-Verlag, Wien-New York , 1995

FIRE RESISTANCE OF STEEL BEAM-COLUMNS SUBJECTED TO AXIAL COMPRESSION AND BIAXIAL BENDING WITH NON-UNIFORM BENDING MOMENT DISTRIBUTION

MARKUS KNOBLOCH[1], MARIO FONTANA[2] and ANDREA FRANGI[3]

ABSTRACT

The fire resistance of steel beam-columns is strongly influenced by the reduction of the elastic modulus during heating and the nonlinear stress-strain relationship of steel at elevated temperatures. Based on a comprehensive numerical parametric study the paper analyses the spatial buckling behaviour of steel members subjected to combined axial compression and biaxial bending with both uniform and non-uniform bending moment distribution. The results of the parametric study are compared to results of the interaction formulae according to the current European fire design rules as well as a calculation model based on the current rules for the ambient temperature design directly adapted for the fire design using temperature-dependent material properties. The comparative analysis shows that the interaction and plasticity factors for the calculation models must be further developed to take advantage of using similar interaction formulae for ambient temperature and fire design.

1. INTRODUTION

Fire design of steel beam-columns has attracted world-wide attention during recent years. Beam-columns are structural members subjected to combined axial compression and bending. Under fire conditions, steel members heat up quickly, primarily because of their usually high surface area-to-volume ratio and the good thermal conductivity of steel. At elevated temperatures, the strength and stiffness of steel decreases rapidly, and the typical linear-elastic perfectly-plastic stress-strain relationship becomes distinctly nonlinear. As a result, very large strains are required for reaching the so-called effective yield strength and to

[1] ETH Zurich, Institute of Structural Engineering, 8093 Zurich, Switzerland,
email: markus.knobloch@ethz.ch.
[2] ETH Zurich, Institute of Structural Engineering, 8093 Zurich, Switzerland,
email: mario.fontana@ethz.ch.
[3] ETH Zurich, Institute of Structural Engineering, 8093 Zurich, Switzerland,
email: andrea.frangi@ethz.ch.

activate an increase in cross-sectional capacity due to plastification. The decreasing stiffness of steel during heating and the nonlinear material behaviour strongly influence the stability behaviour of steel members subjected to fire. The overall buckling behaviour mainly influences the load-carrying capacity of steel beam-columns. Slender beam-columns with torsionally stiff profiles, like rectangular hollow sections, or profiles with sufficient torsional and lateral restraints develop flexural buckling. The buckling resistance of torsionally flexible profiles, like I sections without restraints, is mainly affected by the lateral-torsional buckling behaviour.

The buckling behaviour of axially and eccentrically loaded slender columns under fire conditions is numerically and experimentally studied by Talamona et al. [1] and Franssen et al. [2]. Based on their finite element results and a comparison to fire tests, Franssen et al. [3] develops a calculation model for steel columns whose stability failure mode is in the plane of the loading, later adopted by EN 1993-1-2 [4]. The lateral-torsional buckling behaviour of steel beam-columns in bending about the strong axis at elevated temperatures is recently studied by Vila Real et al. [5]. Another recent study [6] shows that the AISC specifications [7] lead to unconservative results for the lateral-torsional buckling resistance of steel members subjected to combined axial compression and strong axis bending at elevated temperatures. The flexural and lateral-torsional buckling behaviour of steel beam-columns in combined axial compression and both uniaxial and biaxial bending at ambient temperature is numerically analysed by Ofner [8]. These numerical results are used for verifying the novel Method 1 (French-Belgian) and Method 2 (Austrian-German) approaches for beam-columns adopted in EN 1993-1-1 [9]. The calculation method used for the fire design of steel beam-columns [4] is based on the model of ENV 1993-1-1 [10]. Hence, the current European rules for ambient temperature design and the fire design situation use different M-N interaction curves. However, it is the aim to restore the similarity between both designs and to adopt the interaction curves used for ambient temperature design also for the fire design situation. Research carried out on the lateral-torsional buckling behaviour of steel beam-columns in uniaxial bending about the strong axis seems to indicate that it might be possible to use the ambient temperature design approach even for fire design considering the temperature-dependent material properties [11]. However, more research on the lateral-torsional and especially the flexural buckling behaviour is necessary for developing a safe, economical and easy applicable calculation method for the design of steel members in combined axial compression and bending. In particular, the spatial buckling behaviour of steel beam-columns in biaxial bending under fire conditions, i.e. the interaction between flexural buckling, biaxial bending, lateral-torsional buckling and the nonlinear stress-strain relationship of steel at elevated temperatures has been rarely analysed. Thus, the paper aims at analysing the overall buckling behaviour of steel members in combined axial compression and biaxial bending at elevated temperatures as well as determining their flexural and lateral-torsional buckling resistance.

The paper first describes the numerical model used for a comprehensive parametric study. Next, the current European fire design model for beam-columns as well as a calculation model based on the Method 1 and 2 approaches for the fire design are reviewed. Finally, the paper numerically analyses the spatial buckling behaviour of steel beam-columns in fire and compares the buckling resistances according to the analytical models to the numerical results.

2. NUMERICAL MODEL

The load-carrying behaviour of steel beam-columns subjected to fire was analysed in a comprehensive numerical study. By using the finite element program Abaqus [12] with three-

dimensional beam-elements, geometrically and physically nonlinear calculations were performed. The study distinguished between torsionally stiff members (members not susceptible to torsional deformations), in particular rectangular hollow sections (RHS), failing in in-plane and spatial flexural buckling, and torsionally flexible members (members susceptible to torsional deformations), in particular I sections, failing in lateral-torsional buckling (Fig. 1). Hence, two types of analyses were performed: First, analyses with warp-free torsionally stiff elements (designated as B31 according to the Abaqus element library) without rotation around the x-axis and secondly, analyses with torsionally flexible elements considering warping effects according to Vlassov's theory (designated as B31OS according to the Abaqus element library). Both elements considered Timoshenko's hypothesis, however, neglecting the interaction between normal and shear stress in the elastic-plastic range of the constitutive law.

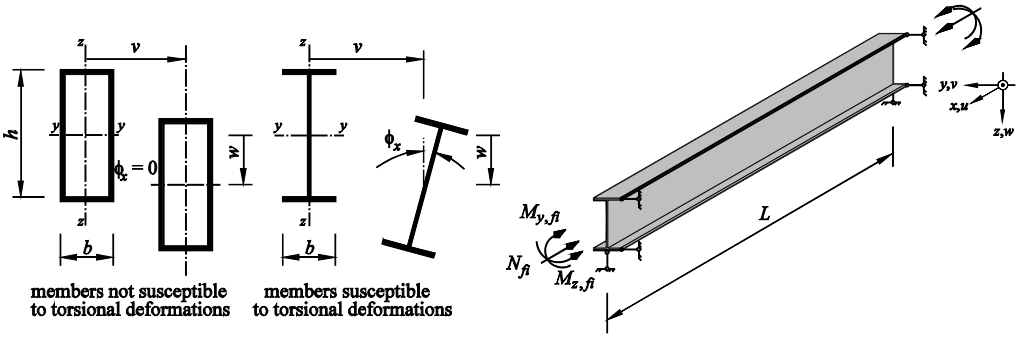

Fig. 1 – Members susceptible and not susceptible to torsional deformations and single-span beam-column with fork support.

The parametric study considered only stocky double symmetrical cross-sections, allowed for plastic design without local buckling at both ambient and elevated temperatures (class 1). However, local buckling gets more important in fire design than in ambient temperature design and even stocky cross-sections may develop local buckling in compression before reaching the plastic resistance [13]. Therefore, for this study it was checked whether due to local buckling effects the cross-section still reaches the temperature-dependent plastic resistance [14]. The following hot-rolled cross-sections were used: RHS 200x100x10, IPE 200 (representative of $h/b = 2$), IPE 500 ($h/b > 2$), and HEB 300 ($h/b < 2$). These or similar cross-sections have been used in several studies on the stability behaviour of steel beam-columns both at ambient and elevated temperatures [e.g. 5, 8]. For simplicity, the influence of the fillets was neglected. A few details on the influence of the fillets on the lateral-torsional buckling resistance in finite element studies are given in [15].

The numerical study analysed the overall buckling behaviour of single span members simply supported at both ends (fork supports), Fig. 1. The lengths of the beam-columns corresponded to the non-dimensional flexural buckling slenderness at ambient temperature $\lambda_z = 0.5$, 1.0 and 1.5. Lateral parabolic geometric imperfections were considered simultaneously in the direction of both major axes of the cross-section. The maximum value of the lateral geometric imperfection was $e_{0,y} = e_{0,z} = l/1000$. The analyses of the lateral-torsional buckling behaviour of members with uniform bending moment distribution ($\psi = 1.0$) additionally considered an initial rotation around the x-axis with a maximum value of $e_{0,\varphi} = l/2000$ radians at mid-span leading to a maximum value of the lateral imperfection of $e_{0,y} = l/1000$ at the top flange combined with the adjusted lateral geometric imperfection. The analyses of the lateral-torsional buckling behaviour of members subjected to triangular-shaped bending moment

distribution with a bending moment ratio of ψ = -1.0 considered two different shapes of imperfection: parabolic-shaped – decisive for members mainly subjected to axial compression – and S-shaped imperfection considering an initial rotation – decisive for members mainly subjected to bending moments. The residual stress pattern corresponded to typical distributions for hot-rolled RHS, I, and H sections with maximum values of 0.3 $f_{y,20°C}$ for IPE sections, and 0.5 $f_{y,20°C}$ for HEB sections and RHS sections (Fig. 2). The stress-strain relationship of steel at elevated temperature was based on the model in EN 1993-1-2 for steel grade S235. The parametric study considered uniform temperature distributions in the cross-sections. The temperature analysed were ambient temperature, 400°C, 500°C, 600°C and 700°C covering the critical steel temperature of the majority of practical situations.

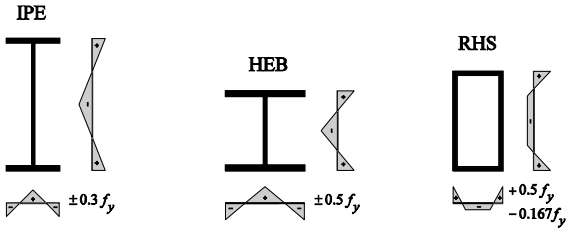

Fig. 2 – Residual stress pattern used for the parametric study.

The parametric study considered axial compression as well as bending moments about both the strong and weak axis. The study considered both end moments (ratio of end moments ψ = 1.0, 0.0, -1.0) and moments due to in-plane lateral loads (uniform load and concentrated load at mid-span). The lateral loads were applied to the centre of gravity. The bending moment distributions about the strong and weak axes were equal. The ratio between the bending moment about the weak axis $M_{z,fi}$ and the temperature-dependent plastic bending moment resistance $M_{pl,z,\theta}$ calculated with plastic moment distribution and the temperature-dependent effective yield strength $f_{y,\theta}$ reached at 2% strain was 0, 0.2, 0.4, 0.6 and 0.8. The finite element model used for the parametric study was verified with the numerical results presented in [8] for ambient temperature and the results presented in [16] for lateral-torsional buckling of member in uniaxial bending at elevated temperatures.

3. INTERACTION FORMULAE FOR STEEL BEAM-COLUMNS IN FIRE

Fire design methods either calculate the critical temperature or the resistance of steel members at a determined elevated temperature. The former methods calculate the so-called critical temperature that a member can sustain under a given load. For the latter methods, standards often distinguish between "advanced", called Level 2 approaches according to the European design standards, and "simple" methods, called Level 1 approaches, where the former requires advanced thermal and structural simulations and the latter method is accomplished through member-based resistance checks. The member-based methods are similar to those for ambient temperature design using temperature-dependent material properties and adapted column and lateral-torsional buckling curves. For example, the calculation method adapted for the European fire design rules essentially adopt the structural resistance approach, where the beam-column resistance under a specified elevated temperature is obtained by substituting the reduced elastic modulus and yield stress into design formulae that are otherwise similar to those used for ambient temperature design. However, the shape of the design formulae for steel beam-columns subjected to fire according

to EN 1993-1-2 is similar to the shape of the equations for ambient temperature design according to ENV 1993-1-1 and, hence, they are different from the shape of the formulae of the Method 1 and 2 approaches for ambient temperature design according to EN 1993-1-1. The current structural fire part of the European design rules (EN 1993-1-2) did not follow the changes for beam-columns and in particular the M-N interaction formulae introduced on EN 1993-1-1 due to the lack of validation for the fire design situation. Nevertheless, it is the aim to restore the similarity and to adapt the interaction formulae present for the ambient temperature design for the fire design situation (Fig 3).

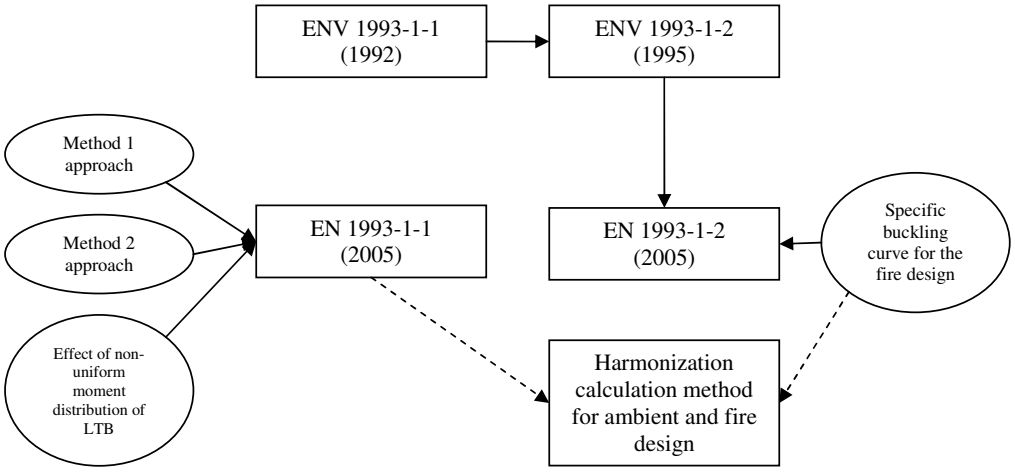

Fig. 3 – Calculation methods for steel beam-columns for fire design.

EN 1993-1-2 uses the effective yield strength reached at 2% strain for the calculation of the cross-sectional resistance of stocky sections. For stability effects, EN 1993-1-2 considers the influence of the material behaviour of steel at elevated temperatures by modifying the non-dimensional slenderness with the temperature-dependent ratio of the effective yield strength to the elastic modulus (Eq. 2c). This simplified method does not consider the nonlinear stress-strain relationship and the larger strains required to reach yield strength. Additionally, the reduction factors for column buckling and lateral-torsional buckling $\chi_{y,fi}$, $\chi_{z,fi}$ and $\chi_{LT,fi}$ are calculated with a specific buckling curve different from those used for the ambient temperature design (Eq. 1). The calculation method for beam-columns uses a linear M-N interaction. The positive effect on non-uniform bending moment distributions on the lateral-torsional buckling resistance is neglected.

$$\chi_{y,fi} = \chi_{z,fi} = \chi_{LT,fi} = \frac{1}{\varphi_\theta + \sqrt{\varphi_\theta^2 - \overline{\lambda}_{i,\theta}}} \tag{1}$$

$$\varphi_\theta = \frac{1}{2} \cdot \left(1 + \alpha \cdot \overline{\lambda}_{i,\theta} + \overline{\lambda}_{i,\theta}^2 \right) \tag{2a}$$

$$\alpha = 0.65 \cdot \sqrt{235 / f_y} \tag{2b}$$

$$\overline{\lambda}_{i,\theta} = \overline{\lambda}_i \cdot \sqrt{\frac{k_{y,\theta}}{k_{E,\theta}}} \tag{2c}$$

The basis of both Method 1 and Method 2 approaches are formed by single span members with double symmetric cross-sections subjected to axial compression, end moments and transverse loading. The Method 1 approach possesses a complex theoretical background

resulting in a wide field of application and high level of accuracy at ambient temperature and uses a smooth transition from flexural to lateral-torsional buckling according to the torsional rigidity of the structural member. The Method 2 approach, however, bases on a semi-empirical approach and strictly distinguishes between torsionally stiff and torsionally flexible members. With respect to the theoretical derivation Method 1 bases on the spatial flexural buckling behaviour and "sinusoidal" moments, while the Method 2 approach bases on the in-plane flexural buckling behaviour and a uniform bending moment distribution. Both methods consider a bi-linear M-N-interaction. Details of Method 1 and 2 at ambient temperature are given in [17].

A possible harmonization may consider the M-N-interaction formulae of the Method 1 and 2 approaches in conjunction with both the temperature-dependent material properties for the effective yield strength and the buckling curve used for the fire design situation according to Eq. (1). The results of the numerical parametric study are compared to results according to the Method 1 and Method 2 approaches of EN 1993-1-1 considering the unmodified shape of the interaction formulae as well as the temperature-dependent effective yield strength, the specific buckling curve for the fire design and the effect of non-uniform bending moment distributions for calculating the reduction factor for the lateral-torsional buckling in the next section (cp. Fig. 3). A similar adoption of the Method 1 and 2 approaches for members in combined axial compression and uniaxial bending is discussed in [16].

4. STABILITY BEHAVIOR OF BEAM-COLUMNS AND COMPARATIVE ANALYSIS OF VARIOUS INTERACTION FORMULAE

The results of the comprehensive numerical parametric study were used for developing non-dimensional axial compression-bi-axial bending moment interaction curves. In addition to the overall stability behaviour, the interaction curves implicitly considered the temperature-dependent cross-sectional capacity. Every interaction curve belongs to a particular cross-section, non-dimensional slenderness, bending moment distribution and steel temperature. An additional parameter of the interaction curves is the ratio between the bending moment about the weak axis $M_{z,fi}$ and the temperature-dependent bending moment resistance $M_{pl,z,\theta}$ calculated with plastic moment distribution.

Figure 4 (left) shows the M_y-N-interaction curves for the different cross-sections analysed with a non-dimensional flexural buckling slenderness λ_z of 1.0 at ambient temperature for a steel temperature of 600°C and a $M_{z,fi}/M_{pl,z,\theta}$ ratio of 0.2, as an example. The bending moment distribution was uniform ($\psi = 1.0$). The RHS profile failed in spatial flexural buckling, whilst the IPE sections developed lateral-torsional buckling deflections leading to markedly smaller bending moment resistances for members mainly subjected to bending moments.

Figure 4 (right) analyses the influence of the steel temperature on the M-N-interaction behaviour of IPE 200 sections. The beam-columns also possessed a non-dimensional flexural buckling slenderness of $\lambda_z = 1.0$ and a weak axis bending moment ratio of $M_{z,fi}/M_{pl,z,\theta} = 0.2$. The overall stability stronger affected the plastic capacity of the cross-section than at ambient temperature. Additionally, the plastic interaction between the axial compression and the bending moment about both the strong and weak axes was affected by the nonlinear stress-strain relationship of steel at elevated temperatures. Due to the reduced stiffness of steel at elevated temperatures and the distinctly nonlinear material behaviour an increase of the cross-sectional capacity as a result of the plastification was not reached until very large strains. The resistance of beam-columns considering stability effects was usually reached for smaller strains, especially for members predominately subjected to axial compression. Thus, the

buckling resistance of steel members mainly subjected to axial compression could not take benefit of the strain hardening due to the nonlinear stress-strain relationship of steel at elevat-

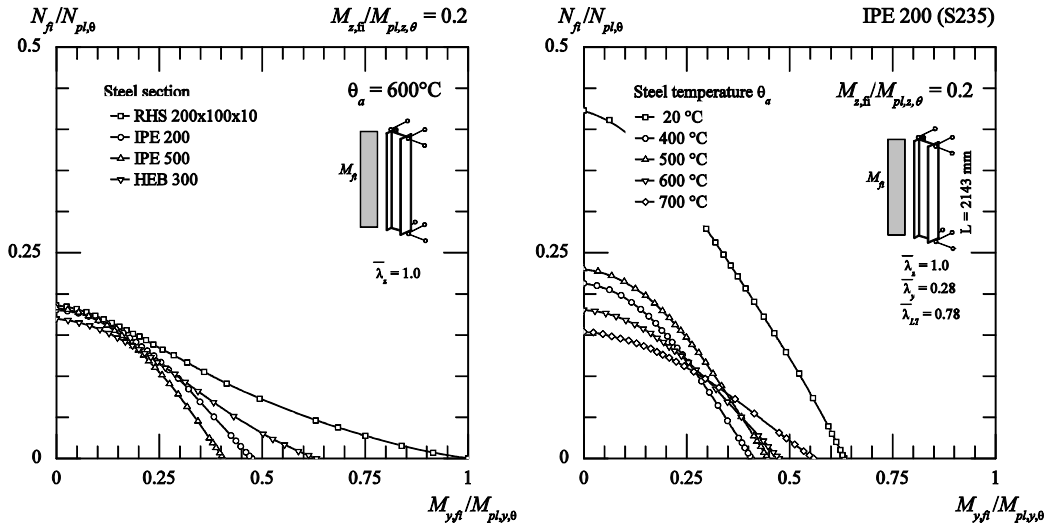

Fig. 4 – Non-dimensional interaction curves for spatial flexural and lateral-torsional buckling. Comparison of the overall stability behaviour of beam-columns with λ_z = 1.0 of different steel cross-sections ($M_{z,fi}/M_{pl,z,\theta}$ = 0.2, θ_a = 600°C) (left) and analysis of the influence of the steel temperature on the M-N-interaction behaviour of IPE 200 sections ($M_{z,fi}/M_{pl,z,\theta}$ = 0.2) (right).

ed temperatures. The ratio between the temperature-dependent proportional limit $f_{p,\theta}$ and the effective yield strength $f_{y,\theta}$ strongly influenced the non-dimensional resistances $N_{fi}/N_{pl,\theta}$ and $M_{y,fi}/M_{pl,y,\theta}$. A large ratio $f_{p,\theta}/f_{y,\theta}$, for example at 500°C, led to a large non-dimensional resistance $N_{fi}/N_{pl,\theta}$ on the on hand and a small resistance $M_{y,fi}/M_{pl,y,\theta}$ on the other, whilst a small ratio $f_{p,\theta}/f_{y,\theta}$, for example at 700°C, resulted in a small non-dimensional resistance to axial compression and a large one to bending moments. The marked influence of the $f_{p,\theta}/f_{y,\theta}$ ratio was already observed for the local buckling behaviour in [18].

Figure 5 analyses the influence of the non-dimensional flexural buckling slenderness on the M-N-interaction curves for RHS 200x100x10 (left) and IPE 200 sections (right) at a steel temperature of 600°C with a $M_{z,fi}/M_{pl,z,\theta}$ ratio of 0.2, as an example. Steel members subjected to combined axial compression and bending develop a specific load-carrying behaviour in the different ranges of slenderness. At very low slenderness the cross-sectional resistance dominates. The cross-sectional resistance is a function of the cross-section shape, the M-N interaction, steel grade, and temperature and is described by the temperature-dependent material properties and the interaction formulae. With increasing slenderness a pronounced second-order effect appears. The slenderness limit for considering second-order effects is strongly effected by the large strains necessary for reaching yield strength at elevated temperatures. The second-order effect in the medium slenderness range is significantly influenced by geometrical imperfections, residual stresses, and the non-linear stress-strain relationship of steel at elevated temperatures in fire. The resistance of beam-columns mainly subjected to axial compression is reached for smaller strains compared to the large strains required to reach yield strength at elevated temperatures. The actual spatial buckling behaviour of steel beam-columns not susceptible to torsional deformations depends on the cross-section shape, the ratio of the slenderness' λ_z/λ_y and the ratio between the axial force and the bending moment. In comparison to the load-carrying behaviour at ambient temperature, e.g. illustrated in [8], the beam-columns developed spatial and out-of-plane

buckling for smaller $N_{fi}/N_{pl,\theta}$ ratios. In the high-slenderness range, member buckling is dominated by the elastic behaviour. Therefore, the decreasing elastic modulus during heating

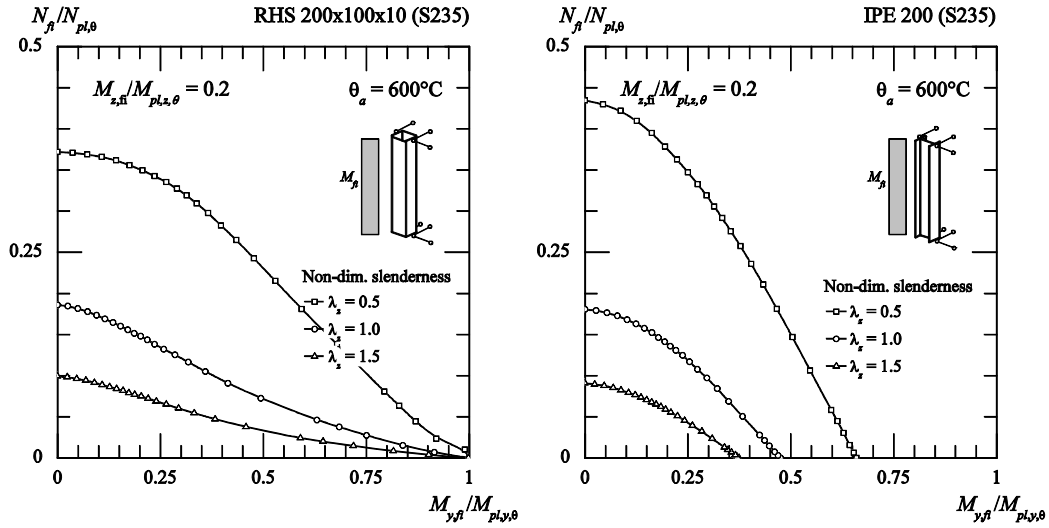

Fig. 5 – Non-dimensional interaction curves for RHS 200x100x10 sections (left) and IPE 200 section (right). Analysis of the influence of the non-dimensional flexural buckling slenderness on the M-N-interaction behaviour ($M_{z,fi}/M_{pl,z,\theta} = 0.2$, $\theta_a = 600°C$).

mainly affects the stability behaviour in the high-slenderness range.

The buckling curve for the fire design (Eq. 1) aims at implicitly considering theses effects for the different ranges of slenderness and correcting the use of the yield strength reached at 2 % strain. For example, the buckling curve for the fire design reduces the cross-sectional resistance due to buckling effects in the low slenderness range even for very stocky members. For medium slender members, the buckling curve is located between curve c and d, although the residual stresses shall less influence the resistance in fire than in ambient temperature (for almost uniform temperature distribution). Using the correct strain-dependent cross-sectional resistance for calculating the member slenderness leads to a less conservative buckling curve for the fire design [19].

The M-N-interaction curves developed from the results of the numerical parametric study were used for a comparative analysis of the various interaction formulae for steel beam-columns subjected to fire. Figures 6-10 compare the analytical M-N-interaction curves according to EN 1993-1-2 (dashed lines) and the Method 1 (dash dotted lines) and 2 (dotted lines) approaches considering the temperature-dependent material properties and the specific buckling curve for the fire design (Eq. 1) to the numerical results. The analytical curves consider the cross-sectional capacity of the profiles in addition the overall buckling effect. The curves are given for RHS 200x100x10 profiles (left), developing spatial flexural buckling, and IPE 200 sections (right), developing lateral-torsional buckling deflections, as examples. The results are given for $M_{z,fi}/M_{pl,z,\theta}$ ratios of 0.0, 0.4 and 0.8. The bending moment distribution was either affected by end moments or in-plane lateral loads. The bending moment ratios ψ caused by the end moments were 1.0 (Fig. 6), 0.0 (Fig. 7) and -1.0 (Fig. 8). Figure 9 shows the results for triangular-shaped bending moment distributions caused by lateral loads at mid-span and Fig. 10 shows the results for parabolic-shaped distributions caused by uniformly distributed lateral loads.

The specific column buckling curve for the fire design according to Eq. (1) in conjunction with the effective yield strength reached at 2% strain led to unconservative results

for all interaction formulae for the column resistance of members mainly subjected to axial compression. The flexural buckling resistance of steel beam-columns mainly subjected to

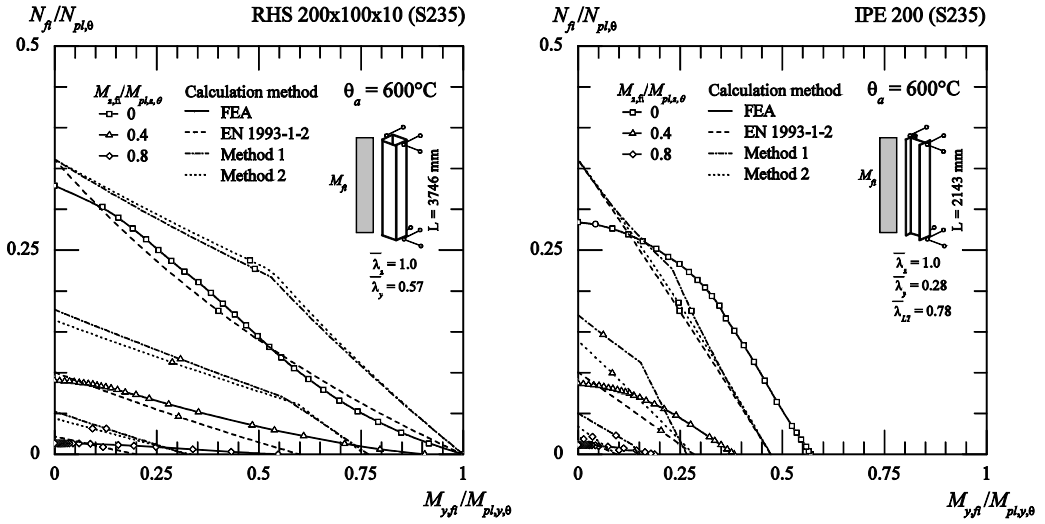

Fig. 6 – Non-dimensional interaction curves for RHS 200x100x10 sections (left) and IPE 200 section (right) for uniform bending moment distribution ($\psi = 1.0$); $\lambda_{z,\theta} = 1.23$, $\lambda_{y,\theta} = 0.70$ (left) and $\lambda_{z,\theta} = 1.23$, $\lambda_{y,\theta} = 0.34$, $\lambda_{LT,\theta} = 0.97$ (right).

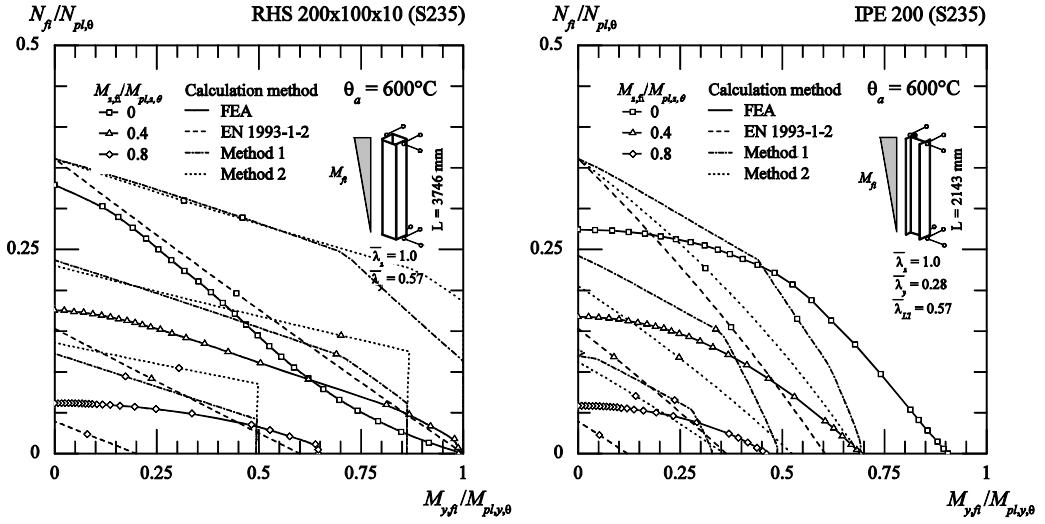

Fig. 7 – Non-dimensional interaction curves for RHS 200x100x10 sections (left) and IPE 200 section (right) for triangular-shaped bending moment distribution ($\psi = 0.0$); $\lambda_{z,\theta} = 1.23$, $\lambda_{y,\theta} = 0.70$ (left) and $\lambda_{z,\theta} = 1.23$, $\lambda_{y,\theta} = 0.34$, $\lambda_{LT,\theta} = 0.70$ (right).

axial compression is reached for smaller strains compared to the large strains required to reach yield strength at elevated temperatures. For steel beam-columns subjected to combined axial compression and weak axis bending moments, the N-M_z-interaction formulae of the Method 1 and 2 approaches led to unconservative results.

The spatial buckling behaviour of steel beam-columns is approached using two branches for the interaction curve according to the Method 1 and 2. However, the direct adoption of the shape of the interaction formulae as well as the interaction and plastification

factors according to the Method 1 and 2 approaches for the fire design led to unconservative results for the flexural buckling (Figs. 6-10 left).

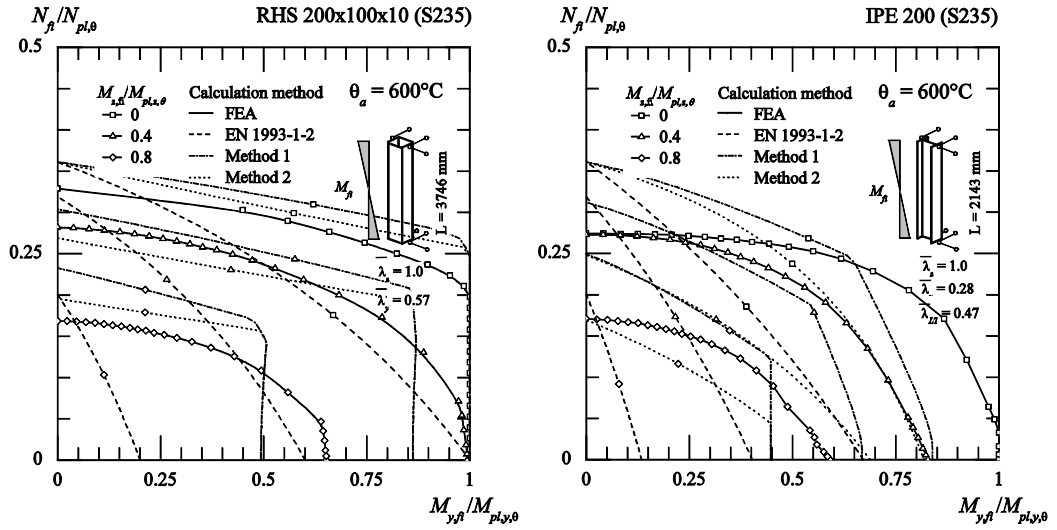

Fig. 8 – Non-dimensional interaction curves for RHS 200x100x10 sections (left) and IPE 200 section (right) for triangular-shaped bending moment distribution (ψ = -1.0); $\lambda_{z,\theta}$ = 1.23, $\lambda_{y,\theta}$ = 0.70 (left) and $\lambda_{z,\theta}$ = 1.23, $\lambda_{y,\theta}$ = 0.34, $\lambda_{LT,\theta}$ = 0.58 (right).

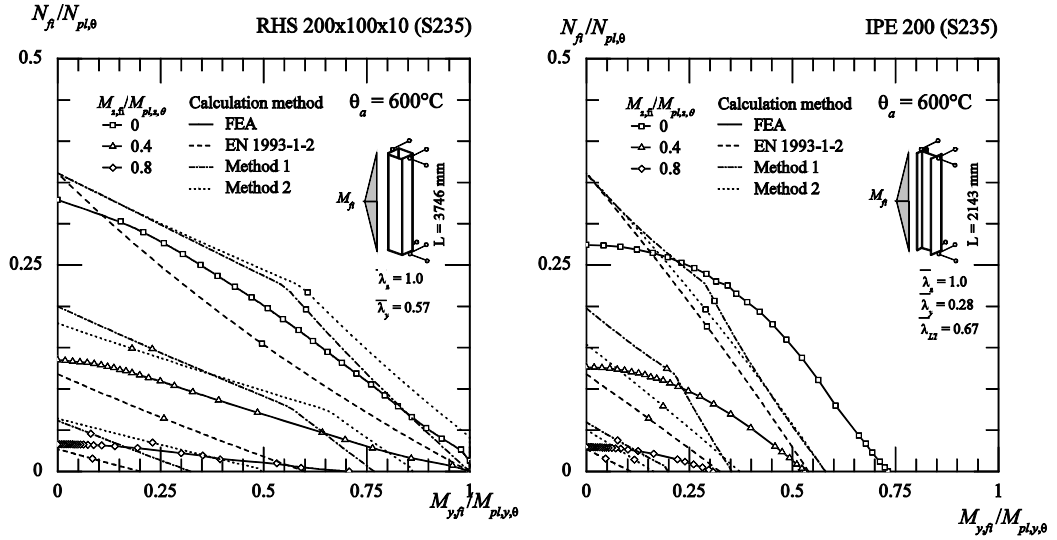

Fig. 9 – Non-dimensional interaction curves for RHS 200x100x10 sections (left) and IPE 200 section (right) for triangular-shaped bending moment distribution (lateral loads at mid-span); $\lambda_{z,\theta}$ = 1.23, $\lambda_{y,\theta}$ = 0.70 (left) and $\lambda_{z,\theta}$ = 1.23, $\lambda_{y,\theta}$ = 0.34, $\lambda_{LT,\theta}$ = 0.82 (right).

The specific buckling curve led to conservative results for the lateral-torsional buckling resistance of steel members mainly subjected to strong axis bending moments of all calculation methods. The lateral-torsional and flexural buckling resistance of steel beam-columns mainly subjected to bending moments was reached for larger strains than for members in compression. Therefore, the use of the yield strength reached at 2% strain led to adequate or even conservative results. The M/N ratio and the shape of the nonlinear stress-

strain relationship ($f_{p,\theta}/f_{y,\theta}$ ratio) markedly influenced the strain corresponding to the buckling resistance. Therefore, a strain-based calculation model which considers the strain-dependent

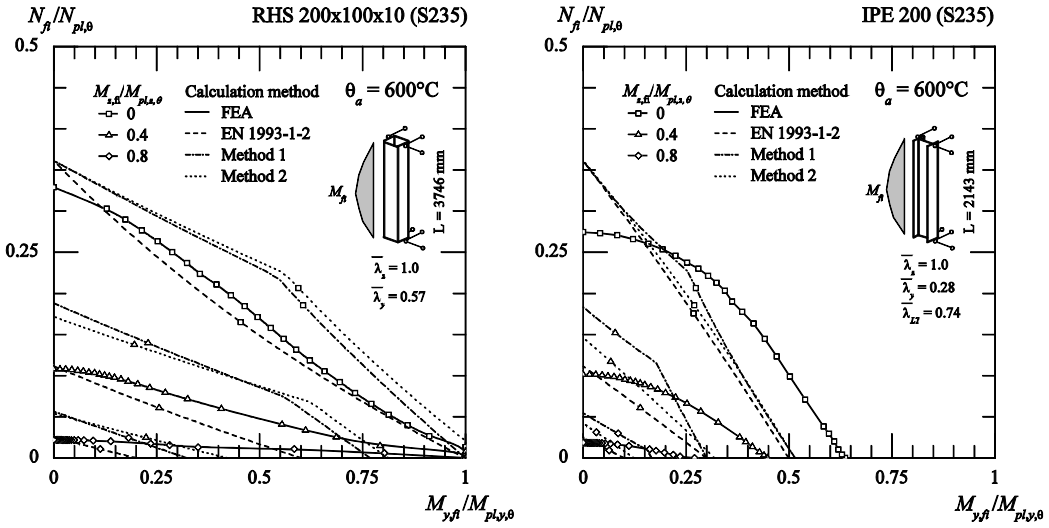

Fig. 10 – Non-dimensional interaction curves for RHS 200x100x10 sections (left) and IPE 200 section (right) for parabolic-shaped bending moment distribution (uniformly distributed lateral loads); $\lambda_{z,\theta} = 1.23$, $\lambda_{y,\theta} = 0.70$ (left) and $\lambda_{z,\theta} = 1.23$, $\lambda_{y,\theta} = 0.34$, $\lambda_{LT,\theta} = 0.90$ (right).

cross-sectional capacity could lead to more consistent results for steel beam-columns subjected to fire.

5. CONCLUSIONS

This paper has analysed the spatial flexural and lateral-torsional buckling behaviour of steel beam-columns subjected to fire. The reduction of the elastic modulus during heating and the nonlinear stress-strain relationship of steel at elevated temperatures strongly influence the buckling resistance. The spatial buckling behaviour reduces the plastic capacity of beam-columns for already smaller slenderness in fire than in ambient temperature due to the nonlinear material behaviour and the large strains required to reach yield strength. The results of a comprehensive numerical parametric study on the spatial buckling behaviour of RHS and I sections in combined axial compression and biaxial bending has been presented as temperature-dependent non-dimensional interaction curves. Further, the influence of the bending moment distribution on the flexural buckling and lateral-torsional buckling resistance has been numerically studied. In addition, the results have been compared to the resistances according to EN 1993-1-2 as well as to a calculation method based on the Method 1 and Method 2 approaches of EN 1993-1-1 using temperature-dependent material properties and the buckling curve for the fire design of EN 1993-1-2. This buckling curve may lead to unconservative results for steel members mainly subjected to axial compression, but to conservative results for the lateral-torsional buckling resistance of members in almost pure bending. To take advantage of using the same interaction formulae for ambient temperature and fire design the interaction and plasticity factors for the calculation models must be further developed. In particular, the influence of the overall stability on the maximum strains at ultimate load vs. the large strains required to reach the plastic bending capacity of beam-columns in combination with the nonlinear stress-strain relationship must be considered.

Temperature-dependent interaction coefficients could be derived from the numerical results of this study and validated on fire tests. However, it is difficult to estimate whether an improved simplified design method is possible by adapting the EN 1993-1-1 interaction format, particularly without prior work on the calculation models for column buckling in fire. A strain-based calculation model could lead to more consistent fire design methods for both column and steel beam-column buckling.

ACKNOWLEDGMENTS

The authors gratefully acknowledge the support of the research projects No. 200021-117906 and PI0I2-119560 of the Swiss National Science Foundation.

REFERENCES

[1] Talamona D., Franssen J.M., Schleich J.B., Kruppa J. "Stability of Steel Columns in Case of Fire: Numerical Modeling". *Journal of Structural Engineering* 123(6): 713-20, 1997.
[2] Franssen J.M., Talamona D., Kruppa J., Cajot L.G. "Stability of Steel Columns in Case of Fire: Experimental Evaluation". *Journal of Structural Engineering* 124(2): 158-63, 1998.
[3] Franssen J.M., Schleich J.B., Cajot L.G. "A Simple Model for the Fire Resistance of Axially-loaded Members According to Eurocode 3". *Journal of Constructional Steel Research* 35(1): 49-69, 1995.
[4] EN 1993-1-2: 2005. Eurocode 3: Design of steel structures – Part1-2: General rules – Structural fire design.
[5] Vila Real P.M.M., Lopes N., Simoes da Silva L., Franssen J.M. "Parametric analysis of the lateral-torsional buckling resistance of steel beams in case of fire". *Fire Safety Journal* 42(6-7): 416-24, 2007.
[6] Takagi J., Deierlein G.G. "Strength design criteria for steel members at elevated temperatures". *Journal of Constructional Steel Research* 63(8): 1036-50, 2007.
[7] AISC: 2005. Specification for structural steel buildings.
[8] Ofner R. *Traglasten von Stäben aus Stahl bei Druck und Biegung*. PhD thesis, TU Graz, Institut für Stahlbau, Holzbau und Flächentragwerke, Heft 9, 1997.
[9] EN 1993-1-1: 2005. Eurocode 3: Design of steel structures – Part 1-1: General rules and rules for buildings.
[10] ENV 1993-1-1: 1992. Eurocode 3: Design of steel structures – Part 1-1: General rules and rules for buildings.
[11] Franssen J.M., Zaharia R. *Design of Steel Structures subjected to Fire: Background and Design Guide to Eurocode 3*, University of Liege, Liege, 2005.
[12] ABAQUS, Hibitt, Karlson & Sorensen Inc., Version 6.7-1, 2007.
[13] Knobloch M., Fontana M. "Strain-based approach to local buckling of steel sections subjected to fire". *Journal of Constructional Steel Research* 62(1-2): 44-67, 2006.
[14] Knobloch M. *Zum Tragverhalten beulgefährdeter Stahlquerschnitte bei Brandeinwirkung*. [Local buckling behaviour of steel sections subjected to fire]. IBK report No. 303, ETH Zurich, vdf Hochschulverlag, 2007.
[15] Nasdala L., Hohn B., Schröder K.U. „FE-Untersuchungen zur Interaktion von Biegedrillknicken und plastischem Querschnittsversagen bei Durchlaufträgern". *Stahlbau* 74(5): 319-330, 2005.
[16] Vila Real PMM., Lopes N., Simoes da Silva L., Piloto P., Franssen JM. "Towards a consistant safety format of steel beam-columns: application of the new interaction formulae for ambient temperature to elevated temperatures". Steel and Composite Structures 3(6), 2003.
[17] Boissonnade N., Greiner R., Jaspart J.P.- Lindner J. *Rules for Member Stability in EN 1993-1-1: Background documentation and design guidelines*. ECCS, 2006.
[18] Knobloch M. "Local buckling behavior of steel sections subjected to fire". Proceedings of the Ninth International Symposium in Fire Safety Science, Karlsruhe, Germany, 2008, in press.
[19] Knobloch M., Fontana M., Frangi, A. On the interaction of global and local buckling of square hollow sections in fire. *Proceedings of the Fifth International Conference on Coupled Instabilities in Metal Structures*, Sydney, Australia, 2008.

DEFLECTION BEHAVIOUR OF PLATE GIRDERS LOADED IN SHEAR AT ELEVATED TEMPERATURE

ZHEN-HAI QIAN[1], KANG-HAI TAN[2]

ABSTRACT

This paper presents a theoretical investigation about out-of-plane and in-plane deflection behaviour of plate girders loaded in shear at elevated temperatures at the pre- and post-buckling stages. Theoretical elastic analysis of plate out-of-plane deflection employs an approximate approach using a combination of classical plate theory and Galerkin's method. These elastic analytical solutions are compared with experimental results and numerical predictions. A combination of shear strength theory for plate girders and energy method is adopted to describe the in-plane vertical deflection of plate girders.

Keywords: *Plate girder, Shear buckling, Thermal restraint, Out-of-plane deflection.*

1. INTRODUCTION

Plate girders have been widely used as load-carrying structural members in multi-storey high rise structures and steel bridges. For such structural components, pre- and post-buckling behaviour is significantly crucial for design considerations. Buckling of this type of members at normal temperature has been rigorously studied by a number of researchers since 1930s. However, until 1959, Basler and Thurlimann performed an extensive study on the post-buckling strength of plate girder web panels subjected to shear [1-4]. Rockey's approach was eventually adopted by the British standard (BS 5950: 1990 [5]) for design practices. Based on Rockey's failure theory, just recently, Vimonsatit et al., [6] proposed a mechanical approach to

[1] Research Staff, Nanyang Technological University, School of Civil and Environmental Engineering, Blk N1, #1A-37, Nanyang Avenue, Singapore 639798, email: zhqian@ntu.edu.sg

[2] Associate Professor, Nanyang Technological University, School of Civil and Environmental Engineering, Blk N1, #1A-37, Nanyang Avenue, Singapore 639798, email: ckhtan@ntu.edu.sg

predict the shear capacity of plate girders at elevated temperatures. This model also incorporated the compressive force induced by thermal restraints arising from adjacent unheated structures in fire. To validate this analytical approach, two series of experimental investigations about plate girders have been conducted at high temperatures [7, 8]. However, there are no suitable mechanical models to represent the out-of-plane and in-plane deformation characteristics of plate girders under shear force at elevated temperatures. Thus, the objective of current study is to derive analytical equations to describe the plate out-of-plane and in-plane deformation characteristics, and to obtain pre- and post-buckling stiffnesses at normal and elevated temperatures. The findings will be beneficial for design practices.

2. BRIEF DESCRIPTIONS OF EXPERIMENTAL INVESTIGATIONS

Before the introduction of current analytical approaches, as a necessary verification, six series of plate girder tests have been conducted by the authors [7-8] in two categories, viz. unrestrained and restrained in the longitudinal direction. At the first stage, three series of plate girders, viz. TG3, TG4 and TG5, have been tested at 20 ^{o}C, 400 ^{o}C, 550 ^{o}C and 700 ^{o}C, respectively. At the second stage, additional three more series, viz. RTG3, RTG4 and RTG5, have also been tested subjected to axial compressive stresses applied onto plate girders. The plate girders were purposely designed so that only two end panels would fail primarily in shear, with negligible effect from bending. Geometrical dimensions for these end panels are 305 mm (width) x 305 mm (height), with web plate thicknesses as 2 mm, 2.7 mm and 1.5 mm. To investigate the effect from axial compressive stress, RTG3, RTG4 and RTG5 series have the same geometrical characteristics as TG3, TG4 and TG5 series. The behaviour is in accord with analytical descriptions proposed by Vimonsatit et al. [6].

3. OUT-OF-PLANE DEFLECTION OF PLATE GIRDER WEB PANEL

Theoretical studies of plated structure defections have been carried out by several researchers more than a century ago. With introduction of special stress function, von Karman [9] first proposed the governing equations, which satisfy both force equilibrium and deflection compatibility for perfectly flat thin plates. With incorporation of initial imperfections, Marguerre [10] modified von Karman's governing equations to predict the post-buckling behaviour using large-deflection analysis. This work forms the basis for current theoretical investigations on plate behaviour loaded in shear. Later, Levy and Greeman [11] used six terms of truncated double Fourier series to seek alternative solutions for Marguerre's equations. Since then, pre- and post-buckling plate problems have been widely examined by several researchers [12-19]. In this study, aforementioned classical plate theory has been extended to elevated temperature situations, with especial insights gained from the incorporation of (i) initial imperfections on mechanical behaviour of plate, and (ii) thermal restraints induced by surrounding unheated structural members.

3.1 Basic assumptions and boundary conditions

For a plate girder loaded in shear, the web panel plate can be modelled as a simply supported flat plate subjected to shear stress (τ) and compressive stress (σ) as shown in Fig. 1. The longitudinal compressive stress in $x-$direction represents thermal restraint forces

induced by surrounding unheated structures. The idealized uniformly distributed shear stress acts along both longitudinal and vertical edges of the web plate.

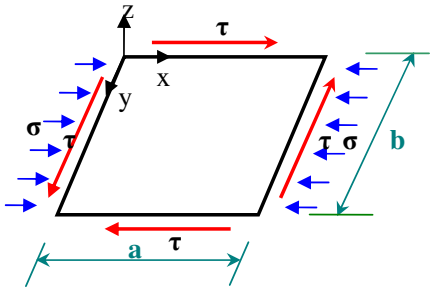

Fig.1-Load Distributions and Geometrical Property for Investigated Plates

Assumed vertical simply supported boundary conditions at $x=0$ and $x=a$ represent the vertical edges of transverse web stiffeners in the end web panels as shown in Fig.1. The assumed simply supported boundary conditions at $y=0$ and $y=b$ are valid for the junction lines between the web panel and the top and bottom flanges.

3.2 Deflection Functions and Stress Function

Out-of-plane deflection w of the buckled plate is normally represented by an infinite double sine series [16], which automatically fulfils the assumed boundary conditions.

$$w=\sum_{m=1}^{\infty}\sum_{n=1}^{\infty}w_{mn}\sin\frac{m\pi x}{a}\sin\frac{m\pi y}{b} \tag{1}$$

However, it is noticed that acceptable accuracy within one percent error can be achieved by considering only the first few terms in this series. Timoshenko et al. [16] utilized five terms of double sine series to calculate the shear buckling strength of a simply-supported plate as follows.

$$w=w_{11}\sin\frac{\pi x}{a}\sin\frac{\pi y}{b}+w_{21}\sin\frac{2\pi x}{a}\sin\frac{\pi y}{b}+w_{22}\sin\frac{2\pi x}{a}\sin\frac{2\pi y}{b}+ w_{23}\sin\frac{2\pi x}{a}\sin\frac{3\pi y}{b}+w_{33}\sin\frac{3\pi x}{a}\sin\frac{3\pi y}{b} \tag{2}$$

Considering the displacement compatibility and stress equilibrium conditions of plates under in-plane loading, governing differential equations were first derived by von Karman [9] and improved later by Marguerre [10] with considerations of initial imperfections of a plate as follows.

$$\nabla^4\Phi+E_{(T)}t\left[\frac{\partial^2 w_0}{\partial x^2}\frac{\partial^2 w}{\partial y^2}+\frac{\partial^2 w_0}{\partial y^2}\frac{\partial^2 w}{\partial x^2}-2\frac{\partial^2 w_0}{\partial x\partial y}\frac{\partial^2 w}{\partial x\partial y}+\frac{\partial^2 w}{\partial x^2}\frac{\partial^2 w}{\partial y^2}-\left(\frac{\partial^2 w}{\partial x\partial y}\right)^2\right]=0 \tag{3}$$

$$D_{(T)}\nabla^4 w-\frac{\partial^2\Phi}{\partial y^2}\frac{\partial^2(w+w_0)}{\partial x^2}-\frac{\partial^2\Phi}{\partial x^2}\frac{\partial^2(w+w_0)}{\partial y^2}+2\frac{\partial^2\Phi}{\partial x\partial y}\frac{\partial^2(w+w_0)}{\partial x\partial y}=0 \tag{4}$$

In addition, w_0 represents the initial out-of-plane imperfection of a plate, similar to Equation (2) for out-of-plane deflection.

$$w_0=w'\sin\frac{\pi x}{a}\sin\frac{\pi y}{b}+w'\sin\frac{2\pi x}{a}\sin\frac{\pi y}{b}+w'\sin\frac{2\pi x}{a}\sin\frac{2\pi y}{b}+w'\sin\frac{2\pi x}{a}\sin\frac{3\pi y}{b}+w'\sin\frac{3\pi x}{a}\sin\frac{3\pi y}{b} \tag{5}$$

Applying compatibility Equation (4), the Airy stress function can be expressed in the following form.

$$\Phi = E_{(T)}t\sum_{i=1}^{30} a_i \cos\frac{m_i\pi x}{a}\cos\frac{n_i\pi y}{b} + \left(-\frac{\sigma}{2}ty^2 - \tau xy\right) \tag{6}$$

in which: the corresponding coefficients of a_i, m_i and n_i are first proposed by Zaras [19] for perfectly flat plates. Considering initial imperfections, the detailed coefficients have been derived by the authors, which satisfy compatibility condition.

3.3 Buckling and Post-buckling Analysis

Exact theoretical solutions of governing differential Equations (3) and (4) are very rare. However, some indirect analytical methods have been developed which give satisfactory results. Current investigations utilize Galerkin's energy method to solve the governing differential equations. Since the assumed deflected shape is only an approximation to the real deflected shape of plate, the values of w and stress function Φ may not satisfy the equilibrium Equation (4). The numerical error can be treated as a force acting normal to the plate surface. Total work performed by this force undergoing a small out-of-plane defection increment dw is set to zero:

$$\iint_A \left[D_{(T)}\nabla^4 w - \frac{\partial^2\Phi}{\partial y^2}\frac{\partial^2(w+w_0)}{\partial x^2} - \frac{\partial^2\Phi}{\partial x^2}\frac{\partial^2(w+w_0)}{\partial y^2} + 2\frac{\partial^2\Phi}{\partial x\partial y}\frac{\partial^2(w+w_0)}{\partial x\partial y}\right] dwdxdy = 0$$
$$dw(x,y) = \sum_{i=1}^{n} dw_i f_i(x,y) \tag{7}$$

The undetermined coefficients w_i in Equation (7) can be obtained by a semi-numerical solution with successive approximations and optimization method. Detailed numerical codes have been developed by the authors using symbolic math function in the Matlab environment. From these analytical predictions, detailed second-order linear elastic analytical predictions have been derived and compared with numerical predictions in the following sections.

3.4 Analytical predictions for out-of-plane deflection

3.4.1 Accuracy Verifications for Analytical Predictions

To verify the proposed analytical approach, load-deflection characteristics of rectangular plates subjected to one-directional compression are first studied with various initial imperfection ratios. These results have been compared with analytical predictions by Williams and Walker [20], who first adopted perturbation method to study the pre- and post-buckling behaviour of isolated plate structures. With this method, an explicit load-deflection expression has been obtained for square plates loaded in one-directional compression. In order to incorporate the effect of initial imperfections, this perturbation method can be easily extended by using the findings by Dawson [21].Detailed comparisons among these three approaches are shown in Fig. 2. Two different case studies have been conducted, including both perfectly flat plates and initial imperfect plates with a maximum imperfection assumed as $w' = t/10$.

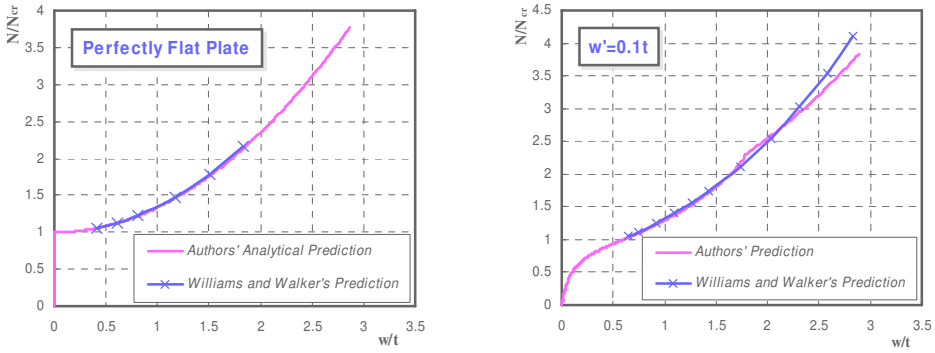

(a) (b)

Fig. 2-Comparisons between Different Analytical Approaches for One-Directional Compression

3.4.2 Analytical Predictions for Pure Shear Case

In this Section, the out-of-plane defection characteristics of plated structures under pure shear are first introduced, focusing on effects from various initial imperfection magnitudes. Three series of square plates (305 mm x 305 mm) with three different plate thicknesses as 1.5 mm, 2 mm and 2.7 mm (in accordance with unrestrained plate girder beam web panels tested by the authors), were examined with three initial imperfection magnitudes at normal temperature. As shown in Fig 3(a), it is clear that, for certain initial imperfection level, the curves for different plate thicknesses illustrate exactly the same dimensionless load-deflection behaviour, which can be proved by Equation (7). In addition, as shown in Fig. 3 (b), with a higher initial imperfection ratio ($w'=t/10$), 2.7 mm thick plate starts to buckle at a much lower shear load ratio compared with perfectly flat plates, or plates with small initial imperfections ($w'=t/1000$, $w'=t/100$). The transition between pre- and post- buckling stages for plates with larger initial imperfections, say $w'=t/10$, becomes much less distinguishable.

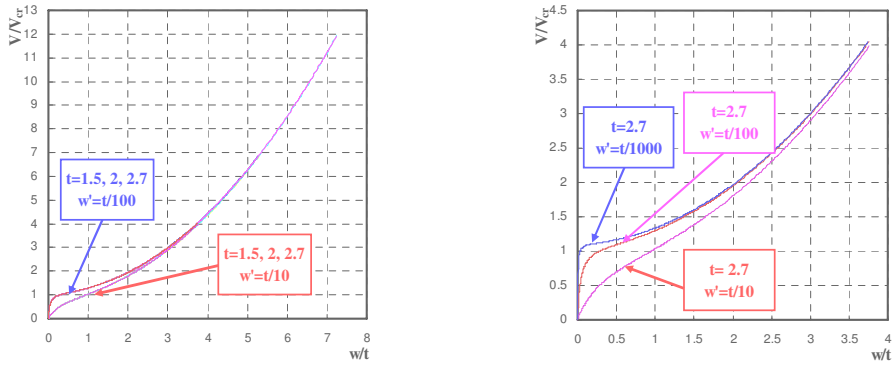

(a) (b)

Fig. 3-Non-Dimensional Load-Deflection Behaviour of Imperfect Plates under Pure Shear

Based on proposed analytical approach, load-deflection relationships of plates subjected to a combination of shear and compression stresses can be derived and compared with corresponding numerical simulations. Numerical investigations have also been conducted to verify the derived plate load-deflection behaviour. Simply-supported square plates with

different thicknesses and initial imperfections are simulated with commercial finite element (FE) software MSC.Marc [22]. An eight-noded shell element is used to simulate the plate, with initial imperfections applied exactly onto the mesh nodes. Square plates (305 mm x 305 mm, $\lambda = 1$) have been investigated to compare with numerical predictions at normal temperature. These analytical studies consist of web plates with three thicknesses of 1.5 mm, 2 mm and 2.7 mm and also with initial imperfection magnitude typically assumed as $w' = t/100$. For each plate model, two compression stress ratios were considered as $k = \sigma/\sigma_{cr} = 0.1$ and $k = \sigma/\sigma_{cr} = 0.3$ (σ_{cr} is the compressive buckling stress for simply supported plates under one-direction compression load presented by Timoshenko *et al.*, 1961), which were selected to ensure the plate fails predominantly due to shear. Typical comparisons between analytical and numerical predicted load-deflection curves are presented in Fig. 4 (a) and (b).

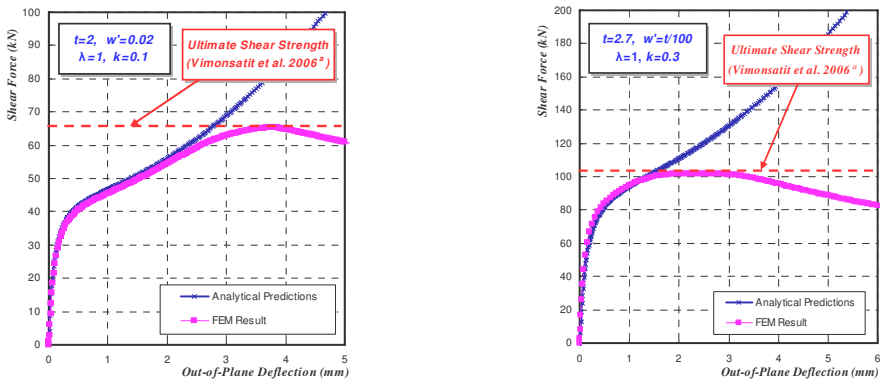

(a) (b)

Fig.4 Comparisons of Load-Deflection Behaviour between Numerical and Analytical Predictions for Square Plates under Combination of Shear and Compression

3.4.3Comparisons with Experimental Measurements

As a typical example, experimental out-of-plane deflection versus analytical predictions are presented in Figs. 5 (a) and (b) for TG4-4 (tested at 700 ^{o}C, with $w' \approx t/10$) and RTG4-4 (tested at 670 ^{o}C, with $w' \approx t/10$), respectively. The difference between the two tests was that the former was subjected to shear while the latter to shear and compression due to thermal restraints. Clearly, proposed second-order linear elastic theory slightly underestimates actual out-of-plane deflections, since the mechanical model neglects the boundary stiffening effect from top and bottom flanges. However, this analytical approach still gives reasonable agreement with test results. In addition to comparisons with analytical predictions, experimental measurements have also been compared with numerical simulations. It can also be observed that the FE simulations gave slightly conservative deflection characteristics prediction, which is due to difficulties in obtaining accurate temperature distribution. However, in general, the difference in ultimate shear strength prediction is small, indicating a good fit to test results.

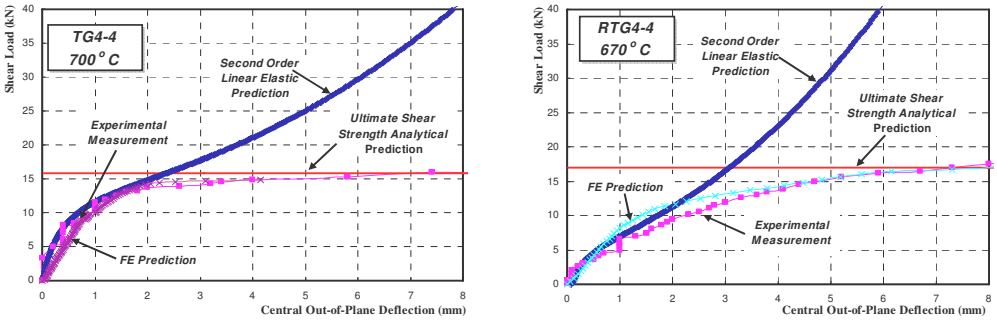

(a) (b)

Fig.5-Out-of-Plane Deflection Characteristics Comparisons between Experimental and Analytical Predictions

4. ANALYTICAL PREDICTIONS FOR PLATE IN-PLANE DEFLECTION

Based on theoretical plate investigations [1-4], the authors proposed a mechanical approach to predict the shear capacity of plate girders at elevated temperatures. In this approach, the overall behaviour of plated structures under shear can be divided into three stages, viz. *(1) Unbuckled*, *(2) Post-buckled*, and *(3) Collapsed stage*. Similar to the pre- and post-buckling shear strength investigations [6], development of in-plane deflection as shown in Fig. 6 (a) can be classified into two stages, that is, pre- and post-buckling stages as shown in Fig. 6 (b). This simple analytical model was improved by the authors, based on research works conducted by Kharrazi et al. [23] about bending and shear analysis of ductile steel plate walls.

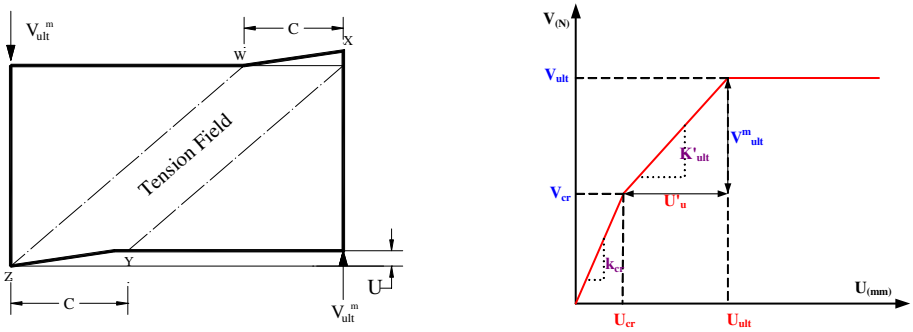

(a) (b)

Fig.6-In-Plane Deflection Development of Plate Girder Web Panel

4.1 Pre-buckling Stage

For plates subjected to shear or a combination of shear and compressive load, critical shear stress can be easily obtained at both normal and elevated temperatures [6]. Critical shear displacement U_{cr} as shown in Fig. 7 (b) can be obtained as:

$$U_{cr} = \tau_{cr} b / G_{(T)} = 2\tau_{cr} b(1+\nu) / E_{(T)} \quad (8)$$

4.2 Post-buckling Stage

After the plate starts to buckle, shear displacement $U_u^{'}$ from post-buckling component of shear force (as shown in Fig. 7 (b)) can be derived by equating work done from post-buckling shear force component with work done by normal stresses acting on flanges (internal work done at the four plastic hinge locations (W, X, Y and Z), as shown in Fig. 7 (a) plus strain energy of the tension field. This leads to the following formulation.

$$U_{ult} = \frac{\left(\sigma_t^y\right)^2 c^2 dt}{E\left(V_{ult}^m c - 4M_{pfr}\right)} + U_{cr} = \frac{\left(\sigma_t^y\right)^2 c^2 dt}{E\left(V_{ult}^m c - 4M_{pfr}\right)} + \frac{\tau_{cr} b}{G} \tag{9}$$

$$k_{cr} = \frac{G_{(T)} dt}{b} = \frac{E_{(T)} dt}{2b(1+\nu)} \qquad k_u^{'} = \frac{EV_{ult}^m \left(V_{ult}^m c - 4M_{pfr(T)}\right)}{\left(\sigma_t^y\right)^2 c^2 dt} \tag{10}$$

4.3 Experimental Verification of Analytical Predictions

Fig. 7 presents typical comparisons among analytical predictions, numerical simulations and test measurements for TG4-1 and TG4-2 tested at normal temperature and 400 ^{o}C, respectively. Numerical simulations in these comparisons consist of two different cases, viz. single web panel and whole beam FE predictions. At the first stage of FE analyses, only those buckled end web panels have been simulated separately, to eliminate influences from bending effects. At the second stage of FE analyses, in order to have a clear numerical representation of tested specimens, entire beam FE models have been constructed to represent whole tested plate girders. From comparisons as shown in Fig. 7, it is apparent that there exist slight discrepancies (approximate 0.3 mm and 0.2 mm for TG4-1 and TG4-2, respectively) between experimental measurements and analytical predictions for single web panel. This is because that current analytical approach only considers a plate subjected to shear or a combination of shear and compression forces. But, web panels of tested beams and FE simulations (whole beam FE prediction) were subjected to not only dominant shear force but also bending moment effects. However, analytical predictions are in reasonable agreement with single web panel FE prediction, in which only shear forces have been considered. Discrepancies between experimental measurements and whole beam FE predictions at initial loading stage (especially for TG4-1) were due to inevitable testing facility inaccuracies, viz. frictions at supporters, slight instabilities of deflection transducers at beginning of loadings, etc. These initial differences were very small, typically in the order of 0.2 mm, and can be easily deducted. Although there are still slight deviations between analytical predictions and experimental results, whole beam FE models still exhibit acceptable accuracy compared with these tests.

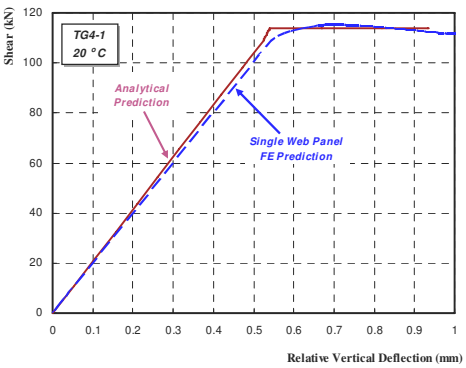

(a)

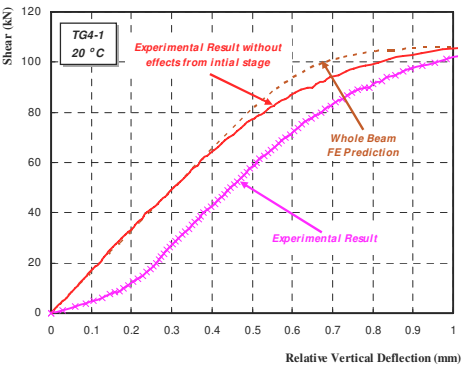

(b)

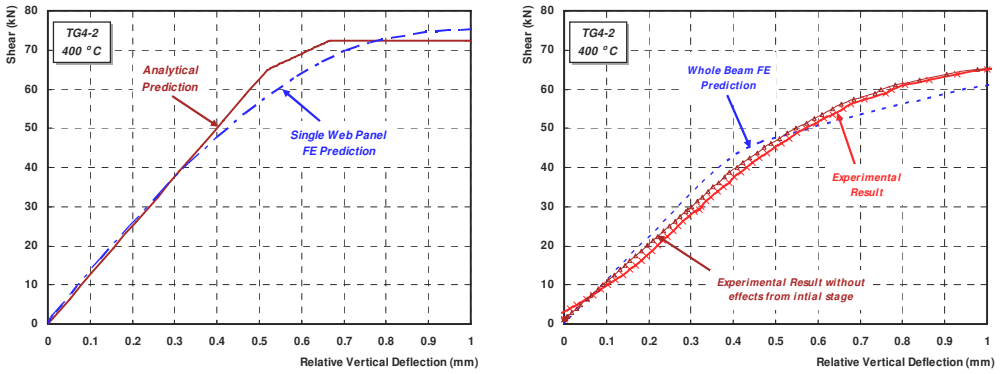

(c) (d)

Fig.7-In-Plane Deflection Characteristics Comparisons among Analytical Prediction, Experimental Measurements and Numerical Predictions

5. CONCLUSION

In this research, Galerkin's energy method has been applied to analyse deflection characteristics for simply-supported web plates of plate girders at elevated temperatures. With a combination of shear and compressive loads, investigated plates also exhibit similar load-deflection relationships compared with that of plates under pure shear, due to lower compressive stress ratios. Besides, a simple analytical approach has also been presented to depict in-plane deflection developments for web plates. Proposed analytical approaches for both out-of-plane and in-plane web plate deflection predictions have been verified by experimental measurements and numerical simulations.

REFERENCES

[1] Basler K, and Thurlimann B. Plate girder research. In proc. AISC National Engineering Conference 1959; New York.

[2] Rocky KC, and Skaloud M. The ultimate load behaviour of plate girders loaded in shear, The Structural Engineer, 1972; Vol.50, No.1, 29-47.

[3] Porter DM, Rockey KC, and Evans HR. The collapse behaviour of plate girders loaded in shear, The Structural Engineer, 1975; Vol. 53, No.8, 313-325.

[4] Rockey KC, Evans HR, and Porter DM. A design method for predicting the collapse behaviour of plate girders, Proceedings of the Institution of Civil Engineers; 1978; Part 2, 85-112.

[5] BS 5950: Part 1. Structural use of steelwork in building, Code of practice for design in simple and continuous construction: Hot rolled sections, British Standards Institution; 1990.

[6] Vimonsatit V, Tan KH, and Ting SK. Shear strength of plate girder web panel at elevated temperature, Journal of Constructional Steel Research 2007; Vol. 63 (11), 1442-1451.

[7] Vimonsatit V, Tan KH, and Qian ZH. Testing of plate girder web panel loaded in shear at elevated temperature, Journal of Structural Engineering ASCE 2007; Vol.133 (6), 815-824.

[8] Tan KH, and Qian ZH. Experimental behaviour of thermally restrained plate girder loaded in shear at elevated temperature, Journal of Constructional Steel Research, 2007; accepted with revisions.

[9] von Karman. Festigkeitsprobleme im maschinenbau, Encyklopadie der Mathematischen Wissenschaften, Vol. 4, B.G. Teubner, Leipzig, 1910.
[10] Marguerre K. Zur Theorie der gekrummmter plate grosser formanderug, Proc. Fifth int. Congress appl. Mech. 93, 1938.
[11] Levy S, and Greeman S. Bending with large deflection of a clamped rectangular plate with length width ratio of 1.5 under normal pressure, NACA, TN No.853, 1942.
[12] Green JR, and Southwell RV. Relaxation applied to engineering problems VIIIA: Problems relating to large transverse displacements of thin elastic plates, Phil. Trans., Serial. A. 59, 1946.
[13] Wang CT. Non-linear large deflection boundary value problems of rectangular plates, NACA, TN No.1425, 1948.
[14] Coan JM and Urbaba I. Large-deflection theory for plate with small initial curvature loaded in edge compression, Journal of Applied Mechanics, ASME, 1951; Vol.43, 143-151.
[15] Yamaki N. Post-buckling behaviour of rectangular plates with small Initial curvature loaded in edge compression, Journal of Applied Mechanics, 1959; Vol.26.
[16] Timoshenko SP, and Gere JM. Theory of elastic stability, (Second Edition), McGraw-Hill Book Company, New York, 1961.
[17] Rhodes J, and Harvey JM. The local buckling and post local buckling behaviour of thin-walled beams, The Aeronautical Quarterly, November, 1971.
[18] Fok CD. Effects of initial Imperfections on the elastic post-buckling behaviour of flat Plates, Ph.D. Thesis, Monash University, 1980.
[19] Zaras J, Rhodes J, and Krolak M. Buckling and post-buckling behaviour of rectangular plates under linearly varying compression and shear: Part 1-Theoretical analysis, Thin-Walled Structures, 1992; Vol. 14, 59-87.
[20] Williams DG, and Walker AC. Explicit solutions for the design of initially deformed plates subjected to compression, Proc. Inst. Civil Engineers, 1975; Vol.59, 763-787.
[21] Dawson RG. Local buckling of thin-walled structural forms, PhD Thesis, University of London, 1971.
[22] MSC. MARC User Guide Version 2001, MSC. Software Corporation, USA; 2001.
[23] Kharrazi MH, Ventura CE, and Prion HGL. Bending and shear analysis and design of ductile steel plate walls, 13th Word Conference on Earthquake Engineering, Vancouver, B.C., Canada, 2004.

FIRE PERFORMANCE OF STEEL BEAM-COLUMNS UNDER DESIGN FIRE EXPOSURES

MAHMUD DWAIKAT[1] and VENKATESH KODUR[2]

ABSTRACT

Restrained steel beams when exposed to fire develop significant restraint forces and often behave as beam-columns. The response of such restrained steel beams under fire depends on many factors including fire scenario, load level, degree of restraint at the supports, and high-temperature properties (including creep) of steel. A set of numerical studies, using finite element computer program ANSYS, is carried out to study the fire response of steel beam-columns under realistic fire, load and restraint scenarios. The finite element model is validated against experimental data, and the importance of high-temperature creep on the fire response of steel beam-columns is illustrated. The validated model is used to carry out a set of parametric studies. Results from the parametric studies indicate that fire scenario, load level, degree of end-restraint and high-temperature creep have significant influence on the behavior of restrained beams under fire conditions. Severe fires produce high axial forces at early stages of fire exposure, whereas in moderate fires, significant axial force develops only at later stages of fire exposure. Increased load level leads to higher catenary forces, resulting in lower fire resistance. Rotational restraint enhances the fire resistance of the laterally-unrestrained steel beam, while the axial restraint has detrimental effect on fire resistance. These numerical studies clearly indicate that the performance of restrained steel beams under design fire exposures is significantly different from that of "standard fire" exposures.

1. INTRODUCTION

Fire represents one of the most severe environmental conditions to which structures may be subjected, and hence, the provision of appropriate fire resistance is an important consideration

[1] PhD candidate, Michigan State University, Department of Civil and Environmental Engineering, email: dwaikat1@msu.edu.
[2] Professor, Michigan State University, Department of Civil and Environmental Engineering, email: kodur@egr.msu.edu.

in design of the buildings. Steel structural systems are quite frequently used in high-rise buildings due to high structural performance such as ductility and strength that steel can provide, compared to other materials. There are many drawbacks in the current approaches of evaluating fire resistance of steel members since these methods are based on "standard" conditions and do not account for "realistic" fire, loading and restraint scenarios. Thus, there is dearth of experimental data, mathematical models and design specifications for predicting the response of restrained steel beams under design fire scenarios.

Restrained steel beams, when exposed to fire, develop significant axial compressive force that results due to high thermal expansion of steel. This resultant axial compressive force, which can often reach 30% of the room-temperature axial capacity of the beam, transforms the behavior of the beam to that of a beam-column.

At ambient temperature, the axial force in a beam is negligible; therefore, the design capacity of the beam does not depend on the applied bending moment. However, for beams-columns, the design capacity depends on the interaction between the applied forces, and is generally expressed in terms of the bending moment and the axial force. The typical interaction relation between the applied forces and the resistive internal forces is expressed as:

$$\frac{P_u}{\Phi P_n} + c\frac{M_u}{\Phi M_n} \leq 1.0 \tag{1}$$

Where: P_u and M_u are the applied axial force and bending moment, ΦP_n and ΦM_n are the axial force and bending moment design capacities, and c is an interaction coefficient.

Under fire conditions, the axial force, P_u, in the restrained steel beam can be quite significant. This increased axial force can reduce the moment carrying capacity as can be seen from Eq. (1).

The resistive capacities and the developing internal forces of steel beam-column under fire conditions depend on the properties of steel, such as specific heat, thermal conductivity, thermal expansion, stress-strain curves, and high-temperature creep, which vary as a function of temperature. As an illustration, under high stress levels and high temperatures, creep effect becomes predominant, and significantly influences the fire response of steel structural members. In addition, fire scenario and degree of restraint which have significant influence on the fire resistance, also influences the extent of creep deformations.

A review of literatures indicates that there have been limited studies on the behavior of laterally unrestrained beams under fire conditions[1-5]. These studies mainly focused on evaluating the fire resistance of a steel beam under standard fire exposure, without any consideration to realistic fire scenarios. The effect of significant parameters, such as, fire scenario, end restraints, support conditions and high-temperature creep on the fire response of restrained beams were not fully investigated under design fire. Also, in most studies the rotational restraint, which is influenced by fire scenario, was assumed to remain constant during fire exposure.

In this paper, the effect of creep is incorporated in the analysis, and its influence on fire response of steel beams is illustrated by comparing predictions from the model with test data. The validated model is used to carry out a set of parametric studies to demonstrate the influence of various factors on the fire response of restrained beams.

2. NUMERICAL ANALYSIS

The analysis of the restrained beams was carried out using the general-purpose finite element software ANSYS, which is capable of handling thermal gradients and highly nonlinear structural problems. A steel space subframe was discretized with beam elements in ANSYS. Temperature-dependent thermal and mechanical properties of steel were incorporated in the analysis. The analysis was carried out by incorporating all significant parameters, namely; high-temperature creep, load level, degree of axial and rotational restraints, and fire scenarios. More information about the finite element analysis is provided in the following sections.

2.1 Thermal Analysis

The thermal analysis was carried out using two types of elements, namely PLANE55 and SURF151. PLANE55 was used as a plane element with two-dimensional thermal conduction capability. The element has four nodes with a single degree of freedom, temperature, at each node. The element is applicable to a two-dimensional, steady-state or transient thermal analysis. SURF151 element is generally used for various load and surface effect applications. In this study, SURF151 element is overlaid onto the face of PLANE55 2D thermal solid element to simulate the effect of thermal radiation from ambient air to steel section.

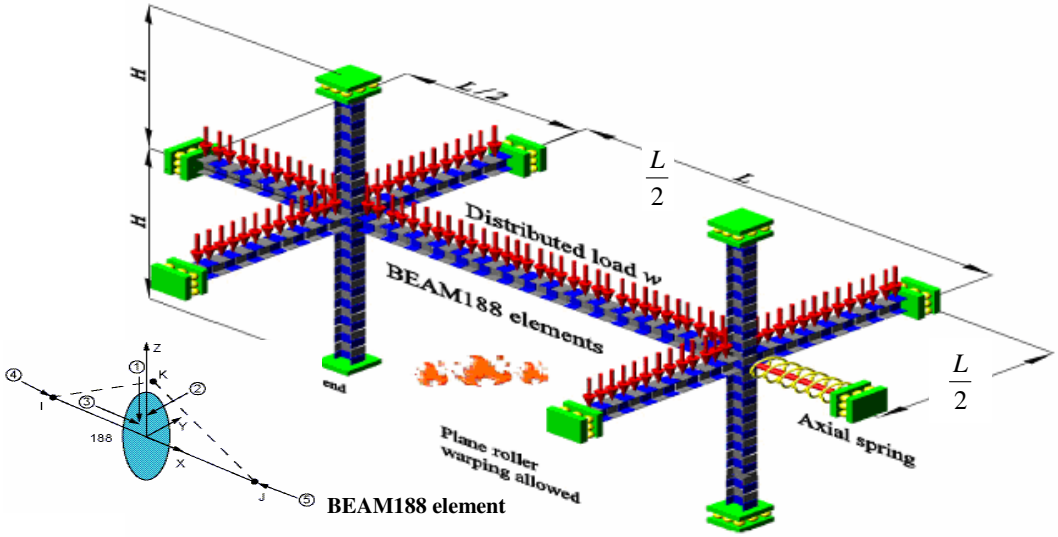

Fig. 1- Discretization of the steel subframe using BEAM188 elements

2.2 Structural Analysis

The structural analysis was carried out by discretizing the space subframe with BEAM188 elements. Fig. 1 shows discretization of a space subframe with the boundary conditions and applied loading. BEAM188 element, suitable for analyzing slender to moderately thick beam-column structures is based on Timoshenko beam theory and shear deformation

effects are taken into consideration. BEAM188 element supports 7 degrees of freedom per node; 3 translations and 3 rotations, in addition to a warping degree of freedom. This element is well-suited for nonlinear large strain applications; therefore, it is used to model the lateral torsional buckling of the members. BEAM188 element can account for non-uniform temperature distribution over either the length of the element and/or the cross-section of the element. Each member was meshed into 90 elements along its length.

To simulate partial resistance to horizontal elongation of beam due to thermal exposure, an axial spring was used to exert lateral resistance that is proportional to the lateral movement of the space subframe. Both the axial spring and the supporting columns, which are fixed at the bottom, provide a more realistic orientation for different types of end restraints. More details about the specifics of the end restraints are discussed in the subsequent sections.

2.3 Failure criteria

Since one of the main objectives of this study is to investigate the effect of high-temperature creep on the response of restrained steel beam, it was necessary to continue the analysis beyond traditional limiting criteria used to define failure, namely attaining a critical temperature in steel. Therefore, the failure criterion that was adopted in this study is based on overall instability failure in the beam-spring system. Energy-based stabilization techniques available in ANSYS were utilized to ensure convergence until overall stiffness of the system becomes negative, leading to instability failure in the steel beam. This failure criterion is more realistic than that based on critical temperature in steel, which has been used in most of the previous studies.

2.4 High-temperature material properties

In the analysis, high-temperature material properties specified in Eurocode[6] for structural steel are implemented. The creep model of ANSYS is used explicitly in the analysis to account for the creep deformations at high temperature. Nonlinear transient analysis was carried out since all material properties vary as a function of steel temperature.

Since the Eurocode provisions do not specify high-temperature creep properties for structural steel, ANSYS built-in "implicit creep model 11" was used to model the primary and secondary effects of creep. Equation 2 gives the two parts of the high-temperature creep model that was used in the finite element analysis.

$$\varepsilon_{\text{cr}} = \varepsilon_{\text{primary}} + \varepsilon_{\text{secondary}} = c_1 \sigma^{c_2} \frac{1}{c_3} t^{c_3} \exp(-\frac{c_4}{T_s}) + c_5 t \sigma^{c_6} \exp(-\frac{c_7}{T_s}) \quad (2)$$

where: $c_1 = 5\times10^{-6}$ per minute, $c_2 = 6.95$, $c_3 = -0.4$, $c_4 = 16500^{\circ}$C, $c_5 = 6.0\times10^{-6}$ per minute, $c_6 = 6\times10^{-5}$, $c_7 = 5\times10^{-3}{}^{\circ}$C, t = time (min), σ = steel stress (MPa), T_s = steel temperature (°C), and ε = steel strain.

Because of its anticipated significance, the creep material model was calibrated using two independent sets of creep material test data; namely, those published by Nippon Steel Corporation[7] for structural steel SM50A (equivalent to Grade 50 American structural steel), and those reported by Kirby and Preston[8, 9] for A36 steel. The results of calibration is shown in Fig. 2, which shows the comparison of high-temperature creep strain computed using Eq. (2) with that

of test data for various stress levels. It can be seen from Fig. 2 that creep strain can become very significant at high temperatures and increased stress levels. Also, the adopted creep model shows good agreement with the test data as plotted in Fig. 2 for both types of A36 and Grade 50 steel. The calibrated creep model of ANSYS was integrated into the finite element structural model.

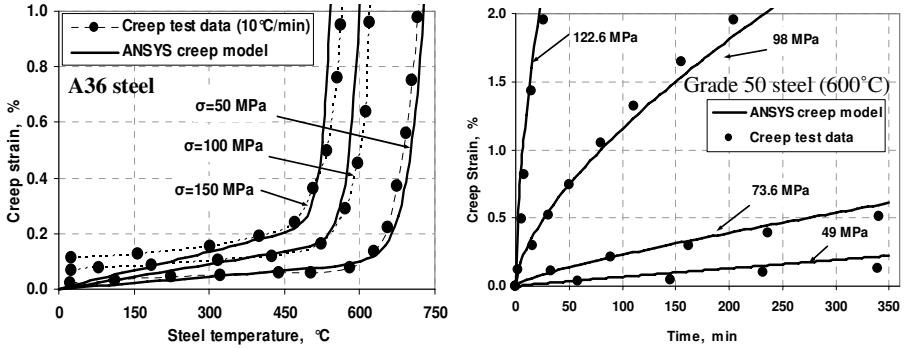

Fig. 2- High-temperature creep model for structural steel

3. MODEL VALIDATION

The ANSYS finite element model was validated by comparing the predictions from the analysis with test data reported in literature. The validation process covered both thermal and mechanical predictions from the analysis. In the reported experiments, unprotected, axially-restrained steel beams were tested under a random design fire scenario[10]. In the analysis, the beams were exposed to similar fire scenario from four sides, but with the top flange covered with heavy insulation to simulate three-side fire exposure (as in fire tests).

Fig. 3 shows the fire temperature and the resulting steel temperatures as predicted by the finite element model and measured in the test. It can be seen that the top flange experienced slow rise in temperature, while the web and bottom flange experienced faster increase in temperature. This is due to the heavy insulation that was applied to the top flange. As the fire entered the decay phase (at 19 minutes), the top flange continued to heat up while the temperature in rest of the section started to decrease. It can be seen in the Fig. that the temperature predicted from the analysis compare well with measured data from test. The result of the thermal analysis was applied as a body thermal load on the finite element structural model.

To illustrate the significance of high-temperature creep, the analysis was carried out for two cases, one including creep and the other without accounting for creep. Fig. 3 shows comparison of measured and predicted mid-span deflection and the axial restraint force in the steel beam. Overall, predictions from the model match well with test data when high-temperature creep is included in the analysis. It can be seen in Fig. 4 that the high-temperature creep has a significant effect on the deflections and fire induced axial force, especially towards the later stages of fire exposure. When the creep effect is not included, the predicted deformations and restraint forces are under-predicted in the later stage of fire exposure. Therefore, neglecting high-temperature creep in the analysis can lead to inaccurate predictions of both deflection and fire induced restraint force.

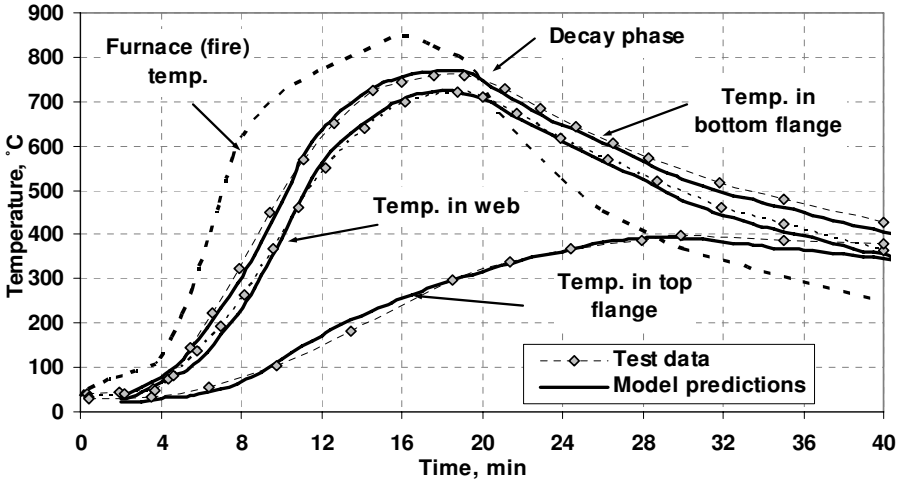

Fig. 3 - Predicted and measured temperatures in the steel beam

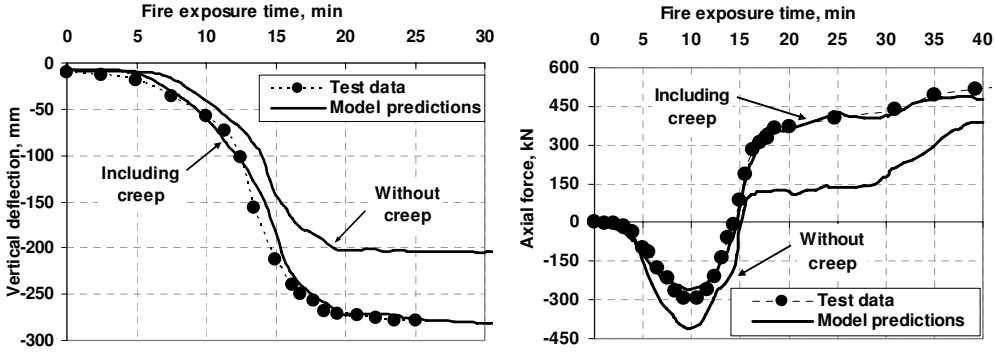

Fig.4- Predicted and measured deflection and restraint force as a function of fire exposure time

4. PARAMETRIC STUDY

The validated finite element model was used to investigate the influence of significant parameters on the response of unprotected, laterally-unrestrained, but axially and rotationally restrained steel beams under fire. In the parametric study, the main beam and the supporting columns in the steel subframe (shown in Fig. 1) were exposed to fire from three sides. The factors considered in the parametric study are: high-temperature creep, load level, degree of end-restraint, and fire scenario.

4.1 Effect of creep and load level

It is well known that creep, at room temperature, influences the behavior of steel structures, however, at elevated temperatures creep becomes a dominant factor and significantly affects the response of steel structures. This was seen in the previous section (Fig. 4), which

illustrated a significant deviation in the fire response of steel beam when high-temperature creep was not considered in the analysis. To further study the effect of creep, a restrained steel beam (W24X76) of span 7m, and supported on columns (W12X79) of height 4m (see Fig. 1), was analyzed under varying load levels and under ASTM E119 fire exposure[11]. The deflection and fire induced restraint forces are plotted in Fig. 5(a) and (b) for three load levels (30%, 40% and 60%) and for two cases; creep effect included and creep effect excluded. The load level (as seen in Fig. 1) represents the ratio of the applied distributed load to the load corresponding to room-temperature capacity of the steel subframe. Results from the analysis are presented in Fig. 5, which shows the effect of load level on the fire response of restrained steel beam. Higher load ratios induce higher mechanical stresses in the steel; therefore, high-temperature creep produces higher strain, leading to increased deflection in the beam.

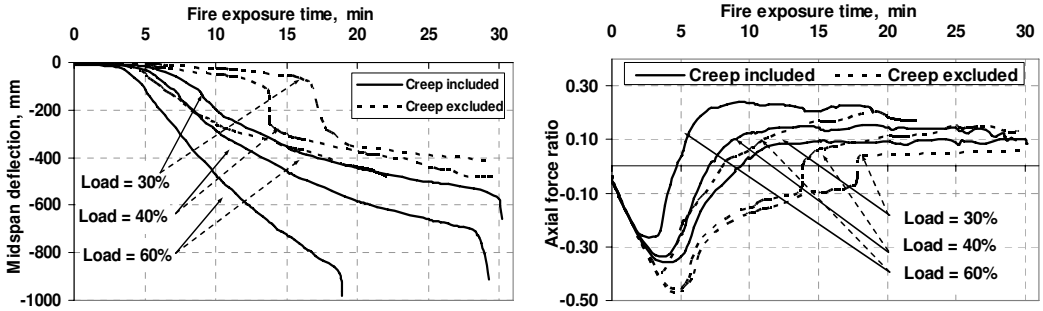

(a) Mid-span deflection (b) Fire induced axial force

Fig.5- Effect of creep on the fire response of restrained steel beam with increasing load level

4.2 Effect of end restraints

4.2.1 Effect of axial restraint

To study the effect of restraint on the fire response, a laterally-unrestrained steel beam within the space subframe was subjected to two types of restraints at its ends, namely, axial and rotational restraints. In order to better represent the practical scenarios, the axial restraint was considered from two components. The first component is the one arising from flexural rigidities of the supporting columns, while the second component is that resulting from the lateral stiffness provided from the adjacent subframes. To simulate this effect, an axial spring was used to represent the lateral stiffness from the adjacent subframes (see Fig. 1). The stiffness of the spring, k_s, was computed as:

$$k_s = \alpha(E\ A/L)_{Beam} \tag{3}$$

Where α is axial spring stiffness parameter, E_o, A and L are room-temperature elastic modulus of steel, cross-sectional area and span length of the beam, respectively. The value of α was varied to arrive at different values of the spring stiffness k_s.

Fig. 6 shows the effect of restraining axial stiffness (of the lateral spring) on the fire response of a laterally-restrained beam. The variation of deflection (Fig. 6(a)) and axial force ratio (Fig. 6(b)) is plotted as a function of fire exposure time for various values of axial spring stiffness (α). The trends in Fig. 6(b) indicate that an increase in the axial restraint (α) is accompanied by an increase in the resulting compressive axial force. The peak values of the axial force occur at early stages of fire exposure, and the resulting force is higher for larger values of α. The axial force, resulting from restraint effect, tends to increase the second order moment at the mid-span because of the P-δ effect. The higher moment will increase the curvature at the mid-span, and hence will further increase the deflection of the beam as can be seen in Fig. 6(a). However, as the vertical deflection increases, and the strength of the beam deteriorates (due to degradation of steel properties at elevated temperature), the fire induced axial force becomes completely tensile (Fig. 6(b)). Therefore, at this stage, the effect of the restraining axial stiffness becomes favorable. This is seen in Fig. 6(a), where the mid-span deflection becomes smaller with increasing axial restraint on the onset of catenary action.

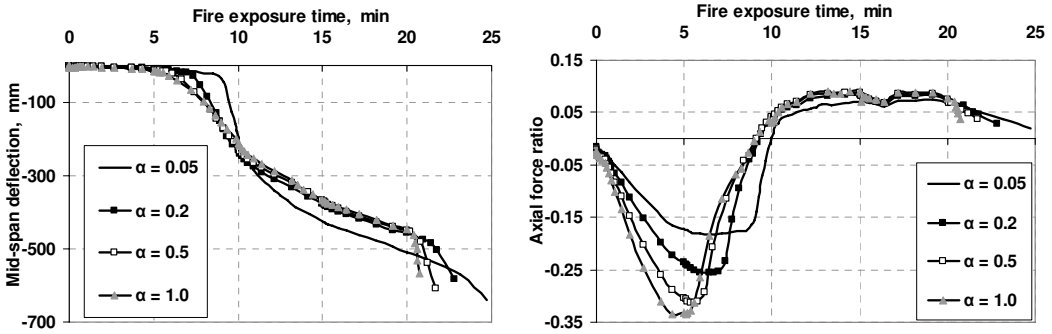

(a) Mid-span deflection (b) Fire induced axial force

Fig.6- Effect of restraining axial stiffness on the fire response of laterally-unrestrained beams

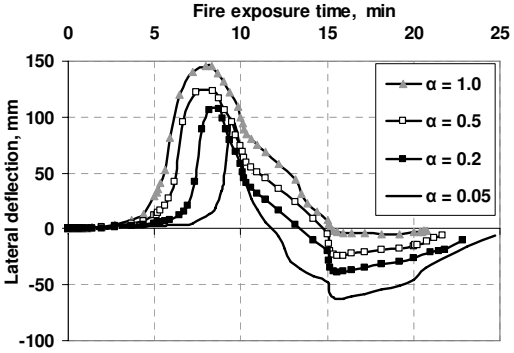

Fig.7- Effect of the restraining axial stiffness on the lateral deflection of the laterally-unrestrained steel beam

Fig. 7 shows the effect of the axial restraint on the lateral deflection of the restrained beam. The axial restraint tends to increase the lateral deflection at early stages of fire exposure. This can be explained by the fact that higher degree of axial restraint produces large value of

compressive force in the beam under fire (see Fig. 6(b)). Therefore, the beam acts like a beam-column under fire induced axial force, and tends to buckle in the lateral direction. However, at later stages of fire exposure, the lateral deflection of the beam at mid-span subsides due to the development of catenary forces.

4.2.1 Effect of rotational restraint

The effect of rotational restraint was investigated by considering the rotational stiffness from the columns in a space subframe (see Fig. 1). The magnitude of this rotational restraint varies as a function of fire exposure time due to the degradation in stiffness properties of the columns. Therefore, the rotational restraint on the beam is not constant and is affected by fire scenario. To quantify the effect of rotational restraint on the laterally-unrestrained steel beam, a parameter β was varied such that:

$$\beta = \sum\left(\frac{E\ I}{H}\right)_{column} \Big/ \sum\left(\frac{E\ I}{L}\right)_{Beam} \tag{4}$$

Where β represents a measure of rotational restraint, E_o, I, L and H are room-temperature elastic modulus of steel, second moment of area of the relevant section, beam span and column length, respectively.

Results from the analysis are plotted in Fig. 8(a) and (b) to illustrate the effect of rotational restraint on mid-span deflection and fire induced axial force. It can be seen in Fig. 8(a), that the rotational restraint slightly enhances the fire response of the beam. This enhanced behavior under fire can be attributed to the fact that higher rotational restraint (β) leads to higher stiffness of the beam. Therefore, the deflection remains smaller for prolonged fire exposure duration until significant degradation in the steel properties occurs, after which large deflection occurs leading to failure.

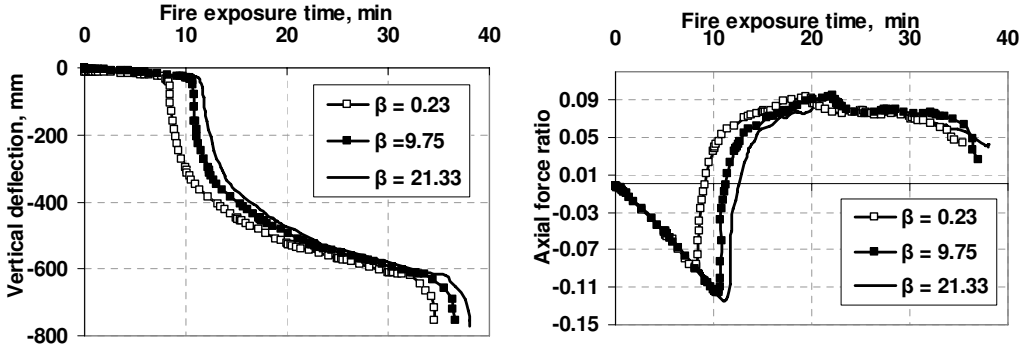

(a) Mid-span deflection (b) Fire induced axial force

Fig.8- Effect of pure rotational restraint on the laterally-unrestrained beam under fire

However, the thermally-induced axial force increases with the increase in the rotational restraint at the supports as can be seen in Fig. 8(b). This can be thought of as a direct consequence of the reduction in the mid-span deflection of the beam. With reduced deflection, due to increased rotational restraint, the *P-δ* effect will be smaller at later stages of fire exposure.

This leads to the development of higher axial force due to expansion before switching to catenary action. Therefore, the peak value of the fire induced axial compressive force (negative value) occurs at later stage of fire exposure time as seen in Fig. 8(b). Consequently, the mid-span deflection reaches values that are large enough to cause lateral buckling in the beam (see Fig. 9) and this leads to development of catenary action.

The lateral torsional buckling (LTB) resistance of the beam is enhanced under fire with the increased rotational restraint. This can be seen from Fig. 9, which shows the effect of rotational restraint on the lateral deflection of the restrained beam. This enhanced LTB resistance can be attributed to the fact that rotational restraint causes an increase in the support moment and a corresponding decrease in the mid span moment. Therefore, the compressive stresses in the top flange, which causes the buckling in the mid span zone, are reduced with increased rotational restraint (β). This can be seen in Fig. 9 where the buckling occurs more quickly when rotational restraint is reduced.

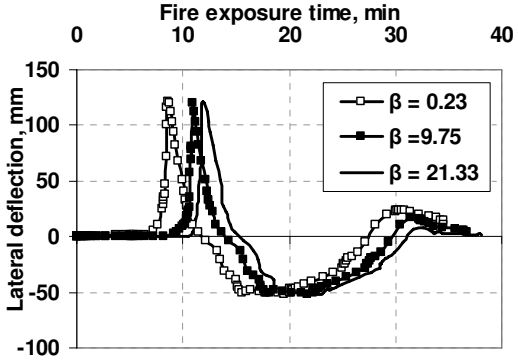

Fig.9- Effect of pure rotational restraint on lateral deflection of beam

4.3 Effect of fire scenario

To study the influence of fire scenario on response of restrained beam, three types of fire exposures were selected for analysis, namely: ASTM E119 standard fire[11], design fire I and design fire II. The time-temperature curves for the three fire scenarios are shown in Fig. 10. ASTM E119 scenario, which does not have a decay phase, represents a baseline case for comparing the response of the steel subframe under different fire scenarios. The other two fire scenarios, selected from the Eurocode parametric fires, have well-defined decay phase. Design fire I represents moderate fire exposure, whereas design fire II represents a severe fire scenario with steeper growth and decay phase and higher peak temperature.

Results from the analysis are presented in Fig. 11(a) and (b) to illustrate the effect of fire scenario on beam-column response. It can be seen that the resulting mid-span deflection and the axial restraint force are dependent on the fire scenario. The laterally-unrestrained beam in the space subframe experiences failure under ASTM E119 fire, while no failure occurs in the beam under design fire scenarios. Also, for the case of severe fire scenario (design fire II), large deflection occurs within the short growth phase of the fire, as seen in Fig. 11(a).

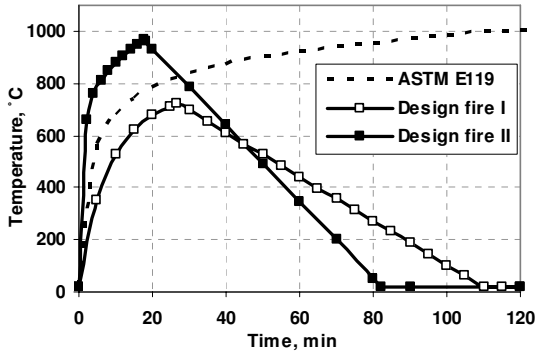

Fig.10- Fire scenarios used in the analysis

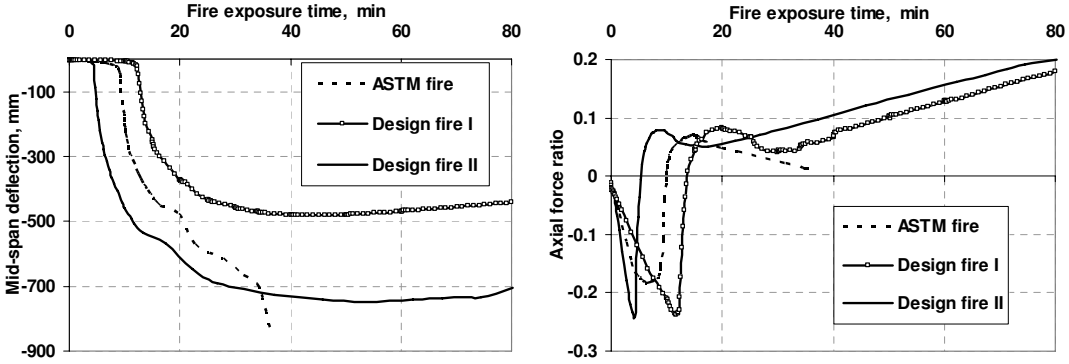

(a) Mid-span deflection (b) Fire induced axial force

Fig.11- Effect of fire scenario on the response of laterally-unrestrained steel beam in a space subframe

The fire induced axial restraint force follow similar trend in the case of the two design fires, but with peak values occurring at different fire exposure times as can be seen in Fig. 11(b). This is a direct consequence of the fact that in the design fire II the peak temperature is attained at earlier times, compared to design fire I. Thus, axial restraint compressive force due to thermal expansion of steel develops at earlier stages of exposure under design fire II. However, the restraint axial tensile force increases when the beam enters the decay phase, as seen in Fig. 11(b). This is because steel regains much of its strength upon cooling (as a result of decay phase in design fire I and II), and starts to contract in cooling phase. In the case of ASTM E119 standard fire scenario, mid-span deflection continues to increase with temperature due to the absence of decay phase. Therefore, the beam attains failure quickly under ASTM E119 fire exposure.

5. CONCLUSIONS

A laterally-unrestrained steel beam confined within a space subframe can develop significant axial restraint force when subjected to fire. This axial force alters the behavior of a beam to that

of a beam-column. Based on the results of parametric studies presented in this paper, the following conclusions can be drawn:

- High-temperature creep has a significant influence on the fire response of restrained steel beams. Therefore, the creep effects have to be properly accounted in the analysis to obtain realistic response of beams under fire conditions.
- The load level influences the fire response of a restrained steel beam. Higher load levels lead to smaller axial compressive forces due to the accelerated development of catenary action.
- Increased axial restraint has detrimental effect on fire response of restrained beam as it generates higher axial compressive force. Such large axial compressive forces lead to lateral buckling, which in turn leads to larger deflections.
- The rotational restraint can enhance the fire response of steel beams.
- Fire scenario plays a significant role in determining the response of restrained steel beams. Severe fires produce high axial forces at early stages of fire exposure, whereas in moderate fires, significant axial force develops only at later stages of fire exposure.

6. ACKNOWLEDGMENT

The research presented in this paper is supported by the National Science Foundation (Grant No. 0652292) and Department of Commerce/National Institute of Standards and Technology (Grant No. 60NANB7D6120). Any opinions, findings, and conclusions or recommendations expressed in this paper are those of the authors and do not necessarily reflect the views of the sponsors.

7. REFERENCES

[1] Bailey, C.G., I.W. Burgess, and R.J. Plank, *The lateral-torsional buckling of unrestrained steel beams in fire.* Journal of Constructional Steel Research, 1996. 36(2): p. 101-119.

[2] Tan, K.-H. and Z.-F. Huang, *Structural responses of axially restrained steel beams with semirigid moment connection in fire.* Journal of Structural Engineering, 2005. 131(4): p. 541-551.

[3] Vila-Real, P.P.M., et al., *Parametric analysis of the lateral-torsional buckling resistance of steel beams in case of fire.* Fire Safety Journal, 2007. 42: p. 416-424.

[4] Wang, Y.C. and Y.Z. Yin, *A simplified analysis of catenary action in steel beams in fire and implications on fire resistant design.* Steel and Composite Structures, 2006. 6(5): p. 367-386.

[5] Yin, Y.Z. and Y.C. Wang, *Numerical simulations of the effects of non-uniform temperature distributions on lateral torsional buckling resistance of steel I-beams.* Journal of Constructional Steel Research, 2003. 59: p. 1009-1033.

[6] EN1993-1-2, *The European standard; Part 1-2: General rules - Structural fire design.* European Committee for Standardization, Brussels, 2005.

[7] NKK, *Fire-Resistant Steel for Building Structural Use*. 1989, Nippon Steel Corporation: Tokyo.

[8] Kirby, B.R. and R.R. Preston, *High temperature properties of hot-rolled, structural steels for use in fire engineering design studies.* Fire Safety Journal, 1988. 13: p. 27-37.

[9] Buchanan, A.H., *Structural design for fire safety*. 2002, Chichester,England: John Wiley & Sons Ltd.

[10] Li, G.-Q. and S.-X. Guo, *Experiment on restrained steel beams subjected to heating and cooling.* Journal of Constructional Steel Research, 2007. In Press.

[11] ASTM, *Standard methods of fire test of building construction and materials: Test method E119-01*. 2001, American Society for Testing and Materials: West Conshohocken, PA.

DUPLEX STAINLESS STEEL COLUMNS AND BEAM-COLUMNS IN CASE OF FIRE

Nuno LOPES[1]; Paulo VILA REAL[2];
Luís SIMÕES da SILVA[3] and Jean-Marc FRANSSEN[4]

ABSTRACT

It is the purpose of this paper to evaluate the accuracy and safety of the currently prescribed design rules in Eurocode 3: Part 1.2 for the evaluation of the resistance of duplex stainless steel columns and beam-columns. This evaluation is carried out by performing numerical simulations on Class1 and Class 2 stainless steel H-columns. These numerical simulations are performed using the program SAFIR.

Eurocode 3 states that stainless steel structural members, subjected to high temperatures, must be designed with the same formulae used for carbon steel members. However, as these two materials have different constitutive laws, it should be expected that, different formulae for the calculation of member stability should be used for fire design.

It is considered buckling in the two main cross-section axis, and, in the case of the beam-columns, different bending moment diagrams.

Parametric studies of the behaviour of the duplex EN 1.4462 stainless steel grade (austenitic-ferritic in Eurocode 3) columns and beam-columns subjected to fire are presented.

[1] Research Assistant, LABEST - University of Aveiro, Department of Civil Engineering, 3810-193 Aveiro, Portugal,
email: nuno.lopes@ua.pt.
[2] Professor, LABEST - University of Aveiro, Department of Civil Engineering, 3810-193 Aveiro, Portugal,
email: pvreal@ua.pt.
[3] Professor, ISISE - University of Coimbra, Dep. Civil Engineering, 3030 Coimbra, Portugal,
email: luisss@dec.uc.pt.
[4] Professor, ArGEnCo, University of Liege, Belgium
email: jm.franssen@ulg.ac.be.

1. INTRODUTION

The stainless steels can be subdivided in five basic groups, according to their metallurgical structure: the austenitic, ferritic, martensitic, duplex austenitic-ferritic and precipitation-hardening groups [1]. The austenitic stainless steels give good combination of corrosion resistance, forming and fabrication properties. The duplex stainless steels have high strength and wear resistance with very good resistance to stress corrosion cracking. The most commonly used grades, for structural applications, are the austenitics 1.4301 (widely known as 304) and 1.4401 (widely known as 316). However increasing interest in duplex steels has been recently noticed due to its low cost. The high final cost of the austenitic stainless steel is due to the price of nickel. Typically they contain 8.0-13.0% of nickel whereas duplex stainless steels contain a lower nickel level. The stainless steel 1.4462 studied in this work contains 4-5%.

The use of stainless steel is increasing however it is still necessary to develop the knowledge of its structural behaviour. Stainless steels are known by their non-linear stress-strain relationships with a low proportional stress and an extensive hardening phase. There is not a well defined yield strength, being usually considered for design at room temperature the 0.2% proof strength, $f_y=f_{0.2proof}$.

The EN 1993-1-4 "Supplementary rules for stainless steels" [2] gives design rules for stainless steel structural elements at room temperature, and only makes mention to its fire resistance by referring to the fire part of the Eurocode 3, EN 1993-1-2 [3]. In a fire situation higher strains than at room temperature are acceptable, so Part 1.2 of Eurocode 3 suggests the use of the stress at 2% total strain as the yield stress at elevated temperature θ, $f_{y,\theta}=f_{2,\theta}$, for Class 1, 2 and 3 cross-sections and $f_{y,\theta}=f_{0.2proof,\theta}$, for Class 4. Comparison of the reduction of strength and elastic stiffness of structural carbon steel and stainless steel at elevated temperature for several grades of stainless steels (as defined in EN 1993-1-2 [3]) is shown in figure 1, where $k_{y,\theta}=f_{y,\theta}/f_y$ and $k_{E,\theta}=E_\theta/E$, being $f_{y,\theta}$ and f_y the yield strength at elevated temperature and at room temperature respectively, and E_θ and E the modulus of elasticity at elevated temperature and at room temperature.

The stainless steel mechanical and thermal properties at high temperatures, used in this paper, can be found in Part 1.2 of Eurocode 3 [3]. For the evaluation of the yield strength reduction factor, the Eurocode states that the following equation should be used:

$$k_{y,\theta} = \frac{f_{y,\theta}}{f_y} = \left[f_{0.2p,\theta} + k_{2\%,\theta}\left(f_{u,\theta} - f_{0.2p,\theta}\right)\right]\frac{1}{f_y} \quad (1)$$

where $f_{0.2p,\theta}$ is the proof strength at 0.2% plastic strain, at temperature θ, $k_{2\%,\theta}$ is the correction factor for determination of the yield strength $f_{y,\theta}$ and $f_{u,\theta}$ is the ultimate tensile strength, at temperature θ.

Despite both carbon and stainless steel exhibiting different constitutive laws, whereby stainless steel presents a pronounced non-linear behaviour even for low stress values, the stainless steel design rules are based on those developed for carbon steel. In a previous paper [4] a new proposal for the flexural buckling of austenitic grades stainless steel columns was made. In the present paper a similar study is made for the duplex stainless steel grade 1.4462 (the only austenitic-ferritic stainless steel presented in Part 1.2 of the Eurocode 3).

The reduction of the yield strength and the reduction of the modulus of elasticity (see figure 1) are used in the determination of the non-dimensional slenderness at high temperatures, as it will be shown later in this work.

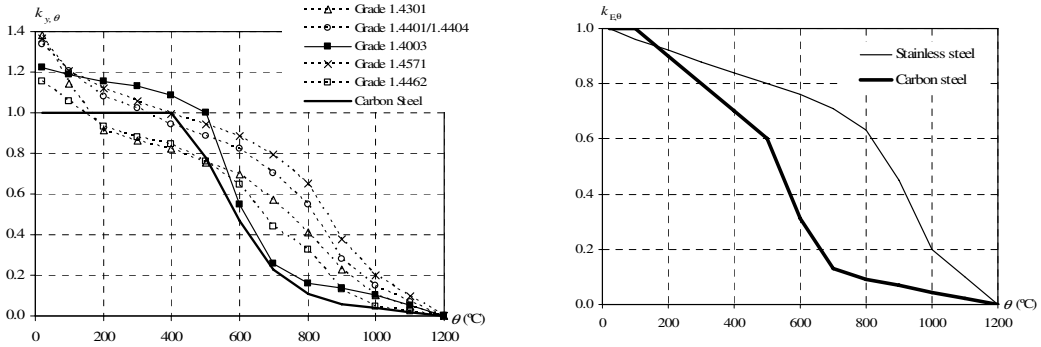

a) Strength reduction b) Elastic stiffness reduction

Fig. 1 – Mechanical properties at high temperatures.

The program SAFIR [5], a geometrical and material non linear finite element code, which has been adapted according to the material properties defined in EN 1993-1-4 [2] and EN 1993-1-2 [3], to model the behaviour of stainless steel structures [6], has been used in the numerical simulations. This program, widely used by several researchers, has been validated against analytical solutions, experimental tests and numerical results from other programs, and has been used in several studies that lead to proposals for safety evaluation of structural elements, already adopted in Eurocode 3.

The objective of the study presented in this paper is to evaluate the accuracy of the flexural buckling design procedures for columns and of the interaction between the axial compression and bending in beam-columns, prescribed in Eurocode 3, for welded I cross-sections in stainless steel grade 1.4462, at high temperatures. This study concluded that the Eurocode 3 formulae need to be improved and new proposals are made.

The equivalent welded HEB 200 cross-section of the Austenitic-ferritic stainless steel grade 1.4462 was used in the numerical simulations. It was studied the possibility of buckling around the weak axis (*zz*) and around the strong axis (*yy*).

For the columns the temperatures chosen were 400, 500, 600 and 700 ºC, deemed to cover the majority of practical situations, for the beam-columns it was chosen 600ºC. A uniform temperature distribution in the cross-section was used so that comparison between the numerical results and the Eurocode could be made. In the numerical simulations, a sinusoidal lateral geometric imperfection was considered [4]. The adopted residual stresses follows the typical pattern for carbon steel welded sections [4, 7, 8], considered constant across the thickness of the web and flanges.

2. FLEXURAL BUCKLING OF STAINLESS STEEL COLUMNS IN CASE OF FIRE

2.1 Formulae from Eurocode 3

For stainless steel structural elements subjected to high temperatures, Part 1.4 of Eurocode 3, refers that the same formulation prescribed for carbon steel elements should be used, following EN 1993-1-2 [3], where the flexural buckling resistance for class 1, 2 and 3 sections, is given by

$$N_{b,fi,t,Rd} = \chi_{fi} A k_{y,\theta} f_y \frac{1}{\gamma_{M,fi}} \quad (2)$$

where χ_{fi} is given by

$$\chi_{fi} = \frac{1}{\phi_\theta + \sqrt{\phi_\theta^2 - \bar{\lambda}_\theta^2}} \tag{3}$$

with

$$\phi_\theta = \frac{1}{2}\left[1 + \alpha\bar{\lambda}_\theta + \bar{\lambda}_\theta^2\right] \tag{4}$$

In this expression, the imperfection factor α depends on the steel grade and is determined with

$$\alpha = 0.65\varepsilon \tag{5}$$

where ε is given in part 1.1 of Eurocode 3 [9] as

$$\varepsilon = \sqrt{235 / f_y} \tag{6}$$

The imperfection factor is then given by

$$\alpha = 0.65\sqrt{235 / f_y} \tag{7}$$

The normalized slenderness for buckling at high temperatures is given by

$$\bar{\lambda}_\theta = \bar{\lambda}\left[\frac{k_{y,\theta}}{k_{E,\theta}}\right]^{0.5} \tag{8}$$

As it can be observed, in figure 2, the curve resulting from the Eurocode 3 is not on the safe side, when the buckling of an HEB200 profile is compared with the numerical values.

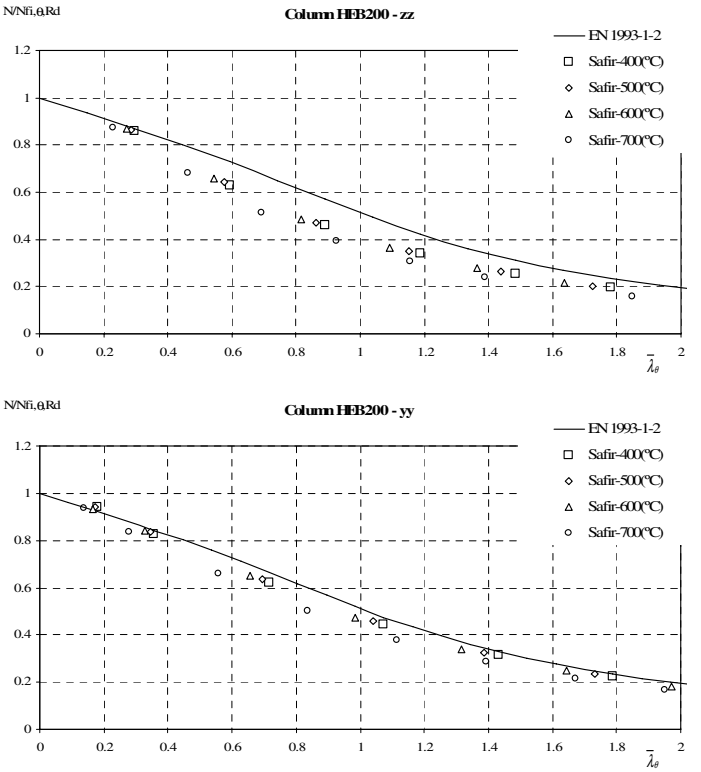

Fig. 2 – Flexural buckling at high temperatures for the stainless steel grade 1.4462 (Duplex)

2.2 Proposals for the austenitic-ferritic grade (Duplex)

To improve the accuracy of the design curve from Eurocode 3, bringing it down, a new reduction factor χ_{fi} is proposed according to [4]

$$\chi_{fi} = \frac{1}{\phi_\theta + \sqrt{\phi_\theta^2 - \gamma \bar{\lambda}_\theta^2}} \tag{9}$$

with

$$\phi_\theta = \frac{1}{2}\left[1 + \alpha \bar{\lambda}_\theta + \gamma \bar{\lambda}_\theta^2\right] \tag{10}$$

where the factor γ should take the value 1.5.

A new imperfection factor α as function of a severity factor β, is used, based on equation (5)

$$\alpha = \beta \varepsilon \tag{11}$$

and using ε given in part 1.4 of the Eurocode 3

$$\varepsilon = \sqrt{\frac{235}{f_y}\frac{E}{210000}} \tag{12}$$

The imperfection factor can be written in function of the temperature as

$$\alpha = \beta \sqrt{\frac{235}{f_y}\frac{E}{210000}}\sqrt{\frac{k_{E,\theta}}{k_{y,\theta}}} \tag{13}$$

The proposal for the value of the factor β to be used with equation (13) is $\beta = 0.8$. This proposal is shown in figure 3.

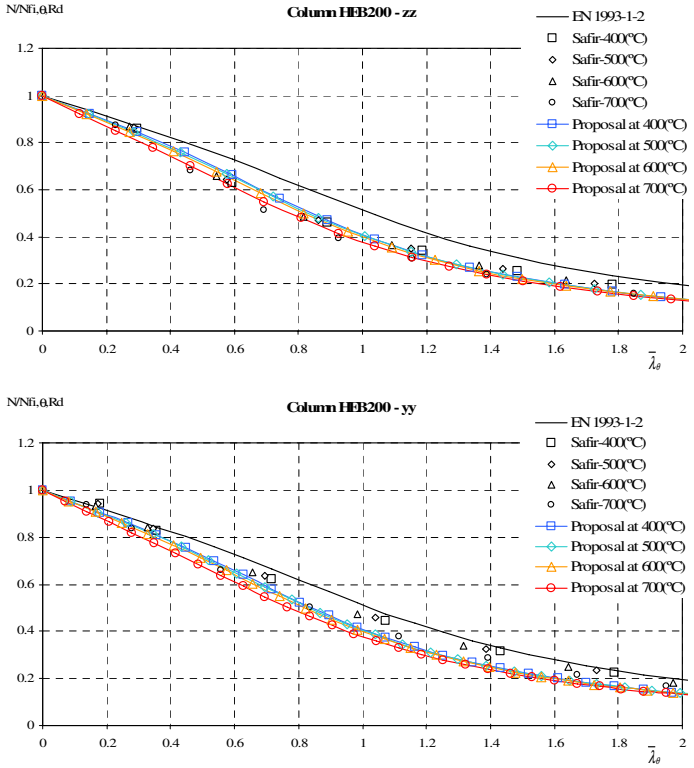

Fig. 3 – Proposed buckling curves for the duplex.

Although it is more accurate, to avoid the use of an imperfection factor depending on the temperature, it is proposed to use equation (11) with ε defined by equation (6) and $\beta = 1.0$. This proposal is called "New proposal" and is shown in figure 4.

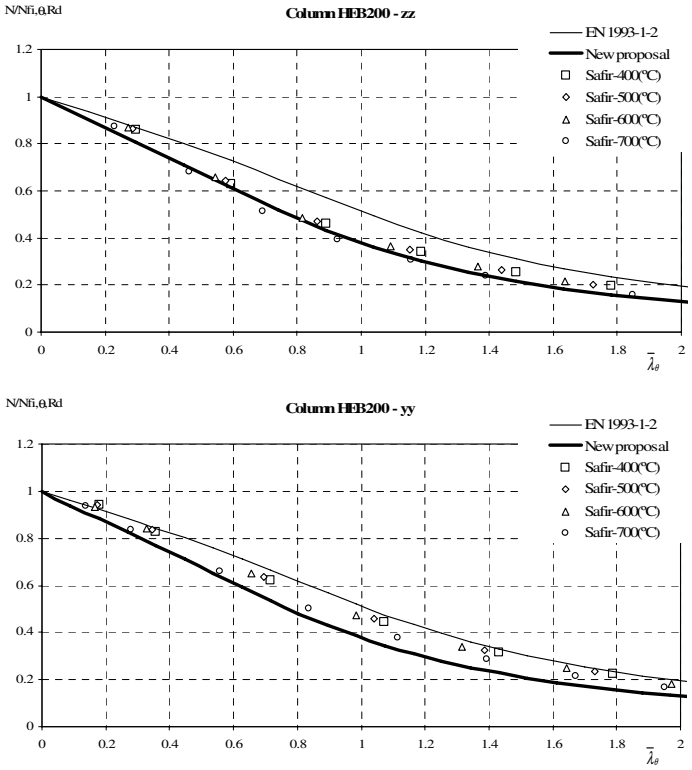

Fig. 4 – Proposed buckling curves for the duplex.

3. DUPLEX BEAM-COLUMN DESIGN IN CASE OF FIRE

In this section a study of the fire resistance of duplex stainless steel beam-columns is made. It is shown an evaluation of the performance of the interaction curves obtained with part 1.2 of Eurocode 3 [10], this study concluded that these interaction curves don't provide a good approximation to the numerical results obtained with SAFIR. Therefore it was necessary to find other curves that could fit better these numerical results.

The proposal made in section 2 of this paper for the fire resistance of duplex stainless steel columns will be taken into account and the letters "NP" will be added to the legend of the charts when it is used.

3.1 Eurocode 3 proposals for fire situation

The Eurocode 3 states that the safety evaluation should be made with the same expressions used in carbon steel elements, which are

$$\frac{N_{fi,Ed}}{\chi_{i,fi} A k_{y,\theta} \dfrac{f_{y,\theta}}{\gamma_{M,fi}}} + k_i \frac{M_{i,fi,Ed}}{W_{pl,i} \dfrac{f_{y,\theta}}{\gamma_{M,fi}}} \le 1 \tag{14}$$

where, $i = y$ or z, and

$$k_i = 1 - \frac{\mu_i N_{fi,Ed}}{\chi_{i,fi} A k_{y,\theta} \dfrac{f_y}{\gamma_{M,fi}}} \le 3 \tag{15}$$

with, according to [10],

$$\mu_{y,\theta} = (2\beta_{M,y} - 5)\overline{\lambda}_{y,\theta} + 0.44\beta_{M,y} + 0.29 \le 0.8 \text{ with } \overline{\lambda}_{y,20^oC} \le 1.1 \tag{16}$$

and

$$\mu_{z,\theta} = (1.2\beta_{M,z} - 3)\overline{\lambda}_{z,\theta} + 0.71\beta_{M,z} - 0.29 \le 0.8 \tag{17}$$

The equivalent uniform moment factor $\beta_{M,y}$ and $\beta_{M,z}$ is determined according to the expression (18), in function of the bending diagram shape.

$$\beta_{M,i} = 1.8 - 0.7\psi_i \tag{18}$$

The curves obtained with these formulae are denoted "EN 1993-1-2" in figure 5, being the curve "EN 1993-1-2 NP" obtained together with the proposal for columns presented in section 2..

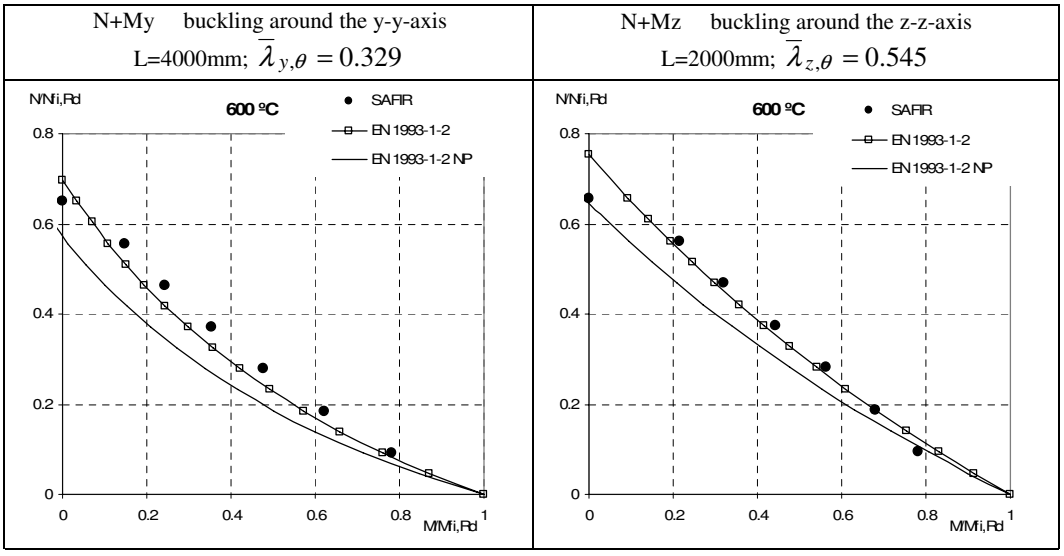

Fig. 5 – Beam-column interaction curves for ψ=1.

From figure 5 it can be concluded that the interaction curves, obtained with the new proposal for columns presented in section 2, are too conservative.

3.2 Proposal for the design of duplex beam-column in case of fire

Based in the same procedure adopted by Talamona [11], new factors μ_y and μ_z to be used with equations (14) and (15) are proposed

$$\mu_y = \left(1.27\beta_{M,y} - 2.68\right)\overline{\lambda}_{y,\theta} + 0.44\beta_{M,y} + 0.13 \le 0.8 \quad (19)$$

$$\mu_z = \left(1.17\beta_{M,z} - 2.66\right)\overline{\lambda}_{z,\theta} + 0.64\beta_{M,z} - 0.01 \le 0.8 \quad (20)$$

Figure 6 shows the evolution of μ_θ as a function of the slenderness $\overline{\lambda}_\theta$ for the strong and weak axis..

In this figure, "Average" corresponds to the average of the numerical results obtained with SAFIR, and the curve "New proposal" corresponds to the use of equations (19) and (20). These equations were developed to be a good approximation of the points "Average".

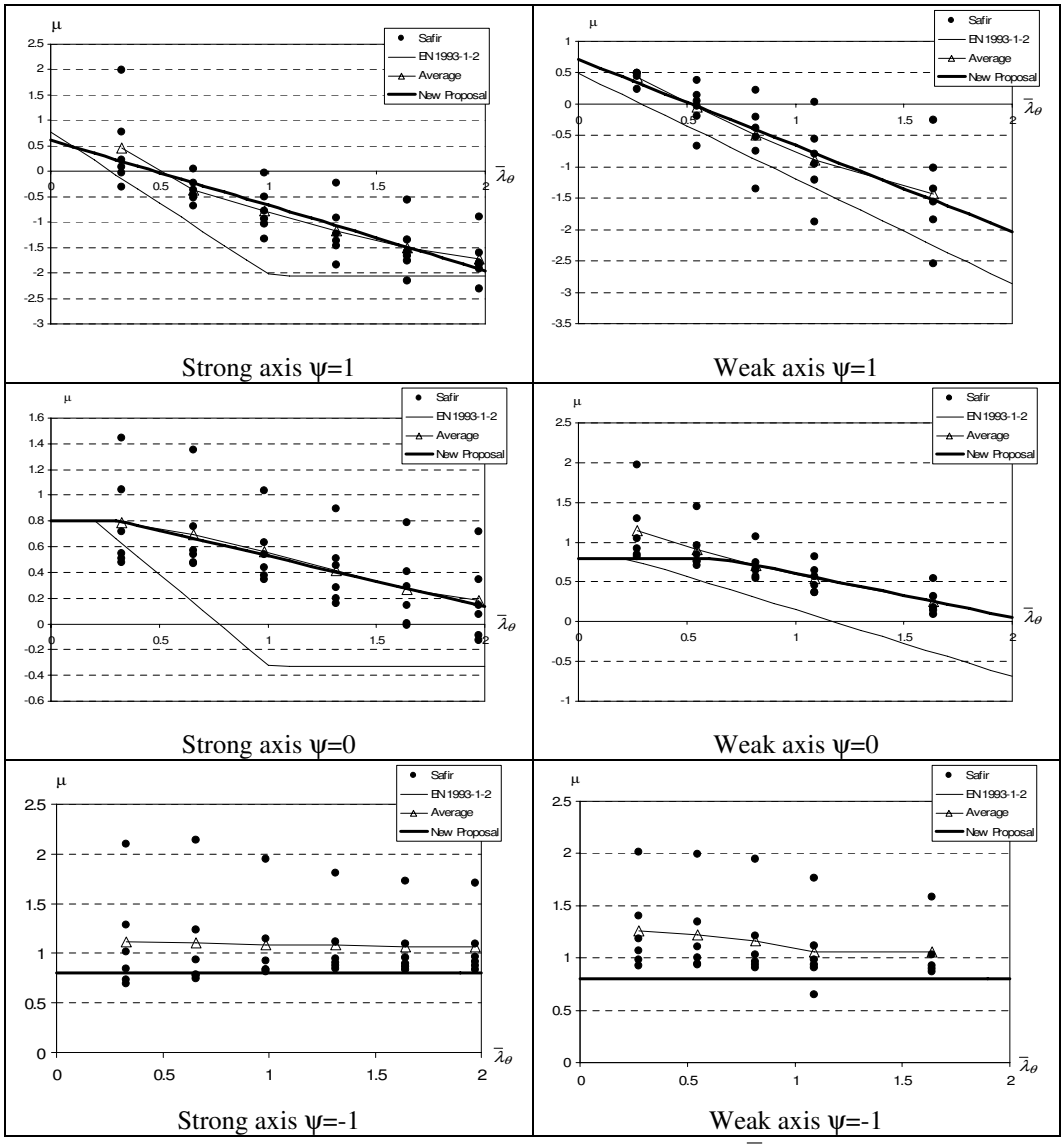

Fig. 6 – μ_θ as a function of the slenderness $\overline{\lambda}_\theta$.

The interaction curve given by (14) and (15) can be written in the following schematic way if bending is only around one axis (weak or strong).

$$N^* + M^* - \mu N^* M^* = 1 \tag{9}$$

Where

$$N^* = \frac{N_{fi,Ed}}{\chi_{i,fi} A k_{y,\theta} \dfrac{f_{y,\theta}}{\gamma_{M,fi}}} \quad \text{and} \quad M^* = \frac{M_{i,fi,Ed}}{W_{pl,i} \dfrac{f_{y,\theta}}{\gamma_{M,fi}}} \tag{9}$$

Figure 7 shows the shape of the interaction curves for different values of the coefficient . It is concave for positive values of (meaning that higher resistance is available) and turns convex with negative values of (meaning that lower resistance is available). The short linear branch near the N^* axis comes from the limitation of $k_i = 1 - \mu N^*$ to the value of 3 in equation (15).

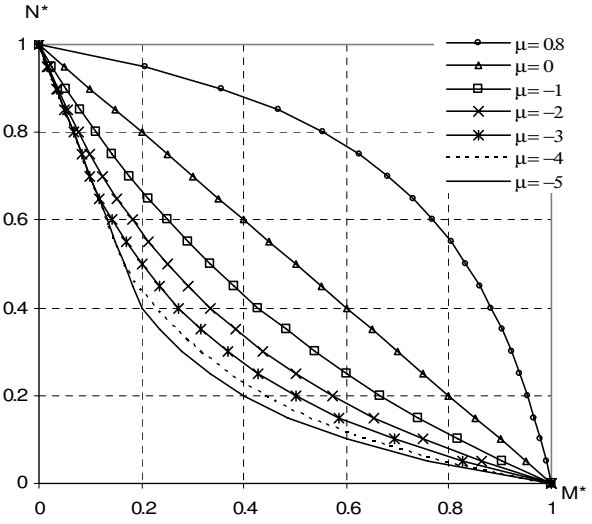

Fig. 7 – Interaction curves.

Figure 8 compares the interactions curves obtained with the Eurocode 3 and with the proposal made in this paper, for only one length of the beam-column for each buckling direction.

From this figure it can be concluded that the new proposal for duplex beam-columns presents good approximation to the numerical results, being safer then the Eurocode 3.

For bi-triangular bending moment distribution ($\psi = -1$) the curves denoted "EN 1993-1-2" and EN 1993-1-2 NP" are coincident.

4. CONCLUSIONS

In this paper new proposals, for the flexural buckling resistance of stainless steel columns and for beam-columns under fire loading were proposed. A new imperfection factor that takes into account the influence of the steel grade, and the variation of the yield strength with the temperature, has been proposed being in good agreement with the numerical results obtained with the program SAFIR.

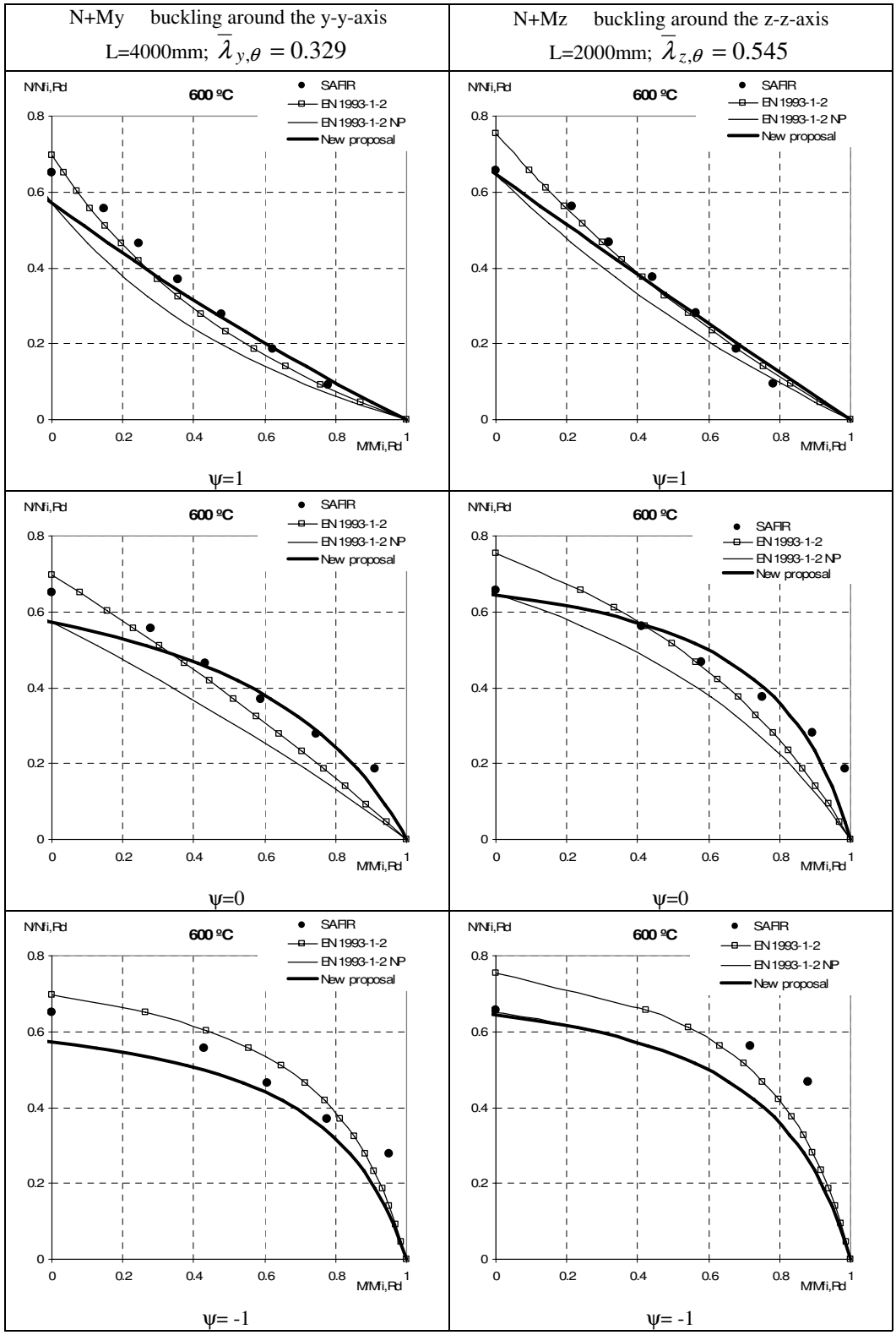

Fig. 8 – New proposal for the interaction curves.

It should be pointed out that as the parametric study shown in this paper contemplates only few cases, more studies considering other cross sections should be made to check the accuracy of the presented proposals.

ACKNOWLEDGEMENTS

The authors wish to acknowledge the Calouste Gulbenkian Foundation (Portugal) for its supports through the scholarship given to the first authors.

REFERENCES

[1] Euro Inox and Steel Construction Institute, "Design Manual for Structural Stainless Steel", 3rd edition, 2006.
[2] European Committee for Standardisation, "prEN 1993-1-4 Eurocode 3, Design of Steel Structures – Part 1.4. General rules – Supplementary Rules for Stainless Steels", Brussels, Belgium, 2005.
[3] European Committee for Standardisation, "EN 1993-1-2 Eurocode 3: Design of Steel Structures - Part 1.2: General rules - Structural fire design", Brussels, Belgium, April 2005.
[4] Lopes, N., Vila Real, P., Silva, L., Franssen, J.-M., Mirambell, E., "Numerical modelling of axially loaded stainless steel members under fire conditions", proceedings of the International Colloquium on Stability and Ductility of Steel Structures, SDSS'06, vol. 2, pp. 797 a 802, ISBN 972-8469-61-6, Lisboa, Portugal, 6 to 8 of September of 2006.
[5] Franssen, J.-M., "SAFIR. A Thermal/Structural Program Modelling Structures under Fire", Engineering Journal, A.I.S.C., Vol. 42, No. 3, pp. 143-158, 2005.
[6] Lopes, N., Vila Real, P.M.M., Piloto, P., Mesquita, L.; Simões da Silva, L., "Modelação numérica da encurvadura lateral de vigas I em aço inoxidável sujeitas a temperaturas elevadas", (in portuguese) Congreso de Métodos Numéricos en Ingeniería, Granada, Spain, 2005.
[7] Chen, W. F. and Lui, E. M., "Stability design of steel frames", CRC Press, 1991.
[8] Gardner, L., Nethercot, D. A., "Numerical Modeling of Stainless Steel Structural Components - A consistent Approach", Journal of Constructional Engineering, ASCE, pp. 1586-1601, 2004.
[9] European Committee for Standardisation, "EN 1993-1-1, Eurocode 3, Design of Steel Structures – part 1-1. General rules and rules for buildings", Brussels, Belgium, 2005.
[10] Talamona, D., Franssen, J.-M., Schleich, J.-B., Kruppa, J., "Stability of Steel Columns in Case of Fire: Numerical Modeling", Journal of Structural Engineering, 1997.
[11] Talamona, D., "Flambement de poteaux métalliques sous charge excentrée, à haute température", (in french); Ph.D. thesis, Université Blaise Pascal Ecole Doctorale Sciences pour l'Ingenieur de Clermont-Ferrand, 1995.

COMPARATIVE STUDY OF ANALYTICAL FORMULAE FOR THE FIRE RESISTANCE OF STEEL BEAM-COLUMNS

DIDIER TALAMONA[1], SYLVIE CASTAGNE[2], NUNO LOPES[3],
PAULO VILA REAL[4] and JEAN-MARC FRANSSEN[5]

ABSTRACT

This paper investigates the difference between the buckling formulae published in the Eurocode 3 part 1.2 and the recommendations made in the final report of the Buckling Curves in Case of Fire (BCCF) research project. This study compares the critical temperatures obtained with both formulations to assess the impact on the fire endurance of steel columns subjected to axial compression and bending. An extensive comparison of the ultimate temperatures obtained with both formulations has been performed (382 profiles, buckling about the strong and weak axis, 12 column lengths, 6 M/N ratios and uniform and triangular bending moment distributions). Failure temperatures between 400°C and 860°C have been considered. The formulations are also compared with Finite Elements (F.E.) calculations performed for a S235 HEA 200 at 600ºC. This analysis shows that for buckling about the strong axis the BCCF method is better than the EC3 but for buckling about the weak axis the EC3 predicts failure temperatures closer to the F.E. model than the BCCF formulation. Finally, the ultimate temperatures predicted by the two formulations have also been compared with experimental results from the database SCOFIDAT. This comparison shows that there is no major difference between the two formulations for small and large bending moments. This study concludes that the EC3 and BCCF formulations are generally equivalent and that either formulation can be used.

[1] Senior Lecturer, University of Newcastle, Australia, School of Mechanical Engineering, Singapore
email: didier.talamona@newcastle.edu.au
[2] Research Fellow, Queen's University, Belfast, UK
email: skstagne@yahoo.fr
[3] Research Assistant, University of Aveiro, Department of Civil Engineering, 3810-193 Aveiro, Portugal
email: nuno.lopes@ua.pt
[4] Professor, University of Aveiro, Department of Civil Engineering, 3810-193 Aveiro, Portugal
email: pvreal@civil.ua.pt
[5] Professor, University of Liege, Department ArGenCo, Belgium
email: jm.franssen@ulg.ac.be

1. INTRODUCTION

In 1995, a new procedure for the calculation of steel beam-columns interaction curves in case of fire was proposed as a result of the Buckling Curves in Case of Fire (BCCF) research project funded by the European Convention for Coal and Steel (ECSC agreement: 7210 SA 316/515/618/931). The results were published by Talamona [1], Profil Arbed Recherche [2, 3], the European Commission [4] and in international journals (Franssen et al. [5] and Talamona et al. [6]).

The proposed formulation was later accepted to become part of the Eurocode 3 part 1.2 to calculate the fire resistance of steel beam-columns. First they were adopted in the French National Annex, later in the ENV version of the EC3 and finally in the EN version [7].

It appeared recently that the equations published in the official version of EN 1993-1-2 [7] differ somehow from the equations proposed in the original work [1, 2, 4].

The motivation for this project is to clarify the doubt concerning the safety level of the Eurocode 3 created by the modification of the formulae originally proposed in 1995. The objectives are to identify precisely the differences between the two formulations and to examine their consequences on the fire endurance of steel columns subjected to axial compression and bending.

2. DESCRIPTION OF THE FORMULATIONS

2.1. BCCF Formulae

The original formulation proposed to calculate the fire resistance of steel beam-columns was published by the BCCF research partners in 1995 [1, 2, 4]. In accordance with this proposal, elements with cross-sections in classes 1 and 2 submitted to bending and axial compression must satisfy the following condition in case of fire:

$$\frac{N_{fi,Ed}}{\chi_{\min,fi}\cdot A\dfrac{k_{y,\theta}\cdot f_y}{\gamma_{M,fi}}}+\frac{k_{y,fi}\cdot M_{y,fi,Ed}}{W_{pl,y}\dfrac{k_{y,\theta}\cdot f_y}{\gamma_{M,fi}}}+\frac{k_{z,fi}\cdot M_{z,fi,Ed}}{W_{pl,z}\dfrac{k_{y,\theta}\cdot f_y}{\gamma_{M,fi}}}\le 1 \qquad (1)$$

The subscripts "y" and "z" refer to the strong axis (or y-axis) and to the weak axis (or z-axis) respectively (except for f_y which is the yield strength and $k_{y,\theta}$ its reduction factor).
The interaction factors $k_{y,fi}$ and $k_{z,fi}$ should be determined by:

$$k_{y,fi}=1-\frac{\mu_{y,\theta}\cdot N_{fi,Ed}}{\chi_{y,fi}\cdot A\cdot k_{y,\theta}\dfrac{f_y}{\gamma_{M,fi}}} \qquad \text{but } k_{y,fi}\le 3 \qquad (2)$$

$$k_{z,fi}=1-\frac{\mu_{z,\theta}\cdot N_{fi,Ed}}{\chi_{z,fi}\cdot A\cdot k_{y,\theta}\dfrac{f_y}{\gamma_{M,fi}}} \qquad \text{but } k_{z,fi}\le 3 \qquad (3)$$

Where the coefficients $\mu_{y,\theta}$ and $\mu_{z,\theta}$ are given by:

$$\mu_{y,\theta}=\left(2\cdot\beta_{M,y}-5\right)\bar{\lambda}_{y,\theta}+0.44\cdot\beta_{M,y}+0.29 \text{ but } \mu_{y,\theta}\le 0.8 \text{ and } \bar{\lambda}_{y,20}\le 1.1 \qquad (4)$$

$$\mu_{z,\theta}=\left(1.2\cdot\beta_{M,z}-3\right)\bar{\lambda}_{z,\theta}+0.71\cdot\beta_{M,z}-0.29 \qquad \text{but } \mu_{z,\theta}\le 0.8 \qquad (5)$$

Using the equivalent uniform moment factors $\beta_{M,y}$ and $\beta_{M,z}$ defined as:

$$\beta_{M,i}=1.8-0.7\cdot\psi_i \qquad (6)$$

In equation (6), the subscript "*i*" is defined as "*y*" or "*z*" depending on the buckling axis considered. The non-dimensional slenderness estimated at elevated temperature is given by:

$$\overline{\lambda}_\theta = \overline{\lambda}_{20} \cdot \sqrt{\frac{k_{y,\theta}}{k_{E,\theta}}} \tag{7}$$

2.2. Formulae from the EC3

The differences between the original formulae and the ones stated in EN 1993-1-2 lie in the equations used to determine the values of coefficients $\mu_{y,\theta}$ and $\mu_{z,\theta}$. In EN 1993-1-2 they are given by equations (8) and (9), which should be compared with equations (4) and (5) of the original proposal.

$$\mu_{y,\theta} = \left(1.2 \cdot \beta_{M,y} - 3\right)\overline{\lambda}_{y,\theta} + 0.44 \cdot \beta_{M,y} - 0.29 \qquad \text{but } \mu_{y,\theta} \le 0.8 \tag{8}$$

$$\mu_{z,\theta} = \left(2 \cdot \beta_{M,z} - 5\right)\overline{\lambda}_{z,\theta} + 0.44 \cdot \beta_{M,z} - 0.29 \quad \text{but } \mu_{z,\theta} \le 0.8 \text{ and } \overline{\lambda}_{z,\theta} \le 1.1 \tag{9}$$

The equivalent uniform moment factors $\beta_{M,y}$ and $\beta_{M,z}$ remain unchanged.

2.3. Description of the Main Diferences

Figures 1 and 2 show a comparison of the evolution of the ratios $\mu_{y,\theta}$ and $\mu_{z,\theta}$ as function of the relative slenderness calculated at elevated temperature ($\overline{\lambda}_\theta$) and of the shape of the bending diagram (see Figure 3).

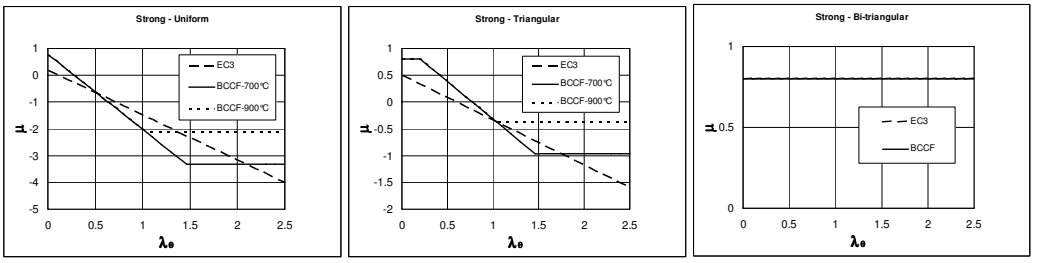

Fig. 1. $\mu_{y,\theta}$ as function of $\overline{\lambda}_\theta, y$

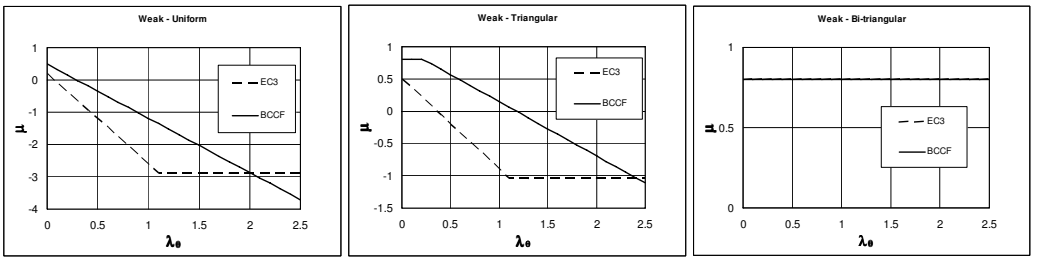

Fig. 2. $\mu_{z,\theta}$ as function of $\overline{\lambda}_\theta, z$

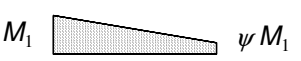

$$-1 \le \psi \le 1$$

Fig. 3. Linear bending diagram

Equation (4) of the original proposal has a limitation of the slenderness expressed at room temperature, $\overline{\lambda}_{20} \le 1.1$, which creates a variation of $\mu_{y,\theta}$ as function of temperature (see equation (7)). The curves established at 700°C and 900°C represent the maximum and minimum values of the ratio $\sqrt{k_{y,\theta}/k_{E,\theta}}$ (1.33 and 0.9428 respectively).

For bi-triangular bending moment distribution (ψ = -1), the coefficients $\mu_{y,\theta}$ and $\mu_{y,\theta}$ are equal to the maximum value of 0.8 for both formulations. In this case, as the two formulations have the same $\mu_{y,\theta}$ and $\mu_{z,\theta}$ as input coefficients, the same ultimate temperature will be predicted. Thus this load case will be left out of this investigation.

The interaction curve given by equation (1) can be written in the following schematic way if the member is subjected to compression and bending only about one axis (y-axis or z-axis). If N^* and M^* are defined as:

$$N^* = \frac{N_{fi,Ed}}{\chi_{min,fi} \cdot A \dfrac{k_{y,\theta} \cdot f_y}{\gamma_{M,fi}}} \tag{10}$$

and

$$M^* = \frac{M_{i,fi,Ed}}{W_{pl,i} \dfrac{k_{y,\theta} \cdot f_y}{\gamma_{M,fi}}} \tag{11}$$

then equation (1), (2) and (3) become equal to the following system of equations:

$$N^* + M^* - \mu_{i,\theta} \cdot N^* \cdot M^* = 1 \quad \text{if} \quad k_{i,fi} = 1 - \mu_{i,\theta} \cdot N^* \le 3 \tag{12}$$

and

$$N^* + 3 \cdot M^* = 1 \quad \text{if} \quad k_{i,fi} = 1 - \mu_{i,\theta} \cdot N^* > 3 \tag{13}$$

The other coefficients obtained from equations (4) to (9) remain unchanged.

In equation 11 and 12, the subscript "*i*" for $M_{i,fi,Ed}$ $W_{pl,i,}$ $k_{i,fi}$ and $\mu_{i,\theta}$ correspond to the letter "*y*" and "*z*" depending on the bending axis considered. Figure 4 shows that the shape of the interaction curves is very sensitive to variations of the coefficient $\mu_{i,\theta}$ when it varies from 0.8 to 0, which is the case for bi-triangular bending moment distribution and also short columns subjected to other bending moment distributions. As $\mu_{i,\theta}$ decreases the M-N interaction curve becomes less and less sensitive to its variation. For example if $\mu_{i,\theta}$ varies from -3 to -4, which are typical values of slender columns submitted to uniform bending moment distribution, the variation of the shape of the M-N curve is less than the previous variation from 0.8 to 0 (see figure 4). The linear descending branch near the N^* axis comes from the limitation of $k_{i,fi}$ to a maximum value of 3 (from equation (2) and (3)) which means that equation (13) should be used instead of equation (12).

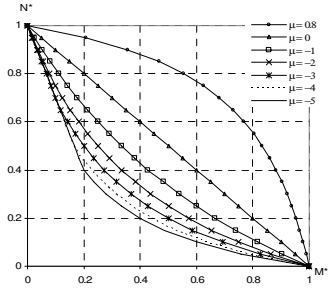

Fig. 4. Influence of the coefficient μ on the M-N interaction diagram

As the ultimate axial load capacity in pure compression and ultimate bending moment (M_{pl}) in pure bending are independent from the coefficients $\mu_{y,\theta}$ and $\mu_{z,\theta}$, these values are not affected by the modifications introduced in the Eurocode 3 part 1.2. This implies that the starting and ending points of the M-N interaction curves are not affected by the modifications of the formulae and only the shape of the curve between pure compression and pure bending is modified.

3. COMPARISON OF THE FAILURE TEMPERATURES

3.1. Comparison Between the Two Formulations

A comparison of the failure temperatures obtained with both formulations has been performed using the following assumptions:

- Profiles in class 1 and 2 in compression and bending have been considered (382 profiles).
- Steel S235 with reduction of the yield strength depending on the thickness of the flanges
  - 235 MPa for $t_f \leq 16$ mm
  - 225 MPa for $t_f \leq 40$ mm
  - 215 MPa for $t_f \leq 100$ mm
  - 195 MPa for $t_f \leq 150$ mm
- Twelve reduced slenderness have been considered ($\bar{\lambda}_{20}$ from 0.2 to 2.4 with an increment of 0.2)
- Six M/N ratios (0.05, 0.1, 0.5, 1.0, 3.0 and 5.0 multiplied by the radius of gyration about the buckling axis considered)
- Buckling about the strong and weak axis
- Two bending moment distributions (uniform: $\psi = 1$ and triangular: $\psi = 0$)
- Failures temperatures between 400°C and 860°C

Note: axially loaded columns, columns in pure bending and bi-triangular (ψ = -1) bending moment distribution have not been considered, as these load cases are not affected by the modification introduced in the EC3.

Figures 5, 6, 7 and 8 show a comparison of the failure temperatures obtained with the Eurocode 3 and the BCCF formations for: profiles in class 1 and 2, non-dimensional slenderness from 0.2 to 2.4, uniform (ψ = 1) and triangular (ψ = 0) bending moment and buckling about the "*y*" and "*z*" axis. As can be seen there is no major difference between the temperatures predicted by both formulations. The biggest differences in ultimate temperatures are obtained for short columns submitted to a triangular bending moment and heavily loaded (failure temperatures under 600 °C). These discrepancies are due to the fact that under these conditions the values of $\mu_{y,\theta}$ and/or $\mu_{z,\theta}$ are between 0.8 and -1 and it has been shown that in this range the M-N interaction curve is extremely sensitive to variations of $\mu_{y,\theta}$ or $\mu_{z,\theta}$. Noticeable differences also appear for slender columns ($\bar{\lambda} \geq 2.0$).

3.2. Comparison with Finite Element Results

Figure 9 and 10 show the interaction curves for the case of a welded HEA 200 in S235, at 600 ºC submitted to flexural buckling around the *y*-*y* axis and the *z*-*z* axis respectively. These figures show that for the major axis buckling the BCCF method is better that the Eurocode 3 but in the minor axis the Eurocode 3 seems to be better. Nevertheless both formulations provide similar results.

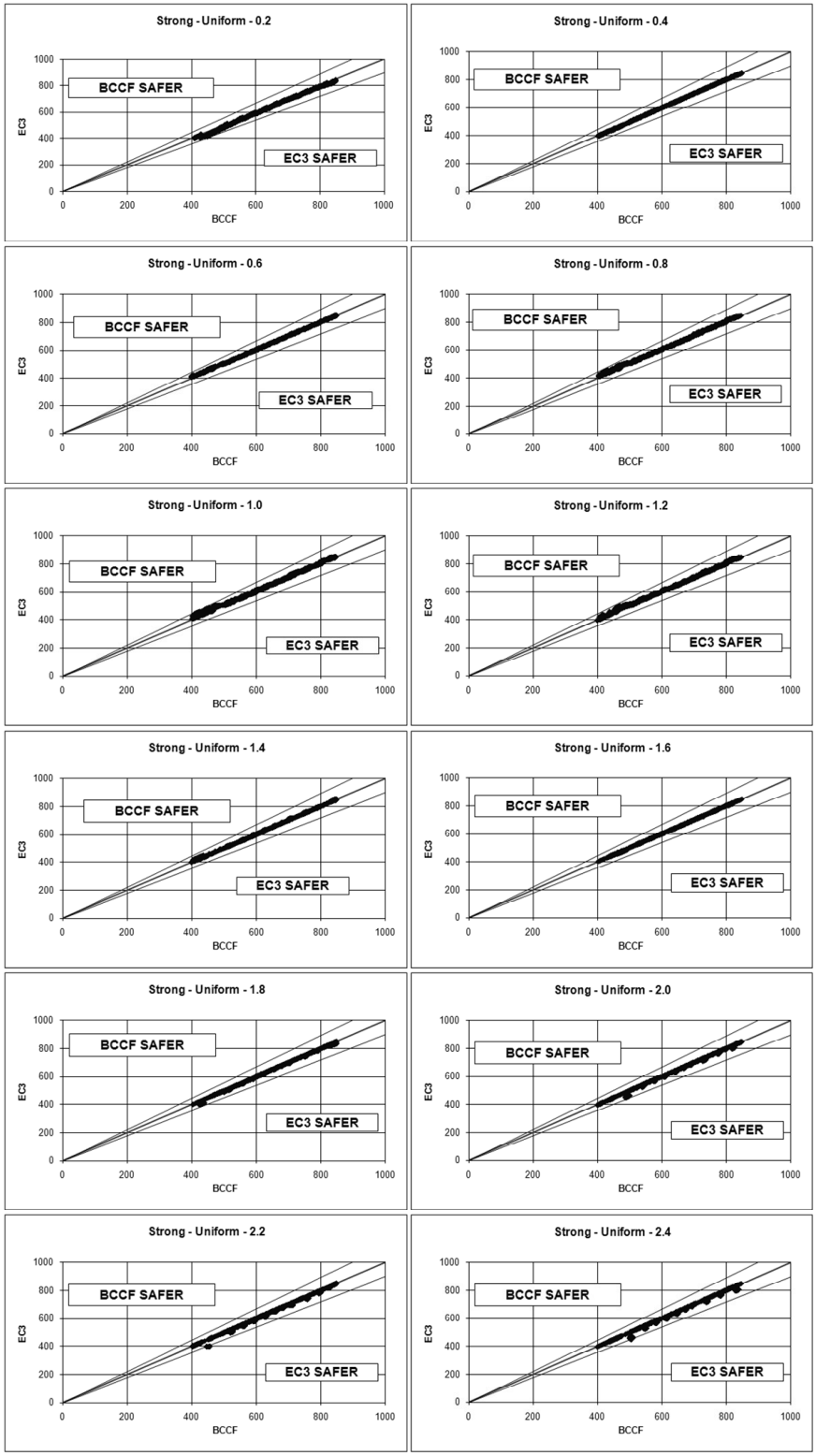

Fig. 5 - Buckling strong axis for $\psi = 1$ and $0.2 \leq \overline{\lambda}_{20} \leq 2.4$

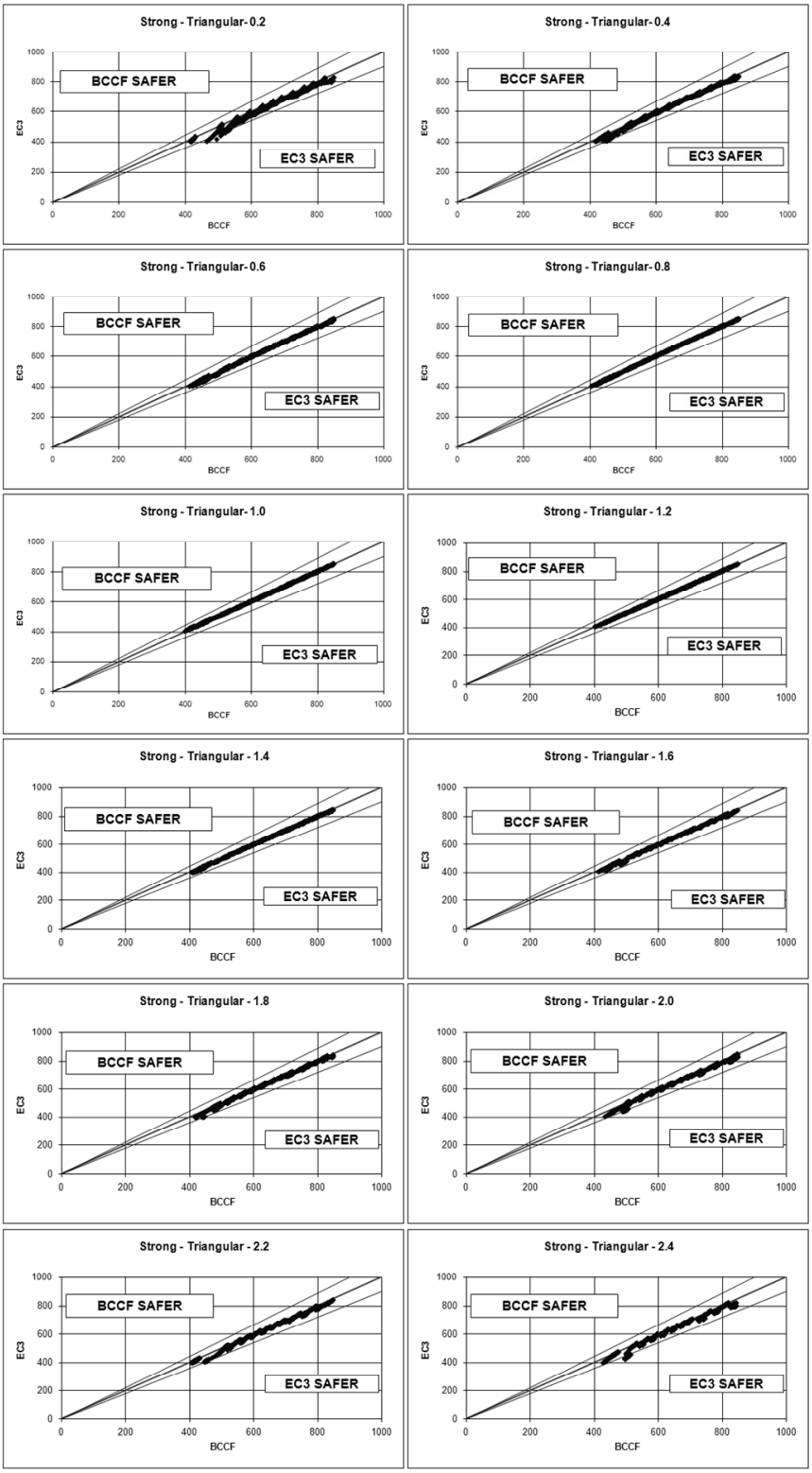

Fig. 6 - Buckling strong axis for $\psi = 0$ and $0.2 \leq \overline{\lambda}_{20} \leq 2.4$

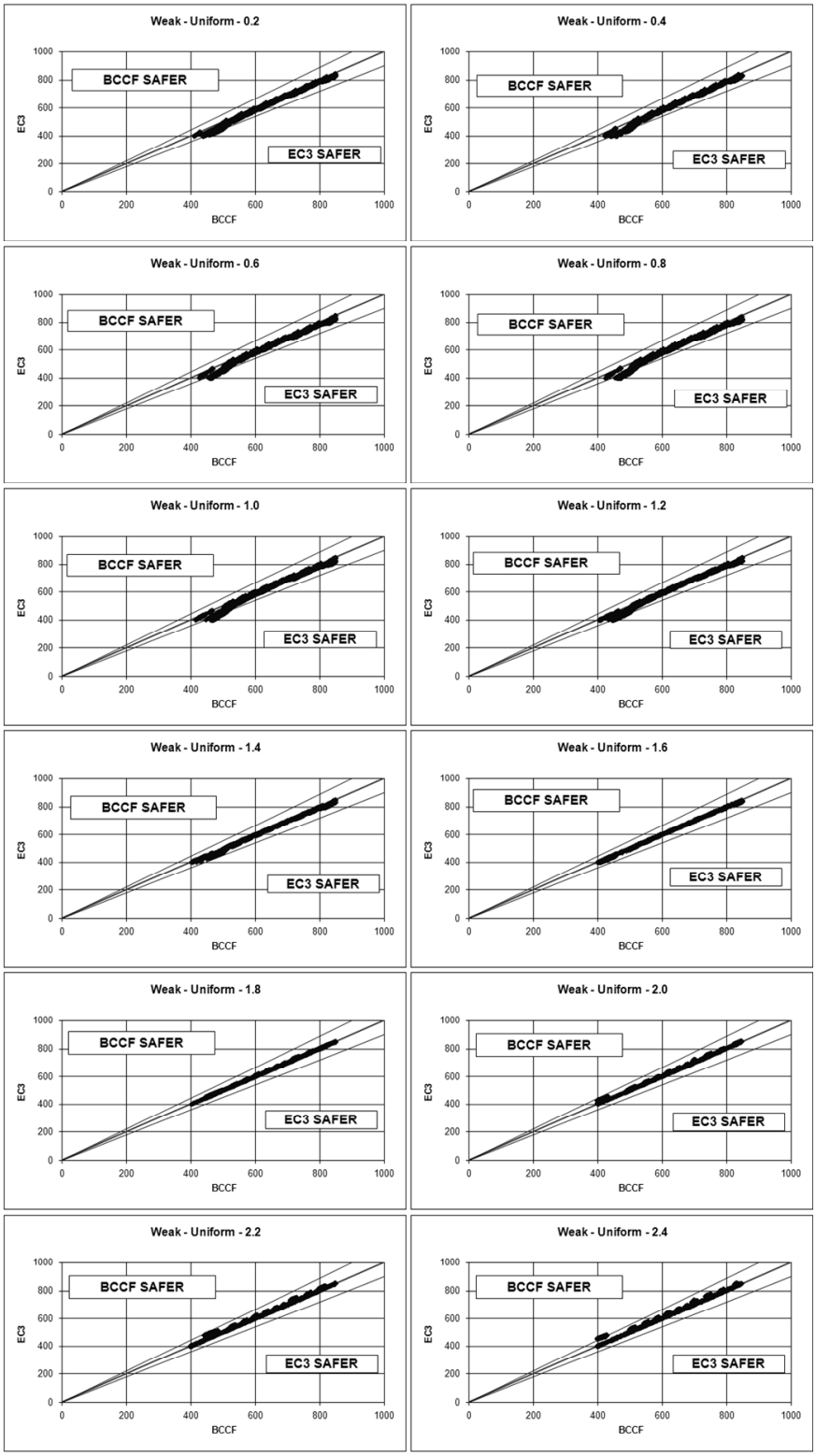

Fig. 7 - Buckling weak axis for $\psi = 1$ and $0.2 \leq \overline{\lambda}_{20} \leq 2.4$

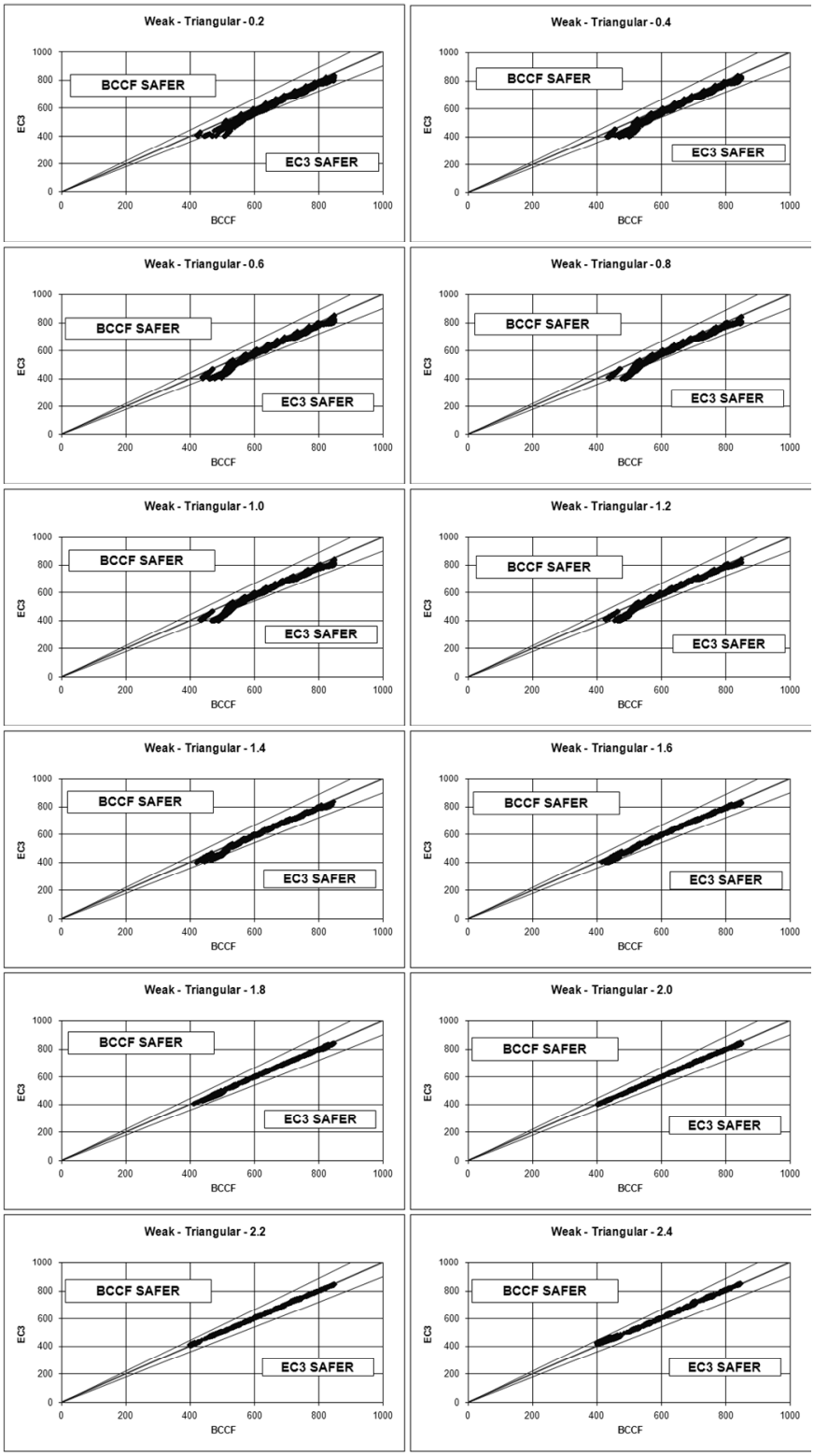

Fig. 8 - Buckling weak axis for $\psi = 0$ and $0.2 \leq \overline{\lambda}_{20} \leq 2.4$

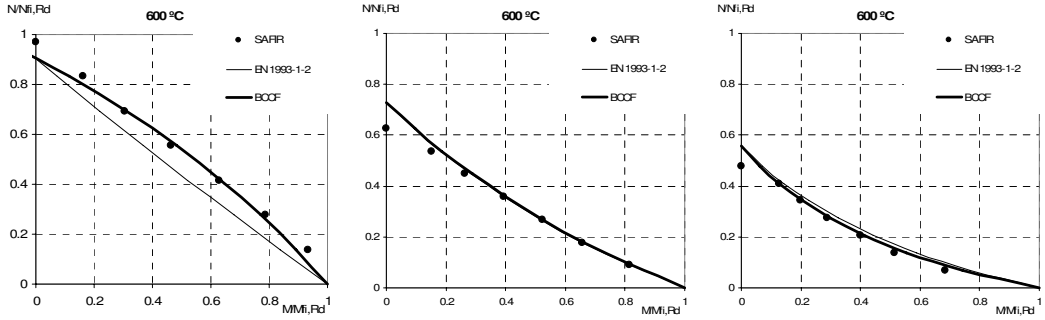

L=1000mm; $\overline{\lambda}_{y,\theta} = 0.159$ L=3000mm; $\overline{\lambda}_{y,\theta} = 0.477$ L=5000mm; $\overline{\lambda}_{y,\theta} = 0.795$

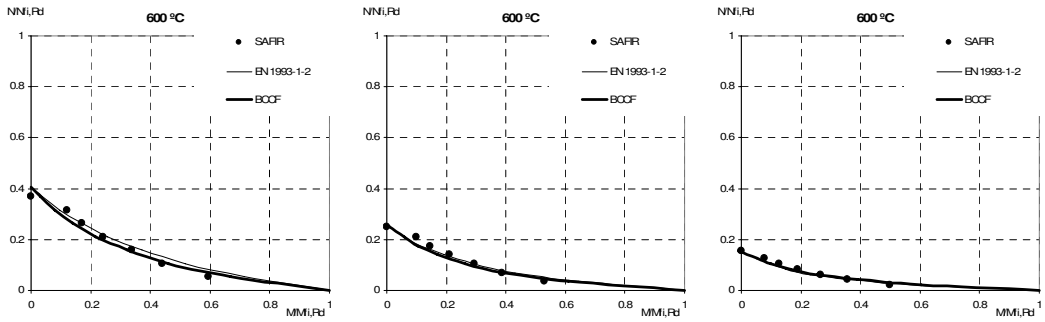

L=7000mm; $\overline{\lambda}_{y,\theta} = 1.112$ L=10000mm; $\overline{\lambda}_{y,\theta} = 1.589$ L=14000mm; $\overline{\lambda}_{y,\theta} = 2.225$

Fig. 9 - Interaction curves for beam column with bending around the major axis, ($N+M_y$)

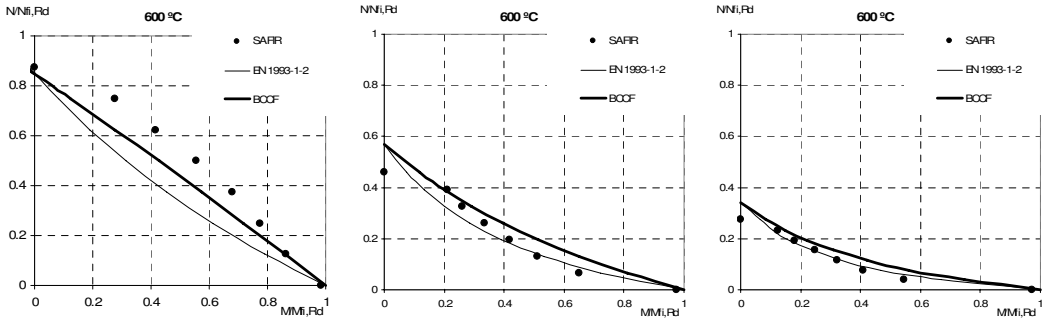

L=1000mm; $\overline{\lambda}_{z,\theta} = 0.258$ L=3000mm; $\overline{\lambda}_{z,\theta} = 0.773$ L=5000mm; $\overline{\lambda}_{z,\theta} = 1.289$

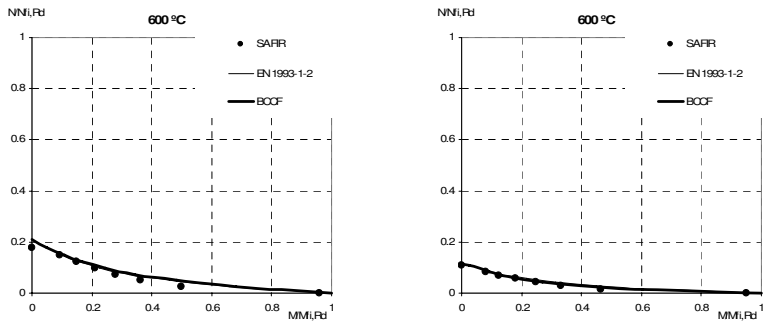

L=7000mm; $\overline{\lambda}_{z,\theta} = 1.804$ L=10000mm; $\overline{\lambda}_{z,\theta} = 2.578$

Fig. 10 - Interaction curves for beam column with bending around the minor axis, ($N+M_z$)

3.3. Comparison with the Database SCOFIDAT

SCOFIDAT is a database that contains over 140 fire tests results performed on steel beam-columns under a wide range of loading, boundary conditions and fire exposures. The data was provided by seven labs. The experimental results obtained from axially loaded columns and tests with failure temperatures under 400ºC were left out of this study, giving just above 60 experimental results that are considered. It has to be noted that all members were subjected to compression and uniform bending moment distribution.

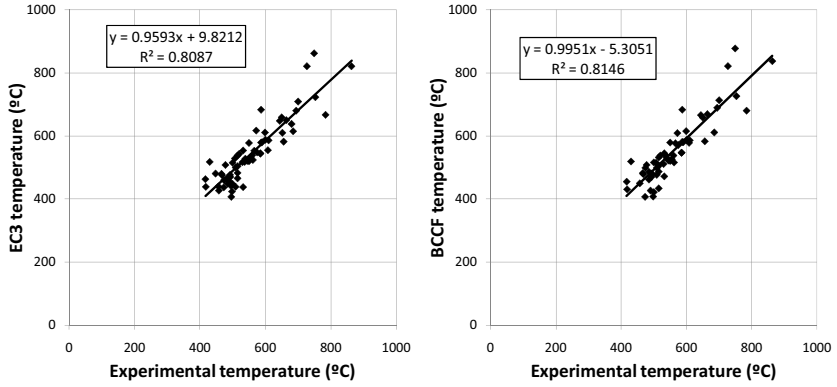

Fig. 11. Comparison of the formulations with experimental results

As can be seen figure 11, both formulations are in good agreement with experimental results. The slopes of the curves are both close to 1.0, the Y-intercept is small, and the regression coefficient above 0.8.

4. CONCLUSIONS

From this investigation, it can be concluded that the formulations from the Eurocode and BCCF research project are:

- Usually similar in terms of failure temperature
- When differences are observed the Eurocode 3 is usually conservative.
- Both formulations provide similar failure temperatures when the predicted temperatures are above 550°C
- Both formulations provide reasonable agreement with experimental results.

From the results presented in this paper it can be concluded that the new formulation is not likely to decrease the safety level of constructions. More investigation needs to be performed to assess the impact of these modifications on the competitiveness of steel structures.

5. NOMENCLATURE

A	area of the cross-section
f_y	yield strength at 20°C
$k_{y,\theta}$	reduction factor for the yield strength of steel at the steel temperature θ
$k_{E,\theta}$	reduction factor for the elastic modulus of steel at the steel temperature θ
$k_{y,fi}$	interaction factor about the y-axis

$k_{z,fi}$ interaction factor about the z-axis
$M_{y,f,Ed}$ design moment resistance about the y-axis
$M_{z,f,Ed}$ design moment resistance about the z-axis
$N_{fi,Ed}$ applied axial load
$W_{pl,y}$ plastic section modulus about the y-axis
$W_{pl,z}$ plastic section modulus about the z-axis
$\beta_{m,y}$ equivalent uniform moment factor
$\beta_{m,z}$ equivalent uniform moment factor
$\gamma_{M,fi}$ partial factor for the relevant material property, for the fire situation
$\overline{\lambda}_{20,y}$ non-dimensional slenderness at 20°C
$\overline{\lambda}_{20,z}$ non-dimensional slenderness at 20°C
$\overline{\lambda}_{\theta,y}$ non-dimensional slenderness at temperature θ
$\overline{\lambda}_{\theta,z}$ non-dimensional slenderness at temperature θ
$\mu_{y,\theta}$ interaction coefficient about the y-axis
$\mu_{z,\theta}$ interaction coefficient about the z-axis
$\chi_{min,fi}$ minimum value of $\chi_{y,fi}$ and $\chi_{z,fi}$
$\chi_{y,fi}$ reduction factor for flexural buckling about the y-axis in the fire design situation
$\chi_{z,fi}$ reduction factor for flexural buckling about the z-axis in the fire design situation
ψ_i ratio between lowest and highest bending moment about the y-axis or z-axis

6. REFERENCES

[1] D. Talamona, Flambement de Poteaux Métalliques sous Charge Excentrée, à Haute Température. Thèse (PhD), Université Blaise Pascal, Clermont-Ferrand, France, September 1995 (in French).
[2] J. B. Schleich, L-G. Cajot, J. Kruppa, D. Talamona, W. Azpiazu, J. Unanue, L. Twilt, J. Fellinger, R-J. Van Foeken, J-M. Franssen, Buckling Curves in Case of Fire. (Draft Final Report) Part I. Profil Arbed Recherches, March 1996.
[3] J. B. Schleich, L-G. Cajot, J. Kruppa, D. Talamona, W. Azpiazu, J. Unanue, L. Twilt, J. Fellinger, R-J. Van Foeken, J-M. Franssen, Buckling Curves in Case of Fire. (Draft Final Report) Part II. Profil Arbed Recherches, March 1996.
[4] J. B. Schleich, L-G. Cajot, J. Kruppa, D. Talamona, W. Azpiazu, J. Unanue, L; Twilt, J. Fellinger, R-J Van Foeken, J-M. Franssen, Buckling Curves of Hot Rolled H Steel Sections Subjected to Fire. Office for Official Publications of the European Communities (Luxembourg), 1998, ISBN 92-828-4603-2.
[5] J. M. Franssen, D. Talamona, J. Kruppa, L. G. Cajot, Stability of steel Columns in Case of Fire: Experimental Evaluation. Journal of Structural Engineering, Vol. 124 N 2, February 1998, pp. 158-163.
[6] D. Talamona, J-M. Franssen, J.B. Schleich, J. Kruppa, Stability of Steel Columns in Case of Fire: Numerical Modeling. Journal of Structural Engineering, Vol. 123, N 6, June 1997, pp. 713-720.
[7] European Committee for Standardization (CEN) – Eurocode 3: Design of Steel Structures - Part 1-2: General rules - Structural fire design, EN 1993-1-2:2005, Brussels, Belgium, April 2005.
[8] European Committee for Standardization (CEN) – Eurocode 3: Design of Steel Structures - Part 1-1: General rules and rules for buildings, DD ENV 1993-1-1:1992, Brussels, Belgium, November 1992.

NUMERICAL MODELLING OF THIN-WALLED STAINLESS STEEL STRUCTURAL ELEMENTS IN CASE OF FIRE

NUNO LOPES[1]; PAULO VILA REAL[2]
LUÍS SIMÕES DA SILVA[3] and JEAN-MARC FRANSSEN[4]

ABSTRACT

In this paper, numerical tests made in stainless steel thin-walled elements, using the program SAFIR, will be presented.

In order to make these simulations, two main changes in SAFIR were made: i) the program was changed in order to deal with the stainless steel 2D material properties to be used with shell elements and ii) the possibility of the program to take into account residual stresses in shell elements was introduced.

The stainless steel stress-strain relationship at high temperatures, was based on the one presented in part 1.2 of Eurocode 3 [1], which has no initial linear branch as the case of carbon steel.

The hardening rule to be used on the shell element formulation could not be exactly established without an approximation of the Eurocode 3 constitutive law [1].

Due to the fact that the SAFIR procedure to take into account the residual stresses consists in transforming them first into residual strains and adding them after to the other initial strains [2], it was necessary to implement a procedure that took in consideration the non-linearity of the material stress-strain relationship.

The paper shows the influence of the residual stresses on the ultimate load bearing resistance of thin-walled stainless steel structural elements in case of fire.

[1] Research Assistant, LABEST - University of Aveiro, Dep. of Civil Engineering, 3810-193 Aveiro, Portugal, email: nuno.lopes@ua.pt.
[2] Professor, LABEST - University of Aveiro, Dep. of Civil Engineering, 3810-193 Aveiro, Portugal, email: pvreal@ua.pt.
[3] Professor, ISISE - University of Coimbra, Dep. of Civil Engineering, 3030 Coimbra, Portugal, email: luisss@dec.uc.pt.
[4] Professor, ArGEnCo, University of Liege, Belgium email: jm.franssen@ulg.ac.be.

1. INTRODUTION

Stainless steel has countless desirable characteristics for a structural material [3, 4, 5]. Even though its use in construction is increasing, it is still necessary to develop the knowledge of its structural behaviour. Stainless steels are known by their non-linear stress-strain relationships with a low proportional stress and an extensive hardening phase. A well defined yield strength does not exist, the conventional limit of elasticity at 0.2% is usually considered.

The EN 1993-1-4 "Supplementary rules for stainless steels" [6] gives design rules for stainless steel structural members at room temperature, mentioning fire resistance making reference to the fire part of the Eurocode 3, EN 1993-1-2 [1], see figure 1.

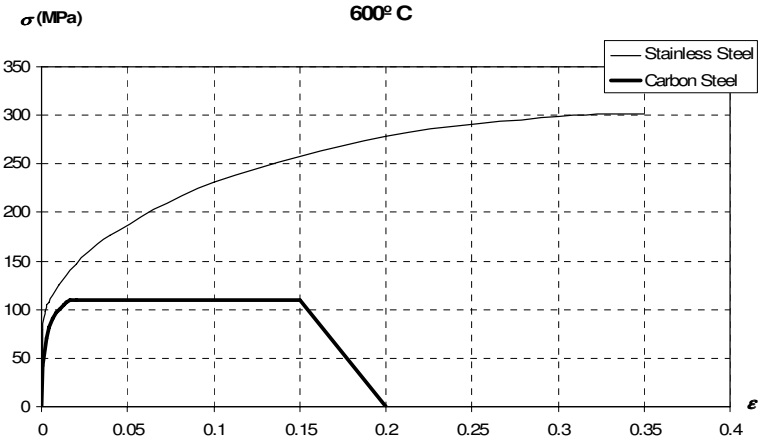

Fig. 1 – Stress-strain relationships of carbon steel S 235 and stainless steel 1.4301 at 600 ºC.

Program SAFIR [7], a geometrical and material non linear finite element code, which has been adapted according to the material properties defined in EN 1993-1-4 [6] and EN 1993-1-2 [1], to model the behaviour of stainless steel structures has been used in the numerical simulations. This program, widely used by several investigators, has been validated against analytical solutions, experimental tests and numerical results from other programs, and has been used in several studies that lead to proposals for safety evaluation of structural elements, already adopted in Eurocode 3. In the numerical simulations, geometrical imperfections and residual stresses were considered.

The stainless steel stress-strain relationship at high temperatures has no initial linear branch as for carbon steel, and the hardening rule to be used on the shell element formulation could not be exactly established without an approximation of the Eurocode 3 constitutive law [1].

Due to the fact that the SAFIR procedure to take into account the residual stresses consists in transforming them first into residual strains and adding them after to the other initial strains [2], it was necessary to implement a procedure that took in consideration the non-linearity of the material stress-strain relationship.

The objective of the study presented in this paper is to evaluate the accuracy of the hardening law introduced for the shell elements in SAFIR, and with these introduced 2D material properties of stainless steel it is evaluated the influence of the residual stresses in thin-walled stainless steel cross-section. Thus this paper shows the influence of the residual

stresses on the ultimate load bearing resistance of Class 4 stainless steel structural elements, in case of fire.

2. SOFTWARE DEVELOPMENT

In order to make this study it were introduced some modifications in the program SAFIR. The two main changes were:

- changing the program SAFIR in order to deal with the stainless steel 2D material properties, with the purpose of using shell elements in the numerical simulations of thin walled stainless steel structural elements.
- introducing the possibility of the program SAFIR accounts with residual stresses in shell elements in elastic materials and in stainless steel.

2.1 Stainless steel 2D material properties introduced in SAFIR

The modelling of the material stainless steel was made by a non-elastic plane stress based on the von Mises surface and on isotropic hardening. The constitutive law of the stainless steel has a permanent non-linear behaviour.

The Shell element from SAFIR is programmed to be used in large displacements in the plane stress state. This finite element was first introduced for elastic materials and then for bi-dimensional elastic-plastic material law [8].

For the stainless steel it was used the same formulation used in the carbon steel [8], but, due to the different stress-strain relationship (see figure 1) it was necessary to achieve a different hardening rule for the stainless steel.

The stainless steel stress-strain relationship at high temperatures used in this work was the one prescribed in part 1.2 of Eurocode 3 [1] and is described in Table 1 and in Figure 2.

Table 1 – Expressions of the constitutive law of the stainless steel at high temperatures

Strain range	Stress σ	Tangent modulus
$\varepsilon \le \varepsilon_{c,\theta}$	$\dfrac{E \cdot \varepsilon}{1 + a \cdot \varepsilon^b}$	$\dfrac{E\left(1 + a \cdot \varepsilon^b - a \cdot b \cdot \varepsilon^b\right)}{\left(1 + a \cdot \varepsilon^b\right)^2}$
$\varepsilon_{c,\theta} < \varepsilon < \varepsilon_{u,\theta}$	$f_{0.2p,\theta} - e + (d/c)\sqrt{c^2 - (\varepsilon_{u,\theta} - \varepsilon)^2}$	$\dfrac{d(\varepsilon_{u,\theta} - \varepsilon)}{c\sqrt{c^2 - (\varepsilon_{u,\theta} - \varepsilon)^2}}$
Parameters	$\varepsilon_{c,\theta} = f_{0.2p,\theta} / E_{a,\theta} + 0.002$	
Functions	$a = \dfrac{E_{a,\theta}\,\varepsilon_{c,\theta} - f_{0.2p,\theta}}{f_{0.2p,\theta}\,\varepsilon_{c,\theta}^{\ b}}$ $\quad b = \dfrac{(1 - \varepsilon_{c,\theta}\,E_{ct,\theta} / f_{0.2p,\theta})E_{a,\theta}\,\varepsilon_{c,\theta}}{(E_{a,\theta}\,\varepsilon_{c,\theta} / f_{0.2p,\theta} - 1)\,f_{0.2p,\theta}}$ $\quad c^2 = (\varepsilon_{u,\theta} - \varepsilon_{c,\theta})\left(\varepsilon_{u,\theta} - \varepsilon_{c,\theta} + \dfrac{e}{E_{ct,\theta}}\right)$ $\quad d^2 = e\,(\varepsilon_{u,\theta} - \varepsilon_{c,\theta})E_{ct,\theta} + e^2$ $\quad e = \dfrac{(f_{u,\theta} - f_{0.2p,\theta})^2}{(\varepsilon_{u,\theta} - \varepsilon_{c,\theta})E_{ct,\theta} - 2(f_{u,\theta} - f_{0.2p,\theta})}$	

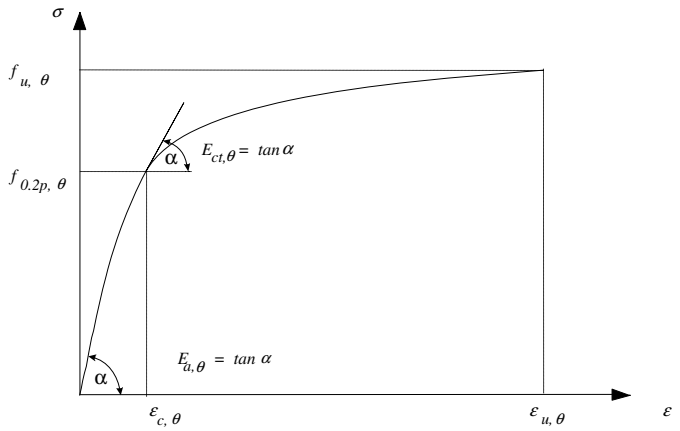

Fig. 2 –Stress-strain relationship of the stainless steel at elevated temperatures

In table 1 it can be found the constitutive law given by the function $\sigma = f(\varepsilon)$. The hardening rule used in SAFIR, $\tau = g(k)$, can be obtained using $\varepsilon = k + \frac{\sigma}{E}$ and making $\tau = \sigma$.

For the second branch ($\varepsilon_{c,\theta} < \varepsilon < \varepsilon_{u,\theta}$) it was possible to use this process to achieve the hardening rule, but for $\varepsilon < \varepsilon_{c,\theta}$ the equation $\sigma = E \cdot \varepsilon / (1 + a \cdot \varepsilon^b)$ did not allow this conversion. Therefore it was developed the equation (1) that approximates the hardening function for the first branch of the stainless steel constitutive law.

$$\tau = b \cdot k^2 + c \cdot k + d + a \cdot \sqrt{k} \tag{1}$$

The parameters *a*, *b*, *c* and *d* were obtained imposing that equation (1) should satisfy the boundary conditions, resulting in

$$\begin{cases} a = 56.0362 \cdot f_{0.2p,\theta} - 0.112 \cdot h \\ b = 63501.9 \cdot f_{0.2p,\theta} - 127.1 \cdot h \\ c = -880.512 \cdot f_{0.2p,\theta} + 2.763 \cdot h \\ d = 0.001 \cdot f_{0.2p,\theta} \end{cases} \tag{2}$$

where *h* is the value of $\frac{\partial \tau}{\partial k}(0.002)$ in the second branch.

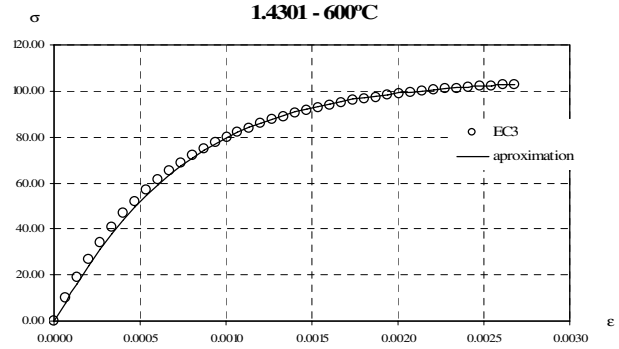

Fig. 3 – Stainless steel constitutive law: comparison between the approximation used for 2D analysis and the Eurocode 3 at 600ºC, for the 1.4301.

Figure 3 shows a comparison between the stress-strain relationship obtained with Eurocode 3 and with the approximation given by equation (1).

2.2 Shell elements residual stresses introduced in SAFIR

In order to introduce the possibility of the SAFIR accounts with residual stresses it is first necessary to transform them into residual strains and then to add them to the other initial strains. This was the formulation adopted in SAFIR for the others finite elements [2].

Due to this procedure the methodology to be adopted for the consideration of the residual stresses, depends on the linearity or non-linearity of the material stress-strain relationship. Therefore the introduction of this consideration was made for all the materials, that have a first elastic phase in its material behaviour and provided that the residual stresses are always in that elastic phase, which is not the case for stainless steel.

As the stainless steel has a non-linear stress-strain relationship, another procedure was used. This procedure begins with the determination of a "comparison stress" of von Mises (see equation 3) of the residual stresses introduced.

$$\sigma_{c,res} = \sqrt{\sigma_{x,res}^2 - \sigma_{x,res} \cdot \sigma_{y,res} + \sigma_{y,res}^2 + 3 \cdot \tau_{xy,res}} \tag{3}$$

With this "comparison stress" and with the constitutive law it is possible using the Newton-Raphson method to achieve a residual "comparison strain". Due to the fact that it was used in SAFIR an approximation to the hardening law of the stainless steel, as explained in the section 2.1 of this paper, this approximation of the hardening law was also used to determine the residual "comparison strain".

With the comparison residual strain and with the comparison residual stress it is possible to determine a secant modulus $E_{\sec} = \dfrac{\sigma_{c,res}}{\varepsilon_{c,res}}$. This modulus is used in the elasticity matrix [D] necessary to evaluate the residual strains

$$\{\varepsilon_{res}\} = [D]^{-1} \cdot \{\sigma_{res}\} \tag{4}$$

3. VALIDATION OF THE SOFTWARE DEVELOPMENT

These developments in the Shell finite elements of the program SAFIR are analysed in this section, being the results obtained with them, compared with the 3D Beam finite element of SAFIR, with the 3D Beam finite element of the commercial software ANSYS and with some experimental tests made by Ala-Outinen et al [9].

Here, the approximation to the stainless steel hardening law described in section 2.1 is tested. These comparisons are made for elements with Class 1 sections. The flexural buckling of a square hollow section and the lateral-torsional buckling of an I-cross section are analysed with shell and beam finite elements, and the results compared between them.

3.1 Flexural buckling in a Class 1 stainless steel square hollow section

The same Class 1 hollow section SHS40x40x4 used in reference [9] to make experimental test on stainless steel columns in case of fire, has been adopted. The round corners were not considered in the finite element mesh used to discretize the cross-section.

In the numerical simulations, a lateral geometric imperfection given by the following expression was considered [10]:

$$y(x) = \frac{l}{1000}\sin\left(\frac{\pi x}{l}\right) \tag{5}$$

where l is the length of the column.

No residual stresses were introduced in these first simulations. The yield strength and the ultimate strength considered were, according to the Eurocode 3, 210MPa and 520MPa respectively. It wasn't considered the increasing of the yield strength in the corner regions [11]. The comparisons were made with uniform temperature in the cross-section.

In figure 4 it is shown the results obtained for different temperatures using the beam-finite elements from SAFIR and from ANSYS. These results are compared with the Eurocode 3 (denoted "EN 1993-1-2").

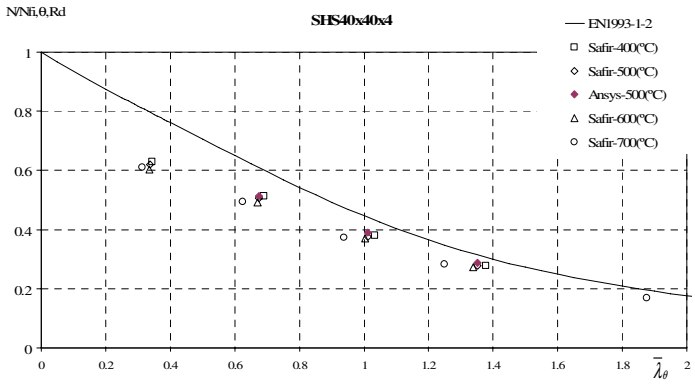

Fig. 4 – SHS40x40x4 numerical results using 3D beam finite elements.

The yield strength and the ultimate strength measured in the experimental tests in reference [9] had the value of 595MPa and 736MPa respectively, therefore these were the values considered in the results presented in figure 5. The load level, the length and the support conditions of the simulations with SAFIR are the same used in the experimental tests. In the graphic "Outinen tests" correspond to the experimental tests, "Outinen tests SAFIR B" are the simulations of the experimental tests with the beam elements from SAFIR and "Outinen tests SAFIR S" are the simulations of the experimental test with the shell elements from SAFIR (see figure 6).

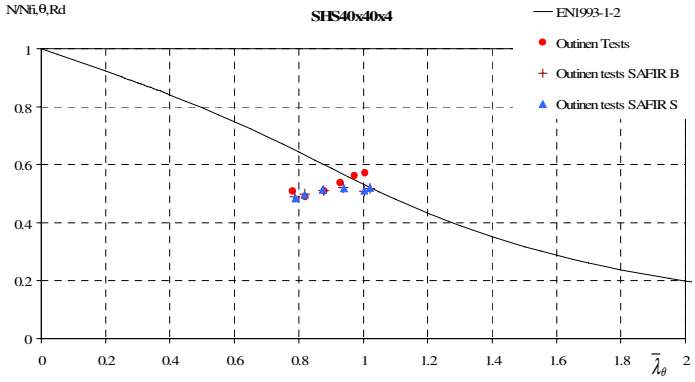

Fig. 5 – SHS40x40x4 numerical results with SAFIR using beam and shell finite elements compared with the experimental tests [9].

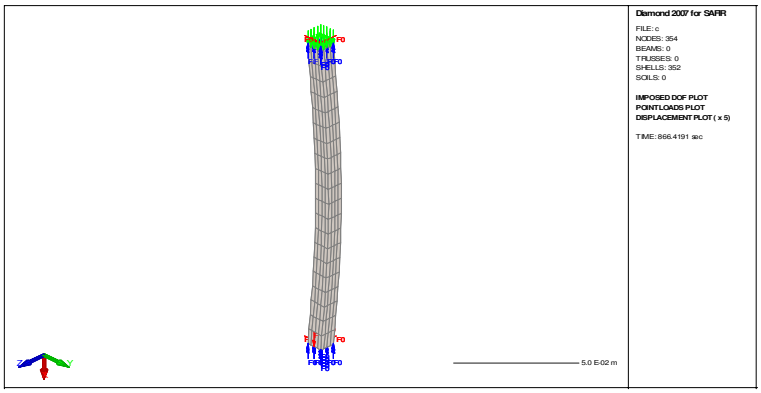

Fig. 6 – SHS40x40x4 column simulated with shell elements.

From figure 4 and 5 it can be concluded that the approximation used for the stainless steel hardening rule used in SAFIR gives a good approximation when compared with the results from others softwares and with experimental results.

3.2 Lateral-torsional buckling of a Class 1 stainless steel IPE welded section

In this section a comparison between the results obtained using the 2D material properties introduced in SAFIR for shell elements with the results obtained using 3D beam elements from SAFIR, with and without residual stresses, is presented.

It was chosen to test simply supported beams subjected to uniform bending with Class 1 welded IPE220 cross-section (see figure 7). In the numerical simulations, a lateral geometric imperfection given by expression (5) was considered. The yield strength and the ultimate strength considered were, according to the Eurocode 3, 210MPa and 520MPa respectively. The comparisons were made with uniform temperature of 600ºC in the cross-section.

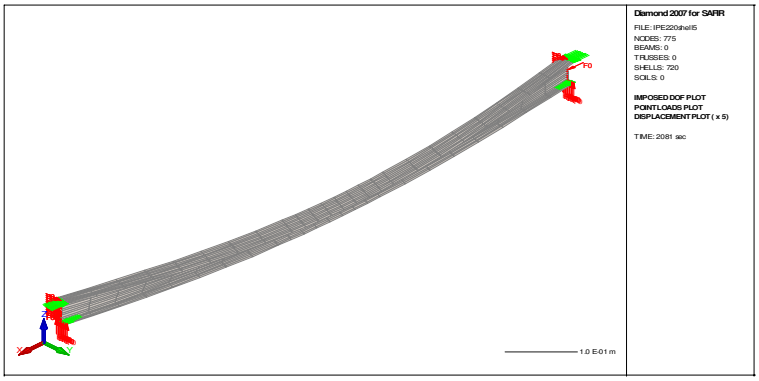

Fig. 7 – Simply supported stainless steel beam subjected to uniform bending.

The adopted residual stresses are considered as constant across the thickness of the webs and flanges. For the welded IPE section, the distribution shown in figure 8, that has the maximum value of f_y (yield strength) [12] was used.

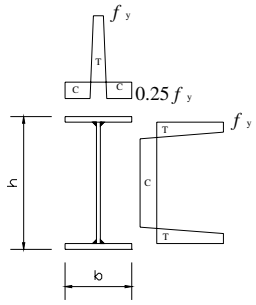

Fig. 8 – Residual stresses in an IPE welded section: C – compression; T – tension.

Table 2 – Results

		Without residual stresses	With residual stresses	Eurocode 3
L=3m	3D-Beam	20.6 kNm	19.9 kNm	20.3 kNm
	Shell	19.3 kNm	19.2 kNm	
L=5m	3D-Beam	15.7 kNm	15.0 kNm	14.1 kNm
	Shell	14.3 kNm	14.0 kNm	

From table 2 it can be concluded that the introduction of the residual stresses in shell elements, gives results that are in good agreement with the results obtained with the 3D beam elements.

4 RESIDUAL STRESSES IN CLASS 4 STAINLESS STEEL SQUARE HOLLOW SECTIONS

In order to study the influence of the residual stresses in Class 4 sections it is presented here a study.

It is compared the numerical results obtained for columns with the square hollow sections SHS150x150x3 and SHS200x200x5 of the stainless steel grade 1.4301. The yield strength and the ultimate strength considered were, according to the Eurocode 3, 210MPa and 520MPa respectively. The comparisons were made with uniform temperature of 600ºC in the cross-section. The tested columns had lengths of 0.9m with fixed ends and were subjected to centric axial compression (see figure 9). This length was chosen so that the collapse would be by local buckling instead of global buckling. In these numerical tests the curvature of the corners was considered.

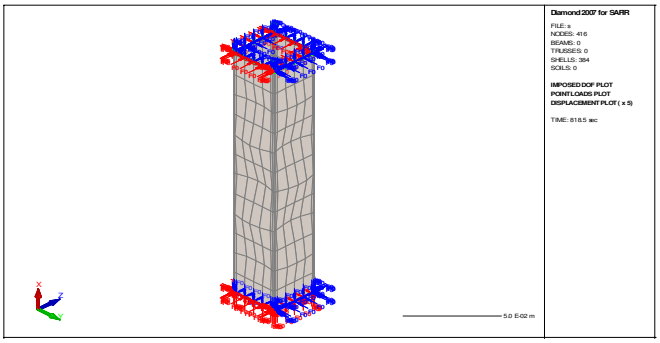

Fig. 9 – Stainless steel beam analysed with shell elements with residual stresses.

For the tested columns without residual stresses it was considered the following possibilities:

a) not having geometric imperfections and not introducing higher corners yield strength according to [11];
b) not having geometric imperfections but introducing higher corners yield strength;
c) having only global imperfections given by expression (5) and introducing higher corners yield strength;
d) having only local imperfections with a maximum value of b/200 [13] and introducing higher corners yield strength;
e) having global imperfections given by expression (5), local imperfections with a maximum value of b/200 and introducing higher corners yield strength;

Table 3 – Ultimate axial compression effort without residual stresses

Case	SHS150x150x3	SHS200x200x5
a)	160.5 kN	423.8 kN
b)	175.5 kN	473.6 kN
c)	174.5 kN	465.6 kN
d)	149.5 kN	387.9 kN
e)	149.5 kN	387.9 kN

From table 3 it can be concluded that no global imperfections are needed to be considered. Therefore it were introduced the residual stresses only in the case d).

The adopted residual stresses are considered as constant across the thickness of the internal section members. For the square hollow section, the distribution shown in figures 10, which has the maximum value of half of f_y [14] was used.

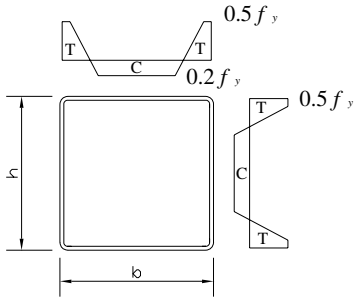

Fig. 10 – Residual stresses in a hollow section: C – compression; T – tension.

Table 4 shows the obtained results for columns with local imperfections with and without residual stresses

Table 4 – Ultimate axial compression effort with local imperfections

	SHS150x150x3	SHS200x200x5
Without residual stresses	149.5 kN	387.9 kN
With residual stresses	139.5 kN	376.5 kN
With/Without residual stresses	0.93	0.97
EN 1993-1-2 [1, 6, 13]	136.9 kN	356.8 kN

From these results it can be concluded that the influence of the residual stresses is low. However this influence is of the same magnitude of the one observed in table 2 for a Class 1 section.

The comparison with EC3 appears to show a good approximation to the numerical results.

4. CONCLUSIONS

This paper has shown that the approximation made for the stainless steel hardening law at high temperatures, to be used in the SAFIR shell elements, gives good results.

The influence of the residual stresses in the resistance of stainless steel Class 4 sections is low. However this influence is of the same magnitude to the one observed in table 2 for a Class 1 section, which leads to think that they should be also taken into consideration.

ACKNOWLEDGEMENTS

The authors are very grateful the Calouste Gulbenkian Foundation (Portugal) for its supports through the scholarship given to the first author and would like to thank Prof. Paulo Piloto for the numerical results obtained with ANSYS.

REFERENCES

[1] European Committee for Standardisation, “EN 1993-1-2 Eurocode 3: Design of Steel Structures - Part 1.2: General rules - Structural fire design”, Brussels, Belgium, April 2005.
[2] Franssen, J.-M., “Residual stresses in steel profiles submitted to the fire: an analogy”, 3rd CIB/W14 Workshop “Modelling”, TNO Building and Construction Research, Rijswijk, The Netherlands, 1993.
[3] Estrada, I., “Shear Design of Stainless Plate Girders”, PhD Thesis, Universitat Politècnica de Catalunya, Barcelona, Spain, 2005.
[4] Gardner, L., “The use of stainless steel in structures”, Progress in Structural Engineering and Materials, 7(2), pp. 45–55, 2005.
[5] Euro Inox and Steel Construction Institute, “Design Manual for Structural Stainless Steel”, 3rd edition, 2006.
[6] European Committee for Standardisation, “prEN 1993-1-4 Eurocode 3, Design of Steel Structures – Part 1.4. General rules – Supplementary Rules for Stainless Steels”, Brussels, Belgium, 2005.
[7] Franssen, J.-M., “SAFIR. A Thermal/Structural Program Modelling Structures under Fire”, Engineering Journal, A.I.S.C., Vol. 42, No. 3, pp. 143-158, 2005.
[8] Doneux, C.; Franssen, J.-M., “2D constitutive models for the shell elements of the finite element software SAFIR”, M&S report, translation of "Rapport interne - SPEC/97_01" by C. Doneux, University of Liege, Liege, Belgium, 2003.
[9] Ala-Outinen T., Oksanen T., “Stainless steel compression members exposed to fire”, VTT Research Notes 1864. Espoo, Finland; 1997
[10] European Committee for Standardisation, “EN 1090-2. Execution of Steel and aluminium Structures – Part 2: Technical Requirements for the execution of steel structures”, 2005.

[11] Ashraf M., Gardner L., Nethercot DA., "Strength enhancement of the corner regions of stainless steel cross sections", in Journal of Constructional Steel Research, 2005;61(1): 37-52.
[12] Chen WF, Lui EM., "Stability design of steel frames", CRC Press, 1991.
[13] European Committee for Standardisation, "EN 1993-1-5 Eurocode 3: Design of Steel Structures - Part 1.5: Plated structural elements", Brussels, Belgium, February of 2003.
[14] ECCS, "Ultimate Limit State Calculation of Sway Frames with Rigid Joints", first edition, 1984.

Connections in Steel and Composite Structures

MODELLING OF FLEXIBLE END PLATE CONNECTIONS IN FIRE USING COHESIVE ELEMENTS

Ying Hu[1], Ian Burgess[2], Buick Davison[3], Roger Plank[4]

ABSTRACT

In the UK, simple steel connections, including flexible end plates, fin plates and web cleats, are the most popular for steel structures. Experimental tests completed in Sheffield have shown that issues concerning tying resistance and ductility are problematic for simple steel connections at elevated temperatures, which could significantly affect the overall performance of steel structures due to a loss of structural integrity in a fire situation.

Conducting experimental tests is an attractive and straight-forward research approach but is time-consuming and expensive in comparison with finite element modelling. A numerical approach has been developed in this project to investigate the performance of simple steel connections in fire conditions. This paper presents a quasi-static analysis with cohesive elements to investigate the resistance and ductility (rotation capacity) of simple steel connections (flexible end plates) in fire conditions. In comparison with experimental test data, a good correlation with the finite element analysis is achieved and the method is suitable to study the tying resistance and ductility for simple steel connections with various dimensions at different temperatures.

1. INTRODUCTION

Simple steel connections including flexible end plates (header plates), fin plates and web cleats (double web angles), are the most popular steel connection types currently in use

[1] PhD research student, Department of Civil and Structural Engineering, The University of Sheffield, Sheffield S1 3JD, UK, Email: cip05yh@sheffield.ac.uk

[2] Professor, Department of Civil and Structural Engineering, The University of Sheffield, Sheffield S1 3JD, UK, Email: ian.burgess@sheffield.ac.uk

[3] Associate Professor, Department of Civil and Structural Engineering, The University of Sheffield, Sheffield S1 3JD, UK, Email: j.davison@sheffield.ac.uk

[4] Professor, School of Architecture, The University of Sheffield, Sheffield S10 2TN, UK Email: r.j.plank@sheffield.ac.uk

for building construction in the UK, owing to the simplicity and economy in both fabrication and assembly[1]. The fire research group at the University of Sheffield developed an extensive series of tests to investigate the robustness of steel connections in a fire situation; the experimental tests demonstrated that issues concerning the resistance and ductility of connections are problematic in fire conditions. Conducting experimental tests is always time-consuming, expensive, and poses the additional difficulties of recording movement and strain within a furnace. Thereafter using experimental data for validation, but simulating the connection behaviour with finite element modelling, provides an opportunity for wider parametric investigations and eliminates the limitations associated with experiments [2]. Initial attempts to simulate steel connections started with two dimensional models (2D models), owing to the limitations in computational resources both in terms of software and hardware. In a 2D model, each component of a connection can be represented by using shell or truss elements, and the interactions between these components are numerically simplified to avoid convergence difficulties in the numerical computation. Because of the rapid improvement in hardware and software, computers are now able to perform more detailed simulations for connections in 3D models. Krishnamurthy *et al.* [3] and Kukreti *et al.* [4] compared numerical results produced by two-dimensional and three-dimensional simulations, and found the three-dimensional numerical model to be more flexible than the two-dimensional counterpart, resulting in larger displacements and stresses. Vegte *et al.* [5] believe that, since bolted steel connections are three-dimensional in nature, two-dimensional numerical models are therefore unable to represent the three-dimensional behaviour satisfactorily. Hence, a three-dimensional non-linear finite element analysis approach has been developed as an alternative method for the investigation of connection robustness in fire.

2. THE FINITE ELEMENT MODEL DESCRIPTION

Sherbourne and Bahaari [6 7] developed a three-dimensional finite element model for simulating endplate connections by using brick elements. The model was assumed to have a continuous connection between the nodes of the bolt head and nut, and the nodes of end plates, and as a consequence, the relative motions between bolt, column flange and end plates were numerically simplified. The bolt shank behaviour was represented using truss elements instead of brick elements which prevents the numerical model reproducing properly the bearing action between bolts and bolt holes, because the interface between the bolt shank and the hole boundary was neglected. Bursi and Jaspart [8] presented a more realistic finite element model for T-stub connections. This numerical model is capable of simulating the complex interactions such as contact, friction, stick and slip conditions, stress concentrations and prying actions in a real connection. Bolts and endplates in the simulation are represented as individual components using brick elements, and are no longer connected through common nodes, enabling relative movement between these components [9]. Although this numerical approach results in finite element simulations which are much more complicated and computationally expensive in terms of time, it has nevertheless been adopted by many researchers owing to the improvement in numerical accuracy.

A three dimensional numerical model was created for a flexible end plate connection, using the ABAQUS finite element code, in order to investigate its resistance and ductility at ambient and elevated temperatures. This model started with the creation of individual components such as bolts, endplates, beams and columns, and then assembled these components, as shown in *Fig. 1*.

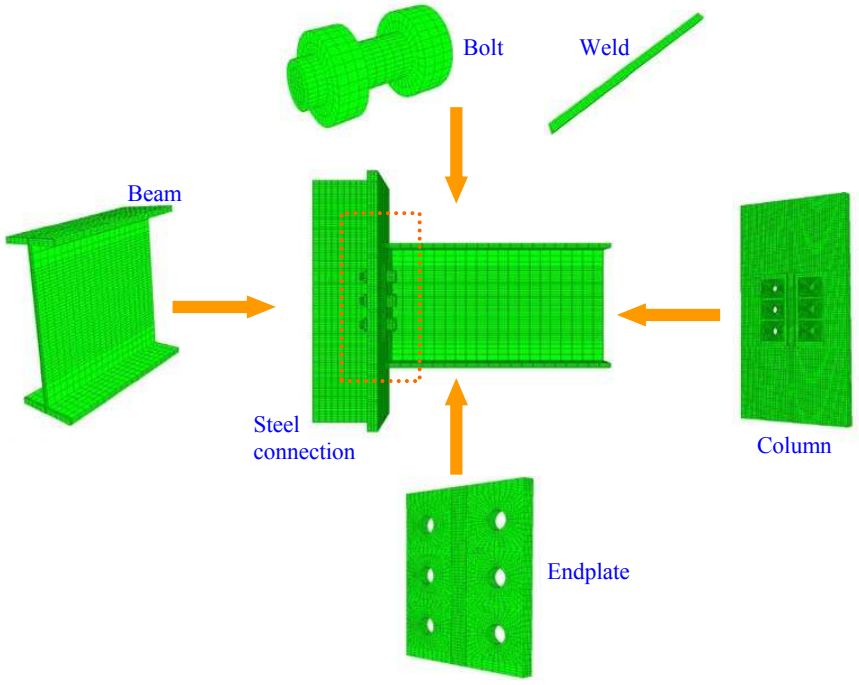

Fig. 1 - FE model for a flexible end plate connection

All these components were modelled using eight-node continuum hexahedral brick elements, and a small number of cohesive elements were used in the heat affected zone (HAZ) where the failure of endplates was seen to occur. The brick element has the capability of representing large deformation, and geometric and material nonlinearity, whilst the traction separation law of cohesive elements is able to demonstrate the rupture of end pates in a real connection. The contacts among bolts, endplates and column flanges were simulated by surface-to-surface formulations. In order to simulate this nonlinear performance, an intensive mapped mesh was made within the bolts and the vicinity of the bolt holes, shown in *Fig. 1*. The following discusses the details of how to create a FE model for a flexible end plate connection.

2.1 Solution Strategy

Within ABAQUS, two different solution strategies are available: the standard analysis and the explicit solution procedure. The standard analysis is implicitly based on static equilibrium, characterized by the assembly of a global stiffness matrix and simultaneous solution of a set of linear or nonlinear equations [9], which enables a wide range of linear and nonlinear engineering simulations to be carried out efficiently. For most nonlinear analyses, the Newton-Raphson method is used to converge the solution at each time step along the force deflection curve. However, if the tangent stiffness is zero, Newton-Raphson method is unable to achieve the convergence. To avoid this problem, the Arc-Length algorithm (Riks method) should be used to allow the load and displacement to vary throughout the time step [10]. Nevertheless, for a numerical model with complicated contact interactions, these two solution algorithms are unlikely to produce an easy and smooth solution in the computation.

The explicit solution procedure is a dynamic procedure originally developed to simulate high-speed impact events in which inertia plays a dominant role in the solution, and

achieving the convergence is not needed in the simulation. This approach has proved to be valuable in solving static problems as well. One advantage of the explicit procedure over the implicit procedure is the greater ease in resolving complicated contact problems. In addition, for very large models, the explicit procedure requires less system resources than the implicit procedure [10].

Applying the explicit dynamic procedure for quasi-static simulations requires some special considerations. Since a quasi-static event is a long-time process, it is often computationally impractical to have the simulation in its natural time scale, which would require an excessive number of small time increments[10]. Hence, this event must be accelerated in some way in the simulation; however, the arising problem is that inertial forces (dynamic effects) become more dominant as the event is accelerated. So the crucial point for a quasi-static simulation is to model the event in the shortest time period in which inertial forces remain insignificant. To achieve this point, Vegte [9] recommends researchers to monitor the various components of the energy balance throughout the loading process. In a quasi-static simulation, the work applied by the external forces is nearly equal to the internal energy of the system; as a general rule, the kinetic energy of the deforming material should not exceed a small fraction (typically 5% to 10%) of its internal energy throughout most of the process [10]. In order to reduce the solution time in simulations, *mass scaling* (artificially increase the mass to reduce inertial effects) is the only option for researchers, which enables an analysis to be performed economically without artificially increasing the loading rate [10].

2.2 Element Types

ABAQUS contains a large variety of hexahedron (brick), shell, contact and beam elements endowed with different features depending on the application. Kukreti *et al.* [4] and Gebbeken *et al.* [11] carried out a comparative investigation on numerical techniques in analyzing bolted steel connections with the intention of reproducing the experimental results in a finite element fashion. They set up a two-dimensional finite element model (using shell elements) and a three-dimensional finite element model (using brick elements) within ABAQUS. The comparison between numerical results and experimental data illustrated that the two-dimensional model is too stiff for the representation of the real deformations [11], and the hexahedron (brick) element is much more suitable to model the continuum behaviour of bolted connections compared to standard shell elements.

The current ABAQUS element library offers engineers and numerical analysts a number of hexahedron elements in finite element simulations. For hyperbolic problems (plasticity-type problems), Bursi and Jaspart [13] suggest that the first order elements are likely to be the most successful in reproducing yield lines and strain field discontinuity. This is because some components of the displacement solution can be discontinuous at element edges. Simulations performed by Bursi and Jaspart [13] compared three eight-node brick elements: (1) The C3D8 element with full integration (8 Gauss points). This element is accurate in the constitutive law integration; but the shear locking phenomenon is commonly associated with it when simulating bending-dominated structures [10]. (2) The C3D8R element with reduced integration (1 Gauss point). This element supplies a remedy for the shear locking problem caused by using C3D8, but the rank-deficiency of the stiffness matrix may produce spurious singular (hourglassing) modes [10], which can often make the elements unusable unless it is controlled. In order to control the hourglass modes in elements, Flanagan and Belytschko [14] proposed the artificial stiffness method and the artificial damping method in the ABAQUS code; although the artificial damping approach is available only for the solid and membrane elements in ABAQUS Explicit. (3) The C3D8I element with full integration (8 Gauss points) and incompatible modes. This element has 13 additional degrees of freedom

and the primary effect of these degrees of freedom is to eliminate the so-called parasitic shear stresses that are observed in regular displacement elements in analyzing bending-dominated problems [10]. In addition, these degrees of freedom are also able to eliminate artificial stiffening due to Poisson's effect in bending.

Through comparative modelling with the aforementioned three brick elements, the C3D8I elements were found to perform particularly well both in the elastic and inelastic regimes, and are suitable for representing the bending-dominated behaviour of a structure [8]. As expected from the theoretical formulation, C3D8R elements underestimate the strength value and the plastic failure load in the finite element modelling. From calibration tests, Bursi and Jaspart [8] also state that C3D8 elements appear to be unsatisfactory, owing to the overestimation of the plastic failure load and the shear locking phenomenon. Therefore, in order to predict the behaviour in a conservative fashion, the element selected for bolted steel connections is the reduced integration brick element C3D8R. In order to control the hourglass modes, a very dense mesh finite element model has been set up for a finite element model.

2.3 Contact Modelling within ABAQUS

In numerical simulations, obtaining realistic representation of connection performance depends upon handling the difficult issues of modelling the contact interaction between various joint components. Within ABAQUS, the contact behaviour can be simply reproduced by using so-called "gap elements", which require the user to define pairs of nodes and specify the value of a clearance gap. These elements allow for two nodes to be in contact (gap closed) or separated (gap open) under large displacements [8]. The limitation of this sort of element is the friction between two contacted components being ignored in the simulation. Furthermore, simulation using these elements is a tedious and time-consuming task [9].

In order to overcome these problems, a "surface-to-surface" contact interaction was developed for the numerical model. The simulation requires the researcher to first determine the slave and master surfaces for two deformable bodies and then define the interaction behaviour between these two surfaces. In the standard analysis, ABAQUS affords two formulations, small-sliding formulation and finite-sliding formulation, for modelling the interaction between two discrete deformable bodies. In the explicit analysis, the interactions between surfaces are modelled by a different contact formulation, which includes the constraint enforcement method, the contact surface weighting, the tracking approach and the sliding formulation. In the explicit analysis, the friction conditions (sliding and sticking) between the master and slave surfaces may be represented by the classical isotropic Coulomb friction model, which has proved to be suitable to steel elements [15]. However, it is of great importance to be careful with the assignment of the slave and master surfaces [2]. It is generally accepted that the surfaces working as master surfaces should belong to the bodies with the stronger material or a finer mesh. In simulating bolted steel connections, experience shows that heat generation caused by frictional sliding is not significant in experimental tests and therefore may be ignored in the finite element modelling.

2.4 Material Properties for the Finite Element Model

For realistic simulations, Bursi and Jaspart [13] state that proper material properties are required in the explicit solution procedure. The material properties for the various components of steel connections may be determined from the engineering stress-strain relationship using nonlinear material curves recommended in Eurocode 3. They may also be defined according to stress-strain relationships obtained in standard tensile tests of steel.

In the connection tests, a 254UC89 was used for the column and a 305x165UB40 for the beam. The thickness of the end plate was 10 mm. The steel used was S275 for endplates

and UB sections; and S355 was used for UC sections. All the bolts are M20 grade 8.8 used in 2 mm clearance holes. The nominal material properties of these components are summarised in *Table 1*.

Table 1 - Material properties

Material type	Yield stress [N/mm^2]	Ultimate stress [N/mm^2]	Density [kg / m^3]	Young's modulus [kN/mm^2]	Poisson's ratio
S275	275	450	7850	205	0.3
S355	355	550	7850	205	0.3
8.8 bolt	640	800	7850	205	0.3

However, material properties used for FE modelling are between the tensile test data from testing labs and the material properties determined according to Eurocode 3, which is shown as a green dotted curve in Fig. 2 (dashed blue line and solid red curve in the figure respectively represent the material properties determined from tensile tests and Eurocode 3).

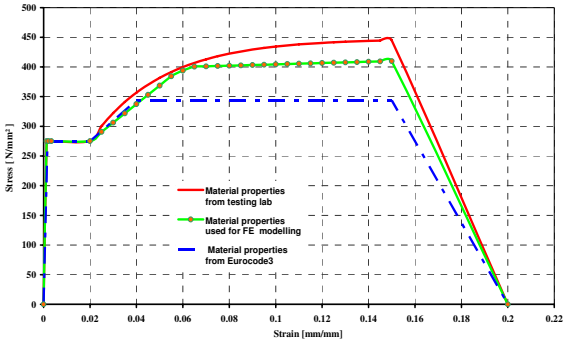

Fig. 2 - Material properties for steel

Since ABAQUS codes operate in a large deformation setting, in order to consider the deformed area the nonlinear relationship of *true stress* versus *true strain* is required to be defined for steel components. However, most material test data are supplied with engineering stresses and strains (nominal stresses and nominal strains) according to the uniaxial material testing response [16]. In such situations, it is necessary to convert material data from engineering stress and strain to true stress and strain using the following relationship:

$$\sigma_{true} = \sigma_{nom} (1 + \varepsilon_{nom}) \quad (1)$$

σ_{true} is the true stress
σ_{nom} is the nominal stress
ε_{nom} is the nominal strain

The relationship between the true strain and nominal strain is defined as:

$$\varepsilon_{true} = \ln (1 + \varepsilon_{nom}) \quad (2)$$

The true stress (σ_{true}) is a function of the nominal stress and nominal strain; and the true strain (true total strain, ε_{true}) is determined by the logarithm of nominal strain (total strain, ε_{nom}). For inputting into ABAQUS, the total strain values (ε_{true}) should be decomposed into the elastic and plastic strain components ($\varepsilon_{el, true}$ and $\varepsilon_{pl, true}$). The true elastic strain ($\varepsilon_{el, true}$) can be captured by the true stress (σ_{true}) divided by the Young's modulus (E); and the true plastic strain, required for the explicit solution procedure, can be obtained using the following relationship:

$$\varepsilon_{pl,\,true} = \varepsilon_{true} - \varepsilon_{el,\,true} = \ln(1 + \varepsilon_{nom}) - \sigma_{true}/E \quad (3)$$

Hence, the elastic-plastic material curves, shown in Figures 2 and 3, are used for the aforementioned steel components in the connection simulations.

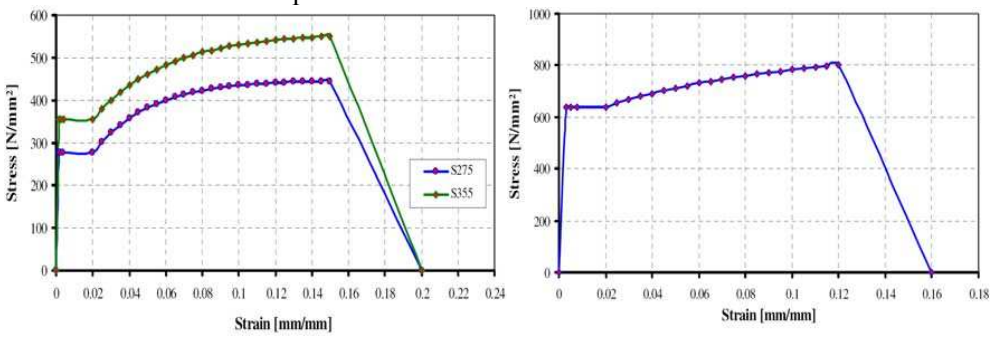

(a) (b)

Fig. 3 - Stress-strain curves for (a) S275 and S355 steel and (b) grade 8.8 high strength bolts [2]

2.5 Modelling the Rupture with Cohesive Elements

To simulate the rupture of endplates, a small number of cohesive elements have been embedded into the heat affected zone (HAZ) in the numerical model. When the cohesive elements and their neighbouring components have matched meshes, it is straightforward to connect cohesive elements to other elements in a model simply by sharing nodes. If the neighbouring elements do not have matched meshes, ABAQUS enables the cohesive elements to be connected to other components by using surface-based tie constraints [10].

The cohesive elements (cohesive zone) represent a fracture of a material as separation across surface and the constitutive response of these elements is determined by the relationship of traction versus separation (*traction separation law*). The available traction-separation model in ABAQUS assumes initially linear elastic behaviour followed by the initiation and evolution of damage. To determine this constitutive response, a number of parameters, such as critical separation (δ_0), cohesive energy (Γ_o) and cohesive strength (T_0), are required for the explicit solution procedure, as shown in *Fig. 4* .

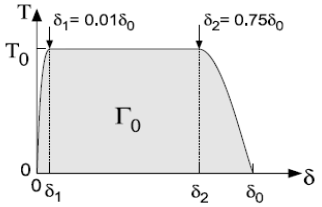

Fig. 4 - Traction-separation law for fracture [12]

Cornec *et al.* [12] recommend that the cohesive strength (T_0) may be taken as the maximum stress at fracture in a round notched tensile bar. But Scheider *et al.* [17] add that this procedure might not be applicable to thin specimens, as round notched bars can not be machined from sheet metal and the individual failure mode (normal fracture) would be different from that in the flat specimen (slant fracture). As an estimation for the simulation, Scheider *et al.* [17] recommend that the nominal stress of the flat tensile specimen at fracture (load divided by the area of the normal projection of its inclined fracture surface, $F_{frac}/A_{frac} \approx 470.5$ Mpa) may be used as T_0 . To simulate the progressive damage in the cohesive zone, it is of great importance to determine the critical separation (δ_0) and cohesive energy (Γ_0). The determination of δ_0

heavily relies on experience in numerical simulation and experimental tests, and three times the separation value at damage initiation (δ_1, shown in *Fig.*4) or over has been adopted for the explicit solution procedure. Thus the cohesive energy (Γ_0) may be estimated by using the following relationship [12]:

$$\Gamma_o = 0.87\ T_0\ \delta_0 \quad \text{.....(4)}$$

or

$$\Gamma_o = T_0\ \delta_0 \quad \text{.....(5)}$$

3. COMPARISON OF NUMERICAL RESULTS WITH EXPERIMENTAL TESTS

The numerical simulations were validated against experimental results at ambient temperatures and also at elevated temperatures. Experimental data was taken from connection test results carried out at the University of Sheffield [18].

3.1 Comparison of Flexible End Plate Model at Ambient Temperatures

Hu *et al.* [18] investigated the resistance and rotation capacity (ductility) of simple steel connections at ambient and elevated temperatures, focusing on flexible end plates. In the programme, twelve tests have been performed for end plate connections, including three tests at ambient temperatures and nine tests for high temperatures. The deformation (rotation) in the connection zone was recorded by inclinometers (angular transducers) for the first three tests at ambient temperatures, and the applied external force was captured by strain gauges on the loading system (three Macalloy bars: oven, link and jack).

The numerical model was created for flexible end plates by using the ABAQUS commercial software package, and the geometrical details of the model are shown in *Fig. 5*. A 254UC89 was used for the column and a 305x165UB40 for the beam, and the thickness of endplate is 10 mm. The steel used was S275 for universal beams and end plates, whereas the column was S355. Dimensions in *Fig. 5* are shown in mm.

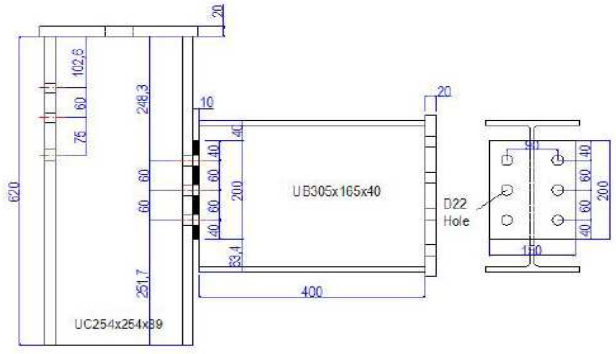

Fig. 5 - Geometrical details of the flexible endplate connection

The deformed and undeformed shapes of the numerical model are displayed for flexible end plates in *Fig.6*, including the contour plots for the components as well, such as bolts and endplates. The FE analysis clearly demonstrates that the rotation capacity of these connections is mainly produced by deformation in the end plates, welds and bolts, and the deformation of the column flange and beam web may be neglected in the analysis.

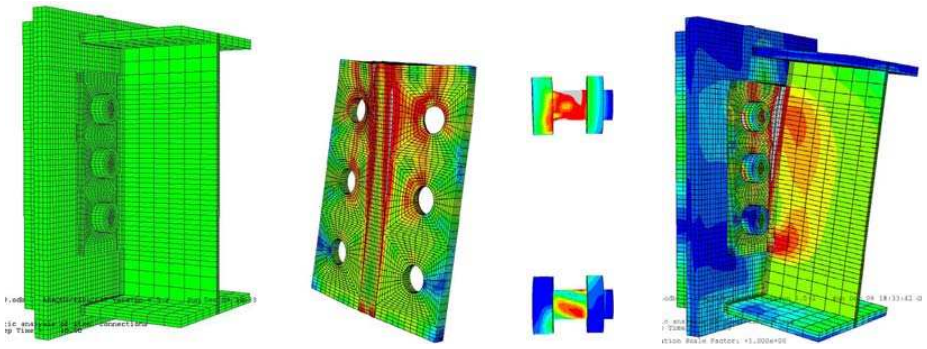

Fig. 6 - FE model of flexible end plate connection: deformed and un-deformed shapes

The relationships of loads and rotations of the numerical model have been compared with experimental data of three connection tests, as shown in *Fig. 7* . The red curves in *Fig. 7* (a), (b) and (c) are the numerical plots produced in ABAQUS; and the loads and rotations, recorded in experimental tests, are displayed as green. The kink in the green curve is at about 6^o rotation as an evidence of the beam bottom flange contacting with the column flange. It is apparent in *Fig7.* (a) and (c) that the numerical plots are in good agreement with experimental plots, and also noted in *Fig7.* (b) that the discrepancy exists between the numerical and experimental results, as variation between the real specimens cannot be represented in a numerical model.

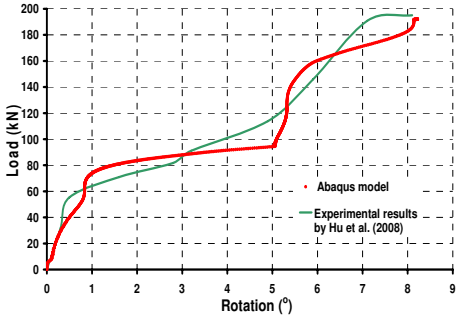

(a) 35^o

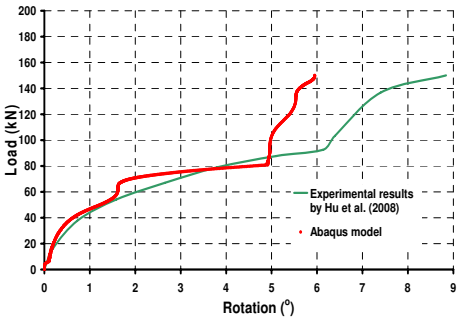

(b) 45^o

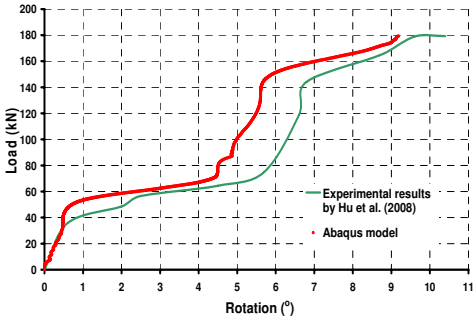

(c) 55^o

Fig. 7 - Load-Rotation comparisons between FE model and experimental results for flexible end plate connections (a) 35^o (b) 45^o (c) 55^o

3.2 Comparison of Flexible End Plate Model at Elevated Temperatures

Nine tests for flexible end plates have been carried out at the temperatures of 450 °C , 550 °C and 650 °C, and the relationships of loads versus rotations are plotted in *Fig. 8*. To simulate the performance of these connections in fire conditions, the numerical model requires the material properties to be applied at the predetermined temperatures, and the reduction retention factors used are recommended from EC3 (BSI, 2005). The deformed shapes of connections are also shown in *Fig. 8* for each temperature. It was observed that the connections both in numerical simulation and experiments failed by the rupture of endplates before the beam flange contacted with the column flange. Except for *Fig. 8* (g), the curves of loads and rotations, produced by numerical simulation, are in good agreement with recorded experimental data.

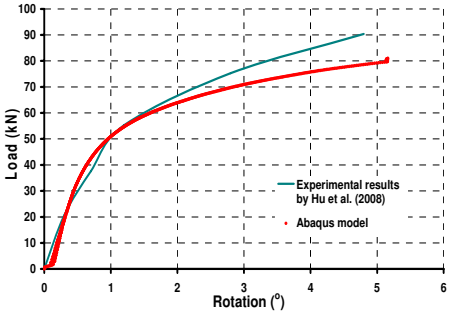

(a) 35° - 450 °C

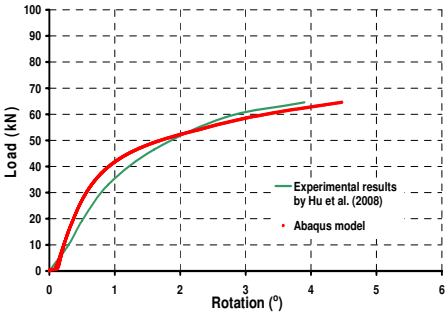

(b) 45° - 450 °C

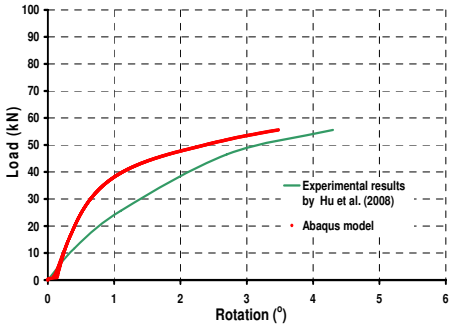

(c) 55° - 450 °C

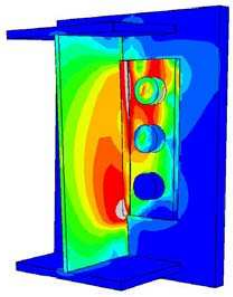

(d) Deformed shape at 450 °C

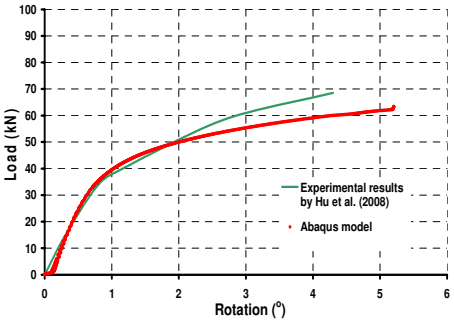

(e) 35° - 550 °C

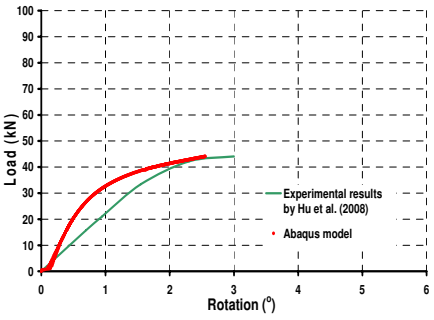

(f) 45° - 550 °C

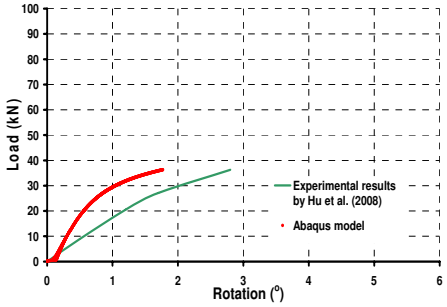

(g) 55° - 550 °C

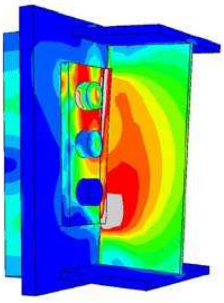

(h) Deformed shape at 550 °C

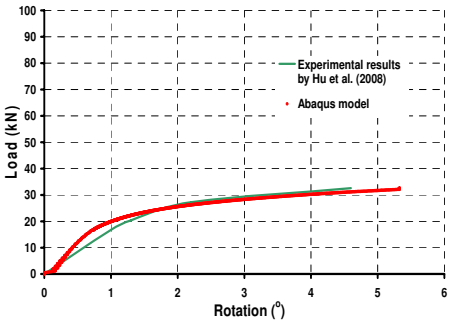

(i) 35° - 650 °C

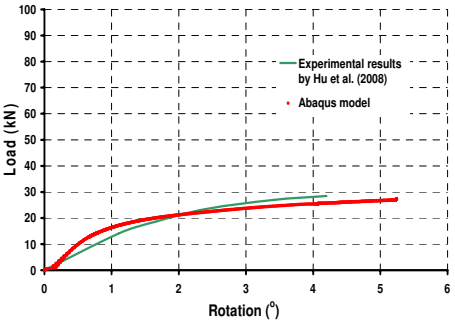

(j) 45° - 650 °C

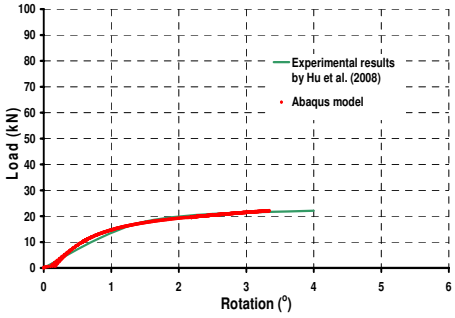

(k) 35° - 650 °C

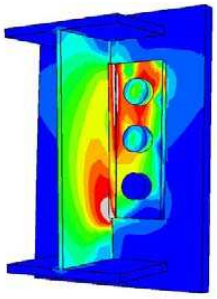

(l) Deformed shape at 650 °C

Fig. 8 - Load-Rotation comparisons between FE model and experimental results for flexible end plate connections

4. CONCLUSIONS

This paper reports on the development of a finite element model embedded with cohesive elements to estimate the resistance and ductility of flexible endplate connections in fire conditions. From the comparative results in *Fig. 7* and *Fig. 8*, the numerical model with cohesive elements is able to estimate the failure of steel connections due to the rupture of endplates. In addition, the results from the aforementioned two figures also showed that the explicit solution technique is a reliable and suitable tool to effectively simulate the performance of bolted connections. Therefore, the simulation strategies employed in this paper may be use for further parametric studies of flexible endplate connections.

5. ACKNOWLEDGEMENT

The research work described in this paper is part of a project funded under Grant EP/C 510984/1 by the Engineering and Physical Sciences Research Council of the United Kingdom. This support is gratefully acknowledged by the authors.

6. REFERENCES

[1] Steel Construction Institute, "Joints in Simple Construction", SCI, Berkshire, Publication No. P206, 2002
[2] Sarraj, M. " The Behaviour of Steel Fin Plate Connections in Fire ", PhD Thesis, The University of Sheffield, 2007
[3] Krishnamurthy, N. and Graddy, D.E. , "Correlation between 2- and 3- Dimensional Finite Element Analysis of Steel Bolted End-Plate Connections", *Computers and Structures*, Vol. 6, pp. 381-389, 1976
[4] Kukreti, A. R. , Murray, T.M. and Abolmaali, A. , "End plate connection moment-rotation relationship", *Journal of Constructional Steel Research*, Vol. 8, pp. 137-157, 1987
[5] Vegte, G.J. van der, Makino, Y. and Sakimoto, T., "Numerical Research on Single-Bolted Connections Using Implicit and Explicit Solution Techniques", Memoirs of the Faculty of Engineering, Kumamoto University, Vol. 47, No.1, 2002
[6] Sherbourne, A.N. and Bahaari, M.R. , "3D Simulation of End-Plate Bolted Connections", *Journal of Structural Engineering*, Vol. 120, No. 11, pp. 3122-3136, 1994
[7] Sherbourne, A.N. and Bahaari, M.R. , "Finite Element Prediction of End-Plate Bolted Connections Behaviour. I : Parametric Study", *Journal of Structural Engineering*, Vol. 123, No. 2, pp. 157-164, 1997
[8] Bursi, O.S. and Jaspart, J.P. , "Benchmarks for finite element modelling of bolted steel connections", *Journal of Constructional Steel Research*, Vol. 43, No. 1-3, pp. 17-42, 1997
[9] Vegte, G.J. van der, "Numerical Simulations of Bolted Connections: The Implicit Versus The Explicit Approach", *@http://www.bouwenmetstaal.nl/congres_eccs_04/ Vegte_Makino_bolted.pdf* , 2008
[10] ABAQUS analysis user's manual version 6.6, ABAQUS inc 2006
[11] Gebbeken, N. , Rothert, H. and Binder, B. , "On the numerical analysis of end plate connections", *Journal of Constructional Steel Research*, Vol. 30, pp. 177-196, 1994
[12] Cornec, A. , Scheider, I. and Schwalbe, K. H. "On the practical application of the cohesive model", *Engineering Fracture Mechanics*, Vol. 70, pp.1963-1987, 2003
[13] Bursi, O.S. and Jaspart, J.P. , "Basic issues in the finite element simulation of extended end plate connections", *Computers and Structures*, Vol. 69, pp. 361-382, 1998
[14] Flanagan, D.P. and Belytschko, T.A. , "A uniform strain hexahedron and quadrilateral with orthogonal hourglass control", *International Journal for Numerical Methods in Engineering*,Vol. 17, No.5, pp. 679-706, 1981
[15] Charlier, R. and Habraken A.M. , "Numerical metallisation of contact phenomena by finite element method" , *Comput. Geotech.*, Vol.9, pp. 59-72, 1990
[16] Bathe, K. J. , "Finite Element Procedures", Prentice Hall, Englewood Cliffs, New Jersey, 1982
[17] Scheider, I. , Schődel, M. , Brocks, W. and Schőnfeld, W. , "Crack propagation analyses with CTOA and cohesive model: Comparison and experimental validation", *Engineering Fracture Mechanics*, Vol. 73, pp. 252-263, 2006
[18] Hu, Y., Davison, B., Burgess, I. and Plank, R. , "Experimental Study on Flexible End Plate Connections in Fire", Eurosteel 2008: 5th European Conference on Steel and Composite Structures, in press, 2008

BEHAVIOR OF STEEL PLATE CONNECTIONS SUBJECT TO VARIOUS FIRE SCENARIOS

SERDAR SELAMET[1] and MARIA E. M. GARLOCK[2]

ABSTRACT

Shear connections connect a beam to a girder or to a column, and they are designed to resist only shear loads. In a fire event, the axial restraint provided by adjacent structure creates compressive and tensile forces in the beam and thus the connection. Using finite element (FE) models, this study examines single-plate shear connections that are bolted to the beam and welded to the supporting girder. The model is validated with experiments of bolted lap splice plates at elevated temperatures as well as full-scale experiments. A floor subassembly, i.e., the beam and girder and connection, is modeled so that appropriate forces (shear, axial, and moment) are applied to the connection. This floor subassembly is subject to a few fire scenarios to evaluate effects of rate of heating on the beam and connection components.

1. INTRODUCTION

Recent experimental research in the UK has shown that it is possible to design a steel beam without fire protection if tensile forces can develop in the connection at elevated temperatures[1, 2, 3]. This same experimental research has shown that failure in the joint region may develop from tensile forces that arise from beam catenary action (where the beam hangs in tension) or beam contraction (during the cooling phase of the fire). Failure in the connection region is not a surprise since the connections are not designed to resist significant tensile forces at elevated temperatures.

Previous studies of steel frames under fire indicate that to get accurate predictions of the global response of a steel frame under fire, it is essential to understand how the

[1] Graduate Student, Princeton University, Dept. of Civil and Environmental Engineering, Princeton, NJ, 08544
email: sselamet@princeton.edu
[2] Assistant Professor, Princeton University, Dept. of Civil and Environmental Engineering, Princeton, NJ, 08544
email: mgarlock@princeton.edu

connections perform. The connections essentially define the boundary conditions (restraint) of the members, which in turn define the response of the steel frame. In a steel framed building, the connections support the floor beams and provide overall stability to the structure. In a fire scenario, the performance of the connections therefore plays a crucial role on the response of the structure as a whole.

Furthermore, a recent survey[4] has shown that where partial floor collapse ensued in steel buildings under fire, that collapse always originated in the steel *shear* connections. Shear connections connect a beam to a girder or to a column, and they are designed to resist only shear loads. In a fire event, the axial restraint provided by adjacent structure creates compressive and tensile forces in the beam and thus the connection.

This paper presents some work that has recently begun at Princeton University on examining steel connections under fire. Specifically, *single-plate* (also called shear tab or fin plate) connections are presented in this paper (Figure 1). Using 3D finite element (FE) models, we examine single-plate shear connections that are bolted to the beam and welded to the supporting girder or column. This connection is studied as a part of a floor subassembly for reasons described below. The subassembly is subject to various fire scenarios to examine the effects of rate of heating on the beam and connection components.

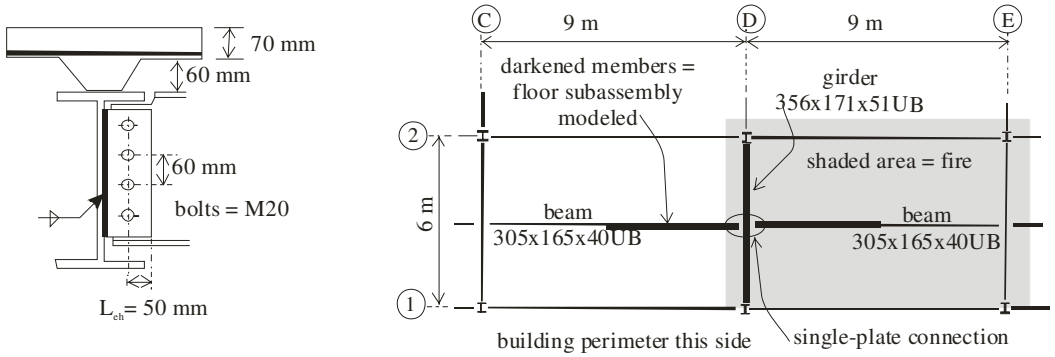

Fig. 1 - Structural design of the 2003 Cardington tests [Wald et al. 2006].

2. MODEL DESCRIPTION AND VALIDATION

2.1 Model Description

In a fire, the response of the beam, and hence the connection forces, are continually changing due to the thermal effects, the boundary conditions, and the large displacements that affect the mechanical response. The thermal effects produce changes in axial load and moment (if there is a thermal gradient) with time. It is therefore necessary to model the connections as a part of a floor subassembly that considers the interaction of the surrounding structure. The prototype for this floor subassembly and connection detail is the 2003 full scale test done in Cardington[3, 5]. A compartment in an 8 story steel frame with concrete composite slab was tested under fire loads by BRE at the Cardington laboratory with the objective of examining the thermal and structural response of the slab, beams, columns and connections. A plan of the compartment that was tested and the corresponding beam sizes and connection details are shown in Figure 1.

Figure 2 shows the floor subassembly and connection finite element model. The slab is represented in the thermal analysis by not applying a fire load to the top flange. In the structural analysis, the lateral restraint provided by the slab is represented by fixing such movement at the centerline nodes on the beam top flange. The slab vertical restraint (i.e., the flexural stiffness) is represented with elastic axial springs attached along the top flange of the beam. The stiffness of the springs was calibrated with experimental results. The flexible axial restraint provided to girder by column D1 is represented by springs with a stiffness based on Quiel and Garlock[6]. Symmetry boundary conditions are imposed on the beam ends (i.e., fixed horizontal translation at every node). The strength of the connection weld (Fig. 1) is not represented in the model; therefore it is assumed that this weld will not fail.

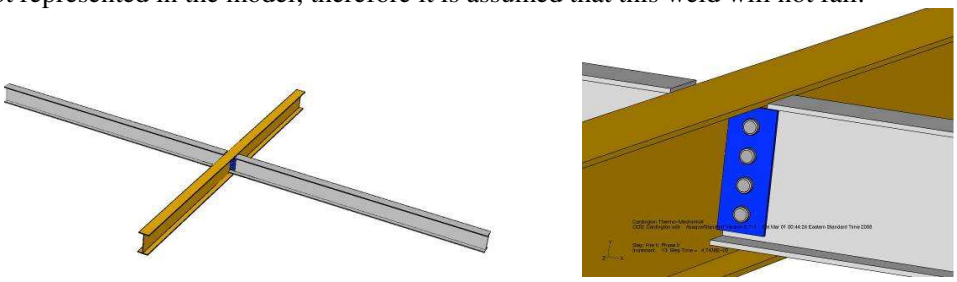

Fig. 2 - Finite element model of floor subassembly.

Commercially available ABAQUS/Standard is used to create the finite element models. 3D continuum stress eight node brick elements (C3D8) elements are used to represent the bolts and all steel plate elements. For the girder and two beams; C3D8 elements are used in proximity of contact areas and reduced integration elements (C3D8R) are used where no contact surfaces are defined and no local stress concentrations are expected. An uncoupled thermo-mechanical analysis is used on the subassembly where in the first phase (the thermal analysis) the heat transfer (Laplace equation) method is used to provide consistent transient nodal temperatures with respect to time. In the second phase (the mechanical analysis), the nodal temperatures are read from the thermal analysis and corresponding temperature dependent mechanical material properties are used.

The fire load imposed on the beam was related to thermocouple readings in the proximity of the beam region. For example, at midspan the beam had an imposed fire load that was slightly different from the beam at the connection region. The imposed fire load on the connection components (plates and bolts) were scaled down from that imposed on the beam so that the finite element thermal response matched closely to the results measured in the test (see Figure 3).

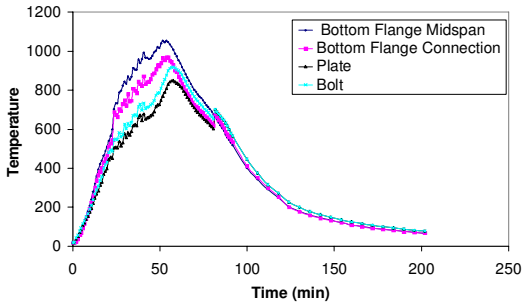

Fig. 3 - Applied fire loads to different parts of floor subassembly to represent heat sink effects as measured in the test.

The measured ambient yield stress of the beam (S275) and girder (S355) were 303 MPa (44 ksi) and 396 MPa (57 ksi), respectively. The bolts were grade 8.8 with a measured ultimate stress of 869 MPa (126 ksi)[6]. The connection plates were Grade 43 with a nominal yield and ultimate stress of 275 MPa (40 ksi) and 430 MPa (62 ksi). Eurocode reduction factors were used to reduce the stress-strain material properties at high temperatures of plate, girder and beam members[7]. For the bolts, Kirby's suggested reduction factors are used[8].

2.2 Validation: Lap Splice Experiments

Before constructing the floor subassembly with the connection details discussed above, we developed models of simple lap splices in order to (1) gain confidence using ABAQUS to represent connection details using smaller and simpler models; and (2) confirm that the ABAQUS models that we were building would be able to properly capture limit states such as bolt bearing and bolt shear. Our high temperature (steady-state) lap splice models were validated with experiments done by Yu[9]. Yu examined single bolt splice plate connections as well as double bolt. He tested these splices at ambient temperature and at varying levels of other temperatures up to 800º C. The specimens failed in a variety of manners including bearing, bolt shear, and block shear (in the case of the double bolts). Yu also examined the effects of varying the edge distance (L_{eh} in Figure 1) from 1 times to 1.5 times the bolt diameter (d_b).

Figure 4 shows the finite element ABAQUS model of the single bolt splice plate detail based on Yu. This figure shows how the finite element model can capture the limit states with reasonable accuracy. The finite element model was also able to capture the peak load reasonably well as shown in Table 1.

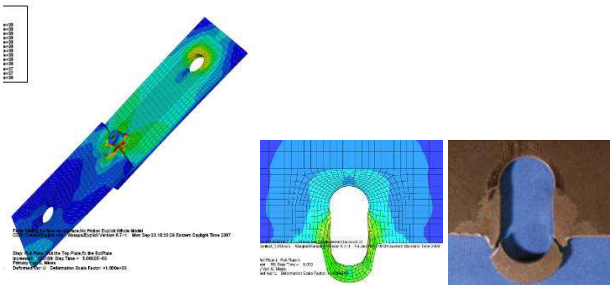

(a) Bearing of Plate ($L_{eh} = 1.0d_b$, at 100 ℃)

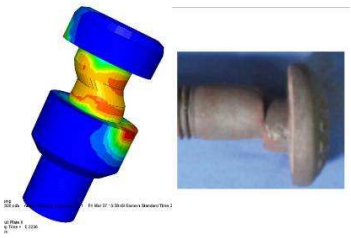

(b) Bolt shear failure
($L_{eh} = 1.5d_b$, at 500 ℃)

Fig. 4 - Finite element models of lap splices and photographs of experiments by Yu [2006] validating the results.

Table 1. Comparison of finite element results to Yu's experiments of a single splice plate connection with and $L_{eh} = 1.5d_b$. and $L_{eh} = 1.0d_b$.

Test	Temp(ºC)	Maximum Load (kips)			Limit State	
		Experiment	Finite Element	Difference	Experiment	Finite Element
$L_{eh}=1.5d_b$	20	41.8	38.5	8%	bearing	bearing
	100	42.8	36.3	15%	bearing	bearing
	500	23.6	21.1	10%	bolt shear	bolt shear
	700	6.0	6.1	2%	bolt shear	bolt shear
$L_{eh}=1.0d_b$	20	25.6	24.2	5%	bearing	bearing
	100	27.9	22.7	19%	bearing	bearing
	500	20.2	17.4	14%	bearing	bearing
	700	5.5	5.3	5%	bolt shear	bearing

2.3 Validation - Full Building Experiment

The floor subassembly described in Section 2.1 was set up to represent as closely as possible BRE's multi-story full scale fire experiments performed at Cardington in 2003 as described previously. At the end of the experiment, the single-plate connection showed ovalization (plastic deformation) of the holes but no failure. The test also exhibited buckling of the beam lower flange as well as coped beam web near the connection. These experimental limit states are shown in the photograph of Figure 5. The finite element model captured these limit states as shown in Figure 6 and Figure 7. Experimental observations indicate that the beam lower flange buckling occurred during the early stages of fire, namely about **23** minutes into the heating phase. The Numerical model predicted lower flange buckling at **23.8** minutes, indicating a close match to the experiment.

Figure 8 shows the beam deflections at midspan. The difference in the vertical midspan deflection between the experiment and numerical model gets significantly larger once the beam web buckles at about **15** minutes into the heating phase. The numerical model fails to sustain the gravity load at about **27** minutes into the heating phase and fails by runaway. This behavior illustrates the importance of composite action and catenary effects of a slab on top of the steel frame. More sophisticated versions of the model will consider using 3D continuum elements to represent the slab.

Fig. 5 - Local buckling after 2003 Cardington experimental fire[5].

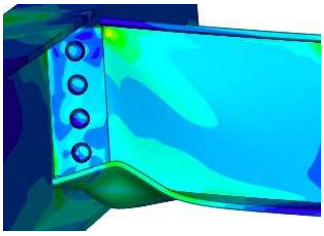

Fig. 6 - Finite element results showing flange local buckling.

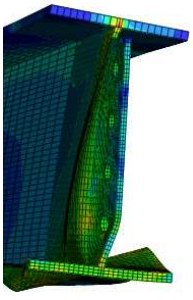

Fig. 7 - Finite element results showing beam web buckling.

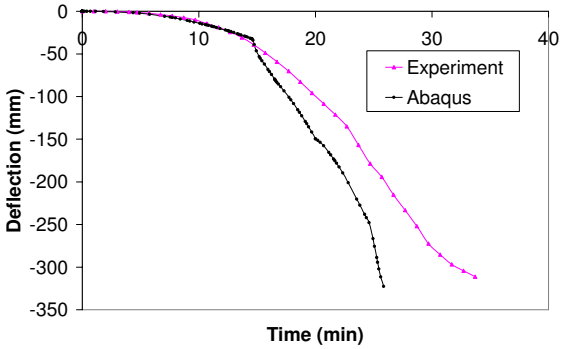

Fig. 8 - Vertical deflection at the beam midspan.

3. EFFECTS OF FIRE PARAMETERS

The parametric study described below uses the structural design, details, and loads of the 2003 Cardington experiments that were described previously. The differences between the parametric study and the Cardington test relate to the fire load and fire protection as follows: (1) the fire is assumed to be in the compartment bound by lines 1 and 2 and D and E and do not go beyond (see Figure 1); and (2) the girder on line D is assumed to have 15 mm thick fire protection on all fire exposed surfaces.

The reason for imposing these differences in the study is to force the limit states to develop on the beam and/or connection. Experimental observations of the Cardington test suggest that lateral-torsional buckling occurs at the girder ends during early stages of fire. Such global buckling would create convergence difficulties to the highly nonlinear (contact and geometric nonlinearity) static analysis.

Temperature recordings in Cardington compartment[5] suggest that the predicted fire curve using Eurocode[10] (i.e., "Cardington Design Fire Curve") correctly predicted the duration of the burning period and the maximum temperature. However, it was not able to capture the fire growth rate within the compartment as seen in Figure 9. Furthermore, using the design fire curve, researchers predicted that local collapse would ensue. Hence one of the fire scenarios used in the parametric study was the recorded time-temperature history of the Cardington tests which is shown in Figure 9.

3.1 Fire Matrix

In the parametric study of different fires, the fire loads were scaled to the same ratio as that measured in the test (as described in Section 2.1 and Figure 3) to represent a cooler connection region due to heat sinks and a more realistic distribution of gas temperatures in the compartment. Figure 9 shows the first 2 hours of the different fire scenarios used in the study where the temperatures shown represent the temperature on beam midspan region. The parameters that were used to develop each parametric fire are described in Table 2. The time-temperature relationship is derived based on Eurocode provisions.[10]

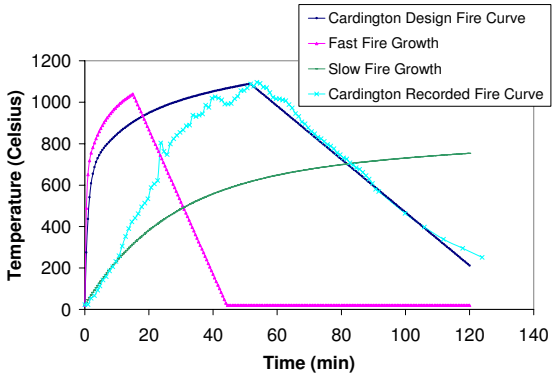

Fig. 9 - Several Fire Scenarios based on Cardington Compartment

The "Cardington Design" fire curve is a ventilation controlled fire that reaches a maximum temperature 1088 °C in about 52 minutes. The "Fast Fire Growth" parametric curve is created by taking the same compartment dimensions but using a larger opening factor, increasing the thermal inertia of surrounding materials for more heat absorption within the compartment and having a slightly smaller fire load density. This leads to a much faster fire growth reaching max temperature 1039 °C in about 15 minutes. This fire curve is severe but it is still within the limit of ventilation controlled fire category. The duration of heating gets smaller compared to the "Cardington Design" fire curve"; but the maximum temperature reached within the compartment stays relatively same. The decay rate of "Fast Fire Growth" fire curve is faster than "Cardington Design" fire curve.

The "Slow Fire Growth" parametric curve is created by taking a much higher fire load density combined with very small opening factor while taking the thermal inertia of surrounding materials about the same as in "Fast Fire Growth" fire curve. This leads to a relatively slow fire growth rate with reached temperature of 839 °C in 4 hours. The decay period would begin after 7 hours, if the fire lasts that long.

Table 2. Summary of Fire Curve Characteristics

Fire	Thermal Inertia (J/m^2*s^.5K)	Energy Density Per floor area (MJ/m^2)	Opening Factor	T_{max} (°C)
Cardington Design	720	720	0.043	1088
Fast Fire Growth	1205	540	0.11	1039
Slow Fire Growth	1135	800	0.013	839

3.2 Results

Figures 10a and 10b show the axial force in the beam (P) versus the time of the fire at the midspan and at the connection region, respectively. As expected, a larger fire growth rate leads to a larger P growth rate and the axial force is essentially the same at both locations.

Figures 11a and 11b also show the axial force in the beam at both midspan and at the connection regions. This time however, P is plotted against the average beam temperature. One interesting result is that the slow fire growth scenario produces larger P. Since in a slow growing fire the temperature in the section will be more uniform through its depth, the thermal elongation is mostly taken out by axial elongation as opposed to curvature, which develops with thermal gradients.

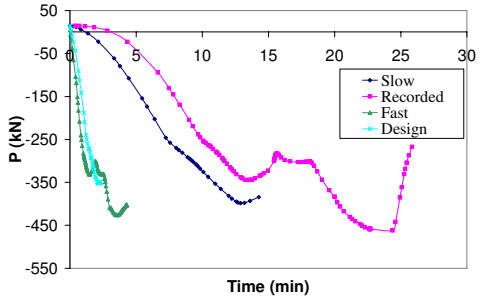

Fig. 10(a) - P vs. time at beam midspan.

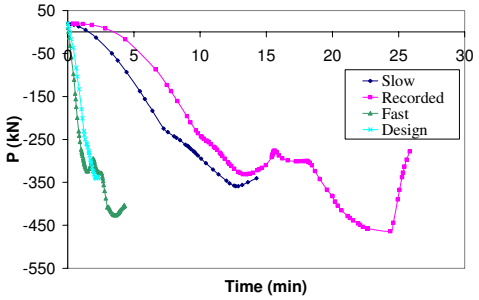

Fig. 10(b) - P vs. time near connection.

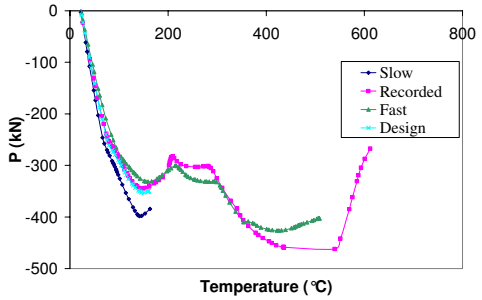

Fig. 11(a) - P vs. avg. beam temperature at midspan

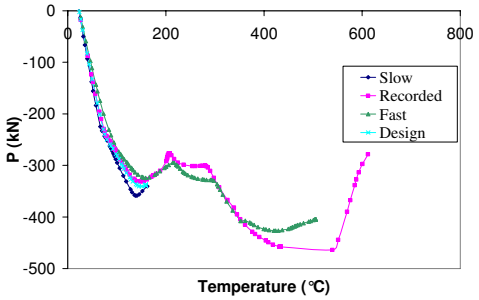

Fig. 11(b) - P vs. average beam temperature near connection.

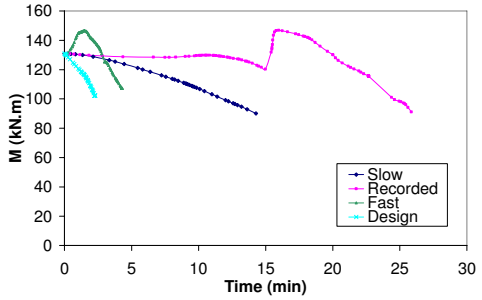

Fig. 12(a) - M vs. time at midspan

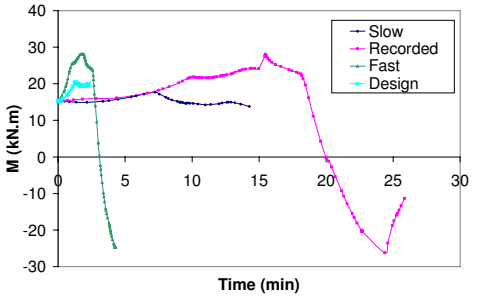

Fig. 12(b) - M vs. time near connection.

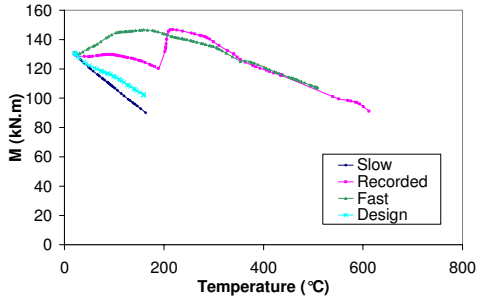

Fig. 13(a) - M vs. avg. beam temperature at midspan

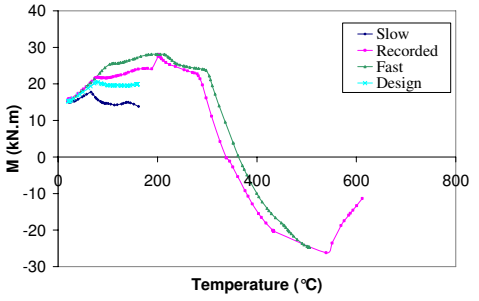

Fig. 13(b) - M vs. average beam temperature near connection.

Figure 12 and 13 plot the moment in the beam both at the connection region and at the midspan. We observe that the rate of heating has an effect on the moments that develop in the beam. This is due to the thermal gradients that are produced. In the fires that were able to reach elevated temperatures (recorded and fast fires), the moments in the connection region reversed direction (become negative) as seen in Figures 12(b) and 13(b). This is due to both the thermal gradients as well as the partial restraint provided by the connection (i.e., it is not an ideal pin connection). This negative moment develops as the deflections at beam midspan become large as seen in Figure 14.

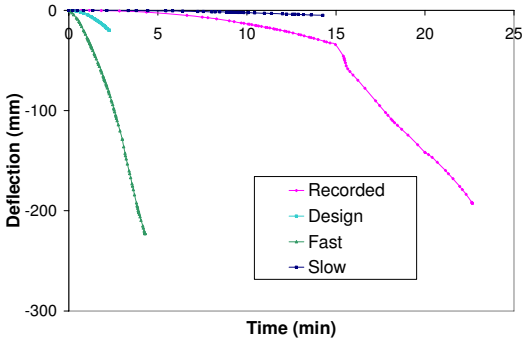

Fig. 14 - Vertical Deflections at Midspan.

Table 3 summarizes the parametric study results. For all parametric fires, beam web buckling is observed in the early stages of the fire due to the weak resistance of the coped beam web to the high temperature induced axial forces. However, the time and average beam temperature at which it is reached changes considerably as seen in Table 3.

While in the actual Cardington test local buckling of the beam lower flange is observed (as seen in Figures 5 and 8), only the "Fast Fire Growth" analysis reached this limit state. It is possible that when the numerical instabilities are overcome, the other analyses will also reach this limit state. Based on the automatic stabilization techniques employed by ABAQUS, we suspect that the other analyses terminated due to lateral torsional buckling near the beam support. This type of global buckling is observed in the Cardington test in the unprotected girder[5], which is restrained in the axial direction by columns.

Table 3. Summary of Parametric Study Results

Test	Web buckling	Lower flange buckling	Analysis End	
			time (min)	temperature (℃)
Cardington Recorded	Yes (13 min)	No	23	436
Cardington Design	Yes (2.1min)	No	2.3	159
Fast Fire Growth	Yes (3.0 min)	Yes (4.2 min)	4.3	507
Slow Fire Growth	Yes (12.6 min)	No	14.3	163

4. SUMMARY AND CONCLUSION

A finite element model of a single plate shear connection was developed and validated against extensive experimental data. The model is successfully capable of predicting the limit states of bolt bearing, bolt shearing, flange local buckling, and the peak loads. This validation was performed against simple splice plate connection tests as well as a full-scale building test done at Cardington.

A parametric study was then performed to examine the effects of different fire characteristics. Since at the time of submission of this paper the analyses ended before the peak temperatures were reached, this study evaluated only the effect of heating rate. In all cases web buckling developed first due to the large compressive forces on the web and the lack of restraint due to the coping detail. The local instabilities occur during the very early stages of fire while most of the beam remains in elastic region.

A slow heating rate also produces higher axial compressive forces in the connection since there will be less thermal gradients and therefore less curvature to take out the thermal expansion of the beam. While the rate of heating does not affect the axial forces, it does affect the moments that develop in the connection region and therefore connection.

The rate of heating and the compressive connection forces that develop do not have a significant effect on the connection response as designed in this study. It does however have an effect on the beam response. It is expected that the effects of peak temperature and decay rate will have more of an impact on the connection performance.

Current research by the authors is not only developing modeling strategies to overcome numerical instabilities, but also looking at alternative means of representing the slab, which will play a crucial role during beam runaway. Future research will also examine the strength of welds in such connection details.

5. ACKNOWLEDGEMENTS

The authors are grateful to Professor Panos Papadopoulos (Dept. of Mechanical Engineering, University of California at Berkeley) for his assistance with ABAQUS and developing the finite element model.

6. REFERENCES

[1] Wang, Y. and Ding, J. “Experimental Behaviour of Steel Joints to Concrete Filled Steel Tubular Columns in Fire,” Proceedings of Fourth International Symposium on Steel Structures, Seoul, Korea, 16-18 November 2006.

[2] Bailey, C.G., Lennon, T., and Moore, D.B., “The behavior of full-scale steel-framed buildings subjected to compartment fires,” The Structural Engineer, Vol. 77, No. 8, pp. 15-21, 1999.

[3] Lennon,T., and Moore, D. (2004). Client Report :Results and observations from full-scale fire test at BRE Cardington, 16 January 2003 Client report number 215-741.

[4] Beitel, J., and Iwankiw, N. “Analysis of needs and existing capabilities for full-scale fire resistance testing.” National Institute of Standards and Technology: NIST GCR 02-843. 1-86, 2002.

[5] Wald, F., Simões da Silva, L., Moore, D.B., Lennon, T., Chadná, M., Santiago, A., Benes, M. and borges, L. "Experimental Behaviour of Steel Structures under Natural Fire", Fire Safety Journal 41 (7), pp. 509-522, 2006.
[6] Garlock, M.E.M. and Quiel, S.E. (2008). "A Closed-Form Analysis of Perimeter Member Behavior in a Steel Building Frame Subject to Fire" (submitted for publication in *Engineering Structures*).
[7] Eurocode 3: Design of steel structures – Part 1.2: General Rules – Structural fire design/./ ENV 1993-1-2:2001/. European Committee for Standardization, Brussels, Belgium, 2001.
[8] Kirby, B.R. "The Behavior of High-strength Grade 8.8 Bolts in Fire", Journal of Constructional Steel Research, Vol 33, p.3-38, 1995.
[9] Yu, L. Behavior of Bolted Connection during and after a Fire, Ph.D. Dissertation, University of Texas at Austin, August 2006.
[10] Eurocode 1: Actions on structures – Part 1-2: General actions – Actions on structures exposed to fire. EN 1991-1-2:2002. European Committee for Standardization, Brussels, Belgium, 2002.

EXPERIMENTAL INVESTIGATION OF THE BEHAVIOUR OF FLUSH ENDPLATE CONNECTIONS IN FIRE

Hongxia Yu [1], I.W. Burgess [2], J.B. Davison [3], R.J. Plank [4]

ABSTRACT

This paper reports a set of test results on flush endplate connections at ambient and elevated temperatures. This set of tests was aimed to investigate mainly the behaviour of connections at the ends of unprotected beams in fire situations, which may be subjected to significant tying forces and large rotations at high temperatures as a consequence of the beam deflection. Observed failure modes in the tests tended to change the failing component from the endplate to the bolts with increase of temperature, as the bolt strength reduces faster than that of steel in fire. Most of the tested connections reached their maximum resistance at about 2° of rotation, and were then able to maintain a moderate amount of resistance up to a rotation of 7°, irrespective of their failure mode. At elevated temperatures, the use of thick endplates can enhance the peak resistance, but reduces the rotational capacity of the connection.

1. INTRODUCTION

A recent trend in the performance-based design of composite framed structures has been to fire-protect beams on the main column grid, while leaving other beams unprotected. The unprotected beams tend to develop large deflections and may achieve some catenary action at very high temperatures. This requires the connections at their ends to be able to resist significant tying forces. At the same time, large deflection of the beam causes the connections to rotate simultaneously. The connections then need either to have high rotational capacity to accommodate the deformation, or need to be very strong in order to shift the rotation towards a hogging curvature of the beam end. Therefore, depending on the type of connection adopted, various levels of moment may be transferred through the connection.

Flush endplate connections are widely used in construction practice in the UK, and their moment-rotation characteristics have been investigated previously [1] [2], both at ambient

[1] PhD, Department of Civil and Structural Engineering, University of Sheffield, UK, h.yu@sheffield.ac.uk
[2] Prof., Department of Civil and Structural Engineering, University of Sheffield, UK, ian.burgess@sheffield.ac.uk
[3] PhD, Department of Civil and Structural Engineering, University of Sheffield, UK, j.davison@sheffield.ac.uk
[4] Prof., School of Architecture, University of Sheffield, UK, r.j.plank@sheffield.ac.uk

and elevated temperatures. However, calculation of the tying capacity specified by the UK design recommendation [3] are based on the assumptions that the connection is subjected to pure tension, and that each bolt row can make full contribution to the total resistance of the connection. This situation is obviously impossible in practice. Co-existence of other actions may reduce the resistance of individual fasteners, and for the whole connection may mean that all the bolt rows cannot reach their maximum resistance at the same time if their behaviour is not ductile enough, and this may cause an "unzipping" failure.

The Universities of Sheffield and Manchester have conducted a joint research programme with the aim of investigating the tying capacity and ductility of steel connections at elevated temperatures. Previous tests [4] have shown that connections can be subjected to tying forces varying from 0.65 to 1.6 times the coincident shear force at high temperatures. Various levels of moment may be transferred through the connections, depending mainly on the connection type. Hence, the current investigation adopted a test setup in which the connections were subjected to combinations of tying and shear forces. Moments were generated at the connection due to the lever arm of the applied force. In total, four types of connection were studied; flush endplates, flexible endplates, fin plates and web cleats. This paper reports the test results on flush endplate connections. The resistance of the connections at various temperatures and subjected to different load combinations are shown in the paper. Different failure modes are described and their effects on the behaviour of the connections are illustrated.

2. TEST SETUP

A detailed description of the test setup and test measurements has been given in a previous paper [5], so only a brief overview will be given here. The tests were performed in an electrically-heated oven of 1.0m^3 internal capacity, as shown schematically in Figure 1. The specimens were heated slowly to the specified temperature, and then loaded to failure at constant temperature. A special loading system was designed to allow very high rotation of the connection. It includes three link bars, one end of each connected to a central pin, with the other ends respectively connected to the jack, the specimen and a fixed hinge. When the head of the jack moves downward, it applies a tensile force to the end of the specimen through the action of the linkage. The loading jack was displacement-controlled. The applied load was measured from strain-gauges attached to the bars. The deformations of the connection were measured using a digital camera facing the connection through a glass window in the oven wall.

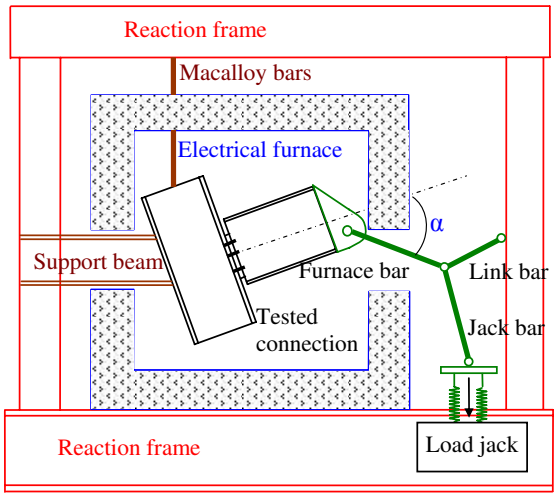

Fig. 1 - Test setup

A UC254×89 section was used for the column, and the beam specimens were all UB305×165×40. Figure 2 shows the details of the connection. The arrangement of the bolts

is typical of practical designs in accordance with current UK design recommendations [1]. However, it is common practice to use an endplate 20mm thick. In the testing program, to serve the final objective of developing a component-based model, it was desirable that various failure modes could be observed. Therefore, three endplate thicknesses, of 8, 10 and 15mm, have been tested. Most tests adopted an arrangement of three bolt rows, as shown in Figure 2. Two tests used two bolt rows, for which the middle bolt row was removed. A custom-made connector was bolted to the end of the beam, and the load from the tie-bar was applied to this connector through a pin.

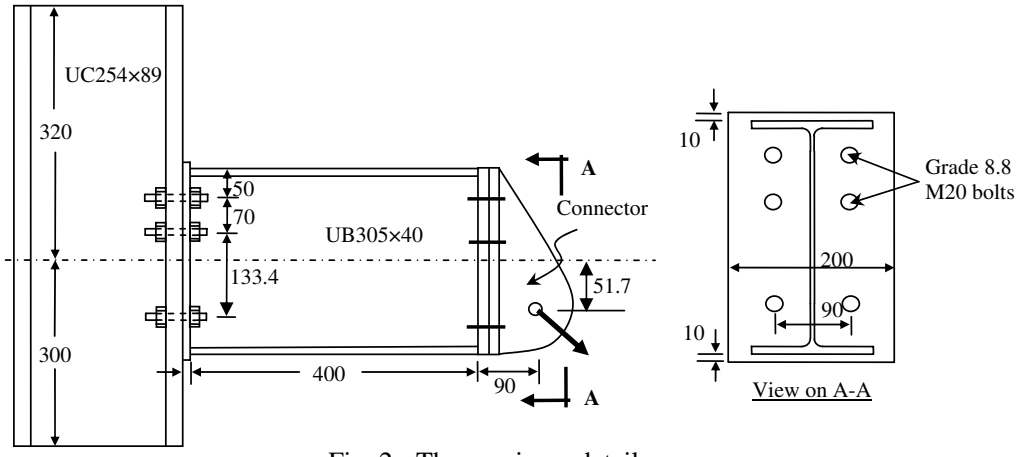

Fig. 2 - The specimen details

3. TEST RESULTS

A summary of the test results is given in Table 1. The endplate thickness is t_p and n row indicates the number of bolt rows adopted in a connection. Connections were designed to be tested at three different combinations of shear and tying force, corresponding to different angles α in Figure 1. Three nominal initial angles α, of 55°, 45° and 35°, shown as "Load angle" in Table 1, were chosen. This angle α is actually that between the axis of the steel beam and the furnace bar. Its value is the algebraic sum of their respective inclinations to the horizontal axis, which were measured using two cameras. However, it was not possible to set these exactly at the start of any test, and so the exact initial value is given in the Table as "Initial α". During each test the angle α changed progressively from its initial value, the degree of variation depending on the exact geometry of the loading system. Its value at the end of each test is shown as "Ending α" in Table 1. The final two columns show the maximum resultant applied force and the connection rotation at maximum resistance. In total, 17 tests were planned, but only 15 were successfully finished. During test 5, the support to the column failed due to thread-stripping of the fixing bolts, and the test results are completely unusable. Test 1 was loaded up to nearly 340kN at which it fractured the loading equipment, and hence maximum resistance was not achieved.

The force-rotation relationships for tests 1-12 are shown in Figure 3. At 550°C, the test at 45° was the first test performed in this series. During this test, the bolts failed by thread-stripping from the nuts. For this reason the force is seen to decrease progressively after a rotation of around 1.5°. After this test, two nuts were used on each bolt to prevent thread-stripping. Except for this case, the other tests were able to maintain a relatively stable resistance until around 7°. The resistance of the connection reduced rapidly with increase of temperature. The load angle has some effect on the overall connection resistance, but not on

the failure mode. Comparison of Tests 3, 14 and 15 shows the effect of endplate thickness on the responses of the connection, as shown in Figure 4. The use of a thick endplate enhances the resistance, but significantly reduces the ductility. The effect of removing one bolt row is shown in Figure 5, comparing Tests 1, 3, 16 and 17. Removing the middle bolt row obviously reduces the resistance of the connection, and according to the results at 550°C, it reduces the ductility as well.

Table 1. List of test results

Test ID	t_p	n_row	Temperature (°C)	Load angle (Degree)	Initial α (Degree)	Ending α (Degree)	Force (kN)	Rotation (Degree)
1	10	3	20	35	unfinished			
2	10	3	450	35	40.5	35.1	180.9	6.1
3	10	3	550	35	41.2	30.7	105.9	2.2
4	10	3	650	35	43.3	32.5	43.6	3.4
5	10	3	20	45	unfinished			
6	10	3	450	45	46.3	43.7	164.6	6.4
7	10	3	550	45	44.7	43.1	81.8	1.4
8	10	3	650	45	46.6	38.9	36.0	4.9
9	10	3	20	55	54.7	43.8	259.0	4.4
10	10	3	450	55	55.7	46.7	182.5	5.6
11	10	3	550	55	55.4	47.2	87.8	2.2
12	10	3	650	55	55.4	48.1	39.2	3.1
13	8	3	20	35	37.8	27.2	258.1	5.3
14	8	3	550	35	41.8	33.3	101.0	7.5
15	15	3	550	35	42.2	37.0	124.6	2.5
16	10	2	20	35	36.5	32.8	303.0	6.6
17	10	2	550	35	41.7	39.5	79.9	2.6

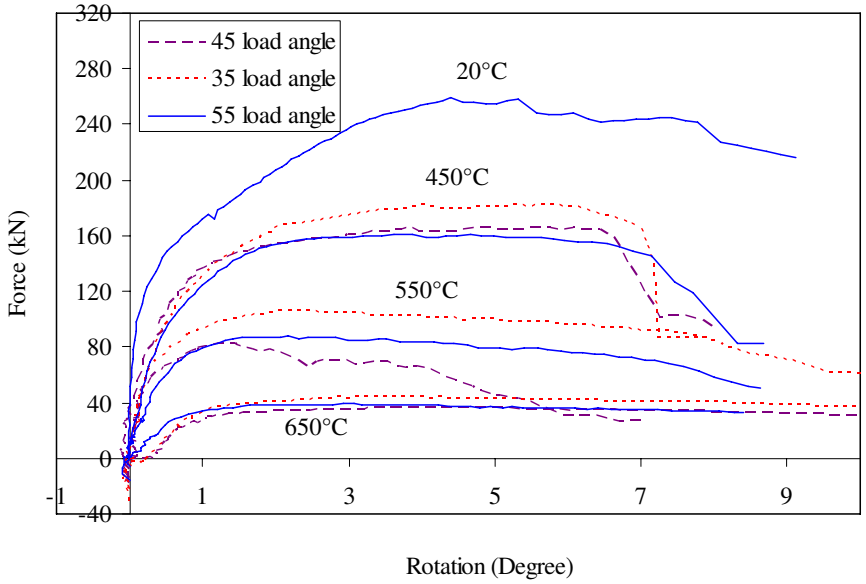

Fig. 3 -The force-rotation relationships for tests 1-12

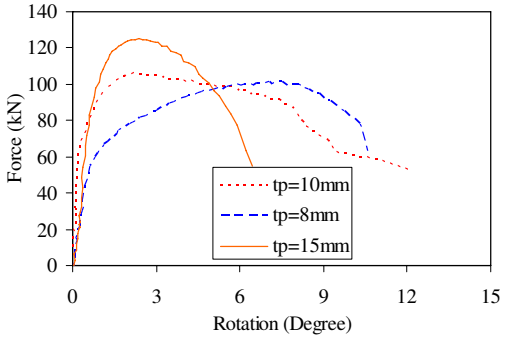

Fig. 4 - Effect of the endplate thickness

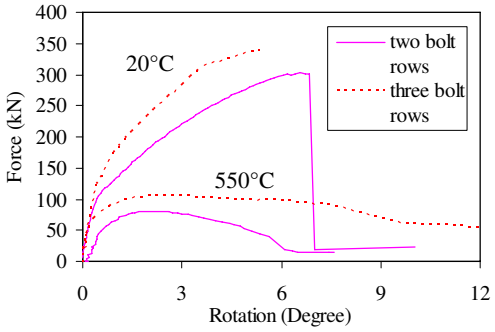

Fig. 5 - Effect of the number of bolt rows

For tests 1-12, which used a typical design of t_p=10mm and three bolt rows, two failure modes were observed. At 20°C and 450°C, the failure was controlled by fracture of the endplate. Figure 6 shows one failed connection after a test at 450°C. The typical failure at this temperature is a block shear fracture of the endplate in the heat-affected zone adjacent to the welding extending from the beam web to the free edge of the beam flange. This fracture corresponds to the sudden drop of resistance at around 7° in Figure 3. At 20°, the fracture is less severe. A small crack was initially developed close to the beam web. This corresponds to the peak resistance at 4.5° in Figure 3. On further loading this crack extended upward and, after reaching the flange weld, started to develop horizontally parallel to the beam flange. The gradual development of the crack was reflected by the slow drop in resistance shown in Figure 3. Apart from resisting tensile forces, the bolts were found to have significant bending deformations.

a. fracture of the endplate

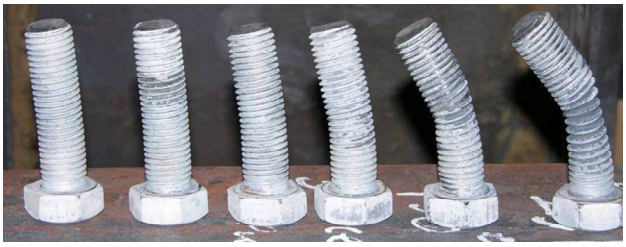

b. deformation of the bolts

Fig. 6 - Failure of endplate connections at 20°C and 450°C

At 550°C and 650°C, the failure was controlled by the bolts, and the bolt extension characteristics were very ductile. Figure 7 shows a typical failed connection. The endplate can be seen to have a moderate amount of bending deformation. A small crack was developed close to the beam web. This crack started from the inside of the endplate next to the weld, and in some tests it was so small that it did not extend through to the opposite surface. Bolts were actually gradually pulled apart, with no obvious breaking point. The top two bolts were completely fractured after very large deformation. By this stage, the middle two bolts had shown quite visible necking. Both rows of bolts had acquired significant bending deformations.

a. endplate with micro crack

b. Deformation of bolts

Fig. 7 - Failure of flush endplate connections at 550°C and 650°C

Two tests were performed using the endplate thickness of 8mm, one at ambient temperature and one at 550°C. At ambient temperature, the failure was concentrated in the endplate, and the bolts remained basically undeformed, as shown in Figure 8. Damage to the endplate started as significant bending. Two cracks were then developed close to the beam web. These cracks soon developed to extend across the top two rows of bolts, so that the endplate worked in uniaxial bending. After that, the top two bolts tore some bearing material from the bolt holes. Formation of the two cracks caused a rapid drop in resistance, as shown in Figure 5. At 550°C, The failure was again controlled by the bolts. The observations were similar to those for the 10mm thick endplate, but bending of the endplate was more severe and no crack along the beam web was observed.

a. Endplate at 20°C

b. Bolts at 20°C

c. Endplate at 550°C

d. Bolts at 550°C

Fig. 8 - Failure of the connections when t_p=8mm

One test was performed using a 15mm thick endplate at 550°C. The test observations are shown in Figure 9. Unsurprisingly the failure was controlled by bolts. However, compared with other tests using thinner endplate, the bolts in this test remained almost straight, which showed that the bolts in this test had been subjected to little bending moment. This explains why in Figure 4, although all three tests failed by breaking the bolts, the resistances are different. Bolts in the other two tests must have been subjected to a large amount of bending moment concurrent with the tension, which must have reduced their tensile capacity. The endplate in this connection remained straight after the test.

a. Deformation of the endplate

b. Deformation of the bolts

Fig. 9 - Failure of the connection at 550°C when t_p=15mm

a. Endplate at 20°C

c. Bolts at 550°C

b. Bolts at 20°C

d. Endplate at 550°C

Fig.10 - Failure of the connections when only two rows of bolts were used

Two tests were performed using two rows of bolts. These were designed to test the difference between bolts working individually and bolts working in group. As a result of there being less bolts in the tension zone, bolt fracture controlled the failure of the connection in

both ambient-temperature and high-temperature tests, as shown in Figure 10. At 20°C, the bolts caused significant bending deformation to the endplate before they underwent a brittle fracture. At 550°C, the endplate remained relatively straight. Comparison of the force-rotation relationships of these two tests shows that a weaker endplate with strong bolts is the better arrangement, as it provides higher ductility and a prolonged phase of increasing resistance with deformation.

4. CONCLUSIONS

This paper reports a series of tests on flush endplate connections subjected to combinations of tying force and shear force at elevated temperatures. The test results have shown that flush endplate connections have relatively stiff responses compared to simple connections [3]. The tested connections reached their maximum resistance at a rotation of about 2°, and maintained this resistance until about 7°. The failure mode of a connection is less affected by the ratio of tying force to shear force, but is significantly dependent on the steel temperature. At lower temperatures, failure was generally controlled by the endplate, which developed a shear fracture close to the weld. At high temperatures, failure always occurred in the bolts. Bolts are extremely ductile at high temperatures, which gives the connection a moderate amount of rotational capacity.

Thicker endplates were subject to less bending deformation, and caused less bending deformation to the bolts. This enhanced the resistance of individual bolts, and in consequence the resistance of the connection as a whole, if the bolts are ductile.

Acknowledgment*: The authors gratefully acknowledge the support of the Engineering and Physical Sciences Research Council of the United Kingdom under Grant EP/C510984/1. Provision of the steel sections by Corus Ltd is also acknowledged.*

5. REFERENCES

[1] Aggarwal A.K., Comparative Tests on Endplte Beam-to-Column Connections, J. Construct. Steel Research, 30, 151-175, 1994.

[2] Al-Jabri K.S., Burgess I.W., Lennon T., Plank R.J., Moment-rotation-temperature curves for semi-rigid joints, Journal of Constructional Steel Research, 61, 281-303, 2005.

[3] SCI & BCSA, *Joints in steel connection, Simple connections,* The Steel Construction Institute and The British Constructional Steelwork Association Limited, UK, 2002.

[4] Ding, Jun, Behaviour of Restraint Concrete Filled Tubular Columns and Their Joints in Fire, Ph.D Thesis, The University of Manchester, 2007.

[5] Yu, H.X., Burgess, I.W., Davison, J.B. and Plank, R.J., *Experimental Investigation of the Behaviour of Fin Plate Connections in Fire*, accepted by JCSR in February, 2008.

BEHAVIOUR AND MECHANICAL MODELLING OF COMPOSITE TOP-AND-SEAT AND WEB ANGLE JOINTS AT AMBIENT AND ELEVATED TEMPERATURES

ZHEN YUAN[1], KANG HAI TAN[2] and SENG KIONG TING[3]

ABSTRACT

This paper describes four experimental tests from part of a test programme carried out at ambient and elevated temperatures on composite top-and-seat and web angle joint. This is part of an experimental programme conducted to study the behaviour of these joints at ambient and elevated temperature conditions. To the authors' best knowledge, there has not been any reported fire tests on this type of joints. Thus, the objective of this experimental study is to provide the test results for the purpose of validating a proposed component-based mechanical model for this type of joints. This experimental programme included three different joint configurations to investigate the effect of beam depth and temperature on the joint behaviour. At the time of writing, only four test results (C1-1, C1-2, C1-3 &C1-5) were fully analysed and compared with component-based mechanical model predictions. The proposed model can accurately predict the behaviour of composite top-and-seat and web angle joints for both ambient and elevated temperatures.

1. INTRODUCTION

Composite structures have become increasingly popular over the last few decades in the USA, Japan and some European countries. However, composite construction is still not as prevalent in Singapore. This may be due to common misconception that analysis of

[1] PhD Candidate, Nanyang Technological University, School of Civil and Environmental Engineering 50 Nanyang Avenue, Singapore, email: yuan0004@ntu.edu.sg.

[2] Associate Professor, Nanyang Technological University, School of Civil and Environmental Engineering 50 Nanyang Avenue, Singapore,email: ckhtan@ntu.edu.sg.

[3] Associate Professor, Nanyang Technological University, School of Civil and Environmental Engineering 50 Nanyang Avenue, Singapore,email: cskting@ntu.edu.sg.

composite steel structure is difficult and there is a lack of engineering software to analyse and design the complex composite joints. Many research works had been conducted on composite joint behaviour since the 1970s and these were neatly summarised by Zandonini[1] and Simoes de Silva et al.[2]. It was found that concrete slab, steel reinforcement, quantity of shear stud, steel joint type, and slab rib direction have great influence on the behaviour of these joints. The EC3: 1.8[3] and EC4[4] presented some principles for the design of joints. Therefore, in practice due to a large number of combinations of geometrical and mechanical parameters of joints, a typical composite joint is designed as either perfectly pinned or completely fixed. In fact, the actual joint behaviour falls in-between these two extreme cases and is conventionally classified as "semi-rigid".

Despite extensive experimental studies and the available analytical and numerical models that can give designers good results or predictions for certain geometries and loads, there are limited test results (if at all) on composite top-and-seat and web angle joints under elevated temperature condition. Most experimental works were conducted on bare-steel joints without composite slabs, viz. flush or extended end plate joints, or top-and-seat angle joints. However, composite top-and-seat and web angle joints are commonly used in some seismic zones (USA, Japan) as they have high strength and ductility characteristics, large rotation range and good energy absorption capacity. Moreover, most of the tests were conducted at ambient temperature; only a few full-scale joint tests on steel and composite flush/extended end plate joints were conducted under fire conditions (Leston-Jones[5], Al-Jabri[6] and Spyrou[7]).

To the authors' best knowledge, no elevated temperature test has been conducted on steel composite top-and-seat and web angle joint. Therefore, the objective of this paper is to present some experimental test results to shed light on the behaviour of these joints at ambient and elevated temperature. The authors will touch on the detailed information on four tests, namely C1-1, C1-2, C1-3 and C1-5. Specimens C1-1 and C1-3 were tested at ambient temperature whereas C1-2 and C1-5 were tested at 430°C (measured at the beam bottom flange).

The results will be used to validate the proposed mechanical model for analysis of these joint. In the following sections, the experimental set-up for the ambient and elevated temperature tests will be described. The test results will be compared with predictions from the proposed mechanical model.

2. EXPERIMENTAL TEST

2.1 Introduction

For the test programme, three series of joints (GR1, GR2, GR3) were designed, fabricated and tested under elevated temperature conditions. Each series has five specimens. Out of a total of fifteen specimens, six of them were carried out at normal ambient temperature and the rest at isothermal elevated temperatures. The geometrical descriptions of these series are given in Fig. 1, which shows a typical composite angle joint. Each specimen consisted of two cantilevered beams of 1.625 m long and a 1 m long central column. Two beams on either side were connected to the column flanges through angles in Grade S355, The overall length of the specimen is 3650 mm and the two roller supports are 3450 mm apart. Since this research focused on the isolated behaviour of these joints at elevated temperatures no axial restraint was introduced into the beams.

The joint configuration is representative of those internal joints in steel structures designed against lateral drift. The joints were designed according to the guidelines given in Joints in Simple Construction – Volume 1: Design Methods[8] and Joints in Steel Construction

- Composite Joints[9]. Thus, the joint details conform to common industry practice and its behaviour is ductile. The selection of specimen details was based on predicted failure modes and the size of existing electrical heating furnace in Nanyang Technological University. For the GR1 series, the predicted failure mechanism consisted of local buckling at the beam flange in compression for both ambient and elevated temperature conditions.

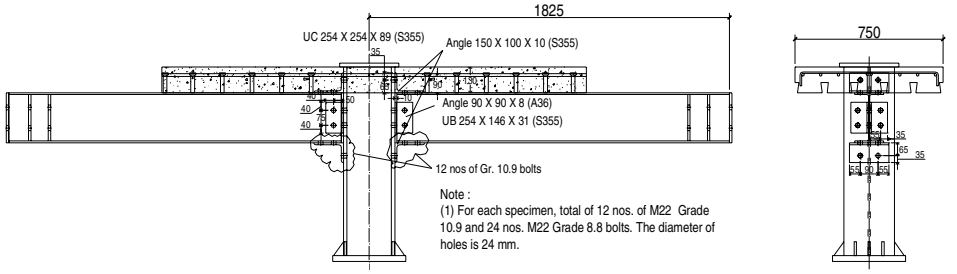

(1.a) Detail of GR 1 Joints

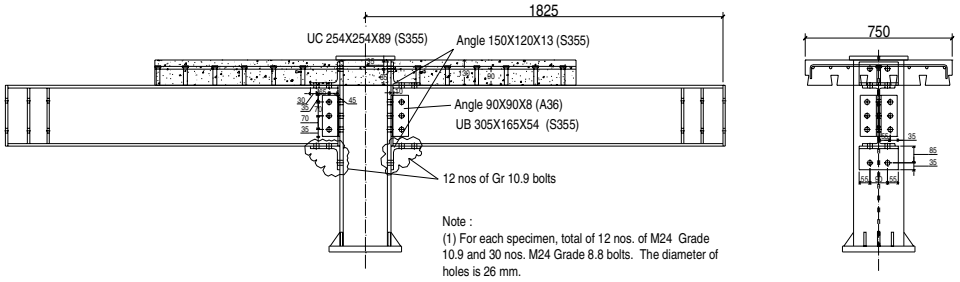

(1.b) Detail of GR 2 Joints

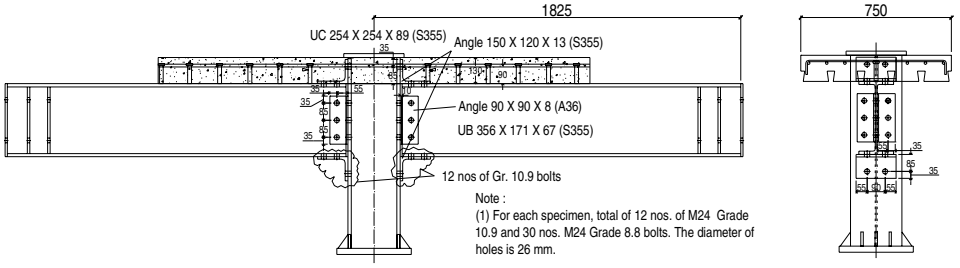

(1.c) Detail of GR 3 Joints

Figure 1. Details of composite top-and-seat and web angle joint Joints

2.2 Specimen arrangement and material properties for C1-1 and C1-2

The material properties of specimens C1-1, C1-2, C1-3 and C1-5, which belong to GR1 series, are given in Table 1a and 1b. Each cruciform specimen was constructed from two UB 254x146x31 beams, one UC 254x254x89 column, four 10 mm thick top and seat angles and two 8 mm thick web angles, as shown in Fig. 1. All the steel sections were Grade S355. Twenty-four M22 Grade 8.8 bolts and twelve M22 Grade 10.9 bolts in 24 mm diameter holes were used. For C1-1 and C1-2 specimens the bolts were tightened by a torque wrench to 600 Nm for M22 Grade 8.8 bolts and 750 Nm for M22 Grade 10.9 bolts. This is above the torque typically achieved in industry practice. Since the C1-3 and C1-5 joints were produced in the second batch of test specimens, the bolts were tightened to 180 Nm for M22

Grade 8.8 bolts and to 240 Nm for M22 Grade 10.9 bolts. This is generally the same as the torque typically achieved in industry practice.

Table 1a. Material Properties for C1-1 and C1-2 Specimen

Concrete Test No.	Compressive Strength (N/mm^2)	Tensile Splitting Strength (N/mm^2)	Density (kg/m^3)	Days	Remarks
1	33.4	2.6	2288	28	For C1-1
2	42.4	3.0	2305	57	For C1-2

Steel Component	Yield Strength (N/mm^2)	Ultimate Strength (N/mm^2)	Elastic Modulus (N/mm^2)
Top/Seat Angle	345	566	206711
Beam Flange	394	543	191142
Beam Web	403	541	208872
Column Flange	397	509	201432
Column Web	416	530	203555
Rebar	524	610	192967
Web Angle	241	394	192834

Table 1b. Material Properties for C1-3 and C1-5 Specimen

Concrete Test No.	Compressive Strength (N/mm^2)	Tensile Splitting Strength (N/mm^2)	Density (kg/m^3)	Days	Remarks
3	31.4	2.2	2234	28	For C1-3
4	31.8	2.2	2245	45	For C1-5

Steel Component	Yield Strength (N/mm^2)	Ultimate Strength (N/mm^2)	Elastic Modulus (N/mm^2)
Top/Seat Angle	380	526	197362
Beam Flange	404	558	206887
Beam Web	415	565	200705
Column Flange	398	503	206887
Column Web	425	539	200700
Rebar	507	604	195934
Web Angle	304	469	192967

To obtain the load-slip characteristics of the shear stud connectors in the composite slab, two push-out tests were conducted following the EC4:1.1[4] provisions. The average maximum shear strength was 115 kN per connector. But based on EC4: 1.1 provisions, the calculated nominal shear strength of this connector was 99.7 kN.

2.3 Test set-up

The arrangement of the test rig and the electrical heating furnace for the cruciform specimen is shown in Fig. 2.During the test, the specimen was inverted within the furnace. It should be noted that for ease of readers, the portion of flange connected to the decking slab

will be referred to as the top flange in the ensuing discussions. The specimen was laterally restrained to prevent it from deflecting out-of-plane under the loading.

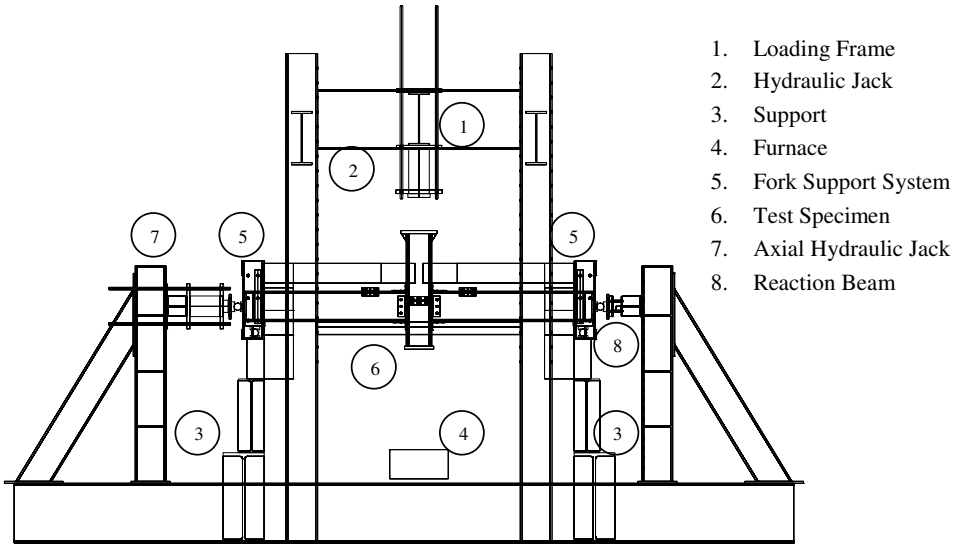

Figure 2. Elevation View of the Cruciform Test Set-up

2.4 Instrumentation and Thermal Proofing

The instrumentation system included readings from load cells, thermocouple measurements, vertical and rotational deflections measured by LVDTs, as shown in Fig. 3. The load level was read from the compressive load cell and stored directly in computer in every 15 seconds during the tests. The load cell was calibrated before the test programme.

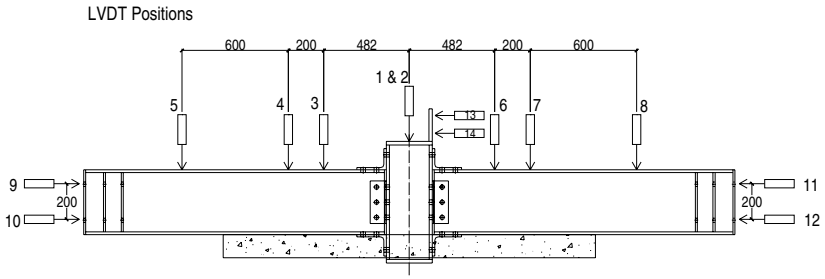

Figure 3. LVDT Positions

The displacements were measured by LVDTs as shown in Fig. 3. The temperatures across the joint depth were measured by Type K thermocouples. Forty of them were used to measure each joint section. The temperatures of beams, columns, angles and bolts were recorded accordingly. Four thermocouples measured the temperature of rebar, and three thermocouples measured the temperature profile across concrete slab at the top, middle and bottom position. Another two thermocouples were used to measure the shear stud temperature. The specimen was protected from heating by wrapping it with a rockwool blanket all-around at both ends of the beams. The only exposed region was the 400 mm beam length from the face of column flange.

2.5 Test Procedure

The ambient test (C1-1) was conducted by increasing the load at centre position until the specimen failed. The elevated temperature test (C1-2) was conducted in two stages, namely, (1) heating up the joint specimen to the desired temperature and (2) applying load until the specimen failed.

3. BRIEF DESCRIPTION OF THE PROPOSED MECHANICAL MODEL

Based on the work conducted on steel top-and-seat and web angle joints by Faella et al. [10, 11, 12], the authors[13,14] have proposed a mechanical model for predicting the moment-rotation response of composite top-and-seat and web angle joints shown in Fig. 4. The joint components included reinforced concrete (hereafter referred as 'RC') slab in tension (rt), shear stud in shear (st), column web in tension (cwt), column flange in bending (cfb), bolt in tension (bt), top angle in bending (ta), bolt in shear (bs), top angle in bending (tab), beam flange in bearing (bfb), top angle in tension (tat), web angle in bending (wa), beam web in bearing (bwb), web angle in bending (wab), beam web in tension (bwt), column web in shear (cws), column web in compression (cwc), seat angle in bearing (sab), beam flange in compression (bfc), and seat angle in compression (sac).

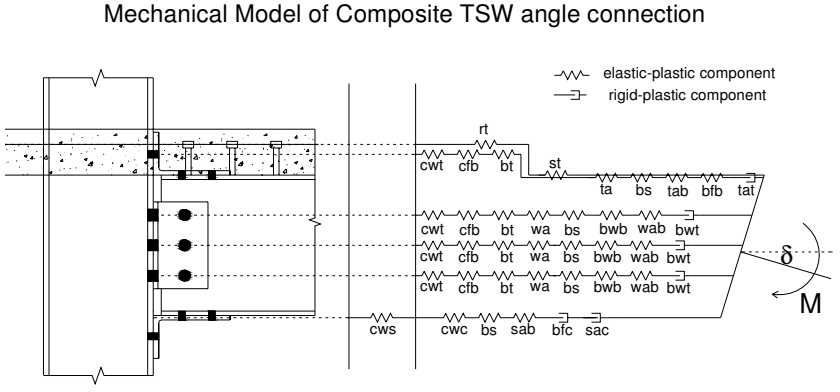

Figure 4. The proposed mechanical model for composite top-and-seat and web angle connection.

The full-range tension-displacement response of reinforced concrete slab was proposed by the authors[13,14] which was developed further from the analytical model developed by Maekawa et al.[15]. The concrete stress-strain relationship in tension was used for the slab element under tension due to cantilever action. Strain-hardening characteristic is incorporated to model the post-yielding behaviour of joint components. Key parameters such as reinforcement length and quantity of shear studs in the composite slabs are described in the proposed model for the respective components.

For advanced analysis of steel frame structures, the accurate prediction of full-range moment-rotation behaviour is indispensable for a successful prediction of overall structural behaviour.

The general concept is to superimpose the moment-rotation relationship of each row of components to get the overall moment-rotation behaviour of the joint. The rotation of a joint for a certain moments is calculated on the principles of equilibrium, compatibility and components force-displacement relationship to be satisfied at all rows of components. The complexities of the calculation process result from the interactions among the constitutive relationships and the non-linearity of each row of components.

It should be noted that the evaluation of initial rotational stiffness and moment capacity according to EC3 Part 1.8[3] neglected the influence of strain hardening. Consequently, it was observed that, for semi-rigid connections, the moment capacity was always less than the ultimate moment capacity. However, strain-hardening behaviour of each component after reaching plastic capacity is important for correctly predicting the full-range moment-rotation curve of the connection and ultimate moment capacity.

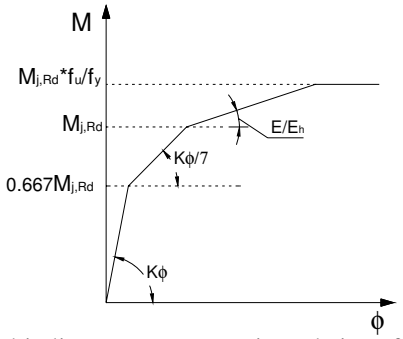

Figure 5. The typical quadric-linear moment-rotation relation of a component row (Faella et al.[10,11,12])

To account for strain-hardening, Faella et al.[10, 11, 12] has proposed a simple method without a significant increase of the computational effort. Fig. 5 shows the typical quadric-linear moment-rotation relation of a component. This approach was adopted in the proposed mechanical model.

This approach allows the engineers to have a means of predicting the full-range moment-rotation response of composite joints through a component-based mechanical model. The model predictions were validated by 28 ambient tests of composite joints in terms of initial rotational stiffness, ultimate moment capacity & moment-rotation response. The comparison showed good agreement and consistency between predictions and test results. With the incorporation of elevated-temperature material (EC3[16]) and component properties, the model can be used for predicting the behaviour of these joints at elevated temperature.

4. TEST RESULTS

The test details for four tests are shown in Table 2. A description of each test is given in the following section.

Table 2. Test Summary of C1-1, C1-2, C1-3 and C1-5.

Test	Temperature (at bottom beam flange)	Predicted Ultimate Moment (kNm)	Test Ultimate Moment (kNm)	Failure Mode
C1-1	ambient	214	215	Buckling of beam flange in compression
C1-2	430°C	200	201	
C1-3	ambient	145	154	Shear stud transfer capacity reached
C1-5	560°C	128	137	

The failure mode of specimen C1-1 is shown in Fig. 6. A close-up view shows slip of horizontal bolts and buckling of the beam flange in compression (Figs. 7 and 8). With the exception of a few damaged thermocouples during installation, there was good consistency

between the temperature profiles recorded for the left and the right hand side of the joint, indicating a reasonably uniform heating environment in the furnace.

Figure 6. Overview of C1-1 after test

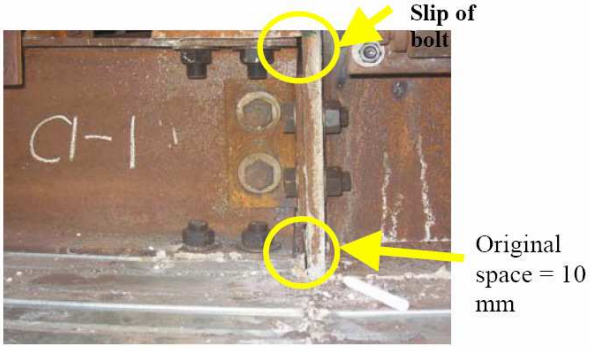

Figure 7. Typical slip of bolts in C1-1

Figure 8. Local view of C1-2

The failure mode of specimen C1-3 and C1-5 is presented in Fig. 9. A close-up view shows detachment of the end of RC slab from the beam flange in Fig. 13. However, the RC slab was still firmly attached to the steel joint without falling apart, which ensured that composite action was present. Detachment of RC slab-end from beam flange showed that the transfer of shear force from RC slab to shear studs was not as effective as in C1-1 and C1-2 joints. Thus, the shear stud capacity should be reduced. Its capacity was modified to 0.6 times the design shear stud capacity in hogging moment area, as stipulated in BS5950 Part 3.1[17].

Moment-rotation response & Failure modes

The moment-rotation curves of C1-1, C1-2, C1-3 and C1-5 specimens are shown in Fig. 10. For C1-1, as the load applied to the joint increased, an almost linear response up to around 160 kNm was observed with a progressive reduction in joint stiffness. This was due to

cracking of concrete slab. At about 160 kNm, a very large noise was heard. This was probably due to horizontal bolts for one seat angle inability to transfer further compressive force to the column flange due to increasing moment. Consequently, they jerked and slid into bearing against the seat angle plate. Fig. 7 shows the slip of bolts after the testing. Initially, there was a gap of 10 mm between the beam end and the column flange.

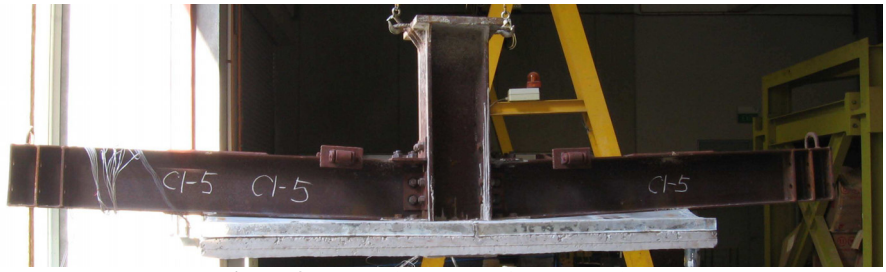

Figure 9. Local view of C1-5 (C1-3 similar)

After this sudden slip of bolts, the load applied to the joint decreased dramatically due to a gradual reduction of joint stiffness. The joint regained a new equilibrium at approximately 95 kNm until the beam flange and seat angle came into contact with the bolts at about 8.5 millirads rotation. This caused a temporary increase in the joint stiffness. Upon further rotation another slip occurred accompanied by a large noise and a reduction in moment, and this zip-zag pattern was repeated in the moment-rotation relation shown in Fig. 10. The test was terminated when there was an abrupt reduction in loading mainly due to local buckling in the beam bottom flange. The maximum moment was around 215 kNm. The observed failure mechanism of the joint was the same as predicted by the component-based mechanical model. Both specimens C1-1 and C1-2 showed buckling of compression flange in Figs. 11 and 12, respectively, and also slip of horizontal bolts.

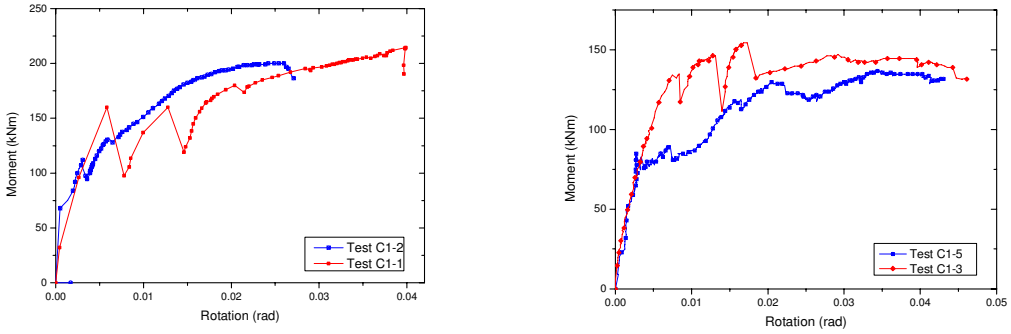

Figure 10. Comparison of Moment Rotation Curve for C1-1 and C1-2

Figure 11. Buckling of beam bottom flange for C1-1

Figure 12. Buckling of beam bottom flange of C1-2 after test

For C1-2, it was observed that the initial response of the joint (at elevated temperature) was slightly stiffer compared to that at ambient temperature. One possible reason was that the lateral restraint system expanded during heating, thus closing up any small gap between the beam flanges and the rollers of the lateral restraint beam system. Subsequently, there was some friction developed between the two surfaces. The initial response of C1-2 joint was approximately linear up to 60 kNm with an almost constant stiffness. At that point the downward movement became apparent with reducing stiffness. The concrete slab had cracks propagating through the thickness. When the moment was about 116 kNm (at about 5 millirads), a reduction in load was observed for a similar reason to the ambient test, that is, the horizontal bolts at one seat angle had slipped causing a relative movement between the seat angle and the beam bottom flange. When compared to the ambient test, the reduction in load is much smaller. This was probably because the clamping force of bolts was reduced to a large extent when the bolt shank expanded longitudinally during heating. So the bolt movement occurred more easily and smoothly compared to the ambient joint test. At approximately 6 millirads the joint regained equilibrium and the load continued to increase up to 135 kNm. At this point another reduction of load on the joint was observed due to the same reason. The test continued and was terminated due excessive deflection. The maximum moment was 201 kNm, close to the predicted 200 kNm. As with the ambient joint test, the observed joint mechanism was similar to the predicted mechanism, with buckling of beam flange in compression.

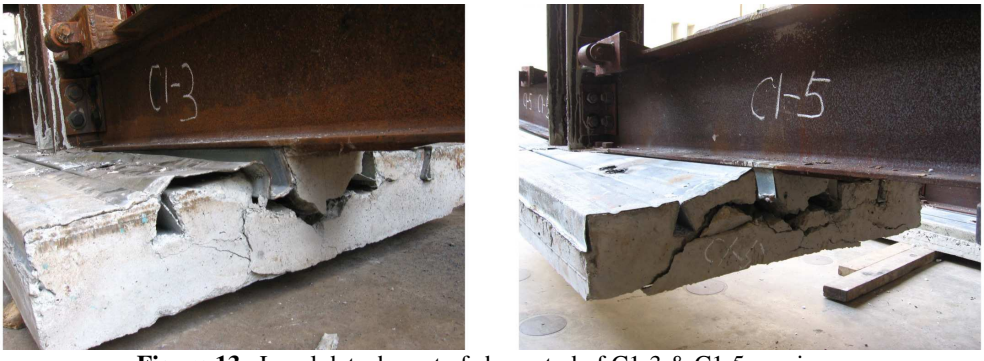

Figure 13. Local detachment of shear stud of C1-3 & C1-5 specimen

For C1-3 and C1-5 specimens the failure mode was different from C1-1 and C1-2 specimens despite the same design. This was because the C1-3 and C1-5 specimens were produced in the second batch. Concrete quality and construction quality were much different from the first batch of specimen fabrication. This resulted in lesser shear-transfer capacity from RC slab to the shear studs, which caused the specimens to reach ultimate moment

capacity when the shear studs could not transmit further shear force from RC slab to the connecting steel beam.

Similarly, sudden reduction of moment occurred twice for C1-3 specimen at ambient conditions. The maximum moment 154 kNm was reached at 17 millirad. But the moment quickly decreased and stabilised at a moment plateau of 147 kNm at approximately 27 millirads when the shear studs failed to transfer any further shear. Compared with ambient test, C1-5 specimen did not exhibit the distinctively sudden reduction of moment. Bolt shift occurred earlier at lower moment than C1-3 specimen. This could be explained by the same reason as in C1-2 elevated temperature test. At approximately 35 millirads the joint also reached its maximum moment of 136 kNm and kept rotating further with almost constant load.

Four points emerged from the four tests. Firstly, the moment capacity of joint decreased with increasing temperature due to material degradation. Secondly, the slip of bolts is characteristic of the behaviour of composite top-and-seat and web angle connection. The effect of bolt slip will cause an additional rotation without any increase in moment. Thirdly, this type of joints exhibited local buckling of the bottom flange in compression when the shear studs did not fail. Besides, the rotation required to reach the ultimate moment capacity is less than that at ambient condition. However, this does not imply that the joint had failed. The joint will continue to rotate at reduced moment, if the loading system allows for displacement control mode. This joint behaviour is borne out of finite element simulations. However, in the elevated temperature test, loading was terminated due to excessive deflection of the specimen to avoid damaging the furnace. Lastly, if the construction quality and concrete quality were not well controlled, the joint would fail when the shear studs could not transfer more shear force from RC slab to steel beam.

5 DISCUSSIONS

For composite angle joints, its characteristic moment-rotation response showed two times of abrupt reduction in moment due to sudden movement of the bolts at two seat angles. The magnitude of reduction in moment depends on the clamping forces of bolts, which in turn depended on the applied torque. The higher the tightening torque, the greater the load required to mobilise the bolts, and the more abrupt was the change in joint behaviour. However, at elevated temperature, the bolt shanks expanded and the clamping forces in the bolts were reduced.

A comparison of moment-rotation curves for the ambient test and elevated test is shown in Fig. 14. Superimposed onto Fig. 14 are the mechanical model predictions with or without bolt slip. There is close correlation between these four sets of results. The ambient response of the joint showed a greater stiffness, a larger moment capacity and a larger rotational capacity than the elevated temperature response of the joint. The initial stiffer response of the joint at elevated temperature could be explained by the unexpected contact between expanded roller restraint and the lateral restraint system at elevated temperatures. Apart from this point, the response of the joint correlated well with that of the ambient test. As mentioned earlier, the shear stud capacity should be reduced for C1-3 and C1-5 joints. It was modified to 0.6 times the design shear stud capacity in hogging moment area, as recommended in BS5950 Part 3.1[17].

The zig-zag pattern in the test curves were due to bolt slip. The component-based mechanical model does not explicitly include the effect of bolt slip. This shortcoming can be overcome by adding an additional rotation in the early stage of loading to simulate bolt slip. The magnitude of this rotation is approximately equal to 1 mm/beam depth (in mm) for bolt under Ø22 mm, or 2 mm/beam depth (in mm). To a lesser extent, the discrepancy in the final

rotation to reach the ultimate moment capacity is due to differences in the assumed materials properties (EC3[16]).

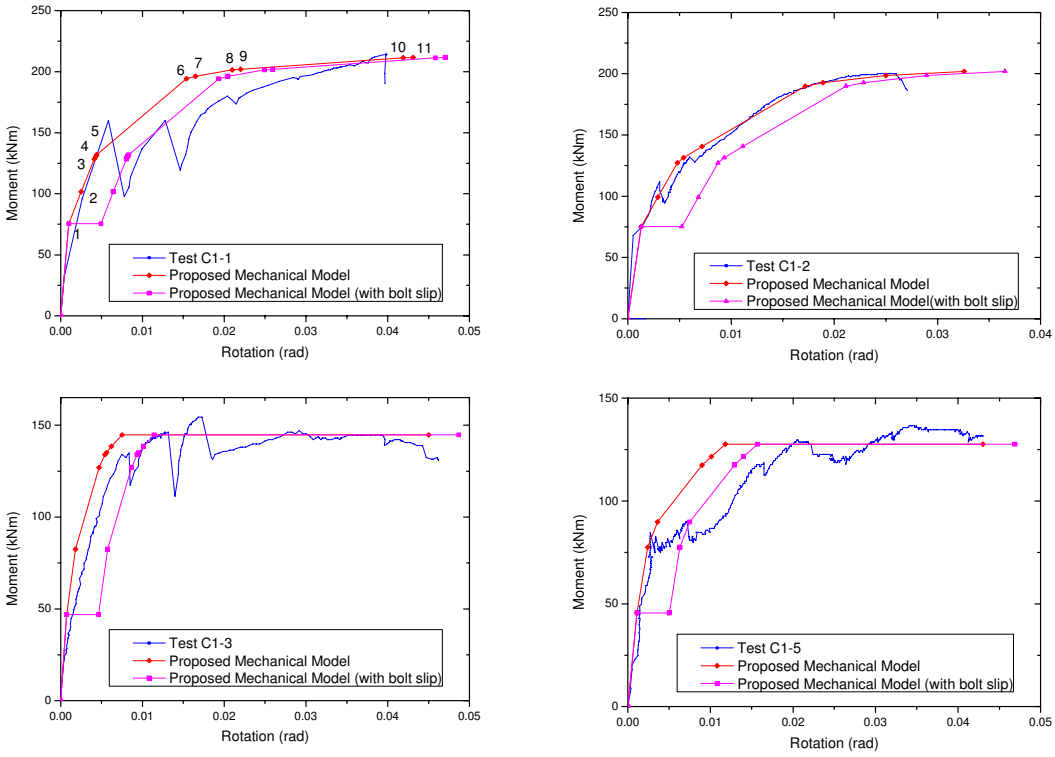

Figure 14. Comparison of test result vs. proposed mechanical model

Despite these shortcomings, the proposed mechanical model is able to trace the sequence of individual component reaching the respective elastic limit, yield limit, or ultimate strength. Generally, the authors assume that each component will behave elastically up to two thirds of its yielding capacity as shown in Fig. 5 (EC3 Part 1.8[3]). For C1-1 specimen, the occurrence of each limit in the predicted moment-rotation response is explained in Table 3. In this manner, the component-based mechanical model gives engineers a very clear picture of the joint behaviour under increasing load.

Table 3. The explanation of points in predicted moment-rotation curve for C1-1 specimen.

Point	Explanation	Point	Explanation
1	Reinforced slab reached elastic behaviour limit.	7	Beam flange in compression reached yielding capacity
2	Shear studs reached elastic behaviour limit.	8	1st row of bolts reached yielding capacity.
3	2nd row of bolts reached elastic behaviour limit.	9	2nd row of bolts reached yielding capacity.
4	Beam flange in compression reached elastic behaviour limit.	10	3rd row of bolts reached elastic behaviour limit.
5	1st row of bolts reached elastic behaviour limit.	11	Beam flange in compression reached ultimate capacity. The joint reached "failure".
6	Reinforced slab reached yielding capacity.		

The greater ultimate moment capacity at ambient condition was due to greater steel strength at ambient temperature. The ultimate steel strength weakens with increasing temperature. From 400°C onwards the ultimate strength is assumed to be the same as decreasing yield strength at 0.02 strain with a truncation for simplification purposed. The strain hardening behaviour is neglected at temperatures above 400°C.

In the mechanical model, since the "failure" mechanism was due to local buckling of the beam bottom flange and web, the loading dropped abruptly when local buckling was detected. The buckling capacity was obtained from the beam flange and web slenderness and post-buckling strength of steel. The steel strain-hardening at ambient temperature provided greater rotation capacity of the joint since greater strains are required to start buckling. However, at 400°C, there was less strain-hardening at elevated temperatures, hence resulting in less rotational of the C1-2 joint to reach the maximum moment capacity.

6 CONCLUSIONS

The "failure" mechanism observed at ambient and elevated temperature tests is similar for C1-1 and C1-2 This failure mechanism belongs to brittle failure because there is no obvious warning sign prior to its occurrence. Although the proposed mechanical model predictions show sufficient strength retention after the occurrence of beam flange and web buckling, both tests were terminated once the loading started to drop abruptly. For C1-3 and C1-5 the "failure" mode changed to failure in shear studs in transferring shear force. After modification of shear stud capacity, the mechanical model can still predict the joint behaviour quite well. The joint can still retention the strength at large rotations after reaching maximum moment.

REFERENCES

[1] Zandonini R. 1989, Semi-rigid Composite Joints. In *Structural Connections : Stability and Strength*. Narayanan R, editor. Elsevier, London. Pg 63-120.
[2] Simoes da Silva L, Simoes R.D., Cruz P.J.S. 2001. Experimental behaviour of end-plate beam-to-column composite joints under monotonical loading. *Engineering Structures* 23(11): 1383-1409.
[3] European Committee for Standardization (CEN) 2003, "Eurocode 3: Design of Steel Structures, Part 1.8: Design of Joints", prEN1993-1-8:2003, Brussels, Belgium.
[4] European Committee for Standardization (CEN) 2003, "Eurocode 4: Design of Composite Steel and Concrete Structures, General Rules and Rules for Buildings" (Draft), prEN1994-1-1:2003, Brussels, Belgium.
[5] Leston-Jones, L.C. 1997. *The influence of semi-rigid connections on the performance of steel framed structures in fire*. PhD thesis. Department of civil and structural engineering. University of Sheffield.
[6] Al-Jabri, K.S. 1999. *The behaviour of steel and composite beam-to-column connections in fire*. PhD thesis. Department of civil and structural engineering. University of Sheffield.
[7] Spyrou, S. 2002. *Development of a Component-Based Model of steel Beam-to-Column Joint at elevated temperatures*, PhD Thesis, Department of Civil and Structural Engineering, University of Sheffield, 2002.
[8] Steel Construction Institute (SCI). 1998, Joints in Steel construction: Composite Connections. SCI and British Construction Steelwork Association Limited. Ascot, London.
[9] Steel Construction Institute (SCI). 1991, Joints in Simple construction: Vol. 1 Design Method. SCI and British Construction Steelwork Association Limited. Ascot, London.
[10] Faella, C., Piluso, V. & Rizzano, G. 1995. Modelling of the moment-rotation curve of welded connections : proposals to improve Eurocode 3 Annex J, C.T.A., *Italian conf. on steel construction. October 1995*. Riva del Garda: Italy.

[11] Faella, C., Piluso, V. & Rizzano, G. 1996. Prediction of the flexural resistance of bolted connections with angles. *IABSE, International colloquium on semi-rigid structural connections. September 1996*. Istanbul, Turkey.
[12] Faella, C., Piluso, V. & Rizzano, G. 2000. *Structural steel semirigid connections : theory, design and software*. Florida, CRC press LLC.
[13] Yuan Zhen, Ting Seng Kiong and Tan Kang Hai. 2007. "Development of a component mechanical model for composite top-and-seat and web angle connection", *The Third International Conference on Steel and Composite Structures*, Manchester, UK.
[14] Yuan Zhen, Tan Kang Hai and Ting Seng Kiong. 2008. "Development of a component-based mechanical model and a finite element model for composite top-and-seat and web angle joint", *Journal of Structural Engineering*, in submission.
[15] Maekawa, K., Pimanmas, A. & Okumura, H. 2003. Nonlinear mechanics of reinforced concrete. Chapter 2, 8 and 9.
[16] European Committee for Standardization (CEN) 1995, "Eurocode 3: Design of Steel Structures, Part 1.2: General Rules – Structural Fire Design", ENV 1993, Brussels, Belgium.
[17] British Standards Institution (BSI) 1990, "BS5950 : Structural use of steelwork in building, Part 3.1 : Code of practice for design of simple and continuous composite beams", BS 5950-3.1:1990, London, UK.

TEMPERATURE DEVELOPMENTS IN PARTIALLY PROTECTED STEEL-CONCRETE COMPOSITE JOINTS USING INTUMESCENT COATING

X H DAI [1], Y C WANG [2] and C G BAILEY [3]
School of Mechanical, Aerospace and Civil Engineering, University of Manchester, UK

ABSTRACT

A series of fire tests on composite steel joint assemblies with different connection components and fire protection schemes have been carried out in the University of Manchester. This paper presents representative temperature distributions in joints, in particular temperature developments in different connection components with full protection of all connection components or protected joints but leaving bolts unprotected. The main conclusion from the experimental observations is that whether or not protecting bolts has little influence on temperatures in other components of a protected joint but in a protected joint with unprotected bolts, the bolt temperatures are higher than those with full bolt protection. Nevertheless, the bolt temperatures were still much lower than bolt temperatures in the completely unprotected joint. Using the measured temperatures, thermal properties of the intumescsent coating used in the tests were derived using the fire protection assessment method in DD ENV13381-4: 2002(E)[1], which were then used to calculate the bolt temperatures according to the simple calculation method in Eurocode: EN 1993-1-2: 2005(E)[2]. It has been found that for protected joints with unprotected bolts, an appropriate exposure factor should be introduced to take into account the additional heat flux to the bolts which are directly exposed to fire.

[1] Research associate, School of Mechanical, Aerospace and Civil Engineering, University of Manchester, UK, email: xianghe.dai-2@manchester.ac.uk
[2] Reader, School of Mechanical, Aerospace and Civil Engineering, University of Manchester, UK, email: yong.wang-2@manchester.ac.uk
[3] Professor, School of Mechanical, Aerospace and Civil Engineering, University of Manchester, UK, email: colin.bailey@manchester.ac.uk

1. INTRODUCTION

Joints are critical members in steel framed structures. The performance of joints in a steel framed structure has critical influence in controlling the progressive collapse of the structure under accidental fire attacks. Although previous researches on steel-framed structures in fire have resulted in the development of design methods being adopted routinely in steel structural design in fire conditions, gaps still exist in understanding joint behaviours. Following the World Trade Center disaster, a number of authoritative organisations [3] [4] have identified joint integrity as a key to maintain structural integrity in fire and have called for extensive research on joints under fire conditions.

Steel being a thermally high conductive material, the temperature rise in unprotected steel exposed to fire attack is quick, resulting in rapid loss in strength and stiffness of steel in fire. To ensure sufficient fire resistance of steel framed structures, fire protection is often required to limit temperature rises in steel. As the most popular type of fire protection material, intumescent coating may be applied either on-site or off-site. However application of intumescent coating to joints can be a time consuming process, therefore how to reduce the effort of applying intumescent fire protection without degrading the fire protection effectiveness is an important practical concern of fire protection professionals. an important issue is whether the bolts can be left unprotected in an otherwise fully protected joint. This is the focus of this paper, which forms part of an extensive experimental and numerical research project on robustness of steel joints in fire, currently under way at the University of Manchester in collaboration with the University of Sheffield, funded by the UK's EPSRC.

2. FIRE TESTS

2.1 Description of test specimens

Fourteen specially designed steel-concrete composite joint assemblies with four typical connection types: web cleat, fin plate, flush endplate and flexible endplate, have been fire tested in the fire lab in the University of Manchester. Each specimen consisted of one column, four beams (two bolted to the column flanges via the aforementioned four different types of joints and the other two bolted to the column web via fin plates) and a concrete slab with profiled steel sheeting and reinforcements on the top of the steelwork. Figure 1 shows the 3D configurations of these joint assemblies. The column in all the test specimens was the same, being UC254X254X89 and with a length of 1000mm. The beam section in all the test specimens was also the same, being UB305X165X40. The length of the steel beams connected to the column flanges was 605mm and the length of the steel beams connected to the column web was 485mm. Table 1 gives detailed dimensions of joints for different test specimens, including the 4 unprotected specimens identified as USP1~USP4 and 10 protected specimens identified as SP1~SP10. Table 2 gives details of joints with full protection or with full protection but unprotected bolts. The dimension of the concrete slab was 1000X1000mm with an overall depth of 130mm.To enable connections of different dimensions to be directly compared, some of the tests used connectors of different dimensions in the same specimen to join the two steel beams connected to the flanges of the column. All specimens tested were not loaded.

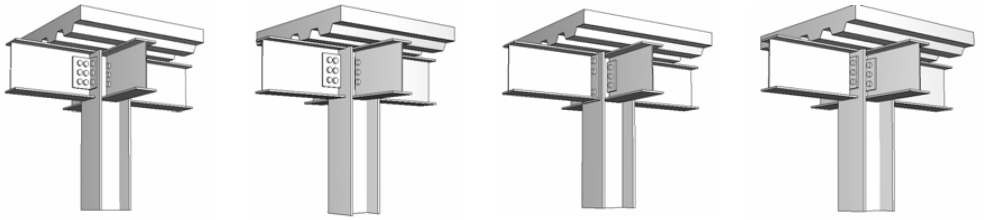

(a) Web cleat joint (b) Fin plate joint (c) Flush endplate joint (d) Flexible endplate joint

Fig. 1- Joint types and configurations

Table 1: Detailed dimensions of connection components

Specimen ID	Join type to column flange	Joint component to one column flange	Joint component to the other column flange	Fin plates welded to column web
USP1	flush endplate	324X200X10		200X100X10
USP2	flexible endplate	200X150X8		
USP3	fin plate	200X150X10	200X100X10	
USP4	web cleats	150X90X10 (depth200)	90X90X10 (depth200)	
SP1-SP3	web cleats			
SP4-SP7	fin plate	200X150X10	200X100X10	
SP7-SP8	Flush endplate	324X200X10		
SP9-SP10	Flexible endplate	200X150X8		

For designation in table 2, full protection (including the bolts) is referred to as FP+B; full protection (excluding bolts) is referred to as FP_B; P300+B or P400+B refers to protecting a segment of 300mm (for beams connected to the column web) or 400mm (for beams connected to the column flanges) of the beams from the corresponding connection ends, including all the beam connectors and bolts; P300_B or P400_B refers to the same beam fire protection scheme as aforementioned but without protecting the bolts. Figure 2 shows typical fire protected specimens before testing. In table 2, Beam 1 and Beam 2 refer to the beams connected to the column flanges (605mm long) and Beam 3 and Beam 4 refer to the beams connected to the column web (485mm long).

(a) Unprotected bolts (b) Protected bolts

Fig. 2 - Examples of fire protection schemes

Table 2: Summary of fire protection schemes

Specimen ID	Join type to column flange	Column	Beam 1	Beam 2	Beam 3	Beam 4
SP1	web cleat	FP+B	FP+B	P400+B	P300+B	P300+B
SP2	web cleat	FP_B	FP_B	P400_B	P300_B	P300_B
SP4	fin plate	FP+B	FP+B	P400+B	FP+B	FP+B
SP5	fin plate	FP_B	FP_B	P400_B	FP_B	FP_B
SP7	Flush endplate	FP+B	FP+B	P400+B	FP+B	P300+B
SP8	Flush endplate	FP_B	FP_B	FP_B	FP_B	FP_B
SP9	Flexible endplate	FP+B	FP+B	P400+B	FP+B	P300+B
SP10	Flexible endplate	FP_B	FP_B	P400_B	FP_B	P300_B

Intumescent coating fire protection was applied by the intumescent coating manufacturer's own application team. The nominal intumescent coating thickness was specified to limit the steel temperature rise to 550^{o}C at 60 minutes of the standard fire exposure to BS 476[5]. However it must be pointed out that although the beams and columns used the same section sizes in all tests, the actual average coating thicknesses (DFT) for different specimens varied considerably, being 1.02~1.43 mm on beams and 0.6~0.95mm on columns. Also DFT measurements at the different locations of the same member showed large variations.

2.2 Test set-up

Fire tests were carried out in a gas fired furnace (internal dimensions: 3500mm×3000mm×2000mm) in the fire laboratory of the University of Manchester. The test specimen was rotated by 90^{o} and hung inside the furnace via three well protected steel ropes, as shown in Figure 3. Fire exposure was according to a standard fire condition (ISO 834[6]).

(a) View from inside the furnace (b) View from outside the furnace

Fig. 3 - Set-up of joint test specimen

2.3 Furnace temperature

In order to compare measured temperatures obtained in different components in the same specimen and also from different specimens, it is assumed that the temperature field inside furnace was uniform and identical for different tests. To verify this assumption, a

supplementary fire test was carried out, in which there was no test specimen but measurements were taken for gas temperatures near where the test specimen would be placed. Figure 4(a) shows the measured gas temperatures at different locations. The small differences confirm the uniformity of gas temperature around the test specimen. Figure 4(b) shows the average gas temperatures calculated using readings from the 6 monitoring thermocouples in the furnace for different specimens. It can be seen that the average temperatures in different tests were very similar and close to the ISO 834[6] standard fire temperature except for tests on specimens USP2 and SP5 where the average gas temperatures were slightly higher than the intended standard fire temperature due to failure of one control thermocouple.

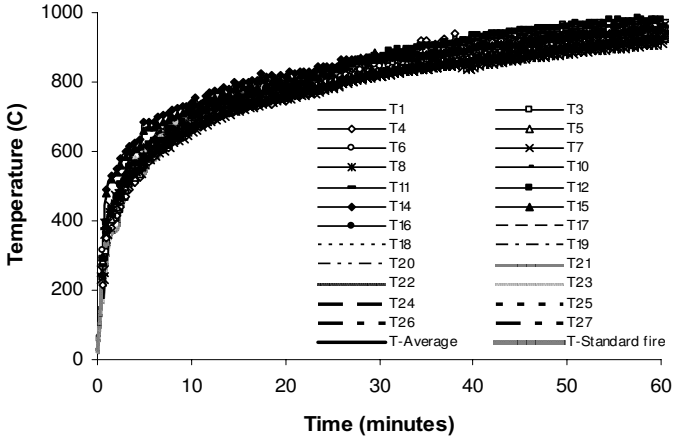

(a) Temperature distribution inside the furnace from a supplementary fire test without a joint specimen

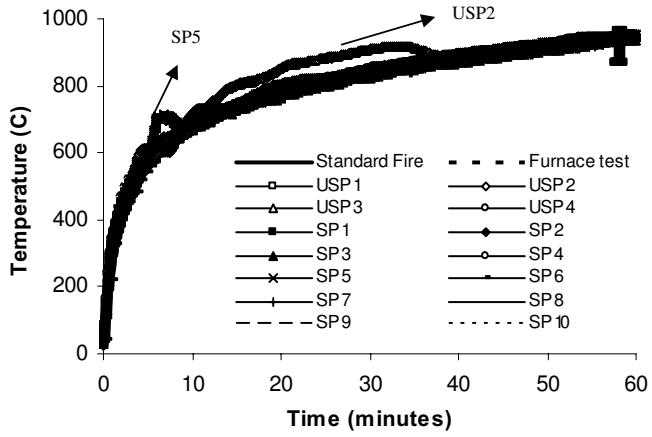

(b) Average furnace temperatures calculated using furnace control thermocouples

Fig. 4 - Furnace temperature uniformity and identity check

2.4 Test observations

Figure 5 and figure 6 compare typical temperature developments in web cleats and associated bolts (representing connection components on the beam web). From which the following conclusions may be drawn: (1) if all the connection components were unprotected, the connection temperatures were much higher than in connections with fire protection regardless of whether or not the bolts were protected; (2) if the connection components (web cleats) were protected, whether or not protecting the bolts had minor influence on temperatures in the protected connection components; (3) if the connection components (web cleats) were protected, the unprotected bolt temperatures were higher than protected bolt temperatures but still much lower than those in a unprotected joint specimen. Similar results were observed from other joint types as fin plate and end plate. Figure 7 shows the unprotected bolts in a protected web cleat before and after the test. The bolts were not covered by the expanded intumescent char. This explains why the unprotected bolt temperature was higher than the temperature in protected bolts.

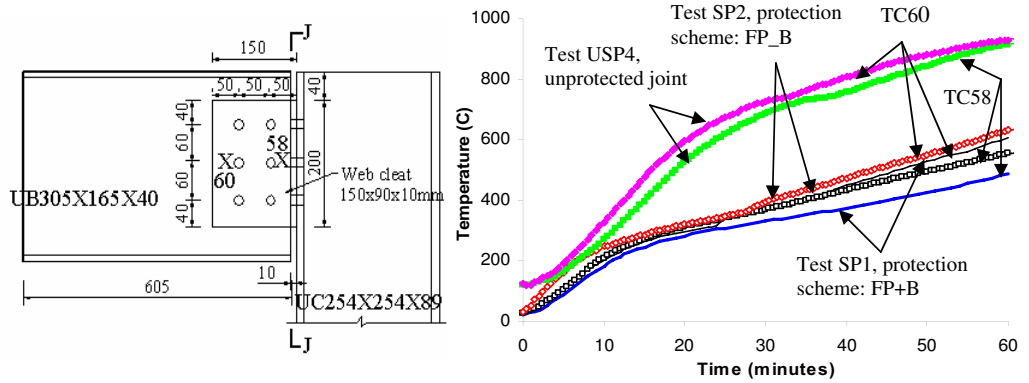

(a) Locations of thermocouples (TC) (b) Temperature – time curves

Fig. 5 - Comparison of temperatures in the web cleat on the beam web

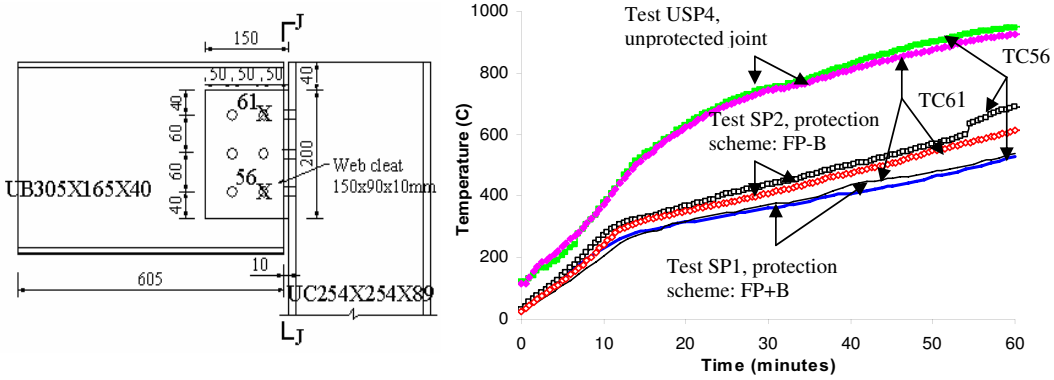

(a) Locations of thermocouples (TC) (b) Temperature – time curves

Fig. 6 - Comparison of temperatures in the bolts connecting web cleat and beam web

Fig. 7 - Unprotected bolts in web cleat before and after 60 minutes fire exposure (Test SP2)

3. PREDICTION OF TEMPERATURES IN JOINT COMPONENTS

3.1 Simple calculation methods in EC3

EN 1993-1-2:2005(E)[2] provides simple calculation methods to calculate temperatures in unprotected and protected steel sections. Figure 8 gives typical examples of comparison of temperatures in column and beam sections measured in tests and calculated by simple methods. In calculations for protected steelwork, the effective thermal conductivity of intumescent coating was obtained following the procedure in DD ENV13381-4:2002(E)[1]. The procedure in DD ENV 13381-4:2002(E)[1] is simply inverse calculation of the method in EN 1993-1-2:2005(E)[2]. Therefore, the results in figure 8(b) only confirm that the calculation procedure was appropriately implemented.

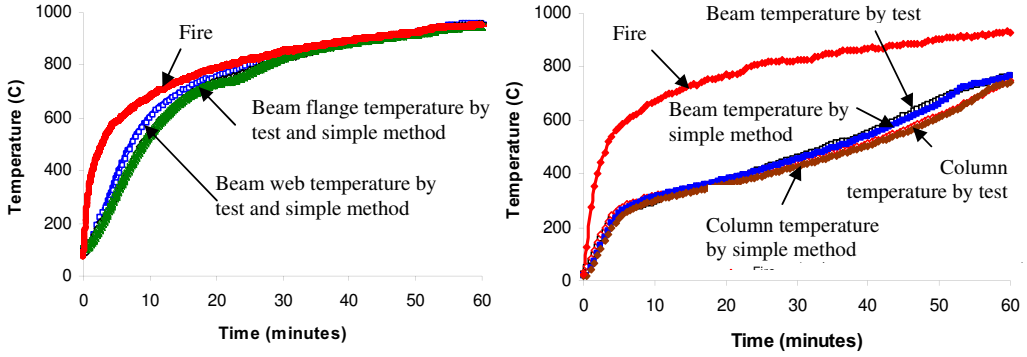

(a) Comparison of temperatures measured in test and predicted using simple method (unprotected steel section)

(b) Comparison of temperatures measured in test and predicted using simple method (protected steel sections)

Fig. 8 - Validation of simple calculation method provided in EN 1993-1-2:2005[2]

3.2 Temperatures in unprotected and fully protected joints

The effectiveness of the simple calculation method, provided in EN 1993-1-2: 2005(E)[2], using predicting temperature developments in fully protected and unprotected steel sections has been approved in the previous section. However joint geometries are much more complicated compared with the simple member cross-sections. Therefore, a method is needed

to calculate the equivalent section factor for joints. Dai *et al.* (2007)[7] proposed and verified a method to calculate the equivalent section factor for a joint if the joint is unprotected. The same effective section factor calculation method may also be used for fully protected joints. figure 9 demonstrates the accuracy of this method by comparing the calculation and experimental results for protected joints using a web cleat (representing the column flange zone) and a fin plate (representing the beam web zone) respectively. In the calculations, the effective thermal conductivity of the intumescent coating was the same as used in member calculations shown in figure 8.

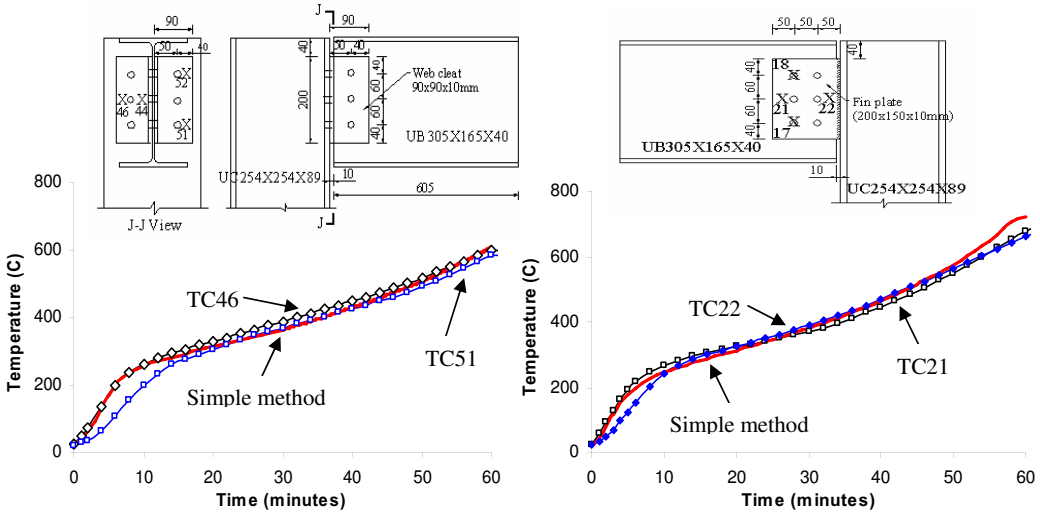

(a) Temperatures in web cleat (SP1) (b) Temperatures in fin plate (SP4)

Fig. 9 - Comparisons of temperatures in fully protected joints obtained from tests and predicted by simple calculation methods

3.3 Temperatures in protected joints with unprotected bolts

Figure 7 shows that for a protected joint assembly with unprotected bolts, it would be appropriate to assume that the bolt top surfaces were not covered by the expanded intumescent coating char. This unprotected top surface of a bolt would increase the bolt temperature compared to a bolt with full protection. In order to account for the effect of unprotected bolt surface, it is recommended to use a coefficient named 'exposure factor' (F_e). This exposure factor expresses the unprotected surface area of a bolt assembly as a proportion of the total surface area of the bolt assembly. Thus, F_e ranges from 0 for a bolt assembly with full protection and 1 for a totally unprotected bolt assembly. Use Q_{up} and Q_p to denote the heat flux to per unit area of unprotected bolt assembly surface and protected bolt assembly surface respectively. If the total surface area of a bolt assembly is A, then the unprotected surface area is $F_e A$ and the protected surface area is $(1-F_e)A$, giving the total heat flux to the bolt assembly as $Q_{up} \cdot F_e \cdot A + (1-F_e) \cdot Q_p \cdot A$. $Q_{up}A$ represents the total heat flux if the bolt assembly is unprotected, which results in a bolt assembly temperature T_{up}. $Q_p A$ represents the total heat flux if the bolt assembly is fully protected, which results in a bolt assembly temperature T_{fp}. Therefore, the temperature in the unprotected bolts of an otherwise protected joint may be calculated by the following formulation:

$$T_{pp} = T_{fp} + (T_{up} - T_{fp}) \cdot F_e \quad (1)$$

T_{up} and T_{fp} can be approximately calculated using the simple calculation method provided in EN 1993-1-2: 2005(E) [2].

Because of the complicated configurations of joints, two methods may be considered to determine the exposure factor F_e: (1) 2-D calculations and (2) 3-D calculations.

In 2-D calculations, the bolts are assumed to be along the entire length of the connected plates. Figure 10 shows how the F_e values for joints using end plates, web cleats and fin plates may be calculated. In figure 10 d_b is the equivalent diameter of the bolt head or the nut and F_s is the approximate section factor for the entire bolt assembly.

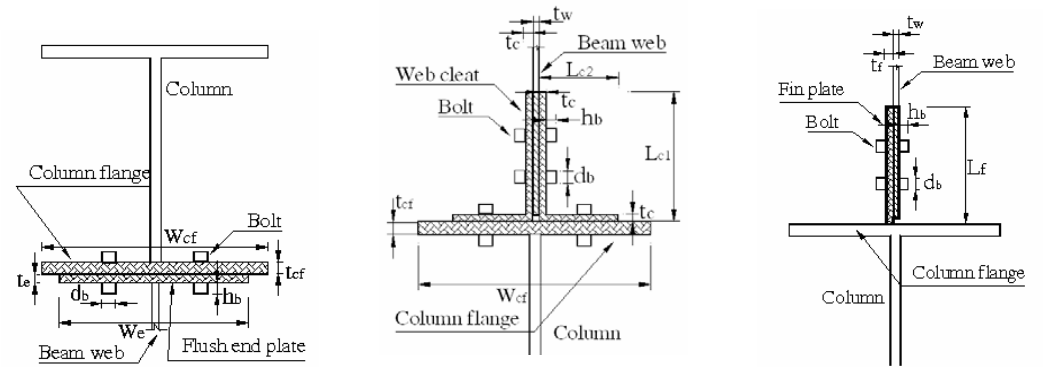

$$F_s = \frac{2 \times (W_{cf} + t_{cf} + t_e)}{W_{cf} \times t_{cf} + W_e \times t_e} \qquad F_s = \frac{2 \times (L_{c1} + t_{cf} + W_{cf})}{(L_{c1} - t_c) \times (2 \times t_c + t_w) + 2 \times L_{c2} \times t_c) + W_{cf} \times t_{cf}} \qquad F_s = \frac{2 \times (L_f + t_f + t_w)}{L_f \times (t_f + t_w)}$$

$$F_e = 4 \times d_b / (2 \times W_{cf} + 2 \times t_{cf} + 2 \times t_e) \qquad F_e = 8 \times d_b / (2 \times L_{c1} + 2 \times t_{cf} + 2 \times W_{cf}) \qquad F_e = 4 \times d_b / (2 \times L_f + 2 \times t_f + 2 \times t_w)$$

Fig. 10 - Simple 2-D calculations of exposure factor and section factor

The 3-D calculation method is similar to the 2-D calculation method. However, in 3-D calculations, the actual quantity and shape of the bolts and nuts in the entire bolt assembly should be considered. It is also assumed that only the top surfaces of bolt heads and nuts are exposed to fire. Figure 11 shows an example for the approximate calculation method for 3-D calculations of exposure factor for a fin plate connection. Based on the 2-D and 3-D calculation methods, table 3 gives the exposure factors for the tested connections studied in this paper.

Table 3: exposure factors for tested joints

Connection types	2-D	3-D calculation
Web cleat (90X90X10)	0.302	0.080
Web cleat (150X90X10)	0.264	0.089
Fin plate (200X100X10)	0.276	0.086
Fin plate (200X150X10)	0.386	0.111
Flush end plate (324X200X10)	0.226	0.047
Flexible end plate (200X150X8)	0.227	0.070

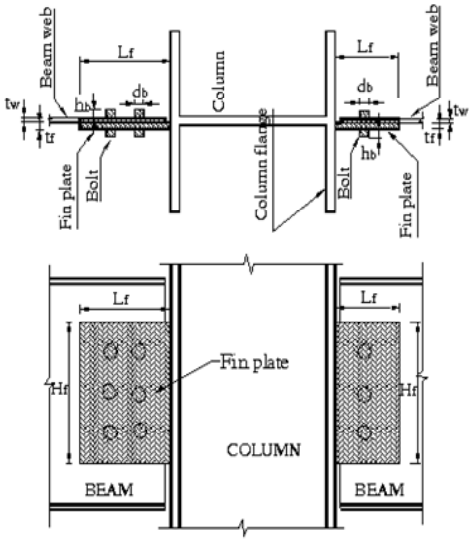

$$F_s = \frac{(2L_f + t_f + t_w)H_f + A_{bs}n_b}{(t_f + t_w)L_f H_f + V_{bo}n_b}$$

$$F_e = A_{be}n_b / [(2L_f + t_f + t_w)H_f + A_{bs}n_b]$$

n_b : Bolt quantity in the analyzed joint.

A_{bs} : Side surface area of a bolt excluding the part inside the connected members.

$$A_{bs} = 2 \times \pi d_b h_b$$

V_{bo} :Volume of a bolt and nut excluding the part inside the connected members.

$$V_{bo} = 2 \times \pi (\frac{d_b}{2})^2 h_b$$

A_{be} : Two end surface area of a bolt.

$$A_{be} = 2 \times \pi (\frac{d_b}{2})^2$$

Fig. 11 - Example for 3-D calculation of exposure factor

Figure 12 shows typical comparisons of temperatures in protected connections with unprotected bolts between test results and predicted results using the simple calculation method. It can be seen that the predicted temperatures are lower than the measured temperatures in the bolts if the bolts were treated as fully protected (F_e =0). However the predicted temperatures are much higher than the measured temperatures when the 2-D exposure factor was employed. The predicted temperatures are close to the measured temperatures when the 3-D exposure factor was used.

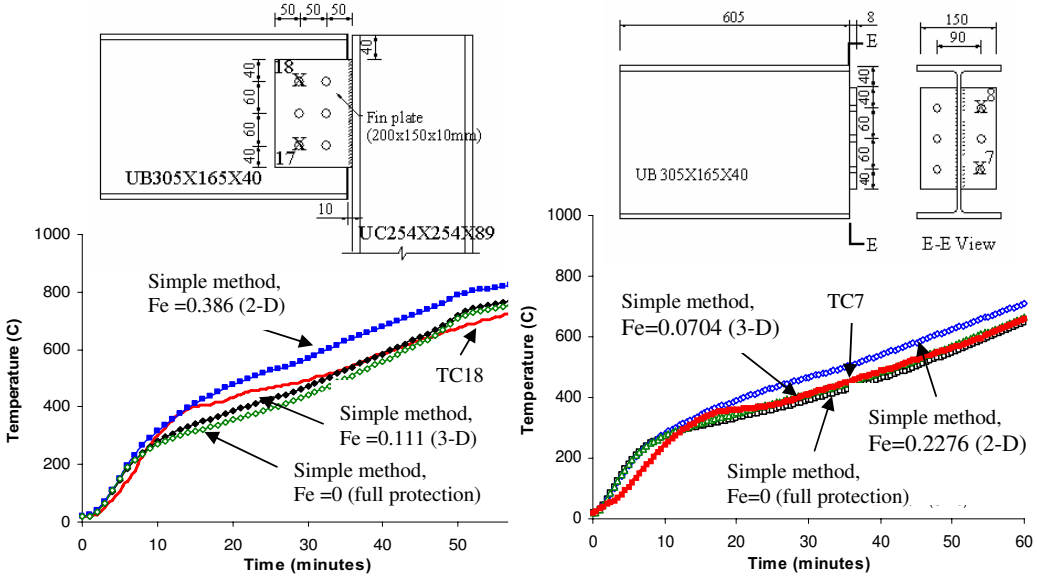

(a) Temperatures in unprotected bolts in a protected fin plate (SP5)

(b) Temperatures in unprotected bolts in a protected endplate (SP10)

Fig. 12 - Comparisons of temperatures in unprotected bolts in a protected joint

The predicted temperatures using the 2-D exposure factors are higher than the measured temperatures. This is because the 2-D exposure factors overestimated the actual unprotected surface area in the bolt assemblies. It may be noticed that at the early heat stage, even using the higher values of 2-D exposure factor would still underestimate the measured temperatures. This is because in the early stage of heating, the side surfaces of the bolts were not covered by intumescent char so the exposure factors should be higher than assuming the side surfaces of the bolts were covered by intumescent char. Nevertheless, since only bolt temperatures in the later stage of heating will be of practical interest, it is acceptable to use the exposure factor based on unprotected bolt head surface only.

4. CONCLUSIONS

This paper describes fire experiments on unloaded steel-concrete composite joints with four types of connection: web cleat, fin plate, flush endplate and flexible endplate. Experimental results are presented for representative temperature distributions in connection components to demonstrate the effects of unprotected bolts in otherwise protected joints. A simple calculation method is described to demonstrate how the unprotected bolt temperatures may be calculated. This method makes use of a quantity called "exposure factor", which is defined as the ratio of unprotected surface area of a bolt assembly to the total surface area of the bolt assembly. Based on comparisons and analyses of temperature distributions in various connection components, the following main conclusions may be drawn:

(1) In a protected joint with unprotected bolts, the unprotected bolt temperatures were higher than those with full bolt protection, but the bolt temperatures were still much lower than those in completely unprotected joints.
(2) In a protected joint, whether or not protecting the bolts had little influence on temperatures in other connection components.
(3) The simple calculation methods provided in EN 1993-1-2: 2005(E) [2] can be used to predict temperature developments in unprotected and protected joint components. However appropriate exposure factors should be used in prediction of temperatures in unprotected bolts in a protected joint. This paper has shown how the exposure factor may be calculated for three different types of connections: end plate connections, web cleat connections and fin plate connections.

5. ACKNOWLEDGEMENTS

This research is funded by a research grant from the UK's Engineering and Physical Science Research Council (EP/C003004/1). The authors would like to thank Mr. Jim Gorst and Mr. Jim Gee for assistance with the fire tests.

6. REFERENCES

[1] DD ENV 13381-4:2002(E), "Test methods for determining the contribution to the fire resistance of structural members. Part 4: Applied protection to steel members". British Standards Institution, London.

[2] EN 1993-1-2: 2005(E), "Eurocode 3: Design of steel structures-Part 1-2: General rules-Structural fire design". British Standards Institution, London.
[3] Federal Emergency Management Authority (FEMA 2002), "World Trade Center Building Performance Study". FEMA, USA.
[4] Institution of Structural Engineers (ISE 2002), "Safety in tall buildings and buildings of large occupancy", Institution of Structural Engineers, London.
[5] British Standards Institution (BSI 1987), "BS476: Fire tests on building materials and structures, Part 20: Methods for determination of fire resistance of elements of construction (general principles)". British Standards Institution, London.
[6] ISO 834 (1975), "Fire Resistance Tests, Elements of Building Construction", Geneva: International Organization for Standardization.
[7] Dai X.H., Wang Y.C. & Bailey C.G. (2007), "Temperature distribution in unprotected steel connections in fire". Proceedings of the 3rd International Conference on Steel and Composite Structures (ICSCS07), Wang & Choi (eds), Taylor & Francis Group.
[8] Wang Y.C. (2002), "Steel and composite structures, behaviour and design for fire safety". London: Spon Press; 2002.

COLUMN WEB PANEL AT ELEVATED TEMPERATURE

MICHAL STREJČEK [1], FRANTIŠEK WALD [2], ZDENĚK SOKOL [3]

ABSTRACT

One of the last studied components exposed to elevated temperature during the exposition of the steel structure to fire is the column panel loaded in shear. At the Czech Technical University in Prague were performed a set of three tests to confirm the analytical prediction model. The model is taking into account the distribution of the internal forces in the shear panel affected by the transfer of the forces by bolt rows in tension. Two panels were tested at ambient temperature and four panels at elevated temperature. The gas temperature in the furnace followed the temperature measured during the seventh Cardington large compartment test in 2003. The contribution is focussed to the presentation of the experimental results and the analytical prediction model by a component method.

1 INTRODUCTION

The analytical prediction of the joint behaviour at the ambient temperature is based on a component method. Firstly is a joint, which consists of connections and a part of the column, decomposed into its components. The behaviour of the components is described in terms of initial stiffness, resistance and deformation capacity by its force-deformation curves $F - \delta$. Based on mechanical/spring model and the loading history is the behaviour assembled into the behaviour of the joint, which may be described by a moment-rotational curve M - ϕ. The curve is introduced into the global analyses. The components in the joints may be divided into components in tension, in compression and in shear, see [1].

The fire resistance of structures is based on the tests of elements at elevated temperatures in furnaces. It is calculated the gas temperature in the fire compartment exposed by localised or compartment fire, the transfer of temperature into the structure, the mechanical

[1] Research assistant, Czech Technical University in Prague, CZ166 29 Praha, Czech Republic.
email: michal.strejcek@fsv.cvut.cz
[2] Professor, Czech Technical University in Prague, CZ166 29 Praha, Czech Republic.
email: wald@fsv.cvut.cz
[3]Assistant professor, Czech Technical University in Prague, CZ166 29 Praha, Czech Republic.
email: sokol@fsv.cvut.cz

loading during the fire and the mechanical resistance of the structure during the fire, see [2]. The structural connections are exposed during the fire to the elevated temperature and forces from thermal expansion during heating and contraction during cooling.

There are two procedures of the design of the connections at elevated temperature. One is based on the protection of the connections as the connecting elements. The alternative is the application of the component method at elevated temperature, see [3]. The changes of the mechanical properties of the components may be described in terms of the initial stiffness and resistance, e.g. for material, welds and bolts. The knowledge of the deformation capacity is namely for the bolted connection limited. The forces during fire may be assumed by shear, moment and normal forces loading at elevated temperature only, if the global analysis at the elevated temperature is based on the ambient temperature design. The assembly may be based on simplified principles according to the material properties changes and temperature distribution in the connection, see [4]. In case of structural analyses at elevated temperature are the internal forces and its changes during fire event evaluated by calculation.

For the temperature development in the connection, there are published two analytical prediction methods. In the step by step method is the temperature calculated as for the elements, where the heat is brought in/brought out by the member surface and the member volume is heated/cooled. Geometrical characteristic of the section is described by the section factor A_m/V of the steel parts of which the joint is composed. The temperature of a joint may be assessed using the local section factor A_m/V, the value of the parts forming the joint. As simplification, it is possible to consider uniform temperature distribution within the section and to take into account the biggest A_m/V value of the steel parts connected into the joint. The temperature of either beam-to-beam or beam-to-column connection covered with a concrete slab can be determined from the temperature of the beam flange in the middle of the span. It is assumed, that the temperature of the particular parts of the connection depends directly only on the distance from the lower edge of the connected beam and indirectly on the prediction of the temperature of the lower flange calculated usually by the step by step procedure.

The set of test with connections and its components at elevated temperature enables to confirm an adequate accuracy. One of the last studied components is the column web in shear. The set of 8 tests by [5] enable to classify the deformation capacity of the beams web loaded in shear and bending. The presented work is focussed on the column web panel, which is loaded in shear by a bolted end-plate connection. There are two methods of the representation of the column web panel in shear in global analyses. The contribution of its deformation may be modelled separately as a zone plus two connections or may be integrated into each connection based on applied shear force to the joint. In the presented work is for simplicity the contribution to the M - ϕ curve taken separately.

2 AMBIENT TEMPERATURES

To study the component column web in shear two sets of tests were prepared. The first set was tested at ambient temperature, the second at elevated temperature. The test set up, which was made of steel S235, consists of two columns HEB 200 and short I-cross-section beam, which was connected by the end-plate joint with the high strength bolts M24-10.9, see Fig. 1. The beam web was stiffened in the compressed part by a U-cross-section. The column was stiffened locally in the position of the applied load. The guiding component, which was design to fail, was the column web panel in shear. Resistance of this component was designed for loading by a bending moment 95 kNm and a normal force 58 kN. Resistance of other components was quantified for loading – column web in tension for 121 kNm and 73 kN, bolts in tension for 155 kNm and 94 kN, column flange in bending for 98 kNm and 60 kN,

end-plate in bending for 97 kNm and 59 kN. Due to the decrease in resistance at elevated temperature in fire test were bolts in tension reinforced by second nut. The transversal forces generated in the joint the bending moment and the normal force, which simulate force from thermal expansion during the fire.

The experiment at ambient temperature was prepared at one set up, with two joints. The loading cells were controlled by deformations to keep the constant force steps. Two linear transducers were used for measuring the deformations of joints. The first at the place of applied load, the second in the middle of the column length, see scheme of the specimen at Fig. 2. The shear deformation of web panel was observed by two short linear transducers, one for compression brace and one for tension brace, see Fig. 1. The moment-rotational diagram of the joint *B* in specimen A58 and its column web panel in shear are shown at Fig. 2. The shear deformation of the column web panel was achieved during the loading. The connection resistance was reached by loading of a bending moment 152 kNm and a normal force 92 kN. The plastic deformations stated with the bending moment 85 kNm and normal force over 51 kN. The measured deformations are included in Tab. 1 with step of 20 kNm.

a)  b) 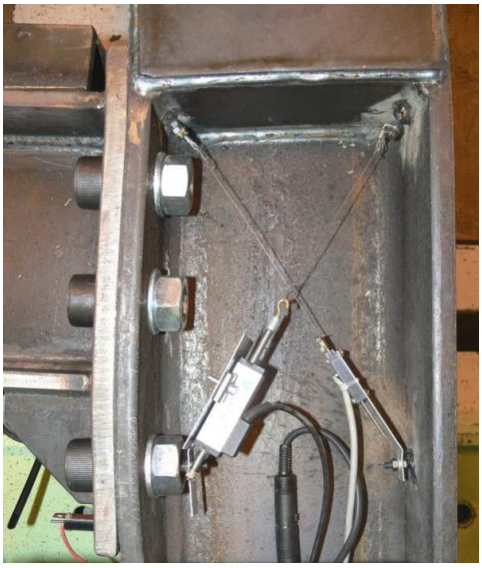

Fig. 1 - Short linear transducers measuring shear deformation of the column web panel a) before the test, b) after the test A58.

The analytical prediction of the column web panel was carried out by component method described in [7]. The moment-rotational diagram can be obtained using eq. (1)-(5). For the prediction the yield strength $f_{y,wc}$ in (1) was replaced by ultimate strength of steel. The steel material characteristics were taken by the coupon tensile test, the characteristic yield strength $f_{y,wc}$ = 309 MPa and characteristic ultimate strength $f_{u,wc}$ = 431 MPa. The stiffness ratio in eq. (2.2) adequately includes the plastification of the web panel. The comparison of the prediction to the test at ambient temperature is included at Fig. 3 and in Tab. 1. The reached accuracy of the initial stiffness and column web plastification is good.

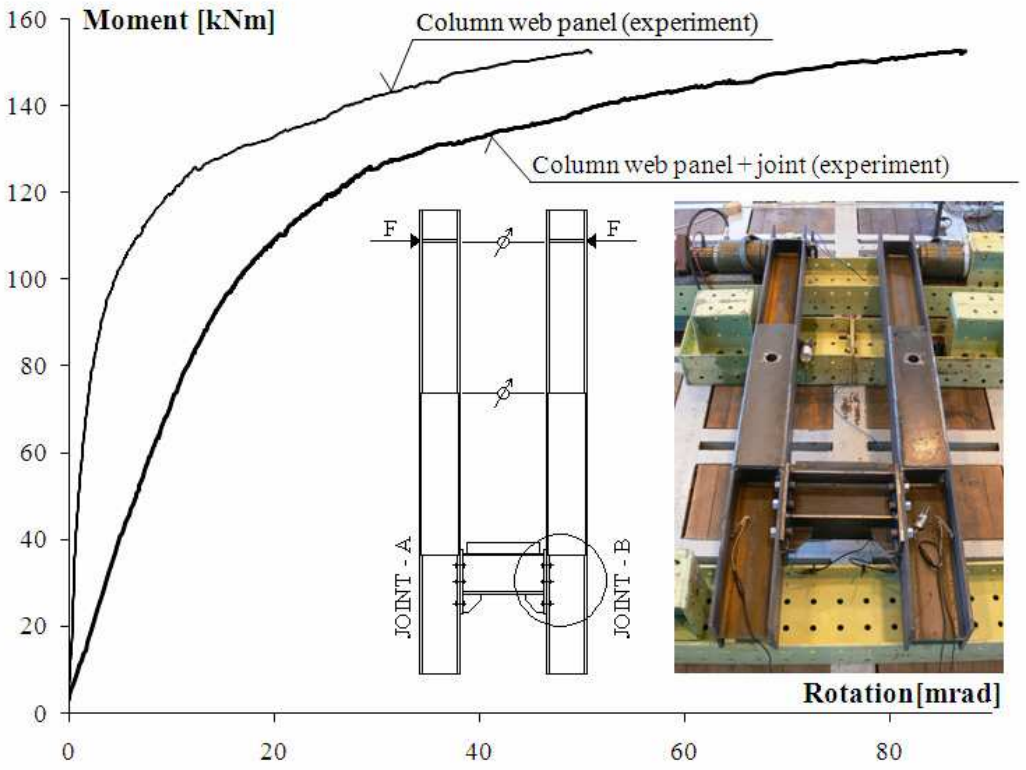

Fig. 2 - M-ϕ diagram of the whole connection and column web panel at ambient temperature, specimen A58.

Shear resistance of transversally unstiffened column web panel can be obtained using:

$$V_{wp,Rd} = \frac{0{,}9 f_{y,wc} A_{vc}}{\sqrt{3}\,\gamma_{M0}} \tag{1}$$

Where A_{vc} is the shear area of the column cross-section; f_{ywc} is the yield stress of the column web. Stiffness of unstiffened column web component can be obtained using:

$$k_1 = \frac{0{,}38 A_{vc}}{\beta z} \tag{2}$$

where: z is the lever arm; β is the transformation parameter (for one-side connection $\beta \approx 1$). Rotational stiffness can be obtained using:

$$S_j = \frac{E z^2}{\mu \sum_i \frac{1}{k_i}} \tag{3}$$

Where k_i is the stiffness coefficient for basic joint component i; is the stiffness ratio $S_{j,ini} / S_j$; $S_{j,ini}$ is the initial stiffness of the joint given by eq. (3) with = 1,0.

The stiffness ratio μ should be determined from the following:

$$\mu = 1 \quad \text{if} \quad M_{j,Ed} \leq 2/3 \; M_{j,Rd}: \tag{4}$$

$$\mu = (1{,}5 M_{j,Ed} / M_{j,Rd})^{\Psi} \quad \text{if} \quad 2/3 \; M_{j,Rd} < M_{j,Ed} \leq M_{j,Rd}: \tag{5}$$

where $M_{j,Rd}$is the design moment resistance of the joint; $\psi = 2{,}7$ for bolted end-plate connections. The equivalent lever arm z_{eq} should be determined from:

$$z_{eq} = \frac{\sum_r k_{eff,r} \, h_r^2}{\sum_r k_{eff,r} \, h_r} \tag{6}$$

where $k_{eff,r}$ is the effective stiffness coefficient for bolt-row r; h_r is the distance between bolt-row r and the centre of compression.

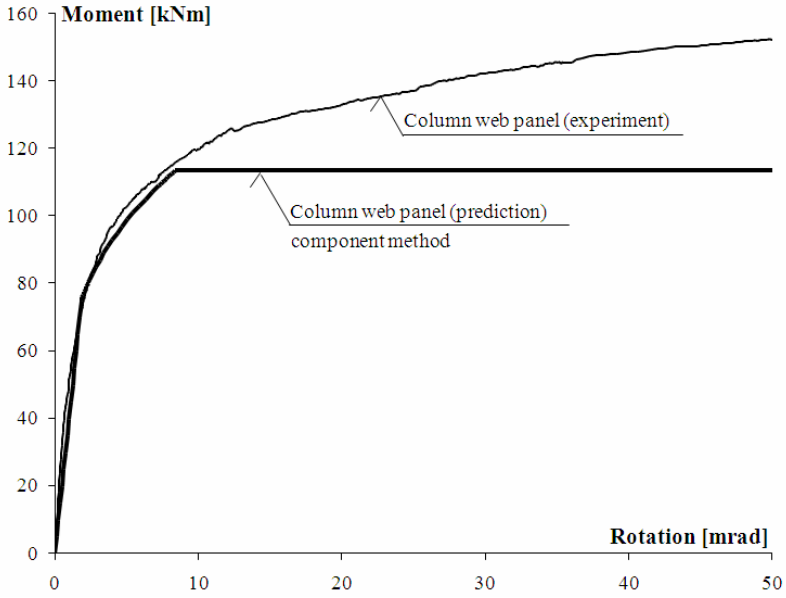

Fig. 3 - Prediction of the column web panel at ambient temperature, specimen A58.

Tab. 1 - Comparison of analytical prediction to test of column web panel at ambient temperature, specimen A58.

Moment [kNm]	Connection	Column web panel	
	Rotation [mrad] measured data	Rotation [mrad] measured data	Rotation [mrad] prediction
20	2,2	0,3	0,5
40	5,0	0,7	1,0
60	8,1	1,3	1,5
80	11,5	2,3	2,3
100	16,4	4,5	5,2
120	26,1	10,2	-
140	51,4	27,2	-
152	87,3	51,0	-

3 ELEVATED TEMPERATURES

The behaviour of the component at elevated temperature was observed on two set ups. The heating was realised in the furnace in the PAVUS laboratory in Veselí n. L. The experiments were suspended from the ceiling of the furnace to expose to heat the joints only, see Fig. 4. The fire curve was simulating by heating of gas burners. The curve measured during the seventhes fire test in Cardington, see [6], was chosen because of tests of restrained beams under the same heating. The mechanical load was introduced by weight unit thought the rope tackle. The different forces for each specimen were generated, (15 kN for specimen marked E15 and 20 kN for specimen marked E20). Two linear transducers were used for measuring deformations of joints. The rotations of joints were observed during the loading by heating only. Due to high temperature there were the deformations of the column web panel observed optically only, but the visibility was not good enough to reach an applicable results. The deformations were derived from chamfering of the whole joint, which is described below.

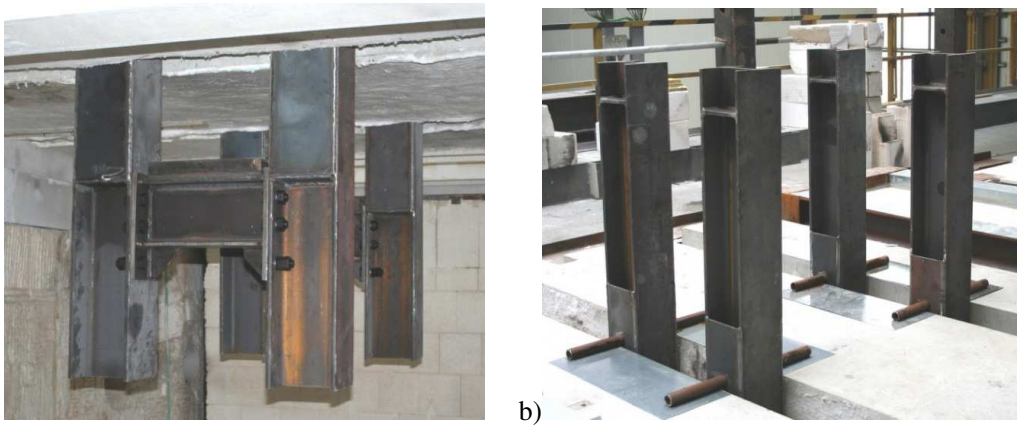

a) b)

Fig. 4 - Specimens E15 and E20 before the test, a) inside the furnace, b) outside the furnace.

During the test of the column panel zone has deform in the shear. The test of the specimen E15 is described at Fig.5. The fast grow of the joint rotation, see Fig. 5a, at 26 and 27 min of the test was observed, which comply to the temperatures 625 °C – 695 °C. This corresponds to the drop on the material reduction curve of the structural steel. The test specimens after the test are documented at Fig. 6.

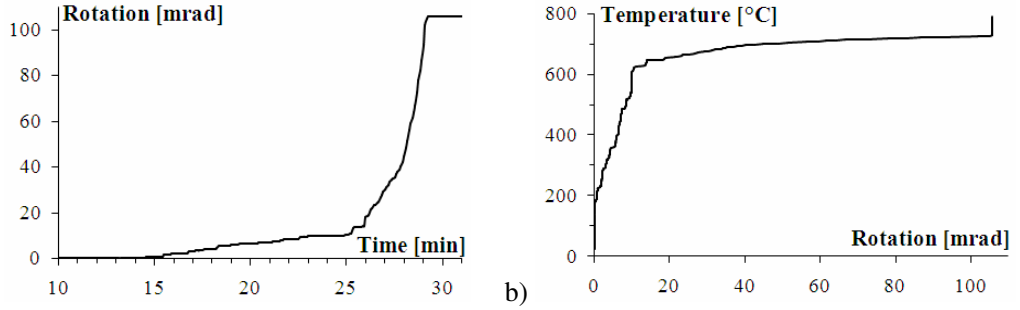

a) b)

Fig. 5 - a) Time – rotation curve, b) Rotation – temperature curve, specimen E15.

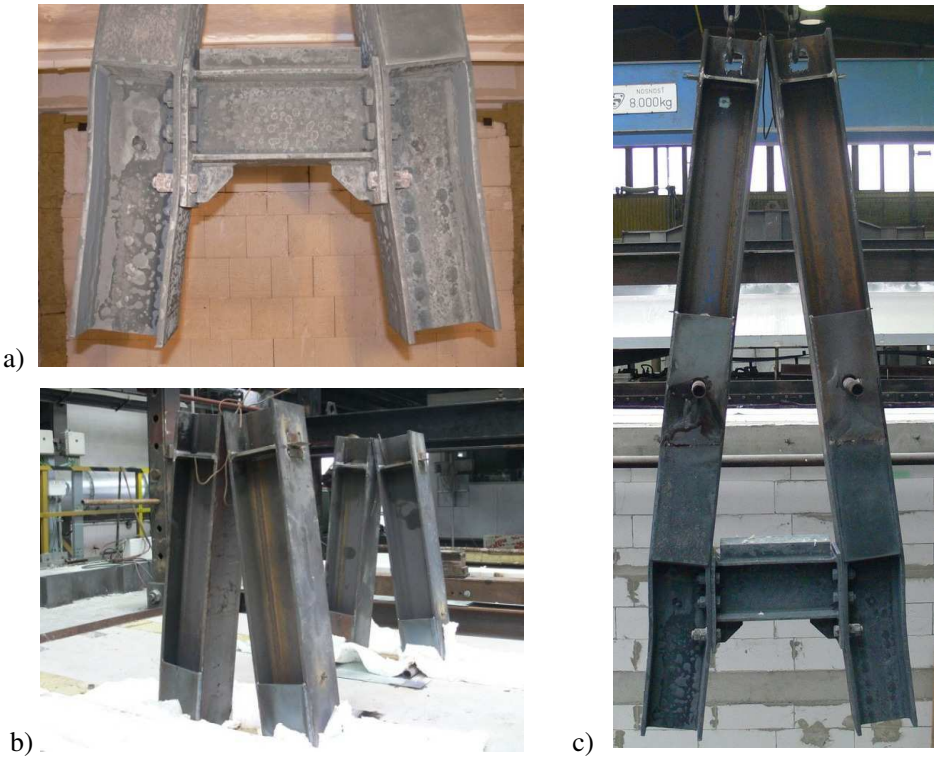

Fig. 6 - Specimens E15 after the test, a) inside the furnace, b) outside the furnace. c) specimen E15 taken out the furnace.

The moment-rotation curve M - ϕ for fire curve is shown at Fig.7. The behaviour of the component column web panel in shear is derived based on the ambient temperature behaviour. The linear dependency between the shear component and the whole joint was observed. The distribution of the deformation in joint was based on reduction factor for yield strength at elevated temperature. Functional dependence of the rotation on the bending moment at ambient temperature is:

$$f_{(\phi)} = a\,M - b \tag{7}$$

where a, b are coefficients ($a = 4*10^{-3}$, $b = 68{,}9*10^{-3}$), M is the applied bending moment. The same dependency was applied at the elevated temperature. M - ϕ curve of the column web panel at elevated temperature is derived from M - ϕ curve of the whole joint by:

$$\phi_1 = \phi_w f_{(\phi)} \tag{8}$$

where ϕ_1 is the column web panel rotation, ϕ_w is the whole joint rotation. The application of the derived function at elevated temperature is verified by the final deformation measured after the test. Total difference between the measured deformation, measured at the point, when the contact of columns were reached, and calculated final deformation is 4,6 mrad only, see Fig. 8.

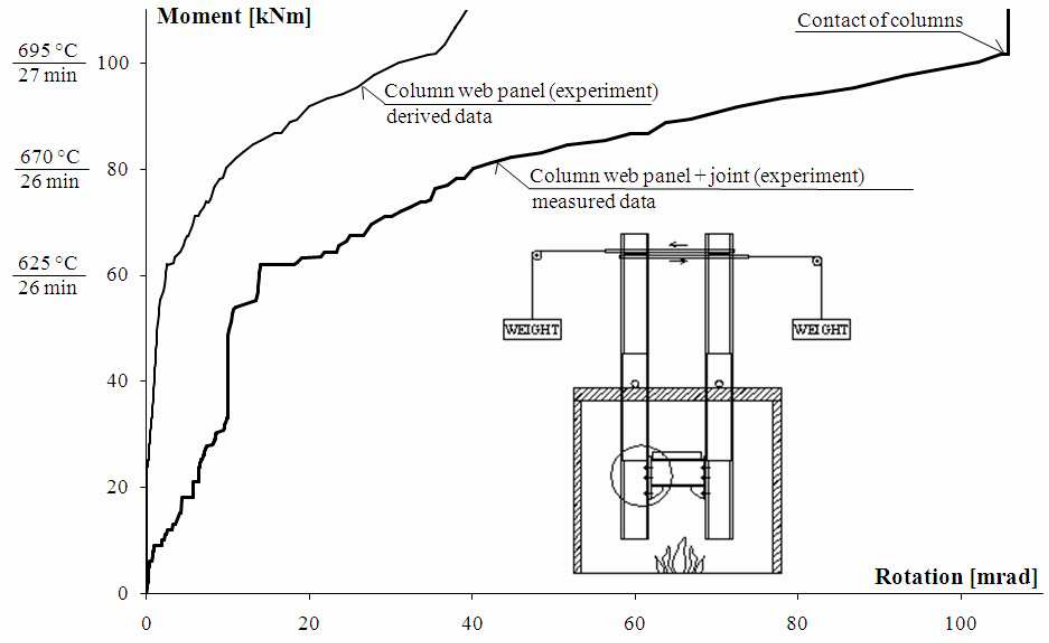

Fig. 7 - M-ϕ diagrams at elevated temperature, specimen E15

The analytical prediction model for joint described in section above was applied to elevated temperature prediction using the reduction factors for modulus of elasticity and yield strength listed in [7]. The moment-rotational diagram at Fig. 8 is calculated for the height of the shear deformation zone 350 mm. The height of the deformed panel zone was confirmed by measurements after the test. The comparison shows a reasonable prediction of the component moment rotational diagram till 600°C, see Tab. 2.

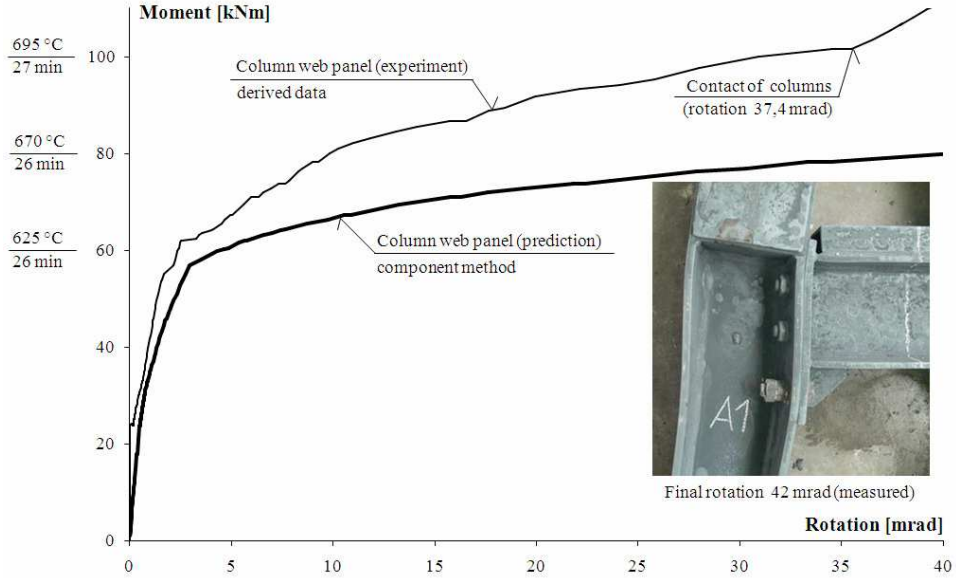

Fig. 8 - Prediction of the column web panel at elevated temperature, specimen E15.

Tab. 2 - Comparison of analytical prediction to test of column web panel at elevated temperature, specimen E15.

Time [min:sec]	Temp. [°C]	Moment [kNm]	Connection	Column web panel	
			Rotation [mrad] measured	Rotation [mrad] from measured data	Rotation [mrad] predicted
15:45	251	10	1,9	0	0,2
18:45	365	20	5,7	0,1	0,4
22:15	492	30	8,5	0,4	0,7
24:00	558	40	10,0	0,9	1,3
24:45	595	50	10,1	1,3	2,2
25:30	623	60	13,8	2,4	4,3
27:45	667	80	39,0	9,8	40,5
28:45	691	90	64,3	19,9	98,2
29:00	694	100	93,1	30,9	213,6
29:15	700	105	105,7	37,4	357,2

4 CONCLUSIONS

The analytical prediction of the component the column web panel in shear was compared to the tests at ambient and elevated temperature. The test at ambient temperature was used to select the ratio of deformation belonging to the shear panel. The ratio was confirmed by the final deformation of the joint at elevated temperature with reasonable accuracy. The good prediction of the initial stiffness and resistance of the component the column web panel in shear by the analytical model with reduction by material properties, e.g. modulus of elasticity and yield strength, was confirmed till the temperature of 600°C.

ACKNOWLEDGMENTS

This project was funded by the Czech Science Foundation, project number GAČR 103/07/1142. The technical assistance of Institute of theoretical and applied mechanics and PAVUS a.s. Veselí nad Lužnicí was much valuable and appreciated.

5 REFERENCES

[1] Jaspart J.P.: Recent advances in the field of steel joints – Column bases and further configurations for beam-to-column joints and beam splices, Universite de Liege, 1997.
[2] Buchanan A.H.: Steel and Composite Structures, John Wiley & Sons 2000, ISBN 0-471-89060-X.
[3] Burgess I.W.: Connection Modelling in Fire, Proceedings of COST C26 Workshop Urban Habitat Constructions under Catastrophic Events, Prague 2007, pp. 25-34, ISBN 978-80-01-03583-2.
[4] Simões da Silva, Santiago A., Vila Real P.: A component model for the behaviour of steel joints at elevated temperatures, Journal of Constructional Steel Research, Vol. 57 (11), 2001, pp. 1169-1195.
[5] Qian, Z.H.: Shear behaviour of steel members and beam-to-column joint under elevated temperarutes. PhD Thesis, Nanyang Technological University, Singapore, 2007, pp. 102-148.
[6] Wald F., Chladná M., Moore D., Santiago A., Lennon, T.: Temperature Distribution in a Full-scale Steel Framed Building Subject to a Natural Fire, Steel and Composite Structures, 2006, vol. 6, no. 2, pp. 159-182, ISSN 1229-9367.
[7] EN 1993-1-8: 2005. Eurocode 3: *Design of steel structures* – Part 1-2: General Rules – Design of Joints, CEN, Brussels, 2005.
[8] EN 1993-1-2: 2005. Eurocode 3: *Design of steel structures* – Part 1-2: General Rules – Structural fire design, CEN, Brussels, 2005.

CONNECTIONS DURING FIRE TESTS ON BUILDING

JIRI CHLOUBA[1], FRANTISEK WALD[2] and ZDENEK SOKOL[3]

ABSTRACT

To study global structural and thermal behaviour, a research project was conducted on a three storey steel frame building at Mittal Steel Ostrava before demolition. The main goal of the experiment was to verify the prediction method of the joint temperature and to improve it during the cooling phase. The fire compartment of floor area of 24 m^2 was build at the second floor. The fire load was 140 kg/m^2 of wood and the ventilation was delimited by an opening of 1400 x 1970 mm. This paper summarises the experimental programme and presents the time-temperature curves of the development of fire in the fire compartment and in the primary and secondary beams and its header plate connections. Comparisons are also made between the test results and the temperatures predicted by the structural Eurocodes.

1. INTRODUCTION

The tests of separate structural elements, e.g. beams, columns and joints in furnaces helped to prepare the prediction design models of elements[1]. The behaviour of the whole structure under a natural fire may be evaluated during the natural fire only. The knowledge related to the structural integrity depends on element stiffness, resistance and deformation capacity of elements and connections. The main aim of the fire test in Mittal Steel Ostrava was to learn more about the connection temperatures and the internal forces into structure. The behaviour of restrained beams during compartment fire at elevated temperatures, the heating of external element as well as column during local fire and the temperature of sandwich panels, light timber based panels and timber concrete element was studied under the heating by natural fire as well.

[1] PhD Student, CTU in Prague, Faculty of Civil Engineering, 166 29 Praha 6, Czech Republic
email: jiri.chlouba@fsv.cvut.cz.
[2] Professor, CTU in Prague, Faculty of Civil Engineering, 166 29 Praha 6, Czech Republic
email: wald@fsv.cvut.cz
[3] Assistant Professor, CTU in Prague, Faculty of Civil Engineering, 166 29 Praha 6, Czech Republic
email: sokol@fsv.cvut.cz

Simplified design of structure in fire is based on the design of structure at ambient temperature. The advanced design takes into account the structure loaded by a temperature fire curve and the joints are exposed to forces caused by the elongation during the warming and by the contraction during the cooling phase as well. In this field is the knowledge limited to a few experiments on real structures, e.g. Cardington experiment[2]. During the fire situation, the temperature development in the joint is different from the temperature development in the adjacent members. The temperature in the joint increases slower than the temperature in the attached members and during the cooling phase is the temperature higher than in the adjacent members. The highest temperature reached in the joint is lower than the highest temperature of the gas. This is caused by the mass concentration in the joint[3].

The standard for fire safety of steel structures EN 1993-1-2:2005[4] for joints recommends usage of the same fire protection for joints as for the adjacent structure. Alternatively it provides the prediction of the temperature distribution within the connection, the reduction of the material properties of connectors by elevated temperature, and the analysis of the structure using the component method[5].

2. NATURAL FIRE TEST

2.1 Fire compartment

A local fire test was performed on June 15, 2006 and a compartment fire test on June 16 on structure of Ammoniac Separator II in company Mittal Steel Ostrava[6]. The structure was composed of tree storey steel structure with the composite slabs, steel beams of hot rolled sections IPN160, IPN180 and IPN300, the beam-to-beam and beam-to-column header plate connections, and the diagonal wind bracings, see Fig. 1. Internal size of fire compartment was designed 3.80 x 5.95 m with height of 2.78 m. The structure of enclosure was made from the light silicate and ceramic bricks. Opening of 2400 x 1400 mm ventilated the room during the fire. The doors of fire compartment 1400 x 1970 mm and columns were equipped by the fire isolation by boards. The mechanical load on the floor above the fire compartment was composed of the dead and life load. The life load was simulated by about 1 m of water, which was placed into 26 steel barrels and 50 plastic boxes equally distributed on the floor. One box was stored on each barrel and the rest of boxes placed at the ends of floor. The barrels and boxes were thermo isolated from the floor by 50 mm of a miner wall and were placed on the timber pallets.

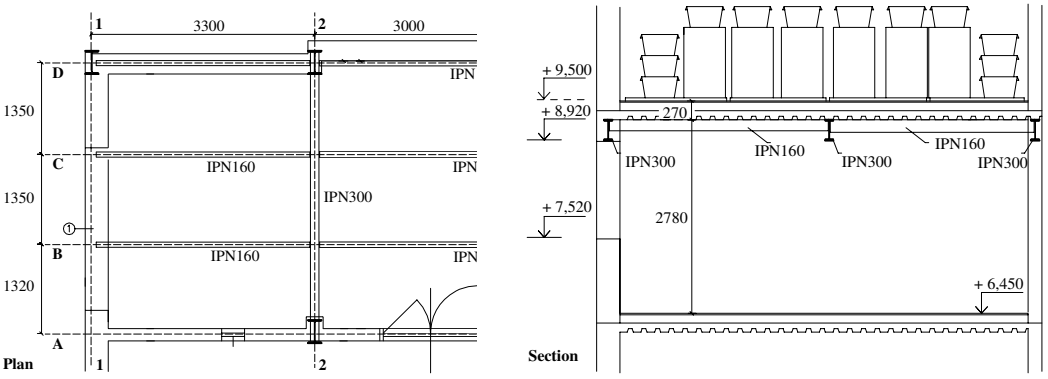

Fig. 1 - Geometry of the fire compartment.

2.2 Fire load

Fire load was represented by the unwrought timber bars 50 x 50 mm of length 1 m from softwood with moisture till 13% For the compartment fire were the bars placed into eight piles, see Fig. 2. A pile consists of 13 rows with ten bars each plus two bars on the top, which means 132 bars per pile. The simultaneous ignition of piles was reached by its connection by the steel thin walled channels filled by a mineral wall and penetrated by paraffin. The channels located onto second layer of bars connected by four piles together.

2.3 Measurements

The gas temperature in the fire compartment was measured by four thermocouples 300 mm below ceiling, marked at Fig. 3 as TGi. Two thermocouples were placed in front of the fire compartment 0.5 m and 1 m from front wall. On steel were located sixth thermocouples, and on joints next seven, in Fig. 4 marked as TCi. The position of thermocouples on the lover flange of beams at their mid span is documented on Fig. 3. Two thermo imagine cameras and seven video cameras scanned the experiment. Two video cameras were installed behind thermo resistant glass in the additionally prepared windows into the compartment internal wall.

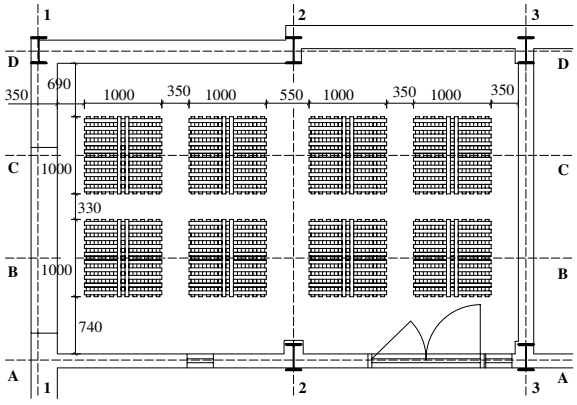

Fig. 2 - Distribution of the timber bars in the plan of the fire compartment.

2.4 Gas and beam temperatures

The comparison of the development of the gas temperatures show, see Fig. 5, that at the beginning of the fire, till 30 min about, was warmer the gas in the front part of the compartment of about 200 °C, TG3 and TG4. During the full developed fire, after 30 min, were the highest temperatures recorded in the back of the fire compartment, max 1050 °C, TG1 and TG2. In the front part was measured only 920 °C. The Fig. 6 shows that the beam lower flange temperatures correspond to the beam positions in the fire compartment. The front beam, TC16, reached maximum temperature of its lower flange of 775 °C compared to the secondary beam in the back of the fire compartment with the measured maximal 970 °C, TC2. The temperature of the beams is at Fig. 6 compared to the average temperature of the gas (TG1 + TG2 + TG3 + TG4) / 4.

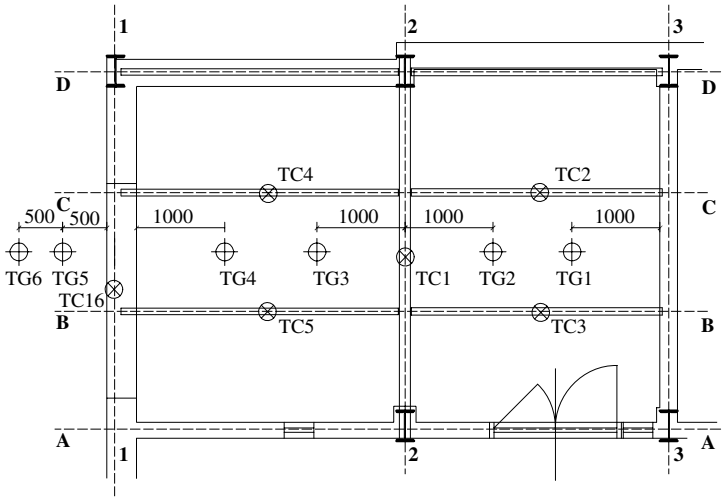

Fig. 3 - The position of the thermocouples for recording of gas and beams temperatures.

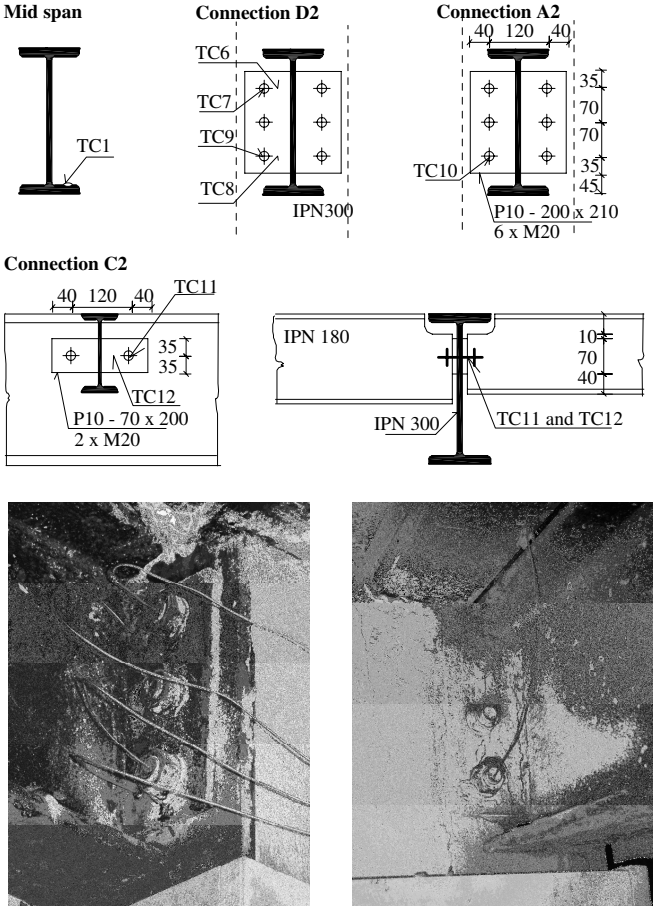

Fig. 4 - Position of the thermocouples on the header plate connection.

3. CONNECTION TEMPERATURES

3.1 Measured temperatures

Fig. 7 shows the gas, beam in the mid span and connection temperatures measured during the experiment. On Fig. 8 are demonstrated the temperature differences inside the connection.

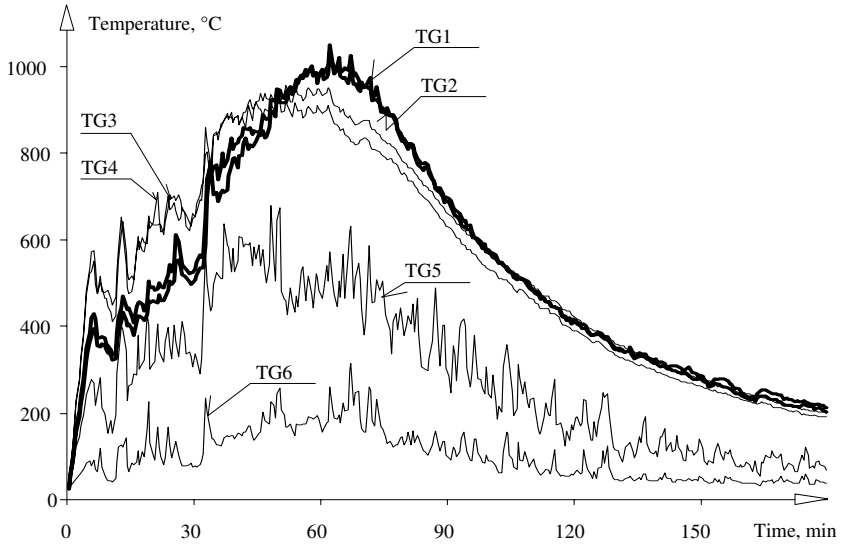

Fig. 5 - Measured gas temperatures.

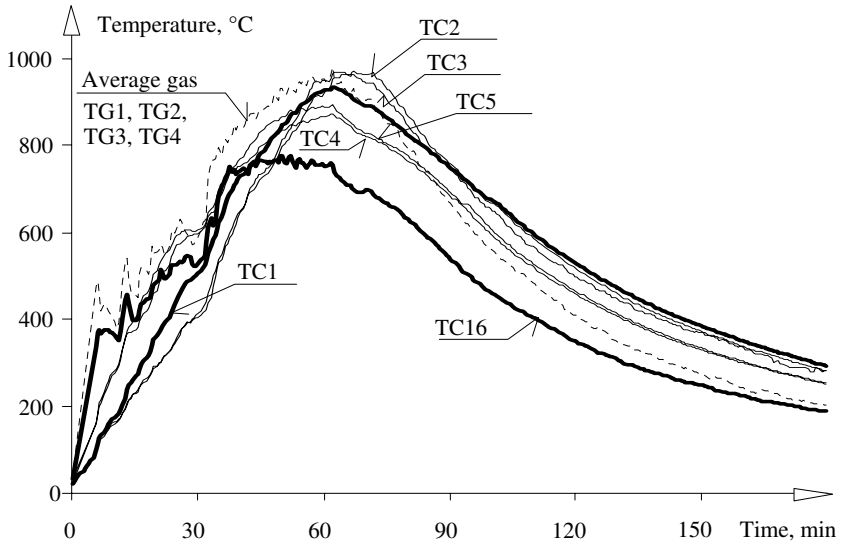

Fig. 6 - Measured temperatures on the top of the beam lower flanges at mid span.

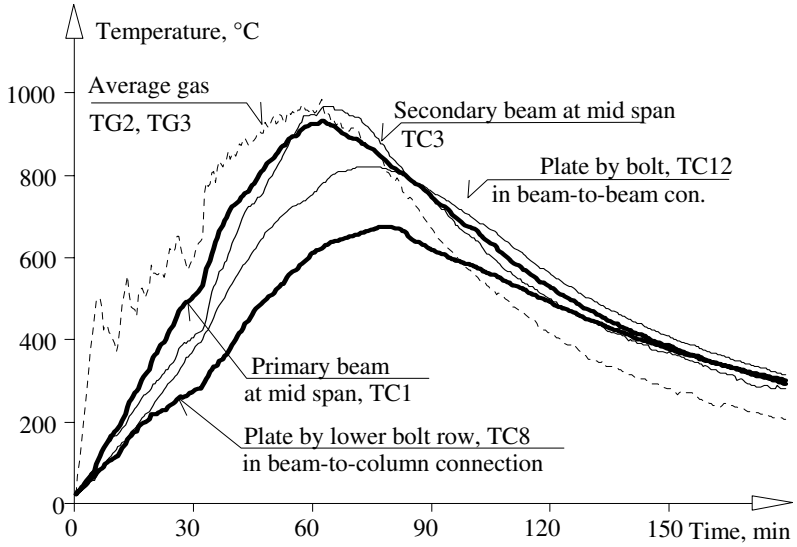

Fig. 7 - Comparison of the measured temperatures on the header plate connection to the gas and beam mid span temperatures.

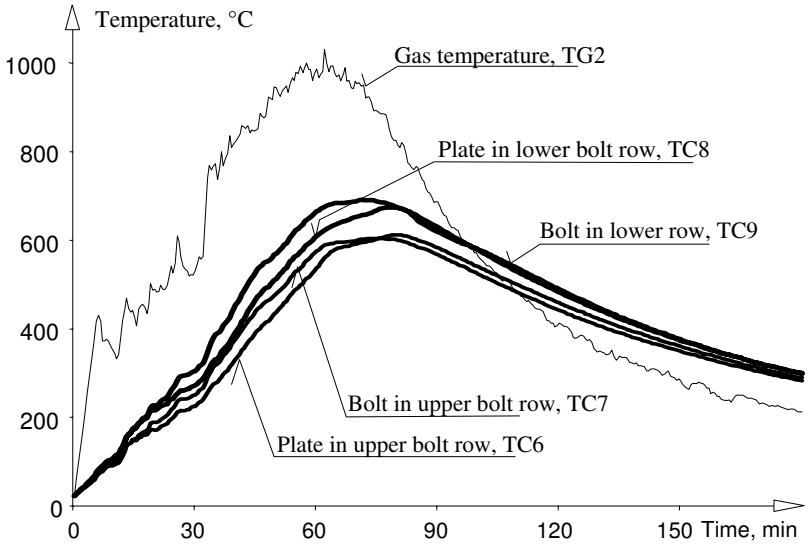

Fig. 8 - Measured temperatures over the height of beam-to-column header plate connection.

3.2 Temperature prediction

For the temperature development in the connection, there are predicted two analytical methods[4]. In the step by step method is the temperature calculated as element, where the heat is brought in/brought out by the member surface and the member volume is heated/cooled. Geometrical characteristic of the section is the section factor A_m/V of the steel parts of which the joint is composed. The section factor indicates the relation between the surface area of the connection A_m per unit of length exposed to the fire and the volume of the connection V per unit length which is being heated. The temperature of the unprotected inner steel structure is given by

$$\Delta\theta_{a,t} = k_{sh}\frac{A_m/V}{c_a\rho_a}h_{net}\Delta t \tag{1}$$

where A_m/V is the section factor in m^{-1}, c_a the specific heat depending on the temperature in J $kg^{-1}K^{-1}$, ρ_a the volume weight of steel in kg m^{-3}, h_{net} the design value of the net heat flux per unit area in W m^{-2}, Δt the time increment in s, and k_{sh} the correction factor for the shadow effect which is used by the heating using the nominal fire curve. The temperature of a joint may be assessed using the local section factor A_m/V, the value of the parts forming the joint. As simplification, it is possible to consider uniform temperature distribution within the section and to take into account the biggest A_m/V value of the steel parts connected into the joint.

The temperature of either beam-to-beam or beam-to-column connection covered with a concrete slab can be determined from the temperature of the beam flange in the middle of the span. It is assumed, that the temperature of the particular parts of the connection depends directly only on the distance from the lower edge of the connected beam and indirectly on the prediction of the temperature of the lower flange calculated usually by the step by step procedure. If the height of the beam is smaller or equal to 400 mm ($h_k \leq$ 400 mm), the temperature is given by

$$\theta_h = 0{,}88\,\theta_0\,[1 - 0{,}3\,(h_k / h)] \tag{2}$$

where θ_h is the temperature in the height h_k of the beam, θ_0 is the lower flange temperature in the mid span and h is the overall beam height.

3.3 Beam-to-column connection

Fig. 9 shows the comparison of the predicted gas temperature in the fire compartment by parametric fire curve[6] according to EN 1993-1-2.2005 Annex A[4] and of the predicted primary beam temperature to the measured values.

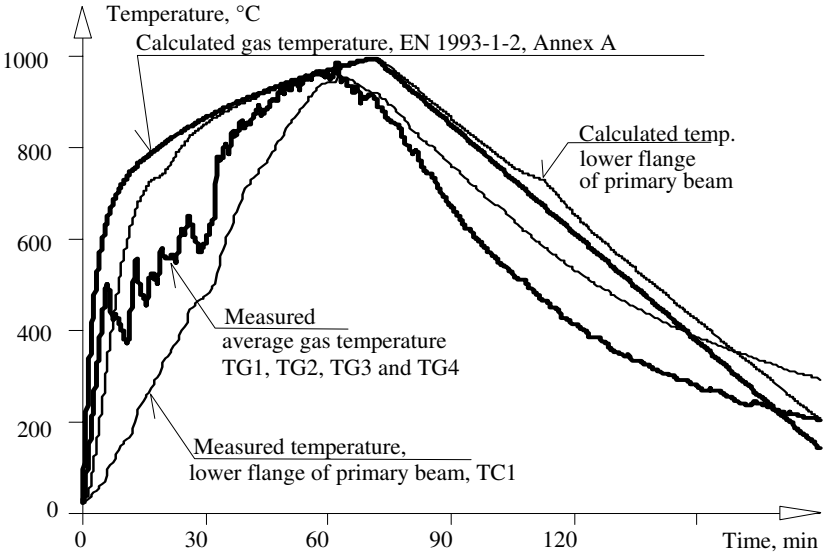

Fig. 9 - Comparison of the predicted temperature with the measured temperatures.

The temperature of the beam-to-column connection was calculated from the measured temperature of the beam's lower flange in the mid span, see Fig. 10 according to eq. (2). The highest temperature is conservative but in the cooling phase is the predicted temperature lower than the actually measured. By applying the section factor, the highest value of section factors of the connected members may be taken into account, e.g. $A_m/V = 138$ m^{-1}, and the results are conservative for the maximum temperature. If the section factor of the head plate is considered, e.g. $A_m/V = 105$ m^{-1} only, the results are less conservative. The difference between these two considerations is 20°C. On Fig. 11 there is a comparison of the predicted and the measured temperatures calculated from the temperatures predicted by the parametric fire curve.

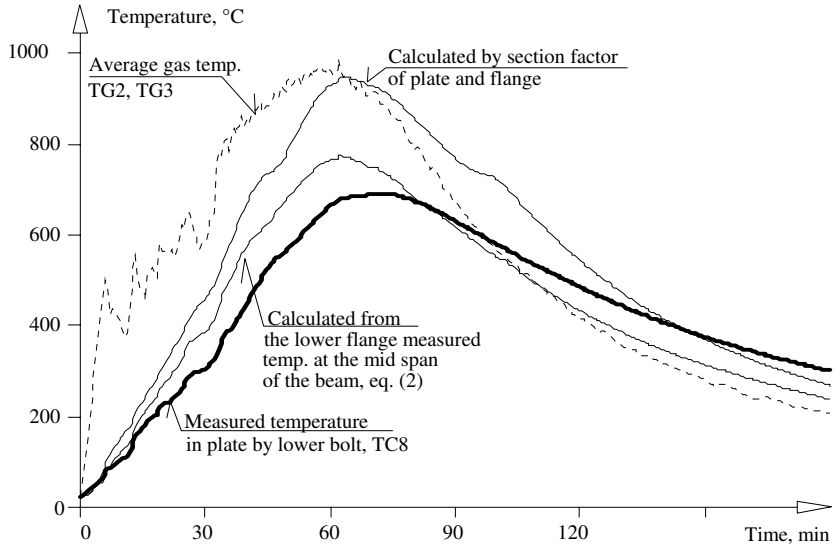

Fig. 10 - Comparison of the predicted temperatures from gas temperature to measured temperatures at the beam to column connection.

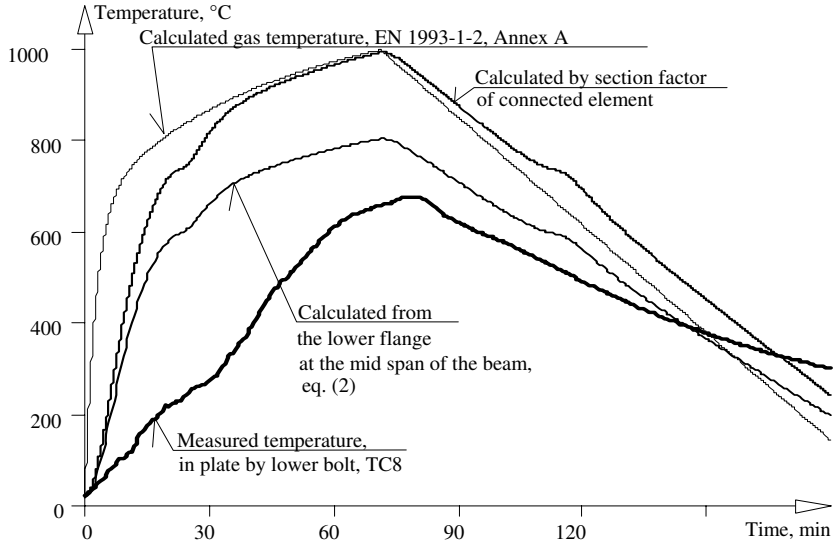

Fig. 11 - Comparison of the predicted temperature by the parametric fire curve to the measured temperatures at the beam to column connection.

3.4 Beam-to-beam connection

Fig. 12 shows the comparison of the prediction of the temperature in the beam-to-beam connection, which was calculated by section factor of the connected beam from the measured gas temperature. The prediction is rather conservative during the heating phase and in the maximal temperature. The prediction based on the measured temperature of the beam's lower flange in the mid span gives lower temperature compared to the measured one. The reduction 1.0 instead of 0.88 in eq. (2) gives closer prediction of the maximal temperature.

$$\theta_h = 1{,}0\,\theta_0\,[1 - 0{,}3\,(h_k / h)] \tag{3}$$

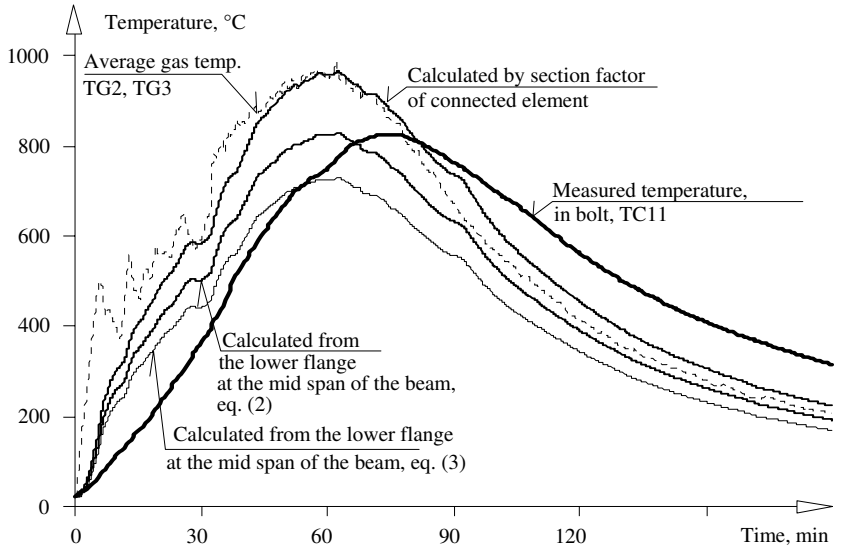

Fig. 12 - Comparison of the predicted temperatures from gas temperature with measured one at the beam-to-beam connection.

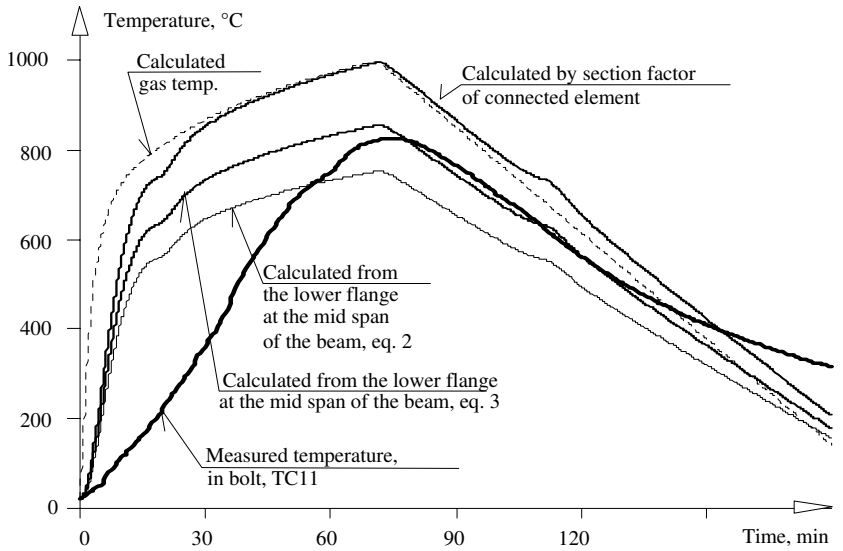

Fig. 13 - Comparison of the predicted temperature by the parametric fire curve with the measured one at beam-to-beam connection.

The comparison of the predicted and the measured temperatures calculated from the temperatures predicted by the parametric fire curve is shown at Fig. 13. The application of the reduction factor 1.0 is in this case conservative, and factor 0.98 gives the closer solution.

3.5 Connection resistance

At elevated temperature the material properties reduced. The reduction may be introduced by factor expressing the ratio between the property under elevated temperature to property at ambient temperature, see Tables 3.1 and D1 in EN 1993-1-2:2005[4].

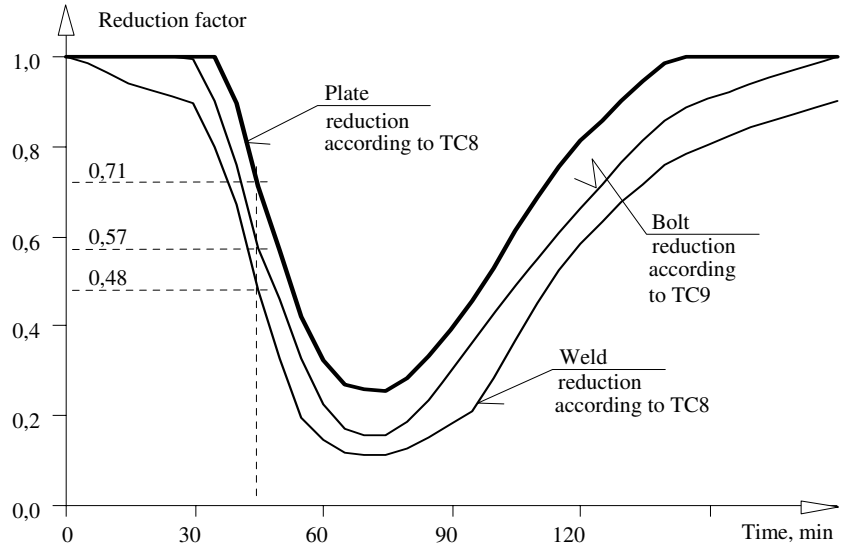

Fig. 14 - Reduction of the resistance of components in connection A2 according to the measured temperatures.

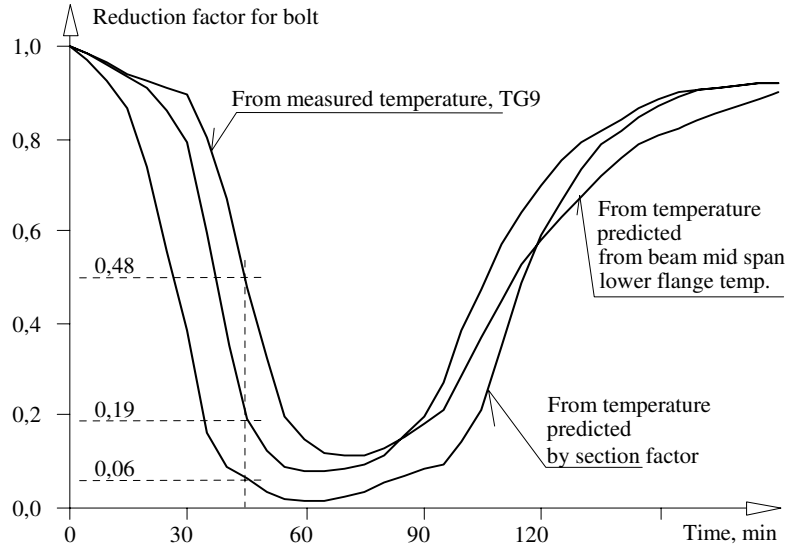

Fig. 15 - Reduction of the resistance of bolts in the lower row of the connection A2 according to the different models compared to the reduction obtained from the measured temperature.

On Fig. 14 is shown the reduction of the plate in connection A2 close to lower bolt row according to thermocouple TC9, of the plate according to thermocouple TC8, and of the weld according to thermocouple TC8. E.g. in 45 min the resistance decrease based on the measured values in plate to 71 %, in the welds to 57 % and in the bolts to 48 %. The sensitivity of the prediction may be expressed by the reduction of the resistance of bolts, see Fig. 15. The bolt resistance decrease in 45 min of fire to 19 % in case of prediction by lower flange temperature and to 6 % by prediction from section factor of connected beam, but the reduction to 48 % only was evaluated based on the measured temperature.

4. CONCLUSION

On the June 15, 2006 a full-scale fire test was carried out at the Ammoniac Separator II in company Mittal Steel Ostrava. One of the main aims of this fire test was to collect data on the distribution of temperatures within the connections. In this paper a comparison is also made with the analytical methods given in EN 1993-1-2: 2005[4] for calculating the temperature and temperature distributions in the structural steel members. From these comparisons it can be concluded that:

The methods for calculating the compartment temperature in EN 1991-1-2: 2003[7] Annex A for parametric fire curve agreed well with the measured data. The incremental analytical models allow presuming temperatures of the unprotected beams with a good accuracy.

Calculating the temperature of the beam-to-column connection from the measured gas temperature in the fire compartment based on the mass of the connection parts is too conservative during the heating phase, see Fig. 10 and Fig. 11. A calculation based on the bottom flange temperature of the supported beam is less conservative.

The prediction of the temperature of the beam-to-beam connections using the measured gas temperature in the fire compartment, based on the mass of the connection parts, during the heating phase is conservative, see Fig. 12 and Fig. 13. The calculation based on the bottom flange temperature of the supported beam may be improved by factor 1.0 instead of 0.88, see eq. 3.

The relatively high sensitivity of the temperature prediction was shown on the reduction of the resistance of bolts for different temperature prediction models, which was compared to the measured values. The next generation of analytical prediction models brings more economical design into highest temperatures and closer prediction into the cooling phase of the fire.

ACKNOWLEDGEMENT

The work was prepared with support of Czech Grant Agency GAČR 103/07/1142.

The paper describes contributions of the Czech partner to the Action Cost C26 Urban Habitat Constructions under Catastrophic Events, which is focused into the connection behaviour prediction and the structural integrity under fire conditions.

REFERENCES

[1] Buchanan A. H.: Structural design for fire safety, John Wiley & Sons 2003, ISBN 0-471-89060-X.

[2] Moore D.B. & Lennon T.: Fire engineering design of steel structures, Progress in Structural Engineering and Materials, 1 (1), 1997, pp. 4-9.

[3] Wald, F., es da Silva, L., Moore, D.B., Lennon, T., , M., Santiago, A., Beneš, M. & Borges, L.: Experimental behaviour of a steel structure under natural fire, Fire Safety Journal ,Volume 41, Issue 7, October 2006, pp. 509-522.

[4] EN 1993-1-2: 2005. Eurocode 3: Design of steel structures – Part 1-2: General Rules – Structural fire design, CEN, Brussels.

[5] Spyrou S., Davison B., Burgess I. & Plank R.: Component-based studies on the behaviour of steel joints at elevated temperatures, in Proceedings of Eurosteel 2002 – 3rd European Conference on Steel Structures, edited by Lamas A., Simões da Silva L., pp. 1469-1478, Coimbra, ISBN 972-98376-3-5.

[6] Kallerová P. & Wald F.: Ostrava fire test, Czech Technical University, Praha, CIDEAS report No. 3-2-2-4/2, p.18.

[7] EN 1991-1-2: 2002. Eurocode 1: Basis of design and actions on structures – Part 2-2: Actions on structures – Actions on structures exposed to fire, CEN, Brussels.

EFFECT OF JOINT TYPOLOGIES ON THE 3D BEHAVIOUR OF A STEEL FRAME UNDER A NATURAL FIRE

ALDINA SANTIAGO[1], LUÍS SIMÕES DA SILVA[2] and PAULO VILA REAL[3]

ABSTRACT

In order to address the complex loading condition of steel joints in fire, and based on the experimental fire tests on steel frames with different joint typologies, performed at the University of Coimbra [1], a detailed three-dimensional model was developed and calibrated to simulate the behaviour of welded and bolted end plate beam-to-column joints. The structural frame is modeled combining 3D shell, solid and joint elements, thereby taking into account the effect of the local failure modes, and the realistic behaviour of the frame exposed to a natural fire. The numerical model accounts for the initial geometrical imperfections, non-linear temperature gradient, geometrical and material nonlinearity and temperature dependent material properties. The results show the performance of each individual structural joint component under heating and cooling conditions and identify the main dependencies of the geometrical and mechanical variables of the components on the joint behaviour. The global behaviour of the frame and the joint failure modes are compared and discussed with the experimental observations.

1. INTRODUCTION

The first developments on the characterization of the steel joints under fire condition were performed at 90's and were mainly based on experimental tests. The results allowed the development of analytical and numerical procedures for the derivation of the moment-rotation relationship of isolated joints at high temperatures, based on the properties at room temperature [2]. However, under fire conditions, large variable axial forces are induced in the

[1] Research Assistant, ISISE - Department of Civil Engineering, U. Coimbra 3030-290 Coimbra, Portugal
email: aldina@dec.uc.pt.
[2] Professor, ISISE - Department of Civil Engineering, U. Coimbra, 3030-290 Coimbra, Portugal
email: luisss@dec.uc.pt.
[3] Professor, LABEST – Department of Civil Engineering, U. Aveiro, 3810-193 Aveiro, Portugal
email: pvreal@civil.ua.pt.

connection and it is no longer predominantly subjected to bending action. The axial force is initially compressive due to the restraint to thermal expansion; at high temperatures, it becomes tensile as catenary action develops when the beams lose their resistance; during the cooling phase the beams contract and stiffens simultaneously, and the tensile forces increase. As a result, research developments follow nowadays several complementary lines: i) characterization of each individual joint component at high temperatures, performing experimental tests that are used to calibrate analytical models [3]; ii) study of the effect of the joint properties on the global behaviour of the structure [4]; and iii) detailed modelling of joints under fire. The first developments on joint modelling in fire were performed by El-Houssieny, who developed a 3D model to simulate the response of extended end plates at room and elevated temperatures [5]. Subsequently, several other authors reported numerical modelling of steel joints under fire; almost all of them were focused on the heating phase of the fire and the cooling effect was neglected. However, observation of real fires and experimental full-scale tests show that one of the main failure modes of bolted end-plate joints is the failure of the brittle components during the cooling phase. This effect is explored in this paper using advanced numerical models, calibrated with experimental tests carried out by the authors [1].

2. MODEL DESCRIPTION

2.1 Structural model

In order to explore the behaviour of a sub-frame steel system under fire loading and study the influence of several beam-to-column joint typologies, the structure of Fig. 1 was chosen. It consists of two thermally insulated HEA300 cross-section columns and an unprotected IPE300 cross-section beam with 5.7 *m* free span, supporting a steel-concrete composite slab.

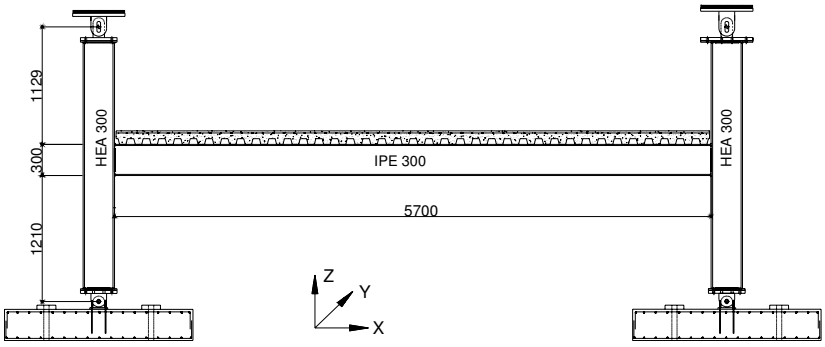

Fig. 1 - Structural model (mm).

The corresponding non-dimensional axial and rotational restraint ratios are given by: $\beta_a = K_{a,c}/K_{a,b} = 0.267$ and $\beta_r = K_{r,c}/K_{r,b} = 7.460$, where $K_{a,b}$ and $K_{r,b}$ are the axial and rotational stiffnesses of the beam and $K_{a,c}$ and $K_{r,c}$ are the axial and rotational stiffnesses of the columns at the beam level, see [6]. The beam was assumed exposed to the fire load, while the columns were unexposed. This structural model corresponds to an experimental fire test program carried out at the University of Coimbra in Portugal, [1]. The parametric numerical study is focused on the joint configurations that were tested (Table 1).

Table 1. Beam-to-column joint configuration.

Test ID	Joint typology	End-plate dimensions (mm) and steel grade	Bolts / Weld
FJ01	Flush end-plate	(320×200×10); S275	2 bolt row M20, 8.8
FJ02		(320×200×16); S275	2 bolt row M20, 10.9
FJ03		(320×200×16); S275	2 bolt row M20, 8.8
EJ01	Extended end-plate	(385×200×16); S275	3 bolt row M20, 8.8
WJ01	Welded joint	----------	$a_f = a_w = 10$ mm

a_f, a_w, are the weld throat thickness

2.2 Numerical modelling

2.2.1 Specimen discretization and bolt modelling

The numerical simulations were carried out using the FE program LUSAS [ref]. In order to reduce the model size and subsequent processing time, symmetry conditions were imposed at the beam mid-span (Fig. 2). The beam, column and plates were modelled with QTS4 shell elements (family of thick shell elements based on the degeneration of a three-dimensional continuum). In the bolted models, the bolts were represented by solid elements (HX8M), the contact was modelled by spring elements (JNT4), but the welds connecting the beam to the end-plate were not reproduced. The bolt is composed by head, nut and shank. Each part constitutes a source of flexibility that should be taken into account in the bolt modelling. Due to the time dispended on the numerical calculation, an optimal mesh discretization was used (Fig. 2a): the bolts were modelled with an equivalent rectangular section, whereby the shank is assigned an area equal to the tensile area of the bolt; in the same way, the head and nut have an area and thickness similar to the real values. The holes were modelled as rectangular cut-outs in the end-plate and in the column flange. The concrete slab was not modelled, although its weight was naturally considered as a uniformly distributed load.

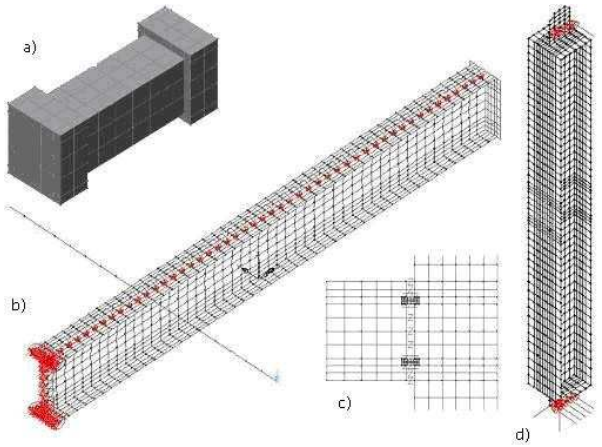

Fig. 2 - Finite element model of a flush end-plate bolted beam-to column sub-structure: a) bolt; b) beam and end-plate; c) detail of joint; d) column and plates at the columns ends.

The contact simulated in these models corresponded to the following interfaces: end-plate – column flange, head of the bolt – end-plate and column flange – nut of the bolt. Concerning the spring element stiffness used to simulate this contact, an individual

calibration study for each bolted sub-structure was performed (Table 2); k_{1c} and k_{1t} are the normal stiffnesses (compression and tension, respectively) and k_2 and k_3 are the tangential stiffnesses. In order to simplify the model, the friction coefficient was not implemented.

In the beam, lateral geometrical imperfections were considered while residual stresses were neglected. A lateral geometrical imperfection given by $y(x) = L/1000\,sin(\pi x/L)$ was applied. The maximum constructional imperfections on the cross-section allowed by EN 1090-2 [7] were also applied: an initial rotation around the x axis with a maximum value of $L/1000$ at mid-span and a curvature on the beam web with a maximum value of 4 mm at the mid-web. These local imperfections on the beam cross-section were implemented following the observation of the main failure modes in the beam during the experimental tests [1].

Table 2. Stiffness coefficients.

	k_{1c} (N/m/m^2)	k_{1t} (N/m/m^2)	$k_2 = k_3$ (N/m/m^2)
FJ01 Test	1.0E12	0	1.0E9
FJ02 Test	5.0E11	0	5.0E8
FJ03 Test	5.0E11	0	5.0E8
EJ01 Test	1.0E15	0	1.0E12

2.2.2 Modelling of the material

The stress-strain curves used to characterize the steel and the bolts in these numerical models were the following:

i) Beams and columns - Four material laws were considered: web of the beams, flanges of the beams, web of the columns and flanges of the columns. In each case, the stress-strain curves were based on the averaged values obtained from tensile tests [6].
ii) Bolts – Two material laws were considered: bolt 8.8 and bolt 10.9. The stress-strain curves at room temperature were based on the averaged values obtained from tensile tests at room temperature [6]. Because no tensile tests were performed at elevated temperature, the corresponding curves were obtained using the reduction factors for bolts [8] applied to those mechanical properties at room temperature.
iii) Plates – Since no tensile tests were performed, the stress-strain laws suggested by EC3 [8] for S275 were used at room and elevated temperatures.

Although the tensile tests performed on the steel after cooling showed an 8% reduction on the yield stress after being subjected to high temperatures [6], this effect was not included in the models. It was assumed that the steel and the bolts regain full strength when cooled down to room temperature. Additionally, experimental stress-strain curves were transformed into true stress-logarithmic strain law and introduced in the FE LUSAS.

2.2.3 Boundary and loading conditions

As mentioned before, only one half of the structure was modelled. This implied that at the beam mid-span, the axial displacement in the X direction was restrained as well the rotational displacement in the Y and Z directions. In order to reflect the experimental set-up, the semicircular plates at the ends of the column restrained the displacement in the X direction and allowed free axial movement at the top of the columns, and behaved as hinges at the bottom of the columns were also modelled. The lateral movement of the beam was prevented.

The mechanical loading applied at room temperature corresponded to a self-weight of 16 kN/m^2 distributed along the top flange of the beam, and the concentrated loads equal to

10 kN at 700 mm from the mid-span cross-section, exactly mimicking the experimental set-up. The thermal loading corresponded to the temperature curves measured for each fire test; as an example, Fig. 3 reproduces the temperature curves applied to the FJ03 model.

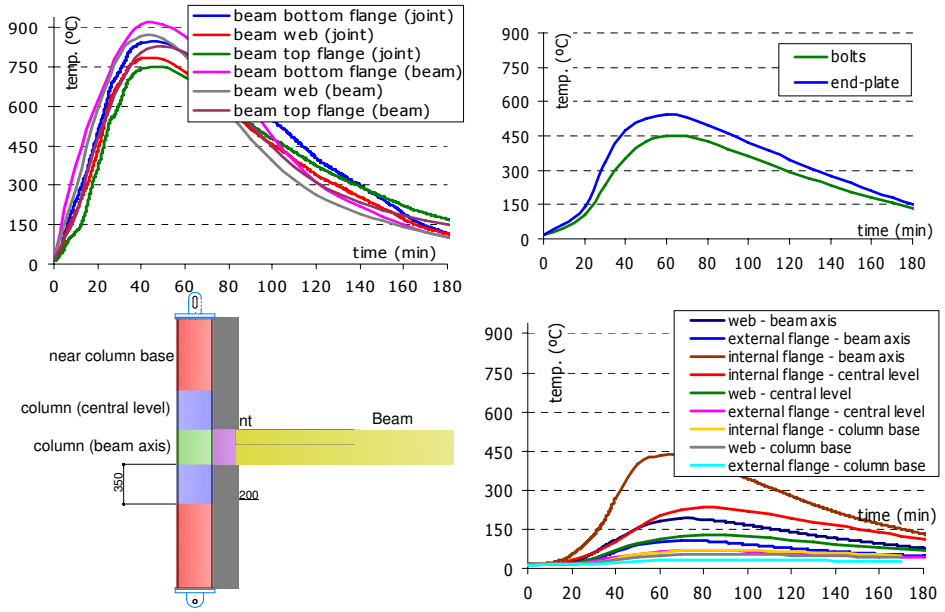

Fig. 3 - Temperature applied to the FJ03 model.

2.3 Failure assessment

In order to assess the occurrence of joint failure throughout the fire event, failure criteria are required. Failure conditions assume that cracking occurs when the ultimate strain ε_u is attained. The steel cracking should be assessed by comparing the equivalent strain ε_E with $\varepsilon_{u,s}$, where $\varepsilon_{u,s}$ is the ultimate strain of steel; for the bolts, the following failure criteria was adopted: $\varepsilon_{11,av} = \varepsilon_{u,b}$, where $\varepsilon_{11,av}$ is the maximum average principal strains and $\varepsilon_{u,b}$ is the ultimate strain of the bolts. The ultimate strains, adopted according to the literature, are reproduced in Table 3. Because the strains ($\varepsilon_{u,s}$) defined in these failure criteria were based on tensile tests [6], and one of the most common failure mode in a fire situation is the beam bottom flange in compression, the equivalent strains obtained from the finite element results (QSI4 elements) should be measured on the tensile surface ($\varepsilon_{E,t}$). It is noted that shell elements provide strains and stresses across the elements thickness: bottom, middle and top surface.

Table 3. Ultimate strains.

		Literature	Assumed in this study
Room temperature	Steel	25-30% [10] 15% [9]	End-plate: 15% [9] Beam and columns: 30% [6]
	Bolts	5-6% [10]	3.5% [6]
High temperatures	Steel	20% [8]	End-plate: 20% [8]] Beam and columns: temperature dependent as shown in [6]
	Bolts	1-6% [11]	3.5%

3. CALIBRATION AT ROOM TEMPERATURE

Even though room temperature tests of the steel sub-frames were not performed, numerical modelling of the joints was carried out to ensure adequate modelling of the bolts and the contact problem for subsequent use in the elevated temperature models. Consequently, these room temperature models correspond to a cantilever beam under an incremental displacement applied downward at the free end of the beam section. Fig. 4 compares the bilinear curve prescribed by EN 1993-1-8 [12] with the numerical moment-rotation response. Concerning the initial stiffness, good agreement was attained. First yielding ($\varepsilon_{E,t} = \varepsilon_y = 0.002$ [9]) and the failure component are also identified numerically in the simulations. The first yielding confirms the critical component obtained by EN 1993-1-8: column web in compression. For almost all bolted end-plate joints, bolt failure was reached before steel cracking.

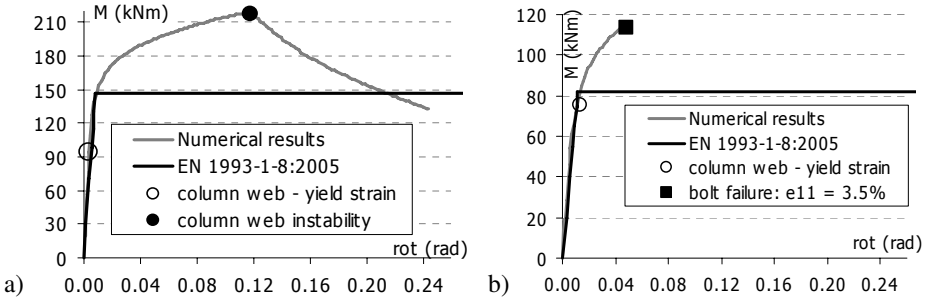

Fig. 4 - Moment-rotation response of a) WJ01 joint, and b) FJ03 joint.

4. NUMERICAL RESPONSE OF A WELDED SUB-FRAME UNDER FIRE

The FE models were calibrated with the experimental data of the tested structures [6]: geometry, temperature evolution; mechanical loading and steel and bolt materials. The numerical results were compared with the experimental ones in terms of mid-span deflection, axial displacement, axial force and failure modes of the joint. Based on the numerical model additional results were obtained: joint bending moment and individual behaviour of each critical connection elements. In the following, the numerical behaviour of each structure during the natural fire will be described and discussed.

Fig. 5 compares the experimental and the predicted failure modes for the WJ01. The deformed configuration was accurately predicted by the FE model: local buckling on the bottom flange and web.

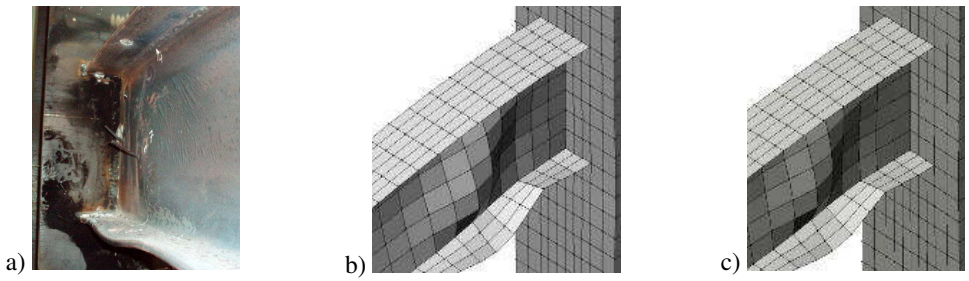

Fig. 5 - Failure mode of the WJ01: a) experimental test (end of the fire); b) FE analysis (t = 55 min); c) FE analysis (t = 170 min – end of the fire); (scale factor: x1).

Comparison of the axial force and displacement responses of the joint under the fire is shown in Fig. 6. The axial force was calculated by integration of the normal stresses at the cross-section B (in the beam, 0.03 m away from the column flange) and the experimental curve of the axial force corresponds to the Yin and Wang expression [13] using the experimental axial displacement (ΔL_m):

$$F_T = K_A' \Delta L_m = \frac{1}{\frac{1}{K_A} + \frac{L}{E_T A} + \frac{1}{K_A}} \Delta L_m \quad (1)$$

where K_A is the axial stiffness of the restraint at the beam ends, E is the Young's modulus of the beam and A and L are the cross-section and the length of the beam, respectively. It can be seen that both curves show good agreement. Special reference should be made to the large tensile forces developed during the cooling phase.

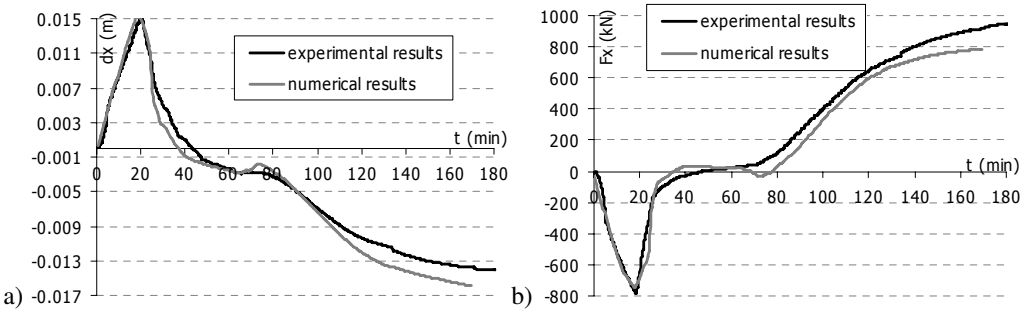

Fig. 6 - FE and experimental results for WJ01: a) axial displacement and b) axial force.

Fig. 7 shows the variation of the bending moment in the joint during the fire. The bending moment was calculated with respect to the centroid of cross-section B. During the first stage of the heating phase, due to the differential thermal expansion across the beam and the reduction of the Young modulus, the hogging moment increases; when the bottom flange reaches about 500ºC, its resistance decreases and the hogging moment also decreases; at high temperatures, the bending moment is minimal along the beam span and the beam resists due to catenary effect (Fig. 6b). During the cooling phase, a reversal of the bending moment is observed and large sagging moments are developed, since the Young modulus and the yield stress recover to the room temperature values and the temperature decreases faster on the bottom flange than on the top. The sequence of the yielding of the components is also identified in this curve; the normative value of $\varepsilon_y = 0.02$ was assumed [8]; consequently, the symbols on the M_y-t curve identify $\varepsilon_{E,t} = \varepsilon_y$. Additionally, the failure of the bottom flange was also identified; it occurred at t = 50 min., for a temperature of 600ºC ($\varepsilon_u = 0.16$ and $\varepsilon_{E,t} = 0.17$).

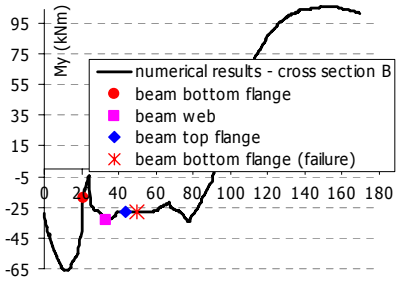

Fig. 7 - Bending moment response in joint (cross-section B).

5. NUMERICAL RESPONSE OF A BOLTED SUB-FRAME UNDER FIRE

5.1 Bolt failure during cooling

As referred in the introduction, one of the main purposes of this work was to prove that brittle joint failure could happen during the cooling phase. Fig. 8 compares the actual and the predicted failure modes for the FJ03 joint. It is observed that local buckling in the bottom flange and bending deformation at the top of the end-plate develops during the heating phase. During the cooling phase, only deformation of the bottom of the end-plate and axial deformation in the bottom bolt-row are noticeable.

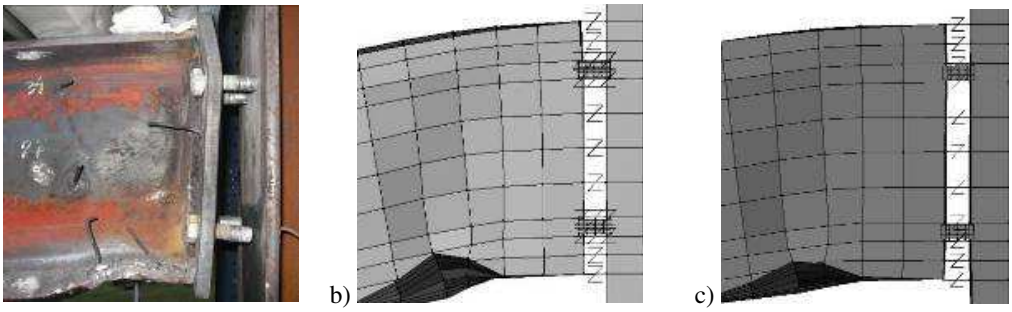

Fig. 8 - Failure mode of the FJ03: a) experimental test (end of the fire); b) FE analysis (t = 55 min); c) FE analysis (t = 167 min); (scale factor: x1).

Fig. 9 compares the evolution of the averaged principal strains ($\varepsilon_{1,1}$) for two bolts, one located at the level of the first row (bolt 1,1) and another in the second row (bolt 2,2); the principal strain contour in bolt 2,2 is also depicted. The bolt strains during the first stage of the heating phase are very low; when the temperature starts to increase, large deflections develop in the beam and the axial tensile strains increase near the joint, especially in the upper zone. During the cooling phase, due to the large tensile forces and the sagging moment, the tensile strains of the 2nd bolt-row increase. According to the failure criteria defined in §2.3, the bolt located on the 2nd row fails during the cooling phase (t = 167 min.). This matches the experimental evidence (bolt failure at t = 190 min.)

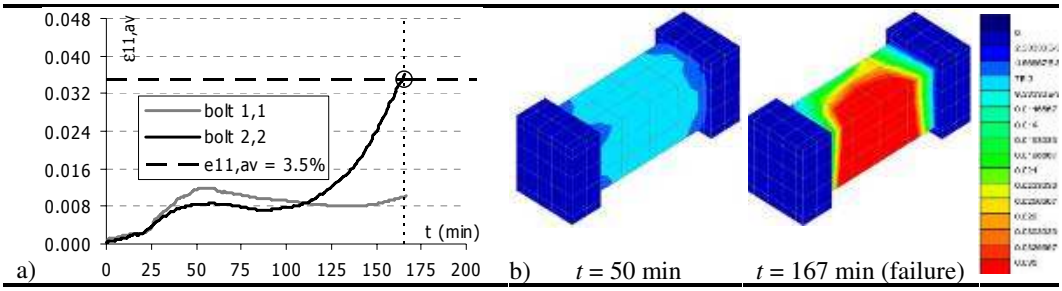

Fig. 9 - a) Averaged principal strains in the bolts; b) Principal strains contour in bolt 2,2.

5.2 Effect of the bolt grade

In this item the effect of the bolt class on the joint behaviour under fire is demonstrated. Since the difference between FJ02 and FJ03 joint is the bolt class.only (grade 10.9 vs. 8.8), comparison between the results for the bolts will be highlighted. The failure

modes of FJ02 were quite similar to FJ03: local buckling in the bottom flange, a slight deformation in the top and bottom of the end-plate and axial deformation in the 2nd bolt-row; however in contrast to test FJ03, and as well as experimentally observed, the bolt failure was not reached in this case (Fig. 10a). Fig. 10b) compares the evolution of the forces measured in the 2nd bolt row of the FJ02 and the FJ03 joints. In this row the bolts forces are developed especially during the cooling phase. The values measured during the heating phase are small and could be neglected. FJ02 bolt developed the highest axial force but its design tension resistance is also higher ($N_{Sd,\theta}$ = 245.5 kN and $F_{ten,t,Rd}$ = 254.0 kN), otherwise the axial force developed in the FJ03 bolt is $N_{Sd,\theta}$ = 192.9 kN while $F_{ten,t,Rd}$ = 191.5 kN; $N_{Sd,\theta}$ was obtained by integration of the axial stresses ($\sigma_{x,x}$) at the middle section of the bolt, and $F_{ten,t,Rd}$ was calculated according to [12] with the experimental ultimate stress for bolts at room temperature [6].

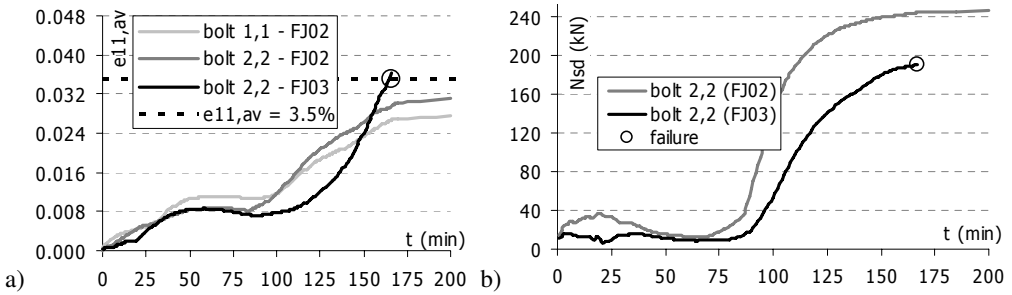

Fig. 10 - a) Averaged principal strains in the bolts; b) Bolt forces.

5.3 Effect of the end plate thickness

Fig. 11 compares the experimental and the predicted failure modes for the FJ01 joint (t_p = 10 mm). The numerical analysis allows the identification of each joint failure mode during the analysis: local buckling in the bottom flange and deformation in the top of the end-plate is developed during the heating phase while deformation at the bottom of the end-plate is only noticeable during the cooling phase. In contrast to FJ03, and in line with the experimental observations, prior to bolt failure, large deformations are observed in the end-plate. These large deformations are confirmed by the equivalent strains contours in the end-plate (Fig. 12).

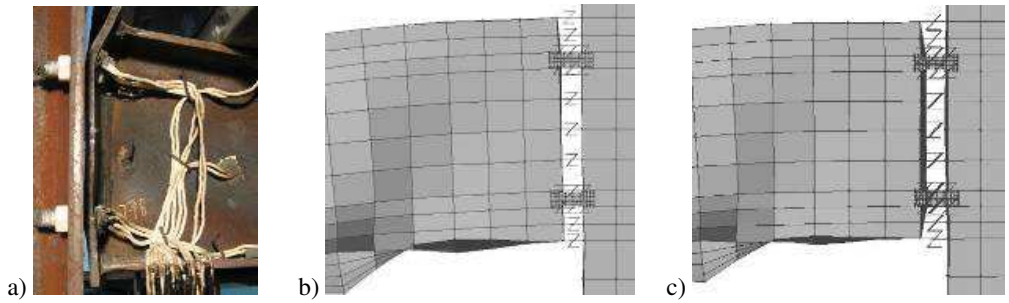

Fig. 11 - Failure mode of the FJ01: a) experimental test (end of the fire); b) FE analysis (t = 55 min); c) FE analysis (t = 170 min); (scale factor: x1).

Significant deformations at the top of the end-plate develop during the heating phase, corresponding to a maximum equivalent strain higher than the yield strain ($\varepsilon_{E,t} > \varepsilon_y = 0.02$);

during the cooling phase, the strains continued to increase, more at the bottom of the end plate than at the top. According the failure criteria reported in §2.3, (ε_u = 0.20) the end-plate did not fails, however large strains on the tensile surface were observed at the level of the 2nd bolt-row during the cooling phase ($\varepsilon_{E,t}$ = 0.12). For the bolts of the 2nd row, principal strains higher than 0.035 are shown in some localised zones; however, the average principal strains in the middle section of the bolts is always lower than this value.

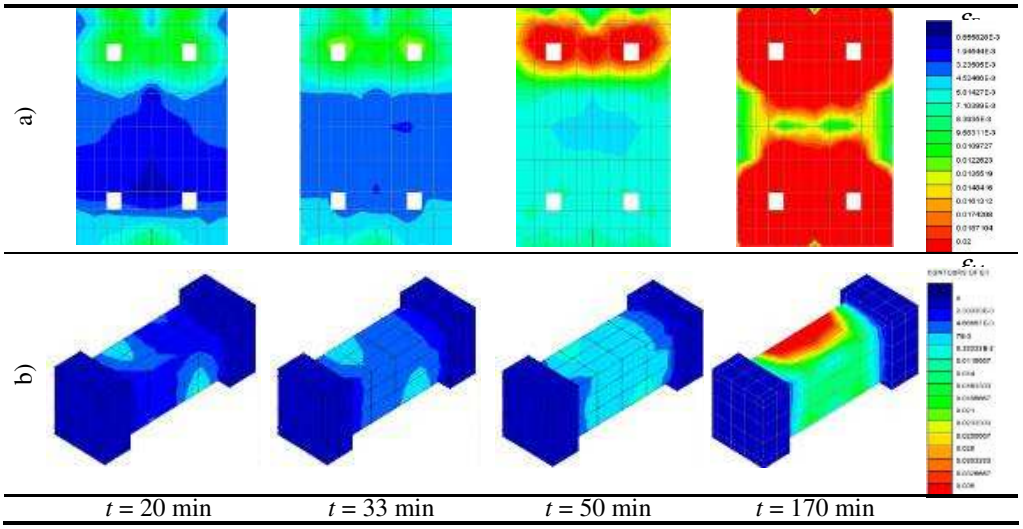

Fig. 12 - a) Equivalent strain contours in the end-plate; b) principal strains in the bolts.

5.4 Behaviour of the extended end-plate joint

In this item, the influence of an extended end-plate on the joint behaviour under fire is described. From the numerical analysis it was observed that local buckling occurs in the bottom flange during the heating phase while deformation at the bottom of the end-plate and deformations on the 3rd bolt-row are only developed during the cooling phase (Fig. 13).

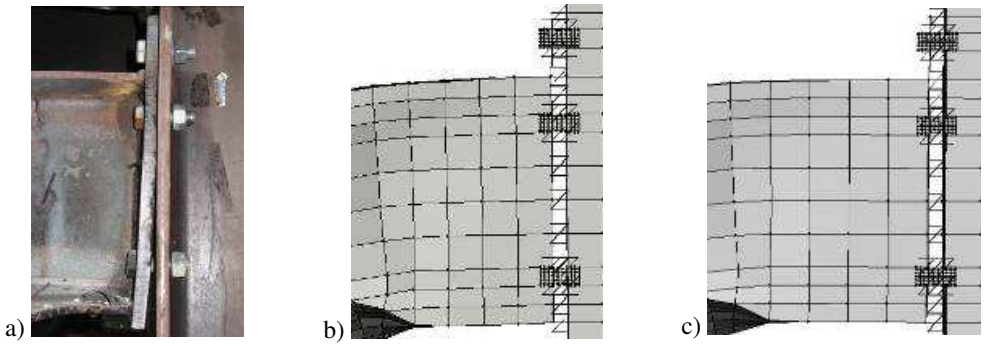

Fig. 13 - Failure mode of the EJ01: a) experimental test (end of the fire); b) FE analysis (t = 55 min); c) FE analysis (t = 157 min); (scale factor: x1).

As for the other joints, the development of the equivalent strain contours starts from the bottom flange to the top flange of the beam; the bottom flange reaches the failure strain at t = 20 min (ε_u = 0.18). In the end-plate, due to the distance between the two first bolts rows, lower deformations are developed. In the bolts, the higher principal strains develop during the

cooling phase in the lower bolt-row (Fig. 14). The numerical failure of this bolt-row was reached at about t = 157 min.; experimentally, it corresponded to stripping-off of the threads of the bolts.

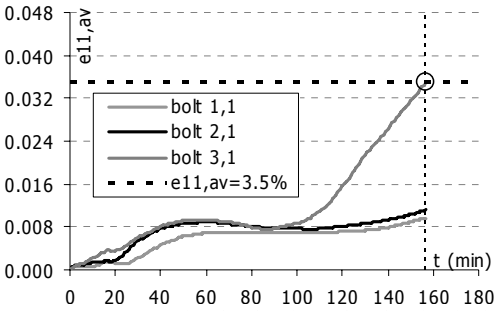

Fig. 14 - Averaged principal strains in the bolts.

6. CONCLUSIONS

In this paper, three dimensional finite element models of the sub-structures tested experimentally were developed. First, the rotational behaviour of each joint at room temperature was studied and compared with the bilinear force-displacement response calculated according to EN 1993-1-8 [12]. Subsequently, these numerical models were calibrated with the experimental data of the tests under fire. It was possible to evaluate the performance of each individual structural joint component, as well as the identification of the main dependencies of the geometrical and mechanical variables of the components on the global joint behaviour. The following conclusions are drawn:

i) As experimentally observed, one of the main problems during the cooling of the fire is the tensile failure of the bolts. In this study, this was numerically demonstrated using a failure criteria based on the averaged principal strains ($\varepsilon_{11,av} \leq \varepsilon_{u,b}$).

ii) During the cooling phase, the lower bolt row showed the highest principal strains. This results from reversal of bending moment, that leads to large sagging moments, since the Young modulus and resistance recover their values, and the temperature decreases faster on the bottom flange than on the top.

iii) Special attention should me made when it is intended to increase the joint resistance under a natural fire. The application of a bolt class with higher resistance reduces the bolt strains (FJ02) and reveals to be a good option to increase the joint resistance. However, a joint typology with a higher resistance at room temperature (EJ01) is not such a good option, because it increases the resistance to the hogging moment, but not to sagging moment that controls the cooling phase.

iv) The application of a thin end-plate demonstrated to be another option to reduce the large bolt strain and consequently the bolt failure (FJ01). However, even if no bolt failure was observed, the equivalent strains on the end-plate increased to values similar to those assumed to the end plate cracking.

ACKNOWLEDGMENTS

Financial support from the Portuguese Ministry of Science and Higher Education (*Ministério da Ciência e Ensino Superior*) under contract grant POCI/ECM/55783/2004 is gratefully acknowledged.

REFERENCES

[1] Santiago, A, Simões da Silva L, Vila Real P, Gameiro Lopes A and Vaz G, "Experimental evaluation of the influence of connection typology on the behaviour of steel structures under fire", *Engineering Journal*, 2008 (*accepted for publication*).
[2] Lawson, R.M., "Behaviour of steel-beam-to-column connections in fire" *The Structural Engineer*, 68(14), pp. 263-71, 1990.
[3] Block F., "Development of a component-based finite element for steel beam-to-column connections at elevated temperature". Doctoral Thesis, Department of Civil and Structural Engineering, University of Sheffield, UK, 2006.
[4] Liu T.C.H., Fahad M.K. and Davies J.M., "Experimental investigation of behaviour of axial restrained steel beams in fire". *J. of Constructional S. Research*, 58, pp. 1211-30, 2002.
[5] El- Houssieny, O.M.; Abdel Salam, S.; Attia, G.A.M. and Saad, A.M., "Behavior of extended end plate connections at high temperature". *J. of Construction S. Research*; 46(1-3), pp. 299, 1998.
[6] Santiago, A, "Behaviour of beam-to-column steel joints under natural fire". Doctoral Thesis, Department of Civil Engineering, University of Coimbra, 2008.
[7] Lusas 13. Lusas manual. Finite element analysis Ltd, Version 13.5. Surrey, UK, 2003.
[8] European Committee for Standardization. EN 1993-1-2: 2005. Eurocode 3: Design of steel structures. Part 1.2: General rules -Structural fire design, Brussels, 2005.
[9] European Committee for Standardization. EN 1993-1-1: 2005. Eurocode 3: Design of steel structures. Part 1.1: General rules and rules for buildings. Brussels, 2005.
[10] Hirt, M.A. and Bez, R. Construction métallique: notions fondamentales et methods de dimensionnement. Traité de Génie Civil de l'École Polytechnique Fédérale de Lausanne, Vol. 10. Presses Polytechniques et Universitaires Romandes, Lausanne, Switzerland.
[11] Li, G-Q, Yin, Y-Z and Li, M-F, "Experimental studies on the material properties of high-strength bolt connection at elevated temperature", *Steel and Composite Structures*, 2(4), pp. 247-58, 2002.
[12] European Committee for Standardization. EN 1993-1-8: 2005. Eurocode 3: Design of steel structures. Part 1.8: Design of joints, Brussels, 2005.
[13] Yin, Y.Z. and Wang, Y.C., "Analysis of catenary action in steel beams using a simplified hand calculation method, Part 1: theory and validation for uniform temperature distribution". *J. Constructional S. Research* 61, pp. 183-211, 2005.

FIRE PERFORMANCE OF STEEL REINFORCED CONCRETE (SRC) BEAM-TO-COLUMN JOINTS

LIN-HAI HAN[1], YONG-QIAN ZHENG[2], ZHONG TAO[3]

ABSTRACT

The present study is an investigation on the fire performance of steel reinforced concrete (SRC) beam-to-column joints under fire. Two new tests on SRC beam-to-column joints subjected to the ISO-834 standard fire were carried out and described. A finite element analysis (FEA) modeling was developed. A comparison of results calculated using this modeling shows generally good agreement with the test results. The FEA modeling is then used to analyze the mechanism of the composite joints under fire.

1. INTRODUTION

It is well known that, the excellent structural and fire resistant properties of steel reinforced concrete (SRC) columns make them particularly suitable to be used in high-rise buildings. In the past, there have been some research studies on structural performance of SRC columns under fire conditions, such as Hass (1986)[1], Yu et al. (2007)[2], Wang and Tan (2006)[3], Huang et al. (2007, 2008)[4, 5]. Some design regulations, such as ECCS (1988)[6] and Eurocode 4 (2005)[7] gave the fire resistance calculating methods for single SRC columns. However, seldom research till now has been reported to investigate the fire performance of beam to SRC column joints.

Set against this background, the authors have recently been engaged in the research project to determine the fire performance of the SRC beam to SRC column joints under fire. Such moment-resisting joints have been widely used in tall buildings in China. ABAQUS software was used to perform a finite element analysis (FEA) in this paper. Two new tests on

[1] Professor, Tsinghua University, Department of Civil Engineering, 100084 Beijing, China, email: lhhan@tsinghua.edu.cn.
[2] PhD, Fujian University of Technology, Department of Civil Engineering, 350007 Fujian, China, email: zhengyongqian@fzu.edu.cn.
[3] Professor, Fuzhou University, College of Civil Engineering, 350108 Fujian, China, email: taozhong@fzu.edu.cn.

this type of joints subjected to the ISO-834 (1999)[8] standard fire were performed to verify the FEA modeling. The FEA modeling was then used to investigate the fire performance of the composite joints.

2. EXPERIMENTAL STUDY

2.1 Specimen preparation

Two SRC beam to SRC column joint specimens were tested. Figure 1 shows the test setup. The column height is 3800 mm and the total beam length is 3900 mm. The two tests were designed to investigate the effect of the load level in the SRC beam m (=0.3, 0.6), which is defined as $m = P_F/P_u$; where P_F is the longitudinal load applied to the beam and P_u is the bearing capacity of the beam at ambient temperature calculated by using the FEA modeling.

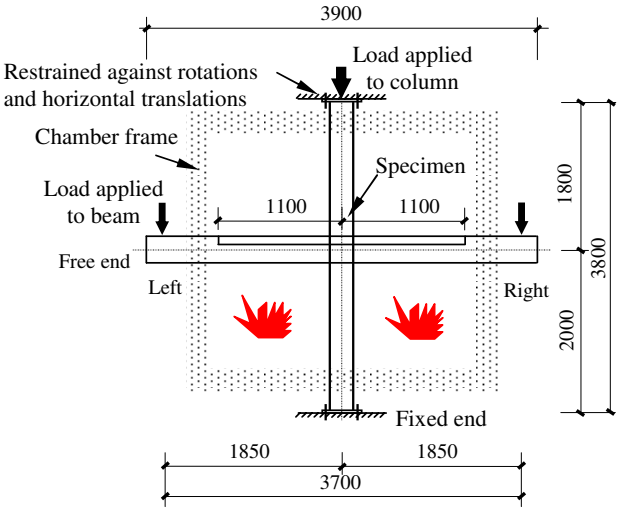

Fig. 1 – Arrangement of test set-up (units: mm)

Table 1 lists the details of each specimen, where k is the beam-column linear stiffness ratio, which is defined as $k = \frac{(EI)_{beam}/L}{(EI)_{column}/H}$, where $(EI)_{beam}$ and $(EI)_{column}$ are the flexural stiffness of beam and column respectively; L and H are the length of beam and the height of column. The flexural stiffness $EI=E_sI_s+ E_{sb}I_{sb}+0.6E_cI_c$, was determined according to Eurocode 4 (2004)[9], where E_s, E_{sb} and E_c are the modulus of elasticity of the section steel, steel bars and concrete, respectively, and I_s, I_{sb} and I_c are the moment of inertia for the section steel, steel bars, and concrete cross section, respectively; n is the level of axial load in the column, which is defined as $n = N_F/N_u$ (N_F is the axial load applied in the column, and N_u is the axial compressive capacity of the column at ambient temperature calculated by using the FEA modeling); t_R is the fire resistance time of the joint specimen.

Table 1. Summary of specimen information

Specimen number	Column dimension (mm)	Beam dimension (mm)	Ratio of beam to column stiffness k	Load level in column n	Load level in beam m	Load in Column N_F (kN)	Load on beam P_F (kN)	Fire resistance time t_R (min)
JSRC1	300×300	300×200	0.706	0.66	0.3	2139	22	127
JSRC2	300×300	300×200	0.706	0.66	0.6	2139	44	94

The two SRC joints were designed based on the Chinese Standard JGJ 138-2001 (2002)[10]. Details of the composite joints are shown in Figure 2.

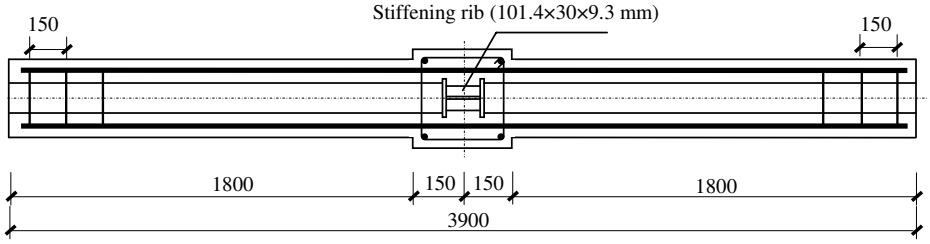

(a) Plan view of SRC beam

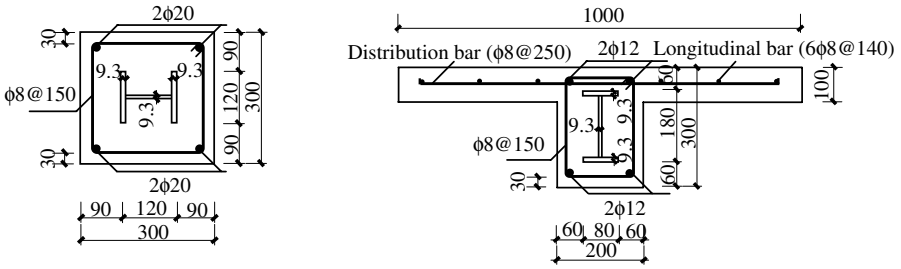

(b) SRC column section (c) SRC beam section

Fig. 2 – Connection configuration (units: mm)

2.2 Material properties

Table 2 lists the measured average yield strength (f_y), tensile strength (f_u), modulus of elasticity (E_s), Poisson's ratio (μ) and yield strain (ε_y). One type of concrete was used to fabricate the composite joints. The mix proportions were: Cement: 315 kg/m^3; Water: 175 kg/m^3; Sand: 744kg/m^3; Coarse aggregate: 1071 kg/m^3; Fly ash: 75 kg/m^3; and Water reducer: 7.02 kg/m^3. The average ambient temperature cube strengths at 28 days and at the time of test were 27.8 and 30.6 MPa, respectively. The modulus of elasticity (E_c) of the concrete at the time of test was 29,200 MPa.

Table. 2 Material properties of steel

Steel type	Thickness/ Diameter (mm)	f_y (MPa)	f_u (MPa)	E_s (MPa)	μ	ε_y ($\mu\varepsilon$)
Section Steel	9.30	260.09	388.19	202500	0.311	2325
Reinforced bar (ϕ20)	19.47	377.46	583.17	200500	0.275	1893
Reinforced bar (ϕ12)	11.27	409.48	588.05	181700	0.270	2399
Reinforced bar (ϕ8)	8.10	430.54	542.00	189800	0.281	2614

2.3 Loading apparatus and fire exposure

Each specimen was then tested under a combined constant axial load (N_F) on the SRC column and two vertical concentrated loads (P_F) on each end of the two SRC beam segments (shown as in Figure 1). The top end of the column was restrained against rotations and horizontal translations, and the bottom end was under a fixed end condition. A hydraulic jack

with a capacity of 5000 kN was used to apply the axial load on the test column and maintain the load constant during the fire exposure. The vertical loads (P_F) on the two beam segments were then applied by two jacks attached to a very rigid beam. Table 1 gives the values of the test loads applied on the column and beams for each specimen.

The ambient temperature at the start of the test was about 20 ^oC. During the test the joint specimen was exposed to heating controlled in such a way that the average temperature in the furnace followed as closely as possible the ISO-834 Standard curve (ISO-834, 1999)[8]. Only the space under the RC slabs was heated (shown as in Figure 1), and the other parts of the specimen were separated from the fire. This was achieved by protecting the slab, the beam and the column in the upper storey using ceramic fiber blankets.

2.4 Test results and discussions

(1) Specimen failure modes

Both the joint specimens behaved in a ductile manner and the tests proceeded in a smooth and controlled way subjected to fire. It was found that, both specimens of JSRC1 and JSRC2 failed due to the failure of their columns. Figure 3 shows the overall failure mode of specimen JSRC1 after tests. It can be found that, because of the fire exposure, the cover concrete cracked and spalled seriously, especially at the corners of the lower columns and the bottom surfaces of the beams. Cracks were also found at the top and bottom surfaces of the slabs. In addition, some of the corner longitudinal bars of the columns have been buckled and the stirrups have been broken. Similar phenomena of concrete were also observed in fire tests on reinforce concrete and steel reinforced concrete joints (Huang et al., 2008; Lie and Irwin, 1990)[5, 11]. In the joint zone, the concrete of the two specimens has retained its integrity in general.

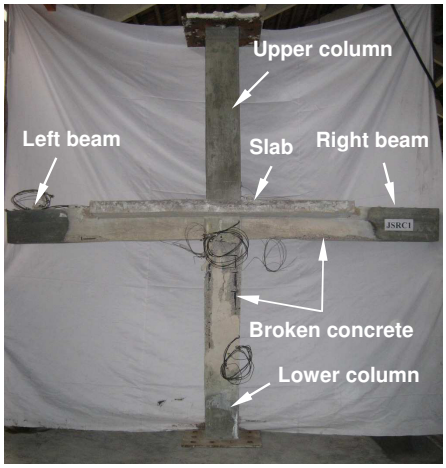

Fig. 3 – Overall failure mode (JSRC1)

(2) Measured results

Figure 4 presents the measured and calculated typical temperature distributions in the columns and beams.

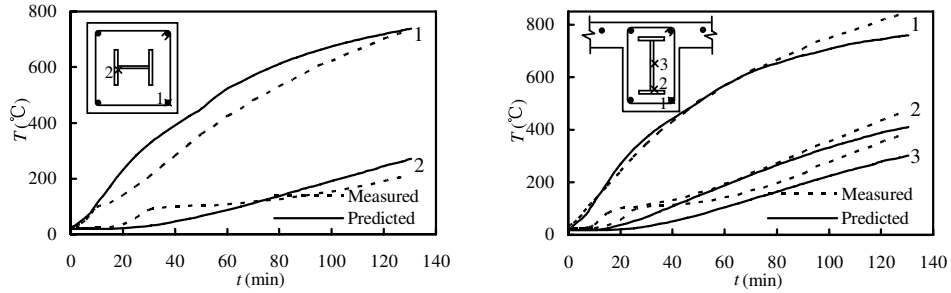

(a) Column (b) Beam

Fig. 4 – Temperature distributions in the column and beams of JSRC1

Figures 5 and 6 show the measured axial deformation (Δ) of the columns and the deflections (f) of the beams with time (t), respectively. It can be found from Figure 6 that the compressive deformation increased during fire exposure, and rapid deformation and rotation occurred in the failure stage. Because of the significant deformation occurred in the column, the deflection developments in the left and right beams were different during the fire exposure. When the column failed, the deflections of the beams increased significantly. For the specimen JSRC1 with a small load ratio, the thermal expansion leaded to a reverse change on deflection in the failure stage.

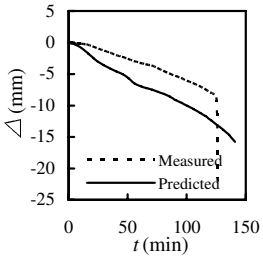

(a) Specimen JSRC1

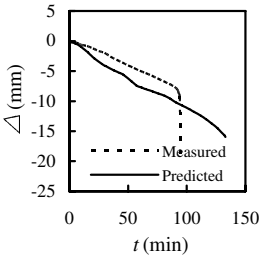

(b) Specimen JSRC2

Fig. 5 – Axial deformation (Δ) versus time (t) relations of the columns

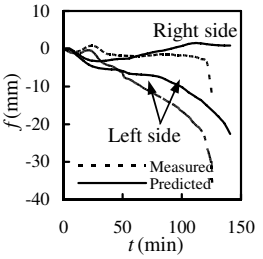

(a) Specimen JSRC1

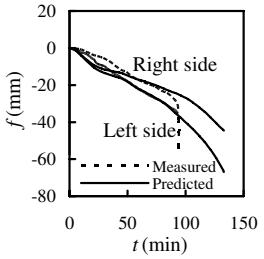

(b) Specimen JSRC2

Fig. 6 – Deflections (f) versus time (t) Relations of the beams

The measured fire resistance time (t_R) of is the composite joints were listed in Table 1.

3. FEA MODELING

The simulation of a SRC joint under fire includes the calculations of the temperature distribution in the joint, and the deformation of the joint under both loading and fire. ABAQUS software is used in this paper for the developing of a finite element analysis (FEA) modeling for the SRC joint under fire. In the modeling, material properties for steel and concrete at high temperatures, element type and element mesh, boundary condition and the steel-concrete interface should be determined rationally.

3.1 Material properties

Elastic-plastic model was used to describe the constitutive behaviour of the steel. The stress-strain model for steel at high temperatures given by Lie and Denham (1993)[12] was adopted herein. Details of the model were described in Lie and Denham (1993)[12]. The initial modulus of elasticity could be determined by the slopes of the stress versus strain curves at high temperatures. The Poisson's ratio for steel in the elastic stage is taken as 0.3 in the calculations.

The residual stress was considered in the FEA modeling for welded I-section steel. A typical residual stress distribution for the steel plates of a section is shown in Figure 7 (Chen, 2006)[13], where "+" and "−" denote the

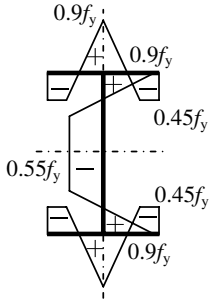

Fig. 7 – Residual stress distributions across plate of a welded I-section

tension and compression zones respectively.

The damage plasticity model defined in ABAQUS/Standard 6.5 is used in the analysis (Hibbitt, Karlson and Sorensen Inc., 2005)[14]. The yielding surface and the description of the plastic behaviour coming from the equivalent stress versus strain relationships of concrete were defined. The initial modulus of elasticity was also obtained by the slopes of stress versus strain curves at high temperatures. The Poisson's ratio for concrete changes at 150°C to reach 50% of its ambient value at 400°C and becomes zero at 1200°C (Izzuddin et al., 2002)[15].

For concrete in tension, tensile soften behaviours need to be set for the analysis of SRC joints under fire in the ABAQUS software. The tensile stress (σ_{tT}) versus strain (ε_{tT}) relationship proposed by Vecchio and Collins (1986)[16] was adopted. Details of the model under high temperatures were presented in Cai et al. (2003)[17] and Huang et al. (1999)[18].

3.2 Geometry, element type, mesh and boundary condition

A cruciform joint in a frame building structure as shown in Figure 8 was selected for analysis in this paper. The joint with a reinforced concrete slab, consists of the left and right beam segments, the upper and lower column segments. Local fire (under the floor) shown as in Figure 8 was assumed.

Finite element divisions of the SRC joint are shown in Figure 9. The concrete in the joint was modeled using 8-node brick elements (C3D8R), and 4-node shell elements (S4R) were used for the section steel and stiffening rib, and the 2-node truss elements (T3D2) were used to model all the steel bars.

Symmetry boundary conditions were applied to the mid-span surfaces of the beams. The mid-height surface of the lower column was restrained to have only the horizontal displacements in X, Y directions, and the mid-height surface of the upper column to have the displacements in X, Y, Z directions, shown as in Figure 9.

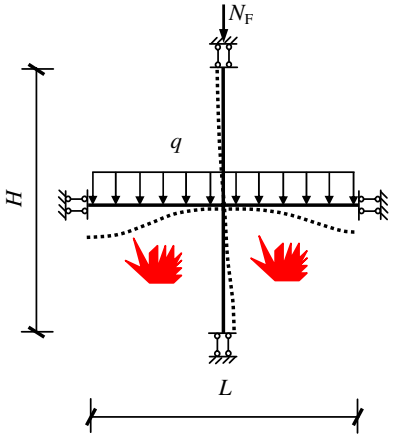

Fig. 8 – Calculating sketch of the composite joint

3.3 Steel -concrete interface

The 2-node spring elements (SPRING2) were used to simulate the interaction of the steel and concrete. The SPRING2 elements in the longitudinal direction were applied to model the bond slip mechanism. The nonlinear behaviour was defined by nodal force-relative displacement relationship, in which the bond strength and limit slip vary with the temperatures. For the bond stress (τ_T) versus slip (S_T) relationship between the steel bar and the concrete, the model provided by Zhu et al. (1990)[19] was adopted in the analysis, as shown in Figure 10. Due to the scarcity of description on the bond stress versus slip relationship between the section steel and concrete at high temperatures, the expression at ambient temperature proposed by Wang and Zhong (1990)[20] were modified to be suitable for the analysis at high temperatures referring to the investigation of Jiang et al. (2003)[21] and Zhu et al. (1990)[19]. Figures 10 and 11 show the bond stress (τ_T) versus slip (S_T) relationships between steel bars (section steel) and concrete at high temperatures. As for all the stirrups, they were embedded in concrete.

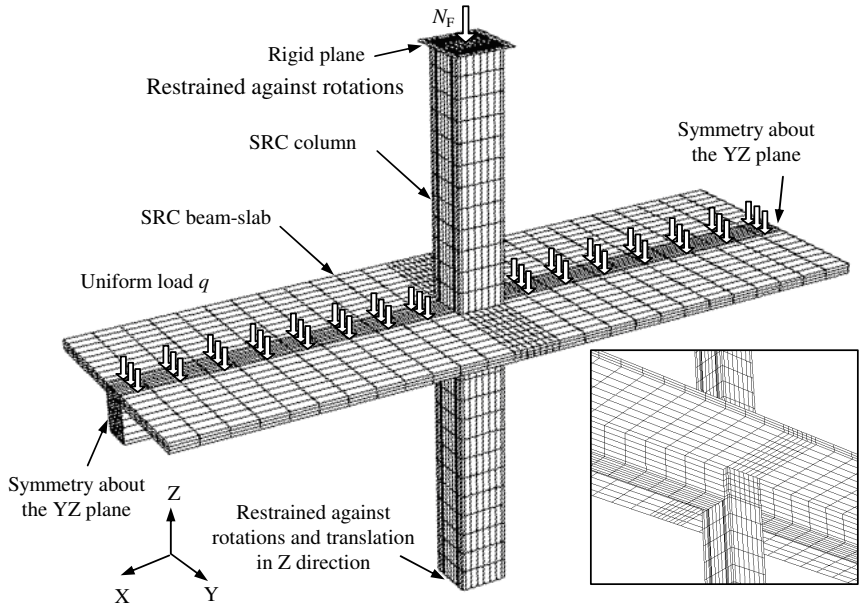

Fig. 9 – Finite element divisions of the SRC joint

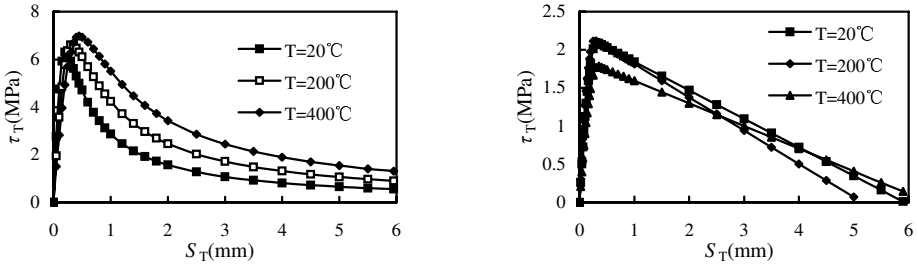

(a) Deformed bars (b) Plain round bars

Fig. 10 – Bond stress-slip relationships between steel bars and concrete

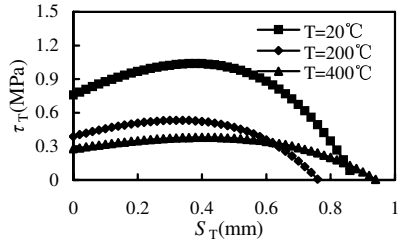

Fig. 11 – Bond stress-slip relationships between section steel and concrete

For the temperature field calculations of the composite joints under fire, the thermal properties for the steel and concrete such as conductivity, specific heat and thermal expansion presented by Lie and Denham (1993)[12] are adopted in this paper.

Figure 4 shows the comparisons between the measured and the calculated typical temperature distributions in the columns and beams. On the whole, the calculated temperatures show good agreement with test results. Figures 5 and 6 show the comparisons between the predicted and measured axial deformation (Δ) of the columns, as well as the

deflections (*f*) of the beams with time (*t*) respectively. It can be found that there are some discrepancies between the predicted and measured results of deformations and fire resistance. The discrepancies can be attributed to the concrete spalling of the columns and beams, leading to a decrease of the effective section area and exposure of reinforcements to the fire. Since this influence was not considered in the simulation, higher predicted fire resistance results (141 min and 133 min for the JSRC1 and JSRC2 respectively) were achieved than the test results (126 min and 94 min for the JSRC1 and JSRC2 respectively).

Figure 12 shows the concrete plastic strain of the JSRC1 at failure predicted by using ABAQUS, where the deformation was magnified five times. As evident from the figure, the concrete at the corners of the heated column at failure have developed greater plastic strains, and the maximum plastic compressive and tensile strains of 15900 με and 23980 με respectively, exist in the lower column at a height of 1250 mm from the bottom end. For the beams, the maximum plastic compressive and tensile strains of 6034 με and 13470 με respectively, exist at the bottoms of 400 mm away from the axis of column. The concrete at locations of highest plastic strain has a tendency to crack and spall, which was observed in the failed specimen JSRC1 as shown in Figure 3.

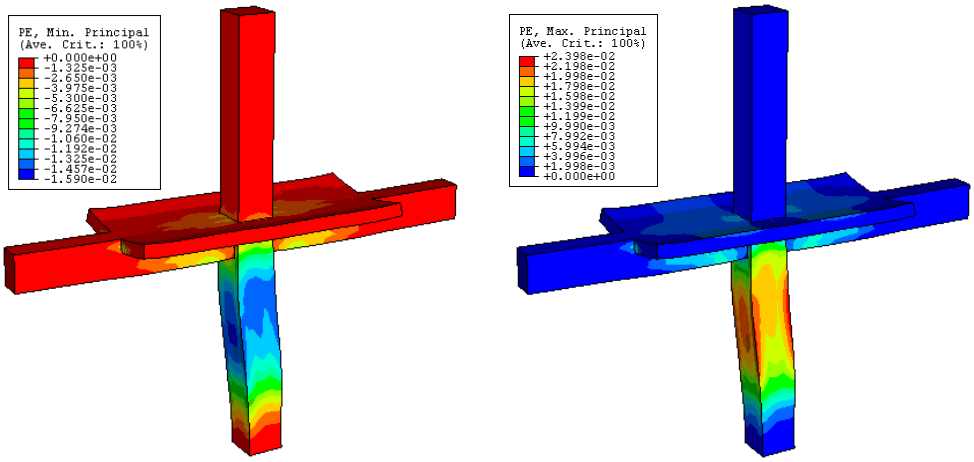

(a) Plastic compressive strain of joint (b) Plastic tensile strain of joint

Fig. 12 – Predicted concrete plastic strain at failure (JSRC1)

4. ANALYTICAL BEHAVIOUR

The FEA modeling can be used to analyze the mechanism of the composite joints under fire. Due to page limitations, only the results regarding stiffness degradation and the stress distribution of the composite joint under fire are given hereinafter.

A typical joint shown in Figure 8 is selected in the analysis. In this case study, the SRC joint was designed according to Chinese Code JGJ 138-2001 (2002)[10]. The geometries of the columns are: square cross section of 600×600 mm, height (*H*) of 6900 mm, section steel of H360×300×16×16, 12 longitudinal steel bars with a diameter of 20 mm, stirrup diameter of 10 mm, stirrup spacing of 200 mm. The geometries of the beams are: rectangular cross section of 600×400 mm, span (*L*) of 9000 mm, section steel of H360×200×14×14, 4 longitudinal tensile steel bars and 2 longitudinal pressed steel bars with a diameter of 20 mm, stirrup diameter of 10 mm, stirrup spacing of 200 mm. The geometries of the slabs are: width of 3000 mm, thickness of 120 mm, diameter of steel bars of 10 mm, spacing of 150 mm and 250 mm of

longitudinal bars and distribution bars respectively. The columns in the joint zones are stiffened with transverse stiffeners connected to the column section steel at the level of the flanges of beam section steel. The yield stresses (f_y) of section steel and steel bars are 345 MPa and 335 MPa respectively. The cubic strengths (f_{cu}) of concrete in the columns and beam-slabs are 60 MPa and 40 MPa respectively.

4.1 Effects of fire on the joint stiffness

The initial stiffness of joints can be used to classify the joints and its change can reflect the fire influence. In the past, there was little research on the stiffness of SRC joints, so the research achievements of steel joints were used herein for reference (Eurocode 3, 2005)[22].

The initial stiffness of joint is determined from the relative rotation versus moment relationships of the beam end section at joint zone in the typical case of non-sway frame joint. Figure 13 shows the calculated SRC joint stiffness (k) as a function of the fire exposure time (t) for the composite joints with different linear stiffness ratios. It can be seen that the joint initial stiffness reduces with the increase of beam-column linear stiffness ratio at ambient temperature. This could be attributed to the less restraint on the beams from the columns. During the fire exposure, the initial stiffness of joint decreases as expected. When the linear stiffness ratio is great than 0.45, the joint stiffness decreases as the time increases until to150 min. At the time of 60 min fire exposure, the stiffness of the joints with the beam-column linear stiffness ratios of 0.45, 0.90, 1.36 reduce to 37.3%, 47.6%, 53.0% of those at ambient temperature respectively. After a fire exposure of 150 min, the joint stiffness shows a slight increase. This is attributed to the beneficial effect from the adjacent members in restraining the expansion during the fire exposure. For the joint with a linear stiffness ratio of 0.23, the initial stiffness increases rapidly after 120 min due to the long span of the beams and the beneficial effect of the expansion.

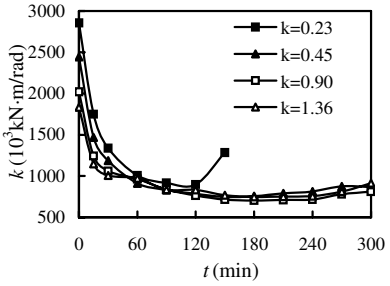

Fig. 13 – Joint stiffeness(k) versus fire exposure time (t)

4.2 Stress distributions in the steel and concrete

In Figures 14 and 15, the Mises stress distributions of the steel and the principal stress distributions of concrete are provided. The maximum Mises stresses in the section steel is 251 MPa before exposure to fire. They are found at the beam end and the web of column section steel near the upper stiffening rib respectively. For the maximum principal stresses of the concrete in beam-slabs, the bottom near the mid-span of beams and the slabs near the joint zone have larger tensile stress due to the bending of beam-slabs, and the maximum tensile value is 2.9 MPa. The maximum tensile value of the column is 3.7 MPa at the location jointed to the top of beams. As the fire duration time increases, the stresses of steel and concrete vary under the combined action of the load and temperature.

Figure 16 shows the longitudinal stress distribution in the concrete section at the mid-height of the lower column with different fire exposure time. It can be seen that the left part of the section is in higher compression than the right one after the load is applied at ambient temperature. At the time of 60 min fire exposure, the load undertook by the concrete reduces because of the deterioration of concrete strength and elastic modulus. However, the concrete stress near the flanges of section steel is still increasing. At a later stage, the deflection of the

lower column greatly increases with time. The concrete stress decreases while the stress near the left flange of section steel is kept increasing. During the whole fire exposure, the concrete section at the mid-height of the lower column is always in compression.

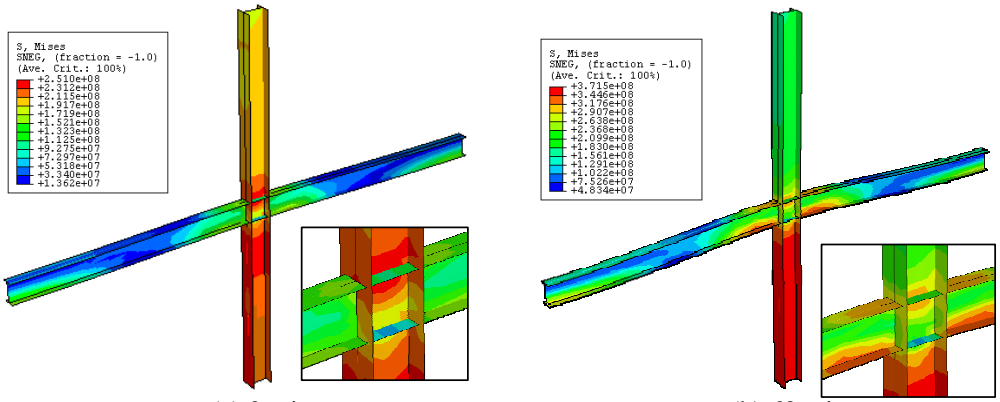

(a) 0 min (b) 60 min

Fig. 14–Mises stress distribution of the Section steel and stiffening ribs

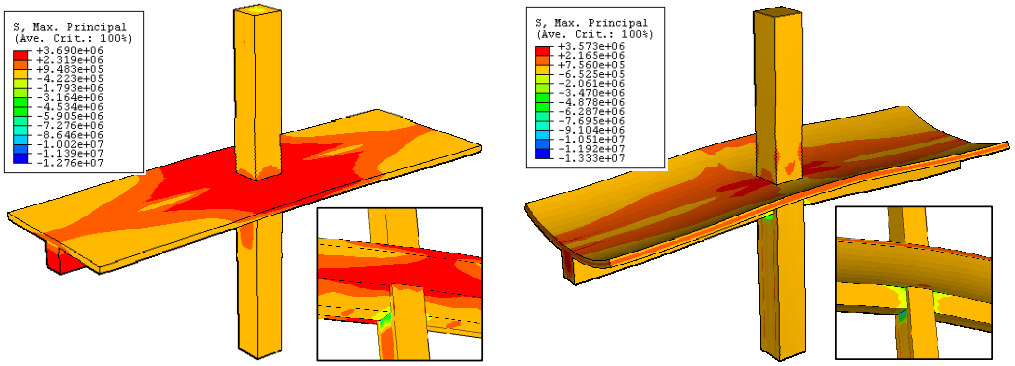

(a) 0 min (b) 60 min

Fig. 15 – Max. principal stress distribution of the concrete

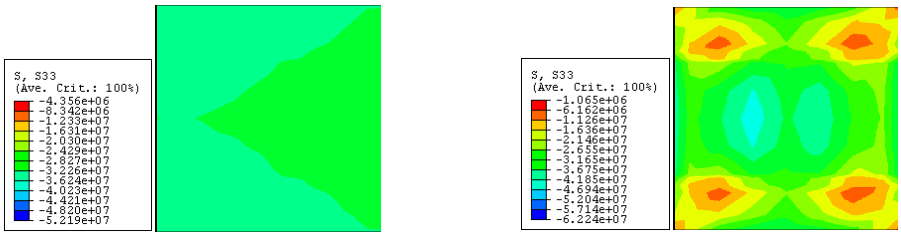

(a) 0 min (b) 60 min

Fig. 16 – Longitudinal stress distribution in concrete section at mid-height of lower column

Figure 17 illustrates the changes of longitudinal stress in the mid-span concrete section of the beam at different time. As expected, the stress of the section shows a band distribution after the joint is loaded before fire exposure. Most of the beam concrete at the bottom is in tension and the slab is in compression. Neutral axis leans toward the compressive zone. During the initial heating stage, the compressive stress of the concrete near exteriors subjected

to higher temperatures increases and the tensile stress at beam bottom even reverses to compressive stress as a result of the effect of thermal expansion. As the time increases, the compressive stress of the concrete with higher temperatures reduces increasingly due to the greatly degradation of material properties. However, the compressive stress at the top slab with lower temperature is increasing until the joint fails, as shown in Figures 17(b).

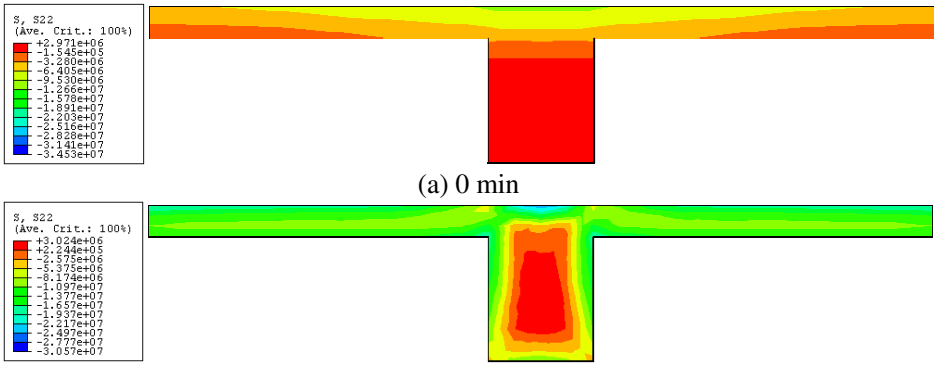

(a) 0 min

(b) 60 min

Fig. 17 – Longitudinal stress distribution in mid-span concrete section of the beam

5. CONCLUSIONS

Two new tests were carried out on steel reinforced concrete (SRC) beam to column joints subjected to the ISO-834 standard fire in this paper. A finite element analysis modeling was presented for the analysis of the composite joints under fire. A comparison of results calculated using this model shows generally acceptable agreement with the test results. Mechanism of the SRC joint under fire was analyzed by using the FEA modeling. The FEA modeling can be used for the parametric studies for providing simplified design methods for the SRC joints subjected to fire.

ACKNOWLEDGEMENTS

The research reported in the paper is part of the Project 50738005 supported by National Natural Science Foundation of China, and the National Key Project of Scientific and Technical Supporting Programs Funded by Ministry of Science & Technology of China (No.2006BAJ06B06). The financial support is highly appreciated.

REFERENCES

[1] Hass, R., “Zur Praxisgerechten Brandschutz-Technischen Beurteilung Von Stützen aus Stahl und Beton”. Institut für Baustoff, Massivbau und Brandschutz der Technischen Universitat Braunschweig, Heft 69, 1986.
[2] Yu, J. T., Lu, Z. D., Xie, Q., “Nonlinear analysis of SRC columns subjected to fire”. Fire Safety Journal, 42(1), pp. 1-10, 2007.
[3] Wang, H. Z., Tan, K. H., “Residual area method for heat transfer analysis of concrete-encased I-sections in fire”. Engineering Structures, 28(3), pp. 411-422, 2006.
[4] Huang, Z. F., Tan, K. H., Phng, G. H., “Axial restraint effects on the fire resistance of

composite columns encasing I-section steel". Journal of Constructional Steel Research, 63(4), pp. 437-447, 2007.
[5] Huang, Z. F., Tan, K. H., Toh, W. S., Phng, G. H., "Fire resistance of composite columns with embedded I-section steel-Effects of section size and load level". Journal of Constructional Steel Research, 64(3), pp.312-325, 2008.
[6] ECCS-Technical Committee 3, "Fire safety of steel structures, technical note, Calculation of the fire resistance of centrally loaded composite steel-concrete columns exposed to the standard fire", 1988.
[7] Eurocode 4, EN 1994-1-2: 2005. "Design of composite steel and concrete structures-part1-2: General rules-structural fire design". European Committee for Standardization, Brussels, 2005.
[8] ISO 834-1, "Fire-resistance tests-elements of building construction-Part 1: General requirements". International Standard ISO 834, Geneva, 1999.
[9] Eurocode 4, EN 1994-1-1: 2004. "Design of composite steel and concrete structures-part1-1: General rules and rules for buildings". European Committee for Standardization, Brussels, 2004.
[10] JGJ 138-2001, "Technical specification for steel reinforced concrete composite structures". China Architecture and Building Press, Beijing, China, 2002. (in Chinese).
[11] Lie, T. T., Irwin, R. J., "Evaluation of the fire resistance of reinforced concrete columns with rectangular cross-section". NRC-CNRC Internal Report, Ottawa, Canada, No.601, 1990.
[12] Lie, T. T., Denham, E. M. A., "Factors affecting the fire resistance of circular hollow steel columns filled with bar-reinforced concrete". NRC-CNRC Internal Report, Canada, No.651, 1993.
[13] Chen, J., "Stability of steel structures-Theory and design (second edition)". Science Press, Peking, China, 2006. (in Chinese).
[14] Hibbitt, Karlson, Sorenson., "ABAQUS Version 6.5: Theory manual, users' manual, verification manual and example problems manual". Hibbitt, Karlson and Sorenson Inc, 2005.
[15] Izzuddin, B. A., Elghazouli, A. Y., Tao, X. Y., "Realistic modelling of composite floor slabs under fire conditions". Proc., 15th ASCE Engineering Mechanics Conf., Columbia University, New York, 2002.
[16] Vecchio, F. J., Collins, M. P., "The modified compression-field theory for reinforced concrete elements subjected to shear". ACI Journal, Proceeding, 83(2), pp. 219-231, 1986.
[17] Cai, J., Burgess, I., Plank, R., "A generalised steel/reinforced concrete beam-column element model for fire conditions". Engineering Structures, 25(6), pp. 817-833, 2003.
[18] Huang, Z. H., Burgess, I. W., Plank, R. J., "Nonlinear analysis of reinforced concrete slabs subjected to fire". ACI Structural Journal, 96(1), pp.127-135, 1999.
[19] Zhu, B. L., Lu, Z. D., Hu, K. X., "Constitutive relationship of steel and concrete at high temperature". Building Science Research of Sichuan, (1), pp. 37-43, 1990. (in Chinese).
[20] Wang, Z. H., Zhong, S. S., "Nonlinear finite element analysis of steel reinforced concrete beam". The second symposium on theory and practice of concrete structures, Beijing, pp. 609-616, 1990 (in Chinese).
[21] Jiang, S. C., Li, G. Q., Li, M. F., "Experimental research on bond strength between profiled steel sheet and concrete at elevated temperatures". Journal of Tongji University, 31(3), pp. 273-276, 2003. (in Chinese).
[22] Eurocode 3, EN 1993-1-8: 2005, "Design of steel structures-Part1-8: Design of joints". European Committee for Standardization, Brussels, 2005.

HEAT TRANSFER MODELLING OF CONNCETIONS

KATE ANDERSON[1] and MARTIN GILLIE[2]

ABSTRACT

Structural fire design is still largely based on single member tests implying the behaviour of the structure as a whole is not usually considered. Consequently, the importance of connection behaviour in fire is often neglected. However, large forces have been shown to develop in connections during a fire as have large deformations and, therefore, it is desirable that connections be designed for such circumstances. To do this, the expected temperatures in connections must be established. This paper presents heat transfer analyses of typical connections using the commercial software ABAQUS to obtain temperature profiles.
Data from the BRE Cardington full scale tests in 2003 and from experimental work carried out at the University of Manchester indicate that lower temperatures are expected at the connections, up to 200^0C lower than that of the beam flange locally. In ABAQUS, 3D composite models were created with linear, 8 noded brick, heat transfer elements. Gas temperature profiles were created based on the experimental data and heat transfer was simulated by defining radiation and convection through the characterization of emissivity and heat transfer co-efficients. Similar temperature trends were produced by the models to those of the experimental data sets.

1. INTRODUCTION

In structural fire design, only individual member design is often considered. This method implies that failure of connections will not be critical due to having a lower temperature than surrounding members. However, this has not been well validated and in

[1] PhD Student, The University of Edinburgh, School of Engineering and Electronics, Edinburgh, EH9 3JL, UK
email: Kate.Anderson@ed.ac.uk.
[2] Lecturer, The University of Edinburgh, School of Engineering and Electronics, Edinburgh, EH9 3JL, UK
email: M.Gillie@ed.ac.uk

order to predict how the behaviour of connections affects the overall structure in fire, connection temperatures must be established in order to evaluate their structural response.

This paper examines the temperature variations across a number of connection types; flush end-plate, flexible end-plate and fin plate by creation of a 3D heat transfer analysis using the commercial finite element package ABAQUS.

Two simpler methods for calculating connection temperatures are also investigated: the lumped capacitance method and a method presented in Eurocode 3 part 1-2[1].

2. SENSITIVITY STUDY

A section of this work was to define the variables which most affect the prediction of connection temperatures by carrying out a sensitivity study. The purpose of this study was to assist in the creation an accurate yet simple heat transfer model. The parameters which were considered were the radiative emissivity, the convective heat transfer co-efficient and the effect of including the composite concrete slab above the connection. In each case, the connection is subject to a 60 minute standard fire[2] and temperatures at the connection are monitored. The cooling phase has not been considered.

The commercial finite element package ABAQUS[3] was used to create a 3D model using 8 noded linear heat transfer brick elements, DC3D8. An unprotected fin plate connection was modelled and, when included in the analysis, the top surface of the concrete was exposed to ambient air. The temperature dependant material properties of the steel and concrete were consistent throughout the study and for the exposed areas of the connection, in the base model, the radiative emissivity was 0.8 and the convective heat transfer coefficient $25W/m^2K^2$**.** All the parts of the model were fixed together using the TIE constraint enabling perfect conduction. The model is shown below in figure 1.

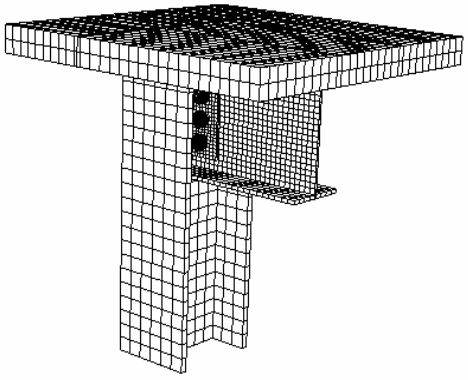

Fig. 1 - Base Model for Sensitivity Study

2.1. Concrete Slab

As the prediction of temperature profiles through the concrete is complex and computationally time consuming, it would be advantageous to exclude it from further modelling. However, to establish whether this is a realistic assumption, the effect of the concrete on the temperature profile of the connection must be examined.

Three models were created to investigate this:

- one including the concrete and adjacent steel decking;
- one including the concrete and excluding the steel decking and;
- one including only the bare steel connection.

Before examining the results, one obvious difference will be that the temperature of the upper beam flange will be higher when the slab is not included. However, this simplification is appropriate within the scope of this research.

A graph showing the temperature at a point next to the middle bolt on the fin plate for the three scenarios is show in figure 2**.** The biggest temperature variation between the models is approximately 15^0C, or 2.5%, and therefore the effect of the concrete being included in the model is negligible.

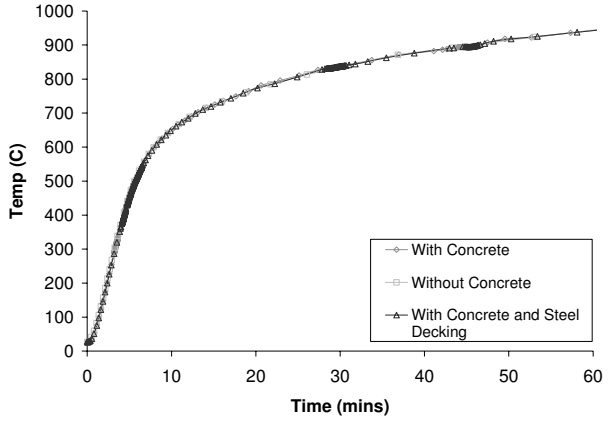

Fig. 2 - Temperature variations when including and excluding the concrete slab

2.2. Convective Heat Transfer Coefficient

Next, the convective heat transfer coefficient for all exposed surfaces was varied between 5 and 30W/m^{2}K at increments of 5W/m^{2}K. Temperatures of the fin plate were again monitored and are shown in the figure 3. This shows a temperature variation of between 5 and 10% between the 5W/m^{2}K and 30W/m^{2}K models, a maximum of 50^0C. This variation, however, is only for a very brief period near the start on the analysis. Generally, models all show similar temperatures. Consequently, the value of heat transfer co-efficient will be kept constant in the heat transfer modelling.

2.3. Radiative Emissivity

For the final part of the sensitivity study, the radiative emissivity for all exposed surfaces was varied between 0.3 and 0.9. When comparing the predicted temperatures on the connection for the various models a notable difference was observed and is shown in figure 4. During the first 20 minutes of heating there were temperature variations of up to 150^0C however, after this time there was substantially less difference, a maximum of 50^0C which is 7% or less. On this basis it would therefore be recommended to use a smaller value for emissivity near the connection where the temperatures are expected to be lower. A value of 0.8 will be used for the majority of the model and at the more bulky and shaded connection area a value of 0.3 will be used.

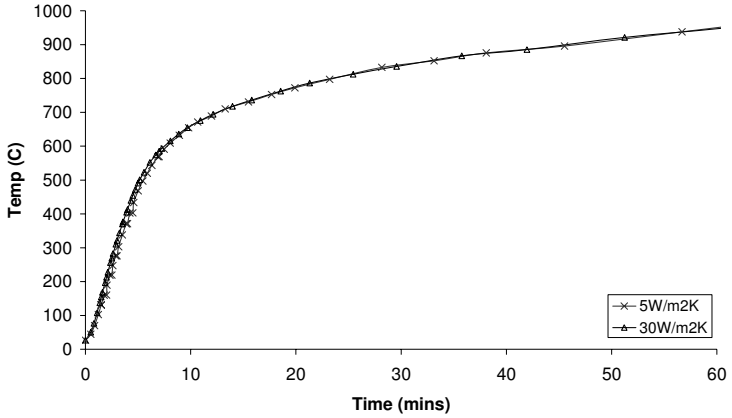

Fig. 3 - Temperature variation for different values of convective heat transfer coefficient

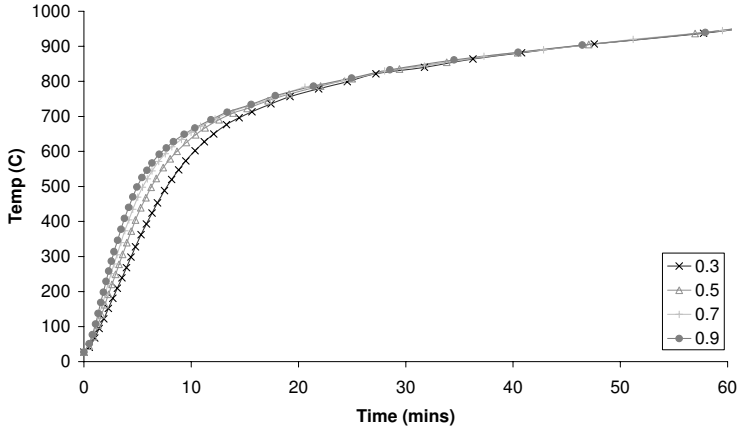

Fig. 4 - Temperature variation for different values of radiative emissivity

3. HEAT TRANSFER MODELLING

3.1. Experimental Tests

For the validation of the heat transfer modelling results from a recent experimental program at Manchester University were used[4]**.** One of the main aims of this program was to look at temperature variations across various connections.

The tests consisted of 4 beams approximately 1 metre in length attached to a column where the beam to column flange connections were flush end plates and the beam to column webs connections were fin plates. There was a reinforced concrete slab and adjacent steel decking above the connection which was connected with shear studs to the top of the beams. The connection was enclosed in a furnace and exposed to temperatures following the standard fire curve. The maximum temperature in the furnace was approximately 950^0C over a time of 60 minutes. The top side of the concrete slab was exposed to ambient air and the system was entirely unprotected.

In section 3.3 simple methods for temperature prediction are discussed and, for validation of these methods, both the experiments discussed above and results from a test carried out at BRE Cardington are used[5].

The test carried out at BRE Cardington, in January 2003, was on the 4th storey of an 8 storey building where one of the objectives was to record the temperature variations of the main structural elements, including across the connections. The fire within the compartment was provided by wooden pallets with 40kg of wood per metre square. The connection considered here was at an interior beam to column join. Here, the columns were protected to the underside of the beam while the beams within the vicinity of the connection and the connection itself remained unprotected.

3.2. Heat Transfer Modelling Parameters and Results

In light of the results of the sensitivity study detailed in section 2, the concrete slab has not been included. Also, the following parameters were used for the 3D heat transfer modelling of the two connection types:

- Heat Transfer Co-efficient[2]: 25 W/m^2.K
- Emissivity for connection area: 0.3
- Emissivity for remainder of model: 0.8

The heat transfer co-efficient and radiative emissivity factors were assigned to the exposed surfaces of the connection using the SURFACE FILM and SURFACE RADIATION TO AMBIENT interactions respectively. Within these interactions a sink temperature is specified which represents the temperature time profile within the furnace.

Over the course of the simulation the temperature was monitored at the connection near to a central bolt and at the edge of the bottom beam flange at a distance of 400mm from the connection.

For both connection types the temperatures predicted in the ABAQUS models have been plotted along side the experimental temperatures as shown in figures 5 and 6. In each case the temperatures predicted by ABAQUS are higher than those found in the experiments. However lower temperatures are predicted at the connections and the relative temperature difference between the two locations are comparable to those in the experiments.

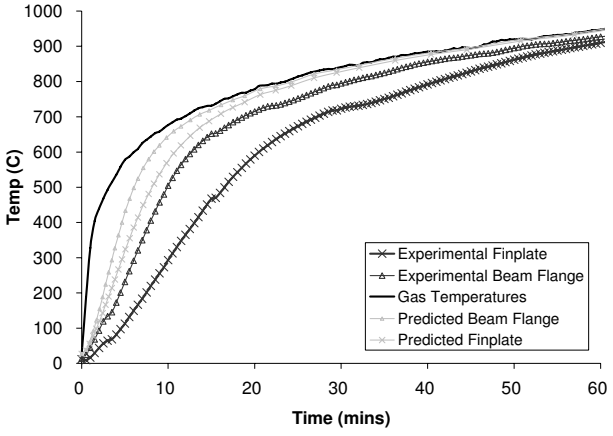

Fig. 5 - ABAQUS predicted temperatures for a Fin Plate Connection

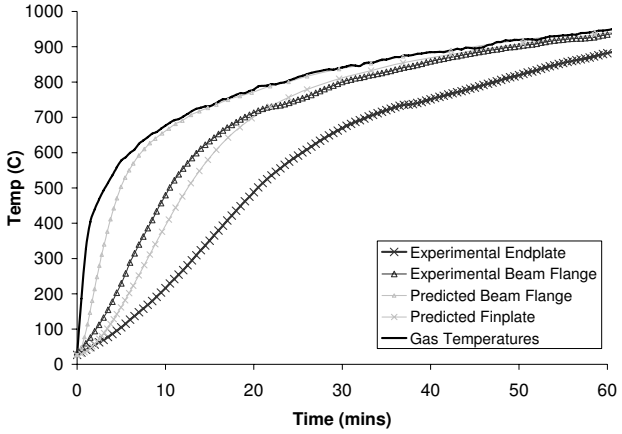

Fig. 6 - ABAQUS predicted temperatures for a Flush End Plate Connection

3.3. Lumped Capacitance and Eurocode Methods

The lumped capacitance method was used to calculate average temperatures of the connections. This method, for unprotected steel members, calculates the temperature rise over a series of finite time steps Δt, using equation 1[6].

$$\Delta T_s = \frac{\alpha}{C_s\,(W/D)}\,(T_f - T_s)\,\Delta t \tag{1}$$

where α is the heat transfer co-efficient, T_f is the furnace temperature, T_s is the steel temperature, C_s is the steel specific heat, D is the heated perimeter and W is the steel weight per meter.

For the purpose of calculating the temperature of the connections, and in order to take into consideration the large volume of steel at the connection, the equation has been modified to use the ratio of steel weight per meter square, V, to heated surface area, A. Temperature dependant values for the heat transfer coefficient and the specific heat of steel were used.

$$\Delta T_s = \frac{\alpha}{C_s\,(V/A)}\,(T_f - T_s)\,\Delta t \tag{2}$$

In figure 7, the temperature predicted using the modified lumped capacitance method has been compared to the average temperature of a fin plate connection. In this case the average temperatures are predicted well. However it is noteworthy that this experiment was carried out in a highly controlled environment.

The same modified lumped capacitance method was then used to calculate the average temperature for the flexible end plate and the results are shown in figure 8. The temperatures predicted are consistently higher than the experimental results and, therefore, conservative. However after about 30 minutes there is a reasonably close correlation between the predicted and experimental results.

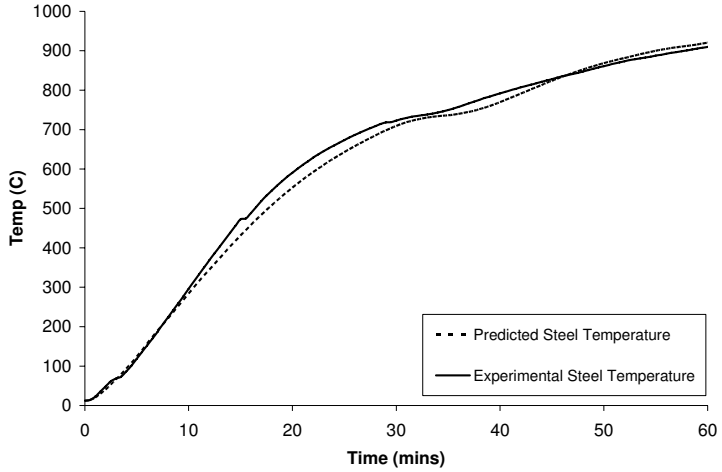

Fig. 7 - Modified lumped capacitance method for a fin plate

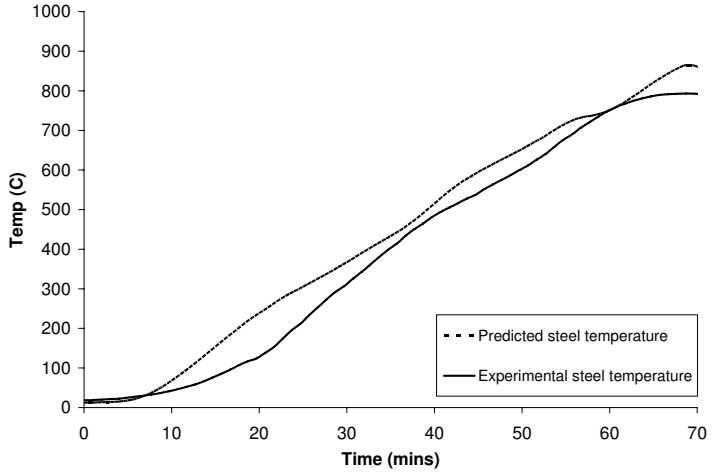

Fig. 8 - Modified lumped capacitance method for a flexible end plate

The method suggested in Eurocode 3 for calculating connection temperatures is to take a percentage of the midspan beam lower flange temperature. For a beam that is less than 400mm deep, these percentages are 62% at the top of the connection near the slab, 75% at mid height and 88% at the bottom[2].

This method has been used to predict the temperatures of the flush end plate and flexible end plate connection types, Fig. 9 and Fig. 10 respectively. The results for the flush end plate show that the temperatures for all locations on the connection are initially over conservative by up to 150^0C but are equally under conservative near the conclusion of the test and the trend of relative temperatures is also not shown.

The flexible end plate temperatures are well predicted for the first half of the experiments. However, after the first 30 minutes the temperatures calculated at the top of the connection are approximately 100^0C less than in the experiments and are similarly under conservative after around 40 minutes at mid depth of the connection. Data was not available to look at the temperatures at the bottom of the connection.

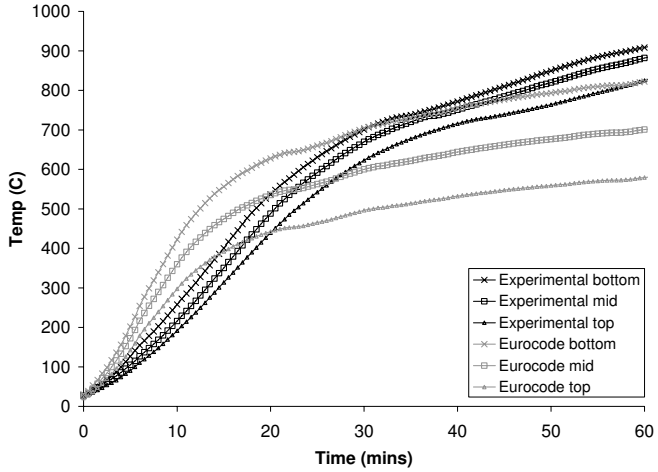

Fig. 9 - Eurocode method for a Flush End Plate

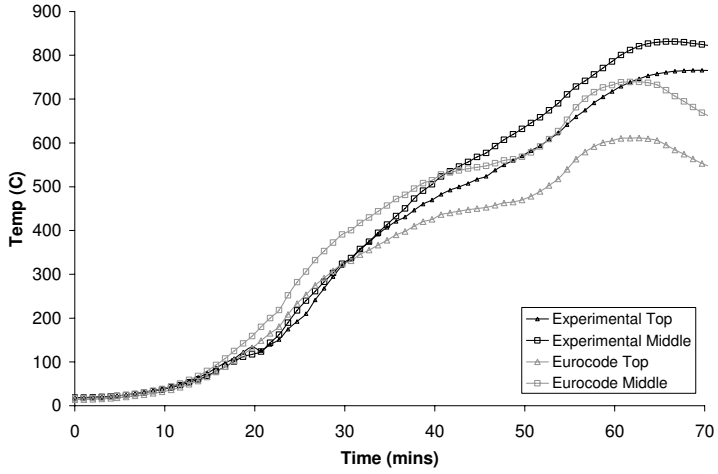

Fig. 10 - Eurocode method for a Flush End Plate

4. CONCLUSIONS

The prediction of temperature in connections using the finite element package ABAQUS and two simpler methods have been examined. Initially a sensitivity study was carried out with the main conclusions being:

- The inclusion of the concrete slab above the connection has a negligible effect on the majority of connection temperatures
- The variation of the convective heat transfer coefficient also has minimal effect
- The value of the radiative emissivity factor affects predicted temperatures mainly during the initial stages of the analysis

After taking into account the findings of the sensitivity study, two connection types were modelled in ABAQUS. While both analyses predicted higher temperatures than shown in the experiments, lower temperatures at the connection and the relative difference between the connection and beam flange temperatures was shown.

Two simple methods of predicting temperatures were then considered. The lumped capacitance method, based on the heated surface area of the connection and its volume, generally showed good correlation with average connection temperatures. However, this method can only be used to predict average temperatures and not the whole temperature profile.

The Eurocode suggests connection temperatures can be calculated as simple percentages of the midspan beam flange temperature. However, results show that this method is considerably under conservative in the latter stage of the experiments.

REFERENCES:

[1] CEN, (2006b) Eurocode 3: Design of Steel Structures part 1.2: General rules - Structural Fire Design, BS EN 1993-1-2:2005, Brussels: CEN, European Committee for Standardisation
[2] CEN, (2002) Eurocode 1: Actions on Structures part 1.2: General Actions – Actions on structures exposed to fire BS EN 1991-1-2:2002, Brussels: CEN, European Committee for Standardisation
[3] ABAQUS User's Manual, version 6.6, Providence, RI, USA
[4] Dai, X. H., Wang, Y. C. and Bailey, C. G. (2007) 'Temperature distributions in unprotected steel connections in fire' Proc. Steel and Composite Structures, Manchester, UK , pp. 535 – 540
[5] Lennon, T. and Moore, D. B (2004) 'Results and observations from full-scale fire test at BRE Cardington, 16 January 2003' BRE, Watford, UK
[6] Buchanan, A. H. (2002) 'Structural Design for Fire Safety' John Wiley & Sons, Chichester, UK
[7] Incropea, F. P., DeWitt, D. P., Bergman, T. L. and Lavine, A. S (2005) Sixth Edition 'Fundementals of Heat and Mass Transfer' John Wiley & Sons, Hoboken, USA

Structural Modeling and Analysis

A *VERY SIMPLE* METHOD FOR ASSESSING TALL BUILDING SAFETY IN MAJOR FIRES

ASIF USMANI[1]

ABSTRACT

The collapse of tall buildings in a densely populated urban setting is a scenario too terrible to contemplate. Buildings are routinely designed to resist this limit state under the extreme loading conditions of high winds and earthquakes etc. However the potential of multiple floor fires to cause such a disaster remains unrecognised in the profession as no current building codes require the consideration of this type of extreme loading. Previous work by the author and his students has demonstrated that the collapse of tall buildings in multiple floor fires is a distinct possibility as the mechanisms that can cause this are easily reproduced using a non-linear finite element analysis programme. This work has been extended by the author and his students to develop a simple analytical method for systematically assessing the collapse of exterior columns of tall buildings for any given fire scenarios. This paper considerably simplifies the method developed previously to the extent that the limit state of collapse under multiple floor fires can be checked even without the need to consider any particular "design" fire and with calculations that can be performed in minutes. This is based on the assumption that in major fires that affect multiple floors, it is quite likely that a number of floors will reach a state of deflection and reduced stiffness that the main load carrying mechanism will be that of catenary action leading to destabilising *pull-in* forces to be exerted on exterior columns. The paper will outline all the steps that must be carried out to check if the remaining structure (columns, floors, connections etc.) will remain stable under the action of the pull-in forces. It will also provide theoretical justification and discussion for all the steps and assumptions made in the assessment. Furthermore the method will be applied to a number of examples, including that of the WTC towers to check if those buildings were safe under major fires involving multiple floors.

[1] Professor, University of Edinburgh, School of Engineering and Electronics, The Kings Buildings, Edinburgh EH16 5AG, United Kingdom,
email: asif.usmani@ed.ac.uk

1. INTRODUTION

There have been relatively few studies of the collapses of the World Trade Centre buildings (chiefly WTC 1, 2 and 7) following the terrorist attacks on September 11, 2001. This is quite surprising given the continued proliferation of high rise buildings all over the world and in particular in the rapidly industrialising economies of Asia. In Europe and North America the engineering community (both academia and industry) have been somewhat shy of seeing these collapses as an engineering problem and have seemingly preferred to see it as chiefly a political problem. The strong linkage of international terrorism to these events and the personally felt shock may explain this attitude of denial in the west, but the absence or any significant investigation in the rest of the world, despite the boom in high rise construction, is less easily explained. With the obvious exception of Japan and possibly Singapore, Hong Kong and South Korea, the research culture in Asia is still maturing and has still to get to a position where it leads, rather than follows. What remains undeniable is the imperative of understanding these collapses in the most fundamental structural engineering sense in order to avoid such failures for other existing and future high-rise construction. This paper will discuss some of the work that has taken place at the University of Edinburgh over the last 5 years.

All the analysis carried out by the author and his collaborators at the University of Edinburgh have focussed on understanding the collapse of the WTC towers purely because of fire. The Edinburgh team have had considerable experience in using computational modelling to understand whole structure behaviour in fire, beginning with the modelling of the full-scale fire tests in Cardington carried out in the mid 90s[1]. This led naturally to applying the same methodology to understanding the collapse of the WTC towers and first hypothesis based on this work was published in 2003[2], followed by a refinement[3]. Further investigation with larger models[4,5], produced another collapse mechanism, however the two were later identified to be of a similar nature, as will be shown in the following sections. The only other significant piece of research on these collapses has been carried out by the official WTC investigation team at the National Institute of Standards and Technology in Maryland, USA[6]. The results from the Edinburgh and NIST work are not strictly comparable as the latter is a forensic investigation taking into account the damage caused by the aircraft and the detailed modelling of the moving fires, while the former assumes an undamaged structure subjected to a large range of simplified fires. Therefore the NIST results are very specific to the WTC 1 & 2 structures while Edinburgh work is much more generally applicable to understanding tall building behaviour in multiple floor fires. This work has now been extended to produce a new and relatively simple methodology for quantitatively estimating the limit load capacity of tall buildings for specified fires without resorting to finite element methods. This will eventually provide a framework for routine assessment of tall building safety in multiple floor fires and hopefully encourage engineers to confront this risk head-on instead of pretending that it doesn't exist.

The following sections will briefly describe the two tall building collapse mechanisms discovered (weak floor collapse and strong floor collapse) in the WTC models, their generalisation to ordinary multi-storey frames and finally the outline of the methodology for determining whether a particular collapse mechanism may or may not occur given a frame, its loading and fire scenario.

2. WEAK FLOOR COLLAPSE MECHANISM

A finite element model of a typical 2D slice of 12 storeys of the WTC 1 & 2 frames was created[2] using the structural information provided in the FEMA report[7], as shown in Figure 1.

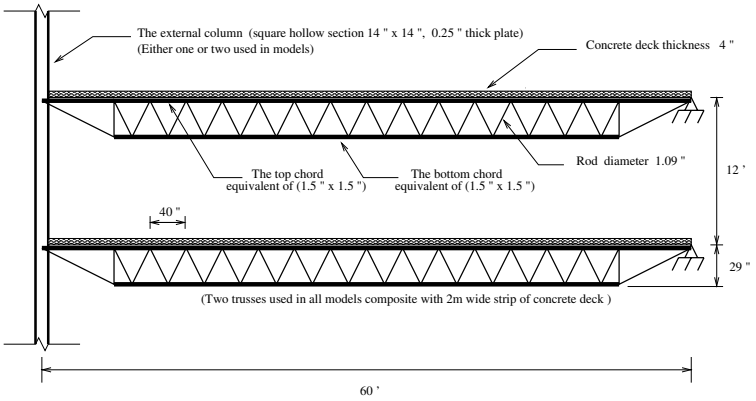

Figure 1: Structural model details and dimensions (feet and inches)

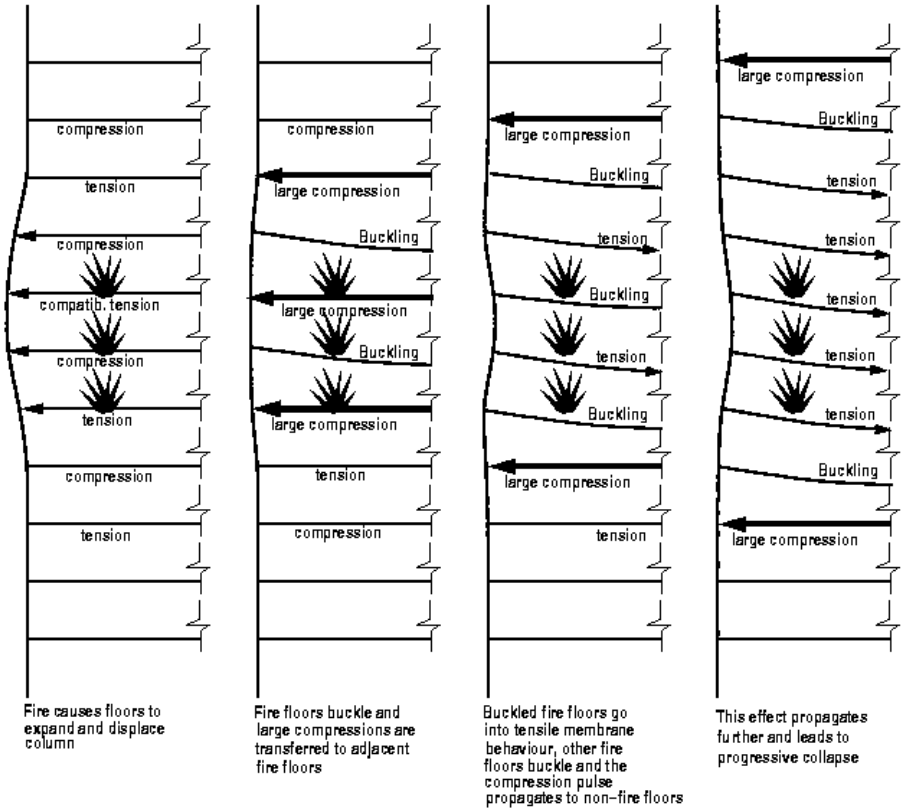

Figure 2: Weak floor progressive collapse

The failure mechanism obtained from this model is shown in Figure 2. This mechanism progresses by sequential overloading of slender floors in axial compression and flexure, spreading the collapse from the fire floors to non-fire floors and then from one failing floor to another. Such a sequence would clearly be arrested if any floor is able to sustain the applied compression and flexure loading without buckling, pointing to the need for strong and stiff floors at suitable intervals over the height of the building, which can sustain such loading.

3. STRONG FLOOR COLLAPSE MECHANISM

When Flint[4] extended his analyses to study larger models, a new and different failure mechanism was discovered. In this mechanism the floors are strong enough to resist the forces of compression and flexure exerted on them because of the membrane (or catenary) action of the fire floors, thus preventing a run-away progressive collapse indicated by the weak floor mechanism. However collapse can still occur as shown in Figures 3 and 4, obtained from analysing 2D and 3D models respectively of structures similar to the WTC towers.

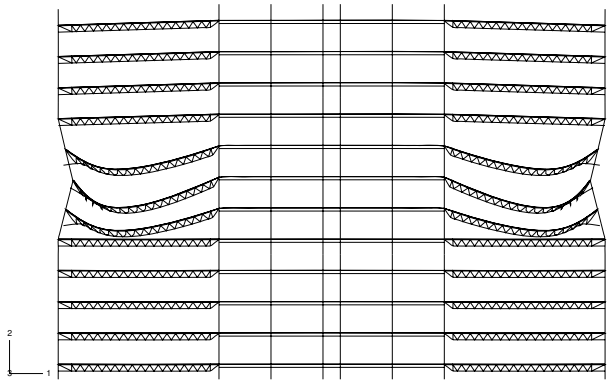

Figure 3: Strong floor localised collapse that will initiate progressive collapse (2D Model)

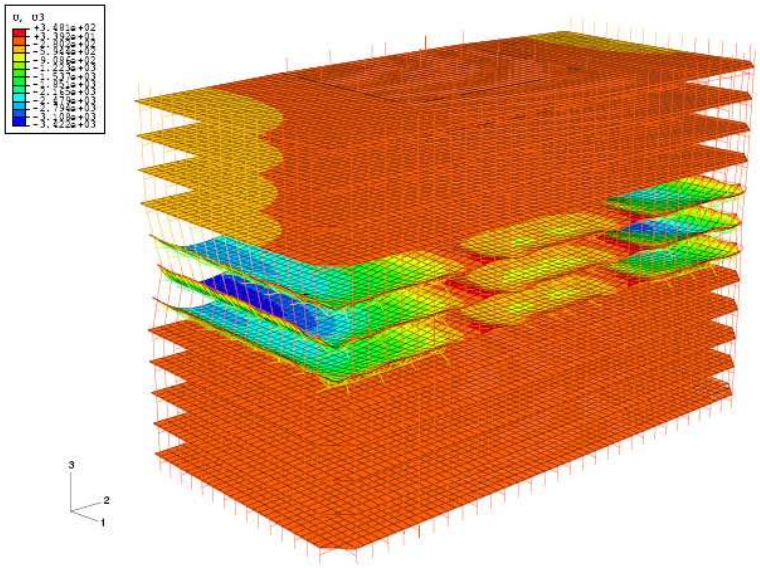

Figure 4: Strong floor localised collapse that will initiate progressive collapse (3D Model)

In these models the pull-in forces exerted on the column by the fire floors acting as membranes causes the formation of 3 plastic hinges (column reaches full plastic yield through a combination of axial compression and bending), thus initiating collapse. This collapse is initiated by localised hinge formation, which is not inherently progressive like the weak floor mechanism, however once the three hinges are formed and there are a considerable number of floors above the location of the fire, then the loads from the superstructure will perpetuate the collapse. If there are only a few floors above the fire floors (say the fire is near the top), the collapse may only be local or not occur at all.

4. GENERIC TALL BUILDING FRAMES IN MULTIPLE FLOOR FIRES

The two main failure mechanisms established in the previous sections are illustrated in Figure 5. Figure 5(a) shows a mechanism that would occur if a stiff column was supported by a floor system relatively weak in membrane compression and bending[2,3]. If however the floors are stiff enough, a plastic collapse type mechanism establishes[4] as a result of the combined compression and bending, as in Figure 5(b). These mechanisms are based on analyses that assume that no connection failure occurs. This assumption allows the focus to be on "global" behaviour as it can be reasonably assumed that this would produce a useful upper bound collapse scenario.

Local effects such as connection failure, local cracking of concrete, failure shear connectors and their endless permutations could potentially produce a whole range of alternative collapse scenarios, which could reasonably be assumed to produce earlier failures than the upper bound scenarios (although this is not by any means certain). In a design context local effects can really only be considered properly in a probabilistic rather than deterministic manner.

The previous analyses were carried out using models close to the WTC towers (using tubular column and truss members for the floor support). This work was extended[8,9] by investigating more "generic" tall building frames made of standard universal beam and column sections to determine whether the same collapse mechanisms are obtained.

A more conventional composite steel frame model using universal beam and column sections respectively was analysed. The beams are laterally restrained by the stiff concrete core but are free to rotate. They are fully fixed to the column, which in turn is fixed at the bottom but restrained only in the horizontal direction at the top. The concrete slabs are designed to act compositely with the beams and are connected with multiple point constraints. All sections are modelled using 2-D beam elements. The structure is subjected to loading on the beams and the column. Each beam supports a UDL which includes the self weight of the concrete slab as well as the imposed load. The column is subjected to a point load which represents the additional floors above the analysed structure. To compare the behaviour of the models several parameters were changed to obtain a wide variety of results. This includes changing loads, section sizes and spans. The assumed material properties are in accordance with Euro Code 3-1. The fire is assumed to affect three floors (floors 6, 7 and 8). The steel is assumed to be unprotected and thus has a uniform temperature equal to that of the fire. The maximum and ambient temperatures are taken as 800ºC and 20ºC respectively with an exponential increase and the columns are protected and are restricted to a maximum temperature of 400 ºC as in reference 2

Figure 6 shows the deformed collapsed shapes for two different models, essentially reproducing the two mechanisms shown in Figure 5. The weak floor mechanism shows that the column forces the floor below the fire floors to buckle, thus increasing the loading on the floor below and starting a progressive collapse. The strong floor mechanism shows a clear plastic collapse with three hinges forming at the floors above and below the fire floors and at the centre fire floor. It also shows that only the fire floors deflect and that no lateral movement of the column

occurs at locations away from the fire floors. This coincides with the three hinge failure assumption that the collapse is localised.

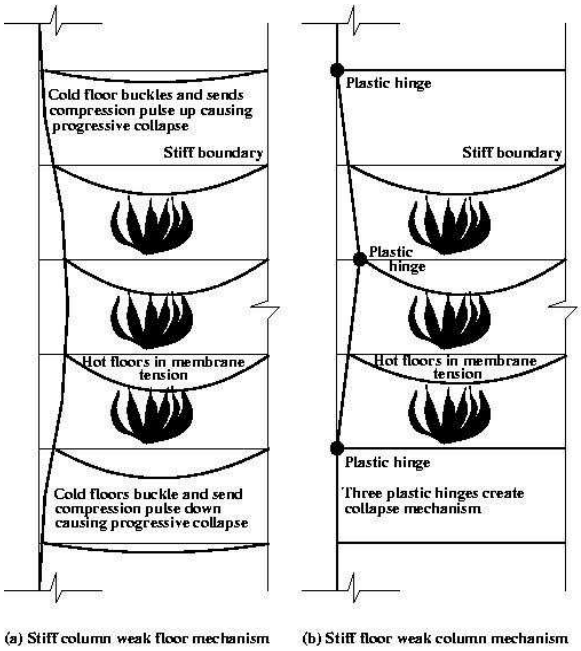

Figure 5: Suggested collapse mechanisms for tall buildings in fire

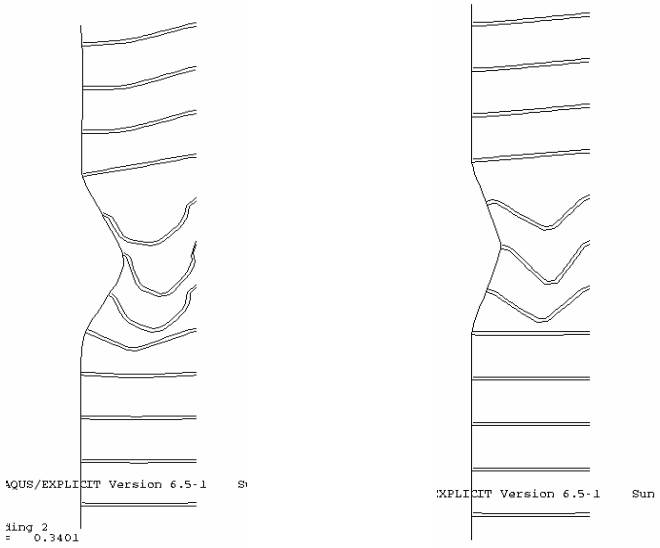

(a) Weak floor mechanism (b) Strong floor mechanism

Figure 6: Deflected shapes with a floor buckling and column plastic collapse respectively

5. VERY SIMPLE ASSESSMENT METHOD

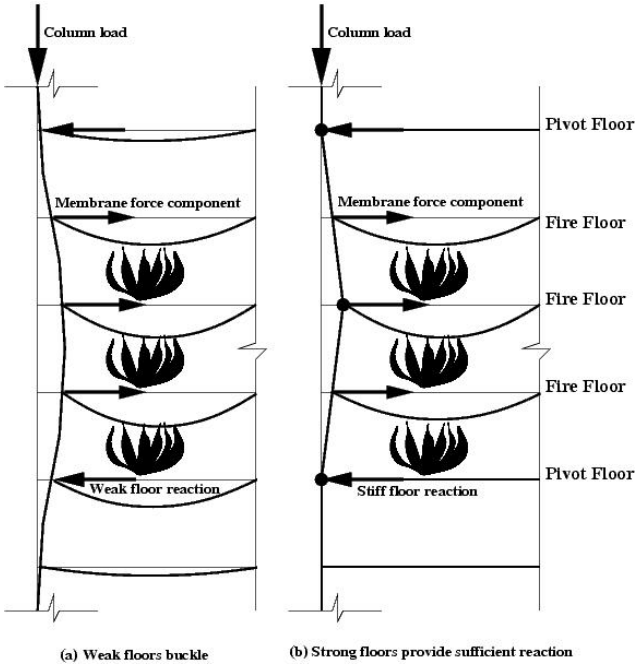

Figure 7: Fire induced collapse of tall building frames

Figure 7 illustrates a simple method for assessing the stability of columns in tall buildings in multiple (or single) floor fires. A two part paper with full details of the method has been submitted to the Structural Engineer[10]. The complete set of steps involved may be described as follows:

A. Structure and Thermal Loading

Based on appropriate risk based criteria, establish the following:

a. An adequate two-dimensional representation of the structural frame, including the exterior columns and the adjacent structural framing, which is assumed to be restrained in the interior by a stiff core;
b. The time dependent magnitude of fire in the compartments adjacent to the exterior columns of the structure (using one of BS476, ISO834, ASTME119 or Eurocode 1 based curves or other more advanced fire models);
c. The number of floors involved in the fire;
d. The temperature distribution in the structural members of the frame (columns and floor systems) at the end of the heating curve using appropriate code formulas or tables or heat transfer calculations;
e. Convert the temperature distribution at the end of the heating phase to an equivalent uniform temperature and through depth thermal gradient.

B. Floor Mechanical Loading

Determine the mechanical state of the floor system after application of the design thermal input (i.e the reduction in strength and stiffness of the component materials and the change in geometry) ignoring the mechanical loading, and follow these steps:

a. Check if the applied uniformly distributed load (using appropriate reduction factors allowed by code) on the floor can be resisted through residual flexural capacity – if this is the case, stop the analysis as the structure can not fail in either of the two collapse mechanisms
b. If the design udl is greater than the flexural resistance of the floor, check to see if the udl can be resisted by the floor system through catenary action, here the concrete tensile resistance is ignored and only the reinforcement and any composite structural steel are assumed to provide catenary resistance. If the floor system is unable to provide the tensile resistance (limited by rupture of reinforcement and fracture of structural steel connection) than the floor system fails, leading potentially to progressive collapse. The floor system should be redesigned until it is able to resist the udl through flexure or catenary action.
c. Determine the "pull-in" forces applied on the column by the fire floors sagging in catenary action.

C. Column Mechanical Loading

Using the catenary "pull-in" forces applied by the floors, obtain the moments induced in the columns at the "pivot" floors (adjacent to the fire floors) and in the centre of the height between the pivot floors. Use an approximation of the column internal displacement to calculate the additional P-δ moments experienced by the columns.

D. Check for Weak Floor Collapse Mechanism

Calculate the reaction of the pivot floors as shown in Figure 1 counteracting the membrane "pull-in" forces. If the floor membrane is unable to provide the reaction calculated, a weak floor failure becomes possible. This failure is relatively less likely to occur as it requires the pull in forces from many floors on fire. However a combination of the membrane compression induced in the floor and the additional moment imposed on the sagging floor by the P-δ effect and by the rotation of the column may also cause a combined bending and compression failure of the floor with only a few floors on fire, also leading to a weak floor failure.

E. Check for Strong Floor Collapse Mechanism

Check the temperature dependent moment-force interaction diagram for the column to ensure that the column has not reached yield surface (and thus formed a plastic hinge). If this is the case at all three locations (pivot floors and middle fire floor) then the strong floor failure mechanism identified can occur as the three hinges form a mechanism.

6. APPLICATION EXAMPLE

Flint et. al.[5] have published the results of their computational analysis of 2D models of WTC (as shown in Figure 3). This analysis shows a strong floor type collapse mechanism with hinges developing in columns. A highly practical and simplified version of the method is presented here to check whether the failure predicted by the finite element model can be reproduced here.

This analysis uses the simple formulas provided in reference 11 to calculate the thermally induced deflections in the 18 meter span of the truss-supported WTC floor system based on the temperature distributions shown in Figure 8. As discussed in reference 2, when exposed to fire the slab first pushes the column out, and then as the thermal gradient effect become dominant and the structural steel loses its strength and stiffness, the floor membrane begins to hang in tension anchored to the core on one side and supported by the perimeter column wall on the other. The horizontal component of the tensile force in the slab (***H***) begins to pull the column wall in, as schematically represented in Figure 9.

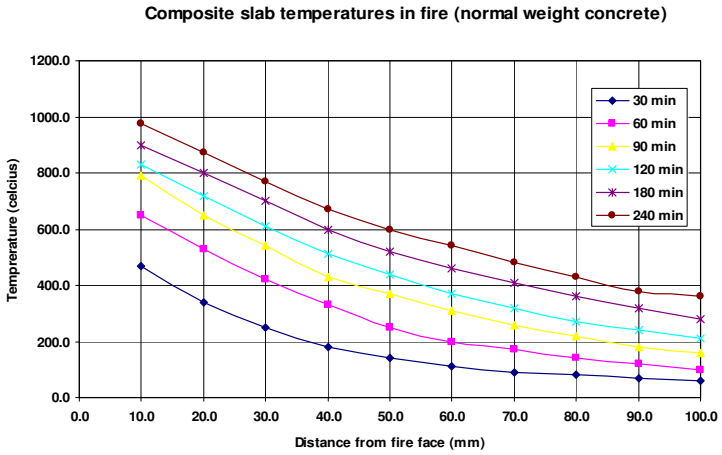

Figure 8: Temperature evolution in composite slabs (see reference 12 for source)

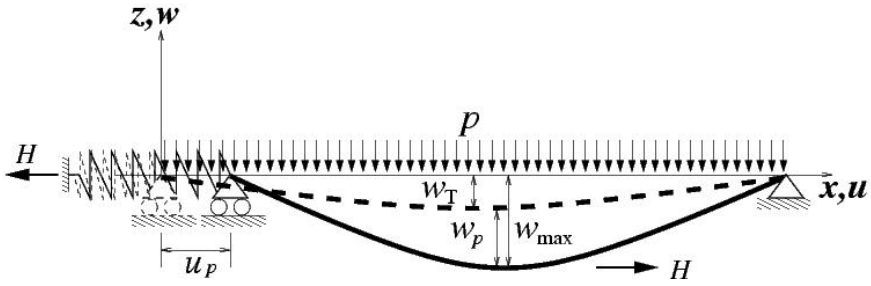

Figure 9: An isolated sagging floor pulling the column (represented as spring)

The force increases as the flexure capacity reduces and reaches a peak value at some value of the floor deflection at midspan (say w_{max}), beyond this point any further deflections reduce the tensile force. The gravity load on the floor system contributes to the deflection, but the predominant portion of this is caused by the thermal gradient. From Figure 8 this can be estimated to be approximately 5 ^{o}C/mm. Over an 18 meter span this translates to a deflection of about 2500mm. However, this deflection accompanies a reduction in span of about 800mm (assuming a 350 ^{o}C average temperature increase, corresponding to a 90 minute fire). The reduction in span will naturally be resisted by the column wall. The formulas for calculating this exactly (and hence the correct floor deflection) can be found in reference 10. From a number of analyses a thumb rule of span(***L***)/10 can be used to for the floor midspan deflection, i.e. 1800mm.

The udl ($\boldsymbol{p}$) on the floor is assumed to be 3 kN/m^2. The column section as modelled is shown in Figure 10. This was necessary as the columns were 1 meter apart and the trusses are two meter apart in the structure. Therefore the udl applied to the member representing the floor was 6kN/m.

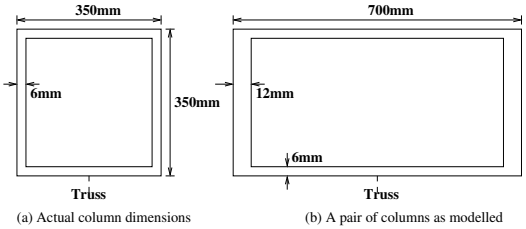

Figure 10: Columns as modelled

Equating the moment $\boldsymbol{pL}^2/8$ to $\boldsymbol{Hw}_{\mathbf{max}}$, the value of $\boldsymbol{H}$ can now be calculated to be $1.25\boldsymbol{pL}$ or numerically 135kN. Now the stability of the perimeter column can be assessed for a three floor fire as discussed below.

Figure 11 shows a simple model of the column, reduced by using symmetry at the point of the middle hinge and truncated at the floor below the lower pivot floor. The symmetry point is assumed to be the 97th floor (WTC tower 1) with 13 floors above that point imposing an estimated load of 700kN at that point.

The model of Figure 11 requires a 2nd order analysis because of the interaction between the axial (representing the load of the superstructure) and lateral loading (representing the tensile pull-in forces from the floor system). This was carried out to obtain results as follows:

1. Lateral displacement at A = 97mm
2. Moment at A = 462.6 kNm
3. Moment at B = 570.4 kNm

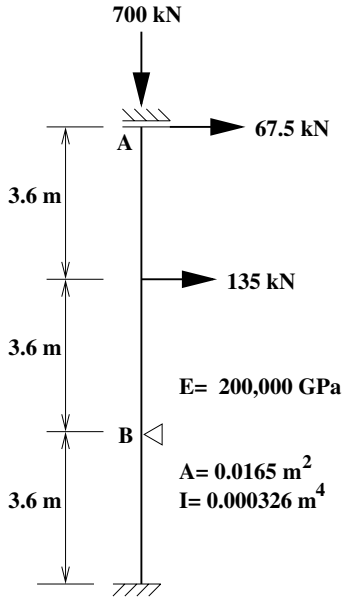

Figure 11: Simple analysis model

Assuming the yield stress of the column to be 300 MPa (the WTC steel ranges from 250 to 690 MPa) the full plastic moment capacity (Mp) of the column section is 639 kNm and its compressive strength (Pp) is 4954 kN. The linear column interaction formula ($M/Mp+P/Pp<1.0$) can be used to conservatively estimate whether the column capacity will be sufficient for this, where M is 570.4 kNm and P is 700 kN. This gives a value of 1.03 which is marginally greater than 1.0 however it does clearly suggest that a hinge is very likely to be formed at point B, which will inexorably lead to a hinge at A because of the P-δ effect, leading to strong floor collapse as discussed earlier. Although the steel yield stress used in this analysis to be on the low side (assuming that the steel on the top level will perhaps be lower strength due to reduced loading), no further reduction is assumed because of the effect of fire and the full ambient value is used. This is not an unreasonable assumption as the perimeter columns has three sides exposed to the atmosphere, however some temperature increase will be expected as fires burn hottest near perimeter openings, i.e. adjacent to the columns.

CONCLUSIONS

The collapse of tall buildings in densely populated urban setting is a scenario too terrible to contemplate. Buildings are routinely designed to resist this limit state under the extreme load conditions of high winds and earthquakes etc. however the potential of multiple floor fires to cause such a disaster remains unrecognised in the profession as no current building codes require the consideration of this type of extreme loading. It is clearly demonstrated in this paper that collapse of tall buildings in multiple floor fires is a distinct possibility as the mechanisms that can cause this are easily reproduced using a non-linear finite element analysis programme, which the real events of September 11, 2001 saw three very tall buildings collapse within hours of each other primarily because of fire.

The simple analysis carried out further confirms the computational models and points to a significant vulnerability in the design of the WTC structure for large fires, albeit no regulations required this, and still don't, which in the light of recent research such as this seems unfortunate.

This paper clearly shows that the assessment of the collapse potential of a frame in multiple floor fires need not always require rigorous, labour intensive and time consuming finite element analyses. It is possible for frames of relatively regular geometry to be assessed using this simple, cost effective and quick method. Therefore there is no real excuse for ignoring the risk that multiple floor fires pose.

REFERENCES

1. Edinburgh University (2001), "Partners in Technology Report: Behaviour of steel framed structures under fire conditions", *Main Report*, University of Edinburgh.
2. Usmani, A. *et. al*. (2003) *How did the WTC Towers Collapse? A New Theory,* Fire Safety Journal, vol. 38, pp. 501-533
3. Usmani A. (2005). *Stability of the World Trade Center Twin Towers structural frame in multiple floor fires*. Journal of Engineering Mechanics, ASCE, vol. 131, pp. 654-657.
4. Flint, G.R. (2005). *Fire Induced Collapse of Tall Buildings*. PhD thesis, University of Edinburgh.

5. Flint, G.R. *et. al*. (2007). *Structural response of tall buildings to multiple floor fires*. Journal of Structural Engineering, ASCE, vol. 133, pp. 1719-1732.
6. NIST (2005). *Global Structural Analysis of the Response of the World Trade Center Towers to Impact Damage and Fire*. Technical report NIST NCSTAR 1-6D.
7. FEMA (2002). *World Trade Center Building Performance Study: Data collection, preliminary observations and recommendations*. Technical Report FEMA 403.
8. Usmani, A. *et. al*. (2006). *Tall building collapse mechanisms initiated by fire*. Proceedings of the 4th Workshop on Structures in Fire (SiF'06), Aveiro, Portugal.
9. Roben, C. *et. al*. (2007). *Tall building collapse mechanisms initiated by fire – Part I: Analysis.* Submitted to the Structural Engineer.
10. Lange, D. et. al. (2007). Tall building collapse mechanisms initiated by fire – Part II: Design method. Submitted to the Structural Engineer.
11. Usmani, A. *et. al*. (2001). *Fundamental principles of structural behaviour under thermal effects*. Fire Safety Journal, vol. 36, pp 721-744.
12. Structural Fire Engineering: One Stop Shop, University of Manchester, www.mace.manchester.ac.uk/project/research/structures/strucfire/

THE IMPACT OF VARIOUS MATERIAL MODELS ON STRUCTURAL FIRE BEHAVIOUR PREDICTION

YNGVE ANDERBERG[1]

ABSTRACT

It is a well-known fact that the material behavior model applied in the structural analysis often has an important influence on the fire behavior prediction. This paper illustrates for concrete as well as for steel structures what differences in behavior you may obtain dependant on the material models chosen.

Fire behavior models of concrete or advanced calculation models (EN 1992-1-2) have four main strain components: thermal strain, instantaneous stress-related strain, creep strain and transient strain. Normally the creep strain is of minor importance but it is most often for simplification reason incorporated in the transient strain. The transient strain is time independent and occurs at a temperature increase under a simultaneous presence of load. The transient strain is very much dominating and cannot most often be neglected in the understanding of the real fire behavior of concrete structures. Deformations, restraint forces and bending moments cannot be realistically predicted by computer programs without taking into account the transient strain in the concrete behavior model. It is also noticed that the transient strain sometimes has a negligible influence on certain structures as concerns fire collapse time and on the result of a fire engineering design based on a limit state. It is discussed at which situations the transient strain has an impact on the structural fire behavior prediction and the fire engineering design of concrete structures.

Fire behavior models of steel have as a sufficiently accurate assumption three main strain components: thermal strain, instantaneous stress-related strain and creep strain. It is however often assumed that the creep of steel is incorporated in the stress-strain relationship at different temperatures in a simplified manner as presented in the Eurocodes, [13-15]. If that model is applied for steel the creep or relaxation effect on the behavior cannot be separated from the total behavior which can be of inconvenience in the understanding of the behavior and the amount of relaxation of pre-stress level in concrete structures. The prediction of structural behavior will also suffer from that simplification.

[1] Docent, PhD, Flight & Safety Design International AB, Vipemöllevägen 111, SE-224 66 Lund, Sweden, email: fsdint@telia.com

1. INTRODUCTION

The understanding of the mechanical behaviour of concrete at high temperature was until the mid of the 1970s very poor. All attempts to use elastic theory when calculating the stress distribution of a concrete member failed. If a concrete member is unloaded and restrained against thermal expansion during heating and the elastic theory is applied, failure will occur at about 350 °C due to high thermal stresses. This behaviour was of course not true. An unloaded and restrained specimen will never fail by itself.

The main key in understanding the mechanical behaviour of concrete exposed to fire was discovered during extensive research in Sweden[1,2] and Germany[3] in the 1970s. An unknown strain component called "transient strain" a nonrecoverable and dominating compressive strain develops during the first heating of concrete under simultaneous load and is time independent. This strain was also discovered later by Khoury[4,5] in 1983 and 1985.
The transient strain contributes to a significant relaxation and redistribution of thermal stresses in heated concrete structures.

A complete constitutive law of concrete at high temperatures was published in 1976[2,6] and used for the first time to obtain a realistic analytical prediction based on a true constitutive model of concrete and steel. The predictions were successfully compared with a great number of fire tests on statically indeterminate concrete slabs which was also published in 1976[6]. The software used for this purpose was a further development and extension of the computer program "Fires-RC" developed by Becker & Bresler within "Fire Research Group" at University of California, Berkeley in 1974[7]. An improved structural software called "CONFIRE" was developed by Forsén 1982[8]. This software was based on the constitutive law of concrete developed in 1976.

Better understanding of the mechanical properties of concrete and new computer program for predicting structural behaviour opened the possibilities to apply a performance-based design and to develop simplified design methods and codes for evaluating fire resistance of concrete structures in general. The result of that was a sectional analysis approach "500°C isotherm method". This hand calculation method was presented at a FIP-congress in London 1978[9]. The method was then introduced in the CEB-Bulletin Information No 145 "Design of concrete structures for fire resistance"[10] in 1982 and later on in the CEB-FIP Model Code.

When modelling the structural behaviour of concrete, independently of how sophisticated FE-software is used, the constitutive model applied must reflect the true behaviour of concrete at high temperatures. Unfortunately this is not always the case when scientists publish their analytical predictions of the behaviour of concrete structures exposed to fire.

2. TEST PROCEDURES AS BASIS FOR MODELLING MECHANICAL BEHAVIOR

When developing an analytical behaviour model of building materials at high temperatures one needs a great amount of data on the stress and deformation characteristics at different temperature histories. The model must be based on reliable and well-documented results from tests carried out under well-defined and controlled conditions. A careful distinction must be made between steady state (stabilized) and transient state conditions. It is important to have in mind the different test procedures for determining the mechanical properties.

There exist two main groups of tests, steady state tests and transient tests. Material properties measured are closely related to the test method used. It is therefore of great importance that the test conditions are well defined.

During a fire situation the material is normally subjected to transient processes varying temperature and stress, and tests cannot be used solely to explain the stress-strain characteristics of steel in all cases.

Mechanical properties of concrete and steel can be established by following a number of different test procedures. The three main test parameters are the heating process, application and control of load, and control of strain. These can have constant values or be varied during testing, giving steady state or transient conditions depending on the heating procedure.

Six practical regimes[11] which can be used for determining mechanical properties are illustrated in Fig.1. Properties in these regimes are as follows:

Steady state tests

- stress-strain relationship (stress rate controlled)
- stress-strain relationship (strain rate controlled)
- creep
- relaxation

Transient tests

- total deformation, failure temperature (stress control)
- total forces, restraint forces (strain control).

Steady state tests are characterized by a heating period, t_H, and a period of time, t_S, during which the temperature of the specimen is stabilized before any load is applied. The time t_S depends on the size of the specimen, but is usually not more than 0,5h. The strain measured before the load is applied corresponds to the thermal expansion.

Transient temperature tests or non-steady state tests are characterized by a varying temperature and a simultaneous load. The load can be applied before heating or developed during heating by restraint against thermal expansion. These two types of transient tests are carried out with load and strain control, respectively.

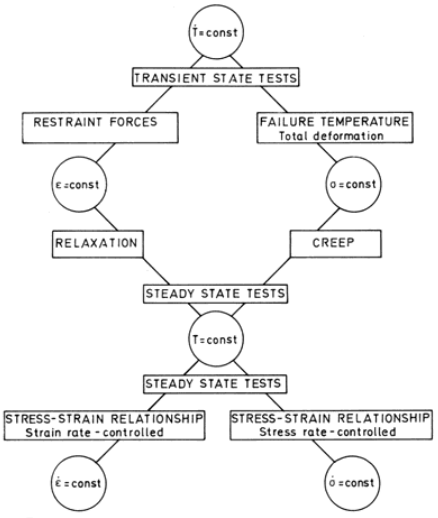

Fig. 1- Different testing regimes for determining mechanical properties[11]. RILEM 44 –PHT (1983)

The principal importance of the stress history on the total strain in a transient process, where the rate of heating T is constant, is illustrated in Fig. 2. Curve 1 corresponds to a constant stress σ_0 during heating up to temperature T, and then a stress σ_0 until temperature T_2 and curve 2 to a stress $\sigma_0/2$ up to temperature T_1, and then a stress σ_0 until temperature T_2 is reached. The difference in total stress is due to the different stress history and a different transient (concrete) or creep strain (steel) developed during the transient process.

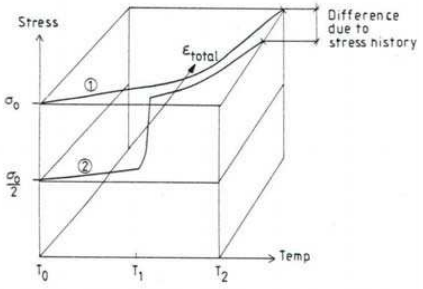

Fig. 2 - Principal influence on total strain on concrete at different stress histories at a transient process.

Curve 1: $\sigma = \sigma_0 \quad T_0 \le T \le T_2$
Curve 2: $\sigma = \sigma_0/2 \quad T_0 \le T \le T_1 \quad ,\sigma = \sigma_0 \quad T_1 \le T \le T_2$

3. BEHAVIOR MODEL OF CONCRETE AT HIGH TEMPERATURES

There exist mainly two constitutive models of concrete for structural analysis at high temperatures which take into account the behaviour under transient conditions:

Model 1: Anderberg Y. & Thelandersson S., 1976[2,6]

Model 2: Khoury G. et al, 1983, 1985[4,5]. This model became fully developed for structural calculations in 1991 by Terro[12]

3.1 Model 1

In model 1 the total strain of concrete (silicious) is the sum of four strain components derived on a phenomenogical basis. The constitutive law can be expressed as follows:

$$\varepsilon_{tot} = \varepsilon_{th}(T) + \varepsilon_{\sigma}(\sigma, T) + \varepsilon_{tr}(\boldsymbol{\sigma}, \sigma, T) + \varepsilon_{cr}(t, T, \sigma) \qquad (1)$$

where

σ =	stress	$\boldsymbol{\sigma}$ =	stress history
$\varepsilon_{tot}(T)$ =	total strain	$\varepsilon_{th}(T)$ =	thermal strain
$\varepsilon_{tr}(\sigma, T)$ =	transient strain	$\varepsilon_{cr}(t, T, \sigma)$ =	creep strain or time dependent strain
$\varepsilon_{\sigma}(\sigma, T)$ =	instantaneous, stress-related strain based on σ-ε relationship		

Transient strain above 100°C is essentially a function of temperature and not of time. This strain is dominating and much larger than the elastic strain which can be observed in Fig 3. The prediction of total deformation at different load levels as function of temperature is presented in Fig 4 and the agreement with measurements is excellent.

Any structural analysis of heated concrete that ignores transient strain will, therefore, be wholly inappropriate and will yield erroneous results, particularly for columns exposed to fire. This phenomenon is still not fully appreciated by structural engineers and should be incorporated more fully into standards and design codes.

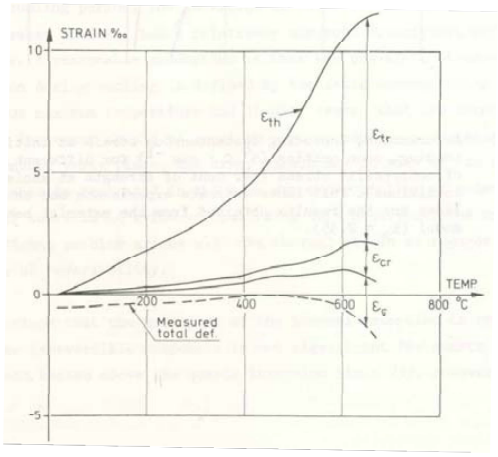

Fig. 3 - Relation between different strain components when the model is applied to a relative stress of 35% of ultimate stress[2]

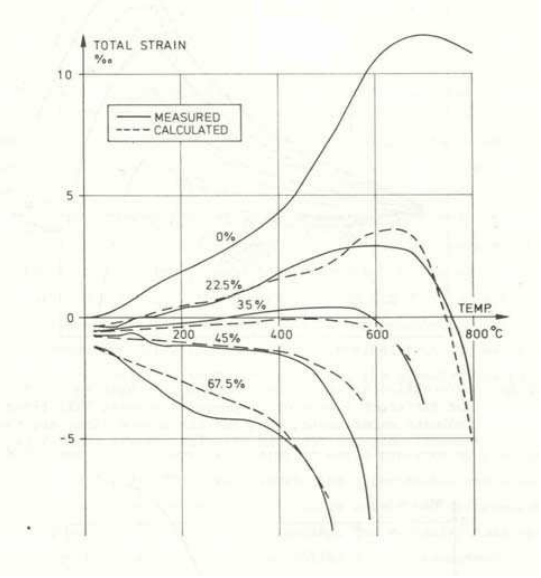

Fig. 4 - Deformation upon heating for different levels of relative compressive stress. Full line curves indicate experiments and dashed line curves prediction with the model[2]

Does concrete have a memory? Is there any influence of load history on stress-strain curves? The answer is yes and can be seen in Fig 5, illustrating the stress-strain relationship at different temperatures with and without the effect of preloading. The preloading is applied before heating starts and heating continues until a stabilised temperature is attained. After that the load is removed, the stress-strain relationship is measured. If concrete is heated without load, tests consistently show the modulus of elasticity or stiffness to reduce considerably with increase in temperature and even by a larger proportion of the initial value than the compressive strength (Fig 5a). Both the compressive strength and elastic modulus reduce far less with increase in temperature for the concrete heated under load (Fig 5b). This evident load history effect is very important and has been observed also for high performance concrete.

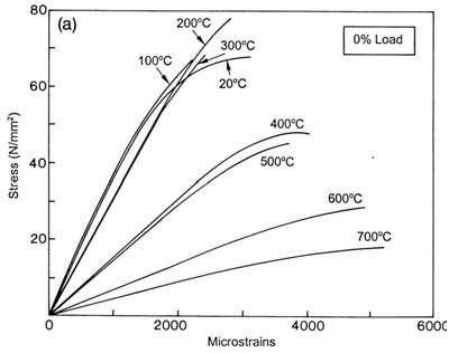

Fig. 5a Stress-strain relationship at different temperatures without any preloading

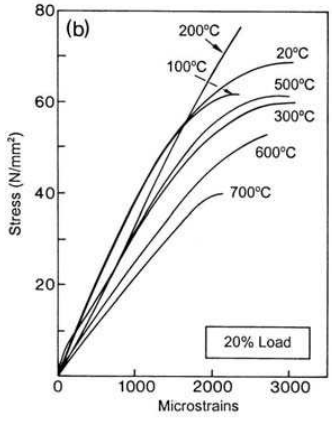

Fig. 5b Stress-strain relationship at different temperatures at 20% preloading

An example of accurate prediction of the deformation behaviour at fire compared with measured results is illustrated in Fig 6. This fig indicates a very good agreement between predictions and measurements where heating curve may have a drop in temperature and a cooling phase and the load level (relative stress) is varying during the test.

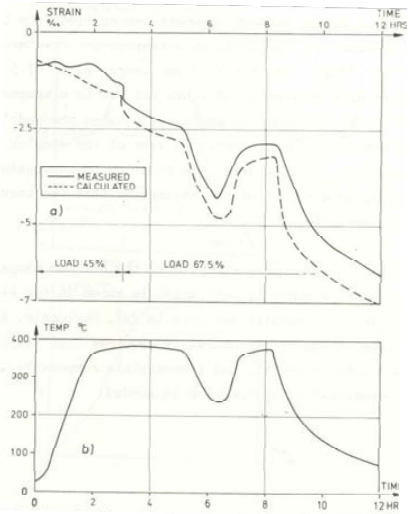

Fig. 6 - Predicted and measured deformation. The temperature versus time is shown in the lower diagram. Load level is changed after 4 hours from 45 to 67 %[2]

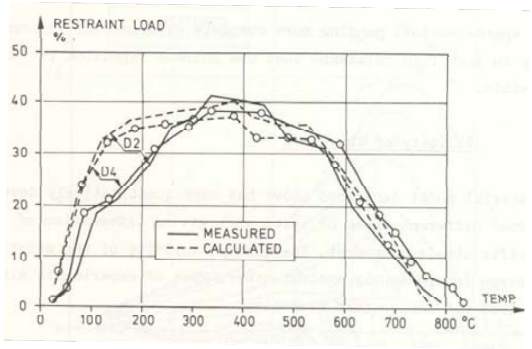

Fig. 7 Predicted and measured restraint load (in % of the ultimate load at ambient conditions) as a function of temperature for specimens heated under fully restrained expansion[2]

In this example the account of load history effect in the prediction had a considerable influence and contributed to a successful calculation. If a concrete specimen is restrained against longitudinal expansion axial restraint forces will develop. Due to the discovery and analytical formulation of the transient strain and the load history effect the prediction of the axial load as function of temperature became possible. In Fig 7 the predicted and measured restraint force as function of temperature is compared for two heating rates with a very good agreement. The maximum restraint load reaches about 40% at 400 °C and decreases to zero at 800°C.

Calculated stress distributions for an axially loaded cylindrical column under heating is characterized by a transition of compressive stresses from the surface to the in the inner part of the specimen after some time[2].

In a concrete structure stresses may change during heating a, compressive stress can be followed by ascending branch and then turn into tensile stress. This feature of behaviour must be modelled, which is fundamentally illustrated in Fig 8[2].

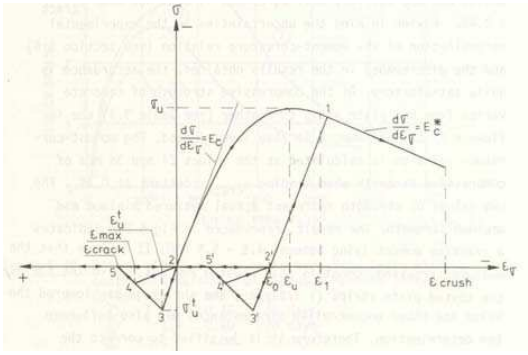

Fig. 8 - Concrete stress-strain model including unloading and loading in compression as well as in tension[2]

3.2 Model 2

This constitutive model was developed on a phenomenogical basis by Khoury et al.[4,5] in 1983 & 1985 based on tests up to 600°C without any refined stress-strain model as illustrated in Fig 8. This further modelling of stress-strain relationship was included in a computer program for structural analysis in 1991 by Terro[12].

In the original model a new concept was introduced where Load Induced Thermal Strain (LITS) was defined as the sum of three components, the stress-related strain (ε_σ), the transient strain (ε_{tr}) and the creep strain (ε_{cr}) as written below

$$\text{LITS} = \varepsilon_\sigma(\sigma, T) + \varepsilon_{tr}(\sigma, T) + \varepsilon_{cr}(\sigma, T, t) = \varepsilon_{tot} - \varepsilon_{th}(T)$$

The effect of load history is missing and not explicitly defined. A further simplification of LITS is the existence of a "*master LITS*" for Portland cement based concrete in general for temperatures up to 450°C irrespective of the type of aggregate or cement blend used.

3.3 Models based on Eurocode stress-strain model

There are several examples of structural analysis published in literature where the transient strain and load history effect have been ignored by using only the stress-strain model under compression from Eurocode 2-4[13-15] as presented in Fig 9 and Table 1. Sometimes it may be possible to obtain a relevant failure time especially for beams and slabs where the fire-exposed zone is in tension without a transient strain effect, because it acts only in compression. The stress and deformation prediction will however not be correct. The reason why the prediction of failure time sometimes can be almost correct depends on the fact that very large strains on the descending branch $\varepsilon_{c1,T}$ and $\varepsilon_{cu,T}$ has been introduced to compensate for the transient strain. These strains are much larger than those, which have been published in literature[13-15]. More realistic strain values are indicated within brackets in Table 1 and the difference is very great.

Table 1 Stress-strain values at different temperatures in accordance with Eurocode 2 Part 1.2

Temp	$f_{c,T}/f_{c,k}$	$\varepsilon_{c1,T}$ (%)	$\varepsilon_{cu,T}$ %	
20	1,00	0,25	2,00	(0,35)
300	0,85	0,70	2,75	(0,50)
600	0,45	(0,3)	3,5	(0.80)
1000	0,04	2,5	4,5	(1,10)
		(0,5)		
		2,5		

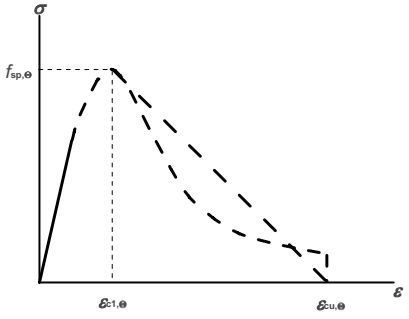

Fig. 9 - Mathematical model for stress-strain relationships of concrete at elevated temperatures.

4. BEHAVIOR MODEL OF STEEL AT HIGH TEMPERATURES

Is is generally agreed that the deformation process of steel at transient high temperatures can be described by three strain components defined by the constitutive equation

$$\varepsilon = \varepsilon_{th}(T) + \varepsilon_\sigma(\sigma, T) + \varepsilon_{th}(\sigma, T, t) \quad (2)$$

where

ε_{th} = thermal strain
ε_{σ} = instantaneous, stress-related strain based on stress-strain relations obtained under constant, stabilized temperature
ε_{ch} = creep strain or time dependent strain.

A computer oriented mechanical behaviour model for steel was developed in Anderberg (1976)[6] and 1983[11].

The strains are found separately in different steady state tests. It is shown that a behaviour model based on steady state data satisfactorily predicts behaviour in transient tests under any given fire process, load and strain history.

Steels behave in many ways differently and therefore hot-rolled and cold-worked reinforcing steel, structural steel and pre-stressing steel must be separated.

4.1 Thermal strain

The thermal strain or thermal expansion is measures on unloaded specimens in a transient test. Investigations published in literature indicate small deviations for structural and pre-stressing steels. Type of steel and strength characteristics seem to have no significant influence. In Fig. 10 thermal strain for structural steel is taken from four different sources. The curves are relatively close together. A linear relationship is most often used in analytical modelling.

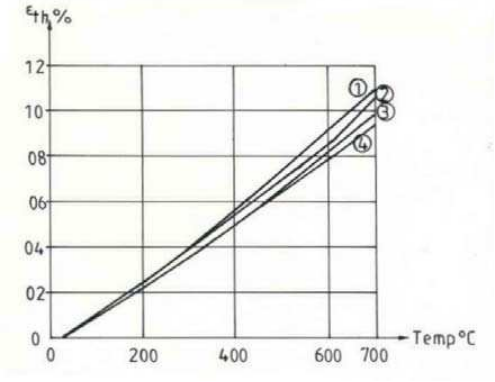

Fig. 10 - Thermal strain (expansion) for structural steel as function of temperature[11]
1. St 37-2, Ruge & Winkelmann (1978-80)
2. Steel 37, Skinner (1972)
3. A 36. Harmathy (1967)
4. Stirland (1980)

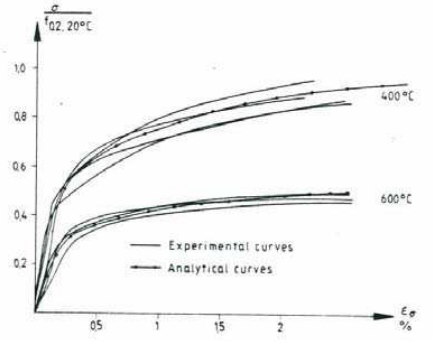

Fig. 11 - Dimensionless σ-ε relationship for 4 different kinds of reinforcing steel at 400°C and 600°C. The theoretical curves are also shown[16]

4.2 Stress-related strain

The σ-ε relationship can be measured under stress rate or strain rate control. The stress-strain relationship must be obtained at a high rate of loading or high rate of strain in order to avoid the influence of creep, which is of importance above about 400°C for ordinary steel (for cold-worked or pre-stressing steel above about 250°C). The influence of creep results in a displaced σ-ε curve and in a lower ultimate (rupture) strength. The σ-ε curves can be used to establish compressive or tensile strength, modulus of elasticity and ultimate strain.

Experimental results published in Anderberg (1978)[16] indicate that reinforcing and structural steel have a similar dimensionless σ-ε relationship as illustrated in Fig. 11 at 400 and 600°C. An analytical description of the σ-ε curve as a function of temperature can be made in different ways to fit the experimental data.

4.3 Creep and relaxation

Creep behaviour is unique for every type of steel and a common description is hard to find. This is due to the fact that the chemical composition and the degree of processing strongly influence this. The creep tendency seems not to be related to the 0,2% proof stress or other strength characteristics at room temperature. Therefore the absolute value of stress is used when describing creep analytically.

The creep strain can only be directly measured in steady state tests and if the stress is kept constant it can be separated into two phases, primary and secondary phase.

A relaxation test is closely related to a creep test but is carried out at constant strain and temperature and the stress decrease is studied as function of time. The relaxation process can analytically be found by using the formulation of creep and the instantaneous stress-related strain as follows. The total strain is kept constant, which means that the sum of ε_σ and ε_{cr} is constant. The increase in creep must be followed by the same decrease in ε_σ. The stress must therefore decrease with time in such a way that ε_σ decreases as ε_{cr} increases.

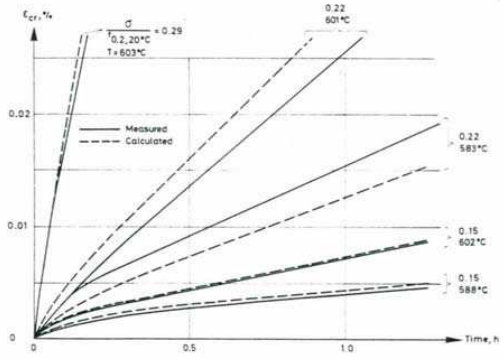

Fig. 12 - Measured and predicted creep (modified Dorn-Harmathy theory) at different stress levels. Reinforcing steel Ks 60 ∅8, $f_{0.2,\,20°C}$ = 710Mpa, Anderberg (1978)[11,17]

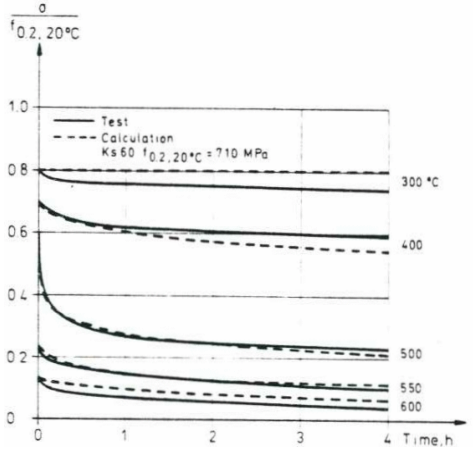

Fig. 13 - Measured and predicted relaxation curves for reinforcing steel (Anderberg 1978)[11,17]

4.4 Simplified model for design purpose

For design purpose a simplified model is used in practice, where the creep strain in an approximate way is incorporated in the stress-strain relationship. The model is solely based on transient tests and the procedure to construct the σ-ε relationships is as follows.

The total deformation measured in a transient test at a constant stress and increasing temperature until failure occurs minus the thermal strain as function of temperature is illustrated in Fig. 14. From these curves, σ-ε relationships can be constructed in which the creep strain corresponding to a specified heating rate is included.

When using constructed σ-ε curves for design one obtains somewhat conservative values which are thus on the safe side. In an analytical study of fire-exposed structures it is often too approximate to use the simplified model because the real temperature and stress history is not accounted for.

Analytical modeling illustrated above makes it possible to couple steady state tests and transient state tests. For instance, the strain or stress rate can be determined in steady state tests to give the same ultimate strength as occurs in a transient test for a given rate of heating.

σ-ε curves from steady state and transient state tests at different temperatures are compared to each other in Fig. 15. Agreement between calculations and measurements is also close. The curve of the steady state conditions contains no creep due to the high stress rate. In the curve of the transient state conditions the influence of creep is, however, of importance. This difference is also very much dependent on the heating rate in the transient test.

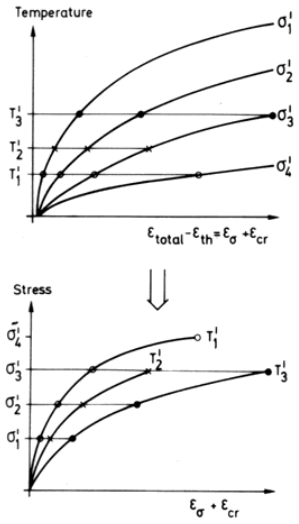

Fig. 14 – Transient tests with load control
Typical Constructed σ-ε curves at different stress levels and below Constructed σ-ε curves at different temperatures

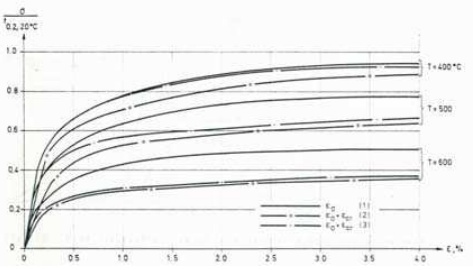

Fig. 15 - Measured and predicted σ-ε curves from steady state and transient state tests[11,17]

1 Steady state test, stress-controlled , dσ/dt= 3.5 MPa/s
2 Transient state test, constructed curve dT/dt=10°C/min
3 Transient process, curve derived analytically, t=10°C/min

The predicted influence of stress and strain rates on the stress-strain relationship under steady state conditions as well as transient conditions can be used to evaluate the ultimate strength as a function of temperature. The rate of stress or strain in a steady state test and the rate of temperature in a transient test are governing the development of creep which causes the change in the ultimate strength. The influence of creep for these procedures is fully illustrated in [11].

5. FIRE BEHAVIOR PREDICTION

5.1 Concrete structure

As an example Fig 16 illustrates the predicted and measured deformation behaviour of a reinforced concrete column exposed to ISO 834 fire on three sides This work was carried out in 1984 by Anderberg & Forsén[18], by using model 1 from 1976. The experimental results on axial as well as the horizontal deformation are predicted very well during the whole fire test and the failure time was very close. It is however very difficult to carry out such a test but still the agreement was exceptional.

If the model based on Eurocode 2:s stress-strain relationships of concrete has been used (as explained above) in this structural prediction the result had been quite different from measurements.

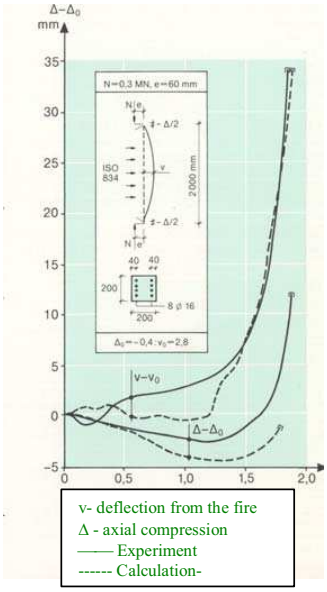

Fig. 16 - Predicted and measured axial and horizontal deformation of a reinforced concrete column fire-exposed (ISO 834) on three sides[18]

5.2 Steel structure

An example on how the influence of creep on the deformation behavior for a fire-exposed steel beam is illustrated in Fig. 17, [19]. The studied case illustrates creep failure under fire attack. If creep is not considered the collapse time is increased from about 17 to 20 min and the failure temperature from 700 to 760°C. For fire-exposed slender steel columns the influence of creep can be furthermore pronounced.

Further predictions on steel beams and columns partially fire-exposed are illustrated in [20].

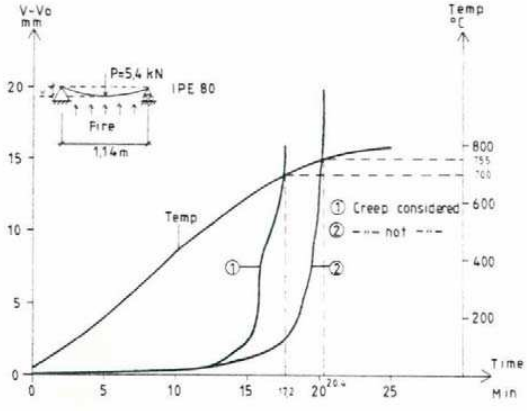

Fig. 17 - Predicted deflection of fire-exposed simply supported steel beam [19].

5. CONCLUSIONS

The constitutive model applied for predicting the structural behaviour of concrete members must reflect the true behaviour of concrete at high temperatures. This means that the transient strain and the load history effect must be considered. It does not help to have the most sophisticated FE-software if the fundamental input is not correct. One may sometimes be lucky to predict the failure time by using the stress-strain relationship of concrete from Eurocode 2 but the "real" behaviour (stress distribution and deformation) will never be correctly calculated. Simply supported concrete beams are not that sensitive but structural members in compression as columns and prestressed members are. However, in a structural design situation practical and simplified methods based on limit state have been developed in order to obtain a safe structure in case of fire.

The constitutive model for steel where the creep is separated is only important for prediction of the total behaviour including deformation from creep and relaxation. From a fire design point of view the creep could be incorporated in the stress-strain relationship (Eurocode 3) if it is based on transient tests with a proper rate of temperature in order to account for the creep influence in a safe way.

5. REFERENCES

[1] Thelanderson, S., "*Mechanical behaviour of Heated Concrete Under Torsional Loading at Transient High Temperature Conditions*". Bulletin No. 46, Lund Institute of Technology, Sweden, 1974.

[2] Anderberg Y. and Thelandersson S., "*Stress and Deformation Characteristics of Concrete at High Temperatures".*
1. "General Discussion and Critical Review of Literature". Lund Institute of Technology. Bulletin 34.
Lund 1973.
2. "Experimental Investigation and Material Behaviour Model", Lund Institute of Technology.
Bulletin 54. Lund 1976.

[3] Schneider U., "*Zur Kinetik Festigkeitsmindernder Reaktionen in Normalbetonen bei Temperaturen bis 1000 °C*". (*Loss of strength due to kinetic reactions of normal concretes up to 1000 °C*). A PhD Thesis at Technical University 1973, Braunschweig, Germany.

[4] Khoury G.A., "*Transient Thermal Creep of Nuclear Reactor Pressure Vessel Type Concretes*". A PhD Thesis at Civil Engineering Department, Imperial College of Science and Technology, University of London, London 1983.

[5] Khoury, G.A., Sullivan, P.J.E. and Grainger, B.N. *Strain of Concrete During First Heating to 600^{o}C Under Load.* Magazine of Concrete Research, Vol. 37, No. 133, pp. 195-215, Dec 1985.

[6] Anderberg, Y., " *Fire-exposed Hyperstatic Concrete Structures. An Experimental and Theoretical Study*". Lund Institute of Technology. Bulletin 55. Lund 1976.

[7] Becker, J., Bresler, B., " FIRES-RC, *A Computer Program for the Fire Response of Structures-Reinforced Concrete Frames*". University of California, Berkeley, Fire Research Group, Report No. UCB FRG 74-3, July 1974.

[8] Forsén N. E., "*A Theoretical Study on the Fire Resistance of Concrete Structures"*. Cement and Concrete Research Institute, The Norwegian Institute of Technology, SINTEF Report No: STF65 A82062, Dec.1982

[9] Anderberg, Y., "*Analytical Fire Engineering Design of Reinforced Concrete Structures Based on Real Fire Characteristics*". FIP Congress, London 1978. Proceedings, Part 1, 1 May 1978, pp 112-121.
[10] CEB-FIP Model Code, "*Design of Concrete Structures for Fire Resistance*". Bulletin d'Information No 145 , January 1982
[11] RILEM 44-PHT: Anderberg, Y., *Behaviour of Steel at High Temperatures*. February 1983.
[12] Terro M., "*Computer Modelling of the Effect of Fire on Structures*". Ph.D. thesis, at Civil Engineering Department, Imperial College of Science and Technology, London University, London 1991.
[13] EN1992-1-2 Design of Concrete Structures – Part 1-2: General Rules – *Structural Fire Design* (December 2004)
[14] EN1993-1-2 Design of Steel Structures – Part 1-2: General Rules – *Structural Fire Design* (2004)
[15] EN1992-1-4 Design of composite Steel and Concrete Structures – Part 1-2: General Rules – *Structural Fire Design* (July 2005)
[16] Anderberg, Y., Mechanical Properties of Reinforcing Steel at Elevated Temperatures (Armeringsståls mekaniska egenskaper vid höga temperaturer). In Swedish with an English summary. Tekniska Meddelanden Nr. 36, Halmstad Järnverk AB, Lund 1978.
[17] Anderberg, Y., *Predicted Fire Behaviour of Steels and Concrete Structures*. Division of Building Fire Safety Design and Technology, Lund Institute of Technology, Lund 1983.
[18] Anderberg Y., Forsen N.E.*," Fire Resistance of Concrete Structures"*. Division of Building Fire Safety and Technology, Lund Institute of Technology, Lund 1982, Lutvdg/TVBB 3009. Nordic Concrete Research.
[19] Yngve Anderberg - Nils Erik Forsen - Bjorn Aasen, *Measured and Predicted Behaviour of Steel Beams and Columns in Fire*. Presented at the First International Symposium on Fire Safety Science in Washington in October 1985. Report LUTVDG/TVBB 3033, 1986
[20] Yngve Anderberg, *Structural Behaviour and Design of Partially Fire-Exposed Slender Steel Columns*. Presented at The second international workshop "Structures in Fire" Christchurch, March 2002. Fire Safety Design, Malmö

BEHAVIOR OF STEEL BUILDING STRUCTURES WITH PERIMETER MRFs UNDER FIRE LOADING EFFECTS

AMIT H. VARMA[1], ANIL AGARWAL[2], SANGDO HONG[3], KULDEEP PRASAD[4]

ABSTRACT

This paper presents a fundamental approach and primer for simulating the behavior of steel building structures subjected to fire loading. A 10-story office building located in Chicago was designed according to current U.S. building codes and design specifications. The structural layout consisted of interior gravity frames and perimeter moment resisting frames (MRFs), which is typical of steel construction in the U.S. The complete 3D building structure was modeled using several 2-node beam (B33) elements for the steel columns and beams, and 4-node (S4) shell elements for the concrete floors.

The 3D structure model was analyzed for two different fire scenarios: (i) corner compartment fire, and (ii) complete story fire. The analyses were conducted using: (i) the modified RIKS (arc-length based) analysis, and (b) the nonlinear implicit dynamic analysis approaches. The analytical results indicated that the thermal expansion of the floor system causes large out-of-plane displacements and inelastic stresses in the perimeter columns, but they do not undergo inelastic buckling failure or collapse. Failure occurs by inelastic buckling failure of the interior gravity columns because they are much lighter sections than the perimeter columns.

The inelastic buckling of interior gravity columns has a significant influence on the overall behavior and collapse of the complete building structure. The normalized story capacity of the building structure can be predicted reasonably using the normalized axial load capacity versus failure temperature curve for heated columns with ambient columns above and below.

[1] Assistant Professor, Purdue University, School of Civil Eng.,
email: ahvarma@purdue.edu
[2] Ph.D. Student and Research Assistant, Purdue Univ.,
email: anilag@purdue.edu
[3] Research Engineer, Indiana Department of Transportation,
email: shong@indot.in.gov
[4] Research Scientist, NIST - Building and Fire Research Laboratory,
email: kprasad@nist.gov

This is recommended as a simple design tool for evaluating the fire resistance and safety of perimeter MRF building structures.

1. INTRODUCTION

The prescriptive fire resistant design approach is emphasized by most of the current building codes including IBC2006[1]. This approach does not account for the effects of realistic fire loading and thermal and structural interactions between the building components during the fire event. Recent events, for example, the 9/11 WTC Tower collapses, and the following analytical investigations directed by NIST, have highlighted the need for fundamental knowledge of the behavior and stability of building structures under realistic fire loading.

The realistic fire behavior of building structures depends on several parameters, the most important of which are: (a) the structural configuration and layout, (b) fire intensity, duration, and spread, (c) structural loading and boundary conditions, and (d) fire protection distribution.

This paper presents an analytical approach for simulating the realistic fire behavior of steel building structures. It focuses on the behavior of a hypothetical 10-story office building located in Chicago, and designed according to current U.S. building codes. The structural layout consists of interior gravity frames and perimeter moment resisting frames (MRFs).

It is expected that the behavior of other structural configurations will be different from those presented in the paper. However, the paper provides a fundamental primer for simulating and evaluating the realistic fire behavior and stability of steel building structures. This primer will be used later in this research effort to further investigate the behavior of other structural configurations and layouts.

2. DESIGN OF A TEN STORY OFFICE BUILDING

A ten story office building was designed according to current building codes and design specifications, namely, IBC 2006, ASCE 2005[2] and AISC 2005[3]. The building was designed to be used as office space in Chicago, IL. USA.

2.1 Building Configuration

Each story is 3.65 m (12 feet) high and the bays are 7.62 m (25 feet) in both horizontal directions. There are a total of 24 equally spaced columns in the building. The building layout is shown in Figure 1. The slabs are composite floor systems with 65 mm (2.5 in.) thick concrete slab on 75 mm (3 in.) deep ribbed deck in full composite action with steel beams.

The steel floor beams are designed to carry the wet concrete weight and the construction live load without any temporary supports (shores). After the concrete sets, the composite floor beams are designed to carry factored design loads. However, the beams of the perimeter MRFs are assumed to resist the moments without any composite action. The gravity beams are provided with pinned (shear only) connections at the two ends, while the perimeter MRF beams have fixed (moment) connections with the columns. The end beams of the larger MRFs are connected to the corner columns using pin (shear) connections to avoid biaxial moments in the corner columns. The columns are designed to remain pin connected at the base.

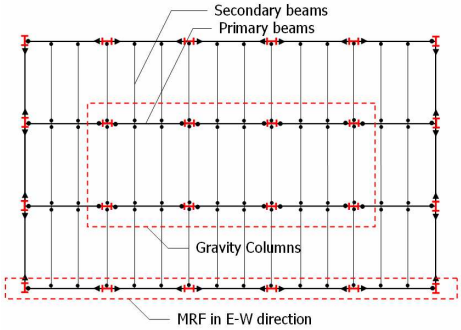

Fig. 1- Structural plan of 10-story building

2.2 Design Requirements

The building is designed for ASCE recommended combinations of dead load, live load, wind load and earthquake load. All the floors are designed for nominal dead loads and live loads equal to 3.1 kN/m^2 (65 psf) and 2.4 kN/m^2 (50 psf), respectively. The building comes under seismic design category B and the lateral load resisting system is designed as an ordinary moment resisting frame, which implies that the values of response modification factor (R), over-strength factor (Ω), and deflection amplification factor (C_d) are 3.5, 3.0, and 3.0 respectively. The inter-story drifts (including the P-Δ effects) are limited to story height/400 for wind loads and story height/50 for seismic loads.

2.3 Member Dimensions

The design process leads to the following A992 steel sections (350 MPa yield stress) for different members. The secondary gravity beams in all floors are W12X19, and the primary gravity beams are W18X35. All the columns are spliced at every 2 floors. The gravity columns for floors 1-2, 3-4, 5-6, 7-8, and 9-10 are made of sections W14X90, W14X74, W12X58, W8X40, and W8X24, respectively. The columns of the N-S perimeter MRFs and the corner columns of floors 1-2, 3-4, 5-6, 7-8, and 9-10 are made of sections W14X311, W14X159, W14X109, W14X90, and W14X53, respectively. The columns of the E-W perimeter MRFs (except the corner columns) for floors 1-2, 3-4, 5-6, 7-8, and 9-10 are made of sections W14X283, W14X145, W14X99, W14X53, and W14X45, respectively. The beams in the E-W perimeter MRFs for floors 1-2, 3-4, 5-6, 7-8, and 9-10 are made of W21X132, W18X71, W18X60, W18X50, and W18X35 sections, respectively. Similarly, the beams in the N-S moment frames for floors 1-2, 3-4, 5-6, 7-8, and 9-10 are made of steel sections W27X217, W21X111, W21X93, W21X83, and W18X50, respectively. It is assumed that the connections are designed so that they don't fail before one of the connecting members does. This assumption is made to simplify the modeling for the further analysis. The limitations of this assumption are well understood and efforts will be made in the future to incorporate the effects of possible connection failures.

3. MODELING THE INDIVIDUAL COMPONENTS OF THE BUILDING

The building structure was modeled and analyzed using the finite element method. The finite element models and nonlinear analysis were conducted using ABAQUS[4], which is commercially available finite element analysis software. ABAQUS was selected for the modeling and analysis because of its excellent range of finite elements and capabilities to perform uncoupled and coupled thermal-structural analysis, while using robust nonlinear temperature-dependent material models and powerful solution algorithms like modified-RIKS and implicit or explicit dynamic analyses.

The steel beams and columns, i.e., all the A992 wide-flange (W) sections mentioned above in Section 2.3, were modeled using 2-node beam elements. The concrete floors (slabs) were modeled using 4-node shell elements. The composite beam models consisted of a combination of beam and shell elements that were connected together using a rigid connection so as to impose full composite action. The details of these models and their validations using experimental results are presented in Hong et al. (2008)[5], and not included here for brevity

4. FAILURE ANALYSIS OF THE BUILDING

The 10-story building structure was modeled as explained above in Section 3. The steel columns and steel beams were modeled using 2-node beam (B33) elements. At least six beam (B33) elements were used to model the length of each column and beam member. The concrete slab of the floor system was modeled using 4-node (S4) shell elements. About 2400 elements were used to model each floor of the building structure. Full composite action was assumed between the steel floor beams and the concrete slabs. Constraint equations were used to define full composite action (i.e., plane sections remain plane) between the steel beam (B33) and concrete slab (S4) elements.

Temperature-dependent material properties were assigned to the steel and concrete materials of the finite element model. The elastic and plastic stress-strain (σ-ε-T) relationships and the thermal expansion (α-T) models were assigned based on Eurocode, ECS 2003 models. The details of these and other material property models are provided in Hong (2007)[6].

The beam-to-girder connections and the girder-to-gravity column shear connections were idealized as pin-end conditions. The girder-to-column connections in perimeter MRFs were idealized as completely fixed or rigid moment connections. There is no steel reinforcement considered in the concrete slab, which is typical for steel construction in the U.S. The vertical offset between the steel beam (B33) elements and the concrete slab (S4) elements is equal to distance between their centroids.

4.1 Analysis Schemes and Assumptions

The objective of the analysis is to compute the complete structural response up to and beyond initial failure and/or local collapse. A typical non-linear static analysis with the Newton-Raphson or modified Newton iteration solution algorithms does not converge beyond the first stability limit, even if it occurs at the local level. The modified-RIKS (arc-length) solution algorithm is capable of continuing the analysis beyond initial or local instability. However, unlike typical non-linear static analysis, it can not be performed for thermal loading. Therefore, the modified-RIKS analysis was conducted by first heating the structure to pre-established or target

temperatures, and then subjecting it to monotonically increasing gravity loading up to failure or limiting displacements.

Another interesting approach is to consider the structure as a dynamic system so that the response is not limited to the equations of static equilibrium, but can include terms with non-zero accelerations and velocities in the equations of dynamic equilibrium. The implicit dynamic analysis approach can be used to investigate the behavior of the complete structure after initial and/or local failure. Therefore, this analysis was also conducted by first subjecting the structure to gravity loads statically, and then increasing the temperatures dynamically (as functions of time) until failure.

The overall behavior and stability of the theme structure under fire loading was investigated using: (i) the modified-RIKS, and (ii) implicit dynamics analysis approaches. Two hypothetical fire scenarios were considered for the theme structure: (i) corner (single) compartment fire, and (ii) complete story fire. These are very simplistic fire scenarios, where the primary input parameters are the structural member temperatures.

Thermal gradients across the depth and length of the members were not included in these analyses. The therrmal gradient in a structural component depends on the thermal properties of the member, the rates of heating and cooling of the compartment air, and the fire protection provided. The effects of time-dependent structural behavior (creep) and cooling of the structure were not included in the analyses. The limitations imposed by these and other modeling assumptions are well understood and will be addressed in future work.

4.2 Corner Compartment under Uniform Fire Loading: Modified-RIKS Approach

All the structural components of one corner compartment [7.62m x 7.62m or (25ft x 25ft)] on the 5th floor of the building were heated to pre-established temperatures. These included all the columns, beams, and composite floors of compartment. The two adjacent compartments were heated to 40% of the corner compartment temperatures. The remaining parts of the structure were assumed to remain at ambient conditions. The modified-RIKS analysis was conducted by subjecting the structure to monotonically increasing gravity loading. Figure 4 shows the deformed shape of the building with corner compartment heated to 600 ^{o}C and loaded under gravity to failure. Figure 4 also includes the plot of normalized gravity loading vs. the vertical displacement of the top node of the failed column. The gravity loading is normalized with respect to the design service loading (DL+LL).

The behavior in Figure 4 shows that the floor system expands and subjects the perimeter columns to significant out-of-plane deformations, stresses, and inelasticity. However, the interior gravity column undergoes inelastic buckling failure before any other component. This occurs because at the 5th story level, the interior gravity columns are W12X58 sections and the exterior and corner perimeter columns are W14X109 and W14X99 sections, respectively. Additionally, the gravity loads acting on the interior columns were about two times that of the exterior columns. It is important to note that the exterior (perimeter) columns were designed to resist the lateral forces in addition to the gravity loads. The interstory drift limits (height/400) for wind loads led to the design of heavier column sections for perimeter MRFs. This is very realistic and typical for building design in the U.S.

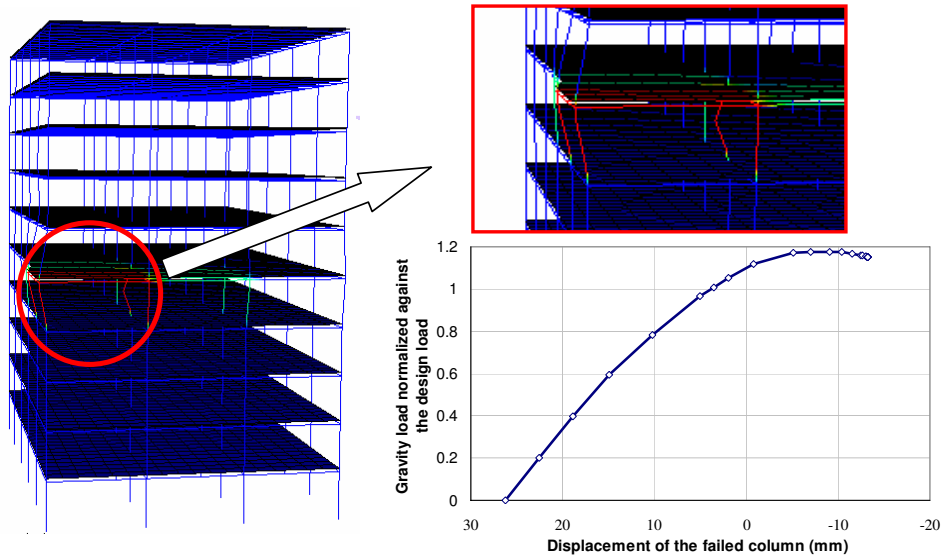

Fig. 4: Corner compartment fire behavior – modified-RIKS analysis

As mentioned earlier, the modified-RIKS analysis can investigate the post-buckling (failure) behavior of the structure. In this case, the corner compartment analysis indicated that at elevated temperatures the *interior gravity column* is the weakest link in the perimeter MRF building structure. However, the analysis procedure could not provide converged solutions significantly after the failure of first gravity column. This raised concerns regarding the redistribution of the forces carried by the interior gravity column to the adjacent columns, and the stability (or progressive collapse) of the complete structure due to the failure of the interior gravity columns. These concerns were addressed using the implicit dynamic analysis procedure in the following section.

4.3 Corner Compartment under Uniform Fire Loading: Implicit Dynamic Analysis

The theme structure was first subjected to design-level service loads (DL+LL). After loading the structure statically, the temperatures of all components in the corner compartment were raised dynamically (with time). The temperatures of the two adjacent compartments were raised at 40% of the rate in the corner compartment. It was observed that for structures with severe nonlinearities and local failures, converged solutions were obtained more easily using the implicit dynamic analysis approach than the modified RIKS method. The results from the nonlinear dynamic analyses confirm the findings and results from the modified-RIKS analysis. They also show that after inelastic buckling, the loads carried by the interior gravity columns are redistributed to the adjacent columns and the system remains stable thereafter.

Figure 5 plots the vertical displacement of the node at the top of the failed column versus the applied temperatures. The initial slow increase in displacements is attributed to the thermal expansion of the column. The drop by about 60mm. represents the buckling of the column. The structural stabilized after initial column buckling by distributing the loads carried by the buckled column to the adjacent columns through catenary action in the composite beams and slabs. The

downward slope in the last portion of the plot represents the stable expansion and softening of the structure with increasing temperatures.

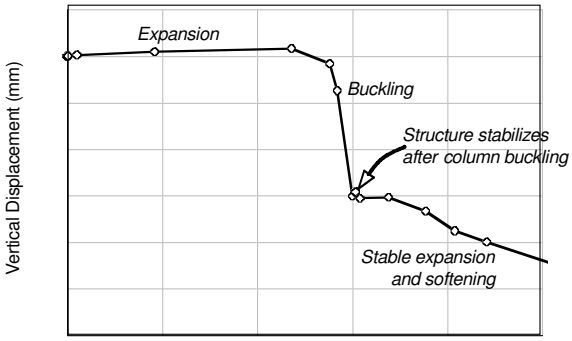

Fig. 5: Corner compartment fire behavior - implicit dynamic analysis

4.4 Complete Floor under Uniform Fire Loading: Modified-RIKS Approach

The second fire scenario considered was the complete story fire. All the structural components of the 5th story of the building were statically heated to a pre-selected temperature. These included the columns, beams, and composite floors of the entire 5th story. The remaining parts of the structure were assumed to remain at ambient conditions. The modified-RIKS analysis was performed by subjecting the building structure to monotonically increasing gravity loading up to failure.

Figure 6 shows the deformed shape of the building structure at the last converged point from the modified-RIKS analysis. The 5^{th} story (under fire) was subjected to a uniform temperature of 600 ^{o}C. The simulated behavior indicates that the horizontal expansion of the composite floor system pushes the exterior and corner columns of the perimeter MRFs in the outward direction. This causes outward deflections and large stresses in the exterior and corner columns, but they do not undergo buckling failure or collapse. Failure or inelastic buckling occurs of the interior gravity columns.

Figure 6 includes a plot of the normalized gravity load versus the arc-length for the analysis. The gravity loading is normalized with respect to the design level service loading (DL+LL). This plot indicates that the structure reaches its peak load capacity and failure initiates due to inelastic buckling of one of the interior gravity columns. This is followed by further reduction in the gravity load capacity of the structure, and buckling of another gravity column, after which the analysis stops due to non-convergence of static equilibrium. The behavior shown in Figure 6 is typical and representative of the behavior of the structure subjected to different uniform temperatures.

The lack of converged solutions after the buckling of two interior gravity columns raised concerns regarding the redistribution of forces carried by the interior gravity columns, and the stability of the complete structure. These concerns were addressed using the implicit dynamic analysis procedure presented in the following section

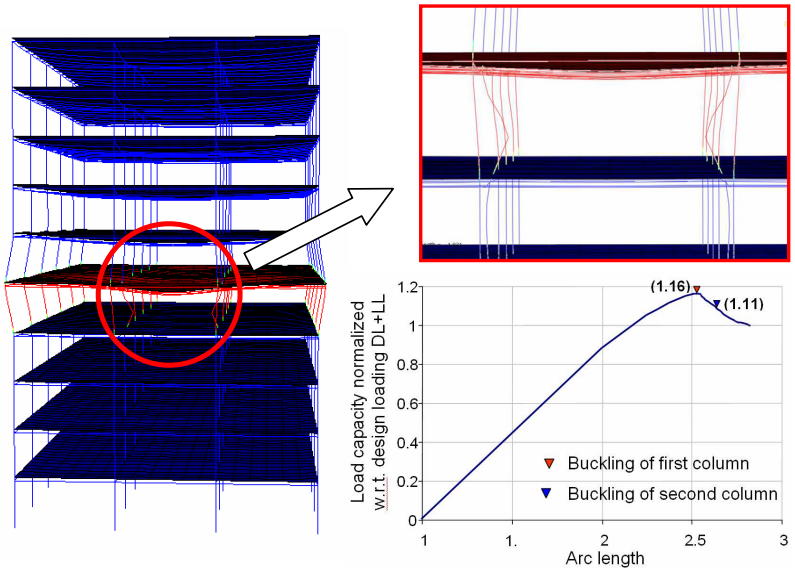

Fig. 6: Complete story fire behavior – modified-RIKS analysis

4.5 Complete Floor under Uniform Fire Loading: Implicit-Dynamic Analysis

The structure was first subjected to the gravity loads (DL+LL) statically, which was followed by dynamically increasing temperatures (heating) to failure. The temperatures of all components of the 5th story were increased dynamically with time. Figure 7 shows the deformed shape of the structure close to failure. The simulated behavior indicated that that the expansion of the floor system caused large out-of-plane displacements and inelastic stresses in the perimeter columns, but failure occurs due to inelastic buckling of all the interior gravity columns. This also confirms the behavior predicted by the modified-RIKS analysis.

Figure 7 includes a plot of the vertical displacement at the top node of one of failing gravity columns vs. elevated temperatures. The plot shows that the column expands (gradually) with increasing temperatures. It undergoes inelastic buckling at the critical or failure temperature, but after buckling the displacement never stabilizes. There may be some redistribution of forces from the buckling columns to the adjacent perimeter columns, but there is not enough capacity (strength or stiffness) for them to stabilize the complete story. The vertical deflections of the failed column (and the story) never stabilize and it has a runaway failure. Thus, the structure fails due to the complete story fire.

The dynamic analysis approach described above was used to determine the critical or failure temperatures for different gravity loading magnitudes. Several complete story fire cases with different gravity loading magnitudes were analyzed dynamically up to failure or collapse. The results were used to develop the normalized story capacity versus failure temperature plot shown in Figure 8. The story capacity was normalized with respect the story capacity at ambient temperatures. As shown in Figure 8, the story load capacity reduces gradually from ambient temperatures to 500 ^{o}C, after which it reduces much more rapidly for temperatures greater than 500 ^{o}C.

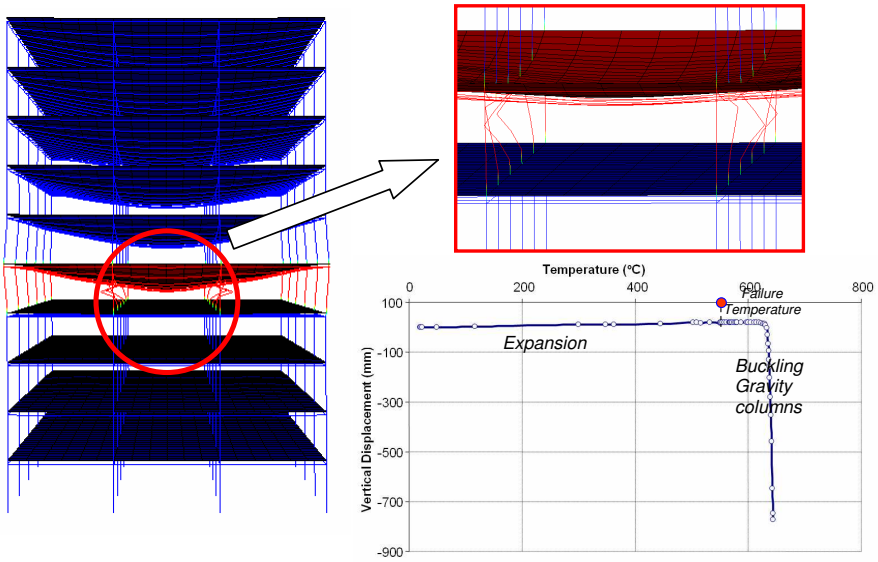

Fig. 7: Complete story fire behavior – implicit dynamic analysis

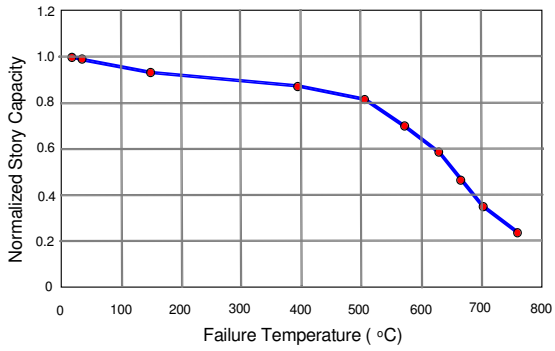

Fig. 8: Normalized story load capacity vs. failure temperatures

4.5 Behavior of Gravity Columns

The discussion in Sections 4.2 to 4.5 indicates that the inelastic buckling failure of interior gravity columns will have a significant influence on the overall fire behavior and stability of building structures with perimeter MRFs. Therefore, the behavior and inelastic buckling failure of gravity columns subjected to elevated temperatures from fire loading was investigated further using three simple cases: (1) Uniformly heated simply supported individual column. (2) Uniformly heated simply supported column with unheated (ambient) column on top. (3) Uniformly heated simply supported column with unheated (ambient) columns at the top and bottom.

Figure 9 (a) shows schematic representations of these three different cases. Their behavior and buckling failure at elevated temperatures was investigated using the modified-RIKS analysis approach. The (heated) columns were first subjected to uniform heating to achieve the pre-established temperatures. This was followed by monotonically increasing the axial loading to failure or collapse.

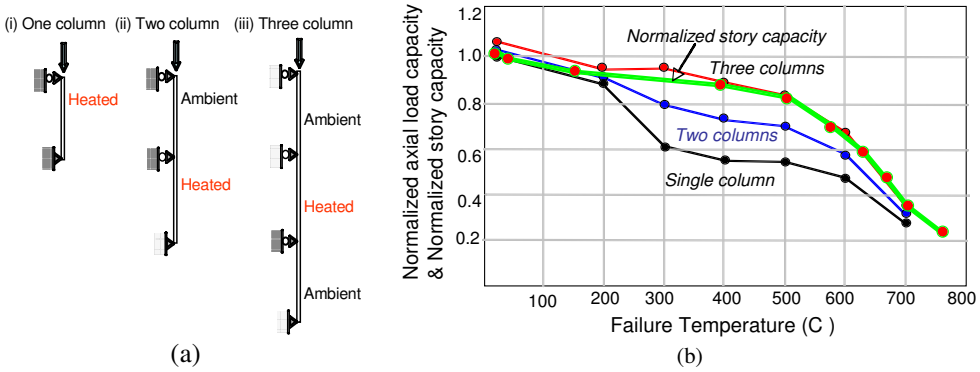

Fig. 9 – Structural behavior of continuous columns subjected to elevated temperatures.

Figure 9 (b) shows the final results from the analyses. For the three cases, it plots the normalized axial load capacities vs. the failure temperature. The axial load capacities were normalized with respect to the axial load capacity of individual column (case 1) at ambient temperatures. Figure 9(b) shows that there are no significant differences in the column axial load capacities up to elevated temperatures of 200 ^{o}C, beyond which the column axial load capacities decrease significantly with increasing temperatures. Between the temperatures of 200 to 700 ^{o}C, the presence of an unheated column above and below improves the axial load capacity of the heated column significantly. The axial load capacity of an individual heated column is much less than that of a similar column with unheated (ambient) columns above and below. This emphasizes the beneficial effects of boundary conditions and the presence of unheated columns (above and below) on the axial load capacities of heated columns.

Figure 9(b) includes the normalized story capacity vs. failure temperature curve developed earlier and shown in Figure 8. Figure 9(b) indicates good correlation between the normalized story capacity curve and the normalized axial load capacity curve for the three-column system (Case 3). This seems reasonable because the normalized story capacity of the structure was governed by the inelastic buckling failure of the interior gravity columns, which had unheated columns in the stories above and below.

Thus, the behavior and inelastic stability failure of perimeter MRFs subjected to the complete story fire scenario can be modeled adequately using the three-column simplification. This will serve as an excellent design tool for evaluating the fire resistance and safety of perimeter MRF building systems subjected to design level gravity loads.

5. SUMMARY AND CONCLUSIONS

This paper developed a fundamental approach and primer for modeling and simulating the behavior of steel building structures subjected to fire loading. A 10-story office building located

in Chicago was designed according to current U.S. building codes and design specifications. The structural layout consisted of interior gravity frames and perimeter moment resisting frames (MRFs), which is typical of steel construction in the U.S. The design of the perimeter MRF columns was governed by interstory drift requirements for lateral loading. As a result, the interior gravity columns were much lighter than the perimeter MRF columns.

The complete 3D building structure was modeled simply using several 2-node beam elements for the steel columns and beams, and 4-node shell elements for the concrete floors. This modeling approach was evaluated in detail in a separate publication (Hong et al. 2008)[5] and is not included here for brevity. This simple modeling approach was selected because it reasonably predicts the experimental results from standard fire tests of columns, composite beams, and frames.

The 3D building structure model was analyzed for two fire scenarios: (i) corner compartment fire, and (ii) complete story fire. The analyses were conducted using: (i) the modified RIKS (arc-length based), and (ii) the implicit dynamic analysis approaches. The implicit dynamic analysis approach was found to provide converged results more easily than the modified-RIKS method after the structure developed significant nonlinearities and local failures.

The analytical results indicate that for a regular perimeter MRF structure subjected to elevated temperatures, the thermal expansion of the floor system causes large out-of-plane displacements and inelastic stresses in the perimeter columns, but they do not undergo inelastic buckling failure or collapse. Failure initiates by inelastic buckling failure of the interior gravity columns because they are much lighter sections than the perimeter columns.

If the fire is confined to a small portion of the story, e.g., a corner compartment, then there is a redistribution of loads from the buckling interior columns to the adjacent columns through catenary action in the composite beams. The structure remains stable after initial buckling failure of the interior column. However, if the fire spreads over the complete story, then all the interior gravity columns fail by inelastic buckling, and there is not enough capacity in the perimeter columns to stabilize the complete story by preventing displacement runaway failure.

The inelastic buckling of interior gravity columns has a significant influence on the overall behavior and collapse of the complete building structure. Further investigations of interior gravity columns indicated that the axial load capacity of heated columns improves significantly with the presence of unheated (ambient) columns above and below. The *normalized story capacity* for the building structure correlated very well with the *normalized axial load capacity versus failure temperature curve* for heated columns with ambient columns above and below. This will serve as an excellent tool for designing and evaluating the fire resistance of perimeter MRF building systems.

The findings presented in this paper are preliminary and based on ongoing research. There are several assumptions and limitations in the analytical models and investigations that are being addressed by current research. Future work will focus on experimental verification and analytical parametric analysis of building structures with various configurations, fire scenarios, and protection details.

ACKNOWLEDGMENTS:

The research presented in this paper has been co-sponsored by the National Science Foundation and the U.S. Department of Commerce through the Extramural Fire Research Grant

Program. This program is administered by the National Institute of Standards and Technology – Building and Fire Research Laboratory (BFRL).

REFERENCES:

[1] IBC (2006). *International Building Code*. International Code Council Inc., Falls Church, VA.
[2] ASCE 7 (2005). *Minimum Design Loads for Buildings and Other Structures*. American Society of Civil Engineers, Reston, VA.
[3] AISC 360 (2005). *Specification for Structural Steel Buildings*. American Institute of Steel Construction, Chicago, IL.
[4] ABAQUS (2007). *ABAQUS/Standard Version 6.3 User's Manuals: Volumes I – III,* Hibbitt, Karlsson, and Sorenson, Inc., Pawtucket, Rhode Island.
[5] Hong, S., Varma, A.H., Agarwal, A., and Prasad, K. (2008). "Behavior of Steel Building Structures Under Fire Loading." *Proceedings of the ASCE Structures Congress-2008, in press, proceedings on CD-ROM*, ASCE, Reston, VA, 10 pp.
[6] Hong, S. (2007) "Fundamental Behavior and Stability of CFT Columns Under Fire Loading", *Ph.D. Dissertation*, School of Civil Engineering, Purdue University, West Lafayette, IN.

3-D VERSUS 2-D MODELING OF A HIGH-RISE STEEL FRAMED BUILDING UNDER FIRE

SPENCER E. QUIEL[1] and MARIA E.M. GARLOCK[2]

ABSTRACT

When using finite element analysis to predict the fire-exposed performance of a high-rise steel-framed building, the analyst must make several decisions regarding the complexity of the model, which is a trade-off between accuracy and computational efficiency. This paper compares the performance of a more detailed but more computationally expensive 3-D model of the perimeter of a prototype high-rise moment-resisting steel frame to that of a simpler but more efficient 2-D plane frame model. The performance of three members that are part of the frame are examined: (1) the perimeter column; (2) the girder, i.e. the beam that frames into the perimeter column perpendicular to the building exterior; and (3) the filler beams, which span between the girders. The results of this study indicate that the 2-D plane frame models deliver similar predictions of behavior and plastic limit states for the perimeter column and girder as larger 3-D models. The 2-D models can therefore be used to obtain reasonable predictions of the fire-exposed performance for these members with significant savings in analysis run time. The filler beam comparison indicates that the deflection of the filler beams is more sensitive to the structural effects of a continuous concrete slab. The more efficient 2-D filler beam models can adequately capture the restraint of the member as well as the trends of axial force and moment, but a 3-D model that includes a continuous slab is recommended for studies of filler beams.

1. INTRODUCTION

Recent fire-induced structural collapses worldwide have raised questions regarding the methods used to predict the fire-induced behavior of high-rise building frames. Such predictions have typically been performed using finite element (FE) models of the building, or a subassembly of the building, for thermal and structural analysis. For a high-rise steel

[1] PhD Candidate, Princeton University, Department of Civil and Env. Eng., Princeton, NJ 08544 USA
email: squiel@princeton.edu
[2] Assistant Professor, Princeton University, Department of Civil and Env. Eng., Princeton, NJ 08544 USA
email: mgarlock@princeton.edu

frame, the analyst must make several decisions regarding the complexity of the model, which is a trade-off between accuracy and computational efficiency. The question remains for many analysts whether to use a more detailed but more computationally expensive 3-D model of the structural frame (including multiple bays on multiple storeys) or if a simpler but more efficient 2-D plane frame model (representing a vertical slice of the frame) will deliver acceptably accurate results.

To date, 2-D FE plane frame models have been widely used to analyze the performance of fire-exposed steel members in high-rise building frames, for example [1-5], as well as single floor elements that are isolated from the frame using idealized boundary conditions, for example [6-8]. In the past decade, an increasing number of researchers have begun to use more complex 3-D frame models of high-rise steel structures in efforts to better capture the interaction among adjacent heated frame members and the behavior of the composite floor system, for example [9-12]. A few studies have been performed that compared the overall performance of 2-D plane frame models to that of 3-D models, such as that by Flint et al. [13] for a portion of the World Trade Center Twin Towers, a unique structural system.

This paper will focus on the performance of a perimeter moment resisting frame (a more common structural system) in a high-rise building that was subjected to an actual fire. This paper compares the use of 3-D versus 2-D FE models to predict the fire-induced behavior of three members that are part of the prototype building frame: (1) the perimeter column; (2) the girder, i.e. the beam that frames into the perimeter column perpendicular to the building exterior; and (3) the filler beams, which span between the girders. The performance of the 3-D and 2-D models will be evaluated in terms of benefits (accuracy) and cost (computational efficiency).

2. MODELING THE PROTOTYPE

In a previous study of the prototype building, the authors examined the fire-induced interaction of perimeter columns (which are braced on three sides only) and the beams that frame into them perpendicular to the exterior wall [1], which will be referred to as girders. The structural system of the prototype building was a moment-resisting frame (MRF), composed of wide-flanged (WF) steel sections carrying a concrete floor slab on a metal deck. Figures 1(a) and 1(b) show the subassembly considered for this study in plan and elevation view, respectively. The "girders" fall on lines A, B, and C, and the "beams" run parallel to lines 1 and 2. The girder-to-column connections are considered rigid (i.e. as a moment connection), and the filler beam-to-girder connections are considered pinned (i.e. no moment transfer due to a shear tab connection). The slab consists of a 64-mm (2½-in.) deep top layer on top of 76-mm (3-in.) deep ribs at 305-mm (1-ft.) spacing. The direction of the ribs is shown in Figure 1(a) to be parallel to the girders. Figure 2(a) shows a cut of the girder and the slab.

Figures 1(a) and 1(b) also show the boundary conditions considered for this subassembly. In general, all boundary conditions except for the fully fixed column base supports are considered to be restrained for all degrees of freedom except vertical translation. The analyses conducted for this study assume that a single compartment in the subassembly on a single floor is subject to fire. The temperature-time history shown in Figure 3 was used as a realistic approximation of the actual fire event [1]. Material models for heated structural steel, concrete, and steel rebar were taken according to Eurocode [14,15]. Building plans specified the following passive fire protection: 39 mm (1½ in.) of spray-on fire resistive material (SFRM) on the floor beams, 39 mm (1½ in.) of SFRM plus 19 mm (¾ in.) of

gypsum plaster boards on the columns, and 19 mm (¾ in.) of SFRM on the underside of the slab.

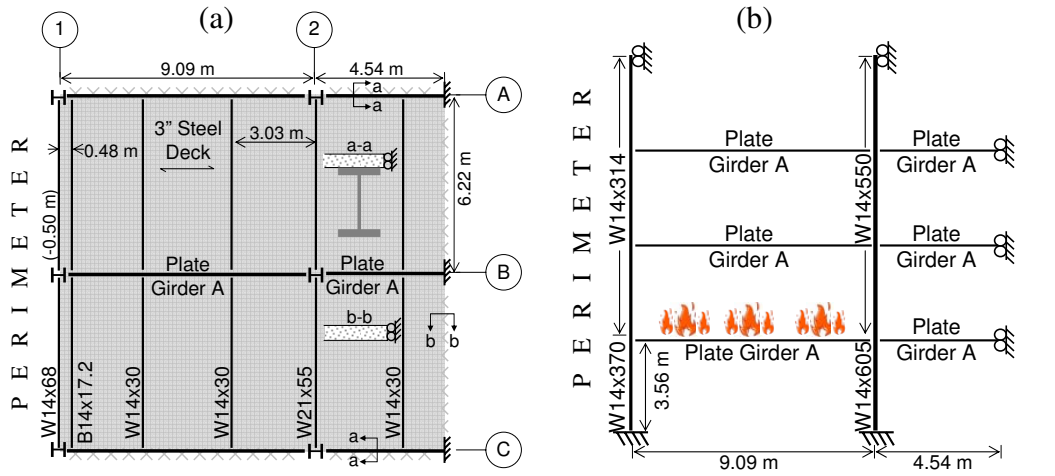

Fig. 1 – Schematics of the prototype building frame in (a) plan view and (b) elevation view.

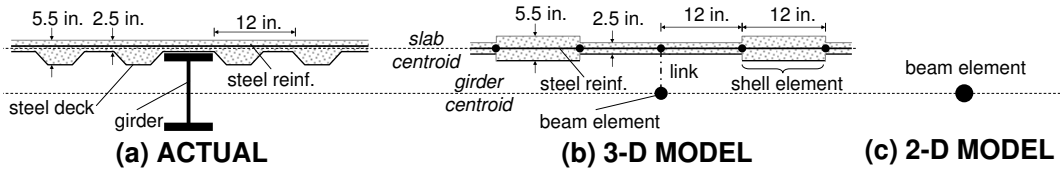

Fig. 2 – Sections of the girder and slab as represented in (a) the actual prototype building plans, (b) the 3-D FE structural model, and (c) the 2-D FE structural model.

Computational FE modeling of this subassembly was conducted using the 2007 version of SAFIR, a computer software developed at the University of Liege specifically for structures exposed to fire [16]. The software uses an uncoupled thermal and structural analysis to model structures subjected to fire. To evaluate the response after sufficient cooling, each analysis case was programmed for a maximum time series of 19 hours even though the fire lasted less than 5 hours (see Figure 3). The maximum and minimum time steps for both the 3-D and 2-D analyses were set to 60 second and 0.0001 seconds, respectively.

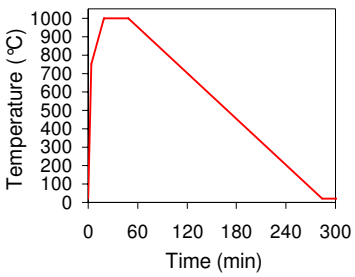

Fig. 3 – Temperature-time history of the prototype fire.

2.1 Modeling the 2-D Frame

In the 2-D frame models, three-noded 2-D non-torsional beam elements were used to represent the girders, columns, and the slab. Before structural analysis of these elements can be performed, a thermal model of each element must be analyzed. Two-dimensional heat transfer is performed for each beam elements, whose cross-sections are discretized into solid

elements. The heated floor members and perimeter columns are exposed to fire on three sides only (i.e. the top face of a floor member is shielded by the slab and one face of the perimeter column is on the building's exterior), and thus these members will develop a thermal gradient through their depth. Figure 4 shows an example of the discretized section used to represent the girder and the filler beam, shown with fire protection and a 2-meter (6.5-ft.) effective width of slab as prescribed by structural codes [17]. The slab in this case is modeled with an average depth of 102 mm (4 in.). Sections that include both the steel beam and the slab will be referred to as *composite*.

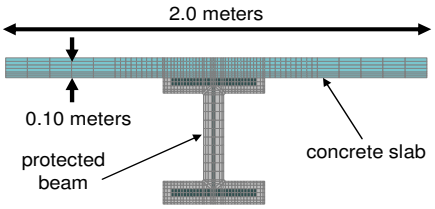

Fig. 4 – Discretized cross section of the protected composite girder.

The thermal results of the column and composite floor cross-sections are input into the structural analysis of the 2-D frame. In the 2-D structural model, each solid element from the thermal model becomes a "fiber" with an area, temperature, and distance to the reference axis. These fibers are represented in the structural model with one "beam element," as shown in Figure 2(c). Note that the structural cross-sections for the girder and filler beam include the fibers of both the steel wide-flanged section and the slab, which have perfect strain compatibility at their interface. The 2-D structural FE model used to analyze the girder and perimeter column is the plane-frame elevation in Figure 1(b) along girder line B in Figure 1(a). Each column is modeled with 16 beam elements, and each girder is modeled with 30 beam elements. The 2-D model used to analyze the filler beam is idealized as a single member spanning between pinned supports with restrained translation (i.e. between the girders), as shown in Figure 5. Each filler beam is modeled with 21 beam elements along its length.

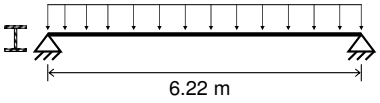

Fig. 5 – 2-D model of the filler beam.

2.2 Modeling the 3-D Frame

The 3-D analyses used the same thermal models for the floor member cross-sections as the 2-D analyses (Figure 4). However, only the thermal results for the steel are input into the beam elements for the girders and filler beams in the 3-D structural analysis. The slab fibers in the thermal cross-section need not be included as part the structural cross-section for the 3-D beam elements because the slab is accounted for with shell elements. Thermal analysis for the shell elements representing the slab is one-dimensional through the slab's thickness, which is discretized into solid element strips.

In the 3-D structural models, three-noded 3-D beam elements (capable of torsion) and four-noded shell elements (with 5 integration points through their depth) were used to represent the steel frame members and the concrete slab, respectively. A wireframe of the 3-D FE model is shown in Figures 6(a) and 7(a). As in the 2-D model, each column was modeled with 16 beam elements, and each girder was modeled with 30 beam elements. Each beam parallel to beam lines 1 and 2 in Figure 1(a) was modeled with 21 beam elements. The slab was modeled with roughly a constant 305-mm (1-ft.) square discretization. As shown in Figure 2(b), adjacent 305-mm (1-ft.) wide strips with uniform depths that represent the minimum and maximum depth of the ribbed slab are used to reasonably approximate the anisotropic two-directional bending properties of the ribbed slab. The location of the slab centroid relative to the girder centroid is preserved. Slab nodes located directly over girder and beam nodes are connected to those nodes via a master-slave relationship of all six

degrees of freedom, labeled as a "link" in Figure 2(b). The slab is included only on the heated floor to cut down the size of the model by about 60%, thus reducing the computational effort needed to perform its analysis. In any case, the slabs on the unheated floors play an insignificant role in the structural response of the subassembly.

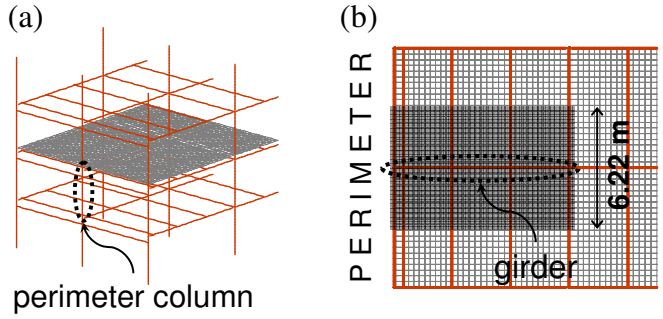

Fig. 6 – Wireframes of the 3-D model for the perim. coln. and girder comparisons: (a) isometric and (b) plan view.

Two representations of the 3-D frame model will be used for this study. The first is shown in Figure 6, which includes a two-bay width of the perimeter frame. As shown in the shaded area in Figure 6(b), the fire compartment for this frame will span one bay width but be centered underneath the girder. This model will be used to analyze the fire-exposed performance of the girder and the perimeter column, as both are the primary target of exposure to this fire. The second representation, shown in Figure 7, includes a three-bay width of the perimeter frame. As shown in the shaded area of Figure 7(b), the fire compartment for this model will span the middle bay, and all beams, girders, and columns in that bay are therefore exposed to fire. This model will be used to analyze the fire-exposed performance of the filler beams, which are the primary members exposed to this fire. The behavior of both filler beams marked in Figure 7(b) will be very similar, and therefore the performance of the filler beam on the left (closer to the building perimeter) has been selected for comparison to the 2-D filler beam model.

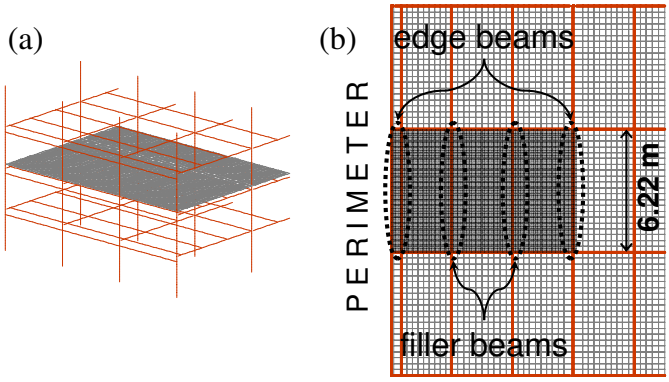

Fig. 7 – Wireframes of the 3-D model for the filler beam comparison: (a) isometric view and (b) plan view.

2.3 Fire Protection Analysis Cases

Four specific analysis cases were chosen for this study, each considering a different combination of fire protection, as specified by the building plans, for the filler beams, girders, and columns. The six-letter notation for each case is defined below:

- **BuGuCp** – The filler **b**eams (including the slab) and the **g**irder (including the edge beams as shown in Figure 7(b)) are **u**nprotected, and the **c**olumns are **p**rotected.
- **BuGpCp** – The filler **b**eams are **u**nprotected, and the **g**irder and **c**olumns are both **p**rotected.
- **BpGpCu** – The filler **b**eams and **g**irder are both **p**rotected, and the **c**olumns are **u**nprotected.
- **BpGpCp** – Fire protection is applied to all members as specified by the building plans.

These analysis cases were selected in order to demonstrate a range of performance for the three members targeted for this study. The assumption of unprotected members, though extreme, allows a worst-case calculation of behavior in the event that the fire-protection is damaged or ineffective. These cases are particularly useful for demonstrating the development of plastic behavior, which results from a combination of axial load (*P*) and bending moment (*M*).

3. RESULTS OF ANALYSIS: 3-D VS. 2-D

As the girder is heated as shown in Figure 6(b) and expands, it laterally displaces the perimeter column, thereby inducing large bending moments in this column and increased axial stress in the girder itself [1]. Likewise, the heated filler beams in Figure 7(b) will expand against the restraint of the girder and the cooler filler beams in the adjacent bays. When these fire-induced reactions develop, the perimeter column, girder, and filler beam are each subject to a combination of *P* plus *M* and therefore act as beam-columns. In addition, all of these members will develop thermal gradients due to three-sided heating, with the exterior face of the perimeter column and the slab-carrying face of the floor beams shielded from fire exposure. These gradients will induce additional bending moments due a shift in the section's effective centroid [18] (i.e. the section's center of stiffness) and a potential shift in plastic *P-M* capacity [19]. The 2-D and 3-D performance of the perimeter column, girder, and filler beam will each be measured in terms of deflection, *P*, and *M* for comparison. The perimeter column and girder, whose 3-D analyses both consider the model shown in Figure 6, will be discussed together because their performance is closely related.

3.1 Comparison of Performance for the Perimeter Column and Girder

Figures 8 and 9 show the 2-D and 3-D performance of the perimeter column and girder for the BuGuCp and BpGpCp analysis cases, respectively. The following measurements of performance are compared: the vertical deflection at the midspan of the girder; the column lateral deflection at the girder-to-perimeter column connection; the *P* and *M* for the girder, measured at its interface with the perimeter column (at which the girder's *M* is greatest due to the moment connection); and *P* and *M* for the heated perimeter column, measured just below its interface with the heated second-floor girder. Note that positive values of *P* denote compression, and positive values of *M* denote tension on the top or exterior face of the member.

Figures 8(a) and 9(a) show that both the girder and perimeter column experience similar deflections in both the 3-D and 2-D models, with the 2-D model experiencing slightly larger deflections for both analysis cases. The 3-D model has larger overall stiffness due to the presence of the adjacent structure and continuous concrete slab, and therefore it experiences smaller deflections. Figures 8(b) and 9(b) show close agreement between the 3-D and 2-D models for *P* in both members, with the 2-D model producing overall conservative values for the girder prior to decrease. The perimeter column experiences slightly higher *P* in the 3-D model as its thermal expansion is partially restrained by the adjacent bays not included in the 2-D model. Figures 8(c) and 9(c) show even closer agreement for *M* in both the girder and perimeter column, with the 2-D model predicting more perimeter column *M* in the BpGpCp case as the heated frame cools. The slab acts somewhat as a compressive diaphragm as the frame cools, preventing the tension in the plastically shortened girder from inducing as much moment in the perimeter column.

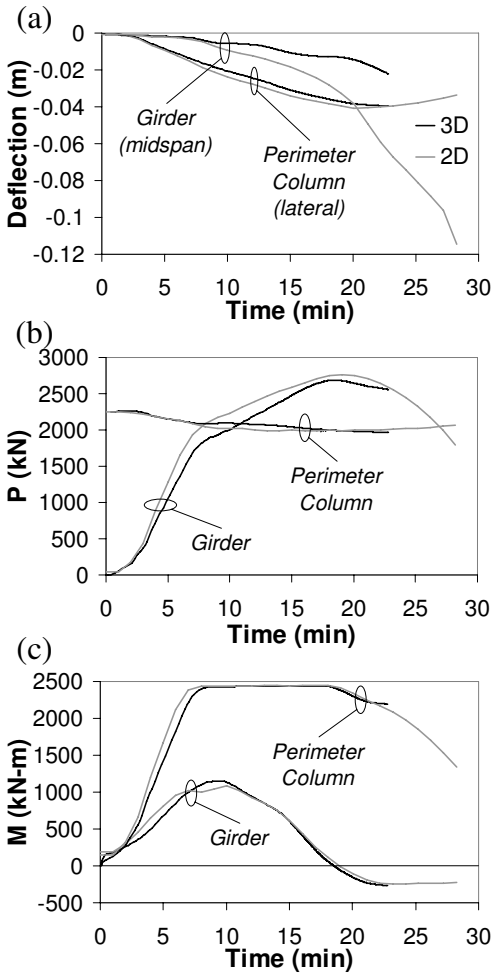

Fig. 8 – Computational results for (a) deflection, (b) axial force, and (c) moment for analysis case BuGuCp.

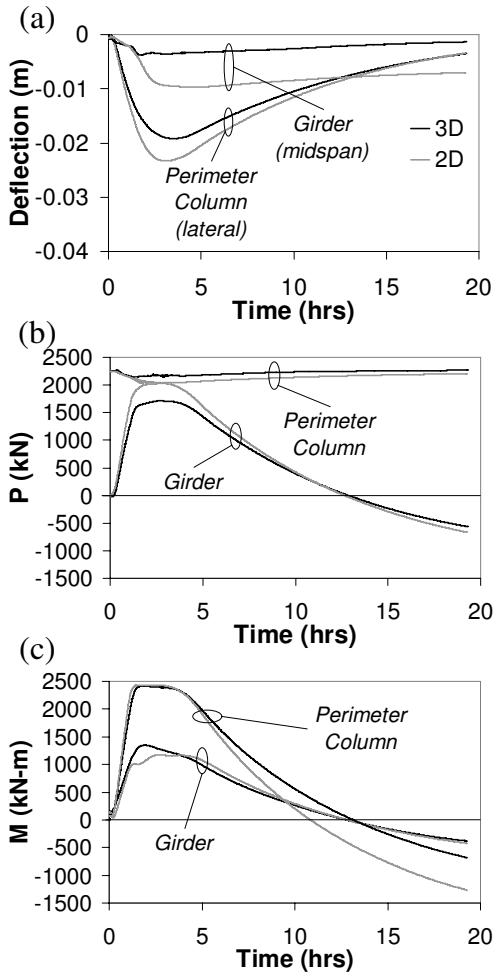

Fig. 9 – Computational results for (a) deflection, (b) axial force, and (c) moment for analysis case BpGpCp.

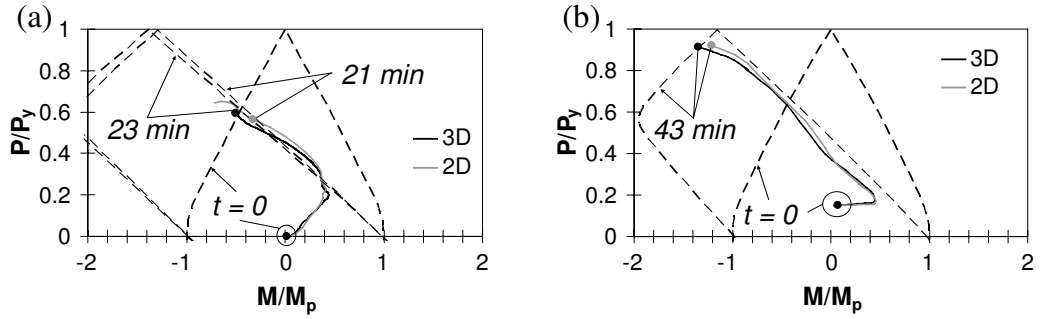

Fig. 10 – Normalized *P-M* interaction for (a) the girder in analysis case BuGuCp and (b) the perimeter column in analysis case BpGpCu.

These plots indicate that perimeter column's lateral deflection is similar in both models and that the girder in the 3-D model experiences slightly less axial force because some of that force is distributed to the slab. Although it predicts more girder deflection, the 2-D model provides a slightly conservative estimate of *P* in the girder, a reasonable prediction of *P* in the column, and an overall conservative estimate of *M* in both elements. These results indicate that the 2-D plane frame model can reasonably be used to calculate the fire-induced behavior of the plane perimeter frame representing a vertical slice of the MRF.

Figures 10(a) and 10(b) show the normalized *P-M* path of the unprotected girder in the BuGuCp analysis case (at its interface with the perimeter column) and the unprotected perimeter column in the not-yet-discussed BpGpCu analysis case (just below its interface with the heated girder). Included are the normalized plastic *P-M* capacity curves at relevant times during the section's exposure to fire. These plastic capacity diagrams, which shift with time due to the presence of a thermal gradient through the depth of the section, are calculated according to Garlock and Quiel [19]. In Figure 10(a), the 3-D and 2-D *P-M* path of the BuGuCp girder reach the plastic *P-M* capacity curve within 2 minutes of each other, showing close overall agreement. Once the 3-D *P-M* curve reaches its plastic capacity, the analysis becomes so nonlinear that it can no longer converge, and the analysis therefore stops. Once the 2-D *P-M* path reaches its plastic capacity, the analysis continues for another 7 minutes as the beam sags prior to post-yield runaway failure. In Figure 10(b), the 3-D and 2-D *P-M* path of the BpGpCu perimeter column reach their plastic capacity at the same time and show excellent agreement. These plots demonstrate that the 3-D and 2-D models are capable of predicting similar *P-M* interaction behavior. A detailed discussion of these *P-M* mechanics, including the moment reversal seen in both Figures 10(a) and 10(b), is provided in [18].

The 3-D and 2-D analyses achieved similar behavior and limit states while progressing to approximately the same time steps at which the analysis of each case terminated. However, the run times of the 3-D analyses using the model shown in Figure 6 were about 250 times greater than those of the 2-D plane frame analyses using the model shown in Figure 1(b). Because of their size and complexity, the 3-D analyses progressed at much smaller time steps, required more run time per time step to converge, and often reverted to the minimum time step to overcome periods of high nonlinearity. Each of these factors contributed to a much large overall run time of the 3-D analyses.

3.2 Comparison of Performance for the Filler Beam

Figures 11 and 12 compare the 2-D and 3-D performance of the filler beam for the BuGpCp and BpGpCp analysis cases, respectively. Measurements for vertical deflection, *P*, and *M* in the filler beam are taken at midspan, where moment is greatest. Figure 11(a) shows that the unprotected 3-D filler beam experiences less downward deflection than in the simple 2-D model, due to the added stiffness provided by the continuous concrete slab. Figure 12(a) shows a similar trend as the filler beam heats (up to t ~ 4 hrs), but then the 2-D beam experiences less residual deflection as it cools. Both Figures 11(b) and 12(b) show a similar trend in *P*, with both the 2-D and 3-D filler beams experiencing a rapid increase until reaching a sudden peak. As seen in Figure 13, which shows the normalized *P-M* behavior for both of these analyses, this peak corresponds to the point at which the filler beam's plastic *P-M* capacity is reached. Figures 13(a) and 13(b) show that once the filler beam reaches the plastic *P-M* capacity envelope, the member's *P-M* path remains on or near the envelope throughout most of the remainder of the simulation. Note that even though the member has yielded, the member will hang from its supports and, in the 3-D case, from the continuous slab in a catenary state.

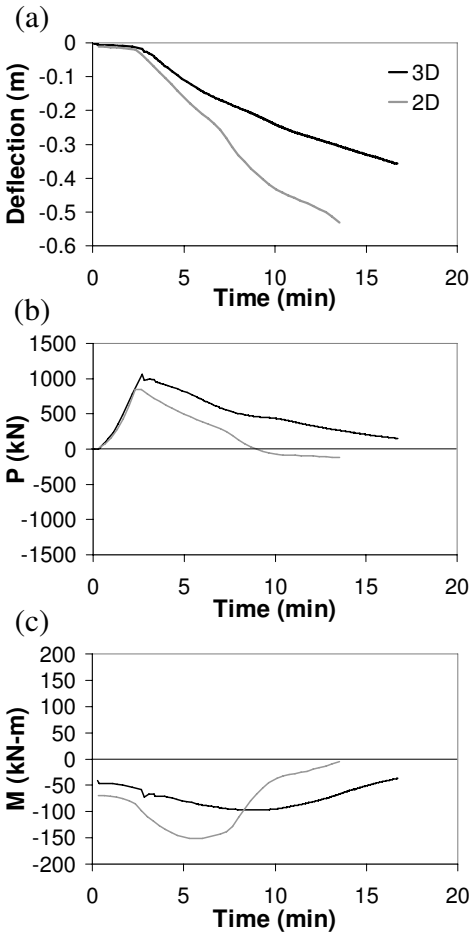

Fig. 11 – Computational results for filler beam (a) deflection, (b) axial force, and (c) moment for analysis case BuGpCp.

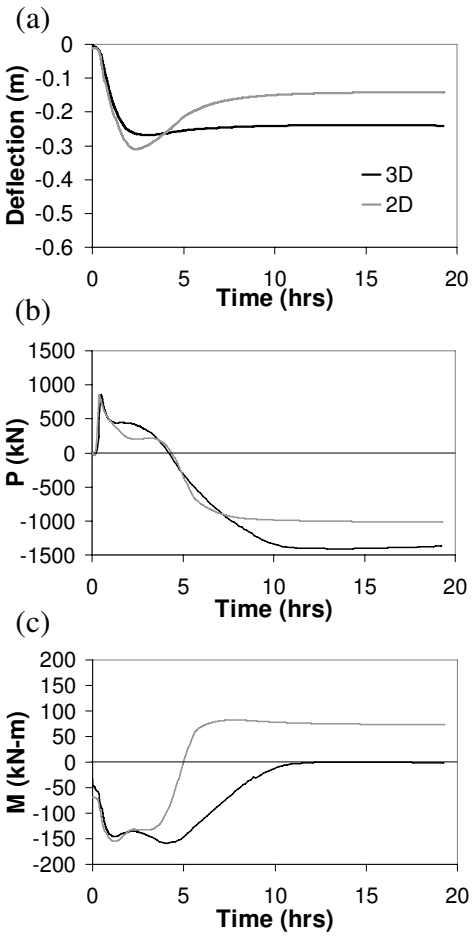

Fig. 12 – Computational results for filler beam (a) deflection, (b) axial force, and (c) moment for analysis case BpGpCp.

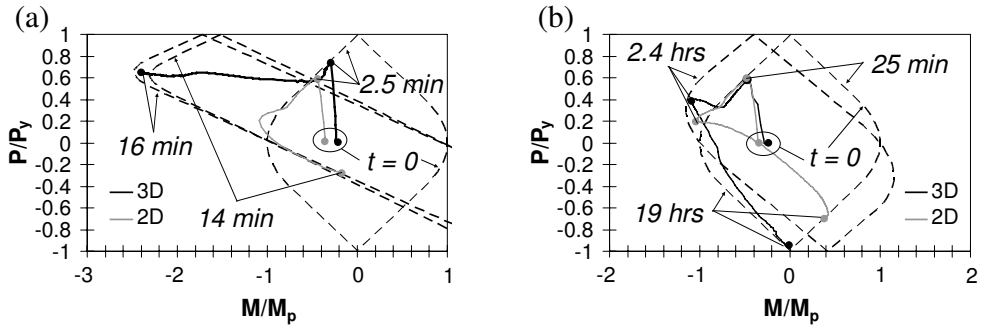

Fig. 13 – Normalized *P-M* interaction for the filler beam in (a) analysis case BuGpCp and (b) analysis case BpGpCp.

In Figure 11(b), the members display similar post-peak behavior until the analysis terminates. In Figure 12(b), the two models show similar post-peak behavior until t ~ 8 hrs, after which the 3-D filler beam experiences more residual *P* in tension as the member cools. The values of residual stress (calculated as the value of *P* divided by steel cross-sectional area) in both models are reasonably consistent with actual post-fire measurements made in floor beams in the prototype structure [20]. Figure 11(c) shows relatively similar moment patterns, as does Figure 12(c) before t ~ 4 hrs. After this time, the 2-D filler beam in Figure 12(c) undergoes a larger moment reversal and eventually experiences a positive moment.

The 2-D filler beam in analysis BpGpCp experiences less residual deflection, less residual *P*, and a larger moment reversal due to its larger initial deflection (before t ~ 4 hrs). The added deflection causes added elongation of the member, which counteracts a portion of the plastic shortening caused by the restraint to thermal expansion. With less plastic shortening, the 2-D filler beam experiences less residual tension as the member cools. The added deflection also creates a larger gradient of plastic strain between the top and bottom flange, with the added deflection having decreased the plastic shortening of the bottom flange and increasing the compression (and thus the plastic shortening) in the top flange. This gradient leads to an increase in positive residual moment in the 2-D model as the top flange will have more tension relative to the bottom flange when the member cools.

The 3-D and 2-D filler beam models achieved relatively similar behavior while progressing to approximately the same time steps for both the BuGpCp and BpGpCp analyses. For the latter case, this was expected as both of the fully protected 3-D and 2-D models progressed through the entire 19-hour time series and did not experience instability or collapse. For the 2-D BuGpCp case, the member experienced a rapid decrease in stiffness, which led to eventual runaway failure as seen by the downward turn at the end of the 2-D member's deflection curve in Figure 11(a). The downward deflection for the 3-D BuGpCp case, however, does not experience runaway as seen in Figure 11(a) and remains stable even as the analysis terminates. This analysis case terminates due to the emergence of negative stiffness at the exterior edge of the slab, which is a local failure and does not indicate instability in the overall floor system. Barring this localized failure, the 3-D BuGpCp case would have progressed further, perhaps lasting the entire analysis due to tensile membrane action as the unprotected filler beams and slab interact with the protected girders, columns, and edge beams. This type of behavior was observed during the Cardington experiments [21] and has been successfully modeled by numerous researchers [9,12]. Future research will attempt to overcome this localized failure at the exterior edge of the slab and allow the analysis to progress to a more realistic final state.

The comparison of 3-D and 2-D models for the filler beam indicate that the two models capture similar restraint to the beam's thermal expansion but that the continuous slab has a non-negligible effect on the member's deflection. Trends for *P* and *M* are similar, but the values for each vary slightly due to variations in deflection, which lead to variations in the development of plastic strain. The difference in run times is even more significant than in the case of the girder and perimeter column comparisons, with the 3-D analyses (using the model shown in Figure 7) running at least 1200 times longer than those of the single member 2-D filler beam (using the model shown in Figure 5). The same factors discussed in Section 3.1 contributed to the large disparity in run time between these two models, except that the 3-D model used to study the filler beam was one-third larger and the 2-D model was much simpler.

4. SUMMARY AND CONCLUSION

As finite element models of high-rise frames have become widely used for studying structures exposed to fire, analysts are increasingly faced with a decision between more complex yet more computationally expensive models versus simpler yet more efficient versions of the same model to obtain acceptable results. This paper compares the performance and computational cost of 3-D and 2-D finite element models for the following three member types in the perimeter of a high-rise steel building frame exposed to fire: (1) the perimeter column; (2) the girder, i.e. the beam that frames into the perimeter column perpendicular to the building exterior; and (3) the filler beams, which span between the girders. The prototype structural system selected for this study was a steel moment resisting frame (MRF), a common high-rise structural system, which had experienced an actual fire.

The results of this study indicate that the 2-D plane frame models, representing a vertical slice of the perimeter frame, deliver similar predictions of fire-exposed behavior and plastic limit states for the perimeter column and girder as larger 3-D models with multiple bay widths. Predictions of axial load and bending moment showed particularly close agreement, while the deflection or the girder was somewhat mitigated in the 3-D model by the added stiffness of the continuous slab. Comparison of these models indicated that the 2-D plane frame model can reasonably be used to predict the performance of the perimeter column and girder in a fire-exposed high-rise MRF with a 250 times savings in analysis run time.

The filler beam comparisons indicated that these members are more sensitive to the structural effects of a continuous concrete slab. The 2-D and 3-D models showed good agreement for peak values of axial force in terms of magnitude and time of occurrence. These models also delivered similar overall predictions of axial force and moment but experienced some variation in residual values following their peak. Downward deflections also showed non-negligible variation, with the 3-D model experiencing less maximum deflection due to the presence of the continuous concrete slab. This difference in maximum deflection was responsible for the variation in residual axial force and moment. These results indicate that the 2-D model can be used to obtain a reasonable prediction of the restraint to the filler beam's thermal expansion as well as the trend of axial force and moment at a significant savings (more than a factor of 1200) in run time. However, it is recommended that the analyst use a 3-D model that includes the continuous slab if deflections are the focus of efforts to model filler beams in the perimeter of a fire-exposed steel MRF.

5. ACKNOWLEDGEMENTS

Mr. Quiel has been involved with this research project while on appointment as a U.S. Department of Homeland Security (DHS) Fellow under the DHS Scholarship and Fellowship Program, a program administered by the Oak Ridge Institute for Science and Education (ORISE) for DHS through an interagency agreement with the U.S. Department of Energy (DOE). ORISE is managed by Oak Ridge Associated Universities under DOE contract number DE-AC05-00OR22750. This material is also based upon work supported by the National Science Foundation (NSF) under grant number CMMI-0652282 and the National Institute of Standards and Technology (NIST) under grant number 60NANB7D6121. All opinions, findings, and conclusions expressed in this paper are the authors' and do not necessarily reflect the policies and views of the DHS, DOE, ORISE, NSF, or NIST.

6. REFERENCES

[1] Garlock, M.E.M. and Quiel, S.E., "The behavior of steel perimeter columns in a high-rise building under fire," *Engineering Journal* (AISC), Vol. 44, No. 4, pp. 359-372, 2007.

[2] Flint, G., Usmani, A., Lamont, S., Lane, B., Torero, J., "Structural response of tall buildings to multiple floor fires," *Journal of Structural Engineering* (ASCE), Vol. 133, No. 12, pp. 1719-1732, 2007.

[3] Landesmann, A. and Batista, E.M., "Refined plastic hinge model for the analysis of steel-framed structures under fire conditions," *Proc. 4th Int. Workshop on Structures in Fire (SiF06)*, Vol. 1, pp. 427-438, 2006.

[4] Duthinh, D., "2D analysis of a building frame under gravity load and fire," *Proc. Computational and Experimental Engineering Sciences Int. Conf.*, pp. 1-6, 2004.

[5] Zaharia, R. and Franssen, J.-M., "Fire design study case of a high-rise steel storage building," *Proc. 3rd European Conf. on Steel Structures (EUROSTEEL)*, 2002.

[6] Chang, J., Buchanan, A.H., Moss, P.J., "Effect of insulation on the fire behaviour of steel floor trusses," *Fire and Materials*, Vol. 29, pp. 181-194, 2005.

[7] Moss, P.J., Buchanan, A.H., Seputro, J., Wastney, C., Welsh, R., "Effect of support conditions on the fire behavior of steel and composite beams," *Fire and Materials*, Vol. 29, pp. 159-175, 2004.

[8] Wang, Y.C. and Moore, D.B., "Steel Frames in fire: analysis," *Engineering Structures*, Vol. 17, pp. 462-472, 1995.

[9] Lamont, S., Lane, B., Flint, G., Usmani, A., "Behavior of structures in fire and read design – a case study," *Journal of Fire Protection Engineering* (SFPE), Vol. 16, No. 2, pp. 5-35, 2006.

[10] Hirashima, T., Li, Y.G., Fujita, M., Segawa, H., Fujimoto, K., Uesugi, H., "Influence of concrete floor slab on stress-deformation behavior of high-rise steel frame exposed to compartment fire," *Proc. 4th Int. Workshop on Structures in Fire (SiF06)*, Vol. 1, pp. 511-518, 2006.

[11] Liew, J.Y.R. and Ma, K.Y., "Advanced analysis of 3D steel framework exposed to compartment fire," *Fire and Materials*, Vol. 28, pp. 253-267, 2004.

[12] PIT Project, *Behavior of steel framed structures under fire conditions – Main Report*, University of Edinburgh, UK, June 2000.

[13] Flint, G., Usmani, A., Lamont, S., Lane, B., Torero, J., "Fire induced collapse of tall buildings," *Proc. 4th Int. Workshop on Structures in Fire (SiF06)*, Vol. 1, pp. 415-426, 2006.

[14] CEN, *Eurocode 3: Design of Steel Structures, Part 1.2: General Rules – Structural Fire Design*, ENV 1993-1-2:2001, European Committee for Standardization (CEN), Brussels, Belgium, 2001.

[15] CEN, *Eurocode 2: Design of Concrete Structures, Part 1.2: General Rules – Structural Fire Design*, ENV 1992-1-2:1996, European Committee for Standardization (CEN), Brussels, Belgium, 1996.

[16] Franssen, J.-M., *User's Manual for SAFIR 2007 – A Computer Program for Analysis of Structures Subjected to Fire*, University of Liege, Belgium, 2007.

[17] ACI, *Building Code Requirements for Structural Concrete (ACI 318-02) and Commentary (ACI 318R-02)*. American Concrete Institute, Farmington Hills, MI, 2002.

[18] Garlock, M.E.M. and Quiel, S.E., "Mechanics of wide-flanged steel sections that develop thermal gradients due to fire exposure," *International Journal of Steel Structures* (KSSC), Vol. 7, No. 3, pp. 153-162, 2007.

[19] Garlock, M.E.M. and Quiel, S.E., "Plastic axial load - moment interaction curves for fire-exposed steel sections." *Journal of Structural Engineering* (ASCE), Vol. 134, No. 6, accepted for publication, 2008.

[20] Dexter, R.J. and Lu, L.-W., "The effects of a severe fire on the steel frame of an office building," *Engineering Journal* (AISC), Vol. 38, No. 4, pp. 167-175, 2001.

[21] Bailey, C.G., Lennon, T., Moore, D.B., "The behaviour of full-scale steel-framed buildings subjected to compartment fires," *The Structural Engineer*, Vol. 77, No. 8, pp. 15-21, 1999.

DEPENDABLE PERFORMANCE OF STEEL STRUCTURES IN FIRE – THE BRITOMART EAST OFFICE BUILDING

MARTIN FEENEY [1], CHARLES CLIFTON [2] and NANDOR MAGO [3]

ABSTRACT

This paper presents a case study of the application of a structural fire model, known as the Slab Panel Method (SPM), to a new 12 level office building, under construction in Auckland. The SPM, developed by the NZ Heavy Engineering Research Association (HERA) in conjunction with the University of Canterbury, accounts for the inelastic reserve of strength available from composite steel/concrete floor systems due to their two way deformation under fully developed fire conditions. . The outcome of the performance based design process is a steel structure with partial fire proofing to the steel beams supporting the floor. Structural elements which are critical for stability are protected with conventional fire proofing materials, and the floor beams for which fire proofing is not necessary for structural stability or integrity are designed without this passive fire protection, for the expected temperatures and associated mechanical properties..

To validate the design solution, the structure has been modelled using finite element analysis to assess the actual performance for the range of structural fire severity expected. As a further comparison, the same structure has been assessed assuming it is fully protected with fire proofing, applied as required by the New Zealand prescriptive solution for fire safety. As expected, the deformations of the floor system in the fully protected steel structure are considerably less when exposed to severe fire than those for the structure as designed (with partial fire proofing). However, the magnitude of this difference does not change the overall outcome in terms of structure performance and post-fire remedial work that would be required.

The paper concludes that design methods are maturing to a level where a dependable and robust performance can be predicted using the Slab Panel Method, so that those parts of

[1] Senior Fire Engineer and Principal, Holmes Fire & Safety, Auckland, New Zealand
email: martin.feeney@holmesfire.com
[2] Associate Professor, Department of Civil Engineering, University of Auckland, New Zealand
email: c.clifton@auckland.ac.nz
[3] Finite Element Analyst, Heavy Engineering Research Association, Manukau City, New Zealand
email: nandor.mago@hera.org.nz

the structure which require fire proofing can be specified with enough protection to maintain structural stability, and those parts which do not need this passive fire protection can be safely constructed without fire protection.

1. INTRODUCTION

The fire resistance of steel structures in office buildings and their inelastic reserve of strength in fully developed fires has received significant attention in recent years. Arising from New Zealand's performance based Building Code [1] – which applies to all aspects of building performance – there has been a strong focus on designing for the expected performance in fire rather than simply adopting prescriptive requirements which typically and traditionally involve the passive fire protection of all structural steel members.

This is especially the case in sprinkler protected buildings, given the very high effectiveness of sprinklers in preventing fire growth reaching full development (eg. Feeney [2]). This means that in sprinkler protected buildings inelastic response in fully developed fires is an acceptable ultimate limit state response provided that the building does not collapse and the floors continue to function as effective fire separations.

One of the principal design procedures developed in New Zealand to take account of this inelastic reserve of strength is the Slab Panel Method (SPM) [3]. The SPM is the outcome of 8 years of research, formulating Bailey's [4] tensile membrane model of floor system response into a design model for general application to steel framed buildings with composite concrete floors on steel deck.

This paper presents the application of the SPM to the steel structure of a multi-storey office building and the resulting performance based design solution which allows for partial fire proofing.

2. REGULATORY ENVIRONMENT

The mandatory provisions for building work are contained in the New Zealand Building Code (NZBC) [1], which comprises the First Schedule to the Building Regulations 1992. The Building Code is performance based and the mandatory clauses are written in non-quantitative performance oriented terms. Compliance with the Building Code is explicitly permitted by "any means". Structural stability during fire is a requirement of NZBC Clauses B1 Structure and C4 Structural Stability During Fire.

The performance requirement in Clause B1 is that "buildings … shall have a low probability of becoming unstable, losing equilibrium, or collapsing throughout their lives. Account shall be taken of all physical conditions likely to affect the stability of buildings including self-weight, imposed gravity loads arising from use, … fire, (etc.)". The functional requirement in Clause C4 is to "maintain structural stability during fire to:(a) Allow people adequate time to evacuate safely, (b) Allow fire service personnel adequate time to undertake rescue and firefighting operations, and (c) Avoid collapse and consequential damage to adjacent household units or other property".

Prescriptive compliance documents (eg. Acceptable Solutions and Approved Verification Methods such as Codes of Practice) can be used to prescribe requirements in familiar terms of fire resistance ratings (as is common in most other countries). A design that complies with the compliance documents is deemed to comply with the Building Code, but this is non-mandatory. A structural fire safety solution that is outside the scope of the

compliance documents is categorised as an alternative solution. This type of solution cannot be rejected simply because it does not follow a prescriptive compliance document.

The building owner is responsible for demonstrating how an alternative solution complies with the non-quantitative performance requirements of Building Code. A common method is to establish that the alternative solution provides an equivalent level of performance (which is distinctly not the same as an equivalent solution). In some situations an appropriate design solution may need fewer components in the fire safety system than prescribed in compliance docs

For the Britomart East building, the acceptance criteria for adequate performance of the structure as prescribed in the fire safety strategy report prepared for the building is based on achieving the level fire resistance stated in the compliance document, which is deemed to comply with the Building Code. Fire resistance of the structure was verified using the HERA Slab Panel Method outlined in this paper. This method has recently been acknowledged by the Authority Having Jurisdiction as an acceptable method for establishing performance of the structure during fire.

3. BRITOMART EAST PROJECT

The Britomart East project is a new 36,000 m2 building under construction in the Auckland City central business district. The building contains predominantly office use, with retail at the ground floor and apartments at the three top most floors.

The building is built on top of an existing underground train station. A 10 storey atrium is built over a public pedestrian street which passes through the centre of the building. The structural design solution was constrained by the location and load capacity of the existing concrete columns and pile foundations of the train station (which had been designed to allow for a building to be constructed above). A steel structure was selected because of its relatively light weight (giving maximum floor area for a given maximum permitted foundation load) and speed of construction. An isometric view of the steel framing and a typical floor plan is shown in Figures 1 and 2.

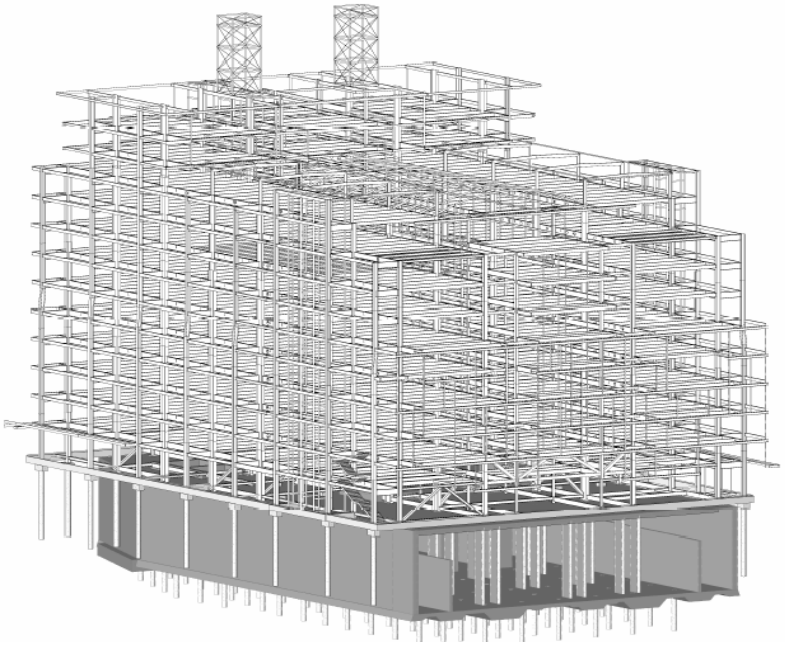

Fig. 1 - Isometric view of the steel structure – Britomart East building

Unfortunately the structural grid for the building (constrained by the existing train station foundations) is not ideal for a steel structure. Seismic design requirements in New Zealand codes also have strong influence on size of structural members. These combined influences resulted in many steel elements being sized for stiffness rather than strength – leaving more reserve strength which improves performance during fire.

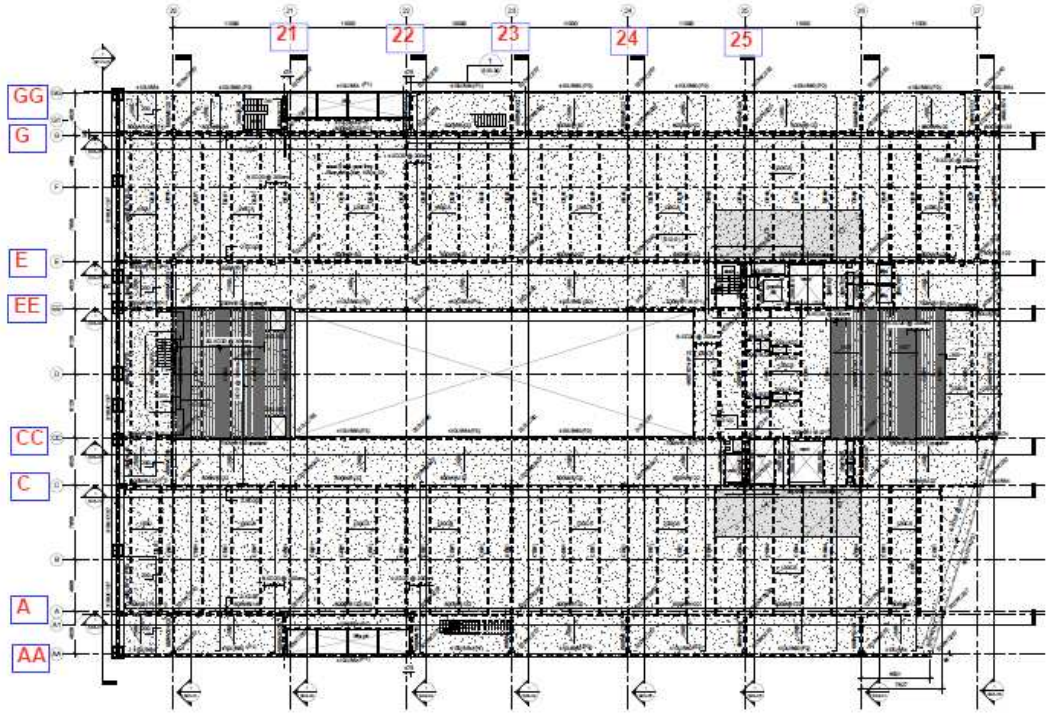

Fig. 2 - Typical structure floor plan – Britomart East building

Two main variations of steel structure were considered for support of floor slab during design development – hot rolled UB sections and cellular beams (cellular beams are custom fabricated beams formed from two tee sections profile cut and welded to form a deep, light beam with regularly spaced circular openings in the webs). The final design selected was the cellular beam option, as this provides much greater flexibility for installation of building services and lower total steel weight per unit floor area. The lateral load resisting system is comprised of rigid steel moment-resisting frames. The external perimeter cladding is a mix of curtain wall glazing and concrete cladding panels.

The building is to be protected with an automatic sprinkler system in all areas (except at the roof level of the 10 storey atrium). It is also provided with passive fire separations between all floors (60 minutes fire resistance rating), automatic smoke detection and a voice messaging system for staged evacuation of different parts of the building.

4. DESCRIPTION OF THE SLAB PANEL METHOD

The Slab Panel Method (SPM) has been used to assess which parts of the steel structure supporting the floor system need passive fire protection to maintain structural stability in order to meet the performance requirements of the Building Code.

The Slab Panel Method is written for application to steel framed buildings with composite floors. It is applicable to a wide range of design fire loads, providing design fire

resistance between 30 to 240 minutes and covers most forms of concrete floor system which are made integral with the supporting steel beams. The procedure is written for application to large regions of floor system in buildings subject to fully developed fire conditions and incorporating unprotected steel members, where these members may be subjected to very high temperatures and the floor system subjected to considerable inelastic demand. The extent of this inelastic demand is determined and a dependable proportion of the additional reserve of strength available from the building when the floor system undergoes this deformation is incorporated into the procedure. The procedure takes into account the temperatures that unprotected steel beams can realistically reach in fully developed fires over large areas.

The method requires a design 'fire resistance rating' to be determined from an appropriate source. Typically this is the equivalent fire severity, t_e, as given by Annex F of Eurocode 1 [5]. The floor system adequacy to support the fire emergency design vertical load for this time is determined using the SPM procedure. The SPM also specifies minimum detailing requirements to ensure the expected deformation can be achieved without premature non-ductile failure in the structure.

The SPM, based on the tension membrane concept presented by Bailey [4], contains design and detailing provisions presented as an integral part of the SPM have been developed from a multi-year research programme involving further theoretical and experimental research carried out by HERA and the University of Canterbury [6, 7, 8].

The key differences between the SPM and the tensile membrane model developed by Bailey (and implemented in the UK in the computer software TSLAB) are:

- TSLAB takes into account only the contribution of the slab panel for flexural strength. The contribution of any supporting beams has to be considered separately and the two summed. SPM incorporates the contribution of the supporting beams directly into the flexural/tensile membrane slab panel load capacity
- SPM implements a check for shear capacity of the slab panel, while TSLAB does not
- The methodology for determining the elevated temperatures of all components in SPM is more comprehensive than in TSLAB and has been developed from the experimental programme by Lim [7]
- SPM allows for the slab panel supports to develop negative moment flexural resistance but does not take into account any lateral restraint of the slab panel edges
- The limits on maximum deflection of the slab panel initially recommended by Bailey have been modified based on the experimental testing and analytical modelling undertaken in the development programme. The deflection is also a function of the fire resistance rating, based on a best fit curve to the experimental and analytical research results
- The SPM procedure contains comprehensive structural detailing requirements to ensure that the floor panel can dependably develop the design deformations without loss of structural stability or integrity

Comparison work by the second author has shown that SPM gives results that are in satisfactory agreement with the specialised finite element program VULCAN [9] developed in the UK. However the SPM is easier and quicker to apply.

5. APPLYING THE SLAB PANEL METHOD TO BRITOMART EAST BUILDING

Regardless of the very low probability that a fire in the sprinklered Britomart building would reach flashover conditions and adversely affect the structure (annual probability less than 1.2×10^{-5}), the fire scenario selected to represent the design case for the analyses covered in this paper is the low probability event of a fire not controlled by the sprinkler system and which reaches full development. This assumes that the sprinklers do not operate and that a fire

grows uncontrolled by any manual or automatic suppression. The analysis of structural stability for elements of the steel structure that are not provided with conventional passive fire protection concentrates on the analysis of effects of fire on the office floors.

The final SPM derived design solution is with the beams along the north and south sides of the slab panels protected (eg. between grid lines A and C) and every 7th cellular beam along the east and west sides of the slab panels protected and stiffened. These beams are shown in Figure 3.

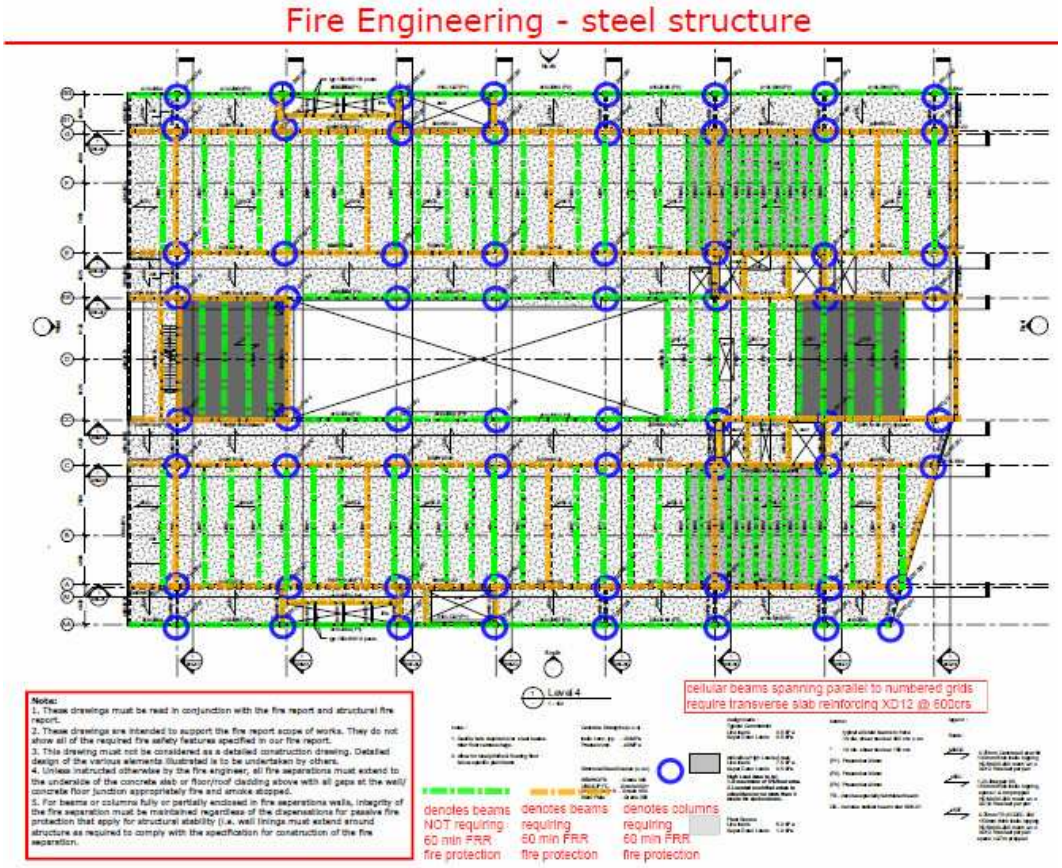

Fig. 3 - Passive fire protection to steel beams for a typical floor – Britomart East building

6. DESCRIPTION OF THE FINITE ELEMENT ANALYSIS AND DISCUSSION

The Britomart floor system comprises composite in-situ concrete floors on steel decking supported by a network of primary and secondary steel beams. Under ambient temperature conditions, this system is designed to act as a series of one-way load spanning elements, taking loads from the slab to the secondary beams, secondary beams to primary beams and primary beams to columns. As specified in the SPM, under severe fire the unprotected secondary beams lose strength and the floor system responds as a two way 'slab panel' element.. Each slab panel has 4 sides, with each side required to have sufficient strength to support the tributary loads direct from the slab panel onto the particular side support. This means that for the sides of the panel supported on secondary beams, designated by the SPM as sides 2 and 4, the supporting beams may carry greater magnitude of fire emergency load than their design ambient temperature vertical loading case, even though the

load per square metre is lower. This is because of the higher tributary area on these secondary support beams. For conventional solid web secondary beams, there is normally sufficient capacity for this as the beam size is governed by deflection and or vibration considerations and they have a high reserve of strength.

However, the secondary beams between grids A and C and grids E and G are cellular beams. These are optimised for a maximum structural efficiency and strength to weight ratio and there is insufficient reserve of strength in these to carry the full fire emergency slab panel secondary beam tributary loading. In contrast, the slab panel primary support beams have sufficient strength to carry the full slab panel loading. The secondary support beams do have sufficient strength to support 1.25 times the yield line load carrying capacity of the slab panel and are sized for this loading condition. To assess (amongst other things) whether the way in which the SPM analysis accounts for the floor system in fire, including this departure from the strict application of the method, is valid, finite element analysis (FEA) of a representative portion of the typical structural floor system was carried out. This type or analysis is not routinely carried out for fire engineering design but was required in this instance due to the modification of the strict application of the SPM.

The FEA was undertaken using ABAQUS/CAE/Explicit version 6.7-4. The structural response of the composite steel-reinforced concrete slab was investigated for several fire loading cases. This has been performed in an explicit "quasi-static FE procedure" with temperature dependent material properties, as described below. A more detailed description of this analysis is given in Mago [10].

Fig. 4 shows part of the building on which FEA was undertaken. Lateral support conditions were varied from free to restrained (symmetrical boundary conditions) along grid lines 21 and 24, since finite element sub modelling was not applicable in this case. In practice, all the slab panels are laterally restrained to some extent, with this incorporated into the FEM, while the SPM assumes no lateral restraint to any panel in the plane of the slab. Symmetry was assumed in the mid plane between grid lines A and C.

Columns were represented as extending to floor levels below and above the compartment in the FE model. At the lower level the columns were fixed or pinned as appropriate, while at the upper level they were axially loaded with design forces from the levels above. The boundary conditions allowed the columns to extend only upwards. All beams in moment frames were fully welded to the columns, while the cellular beam web was bolted to the primary/column web with a web cleat. Equivalent reinforced concrete slab of 100mm thickness was used to represent the floor slab, which in practice is a composite steel-concrete trapezoidal profile. This approximation has been shown to be valid in the modelling of experimental testing undertaken as part of the SPM development, provided that the reinforcement position and area is adjusted to give equivalent load carrying capacity. This approximation significantly simplified the numerical analysis.

The slab was loaded with the self weight of the slab and uniformly distributed vertical superimposed dead load and long term design live load. In the first step, the gravity loads, column forces and payload were applied in a smooth quasi-static explicit procedure. This step was followed by the fire loading step.

Two cases were analysed. One of them is based on applying the prescriptive solution given in the Approved Document for Fire Safety (C/AS1) involving application of passive fire protection to all steel members. The second case, as designed, is a more cost effective solution based on selective fire protection and web stiffening at quarter points of the cellular beams (CBs) comprising slab panel supports in the North-South direction, while leaving unprotected the CBs within the slab panel region. The edge beams were also left unprotected.

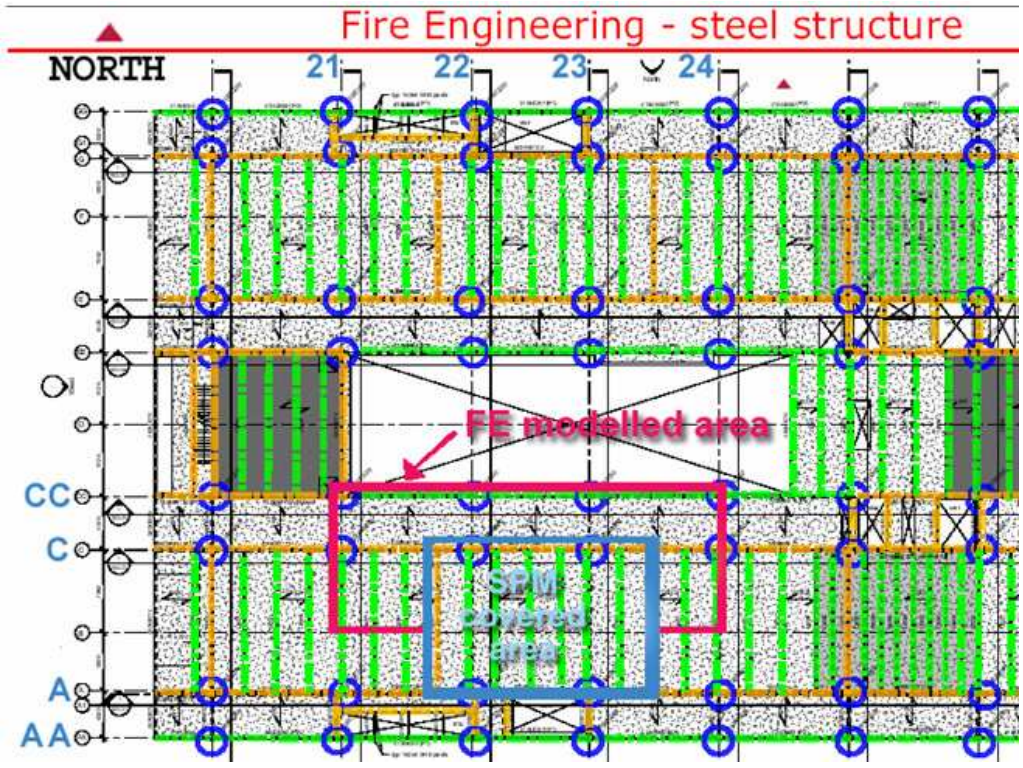

Fig. 4 - Typical floor plan shows the fire engineering design and the part of the building analysed by FEA

The first aim of the FEA was to determine the adequacy of the modified application of the SPM as part of the design solution. The second equally important aim was to determine the likely response of the structure to the range of fire conditions expected and at the end of the post –fire cooling down period. The first part of this second aim required determination of the equivalent time associated with the most severe ventilation condition, (calculated by the fire engineer as 70 minutes) and application of this to the floor system. The second part of the second aim required simulation of the structural behaviour for approximately 45 minutes heating up and for the much longer 255 minutes cooling down period. The simulation of this long lasting fire condition is challenging in explicit codes, therefore "time scaling" and mass scaling were used to obtain the solution within a reasonable time frame (up to one day).

The difficulties in performing successful highly non-linear analyses of concrete structures with temperature dependent material properties are well known. Implicit codes (such as SAFFIR, ABAQUS/Standard) do not always provide a convergent solution and FE simulations like those presented are almost impossible to perform with them. The Britomart finite element model size, complexity and the need for an extended duration deflection history dictated the explicit approach. This allowed the models to progress beyond failure in some of their regions, so large deflections could be captured in many simulations.

Fig. 5 shows the actual deformed shape at the end of the cooling down period of the natural fire condition. Most of the cellular beams are unprotected, with the reduced deflections of the protected slab panel support secondary beams showing up clearly. The figure shows the actual deformed shape and magnitude of vertical deflection at 300 minutes.

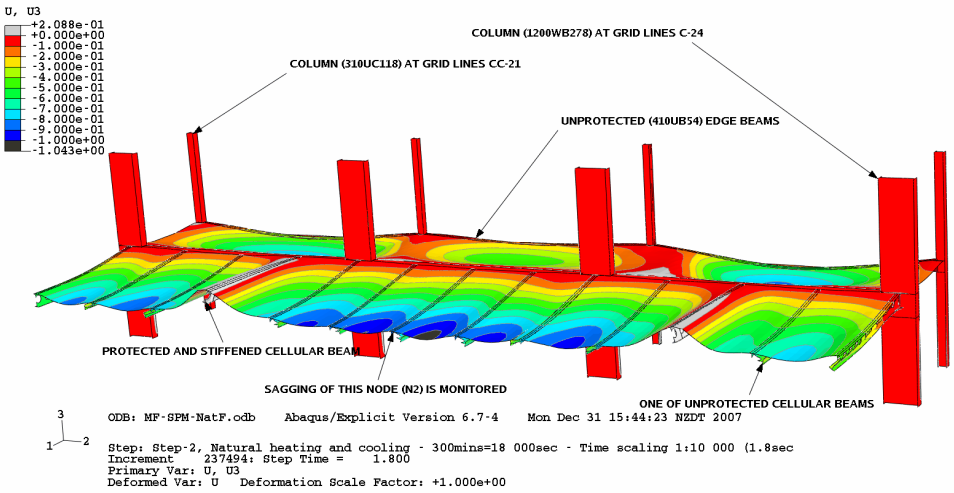

Fig. 5 - Design solution – partial fire protection – based on SPM analysis.

A floor system complying with the Compliance Document for Fire Safety, C/AS1 was also analysed. For this solution all supporting beams are passive fire protected to achieve the fire resistance rating of 45 mins. This was analysed for the natural fire condition conditions followed by cooling down period so that the results of the SPM design solution and the acceptable solution could be compared. The deformed shape for the natural fire condition is shown in Fig. 6.

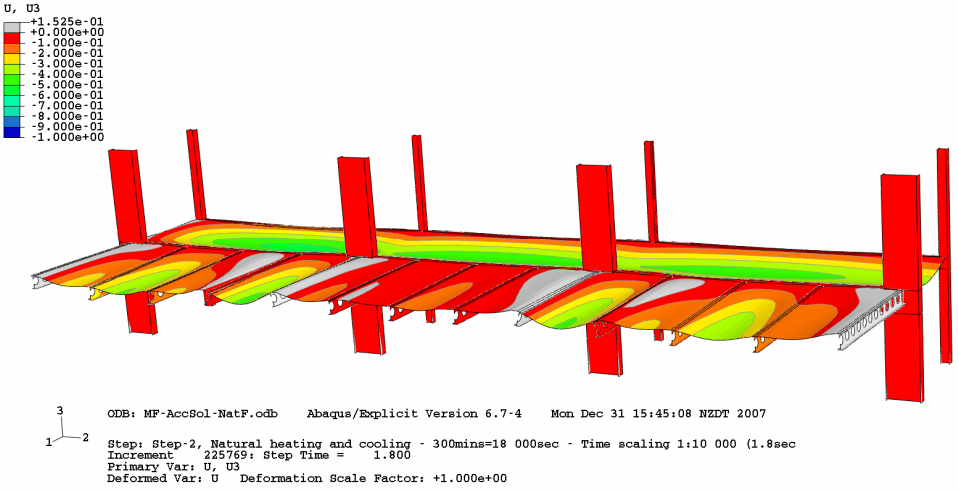

Fig. 6 - Prescriptive solution – full fire protection – based on compliance document.

7. DISCUSSION OF RESULTS FROM THE FINITE ELEMENT ANALYSIS

The key results from the finite element analysis are outlined below.

The slab panel solution between grids A and C and E and G involving the cellular slab panel edge secondary support beams is satisfactory, with all deflections and strains within acceptable limits.

Residual deflections at the centre of the slab panel after the cool down period are approximately 800 mm (span/15 – compare with span/20 limit in the standard fire test) for the structure with partial fire protection and 100 mm for the structure with full passive fire protection. This is shown in Fig. 7.

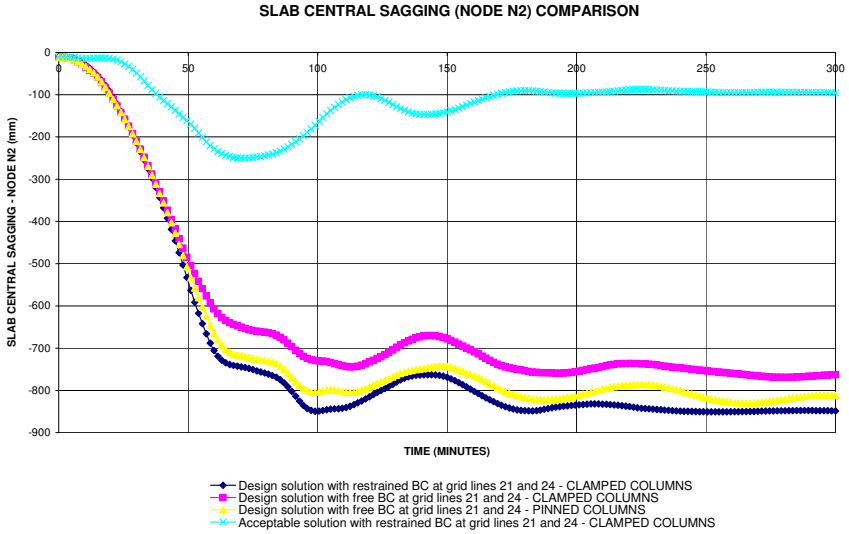

Fig. 7 - Vertical deflection time history at centre of slab panel – partial fire protection (design solution) and full fire protection (Acceptable Solution)

The slab panel itself between grids C and CC (also A and AA and the other side of the building) is satisfactory however the strain demands and deflections of the primary beams on grid CC are too high if these are left unprotected and laterally unstiffened. This is because their strength evaluation as slab panel primary supports was based on an assumed plastic collapse mechanism involving the development of composite positive section moment capacity in the midspan regions and bare steel beam section moment capacity at the support rigid connections. The FEM shows that the latter is achieved but the former is not, as the beam undergoes significant bottom flange lateral buckling in the positive moment regions. For this reason the decision was made to provide passive protection to these supporting beams.

The deflections and strains in the all beams protected solution are much lower than in the SPM complying solution, however the post fire residual deflections are still too large to reinstate the floor without requiring significant remedial work and either in-situ beam re-straightening or replacement. In theory it might be possible to re-level the top of concrete with a levelling compound. However, the structure is unlikely to have the capacity to support the additional weight, particularly if more than one floor needs to be reinstated.

8. SUMMARY OF DESIGN SOLUTION

All structural columns have passive fire protection (60 minute fire rating) to ensure that the slab panel gravity loads are supported. Approximately 80% of the secondary beams do not require passive fire protection. The beams in the main lateral load resisting frames (grid lines A1, C, E and G) are all fire protected. Selected beams on the perimeter (grid lines

AA, CC, EE and GG) are also passively protected. This reduced extent of passive fire protection has resulted in a saving of more than $300,000 for the project.

For the two main variations in extent of passive fire protection modelled by the finite element analysis, the outcome is the same for all practical purposes. The large deflections and corresponding damage to the structure exposed to the effects of a severe uncontrolled fire would require replacement of the affected beams and floor slab, regardless of whether partial of full passive fire protection is provided. In both cases structural collapse is avoided, the load carrying capacity is maintained and the floors would be expected to function as an effective fire separation for the duration of the fire.

Passive protection of all beams does not eliminate the need for detailed assessment and probable repair of the floor after being subjected to fully developed fire. A much more effective fire safety strategy is to rely on the high effectiveness of the sprinkler system (Bennetts et al, [11]), to suppress full fire development and to mobilise the inelastic reserve of strength from the floor in the very remote event of sprinkler failure. That is the approach behind the SPM method and the approach taken in this design.

9. REGULATORY APPROVAL

The Building Consent Authority responsible for regulatory approval, (confirming that a proposed design complies with the Building Code) is Auckland City Environments. Review of structural design requires specialist expertise beyond that available from Auckland City staff, so reliance is placed in external peer review. The structural fire design for the Britomart East building was reviewed independently for Building Code compliance on behalf of the Bldg Consent Authority.

10. CONCLUSION

This paper has outlined as a case study the application of the Slab Panel Method to a new 12 level office building under construction in Auckland, New Zealand. From this case study it can be seen that design methods are maturing to a level where a dependable and robust performance can be predicted using the Slab Panel Method. SPM analysis shows that if sprinklers fail to control a fire such that flashover is prevented structure retains sufficient strength to support design loads for fire load condition. Accordingly, those parts of the structure which require insulative fire proofing can be specified with enough protection to maintain structural stability, and those parts which do not need this passive fire protection can be safely constructed without fire protection. The extent of fire proofing that is not required to satisfy Building Code performance criteria has been identified, resulting in a significant cost saving to the project.

Validation of dependable structure performance consistent with this reduction in extent of fire proofing has been outlined in a brief description of the finite element analyses conducted. The finite element analyses also show that for a structure protected with passive fire protection as required to comply with a prescriptive fire safety solution and exposed to the fire severity of a fully developed fire, large deformations can still be expected (requiring post-fire replacement of affected structure)

This case study demonstrates that the SPM method can be used to assess structure performance in fire in a performance based regulatory environment.

11. ACKNOWLEDGEMENTS

The authors wish to acknowledge the building owner (Bluewater Company Ltd) and the structural engineer (Holmes Consulting Group Ltd) for their cooperation and assistance with the structural fire design for this project and preparation of this paper.

12. REFERENCES

[1.] NZBC (1992). The New Zealand Building Code, Department of Building and Housing, New Zealand.
[2.] Feeney, M., and Buchanan, AH (2000). Accounting for Sprinkler Effectiveness in Performance Based Design of Steel Buildings, University of Canterbury, Christchurch, New Zealand.
[3.] Clifton, G.C., (2006), Slab Panel Method – Design of composite steel floor systems for severe fires, 3rd Edition, HERA Report R4-131, Heavy Engineering Research Association, Manukau City, New Zealand.
[4.] Bailey, C. G. (2000). Design of steel members with composite slabs at the fire limit state, Building Research Establishment, United Kingdom
[5.] ENV1991-1-2 (2002). Eurocode 1: Actions on Structures Part 1-2: General Actions - Actions on Structures Exposed to Fire. CEN, CEN, Brussels, Belgium.
[6.] Moss, P.J and Clifton, G.C., (1999), Behaviour of multi-storey frames in fires, Proc. 16th Australasian Conference on the Mechanics of Structures and Materials, Sydney, December 8-10, pp 461-466
[7.] Lim, L. a. Wade., CA (2002). Experimental Fire Tests of Two-Way Concrete Slabs, Fire Engineering Research Report 02/12. Dept of Civil Engineering, University of Canterbury, Christchurch, New Zealand
[8.] Lim, L. (2003). Membrane Action in Fire Exposed Concrete Floor Systems, Fire Engineering Research Report 03/02. Dept of Civil Engineering, University of Canterbury, Christchurch, New Zealand
[9.] Abu, AK, Burgess, IW and Plank, RJ. "Analysis of Tensile Membrane Action in Composite Slabs in Fire", Proceedings of the 2007 Pacific Structural Steel Conference, Wairakei, New Zealand, 2007; New Zealand HERA. Manukau City, New Zealand
[10.] Mago, N., G.C. Clifton, M. Feeney and T. Porter “Performance of an office building in fire,” 2008 ABAQUS Users’ Conference, Rhode Island, 2008.
[11.] Bennetts, I.D., Goh, C. C., Thomas, I.R. and Poh, K.W. (2000), Low Rise Office Construction - A Guide to Fire Safety, One Steel Market Mills, Newcastle, Australia.

A NEW DESIGN METHOD FOR INDUSTRIAL PORTAL FRAMES IN FIRE

Y. SONG[1], Z. HUANG[2], I. W. BURGESS[3], R. J. PLANK[4]

ABSTRACT

For single-storey steel portal frames in fire, especially when they are situated close to a site perimeter, it is imperative that the boundary walls stay close to vertical, so that fires which occur are not allowed to spread to adjacent properties. A current UK fire design guide requires either that the whole frame be protected as a single element, or that the rafter may be left unprotected if column bases and foundations are designed to resist the forces and moments generated by rafter collapse, in order to ensure the lateral stability of the boundary walls. This can lead to very uneconomical foundation design and base-plate detailing.

In previous studies carried out at the University of Sheffield it was found that a fundamental aspect of the collapse of a portal frame rafter is that it usually loses stability in a "snap-through" mechanism, but is capable of re-stabilising at high deflections, when the roof has inverted but the columns remain close to vertical. Numerical tests performed using the new model show that the strong base connections recommended by the current design method do not always lead to a conservative design. It is also found that initial collapse of the rafter is always caused by a plastic hinge mechanism based on the frame's initial configuration. If the frame can then re-stabilize when the roof is substantially inverted, a second mechanism relying on the re-stabilized configuration can lead to failure of the whole frame.

In this paper, a portal frame with different bases is simulated numerically using *Vulcan*, investigating the effect of different base strength on the collapse behaviour. The test results are compared with the failure mode assumed by the current design method. A new

[1] PhD Student, Department of Civil and Structural Engineering, University of Sheffield, S1 3JD, UK email: y.y.song@sheffield.ac.uk.
[2] Lecturer, Department of Civil and Structural Engineering, University of Sheffield, S1 3JD, UK
[3] Professor, Department of Civil and Structural Engineering, University of Sheffield, S1 3JD, UK
[4] Professor, School of Architectural Studies, University of Sheffield, S10 2TN, UK

method for the estimation of re-stabilized positions of single-span frames in fire, using the second failure mechanism, is discussed and calibrated against the numerical test results.

1. INTRODUCTION

In the UK, fire protection of portal frames differs from that of other structures. Normally the roof of the building need not be protected in fire, but the portal frame is considered as a single structural element due to the rigid connection between rafters and columns, so if any part of it needs to be protected against fire, the whole frame has to be protected. It is also specified by current building regulations [1] for fire safety that the boundary wall of a building has to be fire-protected to stop fire spreading from one building to the next. As a result, the whole portal frame needs to be fully protected in fire as the boundary wall.

The design of pitched portal frames for fire conditions usually follows the SCI document P087 [2]. This design guide allows portal frames to be unprotected if the column bases have the sufficient resistance to the overturning moments (OTM) caused by the collapse of the rafters, in order to guarantee the longitudinal stability of the boundary wall. The calculation of the OTM at the column bases is based on the symmetrical failure mechanism shown in Fig. 1. In this design process, assumptions about haunch length, rafter elongation, fire hinge moments and the limiting inclination of the column are applied to simplify the calculation model. It is worth noting that these assumptions are inconsistent. The assumed rafter elongation implies a steel temperature of 1400°C, while the strength degradation of the rafter fire hinge moments relates to 900°C. The method also implies that the stability of the boundary wall is assured if the inclination of the column is less than 1°. However, the maximum horizontal movement of eaves is specified as 1/300 of the height of column in a well known design guide for masonry walls [3], which means the column inclination should remain within 0.2°. This method also assumes that the haunch length is one tenth of the span, although haunches may be of any size, if they exist.

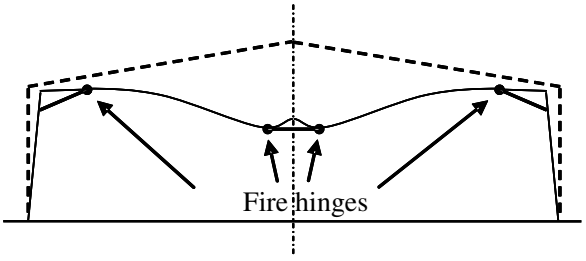

Fig. 1 – Failure mechanism used in current design method

The numerical tests on a typical single-storey industrial frame [4] will show that this symmetric failure mechanism does not always happen in fire, and even nominally rigid bases can not guarantee that the column inclination is always within 1°. The OTM required for a nominally rigid frame could be much bigger than the design value, so the assumptions used to simplify the current design model may not always lead to conservative results in fire.

2. S.Y. WONG'S SIMPLE METHOD

To reveal the true failure mechanism of portal frames in fire, three natural fire tests on a scaled portal frame were carried out at Sheffield University [5]. It can be seen from inspection of one of the tests that the roof frame deflected downward after the rafters initially lost stability in fire and rested in a stable position near to eaves level until the end of the test. It seems that, after initial snap-through of the rafters, the portal frame has re-stabilized with high deflection, and that the inclination of the column can stay within a relatively small region. A simple method, used to predict the critical temperature of single-span portal frames with simple base connections, was developed by S. Y. Wong [5]. According to plastic theory for the mechanism shown in Fig. 2, an equation can be set up equating the work done by the external and internal forces:

$$wL^2\theta = M_p[\theta + \eta_1\theta + \eta_2(\varphi + \theta)] \tag{1}$$

where η_1 and η_2 are the strength reduction factors for the fire hinges at corners 1 and 2 in Fig. 3. If a localized fire is assumed, the strength reduction factor on the unheated corner is set as 1. If the whole roof is assumed to be heated by fire, the critical temperature of the frame can be predicted according to a single strength reduction factor η using Eqn.2.

$$\eta = \frac{wL^2}{M_p(3 + \frac{h_2 + 2h_1}{h_2})} \tag{2}$$

A series of parametric studies on the single-span pitched portal frame performed by Wong [5] using *Vulcan* [6-8] showed that the critical temperatures calculated by this simple method agree with both the numerical and fire test results in predicting the initial collapse of the roof in fire. However, due to the limitations of the iterative solver used in the static model, the numerical analysis was unable to continue beyond this point, so the re-stabilized position observed in the fire test could not be traced.

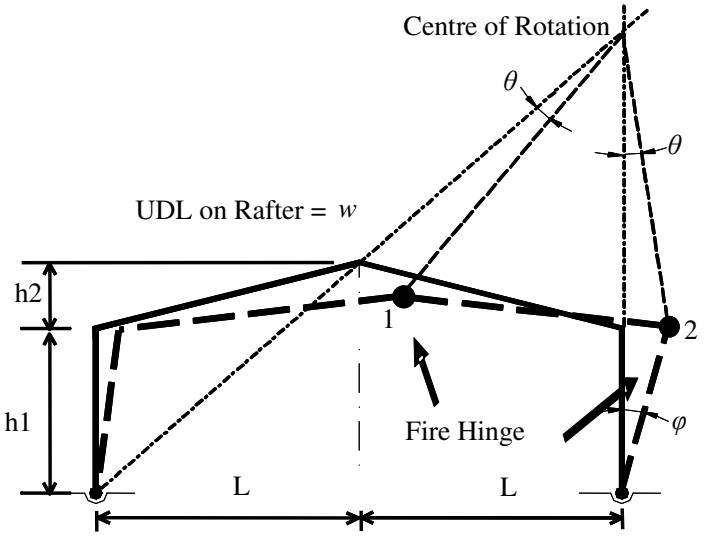

Fig. 2 – The model in Wong's simple design method

3. NUMERICAL TESTS

Recently a new dynamic solver has been incorporated into *Vulcan* [6-8] and a quasi-static solution procedure has been adopted to overcome the problem described above. This new model has been validated on benchmark problems [9] using commercial software, and calibrated against Wong's fire test result [10]. It is evident that the new model is capable of dealing with partial failure and temporary instabilities encountered in structural analysis.

3.1 Numerical model

To model the whole failure sequence of a portal frame in fire, a series of single-span pitched roof frames were tested using the new dynamic model. A uniform section was assumed and the frame was designed according to the load combinations in Table 1 and plastic theory [11], as shown in Fig. 3. As an imperfection to this symmetric structure, the left eave is 0.02m higher than the right eave. It is assumed that the rafters are heated by an ISO834 standard fire [12], and the steel temperature are calculated using the simple Eurocode 3 Part 1.2 method [13].

The semi-rigid base was modelled by dummy elements [14], and no axial restraint was applied at the outer ends of these dummy elements. The capacity of the semi-rigid bases was controlled by the moment resistance of the dummy element according to Eqn. 3.

$$S_{x,dummy} = kS_{x,column} \tag{3}$$

where S_x is the plastic modulus of the column about its major axis and k is the strength reduction factor. Eurocode 3 Part 1.8 [15] assumes that connections can be classified as nominally pinned if their design moment resistance is less than half of the design moment resistance required for a full strength joint, which has the same moment resistance as the connected members. This means that, for a full-strength column base connection, when the moment resistance of the dummy element is equal to the design strength of the column, it represents a full-strength connection, and when its design strength is less than 0.5 times the strength of the column, it can be classified as nominally pinned. As a result, the value of k should lie between 0.5 and 1.0. When the moment resistance of the dummy element is determined, the initial stiffness of the connection can be varied by changing the length of the dummy element, following Eqn. 4.

$$L_{dummy} = k_{flex} \frac{3I_{dummy}L_{column}}{I_{column}} \tag{4}$$

Here L_{dummy} and L_{column} are the lengths of the dummy element and column, I_{dummy} and I_{column} are the second moment of area of the dummy element and column sections, and k_{flex} is the initial stiffness reduction factor. According to the connection classification by stiffness in Eurocode 3 Part 1.8 [15], the initial stiffness of a nominally pinned connection

should be less than $0.5EI_{column}/L_{column}$. The value of k_{flex} was assumed to be 2.0 in all the models used in this study.

Table 1: Load combinations

Load Type	Unfactored load kN/m^2	Ambient Load factors	Fire load factors
Permanent load	0.66	1.4	1.0
Variable load	0.60	1.6	0.5

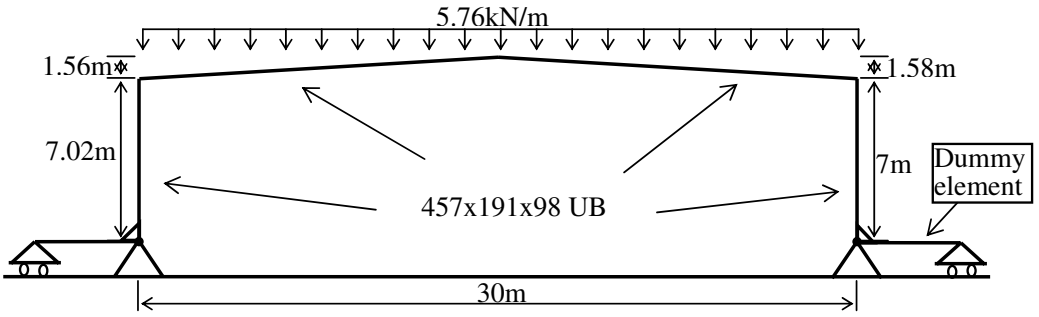

Fig. 3 – Numerical model of the pitched portal frame with semi-rigid bases

3.2 Results of numerical tests

It was found from the numerical tests that, no matter which base strength was applied to the frame, the roof initially lost stability in fire at almost the same temperature of around 563°C, but when the base strength was greater than 55% of the column capacity, the frame was able to re-stabilize, which is shown as the broken lines in Fig. 4.

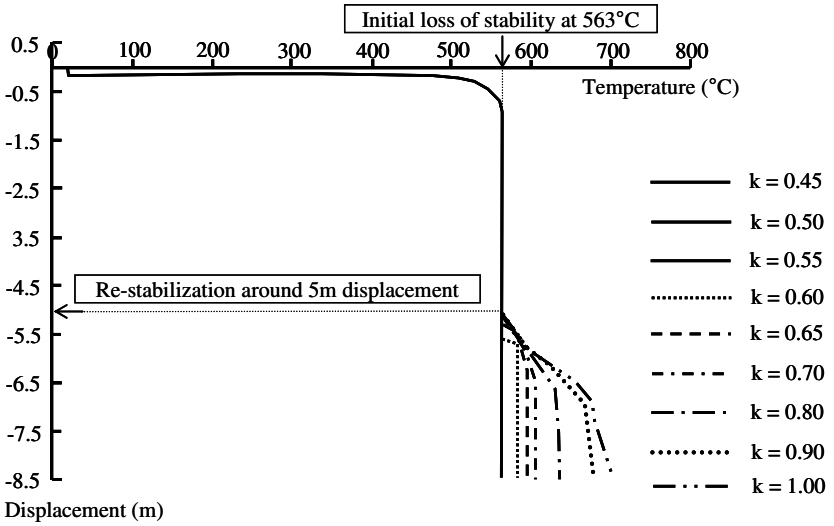

Fig. 4 – Vertical displacements of the apex from numerical modelling

The initial collapse of the pitched roof was caused by the occurrence of fire hinges at the eaves and apex. For the frames with column bases weaker than 55% of the column moment capacity, the roof continued to collapse to base level. This did not happen to the frames with stronger bases, which re-stabilized at an apex displacement of around 5m. In these cases the deformation remained relatively stable against temperature beyond this point. The frame lost stability again when one base began to plastically yield, so that a four-hinge mechanism (with hinges at the two eaves, apex and one base) formed. The temperature at which this second mechanism formed changed with the base capacity. Frames with stronger bases could remain stable to higher temperatures.

3.2 Comparison against current design model

The numerical tests showed that collapse of the single-span portal frame is due to two phases of plastic mechanisms. In the current design model, only the symmetrical collapse mechanism of rafters, shown in Fig. 1, is adopted, and this only concerns the initial loss of stability of the frame in fire. It is worth finding whether the prediction from the current design model is always conservative compared with the numerical tests.

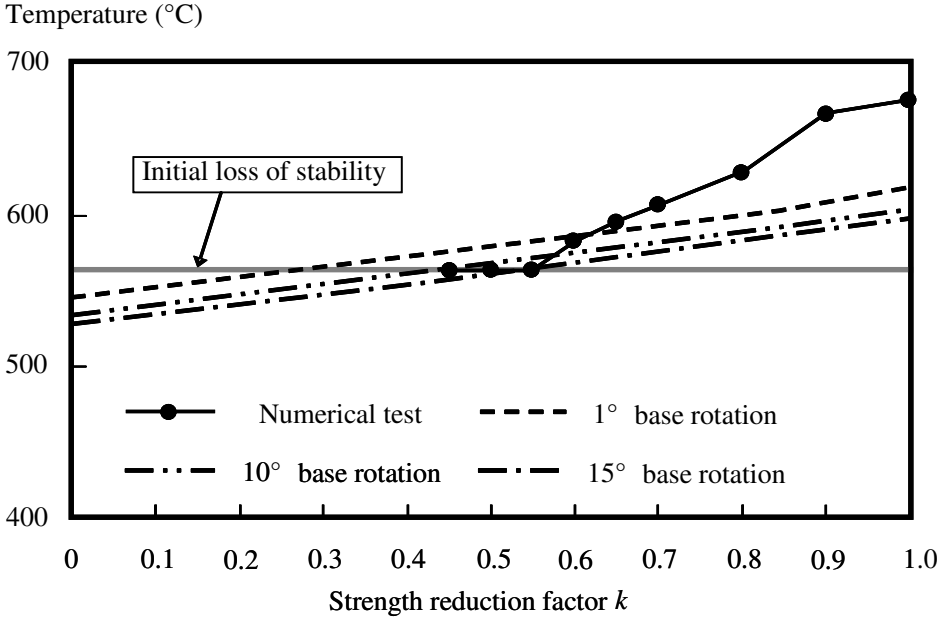

Fig. 5 – Comparison between the numerical results and current design model

In the current design model the effect of haunches, rafter elongations, fire hinge moment and column inclination are known values, so reactions at the base can be calculated from force equilibrium. To compare with the test results, the haunch length was assumed as zero in the design model and the steel properties defined in Eurocode 3 Part 1.2 [13] were used for the rafter elongation and moment capacity at elevated temperatures. It was assumed that the base capacity in the numerical test just equals the OTM required by this model, so the OTM at the base could be given by multiplying the moment resistance of the column by the

appropriate strength reduction factor. Applying different assumptions of base rotation, the relationship between the temperature and strength reduction factor can be represented as the broken lines in Fig. 5.

According to the numerical modeling, all frames initially lose stability at almost the same temperature, which is marked by the grey line in Fig. 5. The temperature that causes the frame either to collapse to ground level directly, or to lose stability a second time before collapsing to ground level, is defined as the critical temperature of the frame in fire. The critical temperatures of frames with different bases are represented in Fig. 5 by the solid line and points.

The critical temperatures predicted by the current design model increase with the base strength, but decrease with higher base rotation. Comparing the current design model with the numerical modeling in predicting initial loss of stability, when the moment capacity of the base is greater than 30% of the column capacity the design model with 1° column inclination gives higher critical temperature for rafter collapse, which suggests longer fire resistance than the numerical model. However when the strength reduction factor is less than 0.3, the collapse temperature from the design model should be lower than the numerical results. If re-stabilization of the roof frame is considered in this comparison, the prediction from the current design model gives a higher critical temperature than the numerical modeling when the base strength reduction factor is between 0.3 and 0.6.

For this specific portal frame, the current design model seems unsuitable for the frames with bases stronger than 30% of the column strength, provided no fire protection is assumed. For frames with simple bases, if fire protection is designed according to the critical temperature, the current design model may not always give conservative results.

4. NEW DESIGN METHOD

A new design method which attempts to predict the collapse of portal frames with simple base connections is being developed as an extension to Wong's work. The heating profile adopted in the current design guide [2] is assumed for this simple method; this is similar to the temperature distribution in a large compartment fire. Two failure mechanisms can be identified during the collapse sequence of pitched portal frames.

4.1 Failure mechanisms

When the roof begins to deform downward in fire under the effect of the degradation of the steel and gravity load, the columns are pushed outward due both to the change of geometry of the rafters and to their thermal expansion. For a portal frame with frictionless base connections, high rotations can be generated at these bases, caused by either elastic or plastic deformation, and these rotations, together with the fire hinges at the apex and eaves, can establish a sway mechanism. Wong's simple model uses this mechanism, whose kinematics is referred to the initial configuration of the portal frame. This method can only

apply to the frame's initial lose the stability at relatively low deflections. This is referred to as the first phase failure mechanism.

The initial collapse of the roof frame may initiate a sway mechanism leading to collapse of the whole frame, or the columns may be pulled back towards the upright position (see shape ABCDE in Fig. 6) due to the collapse of the rafters in fire. In the latter case the change of direction of rotation causes elastic unloading of the base moment and the base rotation is effectively locked. When the apex deflects to below eaves level and the columns are pulled inward this causes the base moments to increase again, and due to the inclination of the column relative to the rotation of the adjacent rafter, the moment on one eave starts to reverse, leading to the locking of the hinge at this eave. This causes the frame to re-stabilise at the position (Shape AB_0C_0DE in Fig. 6) where the internal angle between one column and the connected rafter stops closing and starts opening. With further increase of the pulling force at the column top caused by the catenary action of the inverted roof, the fire hinges at the eave and column base can be mobilised again (shape AB'C'DE in Fig. 6) and a new mechanism is established, which allows complete collapse of the second phase failure mechanism to take place.

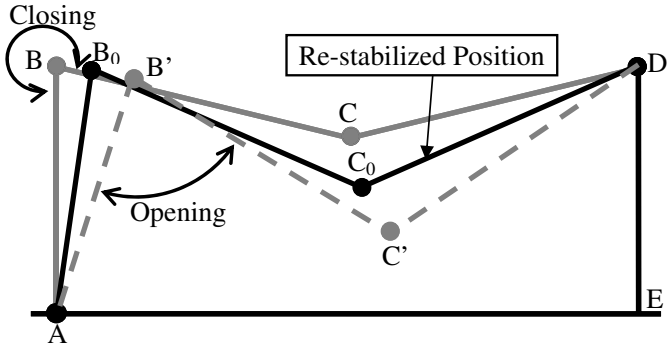

Fig. 6 – Illustration of the second phase failure mechanism

This new design method mainly focuses on the collapse of portal frames caused by the second phase mechanism in fire conditions, and aims to predict the critical temperatures by calculating the strength reduction factor of the fire hinge moment based on a work balance in the second phase failure mechanism. Because of the significant deformation of the roof frame before the mechanism forms, unlike Wong's simple method which can simply refer to the initial configuration of the frame, this method needs to find the re-stabilised position and the critical position at which the second phase mechanism is established including both the elongation of the rafter and the degradation of the moment resistance of the rafter section. Moreover, because a plastic hinge at one column base is essential to the second phase mechanism, the strength of the column bases is included in this new method.

4.2 Estimation of the re-stabilized position

As shown in Fig.7, the re-stabilized position of the frame is determined by the movement of hinges B_0 and C_0. When the angle AB_0C_0 is smallest, the apex (point C_0 in Fig.

7) should lie on the line AD. The coordinates of the point $C_0(x_{C0}, y_{C0})$ and $B_0(x_{B0}, y_{B0})$ can be calculated as follows:

$$x_{B0} = h_1 \sin\left\{\arctan\left(\frac{S}{L}\right) - \arccos\left[\frac{\left(\sqrt{h_1^2 + L^2} - S\right)^2 + h_1^2 - S^2}{2h_1\left(\sqrt{h_1^2 + L^2} - S\right)}\right]\right\} \tag{5}$$

$$y_{B0} = h_1 \cos\left\{\arctan\left(\frac{S}{L}\right) - \arccos\left[\frac{\left(\sqrt{h_1^2 + L^2} - S\right)^2 + h_1^2 - S^2}{2h_1\left(\sqrt{h_1^2 + L^2} - S\right)}\right]\right\} \tag{6}$$

$$x_{C0} = L\left(1 - S/\sqrt{h_1^2 + L^2}\right) \tag{7}$$

$$y_{C0} = h_1\left(1 - S/\sqrt{h_1^2 + L^2}\right) \tag{8}$$

in which h_1 is the column height, L is the span of the frame and S is the length of a rafter.

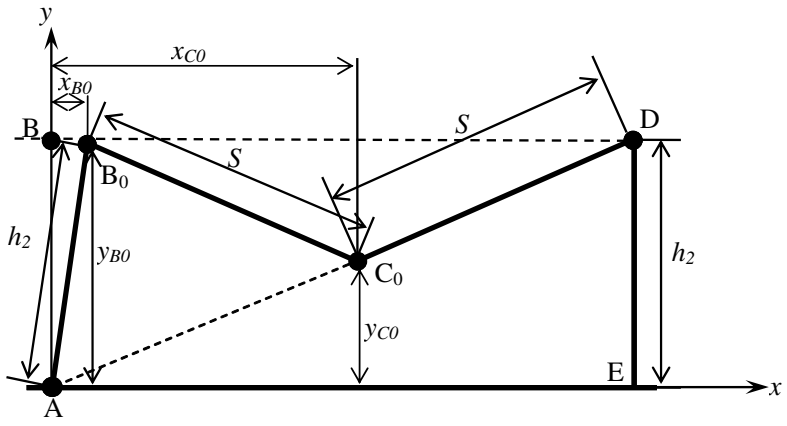

Fig. 7 – Mechanical model for the estimation of the re-stabilized position

This method shows that the frame of Fig. 3 can re-stabilize when the apex deforms to about 3.43m below the eaves level; adding the distance from the apex to the eave level which is 1.58m, the total vertical displacement of the apex should be around 5m, which matches very well with the numerical results presented in Fig. 4. This confirms that the re-stabilization during the collapse of the portal frame is caused by the locking of the plastic hinge near to an eave joint as it unloads. Once the opening of the locked angle exceeds the elastic rotation limit, the frame loses stability again.

5. CONCLUSION AND FUTURE WORK

In this paper, numerical experiments on a single-spanned pitched portal frame with different semi-rigid bases are presented. Numerical results are compared with a current design model which is widely used in the UK. The study shows that re-stabilization of the portal frame at high deflections can postpone the collapse of the whole frame, and its fire resistance may exceed the prediction given by the current design method.

It has been observed in previous physical and numerical tests that the collapse of the portal frame might be caused by a second phase mechanism which happens after inversion of the roof. Based on this failure mechanism, a new approach to estimate the re-stabilized configuration has been developed and the prediction from the new method has been confirmed by the numerical test results.

In the next step of this study, this new design method will be improved by including the prediction of the final (second phase) collapse mechanism. It is expected that the fire resistance of the portal frame with simple base connections can be evaluated using this new method. Instead of only having a single option, of designing moment-resisting base connections, engineers will then have more options to guarantee the fire resistance of portal frames under fire conditions.

The initial rotational stiffness of a "simple" column base can be much greater than that assumed in the numerical testing here. Numerical tests on frames with different initial base stiffness are in progress, and its effect will be reported in due course.

REFERENCES

[1]. The Building Regulations 2000, "Approved Document B, Fire Safety (2006 edn.)", Department of the Environment, Transport and the Regions, RIBA, London, 2006.

[2]. Newman, G. M., "Fire and Steel Construction: The Behaviour of Steel Portal Frames in Boundary Conditions (2nd edn.)", The Steel Construction Institute, UK, 1990.

[3]. "Brick cladding to steel framed buildings", Brick Development Association and British Steel, 1986.

[4]. Song, Y., Huang, Z., Burgess, I. W. and Plank, R. J., "The Design of Pitched-Roof Steel Portal Frames Against Fire", Proceedings of 5th International Conference on Advances in Steel Structures, Singapore, 2007.

[5]. Wong, S. Y., "The Structural Response of Industrial Portal Frame Structures in Fire", PhD Thesis, University of Sheffield, 2001.

[6]. Huang Z., Burgess I. W. and Plank R. J., "Modeling Membrane Action of Concrete Slabs in Composite Buildings in Fire. I: Theoretical Development.", Journal of Structural Engineering, ASCE, 2003, 129 (8), pp 1093-1102.

[7]. Huang Z., Burgess I. W. and Plank R. J., "Modeling Membrane Action of Concrete Slabs in Composite Buildings in Fire. II: Validations.", Journal of Structural Engineering, ASCE, 2003, 129 (8), pp 1103-1112.

[8]. Huang, Z., Burgess, I. W. and Plank, R. J., "3D Modelling of Beam-columns with General Cross-sections in Fire", Paper S6-5, Third International Workshop – Structures in Fire, Ottawa, Canada, 2004, pp 323-334.
[9]. Song, Y., Huang, Z., Burgess, I. W. and Plank, R. J., " The Behaviour of Single-Storey Industrial Steel Frames in Fire", Advanced Steel Construction: an International Journal, In press, 2008.
[10]. Song, Y., Huang, Z., Burgess, I. W. and Plank, R. J., "A New Numerical Model for Industrial Steel Frames in Fire", Research Report F/08/01, University of Sheffield, 2008.
[11]. Horne, M. R. and Morris, L. J., " Plastic Design of Low-Rise Frames", Granada, UK, 1981.
[12]. "ISO834: Fire Resistance Tests – Element of building construction", International Standard Organisation, 1985
[13]. CEN, "Eurocode 3: Design of Steel Structures: Part 1.2: General Rules – Structural Fire Design", European Committee for Standardization, 2005.
[14]. Salter, P. R., Malik, A. S. and King, C. M., "Design of Single-Span Steel Portal Frames to BS 5950-1:2000 (2004 Edition)", SCI Publication P252, The Steel Construction Institute, Ascot, United Kingdom, 2004.
[15]. CEN, "BS EN 1993-1-8: 2005: Eurocode 3: Design of Steel Structures: Part 1.8: Design of Joints", European Committee for Standardization, 2005.

MODELING THE PERFORMANCE OF NON-LOADBEARING GYPSUM-PROTECTED STEEL-STUD WALLS IN FURNACE AND ROOM FIRE TESTS

MARSHALL SHARP[1], BARRY BADDERS[2] and MARC JANSSENS[3]

ABSTRACT

This paper describes the development of a computational method that can be used to predict the performance of a gypsum-protected steel-stud non-loadbearing wall assembly in actual fires based on standard fire resistance furnace data. This work involved three ASTM E 119 fire resistance tests on the assembly, four room fire experiments exposing the assembly to a range of fire severities, BRANZFIRE simulations to model the room fire experiments, and TASEF finite element calculations of the heat transfer through the assembly in the standard fire resistance tests and room fire experiments.

1 INTRODUCTION

In December of 2007, the Fire Technology Department at Southwest Research Institute® (SwRI®) completed a two-year internal research program to develop a computational method that can be used to predict the performance of building elements in actual fires based on standard fire resistance furnace data. The intent was to demonstrate that it is possible to make the standard fire resistance test, ASTM E 119, more useful for performance-based design without discarding the huge database of fire resistance test data that have been obtained over the past five decades. The proposed method consists of the following steps:

[1] Engineer, Fire Technology Department, Southwest Research Institute, 6220 Culebra Road, San Antonio, TX 78238, USA
email: marshall.sharp@swri.org
[2] Group Leader, Fire Technology Department, Southwest Research Institute, 6220 Culebra Road, San Antonio, TX 78238, USA
email: barry.badders@swri.org
[3] Director, Fire Technology Department, Southwest Research Institute, 6220 Culebra Road, San Antonio, TX 78238, USA
email: marc.janssens@swri.org

1. Perform a standard ASTM E 119 fire resistance test on the building element under study (wall assembly, floor/ceiling assembly, beam, etc.);
2. Use a finite element thermal (and structural) analysis program to simulate performance of the building element in the furnace test. Adjust the thermal (and mechanical) properties of the materials used in the construction of the building element to obtain agreement between the calculations and the measurements;
3. Use a compartment fire model to determine the thermal boundary conditions for the building element in actual room fires of varying severity; and
4. Use the finite element program with the "apparent" properties obtained in Step 2 and the boundary conditions in Step 3 to predict the performance of the building element in actual fires. The objective is to determine whether the element will survive burnout of the compartment.

The internal research program confirmed the validity of the proposed method for a non-loadbearing gypsum-protected steel-stud wall assembly. The program involved three standard fire resistance tests on the assembly, four room fire experiments exposing the assembly to a range of fire severities, BRANZFIRE simulations to model the room fire experiments, and TASEF finite element calculations of the heat transfer through the assembly in the standard fire resistance tests and room fire experiments. This paper focuses on the heat transfer calculations performed with TASEF and the challenges that were encountered in modeling the fire performance of gypsum-protected steel-stud walls in room fires due to non-uniformity of gas temperatures and heat fluxes on the exposed side.

2 STEP 1: FURNACE TESTS

The design of the wall assembly that was chosen for the internal research program was identical to that used for a recent proficiency test (PT) program organized by the North American Fire Testing Laboratories Consortium (NAFTL). The assembly was non-loadbearing with a nominal fire rating of one hour. The wall design consisted of a 15.9-mm thick Type X gypsum board (ASTM C 1396) with taped and staggered vertical seams on each side of 25 gauge steel studs, 0.41 m on center.

A total of three ASTM E 119 furnace tests were conducted. The first two furnace tests were conducted on identical 3.05 × 3.05-m wall assemblies to assess repeatability. Since the vertical furnace frames at SwRI are 3.66 m wide, two 0.305-m wide wing walls were installed on the sides of the assembly. ASTM requires a minimum exposed specimen area of 9.29 m^2 and a minimum height of 2.74 m. To determine the effect of variations of wall dimensions and area on the fire resistance rating, it was decided to perform the third test on a 3.66 × 2.74-m assembly.

Additional instrumentation beyond what is specified in the ASTM E 119 standard was used to better characterize the thermal environment in the furnace. In the first test, four differential flame thermometers[1] (DFTs) and four Schmidt-Boelter heat flux gauges were installed through the wing walls. Four of the ASTM E 119 probes, which were inserted into the furnace through holes in the back wall of the furnace, were replaced with plate thermometers[2]. Since the standard requires a minimum of nine furnace thermocouples, the four ASTM E 119 probes that were replaced with plate thermometers were re-inserted through the wing walls. Finally, one bare-bead IMO A.754 thermocouple was installed through an opening in the back wall of the furnace. Furnace instrumentation in the second test was the same as in the first test, except that the plate thermometers were not used. Since there were no wing walls in the third test, the furnace instrumentation consisted of nine ASTM E 119 probes and one IMO A.754 thermocouple.

The three wall assemblies were instrumented with nine thermocouples on the unexposed surface. For the first test, additional thermocouples were placed at various locations inside the cavity. Failure in each test was due to the average temperature rise of the nine thermocouples on the unexposed surface of the assembly exceeding the temperature rise limit of 139 °C. The failure time in the first and third test was 63 min. In the second test the assembly failed at 64 min.

3 STEP 2: MODELING WALL PERFORMANCE IN THE FURNACE TESTS

3.1 The TASEF Finite Element Model

All finite element modeling in the internal research program was performed with TASEF (Temperature Analysis of Structures Exposed to Fire)[3]. TASEF is a finite-element-analysis software package designed to predict the temperature distribution of a two-dimensional structure in a simulated fire environment. The transient two-dimensional heat transfer equation is solved using an explicit forward differencing time scheme. Conduction is the primary mode of heat transfer modeled, although convection and radiation are also included at boundaries and in voids (air cavities).

3.2 TASEF Input

3.2.1 TASEF Geometry to Simulate the Furnace Tests

The geometry used in the TASEF model was a 2-D cross section from the horizontal plane of the steel-stud wall assembly. The assembly consisted of 1 layer of 15.9 mm Type X gypsum board, steel studs 406 mm on center, and another layer of 15.9-mm Type X gypsum board. Due to limitations of TASEF, only a small section with a single steel stud was modeled. The total width of the geometry was equivalent to half the stud spacing such that one stud and one half-width of the air gap were modeled (see Fig. 1a). Symmetry was assumed. This assumption is not entirely correct, but its validity was verified by modeling the same geometry without the flanges of the stud (see Fig. 1b).

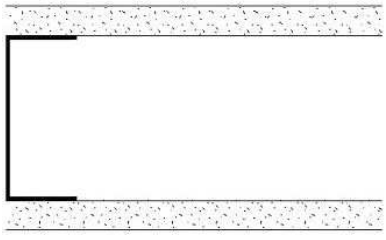

Fig. 1a – Geometry for TASEF Modeling

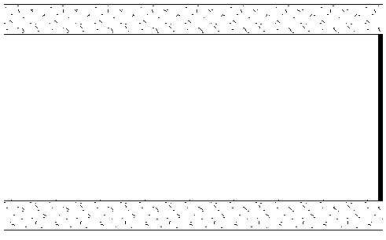

Fig. 1b – Geometry to Verify Symmetry

3.2.2 Material Properties

Fig. 2 and Fig. 3 show the Type X gypsum board properties that were used for the initial TASEF simulation. The thermal conductivity and specific heat were measured by NIST as part of an effort to characterize the construction materials used in the NAFTL ASTM E 119 proficiency testing program (see Fig. 2). The thermal conductivity was measured in a thermal capacitance (slug) calorimeter. The specific heat was obtained from differential scanning calorimetry measurements. It was assumed that the density expressed as a

percentage of the density at room temperature varies with temperature as reported by Jones[4]. The average density at room temperature of the boards that were used in the furnace tests was measured to be 754 kg/m^3. The specific heat and density were combined to obtain the volumetric enthalpy shown in Fig. 3. The property data in the TASEF input file are limited to 20 data pairs. The data pairs are identified by circles in Fig. 2 and Fig. 3. A value of 0.8 was chosen for the emissivity of Type X gypsum board, based on data reported by Jones[4]. For steel, the standard properties in TASEF were selected. The emissivity of steel varies significantly as a function of temperature and an average of 0.6 was chosen[4].

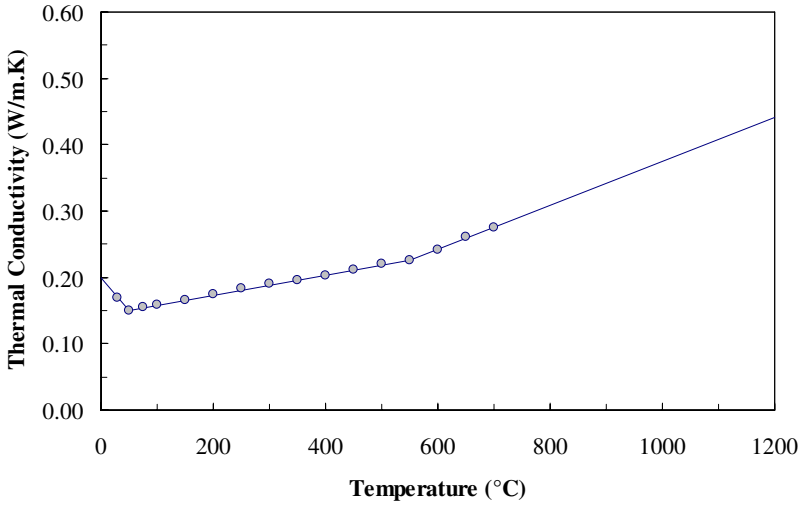

Fig. 2 Thermal Conductivity vs. Temperature for Type X Gypsum Board.

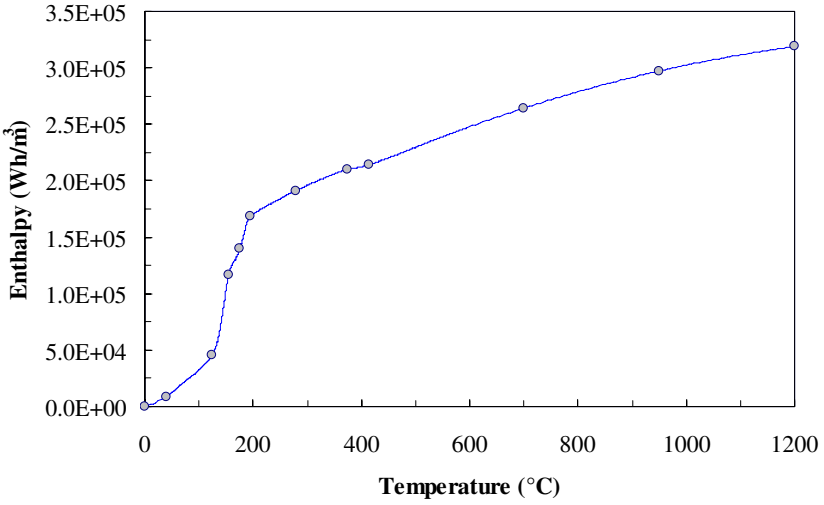

Fig. 3 Volumetric Enthalpy vs. Temperature for Type X Gypsum Board.

3.2.3 Boundary Conditions

The boundary condition at the furnace side of the wall assembly is given by:

$$\dot{q}''_{net} = h_c\left(T_g - T_s\right) + \varepsilon_s \sigma\left(T_g^4 - T_s^4\right) \quad (1)$$

where

$\dot{q}''_{net}$ = net heat flux at the exposed wall surface (kW/m^2);
h_c = convection coefficient (kW/m^2·K);
T_g = gas temperature (K);
T_s = exposed surface temperature (K);
σ = Boltzmann constant ($5.67 \cdot 10^{-11}$ kW/m^2·K^4); and
ε_s = exposed specimen surface emissivity.

A time-temperature curve was obtained (see green curve and circles in Fig. 4) so that Equation 1 gives nearly identical heat flux values as determined from inverse heat transfer calculations with the DFT temperature measurements[5]. The convection coefficient, h_c, was set equal to 0.025 kW/m^2·K. Equation 1 with h_c = 0.009 kW/m^2·K was used as the boundary in the stud cavity and on the unexposed side of the wall assembly. T_g inside the stud cavity was calculated by TASEF. T_g on the unexposed side of the wall assembly was set equal to the initial temperature measured in the test.

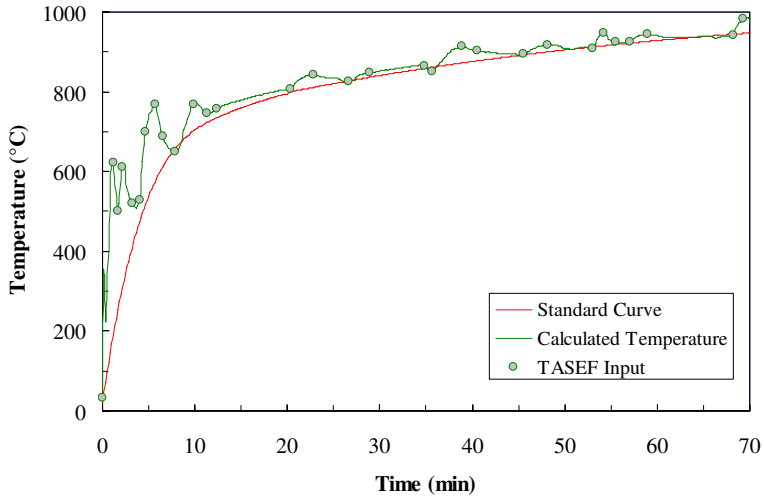

Fig. 4 Furnace Time-Temperature Curve for TASEF Modeling of Furnace Tests.

3.3 Results

With the initial set of property values TASEF calculated a failure time of 56.5 min. The thermal conductivity was then varied to bring the calculations in line with the measurements. Several surveys of thermal conductivity data for Type X gypsum board can be

found in the literature[4, 6, 7]. In most studies the thermal conductivity does not appear to increase much between 200 °C and 600 °C. It was therefore decided to reduce the thermal conductivity at 550 °C in Fig. 2 until the failure time would be close to 63 min. Simulations were performed with a 10%, 20% and 35% reduction. The resulting thermal conductivity vs. temperature curves are shown in Fig. 5. The corresponding predicted failure times are 59, 63, and 69 min, respectively.

Fig. 6 compares the predicted temperature on the unexposed side using a 20% reduction of the thermal conductivity at 550 °C. Although the failure point is the same, TASEF does not do a very good job at predicting the temperature plateau around 100 °C that is observed in the experimental data. This plateau is due to calcination of the gypsum board and moisture evaporation. Another reason for discrepancies between calculated and measured temperatures on the unexposed side is that the thermocouples in the test are attached to the unexposed surface of the assembly with special pads. The effect of these pads on the heat losses from the unexposed side was not modeled. Fig. 7 shows the TASEF prediction of the interior surface temperature of the board on the unexposed side is in good agreement with the measurements, except when calcination and moisture evaporation occurs.

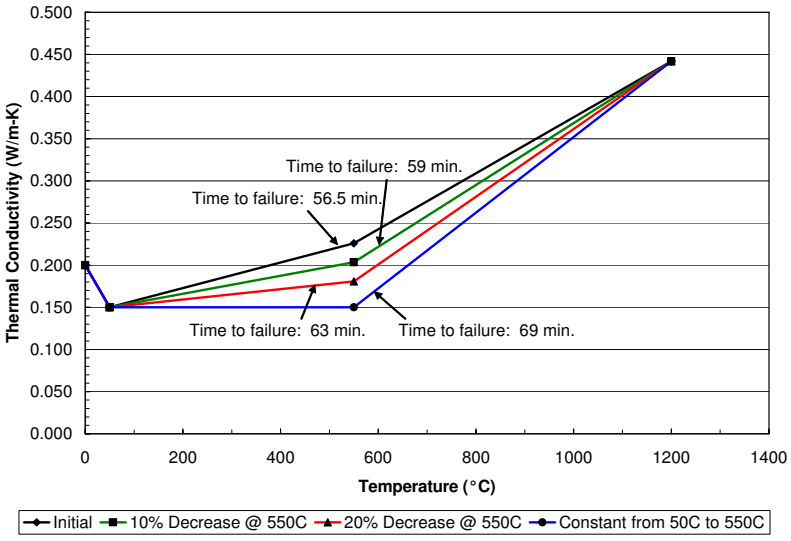

Fig. 5 Effect of Changes to the Thermal Conductivity at 550 °C on Failure Time.

4 STEP 3: ROOM FIRE MODELING

To validate the method, a series of four room tests were conducted to determine the performance of the gypsum-protected steel-stud wall construction in fires of different severity. The results of the validation are discussed in Section 5. The room test matrix was developed based on earlier work by Nyman at the University of Canterbury, Christchurch, New Zealand[8]. The fire severity was varied in the four tests by changing the fuel load (1200 and 800 MJ/m^2) and the ventilation conditions (doorway size, i.e., 1.2 × 2 m vs. 0.8 × 2 m) between tests. As in Nyman's experiments, the fuel load consisted primarily of wood cribs, supplemented with an upholstered loveseat to accelerate initial fire growth.

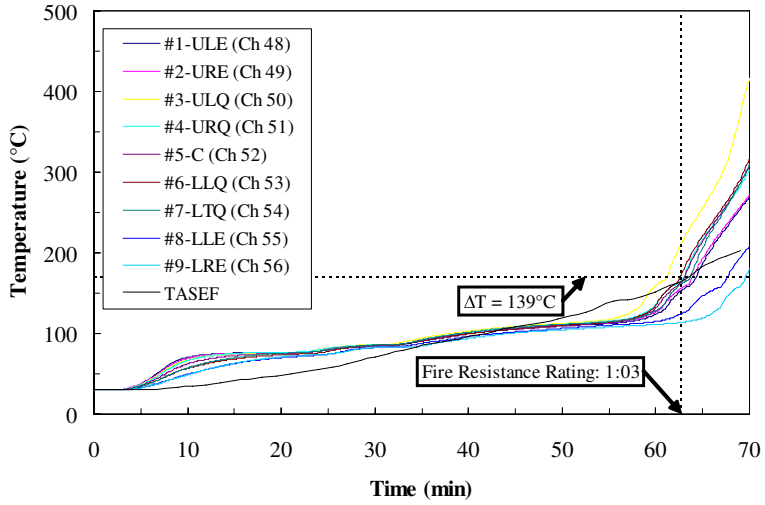

Fig. 6 TASEF Predictions vs. Unexposed Side Stud Temperature Measurements.

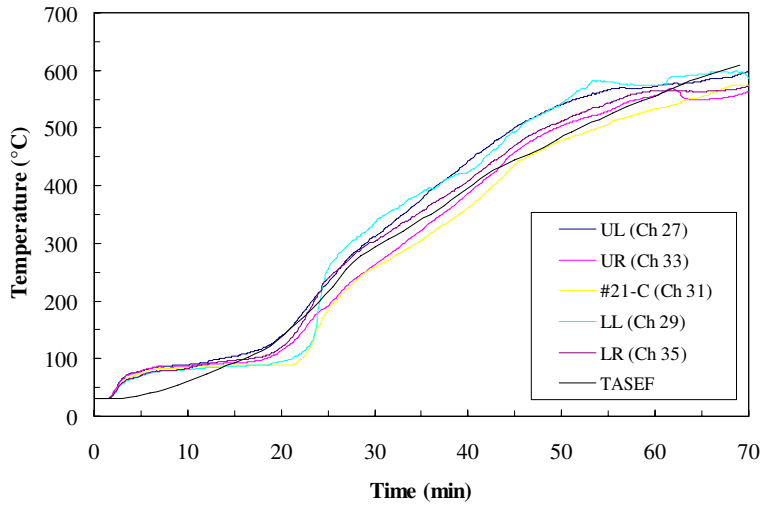

Fig. 7 Prediction vs. Unexposed Board Interior Surface Temperature Measurements.

The rear and one side wall of the 3.05 × 3.05 × 3.05-m room consisted of the gypsum-protected steel-stud wall construction evaluated in the furnace tests. The room was located under the hood of SwRI's industrial-scale oxygen consumption calorimeter to measure heat release rate during the experiments. Forty-six thermocouples were used to measure the gas temperature distribution in the room and doorway. The walls were instrumented with thermocouples in the same way as the wall specimen used for the first fire resistance test.

4.1 BRANZFIRE

BRANZFIRE is a versatile compartment zone fire model that was developed by Colleen Wade at the Building Research Association of New Zealand[9]. It is one of the few models that have an explicit option for simulating fully-developed post-flashover fires.

4.2 Model Input

BRANZFIRE was used to calculate the four room fire tests and to determine the corresponding time-temperature curves.

4.2.1 Material Properties

BRANZFIRE allows different materials on the floor, walls and ceiling of the compartment. An exposed layer and a substrate can be specified. The exposed layer of the walls was specified as 15.9-mm Type X gypsum board. Average properties for the temperature range between ambient and 1000 °C were used, i.e., $k = 0.21$ W/m·K, $c_p = 1558$ J/kg·K, $\rho = 699$ kg/m^3, and $\varepsilon = 0.8$. The thermal properties of the ceramic fiber blanket (Durablanket S 6 pcf) attached to the ceiling were determined on the basis of the manufacturer s spec sheet: $k = 0.13$ W/m·K, $c_p = 1130$ J/kg·K and $\rho = 96$ kg/m^3. An emissivity of 0.8 was chosen for this material as well. The thermal properties for concrete (floor substrate) were taken from the material property database in BRANZFIRE.

4.2.2 Fire Details

The loveseat used in the experiments was the first item ignited. The heat release rate vs. time curve of the loveseat was estimated based on a simple model [10]. This triangular approximation does not require detailed information and can be used in performance-based design when only some basic information is available about the style of the upholstered furniture and the type of frame, foam and fabric. The loveseat serves as the ignition source for the wood cribs. BRANZFIRE calculates the heat release rate from wood crib fires based on an empirical correlation. The user has to enter the total mass of wood (varied with fuel load), density of the wood (495 kg/m^3) and stick size (38 × 38 mm), length (0.77-0.81 m), and spacing (84-91 mm).

4.3 Results

Fig. 8 shows a comparison between the BRANZFIRE time-temperature curve prediction and the temperatures measured with the center tree thermocouples in Test 4. Both fuel load (800 MJ/m^2) and ventilation (0.8 m door width) were low in this test. Note that the test was terminated at 40 min, when the heat release rate started to drop at an accelerated rate. The center tree extended from the floor to the ceiling with thermocouples spaced at 0.305 m. The figure shows that the BRANZFIRE predictions are generally higher than the measured temperatures. This was also observed in the other three room tests, in particular those with the higher fuel load. In addition, the thermocouple tree measurements show that the gas temperature is not completely uniform but varies significantly with height.

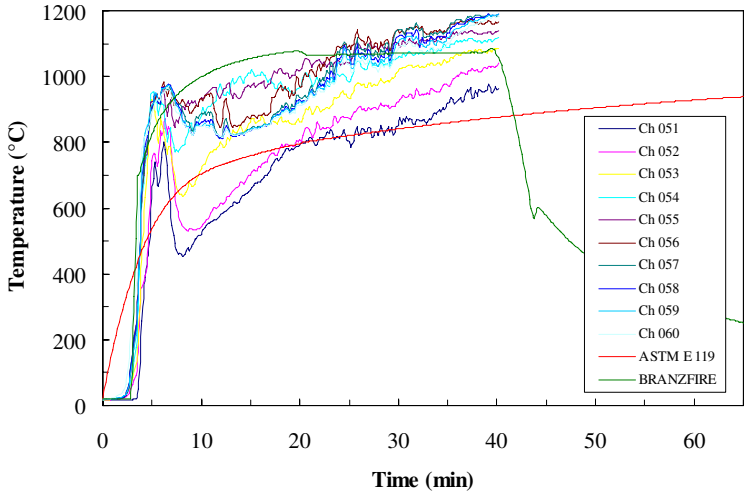

Fig. 8 BRANZFIRE vs. Measured Room Temperatures (Center Tree) for Test 4.

5 STEP 4: MODELING WALL PERFORMANCE IN THE ROOM FIRE TESTS

Fig. 9 compares calculated and measured temperatures on the unexposed side of the rear wall for Test 4. TASEF predicts that, based on the ASTM E 119 unexposed surface temperature criteria, the gypsum wall may survive burnout. For the remaining three tests TASEF predicts that the wall will not survive burnout. This is consistent with the effects of fuel load and ventilation on a fire, e.g., a higher fuel load (Tests 1 and 3) extends the duration of the fire and increased ventilation (Tests 1 and 2) results in a higher burning rate inside the compartment. For example, Fig. 10 shows that the temperature rise on the unexposed side of the wall will exceed the 181 °C single-point limit in ASTM E 119. Babrauskas recently proposed an unexposed surface temperature limit of 400 °C for performance-based design[11]. Based on this higher limit, the wall would be expected to survive burnout in all cases.

6 CONCLUSIONS

A computational method was developed to predict the performance of a gypsum-protected steel-stud non-loadbearing wall assembly in actual fires based on standard fire resistance furnace data. The method consists of four steps:

1. Perform a standard ASTM E 119 fire resistance test on the wall assembly;
2. Use a finite element program to simulate the heat transfer through the wall in the furnace test and adjust the thermal properties of the materials used in the construction of the wall assembly to obtain agreement between calculations and measurements;
3. Use a compartment fire model to determine the thermal boundary conditions for the wall in actual room fires of varying severity; and
4. Use the finite element program with the "apparent" properties obtained in Step 2 and the boundary conditions from Step 3 to predict the performance of the wall in actual fires.

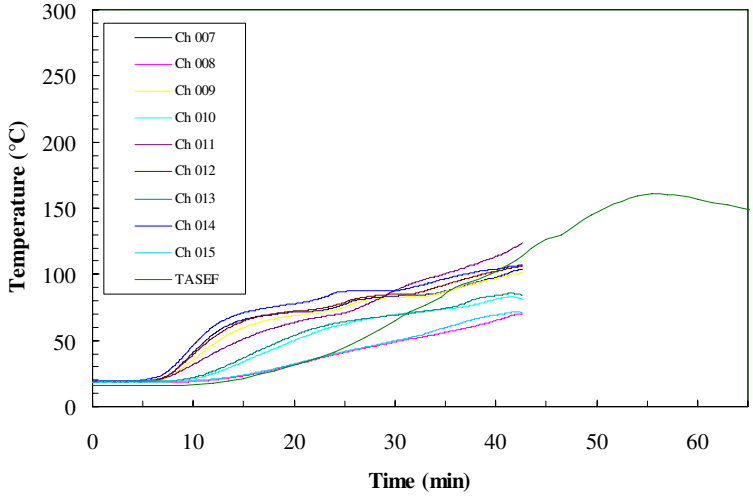

Fig. 9 Predictions vs. Measured Unexposed Back Wall Surface Temperatures (Test 4).

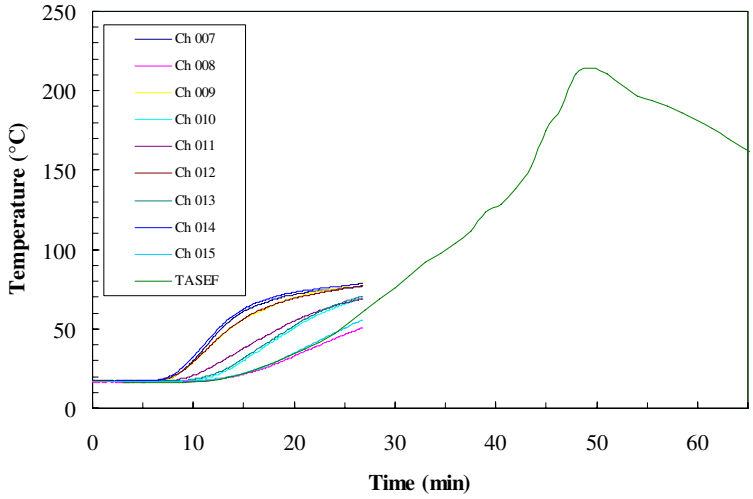

Fig. 10 Predictions vs. Measured Unexposed Back Wall Surface Temperatures (Test 1).

The method was validated by comparing the calculated results from Step 4 to data obtained from four room fire tests exposing the wall assembly to a range of fire severities. The fact that the temperature in the room fire tests varied with height, while it is assumed to be uniform in the compartment fire model, was not an issue because the calculated temperature was generally higher and lead to a conservative estimate of the thermal performance of the wall assembly in actual fires. However, this might present a major problem when applying the method to a loadbearing wall. Additional research is planned to address this issue.

REFERENCES

[1] Keltner, N., "DIRECTIONAL FLAME THERMOMETERS - A Tool for Measuring Thermal Exposure in Furnaces and Improving Control," *11th Interflam Conference*, London, England, 2007.

[2] Wickström, U., "The Plate Thermometer - A Simple Instrument for Reaching Harmonized Fire Resistance Tests," *Fire Technology*, 30, 195-208, 1994.

[3] Sterner, E., and Wickström, U., "TASEF: Temperature Analysis of Structures Exposed to Fire. User's Manual.," *SP Report 1990:05*, Swedish National Testing Institute, Borås, Sweden, 1990.

[4] Jones, B., "Performance of Gypsum Plasterboard Assemblies Exposed to Real Building Fires," *Fire Engineering Research Report 01/4*, University of Canterbury, Christchurch, New Zealand, 2001.

[5] Beck, J., "User's Manual for IHCP1D, a Program for Calculating Surface Heat Fluxes from Transient Temperatures Inside Solids," Beck Engineering Consultants Co., Okemos, MI, 1999.

[6] Bénichou, N., and Sultan, M., "Thermal Properties of Lightweight-Framed Construction Components at Elevated Temperatures," *Fire and Materials*, 29, 165–179, 2005.

[7] Gerlich, J., "Design of Loadbearing Light Steel Frame Walls for Fire Resistance," *Fire Engineering Research Report 95/3*, University of Canterbury, Christchurch, New Zealand, 1995.

[8] Nyman, J., "Equivalent Fire Resistance Ratings of Construction Elements Exposed to Realistic Fires," *Fire Engineering Research Report 02/13*, University of Canterbury, Christchurch, New Zealand, 2002.

[9] Wade, C., "BRANZFIRE Technical Reference Guide," *Study Report No. 92*, Building Research Association of New Zealand, Judgeford, Porirua City, 2004.

[10] Babrauskas, V., and Walton, W., "A Simplified Characterization of Upholstered Furniture Heat Release Rates," *Fire Safety Journal*, 11, 181-192, 1986.

[11] Babrauskas, V., "Unexposed-Face Temperature Criteria in Fire Resistance Tests: A Reappraisal," *10th Fire and Materials Conference*, San Francisco, CA, (abstract, full paper on CD), 2007.

FIRE AFTER EARTHQUAKE

DAN PINTEA[1], RAUL ZAHARIA[2], AUREL STRATAN[3], DAN DUBINA[4]

ABSTRACT

Fire following earthquake can cause substantially loss of life and property, added to the destruction caused by the earthquake, and represents an important threat in seismic regions. Problems related to traffic congestion, water supply and to the possibility of a prompt intervention of the fire brigade in case of a fire arising after an earthquake are some of the aspects of the increased risk.

The authors present a study on two multi-storey moment-resisting steel frame structures subjected to earthquake and fire subsequently. The design of the structures is made according to EN1998-1 and the Romanian seismic code (P100-1/2006).

Standard ISO fire and natural fire scenarios are considered. For the natural fire scenarios, the design fire load density is computed according to Annex E in EN1991-1-2, considering or not the active fire fighting measures, which could be all available in a normal fire situation, but could be partially available after the occurrence of an earthquake. The fire curves are obtained using Ozone V2 program. The structural analysis for the fire situation is done using SAFIR computer program.

1. INTRODUCTION

Fire may be produced by many situations, but international experience confirms that earthquake is a major initiator of fires [1]. As shown in [2], the loss resulting from fires developing after the earthquake are comparable to those resulting from the earthquake itself. Fires following earthquakes were highlighted by the major earthquakes of Northridge, Los

[1] Lecturer, University of Timisoara, Department of Steel Structures and Structural Mechanics
email: dan.pintea@ct.upt.ro.
[2] Assoc Professor, University of Timisoara, Department of Steel Structures and Structural Mechanics
email: raul.zaharia@ct.upt.ro.
[3] Assoc Professor, University of Timisoara, Department of Steel Structures and Structural Mechanics
email: aurel.stratan@ct.upt.ro.
[4] Professor, University of Timisoara, Department of Steel Structures and Structural Mechanics
email: dan.dubina@ct.upt.ro.

Angeles, USA (1994) and Kobe, Japan (1995). The Northridge earthquake from 1994 resulted in fires which challenged the resources of the fire service due to the number of fires, disruption of fire supply and damage to fire protection systems within buildings [3]. The Los Angeles City Fire Department responded to over 2200 emergencies in the day of earthquake [4].

According to the Directive of the European Commission issued on 21 December 1988, the construction works must be designed and built in such way that in the event of an outbreak of fire, the load bearing capacity of the construction can be assumed for a specific period of time, the generation and spread of fire and smoke within the works and to neighbouring construction works are limited, occupants can leave the works or be rescued by other means and the safety of rescue teams is taken into consideration.

When an earthquake occurs, it may cause structural and fire protection damage, and thus the building is more vulnerable to a fire. In the same time, after an earthquake, the loss of water supply or the low water pressure, combined with multiple independent fires, traffic congestion and the limited resources which are not able to respond promptly to all fires, allow to the fire to spread. According to [5], the experience of the impact of fire following earthquake indicates that at wind speeds above 9m/s, the fire spread and associated loss increase dramatically.

After an earthquake, it is supposed that the people already evacuated the building, as usually happens in case of such an event, or are more prone to evacuate in case of a fire resulting after the earthquake. On another hand, concerning the rescue teams, in case of a fire after an earthquake, for the reasons shown above, the increased time needed for firemen to reach the building in fire, associated to the possible lack of the active fire measures and to the increased vulnerability of the building may affect their security.

In recent years, a number of studies on the behaviour of steel structures damaged by earthquakes and exposed to fires have been carried out [6,7], in which a methodology for the analysis of the behaviour of structures subjected to fire has been proposed. The research focused on the fire analysis of frames with different levels of earthquake induced damage, using the standard ISO fire.

In the present paper the authors propose a natural fire approach for the analysis of the structures subjected to a fire after an earthquake. The design fire load density and the fire scenarios are determined according to Annex E in EN1991-1-2 [8], considering or not the active fire fighting measures, which could be all available in a normal fire situation, but could be partially available after the occurrence of an earthquake. The damage induced by the earthquake to the resistant structure of the buildings is also considered.

2 ANALYSED STRUCTURES

The moment resisting steel plane frame considered for the present study has the dimensions given in *Fig.* 1. The building structure is a frame with three spans and three bays. Both spans and bays are of 6 m. The structure is made using European steel profiles of S235 steel grade and all beam-to-column connections are rigid.

In the fundamental combinations of actions, the frame was designed considering the load values given in *Table 1.*

The frame was further verified for two seismic regions in Romania, with different ground motions: a near–field type (Banat region) and a far-field type (Vrancea region). The design was made according to the Romanian seismic code [9], adapted from EN1998. The elastic spectral analysis was applied considering the response spectrum for the Romanian Banat region (moderate seismic area with the design peak ground acceleration a_g=0.16g and

control period Tc=0.7 seconds), given in *Fig. 2* and for Vrancea region (severe seismic area with the design peak ground acceleration a_g=0.32g and control period Tc=1.6 s), given in *Fig. 3*. The behaviour factor for the moment resisting frames was considered q=6.

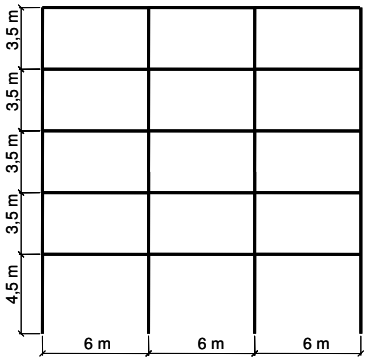

Fig 1. Steel frame dimensions

Table 1. Steel frame loads

Load	Current storey [kN/m^2]	Top storey [kN/m^2]
Dead	4.0	3.5
Live	2.0	1.5
Wind	0.5	

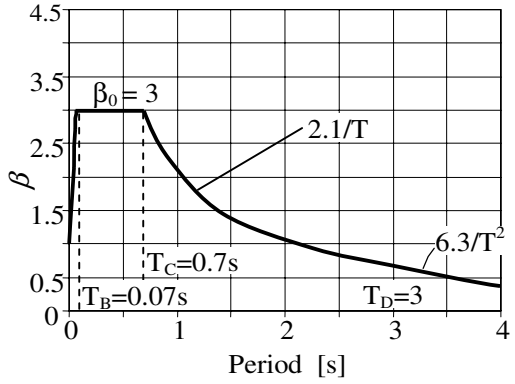

Fig. 2. Normalised elastic response spectrum for Banat

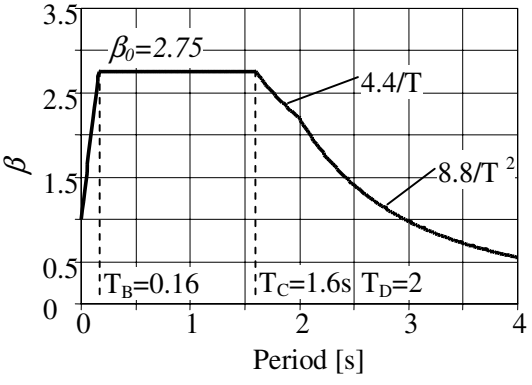

Fig. 3. Normalised elastic response spectrum for Vrancea

The wind conditions for both seismic regions are the same. Finally, the design of the Banat structure was governed by the fundamental load combination, while the design of the Vrancea structure was governed by the seismic combination. Therefore, for the Banat frame, the sections resulted from the fundamental combinations remained the same after the verification for seismic action. *Fig.* 4 shows the steel sections used in the Banat steel frame. The Vrancea frame resulted with stronger beams for some levels and with stronger columns on the height of the building, due to the higher seismic demand, as shown in *Fig.* 5.

The seismic response of the structures was evaluated using a pushover analysis, while the displacement demand under the corresponding seismic event was determined using the N2 method, developed by Fajfar [10], and implemented in EN1998-1. This method combines the push-over analysis of a multi-degree of freedom model (MDOF) with the response spectrum analysis of a single degree of freedom system (SDOF). The push-over analysis was performed by applying an inverted triangular distribution of lateral forces, based on the assumption that the response is governed by the fundamental mode of vibration. The push-over analysis demonstrated that the design requirements expressed by the design code lead to an adequate seismic behaviour. The overstrength requirements for the non-dissipative

members (columns) ensure an elastic behaviour for these members. Until the collapse, the plastic hinges developed only in the beams and at the base of the columns.

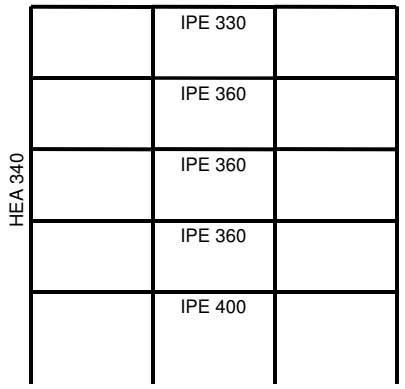

Fig. 4. Steel frame sections for Banat frame

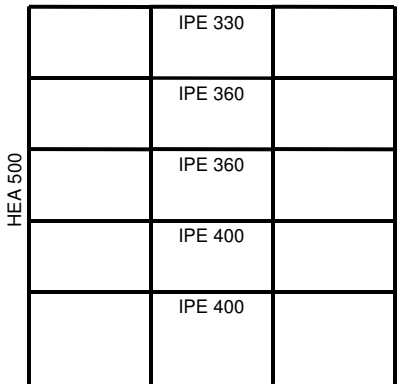

Fig. 5. Steel frame sections for Vrancea frame

According to the N2 method, the seismic demand spectrum is determined for an equivalent SDOF system. The push-over curves were obtained for the MDOF systems, and, therefore it is necessary to determine the simplified force – displacement for the equivalent SDOF systems. The performance point for each SDOF system is defined by the intersection of the capacity curve and the demand spectrum. The displacement demand for the SDOF model, S_d, is then transformed into the top displacement D_t of the MDOF system, called the target displacement.

Figures 6 and 7 show in a graphical form the procedure used to determine the displacement demand of the SDOF systems.

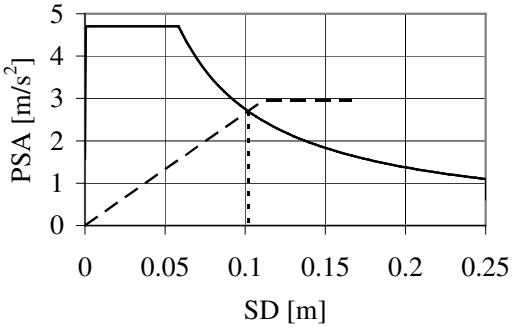

Fig. 6. Seismic demand spectra vs. capacity diagram (SDOF) - Banat earthquake

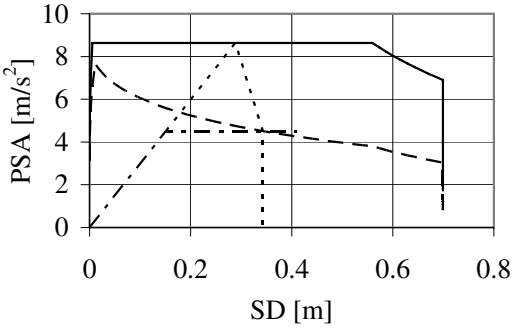

Fig. 7. Seismic demand spectra vs. capacity diagram (SDOF) - Vrancea earthquake

It may be observed that the Banat frame remains elastic after the occurrence of the corresponding earthquake. As mentioned above, the Banat frame was dimensioned from the fundamental combinations, and the steel sections remained the same after the verification for seismic action.

On another hand, Vrancea frame responded to the seismic motion in inelastic range, experiencing maximum interstorey drifts of 2.7%, slightly larger than the 2.5% limit corresponding to "Life safety" performance level according to the informative classification given by FEMA 356 [11]. This means that the structure presents important damages of non-

structural elements and moderate damages of structural elements, but the safety of the people is guarantied.

Consequently, after the earthquake, the Banat structure remains undamaged, while for the Vrancea structure, for the fire analysis, two hypotheses will be considered:

- a lower intensity earthquake occurs and the structure remains undamaged;
- an earthquake with the intensity given by the Romanian code for Vrancea region occurs and the structure suffers the damage determined by the above procedure.

3 FIRE ANALYSIS USING STANDARD FIRE

The standard ISO 834 fire was applied only for the columns and beams of the first storey, in the hypothesis that the ground floor represents a fire compartment. The steel elements have no fire protection. On the beams the fire was applied on three sides (the top being protected by the concrete slab). In the mechanical analysis, the collaboration between the steel beam and the concrete slab was not considered.

The evolution of the horizontal top level displacement of the frames with time is presented in *Figs*. 8-10. *Table 2* summarizes the fire resistance times for each case.

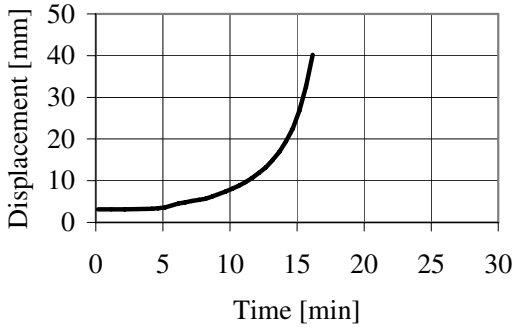

Fig. 8. Banat - ISO

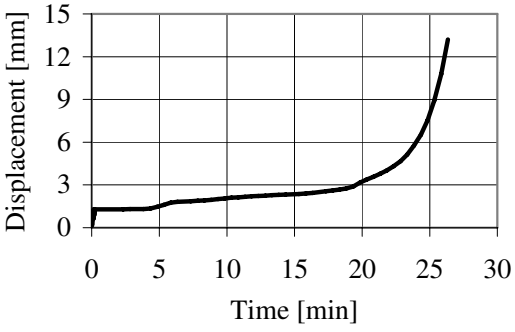

Fig. 9. Vrancea undamaged - ISO

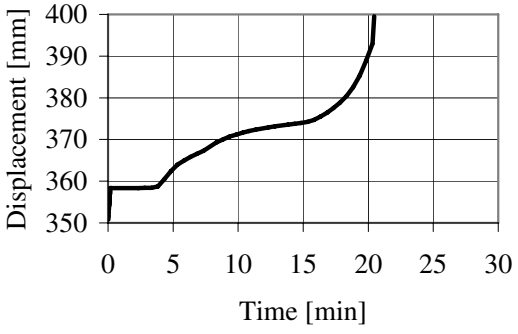

Fig. 10. Vrancea damaged - ISO

Table 2. Fire resistance times under ISO fire [minutes]

Frame	No damage	Damaged
Banat	16	
Vrancea	26	20

It may be observed that for Vrancea frame there is an important difference in time resistance under ISO fire of 6 minutes (30%) between the undamaged structure (before earthquake) and the damaged one (after earthquake). Because after earthquake the Banat frame suffers no damage, before or after the corresponding earthquake the structure has the same time of fire resistance, of 16 minutes. The Vrancea frame, designed for seismic action (the Banat frame sections resulted in fact from the fundamental combination of actions) has

an important reserve of fire resistance in comparison to the Banat frame: 26 minutes for the Vrancea undamaged frame against 16 minutes for the Banat frame. It has to be reminded that both structures were initially designed for the same fundamental load combinations.

4 FIRE ANALYSIS USING FIRE SCENARIOS BEFORE/ AFTER THE EARTHQUAKE

The unprotected steel elements of the first storey of the two frames were subjected to natural fire curves, obtained using the OZone v2 computer model [12]. Several assumptions must be made when dealing with the natural fire scenario, like the maximum fire area, the fire load and the surface of the openings. The most challenging is to establish how the glass panes will behave in a fire situation. In all except very rare circumstances, the flow of oxygen into a room comes largely from open doors and open windows and to a slight extent from any mechanical ventilation systems and from building leakage. Once a fire gets going, however, windows previously closed may crack and break out. Thus, it becomes of significant interest to be able to predict if, and when, glass may break out.

Here, an important distinction needs to be made. When a window pane of ordinary float glass is first heated, it tends to crack when the glass reaches a temperature of about 150 - 200ºC. At that point, there is a crack running through the pane of glass, but there is no effect on the ventilation available to the fire. For the air flows to be affected, the glass must not only crack, but a large piece or pieces must fall out. The only probabilistically-based results concerning glass exposed to a uniform hot temperature come from the Building Research Institute (BRI) of Japan [13]. In that study, researchers used a large-scale high-temperature door-leakage testing apparatus that resembles a large muffle furnace. Only single-glazed, 3 mm thick window glass was studied. The results are presented in *Fig. 11* in terms of a probability of glass breaking out, as a function of temperature rise above ambient.

The fire action is limited to the ground floor of the building (fire area of 324 m), considered as a fire compartment. The walls are made out of normal concrete having a thickness of 20 cm, and the following thermal characteristics: conductivity 0.8 W/mK and specific heat of 840 J/kgK. As shown in *Fig. 12* the windows (openings) in three adjacent walls have a sill height of 1 m and a soffit height of 3 m. In the fourth wall the sill height is 2 m and the soffit is 2.5 m. A linear variation of the openings was considered, i.e. the glass panes. Based on the research mentioned above, at 300°C 30% of the windows were considered broken, while at 500°C all the windows are broken.

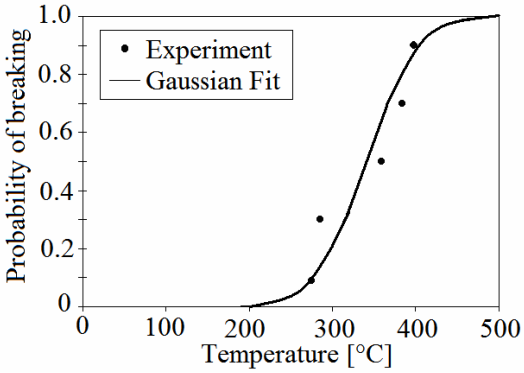

Fig. 11. Glass breaking (Tanaka et al. 1998).

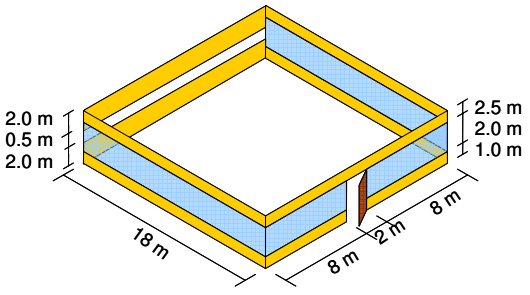

Fig. 12. Fire compartment

The occupancy of the fire compartment is office with a characteristic fire load density $q_{f,k}$ of 511 MJ/m^2. The design fire load density, according to Annex E in EN1991-1-2 [8] is

$$q_{f,d} = q_{f,k} \cdot m \cdot \delta_{q1} \cdot \delta_{q2} \cdot \delta_n \quad (1)$$

in which m is the combustion factor, δ_{q1} is a factor taking into account the fire activation risk due to the size of the compartment, δ_{q2} is a factor taking into account the fire activation risk due to the type of occupancy and $\delta_n = \prod_{i=1}^{10} \delta_{ni}$ is a factor taking into account the different active fire fighting measures i (sprinkler, detection, automatic alarm transmission, firemen, etc.).

Table 3 gives the values of the active fire fighting measure factors considered. Before the earthquake, the building being provided with sprinklers, the coefficient which takes into the account the existence of automatic water extinguishing system (δ_1) and the coefficient which takes into account the existence of the independent water supplies (δ_2) are both sub unitary. After the earthquake, considering the possible disruptions, the sprinkler system and the automatic fire detection are no more considered, and the corresponding coefficients are both 1.00. In relation with the prompt intervention of the fire brigades, which is no more possible due to the number of emergencies and traffic congestion, associated to the possible lack of the active fire measures, the coefficients $\delta_{5\text{-}9}$ are considered with the unit value.

Table 3. Fire fighting measures before and after the earthquake

Fire Scenarios	Autom. Water Exting.	Indep Water Supply	Auto Fire Detection	Alarm Fire Brigade	Fire Brigade	Access Routes	Fire Fight Devices	Smoke Exhaust	Total
	δ_1	δ_2	$\delta_{3/4}$	δ_5	$\delta_{6/7}$	δ_8	δ_9	δ_{10}	$\Pi\delta_n$
Before	0.61	0.87	0.73	0.87	0.78	1.0	1.0	1.0	0.26
After	1.0	1.0	1.0	1.0	1.0	1.5	1.5	1.0	2.25

Using these parameters and running the Ozone software [12], two fire curves were produced (*Fig. 13*). The first curve, for which no flashover occurs, entitled "before earthquake" has a peak temperature of 470°C at 36 minutes and is ventilation controlled. The "after earthquake" curve is fuel controlled with a peak temperature of 670°C at 96 minutes.

These curves were used in SAFIR programme [14] to find the temperature evolutions on each of the exposed profiles, without fire protection. On the beams the fire was applied on three sides (the top being protected by the concrete slab). In the mechanical analysis, the collaboration between the steel beam and the concrete slab was not considered. *Fig. 14* shows the temperature plot on a beam above the ground floor at 44 minutes (peak temperature of the fire "before without sprinklers").

The results of the analysis are presented in *Figs. 15-19*. The evolution of the horizontal top level displacement with time is presented on a single chart for both fire scenarios. *Table 4* summarizes the fire resistance times for the fire scenarios for each frame. It may be observed that considering all fire fighting measures active (in a situation before an earthquake) both frames resist to the fire action.

After earthquake, the stronger Vrancea frame resists the fire, even if the structure is damaged after the seismic action, while the Banat frame collapses, even if its structure remains undamaged. It has to be noted, however, that in the hypothesis of damaged structure after the earthquake, the Vrancea frame is very close to the collapse after around 95 minutes of fire, and experience important displacements in comparison with the undamaged structure (*Fig. 18* and *19*) but, because the fire enters in the decreasing phase at that time, the structure

is able to recover. It is to be therefore underlined again the conclusion emphasised for the fire analysis under standard ISO curve, that the Vrancea frame, designed for seismic action has an important reserve of resistance into a fire situation.

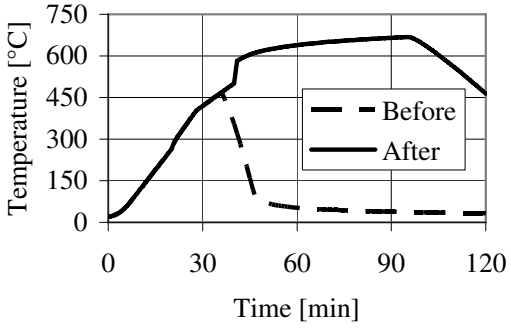

Fig. 13. Temperature-time evolution

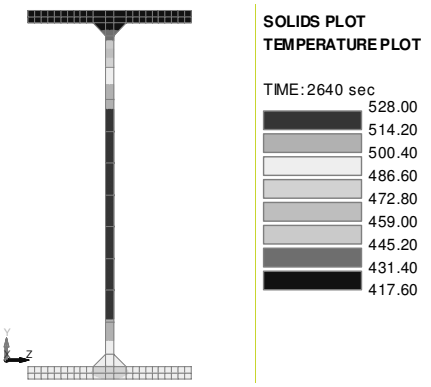

Fig. 14. Temperature plot on beam

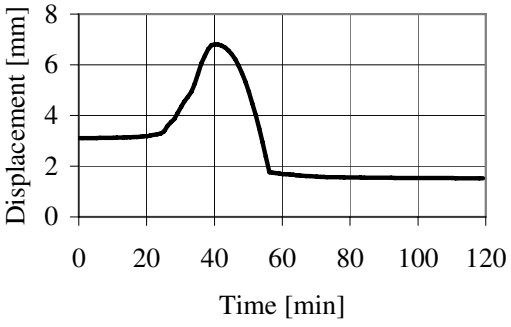

Fig 15. Banat – before earthquake

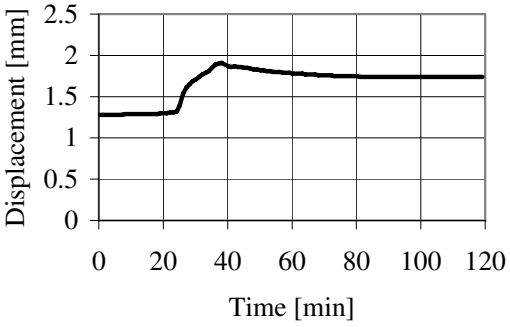

Fig. 16. Vrancea – before earthquake

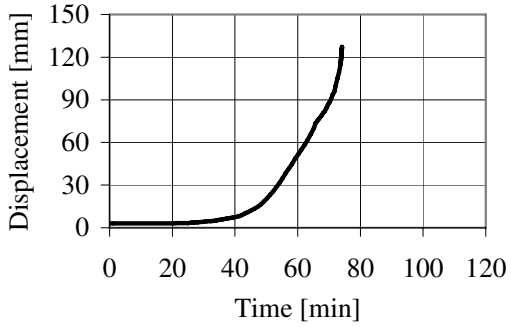

Fig. 17. Banat – No damage – after earthquake

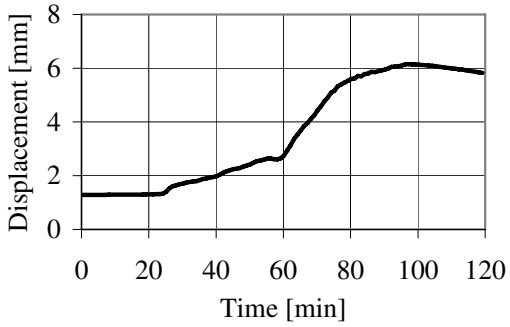

Fig. 18. Vrancea – No damage - after earthquake

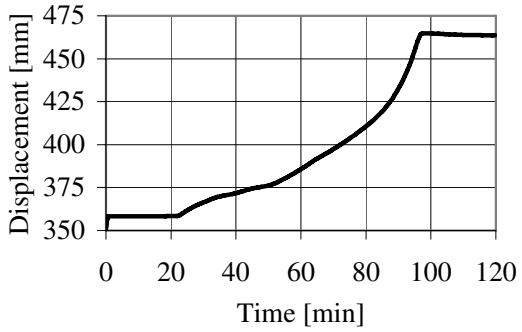

Fig. 19. Vrancea - Damaged – after earthquake

Table 4. Fire resistance times under natural fire [minutes]

Frame	Before earthquake with sprinklers	After earthquake	
		No damage	Damaged
Banat	No collapse	74	
Vrancea	No collapse	No collapse	No collapse

5 CONCLUSIONS

The behaviour analysis of structures subjected to fire after an earthquake consists of the modelling of the fire action and the mechanical analysis of structure under fire action, considering the damage induced in the structure by the earthquake. In the present paper this problem was approached by considering not only the standard ISO fire curve, but also natural fire scenarios and their effect on buildings, in the hypothesis that the earthquake induces or not damage in the resistant structure. The natural fire scenarios were determined considering that the fire fighting measures are available in a regular fire situation, but could be partially available after the occurrence of an earthquake, due to disruptions as water supply, traffic congestion, and overwhelming of the fire brigades.

For the purpose of this study, a building designed for a given fundamental combination of actions, was further adapted to resist to a moderate and severe seismic motion, for two seismic regions in Romania. For the moderate seismic action, the steel moment resisting frame suffered no changes, but for the severe seismic motion the moment resisting frame was changed, considering stronger profiles for beams and columns. For the scenario with all fire fighting measures available in a fire situation both unprotected steel frames resisted to the fire action. In fact, considering all measures available, the fire does not reach flashover. After earthquake, the frame designed for the stronger earthquake resists at the fully developed fire, even if it is damaged by the seismic action, while the frame designed practically from the fundamental load combinations collapses.

In conclusion, the frame adapted for seismic action has an important reserve of resistance in case of a regular fire situation, but also in case of a fire after an earthquake. This conclusion was emphasised considering both standard ISO and natural fire models. The present study represents a first step in a campaign of numerical simulations, in which more structures will be considered.

REFERENCES

[1] Wellington Lifelines Group, Fire following earthquake: Identifying key issues for New Zealand, Wellington, New Zealand, October 2002.

[2] A. H. Buchanan, Structural design for fire safety, John Wiley & Sons, England, 2001

[3] Todd D., Carino N., Chung R.M., Lew H.S., Taylor A.W., Walton W.D., Cooper J.D., Nimis R., Northridge earthquake performance of structures, Lifelines and Fire Protection Systems, NIST Special Publication 862, Gaithersburg MD, 20899, May, 1994

[4] David D. Evans, Wiliam D. Walton, Frederick W. Mowrer, Progress report on fires following the Northridge earthquake, Thirtheen meeting of the UJNR panel on fire research and safety, March 13-20, 1996, Volume 2, Editor Kellie Ann Beall, NIST, Gaithersburg, MD 20899, 1997

[5] All-Industry Research Advisory Council, Fire following earthquake, Estimation of the conflagration risk to insured property in Los Angeles and San Francisco, Oak Brook, IL, 1987

[6] Della Corte G, Faggiano B., Mazzolani F.M., On the structural effects of fire following earthquake, Improvement of buildings, Taylor & Francis Group, London, 2005

[7] Faggiano B, Esposto M., Mazzolani F.M., Landolfo R., Fire analysis on steel portal frames damaged after earthquake according to performance based design, Urban Habitat Constructions under Catastrophic Events, COST C26 Workshop, Prague, March, 2007

[8] EN1991-1-2: Eurocode 1 - Actions on structures - Part 1-2: General actions - Actions on structures exposed to fire, 2005, European Committee for Standardization, Brussels

[9] P100-1/2004, 2005. Seismic design code – Part 1: Rules for buildings (in Romanian) Indicativ P100-1/2004, Buletinul Constructiilor, Vol. 5, 2005

[10] Fajfar P., A non linear analysis method for performance based seismic design, Earthquake Spectra, vol. 16, no. 3, pp. 573-592, August, 2000

[11] FEMA 356, Guidelines for Seismic Rehabilitation of Buildings, Vol. 1:Guidelines, FEMA 356, Washington DC, 2002 (formerly FEMA 273).

[12] Cadorin, J.F, Pintea, D., Dotreppe, J.C, Franssen, J.M, 2003, A tool to design steel elements submitted to compartment fires- Ozone V2, Fire Safety Journal, Elsevier, 38, 439-451.

[13] Tanaka, T., et al., Performance-Based Fire Safety Design of a High-rise Office Building, Building Research Institute, Japan, 1998

[14] J.M. Franssen, VK. R. Kodur, J. Mason, User Manual for SAFIR. A computer program for analysis of structures subbmited to the fire. University of Liege, 2004.

TESTING NEEDS FOR ADVANCEMENT OF STRUCTURAL FIRE ENGINEERING

NESTOR IWANKIW[1], CRAIG BEYLER[2], and JESS BEITEL[3]

ABSTRACT

International standards have long existed and been well recognized for establishing the fire exposure and fire resistance rating features in a standard test of a building construction assembly. However, their primary focus has traditionally been on the thermal protection and performance characteristics of various materials, as recorded by thermocouple measurement of temperatures. Consequently, major voids exist in the documented literature on structural fire response from these prescriptive fire resistance tests, as well as from some research/special testing.

More detailed information on the structural/physical original conditions and response of the test assembly during the fire exposure is greatly needed in order to enable the advancement of structural fire engineering applications. This recorded structural performance information will assist in a better understanding of structural degradation and ultimate failure mechanisms during fire exposures, provide results for validation of analytical models and for the model input properties to structural fire engineering applications. A number of new or revised instrumentation and test procedures, as well as related documentation requirements for these purposes will be outlined. The fire testing issues will principally identify structural performance aspects (such as applied loading, mechanical properties, strength limit states and test termination) and more general needs, though multiple ancillary furnace and fire exposure control variables were also reviewed and considered important to the repeatability and realistic interpretation of the experiments.

[1]Senior Engineer, Hughes Associates, Inc., 5953 N. Oconto Ave, Chicago, IL 60631, USA,
email: niwankiw@haifire.com

[2]Technical Director & Principal, Hughes Associates, Inc., 3610 Commerce Dr., Baltimore, MD, 21227, USA,
email: cbeyler@haifire.com

[3]Senior Scientist and Principal, Hughes Associates, Inc., 3610 Commerce Dr., Baltimore, MD, 21227, USA,
email: jbeitel@haifire.com

1. INTRODUCTION

The continuing trend in Fire Protection Engineering toward Performance-Based Design (PBD) and rational engineering of structural fire protection in lieu of prescriptive requirements is often limited by the availability of reliable experimental data for analysis/design calibration or verification. The PBD approach requires engineering data that existing test methods, like the ASTM E 119[1], ISO 834[2], and the like, for prescriptive fire resistive ratings, were not developed almost 100 years ago to provide[3]. The proprietary nature of most standard fire tests likewise further restricts any such information from being in the public domain of the technical literature. This void of structural engineering data derived from the numerous regular fire resistance tests generally makes it necessary for PBD to utilize results obtained from ad hoc and special test methods performed outside the scope of standard test methodologies. However, special ad hoc tests, by definition, will lack in standardization and possibly in efficiency.

In addition to various limitations with respect to test procedures, number and types of measurements, and reporting, the reproducibility of standard prescriptive fire testing has always been a serious issue. The standard test apparatus and controls are only generally specified in the ASTM E 119 and similar standards. Fuels, burners, furnace linings, furnace dimensions, loading levels, and loading mechanisms are either unspecified or only qualitatively described, thereby allowing for real variances in the fire heating exposure for supposedly identical tests. This has led to situations in which fire test results cannot be reproduced for nominally identical materials and assemblies between different laboratories. Such a lack of experimental consistency and extra source of uncertainty causes significant problems in this PBD environment, which is already difficult due to the nature of normal fire variability.

A number of new or revised instrumentation and fire test procedures, as well as related documentation recommendations for these purposes will be outlined, based on a 2007 NFPA Research Foundation Project[4] completed by Hughes Associates, Inc.

2. BACKGROUND

Standard fire resistance tests of building construction have been used for decades to assess three key performance parameters of the building assembly: integrity as a fire barrier, structural stability under load, and heat transmission. Despite the fact that two of these three fire performance indices are directly related to the structural, or at least the physical/mechanical response of the assembly, the only measurements explicitly required by ASTM E 119 are thermocouple instrumentation for temperatures. The structural/physical original conditions and response of the assembly during the fire exposure are only ambiguously addressed through general provisions for subjective experimental observations, without requirements for any quantitative recorded data or specific acceptance limits. Consequently, the structural/physical conditions before and during the fire have been evaluated from rather "soft" and qualitative observations, rather than hard data and performance limits.

The derived fire resistive assembly listing does not provide any substantive structural fire performance information. Furthermore, the actual supporting fire test data and documentation (e.g., the test report) for the listing is proprietary and not available as a public document under the current practice; this information can only be obtained and used with the permission of the listing's sponsor. While these realities may be customary and satisfactory

for prescriptive uses of products and construction assemblies, they seriously hamper the development and application of PBD.

Acquisition of tangible experimental information on structural fire performance will not only provide a more solid basis for the traditional use of fire resistive ratings, but are an absolute necessity to support PBD developments. However, rather than encumbering or confusing the continuing use of prescriptive fire tests and ratings, a separate series of independent criteria for structural fire performance testing has been suggested.[4] These structurally oriented testing issues will be presented first and in greater detail. Several recommendations relative to furnace and fire controls, and some other more general experimental needs will then conclude this paper. The complete and original source of these recommendations may be found in the cited NFPA Report[4], which can be accessed and downloaded via the NFPA Internet site.

Of course, any and all test procedure items require appropriate documentation and data collection. The great value added to PBE of this additional experimental information lies in better understanding of behavior for purposes of its structural fire resistance modeling, model validation, and subsequent design utilization with better input data.

3. STRUCTURAL ISSUES

Several recommendations for implementation and possibly eventual standardization of structural issues for fire performance testing are presented as follows.

3.1 Test to Failure

All assembly fire tests should be conducted under maximum design load until an imminent, or actual, structural failure limit state is attained, or until an major integrity breach occurs, irrespective of the assembly's other thermal conditions. Currently, many of the prescriptive fire resistance tests, and some others, are stopped when certain limiting acceptance temperatures for the materials are reached, without any insights into the ultimate structural fire endurance time and failure mode.

3.2 Applied Maximum Design Load

The maximum assembly design load should be based on the greater of the design load computed from either allowable stress design or limit states-LRFD, and the controlling strength failure mode to be used for each type of assembly construction. Fire tests with no applied load or with light load may gravely distort the construction's integrity under the worst-case of maximum design load.

3.3 Define Criteria for Imminent Collapse

In lieu of reaching full assembly collapse, quantitative limits and guidelines for imminent structural failure in axial compression and bending should be identified. These would help protect safety and minimize damage to laboratory furnaces and test apparatus, while testing to failure.

Ryan and Robertson[5] had developed in 1959 arguably the first deflection failure criteria for steel beams tested in a standard E 119 fire test under full load. Some prescriptive international fire standards, such as ISO 834, have already included similar type of deflection-based criteria for "loadbearing capacity," but ASTM E 119 has not to date.

3.4 Means of Load Application

Superimposed loading on all assemblies should only be applied through mechanical or hydraulically-controlled equipment, not water-filled tanks, concrete blocks, or sand bags.

Use of such constant weights is inherently less accurate and consistent than load control equipment that has been properly calibrated and serviced. Inconsistencies and differences in the load application methodology alone may lead to discrepancies between tests and/or laboratories. Moreover, in fire tests that reach actual structural failure, the public danger and damage potential to the laboratory furnace is less with controlled loads than with stacked tank, block, and bag weights, whose support and stability cannot be readily maintained after floor collapse.

3.5 Deflections

Record, as a minimum, the time-history of transverse deflections at mid-span in all primary structural members (beams, joists, columns, and wall studs) of the assembly, together with axial shortening of loaded columns and wall studs. The stiffness of a structural assembly is an important performance factor, as is strength. Structural deflections are not only a lead indicator of structural distress in the element tested, but large deflections also can lead to damage of its fire protection materials as well as damage to adjacent construction.

3.6 Strains

Place high-temperature strain gauges at critical sections (typically ends and/or mid-span) of main structural members (beams, joists, columns, wall studs) and of other important load transfer elements (shear studs, metal deck, floor slabs and reinforcement, and connections). Strain data provides key information on load paths, identifies the local member areas where inelastic (yielding) material response is occurring, and whether it is tensile or compressive, thereby revealing the critical structural locations for force redistribution and resistance mechanisms with fire exposure time.

3.7 Loaded Column and Wall Tests (including eccentricity)

Conduct column tests with superimposed compressive load until structural failure; investigate alternative protocol(s) for non-uniform heating of columns and walls, including possible provision for "equivalent" minimum eccentricity of axial load.

The effects of accidental load eccentricity, initial column curvature or imperfections, column mechanical strength properties, length slenderness ratio, and the type of structural failure (squash or stability/buckling) under fire exposures are relatively unknown. Similarly, the effects of non-uniform heating of a column (see Figure 1) or wall can be detrimental to stability and have not been rigorously studied.

A surrogate approach for simulation of wall and column assembly strength degradation due to additional non-uniform heating effects may be the imposition of a minimum eccentricity for compressive loads. Minimum compressive load eccentricity has been required in some test standards, such as ASTM E 72[6], as well as in structural design methods, such as ACI 318-02[7].

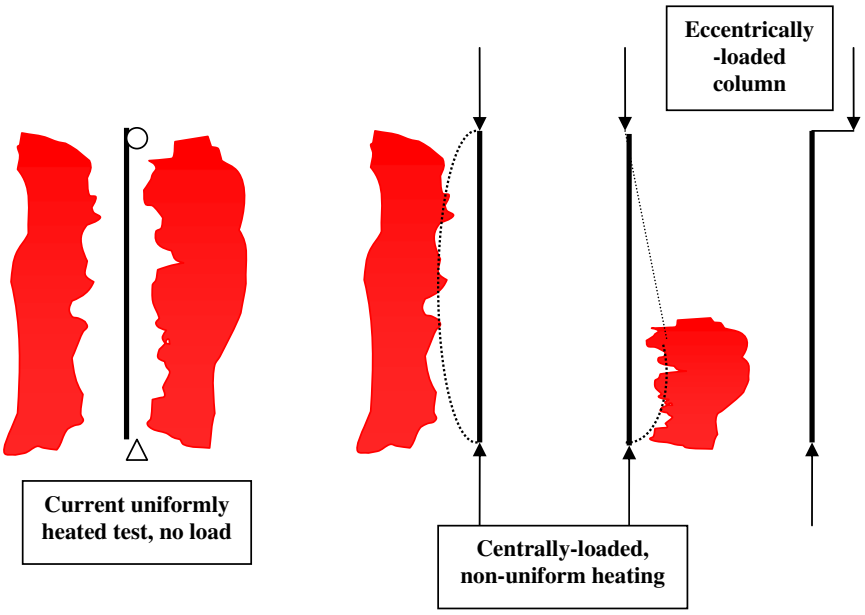

Figure 1 – Column Fire Testing Alternatives

3.8 Actual Mechanical Properties at Ambient

Perform material strength tests on samples extracted from the primary structural assembly members to determine their actual mechanical properties at ambient (including yield and ultimate strength, and elastic modulus). This is more accurate and correct than just relying on the minimum nominal properties of the grade/type of construction material utilized.

3.9 Mechanical Properties at Elevated Temperatures

Perform material strength on samples extracted from the primary structural assembly members to determine their actual mechanical properties at high temperatures (including yield and ultimate strength, and elastic modulus).

3.10 Scaling of Test Results

Develop criteria for when and how furnace- scaled fire tests can be used and interpreted relative to actual construction, as an alternate or supplement to current extrapolation of results to larger and heavier assemblies.

3.11 Thermal End Restraint

Record magnitude of thermal restraining forces on assembly throughout test duration, or at least provide detailed description of the boundary conditions present during the test, especially for floor and ceiling assemblies.

In the US and relative to ASTM E 119 classifications for restrained and unrestrained beam ratings (see Figure 2), this issue presents a common source of confusion, particularly to structural engineers and architects, in that thermal restraint is not necessarily synonymous with structural end restraint. Simple and modest steel shear connections for beam framing,

which are considered to be rotationally unrestrained with negligible moment-resisting strength, have been shown to represent adequate thermally restrained conditions for most cases.[8]

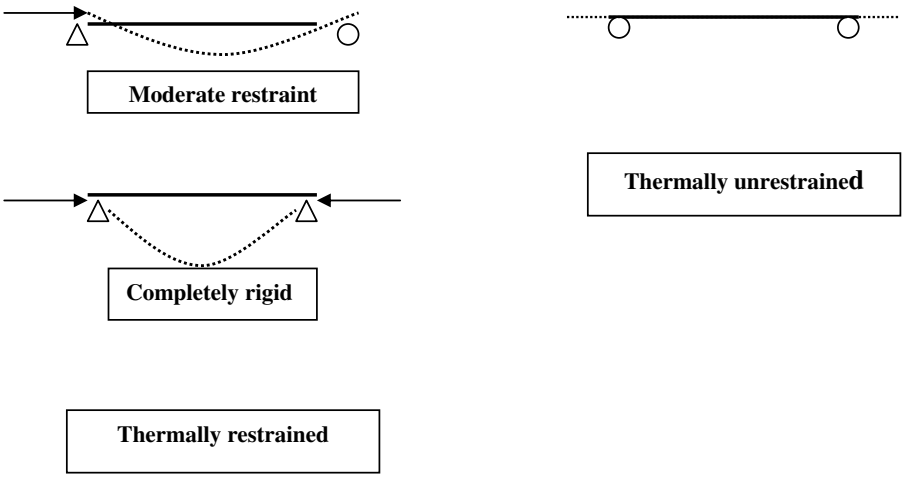

Figure 2 – Thermally Restrained and Unrestrained Floor/Roof Assemblies

4. FIRE/FURNACE ISSUES

The NFPA Report 4 contains an extensive discussion and justification for various recommendations related to the furnace and fire exposure variables, such as:

- Lining
- Gas type
- Burners
- Secondary air flow rate
- Target fire time-temperature curve
- Furnace temperatures
- Furnace temperature controls
- Pressure
- Oxygen concentration
- Tolerances from prescribed exposure

All these generally serve to establish better consistency of the actual heating environment to which the specimens are subjected. Due to the structural focus of this presentation, no more will be said about these, except for the fire time-temperature curve. The latter is a key driving force in the heating and high temperatures of the structural materials, and must commonly be assumed as single or a series of inputs to any structural fire engineering analysis.

4.1 Fire Time-Temperature Curve

In some PBD applications, the standard building fire test curve from ASTM E 119 or ISO 834, or from other more severe exposures based on petrochemical and tunnel incidents shown in Figure 3, is simply used as the design basis exposure. For more in depth studies,

natural fire curves based on the expected combustible fuel content and ventilation in a compartment can be developed.[9] There is not only inherent uncertainty in these fire development parameters, but also variability in the modeling time-temperature predictions for the same set of inputs. This creates a practical quandary about what fire exposure(s) is most appropriate for both PBD and structural fire performance testing.

Review of the literature has confirmed this large variability in actual natural compartment fires in buildings, both in terms of intensity and duration. (see Figure 4) It should be evident that in a number of reported cases, the standard building fire curve (E 119 and similar), which represents the mildest exposure of all the standard fire curves given in Figure 3, can substantially underestimate the temperatures, especially during the 1st hour of burning.

This information indicates that the worst-case scenario for PBD and testing for buildings fires is really a fairly constant and maximum 1,200ºC fire exposure. This has been startling news to many in the building construction profession, including the lead author of this article, given that such high exposure temperatures have been normally associated with only the special hydrocarbon and tunnel fires.

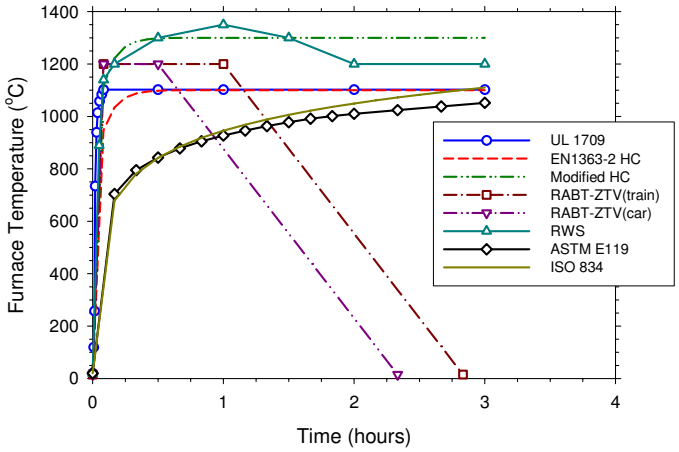

Figure 3 – Different Standard Furnace Time-Temperature Exposure Curves

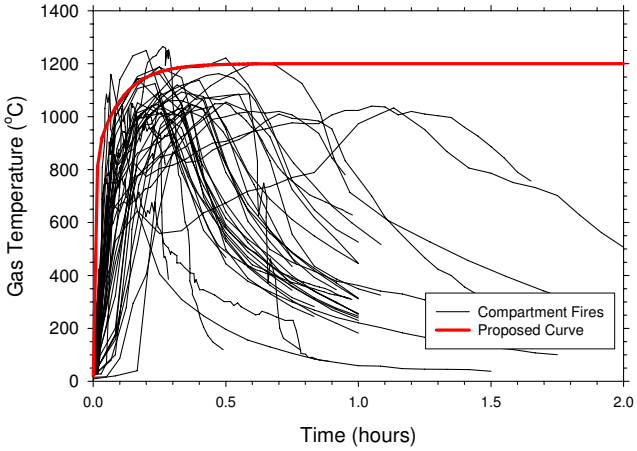

Figure 4 – Average Gas Temperature in Compartment Fires as Function of Time, Compared with 1,200C Maximum Time-Temperature Curve

The impact of this potential high temperature exposure could be immense, in that such a rapid and intense heating can result in both premature structural and protection material damage that has not been previously apparent when subjected to the milder standard fire. This damage, such as early spalling and cracking of concrete, delamination/detachment of low-density spray-on protection, and shrinkage-distortion of gypsum boards, can thereby substantially degrade the overall structural fire performance.

The NFPA Report[4] concludes that the 1,200ºC fire exposure curve is the most appropriate one to use for PBD testing, again since it does represent a worst-case scenario. However, because this is a very severe exposure, it will be over-conservative for some building constructions and occupancies, just like the current E 119 fire curve can be un-conservative for some others. Further work should be undertaken to develop a limited number of standard fire curves for different exposure classes, say light, moderate, and severe, with a good descriptive delineation of their range of applicability, similar to what has been done in the simplification of structural design provisions for seismic and wind loads. In the interim, it should at least be acknowledged that PBD and fire testing to the current standard building fire curve, like ASTM E 119, may not necessarily be a conservative exposure.

5. GENERAL FIRE TESTING RESEARCH NEEDS

5.1 Development of Test Procedure and Data on Fire Performance of Common Structural Connections

In the aftermath of the 9/11 World Trade Center collapses, more attention has been directed at the uncertainties of the high-temperature behavior of structural connections. These include not only the thermally-induced material degradation of welds, bolts, fasteners, adhesives and rebar details, but also the effects of large strains and deformations, together with a possible change in the basic mode of connection load transfer, e.g. from simple shear to tension for catenary action. The standard fire resistance tests essentially address members and small subassemblies, not connections. It would be beneficial to better understand the fire response of the common structural connections, in all materials – flexible/shear and rigid/moment, in order to assess whether they are more or less robust than their supported members, and what detailing and/or fire protection features can be optimized for fire performance.

5.2 Develop, Improve and Standardize Test Methods for High Temperature Thermal, Physical, and Structural Properties of Materials

Test methods for high temperature thermal, physical, and structural properties of materials are needed. Thermal properties (conductivity, specific heat capacity, heat of decomposition) need to be measured at temperatures as close to the highest temperature the material is expected to reach. Physical properties (density, moisture content, expansion/contraction, decomposition kinetics) also need to be measured as a function of temperature up to temperatures the material is expected to reach. Material strength tests need to be performed on materials used in the primary structural assembly members to determine their actual mechanical properties at high temperatures (including yield and ultimate strength, and elastic modulus. Research is needed to develop and evaluate the available methods, and provide suggestions for their improvement.

5.3 Compile Fire Test Database

A central compilation of a comprehensive database on all structural fire tests of members and assemblies, including those that were not successful, is recommended. This database should be regularly updated and also include any prescriptive fire resistance test results that were released to the public.

5.4 Analyze Repeatability (Scatter) of Tests

Once a sufficiently large and diverse database has been compiled, a rigorous statistical study of the random variations in similar fire tests should be performed to determine the expected probability distribution of experimental results.

6. CONCLUSIONS

Standard fire test methods and prescriptive ratings will probably continue to have a place in building design and construction for some time to come. In order to supplement the limited structural fire performance information that can be gleaned from such, a different and more scientific approach to structural fire testing is necessary to assist in the implementation of PBD for projects that so warrant. A parallel perspective has been adopted in seismic engineering. A list of recommendations has been outlined in this paper towards this end, mostly on structural issues, but also touching on fire/furnace controls and general experimental research needs.[4] These should provide a rational path forward to advance PBD and its underlying test validation through enhanced test planning, further standardization, broadened results and better documentation for the future.

7. REFERENCES

[1] ASTM E 119, *Standard Test Method for Fire Tests of Building Construction and Materials*, American Society for Testing and Materials, West Conshohocken, PA, USA.
[2] ISO 834, *Fire-resistance Tests- Elements of Building Construction*, International Organization for Standardization, Geneva, Switzerland, 1999.
[3] Grosshandler, *Fire Resistance Determination and Performance Prediction Research Needs Workshop: Proceedings*, NISTIR 6890, National Institute of Standards and Technology, Gaithersburg, MD, USA, September 2002.
[4] Beyler, C., Beitel, J., Iwankiw, N., and Lattimer, B., "Fire Resistance Testing Needs for Performance-Based Fire Design of Buildings," Report for the Fire Protection Research Foundation of the NFPA, Quincy, MA, USA, June 2007.
[5] Ryan, J. V. and Robertson, A.F., "Proposed Criteria for Defining Load Failure of Beams, Floors, and Roof Constructions During Fire Tests," *Journal of Research of the National Bureau of Standards, C. Engineering and Instrumentation*, Vol. 63C, No. 2, October–December 1959.
[6] ASTM E 72, *Standard Test Methods of Conducting Strength Tests of Panels for Building Construction,* American Society for Testing and Materials, West Conshohocken, PA, USA.
[7] ACI 318-02, *Building Code Requirements for Structural Concrete*, American Concrete Institute (ACI), Farmington Hills, MI, USA, 2002.
[8] Gewain, R.G. and Troup, E.W.J., "Restrained Fire Resistance Ratings in Structural Steel Buildings," *AISC Engineering Journal*, Second Quarter, AISC, Chicago, IL, USA, 2001.

[9] SFPE, *Engineering Guide – Fire Exposures to Structural Elements*, Society of Fire Protection Engineers (SFPE), Bethesda, MD, USA, 2004.

EFFECTS OF FIRE ON A CONCRETE STRUCTURE: MODELLING THE WINDSOR TOWER

IAN FLETCHER[1], STEPHEN WELCH[2], JORGE A. CAPOTE[3], DANIEL ALVEAR[4] and MARIANO LÁZARO[5]

ABSTRACT

A systematic approach has been adopted to studying the possible structural response of the Windsor Tower to various assumed fire scenarios. A simplified single beam model is initially analysed considering heating exposures on the upper and lower surfaces, in order to represent the local effect of the multiple floor fire. The results show that even when subjected to exposures on both sides, the individual concrete floor slab members within the Windsor Tower would have been able to remain intact, though badly damaged and with some residual deflections. The findings are consistent with the observation that the only collapse of the concrete floor slab was in regions where the perimeter steel columns failed due to lack of fire protection.

1. INTRODUCTION

Concrete is a complex non-homogeneous material and as a result modelling concrete structures can be extremely complicated[1]. Here, methods for assessing the performance of concrete structures are first examined in order develop an appropriate strategy for study of the Windsor Tower fire[2].

There is a relative paucity of experimental work carried out on concrete structures compared to steel structures; however useful information can be obtained from fires in real concrete buildings. Unfortunately, as these fires are accidental, it is often difficult to sufficiently categorise the fire load and the temperatures imposed upon the structure are

[1] PhD student, BRE Centre for Fire Safety Engineering, University of Edinburgh
[2] PhD, BRE Centre for Fire Safety Engineering, University of Edinburgh
e-mail: s.welch@ed.ac.uk
[3] Professor, GIDAI, Universidad De Cantabria
[4] PhD, GIDAI, Universidad De Cantabria
[5] PhD student, GIDAI, Universidad De Cantabria

typically uncertain. Methods such as observation of the flame colour and the colour change in the concrete can give indications of peak gas temperatures[3, 4].

In order to give a better understanding of the possible heating history of individual structural members Computational Fluid Dynamics (CFD) modelling of the building can be performed[5]. The initial conditions used within this model will often be uncertain, especially in a large structure, as it is rare that any formal records exist of the distribution of fuel load within a building. Generally this will change from floor-to-floor and room-to-room, and can often be quite different from the fuel loading that was initially assumed during the building design. Assumptions must therefore be made about the fire loading at the time of the fire. While these will clearly affect the duration of the fire, the fire temperatures themselves may exhibit a relatively low sensitivity to the details of the loading during the important post-flashover phase of the fire, when the heat release is normally limited by ventilation control[6]. This possible simplification is however typically confounded by significant uncertainties in the ventilation areas, i.e. the progress of glazing failure.

2. THE WINDSOR TOWER

The Windsor Tower had 32 storeys, 29 above ground, with occupied height of 97m; it was constructed in the late 1970's. The main upper section, above floor three, was a tower block containing offices. The tower consisted of a concrete core, several interior concrete columns, exterior steel columns and a concrete waffle slab floor with permanent clay formwork, see Fig. 1.

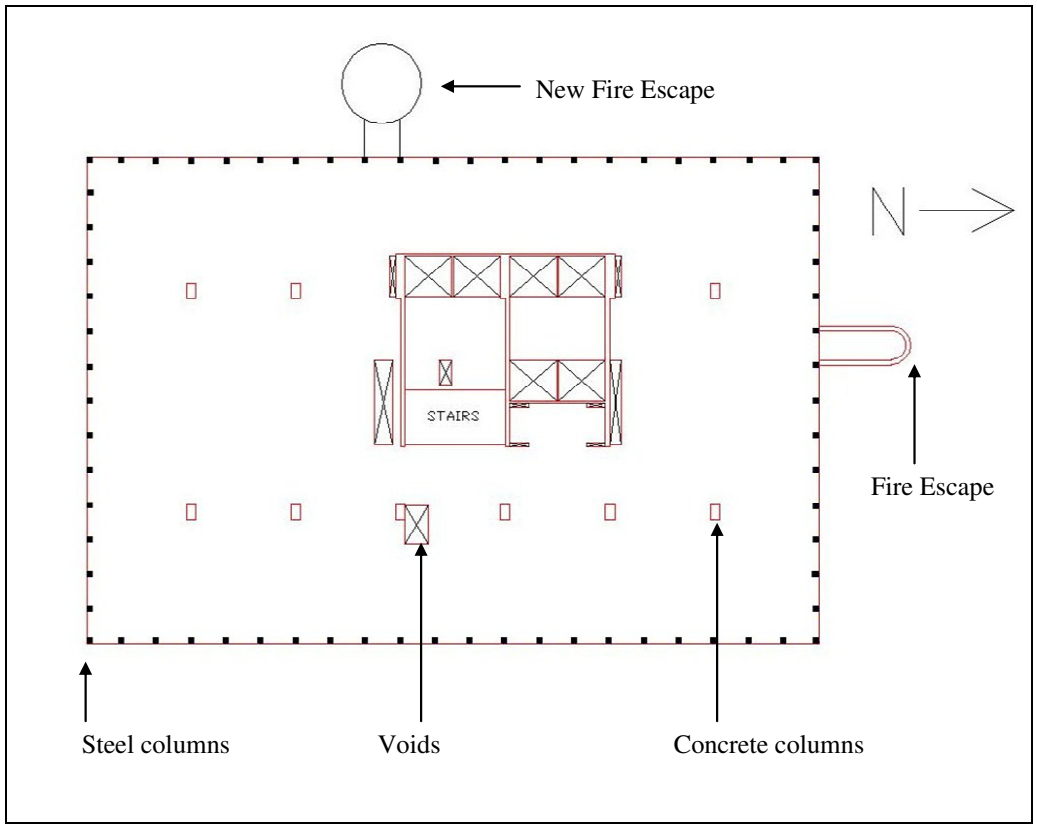

Fig. 1 – Layout of floors above upper transfer floor

There were two "transfer structures" in the tower block, located between floors 3 and 4, and 16 and 17, which were significantly stronger than the average floor, consisting of a series of concrete walls over the entire floorplan of the tower and a solid floor slab.

Below the third floor there was an entertainment and shopping complex, with a different structural layout, and underground parking on several levels; however this part of building was largely unaffected by the fire and did not sustain any structural damage.

The exterior steel columns were not, when the building was first constructed, fire protected. At the time of the fire a programme of fire protection upgrading was being undertaken, and the steel columns up to the upper transfer floor had been protected, with the exception of those on the south and west sides of the 9th floor. An additional fire escape was also added to the west side of the building.

On 12-13 February 2005, the Windsor Tower was involved in a major fire, of duration 18-20 hours. This broke out in an office on the 21st floor of the building, causing extensive structural damage to the upper floors of the building. Damage to the lower floors, below the upper transfer floor, was considerably less[2, 7, 8].

In the region above the upper transfer floor, large areas of the floor slab exterior to the core collapsed and several of the concrete columns were also damaged. It has been suggested that this was due to a failure of the concrete in the fire; however it must be born in mind that this is also the part of the building that had unprotected external steelwork.

On the 9th floor, which had large areas of unprotected steelwork, the exterior steel columns were later found to have buckled severely. However, this part of the building did not collapse. Therefore the concrete structures and the fire protected steel on the floors above and below were proved to be capable of redistributing the loads applied to the weakened steel columns.

3. THE FIRE BOUNDARY CONDITION

When modelling a real structure which has been involved in a fire, rather than a large-scale experiment, such as that at Cardington or Dalmarnock[9, 10], a major obstacle is the lack of knowledge about the fire conditions within the building. It is very rare that there will be any sensor data available other than that provided by CCTV cameras, smoke alarms and often external video footage and photographs taken for news media. While information of this type can sometimes be very useful, it typically lacks the precision which would ideally be available for detailed computational modelling. Methodologies for assessing the likely fire exposures applied to the structural members must therefore be developed to compensate.

The simplest approach is to specify the surface temperature of the structural elements[1]. The value can either be estimated from observational or experimental data, taking into account for example the colour of the flames or the post-fire condition of the exposed materials[3, 4]. In the case of the Windsor Tower, video and other evidence is consistent with gas-phase temperatures reaching around 800-1000°C after flashover and the peak surface temperature of the enclosure boundaries may not have been far below this[5].

A more general approach is to specify the gas-phase boundary conditions, in terms of gas temperatures or incident heat fluxes, and determine the surface temperature using a thermal model. In this case the fire exposures can be represented in a number of different ways. At the simplest extreme, the temperature can be assumed uniform and equated to that of a "standard fire" curve, i.e. ISO 834 or BS 476, or a parametric heating curve, e.g. Eurocode 1, Annex A. A model-based approach can be used in order to define the thermal boundary conditions more realistically[5, 11]. This is a highly challenging process, since sufficient details of the fire development are required, but some simplifying assumptions can

be made, e.g. with regards to the nature of the burning when the fire becomes ventilation-controlled[6]. The advantage of these methodologies is that the simulation can in principle provide spatially and temporally varying exposures which are consistent with the assumed fire development. In particular, a CFD method provides prediction of heat fluxes, which can be used to define the effective boundary conditions for the structural members, rather than gas-phase temperatures which can only represent local conditions. Heat flux boundary conditions automatically accommodate the effects of remote heating – for example, where local gas temperatures are suppressed, in inflow regions and lower layers, but where heat fluxes may nevertheless be high. Furthermore, the influence of different optical properties can be considered, since these will affect the amount of radiation reaching a structural element[12].

In the current work, thermal exposures derived from elements of standard fire curves have been adopted for simplicity, cross-referenced to predictions of fire temperatures from CFD models and observational evidence[6]. The standard curves have been modified in two key respects – their start times have been adjusted for different surfaces, i.e. for the floor and ceiling sides of a floor slab, and they have been terminated at times consistent with the observations of burn-out, with a decay phase appended. Though representation of the detailed spatial variation in heating conditions is necessarily sacrificed in this approach, the main impact of the fire on the structure is described to a level consistent with the other uncertainties in the modelling.

4. FAILURE MODES

Apart from the failures of unprotected steel, a number of possible failure modes for the Windsor Tower have been identified, and the likelihood is that a variety of these took place. Two of the most important mechanisms considered are:

- Failure of the floor slab due to the failure of the steel edge columns. This will have forced the floor slab to act as a cantilever.
- Failure of the floor slab between the core and the concrete columns exterior to the core This may have come about due to the large service void just outside the core, which would have prevented the slab carrying the large tensile load imposed by a collapse of the floor.

The multi-floor nature of the fire is important, as it is likely that if the fire had only broken out on one floor, then the majority of the building would have survived intact. The 9th floor, which did not have fire protection to the steel columns in large areas, is of particular interest; no collapse occurred on this floor, highlighting the importance of the vertical connections to fire-protected floors, allowing redistribution of the loading and preventing the floor slab from acting as a cantilever.

It has been previously documented[13, 14] that fires on multiple floors of a building can have a severe effect beyond that directly associated with the fire itself, due to the forces exerted by expansion of heated members and eccentricities which are induced in supporting members. However, detailed study the majority of these phenomena, and their relationship to a concrete-framed building, is outwith the scope of this paper.

5. FIRE AND STRUCTURAL MODELS

In many cases, even where an entire structure has been involved in a fire, it will not be necessary or desirable to represent the entirety of the building in a simulation. A more simplified model, consisting of either one or several floors, will provide a great deal of information that may be extrapolated to the rest of the structure[13].

In order to define the thermal exposure durations the passage of the fire through the building must be carefully analysed. Where these are based on fire models, i.e. CFD, the domain can be simplified by making recourse to symmetry, i.e. using a quarter floor model. While on a full floorplan there may be differences between the fire loading of each quarter of the floor, and the floorplan may not be exactly bi-axially symmetrical, these variations can be neglected considering the overall uncertainties and the effect of floor-to-floor variations.

Also, when creating a finite element model of the structure, it may not be necessary to create 3-D models of the entire floor. Where possible, rather than using "block" type finite elements, "beam", "shell" or "membrane" entities should be used in order to reduce the number of elements necessary. The model can be further simplified by taking a cross-section of the floor and examining it as a beam, as is common practice in structural engineering.

While this approach will preclude accounting for much of the load redistribution that commonly takes place within a 3-D structure, it can be used to provide some simplified models to examine factors such as the failure of individual members. For example the effect of the failure of the non-fire protected steel edge columns upon the floor slab can be examined by simplifying the floor slab as a beam spanning between the concrete core of the building and the perimeter column.

In the case of the Windsor Tower the member of interest will be a small section of the concrete floor slab, idealized as a beam. Given the waffle slab method of construction, this can be seen to be a fairly reasonable simplification, and will allow the examination of the effects of a variety of physical property changes which occur in concrete with temperature, such as expansion, loss of strength, thermal bowing, etc. Once the physical phenomena deemed important to the performance of the structure have been examined in this way, and their sensitivities are understood, then the model can they be extrapolated into the larger 2D and 3D representations. A systematic approach to the finite element modelling has therefore been adopted here, proceeding from individual elements of the structure and progressively increasing the complexity, as described below.

The first structural element to be modelled is the concrete floor slab. Due to the nature of its construction, it cannot simply be modelled as a membrane supported by beams. As a waffle slab, it behaves as a grillage of beams with an additional layer of concrete overlaid on top to provide a floor surface.

The Windsor Tower waffle slab uses a method of construction involving permanent clay formwork, see Fig. 2. Within the tower block section of the building, the same waffle slab depth is used throughout, though the reinforcement used within the beam sections of the waffle varies throughout the building.

When defining the reinforcement for the slab, it is noted that the bottom reinforcement is set onto a channel within the clay formwork. This clay formwork is nominally 10mm thick, and a further 10mm layer of concrete is used to bring the cover of the bottom steel up to c. 20mm, as discussed in the INTEMAC report[7]. This is representative of a beam running North to South. The bottom reinforcement bars in the beams running East to West are placed on top of this, and therefore have a minimum level of cover of 30mm. For the purposes of initial modelling of the floor slab, rather than using a different material for the concrete and the clay formwork, the entire cover to the bottom steel has been idealised as concrete. This

reduces the complexity of the model. The beam to be modelled in this study runs East to West.

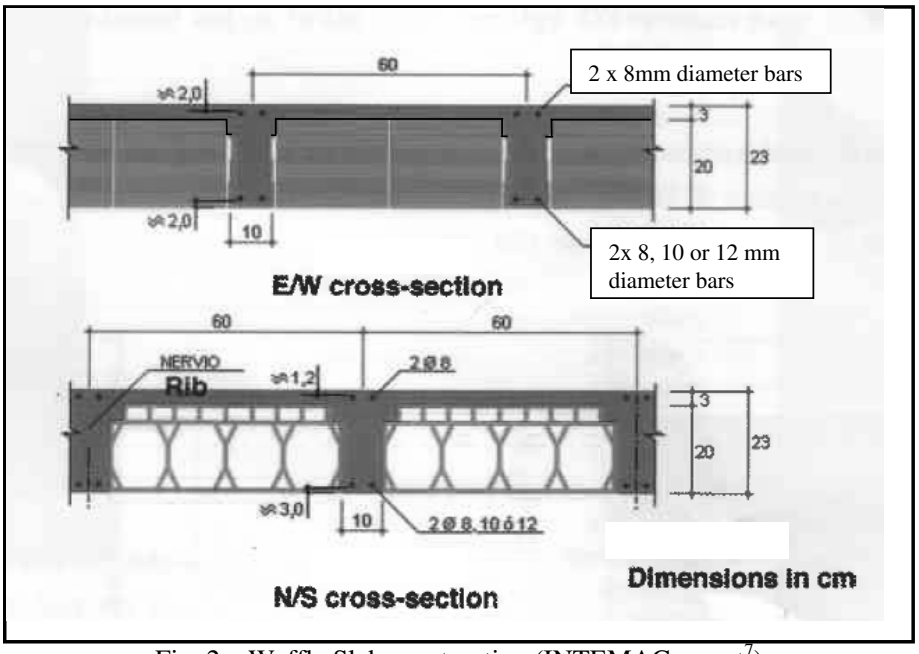

Fig. 2 – Waffle Slab construction (INTEMAC report[7])

From the plans of the Windsor Tower it is clear that the floor slab acts as a network of beams. These can be modelled as primary beams, which in turn support secondary beams. The beams are 0.23m deep and 0.1m wide at 0.6m centres in both directions. The loading acting on the beam per metre is therefore calculated as 0.6 times the pressure acting on the floor slab, given in the building plans as 430kg/m^2.

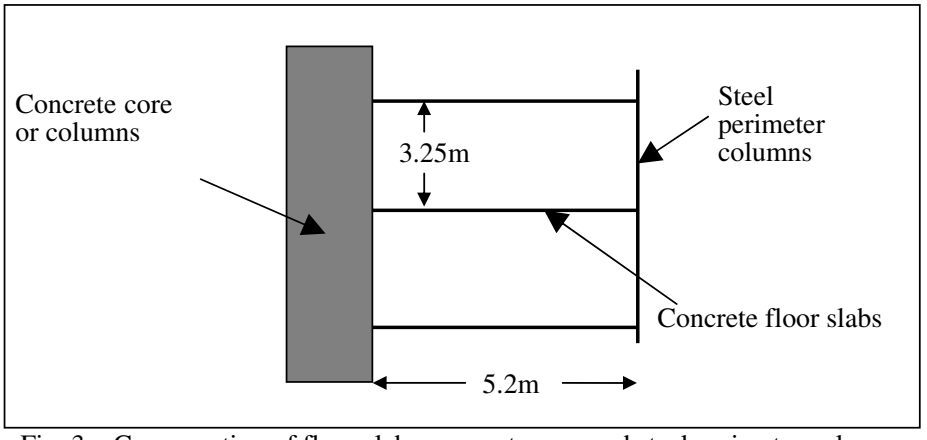

Fig. 3 – Cross-section of floor slabs, concrete core and steel perimeter columns

It is also necessary to make assumptions about the boundary conditions on the beam model. Where the "beam" is attached to the concrete core of the building, cf. Fig. 3, it is assumed that a fixed end connection can be used. At the other end, where the beam attaches to the steel columns, it is assumed that the connection is pinned. While the column is in fact

built into the floor slab at this location, the relatively small size of these columns (140mm by 120mm) means that they are unlikely to resist any significant moments transmitted from the slab. It has been decided to use a totally simply supported beam to give a "worst case" scenario where no moment can be transferred into the core of the building.

The initial Finite Element model of the Windsor Tower structural behaviour therefore consists of a single beam. This is a representative beam from the waffle slab with a span of 5.2m, with 12mm diameter bottom reinforcement and 8mm diameter top reinforcement, cf. Figs. 2 & 3. This reinforcement was laid out as shown in the East-West section in Fig. 2, with 30mm cover to the bottom reinforcement and 12mm cover to the top reinforcement. It was modelled in accordance with the information available from the building plans, with simply supported end conditions and an assumed uniform loading distribution, conservatively taken to be unfactored. The concrete strength was taken as 17.5kN/m^2, in accordance with the building plans and tests carried out in for the INTEMAC report[7]. Both the concrete and steel material properties were defined to be temperature dependent in accordance with the methods from Eurocode 4.

The primary tool used for finite element structural modelling is ABAQUS. When using beam elements in ABAQUS, there are limitations in modelling thermal properties and collapse mechanisms. For the structural model the concrete beam has therefore been modelled as a narrow, deep shell element.

Once the overall structural model has been defined, it is necessary to examine the effects of imposed heating, specifically the evolution of the temperature within the depth of the material, i.e. the penetration of the thermal wave into the concrete structural elements and the temperatures developed within the reinforcing bars. In earlier work, uniform heating conditions were considered, together with approximated equivalent temperature gradients through the material depth, assumed linear and obtained from an in-house thermal analysis code[11]. In the current analyses, a more general approach has been adopted, using a separate analysis undertaken with the numerical heat transfer model in ABAQUS to represent the heating through the depth of the slab. Heat flux boundary conditions are defined on either side and temperature dependent material properties are invoked, accommodating the effects of moisture content using a modified specific heat approach. A one-dimensional representation has been adopted, using shell elements, taking 19 subdivisions of the section thickness; the moisture content was assumed to be 3%. The results of this analysis, i.e. the predicted solid-phase temperatures, are then imported directly into the structural model.

Video evidence and observational analysis of the Windsor Tower fire suggests an approximate fire duration per floor of around one hour for intense fully flashed-over burning, and two hours in total including the burn-out phase[2, 8]. While the standard fire curve is often a poor representation of the temperatures likely to be present within a fire compartment, it may provide a convenient means of specifying temperature development. In the case of the Windsor Tower, the temperature evolution of the standard fire is not too dissimilar to other estimates of compartment temperature evolution[5]. Hence, an element of the standard fire curve, i.e. of finite duration, has been used here to provide a well-defined initial fire loading upon the structural members. By default, a one-hour duration full-scale fire, followed by a one-hour linear cooling phase was specified, with a continuous period of ambient temperature specified thereafter. This exposure was applied respectively to the lower surface of the floor slab, to represent the initial single floor fire, and to both the upper and lower surfaces of the slab, to represent the effects of the multi-floor fires which were a key determinant of the structural response in the Windsor Tower[2, 8]. Where heating from both below and above is adopted, a variable time delay has been applied between the respective exposure curves, in order to represent the effect of the varying floor-to-floor fire spread rate. Different values have been investigated, varying between 0 and 60 minutes, based on the observational

evidence[2, 8], with longer delays representing conditions during the early stages of the upward spread, and *vice versa*. Negative values were also studied for the case of downward spread.

6. RESULTS AND DISCUSSION

When the two hour fire exposure is applied to the lower surface of the beam only, the member is predicted to deflect up to a maximum of 15cm and the bottom reinforcement develops plastic strain as its strength reduces due to the effects of heating (cf. Fig. 4). However, no collapse takes place and the top reinforcement does not develop plastic strain. This demonstrates that in the event of a fire developing on one floor, the floor above should be able to resist the applied loading if its supports remain intact.

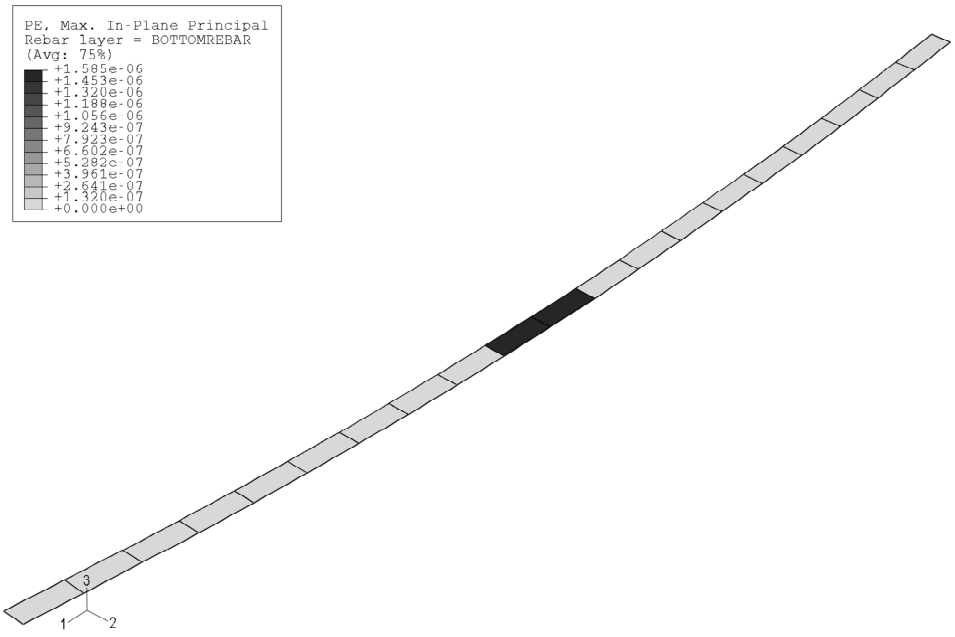

Fig. 4 – Plastic Strain in bottom reinforcement with fire applied to underside of beam

In order to investigate the possible effect of the multiple floor fire, an initial fire loading situation was assumed where both floors were subject to the same fire at approximately the same time; this is an approximation to the situation in the upper stories of the building as the fire travelled quickly upwards[2, 7, 8].

The results of this analysis were that the beam was subject to a substantially larger deflection of 39cm, and that both the top and bottom steel became subject to plastic strain (cf. Figs. 5 & 6). However, again no collapse was predicted to occur in the model, demonstrating that while the deflections involved were large, the floor slab of the Windsor Tower should have been able to withstand a multiple floor fire without collapse.

No major differences in the model predictions were observed when time lags of up to ±60 minutes were introduced for the heating exposure to the top surface of the slab, and failure was not predicted to occur.

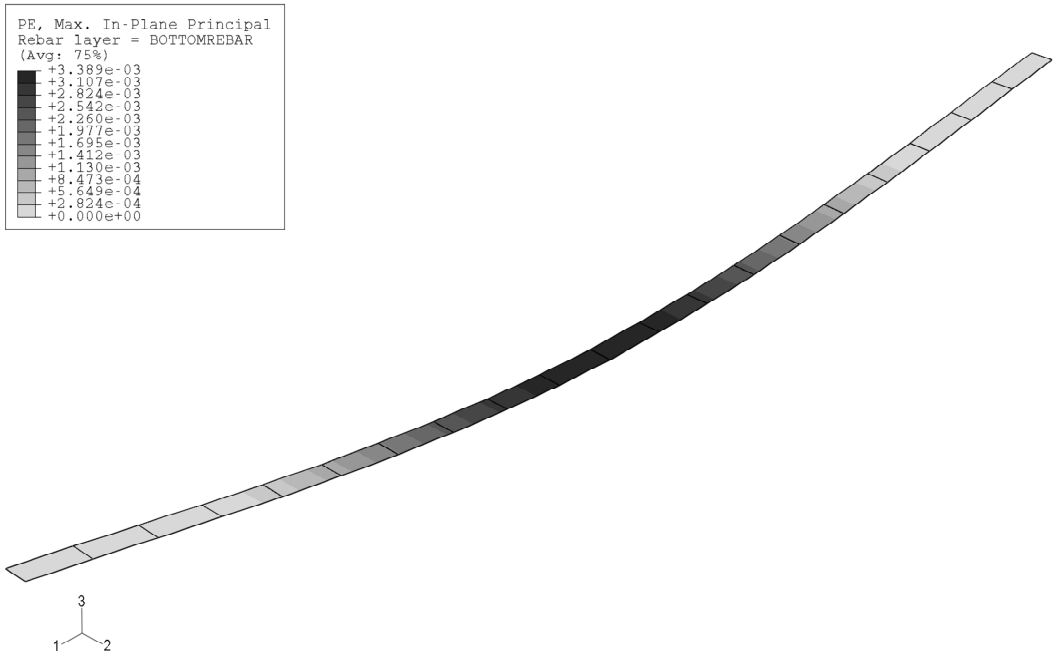

Fig. 5 – Plastic Strain in bottom reinforcement with fire applied to both sides of beam

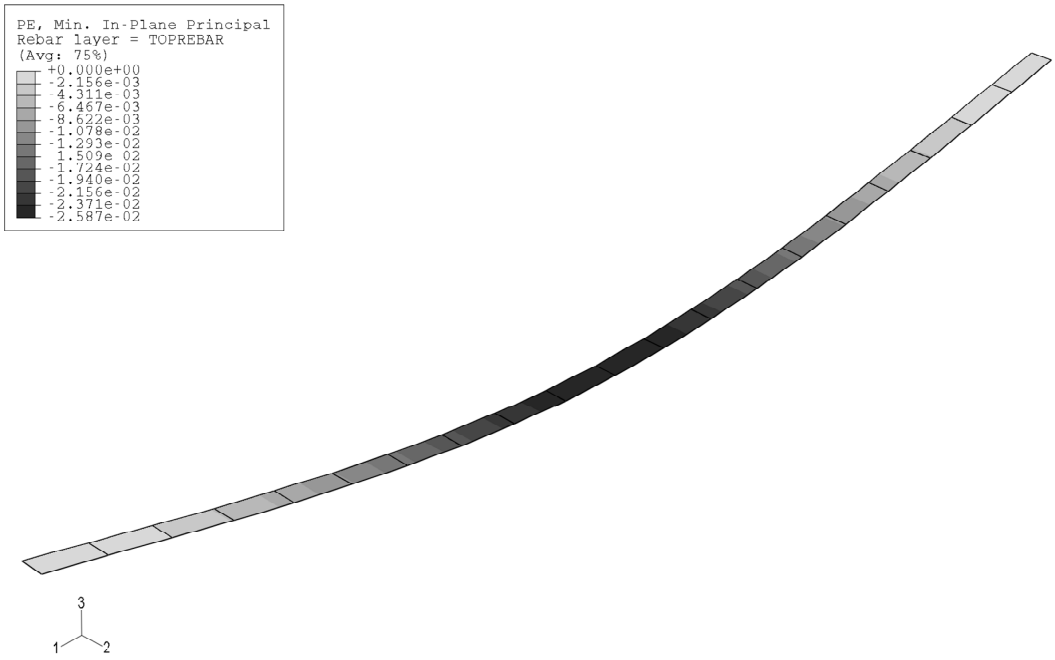

Fig. 6 – Plastic Strain in Top reinforcement with fire applied to both sides of beam

It should be noted that a number of the assumptions made for the initial conditions of these models should have resulted in a "worst case scenario". These are:

- The loading applied to the floor slab, 430kg/m^2, is the unfactored load given in the building plans. In a fire scenario, it is probable that the load imposed on the floor slab will have been significantly lower than this, as the fire took place outwith working hours.
- The support conditions of the beam, simply supported on rollers, do not impose any restraint on the expansion of the beam, which will often create a compressive force to prevent beam failure by mechanical arching.
- The floor surface itself, a 30mm deep membrane which coincides with the top 30mm of the beams, has not been taken into account, reducing the available area of concrete to resist forces.
- The effects of redistribution of the loads into surrounding beams has not been considered. By adopting more generalised thermal exposure distributions, e.g. from CFD, it will be possible to examine the behaviour when areas of the floor slab are subjected to differing exposures, and therefore not all of the beams would have been weakened to the same degree at the same time.

On the other hand, the effects of concrete spalling, which may well have reduced the cover to the steel reinforcement, have thus far been neglected. Other uncertainties in the model, in particular the definition of the heating regime and the thermal response, mean that the initial results can only be taken as indicative and will require support from more detailed and generalised analyses, as described briefly below.

7. FURTHER WORK

This paper presents a variety of work which has taken place so far to examine the effects of the fire on the Windsor Tower. Further work is ongoing, with the main areas of interest being:

- Modification of the temporal and spatial heating exposure variations in accordance with the range of predictions of the CFD models; in particular, variation of the peak temperatures reached in the fire compartment, which remain an area of considerable uncertainty, and also the effect of exposure variation along the length of the beam.
- Further examination of the effects of the differential heating on the floor slab; in particular, use of different exposures and heating curve time offsets so that the slab is subjected to different conditions on either side.
- Further study of the influence of the thermal model, including material property effects on the in-depth temperature distribution.
- Extending the model into a section of the building to investigate the behaviour of the 9th floor, where no collapse took place even with unprotected external steelwork. This will allow examination of the method by which load redistribution takes place vertically within the building and any eccentricities caused by expansion.
- Extending the model into a 3 dimensional "grillage" of beams in order to examine the load redistribution within the individual floors.

8. ACKNOWLEDGEMENTS

The first author acknowledges the support of his industrial sponsors, The Concrete Centre/British Cement Association. Thanks also to Jennifer, for constant support.

The work reported in this paper has formed part of FireGrid, www.firegrid.org. This project was/is co-funded by the Technology Strategy Board's Collaborative Research and Development programme, following an open competition.

9. REFERENCES

[1]. Fletcher, I.A., Welch, S., Torero, J.L., Carvel, R.O. & Usmani, A., *Behaviour of concrete structures in fire.* Thermal Science, 2007. **11**(2): pp. 37-52.

[2]. Fletcher, I.A., Welch, S., Borg, A. & Hitchen, N. *Performance of concrete in fire: A review of the state of the art, with a case study of the Windsor Tower fire*. in Proc. *SiF '06 - 4th international workshop on Structures in Fire*. 2006. Universidade de Aveiro, pp. 779-790.

[3]. Arioz, O., *Effects of elevated temperatures on properties of concrete.* Fire Safety Journal, 2007. **42**(8): pp. 516-522.

[4]. Georgali, B. & Tsakiridis, P.E., *Microstructure of fire-damaged concrete. A case study. Cement & Concrete Composites*, 2005. **27**: pp. 255-259.

[5]. Capote, J.A., Alvear, D., Lázaro, M., Espina, P., Fletcher, I.A., Welch, S. & Torero, J.L. *Analysis of thermal fields generated by natural fires on the structural elements of tall buildings*. in *International Congress Fire Safety in Tall Buildings*. 2006. Santander, Spain, pp. 93-109.

[6]. Rein, G., Zhang, X., Williams, P., Hume, B., Heise, A., Jowsey, A., Lane, B. & Torero, J.L. *Multi-storey fire analysis for high-rise buildings*. in Proc. *Interflam 2007*. 2007. London, pp. 605-616.

[7]. Calavera, J., González-Valle, E., Díaz-Lozano, J., Fernández-Gomez, J., Ley, J. & Izquierdo, J.M., *Fire in the Windsor building, Madrid. Survey of the fire resistance and residual bearing capacity of the structure after the fire.* 2005, Instituto Técnico de Materiales y Constructiones (INTEMAC), ISSN 1885-4575, 35 pp.

[8]. Kono, M., *et al.*, *The Madrid city Windsor building fire inspection report*. 2005, The Madrid city Windsor building fire investigation committee (BCS, JSCA et al) (In Japanese). 133 pp.

[9]. Rein, G., Abecassis Empis, C. & Carvel, R.O. (eds.) *The Dalmarnock Fire Tests: Experiments and Modelling*. Fire SEAT. 2007, The University of Edinburgh.

[10].Lennon, T., *Whole building behavior - results from a series of large scale tests.* CIB Publications No. 290, eds. F. Shafi, R. Bukowski, R. Klemencic, in Proc. CIB-CTBUH International Conference on Tall Buildings, 8-10 May 2003, 2003, pp. 345-351.

[11].Fletcher, I.A., Welch, S., Capote, J.A., Alvear, D. & Lázaro, M. *Effects of fire on a concrete structure: Modelling the Windsor Tower*. in *Fire Design of Concrete Structures - From Materials Modelling to Structural Performance, Proc. FiB 2007*. 2007. University of Coimbra, Portugal.

[12].Welch, S., Jowsey, A., Deeny, S., Morgan, R. & Torero, J.L., *BRE large compartment fire tests - characterising post-flashover fires for model validation.* Fire Safety Journal, 2007. **42**(8): p. 548-567.

[13].Flint, G., *Fire induced collapse of tall buildings*. 2005, PhD thesis, University of Edinburgh: Edinburgh.

[14].Lange, D., Roben, C. & Usmani, A., *Tall building collapse mechanisms initiated by fire, Part I: Analysis, Part II: Design Method.* The Structural Engineer, 2008, **In Press**.

Concrete Structures

COMPUTATIONAL MODELLING OF CONCRETE EXPOSED TO FIRE: THE EFFECTS OF COUPLED HYGRO-THERMAL-MECHANICAL BEHAVIOUR ON THE DEVELOPMENT OF SPALLING IN CONCRETE STRUCTURES

COLIN T. DAVIE[1], HONGLIN ZHANG[2], CHRIS J. PEARCE[3] AND NENAD BIĆANIĆ[4]

ABSTRACT

In this article, through finite element analysis of the coupled hygro-thermal-mechanical (HTM) behaviour of the concrete exposed to high transient temperatures (i.e., standard ISO fire), the relative importance of pore pressure and thermally induced stresses on mechanical damage of concretes with different values of material properties, such as relative humidity, permeability and tensile strength, are particularly investigated and are considered in the light of thermal spalling behaviour observed in concrete structures.

1 INTRODUCTION

When concrete is exposed to high temperature, extremely complex phenomena, including heat conduction and convection, dehydration, thermal expansion, micro-fracturing, pressure driven fluid flow, diffusion, evaporation/condensation, and changes in strength, stiffness, fracture energy, thermal conductivity, permeability, porosity and the mechanical stress field, will occur. Through a variety of processes these phenomena can lead to damage of the concrete and thermal spalling. For accurate prediction of the occurrence of spalling, a complete and fully coupled hygro-thermal-mechanical (HTM) analysis is required. Gawin et al. [1, 2], Khoury et al. [3-5] and Tenchev et al. [6] have undertaken much of the recent pioneering work in the theoretical and numerical modelling of the HTM behaviour of concretes.

[1] Lecturer, School of Civil Engineering and Geosciences, Newcastle University, Newcastle upon Tyne, UK, NE1 7RU, email: colin.davie@ncl.ac.uk
[2] Research Assistant, School of Civil Engineering and Geosciences, Newcastle University, Newcastle upon Tyne, UK, NE1 7RU, email: honglin.zhang@ncl.ac.uk
[3] Senior Lecturer, Department of Civil Engineering, University of Glasgow, Glasgow, UK, G12 8QQ, email: c.pearce@civil.gla.ac.uk
[4] Regius Professor, Department of Civil Engineering, University of Glasgow, Glasgow, UK, G12 8QQ, email: bicanic@civil.gla.ac.uk

Although the coupled hygro-thermal-mechanical behaviour of concrete at high temperature has been well modelled, the causes of spalling are still not fully understood due to the difficulties associated with experimental measurement under high temperature conditions and to the lack of effective and convincing models for prediction of spalling. Several numerical investigations for prediction of spalling have previously been conducted by various authors using a variety of approaches and based on different critical parameters. Tenchev [5] used a damage based approach and determined spalling to have occurred when the damage variable reached its maximum value of unitity. Fu et al. [7] concluded that appropriate modelling of fracture energy is key for predicting the occurrence of spalling. Gawin et al., proposed three criteria based on different simplified hypotheses for the failure mechanisms of concretes to assess the risk of thermal spalling [8].

Based on the previous work, thermally induced stresses and pore pressure can be identified as being contributory to spalling. However, their relative importance for spalling is still a matter of controversy. Some researchers consider pore pressure as the critical factor [9-12], some consider that thermally induced stresses are prevalent [8, 13, 14], and others believe that a combination of the two is required [15-17].

In this article, through finite element analysis of the coupled hygro-thermal-mechanical (HTM) behaviour of the concrete exposed to high transient temperatures (i.e., standard ISO fire), the relative importance of pore pressure and thermally induced stresses on mechanical damage of concretes with different values of material properties, such as relative humidity, permeability and tensile strength, are investigated and are considered in the light of thermal spalling behaviour observed in concrete structures. In the first part of this paper the numerical model is presented in detail. In the second part the model is applied to a simple benchmark problem in an attempt to begin to understand the relative roles of pore pressures and thermally induced stresses in the development of damage and spalling in concrete.

Nomenclature

b	body forces
b	Klinkenberg slip-flow constant
D	total damage parameter
D_{AV}	coefficient of diffusion for the dry air/water vapour mixture
$\mathbf{E}_0$	fourth order elastic strain tensor of the initial elastic moduli
f_{c}^{0}	initial uniaxial compressive strength
h_{qr}	convection/radiation heat transfer coefficient on the boundary
K	intrinsic permeability of the dry concrete
K_θ	relative permeability of concrete
k	thermal conductivity of concrete
k_g	gas-slip modification factor
$\mathbf{N}_\theta$	shape functions
P_{Atm}	atmospheric pressure (101325 Pa)
P_C	capillary pressure
$P_{G,\infty}$	pressure of the atmosphere external to the concrete
P_{Pore}	pore pressure
$\mathrm{P}_{\mathrm{Sat}}$	saturation pressure of water vapour in air
$P_{\mathrm{V}}/P_{\mathrm{Sat}}$	relative humidity
P_θ	pressure of phase θ
R_A	ideal gas constant for dry air

R_V	ideal gas constant for water vapour
S	degree of saturation with liquid water
S_{SSP}	solid saturation point, which is the degree of saturation below which all 'liquid' water exists as adsorbed water
T	absolute temperature
T_∞	temperature of the atmosphere.
t	time
$\mathbf{v}_G$	Darcian velocity of the gas phase
$\mathbf{v}_L$	Darcian velocity of the water phase
X, Y, Z	coefficients of a parabolic curve
β	coefficient of water vapour mass transfer on the boundary
β^{lits}	coefficient of uniaxial thermo-mechanical strain
$\gamma(T)$	coefficient of fracture energy release rate
$\boldsymbol{\varepsilon}^{\mathbf{e}}$	elastic strain tensor
ε_θ	volume fraction of a phase θ ($\theta = L, V, A, D$ refer to liquid water, water vapour, dry air, and dehydrated water phases respectively)
$\varepsilon_{Cem}\rho_c$	cement content per unit volume of concrete
$\varepsilon^m(\sigma,T)$	mechanical strain rate
$\varepsilon^{ft}(T)$	free thermal strain rate
$\varepsilon^{lits}(\sigma,T)$	load induced thermal strain rate (or transient thermal creep)
$\bar{\theta}$	dimensionless transition temperature (equivalent to 470°C)
λ_D	specific heat of dehydration
μ_θ	dynamic viscosity of phase θ
ρC	heat capacity of concrete
$\tilde{\rho}_{G,\infty}$	vapour content in the atmosphere
σ'	Bishop's stress (known as the 'effective stress' in geomechanics)
ϕ	porosity of the concrete
χ	coefficient if thermal damage
ω	coefficient if mechanical damage

2 MATHEMATICAL MODEL

The model employed in this work consists of a fully coupled hygro-thermal-mechanical formulation where concrete is treated as a multiphase system consisting of solid, liquid and gas phases. The solid skeleton is considered to exhibit isotropic elastic-damage behaviour and degradation of the material due to both mechanical and thermal loading is accounted for, in conjunction with other significant thermo-mechanical behaviour. The liquid phase is considered to include adsorbed water (physically bound to the surface of the solid skeleton) the behaviour of which is taken into account where appropriate. The gas phase is considered to be a (variable) mixture of dry air and water vapour, both of which are assumed to behave as ideal gases.

The model is formulated as a coupled system of partial differential equations which are discretised in space by a finite element formulation and discretised in time by a generalised mid-point finite difference scheme.

The model is composed of four governing equations, defining the conservations of mass of dry air, mass of moisture, energy and momentum (1)-(4) [18, 23, 24].

$$\frac{\partial(\varepsilon_G \tilde{\rho}_A)}{\partial t} = -\nabla \cdot \mathbf{J}_A \tag{1}$$

$$\frac{\partial(\varepsilon_G \tilde{\rho}_V)}{\partial t} + \frac{\partial(\varepsilon_L \rho_L)}{\partial t} - \frac{\partial(\varepsilon_D \rho_L)}{\partial t} = -\nabla \cdot (\mathbf{J}_V + \mathbf{J}_L) \tag{2}$$

$$(\underline{\rho C})\frac{\partial T}{\partial t} - \lambda_E \frac{\partial(\varepsilon_L \rho_L)}{\partial t} + (\lambda_D + \lambda_E)\frac{\partial(\varepsilon_D \rho_L)}{\partial t} = \nabla \cdot (k \nabla T) + \lambda_E \nabla \cdot \mathbf{J}_L \tag{3}$$

$$\nabla \cdot (\boldsymbol{\sigma}' - P_{Pore}\mathbf{I}) + \mathbf{b} = 0 \tag{4}$$

2.1 Constitutive Laws for Energy and Fluid Transport Behaviour

Transport of the liquid water phase is assumed to obey Darcy's law of pressure driven flow while the gas phase is assumed to obey with both Darcy's law and Fick's law of concentration driven diffusion. The mass fluxes of dry air, water vapour and liquid water per unit area of concrete are then given by (5), (6) and (7) respectively.

$$\mathbf{J}_A = \varepsilon_G \tilde{\rho}_A \left(-\frac{k_g K K_G}{\mu_G} \right) \nabla P_G - \varepsilon_G \tilde{\rho}_G D_{AV} \nabla \left(\frac{\tilde{\rho}_A}{\tilde{\rho}_G} \right) \tag{5}$$

$$\mathbf{J}_V = \varepsilon_G \tilde{\rho}_V \left(-\frac{k_g K K_G}{\mu_G} \right) \nabla P_G - \varepsilon_G \tilde{\rho}_G D_{AV} \nabla \left(\frac{\tilde{\rho}_V}{\tilde{\rho}_G} \right) \tag{6}$$

$$\mathbf{J}_L = \varepsilon_L \rho_L \left(-\frac{K K_L}{\mu_L} \right) \nabla P_L \tag{7}$$

It may be noted that the diffusion of adsorbed water along the surface of the solid skeleton is considered to be accounted for within the empirically derived liquid water relative permeability term, K_L, and is not therefore treated separately.

In order to account for capillary suctions the liquid pressure is calculated from (8).

$$P_L = P_G - P_C \tag{8}$$

where the capillary pressure, P_C, is then calculated by way of the Kelvin Equation (9).

$$P_C = \begin{cases} -R_V T \rho_L \ln\left(\dfrac{P_V}{P_{Sat}}\right) & \text{for } S > S_{SSP} \\ 0 & \text{for } S \le S_{SSP} \end{cases} \tag{9}$$

The dry air and water vapour within the gas phase are assumed to behave as ideal gases, as described by (10) while their partial pressures and densities are assumed to obey Dalton's law of additivity as described in (11).

$$P_A = R_A \tilde{\rho}_A T; \quad P_V = R_V \tilde{\rho}_V T \tag{10}$$

$$P_G = P_A + P_V; \quad \tilde{\rho}_G = \tilde{\rho}_A + \tilde{\rho}_V \tag{11}$$

For the calculation of the total stress (4) the combined pore pressure, P_{Pore}, is derived from the weighted contributions of the gas and liquid pressures, assuming that adsorbed water applies no pressure, according to equation (12).

$$P_{Pore} = \begin{cases} P_G - P_{G,\infty} & \text{for } S \le S_{SSP} \\ \left(\frac{S - S_{SSP}}{1 - S_{SSP}}\right) P_L + \left(\frac{1 - S}{1 - S_{SSP}}\right) P_G - P_{G,\infty} & \text{for } S > S_{SSP} \end{cases} \tag{12}$$

Finally, the volume fraction of liquid water in the concrete is calculated from the sorption isotherms, which are a function of relative humidity and temperature (13).

$$\varepsilon_L = \frac{\varepsilon_{Cem} \rho_{Cem}}{\rho_L} \cdot f\left(\frac{P_V}{P_{Sat}}, T\right) \tag{13}$$

2.2 Constitutive Laws for Mechanical Behaviour

The total strain rate decomposition for the mechanical component of the model is shown in (14).

$$\varepsilon = \varepsilon^m(\sigma, T) + \varepsilon^{ft}(T) + \varepsilon^{lits}(\sigma, T) \tag{14}$$

2.2.1 Mechanical Strains

Mechanical strains are developed by way of an isotropic damage model, which accounts for the loss of the elastic stiffness that is caused by the micro-fracturing of concrete that develops under loading and under heating. The classical mechanical damage formulation is modified to include a second thermal damage parameter, χ, in a multiplicative form (15) [2, 19].

$$\boldsymbol{\sigma} = (1 - \omega)(1 - \chi)\mathbf{E_0} : \boldsymbol{\varepsilon}^{\mathbf{e}} = \mathbf{E}_{\sec} : \boldsymbol{\varepsilon}^{\mathbf{e}} \tag{15}$$

The mechanical damage parameter is defined by the temperature dependent function shown in (16) as adapted from Peerlings et al. [20]

$$\omega = 1 - \frac{\kappa_0^{md}(T)}{\kappa^{md}} e^{-\gamma(T)\left(\kappa^{md} - \kappa_0^{md}(T)\right)} \tag{16}$$

where, $\kappa_0^{md}(T)$, which defines the onset of damage, is a function of the tensile strength, $f_t(T)$, and elastic modulus, $E(T)$.

$$\kappa_0^{md} = \frac{f_t(T)}{E(T)} \tag{17}$$

The thermal damage parameter is defined by the temperature dependent function shown in (18), which is derived from the degradation of the elastic modulus that results from increased temperatures, $E(T)$.

$$\chi = 0.2\theta - 0.01\theta^2 \tag{18}$$

2.2.2 Free Thermal Strains

To capture the non-linear expansion of concrete observed upon heating a simple, empirically derived, temperature dependent function is adopted (19).

$$\varepsilon_{ij}^{ft} = \alpha T \delta_{ij} \tag{19}$$

The coefficient, α, employed here is representative of a generic concrete made with a quartzite aggregate. Alternative functions may be used to capture the behaviour of other aggregate types.

2.2.3 Load Induced Thermal Strains

Concrete specimens that are heated under load are observed to strain very differently to similar specimens that are heated prior to loading. The difference in the observed strains is defined as the load induced thermal strain [3]. This phenomenon is recognised to be irreversible and to occur only during first heating to a given temperature, and not during subsequent cooling or re-heating.

Following the work of Khoury [4], Thelanderson [21], de Borst et al. [22] and Pearce et al.[18], the load induced thermal strain is given by the parabolic formulation (20) & (21).

$$\varepsilon^{lits} = \frac{\sigma}{f_c^0} \beta^{lits} T \tag{20}$$

$$\beta^{lits} = 0.01 \times \begin{cases} 2X\theta + Y & \text{for } 0 \le \theta \le \bar{\theta} \\ 2Z\left(\theta - \bar{\theta}\right) + 2X\bar{\theta} + Y & \text{for } \theta > \bar{\theta} \end{cases} \tag{21}$$

Full details for the formulation of the model described above including the constitutive relationships and material parameters may be found in Davie et al. [23].

3 NUMERICAL FORMULATION

Employing the Galerkin weighted residual method and application of the divergence theorem the weak form of the governing equations (1) - (4) is obtained and may be expressed in matrix-vector form as (22).

$$\mathbf{C}\mathbf{x} + \mathbf{K}\mathbf{x} = \mathbf{f}^{ext} \tag{22}$$

where, the coefficient matrices, **C** & **K**, and the array of nodal variables, **x**, are given below for the chosen set of primary variables (23).

$$\mathbf{C} = \begin{bmatrix} 0 & 0 & 0 & 0 \\ 0 & \mathbf{C}_{TT} & \mathbf{C}_{TP} & \mathbf{C}_{TV} \\ 0 & \mathbf{C}_{AT} & \mathbf{C}_{AP} & \mathbf{C}_{AV} \\ 0 & \mathbf{C}_{MT} & \mathbf{C}_{MP} & \mathbf{C}_{MV} \end{bmatrix}; \quad \mathbf{K} = \begin{bmatrix} \mathbf{K}_{uu} & \mathbf{K}_{uT} & \mathbf{K}_{uP} & \mathbf{K}_{uV} \\ 0 & \mathbf{K}_{TT} & \mathbf{K}_{TP} & \mathbf{K}_{TV} \\ 0 & \mathbf{K}_{AT} & \mathbf{K}_{AP} & \mathbf{K}_{AV} \\ 0 & \mathbf{K}_{MT} & \mathbf{K}_{MP} & \mathbf{K}_{MV} \end{bmatrix}; \quad \mathbf{x} = \begin{Bmatrix} \mathbf{u} \\ \mathbf{T} \\ \mathbf{P}_G \\ \boldsymbol{\rho}_V \end{Bmatrix} \tag{23}$$

The governing equations are discretised using the standard finite element approximation and the chosen primary variables of displacements, u, temperature, T, gas pressure, P_G, and vapour content, $\tilde{\rho}_V$, are expressed in terms of their nodal quantities (24).

$$u = \mathbf{N}_u \mathbf{u}; \quad T = \mathbf{N}_T \mathbf{T}; \quad P_G = \mathbf{N}_P \mathbf{P}_G; \quad \tilde{\rho}_V = \mathbf{N}_\rho \boldsymbol{\rho}_V \tag{24}$$

Full definitions of the matrix coefficients $\mathbf{C}_{\theta\theta}$ and $\mathbf{K}_{\theta\theta}$ may be found in Davie et al. [23]. The equations are discretised in time using a generalised finite difference scheme (25).

$$\mathbf{x}^{t+\alpha\Delta t} = \frac{\mathbf{x}^{t+\alpha\Delta t} - \mathbf{x}^{t}}{\Delta t}; \quad \mathbf{x}^{t+\alpha\Delta t} = (1-\alpha)\mathbf{x}^{t} + \alpha\mathbf{x}^{t+\Delta t} \tag{25}$$

Combining the temporal discretisation with a Newton-Raphson type iterative solution technique, the finite element formulation becomes (26).

$$\overline{\mathbf{K}} d\mathbf{x} = \mathbf{f}^{ext} - \mathbf{f}^{\text{int}} \tag{26}$$

where, the effective stiffness matrix, $\overline{\mathbf{K}}$, and the internal "force" vector terms, $\mathbf{f}^{\text{int}}$, are given as (27) & (28):

$$\overline{\mathbf{K}} = \begin{bmatrix} \mathbf{K}_{uu} & \mathbf{K}_{uT} & \mathbf{K}_{uP} & \mathbf{K}_{uV} \\ \mathbf{0} & \frac{1}{\Delta t}\mathbf{C}_{TT} + \alpha\mathbf{K}_{TT} & \frac{1}{\Delta t}\mathbf{C}_{TP} + \alpha\mathbf{K}_{TP} & \frac{1}{\Delta t}\mathbf{C}_{TV} + \alpha\mathbf{K}_{TV} \\ \mathbf{0} & \frac{1}{\Delta t}\mathbf{C}_{AT} + \alpha\mathbf{K}_{AT} & \frac{1}{\Delta t}\mathbf{C}_{AP} + \alpha\mathbf{K}_{AP} & \frac{1}{\Delta t}\mathbf{C}_{AV} + \alpha\mathbf{K}_{AV} \\ \mathbf{0} & \frac{1}{\Delta t}\mathbf{C}_{MT} + \alpha\mathbf{K}_{MT} & \frac{1}{\Delta t}\mathbf{C}_{MP} + \alpha\mathbf{K}_{MP} & \frac{1}{\Delta t}\mathbf{C}_{MV} + \alpha\mathbf{K}_{MV} \end{bmatrix} \tag{27}$$

$$\begin{aligned} \mathbf{f}_{\theta}^{\text{int}} = \frac{1}{\Delta t}\begin{bmatrix} \mathbf{0} & \mathbf{C}_{\theta_n\theta_2} & \mathbf{C}_{\theta_n\theta_3} & \mathbf{C}_{\theta_n\theta_4} \end{bmatrix}\left(\mathbf{x}_{j-1}^{t+\Delta t} - \mathbf{x}^{t}\right) \\ + \begin{bmatrix} \mathbf{K}_{\theta_n\theta_1} & \mathbf{K}_{\theta_n\theta_2} & \mathbf{K}_{\theta_n\theta_3} & \mathbf{K}_{\theta_n\theta_4} \end{bmatrix}\left(\alpha\mathbf{x}_{j-1}^{t+\Delta t} - (1-\alpha)\mathbf{x}^{t}\right) \end{aligned} \tag{28}$$

The formulation is completed with the following boundary conditions. Transfer of heat across the boundary is described by (29).

$$\frac{\partial T}{\partial n} = \frac{h_{qr}}{k}(T_{\infty} - T) \tag{29}$$

Transfer of water vapour across the boundary is described by (30).

$$\frac{\partial \tilde{\rho}_V}{\partial n} = -\frac{K_{VT}}{K_{VV}}\frac{h_{qr}}{k}(T_{\infty} - T) + \frac{\beta}{K_{VV}}\left(\tilde{\rho}_{V,\infty} - \tilde{\rho}_V\right) \tag{30}$$

Finally, the gas pressure on the boundary is given by (31).

$$P_G = P_{G,\infty} \tag{31}$$

4 NUMERICAL ANALYSES

For the work described here the model has been applied in the analysis of a concrete wall with its two faces exposed to the standard ISO834 fire, as described by Davie et al. [24]

$$T_{\infty} = 20 + 345\log_{10}(8t+1) + 273.15 \tag{32}$$

This problem can be simplified as a one-dimensional symmetric problem as shown in Fig. 1. One (left) side is heated by fire. The other (right) side is a symmetric plane, and thus no heat and mass transfer across it. Moreover, the concrete can only expand towards the left due to thermal dilation. The initial internal temperature, gas pressure and porosity of the concretes used in the simulation are 293K, 0.1MPa and 12.2%. Young's modulus and Poisson's ratio are kept constant at 30GPa and 0.2. To investigate damage of the concretes

under various conditions, 8 simulation cases are performed. The varied parameters used in the simulation cases are given in Table 1.

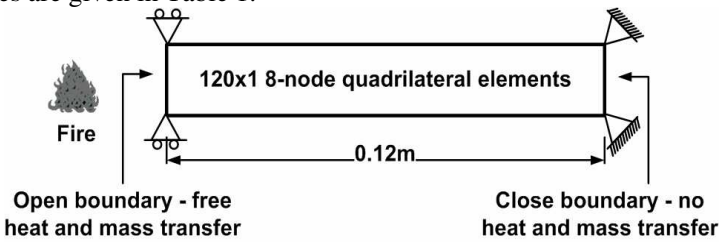

Fig. 1 - Schematic diagram

Table 1. Varied parameters used in the simulation

Case	Permeability (m^2)	Relative Humidity	Tensile strength (MPa)
1	$5x10^{-21}$	1%	3
2	$5x\ 10^{-21}$	90%	3
3	$5x\ 10^{-21}$	1%	11
4	$5x\ 10^{-21}$	90%	11
5	$5x\ 10^{-17}$	1%	3
6	$5x\ 10^{-17}$	90%	3
7	$5x\ 10^{-17}$	1%	11
8	$5x\ 10^{-17}$	90%	11

Figs. 2-4 demonstrate the evolutions of thermal damage, mechanical damage and total damage in the concretes of different tensile strength. As seen in Fig. 1, thermal damage is almost the same for the concretes of different tensile strength. This is to be expected as thermal damage is primarily a function of temperature. However, as seen in Fig. 2, mechanical damage is significantly different for the two different concretes. For example, after 600s mechanical damage is observed only in the concrete of lower tensile strength. Consequently, the difference in total damage between the concretes of different tensile strength is mainly due to the difference in mechanical damage (see Fig. 4). However, for these cases, thermal damage accounts for most of the total damage. The results imply that the most severe degradation and damage of the concrete material occurs at the exposed face and works backwards into the structure. This is not however, completely consistent with the observed occurrence of spalling, which tends to involve the development of fractures at depths 10s of millimetres behind the exposed surface. Furthermore, as indicated in previous work [3-12], thermal degradation of the material is not considered a primary driving factor for the occurrence of spalling. Instead, thermally induced stresses and/or pore pressure are the critical factors. More consistent with observed spalling behaviour is the zone of mechanical damage predicted by the model (Figs. 3-4). This consistency is further reinforced by the mechanisms associated with mechanical damage, which is related to the development of micro-fractures in the concrete (rather than thermo-chemical degradation as is the case for thermal damage), and therefore the mechanical damage parameter (ω) is here considered to be the most appropriate indicator for prediction of spalling.

The contribution of thermally induced stress to mechanical damage is investigated by considering the concretes of higher permeability and/or lower humidity. When humidity of the concrete is low (e.g., in cases 1 and 3 in Fig. 5), the maximum pore pressure is less than 0.5MPa due to the lack of moisture content in the concrete. When the permeability of the concrete is high (see Fig. 6), the maximum pore pressure is also less than 0.5MPa. This is because fluids can transport freely away from the heated surface of the concrete and thus pore pressure cannot built-up. In these cases, the maximum pore pressure is much lower than the

tensile strength of the concrete, and is thus a negligible factor in the development of mechanical damage. Therefore, under these circumstances, thermally induced stress can be considered the primary factor causing mechanical damage. Figs. 7 and 8 demonstrate the mechanical damage mainly caused by thermally induced stresses after 1800s and it can be seen that the concrete experiences mechanical damage in excess of 50% in a zone up to 20mm depth from the heated surface. It may again be noted that this is consistent with the zone where spalling could be expected to occur [6, 8, 9] although it is acknowledged that total damage does is not shown to reach a value of unity in this region. In the above cases, mechanical damage is mainly caused by thermally induced stresses. Considering the fact that the concrete can expand freely towards the heated surface in this simplified problem, it can be expected that mechanical damage caused by thermally induced stresses will be even more significant for concrete with more constraints on the heated surface. Under such conditions damage may reach unity in the spalling zone.

For the concretes of high humidity and low permeability, the contribution of pore pressure to mechanical damage is demonstrated by comparing the mechanical damage of the concretes of high humidity with that of the concretes of low humidity, where pore pressure is negligible. As seen in Fig. 9, although pore pressure may be significant in some cases (e.g., case 2), its significance for mechanical damage is secondary to thermally induced stress. Moreover, because the permeability of the concrete increases with the development of total damage (due to the development of micro-fractures), the pore pressure decreases with the development of damage. Thus as damage develops the role of pore pressure in its continued development reduces (see Fig. 10).

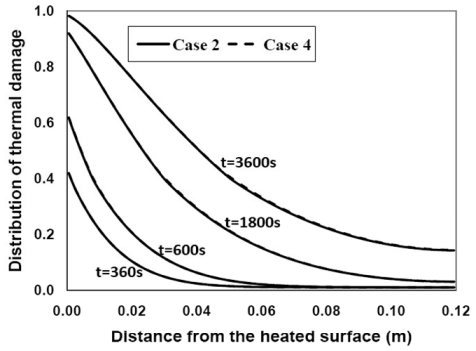

Fig. 2 Development of thermal damage for the concretes of different tensile strength

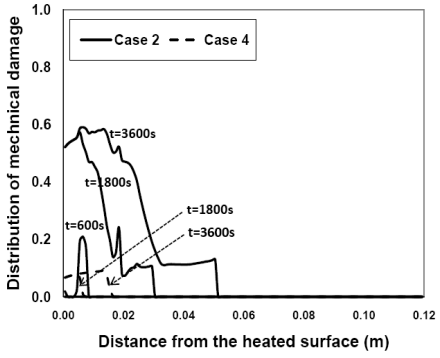

Fig. 3 Development of mechanical damage for the concretes of different tensile strength

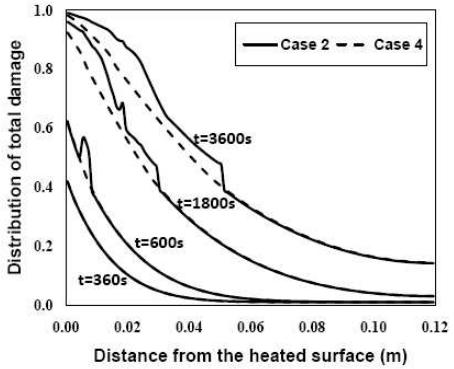

Fig. 4 Development of total damage for the concretes of different tensile strength

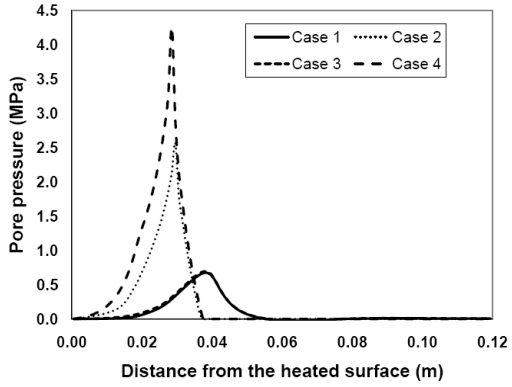

Fig. 5 Pore pressure build-up in concretes of different humidity (t = 1800s)

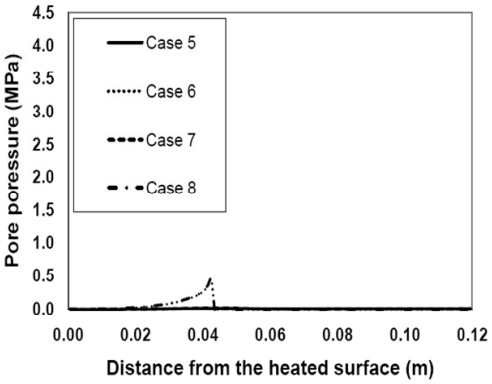

Fig. 6. Pore pressure build-up in concretes of different permeability (t=1800s)

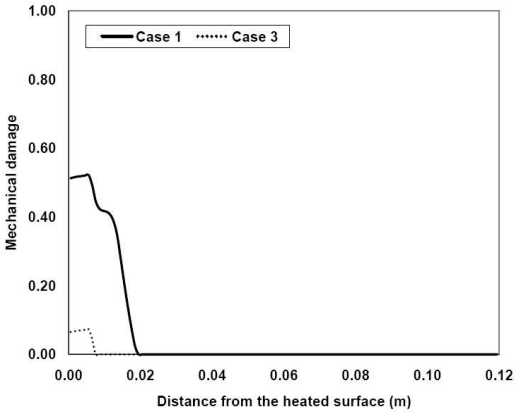

Fig. 7 Mechanical damage mainly caused by thermally induced stresses for the concretes of low humidity (t = 1800s)

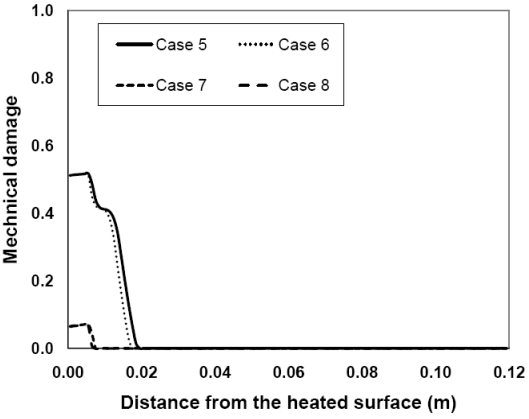

Fig. 8 Mechanical damage mainly caused by thermally induced stresses for the concretes of high permeability (t = 1800s)

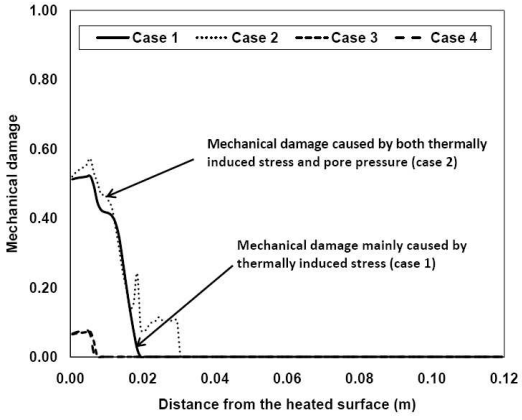

Fig. 9 Significance of pore pressure for mechanical damage

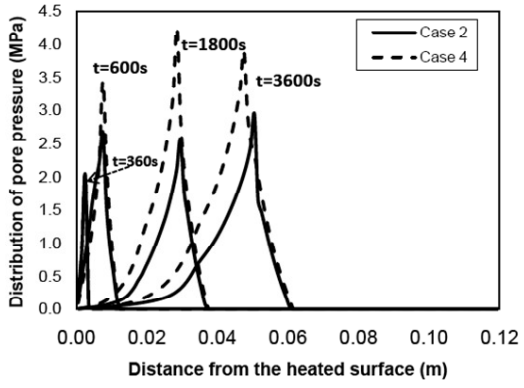

Fig. 10 Pore pressure in the concretes of high humidity and low permeability

5 CONCLUSIONS

In this article, the relative importance of pore pressure and thermally induced stress on the development of damage in various concretes was investigated by finite element analysis of their fully-coupled hygro-thermal-mechanical behaviour. Examination of the results suggested that although thermal damage (related to thermo-chemical degradation of the concrete on exposure to elevated temperatures) was the dominant form of damage, the evolution of mechanical damage (related to the development of micro-fractures due to stress) was more consistent with observed spalling behaviour in concrete structures. Among the causes of mechanical damage (and hence spalling), thermally induced stress was identified as the primary factor and, where high enough to contribute, pore pressure played a secondary role. While it may initiate damage pore pressure cannot contribute to its continued development and furthermore, the contribution of pore pressure to mechanical damage was found to be negligible in concretes of low humidity and/or high permeability.

Although in all the cases the mechanical damage was seen to develop in a pattern consistent with thermal spalling behaviour observed in concrete structures, in the current model, the location where spalling occurs cannot be accurately determined in terms of the mechanical damage parameter. This may be due, in part, to the boundary constraints of the problem employed here and more work is required to investigate the role of different constraint conditions. However, it is also considered here that discrete fracturing behaviour may be required in order to capture accurately thermal spalling and it is the further aim of this continuing work to develop the model to include this behaviour.

6 ACKNOWLEDGEMENTS

This work was carried out as part of a research project (EP/E048935/1 - An Advanced Numerical Tool for the Prediction and Analysis of Spalling in Concrete Structures Exposed to Combined Thermal and Mechanical Loading) funded by the Engineering and Physical Sciences Research Council, UK.

7 REFERENCES

[1] Gawin, D., Majorana, C. E. and Schrefler, B. A. Numerical analysis of hygro-thermal behaviour and damage of concrete at high temperature. Mechanics of Cohesive-Frictional Materials, 4, pp. 37-74, 1999

[2] Gawin, D., Pesavento, F. and Schrefler, B.A., Modelling of hygro-thermal behaviour of concrete at high temperature with thermo-chemical and mechanical material degradation, *Computer Methods in Applied Mechanics and Engineering*, **192**, pp. 1731-1771, 2003

[3] Khoury, G. A., Strain components of nuclear-reactor-type concretes during first heat cycle, *Nuclear Engineering and Design*, **156, p**p. 313–321, 1995

[4] Khoury, G. A., Performance of heated concrete: mechanical properties, Report Submitted to the Nuclear Installations Inspectorate of the Health and Safety Executive, 1996.

[5] Khoury, G. A., Majorana, C. E., Pesavento, F. and Schrefler, B. A. Modelling of heated concrete. Magazine of Concrete Research, 54 (2), pp. 77-101, 2002

[6] Tenchev, R. and Purnell, P. An application of a damage constitutive model to concrete at high temperature and prediction of spalling. International Journal of Solids and Structures, 42 (26), pp. 6550–6565, 2005

[7] Fu, Y. F., Wong, Y. L., Poon, C. S. and Tang, C. A. Numerical tests of thermal cracking induced by temperature gradient in cement-based composites under thermal loads. Cement & Concrete Composites 29, pp. 103–116, 2007
[8] Gawin, D., Pesavento, F. and Schrefler. B. A. Towards prediction of the thermal spalling risk through a multi-phase porous media model of concrete, *Computer Methods in Applied Mechanics and Engineering*, 195, pp. 5707–5729, 2006
[9] Hertz, K. D. Limits of spalling of fire-exposed concrete, Fire Safety Journal, 38, pp. 103-116, 2003
[10] Phan, L. T., Lawson, J. R. and Davis, F.L., Effects of elevated temperature exposure on heating characteristics, spalling and residual properties of high performance concrete, Materials and Structures, 34, pp. 83 – 91, 2001
[11] England, G. L. and Khoylou, N. Moisture flow in concrete under steady state non-uniform temperature states: experimental observations and theoretical modelling, Nuclear Engineering Design, 156, pp. 83–107, 1995
[12] Ichikawa, Y. and England, G. L., Prediction of moisture migration and pore pressure build-up in concrete at high temperatures, Nuclear Engineering and Design, 228(1-3), pp. 245-259, 2004
[13] Ulm, F.-J., Coussy, O. and Bažant, Z.P., The "chunnel" fire. I: chemoplastic softening in rapidly heated concrete, Journal of Engineering Mechanics, 125(3), pp. 272–282, 1999
[14] Msaad, Y. and Bonnet, G., Analyses of heated concrete spalling due to restrained thermal dilation: application to the "channel" fire, Journal of Engineering Mechanics, 132(10), pp. 1024–1132, 2006
[15] Kalifa, P., Menneteau, F. D. and Quenard, D., Spalling and pore pressure in HPC at high temperatures, Cement and Concrete Research, 30, pp. 1915–1927, 2000
[16] Anderberg, Y., Spalling phenomena of HPC and OC, in International Workshop on Fire Performance of High-Strength Concrete Proceeding, NIST Special Publication 919, NIST: Gaithersburg, MD, 1997
[17] Consolazio, G. R., McVay, M. C. and Rish, J. W., Measurement and prediction of pore pressures in cement mortar subjected to elevated temperature, in International Workshop on Fire Performance of High-Strength Concrete Proceeding, NIST Special Publication 919, NIST: Gaithersburg, MD, 1997
[18] Pearce, C. J, Davie, C. T, Nielsen, C. V. and Bićanić, N., A transient thermal creep model for the hygral-thermal-mechanical analysis of concrete. In: Proceedings of VII International Conference on Computational Plasticity (COMPLAS VII), CIMNE, Barcelona, 2003
[19] Stabler, J., Computational modelling of thermo-mechanical damage and plasticity in concrete, PhD Thesis, The University of Queensland, Australia, 2000
[20] Peerlings, R. H. J., de Borst, R., Brekelmans, W. A. M. and Geers, M. G. D., Gradient-enhanced damage modelling of concrete fracture, *Mechanics of Cohesive-Frictional Materials*, **3**(4), pp. 323-342, 1998
[21] Thelandersson, S., Modeling of combined thermal and mechanical action in concrete, *Journal of Engineering Mechanics-ASCE*, **113**(6), pp. 893-906, 1987
[22] de Borst, R. and Peeters, P., Analysis of concrete structures under thermal loading, *Computer Methods in Applied Mechanics and Engineering*, **77**(3), pp. 293-310, 1989
[23] Davie, C.T., Pearce, C. and Bicanic, N., A strongly coupled, fully generalised, multi-phase, hygro-thermal-mechanical model for concrete, *Due for submission*, 2008
[24] Davie, C. T., Pearce, C. J. and Bićanić, N. Coupled heat and moisture transport in concrete at elevated temperatures - effects of capillary pressure and absorbed water. *Numerical Heat Transfer, Part A*, 49: 733-763, 2006.

EFFECT OF FIRE SCENARIO, RESTRAINT CONDITIONS, AND SPALLING ON THE BEHAVIOR OF RC BEAMS

DWAIKAT M.B.[1] and KODUR, V.K.R.[2]

ABSTRACT

A macroscopic finite element model is applied to investigate the effect of four parameters; namely, fire scenario, axial restraint effect, spalling and failures criteria on the fire response of reinforced concrete (RC) beams. Results from the analysis indicate that the fire scenario has significant influence on fire resistance of RC beams. The fire resistance of RC beams generally increases with the degree of axial restraint. Fire induced spalling in concrete, which is influenced by material characteristics and fire scenario, reduces the fire resistance of RC beams. Further, the limiting criteria used to define failure can have significant influence on the resulting fire resistance. These factors, which are not taken into account in conventional prescriptive based approaches, should be given due consideration for realistic assessment of fire resistance of RC beams.

1. INTRODUCTION

Reinforced concrete (RC) structural systems are quite frequently used in high rise buildings and other built infrastructure due to a number of advantages they provide over other materials. When used in buildings, the provision of appropriate fire safety measures for structural members is an important aspect of design since fire represents one of the most severe environmental conditions to which structures may be subjected in their life time. The basis for this requirement can be attributed to the fact that, when other measures for containing the fire fail, structural integrity is the last line of defense.

[1] PhD Candidate, CEE Dept., Michigan State University
dwaikatm@msu.edu
[2] Professor, CEE Dept., Michigan State University
kodur@egr.msu.edu

The current practice of evaluating fire resistance of RC beams is based on standard fire tests, in which the beam is exposed to a standard fire as specified in standards such as ASTM E119[1] and ISO 834[2]. While fire resistance tests are useful benchmarks to establish the relative performance under standard fire condition, they should not be relied upon to determine the survival time of RC beams under realistic fire, loading and restraint scenarios. Nor does the standard heating condition bear any relation to the often less severe heating environments encountered in real fires.

Figure 1 illustrates various time temperature curves for standard and some realistic fire scenarios. In the standard fires (ASTM E119[1] fire and ASTM E1529 hydrocarbon fire[3]), the fire size is the same (irrespective of compartment characteristics), temperature increases with time throughout the fire duration, and there is no decay phase. However, in real fires, the fire size is a function of compartment characteristics, such as ventilation, fuel load and lining materials, and there is a decay phase as clearly shown in Fig. 1 (design fires, Fire I and Fire II). Under real fire scenarios, the cross section of the beam enters the cooling phase during decay phase and the reinforcing steel recovers parts of its strength and stiffness leading to higher fire resistance.

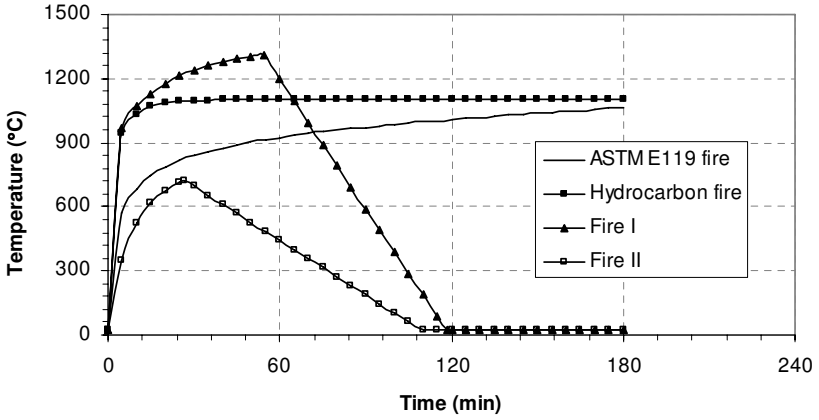

Fig. 1 – Various fire scenarios for fire resistance analysis

RC beams can develop significant restraint forces under fire exposure. The degree of restraint, which is dependent on the support conditions, determines the behavior and fire resistance of RC beams. In addition, the vertical location of the restraint force determines the extent of the effect of the axial restraint on fire resistance. Generally, the axial restraint force is expected to improve the fire resistance of the RC beam through the arch action, which increases the strength and the stiffness of the beam under fire exposure[4]. However, axial restraint forces may lead to increased spalling in concrete or buckling (particularly for slender beams) which in turn might reduce the fire resistance of RC beams. At present, design codes, such as ACI 216.1[5], do not fully account for the fire induced restraint effects in RC beams.

Spalling is one of the major phenomena that occur under fire conditions and has to be considered in evaluating the response of RC members. Although fire induced spalling may not be significant in normal strength concrete (NSC) members, it can be predominant factor in the case of high strength concrete (HSC) members due to low permeability and the presence of silica fume. The reduced permeability increases the fire induced pore pressure leading to spalling

(often explosive in nature). Spalling has the effect of reducing the cross sectional area of the structural member, and increasing the heat penetration to the steel reinforcement. Thus, fire induced spalling might result in significant reduction in the strength and stiffness of RC structural members, which in turn might lead to early failure[6].

To obtain rational assessment of fire resistance, realistic fire, restraint, spalling and failure criteria are to be implemented in the analysis. This paper presents the effect of these four parameters on the flexural behavior of RC beams exposed to fire.

2. NUMERICAL MODEL

2.1 General

The fire resistance analysis is carried out using a macroscopic finite element model developed by Dwaikat and Kodur[4]. In this model, the RC beam is divided into a number of segments along its length and the mid-section of the segment is assumed to represent the behavior of the whole segment. The cross section, representing each segment, is subdivided into elements forming a two dimensional mesh. The fire resistance analysis is carried out by incrementing time in steps. At each time interval, the analysis is performed through four main steps:

- Establishing fire temperature due to fire exposure,
- Carrying out heat transfer analysis to determine temperature distribution across each segment,
- Carrying out mass transfer analysis to determine the extent of spalling in each segment, and
- Performing strength and deflection analysis, which is carried out, through three substeps:
  - Calculating the axial restraint force in the RC beam,
  - Generation of M-κ relationships (utilizing the axial restraint force computed above) for each beam segment, and
  - Performing structural analysis of the beam to compute deflections and internal forces.

The numerical model uses segmental moment curvature relationships to trace the response of an RC beam in the entire range of loading up to collapse under fire. The axial restraint force is computed through an iterative procedure that satisfies compatibility, equilibrium and convergence criteria along the span of the beam. The effect of fire induced axial restraint force is accounted for in the generation of the moment curvature relationships. In the model, the boundaries restraining the beam are idealized as a spring of stiffness (k) as shown in Fig. 2. The value of k can be changed to account for varying degrees of restraint. The second order effects are considered in the model by incorporating the developed secondary moments and forces to the applied loading.

The model is capable of undertaking fire resistance analysis for beams exposed to any given fire time temperature curve. Various strain components including mechanical strain, thermal strain, and creep strain for both concrete and reinforcing steel and the transient strain in concrete are accounted for in the model based on the models proposed by Harmathy[7,8], and Anderberg and Thelandersson[9], respectively. The high temperature creep and transient strains, which are not often accounted for, might play a significant role in predicting the fire behavior of RC beams, particularly deflection and rate of deflection.

The computer model generates various critical output parameters, such as temperatures, stresses, strains, deflections, fire induced axial restraint force and moment capacities at various fire exposure times. The output parameters can be used to check against predetermined four sets of failure criteria, which include prescriptive thermal limit state, strength and deflection considerations. Full details of the numerical procedure, including the derivation of appropriate equations, are presented in Dwaikat and Kodur[4].

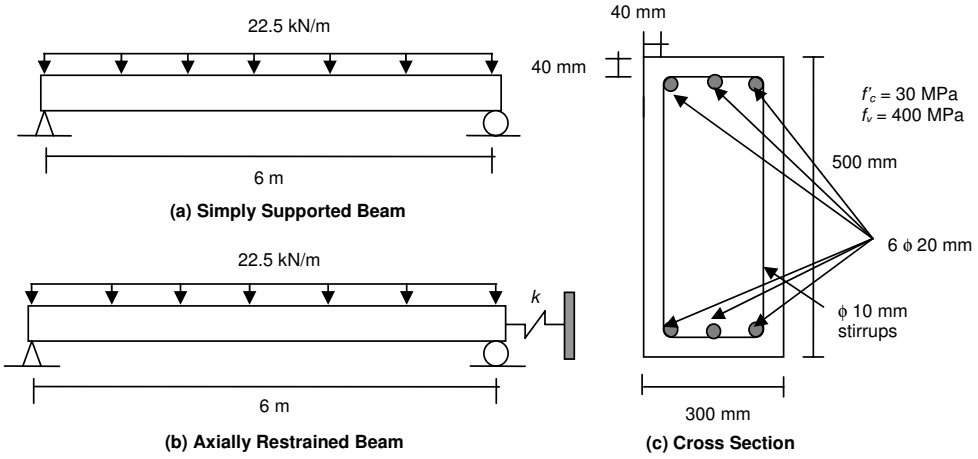

Fig. 2 – Cross section and elevation of RC beam used in parametric studies

2.1 Spalling Model

Spalling is accounted for through a simplified hydrothermal model that involves the calculation of pore pressure in concrete when it is subjected to fire. The hydrothermal model uses the principles of mechanics and thermodynamics including the conservation of mass of liquid water and water vapor to predict the pore pressure in the concrete exposed to fire. In the hydrothermal model, the mass transfer equation for water vapor inside heated concrete can be written as:

$$A\frac{dP_V}{dt} = \nabla B \nabla P_V + C \qquad (1)$$

where: P_V = pore pressure, t = time, A, B and C = parameters that depend on pore pressure, temperature, rate of increase in temperature, permeability of concrete, initial moisture content, and the isotherm used in the analysis. Isotherms are used to predict the liquid water inside concrete as a function of pore pressure for a constant temperature.

Finite element analysis is used to solve Eq. (1) and compute the pore pressure distribution within the midsection of each segment along the length of the structural member. The resulting pore pressure is compared with the temperature dependent tensile strength of concrete. Spalling is said to occur when the pore pressure exceeds the tensile strength of concrete; i.e., when the following expression is satisfied:

$$nP_V > f_{tT} \qquad (2)$$

where: n = porosity of concrete = $V_V + V_L$, f_{tT} = tensile strength of concrete for temperature, T. Once spalling of concrete occurs, the reduced concrete section and the new boundary surface are considered in the thermal and strength analyses in subsequent time steps. In this way, the spalling and thermal calculations are coupled in the analysis.

3. CASE STUDIES

3.1 Analysis Procedure

Two sets of RC beams were analyzed to investigate the influence of fire scenario, axial restraint effects, spalling and failure criteria on the fire resistance of RC beams. The two beams in each set are made of NSC and HSC, respectively. The beams in the first set are simply supported (SS), while the beams in the second set are axially restrained (AR). The axial restraint stiffness (k) is assumed to be 50 kN/mm for the axially restrained beams. This value of the axial restraint stiffness is selected in such a way that it represents a reasonable value encountered in practice[4]. Each beam is analyzed under four fire scenarios including standard and design fire exposures. The analysis was carried out using the macroscopic finite element model in 5 minute time increments till failure occurred in the beam. Results from the analysis are summarized in Table 1.

3.2 Beam Details

All the analyzed beams are of rectangular cross section (300 mm × 500 mm) and have a span length of 6 m as shown in Figure 2. The compressive strength and permeability for the NSC and the HSC are assumed to be 30 MPa, 100 MPa, 1×10^{-16} m^2 and 5×10^{-19} m^2, respectively. The beams were reinforced with steel rebars having yield strength of 400 MPa. The room temperature capacity of the analyzed beams was calculated based on ACI 318 provisions[10]. The applied loading on the beam shown in Figure 2, is calculated for a dead load to live load ratio of 2, based on ASCE 07[11] (1.2 dead load + 1.6 live load for room temperature calculation, and 1.2 dead load + 0.5 live load under fire conditions). For load calculations, the ultimate load at room temperature is equated to the room temperature capacity of each beam. For HSC beams, the spalling depth (thickness of concrete layers that spall off from the concrete section) is assumed not to exceed the clear concrete cover thickness for the analyzed beams.

3.3 Material Properties

The temperature dependent properties that are important for establishing the fire response of RC structures include: thermal, mechanical and material specific properties such as permeability of concrete. For the analysis presented here, the thermal and mechanical properties of concrete and reinforcing steel specified in the ASCE Manual[12] are used. In the cooling phase, the thermal properties of the constituent material are assumed to be similar to that in the heating phase. For mechanical properties, as a conservative estimate, concrete is assumed not to recover any strength in the cooling phase. Thus, the stresses in concrete are determined based on the maximum temperature attained in the concrete. However, the same mechanical properties are assumed for reinforcing steel in both the heating and the cooling phase. For spalling calculations,

the variation of the permeability of concrete is assumed to follow the expression developed by Gawin et al.[13]. Also, the temperature dependent tensile strength of concrete is assumed as per Eurocode 2[14] but with some modifications to avoid the conditions where the tensile strength becomes zero at relatively low temperatures (600 °C). Accordingly, the adopted model follows the temperature dependent tensile strength of concrete specified in Eurocode 2 for temperatures up to 550 °C. Then, the tensile strength of concrete is assumed to decrease gradually until it vanishes at 1200 °C. It should be noted that tensile strength of concrete at 550 °C is only 10% of the room temperature tensile strength.

3.4 Fire Exposure

To investigate the effect of fire scenario on fire resistance, all the beams were analyzed under two standard fire scenarios, namely the ASTM E119[1] standard fire, and the ASTM E1529[2] hydrocarbon standard fire, as well as two design fire scenarios; namely Fire I and Fire II, taken from Eurocode 1[15]. There is no decay phase in the time temperature curves of standard fires. However, in realistic fires, there always exist a decay phase, since the amount of fuel or ventilation runs out leading to burn out in the compartment.

The parametric fire time temperature curve proposed in Eurocode 1[15] together with the recent modifications suggested by Feasey and Buchanan[16], are selected to represent the design fire scenarios used in the analysis. According to Eurocode 1, the design fire consists of a growth phase and a decay phase. Feasey and Buchanan[14] showed that both the growth and decay phases of the fire are influenced by compartment properties such as the fuel load, ventilation opening and wall linings. The time temperature curves for the two standard fire scenarios and the two design fire scenarios are shown in Figure 1.

Table 1 – Summary of the fire resistance values for the analyzed beams

Case	Beam designation	Concrete Type	Type of fire exposure	Fire resistance (minutes)			
				Rebar temperature	Strength	Deflection	Rate of deflection
SS beam	BN11	NSC	ASTM E119	180	145	127	124
	BN12		Hydrocarbon	148	120	101	95
	BN13		Design Fire I	****	****	95	90
	BN14		Design Fire II	****	****	****	****
	BH11	HSC	ASTM E119	72	55	53	46
	BH12		Hydrocarbon	47	35	****	29
	BH13		Design Fire I	36	25	****	21
	BH14		Design Fire II	****	****	****	****
AR beam	BN21	NSC	ASTM E119	180	175	****	****
	BN22		Hydrocarbon	148	150	****	145
	BN23		Design Fire I	****	****	****	****
	BN24		Design Fire II	****	****	****	****
	BH21	HSC	ASTM E119	72	75	****	****
	BH22		Hydrocarbon	47	50	****	49
	BH23		Design Fire I	36	44	****	****
	BH24		Design Fire II	****	****	****	****

4. RESULTS AND DISCUSSION

4.1 Effect of Fire Scenario

The variations of mid-span deflection with fire exposure time for all the beams analyzed under the four fire scenarios are shown in Figs. 3-6. It can be seen from the figures that the deflection increases with time for all the beams at early stages of the fire exposure. However, the figures show reduction (recovery) in the deflection for most of the beams exposed to the design fires at later stages of the fire exposure time. This is because of the decay phase in the design fires in which the beam starts cooling and recovers part of its strength and stiffness. Figures 5 and 6 show no deflection recovery for beams BH13 and BH 23, which are made of HSC and exposed to the sever design fire, Fire I. This is because of the occurrence of severe spalling in these two HSC beams before they enter the cooling phase, which leads to early failure in the two beams as can be seen from Figs 5 and 6.

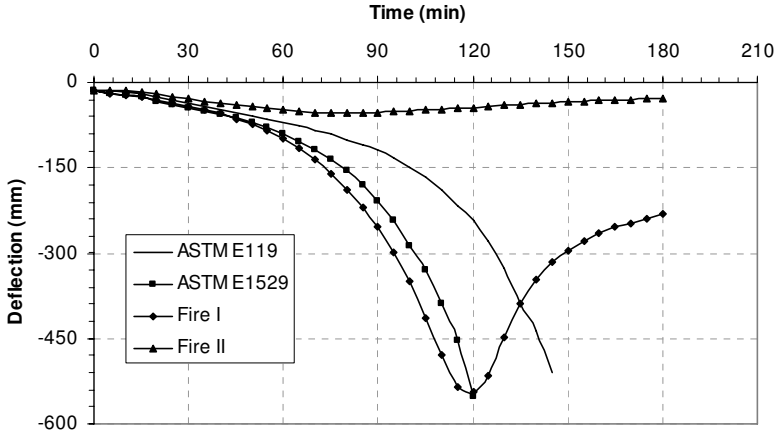

Fig. 3 – Variation of deflection with fire exposure time for simply supported NSC beam

Results from the analysis show that the type of fire exposure has significant effect on the fire resistance of RC beams (Table 1). This variation is dependent on the limiting criteria used to define failure and this is further discussed in following sections. Table 1 shows that, except for beams BH13 and BH23, the lowest fire resistance is obtained for the beams exposed to the hydrocarbon fire, and it is about 25 minutes lower than that for the beam under the ASTM E119 standard fire exposure. This is due to the rapid increase in fire temperature for the hydrocarbon fire as can be seen in Fig. 1. However, lower fire resistance values were obtained for beams BH13 and BH23, which are exposed to Fire I, than those obtained for beams exposed to other fire scenarios. This can be attributed to the rapid increase in temperature for Fire I which causes excessive spalling in the concrete beams and leads to early failure before the fire enters the cooling phase. Table 1 also shows that only three out of the eight beams exposed to design fire exposure attain failure. It can also be noted that the three beams failing under design fire exposure were assumed to be exposed to Fire I (severe design fire). However, none of the beams exposed to Fire II attained failure based on any failure criteria. Hence, in spite of the severe

conditions assumed for design fire (Fire I), failure is attained only in few beams particularly those made of HSC. This result shows that in many applications, the fire resistance values computed based on standard fire scenarios, may be conservative if the resulting fires have a decay phase, similar to the ones used in this study.

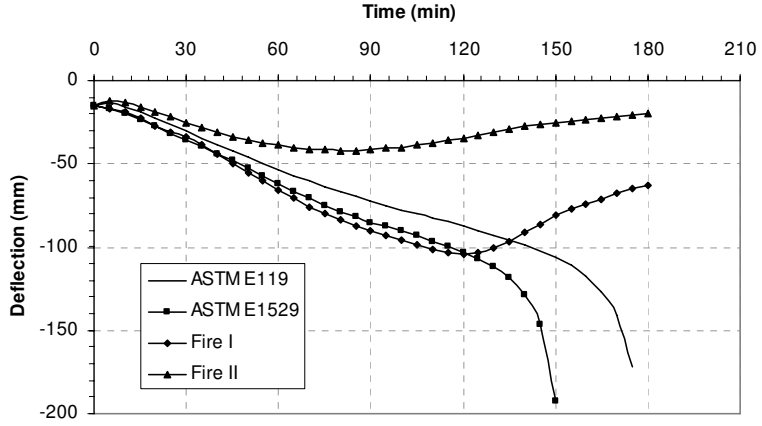

Fig. 4 – Variation of deflection with fire exposure time for axially restraint NSC beam

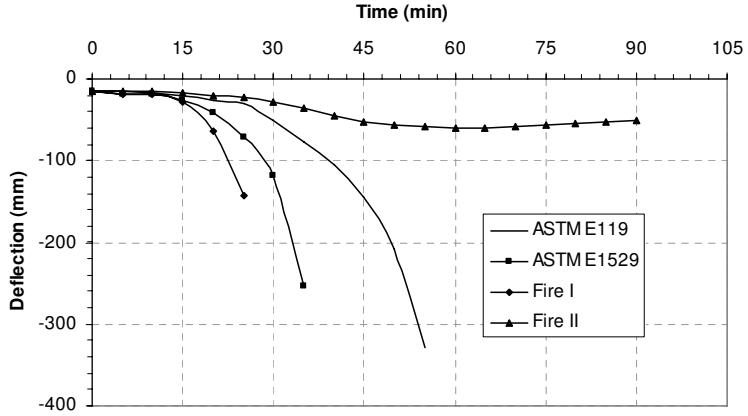

Fig. 5 – Variation of deflection with fire exposure time for simply supported HSC beam

4.2 Effect of Axial Restraint

Figures 3-6 show that axial restraint reduces the deflection of the beam at any fire exposure time. This is because increasing the axial restraint leads to the higher axial restraint forces. These restraint forces create an arch action leading to the development of a counter acting moment that reduces the effect of the applied loading[4].

The fire resistance values computed based on strength, deflection and rate of deflection are given in Table 1. It can be seen, from Table 1, that the axial restraint has significant effect on

the fire resistance of RC beams. For all the analyzed RC beams, the fire resistance computed based on strength and deflection failure is higher for axially restrained beams than that for simply supported beams as shown in Table 1. As an illustration, the fire resistance of beam BN21, which is axially restrained, is 30 minutes higher than that of beams BN11 which is simply supported. This could be attributed to the arch action that is developed due to the axial restraint effect which improves the fire response of the RC beam.

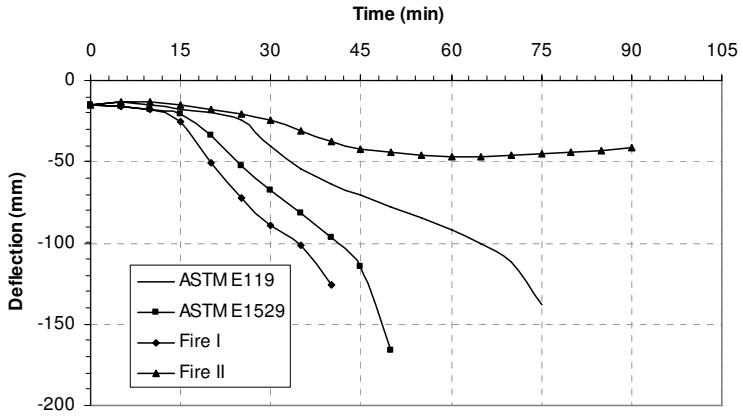

Fig. 6 – Variation of deflection with fire exposure time for axially restraint HSC beam

4.3 Effect of Concrete Spalling

Results from the analysis show that no spalling occurs in NSC beams, whereas excessive spalling was observed for HSC beams. This is mainly attributed of the low permeability of HSC beams. The reduced permeability prevents the water vapor from escaping and this leads to build-up of vapor pressure in concrete and thus leads to concrete spalling. However, for NSC, the high value of permeability allows the water vapor to escape from the concrete and thus there is no significant vapor pressure build up. Therefore, the developed vapor pressure in NSC is too low to cause concrete spalling. The excessive spalling in HSC beams has significant effect on the deflection of the RC beams as can be seen by comparing Figs 5 and 6 with Figs. 3 and 4. It can be seen that the deflection of HSC beams is much larger than that of NSC beams at any fire exposure time. This is primarily due to excessive spalling observed in HSC beams, which in turn reduces the stiffness of the beam.

Spalling has detrimental effect on the fire resistance of RC beams as can be seen from Table 1. As an illustration, the fire resistance of beam BN11 (made of NSC) is 145 minutes, whereas the fire resistance of beam BH11 (made of HSC) is only 55 minutes. The large reduction in the fire resistance for HSC beams is due to the occurrence of severe spalling in HSC beams. Spalling reduces the concrete cover thickness and thus accelerates the heat penetration to the steel reinforcement. Spalling also reduces the cross sectional area of the concrete beam. Thus, spalling significantly reduces the beam strength and stiffness which in turn leads to early failure and lower fire resistance values as can be seen in Table 1.

4.4 Effect of Failure Criteria

The fire resistance for all analyzed beams was computed according to the four sets of failure criteria, namely; rebar temperature, strength, deflection and rate of deflection. The computed fire resistance values are tabulated in Table 1. Based on thermal failure criteria, no failure is attained for the beams exposed to design fire, Fire II. No failure is also attained in the NSC beams exposed to both design fires (Fire I and Fire II) when the rebar temperature criteria is applied to determine failure. This is because of the presence of decay phase, in these two design fires, during which the beams start cooling. The early failure of the HSC beam exposed to Fire I (based on rebar temperature failure criteria) can be attributed to the occurrence of excessive spalling in that beam under fire conditions as discussed above. Results from the analysis show that the fire resistance, based on thermal failure criterion, is not affected by the axial restraint of the beam. This is because thermal failure criterion (limiting rebar temperature) is derived based on the results of thermal analysis only and thus it is independent of the mechanical properties (support conditions, load, strength and stiffness) of the beam.

Deflection and rate of deflection failure criteria generally predict smaller fire resistance values than those predicted by strength failure criterion as can be seen from Table 1. Although, actual failure of an RC beam occurs when the strength limit state is reached, deflection and rate of deflection may be important in many applications to maintain the integrity of the structure so as to facilitate the work of fire fighters, and to safely evacuate the occupants before the collapse of the structure[17]. Therefore, under some fire scenarios, deflection or rate of deflection failure criterion may determine the failure of RC beams and govern their fire resistance. It should be noted that ASTM E119 does not specify deflection or rate of deflection failure criterion.

The above results clearly illustrate that the thermal failure criterion, which is often used, is insufficient to define the failure of RC beams since it does not account for the degradation of the mechanical properties of the beam. It should be noted that the current fire resistance provisions in ASTM E119 are mainly based on thermal failure criterion and thus may not provide realistic assessment of fire resistance.

CONCLUSIONS

Based on the results of this study, the following conclusions can be drawn:

- The type of fire exposure has significant influence on the fire resistance of RC beams. The conventional method of evaluating fire resistance, based on "standard" fire exposure, may be conservative under even severe design fire scenarios.
- The axial restraint has a significant effect on the fire resistance of RC beams. Generally, the fire resistance of axially restrained beams is higher than that of simply supported beams.
- Spalling of concrete, which is directly related to concrete permeability, has detrimental effect on the fire resistance of RC beams. The fire resistance in HSC beams, with low permeability, can be reduced by more than 50% due concrete spalling.
- The limiting failure criterion, used for determining failure, has significant influence on the fire resistance of RC beams. The conventional failure criterion, such as limiting rebar temperature may not be conservative under some fire scenarios. The strength, the deflection and the rate of deflection failure criteria should be considered for realistic assessment of the fire resistance of RC beams.

ACKNOWLEDGMENT

The research, presented in this paper, is primarily supported by the Michigan State University Foundation, through Strategic Partnership Grant (Award No. SPG 71-4434).

Reference

1. ASTM Test Method E119-01, "Standard Methods of Fire Test of Building Construction and Materials", American Society for Testing and Materials, West Conshohocken, PA, 2001.
2. ISO 834-1975, "Fire resistance tests – elements of building construction", International Organization for Standardization, 1975.
3. ASTM Test Method E1529, "Standard Test Methods for Determining Effects of Large Hydrocarbon Pool Fires on Structural Members and Assemblies", American Society for Testing and Materials, West Conshohocken, PA, 1993.
4. Dwaikat M.B., and Kodur V.K.R., "A Numerical Approach for Modeling the Fire Induced Restraint Effects in Reinforced Concrete Beams", *Fire Safety Journal*, In Press, 2008.
5. ACI Committee 216.1-07, "Standard Method for Determining Fire Resistance of Concrete and Masonry Construction Assemblies", American Concrete Institute, Detroit, 2007.
6. Kodur V.K.R., and Phan L., Critical Factors Governing the Fire Performance of High Strength Concrete Systems. Fire Safety Journal, Vol. 42, 2007, pp. 482-488.
7. Harmathy T.Z., "A comprehensive Creep Model", *Journal of Basic Engineering*, 1967, Vol 89, No 2, pp. 496-502.
8. Harmathy T.Z., "Fire Safety Design and Concrete", *Concrete Design and Construction Series*, Longman Scientific and Technical, UK, 1993.
9. Anderberg Y., and Thelandersson S., "Stress and Deformation Characteristics of Concrete at High Temperatures, 2. Experimental Investigation and Material Behaviour Model", Lund Institute of Technology, Sweden, 1976.
10. ACI 318R-2002, "Building Code Requirements for Reinforced Concrete", *ACI 318-02 and Commentary*, American Concrete Institute, Detroit, MI, 2002.
11. ASCE 7-05, "Minimum Design Loads for Buildings and Other Structures", American Society of Civil Engineers, Reston, VA, 2005.
12. Lie, T.T. (Editor), "Structural Fire Protection", *ASCE Manuals and Reports of Engineering Practice, No 78*, American Society of Civil Engineers, New York, 1992.
13. Gawin D., Majorana C.E., and Schrefler B.A., "Numerical Analysis of Hygro-thermic Behaviour and Damage of Concrete at High Temperature", *Magazine of Cohesive Frictional Material*, 4, 1999, pp. 37-74.
14. Eurocode 2, "prEN1992-1-2: Design of Concrete Structures. Part 1-2: General Rules - Structural Fire Design", Comité Europeén de Normalisation (CEN), Brussels, 2004.
15. Eurocode 1, "ENV 1991-2-2: Basis of Design and Design Actions on Structures", Part 2-2: Actions on Structures Exposed to Fire, European Committee for Standardization, 1994.
16. Feasey R., and Buchanan A.H., "Post Flash-over Fires for Structural Design", *Fire Safety Journal*, Vol 37, No 1, 2002, pp. 83-105.
17. Kodur V.R, and Dwaikat M.B., "Performance-Based Fire Safety Design of Reinforced Concrete Beams", *Journal of Fire Protection Engineering*, Vol 17, 2007, pp. 293-320.

EFFECTS OF EDGE SUPPORT AND REINFORCEMENT RATIOS ON SLAB PANEL FAILURE IN FIRE

ANTHONY K. ABU[1], IAN W. BURGESS[2] AND ROGER J. PLANK[3]

ABSTRACT

The advancement in structural fire engineering towards more cost-effective solutions has necessitated the increasing use of performance-based approaches to the design of multi-storey composite buildings. These methods consider the real behaviour of structures and provide economic solutions which optimise fire protection usage. Optimising structures to use tensile membrane action requires the structural use of slab panels. These are vertically supported lightly-reinforced composite floor systems, allowing biaxial bending at elevated temperatures. Vertical support is achieved, in practice, by protecting a panel's perimeter beams to achieve temperatures of no more than 620°C at the required fire resistance time.

The Bailey-BRE design method, which incorporates tensile membrane action, uses these vertically supported panels to establish composite slab capacities in fire. The slab panel resistance is determined by a combination of the residual composite beam strength and the large-deflection enhanced slab resistance. The simple calculations of the Bailey-BRE method imply improved performance with higher reinforcement ratios. However, proportional increases have not been observed in the modelling work reported here. The discrepancy may be due to the geometry, composition or support conditions of the slab panels. Also, with exposure to fire, a panel's 'vertical' support can be lost. This will in turn affect the tensile membrane capacity, pre-empting a structural failure of the floor system.

This paper presents the results of a finite element investigation into the effects of reinforcements and vertical support on slab panel failure. The study examines the effect of various degrees of protection on the development of the tensile membrane action mechanism. It examines the development and failure of this mechanism, considering various degrees of edge-beam protection, and makes comparisons with the predictions of the Bailey-BRE method and various design acceptance criteria.

[1] Research Student, Dept. of Civil & Structural Engineering, University of Sheffield, Sheffield S1 3JD, UK
Email: cip04aka@sheffield.ac.uk
[2] Professor, Dept. of Civil & Structural Engineering, University of Sheffield, Sheffield S1 3JD, UK
Email: ian.burgess@sheffield.ac.uk
[3] Professor, School of Architectural Studies, University of Sheffield, Sheffield S10 2TN, UK
Email: r.j.plank@sheffield.ac.uk

1. INTRODUCTION

The traditional approach to structural fire engineering has been to apply prescriptive fire protection to all exposed steelwork, after completing ambient-temperature design, to achieve a fire resistance rating specified on the basis of the height and use of the building[1]. This design methodology stems from the assumption that individual structural elements behave independently in fire, ignoring interactions that may be present between various parts of the structure. Research, and observations of structural behaviour under fire conditions, over the past 20 years, have shown that load redistribution and large deflections of parts of the structure at the Fire Limit State are essential to the survival of the entire structure. Accidental fires and tests on full-scale buildings have shown that designing composite floors for tensile membrane action yields considerable savings in protection costs, and structural stability is maintained by taking advantage of this real building behaviour in fire[2]. Tensile membrane action is a mechanism that produces increased load-bearing capacity in thin slabs undergoing large vertical displacements, in which radial tension in the central area of a slab induces an equilibrating peripheral ring of compression. The conditions necessary for the effective use of this mechanism are two-way bending of the slab and vertical support along all of its edges. Due to its self-equilibrating nature, horizontal edge restraint is not required for the mobilisation of tensile membrane action.

To optimise composite floors to take advantage of this higher load capacity in structural fire engineering design, a composite floor is divided into several fire-resisting rectangular zones of low aspect ratio, called slab panels; each comprising a set of adjacent unprotected composite beams in the interior of the panel, with edges that primarily resist vertical deflection[4]. This vertical support is usually provided by protected beams along all four edges, and the panels are generally set out to lie between column gridlines, as shown in Fig. 1. The composite slabs are reinforced with light meshes (typically between 142mm^2/m and 393mm^2/m), primarily to control cracking during construction. In fire the unprotected beams lose strength and stiffness rapidly, and their loads are borne by the composite slab, which undergoes two-way bending and increases its resistance as its deflections increase.

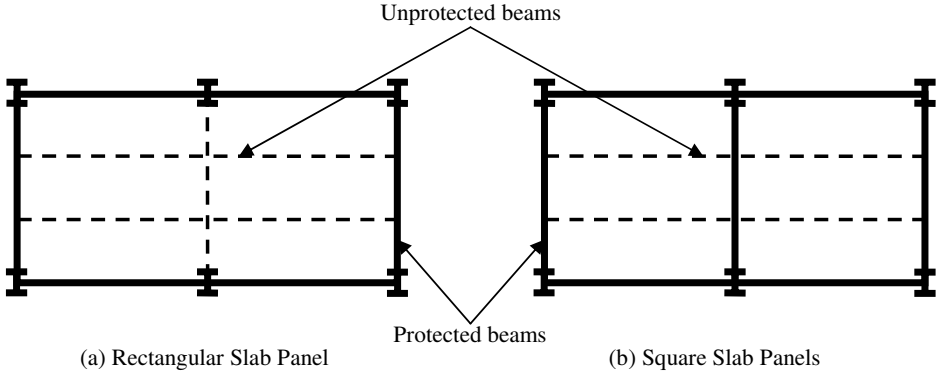

Fig. 1: Rectangular and Square Slab Panels

At large deflections and high temperatures, the slab panel capacity is dependent on the tensile capacity of the reinforcement, provided sufficient vertical support is available at the slab panel boundary. The merits of incorporating tensile membrane action into fire engineering design have prompted the development of several software packages to help quantify slab capacities in fire. Tensile membrane action, and whole-structure behaviour at high temperatures, can be modelled in a three-dimensional framework with sophisticated

finite element software, such as *Vulcan*[4,5], TNO DIANA and ABAQUS, that incorporates geometrically nonlinear effects of structures. Although finite element simulations provide useful information on complete load-deformation and stress development at elevated temperatures, they can be very costly processes. Simpler performance-based methods, such as the Bailey-BRE membrane action method (which can easily be set up as a spreadsheet), are often preferred for routine design. However, there is a suspicion that the simplifications applied in some of these approaches can lead to unrealistic or over-conservative designs.

In order to assess their efficiency as tools for preliminary investigations, there is an implicit need to determine the limits of these simplified methods. The reliance of the Bailey-BRE method on the determination of enhancements to the traditional yield-line capacity of the slab, and the assumption of continuous vertical support throughout the duration of a fire, are two of the issues that need to be addressed.

The study reported here has therefore examined the credibility of the Bailey-BRE method through the use of a finite element study, with the aim of establishing slab panel capacities with respect to the amount of reinforcement within the panel and the degree of vertical support available along the slab panel boundary.

2. THE BAILEY-BRE METHOD

Based on a conservative assumption that the light slab reinforcement over protected beams will fracture in hogging moment areas of continuous composite slabs, the Bailey-BRE method[3, 6] proceeds by dividing a composite floor into several horizontally unrestrained, vertically supported slab panels. Each of these panels is composed internally of simply supported unprotected composite beams. With increasing exposure to elevated temperatures, the formation of plastic hinges in the unprotected beams re-distributes their loads to the two-way bending slab, undergoing large vertical deflections. By employing rigid-plastic theory with large change of geometry, the additional slab resistance provided by tensile membrane action is calculated as an enhancement to the small-deflection yield-line mechanism capacity. Failure is determined by the formation of a full-depth tension crack across the shorter span of the slab or by compressive failure of concrete at the corners. The method conservatively ignores any contribution of the tensile strength of concrete to the capacity of the slab, and does not provide any information on the state of the protected boundary beams, apart from the assumption that they remain vertically supported throughout a fire.

The procedure, developed from ambient-temperature conditions, assumes that the tensile membrane action mechanism at ambient temperature is maintained at elevated temperatures[3]. Research has, however, shown[7] that the development of tensile membrane action at elevated temperatures differs from the ambient-temperature development.

2.1. SCI Level 1 Design Guide and TSLAB

To facilitate the use of the Bailey-BRE method in the United Kingdom, the Steel Construction Institute (SCI) prepared a design guide (P-288)[2], which lists tables of minimum reinforcement mesh sizes required to satisfy an allowable deflection limit criterion (v) at a defined fire resistance time. This limit is based on the mechanical strain allowed in the reinforcement at yield and thermal bowing in the slab, as observed from Equations 1 and 2.

$$v = \frac{\alpha(T_2 - T_1)l^2}{19.2h} + \sqrt{\frac{0.5 f_y}{E}_{t=20^o C} \times \frac{3L^2}{8}} \quad (1)$$

$$v \leq \frac{\alpha(T_2 - T_1)l^2}{19.2h} + \frac{l}{30} \quad (2)$$

In the above equations, α is the coefficient of thermal expansion; T_2 and T_1 are the bottom and top surface temperatures of the slab respectively; h is the average depth of the concrete slab; l and L are the shorter and longer spans of the slab panel and f_y and E are respectively the yield strength and Young's modulus of the reinforcing steel at room temperature.

The reinforcement sizes are based on the type of concrete, the slab panel geometry and the type of steel decking used. In addition to the design tables, the SCI has developed a Microsoft Excel-based spreadsheet called TSLAB. This tool determines whether the reinforcement selected for particular slab panel geometries will be satisfactory, and includes all the advances which have been incorporated into the method recently. However, Toh and Bailey[8] have found differences between TSLAB and the original Bailey-BRE derivation.

TSLAB performs thermal analyses on the unprotected intermediate beams and the composite slab, and then generates the total capacity of the simply-support slab panel model (by summation of the residual unprotected beam capacity and the enhanced slab capacity), using the allowable vertical deflection criterion (Equation 1) at each time step. This capacity is then checked against the applied load at the Fire Limit State. If the capacity of the panel is found to be below this applied load, then either the capacity of the internal beams or the reinforcement mesh size must be increased[2].

2.2. Influence of Reinforcement Ratios and Slab Panel Vertical Support

The Bailey-BRE method determines slab capacities by calculating the enhancements to the theoretical yield-line capacity provided by large deflections. This suggests that increasing reinforcement diameter increases the capacity of the slabs, since the yield-line capacities will be considerably increased. Therefore, with enhancement from large deflections, a considerable slab capacity is obtained by using modest increases in reinforcement area. Composite slabs are normally lightly reinforced to control cracking during construction, and therefore, may fail in compression if they are over-reinforced.

In practice, slab panel vertical support is achieved by protecting the beams around the perimeter of each panel. The assumption of continuous vertical restraint at all times during the fire is therefore unrealistic. At some point during the fire, the combination of imposed loads, together with loss of strength and stiffness of the perimeter beams, will induce vertical displacements, allowing the formation of a single-curvature slab-bending ("folding") mechanism. The slab panel will then hang from its connections, leading to a catenary-type failure of the structure. The potential for these two modes of failure has led to the series of finite element studies reported here, into the effects of reinforcement and slab panel vertical support on composite slab failure in fire.

2.3. Review of the Bailey-BRE Method

A limited number of previous studies [9-11] have compared the Bailey-BRE membrane action method with more fundamental approaches based on finite element analysis. These have highlighted a number of discrepancies between the two approaches.

An investigation by Huang *et al.* [11] into the effects of a panel's horizontal edge support conditions revealed that the Bailey-BRE method correlated very closely with a hinge-supported slab, although it was developed on the basis of simple supports. Another investigation into the effects of reinforcement ratios on slab panel capacity showed that only a marginal increase in slab panel resistance was observed in finite element models with an

aspect ratio of 1.0, while disproportionately large increases in strength were observed in the Bailey-BRE models. It was also observed[11] that the finite element models compared closely with the Bailey approach when high reinforcement ratios were used in slabs of aspect ratio 2.0. The observations led Foster[7] and Bailey and Toh[6] to perform experimental tests on small-scale slabs at ambient and elevated temperatures. They examined various reinforcement ratios with varying ductilities. The experiments showed that high reinforcement ratios could cause compressive failure. The Bailey method was modified accordingly[6].

A more recent comparison by the same authors[8] between the new method and the finite element code *Vulcan* showed that long span (between 14m – 16m) finite element slab panels with aspect ratios not exceeding 1.56 satisfied the Bailey-BRE deflection limit for their design fire resistances, with the protected edge beams reaching a temperature of 550°C at the specified fire resistance time. The article, however, does not describe in detail the support conditions used in the finite element analyses.

3. SLAB PANEL FAILURE STUDY

The investigation into the Bailey-BRE method was conducted in two stages. The first stage was devoted to the effects of vertical support on slab panel failure, while the second stage examined the effects of reinforcement ratio. In total four slab panel sizes were used in the study. These are shown in Fig. 2. The 7.5m x 9m slab panel was used for the vertical support study, while the other panels were restricted to the reinforcement ratio study. For clarity, the following terminology is adopted for the research:

- Primary beams – the beams spanning between panel corners and parallel to the span direction of the decking of the composite floor.
- Secondary beams – the beams spanning between panel corners and perpendicular to the span direction of the decking of the composite floor.
- Intermediate beams – the beams spanning in the same direction as the secondary beams but end-supported at points along the lengths of the primary beams which are off the column grid.

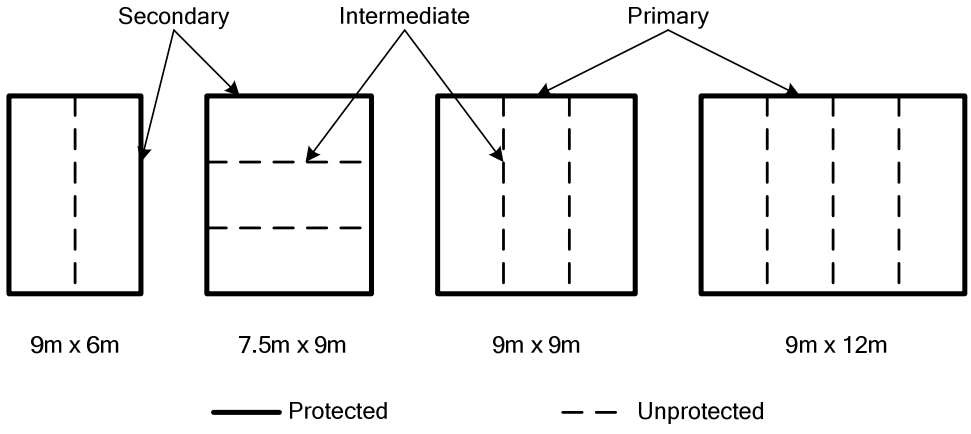

Fig. 2: Slab Panel Sizes

Using BS5950-3 and BS5950-8, the beams were designed for full composite action, using normal-weight concrete, the trapezoidal slab profile shown in Fig. 3 and the slab panel design requirements given in Table 1 (derived from SCI P-288) for a 60-minute fire resistance. The

temperatures of both the primary and secondary beams were restricted to a maximum of 550°C at 60 minutes when exposed to the standard temperature-time relationship, using lightweight fire-resisting gypsum boards (density = 800kg/m^3; specific heat capacity = 1700Jkg/K; conductivity = 0.2W/mK). The results are shown in Table 2.

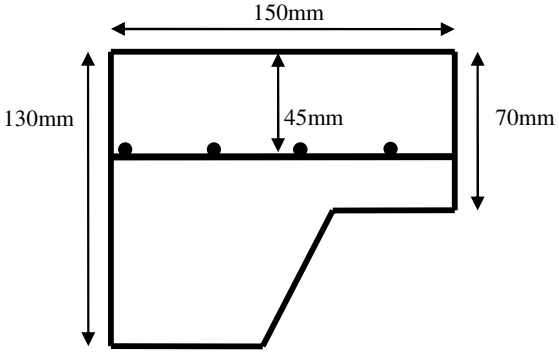

Fig. 3: Concrete slab cross-section

Table 1: Slab panel design requirements

Slab Panel size	7.5m x 9m	9m x 6m	9m x 9m	9m x 12m
Dead load (kN/m^2)	4.33	4.33	4.33	4.33
Live load (kN/m^2)	3.5	5.0	5.0	5.0
Additional load (kN)	20	14	37	49
Beam design factor	1.00	0.77	1.00	0.83
Min. Mesh size	A193	A193	A193	A252

Table 2: Protected beam design data

Slab Panel Size	Beam Type	Beam Section	Load Ratio	Limiting Temperature	Temperature at 60 minutes
7.5m x 9m	Secondary	356 x 127 x 33 UB	0.440	631°C	533°C
	Primary	533 x 210 x 82 UB	0.396	647°C	539°C
9m x 6m	Secondary	356 x 171 x 57 UB	0.426	636°C	548°C
	Primary	406 x 378 x 60 UB	0.452	627°C	549°C
9m x 9m	Secondary	356 x 171 x 67 UB	0.442	630°C	550°C
	Primary	533 x 210 x 101 UB	0.446	629°C	548°C
9m x 12m	Secondary	406 x 178 x 67 UB	0.447	629°C	548°C
	Primary	610 x 305 x 179 UB	0.471	620°C	547°C

The finite element analyses were conducted with *Vulcan*[4, 5]. This is a geometrically nonlinear specialist finite element program for structural fire engineering, developed at the University of Sheffield. Nonlinear layered rectangular elements, capable of modelling both membrane and bending effects, are used to represent slab behaviour, while beam and column behaviour are adequately modelled with nonlinear beam-column elements. Failure of concrete follows a biaxial peak-stress interaction surface.

3.1. Thermal analyses

Because of debonding of concrete from the steel deck, which is usually observed after fires, and the high temperatures applied to the soffit of a composite slab in fire, TSLAB and the Bailey-BRE method use an average-depth flat concrete slab for their structural analyses.

Therefore, with exposure to the standard temperature-time curve, a one-dimensional thermal analysis was performed on a 100mm thick flat concrete slab, using FPRCBC-T[12]. The results are compared with TSLAB temperature distributions, and are shown in Fig. 4. The finite element thermal distributions are shown as continuous lines, while those from TSLAB are shown as broken lines. It is observed that a close comparison was obtained. For unprotected beams, the TSLAB beam temperatures were used in the *Vulcan* analyses.

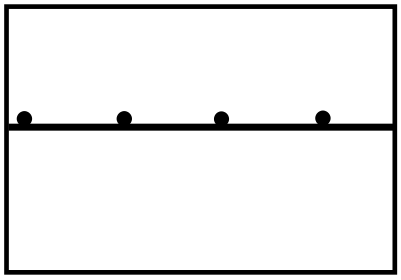

Fig. 4a: Schematic diagram of the 1D thermal analysis

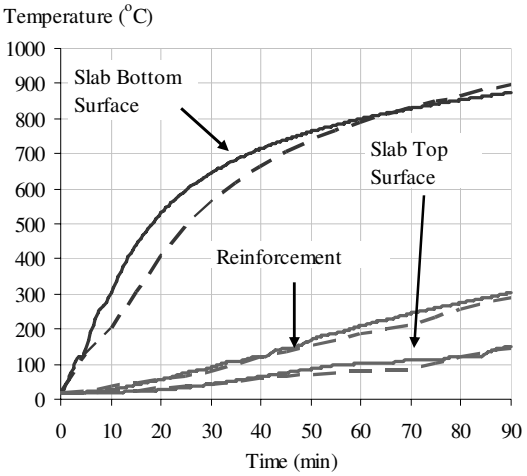

Fig. 4b: Comparison of thermal distribution through the depth of the 1D slab profile

3.2. Structural analyses

The study on the 7.5m x 9m slab panel examined various support conditions intended to provide the necessary vertical support for tensile membrane action. At this stage only one reinforcement mesh size (A193) was used, in order to adequately observe the difference in failure times which can be attributed solely to the support conditions. In trying to simulate reality, the *Vulcan* analyses model slab panel vertical support as protected perimeter beams and corner supports. For comparison, other *Vulcan* analyses were performed with differing edge support conditions, in order to determine their effects on tensile membrane action. For ease of representation of the results the various *Vulcan* models are numbered. They are:

- Generic protection and vertical support at corners (V_1),
- Generic protection with rigid vertical support along slab panel edges (V_2),
- Rotational restraint along the perimeter of the panel (V_5- V_8),
- The assumption of cold perimeter beams (V_3).

Other analyses were conducted with A252 and A393 meshes in order also to observe the behaviour of the panels. The second study was therefore designed to follow up on this aspect with the three slab panel sizes to cover a greater number of aspect ratios.

3.3. Results and discussion

The *Vulcan* and Bailey-BRE analyses were compared using three different deflection limits as 'failure' criteria. These were:

- The TSLAB limiting deflection curve (Equation 1),
- The maximum allowable deflection defined in the generic BRE method,
- Short span/20.

The BRE maximum allowable deflection limit is obtained by setting T_2-T_1 to 770°C for fire exposure below 90 minutes. It should be noted that, unless otherwise stated, the results show absolute maximum vertical displacements of the middle of the slab panel.

Slab panel vertical support

Fig. 5 shows the various deflection limits used in the 7.5m x 9m slab panel analyses. The Bailey-BRE method deems the A193 mesh to be adequate for this panel, as shown in the figure. A comparison of the Bailey displacement and central vertical displacements given by the *Vulcan* models V_1 – V_3 are shown in Fig. 6. The V_1 curve is the ideal representation of slab panel behaviour in fire. It however exceeds all the deflection criteria at 40 minutes, while *Vulcan* V_3, which shows the panel central displacement with edge vertical support and cold perimeter beams, just satisfies the allowable deflection limit at 60 minutes. The model with generic protection and edge vertical support (V_2) satisfies the span/20 criterion and the deflection required by the Bailey method to generate the required enhancement.

An investigation into the apparent failure of the *Vulcan* V_1 model is shown in Fig. 7 Displacements of the centre of the panel relative to the midpoints of the secondary and primary beams are plotted. It is observed that, at about 45 minutes, a reduction in the difference in deflection between the slab centre and the secondary beam begins. This continues until failure, but an accelerated reduction occurs from about 70 minutes. This is seen as the point where fully-developed plastic hinges occur in the secondary beams, thus allowing the formation of a single-curvature mechanism which runs away at failure. Increasing the mesh size does not seem to have any effect on the time at which the accelerated displacement occurs, as shown in Fig. 8. This confirms the failure of the edge beams, as the vertical support necessary to maintain the double-curvature tensile membrane mechanism is no longer available.

In Fig. 10, the Bailey-BRE displacement is compared with four continuous slab panels labelled V_5-V_8, as shown in Fig. 9. The slab panels in Fig. 9 were analysed separately, to isolate the contributions of axial restraint across a slab panel boundary. All the edge beams had generic protection, as in the previous models. Rotations were restrained across boundaries where adjacent slabs existed. The necessary additional loads on these boundaries were included in the models. The results indicate that the conservative assumption of a simply-supported slab panel in the Bailey-BRE method is aided by rotational edge-restraints of continuous slab panels for internal bays, while edge and corner bays may fail once their edge beams deflect by a considerable amount.

3.4. Edge panel failure mechanism

The results of the preceding section have identified a potential slab panel failure when edge beam stiffness is lost. They show that tensile membrane action is maintained up to a point at which the combined effects of increased edge beam loading and thermal degradation cause failure of the protected beams. Additional restraint along any slab panel boundaries improves slab panel capacity. A simple edge-support failure mechanism is therefore proposed in order to address the failure of continuous vertical support in the Bailey method.

The mechanism considers the failure of the protected primary and secondary beams, assuming they are simply-supported. The model distributes the fire limit state floor load to parallel arrangements of either primary or secondary beams (protected edge beams and unprotected intermediate beams). Failure is then determined by the loss of strength of the slab panel system. A schematic representation of the loading and failure modes is given in Fig. 11

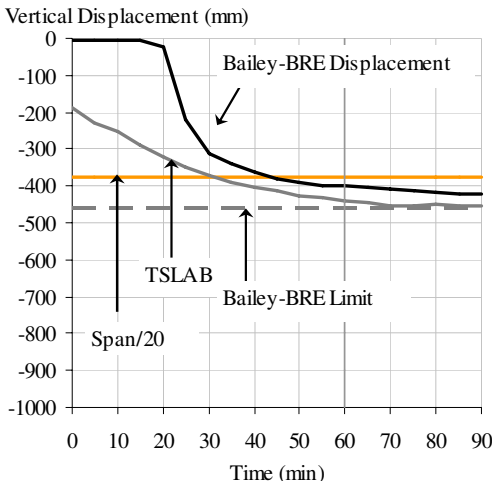

Fig. 5: Deflection limits for the7.5m x 9m slab panel

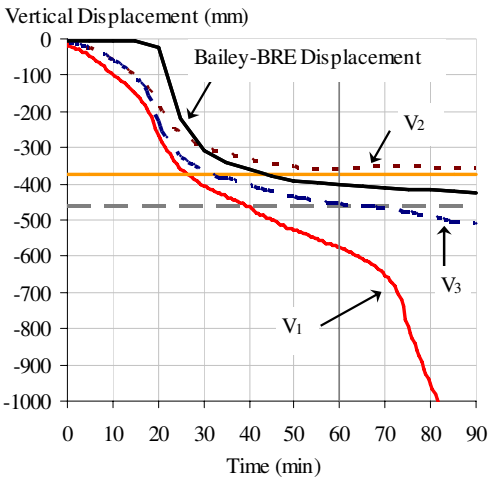

Fig. 6: Comparison of Bailey Displacement and Vulcan V1, V2 and V3

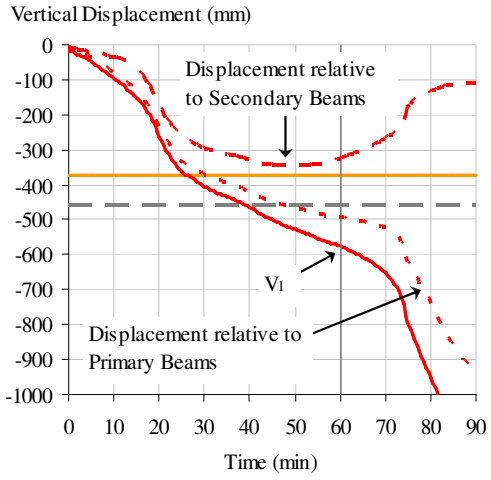

Fig: 7: Vulcan V1 edge beam failure

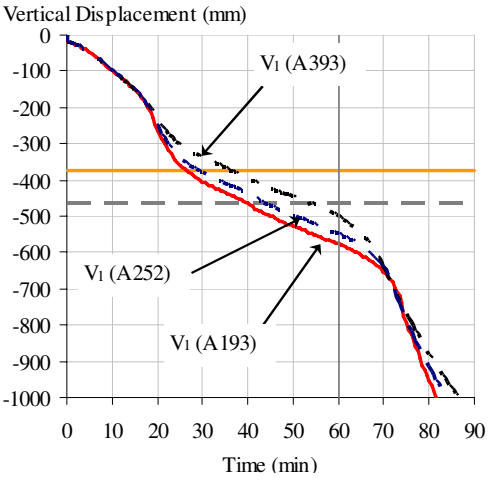

Fig. 8: Reinforcement ratio comparison

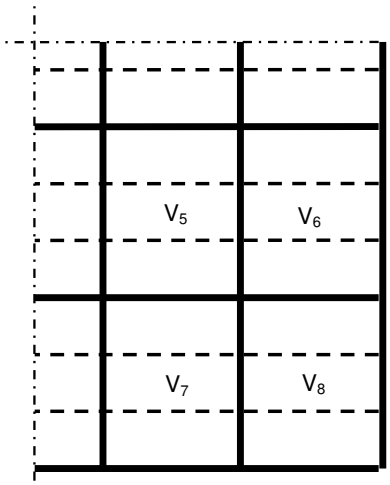

Fig. 9: Continuous slab panels – layout for fig. 10

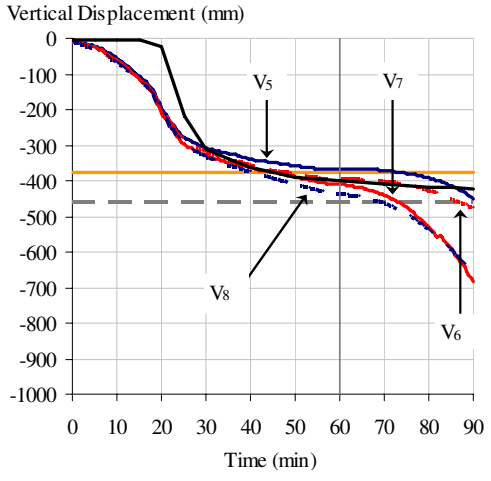

Fig.10: Influence of Rotational restraint

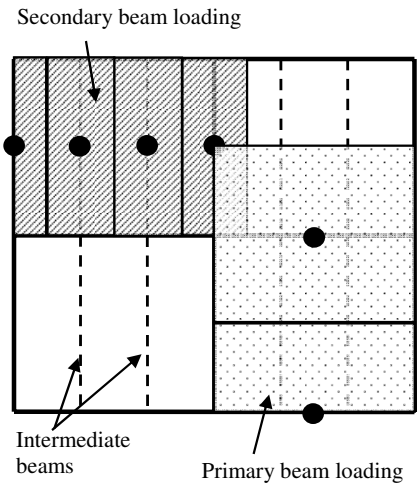

Fig. 11a Load distribution – Type 1 failure

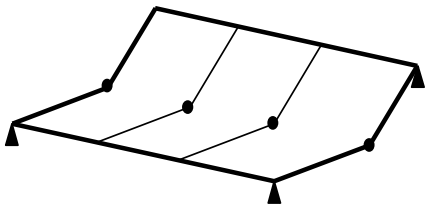

Fig. 11b: Failure of secondary beams

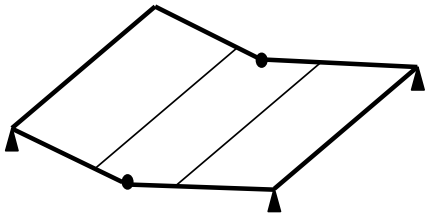

Fig. 11c Failure of primary beams

For either primary beams or secondary (and intermediate) beams, failure occurs when:

$$\sum_{i=1}^{n} M_{applied,i} - \sum_{j=i}^{n} M_{fi,t,Rd,j} \geq 0 \qquad (3)$$

In the above equation, $M_{applied,i}$ is the applied moment on each beam in the parallel arrangement, while $M_{fi,t,Rd,j}$ is the capacity of each composite beam in the arrangement at a particular time t into the fire; n is the total number of beam sections in the parallel arrangement (for primary beams, $n = 2$).

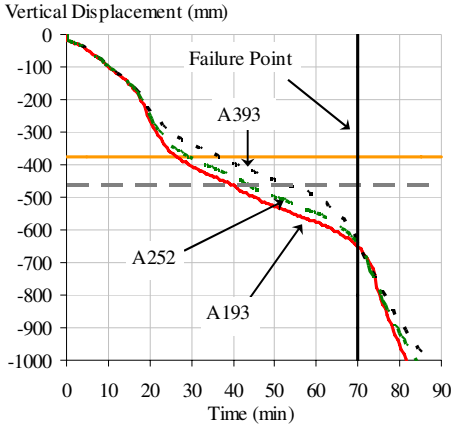

Fig. 12: Plastic failure of 7.5m x 9m slab panel

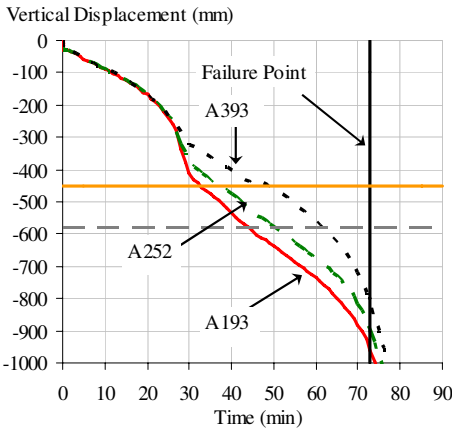

Fig. 13: Plastic failure of 9m x 9m slab panel

Figs. 12 and 13 show the 7.5m x 9m and 9m x 9m slab panels, analysed using *Vulcan* model V_1. A comparison of mesh sizes A193, A252 and A393 and the plastic failure limits of the edge beams are shown. The failure mechanism is tested for the two parallel arrangements of either primary or secondary beams. For the 7.5m slab panel, failure of the secondary beams occurred at 70 minutes with protected secondary beam temperatures at 600°C, while failure of

the primary beams did not occur in 90 minutes of fire exposure. For the 9m x 9m slab panel, secondary beam failure was observed at 73 minutes, with a corresponding temperature of 621°C. Again failure of the primary beams did not occur within 90 minutes of exposure. Failures of the 9m x 6m and 9m x 12m slab panels occur at 82 minutes and 68 minutes respectively, with secondary beam temperatures at 662°C and 594°C.

3.5. Effects of reinforcement ratios

This section presents results on the effects of varying reinforcement ratios on the two slab panel models (*Vulcan* and the Bailey-BRE method). Standard and fictitious reinforcement mesh sizes were used to highlight the differences in the two methods; these were: 142, 166, 193, 221, 252, 318 and 393 (all in mm^2/m). The results (Figs. 14 and 15) show comparisons of the failure times of the Bailey method and *Vulcan* analyses by finding the equivalent times at which their deflections exceed the deflection criteria of TSLAB, the BRE vertical deflection limit and span/20. The solid lines show results from the membrane action method. Those from *Vulcan* are shown as broken lines. The unlabelled lightly-coloured lines show the failure times obtained using the BRE allowable deflection limit.

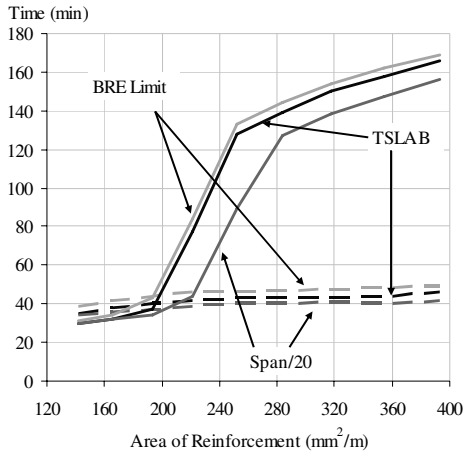

Fig. 14: Comparison of Bailey-BRE and Vulcan Failure times for 9m x 6m slab panel

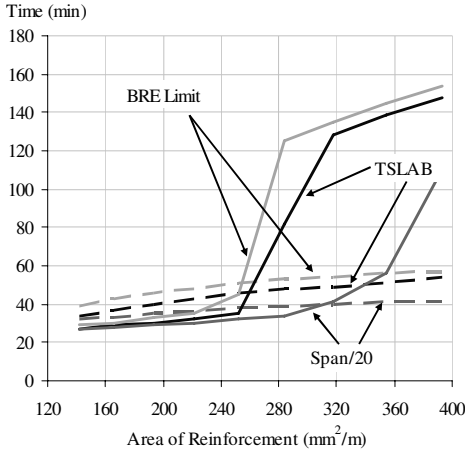

Fig. 15: Comparison of Bailey-BRE and Vulcan Failure times for 9m x 12m slab panel

The results of the 9m x 9m slab panel (not shown here for lack of space) compared very closely with the 9m x 6m slab panel (Fig. 14). The results show that, for smaller panels, there is good comparison between *Vulcan* and the BRE approach for reinforcement areas below the $195mm^2/m$ to $230mm^2/m$ range, but divergence thereafter. However, for larger panels, this good comparison stretches to about $320mm^2/m$, with a span/20 criterion (Fig. 15).

4. CONCLUSIONS

A number of protection schemes and support conditions have been analysed. It has been observed that the tensile membrane action mechanism is lost when slab panel edge beams experience significant deflections. Considerable restraint is provided by either vertically supported edges or continuous slab panels. The results show that the Bailey-BRE method gives a good prediction of slab panel behaviour if the perimeter beams remain stiff for long periods of time. A plastic failure mechanism for slab panel edge beams has been proposed. It should be noted that these beams would normally be designed for critical

temperatures of about 620°C. The analyses have shown that a combination of the imposed load and material degradation will cause failure. Therefore, specifying a temperature of 620°C at the required fire resistance time is not sufficient.

For slabs in the interior of a building, the restraint from adjacent slabs is clearly beneficial, but for edge or corner slab panels increasing the level of protection seems a viable option. This could potentially counter the reduction in cost given by employing tensile membrane action. However, producing safe structures should be a priority over economy.

This comparative study has shown that the Bailey-BRE method is conservative when an A142 or A193 mesh is used on a 'small' slab panel. However, the method predicts more optimistic fire resistance times than advanced analysis when higher reinforcement ratios are used on these 'small' panels or when larger panels are used with reinforcement meshes above A252. It is implied from the preceding analyses that the minimum area of reinforcement for any slab panel is proportional to its dimensions. Therefore, an increase in reinforcement ratio is required if slab panel sizes increase.

REFERENCES

[1] *The Building Regulations 2000, Approved Document B, Volume 2 – Buildings other than Dwelling Houses*, ISBN 10 1 85946 262 6, Department of Communities and Local Government, 2007

[2] Newman, G. M., Robinson, J. T. and Bailey, C. G., *Fire Safe Design: A New Approach to Multi-Storey Steel-Framed Buildings*, Second Edition, SCI Publication P288, The Steel Construction Institute, UK, 2006

[3] Bailey, C. G., *Design of Steel Structures with Composite Slabs at the Fire Limit State, Final Report No. 81415, prepared for DETR and SCI*, The Building Research Establishment, Garston, UK. 2000

[4] Huang, Z., Burgess I. W. and Plank R. J., "Modelling membrane action of concrete slabs in composite slabs in fire. I: Theoretical Development", ASCE Journal of Structural Engineering, **129** (8), 2003, p1093-1102

[5] Huang, Z., Burgess, I.W. and Plank, R.J., "3D Modelling of Beam-Columns with General Cross-Sections in Fire", Paper S6-5, Third International Workshop on Structures in Fire, Ottawa, Canada, 2004, p323-334

[6] Bailey, C. G. and Toh, W. S., "Behaviour of concrete floor slabs at ambient and elevated temperatures" *Fire Safety Journal,* **42**, 2007, p425-436

[7] Foster S. J., *Tensile Membrane Action of Reinforced Concrete Slabs at Ambient and Elevated Temperatures*, PhD thesis, University of Sheffield, 2006

[8] Toh, W. S. and Bailey, C. G., Comparison of simple and advanced models for predicting membrane action on long span slab panels in fire, Proc. Interflam 2007, 2007

[9] Huang, Z., Burgess, I.W. and Plank, R.J., 'The Influence of Tensile Membrane Action on the Behaviour of Composite Steel-Framed Buildings in Fire', Proc. ASCE Structures Congress, Washington DC, 2001

[10] Huang, Z., Burgess, I.W., Plank, R.J. & Bailey, C.G., 'Strategies for Fire Protection of Large Composite Buildings', Proc. Interflam 2001, 2001, p395-406

[11] Huang, Z., Burgess, I.W., Plank, R.J. and Bailey, C.G., 'Comparison of BRE Simple Design Method for Composite Floor Slabs in Fire with Non-Linear FE Modelling', *Fire and Materials*, **28** (2-4), 2004, p127-138

[12] Huang, Z., Platten, A. and Roberts, J., "Non-linear Finite Element Model to Predict Temperature Histories within Reinforced Concrete in Fires", *Building and Environment*, **31**(2), 1996, p109-118.

TESTING AND MODELLING OF BONDED AND UNBONDED POST-TENSIONED CONCRETE SLABS IN FIRE

EHAB ELLOBODY[2] and COLIN G. BAILEY[1]

ABSTRACT

This paper presents new fire tests conducted on bonded and unbonded post-tensioned concrete slabs. A total of 16 tests were carried-out, of which four were conducted at ambient temperature to evaluate the capacity of the slabs in the cold condition. The remaining 12 tests were conducted under fire conditions, with the slabs subjected to the standard fire curve under a static load equal to 50% of the capacity of the unbonded slabs in the cold condition. The slabs were one-way simply-supported and reinforced with 15.7mm nominal diameter seven-wire mono-strand tendons. The effects of different aggregate types, boundary conditions and duct material (steel and plastic) in the bonded slabs have been investigated in the tests. The temperature distribution throughout the slab, the strains in the tendons, the deflection behaviour and the longitudinal expansion were recorded during the tests. A nonlinear finite element model for the analysis of the slabs at elevated temperatures was also developed. The mechanical and thermal material nonlinearities of the concrete, prestressing tendon and anchorages were accurately modelled. The effects of aggregate type and boundary conditions on the structural behaviour of the slabs were considered in the finite element analysis. The interface between the tendon and surrounding concrete was also modelled, allowing the tendon to retain its profile shape during the deformation of the slab. In addition, the thermal properties of the interface element were also included in the model. The temperature distribution throughout the slab, time-deflection behaviour, time-longitudinal expansion, time-stress in the tendon, the failure modes and the fire resistance were predicted by the model and verified against the test results. A parametric study has been conducted to investigate the effects on the global structural behaviour due to the change in the aggregate type, load ratio and boundary conditions, with conclusions presented.

[1]Professor of Structural Engineering, Head of the School of MACE, The University of Manchester, Manchester, United Kingdom. *E-mail address:* Colin.Bailey@manchester.ac.uk
[2]Associate Professor, Department of Structural Engineering, Faculty of Engineering, Tanta University, Tanta, Egypt. *E-mail address:* ehab_ellobody@tanta.edu.eg

1. INTRODUCTION

Post-tensioned concrete slabs are commonly used throughout the World due to their readily achievable clear spans, small construction depth, optimum use of reinforcement and rapid construction. Post-tensioning of concrete slabs can be constructed using unbonded or bonded tendons. For unbonded slabs the transfer of force from the tendons to the concrete is mainly via the end anchors, with strains in the tendons distributed throughout their entire length. In bonded slabs the transfer of the force is mainly via the end anchors and the bond between the tendons and concrete. The bond between the tendon and concrete is created by pumping grout between the tendon and sheathing after tensioning the tendon. Although the use of post-tensioned concrete slabs is increasing there has been some debate within industry relating to the fire resistance of this form of construction.

Very limited test data were found in the literature on unbonded post-tensioned concrete slabs at elevated temperatures. On the other hand, no test data were found on bonded post-tensioned concrete slabs under fire conditions. The previous tests on unbonded slabs comprise three standard fire tests[1,2] carried out in the 1950's and 1960's and nine tests on unbonded slab strips carried out by Herberghen and Damme[3]. In addition to these tests, observations from real fires in buildings with unbonded slabs have highlighted various responses as presented by Lukkunaprasit[4], Troxell[5] and Sarkkinen[6]. A detailed review of these previous tests and observations from real fires has been provided by Lee and Bailey[7]. Finite element models have been used previously to predict the behaviour of concrete structural members in fire conditions, as discussed previously by Ellobody and Bailey[8]. However, numerical models investigating the behaviour of post-tensioned concrete slabs in fire have not been adequately developed to-date with some progress presented by Lee and Bailey[7] and Ellobody and Bailey[8].

This paper presents the results of sixteen tests conducted on unbonded and bonded post-tensioned one-way spanning concrete slabs at ambient temperature and under fire conditions. An efficient nonlinear 3-D finite element model was developed using ABAQUS[9] and verified against the tests. A parametric study has been conducted to study the effects of the change in the aggregate type, load ratio, and boundary conditions on the behaviour of the slabs at elevated temperatures. The experimental and numerical results have been compared with the design values specified in BS 8110-2[10], and BSEN 1992-1-2[11], with conclusions being drawn.

2. TEST PROGRAMME

2.1 General

The test programme, shown in Table 1, includes six tests - two at ambient temperature (T1 and T2) and four at elevated temperature (T3-T6) - conducted on unbonded post-tensioned slabs. In addition, ten tests - two at ambient temperature (TB1 and TB2) and eight at elevated temperature (TB3-TB6) and (TB7-TB10) - carried out on bonded post-tensioned slabs. The main variable parameters in the tests are the boundary conditions (free and restrained longitudinal expansion), the aggregate type (Limestone

and Thames Gravel) and the duct type used within the bonded slabs (plastic and steel). The slabs were designed according to BS 8110-1[12] and the Concrete Society Technical Report 43[13]. The slabs were 4.3m long, 1.6m wide, and 160mm deep. Each slab had three longitudinal parabolic tendons with a nominal diameter of 15.7mm and an area of 150mm^2. One tendon was positioned in the middle of the slab with the other two positioned either side, at a spacing of 530mm, as shown in Fig. 1. The plain tendon was a mono-strand with seven high-strength steel wires, with an average measured tensile strength of 1846MPa. The tendon used in the unbonded slabs was greased and housed in a thin polypropylene extrusion sleeve which had been moulded directly onto the strand, while the tendon used in the bonded slabs was plain (non-greased) tendon. In the unbonded slabs, each tendon was supported on seven steel chairs and passed through the dead and live anchorages which were placed at mid-height at the ends of the slab, as shown in Fig. 1a. In the bonded slabs, the plastic and steel ducts (housing the plain tendon) were supported on seven steel chairs between the dead and live anchorages, as shown in Fig. 1.b. The distance from the bottom of the slab to the centre of the tendon, at the mid-span of the slab, was 42mm. The plastic ducts had a 23mm internal diameter and were supplied by General Technologies Inc., while the metallic ducts were galvanised steel ducts having 40mm internal diameter and supplied by Wells Ltd. The dead and live anchorages were identical and supplied by CCL Ltd.

Table 1. Tests on unbonded and bonded post-tensioned concrete slabs

Test	Concrete strength (MPa)	Moisture content (%)	Fire	Bond		Long. Exp.		Duct		Coarse Aggregate	
				Unbonded	Bonded	Free	Res.	Plastic	Steel	Lime-stone	Thames Gravel
T1	44.4	---		X		X				X	
T2	48.2	---		X		X					X
T3	48.0	2.54	X	X		X				X	
T4	41.0	2.15	X	X			X			X	
T5	40.0	2.34	X	X		X					X
T6	39.7	1.70	X	X			X				X
TB1	41.2	---			X	X		X		X	
TB2	30.3	---			X	X			X	X	
TB3	36.6	1.19	X		X	X		X		X	
TB4	40.9	1.93	X		X		X	X		X	
TB5	35.5	1.07	X		X	X		X			X
TB6	38.6	2.50	X		X		X	X			X
TB7	40.4	2.43	X		X	X			X	X	
TB8	42.3	1.84	X		X		X		X	X	
TB9	36.9	2.27	X		X	X			X		X
TB10	39.3	2.18	X		X		X		X		X

Bursting reinforcement was designed according to BS8110-1[12] to resist tensile bursting forces around individual anchorages. No other non-tensioned reinforcement was included. Table 1 summarises the measured concrete strength at testing and moisture content for the slabs tested under fire conditions. Grouting of the bonded slabs followed BS EN 447[14] using a mixing ratio of Ordinary Portland Cement to water 2.5:1. The grouting equipment was supplied by Pennine Grouting Ltd. Grouting was conducted immediately after post-tensioning.

(a) Unbonded

(b) Bonded

Fig. 1. Moulds used for casting the post-tensioned concrete slabs

Twenty thermocouples were used to measure the distribution of temperatures throughout each slab during the fire tests. The thermocouples were positioned throughout the depth of the slab at the mid-span and quarter-span of the slab. The positions were at the bottom of surface (HS), the top surface (CS), adjacent to the tendons (T) and at the mid-height of the slab (MS). Three strain gauges were fixed on three spiral wires of each of the three tendons (right tendon 'RT', middle tendon 'MT' and left tendon 'LT') near the dead anchorages. Six displacement transducers were used to measure the deflections and the longitudinal expansion at the end of the slab near the movable support.

The full applied design prestressing force to the slabs was 195kN, with an average measured 13% losses. Further details of the post-tensioning process are presented in Ellobody and Bailey [15]. The slabs were tested over a span of 4.0m. In the ambient tests, the slabs were loaded to failure, while in the fires tests, the slabs were subjected to a static load equal to 50% of the capacity of the unbonded Slab T1 (156.6kN) in the cold condition. The slabs were loaded at four locations using spreader plates as shown in Fig. 2a. The applied load, the strains in the tendons, and the vertical deflections were measured in all tests. In the fire tests, temperatures through the slab were also measured together with horizontal longitudinal displacements in the unrestrained slabs. The slabs were heated in the fire tests using two burners with the aim of following the standard time-temperature curve specified in BSEN 1991-1-2[6].

2.2 Unbonded test results

Slabs T1 and T2 (Table 1) were tested in the cold condition. The ultimate failure load was 156.6kN with a central deflection of 82mm for Slab T1 and 178.2kN with a central vertical deflection of 93mm for Slab T2. The mode of failure for both slabs was concrete crushing in the compression zone under one of the middle spreader plates. Further details regarding the tests have been discussed in Ellobody and Bailey[15].

The unbonded post-tensioned concrete Slab T3 was positioned on the top of the gas furnace as shown in Fig. 2a. The longitudinal sides of the slab above the furnace were insulated, as shown in Fig. 2a. The slab was subjected to a static load equal to 78.3kN which was kept constant during all the fire tests. After 20mins into the test for Slab T3, longitudinal cracks appeared on the unexposed surface directly above and parallel to the position of the tendons and remained throughout the test, as shown in Fig. 2a. The cracks appeared in all the unbonded and bonded fire tests. The test continued until collapse of the slab after 178mins. The three tendons fractured and a transverse crack occurred in the

maximum bending moment zone under one of the middle spreader plates causing overall collapse, as shown in Fig. 2.b. On removal of the slab there was no evidence that concrete spalling occurred on the heated surface. Slab T4 was similar to Slab T3 except it was restrained against longitudinal thermal expansion. Initially, the slab expanded longitudinally until it became in full contact with the restraining beams and until the bolts fixing the restrained beams became intact with the edges of the holes. This occurred in all the restrained fire tests. The vertical deflection remained constant after 36mm as shown in Fig. 3a. The test was stopped after 85mins, when the temperature of the tendons reached 350°C, to ensure damage to the furnace did not occur due to overall collapse of the slab. Minor concrete spalling was observed on the bottom surface after the test, however the spalling did not expose the tendons.

(a) Cracking on top surface (b) Collapse of Slab T3

Fig. 2. Cracking and collapse of Slab T3

Slab T5 had Thames Gravel aggregate, and similar to Slab T3 was allowed free thermal expansion. Compared to Slab T3, Slab T5 developed higher vertical deflections immediately after starting heating, as shown in Fig. 3a. This can be attributed to the higher thermal expansion coefficient of Thames Gravel compared to Limestone. The test was stopped after 72mins from the start of heating when the recorded temperature of the tendons reached 350°C and no spalling was observed on the bottom surface. Slab T6 was similar to Slab T5 except it was restrained against longitudinal thermal expansion. Horizontal shear was observed near the slab ends. The test was stopped once the temperatures in the tendon reached 350°C. No concrete spalling occurred for the Slab T6.

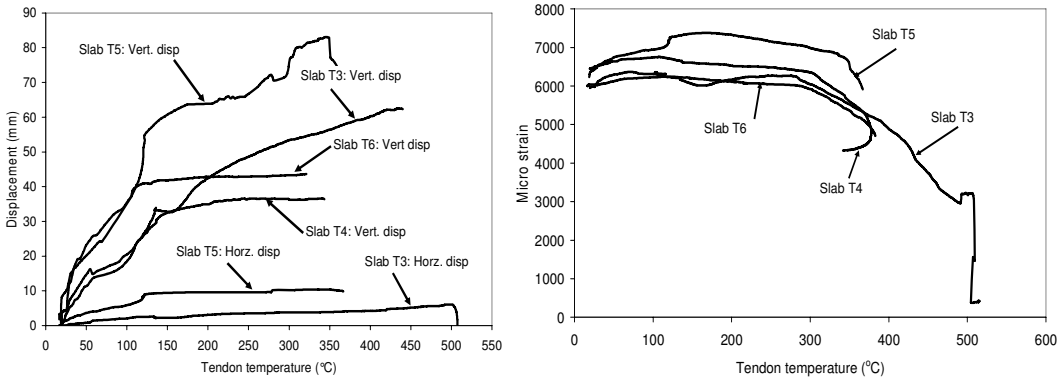

(a) Tendon temperature-displacement curves (b) Tendon temperature-tendon strain curves

Fig. 3. Tendon temperature-displacement and strain curves for the unbonded tests

The tendon temperature-central deflection relationships for all the unbonded fire tests are shown in Fig. 3.a. The Slabs T3 and T4 had concrete with Limestone aggregate. Slab T3 was allowed to expand longitudinally and laterally in the fire test, while Slab T4 was restrained longitudinally against thermal expansion. It can be seen that Slab T3 had higher vertical deflection than that observed for Slab T4. The maximum deflection observed for Slab T3 was 63mm compared to 37mm for Slab T4. Since the slab was not rotationally fixed at its ends, the resultant longitudinal applied restraining force in Slab T4, as it expanded, would have been below the mid-height of the slab and would have led to a restoring moment in the slab reducing its displacement compared to Slab T3 which was unrestrained. Similar behaviour was observed when comparing Slabs T5 and T6, except the displacements were larger. Comparison between the unrestrained Slabs T3 and T5, and the restrained Slabs T4 and T6, shows that the slabs with Thames Gravel aggregates have larger displacements compared to the slabs with Limestone aggregates, due to the greater thermal expansion of Thames Gravel. Due to the variation of temperature through the depth of the slab, thermal curvature contributes to the vertical deflection (together with the loss of strength of the slab) with the Thames Gravel slabs having the greater displacement. The axial deformation is shown in Fig. 3.a where it can be seen that Slab T5, with Thames Gravel expands greater than Slab T3, which had Limestone aggregate. The average strains against temperature for the tendons are shown in Fig 3.b for all the fire tests. It can be seen that Slabs T3, T4 and T6 had similar behaviour in terms of strain values with increasing temperature. For Slab T5 the strains increased considerably at 116°C (Fig. 3.b) due to a plateau in the temperature increase in the tendon, due to water migration, at this temperature with the strains continuing to increase up to a temperature of 186°C. Further details regarding the results of the unbonded fire tests and mode of failure have been discussed in Bailey and Ellobody [17].

In all the fire tests longitudinal cracks occurred on the top surface parallel and directly above the tendons. The cracks appeared in the fire tests between 15 and 21mins corresponding to a tendon temperature between 95°C and 119°C. The observed cracks suggest that there are tensile stresses being induced perpendicular to the trajectory of the tendons due to the additional thermal stresses. No significant spalling occurred in any of the tests mainly due to the low moisture content, as shown in Table 1. Looking at Slab T3 which was tested to overall collapse, the temperature of the tendons at failure was 492°C, which corresponds to reduction factor of 0.32 using EN1992-1-2[11] and a design moment capacity of 30kNm. This design capacity is lower than the applied moment of 38kNm suggesting that the reduction factors in EN1992-1-2 may be slightly conservative.

2.3 Bonded test results

Slabs TB1 and TB2 (Table 1) were tested in the cold condition to define the capacity of the bonded slabs. The testing procedures were identical to Slabs T1 and T2. The ultimate failure load for Slab TB1 was 215.6kN with a central deflection of 119.5mm, as shown in Fig. 4.a. The mode of failure was concrete crushing in the compression zone under one of the middle spreader plates. The ultimate failure load for Slab TB2 was 187.9kN with a central deflection of 107.4mm, as shown in Fig. 4.b. The mode of failure was similar to Slab TB1. Further details regarding the results of the bonded ambient tests and mode of failure have been discussed in Bailey and Ellobody [18].

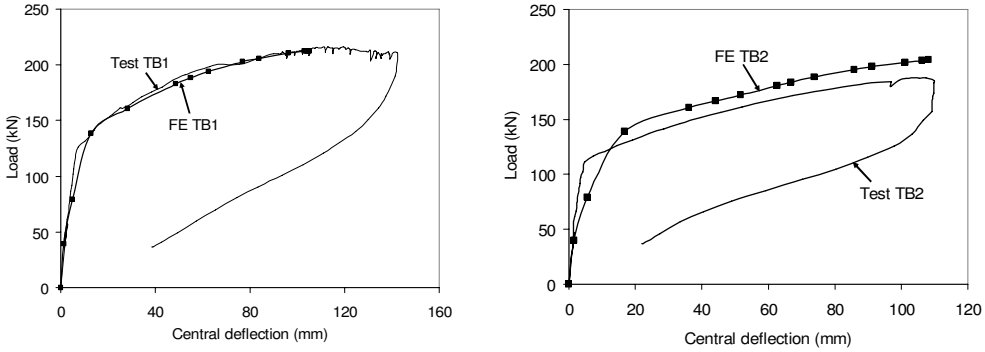

(a) Load-central deflection curves for TB1 (b) Load-central deflection curves for TB2

Fig. 4. Load-central deflection curves for the ambient bonded tests

The bonded post-tensioned concrete Slab TB3 was tested similar to Slab T3. The slab was constructed using plastic ducts. The average furnace temperature against time for all the bonded fire tests is shown in Fig. 5.a. It can be seen that the furnace temperature closely followed the standard fire curve. The test was stopped after 95mins, when the temperature of the tendons exceeded 400°C and no evidence of concrete spalling occurred. The measured central deflection was plotted against time for the slab as shown in Fig. 5.b. The temperature distribution throughout the slab was recorded, as shown in Fig. 6.a. The strains were recorded for all the fire tests. It can be seen from Fig. 7.b that the stresses in the tendons started to decrease after approximately 30mins.

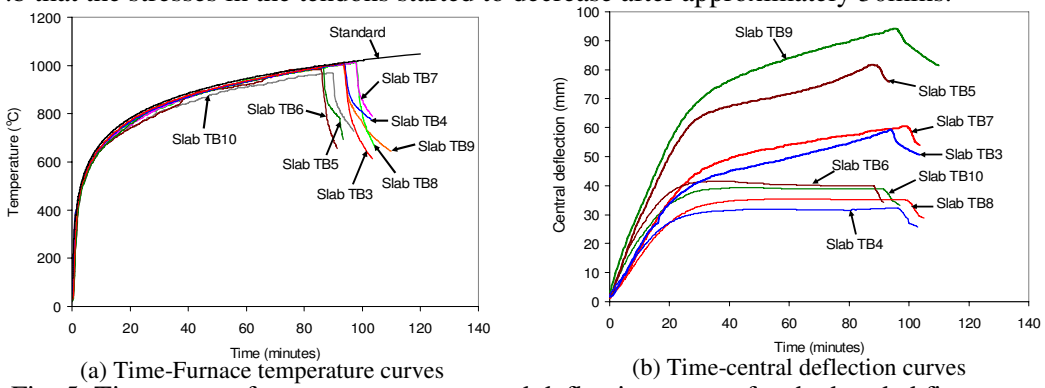

(a) Time-Furnace temperature curves (b) Time-central deflection curves

Fig. 5. Time versus furnace temperature and deflection curves for the bonded fire tests

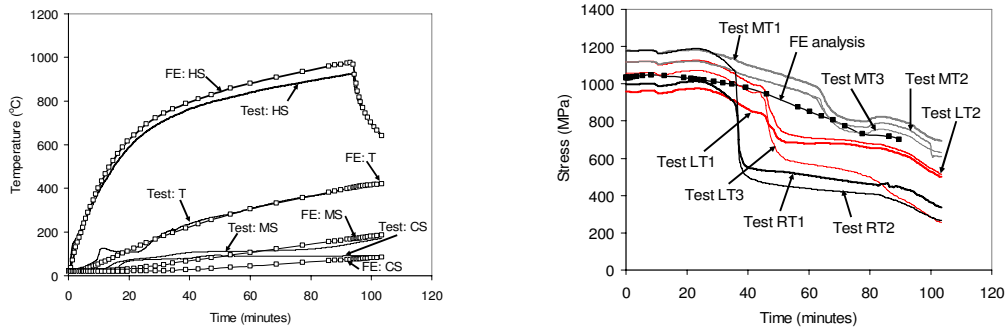

(a)Time-temperature curve (b)Time-tendon stress curve

Fig. 6. Time versus temperature and tendon stress curves for Slab TB3

Slab TB4 was similar to Slab TB3 except it was restrained against longitudinal thermal expansion. As shown in Fig. 5b, the vertical deflection remained constant around 32mm after 46 minutes. The test was stopped after 97mins, when the temperature of the tendons exceeded 400°C. No concrete spalling was observed for Slab TB4, although horizontal shear was observed near the slab ends. Slab TB5 had Thames Gravel aggregate, and similar to Slab TB3 was allowed free thermal expansion. The test was stopped after 87mins from the start of heating when the recorded temperature of the tendons reached 366°C. Minor spalling was observed on the bottom surface. Slab TB6 was similar to Slab TB5 except it was restrained against longitudinal thermal expansion. The slab had a concrete with Thames Gravel. Horizontal shear was observed near the slab ends. The test was stopped after 86mins once the temperatures in the tendon exceeded 400°C. Discrete concrete spalling occurred for Slab TB6.

Slab TB7 was similar to Slab TB3, except Slab TB7 had steel ducts instead of plastic ducts used with Slab TB3. Excessive steam was observed coming through the end anchorages which was not observed in the slabs with plastic ducts. The test was stopped after 99mins when the recorded temperature of the tendons reached 393°C and no spalling was observed. Slab TB8 was similar to Slab TB4 except it had steel ducts instead of plastic ducts. The deflection became constant around 35mm after 46mins as shown in Fig. 5b. Horizontal shear was also observed near the slab ends. The test was stopped after 98mins at a tendon temperature of 366°C and very minor concrete spalling was observed. Slab TB9 was similar to Slab TB5, except again Slab TB9 had steel ducts instead of the plastic ducts used with Slab TB5. Compared to Slab TB5, Slab TB9 had higher central deflection as shown in Fig. 5b. The test was stopped after 94mins from the start of heating when the recorded temperature of the tendons reached 372°C and very minor spalling was observed. Finally, Slab TB19 was exactly the same as Slab TB6 except it had steel ducts instead of plastic ducts. The slab had a concrete with Thames Gravel. The deflection became constant around 39mm after 41mins as shown in Fig. 5b. Horizontal shear was also observed near the slab ends. The test was stopped after 90mins when the tendon temperature reached 382°C. Concrete spalling occurred for the Slab TB10 at one end of the slab and on the bottom surface however it did not expose the tendons.

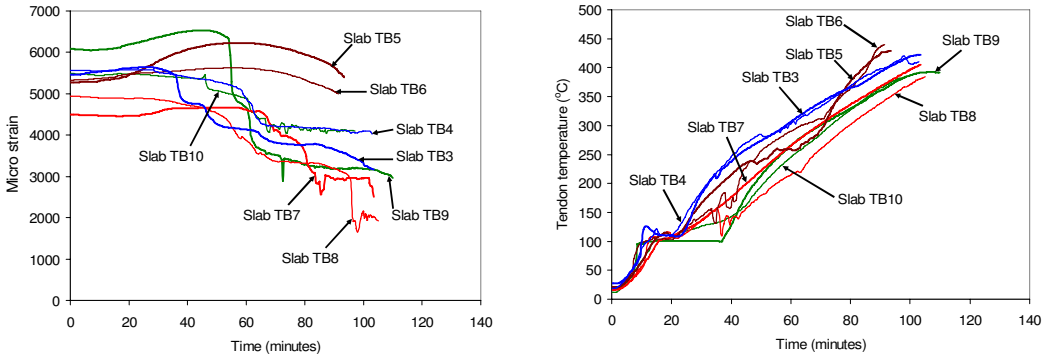

(a)Time-tendon strain curves (b)Time-tendon temperature

Fig. 7. Time versus tendon strain and temperature curves for the bonded fire tests

The time-central deflection relationships for the bonded fire tests are shown in Fig. 5b. Similar to the unbonded tests, the unrestrained slabs had higher defections compared

to the restrained slabs. Also, the slabs with Thames Gravel aggregates have larger deflections compared to the slabs with Limestone aggregates. Comparison between the unrestrained Slabs TB3 and TB7, and the restrained Slabs TB4 and TB8, with Limestone aggregate, shows that the slabs with steel ducts have generally slightly larger deflections compared to the equivalent slabs with plastic ducts. A maximum increase of 15% in deflections was observed between Slab TB9 and Slab TB5. More investigation is in progress to understand the reason behind this increase. The average strains against time for the tendons are shown in Fig 7a. The average strains in the tendons remained approximately constant during the first 30mins for all the slabs, except for Slabs TB5 and TB6 having concrete with Thames Gravel aggregate and plastic ducts. After 30mins, the strains in the tendons started to decrease. It can also be seen that the behaviour of Slabs TB3 and TB4 (having Limestone aggregate and plastic ducts is similar to that of equivalent Slabs TB7 and TB8 (having Limestone aggregate and steel ducts). Fig. 7b shows the time versus tendon temperature curve for all the bonded fire tests. It can be seen that there is a plateau in the curves in all the tests around 100^{o}C due to water migration. The bonded slabs investigated in this study had a minimum cover of 34mm under the prestressing tendons at the middle of the slab, which according to the BS8110-2 should have at least 90 minutes fire resistance. The distance from the axis of the tendon to the bottom surface of the slab was 42mm at the middle of the slab (including 15mm increase), which according to the BSEN 1992-1-2 should have at least 60mins fire resistance. It was found that the BS code was unconservative for unbonded slabs but acceptable for bonded slabs. The fire resistances specified in the EC were conservative for all the slabs.

3. FINITE ELEMENT MODELLING

3.1 General

A combination of 3-D solid elements (C3D8 and C3D6) available within ABAQUS [9] was used to model the concrete, tendon, duct, grout and anchorage elements. The elements have three degrees of freedom per node. Due to symmetry, only one quarter of the slab was modelled. Fig. 8 shows the finite element meshes used for the unbonded and bonded slabs. The boundary conditions and load application were identical to that used in the tests.

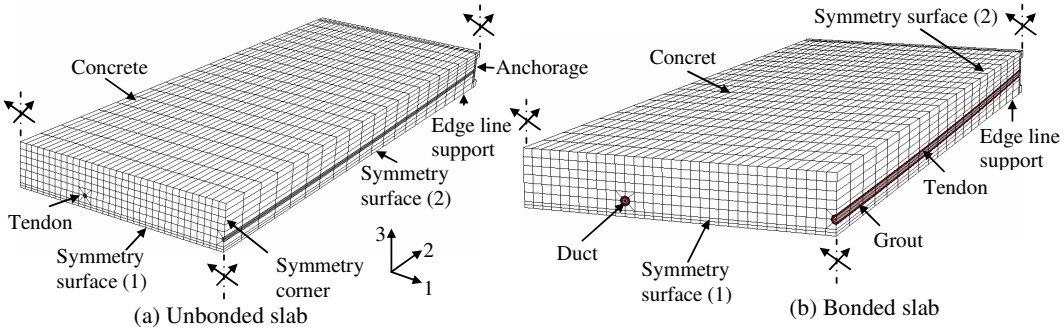

Fig. 8. Finite element meshes for the unbonded and bonded slabs

For the modelling of the fire tests a thermal analysis was conducted, using the *HEAT TRNSFER option, to evaluate the temperature distribution throughout the slabs. A constant convective coefficient (α_c) of 25w/m^{2}k was assumed for the exposed surface and 9w/m^{2}k was assumed for the unexposed surface. The radiative heat flux was calculated using a concrete emissivity (*e*) value of 0.7. Concrete was modelled using the damaged plasticity model. Under uniaxial compression the response is linear until the proportional limit stress, (f_{co}) is reached, which is assumed to equal 0.33 times the compressive strength (f_c). Under uniaxial tension the stress-strain response follows a linear elastic relationship until the value of the failure stress. The tensile failure stress is taken as 0.1 times f_c, which is assumed to be equal to 0.67 times the measured concrete cube strength (f_{cu}). The softening stress-strain response was represented by a linear line defined by the fracture energy and crack band width. The contact between the concrete and the tendon was modelled by interface elements (using the *CONTACT PAIR option). The interface elements consisted of two matching contact faces from the tendon elements and surrounding concrete or grout elements. A friction coefficient of 0.25 was considered between the two faces in the bonded tendons. The interface element allowed the surfaces to displace relative to each other but ensured that the contact elements could not penetrate each other. More details regarding the concrete model could be found in Ellobody and Bailey[8,15]. The stress-strain-temperature curves for concrete in compression and tension were based on the reduction factors given in BSEN1992-1-2[11] for calcareous aggregate and siliceous aggregate. The specific heat and thermal conductivity were also calculated according to BSEN1992-1-2[11], with the measured moisture content considered in the calculation of the specific heat of concrete. The measured stress-strain curve for the tendon at ambient temperature[15] was used to calculate the stress-strain curves at elevated temperatures following the reduction factors given in BSEN1992-1-2[11]. Similar curves were used for the anchorages with material properties at ambient temperature conforming to BS 4447[19]. A linear thermal expansion coefficient of 8.1×10^{-6} per ^{o}C was used for the concrete with Limestone aggregate based on measurements by Ndon et al.[20] and a linear thermal expansion coefficient of 13.2×10^{-6} per ^{o}C was used for the concrete with Thames Gravel based on measured values given by the Building Research Board[21]. The modelling results obtained using the measured and specified[11] thermal expansion coefficients were compared. Further details regarding the modelling in fire could be found in Ellobody and Bailey[22].

3.1 Verification of finite element models

At ambient temperature, the load-deflection behaviour, deformed shape at failure, stresses in the tendons and failure modes obtained from the finite element analysis for the unbonded slabs T1 and T2 were compared with the experimental results[15]. Generally good agreement was achieved. The model was extended to study the behaviour of the bonded slabs. Figs. 4a and 4b show the load-central deflection curves for Slabs TB1 and TB2, respectively. It can be seen that generally good agreement was achieved between experimental and numerical results. The failure load observed experimentally for Test TB1 was 215.8kN, at a central deflection of 111.7mm, compared to 212.5kN and 105mm obtained from the model. The failure load predicted using the model was 2% lower than that observed from the Test TB1. The failure load observed experimentally for Test TB2

was 187.9kN at a central deflection of 107.4mm, compared with 203.9kN and 108.3mm obtained from the model. The failure load predicted using the model was 9% higher than that observed in the Test TB2.

Under fire conditions, to indicate the accuracy of the thermal modelling, the predicted temperatures at the hot surface (HS), the tendon (T), the mid-surface (MS) and the cold surface (CS) for the bonded Slab Test TB3 is shown in Fig. 6a in comparison with test results. Similar accuracy was obtained when the model was compared against the other fire tests. The time-central deflection curves obtained from the tests and the finite element analysis were also compared for all the unbonded and bonded tests. Fig. 9a shows the central deflection-time curves for Tests T3 and T5 using the measured thermal expansion coefficients and that presented in BSEN1992-1-2[11] for normal weight concrete. For Test T3, the central deflection observed experimentally was 62mm at 129 minutes from the start of heating, compared with 67mm at 130 minutes and 76mm at 112 minutes obtained from the model using the measured and the code thermal expansion coefficients. Similarly the central deflection-time curves are plotted for the Test T5 in Fig. 9a. The central deflection experimentally was 85mm at 72 minutes from the start of heating, compared with 85mm at 71 minutes and 115mm at 43.5 minutes obtained from the model using the measured and the code thermal expansion coefficients respectively. It can be shown that the time-deflection behaviour predicted from the model using the EC code coefficients of thermal expansion is inaccurate compared with that predicted using the measured thermal expansion coefficients. Hence, the measured thermal expansion coefficients were used in simulating the remaining fire tests as well as carrying out the parametric studies. The axial deformations were also compared experimentally and numerically for all the free unbonded and bonded tests. The axial deformations for the bonded slabs TB3 and TB5 were compared experimentally and numerically, as an example in Fig. 9b. Generally good agreement was achieved. The maximum axial deformations were 4.3 and 7.2mm at the mid-height of the slabs TB3 and TB5 recorded experimentally, respectively, compared with 4.1 and 7.5mm numerically.

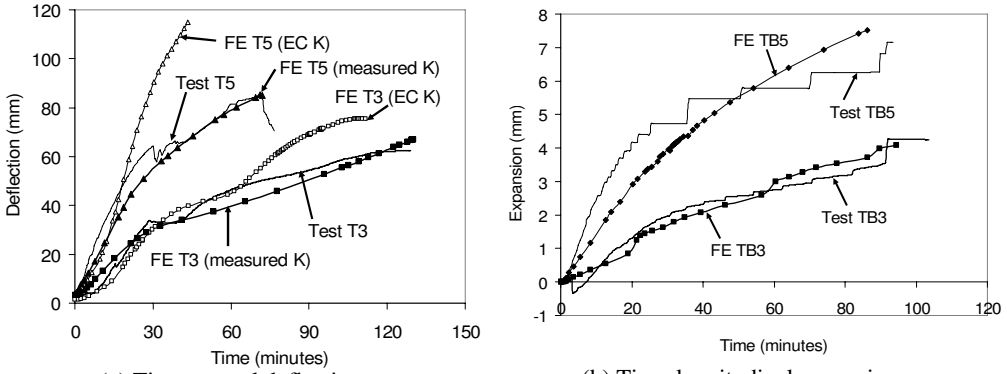

(a) Time-central deflection curves (b) Time-longitudinal expansion curves

Fig. 9. Comparison between test and finite element results

The stresses in the tendons were predicted from the finite element analysis for all the unbonded and bonded slabs. The measured strains were used to predict the stresses in the tendons adopting the reduction factors given in the BSEN1992-1-2[11]. As an example,

the stresses predicted numerically were compared with those obtained experimentally for Slab TB3, as shown in Fig. 6b. Generally good agreement was achieved.

4. PARAMETRIC STUDIES

The verified finite element models were used to investigate the effects of the change in the position of restraint over the slab's depth, load ratio and aggregate type on the structural behaviour of the post-tensioned one-way concrete slabs in fire.

Test T4 was analysed with different height positions for the line of longitudinal restraint. The restraint position was taken at a height of 0.17h, 0.34h, and 0.5h from the bottom of the slab, where h is the overall depth of the slab. The longitudinal restraint was assumed to be ideally rigid along the width of the slab. The central deflection-time relationships were plotted as in Fig. 9a. It can be seen that the lower the restraint position the lower the overall vertical displacement of the slab. This is due to the thrust from the restraint position, as the slab tries to expand, creating a restraining moment at the ends which reduces the central vertical displacement. The lower the line of thrust, the higher the restraining moment. The fire resistance period from the model ranged from 31 minutes to 85 minutes showing clearly the significant effect of the position of the restraint to thermal expansion. Interestingly, although the vertical displacement was smaller as the position of restraint tended towards the bottom of the slab, the fire resistance period was also lower. This was due to localised failure in the proximity of the restraint being induced earlier as the restraint position tended towards the bottom of the slab.

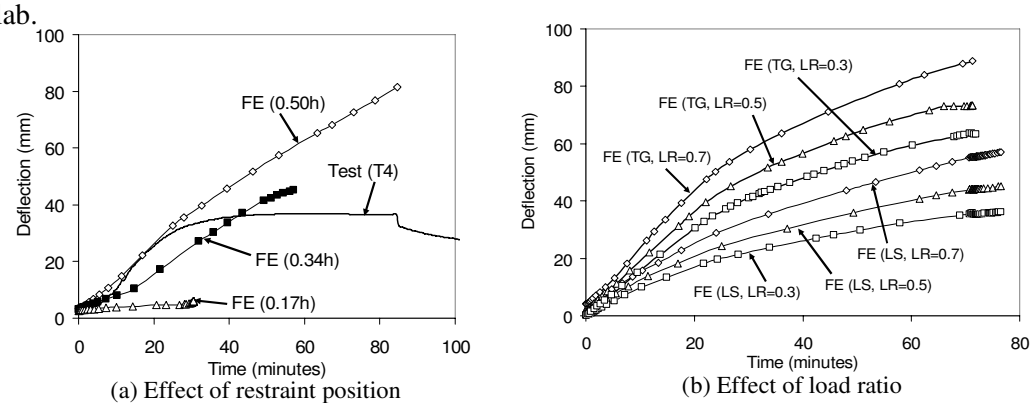

(a) Effect of restraint position (b) Effect of load ratio

Fig. 9. Results of the parametric study

The effect of the load ratio on the post-tensioned slabs with limestone and Thames gravel aggregates was investigated by modelling slabs with different load ratios 0.3, 0.5 and 0.7. All the modelled slabs were unbonded with identical dimensions, material properties and boundary conditions as Slab T5 (free to expand). It can be seen, from Fig. 9b, that the greater the load ratio the greater the vertical deflection of the slab for a given time. Of interest is the fact that all the slabs with Limestone aggregate failed at the same time (77mins) irrespective of the load ratio. Previous experience has shown that the increase in the load ratio generally results in a decrease in the fire resistance. However, for the post-tensioned concrete slabs investigated in this study, failure in the model was initiated due to a crack occurring directly inline and parallel to the tendons.

From the study presented here it can be concluded that the splitting mode of failure is not affected by the applied static load. Similar conclusions can be drawn from the slabs with Thames gravel as shown in Fig. 9b.

5. CONCLUSIONS

Sixteen tests have been carried out, four at ambient temperature and twelve at elevated temperatures, on unbonded and bonded post-tensioned concrete slabs. The fire tests showed that the behaviour of the slabs at elevated temperature is governed by the type of aggregate used in the concrete. The slab with Thames Gravel aggregate had higher vertical and horizontal displacements, compared to an equivalent slab with Limestone aggregate. The slabs which were restrained against thermal expansion had similar vertical displacements to the equivalent unrestrained slabs in the initial part of the tests but then maintained a fairly constant displacement as the temperature continued to rise.

A nonlinear finite element model, for the analysis of unbonded and bonded post-tensioned concrete slabs at elevated temperatures has been developed and presented. The temperature distribution throughout the slab, time-deflection behaviour, time-longitudinal expansion, time-stress behaviour of the tendon, fire resistance and the failure modes have been predicted by the model and verified against experimental results. The comparison between the experimental and numerical results has shown that the model can accurately predict the behaviour of the unbonded and bonded post-tensioned one-way concrete slabs under fire conditions. The study has shown that the coefficients of thermal expansion currently used in EN1992-1-2 for calcareous and siliceous concrete are inaccurate. The developed model was used to investigate the effects on the global structural behaviour due to the change in the aggregate type, load ratio and boundary conditions. It is also shown that the central deflection is increased with the increase of the load ratio but the fire resistance time remains the same, due to the mode of failure comprising cracking (splitting) above the tendons not being influenced by the magnitude of load.

Acknowledgements

The work in this paper was conducted at the University of Manchester, under the direction of Professor Bailey, and was funded by EPSRC (Grant No. EP/D034477/1). The authors are grateful to Tarmac Ltd. for supplying the concrete, Bridon Ltd. for supplying the tendons, CCL Ltd. for supplying the dead and live anchorages, General Technologies Inc. for supplying the plastic ducts, Wells Ltd. for supplying the metallic ducts and Pennine Grouting Ltd. for supplying the grouting equipment. The authors are also grateful to Mr Paul Nedwell, for his continuous support and useful discussions and the support provided by the technical staff at The University of Manchester.

References

[1] Laboratories, U. Report on unbonded post-tensioned prestressed, reinforced concrete flat plate floor with expanded shale aggregate. PCI Journal, 45-56, April 1968.

[2] Gustaferro, A.H. Fire resistance of post-tensioned structures. PCI Journal, 38-63, March/April 1973.
[3] Herberghen, P.V. and Damme, M.V. Fire resistance of post-tensioned continuous flat floor slabs with unbonded tendons. Journal of Fédération Internationale de la Précontrainte, 3-11, 1983/1984.
[4] Lukkunaprasit, P. Unbonded post-tensioned concrete flat plates under 5-hours of fire. FIP-XIth International Congress on Prestressed Concrete, S61-S64, Hamburg, Germany, 4-9, June, 1990.
[5] Troxell, G.E. Prestressed lift slabs withstand fire. American Society of Civil Engineers, ASCE, 64-66, September, 1965.
[6] Sarkkinen, D. Fire damaged post-tensioned slabs. Structural Forensics, 32-34, 2006.
[7] Lee, D.Y.C. and Bailey, C.G. The behaviour of post-tensioned floor slabs under fire conditions. International Technical Congress, Fire Safety in Tall Buildings, Universidad de Cantabria, Santander, Spain, 183-201, October, 2006.
[8] Ellobody, E. and Bailey, C.G. Experimental and numerical investigation of post-tensioned unbonded concrete slabs in fire. Interflam 2007, Interscience Communications Ltd., London University, Royal Holloway College, London, , pp. 617-628, 3-5 September, 2007.
[9] ABAQUS Standard/Explicit User's Manual. Hibbit, Karlsson and Sorensen, Inc. Vol. 1, 2 and 3, Version 6.6-1, USA, 2008.
[10] BS 8110-2. Structural use of concrete. Code of Practice for Special Circumstances. British Standards Institution, London, 1985.
[11] Eurocode 2. Design of concrete structures. General rules. Structural fire design (together with United Kingdom National Application Document). British Standards Institution, BSEN 1992-1-2,London, 1992.
[12] BS 8110-1. Structural use of concrete. Code of Practice for Design and Construction. British Standards Institution, London, 1997.
[13] Technical Report 43. Post-tensioned concrete floors: Design handbook. Concrete Society, Surrey, U.K., 2005.
[14] BS EN 447. Grout for prestressing tendons – Basic requirements. British Standards Institution, London, 2007.
[15] Ellobody, E. and Bailey, C.G. Behaviour of unbonded post-tensioned concrete slabs. Advances in Structural Engineering, Vol. 11, No. 1, pp. 107-120, 2008.
[16] Eurocode 1. Actions on structures. General actions. Actions on structures exposed to fire. British Standards Institution, BSEN 1991-1-2,London, 2002.
[17] Bailey, C.G. and Ellobody, E. Fire tests on unbonded post-tensioned concrete slabs. Magazine of Concrete Research, In press, 2008.
[18] Bailey, C.G. and Ellobody, E. Bonded post-tensioned one-way concrete slab fire tests. 2008.
[19] BS 4447. Specification for the performance of prestressing anchorages for post-tensioned construction. British Standards institution, London, 1999.
[20] Ndon, U.J., and Bergeson, K.L. Thermal expansion of concretes: case study in Iowa. Journal of Materials in Civil Engineering, ASCE, 7(4), 246-251, 1995.
[21] Building Research Board. The thermal expansion of concrete. National Building Studies, Technical paper, No. 7, HMSO, 1950.
[22] Ellobody, E. and Bailey, C.G. Modelling of unbonded post-tensioned concrete slabs under fire conditions. Fire Safety Journal, Under Review, 2008.

EFFECT OF ASPECT RATIO ON FIRE RESISTANCE OF HOLLOW CORE CONCRETE FLOORS

JEREMY CHANG[1], PETER J. MOSS[2], RAJESH P. DHAKAL[3] and ANDREW H. BUCHANAN[4]

ABSTRACT

Previous studies have shown that the fire performance of hollowcore units is significantly affected by the end support conditions, but it has not been clear how the fire resistance of the overall floor system can be improved by providing side supports. The previous studies used beam grillage and shell elements to separately model the hollowcore units and the topping concrete slab using the platform of the non-linear finite element program SAFIR. The modelling method required a lot of computational resources and is not ideal to model a large floor area. This paper describes the effect of the side supports and the aspect ratio of the floor on the predicted fire resistance. It also compares the efficiencies of shell elements and short beam elements for finite element modelling of the topping concrete in fire conditions. The results show that integrating the topping concrete slab into the beam grillages reduces the complexity of the model and also provides satisfactory results. Side supports can increase the fire performance of hollowcore floor slabs provided that the spacing of the side supports does not greatly exceed the span length.

[1] Assistant Lecturer, Department of Civil and Natural Resources Engineering, University of Canterbury, Private Bag 4800, Christchurch, New Zealand,
email: jeremyjchang@gmail.com
[2] Associate Professor, Department of Civil and Natural Resources Engineering, University of Canterbury, NZ
email: peter.moss@canterbury.ac.nz
[3] Senior Lecturer, Department of Civil and Natural Resources Engineering, University of Canterbury, NZ
email: rajesh.dhakal@canterbury.ac.nz
[4] Professor, Department of Civil and Natural Resources Engineering, University of Canterbury, NZ
email: andy.buchanan@canterbury.ac.nz

1. INTRODUCTION

Precast, prestressed hollowcore concrete floors are very popular in multi-storey buildings because of their excellent structural performance in ambient conditions, high quality control and low on-site labour costs. Hollowcore concrete floors are designed as one-way slab systems, with the units sitting side-by-side, spanning between supporting walls or beams. Most hollowcore concrete floors have in-situ reinforced concrete topping. Structural behaviour of hollowcore concrete floors is dominated by action parallel to the units and their prestressing strands. Two-way action can sometimes occur in such slab systems, resulting from transverse structural behaviour of the topping concrete, depending on the vertical supports parallel to the hollowcore units[1-4].

The fire resistance of hollowcore concrete slab has not been outlined specifically in Eurocode 2[5]. However, Eurocode 2 provides separate measures for the fire resistance of flat slabs and solid slabs. The tabulated data in Eurocode 2 relate the fire resistance of a flat slab or of a one way solid slab to the slab thickness and the axis distance of the reinforcements to the surface; they also associate the fire resistance of a two-way solid slab to the aspect ratio which serves as an additional parameter. The British Standard BS EN1168 "Precast Concrete Products – Hollow Core Slabs"[7] suggests that the fire resistance of hollowcore concrete floors follows the table for flat slabs which does not include the effect of the vertical supports parallel to the hollowcore units. The New Zealand Standard NZS 3101 "The Design of Concrete Structures"[8], however, suggests the fire resistance of hollowcore concrete floors follows the table for solid slabs, which considers the influence of the two-way effect.

In the tabulated data from Eurocode 2, the fire resistance of a two-way supported slab can be affected by the aspect ratio when the ratio of the longer span to the shorter span is less than 2. Nevertheless, whether the same criteria are appropriate for the hollowcore concrete floor is still unanswered, and to the authors' knowledge, currently there are no such studies available, either numerical or experimental, to justify these criteria.

Since conducting experiments to study the effect of aspect ratio of hollowcore floors is very expensive, and also because previous study[4] has successfully predicted the fire performance of hollowcore concrete floor systems with different end and side connections using the non-linear finite element program SAFIR[6], numerical modelling of hollowcore concrete floor systems is carried out to study the effect of aspect ratio on the fire performance of hollowcore concrete slabs.

2. MODELLING OF HOLLOWCORE SLABS IN SAFIR

The analytical simulations were carried out using SAFIR, a non-linear finite element analysis program which is able to carry out both structural and thermal analysis, with thermal and mechanical properties from Eurocodes 2 and 3[9] integrated into the program. Chang et al.[4] have showed that SAFIR can successfully predict the performance of hollowcore floor systems in fire by using a grillage of 3D beam elements to simulate the hollowcore units and a layer of shell elements to represent the topping concrete slab which covers the hollowcore units and connects the hollowcore units to each other and to the surrounding structural members.

In the beam grillages, the longitudinal beams run in the direction of the span and represent the webs and flanges of the hollowcore units. The prestressing effect is considered in the longitudinal beam by SAFIR through calculating the stress equilibrium in the first time step of the structural analysis. The transverse beams in the grillage model both the top and bottom flanges and run in the direction across the hollowcore unit. These transverse beams

are to capture the affect of thermal expansion in the transverse direction of each hollowcore unit. In thermal analysis the topping is included in both longitudinal and transverse beams to calculate the thermal gradient correctly, but as the topping is simulated using shell elements in structural analysis, the section representing the topping in beam elements in the thermal analysis is taken as an arbitrary material without strength or stiffness. In the shell elements, the reinforcing bars in the topping slab are simulated as layers of smeared steel section across the shell element with each layer exhibiting a uniaxial behaviour.

This modelling scheme does not consider shear and anchorage failures. As perfect bond between the concrete and the reinforcing steel is assumed for both beam and shell elements, as well as between the topping slab (shell elements) and the hollowcore units, bond failures are also not accounted for. It also does not consider spalling or the vertical tensile stresses in the web of hollowcore units. Nevertheless, the model considers the prestressing effect, the thermal strains as well as the mechanical stresses induced by incompatible thermal strains in both lateral and longitudinal directions, and the continuity between the hollowcore units which subsequently allows the model to take account of the effects of the end and side supports. Most importantly, the results from this modelling method showed good agreement with experimental results available in literature[4].

The model developed in the previous study worked well for small subassemblies. However, although the sections representing the topping in the beam elements needed in the thermal analysis (Fig. 1) do not contribute to the performance of the slab, they are modelled as non-load bearing material and still consume a lot of computer resources in the structural analysis. As a result, the model becomes too complicated for SAFIR when analysing subassemblies containing more than 4 parallel hollowcore units. Therefore, a new model is needed in order to study the effect of aspect ratio on the fire performance of hollowcore concrete floor systems.

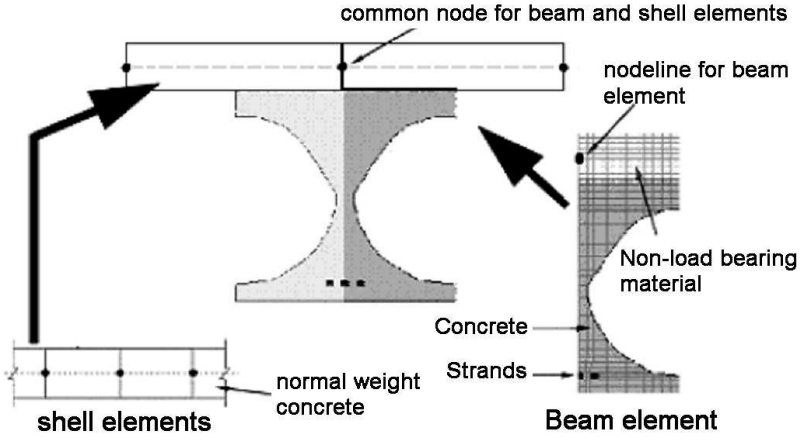

Fig. 1 –Discretisation of the cross section of hollowcore unit in the original method

It was found during the development of the original model that, when modelling the floor slab with only one hollowcore unit, simulating the topping slab as part of the beam elements or separately by the shell elements gave the same result[10]. Hence, instead of giving the section representing the topping in the beam elements zero strength and using shell elements to simulate the topping, the topping can be modelled as part of the beam elements and the shell elements can be removed from the model completely. The schematic drawings of the two modelling methods are shown in Fig. 2. This new modelling method need to be

validated for floors with more than one hollowcore unit, as problems may arise when modelling the topping slab connecting two parallel hollowcore units together.

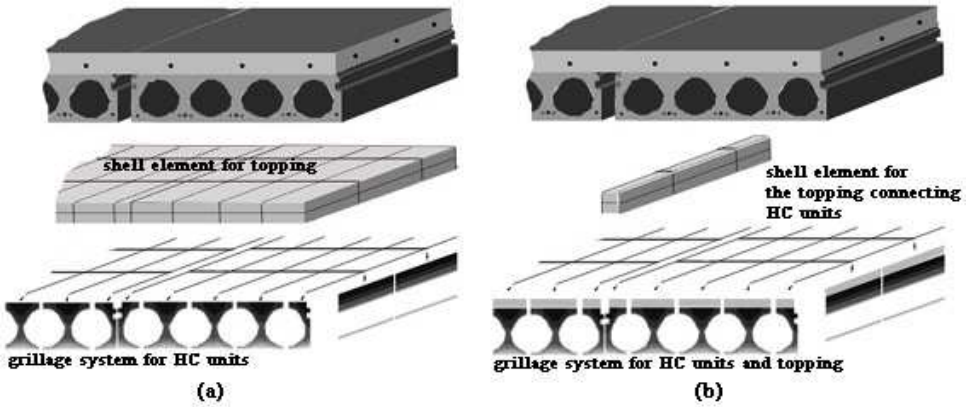

Fig. 2 –Schematic drawing for the (a) original (b) new method to model hollowcore floor systems.

3. VALIDATION OF THE NEW COMPUTER MODEL FOR SIMULATING HOLLOWCORE SLABS

In the first step of the validation, the experimental results of from Universities of Ghent and Liege carried out in 1998 were compared to the simulation results calculated from both the original and new modelling method. Detailed descriptions and the explanations of the designs are given in the test report[11]. The modelled test (Test 1 in the test reports) comprised two independent floor slabs of 2.4m width made of two HC units, spanning 3m and supported on three beams as shown in Figure 3(a). The floor was made of 200mm hollowcore unit (SP200Ergon) with 50mm reinforced topping slab and was exposed to 2 hours of ISO834 standard fire from underneath. A line load of 100kN was applied at the middle of each of the two spans, which makes the load ratio to be 37%. After two hours of fire exposure, extra load was applied to check the remaining load capacity. Due to symmetry, only half of the floor was simulated (one 1.2m wide floor span of 3m) as shown in Fig. 3(b).

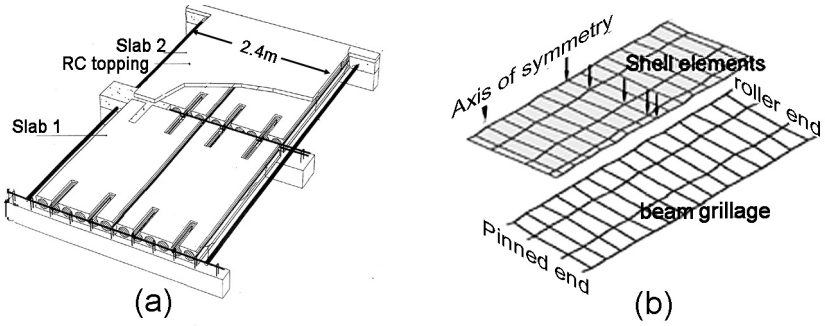

Fig. 3 – a) Layout (b) illustration of the simulation model using the original method for the test in Universities of Ghent and Liege[11]

In the modelled test, the compressive strength of the concrete in the hollowcore units was 45MPa, and the strand strength was 1.85GPa. The level of prestressing was unspecified in the report and was assumed to be 75% of the strand strength in the simulations, which is

the level usually used in practice. The slab is simulated using both the original method, which has the shell elements representing the topping slab, and the new method, where the topping slab is included in the beam grillage. The end supports of the grillage are assumed to be fixed in the simulations, while in the experiment they had a limited freedom for rotation and displacement. The results are shown in Fig. 4. As explained in the previous study, the difference between the simulated results and the actual data is due to the simulation model not being able to predict the shear displacement or failure, as shear effects are not included in the computer software used, and in the experiment shear cracking was observed as early as 7 minutes into the fire test and at the end the slab experienced shear failure. Nevertheless, the focus here is the comparison between the two modelling methods, and it is obvious that the new simulation method provides almost identical results as the original method. This shows that it does not make much difference whether the topping is included in the beam grillage or modelled separately using shell elements in the structural analysis when simulating slabs with one or two hollowcore units and no side supports.

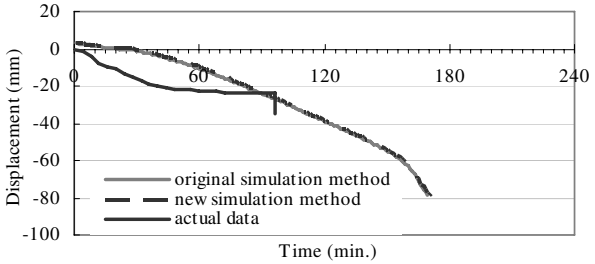

Fig. 4 –Comparison of simulation results and actual data from the test in Universities of Ghent and Liege

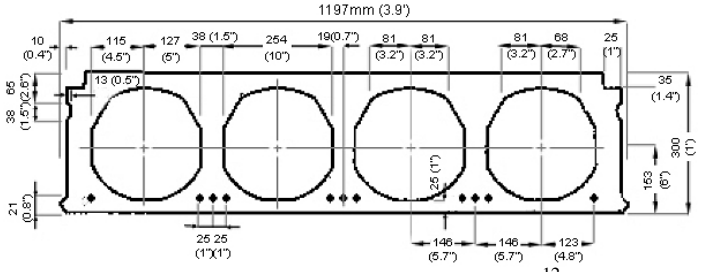

Fig. 5 – Cross section of 300Dycore[12]

The second part of the validation process compares the results of simulating previously modelled subassemblies. The structure comprises a floor made from 300mm thick hollowcore units (300Dycore) with a 75mm reinforced topping. The cross section of the 300Dycore is shown in Fig. 5 and its properties are shown in Table 1. The floor is 12.2m long and 10.2m wide, which includes eight hollowcore units as shown in Fig. 6(a) in the case where the last unit is adjacent to the side beams, or seven units as shown in Fig. 6(b) in the case where there is a concrete infill panel between the last unit and the side beams. The concrete infill panel is suggested in the New Zealand Concrete Standard (NZS 3101:2006) for seismic resistances. The end and side beams of the structure are 750 mm deep by 400 mm wide with three 25 mm diameter bars at both the top and bottom. The hollowcore units simply sit on the end beams, and the floor is connected to the end and side beams via the topping slab. There are six 3.5m high, 750 by 750mm square columns in the subassembly spaced 5.1m apart along the width of the structure as shown in Fig. 6. The beams are connected to the columns at mid-height. The columns are restrained against displacement at both the top and

bottom ends. The slabs and beams were exposed to 3 hours of the ISO 834 standard fire from below, while the columns were fully protected and assumed to remain cool. The applied load on the slab is 8.0kPa, which gives a load ratio in fire of 40%.

Table 1 – Properties of the hollowcore floor system

300Dycore	
Cross sectional area	0.1606 m^2
Self weight	3.20 kPa
Compressive strength	42 MPa
Prestressing strands	
Type	Stress relieved 7-wire strand
Strength	1.87 GPa
Prestressing level	70%
Cross sectional area per strand	112 mm^2
Reinforced concrete topping slab	
Compressive strength of concrete	25 MPa
Strength of reinforcement	450 MPa

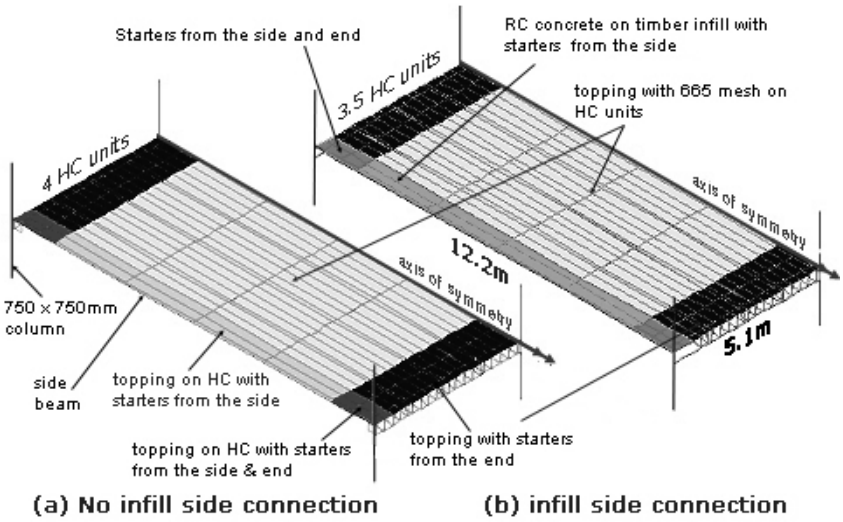

Fig. 6 –Simulation model used in the second step of validation

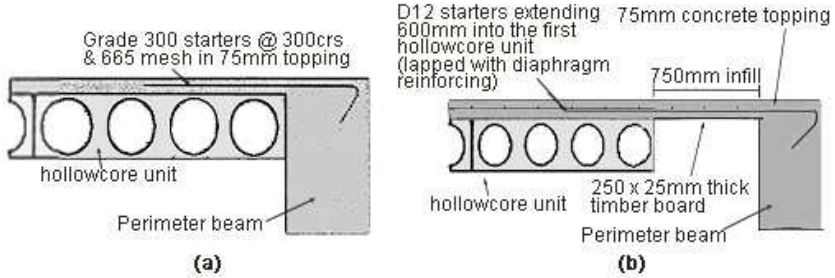

Fig. 7 –Modelled slab-side beam connections (a) without infill (b) with infill

There are three types of side supports considered in this set of validation analyses. The first scenario has no side beams but has restraint against lateral displacement. This represents a slab restrained by the surrounding floor slabs as a portion of a bigger floor system. The other two scenarios with side beams are shown in Fig. 7. The "no infill" side connection scenario (Fig. 7(a)) has the last hollowcore unit immediately adjacent to the side beam. The "infill" side connection scenario (Fig. 7(b)) has a cast-in situ reinforced concrete infill slab between the last hollowcore unit and the side beam to overcome the incompatibility between the displacement of the side beams and the slabs during earthquakes as suggested by NZS3101:2006.

Two simulation methods were examined. The original method (Method I) has the topping slab modelled using a layer of shell elements in the structural analysis (Fig. 2(a)); in Method II the topping slab between the hollowcore units and connecting the hollowcore units to the end beams is modelled using shell elements, but that on top of the hollowcore units is modelled as part of the beam grillage (Fig. 2(b)). Furthermore, the topping slab connecting the hollowcore units to the side beam is modelled using shell elements in Method I and beam elements in Method II.

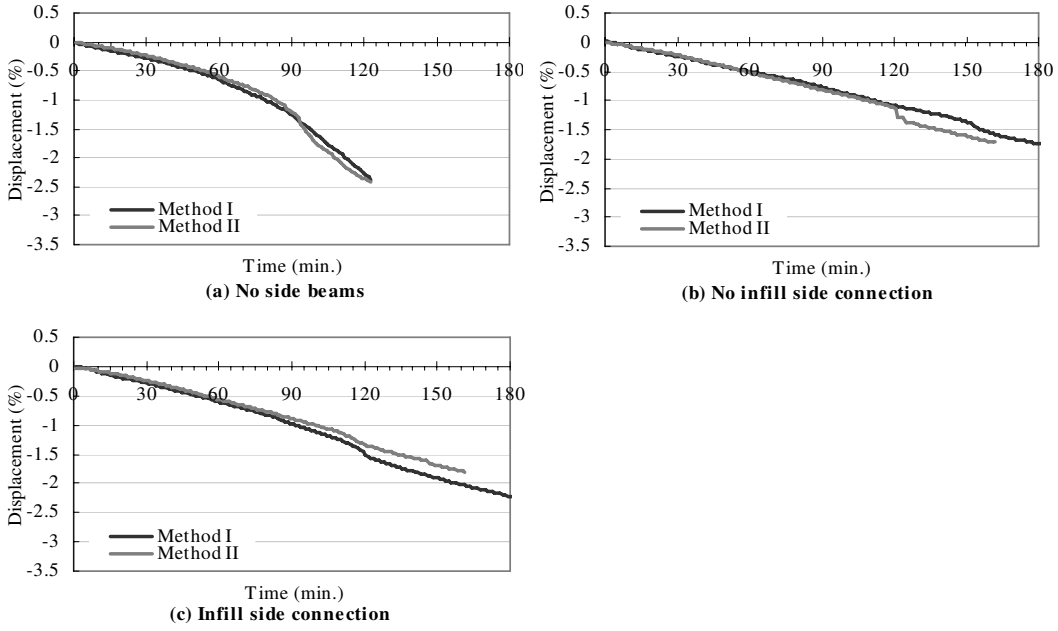

Fig. 8 –Comparison of analysis results of a subassembly with different side supports simulated using two different modelling methods

The vertical deflections from the two simulation methods at the units closest to the centre, where the maximum deflection occurred, are shown in Fig. 8. The deflections are expressed in relation to the span length. It is evident that the results from the two simulation methods are very similar, and Method II can be used to replace Method I. Because Method II requires fewer computational resources and save simulation time by up to 30%, it can be used to model larger structures. The simulations using Method II terminate earlier in the cases with side beams, as in the calculation the stresses are localised in the few remaining shell elements and consequently making stress calculation in the shell elements, especially the ones at the corner, more prone to numerical errors. Nevertheless, because the simulations can be stopped by cracking of shell elements, the stopping time of the simulations does not indicate failure

unless supported by other evidence in the output files, such as yielding of the prestressing strands. As the aim of using computer simulations is to carry out virtual ISO 83416 standard fire tests on the hollowcore floor systems through analysis, the failure criterion of the slab should be taken as either the collapse of the slab, or the time when the maximum deflection exceeds 1/30 of the span length, as in a standard fire test.

4. EFFECT OF ASPECT RATIOS TO THE OVERALL PERFORMANCE IN FIRE

Previous studies have shown that side supports are beneficial to hollowcore concrete floor systems which are normally designed as one-way slabs under cold conditions. To study the extent of the benefit resulting from the side supports, several subassemblies with different floor aspect ratios and three different side support conditions are investigated as shown in Table 2. The subassemblies are the same as those used in the second step of the validation process except the length and width of the floor. The end and side beams as well as the floor were exposed to the ISO fire from underneath, while the columns were assumed to remain cool throughout the fire. The columns are spaced every 5m along the width in the cases where the overall width is 5m or 10m, and every 6m in the other cases. Fig. 9 shows a typical modelled subassembly.

Table 2 – Studied aspect ratios

	Span	Width	Aspect ratio	FRR as 2-way solid slab in Table 5.8, EC2	FRR as flat slab in Table 5.9, EC2
Comparison 1	12m	5m	0.4	60	60
	12m	10m	0.8	120	60
	12m	15m	1.3	120	60
	12m	20m	1.7	90	60
Comparison 2	18m	10m	0.6	90	60
	15m	10m	0.7	120	60
	12m	10m	0.8	120	60
	9m	10m	1.1	120	60

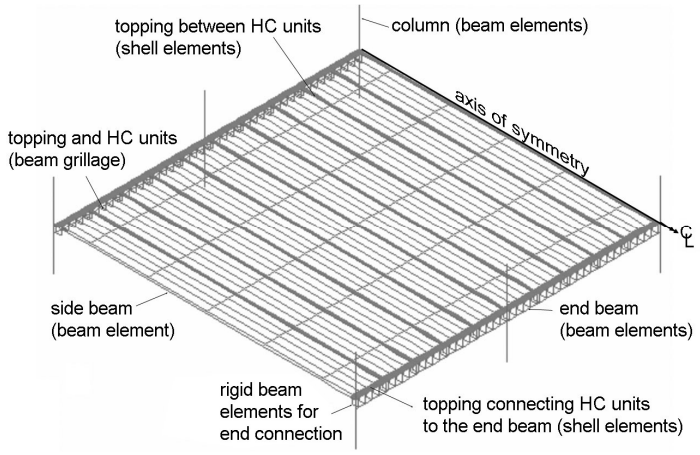

Fig. 9 –Simulation model of the 12m long 20m wide hollowcore floor system with no-infill connection to the side beams

In the tabulated data of Eurocode 2, the benefit of the side supports to a solid slab diminishes when the ratio of the longer side to the shorter side exceeds 1:2, and becomes more significant when the ratio is smaller than 1:1.5. From this study two sets of comparison can be drawn. Comparison 1 fixes the span length to 12m and changes the width of the floor to study the affect of the side supports. Comparison 2 fixes the width to 10m and varies the span length to compare whether the tabulated data of Eurocode 2 for solid slab is applicable to hollowcore floor systems.

Fig. 10 shows the maximum vertical displacement in the slab (at the centre of the slab in the bay farthest from the sides) from Comparison 1, with the deflections expressed as a ratio of the span length. Theoretically, without side beams the width of the subassemblies should not influence the performance of the slab and this is reflected in Fig. 10 (a). Because more elements are included in the model it is more likely for the simulation to encounter numerical errors, which subsequently causes the simulation to stop before reaching failure. Therefore, the simulations for wider slabs stopped earlier than for the 10m wide slab. Fig. 10(b) shows that when the side beams are included in the model, and the closer spaced they are, the less deformation the slab is going to encounter.

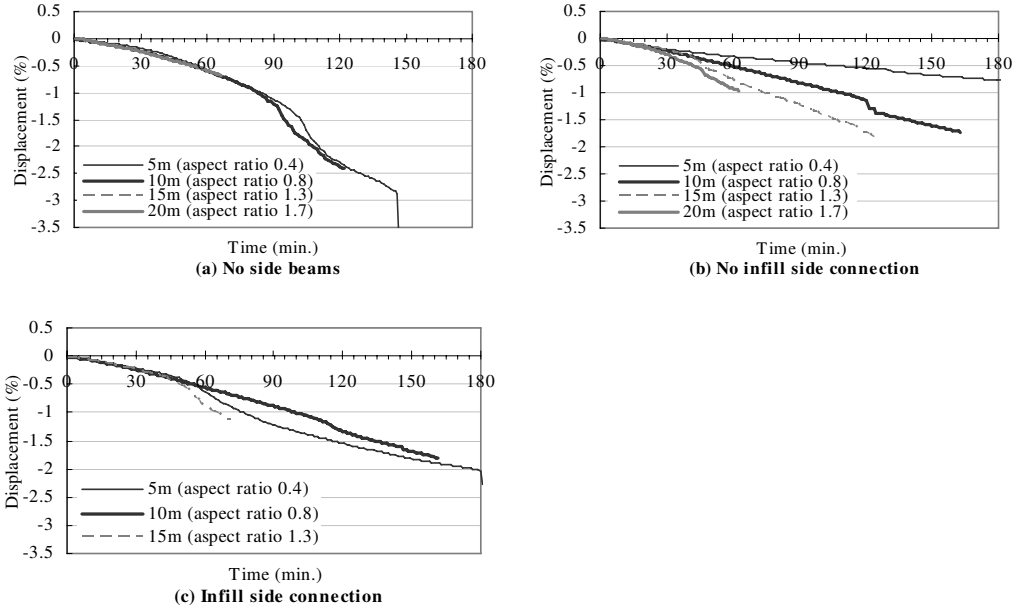

Fig. 10 –Maximum vertical displacement in fire of 12m span subassemblies and various widths with (a) no side beams (b) side beams, connections with no infill (c) side beams, with infill connection

Comparing Fig. 10(b) to 10(a) shows that the presence of side beams slightly aggravated the deflection in the cases of 15m or 20m floor width. Fig. 11 shows the shape of the deformed slab in the slab with two side beams 20m apart. Because the top and the bottom ends of the columns are fixed in position, the end beams have more restraint against horizontal displacement or rotation near the columns (point B) than at mid-span (point A). The increase in horizontal restraint from point A to point B increases significantly when side beams are provided, as shown in Fig. 12(a).

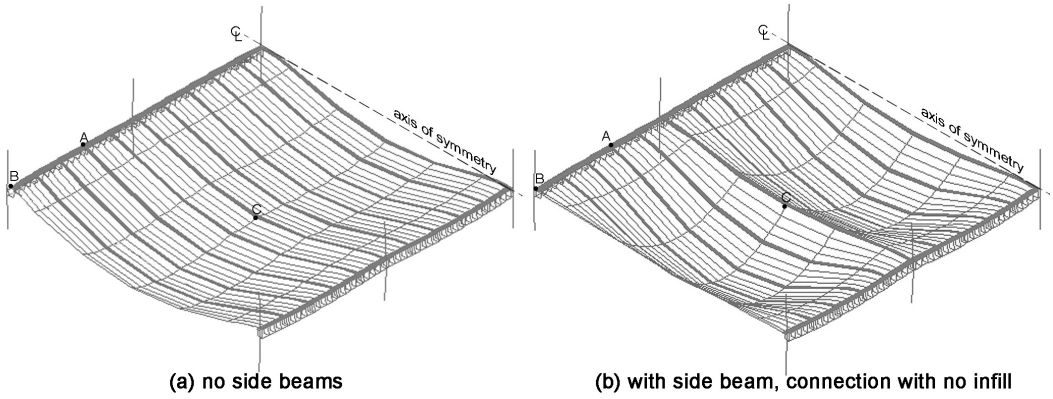

Fig. 11 –Deflected shape of the 12m long 20m wide hollowcore floor system (a) without side beams (b) with side beams after 1 hour of fire exposure (deformation exaggerated 20 times)

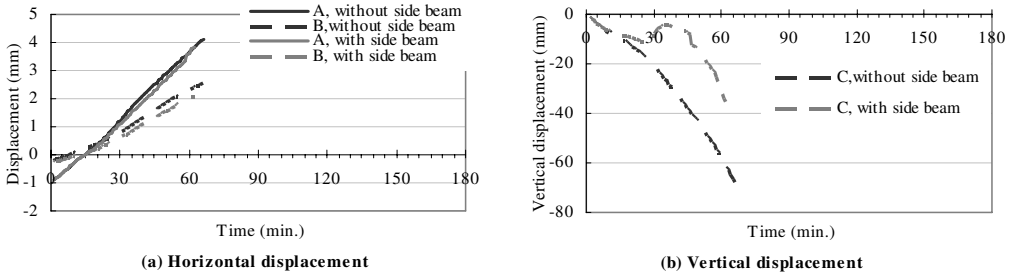

Fig. 12 –Longitudinal displacements of points A and B; and vertical displacement of point C of subassemblies with 12m span and various widths in fire

Fig. 12(b) shows the vertical mid-span displacement directly between the columns (point C in Fig. 11) for the two cases with and without side beams. It can be seen that the additional restraint from the side beams causes much smaller vertical deflections at point C, with the slab briefly rising upwards after about 30 minutes of fire exposure, before increasing again.

In the cases with wide slabs the large curvature near the side beam supports causes a concentration of stress in the shell elements at the corner of the slab, which consequently causes the program to stop. Regardless of the stopping time of the simulation, the results show a clear benefit of providing supports parallel to the span direction, with spacing equal to or smaller than the span length. It also shows that providing side supports with spacing greater than the span length has little benefit.

The results from Comparison 2 are shown in Fig. 13, again with the maximum vertical displacement in the slab expressed as a ratio to the span length. The displacements of the slabs with the infill side connection initially are similar to those with no side beams but became relatively smaller after having further exposure to the fire. Nevertheless, they are always greater than those with no-infill side connection. Fig. 13(a) shows excellent performance for all cases. Fig. 13(b) (aspect ratio 1:0.8) shows the side beams giving much smaller deflections than no side beams after 60 minutes fire exposure. Similar results at much shorter times are seen in Fig. 13(c) and (d) for very long spans.

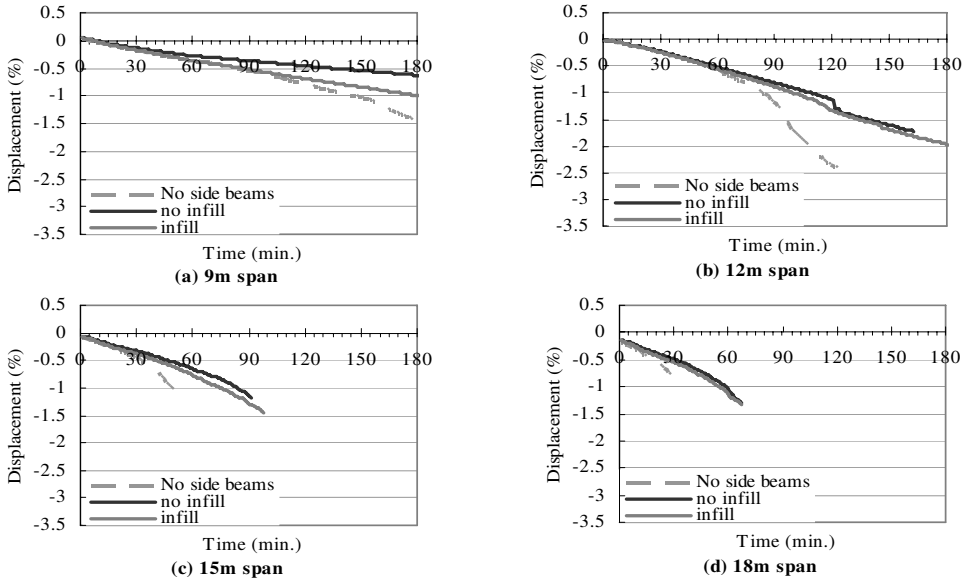

Fig. 13 –Maximum displacement at the midspan of the 10m wide subassemblies with various span lengths and side supports

Based on all the simulation results presented in this paper and in the previous study, it is shown that the performance of the hollowcore floor systems is dominated by the behaviour along the span. Therefore, it is not suitable for the tabulated data for two-way solid slabs in Eurocode 2 to be applied to hollowcore floor systems. Nevertheless, the simulation results showed the benefit of providing supports parallel to the span direction in fire, and it shows that to use the table for flat slabs in Eurocode 2 and ignore the effect of the vertical supports parallel to the hollowcore units is very conservative. To achieve a better performance of hollowcore floor systems in fire it is suggested to provide some side beams spaced as close as the span length of the units, regardless of the type of connection used between the side beams and the units adjacent to them. Because the hollowcore floor systems are usually designed under ambient conditions as one-way slabs and the side supports are ignored, these extra side beams are mainly to enhance the fire performance and they are also called “fire emergency beams”.

5. CONCLUSIONS

The performance of hollowcore concrete floor systems in fire depends on several factors. This paper investigates the influence of the width to floor span aspect ratio on the behaviour of the slab in fire. In order to conduct the investigation, a new version of the previously used model was proposed and validated. Unlike the previous model using shell elements to simulate the topping and beam grillage system to simulate the hollowcore units, the new model includes the topping slab as part of the beam grillage system and uses shell elements only for the area of topping slab where there are no hollowcore units underneath. This new model provides very similar results to the original model but requires less computer resources, therefore is more suitable to simulate large and complex structures.

Several subassemblies with different geometries were simulated to investigate the effect of the floor aspect ratio on the structural behaviour in fire. The results show that for

hollowcore floor systems it is not suitable to use the tabulated data for the two-way solid slab in Eurocode 2 as the table is too optimistic about the effect of the side supports when the aspect ratio is greater than 1:1.5. Using the table for flat slabs in Eurocode 2 as suggested by BS EN 1168, however, can be very conservative. The results also show that providing side supports such as "fire emergency beams" with spacing equal or less to the span length of the unit can increase the performance of the hollowcore concrete floor systems in fire.

6. REFERENCES

[1]. Fellinger, JHH. Shear and Anchorage Behaviour of Fire Exposed Hollowcore Slabs, DUP Science, the Netherlands, 2004
[2]. Fib. Résistance au Cisaillement de Dalles Alvéolées Précontraintes, Studiecommmissie SSTC, University of Liège, Belgium, 1998
[3]. BEF. Hollow Core Slabs and Fire – Documentation on Shear Capacity, Birch & Krogboe A/S, Denmark, 2005
[4]. Chang, J., Buchanan, AH, Dhakal, RP. & Moss, PJ, "Hollowcore concrete slab exposed to fire", Fire and Materials, Online ISSN: 1099-1018, 2008
[5]. EC2. Eurocode 2: Design of Concrete Structures. PrEN 1992-1-2: General rules – Structural fire design, Brussels: CEN; 2002.
[6]. Franssen, JM., Kodur, VKR. & Mason, J. User's Manual for SAFIR2001 Free: A Computer Program for Analysis of Structures at Elevated Temperature Conditions, University of Liège, Belgium, 2002
[7]. BSI, Precast Concrete Products – Hollow core Slabs, BS EN1168, British Standards Institution, London, 1995
[8]. SNZ, The Design of Concrete Structures, NZS 3101, Standards New Zealand, Wellington, 2006
[9]. EC3. Eurocode 3: Design of Steel Structures. PrEN 1993-1-2: General rules – Structural fire design. Brussels: CEN; 2002
[10]. Chang J. Computer Simulation of Hollowcore Concrete Floor systems Exposed to Fire. PhD Thesis, Christchurch: University of Canterbury; 2007
[11]. fib. Résistance au Cisaillement de Dalles Alvéolées Précontraintes. Belgium: Studiecommissie SSTC; 1998.
[12]. Firth Stresscrete & Stahlton Flooring, Precast Concrete Manual 2007, Firth Stresscrete, Porirua, 2007

THE INFLUENCE OF PRESSURE IN THE PORE SYSTEM ON FIRE SPALLING OF CONCRETE

ROBERT JANSSON[1] and LARS BOSTRÖM[2]

ABSTRACT

Recent results from fire tests on Self Compacting Concrete (SCC) have shown that the connection between pressure in the capillary pore system and fire spalling of concrete is not obvious[1]. This issue has been further investigated performing pressure measurement tests on SCC and a concrete designed for tunnel construction. In the tests conducted on SCC concrete data from exposure to the HC fire curve are presented. In the test series conducted on tunnelling concrete, pressure measurements were performed in concrete exposed to the standard fire exposure (EN1363-1) as well as the RWS fire exposure. In general, the highest pressures in the two test series were measured in the concretes that did not exhibit spalling during fire, i.e., in many cases in those concrete specimens containing polypropylene (PP) fibres. A conclusion from the test series is that pressure in the capillary system is not the driving force for spalling during fire exposure. However, the pressure is involved in the redistribution of moisture during fire exposure. As an alternative to the common theory of the spalling reduction function of PP-fibres as "pressure releasers", a new theory, based on the presence and movement of moisture, is put forward to explain the spalling reducing function of PP- fibres.

1. INTRODUTION

The physics behind fire spalling of concrete is not known in detail. In a thesis produced 1935 at the University of Braunschweig in Germany, Hasenjäger[4] summarised the available data at that time and concluded that fire spalling was primarily a result of:

- rapid heating of concrete,

[1] Project Manager, PhD Student, Fire Resistance, SP Technical Research Institute of Sweden, Fire Technology
email: robert.jansson@sp.se.
[2] Manager, Fire Resistance, SP Technical Research Institute of Sweden, Fire Technology
email: lars.bostrom@sp.se.

- exceeding of the tensile strength by one sided strain,
- rapid structure and volume change in the aggregate, and
- pressure from liberation of water vapour and gases from the aggregate and the cement paste.

As seen in the list above, Hasenjäger identified two types of stresses leading to the spalling phenomena: thermal stresses and pressure from moisture. The relative importance of these two factors has since been the subject of intense discussion in the scientific community[5-18]. Important to consider, when comparing different spalling theories, is whether the theory deals with one-side exposure of concrete or exposure from more then one side, such as the web of a beam. The mechanism of fire spalling depends on the type of exposure due to the fact that, e.g., in the case of exposure from more than one side all moisture must be released on one of the hot sides while in the case of single-sided exposure the moisture can be released from the cold side. This means that at some point in multiple-sided exposure no more moisture can be transported inwards, and the role of moisture in prompting spalling is probably amplified relative to that in single-sided exposure[8].

In the experiments described in this paper only one-sided fire exposure has been examined. During this type of test it is common in the later stages of the exposure, after more then 30-40 minutes, that some liquid water pours out of the non-fire exposed side of the test specimens, even for slabs as thick as 400 mm. Although the spalling process usually starts between 2 and 25 minutes depending of the severity of the fire, the fact that moisture is transported away from the fire exposed side indicates that moisture is not entirely restricted by the built up of a moisture clog. According to Harmathy[5], the highest moisture pressures will appear at the front of the moisture clog that has been formed by re-condensation of steam travelling inwards during fire exposure. If the moisture clog can move, the pressure will drop significantly in the high pressure zone. Clearly an experimental investigation of the pressure inside a fire-exposed concrete sample is necessary to resolve the role of moisture in fire spalling. The work presented in this paper continues the work presented at the previous Structures in Fire conference[1], and aims to obtain supporting evidence for the role of pressure in fire spalling.

2. EXPERIMENTAL METHOD

The pressure in the capillary system was measured using oil filled pipes in the fire exposed concrete. The same system was applied in the paper presented at the previous Structures in Fire[1] and is described in detail there. Thus, this paper contains only basic information concerning the applied methodology and no further discussion of alternative pressure measurement systems is given.

During the moulding of concrete, steel pipes with an inner diameter of 2 mm and wall thickness of 0.2 mm, were inserted. The end of the steel pipes, i.e., the pressure measurement point, was placed at different distances from the fire exposed surface of the test specimen with the other end of the pipes extending out of the non-fire exposed side. The exposed end of the tube was then attached to a pressure gauge, type P8AP/100bar from Hottinger Baldwin Messtechnik GmbH, using a T-junction, as shown in figure 1.

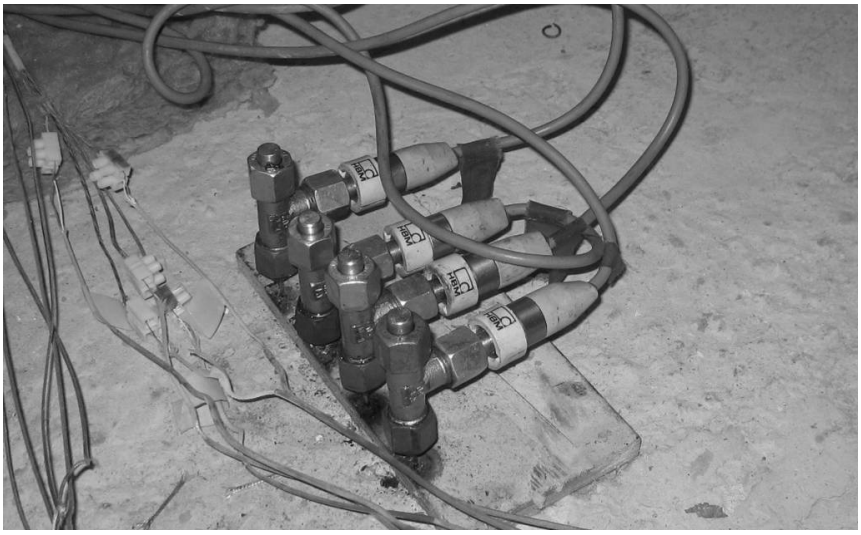

Fig. 1 – The oil filled pressure pipes, extending out of the sample cross-section, attached with T-junctions to the pressure gauges.

During moulding, the pipes were filled with thin welding bars to prevent cement paste from flowing into the pipes. Immediately prior to the fire test the welding bars were taken out and the pipes were filled with silicon oil, type Sil 300, produced by Haake. The pipes were filled by inserting a syringe containing the silicon oil and carefully filling the pipe from the measurement point to the top. This procedure ensured that no air bubbles were trapped inside the pipes. The whole T-junction connected to the pressure gauges was then filled with oil. The oil used expands during heating but this effect was deemed negligible. This was checked in a simple experiment where 5 cm of a plugged oil pipe was exposed to 200 ^{o}C, indicating that the thermal expansion is in an acceptable range, i.e. only a minor overestimation of the pressure will be made with this system. A similar conclusion, i.e., that the oil expansion is only a minor error, was made by Suhanedi[19] when using a similar oil-filled pressure measurement system.

3. MATERIALS AND TEST SCENARIOS

Pressure measurement results from two test series are presented in this paper. The first set of results is from a test program on tunnel concrete. These tests were conducted as part of a research project on fire spalling of tunnel concrete for the Swedish Road Administration. Full data concerning these tests will be available in an SP report yet to be published. Details of the composition of these concretes can be seen in table 1. The aggregate used in all concrete samples was granite.

Table 1 Composition of tunnel concrete.

Name	w/c	Gravel 0-8 mm [kg/m^3]	Gravel 8-16 mm [kg/m^3]	Water [kg/m^3]	Cement CEM I [kg/m^3]	Super-plasticizer [kg/m^3]	Fiber amount [kg/m^3]	Fiber ϕ [m]	Fiber length [mm]
A	0.4	852	896	170	426	2.98	-	-	-
M	0.4	852	896	170	426	2.98	1	32	12

The second set of results is from a test program on self compacting concrete (SCC) conducted as part of a research project funded by SBUF (the construction industry's

organisation for research and development). Full data concerning these tests will be available in an SP report yet to be published. Some pressure measurement results from tests on other SCC in that program were reported in a previous SiF article[1]. Details concerning the composition of the SCC can be seen in table 2.

Table 2 Composition of self compacting concrete.

Name	w/c	w/p	Gravel 0-8 mm [%]	Gravel 8-16 mm [%]	Limus 25	Water [kg/m^3]	Cement CEM I [kg/m^3]	Super-plasticizer [kg/m^3]	Fiber amount [kg/m^3]	Fiber ϕ [m], (length [mm])
39	0.4	0.30	56 %	44%	140	168	420	6.3	-	-
38	0.4	0.30	56 %	44%	140	168	420	8.0	1	18 (6)

The tests presented in this paper have been conducted on a large horizontal furnace at SP Fire Technology. The dimensions of the various test specimens are given together with the presentation of the results in the next section. All tested concretes were loaded in one direction with 10 % of their compressive strength. The fire curves that have been used include the standard fire curve (EN 1363-1), the hydrocarbon curve (HC curve) and the Rijkswaterstaat (RWS) curve. Of these three curves, only the RWS curve has been developed for tunnel applications. The standard fire curve was developed for building applications and the HC curve was originally developed for the off-shore oil industry.

4. RESULTS AND DISCUSSION

Test results from the tests on tunnel concrete can be seen in figure 2-4. Concrete A, the concrete without the addition of PP- fibres started to spall after 8 minutes and resulted in a mean spalling depth of 97 mm and a maximum depth of 140 mm. The spalling was propagating from the surface by flaking of layer after layer. The pressure development in concrete A is shown in figure 2. The initial pressure of approximately 0.1 MPa is a result of the filling process of the silicone oil in the pressure pipes. To enclose the system a screw in the T- junction is tightened leading to a slight rise in the pressure. This pre-pressure in the system is very small compared with the tensile strength of concrete, and its effect is deemed negligible to the spalling process.

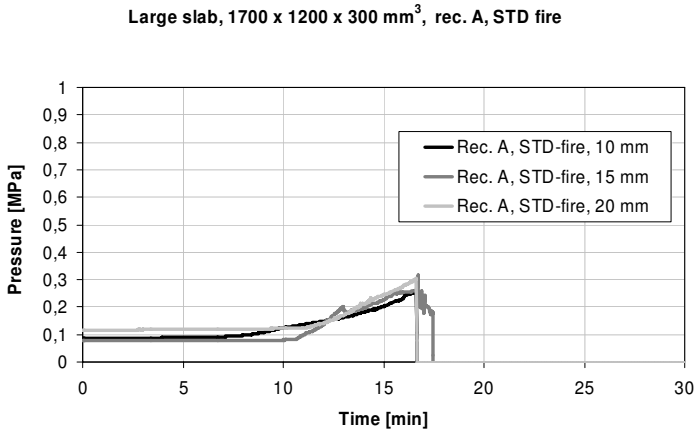

Fig. 2 – Pressure developments in tunnel concrete without PP-fibres that spalled severely during standard fire exposure.

Close inspection of the pressure curves in figure 2 show that the pressure rises first at the depth of 10 mm followed by a rise at the depths of 15 mm and 20 mm. When the pressures begin to rise they are very close to each other until after approximately 17 minutes at which point they are reduced to zero. The similarity of the pressure curves at the three different depths is probably the result of severe spalling and cracking but, as seen in the figure, the pressure does not rise above 0.3 MPa during the spalling process at any of the measurement points.

In figure 3, the results from the same type of concrete as shown in figure 2 with the addition of 1 kg/m^3 of PP-fibres, is shown. When the PP-fibre concrete was fire tested with the standard fire curve (EN 1363-1) no spalling occurred. The pressure development shown in figure 3 exhibits considerably higher maximum pressures compared to those in figure 2. Close inspection of figure 3 shows that the pressure at the depth of 10 mm is the first one to rise but after approximately 13 minutes the pressure at the depth of 15 mm passed that at 10 mm, exhibiting the highest peak close to 0.7 MPa. Recall that these specimens did not spall despite the higher pressures measured in the samples relative to those without PP-fibres.

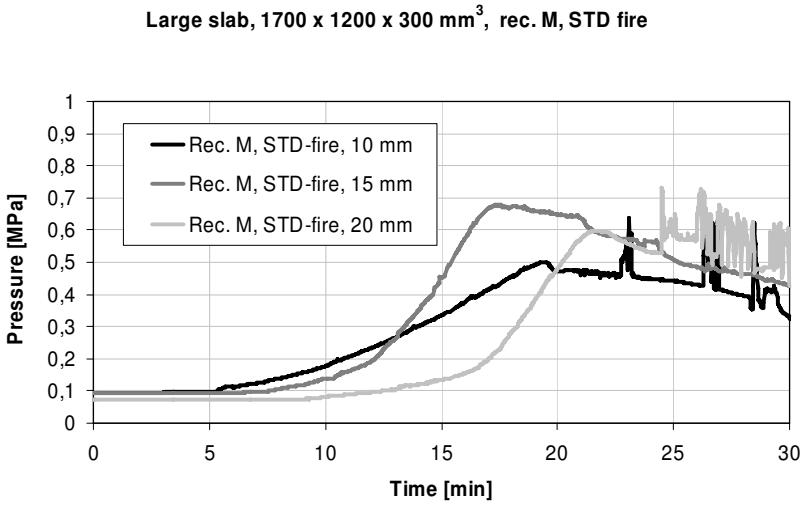

Fig. 3 – Pressure developments in tunnel concrete with the addition of 1 kg/m^3 PP-fibres that did not spall during standard fire exposure.

Figure 4 shows the results of a test on tunnel concrete with the addition of 1 kg/m^3 PP fibres tested with the RWS fire exposure. The concrete spalled to a small degree during the exposure. The mean value of the spalling depth on the surface was 2 mm and maximum spalling depth on the fire exposed surface was 31 mm (the position of the maximum spalling depth was not close to the pressure measurement pipes). When comparing these results with the results from standard fire exposure, the specimens exposed to the RWS fire curve show a faster pressure rise but the maximum value is almost the same as that obtained with the standard fire curve. In this case, however, the maximum value was measured using the oil-filled pipe placed 10 mm from the fire exposed surface. One should keep in mind that the pressure in the fire-exposed specimens is probably not uniform parallel to the exposed surface due to the inherent inhomogeneity of concrete. Thus, one cannot conclude that the pressure is generally higher closer to the surface of a sample exposed to the RWS curve than a sample exposed to the standard fire curve based on the small set of tests presented here. Further testing would be needed to confirm or refute such a postulate.

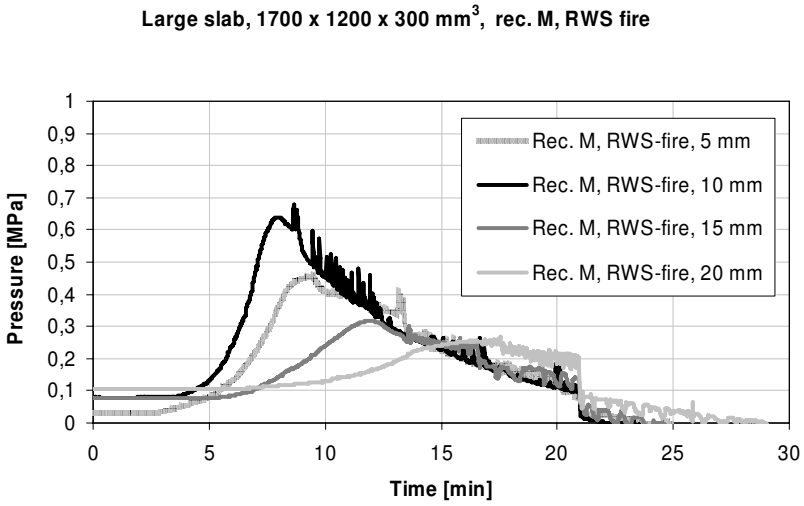

Fig. 4 – Pressure developments in a tunnel concrete with an addition of 1 kg/m^3 PP-fibres that spalled a little during RWS fire exposure.

Pressure measurement tests on SCC exposed to the HC fire curve were also performed. In figure 5 the results of pressure measurements on severely spalling concrete are shown. As in the case of tunnel concrete without PP-fibres the maximum pressure in the tested SCC was low, less then 0.2 MPa.

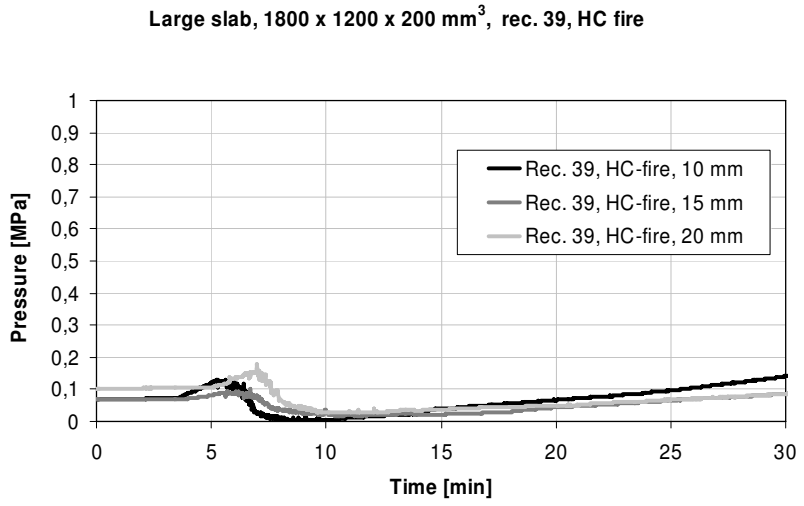

Fig. 5 – Pressure developments in self compacting concrete without the addition of PP-fibres that spalled severely during HC fire exposure.

A similar SCC with 1 kg/m^3 PP- fibres did not spall during HC fire exposure and as in the case of the tunnel concrete, higher pressure was measured in the SCC that did not spalled relative to that which did spall. The maximum pressure measured in the SCC which did not spall, shown in figure 6, was 0.45 MPa.

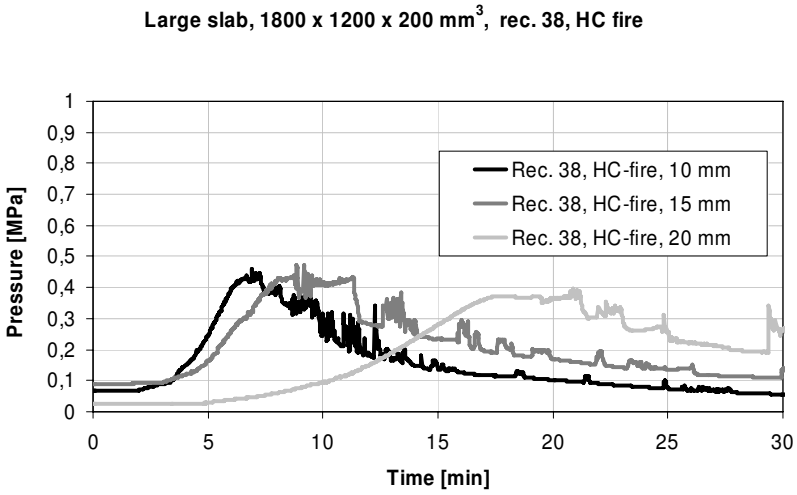

Fig. 6 – Pressure developments in self compacting concrete with addition of 1 kg/m^3 PP-fibres that did not spall during HC fire exposure.

In an additional set of tests on the SCC presented here, with standard fire exposure, the pressures were slightly higher for sample 39 (without PP) when spalling compared to those for sample 38 which did not spall. This is in contrast to the results obtained from the same type of concrete exposed to the HC-curve where the concrete containing PP-fibres exhibited the highest pressure. The propensity to spall was, however, not different for both fire exposure scenarios, i.e. the concrete without PP-fibres spalled. This is an indication that pressure is not always higher in concrete that do not spall but the test series point out that there is no simple correlation between the magnitude of pressure and fire spalling in the investigated concretes. The question is therefore: why do PP-fibres reduce spalling? This effect could not be explained solely by the relative pressure in the capillary pores of the test specimen. Clearly the pressure in itself is not the only factor impacting on the propensity of the concretes to spall, i.e., the pressure is also involved in the redistribution of moisture during fire exposure.

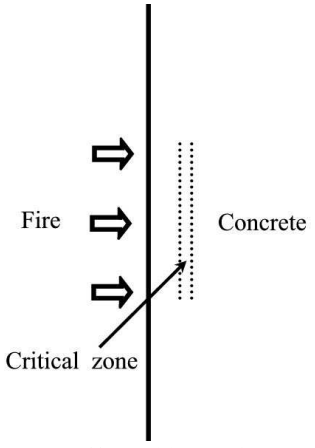

Fig. 7 – Zone affected by moisture presence or movement.

In another part of the project on tunnelling concrete it was shown that an addition of PP-fibres amplifies the moisture transport around 200 °C when fibres melt[20]. This is, or is

close to, the critical zone were the spalling crack occurs, see figure 7. So if moisture can be transported easier it is plausible that high moisture concentrations and even saturation of the pore system can be limited close to the critical zone.

If it is assumed that high moisture transport reduces spalling, the anti-spalling function of PP-fibres in heated concrete may be due to:

- a reduction of the "breaking" pressures in the capillary pores, avoiding pore pressure prompted spalling,
- a modification of the mechanical properties, modulus of elasticity, strength and fracture energy in the spalling zone, or
- local stress relaxation in the spalling zone due to drying creep.

Common for the three hypothesises is that a zone close to the surface, as shown in figure 7, will be affected by the presence or movement of moisture. According to all three hypotheses, this zone will be where the spalling crack occurs which leads to surface fire spalling of concrete.

The test results presented indicate that the first of the three theories is insufficient to explain fire spalling. The investigated concretes that spalled did not exhibit high pressures in the capillary system. Interesting results has been shown in a small scale study on the influence of the heating severity on pressure in concrete[3]. The heating scenarios used were exposure to a heating panel at 600 °C and 800 °C compared to exposure from a standard time temperature exposure, ISO 834. The specimens used for the heating panel test were 30 x 30 x 12 cm and the ISO 834 specimens were 70 x 60 x 15 cm. The maximum measured pressure in a concrete with w/c= 0.54 was 1.5 MPa during exposure from a heating panel at 600 °C and approximately 0.2 MPa during exposure from a heating panel at 800 °C. No spalling occurred during these heating panel tests. When the same concrete was tested with ISO 834 exposure it spalled and the maximum pressure was only approximately 0.2 MPa. A similar behaviour was recorded in a concrete with w/c= 0.38. The main conclusion from the tests was that the origin of spalling was not pore pressure, rather internal cracking released the pressure during fast heating[3]. To investigate the issue further, tests of the residual permeability have been performed on specimens made on tunnel concrete (recipe A) heated with different heating regimes. In the experiments a specimen heated with a thermal shock to 600 °C was compared with one exposed to slow heating, 1 °C/min. The residual permeability of the specimens exposed to thermal shock was twice that of the specimens exposed to slow heating[20]. This indicated larger internal destruction in the specimens exposed to the faster heating scenario. More tests must be carried out to verify the result but these results give an indication that internal cracking is important when discussing pressure development during different heating scenarios. This might partly explain the pressure measurement results from a study made at NIST on high strength concrete where the highest pressure was recorded in the specimens that spalled during a slow heating exposure, 5 ^{o}C/min[2]. The maximum pressure, 2.1 MPa, was measured in the spalled specimens compared with a maximum of 1.4 MPa in a specimen containing PP-fibres.

The presence of PP-fibres facilitates moisture transport, peaking around 200 °C, i.e., the evacuation of moisture at high temperatures from the critical zone shown in figure 7 is probably faster if the concrete contains PP-fibres. Important then is to consider whether the presence of trapped moisture during heating is unfavourable from a mechanical point of view.

The mechanical properties cannot be determined locally in a rapidly heated specimen (containing trapped moisture). However, an indication of the effect of trapped moisture during heating can be seen from experiments conducted on specimens heated and tested under sealed conditions. A literature review conducted by Lankard et al. [21] shows that the compressive strength of concrete heated under sealed conditions exhibits a dramatic decrease.

The same conclusion was drawn by Schneider and Horvat[22] when reviewing results from Berto and Polivka. These results show a 30 % reduction of the compressive strength when testing a sealed specimen compared with an unsealed specimen at 150 °C.

At room temperature, the Young's modulus is higher when more moisture is present[23]. This is explained by the fact that pore water is almost incompressible and if it is not easily moved by the pressure the Young's modulus will increase[24]. It is plausible that a situation will arise when the moisture transport from the gel pores to the capillary pores and further transport away from the high pressure zone will be restricted during heating and the critical zone shown in figure 7 will become stiff.

A stiff cement matrix zone around expanding aggregate can be the reason for the development of a crack parallel to the fire exposed surface. When PP-fibres are present the moisture kept at a high temperature in the critical zone will be lower, leading to less stiffness and less cracking. This plausible effect has not been experimentally verified.

Very few experiments have been conducted to measure the Young's modulus during sealed conditions at high temperature and the conclusions from such experiments are not consistent. Schneider and Horvat[22] concluded that sealing of the specimens did not have a significant effect on the Young's modulus for limestone concretes. In tests performed by Lankard et al.[21] on gravel concrete, however, the effect of sealed conditions was to dramatically decrease the Young's modulus. This is in contradiction to the room temperature behaviour. More work is needed to resolve this issue.

As shown previously, PP-fibres facilitate moisture transport peaking at around 200 °C. The evacuation of moisture at high temperatures from the critical zone shown in figure 7 will be faster if the concrete contains PP-fibres. The effect on mechanical properties in the presence of moisture is discussed above. The effect of moisture transport from the critical region will now be discussed.

During first time heating of a loaded concrete specimen the total strain can be divided into the following components: thermal expansion, transient strain, creep strain, and elastic strain according to Anderberg and Thelandersson[25]. In an analogy to this description, the transient strain will, in a given situation of restrained thermal expansion during heating, relax the stresses originated from thermal expansion. This is very important in the behaviour of heated concrete.

The nature of the transient strain in a heated unsealed specimen is a mix of "transitional thermal creep" (TTC) and drying creep[26]. The TTC component was first found by Hansen and Eriksson[27] when they tested loaded and unloaded cement paste and mortar specimens submerged in water and heated to 100 °C. These experiments illustrated that a specimen first loaded and then heated exhibited larger deformation than a specimen first heated and then loaded. The fact that the tests were performed under water lead to the conclusion that transitional thermal creep is a different phenomenon to drying creep.

How much of the transient strain originates from TTC relative to drying creep during a test has never been determined but according to Bazant and Kaplan[28] the drying creep is totally dominant. The drying creep component was also highlighted by Thelandersson[29] as a highly important phenomenon during heating. In a recent experimental study, Petkovski and Crouch[27] concluded, from tests on concrete under partly sealed conditions, that the Load Induced Thermal Strain (LITS) in concrete is reduced if the moisture movement is restricted, i.e., if drying creep is minimised, thereby confirming the importance of drying creep in transient strain. LITS is the difference between heating without load relative to heating under load, minus the initial elastic strain.

In summary, drying of concrete during heating leads to drying creep which relaxes stresses in the material. Thus, in a material with low permeability the drying is restricted and

higher stresses will occur. When PP-fibres are present an extra "relaxation" peak in the material around 200 °C, will be present, which indicates that the PP-fibres may facilitate drying creep. An indication of this has been seen in free thermal strain experiments performed at the heating rate 1 °C/minute where the presence of PP-fibres introduces a plateau around 200 °C in the strain curve[20]. Thus the fibres probably relax internal stresses due to the temperature gradient in the test specimen.

5. CONCLUSIONS

In general, the highest pressures in the two test series presented in this paper were measured in the concretes that did not exhibit spalling during fire, i.e., in those concrete specimens that included PP-fibres. Conclusions from the test series is that pressure in the capillary system is not the driving force for spalling during fire exposure of the investigated concretes. However, the pressure is involved in the redistribution of moisture during fire exposure.

As an alternative to the common theory of the function of polypropylene (PP) fibres as "pressure releasers", a new theory, based on aspects of the presence and movement of moisture, is put forward to explain the function of PP-fibres in reducing the propensity of concrete to spall. In this context it is hypnotised that PP- fibres reduce moisture content in the critical zone which affects the mechanical properties and moisture movement leads to larger drying creep which locally relaxes the thermal stresses.

REFERENCES

[1] Jansson, R. "Liquid/steam pressure measurement inside concrete exposed to fire", Structures in Fire 06, Proceedings from the 4th international workshop, Aveiro, Portugal, 2006, pp. 747-756

[2] Phan T. L., "High-Strength Concrete at High Temperature – An Overview" Utilization of High Strength/High Performance Concrete, 6th International Symposium. Proceedings. Volume 1. June 2002, Leipzig, Germany, Konig, G.; Dehn, F.; Faust, T., Editor(s)(s), 501-518 pp, 2002.

[3] Mindeguia J.C., Pimienta P., La Borderie C., Carre H, "Experimental study of the influence of polypropylene fibres on material properties and fire spalling of concrete" Proceedings of the fib Task Group 4.3 workshop "Fire Design of Concrete Structures – From Materials Modelling to Structural Performance" Coimbra, Portugal, November 8-9, 2007

[4] Hasenjäger "Über das Verhalten des Betons und Eisenbetons im Feuer und die Ausbildung von Dehnungsfugen im Eisenbetonbau" Dissertation, Techniche Hochschole Braunschweig 1935, , cited in Meyer-Ottens C. (1972) "Zur Frage der Abplatzungen an Betonbauteilen aus Normalbeton bei Brandbeanspruchung", PhD-thesis, Braunshweig, Germany, 1972

[5] Harmathy, T. Z., "Effect of moisture on the fire endurance of building materials", Moisture in Materials in Relation to Fire Tests, ASTM Special Technical Publication No. 385, pp 74-95, 1965

[6] Sato H. "Explosive spalling of prestressed concrete in fire" Fire resistance of prestressed concrete; proceedings of a symposium on the fire resistance of prestressed concrete, held under the auspices of the F.I.P. Commission on Fire resistance of prestressed concrete at Braunschweig, Germany, June 1965

[7] Dougill J. W.,"Modes of failure of concrete panels exposed to high temperature" Magazine of Concret Research, Vol 24, No 79, June 1972
[8] Meyer-Ottens C.,"Zur Frage der Abplatzungen an Betonbauteilen aus Normalbeton bei Brandbeanspruchung", PhD-thesis, Braunshweig, 1972
[9] Waubke N. V., Schneider U."Tensile stress in concrete due to fast vapour flow", Proceedings of the international RILEM symposium "Pore Structure and Properties of Materials", Prauge, September, 1973
[10] Zhukov V. V.,"Reasons of Explosive Spalling of Concrete by Fire", Beton I zhelezobeton (Concrete and Reinforcement Concrete), No. 3, 1976
[11] Copier, W.J., "Spalling of normalweight and lightweight concrete on exposure to fire" Report 24(2), Heron, Holland, 1979.
[12] Connolly R. J.,"The Spalling of Concrete in Fire" PhD thesis, Ashton University, 1995
[13] Khoylou N., "Modelling of moisture migration and spalling behaviour in non-uniformly heated concrete", PhD thesis, University of London, March, 1997
[14] Kalifa P., Menneteau F.D., Quenard D., "Spalling and pore pressure in HPC at high temperatures" Cement and Concrete Research 30 pp.1915-1927, 2000
[15] Arita, Harada, Miyamoto,"Thermal spalling of high-performanceconcrete during fire" Second International Workshop Structures in Fire, Christchurch, New Zeeland, – March 2002
[16] Breunese A.J., Fellinger J. H. H. (2004) "Spalling of Concrete - An Overview of Ongoing Research in the Netherlands", Workshop - Structures in Fire, Ottawa, May, 2004
[17] Bazant, Z. P.,"Concrete Creep at High Temperature and its Interaction with Fracture: Recent Progress", Concreep-7 Conference: Creep, Shrinkage and Durability of Concrete and Concrete Structures, pp 449–460, 2005
[18] Jansson R., Boström L, "Fire spalling- Theories and experiments" Proceedings of the Fifth International RILEM Symposium on Self-Compacting Concrete, 3-5 September 2007, Ghent, Belgium
[19] Suhaendi S. L. "Properties of Fiber Reinforced High Strength Concrete under High Temperature Conditions" PhD thesis, Hokkaido University, September 2007
[20] Jansson R., Boström L. "Experimental study of the influence of polypropylene fibres on material properties and fire spalling of concrete" Proceedings of the fib Task Group 4.3 workshop "Fire Design of Concrete Structures – From Materials Modelling to Structural Performance" Coimbra, Portugal, November 8-9, 2007
[21] Lankard D. R., Birkimer D. L., Fondriest F. F. , Snyter M. J. "Effects of moisture content on the structural properties of portland cement concrete exposed to 500 F" ACI Special Publication SP 25, Detroit 1971
[22] Schneider U. , Horvat J."Behaviour of ordinary concrete at high temperature", Technische Universität Wien, Heft 9, 2003
[23] Guo J. S., Waldron P. "An elastic model to quantify the effect of moisture on the mechanical properties of concrete at time of test" Magazine of Concrete Research, 53, No 3, June 2001
[24] Concrete handbook – Material, (Betonghandbok Material) a publication in Swedish from Svensk Byggtjänst, second edition, 1982
[25] Anderberg Y., Thelandersson S. "Stress and deformation characteristics of concrete at high temperatures", Lund Institute of Technology, Bulletin 54, Sweden, 1976
[26] Khoury G. A., Majorana C. E., Pesavento F., Schrefler B. A. , "Modelling of Heated Concrete" Mag. Of Conc. Research No 2 2002
[27] Petkovski M.,Crouch R. S. "Strains under transient hygro-thermal states in concrete loaded in multiaxial compression and heated to 250 °C" Cement and Concrete Research 38, 2008

[28] Bazant Z. P., Kaplan M. F. “Concrete at High Temperatures- Material properties and mathematical models” Book published by Longman Group Limited, 1996
[29] Thelandersson S. “On the multiaxial behaviour of concrete exposed to high temperature” Nuclear Engineering and Design 75 (1982) 271-282

EFFECT OF ELEVATED TEMPERATURES ON FLEXURAL BEHAVIOUR OF HYBRID FIBRE REINFORCED HIGH STRENGTH CONCRETE

Kazuo WATANABE[1] and Takashi HORIGUCHI[2]

ABSTRACT

The structural property of concrete that has been studied most widely as a function of elevated temperature is compressive strength. Only a limited number of studies on the flexural behaviour as influenced by elevated temperature have been conducted.

In this paper, flexural behaviour (flexural strength and fracture energy) of high-strength concrete (HSC) and hybrid-fiber-reinforced high-strength concrete (HFRHSC) during and after exposure to high temperatures were investigated. In addition, the tensile softening curve was back-calculated with the poly-linear approximation method. Physical properties and fracture energy were evaluated during heat exposure (hot test) and after heat exposure (residual test).

The tests results showed that quite remarkable difference was verified from the strength quality of HFRHSC due to heating test method, hot test and residual test. Especially, at the time of hot heating above 200°C, sudden decrease of maximum load was verified in the case of hot test. For specimens including steel fiber, the maximum load does not drop suddenly in hot test. It was verified from the Load-CMOD curve that it only caused gradual decrease.

In hot test, hybrid fiber reinforcement in high strength concrete mixture is very effective to prevent brittle fracture. It is verified that this type of reinforcement is effective with the favor of fracture energy test.

[1] Ph.D. student, Hokkaido University, Graduate School of Eng., N13 W8, Sapporo 060-8628, Japan, kazuo-be@eng.hokudai.ac.jp

[2] Associate Professor, Hokkaido University, Graduate School of Eng., N13 W8, Sapporo, Japan, horiguti@eng.hokudai.ac.jp

1. INTRODUCTION

Recently, long tunnels are constructed with high strength concrete and have become an important means of traffic infrastructure worldwide. But, damage due to fire accident inside the tunnel occurs in some cases. As a consequence of the damage for the fire in the tunnel, concrete strength decreases. In terms of high strength concrete, there is a characteristic deterioration due to the explosive spalling phenomenon. With respect to structural collapse mechanism, this will cause secondary damage that must be considered as an important problem. In addition to a recent tunnel structure, secondary tunnel linings are often uninstalled due to the aspect of economical efficiency. With this trend increasing, improvement in fire resistance of primary concrete tunnel linings is required. However, research that deals with fracture behavior of high strength concrete under high temperature condition, comparing to normal strength concrete is still limited. Topics on this issue are still open to be investigated. Therefore, detailed examination regarding fire resistance of high strength concrete is needed worldwide.

In this research, flexural behaviour (flexural strength and fracture energy) of high-strength concrete (HSC) and hybrid-fiber-reinforced high-strength concrete (HFRHSC) during and after exposure to high temperatures were investigated. Polypropylene (PP) fiber is utilized to prevent the explosive spalling[1], while steel fiber is expected to retain the remaining strength of the concrete[2,3]. Deterioration behavior of fiber reinforced high strength concrete (FRHSC) exposed to high temperature is examined from the viewpoint of fracture mechanics. This experimental study compares fire resistance of five kinds of FRHSC that utilized various fibers inside HSC mixture during and after exposure to high temperatures. Evaluation of fracture energy is back-calculated using the poly-liner approximation method[4].

2. EXPERIMENTAL PROGRAM

2.1 Fibers, Materials, Specimens, and Experimental Conditions

Mix proportion of concrete is shown in Table 1. All series of concrete were casted using ordinary Portland cement, river sand, and crushed stone. Specific gravity of river sand is 2.70, and specific gravity of crushed stone is 2.65 (maximum nominal size of 20 mm).

Some parameters of mix proportion were kept constant: W/C = 0.3, sand to aggregate ratio (s/a) = 50%, and water content = 170 kg/m^3. A polycarboxylate-based superplasticizer,

Table 1. Mixture proportion of HSC and FRHSC

Series	W/C (%)	s/a (%)	Fiber volume (%)			W (kg/m^3)	Air (%)	SP[*1] (%×c)	AE[*2] (%×c)	BC[*3] (%×c)	compressive strength (MPa-20°C)
			Polypro-pylene	Steel (S13)	Steel (S30)						
Plain	30	50	-	-	-	170	6	0.8	0.012	-	73
PP			0.1	-	-			1.2	0.006	0.001	71
HY1			0.1	0.3	-			1.3	0.008	0.001	81
HY2			0.1	0.5	-			1.35	0.008	0.001	83
HY3			0.1	0.2	0.1			1.35	0.008	0.001	81
HY4			0.1	0.4	0.1			1.4	0.008	0.001	84

[*1]SP: super plasticizer [*2]AE: air entraining agent [*3]BC: bubble cutter agent

air entraining agent, and bubble cutter agent were used to attain desired workability and air content of fresh concrete. Specimens were mixed using a double-axes mixer. All specimens were prisms of 100×100×400mm. Compressive strength of concrete using portions of beams broken in flexure is measured at 20°C and summarized in Table 1.

Polypropylene and two types of steel fibers having 18 , 160 and 600-micron effective diameter were used in this experimental study. All of fibers came in bundles that were well dispersed inside the concrete mixture. Properties of fibers are shown in Table 2.

After casting, the specimens were demoulded after 24 hours, and then cured under lime-saturated water at temperature of 20±2°C for 28 days. The notch with a thickness of 5 mm and a depth of 30 mm was made in the center section of all specimens making use of concrete cutter. Some specimens were heated using electric furnace and heating device. Both heating rates were set at 10°C/min with the maximum temperature kept at 200, 400, and 600°C for 2 hours. In the case of residual test, heated specimens were let to cool inside the furnace until its temperature coincided with room temperature to prevent cracks upon cooling.

Table 2. Properties of fibers

	Polypropylene	Steel (S13)	Steel (S30)
Diameter (mm)	0.018	0.16	0.6
Length (mm)	6	13	30
Shape	Filament	Straight	Indent
Density (gr/cm^3)	0.9	7.8	7.8
T_{melt} (°C)	160-170	1370	1370
$T_{vaporize}$ (°C)	341	-	-

2.2 Fracture Energy Measurement

With a designated loading span of 300 mm, the fracture energy test was executed under load control using a servo jack testing machine. The beam specimen was arranged on some rollers under both fulcrums to let it move freely in horizontal direction.

In the case of fracture energy test, loading rate was set at 0.1 mm/min. The fracture energy test was conducted in accordance with a JCI (Japan Concrete Institute) test method [JCI-S-002-2003] [5].

During the fracture energy test, load (P), crack mouth opening displacement (CMOD), and load point displacement (LPD) were measured. The loading device and measurement points layout are shown in Figure 1.

Fracture energy of specimen was calculated as follows:

$$G_F = \left(0.75W_0 + W_1\right) / A_{lig}$$
$$W_1 = 0.75\left(S/L \cdot m_1 + 2m_2\right)g \cdot CMOD_c \quad (1)$$

where,

G_F : Fracture energy (N/mm)

W_0 : Area under Load-CMOD curve before specimen breaking (N mm)

W_1 : Weight of the specimen and the work from loading jig forms (N mm)

A_{lig} : area of ligament (b h)

m_1 : weight of specimen (kg)

S : loading span (mm)
m_2 : weight of jig appearing in a specimen (kg)
$CMOD_c$: (mm)

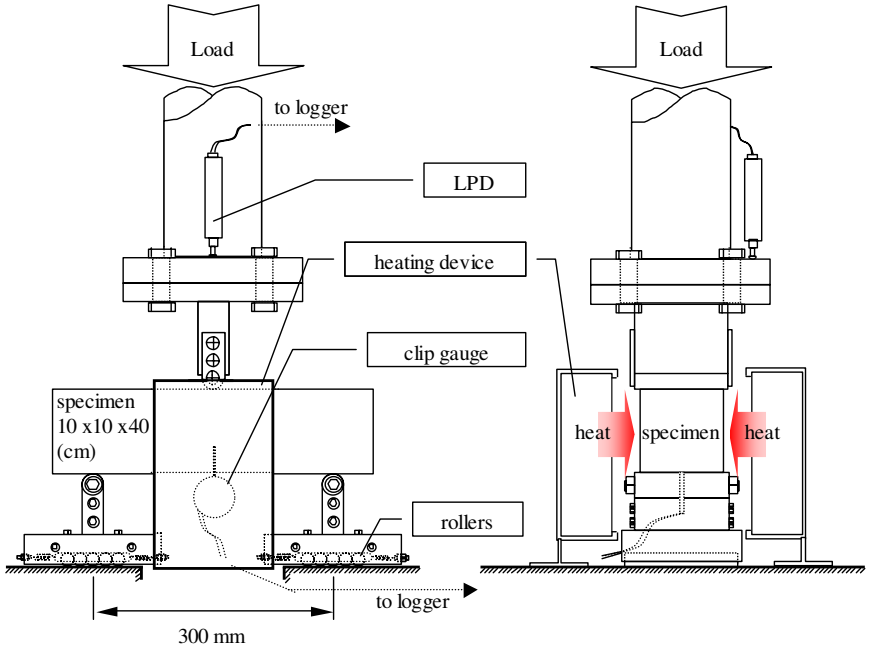

Figure 1. Fracture energy test set-up (with heating device of hot test)

The Young's modulus in bending by considering the self-weight of the notched beam specimens were calculated based on Equation (2). In order to keep the value of modulus of elasticity in bending (E_b) to be in serviceability limit range, calculation of this parameter will be based on CMOD of 0.05mm.

$$E_b = \frac{\left[P_u + 0.5mg(L/S)(2 - L/S)\right]}{4B(H - a_0)^3 D} \tag{2}$$

where,
P_u : maximum load at peak (kN)
L : full length of the beam(mm)
H : specimen depth (mm)
B : width of the beam (mm)
a_0 : initial notch depth (mm)
D : deflection at the center of the beam (mm)

3. TESTS RESULTS AND DISCUSSION

3.1 Bending Strength under Hot Test and Residual Test

Bending strength was evaluated both under the heating stage (hot test) and cooling stage (residual test). Table 3 shows a summary of bending test results with heating

temperature up to 600°C. Bending strength ratio with relation to heating temperatures is shown in Figure 2 and Figure 3. One of the most important findings is the difference of reduction behavior under hot test and residual test. As shown in Figure 2 at residual test, the strength reduction at 200°C isn't significant and even seemed to increase. However, the reduction is significant in Figure 3 at hot test. This interesting phenomenon could be explained by LITS concept [6] (Load-Induced thermal strain) so- called transient creep and also traditional "dry strength" concept[7]. As there are very few bending tests results under hot test, the importance of hot test is not fully recognized. The other hand, inclusion of fiber into concrete will guarantee the residual bending strength, as shown in Figure 2 and Figure 3.

Table 3. Experimental test results of bending strength (N/mm^2)

Series	20°C	Residual test			Hot test		
		200°C	400°C	600°C	200°C	400°C	600°C
Plain	3.25	3.34	2.34	1.66	1.28	1.08	0.72
PP	3.15	3.55	3.25	2.53	1.59	1.43	0.72
HY1	3.65	3.85	3.42	2.25	1.72	1.72	1.11
HY2	3.34	3.84	3.25	2.69	2.25	1.93	1.20
HY3	3.89	4.01	3.62	2.22	2.48	2.32	1.76
HY4	4.15	4.51	4.31	3.29	2.51	2.41	2.10

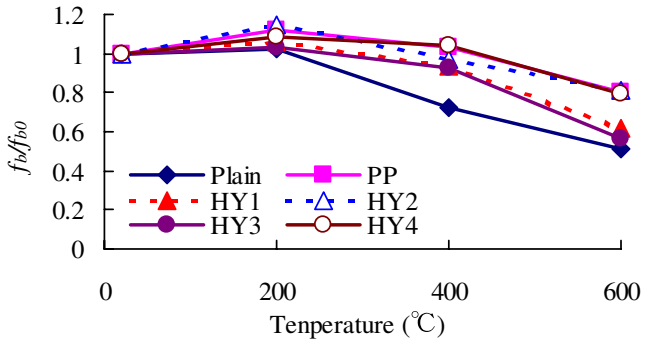

Figure 2. Reduction of bending strength ratio at elevated temperature (Residual test)

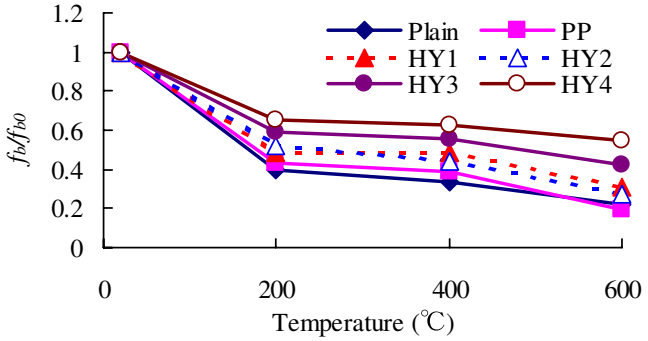

Figure 3. Reduction of bending strength ratio at elevated temperature (Hot test)

3.2 Load - CMOD Curve under Hot Test and Residual Test

Load - CMOD curve is given in Figure 4 (residual test) and Figure 5 (hot test) showing one representative result from the experimental tests.

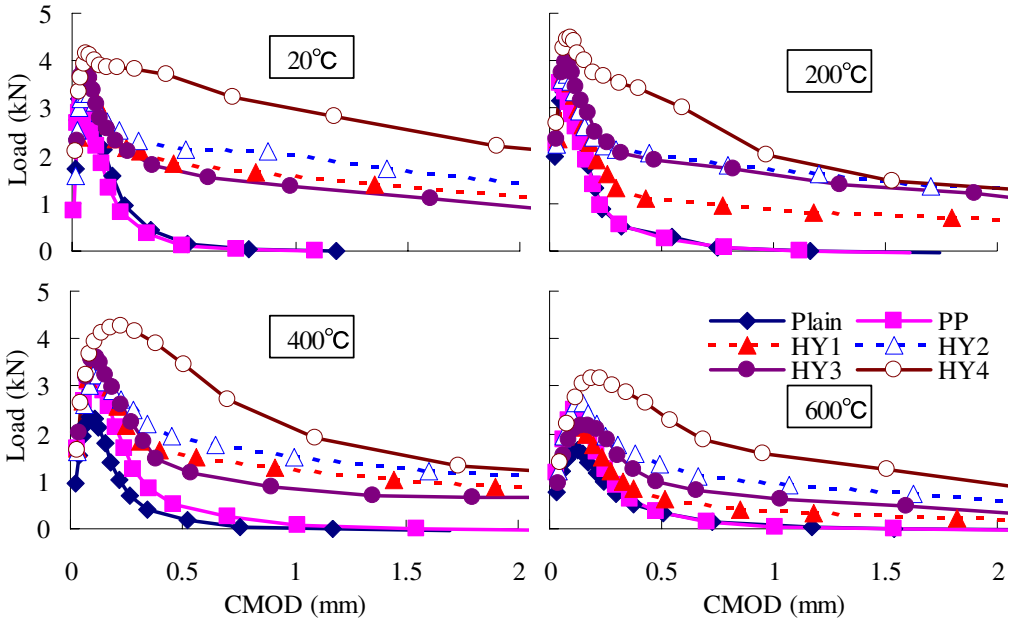

Figure 4. Load–CMOD curve at 20°C, 200°C, 400°C, and 600°C (Residual test)

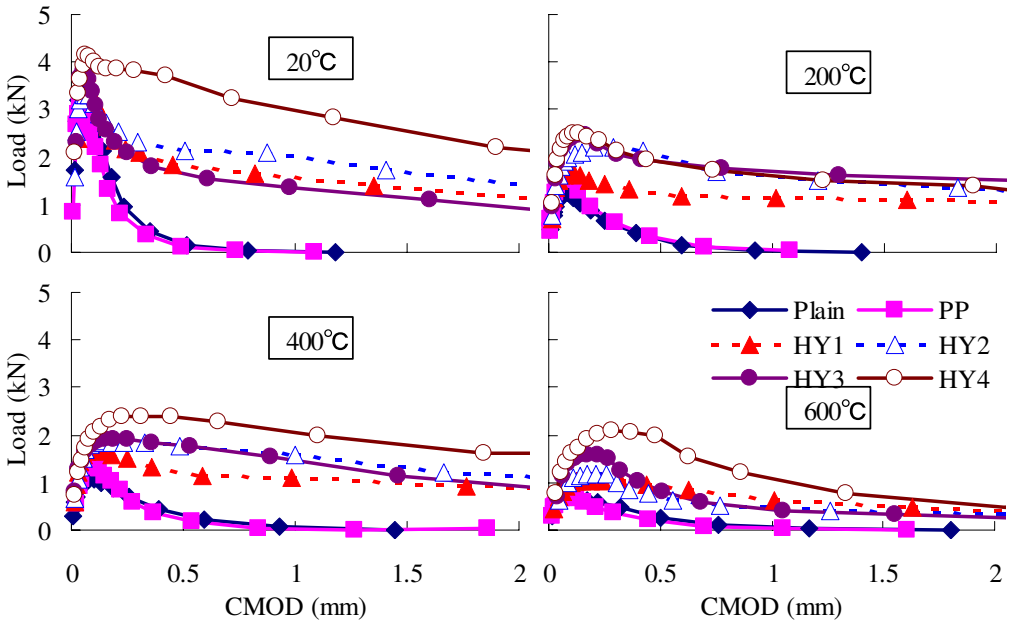

Figure 5. Load–CMOD curve at 20°C, 200°C, 400°C, and 600°C (Hot test)

From Figure 4 and Figure 5, it was verified that the maximum load decreases with increasing heating temperature in both test conditions, and that CMOD at maximum load becomes larger with relation to the increase in heating temperature. With the increase in heating temperature, stiffness decreases, as shown in both Figures. In each heating temperature of both tests, the load decrease of Plain and PP is considerable after the peak. However, not breaking either after the peak is due to steel fiber reinforcement. Especially, HY4 verified that continues to support the large load, in comparison with Plain and PP.

In both tests, the specimens including steel fibers didn't show rapid descending behavior after maximum load. Previous tendency becomes high with the increase in heating temperature. However, in the case of hot test, sudden decrease after maximum load is not observed. The reason of this finding should be investigated further.

3.3 Fracture Energy under Residual Test and Hot Test

Fracture energy of HSC and FRHSC during and after exposure to high temperatures was calculated and summarized in Table 4. The relationships between fracture energy and heating temperatures are shown in Figure 6 and Figure 7. As shown in these figures, large difference of fracture energy between the Plain/PP series and the HY series was observed. As for the fracture energy of the HY series, it was found that the fracture energy decreased with the increase in heating temperature. Especially, at the all muximum heating temperature, G_F of HY4 (three types of fibers)is found to be the highest among of all series.

Especially, when it is exposed to high temperature above 200°C, fracture energy of concrete decreases suddenly and converted to fail in a brittle manner. This phenomenon is thought to be affected by the fiber due to the fact that under hot environment polypropylene fiber melts and disappears.

For both tests, it could be found that the fracture energy of concrete that includes steel fiber exceeds the one of Plain and PP series at any heating temperature. Therefore, it was confirmed that the mixture of the steel fiber improves fracture toughness. But, this result should be verified for other mixture proportions.

As mentioned before, bending strength under residual test and hot test showed significant difference at high temperature, however the fracture energy under both test showed no significant difference.

Table 4 Experimental test results of fracture energy (N/mm)

Series	20°C	Residual test			Hot test		
		200°C	400°C	600°C	200°C	400°C	600°C
Plain	0.12	0.09	0.10	0.08	0.08	0.07	0.07
PP	0.15	0.09	0.16	0.12	0.09	0.06	0.06
HY1	0.82	0.45	0.52	0.36	0.62	0.49	0.35
HY2	1.33	0.63	0.57	0.54	0.81	0.55	0.39
HY3	1.17	0.63	0.56	0.38	0.93	0.56	0.32
HY4	1.55	1.07	1.18	0.76	1.06	0.77	0.47

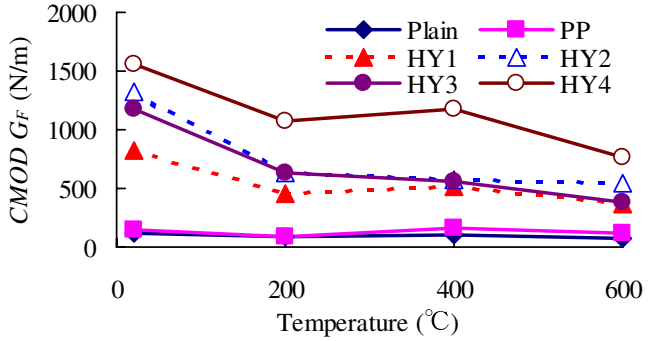

Figure 6. Reduction of fracture energy at elevated temperature (Residual test)

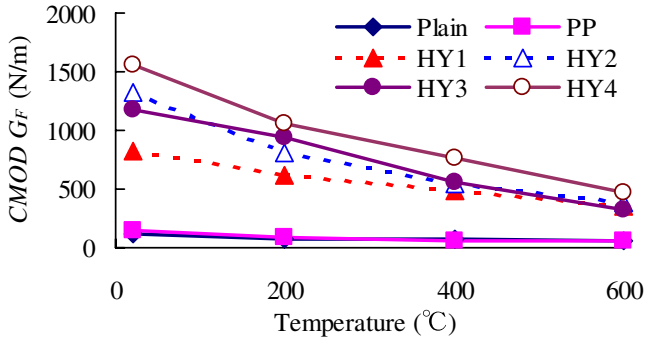

Figure 7. Reduction of fracture energy at elevated temperature (Hot test)

3.4 Young's Modulus under Hot Test and Residual Test

Young's modulus was evaluated both under the heating stage (hot test) and cooling stage (residual test). Table 5 shows a summary of experimental test results with heating temperature up to 600°C.

Relationships between Young's modulus and heating temperatures are shown in Figure 8 and Figure 9. The residual test result of Young's modulus is the tendency to decrease rectilinearly upon heating temperature. But, the case of the hot test sudden decrease at 200°C was noticed and followed by gradual decreases after that. Especially residual test result, it was verified that 40 % of residual Young's modulus properties is maintained even after heating at 600°C.

Table 5. Experimental test results of Young's Modulus (kN/mm^2)

Series	20℃	Residual Test			Hot Test		
		200℃	400℃	600℃	200℃	400℃	600℃
Plain	36.96	22.06	13.68	7.24	14.73	12.04	7.27
PP	29.51	23.86	14.49	10.60	23.15	9.21	7.03
HY1	23.49	19.33	15.27	8.73	15.39	14.84	5.91
HY2	33.91	22.62	14.07	9.77	18.36	13.25	4.42
HY3	29.69	22.26	15.72	8.16	17.91	11.01	6.03
HY4	34.15	23.50	17.87	8.93	18.26	11.85	7.30

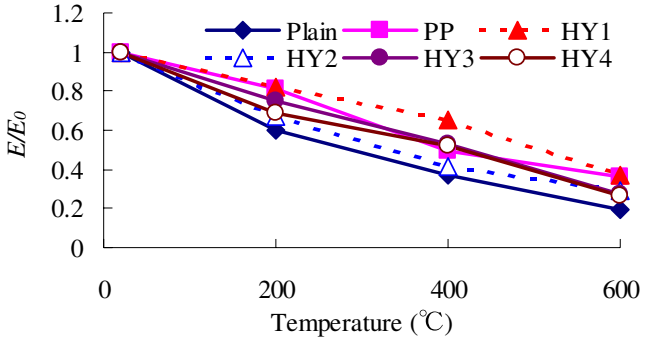

Figure 8. Reduction of Young's Modulus at elevated temperature (Residual test)

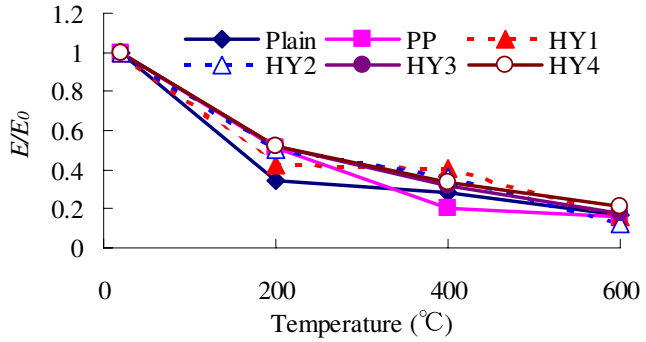

Figure 9. Reduction of Young's Modulus at elevated temperature (Hot test)

4 CONCLUSIONS

Based on the results of this experimental investigation, the following conclusions can be drawn:

(1) Quite remarkable difference was observed from the strength quality of HSC and FRHSC due to heating test method, hot test and residual test. Especially, at the time of hot heating above 200°C, sudden decrease of maximum load was verified in the case of hot test.
(2) It is found that the bending strength at elevated temperature under hot test shows far lower value than that under residual test. This implies the importance of hot test to evaluate the real fire resistance of HSC and FRHSC.
(3) Concrete with hybrid fiber reinforcement that has large initial strength is found to be effective. For specimens including steel fiber, the maximum load does not drop suddenly in hot test. It was verified from the Load-CMOD curve that it only caused gradual decrease.
(4) As for mixing the steel fiber which combines long and short fibers into the concrete (HY4), the effect is larger than single use (HY2).
(5) In hot test, hybrid fiber reinforcement in high strength concrete mixture is very effective to prevent brittle fracture. It is verified that this type of reinforcement is very effective with the favor of fracture energy test.

REFERENCES

[1] S.L. Suhaendi, M. Suto, and T. Horiguchi, "Optimization of polypropylene fibers for high strength concrete under high temperature condition", Proceedings of the 10th East Asia Pacific Conference on Structural Engineering and Construction, Vol. 6, pp. 467-472, 2006

[2] S.L. Suhaendi, K. Shimura, and T. Horiguchi, "Non-destructive test of heated fiber reinforced high strength concrete", Proceedings of the Japan Concrete Institute, JCI, Vol. 28, No. 1, pp. 407-412, 2006

[3] S.L. Suhaendi and T. Horiguchi, "Effect of short fibers on residual permeability and mechanical properties of hybrid fiber reinforced high strength concrete after heat exposition", Cement and Concrete Research, Vol. 36, No. 9, pp. 1672-1678, September 2006

[4] Y. Kitsutaka: Fracture Parameters by Poly-linear Tension Softening Analysis, Journal of Engineering Mechanics, ASCE, Vol. 123, No. 5, pp. 444-450, 1997

[5] Japan Concrete Institute Research Committees: Method of test for load-displacement curve of fiber reinforcement concrete by use of notch beam, JCI-S-002-2003

[6] Gabirel A. Khoury, Brain N. Grainger and Patrick J. E. Sullivan: "Strain of concrete during first heating to 600°C under load" Magazine of Concrete Research, Vo.37, No.133, December 1985

[7] Czernin, Wolfgang, "Zementchemie für Bauingenieure". - 3., neubearb. Aufl. - Wiesbaden [u.a.] : Bauverl., 1977

ON THE ROLE OF SECOND-ORDER EFFECTS IN HSC COLUMNS EXPOSED TO FIRE

PATRICK BAMONTE[1]

ABSTRACT

It is well-known that M-N envelopes of R/C sections are markedly reduced by high temperature and fire, depending on the maximum temperature reached during the heating process, and on fire duration and severity. The thermal properties of the materials and the mechanical decay play an important role, but what prevails in most cases is the structural context, whenever the restraints and the geometry have a direct impact on the sectional behaviour. This is the case of the stability of any structural member, whose behaviour can be investigated by considering only the most stressed section (statically-determinate members are a typical, but not exclusive case). In this paper, an application of the model-column method to the study of the buckling of R/C columns is shown, in the case of high-strength concrete columns with various types of end restraints. The numerical results are compared with some recent experimental results, and the role played by the different factors (restraint conditions, spalling, unintentional eccentricities of the axial loads) are highlighted.

1. INTRODUCTION

Many structural members, such as columns, simply-supported beams and most of the prestressed-concrete members, are usually modelled and designed assuming their structural behaviour to be statically determinate. In these cases, the distribution of the internal forces is not affected by the stiffness of the members and depends only on equilibrium. Consequently, a redistribution of the internal forces cannot take place and the collapse of the structure can be reasonably identified with the failure of the most stressed section.

Usually, the same approach is also adopted at ambient temperature for redundant structures, whenever the structural safety is checked using a statically-admissible approach: the distribution of the internal forces is worked out on the basis of linear elastic analysis, assuming that all the elements are uncracked. In so doing, the degree of safety of the whole

[1]Associate Researcher, Politecnico di Milano, Department of Structural Engineering, Milano, Italy, email: patrick.bamonte@polimi.it.

structure is identified with that of the weakest (or most stressed) section. This procedure does not take into account the possible redistribution of the internal forces with an increase of the bearing capacity, and thus does not allow to exploit the redundancy of the structure.

In fire conditions the redistribution of the internal forces due to the inevitable coupling of the thermal and mechanical problems (through the coefficient of dilation and the ensuing thermal deformations, which are usually restrained) has to be taken into account in almost any type of structure. Hence, the assessment of safety should be performed, at least in principle, on the basis of the behaviour of the whole structure [1], even more since 2nd-order effects are to be taken care of in working out the internal forces [2]. There are, nevertheless, some cases where the structural behaviour can be determined on the basis of simplified kinematic models, that reduce the computational effort, to the advantage of the design of many commonly-found structures. An example is the study of 2nd-order effects in concrete columns. The usual procedure at ambient temperature is to give an approximate formulation to the "critical" deformed shape (i.e. the deformed shape at the onset of buckling) and to evaluate the corresponding bearing capacity of the column. In this way, 2nd-order effects are easily taken into account. This topic is of great interest nowadays, because a few recent dramatic events concerning the collapse of concrete structures in fire have shown that the exposure to high temperature can greatly increase the sensitivity of columns to buckling [3]. Moreover, the increasing use of high-performance and high-strength concrete leads to sectional size reductions and brings in an enhancement of second-order effects.

This paper illustrates the application of the model-column approach to the study of 2nd-order effects in fire-exposed concrete columns. The numerical results are compared to the experimental results obtained on HSC columns recently tested in a furnace under combined bending moment and axial force.

2. NUMERICAL PROCEDURE

2.1 Sectional analysis

The ultimate bearing capacity of a R/C section subjected to combined axial force and bending moment is usually evaluated by means of M-N envelopes. These diagrams can be easily determined if concrete and steel constitutive laws are given monotonic or quasi-monotonic formulations (like Sargin's law and the parabola-rectangle diagram [4]) and plane sections are assumed to remain plane up to failure. In this way, for any linear profile of the longitudinal strain (corresponding to a given load combination), by enforcing the well-known limits for concrete strains in compression (ε_{cu} = 3.5‰) and steel strains in tension (ε_{su} = 10-20‰), the ultimate values of M and N can be evaluated by simply integrating the stresses over the section.

This approach may nevertheless lead to an underestimation of the bearing capacity, should it be used together with non-monotonic stress-strain diagrams (such as the temperature-dependent stress-strain curves for concrete in compression, presented in EN 1992-1-2 [5], Figure 1): in this case, the so-called "moment-curvature method" must be applied [6]. For any given value $N = N_u$ of the axial force, the maximum value M_u of the bending moment has to be worked out, on the basis of the moment-curvature diagram of the section. This calculation is performed for different values of $N = N_u$; these values are then plotted together with the corresponding values of M_u and the envelope is obtained.

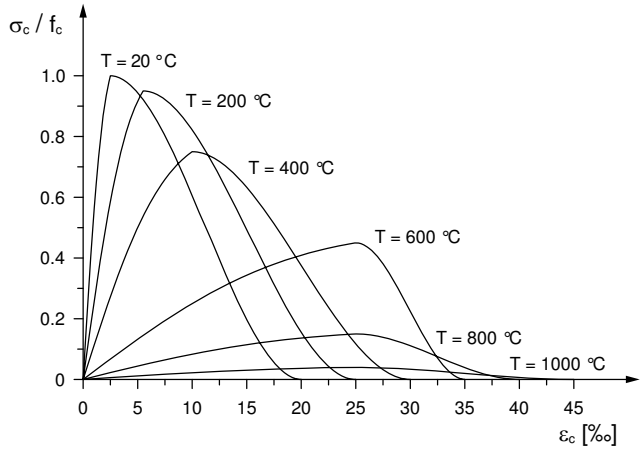

Figure 1 – Temperature-dependent stress-strain curves for concrete in compression [5].

This procedure can be easily extended to the case of fire-exposed concrete members. At first the thermal analysis is performed in order to determine the temperature distribution in the section, and the ensuing level of thermal damage in each point, for any given fire duration. The mechanical properties of the concrete and of the steel in each point can then be related to the maximum temperature reached at that point, on the basis of temperature-dependent stress-strain curves. The evaluation of the moment-curvature diagrams and of the corresponding envelopes can then be determined as explained before, even though the iterative procedure is rather demanding from a computational point of view. An example of this procedure is shown in Figure 2, with reference to the case of a NSC section exposed to the Standard ISO-834 fire on four sides (300 × 300 mm, 4∅16 rebars, f_c = 30 MPa, f_s = 500 MPa). The thermal and mechanical properties were evaluated according to EN 1992-1-2 [5].

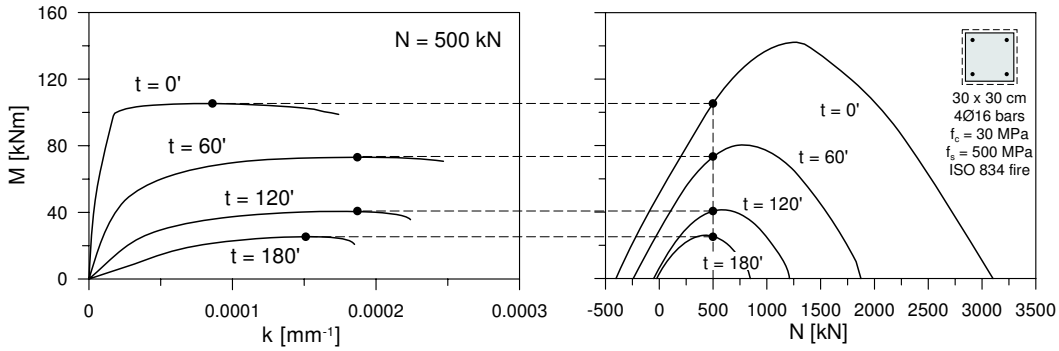

Figure 2 – Square section subjected to different values of the fire duration: M-N envelopes based on the moment-curvature diagrams (value of the axial force N = N_u = 500 kN).

2.2 Extension to the model column

As stated before, plotting the moment-curvature diagrams in fire conditions is rather demanding from a computational point of view. Nevertheless, the information contained in these diagrams allows to extend the previous results (which refer to a single section of a given

concrete member) to the whole structural element. The main steps of the method are the following:

1. the moment-curvature diagrams are determined for the current value of the axial force, for increasing values of the fire duration, taking into account the decay of both the concrete and the reinforcing steel: these diagrams represent the bearing capacity of the column;
2. the nominal 2nd-order moment is evaluated, assuming that the deformed shape of the column is the same as the critical Eulerian deformed shape; the resulting expression of the 2nd-order moment is

$$M_2 = N \frac{k l_0^{\,2}}{\pi^2} \tag{1}$$

where k is the curvature of the most stressed section, N is the axial force and l_0 is the effective length of the column, i.e. the distance between two counter-flexure points in the critical deformed shape (for columns with pinned end sections, l_0 coincides with the total height): it is worth noting that the 2nd-order moment increases linearly with the curvature;

3. the ultimate first order moment M_{1u} is determined as that corresponding to the limit equilibrium state, characterized by the tangency between the straight line representing the total bending moment ($M_{tot} = M_1 + M_2$) and the moment-curvature curve;
4. the values of M_{1u} and of the axial force $N = N_u$ are plotted in the domain M-N, and the "reduced" M-N envelopes accounting for 2nd-order effects are obtained.

It is worth remarking that the same procedure was applied in the past to NSC columns, with a slightly-different formulation (Lie et al. [7,8]): a bilinear curvature along the effective length of the column was assumed, which means that the critical deformed shape is approximated with the deformed shape of a beam subjected to a concentrated load acting in its mid-section.

The reduction due to 2nd-order effects can be rather severe: an example is shown in Figure 3, where the reduced M-N envelope for 90' fire duration of the above-mentioned section is plotted and compared with the original M-N envelope.

A further reduction of the bearing capacity occurs if the contribution of the nonlinear thermal strains and of the ensuing eigenstresses is explicitly taken care of (Figure 3, dashed curves): whereas the effect of the eigenstresses is either negligible or even beneficial when 2nd-order displacements are not present [9] (i.e. when the section is considered as such, with no reference to the whole structure), their effect on the stability of the whole structural element can be highly detrimental.

3. EXPERIMENTAL RESULTS

An application of the numerical procedure presented in the previous section was performed by fitting the experimental results obtained by Kodur et al. [10] on HSC columns.

The experimental program consisted of fire-endurance tests on 10 HSC columns, designated as HS2-1 to HS2-10. All columns had the same square cross-section (406×406 mm) and length (3810 mm). The characteristics of the columns considered in the numerical simulations are listed in Table 1.

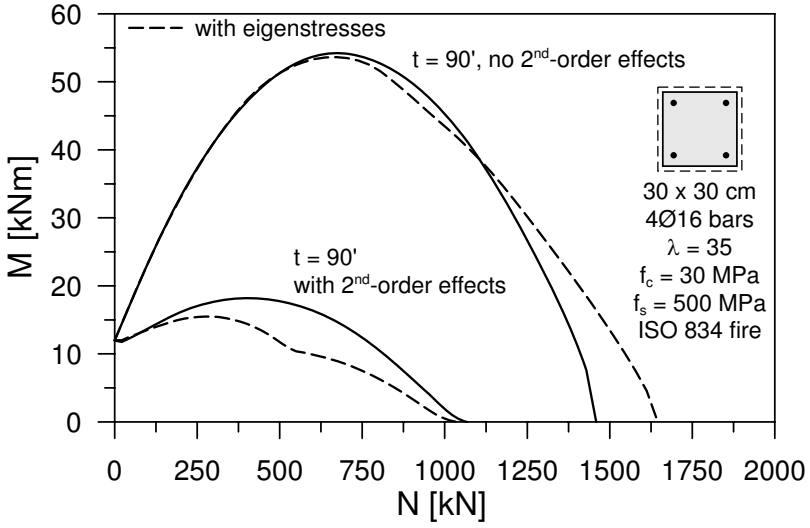

Figure 3 – M-N envelopes, with/without 2nd-order effects and eigenstresses.

Table 1 – HSC columns: summary of test parameters, results and geometry (a × a = 406 × 406 mm; h = 3810 mm; 8∅25 bars).

Column	f_c [MPa]	N_{exp} [kN]	restraints	time [min]	N_{Rd}^{20} [kN]
HS2-4	114	4567	fixed	146	20362
HS2-5	114	5373	fixed	108	20362
HS2-6	114	3546	fixed	142	20362
HS2-7	138	4233	pinned	248	24318
HS2-8	138	4981	pinned	118	24318
HS2-9	138	4981	pinned	117	24318
HS2-10	138	4981	pinned	166	24318

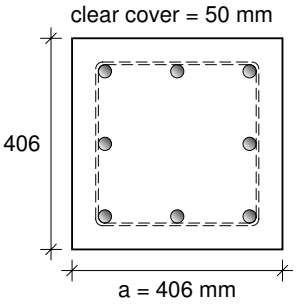

Both calcareous and siliceous aggregates were used. The fine aggregate used in the concrete mix was natural sand.

Deformed bars were adopted for both main longitudinal bars and ties. The reinforcement had a specified yield strength of 400 MPa. The longitudinal reinforcement in all columns consisted in eight 25 mm bars symmetrically placed with 40 mm clear cover to the stirrups. The main reinforcing bars were welded to steel end-plates. The steel ratio in all columns was 2.38%.

Three batches of concrete were used for the columns: Batches 1 and 3 contained carbonate aggregate, while Batch 2 had siliceous aggregate. The compressive strength of the concretes at 28 days ranged from 75 to 128 MPa; the compressive strength at the beginning of each test ranged from 81 to 138 MPa. Columns HS2-4 to HS2-6 were tested with both ends

fixed, i.e., restrained against rotation and horizontal displacement; Columns HS2-7 to HS2-10 were pinned, and consequently no horizontal displacement was possible at the end sections.

Columns HS2-4 to HS2-6 were tested in pure compression, while the remaining columns HS2-7 to HS2-10 were tested with a load eccentricity of 27 mm (Figure 4). The load was applied approximately 45 minutes before the start of each fire test and was maintained until a steady state condition was reached with no further rotations and load increases. This condition was selected as the reference condition of the column deformation. The load was constant throughout the fire-endurance test.

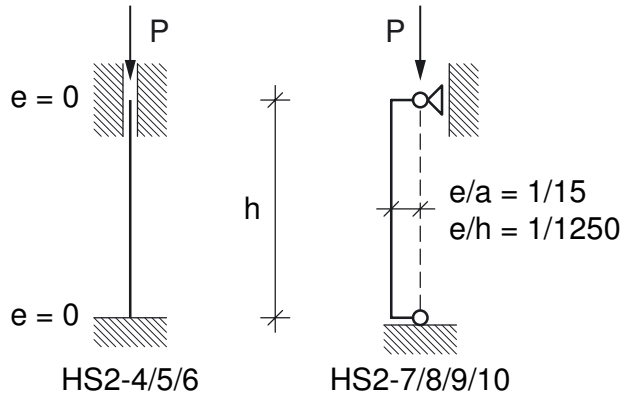

Figure 4 – Structural scheme of the columns tested by Kodur et al. [10].

The ambient temperature at the beginning of each test was approximately 20°C. During each test, the heating process was controlled in such a way that the average temperature in the furnace followed, as closely as possible, the ASTM-E119 standard temperature-time curve. An approximate formulation of the curve is given by Eq. 2:

$$T_f = 20 + 750\left(1 - e^{-3.79533\sqrt{t}}\right) + 170.41\sqrt{t} \tag{2}$$

where t is the time in hours and T_f is the temperature of the furnace in °C. The columns were assumed to be at the onset of failure (and the tests stopped) when the axial hydraulic jack could no longer maintain the load.

In the numerical simulations, the decay of the thermal and mechanical properties was evaluated according to the provisions of EN 1992-1-2. The density and specific heat, which are almost constant with temperature, were given the same values as for NSC (Figure 5a,b). Since the concrete used for these specimens was a high-strength concrete, which is generally characterized by a higher thermal diffusivity, the upper bound suggested in EN 1992-1-2 was assumed for the thermal conductivity (Figure 5c). Moreover, the decay of concrete strength was evaluated according to the provisions given for high-strength concrete (Figure 5d), with the typical steep strength reduction at low temperatures (T = 20-200°C).

3.1 Effect of the end restraints

In the experimental set-up of the first three columns (HS2-4, HS2-5 and HS2-6) the end sections were fixed. Considering an effective length $l_0 = h/2 = 1905$ mm in Eq. 1, the corresponding interaction domains for a time duration of 110 and 140 minutes are plotted in Figure 6 (continuous lines): these values of the fire duration are very close to the measured

fire resistances (108 minutes for the column HS2-5; 146 and 142 minutes for the columns HS2-4 and HS2-6). Consequently, the two M-N envelopes in Figure 6 can be considered as those of the sections HS2-5, HS2-4 and HS2-6 at the onset of failure in fire. In Figure 6 the numerical values of the axial capacities are by far larger than the experimental values ($N_{th}/N_{exp} \approx 2 \div 4$).

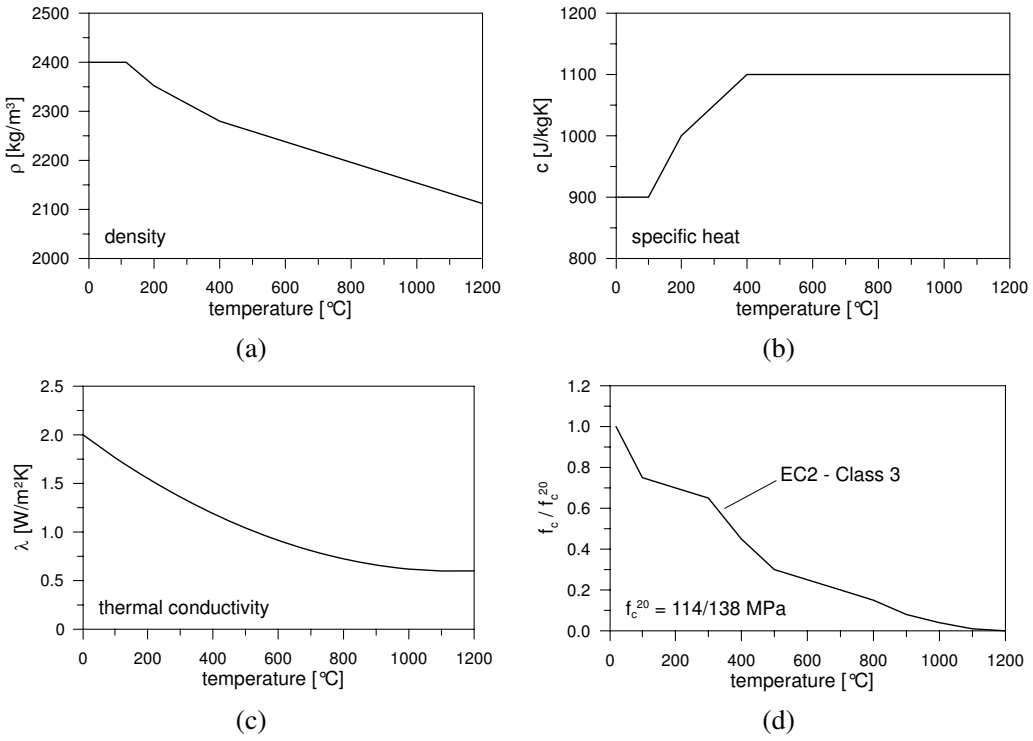

Figure 5 – Thermal and mechanical properties as a function of the temperature: (a) density; (b) specific heat; (c) thermal conductivity; and (d) compressive strength.

This overestimation can be significantly reduced if the end sections are assumed to be partially built-in, which means that a certain degree of rotation is possible: the limit condition is to consider the end sections pinned and therefore to increase the effective length (Eq. 1) to 3810 mm. The corresponding interaction domains are plotted in Figure 6 (dashed curves): the calculated bearing capacities in pure compression are still higher than the corresponding experimental values, but the difference is markedly reduced ($N_{th}/N_{exp} \approx 1.5 \div 2$).

A possible way to explain the difference between the experimental and the numerical values is to assume that the load is not perfectly aligned with the axis of the columns (unintentional eccentricity). Approximate values of the possible unintentional eccentricity can be calculated as shown in Figure 6, by moving vertically the points corresponding to the experimental values of the ultimate axial forces vertically. The intersection between the vertical lines and the failure envelopes makes it possible to identify the eccentricity that might be the culprit of the relatively low axial capacity in each test. This procedure can be adopted for both restraint conditions (built-in and hinged ends): the values of the eccentricity are summarized in Table 2. It is worth noting that only if the columns are assumed to be pinned,

the unintentional eccentricity is of the same order of magnitude of the usual values suggested in the codes (e.g., e ≤ a/30 in EN 1992-1-1 [4]).

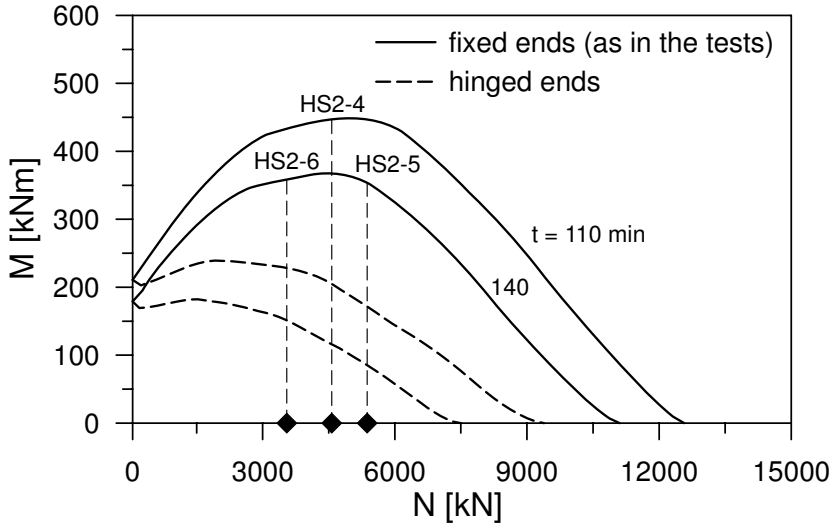

Figure 6 – Interaction envelopes resulting from two different restraint conditions.

Table 2 – Unintentional eccentricity for built-in end sections (as in the tests [10]) and in the limit case of hinged end sections.

column	e [mm] (fixed ends)	e [mm] (hinged ends)
HS2-4	77 (≈ a/5)	22 (≈ a/18)
HS2-5	84 (≈ a/5)	33 (≈ a/12)
HS2-6	100 (≈ a/4)	41 (≈ a/10)

With reference to the remaining columns (HS2-7 to HS2-10), a reduction of the restraint degree is not applicable, since they were all pinned.

Since the values of the unintentional eccentricity are rather large (and definitely larger than those suggested in the codes) cover spalling is probably the main factor in the reduction of the axial capacity, as shown in the following section.

3.2 Effect of cover spalling

During the fire-endurance tests, a more or less severe spalling was observed. The ensuing reduction of the effective cross section might have been the cause of the reduction in the bearing capacity. The spalling of the cover was taken into account in the numerical simulations by simply reducing the concrete section, from the beginning of the thermal and mechanical analyses. As a matter of fact, spalling usually occurs in the early phase of the heating process, when the heating rate is high. For normal-strength elements and typical temperature-time curves, it is reasonable to assume that spalling occurs during the first half hour and that it reduces the section by approximately 15% of the gross concrete section [11]. In

our simulations, the evolution of the spalling was quantified as a percentage of the clear cover, from the surface to the longitudinal reinforcement (50 and 100% of the clear cover). The interaction envelopes are shown in Figure 7. It is worth noting that, whereas the reduction of the restraint at the end sections implies a change in the shape of the domains, a reduction of the section leads to a "shrinkage" of the domains.

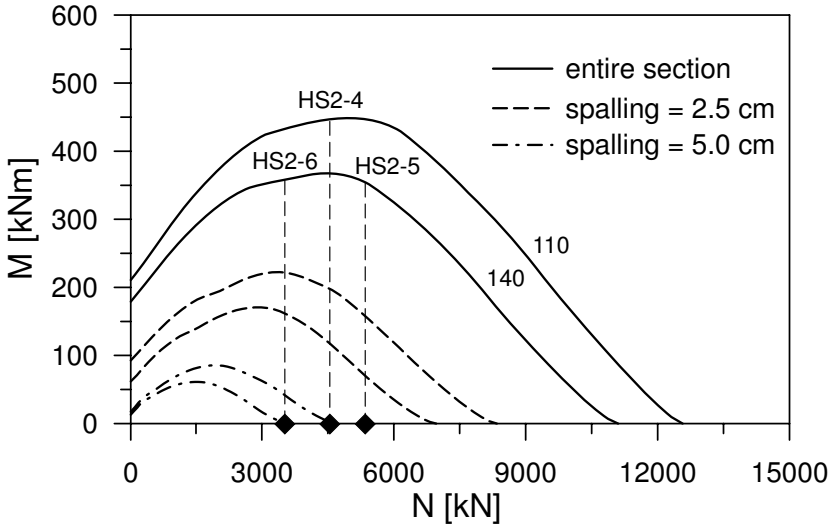

Figure 7 – Interaction envelopes for built-in columns, with/without spalling, as in the tests presented in [10].

In the cases examined in Figure 7, spalling may be an explanation of the limited fire endurance of the columns. As a matter of fact, if the load is assumed to be perfectly aligned with the axis of the column, the numerical and experimental values are rather close and the overestimation of the bearing capacities is significantly reduced:

- $N_{th}/N_{exp} \approx 1.5 \div 2.0$ if the spalling is limited to 50% of the cover;
- $N_{th}/N_{exp} \approx 0.7 \div 1.0$ if the spalling is extended to the entire cover.

The same procedure can be applied to the remaining pinned columns (HS2-7 to HS2-10); in these cases the comparison between the numerical and experimental results (Figure 8) shows that the ultimate situation was reached with no spalling in one case (HS2-10), and in two cases (HS2-8 and HS2-9) with limited spalling (less than 2.5 cm, i.e. less than half the clear cover). In all cases the eccentricity was prefixed (e = 27 mm = a/15). It should be observed that, justifying the reduced bearing capacity in terms of unintentional eccentricity seems hardly possible, because in such a case the calculated total eccentricity would be 60% larger than the prefixed eccentricity (e_{tot} = 44 mm = 27 + 17 mm ≈ a/15). This value is definitely larger than the value specified in the codes (e ≤ a/30 in EN 1992-1-1 [4]).

It is worth noting that the point corresponding to column HS2-7 is not shown in Figure 7, since its fire endurance was definitely too large.

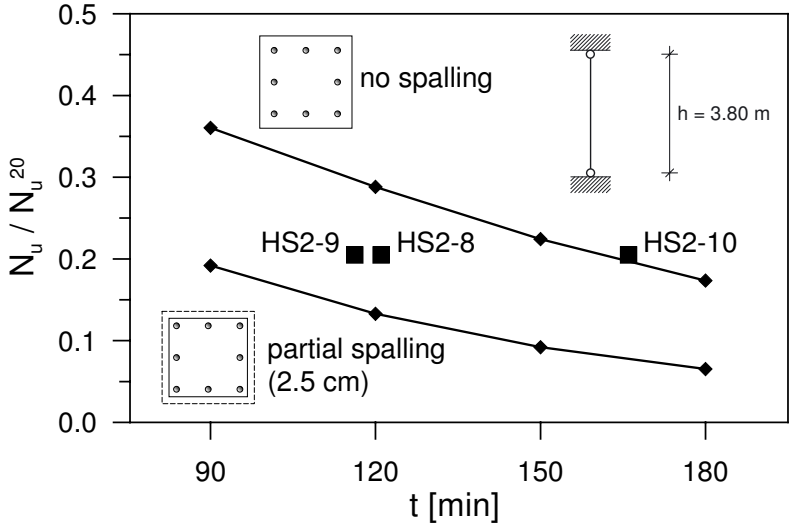

Figure 8 – Reduction of the resisting axial force for pinned columns [10] with/without cover spalling.

4. CONCLUDING REMARKS

The well-known model-column approach has been applied to investigate the buckling of HSC columns, with the end sections either fixed or hinged, in order to have information on the buckling-triggered reduction of the M-N envelopes in fire conditions, and to model a few recent, well-documented tests (without end eccentricities in clamped columns and with a prefixed eccentricity in pinned columns).

While the marked reduction of the envelopes in HSC sections is a confirmation of what is well known in NSC sections, the modelling of the tests poses at least a couple of questions, since the experimental failure loads are definitely smaller than the predicted failure loads. The reasons could be: (a) possible unintentional eccentricities (particularly in clamped columns, where the prefixed eccentricity is zero), and (b) cover spalling, that is unavoidable in any HSC section, unless polypropylene fibers are used in the mix (but this was not the case in the tests reported here).

In the columns with built-in end sections examined in this study, the unintentional eccentricity resulting from the analysis is rather pronounced (from 1/4 to 1/5 of section side). Consequently, the question is whether the unintentional eccentricity alone can explain the rather low experimental failure loads, or other phenomena (like cover spalling) should be considered. As a matter of fact, by introducing the spalling as a uniform reduction of the cover, the experimental and numerical results turn out to be very close, on condition that the spalling is severe (the whole net cover is removed).

In the 3 pinned columns examined here the unintentional eccentricity seems to play a minor role, while – again – the cover spalling plays a substantial role, since a moderate degree of spalling (less than half of the clear cover) justifies the axial-capacity reduction in 2 of the 3 cases examined (in the third case column failure seems to occur without any spalling at all).

Summing up, unintentional eccentricities (mostly due to concrete lack of uniformity), cover spalling and a combination of these phenomena are the main factors that control column stability in fire. Unfortunately, both unintentional eccentricities and cover spalling are rather

unpredictable. However, in the cases examined in this study cover spalling gives a more convincing justification to the discrepancy between the experimental and the numerical results. Hence the designer should introduce a moderate-to-severe cover spalling to be on the safe side in column design.

ACKNOWLEDGEMENTS

This study was financially supported by the Italian National Research Project – PRIN "Optimization of the Structural, Technological and Functional Performance of the Concrete Mixes used in Tunnel Linings" (2007-08). The assistance of Prof. Pietro Gambarova – Head of the Research Team in Milan, and of Giovanni Plizzari – Coordinator at the national level are gratefully acknowledged.

REFERENCES

[1] Biondini F. and Nero A., "Nonlinear Analysis of Concrete Structures Exposed to Fire", Proceedings of the 2nd International *fib* Congress, Napoli (Italy), 5-8 June 2006, Vol. 2, pp. 230-231 (full paper on CD).
[2] Riva P., "Structural Behaviour", *fib* Bulletin "Fire Design of Concrete Structures", edited by the *fib* TG 4.3, 2008, in publication.
[3] Mlakar P.F., Dusenberry D.O., Harris J.R., Haynes G., Phan L.T. and Sozen M.A. – *The Pentagon Building Fire Performance Report*, ASCE, January 2003.
[4] EN1992-1-1 - *Eurocode 2: Design of Concrete Structures - Part 1-1: General rules and rules for buildings*, December 2004, 225 pp.
[5] EN1992-1-2 - *Eurocode 2: Design of Concrete Structures - Part 1-2: General rules – Structural Fire Design*, December 2004, 97 pp.
[6] Buchanan A.H., *Structural Design for Fire Safety*, John Wiley & Sons, 2001.
[7] Lie T.T and Celikkol B., "Method to Calculate the Fire Resistance of Circular Reinforced Concrete Columns", *ACI Materials Journal*, V. 88, No. 1, January-February 1991, pp. 84-91.
[8] Lie T.T. and Irwin R.J., "Method to Calculate the Fire Resistance of Reinforced Concrete Columns with Rectangular Cross Section", *ACI Structural Journal*, V. 90, No. 1, January-February 1988, pp. 52-60.
[9] Bamonte P. and Meda A., "Sectional Analysis", *fib* Bulletin "Fire Design of Concrete Structures", edited by the *fib* TG 4.3, 2008, in publication.
[10] Kodur V., McGrath R., Leroux P. & Latour J. - *Fire Endurance Experiments on High-Strength Concrete Columns*, Report No. RD138, Portland Cement Association, 5420 Old Orchard Road, Skokie (Illinois, USA), 2004.
[11] Dotreppe J.-C., Franssen J.-M. and Vanderzeypen Y., "Calculation Method for Design of Reinforced Concrete Columns under Fire Conditions", *ACI Structural Journal*, V. 96, No. 1, January-February 1999, pp.9-20.

EXPERIMENTAL RESEARCH ON FIRE PERFORMANCE OF AXIALLY RESTRAINED RC COLUMNS WITH L-SHAPED CROSS SECTION

BO WU[1] and YI-HAI LI[2]

ABSTRACT

This paper presents an experimental study on the behavior of four concentrically loaded L-shaped RC columns subjected to ISO834 fire. The main objective of the paper is to investigate the effect of axial restraint on columns during both expanding and contracting phases. The fire tests, which consist of four combinations of two levels of axial load with two degrees of axial restraint, were conducted at the fire laboratory of South China University of Technology. Axial restraints were imposed on columns using a flange steel beam. Different degrees of axial restraint were obtained by varying the length of the restraining beam. The boundary conditions of the columns were considered as fixed-fixed for all tests. In each test, the fire was stopped when approximate 50% of the applied load was transferred from column to the restraining beam, and then the behavior of axially restrained column during the cooling process was also studied to some degree. Special attention was given to eliminate the mechanical slack during both heating and cooling phases. Finally, the finite element program, SAFIR, is employed to conduct a numerical analysis of the tests. It is found that: (a) displacements of columns subjected to the same axial restraint ratio follow similar path (nearly parallel) during the contracting phase and all four columns experienced similar path

[1] Professor, South China University of Technology, Department of Civil Engineering, State Key Laboratory of Subtropical Building Science, 510640,Guangzhou, China, email: bowu@scut.edu.cn

[2] PhD student, South China University of Technology, Department of Civil Engineering, 510640,Guangzhou, China, email: yihai.li@mail.scut.edu.cn

during cooling phase; (b) for columns subjected to same load ratio, the axial restraint ratio seems to have little effect on the development of column axial load during contracting and cooling phases; (c) for test columns with the same load level, the time that the column additional axial force reduces to zero (i.e., the column internal axial force reduces to the initial value before heating) is almost the same, regardless of the axial restraint degrees; and (d) the maximum additional axial forces induced in axially restrained columns with axial restraint ratios of 0.0578 and 0.0875 are, respectively, around 34% and 53% of the designed load for the load ratio of 0.25; for the load ratio of 0.35, the additional forces are 26% and 30% of the designed load

1. INTRODUCTION

Columns acting as part of a frame exhibit different behavior from that of isolated ones in fire, because of the considerable restraint and continuity provided by abutting structure. Axial restraint, in particular, may accelerate the columns failure due to the additional axial forces generated in columns during expanding phase.

In recent years, reinforced concrete (RC) columns with special-shaped have been gaining popularity in the engineering industry for they excel in enlarging useful indoor area, compared with columns with rectangular cross section. The behaviors of columns with special-shaped cross section, such as load bearing capacity or seismic capacity, have been studied extensively. Special-shaped columns, be they L-shaped, T-shaped or +-shaped, are thinner in nature and thus have lower fire resistance. But to the author's best knowledge, their fire resistance has been scarcely reported.

In the past decade, research has been concentrated on the behavior of restrained steel and composite columns in fire.[1-15] However, the same level of development has not taken place for reinforced concrete columns. Ali et al.[16] have reported a research on 93 half–scale restrained high and normal strength concrete columns subjected to fire, with special focus on concrete spalling. Benmarce et al.[17] have conducted a study of 12 restrained high strength concrete columns under fire. In both of the previous two tests, axial restraint was imposed to the columns by employing specially design rubber springs. The main disadvantage lies in that failure occurs when the column displacement and axial force go back to initial equilibrium state during the contracting phase (zero displacement before heating).

The objective of the research is to investigate the full behavior, including expanding and contracting phase, of restrained concrete column during fire. The paper outline the experimental programme and presents the experimental results of four L-shaped reinforced concrete columns that were carried out recently in South China University of Technology. The paper finally employed finite element method to validate the experimental results.

2. EXPERIMENTAL PROGRAMME

2.1. Test specimens

The experimental research focuses on influence of the two main factors, load ratio and axial restraint ratio, as listed in Table 1. k_c, k_l, β and α denote axial stiffness of column, axial restraint stiffness, axial restraint ratio and load ratio, respectively. All columns have a nominal height of 2340mm and only the center portion of 1650mm is exposed to fire on all sides. Each column is reinforced with 12 longitudinal rebars with a diameter of 10mm and the steel ratio is 2.36%. Steel bars with a diameter of 6mm are used for ties, which are spaced at 100mm within the central fire exposed portion. The mechanical properties of materials measured experimentally are summarized in Table 2 and specimen details are shown in Fig. 1. The initial axial load level is relatively low, but this low load ratio ensures that the column would not fail during the heating process.

In order to ensure the connectivity and avoid local failure of concrete near the top and bottom ends of the specimens, the enlarged portion with dimensions of 400×400×325mm plus the 20mm steel plate at both ends of the column were wrapped with ceramic fiber blanket.

Table 1 Summary of specimen parameters

Column NO.	α -	k_c (MN/m)	k_l (MN/m) ABAQUS	k_l (MN/m) measured	β -
RCL11	0.25	596.4	66.0	34.5	0.0578
RCL12	0.25	596.4	108.0	51.9	0.0870
RCL21	0.35	596.4	66.0	34.5	0.0578
RCL22	0.35	596.4	108.0	51.9	0.0870

Table 2 Material properties of tested columns

Concrete	f_c (MPa)	E_c (GPa)	Rebar	f_y (MPa)	E_s (GPa)
C30	29.4	30.4	Main bar	365	200
			Tie	432	200

2.2. Test set-up

The tests were performed under transient heating state conditions, i.e. the column was loaded at room temperature and load was kept constant during the fire exposure. Fig. 2 shows the test set-up. Each test assembly consisted of a RC column and a steel flange beam. The bottom end plate of the RC column is fixed to the ground base by 12 bolts to simulate fixed-end support. The column top steel plate was connected to the bottom flange of the restraining beam by bolts, which was restrained from rotation during the test.

A reaction frame constructed outside the furnace and fixed to ground, was used to apply the vertical loads. Ribbed stiffeners were welded to the reaction frame and the restraining beam to avoid any local failure. The reaction frame had a testing capacity of 1200kN.

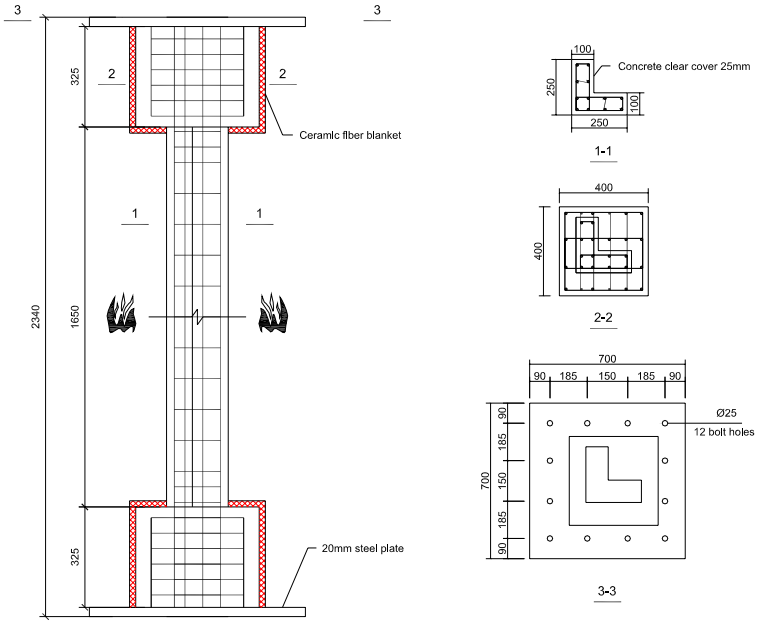

Fig. 1 Details of the test specimens

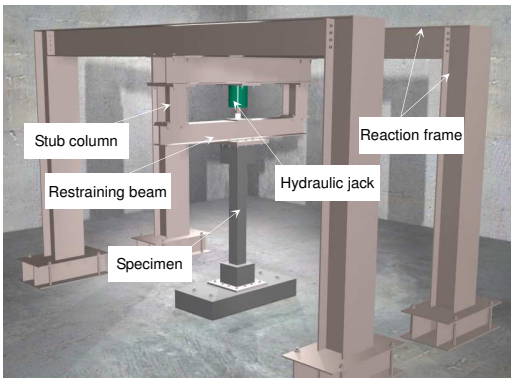

Fig. 2 Arrangement of the test set-up

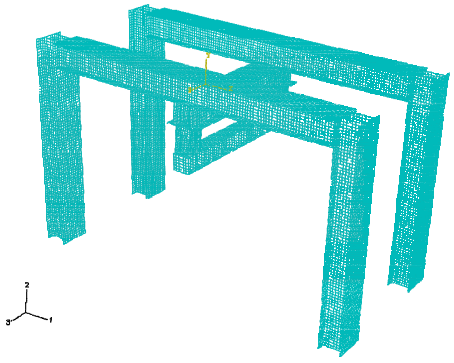

Fig. 3 The numerical model in ABAQUS

2.2.1. Furnace construction

The tests were carried out in one of the two furnaces in the fire laboratory of South China University of Technology. Fig. 4 shows the furnace construction. The internal dimension of this furnace is 4m×3m×1.5m. The upper panel of the furnace is removable to facilitate assembly of the test specimens. Openings of the unheated part were filled with ceramic fiber materials and insulation board, which insures that the restraining beam remains unheated in room temperature.

The furnace consists of 24 gas burners, with firing and control equipment installed and connected to computers. The gas burners are evenly and symmetrically distributed on the

north and south side of the furnace. Average temperature inside the furnace is recorded by 8 embedded thermocouples and automatically controlled by computers to follow the standard ISO834 curve.

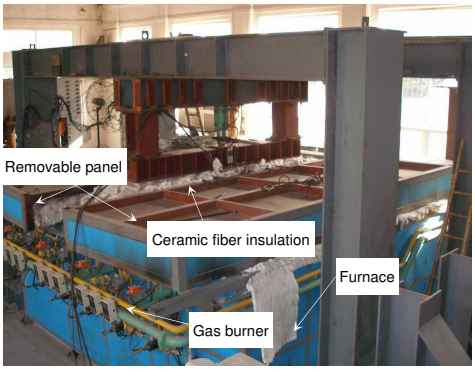

Fig. 4 Furnace construction and test set-up

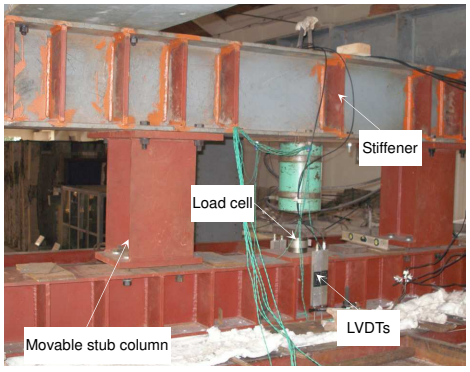

Fig. 5 Restraining beam

2.2.2. Loading facility and axial restraining system

Restraining beam and the column-to-beam connections were projected outside the furnace to facilitate the application of loads. Vertical loading was imposed to the top flange of the restraining beam through a hydraulic jack, which was controlled and recorded manually to maintain constant load. Additional axial load generated during the expanding phase was carried by the transverse steel beam. During the contracting phase beyond the initial equilibrium state, loads were transferred to the restraining beam supported on the reaction frame. Different axial restraint stiffnesses were obtained by varying the length of the restraining beam (by moving the stub columns, see Fig. 5).

The design of the axial restraining system is based on simulations conducted by ABAQUS using shell elements (Fig. 3). The restraint stiffness was also measured experimentally after the fabrication. As we can seen in Table 1, the overall stiffnesses of the restraining system measured are less than the corresponding analytical results. It can be explained by the fact that rigid connection is assumed between members in the numerical simulation, whereas in reality elements were connected by bolts. Therefore, the measured results are used for the later finite element analysis by SAFIR.

2.3. Test measurement

2.3.1. Temperature acquisition

Four K-type thermocouples were embedded within the mid-height cross section for each test specimen. Fig. 6 shows the locations of thermocouples within the cross section. For each test assembly, two additional thermocouples, one attached to the bottom flange of the restraining beam and the other attached to the surface of the enlarged section, were used to see if they were influenced by high temperatures. All thermocouples were connected to computer and the temperatures were recorded automatically every one minute.

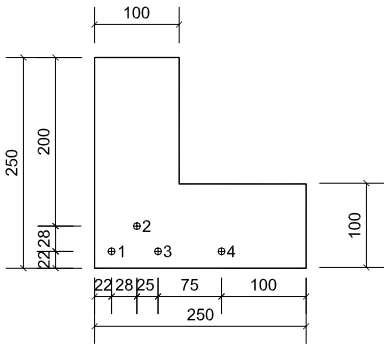

Fig. 6 Locations of the thermocouples

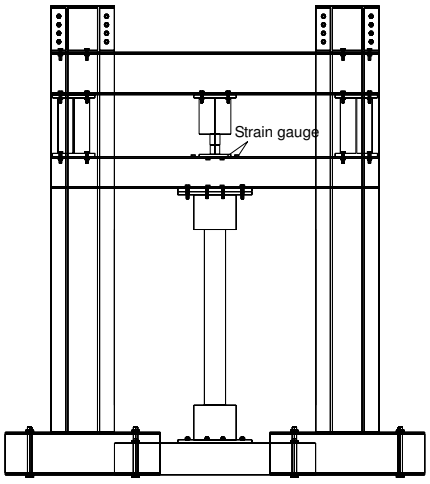

Fig. 7 positions of the strain gauges

2.3.2. Deflection and axial load measurement instrumentation

Axial deformations were measured using four linear variable displacement transducers (LVDTs) symmetrically located at the top end plate of column (Fig. 5). A load cell attached to the hydraulic jack was used to measure the applied loads, which were kept constant during the test. No strain gauge can be placed on columns because of the high temperatures during the fire attack. Thus, the axial load in test columns can not be obtained directly. In this way, a total number of six strain gauges were positioned on the restraining flange beam. For each test, the sum of force taken by the restraining beam and applied load was then deemed to give the axial load in column. Fig. 7 shows the positions of the strain gauges.

2.4. Test procedures

Before the commencement of fire exposure, axial load was imposed on the top flange of restraining beam, which was not connected to the reaction frame. It ensured that the entire load was held by column. Special attention was given to the test set-up and procedures, for there were many possible mechanical loose and gap between the members. All the possible gaps and mechanical slack had been taken care. The procedures for setting up and performing a test on a restrained concrete column under transient heating state are outlined as follows:

1. Setting up the specimen in the test rig and connecting the restraining beam to column.
2. Preloading (50% of the working load) and unloading the specimen twice to minimize the mechanical slacks in the test rig.
3. Applying the working load to the top flange of restraining beam and then holding it constant for 10 minutes to stabilize the deformation.
4. Connecting the restraining beam to reaction frame and securing the possible gaps until the strain gauges give small readings, indicating proper contact.

5. Positioning the LVDTs on the specimen and connecting LVDT wires to a data logger.
6. Joining wires of the thermocouples and strain gauges to a computer system.
7. Turning on the gas burners and heating up the column while maintain the applied load.

Unless columns failed prematurely, fire was stopped when approximately 50% of the working load was transferred from column to restraining beam, followed by a cooling phase. There was a malfunction of the control for test specimen RCL12, thus fire was stopped nine minutes after the designated time. The test was finally terminated when the average temperature in the furnace fell back to around 300°C.

3. EXPERIMENTAL RESULTS AND DISCUSSIONS

The purpose of the research project is to study the behaviors of restrained concrete columns subjected to different load ratios and restraint ratios under both heating and cooling process. The results of temperature fields, axial displacements and axial forces are presented and discussed. Finite element program SAFIR, developed by J. M. Franssen in Belgium, was used for both thermal and structural analysis. Thermal parameters and mechanical parameters for concrete and steel recommended by EC2 Pt.1.2[18] were used in the analysis.

3.1. Thermal responses

Fig. 8 shows the recorded temperature profiles at four different points (Fig. 6) within column mid-height section for test specimen RCL12. Almost the same results were obtained for other three specimens. Since there was no preset cooling-down curve, the furnace parameters were shifted to manual control at the beginning of the cooling phase to ensure similar cooling path for all tests.

Fig. 8 also shows the results of numerical analysis using SAFIR. The temperature within the cross section is highly non-uniform because of inertia of concrete to heat. In despite of the deficiency to model moisture movement towards concrete core during heating, the overall prediction of temperature is quite satisfying. The discrepancy between the experimental results and numerical results was mainly caused by different values of thermal parameters and casting errors of thermocouples. It is very interesting to note that all predicted values are somewhat lower than the recorded ones during the cooling phase. Temperatures of rebar and the outer portion of concrete decreased soon after the commencement of cooling phase. However, temperature of the inner core part of concrete continued to rise. The maximum temperature of steel beam (Point 5) and surface of enlarged cross section (Point 6) is around 30°C and 200°C, respectively, which indicated that the restraining beam and the column enlarged part were hardly influenced by increasing temperature.

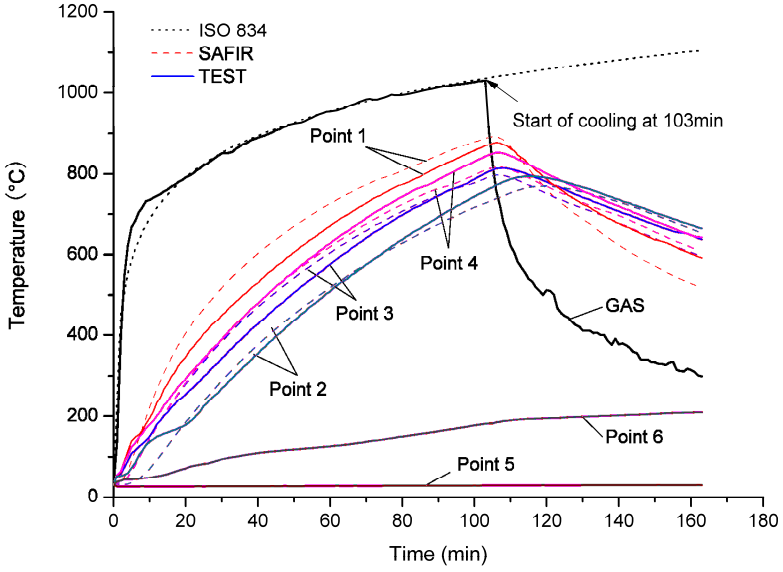

Fig. 8 Recorded temperature developments for test specimen RCL12

3.2. Structural responses

None of the four columns failed during the fire test. Very little could be observed during the test for columns were enclosed in the furnace. Fig. 9 shows the pictures of the elements after test. There were mainly vertical cracks along all sides of columns. Minor spalling (Fig. 9 (e) and (f)) was observed for two columns (RCL11 and RCL21). The axial restraint ratio seemed to have no influence on concrete spalling.

(a) RCL11 (b) RCL12 (c) RCL21 (d) RCL22 (e) Spalling of RCL11 (f) Spalling of RCL21

Fig. 9 Pictures of the columns after test

The structural analysis model in SAFIR is shown in Fig. 10, where the linear spring represents the axial restraint of the whole restraining system. Values of actually measured

ones were adopted for analysis. As tests have shown, the boundary conditions of the columns were considered as fixed-fixed.

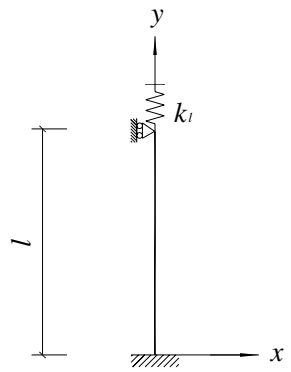

Fig. 10 Structural model in SAFIR

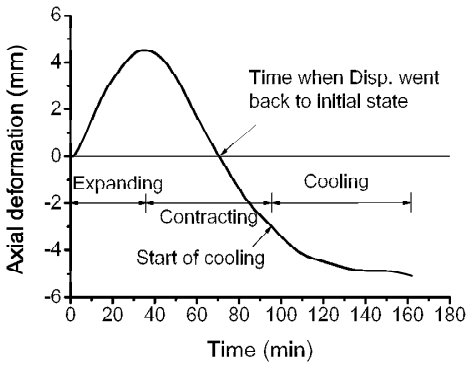

Fig. 11 Typical deformation-time curve

Fig. 11 shows the typical deformation-time curve for the specimens. The curve can be characterized by three different stages, i.e. expanding, contracting and cooling phases. Fig. 12 shows the recorded column axial deformation versus time relationships, together with the numerical results, for all tests. The measured axial deformation was calculated from the readings of four evenly distributed LVDTs. It can be seen that load ratio plays an important role on the fire behaviors of columns. The maximum deformations during expansion were influenced mostly by load ratio. For a given load ratio, axial restraint ratios had a great effect on the development of axial deformation during contraction phase beyond the initial state. We can further find that columns with the same axial restraint ratio followed similar (nearly parallel) contraction path and all four columns experienced similar path during cooling phase.

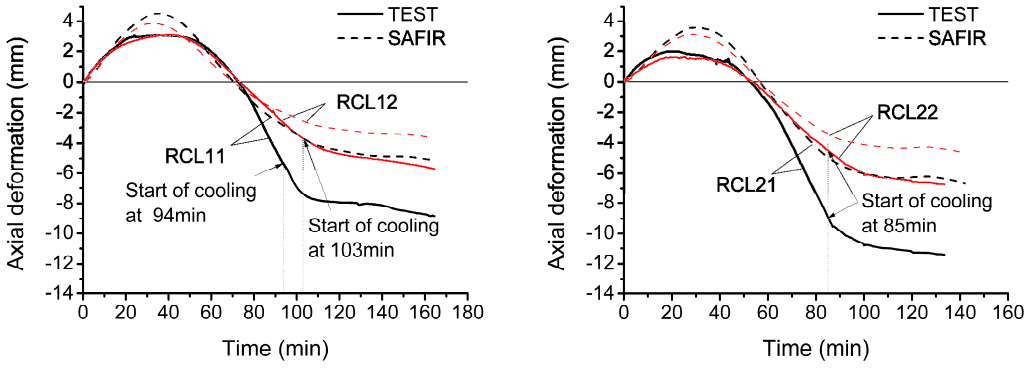

(a) $\alpha = 0.25$ (b) $\alpha = 0.35$

Fig. 12 Axial deformation-time relationships

For columns with a load ratio of 0.25, displacement went back to the initial state

before heating at 73min and 74min. For a load ratio of 0.35, the time was 54min and 57min. Table 3 summarizes the experimental and numerical results. It can be noted that for columns with the same load ratio, the deformation went back to zero at nearly the same time, regardless of the axial restraint ratios. This can also be validated in the numerical analysis. Furthermore, it can be seen that the numerical predictions of the maximum displacement are greater than the test results. It may be due to the fact that creep strain is implicitly incorporated in EC2.

Table 3 Summary of the experimental and numerical results of axial deformation

Column	α	β	Time when Disp. went back to initial state (min)		Max. Disp. during Expansion (mm)	
NO.	-	-	TEST	SAFIR	TEST	SAFIR
RCL11	0.25	0.0578	73	71	3.10	4.50
RCL12	0.25	0.0870	74	71	3.00	3.82
RCL21	0.35	0.0578	54	56	1.99	3.56
RCL22	0.35	0.0870	57	56	1.61	3.08

In each test, the applied load was imposed before connections of the end of restraining beam and kept constant manually during the fire exposure. Any additional load was taken by the restraining beam. Fig. 13 shows the column axial loads, calculated from the strain gauges plus the initial applied loads. The fluctuations of the applied loads during the test, which were fairly small and within 5% of the designated loads, are also shown in Fig. 13.

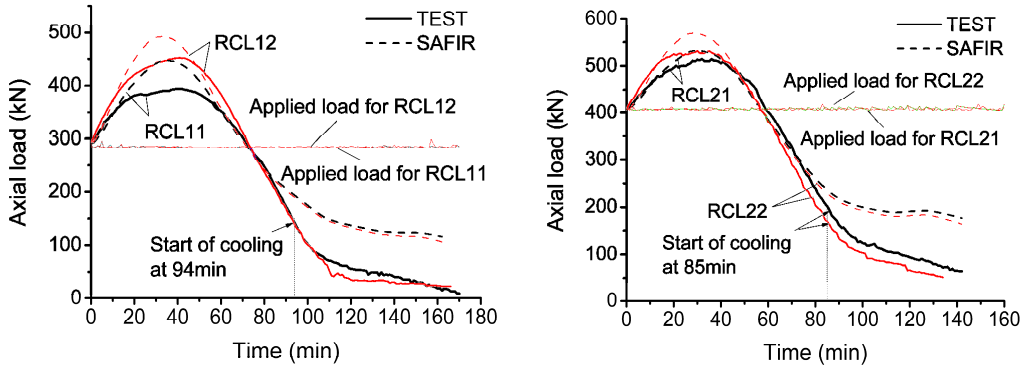

(a) α = 0.25 (b) α = 0.35

Fig. 13 Axial load-time relationships

It can clearly be seen that, for columns under the same load ratio, numerical simulation curves are consistently above the corresponding test curves. The comparison of test results to SAFIR predictions are listed in Table 4. Both numerical simulation and test results show that, for columns subjected to same load ratio, the axial restraint ratio seems to have little effect on the development of column axial load during contracting and cooling phases.

Table 4 Summary of the experimental and numerical results of axial load

Column	α	β	Time when axial load went back to initial state (min)		Max. additional axial load during Expansion (kN)	
NO.	-	-	TEST	SAFIR	TEST	SAFIR
RCL11	0.25	0.0578	72	71	100.2	153.2
RCL12	0.25	0.0870	73	71	157.9	198.4
RCL21	0.35	0.0578	59	56	106.6	123.9
RCL22	0.35	0.0870	57	56	123.7	161.0

4. CONCLUSIONS

Based on the test results and simulation analysis, the following conclusions can be drawn:

- Minor spalling was observed for two columns and axial restraint seemed to have no effect on concrete spalling.
- Temperatures of the inner core part of concrete continue to rise during the cooling phase and thus the load bearing capacity of the column continues to deteriorate.
- Displacements of columns subjected to the same axial restraint ratio follow similar path (nearly parallel) during the contracting phase and all four columns experienced similar path during cooling phase.
- For columns subjected to same load ratio, the axial restraint ratio seems to have little effect on the development of column axial load during contracting and cooling phases.
- For test columns with the same load level, the time that the column additional axial force reduces to zero (and deformation went back to zero) is almost the same, regardless of the axial restraint degrees.
- The maximum additional axial forces induced in axially restrained columns with axial restraint ratios of 0.0578 and 0.0875 are, respectively, around 34% and 53% of the designed load for the load ratio of 0.25. For the load ratio of 0.35, the additional forces are 26% and 30% of the designed load.

ACKNOWLEDGEMENTS

The authors want to express their gratitude to the financial support of National Natural Science Foundation of China (No.50738005, 50478078) and Ministry of Education of China (No.NCET-04-0819). The authors are also grateful to Dr. Zhan-Fei Huang for his discussions and suggestions on the initial design of the restraining system.

REFERENCES

[1] Ali Faris,O'connor David. Structural performance of rotationally restrained steel columns in fire Fire Safety Journal, 36(7): 679-691.2001.

[2] Ali Faris A., Shepherd Paul, Randall Michael, Simms Ian W., O'connor David J., and Burgess Ian. The effect of axial restraint on the fire resistance of steel columns Journal of Constructional Steel Research, 46(1-3): 305-306.1998.
[3] Cabrita Neves I. The critical temperature of steel columns with restrained thermal elongation Fire Safety Journal, 24(3): 211-227.1995.
[4] Cabrita Neves I., Valente J. C., and Correia Rodrigues J. P. Thermal restraint and fire resistance of columns Fire Safety Journal, 37(8): 753-771.2002.
[5] Huang Zhan-Fei,Tan Kang-Hai. Effects of external bending moments and heating schemes on the responses of thermally restrained steel columns Engineering Structures, 26(6): 769-780.2004.
[6] Huang Zhan-Fei, Tan Kang-Hai, and Phng Guan-Hwee. Axial restraint effects on the fire resistance of composite columns encasing I-section steel Journal of Constructional Steel Research, 63(4): 437-447.2007.
[7] Huang Zhan-Fei, Tan Kang-Hai, and Ting Seng-Kiong. Heating rate and boundary restraint effects on fire resistance of steel columns with creep Engineering Structures, 28(6): 805-817.2006.
[8] Rodrigues J. P. Correia, Cabrita Neves I., and Valente J. C. Experimental research on the critical temperature of compressed steel elements with restrained thermal elongation Fire Safety Journal, 35(2): 77-98.2000.
[9] Tan Kang-Hai, Toh Wee-Siang, Huang Zhan-Fei, and Phng Guan-Hwee. Structural responses of restrained steel columns at elevated temperatures. Part 1: Experiments Engineering Structures, 29(8): 1641-1652.2007.
[10] Valente Joaquim C.,Neves I. Cabrita. Fire resistance of steel columns with elastically restrained axial elongation and bending Journal of Constructional Steel Research, 52(3): 319-331.1999.
[11] Wang Y. C. Effects of structural continuity on fire resistant design of steel columns in non-sway multi-storey frames Fire Safety Journal, 28(2): 101-116.1997.
[12] Wang Y. C. The effects of structural continuity on the fire resistance of concrete filled columns in non-sway frames Journal of Constructional Steel Research, 50(2): 177-197.1999.
[13] Wang Y. C.,Davies J. M. An experimental study of non-sway loaded and rotationally restrained steel column assemblies under fire conditions: analysis of test results and design calculations Journal of Constructional Steel Research, 59(3): 291-313.2003.
[14] Wang Y. C.,Davies J. M. An experimental study of the fire performance of non-sway loaded concrete-filled steel tubular column assemblies with extended end plate connections Journal of Constructional Steel Research, 59(7): 819-838.2003.
[15] Wang Y. C.,Davies J. M. Fire tests of non-sway loaded and rotationally restrained steel column assemblies Journal of Constructional Steel Research, 59(3): 359-383.2003.
[16] Ali Faris, Nadjai Ali, Silcock Gordon, and Abu-Tair Abid. Outcomes of a major research on fire resistance of concrete columns Fire Safety Journal, 39(6): 433-445.2004.
[17] Benmarce Abdelaziz,Guenfoud Mohamed. Behaviour of axially restrained high strength concrete columns under fire Construction and Building Materials, In Press, Corrected Proof.
[18] European Committee for Standardization (CEN). Design of concrete structures: Part 1.2. General rules – structural fire design. BS EN 1992-1-2:2004: Brussels (United Kingdom). 2004.

CONSIDERATION OF NONLINEAR CREEP STRAIN OF SILICEOUS CONCRETE ON CALCULATION OF MECHANICAL STRAIN UNDER TRANSIENT TEMPERATURES AS A FUNCTION OF LOAD HISTORY

ULRICH SCHNEIDER[1], MARTIN SCHNEIDER[2], JEAN-MARC FRANSSEN[3]

ABSTRACT

The paper is given of an extended model for concrete in compression at elevated temperature that incorporates elastic, plastic and creep strain as a function of temperature and stress history. The mechanical strain calculated as a function of elastic strain, plastic strain and thermal induced strain. The thermal induced strain is relative independent compared to dependence of Young's Modulus by load history. Actually the term comprises elastic, plastic and (pure) transient creep strains as we will show. A comparison is given between experimental results with cylindrical specimens and calculated results.

1 INTRODUCTION

For the calculation of deformation and load bearing capacity of structures at high temperatures, the material laws depend on loads and temperatures. Both effects are interactive and have to be included in the calculation of deformation and load bearing for the material. Analysis revealed that, at high temperature, restrained parts of the structure show a relative increase of stiffness compared to unrestraint components [1].

[1] Professor, University of Technology Vienna, Karlsplatz 13/206, 1040 Wien, Austria,
email: ulrich.schneider+e206@tuwien.ac.at
[2] PhD Student, University of Technology Vienna, Karlsplatz 13/206, 1040 Wien, Austria,
email: e0527948@stud4.tuwien.ac.at
[3] Professor, NFSR Belgium, University of Liege, 1, Ch. Des Chevreuils, 4000, Liège, Belgium,
email: jm.franssen@ulg.ac.be

Thermal strain doesn't depend on load. The mechanical strain depends on both temperatures and loads [2]. Therefore this behaviour is further referred to as „load history", because we assume transient temperatures, i.e. the temperature is a function of time.

In this paper is presented a concrete model for the calculation of separate strains of concrete under compression based on transient temperature effects. The results relate to temperature and load history.

2 GENERAL DEFINITIONS

It is generally agreed that the total strain ε_{tot} comprises the following parts:

$$\varepsilon_{tot} = \varepsilon_{el} + \varepsilon_{pl} + \varepsilon_{tr} + \varepsilon_{th} \tag{1}$$

where: ε_{tot} total strain, ε_{el} elastic strain, ε_{pl} plastic strain, ε_{tr} total transient creep strain, ε_{th} thermal dilatation

It is therefore convenient to write for the pure mechanical strain:

$$\varepsilon_{m} = \varepsilon_{el} + \varepsilon_{pl} + \varepsilon_{tr} = \varepsilon_{tot} - \varepsilon_{th} \tag{2}$$

During an isothermal creep test the following types of deformation occur, see Figure 1:

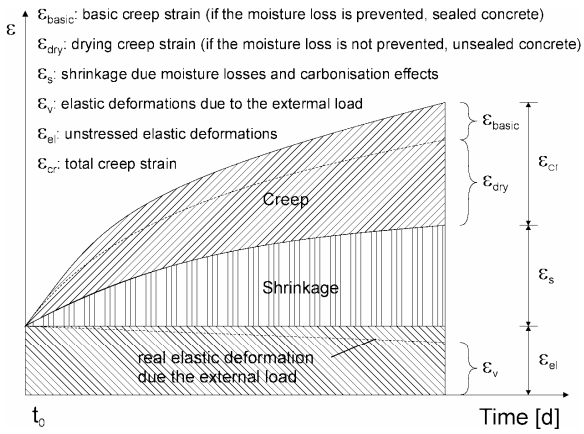

Fig. 1 - Deformations of concrete at ambient temperatures subjected to a constant compressive load, according to [3].

According to [4], in this case the term ε_{m} is called „load inducted thermal strain". It consists of transient creep (transitional thermal creep and drying creep), basic creep and elastic strains.

Figure 2 shows the evolution of the total strain for specimens under different constant loads during heating up based on the calculation with the concrete model presented in this paper. The high influence of load during transient heating up is to be seen. The elastic strain is very small at temperature T = 20°C compared to the high deformation at high temperatures.

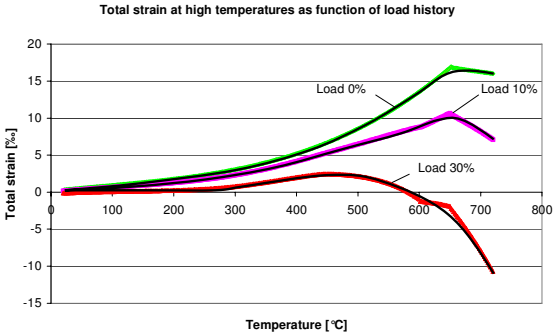

Fig. 2 - Total strain at high temperatures as a function of load history.

In the following the temperature at any time is referred as T and the maximum experienced temperature as T_{max}.

3 THERMAL STRAIN

Figure 3 shows the thermal strains of concrete with different aggregates and the thermal strain of steel compared to it.

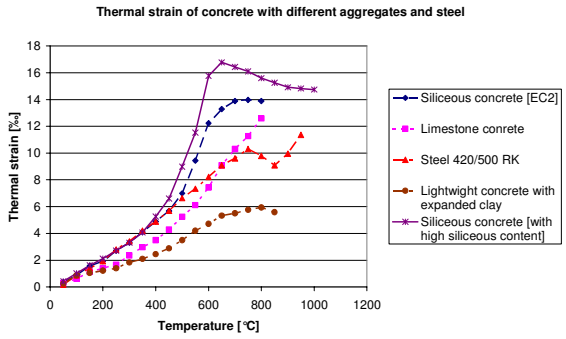

Fig. 3 - Thermal strain of concrete with different aggregates and steel; according to [1, 5].

According to Figure 3, the line of siliceous concrete with a high siliceous content is calculated according to a regression function:

$$\varepsilon_{th} = 6.6*10^{-11}*T^3 - 1.7*10^{-8}*T^2 + 9*10^{-6}*T + 1.369*10^{-4} \qquad (T \le 650°C) \qquad (3)$$

$$\varepsilon_{th} = 2*10^{-8}*T^2 - 3.94*10^{-5}*T + 0.0342 \qquad (T > 650°C) \qquad (4)$$

It is assumed that concrete has different moisture content inside. Drying occurs through capillary pores and micro cracks. Shrinkage is accounted for by the thermal strain as this is usually determined by testing unsealed concrete specimens[3], i.e. shrinkage occurs simultaneously to thermal expansion during transient temperatures.

4 CALCULATION OF MECHANICAL STRAIN

4.1 Consideration of load history

To calculate the mechanical strain a load factor is established. This factor is calculated as follows:

$$\alpha = \frac{\sigma_{hist}}{f_c(20°C)} \tag{5}$$

This factor presents the load history and is used for structures which are loaded in the elastic range $\alpha \leq 0.3$, whereas some researchers adopt $\alpha \leq 0.4$ as upper limit for the application of this method.

In compression, thermal induced cracks will be closed. Therefore one can observe a relative increase of stiffness compared to unstressed concrete during first heating. Even though the dehydratation of cementitious binder generally leads to a decreasing stiffness (see Figure 4).

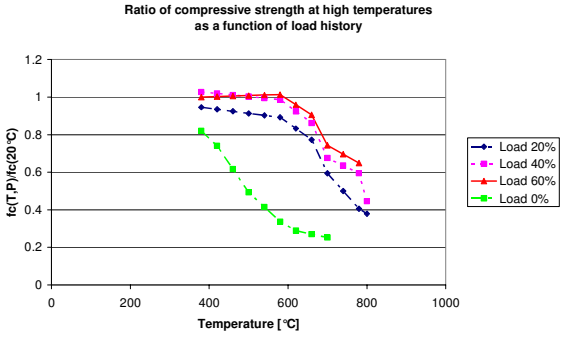

Fig. 4 - Comparison of concrete strength for different stress-temperature history; according to [7].

Figure 4 shows that an increase of the load factor up to $0 < \alpha \leq 0.3$ respective $0 < \alpha \leq 0.4$ indicates very clearly the relative increase of strength compared to $\alpha = 0$. A further increase of the load factor doesn't increase significantly the stiffness.

4.2 Compressive strength

Figure 5 shows the compressive strength as a function of temperature and load history compared to measurements [1]. $f_c(20°C)$ is an experimental result for the OPC tested and cured under RILEM conditions [8].

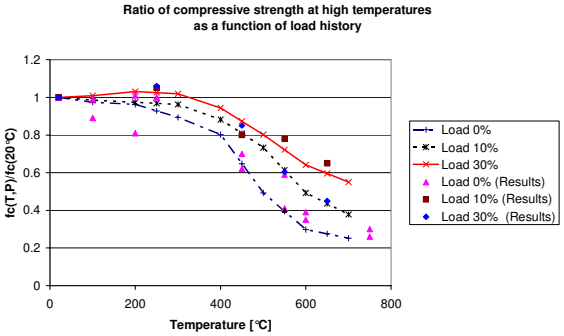

Fig. 5 - High temperature compressive strength of siliceous concrete being loaded or not loaded during heating up – experimental and calculated results, according to [1].

The following equations according to Figure 5 are based on experimental results. Without load history the behaviour of compressive strength as a function of temperature is according to [9]:

$$f_c(T,\alpha_0) = f_c(20°C) \qquad (T \le 250°C) \qquad (6)$$

$$f_c(T,\alpha_0) = f_c(20°C) * [1 - 0.0018 * (T - 250)] \qquad (250°C < T \le 750°C) \qquad (7)$$

$$f_c(T,\alpha_0) = f_c(20°C) * [0.1 - 0.0004 * (T - 750)] \qquad (750°C < T \le 1000°C) \qquad (8)$$

$$f_c(T,\alpha_0) = 0 \qquad (1000°C < T) \qquad (9)$$

With load history the compressive strength is calculated as followed:

$$f_c(T,\alpha = 0.1) = f_c(20°C) * [-2 * 10^{-6} * T^2 + 4.7 * 10^{-4} * T + 0.977] \quad (T \le 750°C) \qquad (10)$$

$$f_c(T,\alpha = 0.3) = f_c(20°C) * [-2 * 10^{-6} * T^2 + 6.8 * 10^{-4} * T + 0.9875] \quad (T \le 750°C) \qquad (11)$$

$$f_c(T,\alpha = 0.1) = f_c(20°C) * [0.25 - 0.001 * (T - 750)] \qquad (750°C < T \le 1000°C) \qquad (12)$$

$$f_c(T,\alpha = 0.3) = f_c(20°C) * [0.38 - 0.00152 * (T - 750)] \qquad (750°C < T \le 1000°C) \qquad (13)$$

$$f_c(T,\alpha = 0.1) = 0 \qquad (1000°C < T) \qquad (14)$$

$$f_c(T,\alpha = 0.3) = 0 \qquad (1000°C < T) \qquad (15)$$

An interpolation is allowed.

4.3 Young's Modulus

The Young's Modulus as a function of load history and temperature, $E(T = 20C°)$ must be measured according to RILEM or National Code with respect to the geometry of specimens being used in the high temperature range.

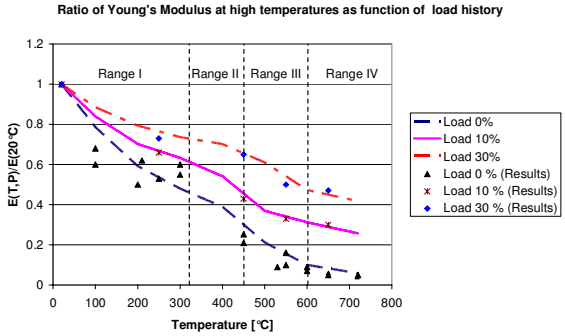

Fig. 6 - Influence of high temperature on the Young's Modulus of siliceous concrete - experimental and calculated results; according to [1].

The following equation can be used with $\alpha = 0$, $\alpha = 0.1$ and $\alpha = 0.3$ to calculate the Young's Modulus at high temperature, based on measurements of $E(T,\alpha)$ according to Figure 6 [10].

Range I ($T \leq 320°C$):

$$E(T) = E(20°C) * \left[1 - 3*10^{-3} * (T-20) + 4.085*10^{-6} * (T-20)^2\right] \quad (16)$$

$$E(T,\alpha = 0.1) = E(20°C) * \left[3*10^{-6} * T^2 - 2.311*10^{-3} * T + 1.04505\right] \quad (17)$$

$$E(T,\alpha = 0.3) = E(20°C) * \left[2*10^{-6} * T^2 - 1.57*10^{-3} * T + 1.0306\right] \quad (18)$$

Range II ($320°C < T \leq 450°C$):

$$E(T) = E(20°C) * \left[0.89406 - 3.2445*10^{-3} * T + 1.0081*10^{-5} * T^2 - 1.2801*10^{-8} * T^3\right] \quad (19)$$

$$E(T,\alpha = 0.1) = E(20°C) * \left[-5.1*10^{-6} * T^2 + 2.73*10^{-3} * T + 0.262\right] \quad (20)$$

$$E(T,\alpha = 0.3) = E(20°C) * \left[-4*10^{-6} * T^2 + 2.5*10^{-3} * T + 0.342\right] \quad (21)$$

Range III ($450°C < T \leq 600°C$):

$$E(T) = E(20°C) * \left[0.45 * e^{-7.52*10^{-3}*(T-400)}\right] \quad (22)$$

$$E(T,\alpha = 0.1) = E(20°C) * \left[-6*10^{-8} * T^3 + 1*10^{-4} * T^2 - 0.056 * T + 10.874\right] \quad (23)$$

$$E(T,\alpha = 0.3) = E(20°C) * \left[1.767 * e^{-0.0022*T}\right] \quad (24)$$

Range IV ($T > 600°C$):

$$E(T) = E(20°C) * \left[e^{-4*10^{-3}*(T-20)}\right] \quad (25)$$

$$E(T,\alpha = 0.1) = E(20°C) * \left[0.82554 * e^{-0.0016*T}\right] \quad (26)$$

$$E(T,\alpha = 0.3) = E(20°C) * \left[0.86 * e^{-0.001*T}\right] \quad (27)$$

Furthermore it was found that the Young's Modulus is relative constant above $\alpha = 0.3$, as shown in Figure 7. Considering $\alpha \equiv 0.3$ is therefore acceptable when $\alpha > 0.3$.

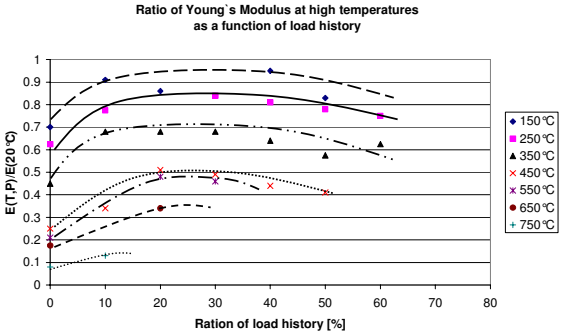

Fig. 7 - Young's Modulus of siliceous concrete being loaded during heating up; according to [9].

4.4 Ultimate strain

The ratio between ultimate strain at 20°C $\varepsilon_u(T=20)$ and ultimate strain as a function of load history and temperature $\varepsilon_u(T,\alpha)$ is shown in Figure 8. It's also based on measurements [1].

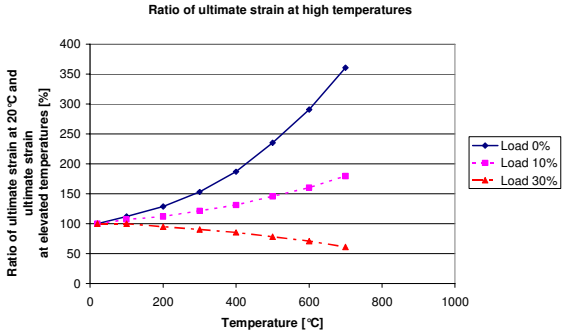

Fig. 8 - Ratio of ultimate strain of heated and loaded/not loaded specimens compared to specimens tested at 20°C; according to [1].

According to Figure 8, the material behaviour is a function of $f(\alpha)$, $\Delta\varepsilon_u(T)$ and $\varepsilon_u(T=20°C)$ [9]. $\varepsilon_u(T,\alpha)$ is calculated as follows:

$$\varepsilon_u(T,\alpha) = \varepsilon_u(20°C) + \Delta\varepsilon_u(T) * f(\alpha) \tag{28}$$

with $\varepsilon_u(T,\alpha) \le 7.8*10^{-3}$ as an upper limit for all cases (α=0). Where:

$$\varepsilon_u(20°C) = 2.2*10^{-3} \tag{29}$$

$$\Delta\varepsilon_u(T) = \left[4.2*10^{-6} + (T-20)*5.4*10^{-9}\right]*(T-20) \tag{30}$$

$f(\alpha)$ is a function of load history. A linear interpolation is applied for intermediate values of load factor α. $f(\alpha)=1$ (α=0), $f(\alpha)=0.227$ (α=0.1), $f(\alpha)=-0.095$ (α≥0.3)

4.5 Elastic strain

Elastic strain is:

$$\varepsilon_{el}(T,\alpha) = \frac{\sigma(t)}{E(T,\alpha)} \tag{31}$$

where: $\sigma(t)$ stress at time *t*,

$E(T,\alpha)$ Young's Modulus as a function of load history and temperature

4.6 Plastic strain

Two parts of the stresses induced strain at high temperatures can be explained as stress-strain relationship according to Figure 9 and the following equations:

$$\sigma(t) = f_c(T,\alpha) * \frac{\varepsilon(\sigma(t))}{\varepsilon_u(T,\alpha)} * \frac{n}{(n-1)+\left(\frac{\varepsilon(\sigma(t))}{\varepsilon_u(T,\alpha)}\right)^n} \tag{32}$$

where: n=3 ordinary concrete,

n=2.5 lightweight aggregate concrete

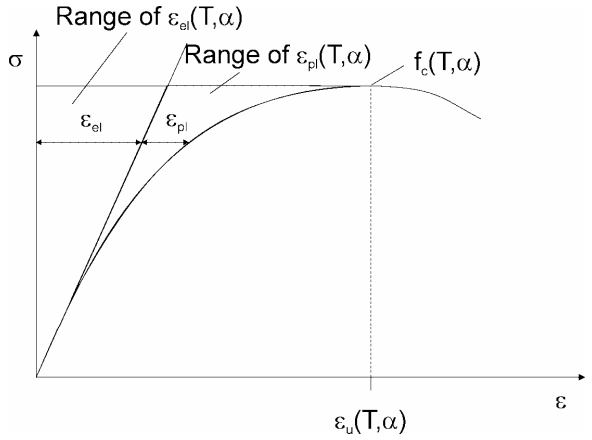

Fig 9 - Range of elastic and plastic strain of stress-strain-relationship.

The elastic and plastic strains should generally be taken from measured stress-strain-relationship. Here is:

$$\varepsilon_{pl}(T,\alpha) = \varepsilon(\sigma(t),\varepsilon_u(T,\alpha),T,\alpha) - \varepsilon_{el}(\sigma(t),T,\alpha) \tag{33}$$

respectively

$$\varepsilon_{pl}(T,\alpha) = \varepsilon(\sigma(t),\varepsilon_u(T,\alpha),T) - \varepsilon_{el}(\sigma(t),T,\alpha) \tag{34}$$

whereby $\varepsilon_{pl} \equiv 0$ if $\varepsilon_{el} > \varepsilon_{pl}$

where: α, $T = T(t)$ are Parameters; ε_u is a function

A numerical approximation for the ascending branch of the stress-strain-relationship is:

$$\varepsilon_{pl}(T,\alpha) = \kappa * \frac{\sigma(t)}{E(T,\alpha)} \tag{35}$$

The function κ given in [2]:

$$\kappa = \frac{1}{2} * \left[1 - \sqrt{1 - \left(\frac{\sigma(t)}{f_c(T,\alpha)} \right)^4} \right] \tag{36}$$

4.7 Total mechanical strain

Thermal induced total strain minus thermal strain is given in the following equation. This equation comprises elastic, plastic and creep contents [5].

$$\varepsilon_m = \varepsilon_{el} + \varepsilon_{pl} + \varepsilon_{tr} = \varepsilon_{tot} - \varepsilon_{th} \tag{37}$$

$$\varepsilon_m(T) = \frac{\sigma(t)}{E(T)} * (1 + \varphi) \tag{38}$$

The thermal induced strain is relatively independent compared to dependence of Young's Modulus by load history [11] and the term $\varepsilon_{tr,cr} = \frac{\varphi * \sigma(t)}{E(T)}$ defined as transient creep in literature [12]. Actually the term comprises elastic, plastic and (pure) transient creep strains as we show below [10]. The elastic strain is calculated in the following equation:

$$\varepsilon_{el}(T,\alpha) = \varepsilon_{el}(T) - \Delta\varepsilon_{el}(T,\alpha) \tag{39}$$

The φ-function is calculated in the next equation. It utilizes new parameters as shown in table 1, those were obtained by recent scientific results [2, 6] based on ongoing research.

$$\varphi = C_1 * \tanh \gamma_w * (T - 20) + C_2 * \tanh \gamma_0 * (T - T_g) + C_3 \tag{40}$$

Tab. 1 - Parameters for transient creep functions of structural concretes; according to [5].

Parameter	Dimension	Quarzit concrete	Limestone concrete	Lightwight concrete
C_1	1	2.50	2.50	2.50
C_2	1	0.70	1.40	3.00
C_3	1	0.70	1.40	2.90
γ_0	$°C^{-1}$	$7.5*10^{-3}$	$7.5*10^{-3}$	$7.5*10^{-3}$
T_g	°C	800	700	600

$$\gamma_w = 0.3 * 10^{-3} * w^{0.5} + 2.2 * 10^{-3} \text{ with } \gamma_w \le 2.8 * 10^{-3} \tag{41}$$

w is the moisture content of concrete in % by weight [5].

The equation above is similar to the equation for creep strain at room temperature. That is why the φ-function is called „transient creep function" in RILEM literature [11], although it was

known that φ contains in addition plastic and small elastic strain parts [11]. Therefore it was also called "thermal induced strain" according to [13]. The separate creep part ε_{tr} will not be calculated within the proposed calculation procedure described below.Figure 10 shows the φ-function for siliceous concrete.

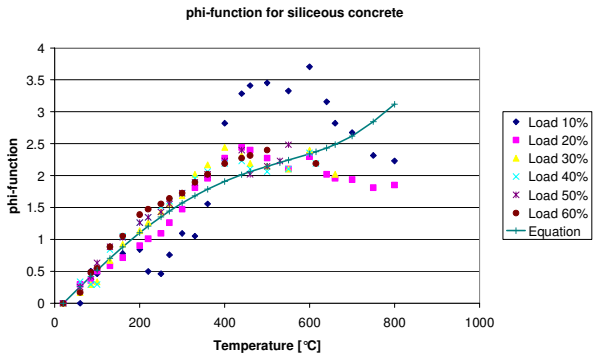

Fig. 10 - Transient creep function for siliceous concrete; according to [5].

After calculation of plastic strains and elastic strains the pure transient creep strain should be calculated as follows:

$$\varepsilon_{tr}(T,\alpha) = \varepsilon_{m}(T) - \varepsilon_{el}(T,\alpha) - \varepsilon_{pl}(T,\alpha) \tag{42}$$

5 DEVELOPMENT OF DIFFERENT STRAINS IN COMPRESSION AT HIGH TEMPERATURES IN A CONCRETE MODEL BY TRANSIENT EFFECTS

5.1 Thermal strain during heating up

The thermal strain increases in any case by heating up to 650°C. Above that point thermal strain gradual slightly decreases until the final strain is 14.8 ‰ at a temperature of 1000°C. At each time step there is a final strain according to the reached temperature. It is essential:

$$\varepsilon_{th}{}^{n} = \varepsilon_{th}(T) \tag{43}$$

During cooling down the thermal strain is irreversible. That is because in concrete crack opening starts during heating up to the maximum temperature. These cracks don't close completely during cooling down, which leads to residual deformations [1].

5.2 Elastic and plastic strain during heating up including load history

Any time in the ascending branch the elastic strain is:

$$\varepsilon_{el}{}^{n} = \varepsilon_{el}(T,\alpha) \tag{44}$$

When cooling down, the elastic strain is reversible. The deformation energy could be released after heating up assuming that further cracking takes places during cooling, which is not always the case.

Plastic strain cannot decrease because it is irreversible. Subsequent behaviour in the ascending and descending branch of the stress-strain-relationship is assumed. The plastic strains are calculated as described before including the load history in stress-strain-relation. If temperature or load history decreases the plastic strain, then the deformation is taken as permanent.

$$\varepsilon_{pl}{}^{n} = \max \varepsilon_{pl}(T,\alpha) \tag{45}$$

For cooling down the deformations are constant. In the range of $\varepsilon_{pl} + \varepsilon_{el} \geq \varepsilon_{u}$ it may be calculated according to the linear model of EC2 [6].

Tab. 2 - Ultimate strain and stress induced strain in ascending and descending branch of the stress-strain-relationship; according to [6].

Concrete temperature	$\varepsilon_u(T,\alpha)$ see chapter 4.4	$\varepsilon_{u,1}(T)$
20 … 1100 °C	$\varepsilon_u(T,\alpha) = \varepsilon_u(20°C) + \Delta\varepsilon_u(T) * f(\alpha)$ and $\varepsilon_u(T,\alpha) \leq 7.8 * 10^{-3}$	$\varepsilon_{u,1}(T) = 3 * 10^{-5} * T - 0.0199$ (46)

where: $\varepsilon_u(T,\alpha)$ ultimate strain in ascending branch

$\varepsilon_{u,1}(T,\alpha)$ maximum strain of the descending branch of stress-strain-relationship, according to [6]

5.3 Transient creep during heating up and load history

The component of deformation of the creep-function is irreversible. The consideration is discrete. For each timestep exists a point of the creep function, that rises to the thermal induced strain and the part of transient creep strain depends on load history and temperature [14].

By increasing the temperature and changing the load simultaneously, the parts of plastic and transient creep are irreversible. The part of elastic strain $\Delta\varepsilon_{el}$ is reversible. The stepwise calculation of strains based on the total strain approach is done as follows:

$$\varepsilon_{tr}{}^{n} = \varepsilon_{tr}{}^{n-1} + \Delta\varepsilon_{tr}(T,\alpha) \tag{47}$$

where: n new timestep with T=T(t) and n-1 old timestep

with $\varepsilon_{tr}{}^{n} \geq \varepsilon_{tr}{}^{n-1}$ (temperature increase and stress increase)

$$\Delta\varepsilon_{tr}(T,\alpha) = \varepsilon_{tr}{}^{n} - \varepsilon_{tr}{}^{n-1} \tag{48}$$

with $\varepsilon_{tr}{}^{n} < \varepsilon_{tr}{}^{n-1}$ (temperature increase and stress decrease)

$$\Delta\varepsilon_{tr}(T,\alpha) = \max \varepsilon_{tr}{}^{n} - \Delta\varepsilon_{el}{}^{n}(T,\alpha) \tag{49}$$

Whereas $\Delta\varepsilon_{el}$ is:

$$\Delta\varepsilon_{el}(T,\alpha) = \varepsilon_{el}(T,\alpha) - \varepsilon_{el}(T) \tag{50}$$

From the basic equations we receive:

$$\varepsilon_{m}(T) = \varepsilon_{el}(T,\alpha) + \varepsilon_{pl}(T,\alpha) + \varepsilon_{tr}(T,\alpha) \tag{51}$$

$$\varepsilon_m(T) = \frac{\sigma(t)}{E(T)} * (1+\varphi) \tag{52}$$

$$\varepsilon_{el}(T) = \frac{\sigma(t)}{E(T)} \tag{53}$$

$$\frac{\varphi * \sigma(t)}{E(T)} = \varepsilon_{pl}(T,\alpha) + \Delta\varepsilon_{el}(T,\alpha) + \varepsilon_{tr}(T,\alpha) \tag{54}$$

For the pure transient creep we receive finally:

$$\varepsilon_{tr}(T,\alpha) = \frac{\varphi * \sigma(t)}{E(T)} - \varepsilon_{pl}(T,\alpha) - \Delta\varepsilon_{el}(T,\alpha) \tag{55}$$

It is astonishing to observe that the influence of load history originates from plasticity effects and to a small extent from the load effect on the modulus of elasticity.

6 Results by transient effects

The calculation results of thermal induced strain, considering unsteady temperatures and loads according to the material laws above, are shown in Figure 11. The specimens are cylinders with 80 mm diameter and 300 mm height. Heating rate is 2 K/min. The compressive strength at 20°C is 38 MPa. The results are obtained from heated specimens under different stress-time-relationships [11].

There is a rather good agreement between measured and calculated results. The results are calculated with consideration of material laws depending on temperature and load history as discussed before.

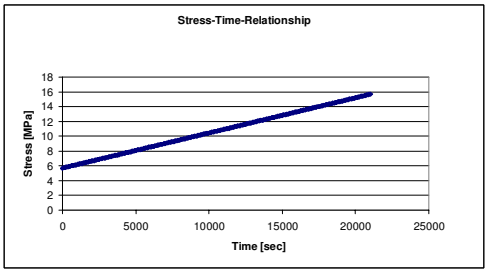

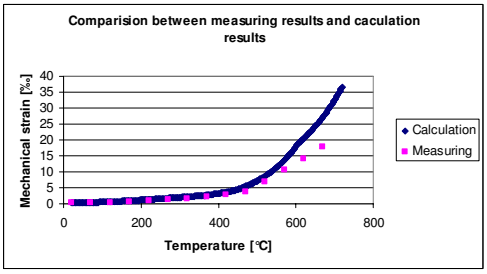

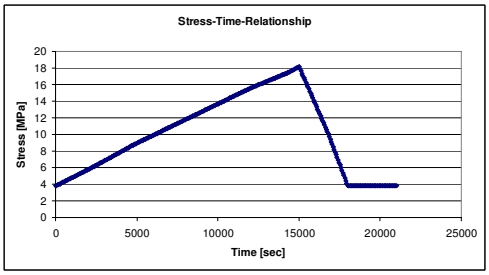

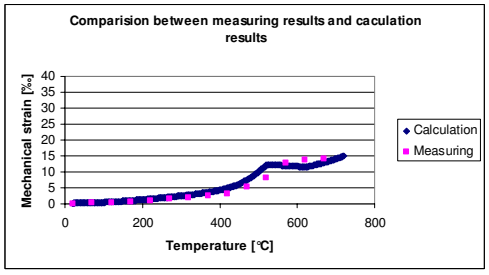

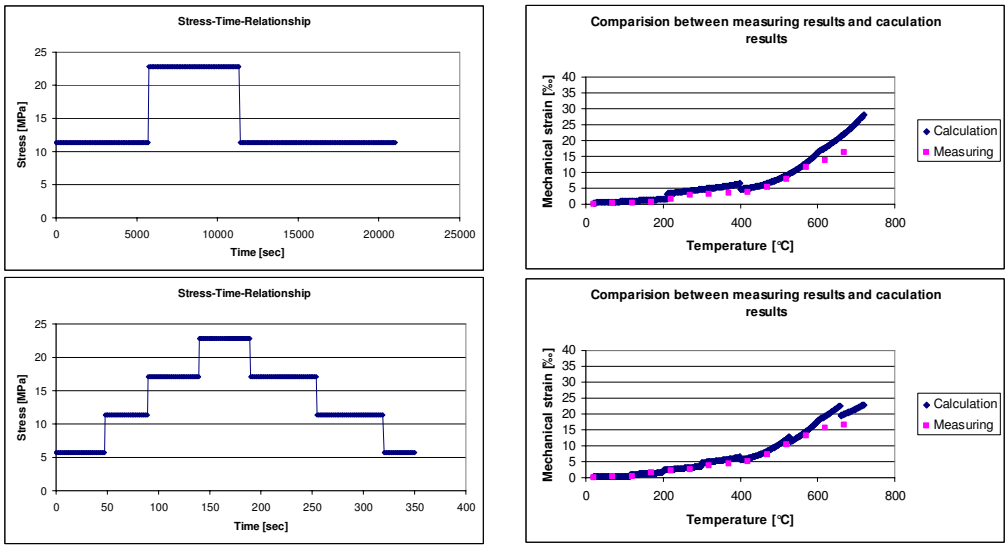

Fig. 11 - Comparison between calculated results and experimental results, according to [11].

7 OUTLOOK

To calculate the load bearing behaviour of structures subjected to fire the material laws for the most important material properties of ordinary concrete were developed. This model was made to complete the existing concrete model of EC2 to consider the thermal creep and the effect of load history. It is possible with this model to consider the load history in all phases of thermal exposition. With this complex model one can calculated total strain with variances of load history and variances of temperature. Different parts of deformations are approximated with discrete equations interacting in concrete model. This technique is usable to calculate realistic behaviour of structures [15, 16], also in the case of cooling, which is not allowed in EC2.

By considering the load history during heating up in several cases an increasing load bearing capacity due to a higher stiffness of concrete may be obtained. With this model it is possible to consider the thermal-physical behaviour of material laws for calculation of structures. By applying this model to the ordinary calculation system of EC2 it will lead to a better evaluation of the safety level. This opens space for optimizing concrete structure and material design.

8 REFERENCES

[1] Schneider, U., Diederichs, U.; Weiß, R.: Hochtemperaturverhalten von Festbeton, Sonderforschungsbereich 148 – Brandverhalten von Bauteilen – TU Braunschweig, 1977

[2] Schneider, U.; Morita, T.; Franssen, J.-M.: A Concrete Model Considering the Load History Applied to Centrally Loaded Columns Under Fire Attack, Fire Safety Science – Proceedings of the Fourth International Symposium, Ontario, 1994

[3] Schneider, U.: Behaviour of Concrete at High Temperatures, Verlag Ernst & Sohn, Berlin 1982

[4] Khoury, G.A.; Grainger, B.N.; Sullivan, P.J.E.: Transient thermal strain of concrete: Literature review, conditions with specimens and behaviour of individual constituents, Magazine of Concrete Research Vol. 37 No. 132, 1985
[5] Schneider, U.; Lebeda, C.; Franssen, J.-M.: Baulicher Brandschutz, Bauwerk Verlag GmbH, Berlin, 2008
[6] Eurocode 2: Design of concrete structures – Part 1-2: General rules – Structural fire design; 2004
[7] Xudong, S. et al: Concrete Constructive Relationships Under Different Stress-Temperature-Paths, Journal of Structural Engeneering, 12/2002
[8] RILEM TC HTC 200: Mechanical Concrete Properties at High Temperature - Recommendation Part 1: Mat.&Struct., Vol. 44, Paris, June 2007
[9] Schneider, U.: Concrete at High Temperatures – A General Review, Fire safety Journal, 13, 1988
[10] Schneider, U., Diederichs, Rosenberger, W.; U.; Weiß, R.: Hochtemperaturverhalten von Festbeton, Sonderforschungsbereich 148 – Brandverhalten von Bauteilen – TU Braunschweig, 1980
[11] Schneider, U.: Ein Beitrag zur Frage des Kriechens und der Relaxation von Beton unter hohen Temperaturen, Institut für Baustoffe, Massivbau und Brandschutz, TU Braunschweig, Heft 42, Braunschweig, 1979
[12] RILEM TC 129-MHT: Test Methods for Mechanical Proberties of Concrete -Recommendation: Part 7: Transient creep for service and accident conditions, Mat.&Struct., Vol. 31, Paris, June 1998
[13] Khoury, G.A.; Grainger, B.N.; Sullivan, P.J.E.: Strain of concrete during first heating to 600°C under load, Magazine of Concrete Research Vol. 37 No. 133, 1985
[14] Bockhold, J.; Stangenberg, F.: Modellierung des nichtlinearen Kriechens von Beton, Beton- und Stahlbetonbau 99, Heft 3, Verlag Ernst & Sohn, Berlin 2004
[15] Franssen, Jean-Marc: Plastic Analysis of Concrete Structures Subjected to Fire in: fib Task Group 4.3 - Fire Design of Concrete Structures: Whats now? What next? Milano 2004
[16] Li, L.; Purkis, J.: Stress-strain constitutive equations of concrete material at elevated temperatures in: Fire Safety Journal (40) 2005

RESULTS FROM TWO RESEARCH PROGRAMS ON SPALLING OF CONCRETE

LARS BOSTRÖM[1] and ROBERT JANSSON[2]

ABSTRACT

Two Swedish research programs concerning fire spalling of concrete have been completed by the end of 2007. In the test program "Innovative self-compacting concrete with good fire spalling properties" the behaviour of 52 different self compacting concretes were investigated. A part of the results from this study were presented at the SiF 06[1]. The other test program, initiated by the Swedish Road Administration, deals with the spalling issue for concrete used for tunnel constructions in Sweden. In this program the spalling behaviour of 20 different construction concretes were investigated by performing tests on 40 small slabs, 500 x 600 x 300 mm^3, and 14 tests on large slabs, 1700 x 1200 x 300 mm^3. On the large slabs the influence on spalling by different fire exposures were also investigated. The standard fire curve (EN 1363-1) and the RWS (Rijkswaterstaat) curve were used. Some results and the material testing part of this program have previously been reported on a workshop[2]. The results from the studies show that all of the investigated concretes without protection spalled more or less when exposed to fire. The main conclusion is the some type of protection is always needed for self-compacting and tunnel concrete if spalling not can be accepted. In most cases an addition of 1 kg/m^3 of polypropylene fibres would prevent the dangerous progressive spalling. Both 18 μm and 32 μm diameter fibres worked well.

1. INTRODUCTION

During the last decade has an increased focus been put on fire issues of concrete and especially the new types of concretes. The reason is that the new concretes such as high performance concrete and self-compacting concrete have been shown to be very sensitive to fire exposure, which in many cases can lead to severe spalling. Therefore has both industries

[1] Manager, Fire Resistance, SP Technical Research Institute of Sweden, Fire Technology
email: lars.bostrom@sp.se.
[2] Project Manager, PhD Student, SP Technical Research Institute of Sweden, Fire Technology
email: robert.jansson@sp.se.

and different authorities in Sweden and Norway financed some large experimental research projects with the aim to find good fire resisting concretes for both building and infrastructure applications.

2. MATERIALS AND SPECIMENS

A total of 52 different self-compacting concretes have been included in the study. Furthermore have 20 different concretes, specific for tunnel applications, been investigated. A summary of the studied parameters are assembled in table 1. The gravel was mainly consisting of granite.

Table 1. Investigated parameters

Parameter	**Self-compacting concrete**	**Tunnel concrete**
Cement type	CEM I 42,5N BV/LA/SR CEM II 42,5R A-LL Norskt ANL	CEM I 42.5 BV/SR/LA
Water cement ratio	0.30 – 0.71	0.40 – 0.45
Water powder ratio	0.25 – 0.55	0.40 – 0.45
Polypropylene fibres, amount (kg/m^3)	0 – 3.0	0 – 1.5
Fibre diameter (μm)	18, 32	18, 32
Fibre length (mm)	6, 12	6, 12
Max gravel size	16	16, 25
Curing time (months)	3, 6, 9, 12, 24	7 - 10

The test specimens of self-compacting concrete were all manufactured by Skanska Prefab in Strägnäs and thereafter transported to SP for conditioning and storage, while the test specimens of tunnel concrete were directly manufactured by SP in Borås.

It was not possible economically to carry out all tests in a large, or medium sized scale. Therefore was the main part of the tests were performed on a small furnace with small slab specimens. This methodology was studied in a previous research project [3], and it gave reasonable good results. In addition to the small scale tests were several medium sized tests performed on both slab and beam specimens. These tests were made in order to verify the tests obtained in small scale. The size of the specimens is shown in table 2.

Table 2. Size of the different specimen types used.

Specimen type	**Dimensions, length x width x thickness (mm^3)**	
	Self-compacting concrete	Tunnel concrete
Large slab	1600 x 1200 x 200	1600 x 1200 x 300
Small slab	600 x 500 x 200	600 x 500 x 300
Beam	3200 x 600 x 200	-

Most test specimens were externally loaded in compression during the fire tests. The loading system consisted of threaded bars (DYWIDAG) going through pipes cast into the specimens. In the small slabs of self-compacting concrete were three bars used and in the large slabs six bars. In the small slabs of tunnel concrete were four bars used and in the large slabs eight bars. Each bar could be loaded up to 800 kN. A schematic drawing of the loading system is shown in figure 1, and in figure 2 is a photo showing large slabs during a fire test.

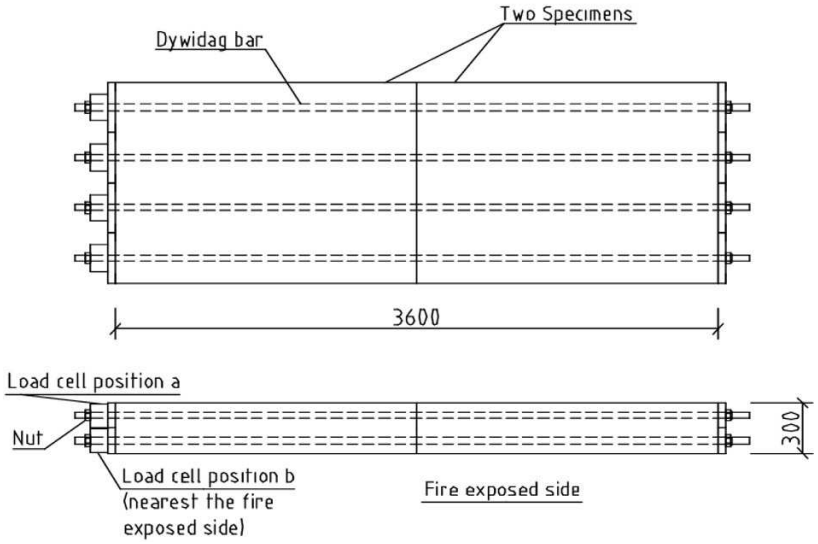

Figure 1. Loading arrangement and coupling of large slab test specimens.

Figure 2. Photo of large test specimens of tunnel concrete during fire testing.

After casting different curings were adopted. Some of the self-compacting concretes were stored in air the whole time from casting until the fire test. The storage was indoor in a heated laboratory with a mean temperature of approximately 20 °C and relative humidity 50 %. Most of the self-compacting concretes were stored outside under a rain protection. The tunnel concretes were stored under water after casting for 5-8 months. Thereafter they were stored in air in the laboratory for 1-3 months before the fire test.

3. TEST PROGRAM

The tests were mainly made with the small slab specimens, and only those results will be presented here. The schematic table showing the test program on self-compacting concrete is presented in table 3. Table 4 show the test program on tunnel concrete. In addition to the fire tests have several other material tests been performed on many of the concretes. The

study includes tests on permeability, thermal properties, different moisture transport tests, mechanical tests, and more. The results on all tests on the tunnel concretes will be published in [4].

Table 3. Test program on self-compacting concrete.

	w/p	Cement type	Curing (months)	Load level (of f_u)	Filler	Type of fibers	Amount of fibers (kg/m^3)	Fiber length	Air content	Fire curve	Total
Concrete quality	0.25 0.30 0.35 0.40	CEM I	6	0 % 10 %	Lime	-	-	-	Std	HC	16
	0.40 0.45 0.50 0.55	CEM II	6	0 % 10 %	Lime	-	-	-	Std	Std	16
Moisture content	0.30 0.40	CEM I	12 9 3	5 % 10 %	Lime	-	-	-	Std	HC	32
	0.40 0.50	CEM II	12 9 3	5 % 10 %	Lime	-	-	-	Std	Std	24
Load level	0.30	CEM I	6	5 % 30 %	Lime	-	-	-	Std	HC	4
	0.40	CEM II	6	5 % 30 %	Lime	-	-	-	Std	Std	4
Filler	0.30	CEM I	6	10 %	Cement	-	-	-	Std	HC	2
	0.40	CEM II	6	10 %	Cement	-	-	-	Std	Std	2
	0.43	CEM II	6	10 %	Lime -40 kg	-	-	-	Std	Std	2
	0.37	CEM II	6	10 %	Lime +40 kg	-	-	-	Std	Std	2
vct = 0.40	-	CEM II	6	10 %	Lime	-	-	-	Std	Std	2
	0.50	CEM II	6	10 %	Lime	PP-filler	0,5 5.0 10.0	-	Std	Std	6
	0.50	CEM II	6	10 %	Non	PP-filler	10	-	Std	Std	2
Type of fibers	0.30	CEM I	6	10 %	Lime	Ø=18 m	1.0	6 mm	Std	HC	2
	0.30	CEM I	6	10 %	Lime	Ø=32 m	2.0	6 mm	Std	HC	2
	0.40	CEM II	6	10 %	Lime	Ø=18 m	1.0	6 mm	Std	Std	2
	0.40	CEM II	6	10 %	Lime	Ø=32 m	2.0	6 mm	Std	Std	2
Amount of fibers	0.25 0.30	CEM I	6	10 %	Lime	Ø=18 m	0.5 1.5	6 mm	Std	HC	8
	0.40	CEM I	6	10 %	Lime	Ø=18 m	0.5	6 mm	Std	HC	2
	0.25 0.30 0.40	CEM I	6	10 %	Lime	Ø=32 m	1.0 3.0	6 mm	Std	HC	12
	0.40 0.45	CEM II	6	10 %	Lime	Ø=18 m	0.5 1.5	6 mm	Std	Std	8
	0.50	CEM II	6	10 %	Lime	Ø=18 m	0.5 1.0	6 mm	Std	Std	4
Glenum	0.50	CEM II	6	10 %	Lime	Ø=18 m	1.0	6 mm	Std	Std	2
	0.40 0.45 0.50	CEM II	6	10 %	Lime	Ø=32 m	1.0 3.0	6 mm	Std	Std	12
Fiber length	0.30	CEM I	6	10 %	Lime	Ø=18 m	1.0	12 mm	Std	HC	2
	0.40	CEM II	6	10 %	Lime	Ø=32 m	2.0	12 mm	Std	Std	2
Air content	0.30	CEM I	6	10 %	Lime	-	-	-	4 % 8 %	HC	6
	0.40	CEM II	6	10 %	Lime	-	-	-	10 %	Std	2
Fire curve	0.30	CEM I	6	10 %	Lime	-	-	-	Std	Slow Std	4
	0.40	CEM II	6	10 %	Lime	-	-	-	Std	Slow HC	4
Total											196

Table 4. Test program on tunnel concrete

	w/p	Cement type	Curing (months)	Load level (of f_u)	Max size aggregate	Type of fibers	Amount of fibers (kg/m^3)	Fiber length	Air content	Fire curve	Total
Concrete quality	0.40 0.45	CEM I	6	10 %	16 mm 25 mm	Ø=18 m Ø=32 m	0 1.0 1.5	6 mm	Std	10 K/min Slow heat Std HC	40

4. TEST RESULTS

4.1 General

A thorough analysis of all test data has not been done yet. The results presented here will mainly be based on analysis of very large samples where different parameters may be influencing on the results. Nevertheless, this will show the overall behaviour of the concretes.

4.2 Effect of age

It was chosen to test some of the concretes after different curing times in order to not only establish the effect of age but also on moisture content since drying will take place during the curing. In figure 3 is the effect of age shown for five different self-compacting concretes. There is no significant effect on the spalling by the age, or curing time, of the concrete.

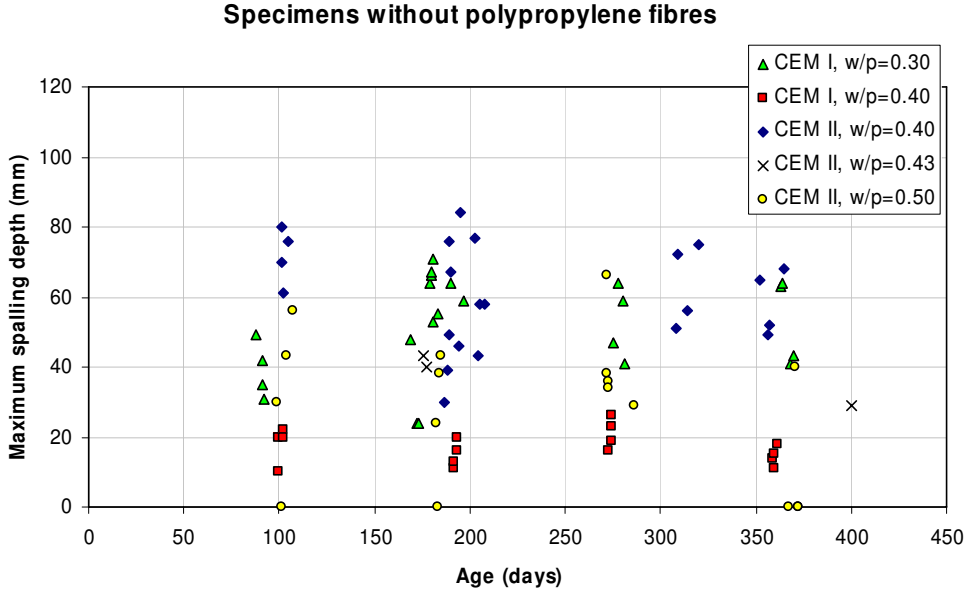

Figure 3. Effect of age on the maximum spalling depth.

The tests were made on specimen with an age from three months up to one year. The moisture content was measured on separate cubes (on which also the compressive strength was measured) stored together with the slabs. The moisture content measurement started the same day as the fire test. All data was not available at the time of writing, so only a part of the tests can be presented. In figure 4 is the effect of moisture content on the spalling shown. It is clear that the drying of these self-compacting concretes is a very slow process. Even after over a year is the moisture content still well above 4 %. The results do not show any significant effect on the spalling due to the moisture content. As should, however, be noted that the moisture content was high in all tests, but probably representative for what is expected in practice.

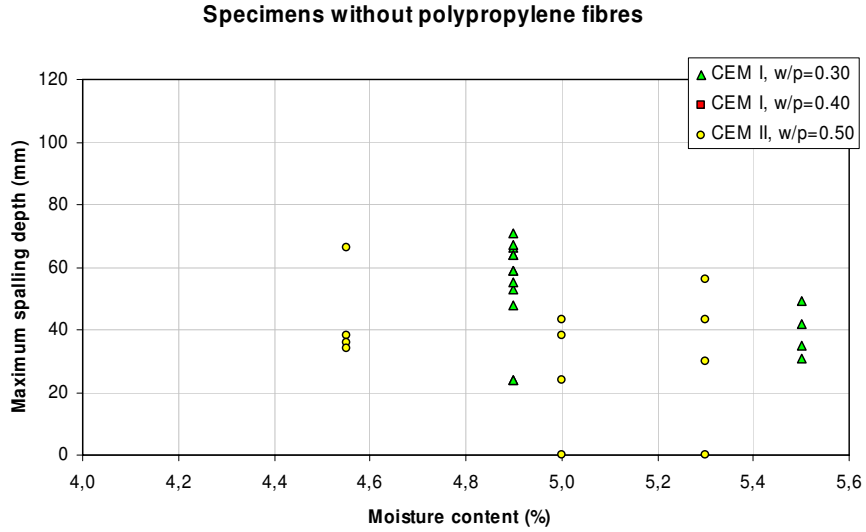

Figure 4. Effect of moisture content on the maximum spalling depth.

4.3 Effect of load level

Tests have been carried out using different compressive stress of the specimens. In figure 5 is the effect of the applied stress on the maximum spalling depth shown and in figure 6 is the effect of stress level, i.e. the ratio between the applied stress and the compressive strength, on the maximum spalling depth shown. There is clearly an effect when the specimens are unloaded. The spalling depth is less for unloaded specimens compared with specimens loaded in compression. Although, there is no significant influence on the spalling depth of the applied stress or the stress level.

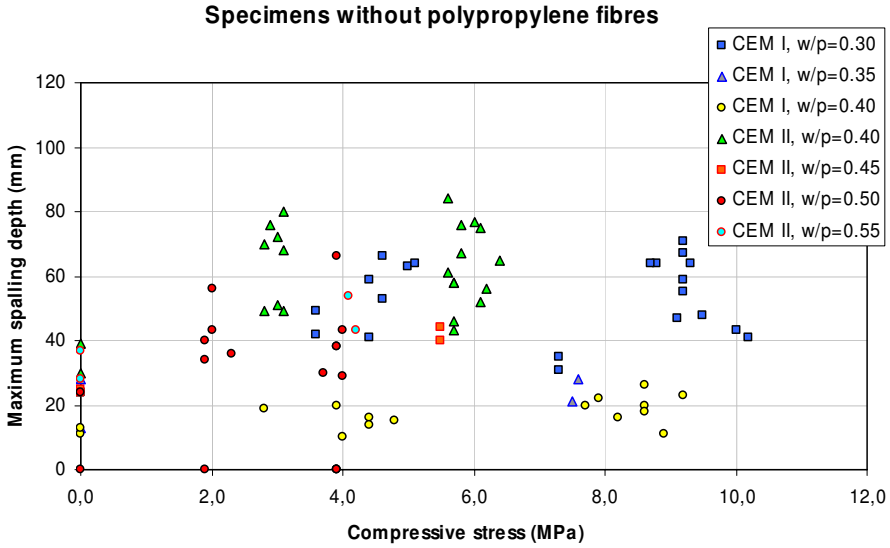

Figure 5. Effect of applied compressive stress on the maximum spalling depth.

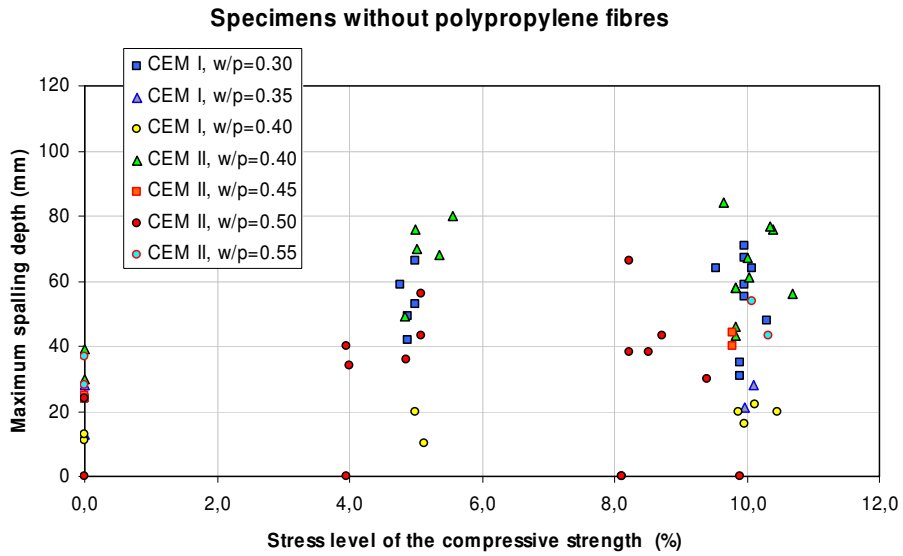

Figure 6. Effect of the stress level on the maximum spalling depth.

4.4 Effect of limestone filler

In figures 7-8 is the effect of the limestone filler on the maximum spalling depth presented. In figure 7 are the results obtained with concrete made with CEM I cement while in figure 8 are the results for the concretes made with CEM II cement. There is clearly no significant effect on the maximum spalling depth by the amount of limestone filler used.

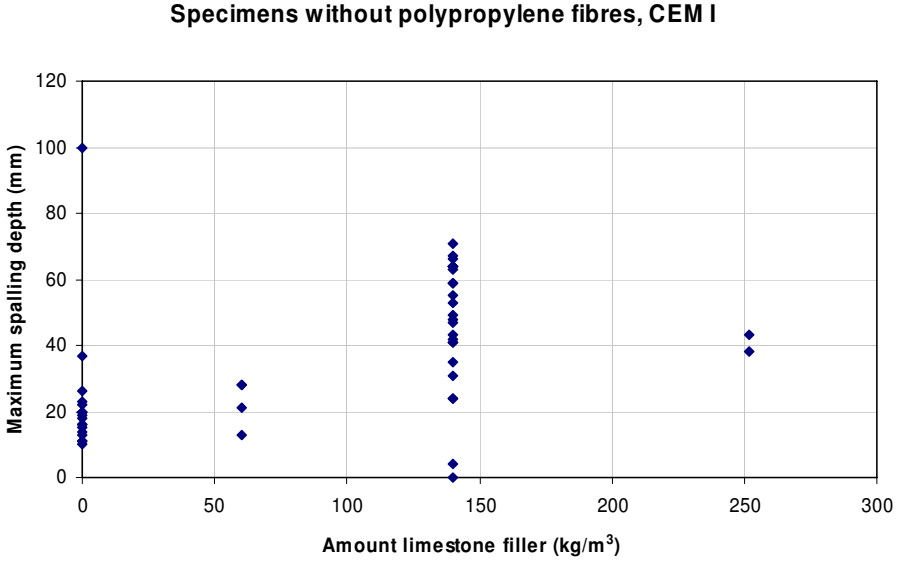

Figure 7. Effect of the amount of limestone filler on the maximum spalling depth of concrete made with CEM I cement.

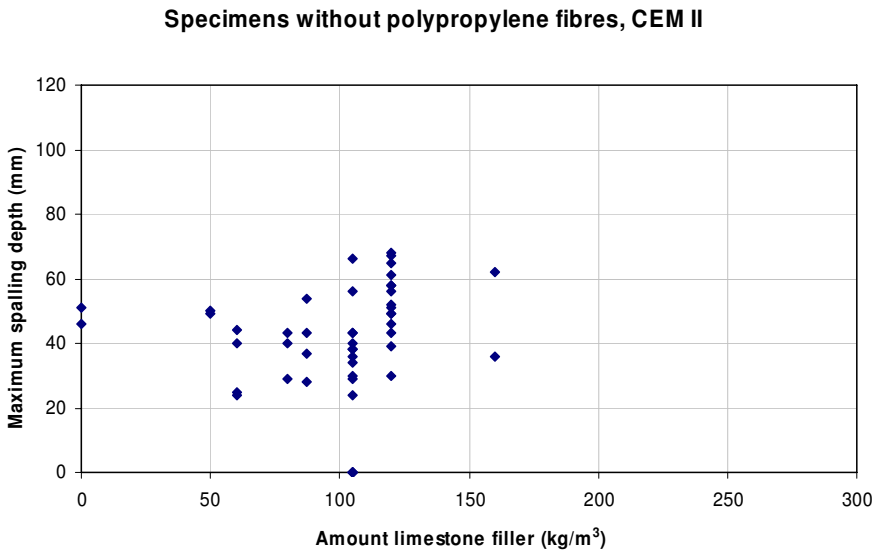

Figure 8. Effect of the amount of limestone filler on the maximum spalling depth of concrete made with CEM II cement.

4.5 Effect of water powder ratio

In figure 9 is the effect of the water powder ratio on the maximum spalling depth shown. In the diagram has the data been divided into groups with the same stress level. These results show that the water powder ratio does not influence on the maximum spalling depth.

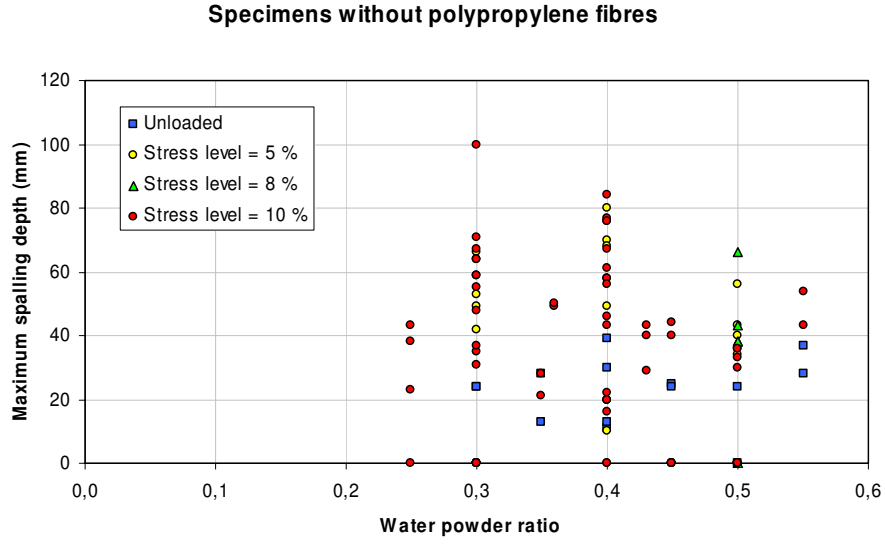

Figure 9. Effect of the water powder ratio on the maximum spalling depth.

4.6 Effect of fire curve

Generally it is assumed that a more severe fire exposure would give more spalling. Two different concretes were examined with regard to the severity of the fire exposure. The test results are presented in figure 10. These tests show that the amount of spalling is not increasing with increasing fire severity, rather the opposite could be the case. Although, the time to the spalling starts is of course dependent on the type of fire curve. In the case of the very low heating rate, i.e. the 10 K/minute ramp test, the spalling started after 50-60 minutes, while in the case with the hydrocarbon curve the spalling started after 2-4 minutes. Generally the spalling started when the furnace temperature was measured to between 500-700 °C.

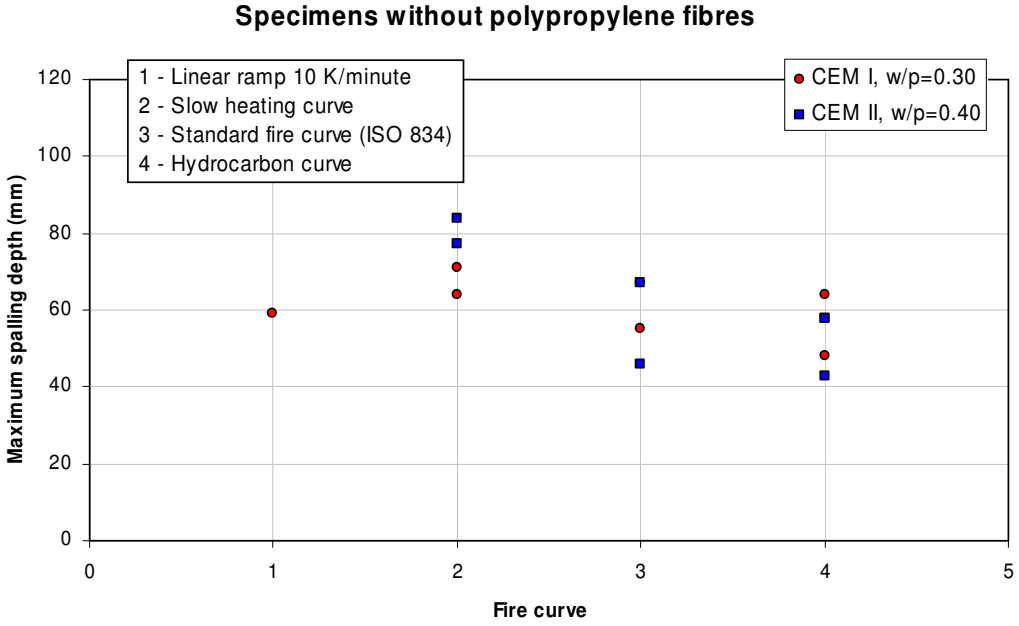

Figure 10. Effect of the fire curve on the maximum spalling depth.

4.7 Effect of polypropylene fibres

Over 60 tests on self-compacting concrete and 16 tests on tunnel concretes have been carried out with polypropylene fibres added to the concrete,. Fibres with two diameters have been used, 18 µm and 32 µm, and two different lengths, 6 mm and 12 mm. The amount of fibres has been varied from 0.5 kg/m^3 up to 3 kg/m^3. Only 18 µm fibres were tested with the amount 0.5 kg/m^3. 13 test specimens were made with 0.5 kg/m^3 polypropylene fibres and of these did 4 spall. With 1.0 kg/m^3 fibres were 14 manufactured with 18 µm fibres and 10 with 32 µm, i.e. a total of 24 specimens. Of these did two spall, one of each fibre diameter. The effect of the amount of fibres on the spalling depth is shown in figure 11.

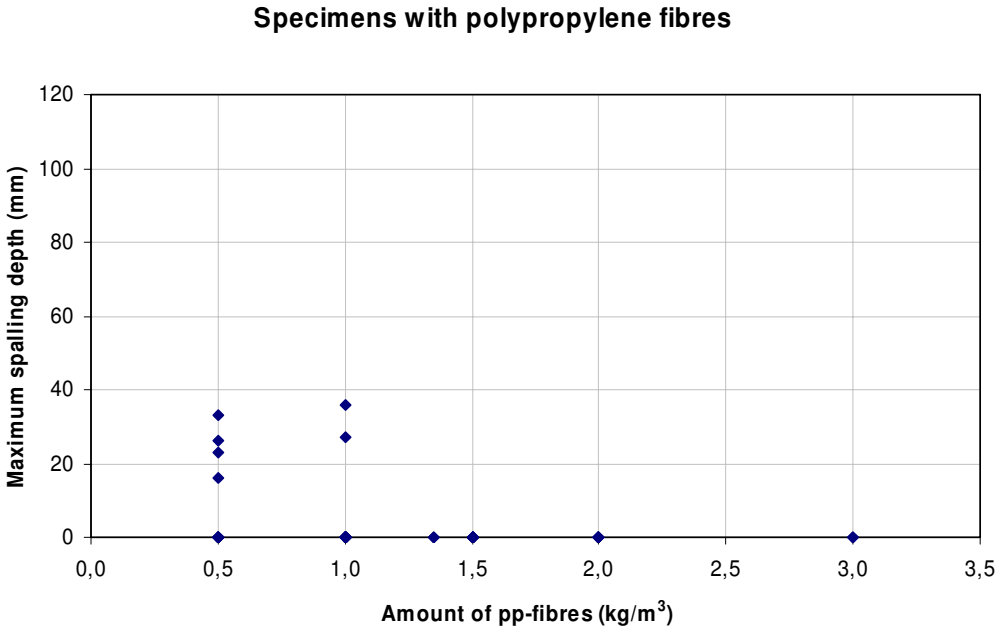

Figure 11. Effect of the amount of polypropylene fibres on the maximum spalling depth.

4.8 Effect of polypropylene filler

Some tests were made on concrete where filler of polypropylene had been added. The amount of filler varied from 0.5 kg/m^3 up to 10 kg/m^3. The advantage with the polypropylene filler compared to the fibres is that they do not influence on the workability of the fresh concrete. The tests showed that the polypropylene filler did not improve the fire resistance of the concrete, i.e. they cannot replace the use of polypropylene fibres.

5. SUMMARY AND CONCLUSIONS

Two experimental test series have been carried out, one with self-compacting concrete and one with tunnel concrete. The tests were mainly carried out on small slab specimens. In order to verify the results from the small scale tests has also medium sized specimens been tested. A total of 40 medium sized specimens (fire exposed surface 1500 x 1200 mm^2) were used in this verification. The tests showed a good agreement regarding when and if spalling occurred. The measured spalling depth was generally larger on the medium sized specimens compared to the small ones. The conclusion was that the small scale specimens give reliable results on the risk for spalling, but they would not fully represent the correct spalling behaviour in larger concrete slabs.

Several different factors regarding the composition of the concrete as well as the loading conditions and age have been examined. The general results, i.e. when looking on all test data on self-compacting concrete, show that these test results contradicts some of the results found in the literature. It should be noted, however, that the analysis has not yet been completed and the discussion here will be on a more general plane. It is possible that some effects on the spalling can be revealed when examining the data in more detail.

The experiments showed that in principle all self-compacting as well as the tunnel concretes without addition of polypropylene fibers spall when exposed to fire. An addition of 1 kg/m^3 polypropylene fibres with a diameter of 18 μm or 32 μm gave a good protection regarding progressive spalling which would be acceptable in most applications. There are, however, cases when more fibres or other types of protection will be required. It could for example be in tunnel applications where no spalling is acceptable or in pre-cast elements where the design and geometry has been optimized.

In the present tests the level of compressive loading did not affect the spalling of self-compacting concrete, except that unloaded specimens spalled slighlty less compared with the ones loaded in compression.

The concrete composition of the self-compacting concretes did not affect the spalling. The factors looking of included water-cement ratio, water-powder ratio and amount of limestone filler and none gave any significant influence on the spalling.

The effect of the fire exposure, i.e. the type of fire curve uesed, was examined on some concretes. It was found that the type of exposure did not affect the risk of spalling, even with such slow heating as 10 K/minute. An interesting finding was that the furnace temperature was 500-700 °C when the spalling started in all cases. Hence the spalling starts after 1-2 minutes when a RWS fire curve is used (tunnelling concrete), and after 50-60 minutes when the 10 K/minute ramp is employed for self-compacting concrete. The amount of spalling was generally larger when slower heating curves were used.

A parameter that is often regarded as a driving force for spalling is the moisture content. In the study was some concretes cured different long time before testing. The moisture content was determined on cube specimens stored together with the fire specimens. The results showed as expected that the drying is very slow for these dense concretes. Even after over one year storage in air the moisture content is well over 4 %. In the fire tests could not any influence of the curig time be shown on the spalling. One explanation could be that the moisture content never decreased below the critical level. A medium sized self compacting concrete specimen made with CEM II cement was tested after over two years storage, and even after this time did it spall severely.

REFERENCES

[1] Boström L., Jansson R. “Spalling of Self Compacting Concrete” *Structures in Fire 06, Proceedings from the 4th international workshop*, Aveiro, Portugal, 2006

[2] Jansson R., Boström L. “Experimental study of the influence of polypropylene fibres on material properties and fire spalling of concrete” *Proceedings of FIB Workshop, Fire Design of Concrete Structures: From Materials Modelling to Structural Performance*, Coimbra, Portugal, 2007 (to be published)

[3] Boström L. “Innovative self-compacting concrete – development of test methodology for determination of fire spalling”, *SP Report 2004:06*, Borås, Sweden, 2004

[4] Jansson R., Boström L. “Spalling of concrete exposed to fire”, *SP Report*, to be published

LOAD INDUCED THERMAL STRAIN: IMPLICATIONS FOR STRUCTURAL BEHAVIOUR

ANGUS LAW[1] and MARTIN GILLIE[2]

ABSTRACT

Load induced thermal strains (LITS) have been studied for many years from a material science perspective. This paper examines the implications of LITS for structural behaviour. The basic principles are presented and the often confusing terminologies used to describe the main LITS components are defined and explained in terms relevant to structural engineering. Given the complexity of LITS, it is tempting to build complicated phenomenological models. However, for structural modelling purposes, it is found that it is not necessary to include all of these phenomena. In fact, for short term transient heating conditions – such as exposure of a structure to fire – it is only necessary to distinguish between the elastic and plastic components of strain. An idealised test on a pinned column demonstrates the influence that effective representation of LITS has on the response of a structure during the cooling phase of a fire. Two material models are applied, and the importance of defining an elastic modulus which is distinct from the 'apparent' modulus of the material is demonstrated.

1. INTRODUCTION

Load induced thermal strain (LITS) is an umbrella term used to refer to a number of different strain components[1] in heated concrete. These components alter the strain behaviour of concrete if the material is heated under applied stress. In fact, concrete heated under high stresses can be observed to shrink – rather than expand due to thermal expansion. The most significant components of LITS (but not all) are non-recoverable; hence, the effects of LITS are only evident on first heating.

There has been a great deal of work concerning LITS over the past four decades[2-5]. Modern development of LITS started in the 1960s with the realisation and confirmation that

[1] PhD. Student, The University of Edinburgh, School of Civil and Environmental Engineering, email: A.Law@ed.ac.uk
[2] Lecturer, The University of Edinburgh, School of Civil and Environmental Engineering, email: M.Gillie@ed.ac.uk

the main LITS component existed[5]. The following decade saw a great deal of work which identified numerous LITS components and isolated them – demonstrating that the main component was distinct and had its own properties.

During the 1980s a large amount of work was carried out – particularly at Imperial College[6] – which suggested the existence of a "master" LITS curve whose properties were independent from other concrete properties such as strength, age, moisture content, and aggregate type. Khoury *et al.* also showed that LITS was physically independent from free thermal expansion.

Despite the volume of work on the material property aspects of LITS, the implications for structural behaviour have yet to be fully understood. The presence of LITS provides opportunities for the development of additional strains that are not identified. These could cause structures to respond differently than previously expected. Since the strains involved are largely irrecoverable, LITS has an active influence during heating, but is not active during cooling. As the development of larger, holistic, structural models becomes more commonplace, the understanding of how a structural member behaves and interacts with the rest of a building under heating *and* cooling becomes more important; the influence of preloading and the development of locked-in strains becomes more pertinent.

Though there are a large number of components involved in LITS it is not necessary to build phenomenological models which include every strain component and its governing factors. On this basis, a number of researchers have developed mathematical models which attempt to describe LITS. Recently, several studies have reviewed the available material models[7-9]. This paper will focus on the models by Terro[10] and Anderberg[11] with reference to Schneider's model[12] and Eurocode 2[13]. Structural modellers have also begun to include these LITS models in their simulations[14, 15]. However, though comparisons of the different material models have been conducted[7], one model has not been found to represent structural behaviour more satisfactorily than another.

2. EXPLANATION OF LITS

LITS is defined as the difference between the free thermal expansion of concrete when it is heated, and the net thermal expansion when the same concrete is heated under a level of pre-stress. Figure 1. shows the difference between an unstressed sample and a pre-stressed sample. This figure is similar to that presented by Khoury[16]. It can be observed that under higher levels of pre-stress the material shrinks.

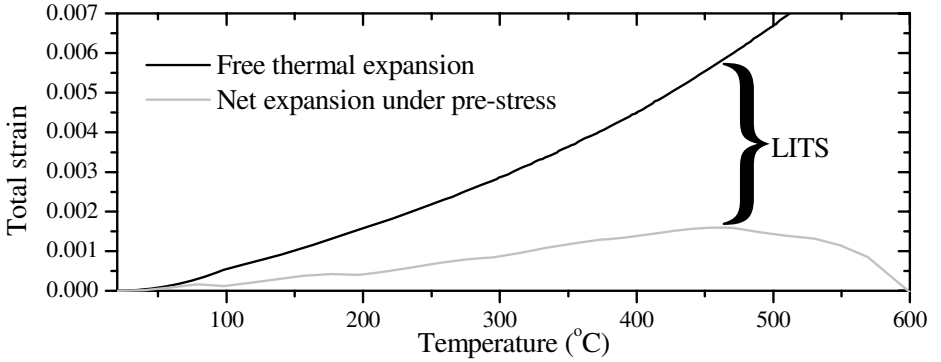

Fig. 1 – Difference between strain when heated with and without applied stress

The existence of a large number of strain components contributing to LITS has led to a number of different terms being used to describe them. This has caused some confusion regarding what different terms mean. The more commonly used terms are disambiguated below.

Transitional thermal creep (ttc) develops irrecoverably during, and for a few days following, first-time heating of sealed concrete under load[5]. Ttc is by far the largest component of LITS[10]. It is thought that the origins of transitional thermal creep are in the cement paste and that the addition of aggregate restrains it.

Drying creep is the shrinkage experienced by the material due to the evaporation of water. This can only occur where the specimen is unsealed and, therefore able to dry out.

Transient creep and *transient strain,* describe the same phenomena and refer to the sum of ttc and drying creep. Though both these terms are technically time dependant, it is believed that – for practical purposes – they can be regarded as quasi-instantaneous. Since drying creep is regularly omitted from the transient strain calculation, and because ttc is such a large component of LITS, the three terms; ttc, transient strain, and LITS have been incorrectly regarded as synonymous. Henceforth, for clarity, transient creep/strain will be referred to as transient strain.

Basic creep is used to describe the strain of thermally stabilised concrete when loaded at constant temperature. In conditions where the temperature is not constant, by definition, the term basic creep cannot be used. Instead, Khoury[1] adopts the term of a 'time dependent' strain which develops under transient heating conditions.

Changes in elastic strain are used to describe the elastic components of LITS which are caused by the change in elastic modulus as temperature increases. This is illustrated in Figure 2.

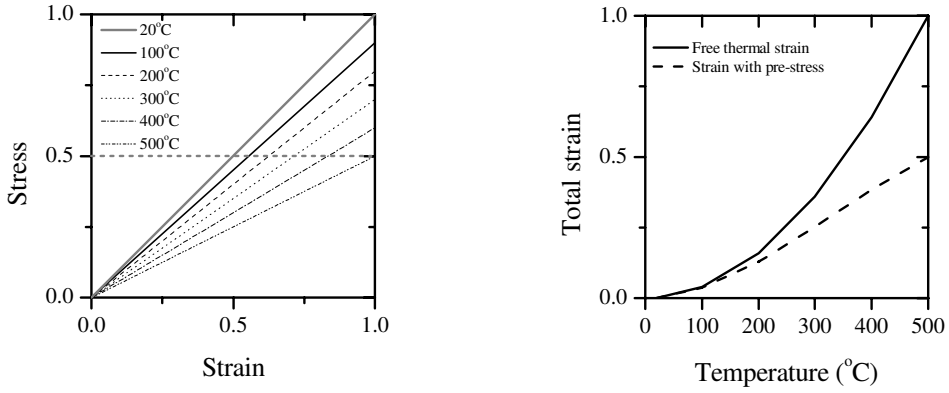

(a) Elastic modulus at different temperatures (b) Effect of different elastic moduli on total strain

Fig. 2 – Modelling LITS as part of the constitutive curve

3. CONSTITUTIVE RELATION

Though LITS appears to manifests itself as a change in the thermal expansion under different pre-stresses and temperatures, it can instead be thought of as being part of the stress-strain definition of the material. Figure 2. (a) shows a material whose elastic modulus degrades with increasing temperature. The influence of this change is demonstrated in Figure 2. (b) where the total strain experienced by the material does not follow free thermal expansion. Instead, the strain at each temperature is reduced by the change in elastic strain.

The path followed by the horizontal line in Figure 2. (a) demonstrates how the stress remains the same while the strain increases. The degree to which the total strain is reduced is dependant upon the level of applied stress.

Of course, the LITS developed in Figure 2. (b) will be fully elastic, and were the material to be cooled back to the starting temperature the strains would be fully recovered. If, however, plastic strains were introduced they would not recover on cooling; the combination of these different strains is what is meant by the multiple components of LITS. Defining LITS in this way allows it to be included in the material model for the concrete.

4. MATERIAL MODELS

Several different models have been developed to describe LITS. However, because of the way that the components of LITS are inseparable from the constitutive curve, a model for LITS cannot be regarded in isolation. For a model to be used in finite-element analysis, the full constitutive curve must be defined. This paper will only describe two academic models which develop a full constitutive relation. The model presented in the Eurocode will also be examined.

4.1 Anderberg's model

In 1976 Anderberg[11] developed a constitutive model for concrete. The present authors were unable to obtain the original presentation of this model, though it has been described extensively in a number of different publications[7, 8]. The instantaneous stress-strain curve is composed of two branches: an ascending branch, represented by a quadratic curve which traverses the peak stress; and a linear descending branch which joins with the ascending branch when their gradients are equal and intersects with the strain axis at a predefined value of peak strain. The model includes a formulation for creep strain. As its name suggests, this is a time dependent component. It is recognised that for short term transient problems – such as fires – creep strain can be regarded as negligible.

When temperature is less than 550ºC degrees, Anderberg's model relates the transient strain term (the largest LITS component) to thermal expansion and the ratio of stress-to-peak-stress. For temperatures greater than 550ºC transient strain is given only in terms of stress-to-peak-stress ratio.

For $T \leq 550$ºC

$$\varepsilon_{tr} = -k_{tr}\left(\frac{\sigma}{\sigma_{u0}}\right)\varepsilon_{th} \tag{1}$$

For $T \geq 550$ºC

$$\frac{\partial \varepsilon_{tr}}{\partial T} = -0.0001 \cdot \left(\frac{\sigma}{\sigma_{u0}}\right) \tag{2}$$

Where Anderberg gives k_{tr} as 2.35 for calcareous concrete. The existence of the link to free thermal strain is the subject of some debate as it has been demonstrated that there is no physical evidence to link it with transient strain. In fact, transient strain has been shown to be independent of free thermal strain. This is exemplified by the fact that a lightweight concrete

with zero free thermal strain can be shown to have the same transient strain curve as a normal weight concrete.

Neilsen [9], proposed a modification to the Anderberg's formulation of transient strain which removes the link to free thermal strain.

$$\varepsilon_{tr} = -0.000038 \cdot \left(\frac{\sigma}{\sigma_{u0}} \right) \tag{3}$$

Unlike Anderberg's transient strain component, this can be used for all values of temperature and stress. Nielsen's formula has been demonstrated to provide a good match to experimental data. The version of Anderberg's model used in this paper adopts the modification proposed by Nielsen.

4.2 Terro's model

The introduction mentioned the large body of work carried out at Imperial College. Though no mathematical model has been directly proposed by the authors of that work, Terro[10] used the experimental data to create a constitutive model which includes LITS components.

The main ascending branch is based on a simplified version of the model proposed by Schneider[12]. In recent studies of constitutive models, though, there has been inconsistency in the application of the instantaneous stress-strain curve. The study by Li[7] regarded the relationship to be linear elastic, whereas, the study by Youssef[8] used a simplified Schneider method. This study will use the latter method since this permits a descending branch and, in the study by Youssef, it was concluded that the model achieved "good accuracy".

The equation for LITS is fitted to Khoury's master curve[6] and is:

$$LITS = LITS(T,0.3) \cdot \left(0.032 + 3.226 \cdot \frac{\sigma}{\sigma_{u0}} \right) \tag{4}$$

Where:

$$LITS(T,0.3) = \left(43.87 - 2.73T - 6.35 \cdot 10^{-2} T^2 + 2.19 \cdot 10^{-4} T^3 - 2.77 \cdot 10^{-7} T^4\right) \cdot 10^{-6} \tag{5}$$

Two versions of the latter equation are provided by Terro since Thames gravel concrete departs from the master curve above 400ºC. A fifth order polynomial is proposed for use in this case. A number of formulae are also presented for strain at peak stress to account for different levels of pre-stress.

In summary, both of the models have key features in common: they both present a constitutive stress strain curve which varies with temperature; the curves are based on the way that material strength and elastic modulus degrades with increased temperature; these curves are then modified by the transient strain component (or the LITS component in the Terro model). This three step method of obtaining a final constitutive curve is demonstrated in Figure 3. (a).

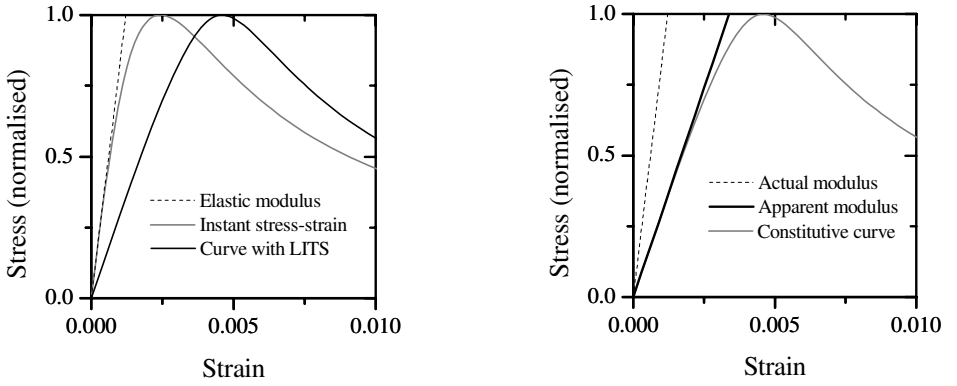

(a) Three step formulation of constitutive curve (b) Apparent and actual elastic moduli

Fig. 3 – Construction of the final constitutive curve

5. APPARENT ELASTIC MODULUS

For most stress-strain curves, it is reasonable to assume that the initial tangent modulus of the constitutive relation is equal to the elastic modulus. Put another way, the first section of the stress-strain curve is within the elastic region of the material. The situation becomes less clear with the inclusion of LITS. The modification of the original stress-strain curve by the LITS components causes plastic strains to develop from very low stresses. The implication of this is that the tangent modulus of the constitutive strain curve is never equal to elastic modulus of the material – even at zero strain, or where the ascending branch is straight.

It is, therefore, impossible to identify the elastic modulus of the material from simple inspection of the constitutive curve. If this is attempted, a value of elastic modulus will be obtained which is the not the actual modulus, but the "apparent" modulus of the material. This will result in significant underestimation of the true plastic strains which would develop if the actual modulus was in use. Figure 3. (b) illustrates the difference between the apparent elastic modulus of a material and the actual modulus as defined by the constitutive equations.

In finite-element applications the difference between the actual and apparent material moduli must be carefully considered. There are circumstances under which the differences between the moduli will not effect the response of a structural model. For example, under direct strain or heating the solution will simply follow the defined curve or move between curves in the appropriate way. However, if the applied strain is reduced, there are multiple heating phases, or there are more complex loading patterns to be considered, the mal-definition of the plastic strains becomes significant. This has not been a major issue for most models as the emphasis has predominantly been on the heating phase of the fire. However, as attention turns to cooling it is necessary to consider these components more carefully.

The concrete constitutive curves described in Eurocode 2[13] have the potential to suffer from these problems. The model is defined by the specification of peak stress, peak strain, and strain-at-peak-stress – not elastic modulus. Thus, the user has to define an elastic modulus to associate with the model. A reasonable assumption might be to assume that the elastic modulus should be equal to the initial gradient of the constitutive curve. However, as illustrated above, this may not be a useful or accurate assumption.

6. SIMPLE EXAMPLE

The influence of the definition of elastic modulus is demonstrated using a series of simple models. A finite-element model was created using the commercially available finite-element package ABAQUS. The model was of a simplified pure concrete column consisting of a single member pinned at both ends. The temperature was raised uniformly to 500ºC and then cooled back down to ambient temperature. Five different models were applied: the Anderbreg model; the Anderberg model with use of the apparent elastic modulus; the Terro model; the Terro model with the use of the apparent elastic modulus; and the Eurocode model. The constitutive curves for ambient and 500ºC are shown in Figure 4. The resulting stress from the heating and cooling regimes was then plotted against the temperature (Figure 5.).

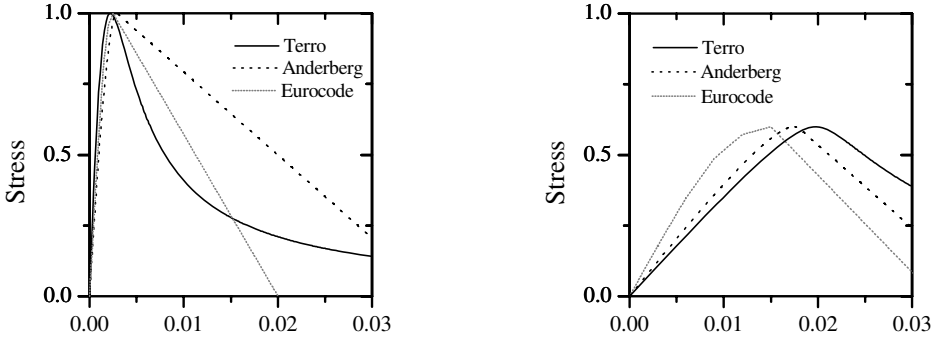

(a) Constitutive curves at ambient (b) Constitutive curves at 500ºC

Fig. 4 – Constitutive curves at different temperatures

Thermal expansion caused compressive stresses to build up as the column was heated due to the fixed ends of the column. Though the associated material models followed the same path through heating, the stains that built up in the models with the apparent moduli were predominantly elastic, whereas, in the models with the actual moduli, most of the strain was plastic. This only became evident on cooling, where the apparent models slowly released the stresses and, were only pulled into tension when the temperature was close to returning to ambient. The models which used the actual moduli, on the other hand, were unable to recover the strains developed and rapidly progressed into tension.

Also presented in Figure 5. is the stress path that the Eurocode 2 model takes under the same heating regime. The first notable difference between this model and the two academic models is that the stresses generated were significantly higher. This was due to the steeper gradient of the constitutive curve in the ascending branch. Though this could be considered as an important difference between the models, it is of no specific relevance to this study which is primarily concerned with the development of elastic and plastic strains.

Analysis of the cooling stress path demonstrated that though the model does not exhibit either strain type – mostly plastic or mostly elastic – in the extreme, it is much more similar to the apparent models. This is expected since the elastic modulus was derived from the gradient of the constitutive curve. The plastic strains are more significant than the other apparent models because the curvature of the ascending branch in the Eurocode is greater than that of the other models.

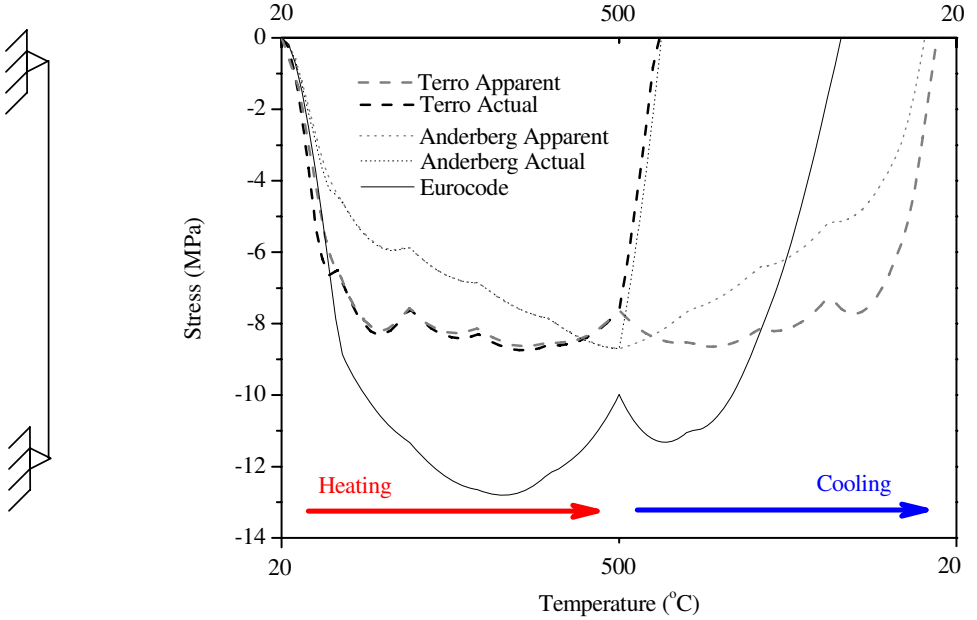

Fig. 5 – Stress response to heating and cooling regime

Though this is a very simplified model, it demonstrates that it is necessary to consider the difference between the apparent and the actual elastic modulus of a model. It shows that a difference of definition can have significant impact on the structural response of during cooling or unloading.

7. CONCLUSIONS

There are several conclusions which can be drawn from this study. These are summarised below:

- LITS contains a number of different components which influence the behaviour of concrete when it is heated under applied stress.
- The most significant component of LITS is transitional thermal creep which is irreversible. However, this is frequently considered in combination with drying creep and termed transient strain.
- The terms transient strain and transient creep refer to the same phenomena.
- Several models exist with which to model LITS. One model has not been found to be significantly superior to another.
- There are significant differences between a constitutive curve which includes LITS, and a model which accurately represents LITS components.
- Consideration of the apparent and actual elastic moduli is necessary to accurately represent LITS in structural models.

REFERENCES

1. Khoury, G.A., "Strain of heated concrete during two thermal cycles. Part 3: isolation of strain components and strain model development", Magazine of Concrete Research, 2006. 58(7): p. 421-432.
2. Thelandersson, S., "Modeling of Combined Thermal and Mechanical Action in Concrete", Journal of Engineering Mechanics, 1987. 113(2): p. 893-906.
3. Schneider, U., "Concrete at High Temperatures - A General Review", Fire Safety Journal, 1988. 13: p. 55-68.
4. Bazant, Z.P. and M.F. Kaplan, "Concrete at High Temperatures: Material Properties and Mathematical Models". 1996, Harlow: Longman Group Limited.
5. Khoury, G.A., B.N. Grainger, and P.J.E. Sullivan, "Transient thermal strain of concrete: literature review, conditions within specimen and behaviour of individual constituents", Magazine of Concrete Research, 1985. 37: p. 131-144.
6. Khoury, G.A., B.N. Grainger, and P.J.E. Sullivan, "Strain of concrete during first heating to 600C under load", Magazine of Concrete Research, 1985. 37(133): p. 195-215.
7. Li, L.-y. and J. Prukiss, "Stress-strain constitutive equations of concrete material at elevated temperatures", Fire Safety Journal, 2005. 40: p. 669-686.
8. Youssef, M.A. and M. Moftah, "General stress-strain relationship for concrete at elevated temperatures", Engineering Structures, 2007. 29: p. 2618-2634.
9. Nielsen, C.V., C.J. Pearce, and N. Bicanic, "Theoretical model of high temperature effects on uniaxial concrete member under elastic restraint", Magazine of Concrete Research, 2002. 54(4): p. 239-249.
10. Terro, M.J., "Numerical Modeling of the Behaviour of Concrete Structures in Fire", ACI Structural Journal, 1998. 95(2): p. 183-193.
11. Anderberg, Y. and S. Thelandersson, "Stress and deformation characteristics of concrete, 2 - experimental investigation and material behaviour model". Bulletin 54. 1976, Sweden: University of Lund.
12. Schneider, U. "Modelling of concrete behaviour at high temperatures". in Design of Structures against Fire. 1986. Aston, Birmingham: Elsevier.
13. Eurocode2, "Design of Concrete Structures". 1992.
14. Bratina, S., M. Saje, and I. Planinc, "The effects of different strain contributions on the response of RC beams in fire", Engineering Strucutres, 2007. 29: p. 418-430.
15. Nechnech, W., F. Meftah, and J.M. Reynouard, "An elasto-plastic damage model for plain concrete subjected to high temperatures", Engineering Structures, 2002. 24: p. 597-611.
16. Khoury, G.A., "Strain of heated concrete during two thermal cycles. Part 1: strain over two cycles, during first heating and at subsequent constant temperature", Magazine of Concrete Research, 2006. 58(6): p. 369-385.

Composite Structures

MECHANICAL CHARACTERIZATION OF FIBRE REINFORCED POLYMERS FOR NUMERICAL FIRE ENDURANCE MODELLING

E. U. CHOWDHURY[1], R. EEDSON[2], L. A. BISBY[3], M. F. GREEN[4], N. BENICHOU[5], V.K.R. KODUR[6] and E. FYFE[7]

ABSTRACT

Concerns associated with fire remain an obstacle to applications of fibre reinforced polymer (FRP) materials in buildings and parking garages due to their sensitivity to high temperatures as compared with other structural materials. This paper presents the preliminary results of an experimental investigation to characterize the mechanical properties of unidirectional infrastructure FRPs under various loading and thermal regimes, ranging from ambient temperature, eventually up to 600°C. Tensile, lap splice bond, and FRP to concrete bond tests are being conducted under both steady state and transient thermal and loading regimes. Results from initial mechanical testing of unidirectional carbon/epoxy FRP (CFRP) coupons are presented in this paper. The CFRP coupons retained 40 to 60% of their room temperature tensile strength and 50 to 80% of their room temperature tensile elastic modulus when tested under steady state thermal conditions between 86°C and 200°C. The implications of these test results for numerical fire endurance modelling of FRP strengthened concrete structures are discussed.

[1] Graduate Student, Queen's University, Department of Civil Engineering, Kingston, ON, Canada, K7L 3N6
email: chowdhury@ce.queensu.ca
[2] Graduate Student, Queen's University, Department of Civil Engineering, Kingston, ON, Canada, K7L 3N6
email: rob.eedson@ce.queensu.ca
[3] Assistant Professor, Queen's University, Department of Civil Engineering, Kingston, ON, Canada, K7L 3N6
email: bisby@civil.queensu.ca
[4] Professor, Queen's University, Department of Civil Engineering, Kingston, ON, Canada, K7L 3N6
email: greenm@civil.queensu.ca
[5] Research Officer, National Research Council of Canada, Ottawa, ON, Canada, K1A 0R6
email: Noureddine.Benichou@nrc-cnrc.gc.ca
[6] Professor, Michigan State University, Lansing, Michigan, USA, 48824
email: kodur@egr.msu.edu
7 President, Fyfe Company LLC, San Diego, California, USA, 92121
email: ed@fyfeco.com

1 INTRODUCTION

Fibre reinforced polymer (FRP) materials are increasingly being used in repairing and retrofitting reinforced concrete structures that have deteriorated from damage caused by electrochemical corrosion or from sustaining loads higher than their design. There are many advantages in externally strengthening concrete structures with FRP materials rather than with steel, including resistance to corrosion, and ease and speed of application. In spite of FRPs' advantages, fire resistance remains a significant obstacle to the application of FRPs in many buildings and parking garages because of these materials' combustibility and susceptibility to degradation of mechanical and bond properties at elevated temperatures. A research study is being conducted at Queen's University in conjunction with the National Research Council of Canada (NRC) and industry partners to investigate the effects of fire on FRP strengthened concrete structures. As part of that overall research effect, this paper presents test results to characterize the mechanical properties of selected currently available infrastructure FRPs under various loading and thermal regimes, ranging from ambient temperature to 300°C. Results from these tests will be used to develop analytical models to represent the stress-strain behaviour of FRPs for subsequent use in predictive fire simulation software which is currently being developed by the authors.

2 RESEARCH SIGNIFICANCE

The current paper represents part of a larger study to investigate the performance of FRP strengthened concrete members under exposure to standard fires. A major component of this larger research program involves developing numerical models that can simulate the heat transfer within these FRP strengthened concrete structures and their structural response at high temperature.[1,2,3] If successful, rational and defensible numerical models could considerably reduce the costs incurred in standard fire testing of full-scale specimens. A detailed knowledge of the thermal and mechanical behaviour of FRP materials at high temperature, which is extremely scarce for the specific systems under consideration, is critical for such models to accurately simulate the behaviour of FRP strengthened concrete structures under fire. In addition, the critical temperature above which the FRP composite will have inadequate structural strength remains unknown. Such information is important for setting defensible service temperature limits for these systems.

3 EXPERIMENTAL PROCEDURE

In this paper, preliminary results from a larger material testing program are presented. In the overall material testing program, selected commercially available FRP strengthening systems will be tested under various loading and thermal regimes. The mechanical properties and bond strength of FRP materials are known to begin degrading at temperatures close to or exceeding the glass transition temperature (T_g) of the polymer resin component of the FRP material, which is typically between 65 and 120°C.[4] Hence, the tests presented herein were conducted at ambient temperature and temperatures near the resin's T_g. Prior to the tension tests, differential scanning calorimetry (DSC) was performed on four samples of FRP composite by the authors to determine the glass transition temperature of the FRP material. Based on the DSC results, tension tests were conducted at temperatures 15°C below and above the glass transition temperatures to investigate the mechanical degradation near the

glass transition temperature. Additional tests were conducted at 200°C to observe the material's performance at temperatures well above the glass transition temperature.

In the overall material testing program, tensile, lap splice, and FRP-to-concrete bond tests will be conducted. The experimental procedure for the current study is based on earlier research performed at Queen's University on the residual properties of FRPs after exposure to elevated temperature.[5,6] Details of the specimens for the three types of tests to be performed are shown in Figure 1. Both steady and transient thermal and loading regimes are being considered. Preliminary results for some of the tensile specimens are included in this paper. The FRP specimens, which were made with two plies of sheet, had a nominal thickness of 2.0 mm. The tension tests were conducted in a Universal Testing Machine (UTM) (Figure 2), which has an integrated, custom designed thermal chamber (with internal dimensions of 250 mm width by 250 mm depth by 300 mm height) and a maximum load capacity of 600 kN.

For this paper, tension tests on carbon/epoxy FRP (CFRP) coupons were conducted under a steady-state heating condition. The CFRP specimens were heated to the specified temperature at a constant heating rate of 10°C/min, held at the specified temperature for 15 minutes, and then loaded at a crosshead stroke rate of 3 mm/min. At this point, no investigation on heating rate or loading rate, both of which may be important, has been conducted. Figure 3 shows the temperature-time curve of the design and measured temperature achieved by the FRP specimens (i.e., the intended chamber ramp and soak regimes, along with the temperature measured on the surface of the FRP coupon at its midpoint). The slight lag in the "actual" curves is due to the fact that these temperatures were measured using bondable surface thermocouples, such that the thermal mass of the coupons decreased the measured temperatures. In general, both the ramp rate and hold temperatures were as desired. During the tension tests, the middle 300 mm of the FRP specimens was heated, as shown in Figure 2(b), to prevent failure near the grip region (which would be a matrix-dominated failure mode). Axial strains were measured using a deformation measurement technique based on particle image velocimetry (PIV) and close-range digital photogrammetry.[7] In this measurement technique, digital images were captured of the FRP specimens inside the thermal chamber using a high-resolution digital camera. Using PIV, 20 virtual strain gauges were created across the width of the coupons by defining 40 pixel "patches" on the images of the FRP specimens, as shown in Figure 4. During PIV analysis, the digital images were processed to track the movement of the pixel patches and thus measure the displacements of the patches between two or more digital images. Based on the displacements measured from the image processing, the variation in axial strain was calculated across the width of the coupons at various load levels. This information was subsequently used to calculate the elastic modulus of the coupons during testing as per ACI 440 requirements[8].

4 RESULTS AND DISCUSSION

Initial results from tensile tests of carbon/epoxy FRP coupons are presented in this paper. The glass transition temperature of the FRP material was determined to be 101 ± 2°C based on an average of four DSC runs (with T_g determined on the second heating cycle). Based on this measured T_g value, initial test temperatures were selected on the basis of recommended service temperature limits as per ACI 440 requirements[9] as 20°C (ambient), 86°C (T_g - 15°C), 116°C (T_g + 15°C) and 200°C. Additional temperatures will be investigated in future tests, up to and including temperatures at which decomposition of the matrix polymer is expected to occur.

Three direct tension tests were performed at each of the above temperatures. Figure 5 shows the normalized tensile strength and elastic modulus data with increasing exposure temperature. Because of the well known difficulty of measuring strain at elevated temperatures during material testing, axial strains in the coupons were measured using PIV analysis. The strain analysis was performed for twenty virtual axial strain gauges across the width of the coupons, and the axial strains were observed to vary by up to 0.05% across the width of the FRP coupon specimens at a given level of total axial load. As an example, Figure 6 shows the axial strain profiles measured across the width of one of the coupons tested at room temperature at three increasing load levels. Interestingly, this figure shows that the axial strain varies considerably (by up to 25% of the average reading) across the coupon's width. It is likely that this strain variation results from non-homogeneities in the coupons, as well as uneven gripping at the coupon's ends (even though these coupons were carefully tested according to applicable guidelines[8]).

Also shown in Figure 6 are horizontal lines showing the strains measured by a bonded foil gauge at the specimen centreline at the same load levels. It is clear that there is good agreement between the foil and optical gauges. Additional validation of this optical technique for measuring strains in FRPs is given by Bisby et al.[10]. Despite the variation in observed axial strain over the coupon width, the axial strains from all 20 virtual strain gauges were averaged across the width to obtain a global stress-strain curve for the coupon. From this global stress-strain curve, the tensile chord modulus was calculated using stress values corresponding to 0.1% and 0.3% strain[8].

At room temperature, the CFRP coupons had a tensile strength of 703 ± 34 MPa and a tensile elastic modulus of 82 ± 3 GPa at 20°C. Figure 5 shows that the CFRP coupons tested thus far experienced strength losses between 20 and 60% and losses of tensile elastic modulus between 20 and 40% at 86°C, or T_g - 15°C. Comparable losses of strength and modulus were observed at both 116°C and 200°C, with little apparent additional degradation in either strength of stiffness at these higher temperatures.

The above data suggest that the coupons tested herein lose up to 60% of their room temperature strength at temperatures 15°C below their matrix T_g, but that further heating does not cause additional strength loss. Thus, the authors suspect that this behaviour is due to loss of interaction and load sharing between fibres for all elevated temperature exposures, due to matrix softening, such that the elevated temperature strength and stiffness values effectively represent the results that would be obtained by testing dry fibres. Tests are currently underway to confirm this hypothesis. The data also suggest that, provided that adequate anchorage is maintained, the CFRP strengthening system tested appears able to retain at least 40% of its room temperature strength at temperatures up to 200°C. Clearly, additional testing is needed to support this conclusion.

While considerable variability exists in the data shown in Figure 5, it should be noted that none of the coupons failed near the grips. Furthermore, all coupons that were tested at high temperature ruptured in the region of the FRP that was inside the thermal chamber, indicating that the reduced strength and stiffness was not a consequence of thermal degradation in the gripping region. Failure of the CFRP coupons at room temperature was sudden and violent and occurred along a horizontal line across the coupons' width. Coupons tested at 86°C were less violent than at 20°C, but displayed a similar failure mode. At 116°C and 200°C, the coupons split longitudinally (refer to in Figure 7) as they approached failure and thus failed more gradually. This behaviour is thought to be associated with loss of interaction between the individual fibre rovings due to resin softening at elevated temperature.

5 IMPLEMENTATION IN STRUCUTRAL FIRE MODELS

As previously mentioned, the long term objective in performing the tests such as those presented above is to develop empirical/analytical relationships to describe the variation in mechanical and bond properties of various currently available FRP strengthening materials and systems with temperature for subsequent use in numerical fire simulation models. To develop analytical descriptions of the data presented previously, the authors have, on the basis of previously published research on the high temperature performance of polymer composites[4,11,12], selected a sigmoid function to represent mechanical property degradation. This function can be expressed using the following form:

$$\frac{f}{f_o} = \left(\frac{1-a}{2}\right)\tanh\left(-b(T-c)\right) + \left(\frac{1+a}{2}\right)$$

In the above expression, f is the material property at elevated temperature, T, f_o is the room temperature material property, and a, b, and c, are parameters that determine the lower asymptote, midpoint, and curvature of the sigmoid curve. Using a non-linear multi-parameter least squares regression analysis, the coefficients, a, b, and c in the above equation can easily be determined to provide an analytical approximation to the observed behaviour. This has been done for the experimental data presented herein in Figure 8. Clearly, given the variability in the data obtained to date, additional data are needed before these predictions can be used with confidence. It is expected[4,12] that degradation of bond properties will follow a similar, although more severe, degradation trend at high temperature.

Once the analytical relationships are derived for strength, stiffness, and bond properties, they will be incorporated into numerical models to predict the fire endurance of FRP strengthened reinforced concrete columns. Details of these column models have been presented elsewhere[2].

6 FUTURE TESTING

The data presented in this paper represent a preliminary investigation only. The reader will recognize that a considerable amount of additional testing is required before the true behaviour of FRP strengthening systems, under load, at elevated temperature can be accurately described. Tests are currently underway to study both the transient and steady-state creep performance of FRP strengthening systems under various loading and thermal regimes. Similar tests are planned to study the FRP-to-FRP and FRP-to-concrete bonds under both static and dynamic thermal and loading regimes. Furthermore, the effects of heating rate and thermal history will also be examined.

7 SUMMARY AND CONCLUSIONS

This paper has presented the initial results of an ongoing experimental study aimed at developing a more complete understanding of the degradation in mechanical and bond properties of FRP strengthening systems for infrastructure at elevated temperatures. Based on the results of these preliminary tests on FRP coupons, the following conclusions can be drawn:

- The wet lay-up carbon/epoxy FRP material tested in the current paper suffered a 20 to 60% degradation of tensile strength and a 20 to 40% degradation of tensile elastic modulus at temperatures 15˚C below the glass transition of its resin matrix.
- The loss of strength and stiffness appears to be due to loss of load sharing between the individual fibre rovings, essentially resulting in dry fibre behaviour at temperatures close to or exceeding the resin's T_g.
- The data presented herein provide preliminary evidence that wet lay-up FRP materials such as that tested in the current paper may be able, with sufficient anchorage, to maintain 40 to 50% of their tensile strength at temperatures well in excess of their resins' T_g. A total loss of tensile strength is expected beyond the thermal decomposition temperature of the polymer resin. Additional testing is required to support these conclusions.

8 ACKNOWLEDGEMENTS

The authors are members of the ISIS Canada Research Network and would like to acknowledge the support of the Networks of Centres of Excellence Program of the Natural Science and Engineering Research Council of Canada. We would also like to thank the National Research Council of Canada, Fyfe Co., and Sika Corp for their support of this project.

9 REFERENCES

[1] Bisby, L.A., Kodur, V.K.R. and Green, M.F. "Fire endurance of fiber-reinforced-polymer confined concrete columns", ACI Structural Journal, 102(6), pp. 883-891, 2005.
[2] Chowdhury, E.U., Bisby, L.A., Green, M.F., Bénichou, N and Kodur, V.K.R. "Fire behaviour of FRP wrapped square reinforced concrete columns", CDCC-07, Quebec City, Canada, pp. 83-90, 2007.
[3] Williams, B., Kodur, V., Green, M.F. and Bisby, L. "Fire endurance of fiber-reinforced polymer strengthened concrete T-beams", ACI Structural Journal, 105(1), pp. 60-67, 2008.
[4] Bisby, L.A., Green, M.F. and Kodur, V.K.R. "Response to fire of concrete structures that incorporate FRP", Progress in Structural Engineering and Materials, 7(3), pp. 136-149, 2005.
[5] Bisby, L.A. and Foster, S.K. "High temperature residual bond properties of FRP strengthening systems for concrete", CDCC-07, Quebec City, Canada, pp. 193-200, 2007.
[6] Foster, S.K. and Bisby, L.A. "High temperature residual properties of externally-bonded FRP systems", FRPRCS-7, Kansas City, USA, pp. 1235-1252, 2005.
[7] White, D.J., Take, W.A. and Bolton, M.D. "Soil deformation measurement using particle image velocimetry (PIV) and photogrammetry", Géotechnique, 53(7), pp. 619-631, 2003.
[8] ACI. "Guide Test Methods for Fiber-Reinforced Polymers (FRPs) for Reinforcing or Strengthening Concrete Structures", ACI 440.3R-04, American Concrete Institute, Farmington Hills, MI, 40 pp, 2004.
[9] ACI. "Guide for the Design and Construction of Externally Bonded FRP Systems for Strengthening Concrete Structures", ACI 440.2R-02, American Concrete Institute, Farmington Hills, MI, 45 pp, 2002.
[10] Bisby, L.A., Take, W.A. and Caspary, A. "Quantifying strain variation in FRP confined concrete using digital image analysis", 1st Asia-Pacific Conference on FRP in Structures (APFIS 2007), Hong Kong, December 12th-14th, pp. 599-604, 2007.
[11] Dimitrienko, Y.I. "Thermomechanics of Composites under High Temperatures", Klewer Academic Publishers, London, 347 pp, 1999.
[12] Katz, A., and Berman, N. "Modeling the effect of high temperature on the bond of FRP reinforcing bars to concrete", Cement and Concrete Composites, 22, pp. 433-443, 2000.

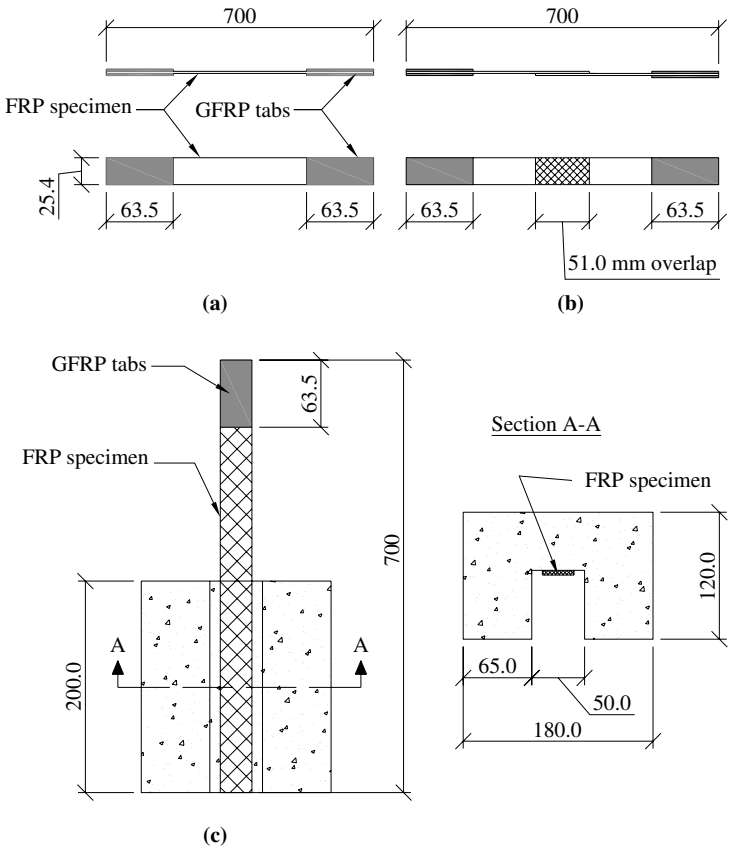

Fig. 1 – FRP specimen schematics for (a) tensile tests (presented), (b) FRP-to-FRP bond-overlap test (not presented), and (c) FRP to concrete bond test (not presented). Dimensions are in mm.

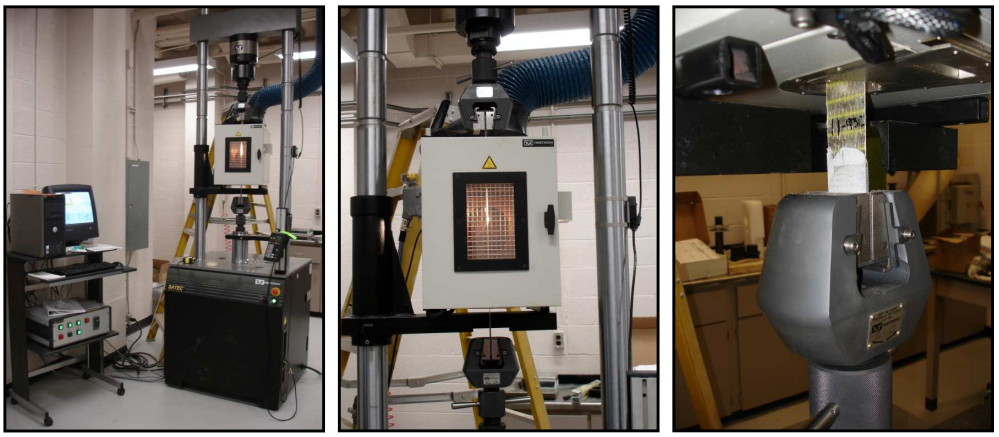

(a) (b) (c)

Fig. 2 – (a) Universal testing machine, thermal chamber, and data acquisition system, (b) thermal chamber, and (c) wedge-action gripping system outside the chamber.

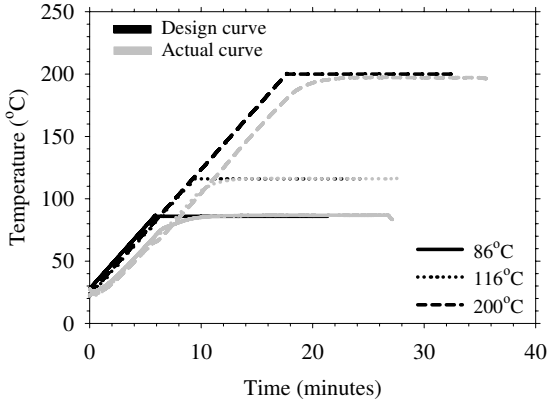

Fig 3. Design (desired) and actual (observed specimen) temperatures during heating.

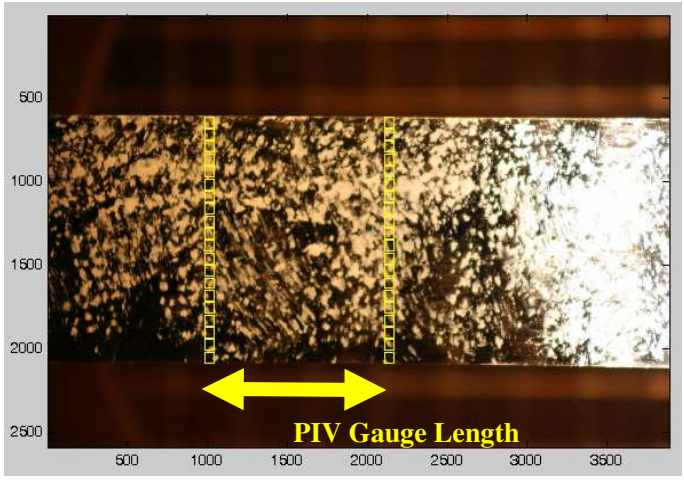

Fig 4. Test patches on FRP specimens for image processing using PIV (photo rotated 90˚ clockwise).

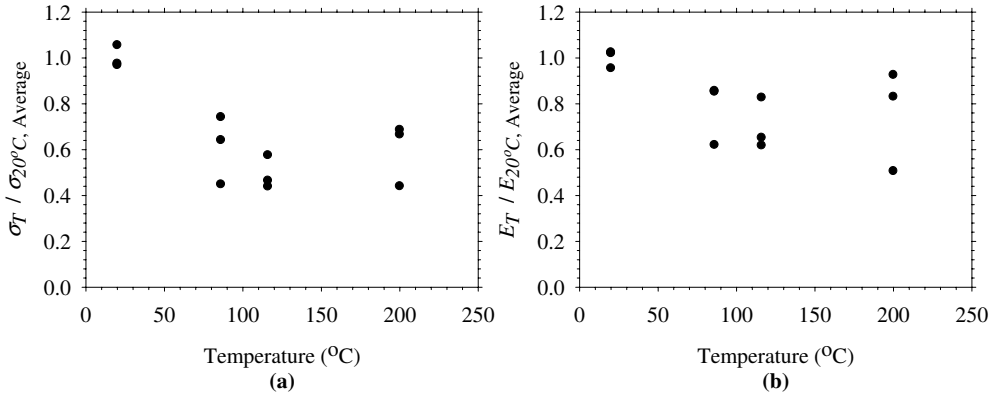

Fig 5. (a) Normalized strength and (b) normalized tensile elastic modulus of CFRP coupons with increasing temperatures.

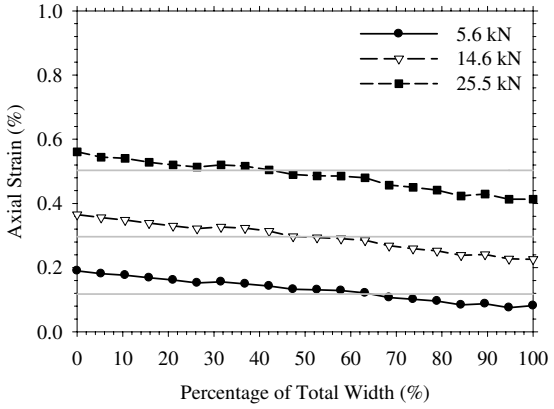

Fig 6. Strain variation across the width of a typical FRP specimen under increasing axial tensile loads

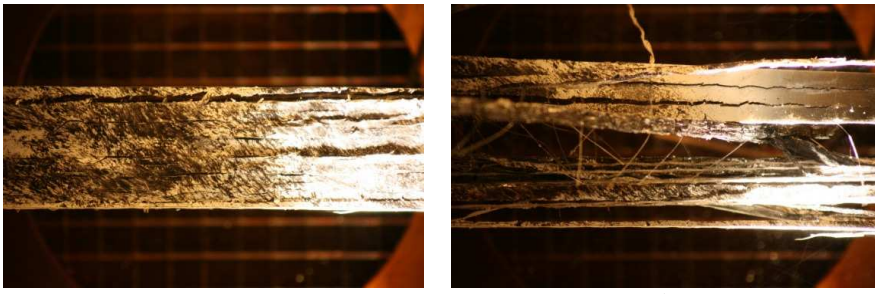

Fig 7. Failure of CFRP coupons at 200°C (a) just before failure, and (b) just after failure. Loss of interaction between rovings is evident (photos rotated 90˚ clockwise).

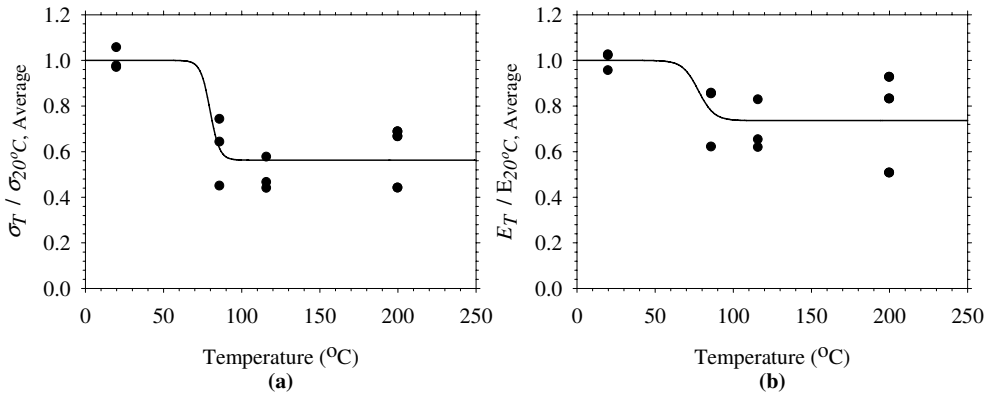

Fig 8. (a) Normalized strength and (b) normalized tensile elastic modulus of CFRP coupons with increasing temperatures, including preliminary analytical least-squares best-fit sigmoid curves.

TENSILE MEMBRANE ACTION OF COMPOSITE SLAB PANELS IN FIRE - SIMPLE VS. ADVANCED MODELS

WEE SIANG TOH[1] and NICK BERNABE[2]

ABSTRACT

This paper presents a comparison, based on real practical case studies, between the simple analytical BRE-Bailey method (BRE-BM) and the advanced finite element model (FEM) Vulcan for the membrane action of composite slab panels with unprotected secondary beams at elevated temperatures. Both approaches predicted the membrane behaviour of the composite slabs, comprising compressive membrane action around the slabs' perimeter and tensile membrane action in the central span region of the slabs. This paper mainly studies the effects of the orientation of unprotected secondary beams and the boundary conditions on tensile membrane action of composite slab panels. The results show that the application of the BRE-BM is generally restricted by the conservative assumption of the maximum allowable vertical displacement. In contrast, the FEM estimates higher load-carrying capacities as well as providing a full displacement-time relationship throughout the heating of the slabs. For slab panels with unprotected secondary beams with an orientation in the short span, tensile membrane action can be easily mobilised without increasing fire protection to the boundary supporting beams. However, the FEM predictions on the slab capacities and deflections in fire are very sensitive to the continuity of the reinforcement over the protected boundary beams.

1 INTRODUTION

A series of seven full-scale fire tests carried out on the real size eight-storey steel-framed building with composite metal deck floors at Cardington in 1995-96 and 2003 had

[1] Senior Fire Engineer, Safe Consulting Limited, 60 Newman Street, London W1T 3DA, UK, email: adam.toh@safe.eu.com.
[2] Associate Director, Safe Consulting Limited, 60 Newman Street, London W1T 3DA, UK, email: nick.bernabe@safe.eu.com.

demonstrated the robustness and resistance to fire of the composite floors comprising of unprotected secondary steel beams [1-2]. Many researchers have identified tensile membrane action of the composite slabs as the mechanism of supporting the applied working load under fire conditions, and the enhancement depends on the slab's aspect ratio, strength and ductility of reinforcement, slab deformation and boundary conditions [3-6].

The Building Research Establishment (BRE) and Steel Construction Institute (SCI) in the UK have published design guidance and a simple calculation method previously derived by Bailey (denoted as BRE-BM) for determining tensile membrane action of composite slabs in fire, based on the lessons learned from the Cardington tests [5, 7]. This design approach allows for the composite floor plates to be divided into a number of slab panels with each panel being surrounded by protected supporting beams and the secondary beams within the panel being unprotected.

In the last decade, the omission of fire protection to secondary beams in composite steel-framed buildings has been widely accepted and applied by the steel construction industry in the UK. Both simple design and advanced calculation methods have been used for a wide range of buildings including office blocks, shopping malls, hospitals and schools etc [7-11]. However, there is a divergence in opinion among consultants and researchers in the UK which of the two methods, the BRE-BM or the FEM should be used in practical designs. The main concern or misunderstanding is the BRE-BM may give unsafe results.

A comparison study was previously carried out by Toh and Bailey on long span slab panels with a span ranging from 14, 16 to 18m [12]. In general, the results showed that the BRE-BM tends to be conservative compared to the finite element software "Vulcan". This paper will continue the research by investigating the effects of the orientation of unprotected secondary beams and the boundary conditions on tensile membrane action of composite slab panels, based on real practical case studies. Both BRE-BM and Vulcan have been used to determine the enhancement of membrane action for slab panels under standard fire conditions.

The following sections contain the brief description of the BRE-BM, an introduction of Vulcan, the details of the case studies and the discussions of the results.

2 BRE-BAILEY METHOD

This approach was developed based on horizontally unrestrained slab panels, in which the resistance of the slabs is based on membrane action consisting of a compressive ring forming around the perimeter and tensile membrane action occurring in the central region of the panel as shown in Fig. 1. The main assumptions embedded within the approach include:

- Fracture of reinforcement mesh over the protected beams in fire situations
- Membrane action based on a lower-bound yield-line pattern
- Low maximum allowable deflections compared to those experienced at Cardington

These assumptions result in a conservative prediction of load carrying capacity, for a given displacement, compared to the condition if the reinforcement remains intact. The calculation equations can be found in FBE Report 5 by BRE [13] which will not be repeated here. Generally, enhancement from membrane action in fire increases proportionally with the allowable deflection. A conservative estimate of the allowable vertical displacement v (mm) is given by:

$$v = \frac{\alpha(T_2 - T_1)l^2}{19.2h} + \sqrt{\left(\frac{0.5f_y}{E}\right)\frac{3L^2}{8}} \quad \text{but} \quad \sqrt{\left(\frac{0.5f_y}{E}\right)\frac{3L^2}{8}} < \frac{l}{30} \tag{1}$$

where:

α is the coefficient of thermal expansion of concrete:
= 18×10^{-6} for normal weight concrete;
= 8×10^{-6} for lightweight concrete;
E is the Young Modulus of reinforcement [= 210 kN/mm^2];
h is the thickness of the slab [mm]. For trapezoidal slabs take depth to mid-height of troughs and for dovetail slabs assume full depth of slab.
L is the long span of the slab [mm];
l is the short span of the slab [mm];
$(T_2 - T_1)$ is the difference between the temperature at the top and bottom of the slab
= 770˚C for R30 to R90; and
= 900˚C for R120.

It can be seen that the maximum allowable deflection are a function of both long and short spans (L & l) of the slabs until the deflection limit of l/30 is reached. The maximum allowable deflection should be taken as relative deflection of the slab centre to the protected boundary beams in long span. The simple approach does not assume that the protected boundary beams do not deform in fire.

3 VULCAN - FINITE ELEMENT SOFTWARE

Vulcan is a be-spoke 3D finite element analysis software, developed in the University of Sheffield, for steel framed structures with composite floor slabs under fire conditions. The composite slabs are modelled by using a quadrilateral 9-noded higher-order isoparametric element (see Fig. 2) with a modified layered orthotropic formulation based on the Mindlin/Reissner theory, and using an effective stiffness model to model the ribbed nature of typical composite slabs. The steel-to-steel connections are represented by a 2-noded spring element and the interaction of steel beams and concrete slabs within a composite floor is represented using a linking two-noded shear-connector element [13-15].

The material properties at elevated temperatures for concrete and steel can be specified independently. A maximum-strain failure criterion has been adopted for the concrete, and a smeared model has been used in calculating element properties after cracking or crushing. After the initiation of cracking in a single direction, concrete is treated as an orthotropic material with principal axes parallel and perpendicular to the cracking direction. Upon further loading of singly cracked concrete, if the tensile strain in the direction parallel to the first set of smeared cracks is greater than the maximum tensile strain then a second set of cracks forms. After compressive crushing, concrete is assumed to lose all stiffness.

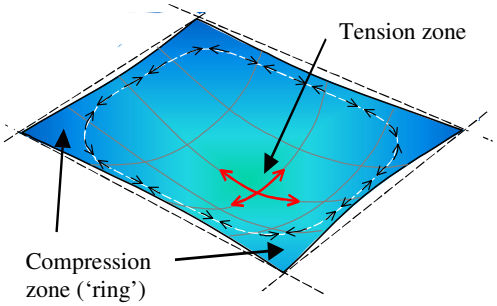

Fig. 1 – Membrane action of horizontally unrestrained composite slab.

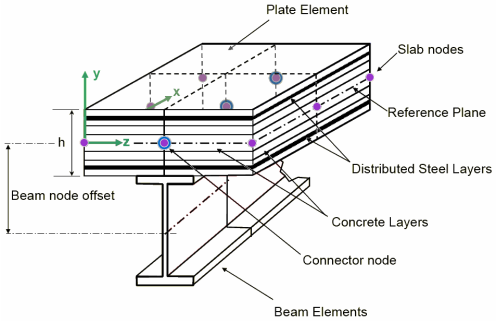

Fig. 2 – Schematic diagram for beam and layered slab elements in Vulcan.

4 CASE STUDIES

The office building studied in this paper is a 8-storey office block in London. The building is a composite steel-framed structure with a required fire resistance of 90 minutes (R90) for the office areas. Fig. 3 shows the typical floor plan with a length of 60m and a depth of 31m. The floor plate is made of a 140mm thick normal weight concrete slab on Richard Lees E60 (1.2 Gauge) profiled decking spanning on composite steel cellular beams. The typical floor beams are made of Grade S355 cellular sections with a finished depth of 450mm. Mesh reinforcement A252 is provided with a concrete cover of 25mm. The factored working load at ultimate limit state (ULS) and fire limit state (FLS) are 11.9 and 6.5kN/m^2 respectively, based on the load factors in accordance with BS5950-8 [17].

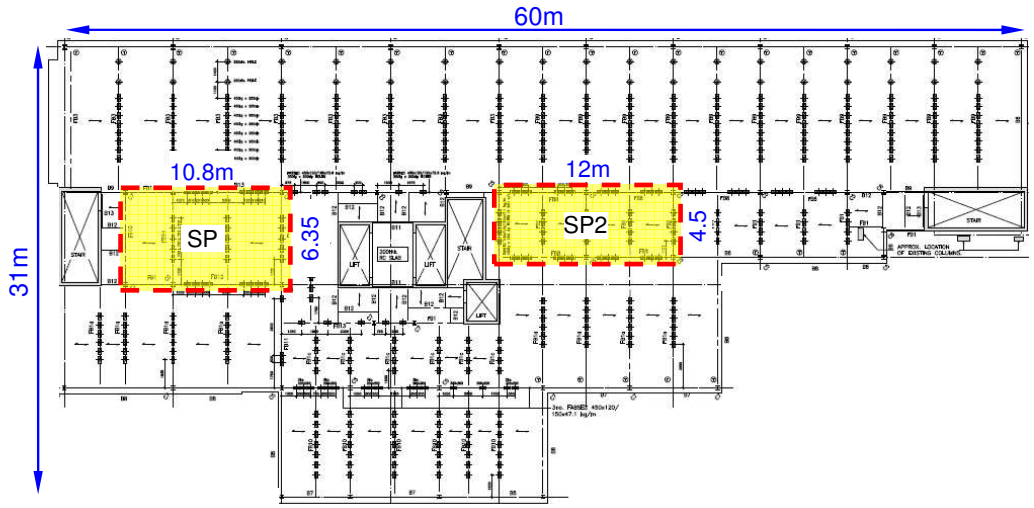

Fig. 3 – Typical floor plate.

This building provides a good opportunity to compare the fire performance of floor plates containing secondary beams with different orientations. The floor plate to the left of the central core comprises three bays of slab panels with secondary beams spanning 6.35m, whereas the floor plate to the right of the central core comprises four bays of slab panels with secondary beams spanning 4.5m. In this study, both floor plates will be adopted in case studies as Series SP1 and SP2 respectively.

In the FEM, reinforcement mesh is normally taken as continuous over the supporting beams in an internal slab panel, which will attribute to moment resistance of the concrete slab over the supporting beams. In contrast, the simple BRE-BM assumes that reinforcement mesh will fracture over the protected beams in fire situations, leading to zero moment resistance of the concrete slab. This study considered both simply and continuous supporting conditions for the edges of slabs over the boundary protected beams in order to investigate the effects of support conditions on the membrane action in fire situations.

The case studies comprise the extended unprotected slab areas to include 2 to 4 bays, leading to 5 slab panels of different sizes with aspect ratios (= L/l) varying from 1.18 to 2.67. Incorporating both simply and continuous support conditions, the total number of case studies were 11 as shown in Table 1.

The original design equations of the BRE-BM have been used to determine the enhanced capacities due to membrane action for all slab panels under standard fire conditions

for R90. In the Vulcan modelling, the analyses were carried out assuming standard fire conditions up to 120min in order to assess the ultimate failure time of the slabs.

Table 1 – Details of case studies and results.

Slab	Size (m×)	Aspect Ratio (-)	Support Condition	BRE-BM			Vulcan	
				v (mm)	e (-)	P (kN/m^2)	T_{eq} (min)	Span/Def. at 90min
SP1-1	6.35×7.5	1.18	Simply	423	4.7	9.1	16	9.6
SP1-2			Continuous	-	-	-	116	17.3
SP1-3	6.35×10.8	1.70	Simply	476	3.9	5.9	15	7.5
SP1-4			Continuous	-	-	-	66	10.7
SP1-5			Continuous*	-	-	-	70	11.7
SP2-1	4.5×6	1.33	Simply	260	3.0	10.5	23	11.6
SP2-2			Continuous	-	-	-	>120	49.5
SP2-3	4.5×9	2.00	Simply	283	2.4	6.4	27	11.0
SP2-4			Continuous	-	-	-	>120	27.1
SP2-5	4.5×12	2.67	Simply	283	1.9	4.6	116	22.1
SP2-6			Continuous	-	-	-	>120	26.6

* Protected beams orientated in the short span have a limiting temperature of 550°C.

4.1 Vulcan Modelling

In the modelling of Vulcan, the finite element densities were derived from sensitivity analyses. The following assumptions were made:

- No horizontal restraints for the slab panels around its four protected boundary beams
- Equivalent sections for beams with openings as illustrated in Figs. 4(a) and (b), ensuring a constant net cross sectional areas with conservative section stiffness
- Effective thickness of 80mm for the concrete slabs ignoring contribution of the ribs within the height of the metal decking
- Pinned connections for all boundary beams
- Full composite action between slabs and beams
- Uniform temperature distribution for all beams
- Steel temperature of unprotected beams equal to the standard fire curve (see Fig. 5)
- Boundary beams protected for R90 with a limiting temperature of 620°C unless otherwise specified (see Fig. 5)
- Bilinear thermal gradient across the effective concrete slabs as shown in Fig. 4(c) – This profile ensures that the temperatures of the reinforcement and top surface of the slabs at 90min are always higher than 400°C and 220°C respectively in accordance with Table 12 of BS5950-8 (see Fig. 5).

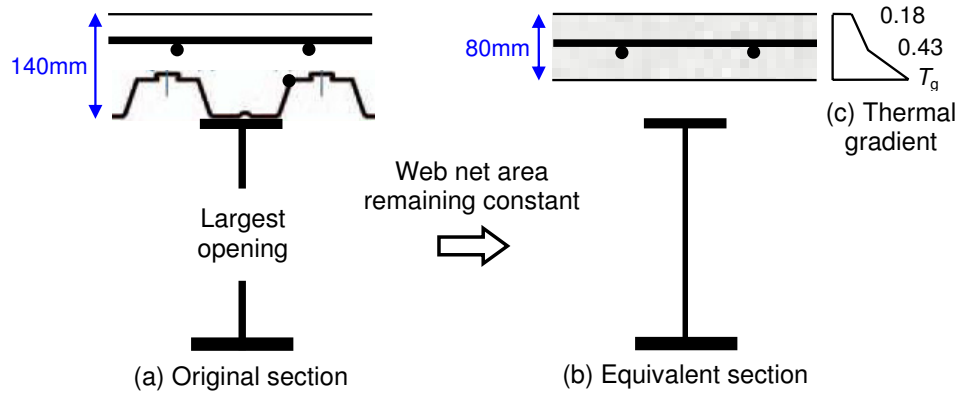

Fig. 4 – Simplification of beam and slab sections.

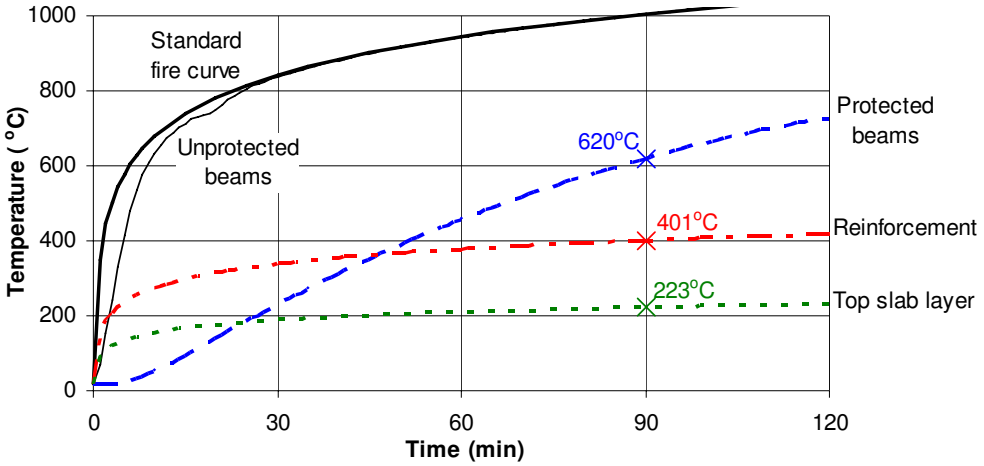

Fig. 5 – Temperature-time relationships adopted in Vulcan.

4.2 BRE-BM Predictions

Table 1 summarises the results of maximum allowable deflection υ, enhancement factor of membrane action e and slab capacity P for the 5 different slab panels by using the BRE-BM. The enhancement factor is governed by the maximum allowable deflection which is proportional to both long and short spans of the slabs but restrained by the deflection limit of $l/30$ (see Eq.(1)). In this study, the limit of $l/30$ is reached when the aspect ratio is equal to or more than 1.87. This explains why Slabs SP2-3 and SP2-5 have the same value of υ.

Generally, the enhancement of membrane action is greater for a slab with smaller aspect ratio. The results proves that the value of e reduces from 3.0 to 1.9 when the aspect ratio of the SP2 slabs increases from 1.33 to 2.67. This is similar in the SP1 slabs.

Fig. 6 shows that the variation of the slab capacities with respect to the aspect ratios of the slabs. It can be seen that only Slabs SP1-1 and SP2-1 have adequate capacity for R90. The capacity of Slab SP2-2 is marginally below the working load at FLS. That means, the BRE-BM only allows for alternative unprotected secondary beams in the middle row of floor plates as shown in Fig. 3. The unprotected slab panels cannot be larger than 2 bays.

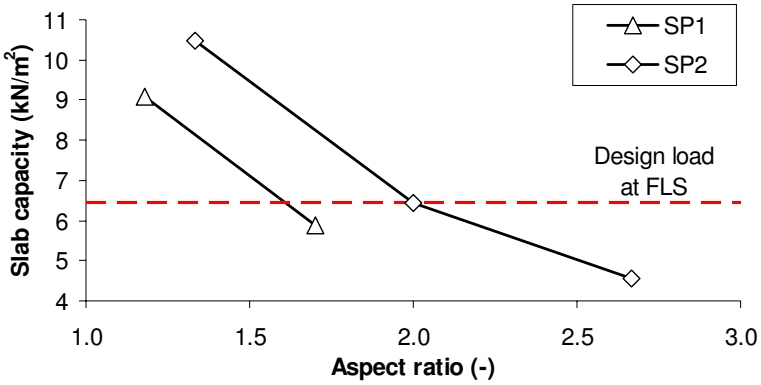

Fig. 6 – Variation of slab capacity with respect to aspect ratio.

4.3 Vulcan Predictions

In contrast to the BRE-BM, the Vulcan analyses proved that all slabs did not fail after 90min of heating although they all experienced large deformation. Figs. 7 and 8 show the deflection-time curves at critical points (denoted by Vc) of the slabs in Series SP1 and SP2 respectively. The deflection curves at the mid-span of the protected boundary beams with the orientation in short span (denoted by PM) clearly indicate that the protected beams had adequate strength and stiffness for providing the vertical support to the highly deformed unprotected slab panels.

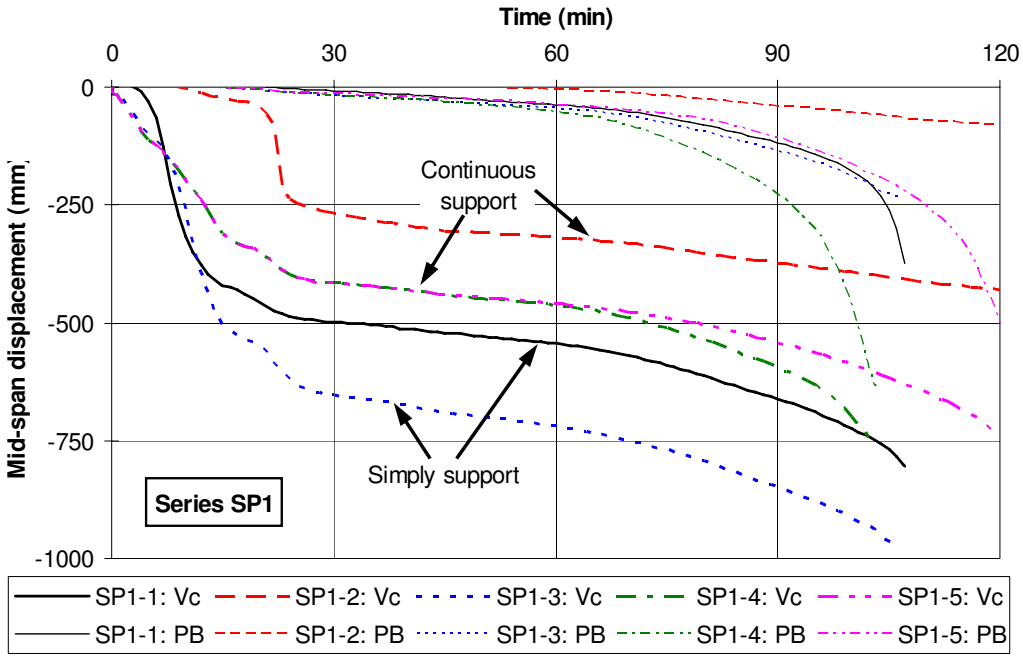

Fig. 7 – Deflection-time curves of slab panels SP1 by Vulcan.

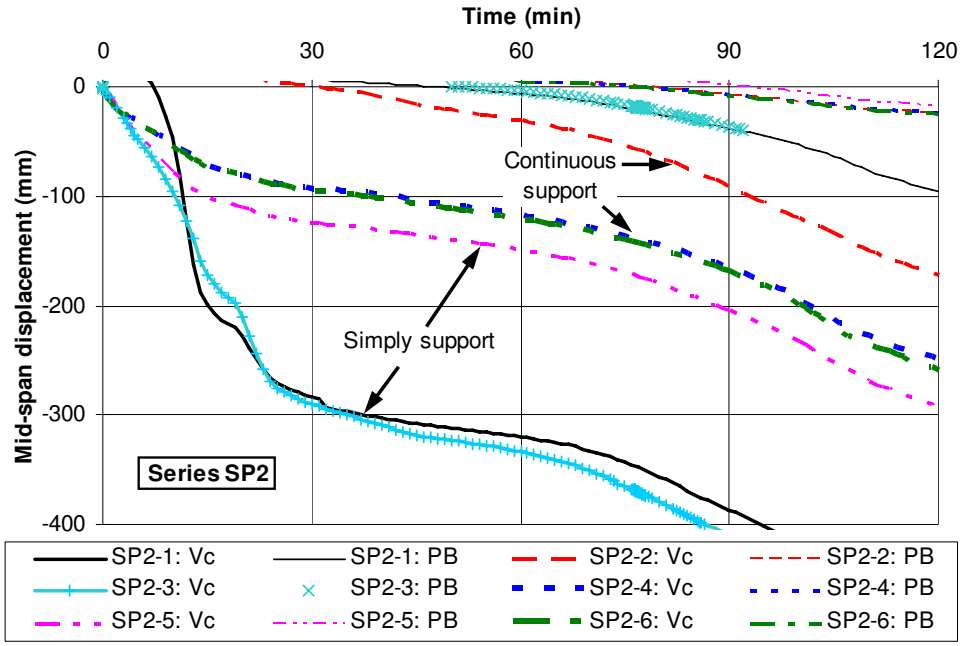

Fig. 8 – Deflection-time curves of slab panels SP2 by Vulcan.

The results show that the slab deflections are very sensitive to the support conditions over the protected beams. By considering the continuity of reinforcement over the protected beams, a significant reduction of the slab deflections can be achieved in fire situations, as shown in SP1-1 vs. SP1-2 and SP1-3 vs. SP1-4. In addition, the slab deflections can also be controlled by increasing fire protection to the supporting beams. By reducing the limiting temperature of the supporting beams in short span from 620 to 550°C, SP1-5 experiences a smaller deflection beyond 60min of heating compared to SP1-4.

In each series of analyses, it is expected that a large panel deflects more than a small panel under same fire and support conditions, with the exception of SP2-5. All slab panels in Series SP2 have the same short span of 4.5m, but with different long spans. With a long span of 6 and 9m respectively, the simply supported SP2-1 and SP2-3 deform similarly at elevated temperatures. However, by increasing the long span to 12m as in SP2-5, Vulcan predicted a much smaller deflection which does not make sense. Further investigation is necessary.

For comparison purposes, the equivalent times of fire resistance T_{eq}, corresponding to the allowable maximum deflections υ in accordance with the BRE-BM, have also been included in Table 1. The results show that all simply supported slabs, except for SP2-5, have T_{eq} much smaller than 90min due to excessive deflections. On the other hand, all continuously supported slabs, except for SP1-3 and SP1-4, have $T_{eq} > 90$min.

It is worth noting that the limits of deflection ($\upsilon = 423$ & 476mm for SP1; $\upsilon = 260$ & 283mm for SP2) correspond to span/13.3 (6350/423) to span/17.3 (4500/260), which are lower than those experienced on the Cardington fire tests in which the maximum slab deflection of one test exceeded span/10 without failure. Table 1 also gives the span/deflection ratios at 90min for all slab panels from the Vulcan analyses, in which only the simply supported SP1-1 and SP1-3 had a span/deflection ratio less than 10.

In summary, continuously supported slabs have a higher fire resistance than the simply supported slabs due to the mobilization of membrane and catenary actions in fire situations. It is believed that, for a very long span slab with an aspect ratio more than 2.50, catenary

action will be greater in proportion to tensile membrane action. Attention should be paid to the prevention of over-stretching of the reinforcement mesh over the protected beams under fire situations.

5 CONCLUSIONS

The case studies on the slab panels with secondary beams orientated in the short span from a real office block development proved that the application of the BRE-BM is generally restricted by the maximum allowable vertical displacement.

On the other hand, Vulcan estimates higher slab capacities compared to the simple methods as the slabs were allowed to deform to a much greater value compared to the limits imposed by the BRE-BM. In addition, it was not required to increase the fire protection and section size of the protected boundary beams because there was no significant load redistribution arising from tensile membrane action.

The boundary conditions of the slab panels have significant influences on the slab capacities. In comparison with the simply supported conditions, if reinforcement is assumed to be continuous over the protected boundary beams, it will enhance the tensile membrane and catenary actions of the slabs in fire situations. The slab deflections can be reduced by more than 40% although the ultimate slab capacities are only slightly enhanced. It would be good practice to prevent over-stretching of reinforcement due to excessive deflection of a slab under fire conditions by imposing a limit on the maximum allowable deflection like the BRE-BM.

REFERENCES

[1] Bailey, C.G., Lennon, T. and Moore, D.B., "The behaviour of full-scale steel framed building subjected to compartment fires", The Structural Engineer, 77(8), pp.15-21, 1999.
[2] O'Conner, M.A., Kirby, B.R. and Martin, D.M., "Behaviour of a multi-storey composite steel framed building in fire", The Structural Engineer, 81(2), pp.27-36, 2003.
[3] Wang, Y.C., "Tensile membrane action in slabs and its application to the Cardington fire tests. Fire, static and dynamic tests of building structures", Proceedings of the Second Cardington Conference, England, 12-14 March, pp.55-67, 1996.
[4] Bailey, C.G. and Moore, D.B., "The structural behaviour of steel frames with composite floor slabs subject to fire: Part 1: Theory", *The Structural Engineer*, 78(11), pp.19-27, 2000.
[5] Bailey, C.G., "Steel Structures Supporting Composite Floor Slabs: Design for Fire", BRE Digest 462, 2001.
[6] Huang, Z., Burgess, I.W. and Plank, R.J., "Modelling of six full-scale fire tests on a composite building", The Structural Engineer, 80(19), pp.30-37, 2002.
[7] Newman, G.M., Robinson, J.T. and Bailey, C.G., "Fire Safe Design: A New Approach to Multi-Storey Steel-Framed Buildings (Second Edition)", SCI Publication P288, Steel Construction Institute, 2006.
[8] Corus Construction & Industrial, "Fire Resistance of Steel-Framed Buildings", SCI Publication P299, Steel Construction Institute, 2006.
[9] University of Manchester, "One Stop Shop Website in Structural Fire Engineering: Case Studies", from http://www.structuralfiresafety.org/, 2007.
[10] Bernabé, N., "Focus: Modern Hazards – Office Hours", Fire Prevention & Fire Engineers Journal, November, pp.27-29, 2006.

[11] Bernabé, N., "Focus on: Fire Engineering – Abbey Mill House, Reading", AJ Specification, 7 April, pp.32-33, 2007.
[12] Toh, W.S. and Bailey, C.G., "Comparison of simple and advanced models for predicting membrane action on long span slab panels in fire", Proceedings of the 11th International Fire Science & Engineering Conference (Interflam 2007), London, pp.791-796, 2007.
[13] Bailey, C.G., "New fire design method for steel frames with composite floor slabs", FBE Report 5, BRE, January, 2003.
[14] Huang, Z., Burgess, I.W. and Plank, R.J., "Three-dimensional analysis of composite steel-framed buildings in fire", Journal of Structural Engineering, ASCE, 126(3), pp.389-397, 2000.
[15] Huang, Z., Burgess, I.W. and Plank, R.J., "Modeling membrane action of concrete slabs in composite buildings in fire. I: Theoretical development", Journal of Structural Engineering, ASCE, 129(8), pp.1093-1102, 2003.
[16] Huang, Z., Burgess, I.W. and Plank, R.J., "Modeling membrane action of concrete slabs in composite buildings in fire. II: Validations", Journal of Structural Engineering, ASCE, 129(8), pp.1103-1112, 2003.
[17] BS5950-8, "Structural Use of Steelwork in Building - Part 8: Code of Practice for Fire Resistant Design", British Standards Institution, 2003.

ULTIMATE BEHAVIOUR OF COMPOSITE FLOOR SLABS AT AMBIENT AND ELEVATED TEMPERATURE

K.A. CASHELL[1], A.Y. ELGHAZOULI[2] and B.A. IZZUDDIN[3]

ABSTRACT

This paper is concerned with the ultimate behaviour of composite floor slabs under extreme loading situations resembling those occurring during severe building fires. The study focuses on the failure state associated with rupture of the reinforcement in idealised slab elements, which become lightly reinforced in a fire situation due to the early loss of the steel deck. The paper summarises recent studies carried out in order to provide a fundamental approach for assessing the failure limit associated with reinforcement fracture in lightly reinforced beams, representing idealised slab strips. In addition, preliminary results from the first phase of ambient tests on isolated strips are outlined and the main conclusions are discussed. Following the completion of subsequent stages of experiments involving full slab members, this work will enable validation of detailed numerical models which will be used for developing simplified design-oriented guidance.

1. INTRODUCTION

The structural fire performance of buildings with composite steel-concrete floors has been the subject of extensive research investigations in recent years, e.g. [1-7]. These studies have identified the crucial role played by the composite floor slab in carrying the gravity loading within the fire compartment after the loss of strength in the supporting secondary steel beams due to elevated temperature. Although the slab exhibits significantly lower bending capacity, the development of tensile membrane action coupled with several sources of over-design leads to considerable fire resistance capabilities. To this end, progress in the development of improved design approaches needs to be based on detailed assessment of the behaviour of floor slabs, using reliable and realistic modelling approaches coupled with the application of appropriate failure criteria.

[1] Dept. of Civil & Environmental Engineering, Imperial College London, e-mail: k.cashell@imperial.ac.uk
[2] Dept. of Civil & Environmental Engineering, Imperial College London, e-mail: a.elghazouli@imperial.ac.uk
[3] Dept. of Civil & Environmental Engineering, Imperial College London, e-mail: b.izzuddin@imperial.ac.uk

One of the most important failure criteria in a composite slab is that related to rupture of the reinforcement. Under fire conditions, the thin steel deck within a composite slab develops high temperature and becomes largely ineffective at an early stage. As a result, the slab behaves primarily as a concrete element with light mesh reinforcement. Prediction of the displacement and load levels corresponding to the fracture of the reinforcement is however a complex issue that necessitates a detailed treatment of the interaction between the concrete material and steel reinforcement, with due account of the appropriate loading and boundary conditions. Due to the uncertainties involved in various important material and response parameters, this problem also requires experimental validation and calibration.

This paper provides an overview of recent studies carried out to examine the performance of floor slabs. Analytical models developed to represent the ultimate behaviour of lightly reinforced beams at ambient and elevated temperature are outlined; these formed the basis of more detailed treatment of full slabs. Selected results from the first set of validation tests, conducted on isolated reinforced concrete beams representing idealised slab strips are presented and preliminary findings are discussed. Further tests on more realistic slab representations are currently underway which, in conjunction with numerical investigations, will be used to carry out design-oriented studies.

2. ANALYTICAL MODELS

2.1 Structural Configuration

A typical composite slab, of the form shown in *Fig. 1*, is normally supported by secondary steel beams acting compositely with the slab through shear connectors. The conventional design procedure is to treat the short direction of the slab as well as the secondary and primary beams as one-dimensional members supporting the load from the floor. The gravity loading considered in an accidental fire situation typically consists of the unfactored dead load and a proportion of the imposed load. Depending on the extent of fire spread within compartments as well as the degree of fire protection, some of the steel beams as well as the thin steel deck develop high temperature and become largely ineffective at an early stage. As a result, the slab behaves primarily as a concrete element with light mesh reinforcement, which is required to span over the ineffective steel beams and hence sustain the gravity load from a larger floor area than that intended by design.

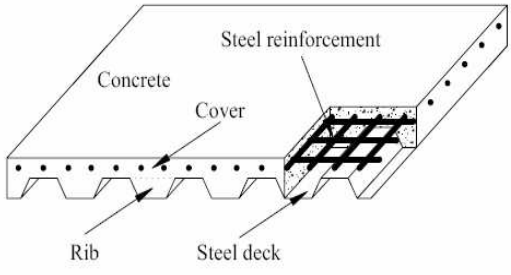

Fig. 1 – Typical configuration of composite profiled slabs

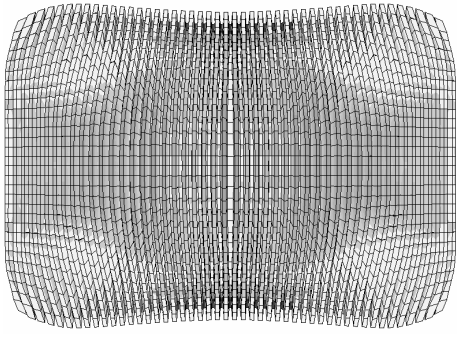

Fig. 2 – Numerical simulation of full-depth crack (magnified deformation) [9]

Although the flexural capacity of the slab is significantly reduced due to the loss of the steel deck, it is still able to provide considerable fire resistance. This is contributed to by several aspects of floor over-design caused by the idealisation of the member behaviour and support conditions. Most importantly, the slab is usually able to develop tensile membrane action, which significantly increases the load-carrying capacity. The existence of considerable planar restraint in most situations has been demonstrated in earlier studies, e.g. [6]. In an internal compartment, this is effectively provided by the surrounding cooler structure. On the other hand, in edge compartments, the perimeter beams retain significant stiffness due to their relatively lower temperatures. Besides, the development of a compressive ring in the slab with the presence of adequate reinforcement anchorage contributes to the provision of a degree of planar restraint.

2.2 Failure Conditions

In the absence of the steel deck, simulating deck integration at elevated temperature, failure occurs by fracture of the reinforcement across a localised through-depth crack. This is illustrated in Fig.2 based on analysis carried out adopting a recently-developed numerical model [8,9] for simulating the response of orthotropic slabs, using computationally efficient shell elements that retain the accuracy of solid representations. This localisation is primarily due to the fact that the only available reinforcement is a nominal steel mesh, which is rather light and hence unable to generate further significant cracks within the concrete, thus leading to high strain concentrations within the steel. In order to take this failure criterion into consideration, it is important to determine the levels of deformation that may safely be sustained by the lightly reinforced floor slab. A conventional smeared crack approach provides good predictions of the load-deflection response of lightly reinforced structures, but cannot assess reliably the strain concentrations across cracks, since such concentrations would be unrealistically dependent on the element size instead of the geometric and material characteristics of the structure.

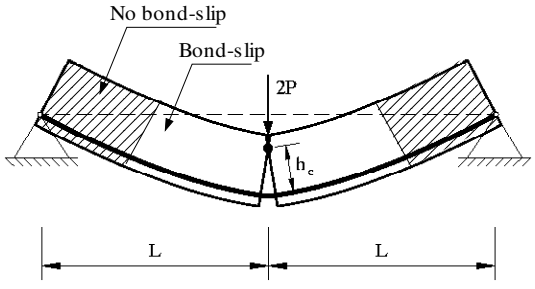

Fig. 3 – Layout of lightly reinforced member indicating bond-slip regions [10]

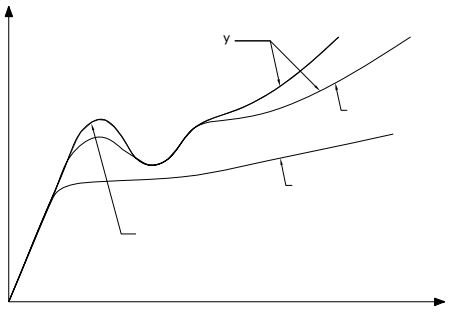

Fig. 4 – Behaviour of reinforced concrete members under various restraint conditions

A fundamental step towards quantifying the failure of lightly reinforced members under ambient and fire conditions has been recently proposed [10] through a simplified model of restrained lightly reinforced concrete members, simulating composite slab strips. The model represents the post-cracking behaviour of an axially restrained member subject to mid-span loading, as shown in Fig. 3. A single layer of reinforcement is located at a prescribed depth, and the centre of rotation is user-defined but typically assumed to be at the top concrete

fibre. Under fire conditions, the temperature distribution over the cross-section is assumed to be linear, but no variation over the length is considered. Depending on the combination of loading, geometry and material properties, the length L consists of two regions, namely the 'bond-slip' and the 'no bond-slip' region', as indicated in Fig. 3. By incorporating the full stress-strain relationship for the steel reinforcement and appropriate properties for concrete, as well as bond strength between the steel and concrete, the load-displacement response of the member can be determined for a given temperature distribution. Most importantly, the deformation and load levels corresponding to the attainment of an ultimate strain limit in the steel can be obtained, hence providing a prediction of the failure limit associated with reinforcement fracture.

Although the model focuses on the tensile membrane behaviour in axially-restrained members as illustrated in Fig. 4, through minor modifications it can also predict the failure displacement and corresponding capacity for other loading, boundary and response conditions. The model has been used to investigate the factors influencing fracture of light reinforcement [11]. For example, Figs. 5 and 6 show representative behaviour of the response at ambient and elevated temperature. The member in this case has a span of 3 m (i.e. L=1.5 m according to Fig 3), depth of 60 mm and width of 200 mm. The reinforcement ratio is assumed as 0.25% and located at mid-depth. The ultimate strength of the reinforcement is 600 N/mm^2 and the concrete strength is 40 N/mm^2. In Fig. 6, the temperatures are varied at the bottom of the member, whilst the top remains at ambient.

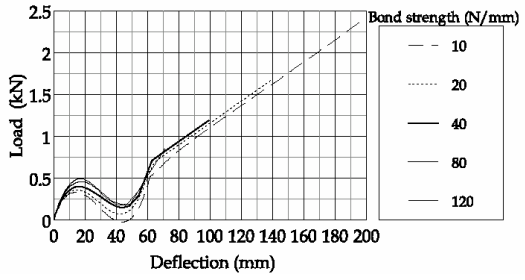

Fig. 5 – Effect of bond strength on response and failure limit at ambient temperature [11]

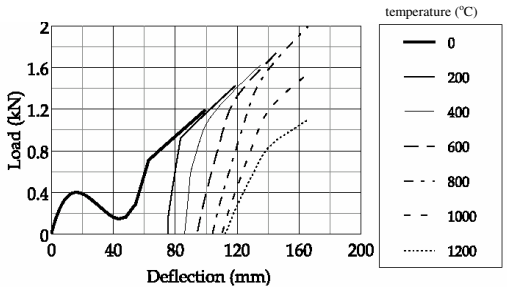

Fig. 6 – Influence of temperature on response of lightly reinforced member [11]

As expected, in addition to a number of important geometric and material characteristics, the bond strength between the steel reinforcement and concrete plays a major role in determining the failure displacement. Furthermore, it has been shown that elevated temperature increases the failure deflection, which is attributed mainly to thermal expansion effects. However, elevated temperature can also have a negative influence on the failure deflection when it leads to a significant thermal gradient over the depth of the member [10,11].

The models for isolated reinforced concrete strips were more recently extended [12,13] to represent slabs of various levels of reinforcement and restraint under ambient and elevated temperature conditions. The approach used for the slab models at elevated temperature differs from that in the beam models in that the underlying shape of the various slab parts is described in three dimensions. The procedure utilises an assumed thermal strain field which captures reasonably well the influence of thermal curvature. Importantly, individual strips within a slab represent fundamental components within the full slab models. Consequently, understanding and validating the behaviour of isolated strips represents a necessary step which would be followed by experimental examination of full slab components.

3. EXPERIMENTAL RESPONSE

The primary objective of the laboratory experiments is to gain a greater understanding of the ultimate behaviour of composite slabs and to provide the necessary information to validate appropriate failure criteria. As noted before, a number of material properties, including the bond-slip characteristics, have a direct influence on the ultimate performance. In order to provide validation for detailed numerical models and simplified analytical approaches, the experimental investigation are planned in stages, starting from material tests, followed by isolated strip tests, and will subsequently be complemented by full slab tests. The tests are carried out at ambient temperature, but simulating one aspect of elevated temperature conditions through the absence of the steel deck. Hereafter, a brief description of selected material and strip tests is presented, and important observations are highlighted.

3.1 Material Characteristics

Several types of reinforcement bars with different properties were considered in the experimental investigation in order to ascertain the behaviour under various conditions. Plain, ribbed and mesh reinforcement were examined in order to provide a range of characteristics and assess their influence on the member response. The yield, or proof, strength of the reinforcement bars varied between under 250 N/mm^2 to over 550 N/mm^2, with a corresponding ultimate strength between 300 N/mm^2 and over 600 N/mm^2. On the other hand, the ultimate strain exhibited by the reinforcement at fracture varied between low values of about 4% to as high as 20% in some bars. Careful attention was given to using equipment that can provide the full stress-strain relationship of the reinforcement bars up to fracture, as the actual shape of the curve can have a significant influence on the behaviour. On the other hand, an average compressive concrete strength of about 40 N/mm^2 was considered in most of the tests.

As noted before, in addition to other material properties, the bond between the reinforcement bars and concrete plays a key role in determining the failure limit of the members. Accordingly, it is important to assess the bond characteristics for the reinforcement used in the tests. There are several possible techniques for bond tests, with the most common being pull-out testing and beam approaches. In selecting the most appropriate test method, consideration should be given to the actual conditions prevailing in the member. However, replicating the exact bond conditions present in a member within a simple testing technique may not be possible. Consequently, to enable a large number of material tests to be conducted, conventional pull-out bond tests were initially adopted to provide the same basis for comparing the relative bond characteristics of various reinforcement bars. Several modifications were made to the typical pull-out test set-up in order to improve the representation of the realistic loading and confinement conditions in a member. Nevertheless, whilst the pull-out tests provide useful information as a comparative measure of bond characteristics, the actual bond characteristics can be more directly obtained from large-scale beam tests, which for comparison were also carried out as part of this investigation for selected cases.

The influence of a number of parameters was examined within the study of bond-slip behaviour. These included the type and diameter of reinforcement, concrete mix, bond length, concrete cover, amongst other properties. As expected, the type of reinforcement had a direct influence on the bond strength. This is illustrated in the example of bond-slip response shown in Fig. 7 for deformed (B1) and plain (B2) bars of the same diameter.

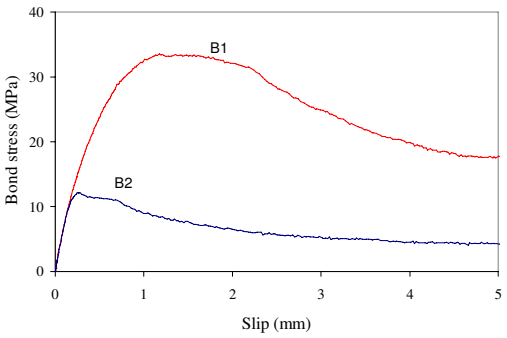

Fig. 7 – Influence of bar type on bond-slip

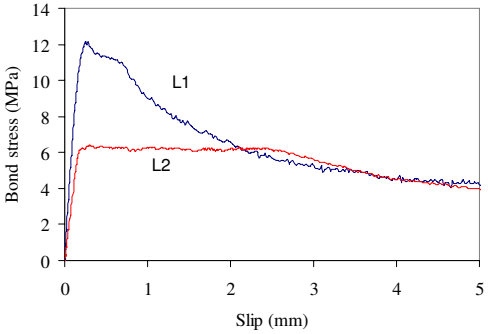

Fig. 8 – Influence of length on bond-slip

The bond embedment length and concrete cover to the reinforcement also had a significant effect on the bond-slip characteristics. For example, Fig. 8 shows the response obtained from two pull-out tests with different embedment lengths L1 and L2 corresponding to 5 and 10 multiples of the bar diameter, respectively. On the other hand, Fig. 9 illustrates the behaviour for specimens with different concrete covers C1 and C2, corresponding in this case to about 75 and 20 mm, respectively. The type of bond failure can also vary between pull-out and splitting behaviour, depending on both the type of reinforcement and the concrete cover. Whilst in pull-out behaviour, some residual bond strength is normally present, in the case of splitting failure the residual bond diminishes with increasing values of slip.

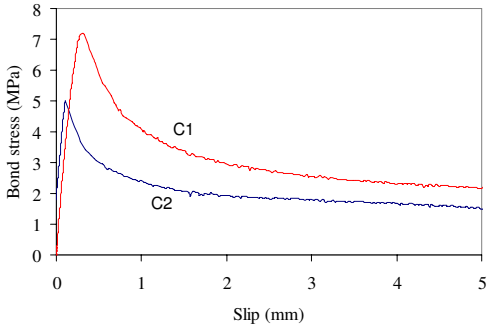

Fig. 9 – Effect of concrete cover

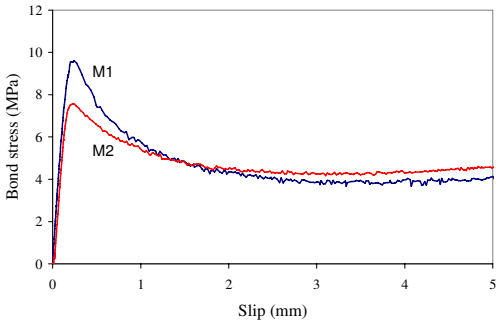

Fig. 10 – Effect of different concrete mixes

Fig. 10 highlights the effect of concrete type on the behaviour, where M1 and M2 represent normal-weight and light-weight concrete respectively. The type of aggregate used in the concrete appeared to have a minor influence on the bond behaviour and mechanisms, in comparison with other parameters, although the peak bond stress was marginally higher for normal-weight concrete.

3.2 Idealised Member Tests

In order to examine the ultimate behaviour of members representing isolated strips of slabs, an experimental arrangement which enables testing of axially restrained specimens was constructed. The arrangement used for the test rig is shown in Fig. 11 and a view of the test set up is shown in Fig. 12. The specimens were rotationally unrestrained, but the axial restraint was varied between conditions related to restraint from pull-in only, axial expansion, or both. Conditions related to full axial restraint was simulated by clamping the ends of the

specimen within stiff plates which were then connected to an arrangement of bearings. Loading was applied at the middle of the specimen through closely spaced points to simulate concentrated mid-span loading. A hydraulic actuator, operating in displacement-control, was used for applying the loading. In each test, the displacement was increased gradually until failure was reached by fracture of the reinforcement, which was typically accompanied by a significant reduction in the load carrying capacity.

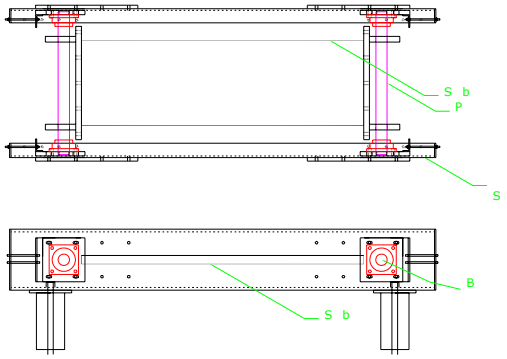

Fig. 11 – General arrangement of test rig

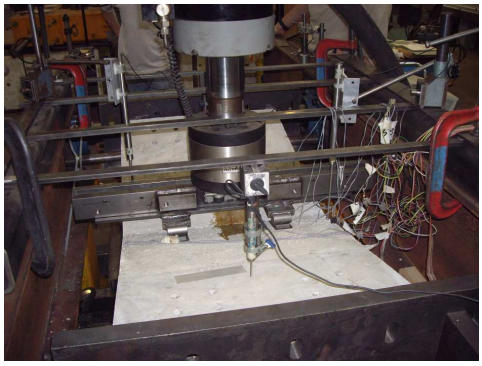

Fig. 12 – View of test set up

The first phase of experiments included tests on specimens with various reinforcement configurations, as discussed before, and employing a number of variations in the loading and boundary conditions. Tests were carried out on members with both flat and ribbed profiles simulating composite slab configurations. The reinforcement ratio was varied between around 0.2% to 1.2%., and the range of material properties for the reinforcement bars was as described in the previous section.

A large amount of data was obtained through the measurements of displacements, loads and strains in the tests. However, emphasis is placed herein on the deformation at failure of the specimen which corresponds to fracture of the reinforcing bars. Typical examples of the overall load-displacement response obtained are given in Figs 13 to 16 below.

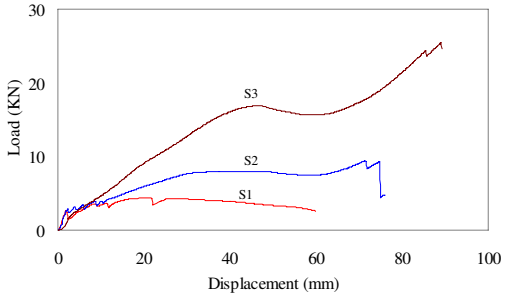

Fig. 13 – Members with deformed bars

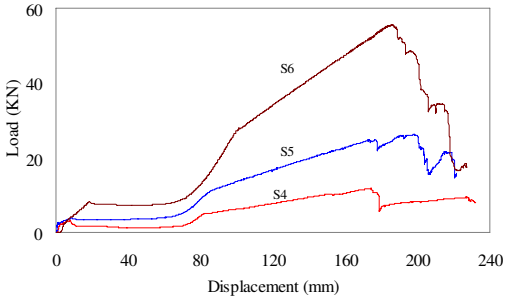

Fig. 14 – Specimens with plain bars

Fig. 13 illustrates the response of three members utilising identical deformed bars but with varying reinforcement ratios of 0.24%, 0.52% and 1.2% for strips S1, S2 and S3, respectively. The specimens had an overall span of 1.5 m; they were rotationally unrestrained but restrained from pull-in deformations, hence able to develop tensile membrane action. In

this case, the specimens with higher reinforcement ratios developed multiple cracks which resulted in an increase in the deformation corresponding to failure.

The overall response from corresponding tests with specimens utilising plain reinforcing bars is demonstrated in Fig. 14. Again, the three specimens S4, S5 and S6 have reinforcement ratios of 0.24%, 0.52% and 1.2%. In this case, significantly more ductile behaviour was obtained, as expected. Moreover, due to the relatively low bond, multiple cracking did not occur, resulting in broadly the same failure displacement in all three specimens. Despite the lower yield capacity of these three specimens, the ability to develop considerable membrane action resulted in higher overall load-carrying capacity compared to the specimens with the deformed bars.

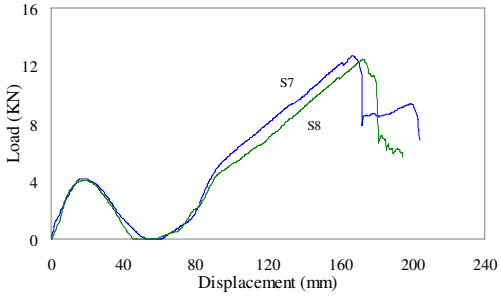

Fig. 15 – Compressive membrane action

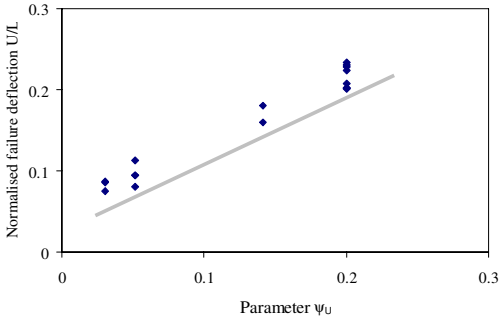

Fig. 16 – Vertical deflection at failure

Fig. 15 on the other hand illustrates the response when an effective restraint enabling compressive membrane action to occur is provided. In this case, the response is shown for two specimens, S7 and S8 with plain bars and a reinforcement ratio of 0.23% but with different cross-section dimensions. In comparison with the plots in Fig. 14, whilst the initial response is markedly different, it subsequently behaves in the same manner within the tensile membrane range, attaining a similar failure deformation level.

In general, whilst the load-deflection response can be predicted through numerical and analytical models adopting smeared cracking approaches, the displacement at failure is more difficult to assess due to its dependence on a number of inter-related parameters.

As expected, the failure deflection was closely related to a number of important parameters, including: the ultimate strain of the reinforcement (ε_{um}); the bond strength per unit length (σ_b) between steel and concrete, the strain hardening properties of the reinforcement, which can be represented through the difference between the ultimate strength (σ_u) and proof ($\sigma_{0.2}$) or yield stress of steel, the reinforcement cross-sectional area (A_s); and the length (L). Both the results of the analytical assessments [10,11] and the findings from the experimental observations, point towards a direct relationship between the failure deflection (U), normalised by the length L, and a parameter ψ_U, which captures the combined influence of the above-noted parameters, such that:

$$\psi_U = \sqrt{\frac{A_s\left(\sigma_u - \sigma_{0.2}\right)}{\sigma_b L}\varepsilon_{um}} \qquad (1)$$

The above parameter is based on the assumption that a single crack would occur at mid-span of the member, which is characteristic of members with relatively light reinforcement. Accordingly, the accuracy of this expression depends on the reinforcement ratio within the member, as it would tend to underestimate the failure deflection if multiple

cracking occurs with increasing steel ratios. This aspect of behaviour was also observed in the experimental investigation where, depending on the type of bars used, several members with reinforcement ratios exceeding 0.5% exhibited multiple cracking which had a direct influence on enhancing the failure deflection. Fig. 16 depicts the normalised failure deflection (U/L) obtained from the tests as a function of the parameter ψ_U. Equation (1) above provides a lower bound prediction of the failure displacement, hence representing a reasonable failure criterion for this type of member.

The above treatment has been extended to the response under elevated temperature [10,11]. It can be shown that the parameters given in Equation (1) above can also be used to predict the failure displacement through the following relationship:

$$U = \sqrt{2L\left(\frac{A_s(\sigma_u - \sigma_{0.2})}{3\sigma_b}\varepsilon_{um} + \alpha t_s L - \frac{(\alpha\nabla t)^2 L^3}{24}\right)} \tag{2}$$

in which t_s is the temperature at the steel reinforcement and ∇t is temperature gradient in the cross-section; σ_b, σ_u, $\sigma_{0.2}$ and ε_{um} are the temperature-dependent material properties, and the coefficient of thermal expansion α can be conservatively considered as the lower of α_c and α_s of the concrete and steel, respectively, if they differ within normal ranges.

Equation (2) above illustrates that, in addition to the temperature related material properties, the thermal expansion and gradient have an influence on the failure displacement. Subject to further experimental validation under elevated temperature conditions, relationships of this form can be used as a basis for implementing appropriate failure criteria in design procedures.

4. CONCLUDING REMARKS

A brief description of recent studies into the ultimate behaviour of composite slabs under idealised fire conditions has been presented in this paper. The slabs are lightly reinforced following the loss of the steel deck; therefore particular attention is given to failure by fracture of the reinforcement. Emphasis is given to lightly reinforced beams, representing isolated slab strips. Based on analytical and experimental investigations, the influential parameters are described and a direct relationship is established between the failure displacement and a number of these parameters. Of particular importance are the steel stress-strain curve and the bond stress-slip characteristics. Examination of these relationships enables a realistic assessment of the ultimate behaviour.

The experimental program associated with this research is continuing presently with the testing of further slab strips and also full two-way reinforced slabs. Similarly to the previous phases, several parameters will be varied in these experiments such as the boundary conditions, specimen geometry and material properties.

5. ACKNOWLEDGEMENTS

The support provided by the Engineering and Physical Sciences Research Council (EPSRC) in the UK for the work described in this paper is gratefully acknowledged. The authors would also like to thank the technical staff of the structures laboratories at Imperial College London for their assistance with the experimental work.

REFERENCES

[1] Wang, Y.C., Lennon, T., and Moore, D.B. "The behaviour of steel frames subject to fire", Journal of Constructional Steel Research, 35, pp. 291–322, 1995.
[2] Huang, Z., Burgess, I. W. and Plank, R. J. "Nonlinear analysis of reinforced concrete slabs subjected to fire", American Concrete Institute Structural Journal 96(1), pp. 127–135, 1999.
[3] Bailey, C.G. and Moore, D.B., "The structural behaviour of steel frames with composite floor slabs subject to fire. Part 1: Theory", The Structural Engineer, 78(11), pp. 19–27, 2000.
[4] Bailey, C.G. and Moore, D.B., "The structural behaviour of steel frames with composite floor slabs subject to fire. Part 2: Design", The Structural Engineer, 78(11), pp. 28-33, 2000.
[5] Gillie, M., Usmani, A.S., and Rotter, J.M. "A structural analysis of the first Cardington test", Journal of Constructional Steel Research, 57, pp. 581-601, 2001.
[6] Elghazouli, A. Y. and Izzuddin, B. A., "Analytical assessment of the structural performance of composite floors subject to compartment fires", Fire Safety Journal, 36, pp. 769–793, 2001.
[7] Lim, L., Buchanan, A. and Moss, P. "Experimental testing and numerical modelling of two-way concrete slabs under fire conditions", Journal of the Structural Engineering Society New Zealand, SESOC, 12-26, 2003.
[8] Izzuddin, B. A., Tao, X. Y. and Elghazouli, A. Y. Realistic modelling of composite and RC floors slabs under extreme loading – Part I: Analytical method", Journal of Structural Engineering, ASCE, 130(12): 1972-1984, 2004.
[9] Elghazouli, A. Y. and Izzuddin, B. A. "Realistic modelling of composite and RC floors slabs under extreme loading – Part II: Verification and Application", Journal of Structural Engineering, ASCE, 130(12): 1985-1996, 2004.
[10] Izzuddin, B. A. and Elghazouli, A. Y., "Failure of lightly reinforced concrete members under fire. I: Analytical modelling", Journal of Structural Engineering, 130(1), pp. 3–17, 2004.
[11] Elghazouli, A. Y. and Izzuddin, B. A., "Failure of lightly reinforced concrete members under fire. II: Parametric studies and design considerations", Journal of Structural Engineering, 130(1), pp. 18–31, 2004.
[12] Omer E., Failure of composite steel-concrete slabs under elevated temperatures, PhD Thesis, Imperial College London, 2006.
[13] Omer E., Izzuddin B. A. and Elghazouli A. Y., "Failure assessment of simply supported floor Slabs under elevated temperature", Structural Engineering International, 16(2), pp. 148-155, 2006.

THERMAL AND STRUCTURAL RESPONSE OF A TWO-STORY, TWO-BAY COMPOSITE STEEL FRAME UNDER FIRE LOADING.

YULI DONG[1] and KULDEEP PRASAD[2]

ABSTRACT

The collapse of the World Trade Center Towers and other recent fires in tall buildings has motivated a study to understand the performance of structural frames under fire loading. A two-story, two-bay composite steel frame was constructed and was subjected to dead loads using load blocks, and to thermal load by placing the frame in a furnace. The furnace was specially designed to allow for controlled heating of the structural elements that form the various compartments of the test frame. This paper describes the experimental results of a furnace test conducted on three full-scale composite frames. The three tests differed from each other in the number of compartments that were heated by the furnace and in the relative location of the heated compartments. For each test, the structural elements were subjected to a heat up phase followed by a cool down phase. The furnace temperatures as well as the steel and the concrete temperatures recorded during the test are discussed. The thermally induced horizontal displacements and vertical deflections of the various structural elements are presented. Observations on local buckling of the steel beam, cracking of the concrete slab and failure of the beam-to-column connection are tabulated. Experimental results of the three tests are compared and contrasted by studying the complete deformation process of the test frames over time. Results indicate that the deformation process and time to failure of a structure is highly dependent on the number of compartments that are heated and the location of the compartments that are subjected to fire loading.

[1] Professor, Harbin Institute of Technology, CHINA
[2] Corresponding Author : Research Engineer, National Institute of Standards and Technology, Gaithersburg, MD 20899, USA.
Email : kprasad@nist.gov

1. INTRODUCTION

Recent large fires in tall buildings, such as One Meridian Square, the World Trade Center Towers and Windsor Tower have renewed interest in studying the response of tall buildings under fire loading. In order to analyze and understand such events, researchers have focused on the development of numerical models to analyze the behavior of isolated steel members [1-4] and to a lesser extent, full scale steel structures under fire loading [3]. Lack of validation of the numerical models with full scale experimental data has limited the use of the numerical models in fire safety design of steel structures [1-4]. Full scale experiments on structures subjected to fire loading are critically important in developing new understanding as well as to serve as a database for validation of numerical models.

Traditionally, the fire resistance of constructional steelwork has been investigated by conducting standard fire tests on single isolated structural members (i.e. steel beams, composite beams, concrete floor slabs) [5-8]. The British Standard Institution [5] compiled a large number of the UK's standard fire resistance test results on steel structures. Franssen et al. [6] have reported a database containing many column fire tests. In such tests involving single isolated elements, aspects of structural behavior that occur due to the interaction between adjacent members cannot be studied. Performance of real structures subject to fires can sometimes be much better than that predicted from standard tests, due to structural continuity and the interaction between members [9-11].

This paper describes experimental results of furnace tests on full-scale two-story, two bay, composite steel frames to evaluate and analyze their structural performance under fire loading. We outline the construction of the test assembly and the furnace, provide specifications and dimensions of the composite steel frame, and include a description of three furnace tests (conducted with different heating conditions). The major experimental results, including temperature measurements as well as displacement data for columns and composite beams have been provided, to serve as a database with which to check and validate the numerical models. Evidence of the failure modes observed in the tests are tabulated and analysed. The results of this study are compared and contrasted with an earlier study on a single compartment, single story frame [12], to understand the differences in the observed structural response.

2. FRAME DESIGN, FURNACE CONSTRUCTION AND INSTRUMENTATION

A two-story, two-bay sway portal frame with fixed bases was constructed to study the response of full-scale composite steel frames under furnace loading. The frame design and the overall frame dimensions are shown in Figure 1. The frame had two-bays, the center-to-center span width of each bay was 3.6 m, and the overall width of the frame was 7.2 m. The test frame was two-stories high, each floor was 2.8 m tall and the overall frame height was 6.0 m. The major structural elements of the test frame consisted of three steel columns and four composite beams. Each column had an H section (H200x200x8x12) and was constructed from Q235 steel (Yield Strength 235 MPa). Each composite beam consists of a re-inforced concrete slab with a single floor steel beam. Composite floor behavior was obtained by using shear studs to connect the floor beam with the concrete slab. The concrete floor slab on each floor was 100 mm deep and 1000 mm wide, and was made of normal weight concrete (NWC 30-40 MPa). The steel beam on each floor (H250x125x6x9) was also made of Q235 steel. The floor slab was re-inforced with anti-crack rebars with a spacing of 150 mm and a bar diameter of 10 mm. The beam-to-column connections in the test frame were designed to transfer both moment and shear forces and were constructed with a 12 mm thick extended-end plate, bolted

with eight, M22 Grade, 10.9 mm diameter bolts [12]. Column bases were welded to a 16 mm thick steel plate, which was fixed to the test bed by four, M22 bolts. The frame was supported in the out of plane direction by three hollow steel pipes (extremely weak) which were not expected to provide any restraint to the frame.

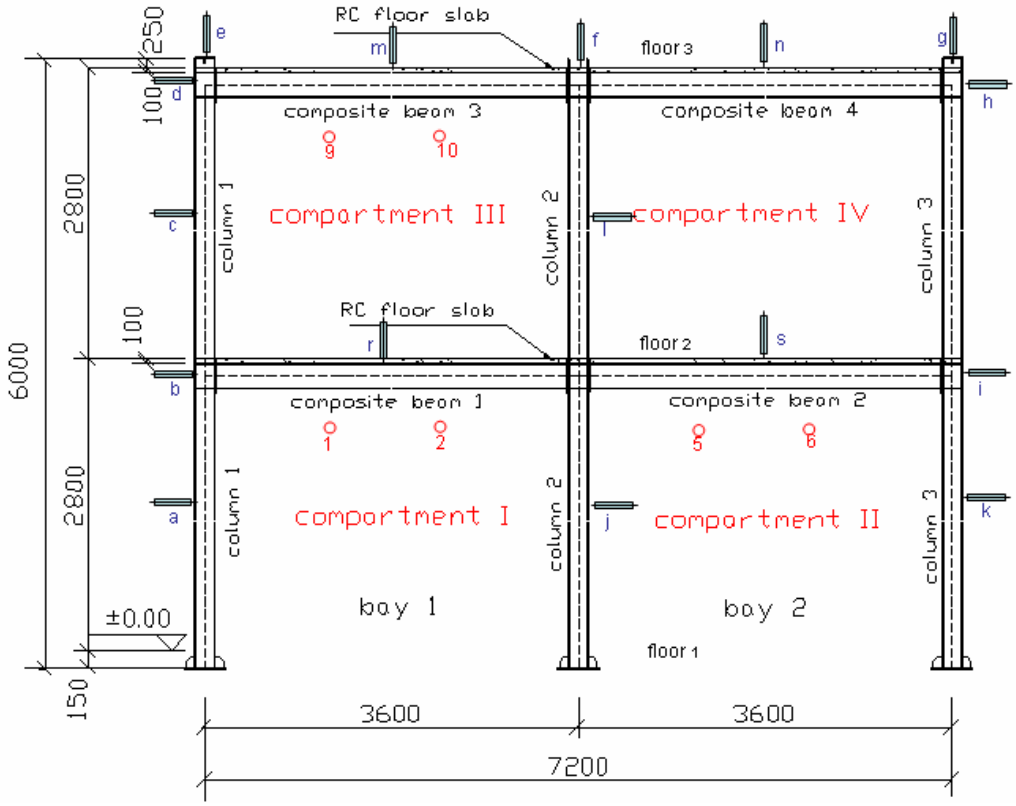

Figure 1. Construction of a two-story, two bay sway portal frame with fixed bases, designed for conducting tests under furnace loading. Location of the thermocouples and the displacement transducers used to measure the temperature of the furnace and the displacement of the frame, respectively are also indicated. All dimensions are in mm.

A furnace was specially designed and constructed to conduct experiments on full-scale structural frames under load. An elevation view of the furnace test setup along with a section side view is shown in Figure 2. The furnace was designed to accommodate the two-story, two bay structural frame, and at the same time allowed for the thermal expansion and large displacement associated with high temperature testing. The outer furnace walls (outside furnace walls) were located in between the reaction frame and the test frame. Inner furnace walls were constructed in each compartment as marked in Figure 2. Both the outside furnace walls and the inner furnace walls were constructed of firebrick. For Compartment I and II, the inner furnace walls were supported on Floor 1. For Compartment III and IV, the inner furnace walls were supported on a cantilever RC beam. A small RC slab was supported on the inside furnace walls of each compartment. The back wall of the furnace (marked in the side elevation view of the furnace) was constructed of firebrick. The concrete slab of the test frame on Floor 3 served as the upper cover of the furnace.

Once the test frame was constructed and placed in-side the furnace, an RC slab was moved in position to cover the front of the furnace. The RC slab, which forms the front cover of the furnace, was specially designed to have four large rectangular holes. The size of each hole was such that it matched the inner furnace walls on two sides, and the RC slab that is supported by the two side walls, on the top. The large holes in the RC slab (front removable RC furnace wall) allows for easy access to a portion of each compartment. This portion of each compartment was protected from furnace heating by the inside furnace wall on the side and the RC slab on the top. This protected area allowed one to observe the test frame during the furnace test through various observation windows located in the inside furnace walls. The protected area of each compartment also helped in instrumentation of the test frame for measuring temperatures and displacements during each test.

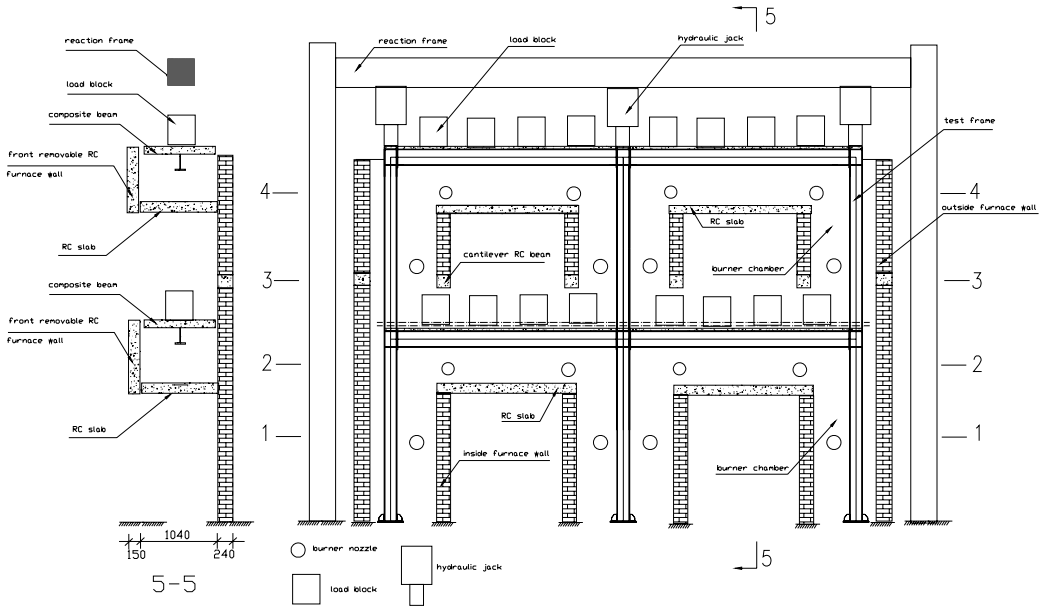

Figure 2. Elevation of the furnace test setup indicating the inner and outer furnace walls, reaction frame, load blocks and burners. A sectional side view at section 5-5 has also been shown (left sub-figure).

Vertical loads were applied at the top of each column by hydraulic jacks mounted on the reaction frame, and were maintained at a constant value of 100 kN. This load was continuously monitored to ensure that it did not change during the course of the test because of thermal expansion. Four load blocks were placed at equi-distant locations on each composite beam as shown in Figure 2. Each load block maintained a constant value of 4.5 kN. The applied loads were allowed to reach the constant pre-determined value before subjecting the test frame to furnace heating. Each compartment was heated by four oil-fired burner nozzles. The nozzles were located in the back wall of the furnace and their locations have been indicated by circles in Figure 2. The operation of each nozzle could be controlled independently from each other and from those in the other compartments.

The furnace and the test frame were heavily instrumented to measure the temperatures as well as the displacement of the frame during the course of a test. Figure 1 shows the instrumentation of the test assembly indicating the location of the thermocouples and the linear variable differential transducers (LVDT), used for measuring the temperatures and the deflections of the structural components. Twelve N type thermocouples were installed (four

each, in compartment I through III), at the locations shown in Figure 1 to measure the temperature of the gas inside the furnace. Four K type thermocouples were installed around each steel column profile at section 1-1 through section 5-5, and eleven K type thermocouples were installed around the steel beam profile or embedded in the reinforced concrete slab, to measure the temperature distribution. Four LVDTs (a, b, c and d) were placed at various heights along the length of column 1 to measure its horizontal displacement during the course of the test. Similarly, three LVDTs (k, i and h) were used to measure horizontal displacement of column 3, while only two LDVT's (j and l) were used for column 2. Vertical displacements at the mid-span of composite beams 1 and 2 were measured by displacement transducers r and s, respectively, while the vertical displacement of floor 3 was monitored by transducers e, m, f, n and g. The LVDTs were protected from the furnace by ceramic rods inserted through the fiber lining of the furnace. The transducer data was calibrated at high temperature to compensate for the effect of thermal expansion and collected through a computerized data recording system. An expanded relative uncertainty value of 5% for the thermocouple temperature measurements and 3% for the displacement data was reported in [12].

3. TEST CONDITIONS, RESULTS AND ANALYSIS

The two-story, two-bay, test frame described in the previous section was tested to understand its response under fire loading. Three tests (referred to as Test 1, Test 2 and Test 3) conducted on identical test frames with different heating conditions are discussed and analyzed. In all three tests, the beam-to-column connections, as well as the columns, were wrapped in an alumino-silicate refractory fiber blanket, and were not expected to heat-up significantly. The composite beam was not protected from furnace heating in any of the three tests. The three tests differed from each other in the manner in which different compartments of the test frame were subjected to furnace loading. In Test 1, the burners in Compartment I were in operation, while in Test 2, the burners in compartment I and II were in operation. In Test 3, the burners in compartment I and III were in operation.

3.1 Thermal Response of the Frame

The test frame was placed in the furnace and load blocks were placed on the various floors. Vertical loads were applied at the top of each column through hydraulic jacks mounted on a reaction frame. Once the loads reached their constant pre-determined value, the front cover plate of the furnace was closed. The furnace was subsequently heated by various oil fired gas burners that were located in each compartment. For each test, the burners in the various compartments were operated so as to replicate the temperature prescribed by the ISO 834 standard. Figure 3 shows the furnace gas phase temperatures plotted as a function of time for Test 1. For Test 1, compartment I was heated, and the temperature measured by thermocouples 1 and 2 are shown. Similarly for Test 2, temperature measurements from thermocouples 1, 2, 5 and 6 are shown, while for Test 3, temperature measurements from thermocouples 1, 2, 9 and 10 are shown. Each sub-figure also shows the average gas phase temperature indicated by a solid line.

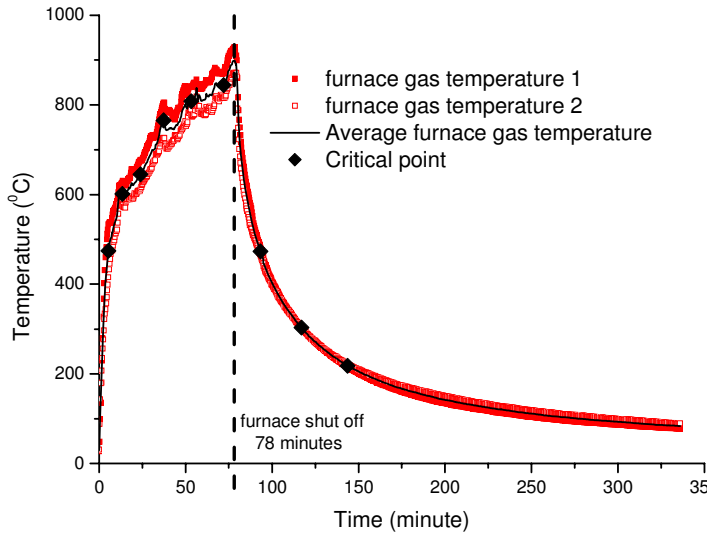

Figure 3. Furnace temperature plotted versus time for Test 1 as measured by the thermocouples in the heated compartment. Average furnace temperature (solid line) is also plotted as a function of time.

As the structural frame is heated, restrained thermal expansion result in thermally induced stresses. Heating of the structural frame also results in weakening of the structure due to material property degradation at high temperature. At some point during the heating phase, the hydraulic jacks mounted on the reaction frame were unable to maintain a constant load value on the columns. For each test, the furnace was shut-off at this point. The furnace shut-off time for Tests 1-3 occurred at 78 min, 112 min and 60 min after ignition, respectively. The maximum temperatures recorded at the shut-off time for Test 1 were 929 ^{0}C and 868 ^{0}C, with an average value of 899 ^{0}C. Similarly, the maximum temperature values recorded in Test 2 were 900 ^{0}C, 816 ^{0}C, 752 ^{0}C and 871 ^{0}C, with an average value of 835 ^{0}C, while in Test 3, the maximum values were 924 ^{0}C, 868 ^{0}C, 864 ^{0}C and 924 ^{0}C, with an average temperature value of 895 ^{0}C. After furnace shut-off, the furnace temperature rapidly reduced and stabilized at the ambient temperature value. All three tests concluded at 350 minutes after furnace ignition.

As the various structural elements are subjected to radiative and convective fluxes from the furnace gases, the temperature of the structural element also changed. The level of structural heating depended on fireproofing status, fire exposure, size and shape of the structural member and thermal properties (thermal conductivity, heat capacity etc.) All columns were protected from furnace heating by an alumino-silicate fireproofing blanket, and did not heat-up significantly. The steel beam was heated on three sides, while the RC floor slab was heated from the bottom and was convectively cooled on its top surface. Thermocouple measurements indicated that the temperature of the RC floor slab rose slowly compared to the steel beam, because of its large thermal mass. There was a significant temperature gradient through the composite floor beam (temperature difference between the bottom flange of the steel beam and top of the concrete slab was as high as 800 ^{0}C). The top flange of the steel beam was in thermal contact with the concrete slab and its temperature was approximately 200 ^{0}C lower than that of the bottom flange. The differential thermal heating of the structural components has a significant effect on the observed structural response as seen in the next section.

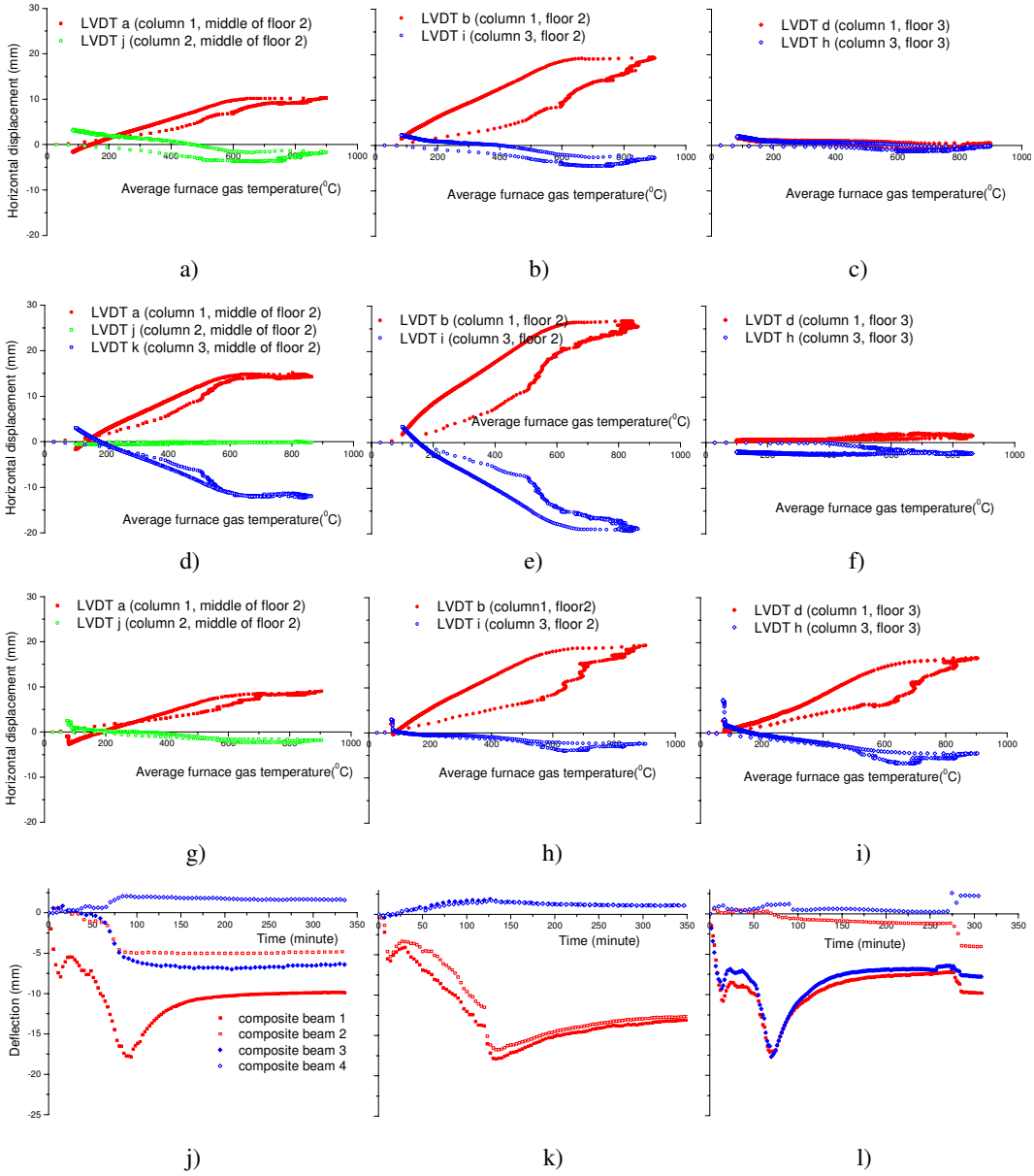

Figure 4. Horizontal displacement measured at various location for Test 1 (sub-figure a, b and c), for Test 2(sub-figure d, e and f) and Test 3(sub-figure g, h and i), plotted as a function of average furnace temperature. Vertical deflections plotted as a function of time (minutes) for Test 1, Test 2 and Test 3 are shown in sub-figures j, k and l, respectively.

3.2 Structural Response of the Frame

This section describes the observed horizontal and vertical displacement of the frame during the heat up and the cool down phase. Figure 4 shows the horizontal displacements measured at various locations on the columns during the three tests, plotted as a function of the average furnace temperatures. Sub-figure a), b) and c) show results for Test 1. Sub-figure a) shows the horizontal displacements of column 1 (LVDT a) and column 2 (LVDT j) between floor 1 and floor 2. Sub-figure b) shows the horizontal displacements of column 1 and column 3 measured at the height of floor 2, while the sub-figure c) shows the horizontal displacements of columns 1 and 3 measured at the height of floor 3. The scale for the vertical axis is shown only in the first sub-figure. Red symbols are used for column 1, green symbols for column 2, and blue symbols are used for column 3. Sub-figures d), e) and f) show similar data for Test 2, while sub-figures g), h), and i) show results for Test 3. The only exception is sub-figure d), where the horizontal displacements of all columns are shown. All of the figures use the same scale as well as consistent symbols and color coding to help compare and contrast the results of the three tests.

In Test 1, the thermal expansion of composite beam 1 results in pushing out of column 1 and column 2. The displacement of column 1 was recorded as a positive number, while that of column 2 was recorded as a negative direction, indicating that the displacements were in two different directions. Since the composite beam 2 was not heated in Test 1, this beam restrained the outward expansion of column 2. Due to this restraining action provided by Compartment II, the horizontal displacement of column 2 was smaller than that of column 1. Similarly, sub-figure b) showed that the displacements of column 1 and column 3 were in the opposite directions, but the magnitude of the displacement for column 1 was significantly higher than that of column 3. Sub-figure c) shows that the horizontal displacement of column 1 and column 3 at the level of the 3rd floor are small throughout the heating and the cooling phase.

In Test 2, the burners in Compartment I and II were operational and as a result, the thermal loading of the frame induced loads that were very symmetric in nature. Sub-figure d) shows that the displacement of column 1 and column 3 were in opposite direction (as in Test 1), but the magnitude of the displacement was approximately equal. The horizontal displacement of Column 2 was approximately zero throughout the heating and cooling phase, again indicating the symmetric nature of the displacements. The maximum horizontal displacements were observed at the level of floor 2. This was due to the heating of floor 2 by the burners in compartment I and II. Since Compartments III and IV stay relatively cold during the test, the displacements of columns 1 and 3 at the level of floor 3 were relatively small.

In Test 3, the thermal loading was asymmetric and the displacements of column 2 and 3 were in the same direction, while that of column 1 was in the opposite direction. The displacements at the middle of floor 2 were similar to those obtained in Test 1, however, the displacements at the level of floor 3 were much larger than those in Test 1. This was due to the heating of the composite beam 3 in Test 3, which pushed Column 1 and Column 3 apart at the level of floor 3.

The mid-span deflection of the composite beams 1, 2, 3 and 4 are plotted as a function of time in the three sub-figures of Figure 4. The results for Test 1 are shown in the left sub-figure, those for Test 2 are shown in the center sub-figure, and Test 3 is shown in the right sub-figure. All three sub-figures use the same scale, as well as consistent symbols, and color coding to compare the results. The mid-span deflection was computed by subtracting the average vertical displacement measured at the edge of the beam from the mid-span displacement. In Test 1, composite beam 1 showed large downward vertical deflections. In

Test 2, composite beam 1 and 2 showed large symmetric vertical deflections, while in Test 3, composite beams 1 and 3 showed large vertical deflections. The vertical deflection of the beams that were not heated by the furnace was relatively small in all the three tests.

The results for Test 1 show vertical downward deflection of composite beam 1 and outward bowing of column 1 due to heating in Compartment I. The structural elements in the other compartments stay relatively cool and do not show appreciable deformation. The deformation of the test frame was smaller than those for the single story, single compartment test reported in [12], since the portion of the frame that does not heat up resisted the deformation of the structural elements in Compartment I. Frame deformation observed for Test 2 clearly shows symmetric outward displacements of column 1 and 3 as well as symmetric downward deflection of composite beams 1 and 2 during the heating phase as well as the cooling phase. The results for Test 3 are similar to those for Test 1 and indicate asymmetric distortion of the test frame.

Table 1. Summary of local buckling on the various steel beams and cracking of the concrete slab, observed at the completion of each test.

		Test 1	Test 2	Test 3
Local Buckling	Steel Beam 1	-100~400 mm from C1 -250~350 mm from C2	-100~500 mm from C1 -200~500 mm from C2	-100~400 mm from C2
	Steel Beam 2	No	-200~ 400mm from C2 -100~400 mm from C3	No
	Steel Beam 3	No	No	-100~300 mm from C1 -100~400 mm from C2
	Steel Beam 4	No	No	No
Cracking	Concrete Slab 1	Five major cracks, symmetrically placed	Nine major cracks, six near C1, one at midspan, and two near C2	Seven major cracks, five near C1, two near C2
	Concrete Slab 2	No	Eight major cracks, four near C2, one at mid-span, and three near C3	No
	Concrete Slab 3	No	No	Three major cracks, one near C1, two near C2
	Concrete Slab 4	No	No	No

4. OBSERVATIONS ON STRUCTURAL FAILURE AND CONCLUSIONS

At the completion of each test, the frame was removed from the furnace, the fireproofing blanket was stripped off and the frame was visually inspected for signs of local failure (local buckling of columns and steel beams, failure of the connection and cracking of the concrete slab). None of the columns in any of the three tests showed signs of local buckling or plastic hinge formation. Structural failure was observed in the beam-to-column connections, the composite beam and the concrete slab. Failure of the beam-to-column

connection was due to gap formation between the end plate and the column. Results indicate that the beam-to-column connection of those beams subjected to furnace heating failed during each of the three tests. During the heating stage, thermal expansion of the beam was restrained and a compressive force was generated in the connection. However, during the cool down stage, the temperature of the concrete slab was higher than the steel beam. The hot concrete slab continued to push the columns outwards, but the steel beam contracted during the cool down phase. This resulted in tensile forces in the connection and ultimately led to the formation of a gap between the end-plate and the column.

The steel beam in the tests reported in this paper was not protected from furnace heating. As a result, the bottom flange and the web plate reached a very high temperature. The temperature of the top flange was lower due to heat losses to the concrete slab. The beam-to-column connections and the columns were protected from furnace heating and as a result did not heat up significantly. Since the bottom flange and the web plate heated-up significantly, they were susceptible to local buckling. Table 1 summarizes the observation of local buckling of the four steel beams for all of the tests. Results for the three tests indicate that the beams that were subjected to furnace heating buckled locally. In most cases, local buckling was observed close to the two ends of the beam, where it connects with the column. The only exception was beam 1 in Test 3, which showed local buckling at one end only (the end close to column 2). Steel beams that were not heated by the furnace did not show signs of local buckling.

The four concrete slabs were also visually inspected at the completion of each test for indications of cracking and spalling. None of the three tests indicated spalling of the concrete slab, however, cracking of concrete slabs that were subjected to furnace heating was observed in each test. Table 1 also summarizes the number of major cracks and the pattern observed on the various concrete slabs for the three tests. For Test 1, five major cracks were observed running along the width of the Concrete Slab 1. These cracks were symmetrically placed along the length of the slab. The cracking pattern for the other tests is indicated in Table 1. In general, the cracks were concentrated near the beam-to-column connection, while fewer cracks were observed in the mid-span section. The cracking of the concrete slab is indicative of the composite action between the concrete slab and the steel beam.

The furnace tests presented in this paper on two-story, two-bay composite steel frames provide an improved understanding of the fire induced response of a structure. Detailed information on furnace temperatures as well as horizontal and vertical displacement of the test frame will serve as a database for validation of numerical models. Test results indicate that the deformation process and time to failure of a structure is highly dependent on the number of compartments that are heated and the location of the various compartments.

REFEERENCES

1. Najjar S.R., Burgess I.W., *Engineering Structure*, 1996;18(1):77-89
2. Bailey. C. G. and Moore, D. B., *The Structural Engineer*, 77(8), pp. 15-21, 1999.
3. Usmani, A. S., Rotter, J. M., Lamont, S., Sanad, A.M., Gillie, M., *Fire Safety Journal*, Vol. 36, No. 8, pp. 721-744, 2001.
4. Buchanan, A.H., *Structural Design for Fire Safety*, John Wiley and Sons, 2001.
5. British Standards Institution (BSI): British Standard 476, Fire Tests on Building Material and Structures, Part 20: Method for Determination of the Fire Resistance of Elements of Construction (General Principles), British Standards Institution, London, 1987.

6. Franssen, J.M, Talamona, D., Kruppa, J. and Cajot, L.G., *ASCE Journal of Structural Engineering,* 124(2):158-163, 1998.
7. Lamont, S., Lane, B., Flint, G. and Usmani, A., Journal of Fire Protection Engineering, Vol. 16, No. 1, 5-35, (2006).
8. Harmathy, T.Z. and Sultan, M. A., Fire Safety Journal, Vol. 13, No. 2-3, 163-168, (1988).
9. Kodur, V. K. R, ASCE Structures Congress, 1-9, 2000.
10. Huang, Z., Burgess, I., Plank, R., Bailey, C., Fire and Materials, Vol. 28, No.2, 127-138, (2004).
11. Lamont, S., Usmani, A. S., Drysdale, D. D., Fire Safety Journal, Vol. 36, No. 8, 815-839, (2001).
12. Dong, Y. and Prasad, K., An Experimental Study on the Behavior of Full-Scale Composite Steel Frames under Furnace Loading, submitted, Journal of Structural Engineering, January 2007.

FULL SCALE TEST OF A STEEL AND CONCRETE COMPOSITE FLOOR EXPOSED TO ISO FIRE

BIN ZHAO[1], MOHSEN ROOSEFID[2] and OLIVIER VASSART[3]

ABSTRACT

The fire performance of composite steel framed buildings with composite floors (concrete slab connected to steel beams by means of headed studs) is shown, through large-scale fire tests conducted in a number of countries and observations of actual building fires, to be much better than indicated by standard fire resistance tests on isolated structural elements, such as composite slab or composite beam alone. Such good performance has led to the development of a new design concept in UK according to which only a part of steel members of a steel and concrete composite floor need to be fire protected and the saving of fire protection with respect to a traditional solution could be as much as 40%, so a great advantage from economical point of view. This design concept, derived from both natural fire tests and analytical investigation, is in principle considered to be also applicable to ISO fire condition, the most common design fire used in fire design of buildings. However, more evidence is still necessary to confirm such good performance of steel and concrete composite floor in case of long ISO fire exposure duration.

The paper is focused on the presentation of a full scale ISO fire test with a steel and concrete composite floor of more than 60 m², within the scope of an European project dealing with the dissemination of above mentioned new design concept over other European markets.

1. INTRODUTION

Large-scale fire tests conducted in some countries and observations of actual building fires have shown that the fire performance of composite steel framed buildings incorporating

[1] Dr. Ing., Fire Research and Engineering Section, CTICM 91193 Saint-Aubin, France
email: binzhao@cticm.com
[2] Dr. Ing., Fire Research and Engineering Section, CTICM 91193 Saint-Aubin, France
email: mroosefid@cticm.com
[3] Ing., Arcelor Profil Luxembourgh S.A Research Centre, L-4009 Esch-sur-Alzette, Luxembourg
email: olivier.vassart@arcelormittal.com

composite floors (concrete slab with profiled steel sheet connected to steel beams by means of headed studs) is much better than that indicated by standard fire resistance tests on isolated structural elements. It is clear that there are large reserves of fire resistance in modern steel-framed buildings and that the standard fire resistance tests on single unrestrained members do not provide a satisfactory prediction of the real performance of such type of structures.

The natural fire tests on the eight-storey building at Cardington (see figures 1 & 2) shows clearly that the stability of composite steel-framed floors with some unprotected steel beams can be fully maintained by the beam/slab interaction, despite the fact that the temperature of unprotected beams exceeds 1000º C. The analysis made after Cardington fire tests shows that this excellent fire behaviour is due to both membrane and diaphragm effects of the reinforced composite slab together with steel beams once the steel beams attain temperatures at which they are no longer capable of supporting the applied load alone.

Fig. 1 – Cardington test building prior to concrete casting of the floor

Fig. 2 – One of the fire tests on Cardington building

Based on observation and analysis of the extensive programme of above full scale natural fire tests, a new fire design concept (design method and corresponding design guide) was developed in UK concerning modern multi-storey steel-framed buildings using composite construction, i.e. the floors are constructed using composite slabs with profiled steel decking attached by shear connectors like headed studs to downstand beams [1]. This design concept allows designers to take advantage of whole building behaviour and allows them to determine which members can remain unprotected while maintaining the same safety levels, as far as the expected overall stability from fully fire protected structures. Moreover, this design method is aimed at fire resistance assessment of partially protected composite floors not only under natural fire condition but also in a standard ISO fire situation. The latest is of particular interest because it means that the design concept may be applied by any design engineers in their fire resistance assessment of multi-storey steel-framed buildings using composite construction. Currently, this design concept is already officially applicable in UK.

On the basis of above evolution in UK, Steel Alliance, with a sponsoring from both ArcelorMittal and CTICM, launched the project FRACOF of which the main objective is to extend this design concept to other European national markets, especially under ISO fire condition with the purpose of getting the maximum benefit from this new design concept. The presentation below will be focused on full scale fire test which constitutes a major step of the project.

2. FULL SCALE TEST UNDER ISO FIRE CONDITION

2.1 Design of the fire test and the corresponding specimen

This fire test is with the objective to provide the evidence that a steel and concrete composite floor if some of its steel beams are not protected may ensure, with an adequate reinforcing steel mesh in concrete slab, a good fire performance even exposed to long ISO fire. Considering the size of used fire furnace, it is decided to adopt a specific test specimen shown in figure 3.

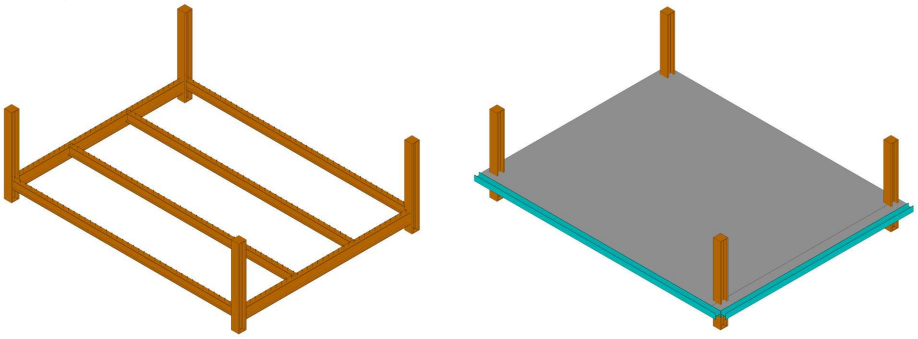

a- View over the steel frame b- View over the composite floor

Fig. 3 – ISO fire full scale test set-up

In fact, the specimen is with a composite floor supported by four short steel columns. The composite floor is composed of four secondary beams and two primary beams covered by a steel and concrete composite slab, all of which are linked together with help of headed studs, a very commonly used type of shear connectors for composite structures. In addition to this shear connection, all steel members are linked together with two common types of steel joints. It can be found that all structural members of a composite floor are present in this specimen leading therefore to a structure within real buildings. Also, in order to simulate the continuity condition of composite floor, the reinforcing steel mesh of two sides of the slab is welded to two additional steel beams which are in turn fixed to furnace structure.

The global dimensions of the specimen can be summarized as follows:

- span of secondary beam: 8.735 m
- span of primary beam: 6.66 m
- span of composite slab: 2.22 m
- total length of steel column: 2.5 m, with 0.8 m below composite slab

The composite slab is with the profiled steel sheet COFRAPLUS60 (trapezoidal), a steel decking very largely used over French market. According to EN1994-1-2 [2], the total depth of the slab should be 155 mm (see figure 4 for more detail) for a fire resistance of 120 minutes. In compliance with the span of the slab (2.22 m), the thickness of the steel sheet is 0.75 mm. The concrete is predicted in normal weight concrete with a quality of C30/37.

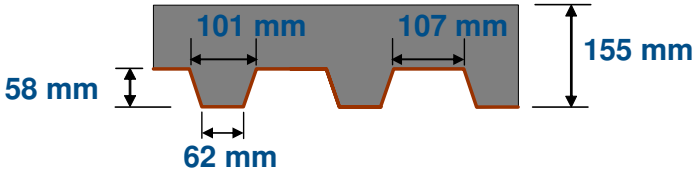

Fig. 4 – Size of composite slab

The cross sections as well as the headed studs of all steel beams are defined in accordance with the requirements of EN1994-1-1 for room temperature design of composite structures [3]. As far as steel joints are concerned, they are designed according to the requirements of EN1993-1-8 [4]. Two common types of steel joints, that is flexible end plates and double angle web cleats using bolts of M20 in grade 8.8, are adopted for this steel frame (see figure 5).

Beam to column joints with flexible end plates and double angle web cleats

Beam to beam joints with double angle web cleats

Fig. 5 – Steel member joints

In addition to the self weight of the structure, the floor construction was designed for a dead load of 1.20 kN/m^2 and an imposed load of 5.00 kN/m^2.

With all above data, the design has led to following cross sections of steel beams:

- secondary beam: IPE300 with the steel grade of S235
- primary beam: IPE400 with the steel grade of S355
- column: HEB260 with the steel grade of S235

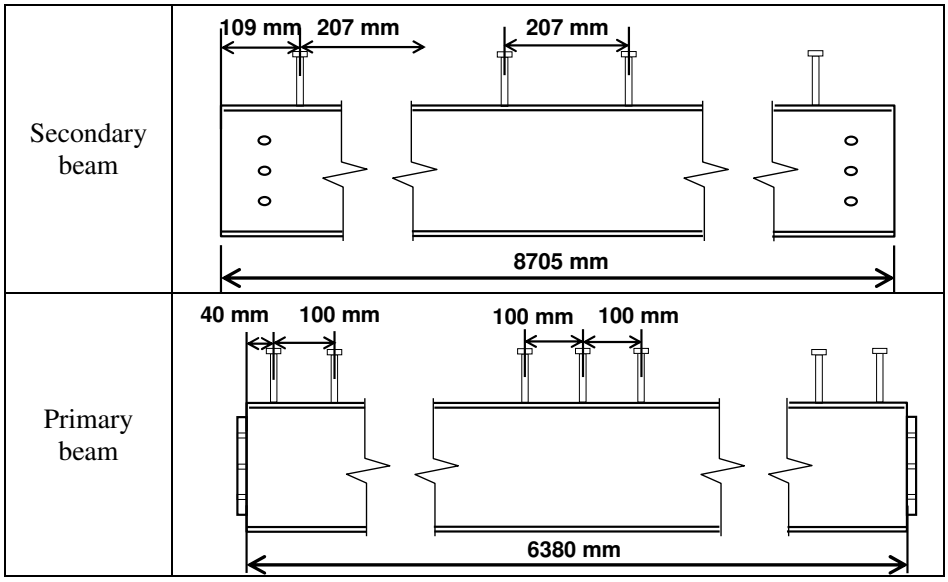

Fig. 6 – Distribution of shear connectors for steel beams

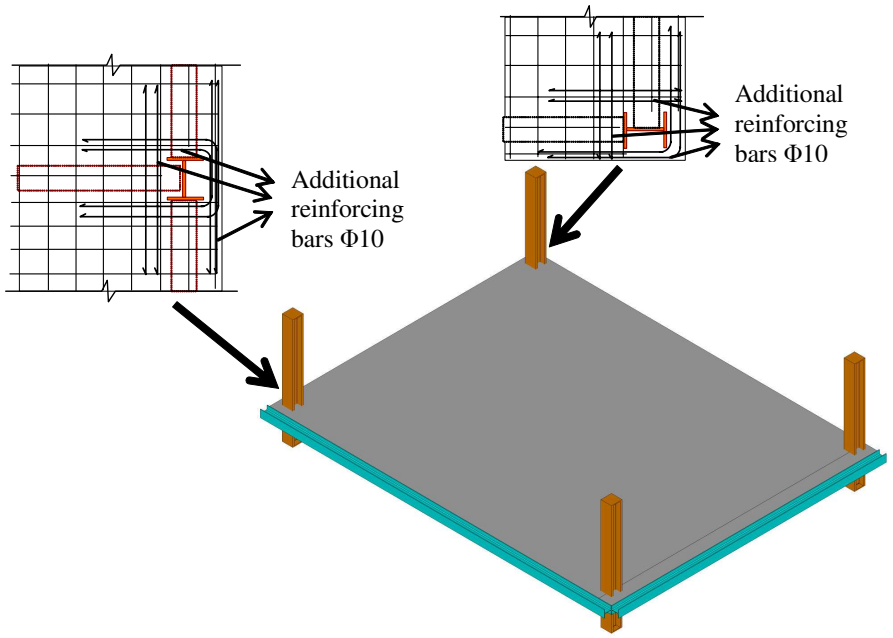

Fig. 7 – Connection configurations to be investigated in the fire test

With respect to shear connectors, they are all in headed studs with a diameter of 19 mm and a height of 125 mm and their distribution over steel beams is shown in figure 6.

The reinforcing steel mesh used in composite slab is located at 50 mm from the top of the slab. The mesh with a steel grade of S500 has a grid size of 150 mm x 150 mm and a diameter of 7 mm. Moreover, the additional reinforcing bars are used for the edge steel and concrete composite connection (see figure 7).

2.2 Fire test condition

For fire test, following three aspects are to be considered:

- mechanical loading condition
- heating condition
- fire protection of steel members

The mechanical loading of the floor is applied with help of fifteen sand bags uniformly distributed over the floor (see figure 8). Each of sand bags weighs exactly 15.0 kN leading therefore to an equivalent uniform load of 3.87 kN/m². This load value is slightly higher than design load of 3.75 kN/m² derived from Eurocode load combination in fire situation for office buildings given below:

- G (dead load) + 0.5 Q (imposed load)

The floor, occupying an area of more than 60 m², was exposed, from below, to the ISO fire condition using a standard fire resistance testing furnace (see figure 9).

In compliance with the fire design concept of such type of floor, the two secondary beams and the composite slab are unprotected. However, all the boundary beams of the floor (all beams in direct connection with columns) are fire protected to ensure a global structural stability for a fire rating of 120 minutes.

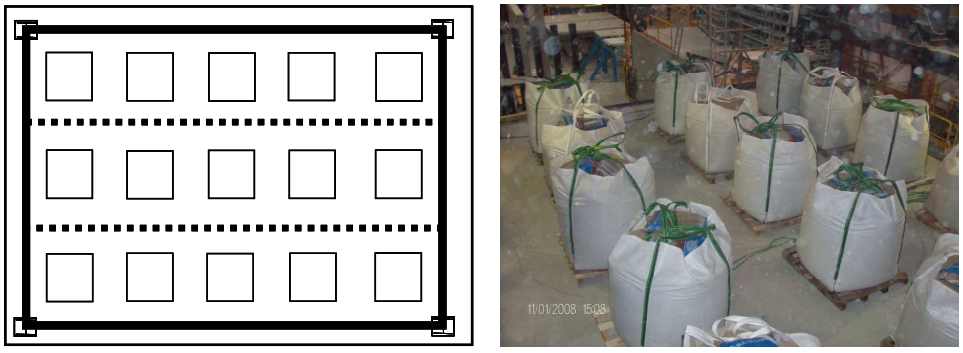

Fig. 8 – Loading of the floor with sand bags

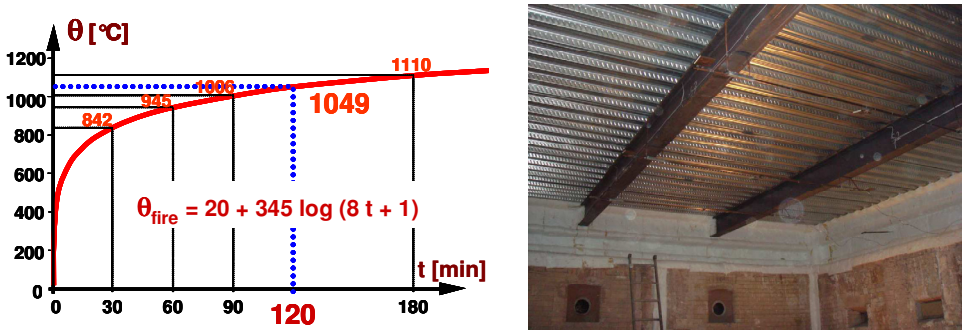

a- ISO standard fire curve b- View below floor inside fire furnace

Fig. 9 – Heating condition of the floor under ISO fire

2.3 Real material properties

The different material investigation performed before the fire test allows to know the real material properties of the specimen as follows:

- Secondary beams: mean value of yield strength is 311 MPa.
- Primary beams: mean value of yield strength is 423 MPa.
- Reinforcing steel mesh: mean value of yield stress is 594 MPa with a minimum elongation capacity of 14.5%
- Concrete: mean value of cylinder compressive strength is 36.7 MPa.

It must be noted that the reinforcing steel mesh is in class A so the elongation capacity is the minimum among all reinforcing steel bars.

2.4 Measurement of test results

A total of 194 measurements were used to record the specimen's behaviour. The main measurements are related to temperature and the deflected shape of the floor. Approximately 170 thermocouples were used to monitor the temperature of the steel frame and the temperature distribution through the slab (see figure 10).

9 displacement transducers of which 7 vertical displacement transducers were installed to measure the deflection of the floor (see figure 11). The two remained transducers were used to measure the horizontal movement of the floor. Moreover, a special high temperature video camera was put inside the furnace which can record visually the floor deformations versus time.

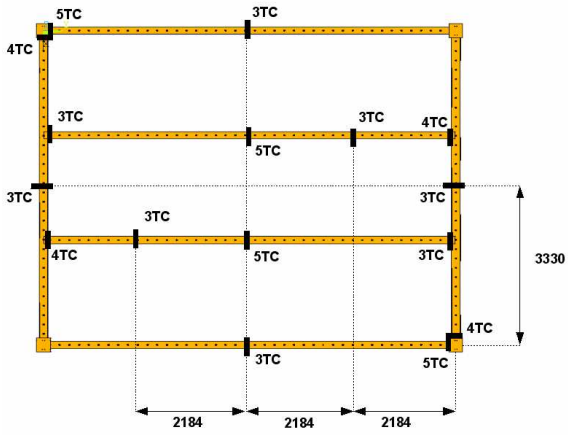

a- Position of temperature measurement of steel frame

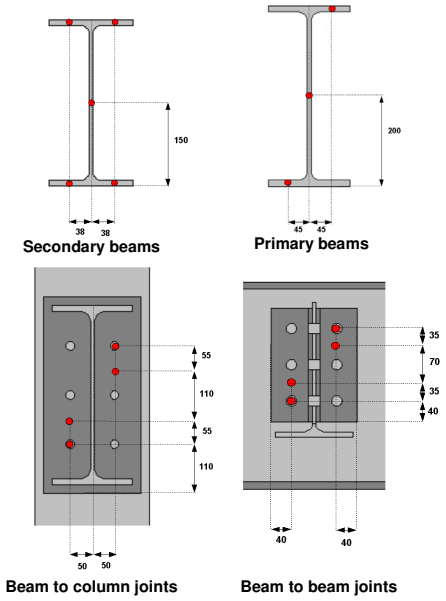

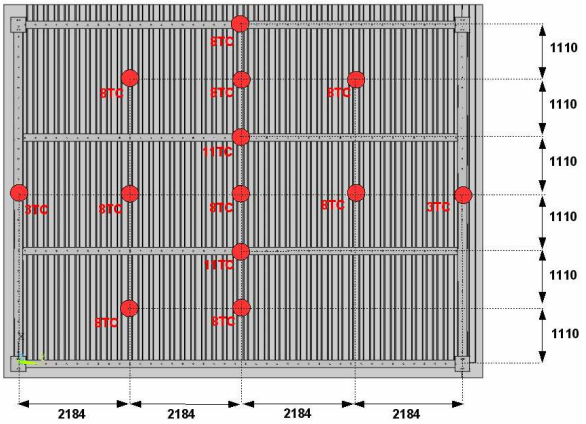

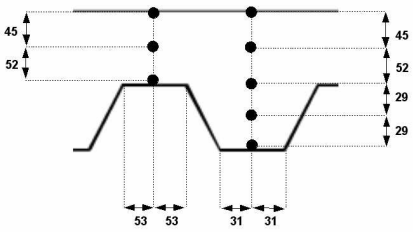

b- Position of temperature measurement of composite slab

Fig. 10 – Position of temperature measurement of the specimen

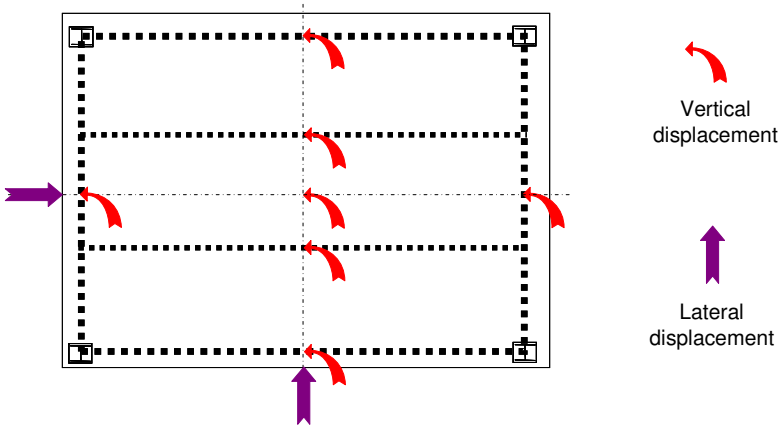

Fig. 11 – Position of displacement transducers

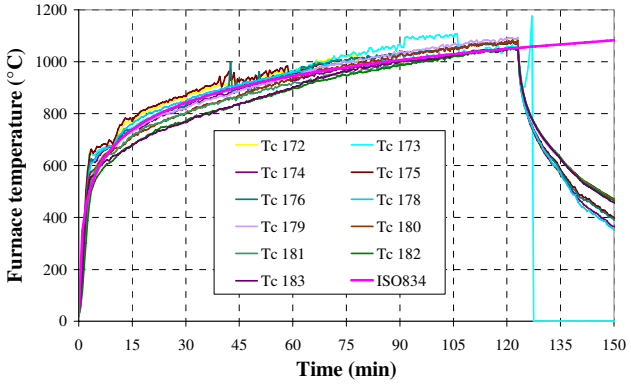

Fig. 12 – Furnace temperature versus ISO-834 fire curve

3. EXPERIMENTAL OBSERVATIONS

The test lasted for more than 120 minutes and the fire was stopped due to integrity failure of the floor. However, the recording of specimen's behaviour continued until 900 minutes allowing also to know the performance of the floor during the cooling phase of the fire. As consequence, the presentation of the test results can be divided in following parts:

- temperature:
- displacement
- observation of concrete cracking

The furnace temperature was controlled during the test with plate thermal meters just below the floor and the recorded temperatures in different places of the furnace show that the ISO standard fire curve is closely followed (see figure 12).

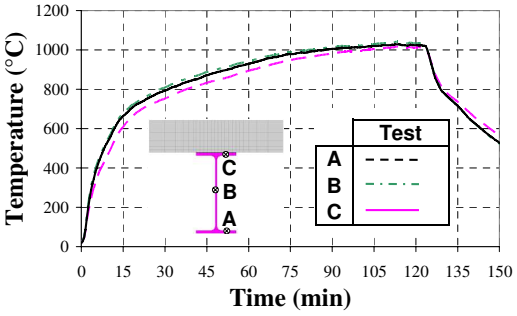

Fig. 13 – Heating of unprotected steel beams

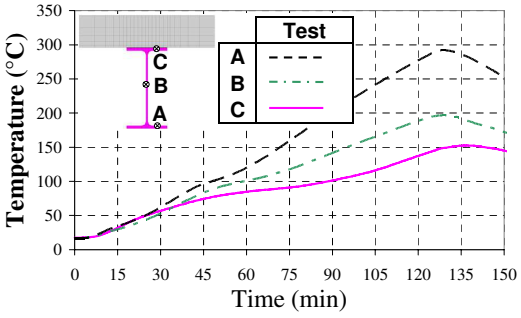

Fig. 14 – Heating of protected steel beams

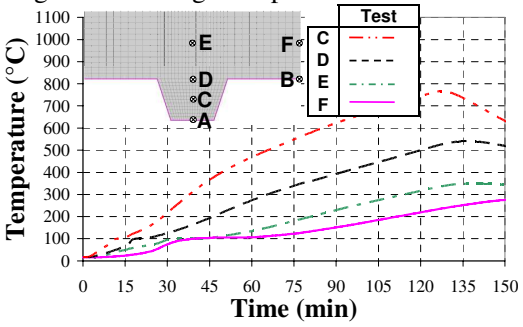

Fig. 15 – Heating of composite slab

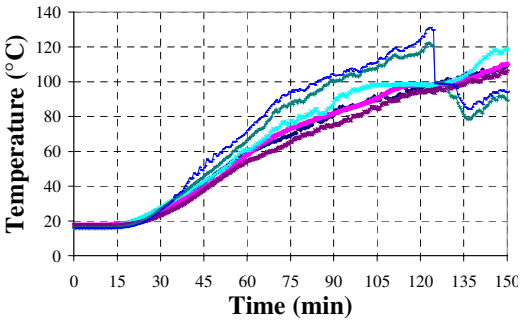

Fig. 16 – Temperatures recoded at unexposed side of the composite slab

As far as the heating of steel beams is concerned, the unprotected steel beams were heated up to around 1040 °C (see figure 13). On the contrary, the protected steel beams were heated up to around 300 °C which is less than predicted due to reduced exposure of these members located at the edge parts of the furnace (see figure 14).

The heating of composite slab was also recorded during the test and an example was given in figure 15. It can be found that the temperatures of points A and B are missing, which is due to the fact that the thermal couples fixed to steel sheet were lost very quickly with the unsticking of steel sheet with respect to concrete once exposed to fire. This phenomenon is observed practically everywhere of the composite slab.

The temperature recorded at the unexposed side of the composite slab is illustrated in figure 16. One can find that the temperature rise at unexposed face of the composite slab after 120 minutes of fire is slightly higher than 100 °C, which is still less than 140 °C, the criterion of insulation performance.

The various displacement transducers installed on the floor permit to know in detail the displacement of the floor. The vertical displacements of the floor are shown in figure 17 over the whole period of recording. A more detailed illustration of these displacements mainly during the heating phase of the floor is given in figure 18. It can be observed that the maximum deflection rise of the floor after 120 minutes of fire is about 450 mm and those of the two unprotected secondary beams are approximately 420 mm so less than the twentieth of their span. During the cooling phase of the fire, the deflection increased still slightly and reached the maximum value at about 135 minutes. At this moment, the furnace temperature has dropped from 1050 °C to only 600 °C (see figure 12). This phenomenon can be explained by the fact that the main component providing the necessary load bearing capacity of the floor, that is the reinforcing steel mesh in concrete slab is still heated up until 135 minutes (see figure 15). Regarding the displacement of edge beams, as they were very few heated, their deflection rise remains also low and does not exceed 100 mm. In addition, the deflection of edge secondary beams is much more increased than that of two primary beams, which complies fully with the load redistribution principle of the floor under membrane effect once subjected to fire.

From the deflection recording of the floor, one can understand easily that it fulfil its load-bearing capacity during the whole period of fire. Apparently after 120 minutes of ISO fire, the resistance capacity of the floor is still strong enough to bear the applied load.

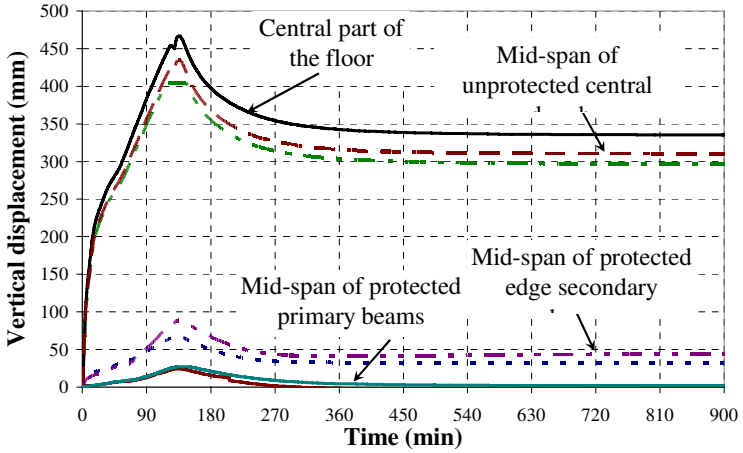

Fig. 17 – Deflection of the floor recoded during the whole period of test

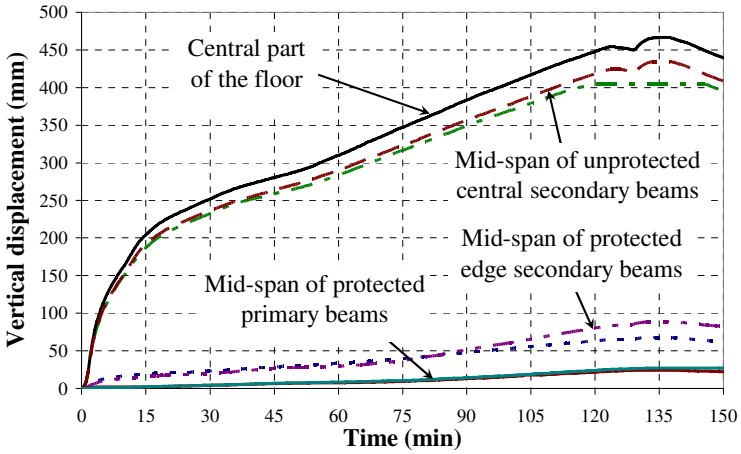

Fig. 18 – Deflection of the floor recoded during the heating period of test

Another important parameter to be mentioned here is the cracking of the composite floor which has a direct influence on fire performance of the floor. Therefore, the cracking of concrete was followed closely during the test and the main observed results are as follows:

- Small cracks occurred in the concrete, particularly around steel columns and continuous edges of the slab, at an early stage of the fire test, as shown in figure 19.
- There was some enlargement of these cracks during the heating phase of the test, but this did not significantly influence the integrity performance of the floor (see also figure 19).
- A more significant crack occurred after 105 minutes of fire exposure, as shown in figure 20. Such cracking has certainly an impact on integrity performance of the floor. Investigation of the crack after the test showed that the crack was caused by the failure of a welded joint between two steel reinforcing meshes as shown in figure 21. This type of failure can be fully avoided if appropriate construction details for lapping tension reinforcement are adopted in accordance with EN1992-1-1 [5].

Despite the occurrence of such an important crack and failure of steel reinforcing mesh in the longitudinal direction in the central part of the floor, its loadbearing capacity was still adequate to achieve a fire resistance in excess of 120 minutes.

a- at the beginning of fire test b- at the end of fire test

Fig. 19 – State of slab around steel column

a- State of the cracking at central part of the floor

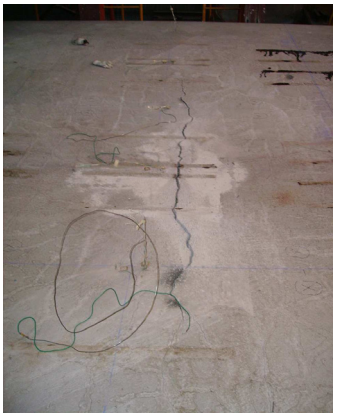

b- State of the cracking after cooling

Fig. 20 – State of slab at central part of the floor during and after the test

a- Welded reinforcement joint prior to the concrete casting

b- State of the reinforcement joint at the location of the crack after cooling

Fig. 21– Joint of reinforcing steel meshes before and after test

4. CONCLUSION

A floor of 7.35 m x 9.53 m was tested under ISO fire up to more than 120 minutes. The first conclusions derived from test results regarding the fire performance of the floor are:

- even with unprotected secondary steel beams of a span of 8.735 m, the criterion R related to fire resistance is fulfilled up to more than 120 minutes,
- the criterion E related to integrity of the floor is fulfilled up to 105 minutes due to premature failure of reinforcing steel mesh. Certainly the criterion I related to insulation of the floor was certainly reached also at the same time. However, the lost of these criteria can be fully avoided by using enough overlapping for joints of reinforcing steel meshes,

- the whole floor remains structurally very robust under long duration fire even with important failure of reinforcing steel mesh in concrete slab,
- the concrete cracking at edge parts of the floor is very limited and without any influence on integrity and insulation criteria of the floor,
- the floor behaved equally in good way during the cooling phase of fire.

It can be stated that the composite floor with reinforcing steel mesh designed to support membrane effect satisfy a REI of more than 2 hours provided that the continuity of reinforcing steel mesh is guaranteed with the construction details according to the state of the art.

Finally, the above experimental results are currently being investigated to check the validity of numerical models and the preliminary results are published in [6].

REFERENCES

[1] Newman, G.M., Robinson, J.T. and Bailey C.G., Fire Safe Design: a New Approach to Multi-Storey Steel-Framed Buildings (second edition), SCI Publication P288, 2006
[2] CEN, EN 1994-1-2 - Eurocode 4 "Design of composite steel and concrete structures" – Part 1-2: General rules - Structural fire design, June 2005
[3] CEN, EN 1994-1-1 - Eurocode 4 "Design of composite steel and concrete structures" – Part 1-1: General rules and rules for buildings, December 2004
[4] CEN, EN 1993-1-8 - Eurocode 3 "Design of steel structures" – Part 1-8: Design of joints, May 2005
[5] CEN, EN 1992-1-1 - Eurocode 2 "Design of Concrete Structures" – Part 1-1: General rules and rules for buildings, March 2004
[6] Zhao, Bin, Roosefid, Mohsen and Vassart, Olivier, "Full scale test of a steel and concrete composite floor exposed to ISO fire and corresponding numerical investigation", Eurosteel Conference 2008.

SIMPLE CALCULATION METHOD OF COMPOSITE CELLULAR BEAMS AT ELEVATED TEMPERATURES

ALI NADJA[1] ,NATHAN GOODFELLOW[1], OLIVIER VASSART[2],
FARIS ALI[1], SEGKWAN CHOI[1].

ABSTRACT

The growing popularity of the use of Cellular steel beams in composite floors comes at the same time as an increasing attention to the fire safety engineering design. The recommendation for their design in fire limit states remains very primitive and this is due to the lack of general research in this area. Six composite cellular steel beams were tested at the University of Ulster with two models of different steel geometries and loading conditions under monotonic loading and at elevated temperatures. This paper presents a simple model to calculate the shear buckling at the web post and the bending resistance of composite cellular beams in fire.

1. INTRODUTION

In the UK and Europe, in particular, the development of a wide variety of innovative composite floor systems has been notable. Investigation of the behaviour of composite beams with isolated web openings in otherwise solid webs has shown that the slab significantly increases the shear-carrying capacity beyond that of the steel beam alone. This is due to the enhanced flexural and shear capacity of the upper part of the beam across an opening, although an unsupported web-post is more susceptible to buckling. The structural behaviour of beams with opening is relatively complex and involves the main failure modes which are included in the design model for ULS design at ambient temperature and in fire conditions described in the literature review [1-4]

[1] University of Ulster , School Built Environment, FireSERT, Belfast BT37 OQB, UK
Email : a.nadjai@ulster.ac.uk
[2]ArcelorMittal Belval&Differdange S.A., Research Centre, Esch/Alzette, G.-D. of Luxemburg

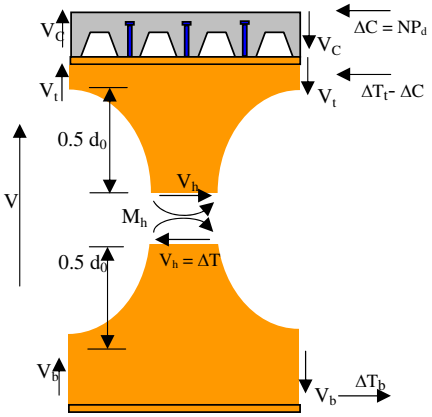

Fig. 1 - Forces acting on the web

Fig.2 - Beam failure at the post web

The model shown in Fig. 1 shows the forces and moments acting on the web post between adjacent openings. Horizontal shear forces are developed in the web post in order to transfer the incremental tension force to the bottom tee. Web posts in asymmetric beams will also be subjected to in-plane moments in order to maintain equilibrium between the top and bottom tees. Due to the shear forces transferred across the web posts between openings failure can occur due to out of plane buckling, as illustrated in Fig. 1. The tendency for the web post to buckle will depends on the width of the web post the height of the opening and the d/t ratio of the web.

The incremental in axial force in the bottom tee ΔT_b, top ΔT_t and concrete slab ΔC correspond to the change in applied moment between the two openings. The horizontal shear force, V_h, applied to the adjacent web post will be equal to ΔT_b. Therefore, the change in the force applied to the bottom tee between adjacent openings and, subsequently, the total force that can be applied to the bottom tee between the support and the maximum moment position, cannot exceed the capacity of the web posts. For a beam with narrow web posts, this will often mean that the actual moment resistance at the point of maximum applied moment is less that the plastic capacity of the section at this point. For beams with low values of slenderness (low d/t ratios), the horizontal shear capacity of the web post will govern the design at ultimate limit state and for higher d/t ratios the buckling capacity of the web post will govern opening

In fire, the temperature distribution across a composite member is non-uniform, since the web and bottom flange have thin cross-sections and a greater exposed perimeter than the top flange [5]. The deterioration of the material properties of the web will therefore become an important effect on the overall performance of the member in the event of fire (Fig.2).

2. CALCULATION MODEL FOR THE BEAMS WITH WEB OPENINGS

The ratio of opening spacing to opening diameter, S/d_0 must be known. The opening spacing, S, is measured between the centre-lines of adjacent openings as shown in Fig. 3. For a series of specific web post widths, the model generates beam with varying depths, opening diameters and opening pitches, giving a range of S/d_0 values between 1.4 and 1.8. The thickness of the web for each beam is also varied to give d/t ratios between 40 and 80.

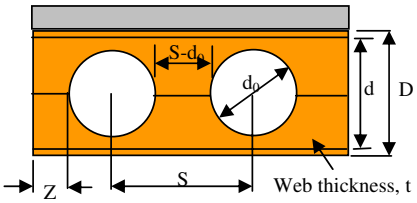

Fig. 3 - Detail information of cellular beams

The structural model assumes that the loading applied to the beam is symmetric. The loading can be defined as a uniformly distributed load (UDL) or as point loads located centrally or at third points of the span.

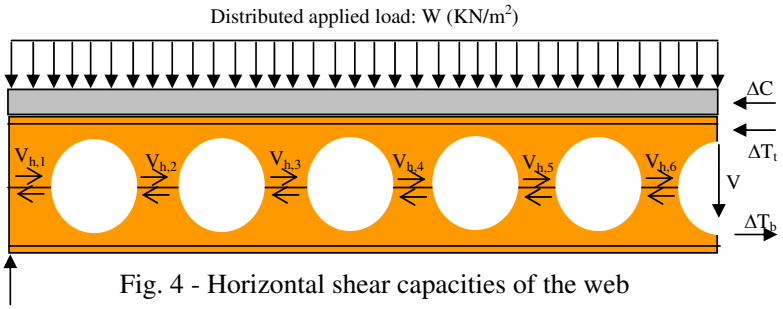

Fig. 4 - Horizontal shear capacities of the web

The bending moment capacity of the beam in both the fire and ultimate limit states can be limited by the horizontal shear capacity and/or the buckling capacity of the web posts, as this limit the axial force that can be generated in the bottom tee (see Fig. 4). The force in the bottom tee at the maximum moment position, T_b, cannot exceed the sum of the horizontal shear capacities of the web posts, $V_{h,i}$.

$$\sum V_{h,i} \geq T_{b,\theta} \tag{1}$$

Where $T_{b,\theta}$ is the plastic tensile capacity of the bottom tee at temperature Θ. $V_{h,i}$ is the lesser of the horizontal shear capacity and the buckling capacity of i-th web post.

The shear buckling capacity of the web post at temperature Θ, expressed in terms of longitudinal shear, is given by:

$$V_{h,buck,\theta} = \frac{\chi \cdot p_{y,\theta}(S - d_o)t_w}{\gamma_m} \tag{2}$$

In which

$$\phi = 0.5\left(1 + \alpha(\lambda_\theta - 0.2) + \lambda_\theta{}^2\right), \ \chi = \frac{1}{\left(\phi \cdot \sqrt{\left(\phi^2 - \lambda_\theta{}^2\right)}\right)} \ \text{and} \ \lambda_\theta = \sqrt{\frac{p_{y,\theta}}{P_{E,\theta}}}$$

Where $P_{E,\Theta}$ is the elastic buckling stress at temperature Θ. The value of $P_{E,\Theta}$ is determined on the basis of an effective length of an equivalent strut. The properties of this equivalent strut were determined from finite element modeling. The effective length used in fire is 0.9 times the effective length used for the cold design.

The horizontal shear capacity of the web post at temperature Θ, is given as follows:

$$V_{h,shear,\theta} = \frac{0.6 \cdot p_{y,\theta}[(S - d_o)t_w]}{\gamma_m} \quad (3)$$

Where: S and d_0 are as defined in Fig. 3, t_w is the thickness of the web and $P_{y,\Theta}$ is the design yield strength at temperature Θ.

The plastic capacity calculated at elevated temperature $M_{c,\Theta}$ is taken as the maximum applied moment for the particular design temperature.

$$M_\theta = T_{b,\theta}(D + D_s - 0.5x_{c,\theta} - x_{eb}) \quad (4)$$

Where: $x_{c,\theta} = \frac{T_{b,\theta}(D_s - D_p)}{0.45 \cdot f_{cu,\theta}(D_s - D_p)B_e}$, $B_e = \frac{L}{4}$

B_e is the effective breadth of concrete flange and L is the span length of beam

and $x_{eb} = \frac{(A_f \cdot y_f + A_w \cdot y_w)}{A_f + A_w}$ (see Fig. 5)

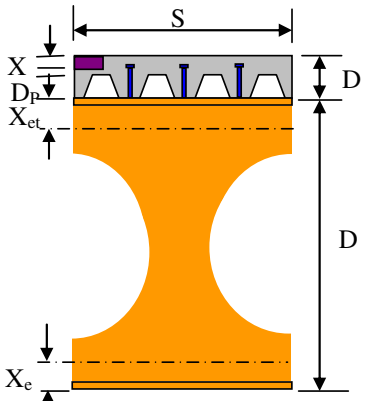

Fig. 5 - Geometric properties of

The plastic capacity $M_{c,\Theta}$ is then divided by the plastic capacity calculated for normal design $M_{c,20,}$ to give the load ratio as fellow:

$$R = \frac{M_{C,\theta}}{M_{C,20}} \quad (5)$$

This load ratio is then compared with the ratio of design load for the fire limit state compared with the design load at ultimate limit state, η_{fi}, calculated below. If the ratios are equal, the temperature at which $M_{c,\Theta}$ was calculated is taken as the limiting temperature for the beam.

The partial safety used to calculate the design load for the fire limit state are defined in BS 5950-8 [5] and are lower than the partial safety factors used for normal design as defined in BS 5950-1 [6].

The ratio of the design load at the fire limit state to the design load at the ultimate limit state may be expressed as:

$$\eta_{fi} = \frac{(\gamma_{GA} + \gamma_f \zeta)}{(\gamma_G + \gamma_Q \zeta)} \quad (6)$$

Where γ_G is the partial safety for dead loads, γ_{GA} is the partial safety for dead loads in fire, γ_Q is the partial safety factor for imposed loads, γ_f is the partial safety factor for imposed loads in fire and ζ is the ratio between the imposed and dead loads.

3. MODEL COMPARISON WITH FIRE TEST

When referring to the standard temperature time curve, the main information needed is the time when the bending moment resistance of a composite cellar beam is lower than the maximum applied moment in the beam span. Using the experimental results data [7] of the University of Ulster and by calculating the moment capacities of the web posts (see Fig. 6) between openings 1 & 2 (web post 1) and between openings 2 & 3 (web post 2) and comparing to the applied moment at that section it can be shown when the web starts to buckle.

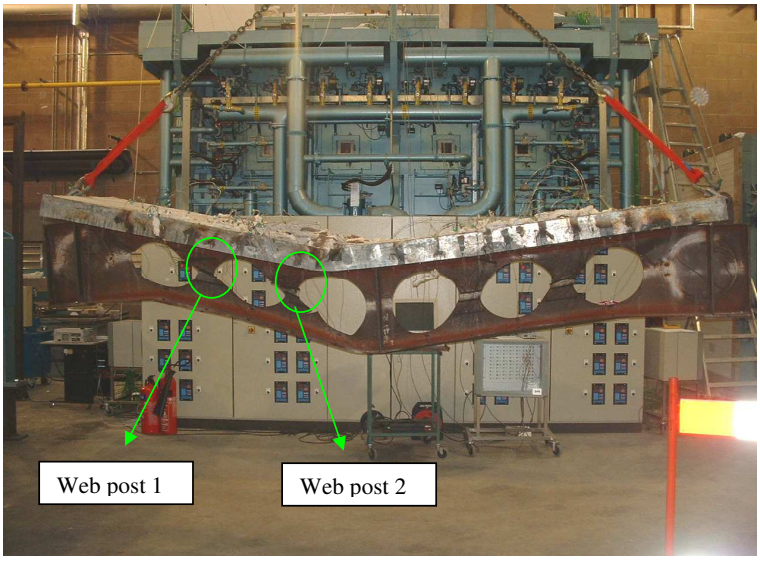

Fig. 6 - Composite cellular beam tested in Ulster

Web post 1 is shown to buckle after 65 mins when the temperature has reached around 690°C, whereas web post 2 buckles after 57 mins when the temperature is 600°C. Beyond these points of failure the applied moment is resisted by the buckling web post and finally by the concrete slab until the point of failure after 78 minutes (Fig. 7).

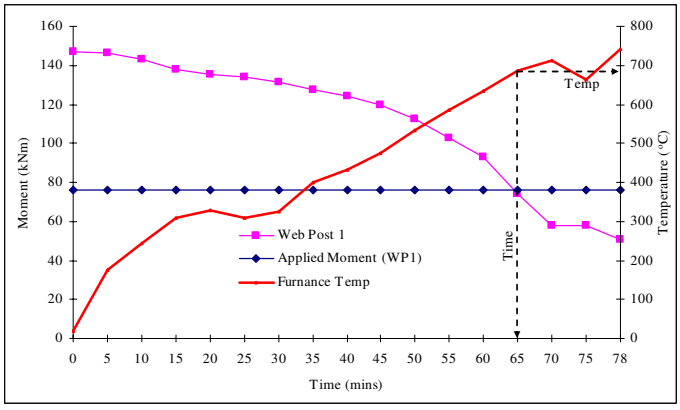

(a)

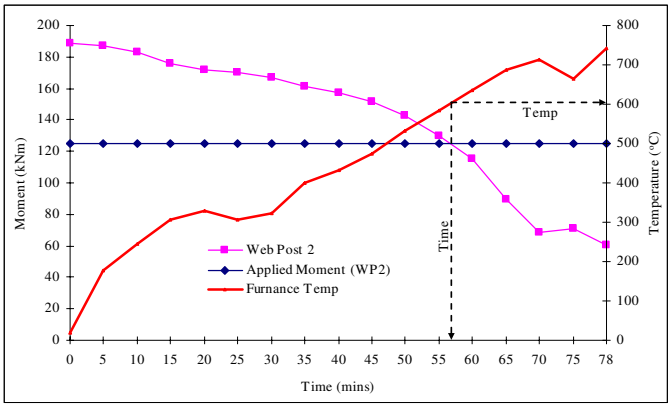

(b)

Fig. 7 - Moment capacity of: a) web post 1, b) web post 2, for slow fire

When the same section is subjected to the ISO fire curve (Fig. 8) and the same web posts are considered, it is shown that the web posts failure occurs after a shorter period of time.

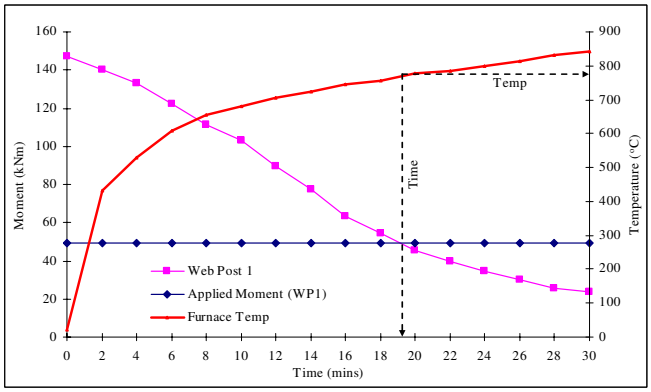

(a)

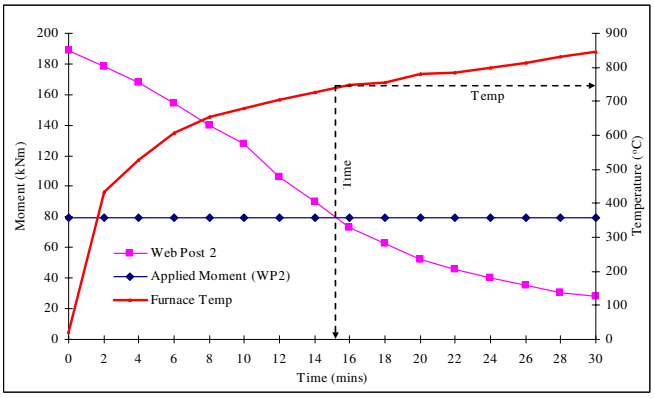

(b)

Fig. 8 - Moment capacity of: a) web post 1, b) web post 2, ISO fire

Web post 1 is shown to buckle after 19 mins when the temperature has reached around 676°C, whereas web post 2 buckles after 15 mins when the temperature is 655°C. The reason for this shorter period of web buckling resistance is due to the severe heat regime that the section is subjected to during the ISO fire. The steel section reaches higher temperatures at a greater rate than the slow fire test resulting in greater loss of strength and stiffness and thus causes the web post to buckle after a short period of time. As before the applied moment is resisted by the buckling web post and the concrete slab after the point of buckling occurs.

4. TEMPERATURE DISTRIBUTION IN THE CROSS SECTION

The temperature rise in a steel section depends very much on the design fire scenario due to the fact that steel has a high thermal conductivity and fairly low thermal capacity. The time lag between the steel temperature and air temperature is small compared to other materials such as concrete. It also depends on Section Factor (H_p/A), a physical quantity which relates the exposed area of the steel section and its volume that absorbs and distributes the heat energy. For sections such as the cellular beams, the volume is considerably reduced and hence the temperature rise is expected to increase faster than conventional solid beams.

The temperatures required for the calculations are shown in Fig. 9. The temperatures are all generated as a function factor (H_p/A) of the bottom tee. This is because the required strength of the beam in fire is calculated iteratively using the bottom Te flange temperatures, θ_{fb}. The temperature of the top flange of the section is set relative the bottom flange using the following relationships given in the SCI reference [2]:

$$\theta_{fb} = 547 + 0.65\left[\frac{H_p}{A} - 150\right] \tag{7}$$

Where

$H_p = 2\cdot B + 2\cdot d_b$, $A = B\cdot T_f + (d_b - T_f)t_w$

$\theta_{ft} = 0.7\cdot\theta_{fb}$

$\theta_{wb} = 1.02\cdot\theta_{fb}$

$\theta_{wt} = 1.02\cdot\theta_{ft}$

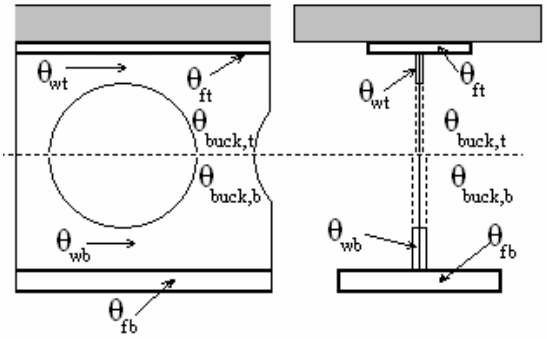

Fig. 9 - Temperatures distribution in the cross section of the cellular beam

The buckling temperature of the web post is given by:

$$\theta_{buck} = \theta_{fb}\left[1.4 - \frac{(1.4-1.1)}{450}\cdot(S - d_o)\right], \text{ but } \theta_{buck} \geq 1.1\cdot\theta_{fb} \tag{8}$$

Where $(S\text{-}d_0)$ is the width of the web post (mm)

Figure 10 shows the temperature profiles of web post 2 at the point at which the buckling capacity of the web post has been reached and the point where the test beam has failed for both the slow and ISO fire tests. It is shown that the temperature of the slab varies considerably between the fire exposure side and the unexposed top side.

Comparing these to the calculated SCI values it can be seen that at the point of web buckling for the slow fire (57mins) the test data only does not correlate well with the SCI value except for the top web temperatures. But when compared to the final failure temperatures of the composite system the only temperatures that are a close match are for the bottom flange and web.

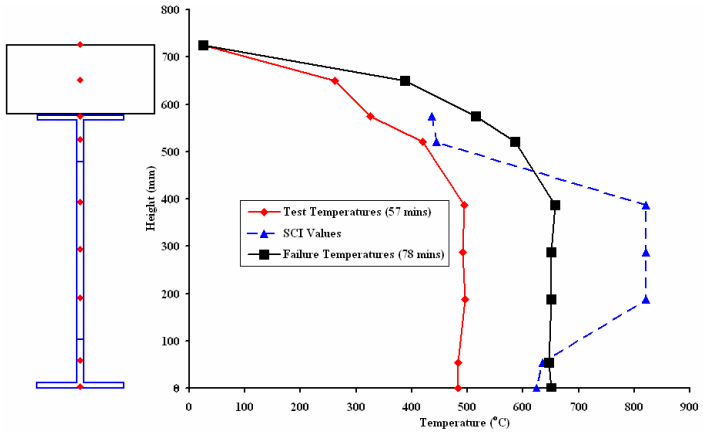

(a) Slow fire Web Post 2

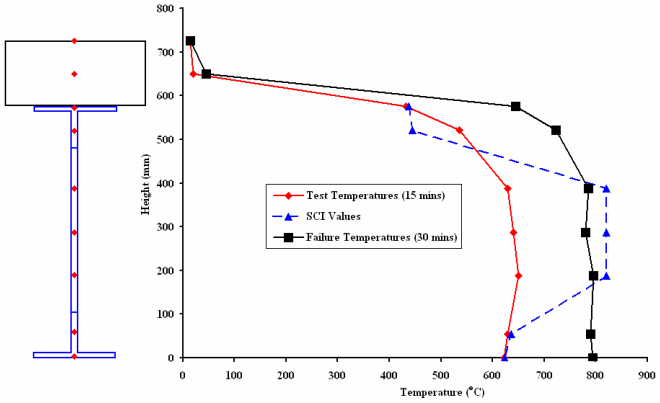

(b) ISO fire Web Post 2

Fig. 10 – Temperatures distribution at the post web buckling of the cellular beam.

When the ISO fire is considered (Fig.10b), the SCI calculated values do have better colorations with the test data only at the bottom and top flange when the moment capacity fail below the applied moment capacity at recorded time of 15 min. At the point of web buckling (30 mins) the SCI values correlate well with the experimental results data. The rest of the values do not mach well with the obtained experimental recorded temperatures at the bottom and top flanges. It can be seen in Fig.10 that the SCI model does not consider the temperatures distribution in the slab cross section. The increase of temperatures of both steel and concrete decrease their mechanical properties. Therefore, the increase in temperature to a difference in the thermal elongation of slab and profile creating an increase of shear force connectors which should be taken in consideration.

5. CONCLUSION

Based on the simple calculation model the bending moment can predict the time of the post web buckling failure and can lead to safe results when used outside the range of experimental evidence. The paper reviews also the method of determining the temperature distribution across the cellular beams according to the SCI model. It was found that the model is very conservative and needs to be improved. Therefore, a proper fire testing programme for cellular beams is needed to consider a range of section geometries. Further testing should also cover protected cellular beams in order to permit the fire protection material to be evaluated over the range of deflections.

6. REFERENCES

[1] Liu, TCH, Liew, KH, Behaviour of Cellular Steel Beams in Fire, Interflam 2004, pp157-168, 2004.
[2] SCI, 2004. RT1006 Version 02 - Fire Design of Cellular beams with Slender Web Posts, SCI, Ascot, 2004.
[3] Bitar, D.; Demarco, T.; Martin, P.O. 2005. Steel and non composite cellular beams – Novel approach for design based on experimental studies and numerical investigations, Proc. 4th Eurosteel Conference, Maastricht, June 2005.
[4] Lawson et al, Design of composite asymmetric cellular beams and beams with large web openings, Journal of Constructional Steel Research, V62, N6, June 2006
[5] BS5950-8:2003 Structural use of steelwork in building - Part 8: Code of practice for fire resistant design
[6] BS5950-1:2000 Structural use of steelwork in building - Part 1: Code of practice for design - Rolled and welded sections
[7] Nadjai, A.; Vassart, O.; Faris, A.; Talamona, D.; Allam, A. & Hawes, M. 2006. Performance of cellular composite floor beams at elevated temperatures, Proc. SIF 2006, pp. 813-823.

A NEW METHOD TO ANALYZE THE MEMBRANE ACTION OF COMPOSITE FLOOR SLABS IN FIRE CONDITION

NA-SI ZHANG [1] and GUO-QIANG LI [2]

ABSTRACT

During 1995 and 1996, a total of six localized fire tests were conducted on a full-scale, eight-storey, steel framed building at Building Research Establishment Laboratory at Cardington. The test results show that the fire performance of steel-concrete composite floor is better than that obtained from traditional design method, and the load capacity of composite floor slab in fire condition is usually higher than the predicted capacity without considering membrane action. In the past decade, researchers have done a series of analyses in this area, such as Bailey, Usmani, and Guo-Qiang Li. In this paper, a new method to calculate the load capacity of simply supported composite floor slabs with considering the membrane action is presented. The slab is divided into five parts at the limit state of load capacity, including a center-elliptic part and four rigid parts around. The deflection of the slab, the force of rebars in high temperature, and the force distribution between four rigid parts are reasonably assumed. According to force and moment equilibrium requirements on the slab, a series of equations are obtained to calculate the ultimate load capacity of floor slabs in fire condition. The effectiveness of this new method is validated through comparison with results from experiments and different theoretical simulations. The comparison shows that this new method is more reasonable in predicting the deflection and ultimate load capacity of floor slabs in fire condition than previous methods.

[1] Master Candidate, Tongji University, College of Civil Engineering, Shanghai, China.
email: chzns0508@hotmail.com.
[2] Professor, Tongji University, College of Civil Engineering, Shanghai, China.
email: gqli@mail.tongji.edu.cn.

1. INTRODUCTION

Steel-concrete composite floor system is the most widely used floor system in steel buildings. In fire condition, most area of the slab is heated, which may have great impact on the load capacity of the slab. However, through the investigation of real fire disasters and fire experiments of slabs, it is noticed that composite floor slab showed higher load capacity than expected by using traditional bending method for fire-resistance. According to detailed analysis [1], that is due to tensional membrane action.

Membrane action occurs at large deflection of slab, when the edges of slab are vertically and horizontally restrained. It is also possible for membrane action to occur when the slab is vertically supported without horizontal restraint. Membrane action can enhance the load capacity of slab by changing the load bearing mechanism from bending action model at small deflection to membrane action model at large deflection. This phenomenon was found in Cardington test and many real fire disasters.

Since 1990s, many researchers, including C.G. Bailey et al, A.S. Usmani et al and Guo-Qiang Li et al, have conducted studies in such membrane action using various methods.

In Bailey's method [1-3], the final deformation of slab at limit state is based on yield-line model. However, in fire, with the temperature elevation of the slab, the strength and stiffness of reinforcement and concrete are continually decreased, and the maximum deflection of slab will be greatly increased. Therefore the traditional bending yield-line model will disappear, and will be taken place by membrane action. So, the assumption of bending yield-line model may not be appropriate for modeling membrane action of slabs subjected to fire.

In the method presented by Usmani [4-5], the distribution of membrane stresses in a slab is calculated by solving the equilibrium equation and compatibility equation which are used for isotropic flat slab. Geometric non-linearity but no material non-linearity is considered in the method. However, most slabs, especially steel-concrete composite floor slabs, are anisotropic plate, and they will experience large non-elastic deflection in fire condition. In this way, Usmani's method is not reasonable enough for determining the ultimate load capacity of composite slab in fire.

At the beginning of 2000s, Guo-Qiang Li et al presented a model to calculate membrane action [6]. In this model, the slab was divided into 5 parts (a center-elliptic part and four rigid parts around) at the limit state. The boundaries of the slab were assumed to be both vertically and horizontally restrained and the ultimate loading capacity could be obtained, according to equilibrium of the forces and bending moments. In this model, to get the horizontal boundary forces, slabs had to be divided into many strips. By summarizing the tensile force induced by deflection and the compression force induced by thermal expansion, the horizontal boundary forces could be obtained. This method exactly considered the final deflection of the slab in fire, and gave a reasonable model to simulate membrane action. However, the processes to get the boundary forces are relatively too complex. On the other hand, to divide the slab into stripes really destroys the global property of the slab, and can lead to force inharmony between different parts.

In this paper, to overcome the problem mentioned above, a new method to analyze the membrane action in slab exposed to fire, based on Guo-Qiang Li's model, is presented.

2. DEVELOPMENT OF MEMBRANE ACTION IN FLOOR SLAB

When a slab is subjected to fire, Guo-Qiang Li suggested that [6]: 1) at the beginning of fire, when the temperature is not very high, the slab bears applied load by bending mechanism; 2) as the temperature becomes higher, the bending yield lines will be formed in the slab due to the decrease of the strength and stiffness of concrete and reinforcement (Fig. 1(a)-(b)); 3) with continual increase of temperature, the bending yield lines will be completely formed (Fig. 1(c)); 4) with further temperature elevation, the load capacity of the slab offered by traditional bending mechanism will not be enough, and the membrane action contribute to keep the stability of the slab(Fig.1 (d)-(e)); and 5) at the final state, most of the load will be carried by membrane action with the reinforcement acting as a mesh, and a concrete compression ring will be formed in the peripheral party to provide anchorage for the reinforcement mesh (Fig. 1(f)).

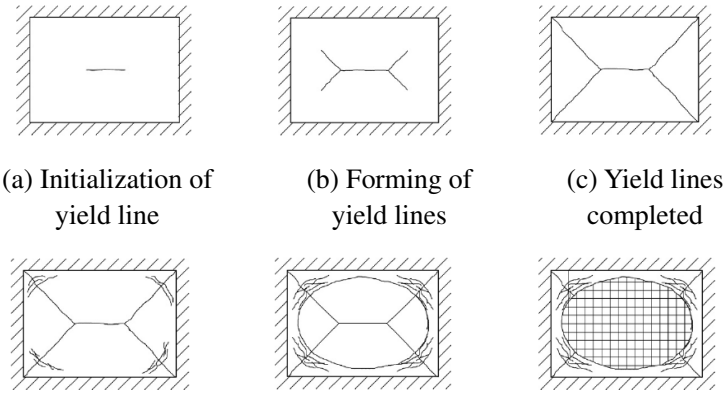

(a) Initialization of yield line (b) Forming of yield lines (c) Yield lines completed

(d) Appearance of membrane action (e) Development of Membrane action (f) Membrane action at the limit state

Fig.1 The development of membrane action in a floor slab

3. ASSUMPTIONS OF MODELING MEMBRANE ACTION

The following assumptions are adopted in the method presented in this paper:

1) The slab is rectangular one, and the ratio between length and width should not be greater than 2;

2) The support-beams bellow the edges of the slab are protected and are strong enough to support the load coming from the slab in fire;

3) The boundaries of the slab are vertically restrained but there are no horizontal and rotational restraints;

4) The reinforcement in the slab is continuous, and arranged in two orthogonal

directions to assure the formation of reinforcement mesh. The strain hardening of the reinforcement is ignored;

5) At the limit state, the deformation of the slab is like Fig.1-f. The slab can be divided into five parts as shown in Fig.2, where (x_0, y_0) is the intersecting point of the bending yield line and the ellipse; α is the separation angle between yield line and long edge of the slab. Plates 1 through 4 are assumed to be rigid, therefore they only have rigid rotational deformation. In the center of the slab, the concrete is cracked and its effect can be ignored, so the central reinforced concrete slab can be simplified as a reinforcement mesh. According to investigation of experiment and real fire disasters, the profile of central part can be supposed to be elliptic paraboloid, governed by the following equation as

$$\frac{x^2}{\frac{1}{w}\cdot(KL)^2}+\frac{y^2}{\frac{1}{w}\cdot(KB)^2}=w-z \tag{1}$$

where L is the length of the slab; B is the width of the slab; w is the maximum deflection of the elliptic part of the slab; K is the ratio of half length of the long or short axis of the ellipse to the corresponding length of the long or short edge of the slab, obviously, $0<K<0.5$;

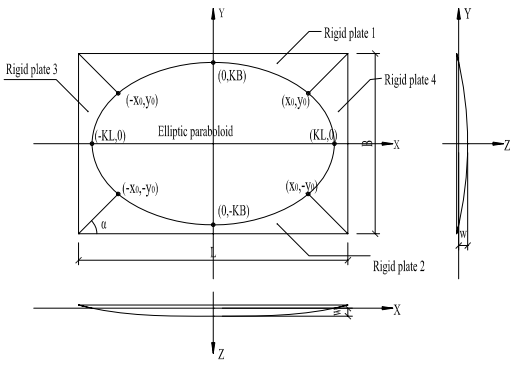

Fig.2 Division and coordinates of the slab at the limit state

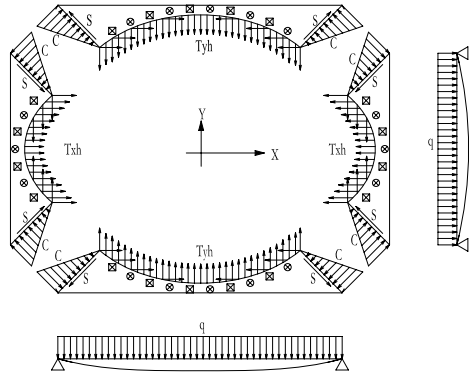

Fig.3 Force distribution in slab at the limit state

6) At the limit state, the force distribution is assumed as Fig.3, where C is the compression force between rigid plates; S is the shear force in the XY coordinate plane between rigid plates; T_{xh} and T_{yh} represent the in-plane components tension force of the reinforcement in X direction and Y direction respectively; $\otimes$ and $\boxtimes$ represent the vertical components force of the reinforcement in X direction and Y direction respectively;

7) At the limit state, the finial deflection of the slab is supposed as shown in Fig.4, where θ_x, θ_y are the rotation of the rigid plates about Y and X axis respectively. The maximum of the deflection can be divided into two parts: d_r and w, where d_r is the deflection caused by the rotation of rigid plates and w is the deflection of elliptic part.

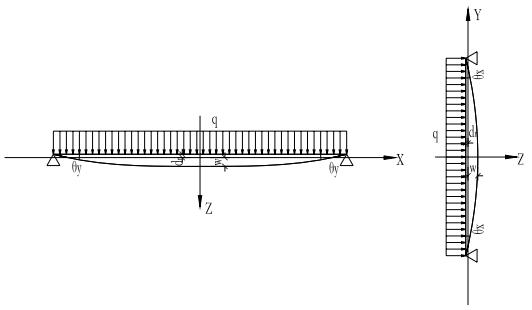

Fig.4 Deflection of slab at limited state

8) The failure criterion of the slab is fracture of the reinforcement mesh or the crushing of the concrete in the rigid plates.

4. DETERMINATION OF THE PARAMETERS

In the model proposed to simulate the membrane action of slab, the main parameters are α, (x_0, y_0), w, d_r, θ_x and θ_y, where α is the angle between yield line and long edge of the slab; (x_0, y_0) is the intersecting point of the yield line and the ellipse; w is the deflection of elliptic part; d_r is the deflection caused by the rotation of the rigid plates; and θ_x, θ_y are the rotations of the rigid plates. The determinations of these parameters are presented as follows.

4.1 Determination of α and (x_0, y_0)

The ultimate deflection of the slab at the limit state is developed from yield line mechanism, therefore α can be determined by the traditional yield line theory [7].

(x_0, y_0) is the intersecting point of the yield line and the ellipse, which can be obtained by using analytic geometry and given by

$$x_0 = \frac{-(B\cdot\tan\alpha - L\cdot\tan^2\alpha)\cdot L^2 + \sqrt{-L^4B^2\cdot\tan^2\alpha - L^2B^4 + 2L^3B^3\cdot\tan\alpha + 4K^2B^4L^2 + 4K^2L^4B^2\cdot\tan^2\alpha}}{2\left(B^2 + L^2\cdot\tan^2\alpha\right)} \tag{2}$$

$$y_0 = \left(x_0 - \frac{L}{2}\right)\cdot\tan\alpha + \frac{B}{2} \tag{3}$$

4.2 Determination of w

It is assumed that the reinforced bar will reach its mechanical strain limit when the ultimate load is reached, so the maximum deflection of the elliptic part should be determined by the limited elongation ratio of the reinforced bars. At the same level of deflection in the middle of the slab, the average strain in the reinforcement along the short span of the slab is larger than that along the long span. In this way, the maximum deflection of the slab is governed by the limited elongation of the reinforcement along the short span. According to

the analysis in [6-7], w can be obtained by using following equation as

$$w_{total} = w + d_r = KB\sqrt{\frac{3}{8}\left(\varepsilon_{uk} + \alpha_s \cdot \Delta T\right)} + \theta_x \cdot \left(\frac{B}{2} - KB\right) \tag{4}$$

where ε_{uk} is the characteristic limited elongation of reinforcement, which is 2.5% when the diameter of the reinforcement is less than or equal to 12mm, or 5% when the diameter of the reinforcement is greater than 16mm [8]; α_s is the average coefficient of thermal expansion, which is $1.4*10^{-5}$; θ_x is the rotation of the rigid plates 1 and 2; and T is the temperature of the slab after t minutes of ISO 834 standard fire exposure, which can be determined by the following equation as [9]

$$T = \left[\frac{0.6 \cdot e^{-\frac{w_2}{w_4}} - 0.1}{H} d + 1\right] \cdot \left[T_0 + \frac{e^{\left(0.05+0.135\frac{t}{20}-0.005\left(\frac{t}{20}\right)^2 - d\right)\Big/\left(0.007+0.0145\frac{t}{20}-0.005\left(\frac{t}{20}\right)^2\right)}}{8}\right] \tag{5}$$

where t (unit: min) is the heating-up time; T_0 (unit: ℃) is the room temperature; d (unit: m) is the distance between reinforcement and the bottom of the slab; H (unit: m) is the thickness of the slab; and w_2 and w_4 are sizes of steel deck for the slab, which are shown in Fig.5.

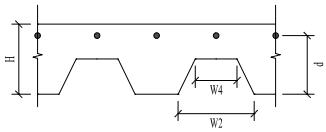

Fig.5 The sizes of slab

4.3 Determination of θ_x and θ_y

It is supposed that the rigid plate 1,2 and the tangent of the elliptic paraboloid are continuous on the boundaries. Therefore θ_x is equal to the gradient of the elliptic paraboloid at point (0, KB), and can be obtained by the following equation as

$$\theta_x = \left.\frac{\partial z}{\partial y}\right|_{y=KB} = \frac{2w}{KB} \tag{6}$$

Based on the deformation compatibility condition of rigid plates 1,2 and 3,4 at the points of (x_0, y_0), $(x_0, -y_0)$, $(-x_0, y_0)$, $(-x_0, -y_0)$, the rotation of plates 3,4 can be determined by

$$\theta_y = \arctan\left(\frac{B/2 - y_0}{L/2 - x_0} \cdot \tan\theta_x\right) \tag{7}$$

5. EQUILIBRIUM OF FORCES AND BENDING MOMENTS IN THE SLAB

5.1 Equivalent force of reinforcement and concrete

With the temperature increase of reinforcement and concrete after t minutes in fire obtained by equation (5), the strength of reinforcement and concrete can be obtained with

using the reduction formulas specified in [10]. Then, the tensile forces per unit width of reinforcement at T℃ in X and Y directions can be determined by

$$T_{xu} = f_{yT} \cdot A_{sx}, \quad T_{yu} = f_{yT} \cdot A_{sy} \tag{8}$$

where f_{xT} and f_{yT} are the strength of reinforcement at T℃ in X and Y direction respectively; and A_{sx} and A_{sy} are the area of the reinforcement per unit length in X and Y direction respectively, which can be calculated by

$$A_{sx} = \frac{\pi d_x^2/4}{D_x}, \quad A_{sy} = \frac{\pi d_y^2/4}{D_y} \tag{9}$$

where d_x and d_y are the diameters of reinforced bar in X and Y direction respectively; D_x and D_y are the bar spacing in X and Y direction respectively.

5.2 Component force of reinforcement

On the boundary of the elliptic paraboloid, the force, exerted from reinforcement, on the rigid plates is shown as Fig.6.

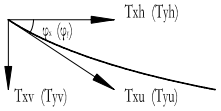

Fig.6 Force of the reinforced bar

In Y direction, tanφ_y is equal to the gradient at the intersection of the elliptic part and rigid plate, and can be obtained by following equation as

$$\tan\varphi_y = \left.\frac{\partial z}{\partial y}\right|_{z=0} = \frac{2w}{KB}\sqrt{1-\left(\frac{x}{KL}\right)^2} \tag{10}$$

therefore,

$$\sin\varphi_y = \frac{2w\sqrt{1-\left(\frac{x}{KL}\right)^2}}{\sqrt{(KB)^2 + 4w^2\left[1-\left(\frac{x}{KL}\right)^2\right]}}, \quad \cos\varphi_y = \frac{KB}{\sqrt{(KB)^2 + 4w^2\left[1-\left(\frac{x}{KL}\right)^2\right]}} \tag{11}$$

So the horizontal and vertical component forces of reinforcement in Y direction are obtained by

$$T_{yh(x)} = T_{yu} \cdot \frac{KB}{\sqrt{(KB)^2 + 4w^2\left[1-\left(\frac{x}{KL}\right)^2\right]}}, \quad T_{yv(x)} = T_{yu} \cdot \frac{2w\sqrt{1-\left(\frac{x}{KL}\right)^2}}{\sqrt{(KB)^2 + 4w^2\left[1-\left(\frac{x}{KL}\right)^2\right]}} \tag{12}$$

In the same way, for the reinforcement in X direction, the horizontal and vertical component forces of reinforcement are given by

$$T_{xh(y)} = T_{xu} \cdot \frac{KL}{\sqrt{(KL)^2 + 4w^2\left[1-\left(\frac{y}{KB}\right)^2\right]}}, \quad T_{xv(y)} = T_{xu} \cdot \frac{2w\sqrt{1-\left(\frac{y}{KB}\right)^2}}{\sqrt{(KL)^2 + 4w^2\left[1-\left(\frac{y}{KB}\right)^2\right]}} \tag{13}$$

5.3 Force equilibrium

At the limit state, the membrane forces in each rigid plate of the slab are shown in Fig.7. The force equilibrium in X and Y direction may be expressed as

$$\begin{cases} 2C \cdot \cos\alpha + 2S \cdot \sin\alpha = 2\int_0^{x_0} T_{yh(x)} dx \\ 2C \cdot \sin\alpha = 2S \cdot \cos\alpha + 2\int_0^{y_0} T_{xh(y)} dy \end{cases} \tag{14}$$

which leads to

$$\begin{cases} S = \dfrac{\sin\alpha \cdot 2\int_0^{x_0} T_{yh(x)} dx - \cos\alpha \cdot 2\int_0^{y_0} T_{xh(y)} dy}{2} \\ C = \dfrac{2\int_0^{x_0} T_{yh(x)} dx - 2S \cdot \sin\alpha}{2\cos\alpha} \end{cases} \tag{15}$$

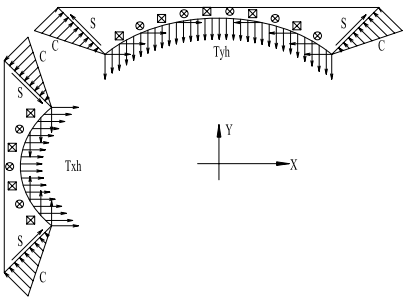

Fig.7 Membrane forces in rigid plates 1 and 3

5.4 Bending moment equilibrium

At the limit state, the force diagrams of each rigid plate are shown in Fig.8, where q_{12} is the loading capacity of plates 1and 2, and q_{34} is the loading capacity of plates 3 and 4.The bending moment equilibriums about axis O' and O may be expressed as

$$\begin{cases} M_{q12} + M_{Tvx} + M_{Thx} - 2C \cdot \cos\alpha \cdot \left[h_{0x} - \frac{1}{3}\left(\frac{B}{2} - y_0\right) \cdot \theta_x\right] - 2S \cdot \sin\alpha \cdot \left[h_{0x} - \frac{1}{2}\left(\frac{B}{2} - y_0\right) \cdot \theta_x\right] - M_{xu} = 0 \\ M_{q34} + M_{Tvy} + M_{Thy} - 2C \cdot \sin\alpha \cdot \left[h_{0y} - \frac{1}{3}\left(\frac{L}{2} - x_0\right) \cdot \theta_y\right] + 2S \cdot \cos\alpha \cdot \left[h_{0y} - \frac{1}{2}\left(\frac{L}{2} - x_0\right) \cdot \theta_y\right] - M_{yu} = 0 \end{cases} \tag{16}$$

where M_{12} and M_{34} are the bending moments induced by q_{12} and q_{34} respectively; M_{Thx} and M_{Tvx} are the bending moments induced by horizontal and vertical component forces of reinforcement in plates 1 and 2 respectively; M_{Thy} and M_{Tvy} are the bending moments induced by horizontal and vertical component forces of reinforcement in plates 3 and 4 respectively; and M_{ux} and M_{uy} are the bending resistance of the slab about the yield line respectively.

The values of M_{12}, M_{Thx}, M_{Tvx}, M_{34}, M_{Thy}, M_{Tvy}, M_{ux} and M_{uy} can be determined by

$$\begin{cases} M_{q12} = q_{12} \cdot A_{12} \cdot dy \\ M_{Thx} = 2\int_0^{y_0} T_{yh} \cdot \left[h_{0x} - \left(\frac{B}{2} - y_0 \right) \cdot \theta_x \right] \cdot dx \\ M_{Tvx} = 2\int_0^{y_0} T_{yv} \cdot \left[\frac{B}{2} - KB\sqrt{1 - \left(\frac{x}{KL} \right)^2} \right] \cdot dx + 2\int_{y_0}^{KB} T_{xv} \cdot \left(\frac{B}{2} - y \right) \cdot dy \\ M_{ux} = A_{sx} f_{yT} \left(h_{cx} - 0.59 A_{sx} \frac{f_{yT}}{f_{cT}} \right) \cdot (L - 2x_0) \end{cases} \quad \begin{cases} M_{q34} = q_{34} \cdot A_{34} \cdot dx \\ M_{Thy} = 2\int_0^{x_0} T_{xh} \cdot \left[h_{0y} - \left(\frac{L}{2} - x_0 \right) \cdot \theta_y \right] \cdot dy \\ M_{Tvy} = 2\int_0^{x_0} T_{xv} \cdot \left[\frac{L}{2} - KL\sqrt{1 - \left(\frac{y}{KB} \right)^2} \right] \cdot dy + 2\int_{x_0}^{KL} T_{xv} \cdot \left(\frac{L}{2} - x \right) \cdot dx \\ M_{uy} = A_{sy} f_{yT} \left(h_{cy} - 0.59 A_{sy} \frac{f_{yT}}{f_{cT}} \right) \cdot (B - 2y_0) \end{cases} \tag{17}$$

where A_{12} and A_{34} are the area of the rigid plates 1 or 2 and plate 3 or 4 respectively; d_y and d_x are the distances between gravity center of rigid plate 1 or 2 and axis O' and between plate 3 or 4 and axis O respectively; h_{cx} and h_{cy} are the distances between reinforcement and the upper side of the slab in Y and X direction respectively.

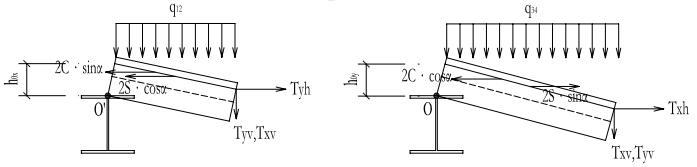

Fig.8 Forces on rigid plate 1 and 3

6. ULTIMATE LOAD CAPACITY OF SLAB

The load capacity of the elliptic part contributed from the vertical component force of reinforcement in the elliptic paraboloid, which can be obtained by

$$q_e = \frac{4\left[\int_0^{KL} T_{yv(x)} \cdot dx + \int_0^{KB} T_{xv(y)} \cdot dy \right]}{\pi \cdot (KL) \cdot (KB)} \tag{18}$$

By making the average load capacity of 4 rigid plates equal to the load capacity of the elliptic paraboloid, the following equation can be obtained as

$$q_e = \frac{q_{12} \cdot A_{12} + q_{34} \cdot A_{34}}{A_{12} + A_{34}} \tag{19}$$

where q_{12}, q_{34} and K can be determined by solving the equations of (16), (18) and (19).

Through averaging the load capacities of the rigid plates and the elliptic part over the whole area of the slab, the ultimate load capacity of slab can be determined by

$$q = \frac{2q_{12} \cdot A_{12} + 2q_{34} \cdot A_{34} + 4\left[\int_0^{KL} T_{yv(x)} \cdot dx + \int_0^{KB} T_{xv(y)} \cdot dy \right]}{LB} \tag{20}$$

7. CHECK THE STRENGTH OF THE CONCRETE COMPRESSION RING

It is possible that, the concrete compression ring may be crushed before the fracture of the reinforcement in the slab exerting membrane action to resist fire, so the strength of the

concrete compression ring should be checked to insure that the membrane action works. At the limit state, the stress of concrete compression ring at the section A-A or B-B will reach the ultimate compressive strength of concrete as shown in Fig.9. The equilibrium of the force in the concrete compression ring can be expressed as

$$\int_0^{K_x B} T_{xh(y)} \cdot dy = \left(\frac{1}{2} - K_x\right) \cdot B \cdot h_c \cdot f_{cT} \quad , \quad \int_0^{K_y L} T_{yh(x)} \cdot dx = \left(\frac{1}{2} - K_y\right) \cdot L \cdot h_c \cdot f_{cT} \tag{21}$$

K_x and K_y can be obtained by solving equation (21). If K_x or K_y is smaller than K, the concrete compression ring will be crushed early than the reinforcement. Taking the smaller one of K_x and K_y to substitute K in the equations (16), (18), (19) and (20), the ultimate load capacity of the slab under fire condition can be obtained.

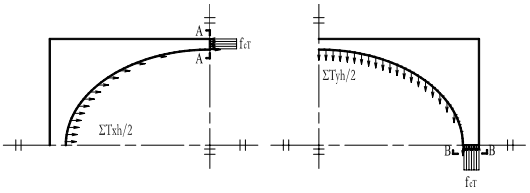

Fig.9 Force distribution over concrete compression ring at limit state

8. VERIFICATION

The method of modeling membrane action for fire-resistance of slab presented in this paper can be verified by previous tests performed by other researchers. The main facts of the slabs tested in fire are given in Table 1. The maximum deflection of the slabs measured in the tests and that predicted by various methods are compared in Table 2; and the test load and the load capacity predicted are compared in Table 3.

Table 1 The base situation of test slabs

Test No.	Reference	Slab size (m)	Effective thickness (mm)	Reinft dia. (mm)	Reinft spacing (mm)	Steel yield strength f_y (N/mm^2)	Max deflection recorded in the test (mm)	Test load (kN/m^2)
1	Sawczuk [1]	1.6*1.1	26	3	30	263	127	45.13
2		2.0*1.0	26	3	60	263	76	17.14
3	Taylor etal [1]	1.829*1.829	43.6	4.8	76.2	376	81	42.9
4		1.829*1.829	37.3	4.8	63.5	376	98	39.03
5		1.829*1.829	69	4.8	122	376	84	38.13
6	Ghoneim& MacGregor [11]	2.745*1.829	68.2	6.36	120	450	106	45.5
7		1.829*1.829	67.8	6.35	120	450	100	75
8	Cardington [11]	9.98*7.57		6	200	460	390	5.48

9	Guoqiang Li [12]	3*2	U76-305-610	4	150	300	130	10

Table 2 Comparison of maximum deflections between measured and predicted

Test No.	Maximum deflection measured w_{test}(mm)	Predicted by Bailey et al w_{Bailey}(mm)	Predicted by Guoqiang Li $w_{Guo\text{-}Qiang\ Li}$ (mm)	Predicted by the method proposed w_{new}(mm)	$\frac{w_{Bailey}}{w_{test}}$	$\frac{w_{\text{Guoqiang Li}}}{w_{test}}$	$\frac{w_{\text{new}}}{w_{test}}$
1	127	25	43	58.6	0.356	0.339	0.461
2	76	31	36	55	0.187	0.474	0.724
3	81	33.5	72	95.9	0.435	0.889	1.184
4	98	33.5	72	92.8	0.409	0.735	0.947
5	84	33.5	72	103.8	0.372	0.857	1.236
6	106			95.1			0.897
7	100			93.6			0.936
8	390			450.2			1.154
9	90			127			1.4

Table 3 Comparison of test load and predicted

Test No.	Test load q_{test} (mm)	Predicted by Bailey et al q_{Bailey} (kN/m^2)	Predicted by Guo-Qiang Li $q_{Guo\text{-}Qiang\ Li}$ (kN/m^2)	Predicted by the method proposed q_{new} (kN/m^2)	$\frac{q_{Bailey}}{q_{test}}$	$\frac{q_{\text{Guoqiang Li}}}{q_{test}}$	$\frac{q_{\text{new}}}{q_{test}}$
1	45.13	45.24	44.18	34.4	1.002	0.979	0.762
2	17.14	14.21	14.63	17.85	0.829	0.854	1.041
3	42.9	35.27	33.60	41.18	0.822	0.783	0.960
4	39.03	40.03	35.51	48.75	1.026	0.910	1.249
5	38.13	31.22	31.22	31.18	0.819	0.819	0.818
6	45.5			41.89			0.897
7	75			58.3			0.735
8	5.48			5.318			0.970
9	10			7.13			0.713

Tests 1-7 were preformed at ambient temperature, and Test 8, 9 were preformed at high temperatures. Because the characteristic limited elongation of the reinforcement at high temperature is larger than that at ambient temperature, the value of characteristic limited elongation of the reinforcement in test 1-7 had been reduced by 30% based on statistical regression analysis.

According to the comparisons, it is shown that the method proposed in this paper can give more reasonable prediction to the maximum deflection and load-bearing capacity of slabs exposed to fire.

9. CONCLUSION

Large deflection is not allowed in the traditional design of reinforced concrete slabs at ambient temperature. However, in fire condition, large deflection can induce membrane action which can keep stability of slabs and avoid collapse. Based on the membrane action model presented by Guo-Qiang Li, a new method to model the membrane action is developed in this paper. This new method can be used for simply supported reinforced concrete slab with continuous reinforcement in two directions. For the slabs, with that predicted horizontal restraint on the boundaries, this method is also applicable with conservation. The good agreement between the test results and predictions provides the validation of this new method.

REFERENCE

[1] C.G. Bailey, "Membrane action of slab/beam composite floor systems in fire". Engineering Structure 26(2004) 1691-1703.
[2] C.G. Bailey and D.B. Moore, "The structural behaviour of steel frames with composite floor slabs subjected to fire: Part 1: Theory". The Structural Engineer 2000, Vol. 78(11):19-27.
[3] Colin G. Bailey, "Membrane action of unrestrained lightly reinforced concrete slabs at large displacements". Engineering Structure 23(2001) 470-483.
[4] S. Lamont, A.S. Usmani and D.D. Drysdale, "Heat transfer analysis of the composite slab in the Cardington frame fire tests". Fire Safety Journal 36 (2001) 815-839.
[5] A.S. Usmani and N.J.K. Cameron, "Limit capacity of laterally restrained reinforced concrete floor slabs". Cement & Concrete Composites 26 (2004) 127-140
[6] Guo-Qiang Li, Shi-Xiong Guo, and Hao-Sheng Zhou, "Modeling of membrane action in floor slabs subjected to fire". Engineering Structures 29 (2007) 880-887.
[7] Hao-Sheng Zhou, "Membrane action in floor slabs of steel structures and its simple fire design method", Tongji University, Shanghai, China, pp57-58.
[8] Eurocode 2: Design of concrete structures. Technical Report ENV 1992-1-1, Brussels, European Committee for Standardisation, 1992.
[9] Guo-Qiang Li, Ying-Zhi Yin and Shou-Chao Jiang, "Analysis of the temperature distribution in composite slabs subjected to fires". Industrial Construction, No. 12, Vol.29, 1999.
[10] Technical Code for Fire Safety of Steel Structure in Buildings. CECS 200:2006.
[11] Zhaohui Huang, Ian W. Burgess and Roger J. Plank, "Modeling Membrane Action of Concrete Slabs in composite Building in Fire. II: Validations". Journal of Structural Engineering, (ASCE) 0733-9445(2003)129:8(1103).
[12] Shou-Chao Jiang, Guo-Qiang Li, Hong-Yu Zhou and Qi Wang, "Experimental study of behavior of steel-concrete composite slabs subjected to fire". Journal of Building Structure, Vol. 25, No.3, June 2004: pp45-50.

FUNDAMENTAL BEHAVIOUR AND OVERALL STABILITY OF STEEL-CONCRETE COMPOSITE COLUMNS UNDER FIRE LOADING

SANGDO HONG[1] and AMIT H. VARMA[2]

ABSTRACT

This paper presents: (i) a unique experimental approach for measuring the fundamental moment-curvature-temperature [M-ϕ-T] behavior of structural members, and (ii) a simple analytical approach for using this fundamental behavior to predict the overall behavior and stability of structural columns under fire loading. Both the experimental and analytical approaches were implemented for steel-concrete composite members, namely, concrete filled steel tubes (CFT) beam-columns

The experimental investigations were conducted using a unique testing approach involving innovative radiation-based heating and photogrammetry-based sensing techniques. The experimental results included: (i) the detailed thermal response of the heated CFT section, and (ii) the fundamental M-ϕ-T response of the heated failure segment of the CFT beam-columns. Several CFT beam-columns were tested, and the results were used to evaluate the effects of various material, geometric, loading, and fire protection parameters on the fundamental behavior.

The analytical approach uses the fundamental M-ϕ-T behavior to predict the overall structural behavior and inelastic buckling failure of columns subjected to axial load (P) and elevated temperatures from fire loading effects. It consists of three parts: (i) The first part conducts a 2D heat transfer analysis of the cross-section. (ii) The second part conducts a fiber-model analysis of the cross-section to predict its M-ϕ-T behavior. And, (iii) the third part conducts inelastic column buckling analysis using Newmark's method, which was modified to use the section M-ϕ-T behavior at elevated temperatures. The approach was validated by using it to predict the standard fire behavior of several CFT column specimens tested by other researchers.

[1] Research Engineer, Indiana Department of Transportation, West Lafayette IN USA,
email: shong@indot.in.gov.
[2] Assistant Professor, Purdue University, Department of Civil Engineering, West Lafayette IN USA,
email: ahvarma@purdue.edu.

The experimental approach is recommended for determining the fundamental M-ϕ-T behavior of structural members, and the analytical approach is recommended for simulating the overall behavior and stability of structural columns subjected to fire loading conditions.

1. INTRODUCTION

The current building design provisions (e.g., IBC 2005[1]) emphasize prescriptive fire resistant design. These design provisions specify required fire resistance rating (FRR) values for the individual building components based on construction type, occupancy, and function. The design FRR values for building components can be determined experimentally by: (a) testing them individually according to the ASTM E119 (ASTM 2003)[2] standard fire test, or (b) using standard calculation methods based on the results of E119 tests and provided in design guides (e.g. IBC 2005). The prescriptive design provisions do not account for the overall thermal and structural behavior of the complete structure during fire loading. Hence, they do not necessarily indicate structural strength or stability during a fire event (Iding 2003[3]). Currently, there is a significant need for structural performance-based fire resistant design provisions that quantify structural stability under fire loading. This leads to a critical need for knowledge of the *fundamental behavior of structural components and system under fire loading*.

Steel-concrete composite structures with concrete filled steel tube (CFT) columns are gaining popularity in the U.S. A potential advantage of such structures is the enhanced fire resistance of the CFT columns. Researchers from Canada, Japan, and China have conducted significant research on CFT columns subjected to fire loading (Kodur *et al.* 2000[4], Sakumoto *et al.* 1994[5], Han *et al.* 2002[6]). However, most of this research is firmly rooted in the current fire resistant design provisions. The results from these studies are adequate for determining the standard fire resistance (FRR) of CFT columns, but they do not provide knowledge of their fundamental behavior under fire loading.

A research project focusing on the fundamental behavior of CFT columns and beam-columns under fire loading has been conducted at Purdue University. This project consists of three phases: (1) Development of 3D finite element models for predicting standard fire behavior. (2) Experimental investigations of the fundamental F-δ-T behavior, and the influence of various geometric, material, loading, and fire protection parameters. (3) Development and verification of a fiber model based analytical approach (utilizing the fundamental F-δ-T behavior) for predicting inelastic stability failure of columns under fire loading. The results from all three phases are summarized in detail in Hong (2007)[7]. This paper summarizes the results from phases 2 and 3.

2. EXPERIMENTAL SETUP, TEST CONDITIONS, AND RESULTS

The experimental investigations focused on the behavior of CFT beam-column specimens with external fire protection subjected to combined axial, thermal, and flexural loading. The experimental test matrix included thirteen CFT beam-column specimens with different tube widths (254 and 305 mm), width-to-thickness b/t ratios (32 and 42), and concrete infill strengths (48 and 68 MPa). The steel tubes for all CFT specimens were made from A500 Grade-B material with 345 MPa nominal yield stress. The steel tubes of the same type (width and b/t ratio) were made from the same heat. The concrete infills with same strength were also from the same concrete mix batches. The steel and concrete material properties (uniaxial stress-strain relationships) were measured according to applicable ASTM

standards. Most of the specimens were fire protected with gypsum plaster with similar thickness, but some specimens had no fire protection.

These specimens were tested by subjecting them to axial loading (15 or 30 % of axial capacity P_o), heating duration (0, 1, or 2 hours), and monotonically increasing flexural loading. *Three* of the specimens were tested at ambient conditions (0 hours of heating) to provide control data for comparison and evaluation. The remaining ten specimens were tested after heating to elevated temperatures. The experimental results included: (a) the lateral load-displacement responses of the CFT beam-column specimens, and (b) the M-ϕ-T responses of the heated plastic hinge regions at the base of the specimens. The experimental results were used to evaluate the effects of various materials, geometric, loading, and fire protection parameters on the M-ϕ-t behavior of the CFT beam-column specimens.

Figure 1 shows the photograph of experimental setup. As shown in the photograph, the CFT beam-column specimens were fixed at the base (foundation) and free at the top. The foundation consists of base concrete blocks that are post-tensioned vertically to the strong floor and horizontally to the CFT specimen. The length of the specimen from the foundation to the free end was equal to 1.828 meters. The testing procedure was as follows: (1) The CFT beam-column specimens were subjected to axial loading (15 or 30% of P_o), which was maintained constant throughout the experiment. (2) The segments at the base of the specimens (with length equal to section width *b*) were subjected to heating following the E119 fire T-t curve. (3) After heating for the specified duration (1 or 2 hours), the specimens were subjected to monotonically increasing lateral loading.

The deformations of the heated base segments subjected to combined axial, thermal, and flexural loading were measured using a specially designed digital imaging system. The focus was on measuring the axial deformations (ε) and curvatures (ϕ) of the base segments. Thus, the fundamental moment-curvature-temperature (M-ϕ-T) responses of the base segments of CFT beam-column specimens were measured experimentally.

The thermal loading was applied to the base segments of the CFT beam-column specimens using radiant heaters. The heating (T-t curves) applied to the exterior surfaces of the CFT specimens was controlled by a temperature control network. The temperature control network consists of four elements: a temperature controller, power controller, heating unit, and temperature sensor. A more detailed discussion of the heaters and control network is presented in Hong (2007).

A close-range photogrammetry based digital imaging system was used to measure the longitudinal and transverse displacements of target points located within the inelastic failure segments of the CFT beam-column specimens. The digital imaging system was needed because the temperatures were too high to use conventional voltage-based sensors, for example, LVDTs or potentiometers. A more detailed discussion of the setup, calibration, and verification of the digital imaging system is provided in Hong (2007).

Small (6 mm diameter) holes were drilled on all four sides of the steel tube for thermocouple installation prior to placing concrete. Heat-shrink tubes were placed on the bare thermocouple wires in order to provide protective insulation against electrical interference from the steel tube and water in the concrete. Ceramic fiber strips were also placed on the thermocouple near the steel tube in order to protect the thermocouple from high temperatures and electrical interference. Figure 2 shows the holes and thermocouple locations on all sides of the steel tube. Additional small (6 mm diameter) holes were drilled in the sides of the steel tubes to provide vent holes to release water vapor pressure.

Figures 2-4 show the measured moment-curvature (M-ϕ-T) responses of the inelastic failure segments (plastic hinges) of Specimens 1-3. The specimen details including the material, geometric, axial load level, fire protection, and heating parameters are summarized in Table 1. These specimens focus on the effects of heating (1 and 2 hours), axial load level

(P/P_o), and b/t ratio on the behavior of CFT beam-column specimens. The M-ϕ–T responses shown in Figures 2-4 are for the cases of: (1) elevated steel temperature of about 300 ^oC with axial load equal to 16% and b/t ratio of 34, (2) elevated steel temperature of about 303 ^oC with axial load equal to 36% and b/t ratio of 34, and (3) elevated steel temperature of about 471 ^oC with axial load equal to 17% and b/t ratio of 42, respectively. The curvatures of the failure segments were calculated using the digital imaging systems and procedure mentioned above. As shown in Figures 2-4, the measured moment-curvature (M-ϕ-T) responses are initially linear followed by some nonlinearity due to concrete cracking and material nonlinearity at elevated temperatures. Additional details and evaluation of the experimental results are presented in Hong (2007).

3. DEVELOPMENT AND VALIDATION OF M-ϕ-T RESPONSE ANALYSIS

The fiber modeling approach was used to predict the section M-ϕ-T responses of the CFT beam-column specimens. The approach consisted of two parts: (i) The first part conducted a 2D heat transfer analysis of the composite cross-section using heat balance equations, and (ii) the second part determined the section M-ϕ–T for the given axial load (P) and temperature distributions from part-1. The results from the experimental investigations mentioned above (in Section 2.0) were used to validate the fiber modeling approach.

The fiber models of the CFT beam-column specimens were developed using the material, geometric, loading, and heating duration parameters for the tested specimens. The empirical σ-ε-T model developed by Poh (2001)[8] was used for the steel fibers, and the σ-ε-T model developed by Lie and Irwin (1995)[9] was used for the concrete fibers. The models were analyzed for the same loading and heating used as the test specimens.

Figures 2-4 show the comparisons of the analytical and experimental M-ϕ–T curves for three of the CFT beam-column specimens. The material, geometric, loading, fire protection, and heating parameters for these specimens were provided in Table 1. As shown, all three specimens were provided with gypsum plaster fireproofing material. Specimens-1 and 2 were subjected to one hour of heating leading to steel surface temperature of 300°C. Specimen 3 was subjected to two hours of heating leading to steel surface temperature of 500°C. Specimens 1, 2, and 3 had axial load levels equal to 16%, 36%, 17%, respectively.

The comparisons in Figures 2-4 indicate that the analytical results compare favorably with the experimental measurements. The fiber model approach can predict the M-ϕ-T behavior of CFT members with reasonable accuracy. Additional details and comparisons of all the analytical and experimental results are reported in Hong (2007).

4. ANALYTICAL PREDICTIONS OF STANDARD FIRE BEHAVIOR

A fiber-based analytical approach was developed to predict the overall behavior and stability failure of columns under standard fire loading. This approach was as an extension of the fiber modeling approach presented above. It consisted of three parts, where the first two parts were the same as those mentioned above:

(1) The first part determined the thermal response of the column by conducting 2D heat transfer analysis of the cross-section using heat balance equations.

(2) The second part determined the fundamental moment-curvature (M-ϕ–T) response of the cross-section for the given axial load (P) and temperature distributions from part-1.

(3) The third part determined the structural behavior of the column using Newmark's method of inelastic buckling analysis, which was modified to account for the elevated temperature distributions from part-1 and the section M-ϕ-T response from part-2.

4.1 2D Heat Transfer and Section Moment-Curvature Analysis

A fiber-model of the CFT column cross-section was developed by discretizing it into a grid of steel and concrete fibers. This fiber model was used to conduct the 2D heat transfer analysis by writing finite difference approximations of the heat balance equations for each node of the grid. The equations are summarized in Hong (2007), and not included here for brevity. These equations used temperature-dependent thermal properties for the steel and concrete, which are also summarized in Hong (2007).

At each time step $t_{i,}$, the section moment-curvature M-ϕ–T behavior was computed using: (a) fiber model of the CFT cross-section, (b) the temperature distribution T_{fib} over the section, and (c) temperature-dependent uniaxial stress-strain-temperature (σ-ε-T) relationships for the steel and concrete materials. For each fiber of the CFT cross-section, the fiber area (A_{fib}), distance from centroid (y_{fib}), temperature (T_{fib}), and associated material σ-ε-T curve are stored.

The empirical uniaxial σ-ε-T model developed by Poh (2001) was used for conventional strength steel. The Sakumoto et al. (1994) σ-ε-T model was used for fire resistant (FR) steel. The Lie and Irwin (1995) σ-ε-T model was used for the concrete infill of the CFT columns. The concrete fibers were assumed to have no stress capacity in tension. The thermal expansion models (α_s-T) for steel and (α_c-T) concrete were assumed based on values reported in the literature (e.g., Lie and Irwin (1995) and preliminary evaluations presented in Hong (2007). The algorithm for calculating the section M-ϕ-T behavior is presented in detail along with a flowchart in Hong (2007). It is not included here for brevity.

4.2 Column Analysis at Elevated Temperatures

The overall behavior of CFT columns under constant axial load (P) and standard fire loading was simulated using Newmark's method of inelastic column analysis. The method was modified to account for the effects of elevated temperatures and the section M-ϕ-T behavior predicted using fiber models of the cross-section. The algorithm for predicting the overall behavior of CFT columns is summarized below. The corresponding flowchart is presented in more detail in Hong (2007).

- The column length is divided into several (n) segments. A slice or station point is assumed to be located at the center of each segment. A fiber model of the CFT cross-section is assumed to be located at each slice or station point.
- The total time duration is divided into smaller time steps (Δt), which were calculated using equations for numerical stability of the thermal solutions.
- At each time step (t_j) of heating, the temperature distribution through the CFT cross-section is calculated using 2D heat transfer analysis and the section M-ϕ-T behavior is calculated using fiber model analysis.
- A lateral displacement profile is assumed for the column length. This specifies the assumed lateral displacements ($v_{i,j\text{-}ass}$) at all stations (j) along the length.
- The moment at each station ($M_{i,j}$) is computed as the axial load (P) multiplied by the assumed lateral displacement ($v_{i,j\text{-}ass}$). The corresponding curvature ($\phi_{i,j}$) and centroidal strain ($\varepsilon_{cen\text{-}i,j}$) are obtained from the section M-ϕ-T response computed earlier.

- The station curvatures ($\phi_{i,j}$) are numerically integrated to compute the average slope ($\theta_{i,j}$) at each station. The slopes are integrated once to compute the lateral deflections ($v_{i,j}$) at each station.
- If the computed lateral displacements ($v_{i,j}$) are within tolerance limits of the assumed lateral displacements ($v_{i,j\text{-}ass}$), then the analysis has converged. Otherwise, the computed lateral displacements should be assumed, and the procedure repeated.
- After the analysis converges, the axial displacement of each station ($u_{i,j}$) is computed using Equation (1). The total axial displacement (u_i) is computed using Equation (2).

$$u_{i,j} = \varepsilon_{cen\text{-}i,j,} \bullet \Delta L + v_{i,j} (1\text{-}\cos \theta_{i,j}) \quad (1)$$

$$u_i = \sum_{j=1}^{n} u_{i,j} \quad (2)$$

- The time step is incremented, and the computational procedure is repeated for the next time step.

If convergence cannot be achieved because the computed moment at any station is greater than the peak moment capacity of the section from the fiber model analysis, then the column has reached its inelastic buckling failure limit. Thus, the column fails by inelastic column buckling at the time instant (t_j) when static force equilibrium cannot be achieved.

4.3 Validation of Analytical Approach

The fiber-based analytical approach was used to predict the standard fire behavior of CFT columns tested by researchers around the world. Fifteen CFT columns with a wide range of material, geometric, loading, and fire protection parameters were included in the test matrix. The analytical results and comparisons with experimental results for all these fifteen CFT columns are presented in detail in Hong (2007). This paper summarizes the results for four CFT columns that were selected from the complete analytical matrix.

Table 2 summarizes the details of CFT Columns 1-4. It includes the values of various parameters for these specimens. As shown, Columns-1, 3, and 4 were made from conventional steel tubes, while Column-2 was made from fire resistant (FR) steel. The specimens were about 300 – 350 mm. in cross-section with different width-to-thickness (b/t) ratios. The measured steel yield stress (f_y) and concrete strength (f'_c) for these specimens are also given in Table 2. The columns had different fire protection conditions as indicated in the Table. Additionally, Column-1 was tested by Lie and Irwin (1995) at the National Research Council in Canada. Columns-2 and 3 were tested by Sakumoto et al. (1994) in Japan, and Column-4 was tested by Han et al. (2002) in China.

Column-1

Column -1 is representative of several CFT columns tested by NRC researchers [Lie and Stringer (1994)[9], Lie and Irwin (1995)]. It was subjected to constant axial load followed by standard E119 fire loading. The column was tested with fix-fix end conditions. Since, the column end conditions were fixed, only the effective length equal to half the total column length (0.5L) was modeled. The Poh (2001) empirical σ-ε-T model was used for the steel fibers, and the Lie and Irwin (1995) empirical σ-ε-T model was used for the concrete fibers. The thermal expansion coefficients for the steel and concrete were assumed based on the preliminary analysis and sensitivity studies conducted as part of this research (Hong 2007).

Figure 5 shows comparisons of the analytical and experimental axial displacement-time curves (u-t) curves for the column. This was the primary experimental result reported by

the researchers. Figure 5 also includes the u-t curve predicted by the 3D finite element analysis of Column-1.

The development and verification of 3D finite element models for the CFT columns was presented earlier in Varma et al. (2005)[11] and are included in detail in Hong (2007). The comparisons in Figure 5 show that the analytical predictions using the fiber-based approach compare favorably with the experimental results and the predictions from the 3D finite element analyses. Additional comparisons of the stress states predicted by the fiber-based analytical approach and the 3D finite element analysis are presented in Hong (2007). These comparisons indicate that the stress states predicted by the two analytical approaches compare favorably.

Columns-2 and 3

Columns-2 and 3are representative of several CFT columns tested by Sakumoto et al. (1994) at the Japan Building Research Institute (JBRI). As shown in Table 2, Column -2 was made from FR steel and Column-3 was made from conventional steel. These columns were tested with pin-pin end conditions. Hence, their complete lengths were modeled. The behavior of FR steel (Specimen-2) was modeled using the empirical σ-ε-T developed by Sakumoto et al. (1994). The behavior of conventional steel (Specimen-3) was modeled using the Poh (2001) σ-ε-T model. In both cases, the concrete infill was modeled using the Lie and Irwin (1995) concrete material model. The rest of the details were the same as that for Column-1.

The comparisons of the analytical and experimental axial displacement-time curves (u-t) curves for the Columns-2 and 3 are shown in Figures 6 and 7, respectively. These figures also include the u-t curves predicted by the 3D finite element analyses of Columns -2 and 3. The comparisons in Figures 6 and 7 show that the analytical predictions using the fiber-based approach compare favorably with the experimental results and the predictions from the 3D finite element analyses.

Column-4 was representative of the several CFT columns tested by Han et al. (2003) in Tianjin, China. The details of the column are noted in Table 1. It was also tested with pin-pin end conditions, and the complete length was modeled. The empirical σ-ε-T model developed by Poh (2001) was used for the steel fibers, and the empirical σ-ε-T model developed by Lie and Irwin (1995) was used for the concrete fibers. The rest of the model details were the same as those noted above for other column specimens.

Figure 8 shows the comparisons of the analytical and experimental u-t curves for Column -4. The figure also includes the u-t curve predicted by the 3D finite element analysis of Column-4. The figure indicates that the u-t curves predicted by the fiber model analyses compare reasonably with experimental results and the predictions from the 3D finite element analysis.

The results in Figures 5-8 indicate that the analytically predicted time to failure (i.e., the time when the axial deformations start increasing rapidly) compare reasonably with the experimental values. These numerical comparisons are not included here for brevity, but are presented in detail in Hong (2007).

5. SUMMARY AND CONCLUSIONS

This paper presented an experimental testing approach for determining the fundamental force-deformation-temperature behavior of structural members. The approach included the use of: (a) innovative heating and control to apply the thermal loading, and (b) digital imaging system for measuring deformations at elevated temperatures. The

experimental results for three CFT beam-columns were presented in detail. These results illustrated the effects of heating and axial load level on the fundamental M-ϕ-T behavior of CFT. Additional results and evaluations are presented in Hong (2007). The experimental approach presented in the paper can be used to determine the fundamental M-ϕ-T behavior of structural members. This information can be used to calibrate macro finite element models for predicting member behavior and stability under fire loading.

This paper also presented a simple fiber-based analytical approach for predicting the thermal and structural behavior of columns under standard fire loading. The approach was implemented and validated for CFT columns using experimental results (thermal and structural) for the fire behavior of CFT members developed as part of this research, and those developed by other researchers from around the world. The thermal and structural behavior predicted by the fiber-based analytical approach compare favorably with corresponding experimental results. The results from the fiber-based analytical approach also compare favorably with the results from detailed 3D finite element analysis of the CFT columns under standard fire loading.

ACKNOWLEDGEMENT

This research project was sponsored by the National Science Foundation (Grant Nos. CMS-0453913 and CMS-0601201) and also by the U.S. Department of Commerce through the Extramural Fire Research Grants Program administed by the National Institute of Standards and Technology – Building and Fire Research Laboratory. The steel tubes for the test specimens were donated by Bull Moose Tube.

REFERENCES

[1] IBC. (2005). *International Building Code*, Intl. Code Council, Inc., Falls Church, VA.
[2] ASTM. (2003). "Standard Test Methods for Fire Tests of Building Construction and Materials," *E119*, American Society for Testing & Materials, W. Conshohoken, PA
[3] Iding, R.H. (2003). "Calculating Structural Response to Fire". *Fire Protection Engineering*. Society of Fire Protection Engineers (SFPE), Sp. 2003, pp. 18 - 23.
[4] Kodur, V.K.R. and Mackinnon, D.H. (2000). "Design of Concrete-Filled Hollow Structural Steel Columns for Fire Endurance," *Eng. Journal*, 1st Qtr., pp. 13-24.
[5] Sakumoto, Y., Okada, T., Yoshida, M., and Tasaka, S. (1994). "Fire Resistance of Concrete-Filled, Fire-Resistant Steel-Tube Columns." *J. of Matrls. In Civil Eng.*, 6(2), 169-184.
[6] Han, L.H., Yang, Y.F., Xu, L. (2002) "An experimental study and calculation on the fire resistance of concrete-filled SHS and RHS columns" *Journal of constructional steel research*. 59 pp427-452.
[7] Hong, S. (2007). "Fundamental Behavior and Stability of Concrete Filled Tubes (CFTs) Members Under Fire Loading", Ph.D. dissertation, School of Civil Engineering, Purdue University, West Lafayette, IN., May 2007
[8] Poh, K.W. "Stress-strain-temperature relationship for structural steel." Journal of Materials in Civil Engineering. Vol. 13 pp 371-379, 2001
[9] Lie, T. T., and Irwin, R. J. (1995). "Fire Resistance of Rectangular Steel Columns Filled with Bar-Reinforced Concrete." *J. of Struct. Eng.,* 121(5), 797-805.

[10] Lie, T.T. and Stringer, D.C. (1994). "Calculation of Fire Resistance of Steel Hollow Structural Steel Columns Filled with Plain Concrete," *Canad. Jour. of Civil Eng.*, 21(3), pp. 382-385.
[11] Varma, A.H., Srisa-Ard, J., and Hong, S. (2004). "Analytical Investigations of the Fire Behavior of Concrete Filled Steel Tube (CFT) Columns," *Proceedings of the ASCE Structures Congress* – 2004, proceedings on CD-ROM, ASCE, Reston, VA, 10 pp.

Table 1 CFT Beam-Column Specimen Details

Col.	Cross-Section	b/t	f_y MPa	$f'c$ MPa	Load (P/P_o)	Heating (hours)	Steel Temp	Fire-protection
1	254x8mm	34	330	48	16	1 hr	300	gypsum
2	254x8mm	34	330	48	36	1 hr	303	gypsum
3	254x6mm	42	372	48	17	2 hrs	471	gypsum

Table 2 CFT Column Details

Col.	Cross-Section	Length *mm*	Bar-reinforced	f_y MPa	$f'c$ MPa	Load kN	Steel type	Fire-protection
1	305x6.3mm	3810	4-25 mm	350	47	2000	Conv.	none
2	300x9.0mm	3500	-	358	38	2020	FR	intumescent
3	300x9.0mm	3500	-	358	38	2020	Conv.	ceramic
4	350x7.7mm	3810	-	284	19	2700	Conv.	spray

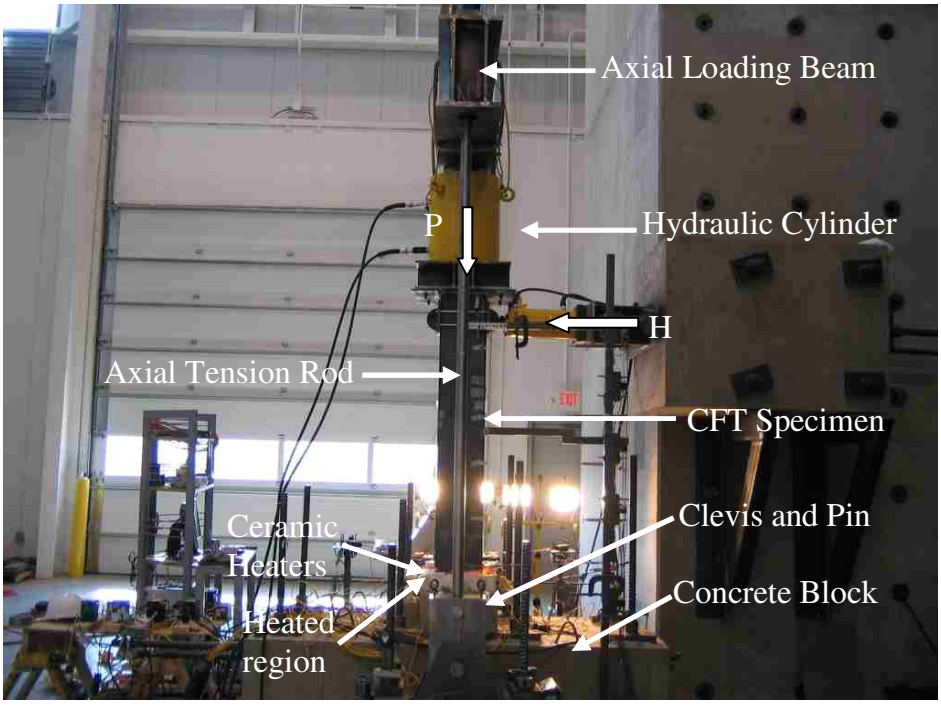

Fig. 1 - Photogragh of experimental set up

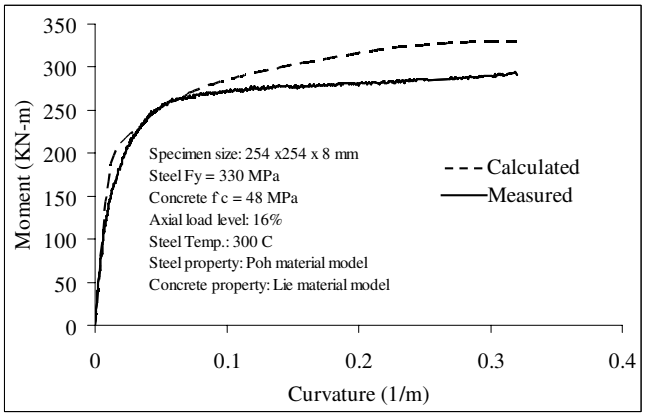

Fig. 2 - Comparison of predicted and measured P-M-ϕ-T of CFT beam-column Specimen-1

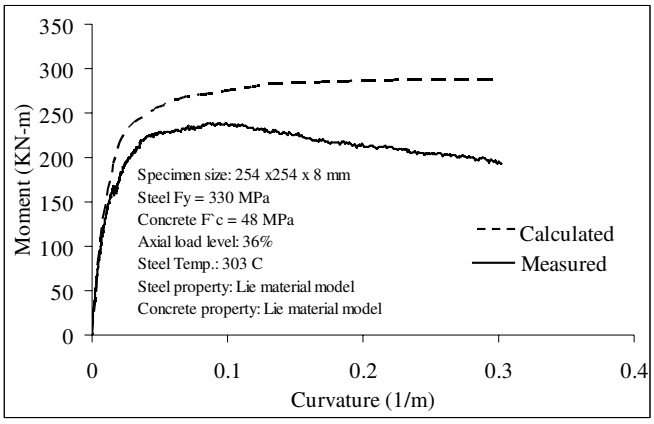

Fig. 3 - Comparison of predicted and measured M-ϕ-T behavior of CFT beam-column Specimen-2

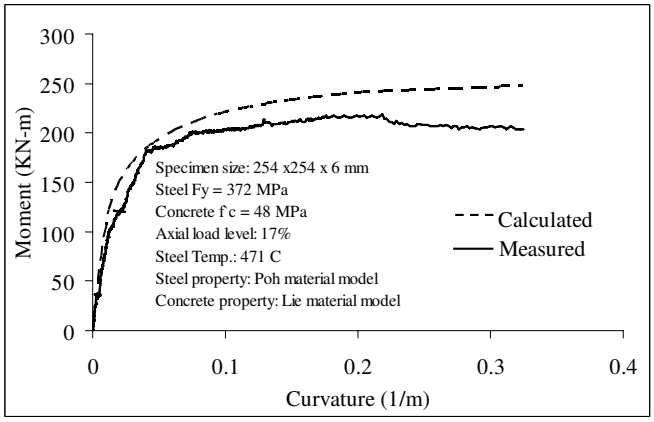

Fig. 4 - Comparison of predicted and measured M-ϕ-T behavior of CFT beam-column Specimen-3

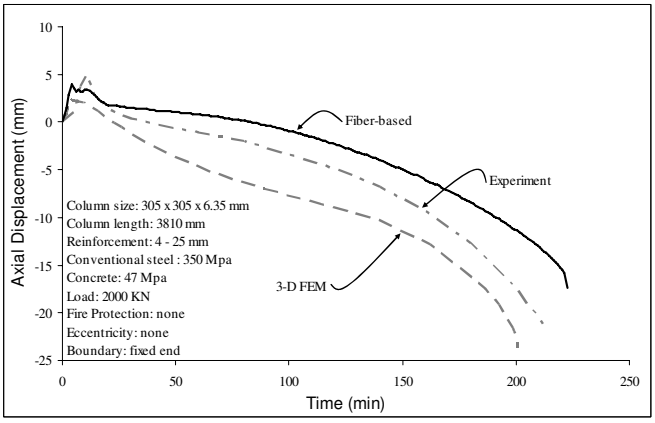

Fig. 5 - Comparison of predicted and measured axial deformation (u-t) for Column-1

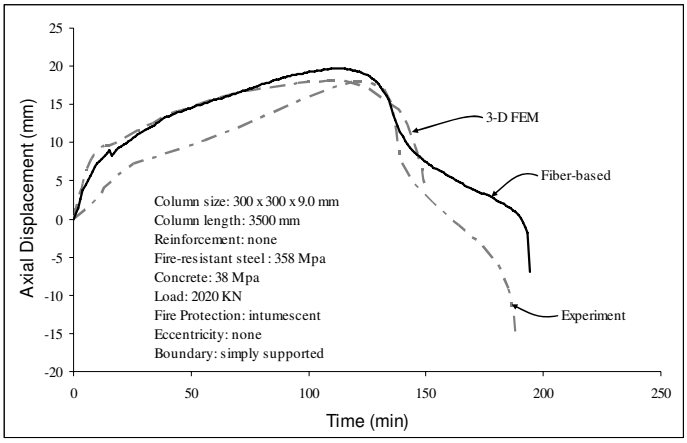

Fig. 6 - Comparison of predicted and measured axial deformation (u-t) for Column-2

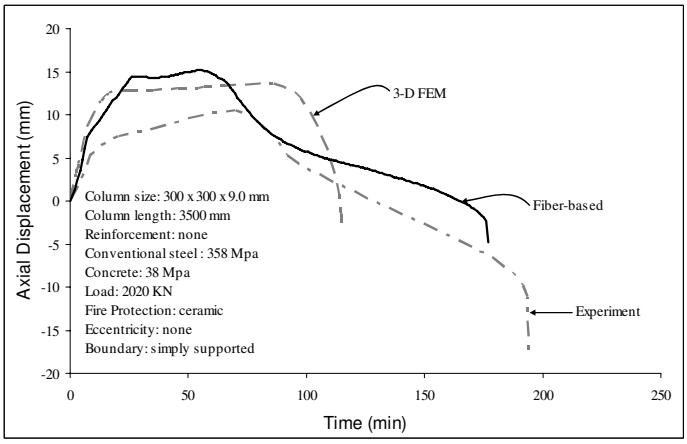

Fig. 7 - Comparison of predicted and measured axial deformation (u-t) for Column-3

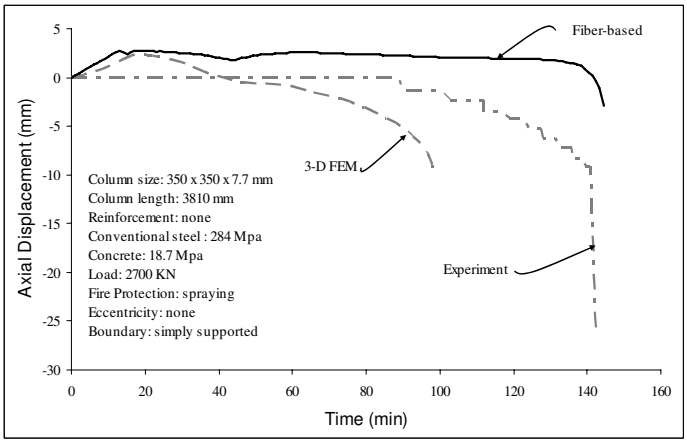

Fig. 8 - Comparison of predicted and measured axial deformation (u-t) for Column-4

CHARACTERISTICS ANALYSIS OF THE PERFORMANCE DESIGN EQUATIONS FOR THE FIRE RESISTANCE OF CONCRETE-FILLED STEEL TUBE COLUMNS

SUHEE PARK[1], KYUNGCHUL SONG[2], KYUNGSOO CHUNG[3] and SUNGMO CHOI[4]

ABSTRACT

The purpose of this study is to analyze the characteristics of the performance design equations provided in various countries for the fire resistance of concrete-filled steel tube structures and to evaluate the safety of the estimation equation provided in Korea. In this study, we compared and evaluated the safety of the performance design equation for concrete-filled steel tube columns provided in various countries in terms of estimating the fire-resistance within their application scope and the influence of each factor. We also analyzed the characteristics of each design equation beyond the scope of application. For this, we collected fire-resistance experiment data for more than ninety concrete-filled steel tube column specimens from 14 studies conducted in Korea and abroad. We made a comparative evaluation of the characteristics of the fire-resistance design equations provided in the U.S and Japan and the estimation equation provided in Korea. Within the scope of application, the ratio of fire-resisting time drawn from the AISC design equation to that obtained from experiment (FR_{de}/FR_{exp}) under the influence of various factors was approximately 1.0, while it was 0.7-0.8 in Korea's equation, presenting that it would yield safe side. The AIJ equation showed larger standard deviations ranging from 0.6 to 1.0 depending on influential factor. Beyond the scope of application, fire-resisting time estimated by the AISC equation increased 1.06-2.58 times as long as the value obtained from experiment as width-length ratio increased, whereas the AIJ and Korea's equations produced more conservative estimation of 0.22 and 0.38, respectively. Deviation from experiment increased significantly in the AIJ equation as sectional dimension and width-length ratio changed, while Korea's equation estimated fire-

[1] Ph. D candidate, University of Seoul, Department of Architectural Engineering, Seoul, 130-743, Korea, email: heehee104@empal.com.
[2] Master course, University of Seoul, Department of Architectural Engineering, Seoul, 130-743, Korea, email: watch48@naver.com.
[3] Senior researcher, Research Institute of Industrial Science & Technology, 79-5, Hwasung, Kyonggi-do, 445-813, Korea, email: kschung@rist.re.kr.
[4] Professor, University of Seoul, Department of Architectural Engineering, Seoul, 130-743, Korea, email: smc@uos.ac.kr.

resisting time more conservatively. All the 3 equations estimated longer fire-resisting time than experiment as concrete strength increased.

Keywords: Fire Resistance, Concrete-Filled Steel Tube Column, Performance Design Equations, Effect Factor, Constant Axial Load, High Temperature

1. INTRODUTION

Concrete-filled steel tube (CFT) columns yield excellent structural performance under strong axial loads because steel tube controls concrete and the concrete prevents the local buckling in the steel tube. And, the columns yield a certain degree of fire-resistance thanks to the heat storage effect of the concrete which fills the steel tube. Having been commenced in Europe in early 1970s and 1980s as part of composite structure research, the studies on the fire-resistance of Concrete-filled steel tube structures have been conducted in advanced countries including Japan ((L.H. Han, 2003)[7], (V.K.R. Kodur, 1998)[11]). In Korea, experimental and analytical studies on non-covered cylinder and square CFT columns have been carried out (D.K. Kim et al, 2005)[16]. The performance design equations for the fire-resistance of CFT columns are provided in various advanced countries. The equations are established as design guidelines in some countries. In others, although they are not established as design guidelines, the application of the equations is allowed if their performance is verified.

The purpose of this study is to analyze the characteristics of the performance design equations provided in various countries for the fire resistance of CFT columns and to evaluate the safety of the estimation equation provided in Korea. In this study, we compared and evaluated the safety of the performance design equations for concrete-filled steel tube structures provided in various countries in terms of estimating the fire-resistance within their application scope and the influence of each factor. We also analyzed the characteristics of each design equation beyond the scope of application. For this, we collected fire-resistance experiment data for more than ninety CFT column specimens from 14 studies conducted in Korea and abroad. We made a comparative evaluation of the characteristics of the fire-resisting design equations provided in the U. S and Japan and the estimation equation provided in Korea.

2. EXPERIMENT DATABASE & FIRE-RESISTANCE DESIGN EQUATIONS

2.1 Experiment database for the fire-resistance of CFT columns

Fire-resistance experiment data for more than ninety cylinder and square CFT columns were collected from 14 studies conducted in Korea and abroad [2-13, 16, 18] to be used as verification data for the characteristics analysis of fire-resisting design equations as shown in Table 1.

Table. 1 – Scope of application of experiment data

Factors		Cylinder CFT	Square CFT
Scope of application	Sectional dimension (D)	141.3-478 mm	150-350 mm
	Axial load ratio (N/N_c)	0.21-0.84	0.27-1.00
	Concrete strength (f_{ck})	23.5-60 MPa	27.5-60 MPa
	Effective heating length (KL)	1,751-3,200 mm	2,280-3,000 mm

2.2 Performance design equations for the fire-resistance of CFT columns

Fire-resistance design equations in the U. S. [1] and Japan [14, 15] and estimation equation in Korea [17] were used. Since the equations were drawn from experiments, there is a big difference in the scope of application among them as shown in Table 2.

$$\cdot AISC : FR = f\frac{(f_{ck}+20)}{(KL-1000)}D^2\sqrt{\frac{D}{N}} \quad (1)$$

Here, f = constant for the type of aggregate

$$\cdot AIJ : FR = EXP\left(\left(\frac{-1}{a}\right)\cdot LN\left(\frac{N}{b\cdot f_{ck}A_c}\right)\right) \quad (2)$$

Here, a, b = constant for the change in cross-sectional shape and concrete strength

$$\cdot Estimationequation : FR = LN\left(\frac{N\cdot 10^3}{\alpha\cdot f_{ck}A_c}\right)\cdot\left(\frac{1}{\beta}\right) \quad (3)$$

Here, α, β = constant for the change in sectional shape and dimension

Table. 2 – Scope of application of fire-resistance design equations

Factors		AISC	AIJ	Estimation equation in Korea
Sectional dimension	Cylinder	140-410mm	≥200mm	300-900mm
	Square	140-305mm		
Axial load ratio (N/Nc)		≤Nr'/Nc	≤na	-
Concrete strength (fck)		20-40MPa	24-60MPa	24-50MPa
Effective heating length (KL)		2,000-4,000mm	KL/D≤8	KL/D≤10

Here, Nr': Compressive load capacity of concrete core at normal temperatures, na: Allowable axial load ratio at a fire

$$N_r^{'} = 0.85\phi_c f_{ck}A_c\lambda_c^{-2}\left(\sqrt{1+0.25\lambda_c^{-4}}-0.5\lambda_c^{-2}\right)$$

$$n_a = \left(a\cdot 10^{-b}\cdot f_{ck}^{c}\cdot T_{ef}+1\right)^{-d}$$

3. CHARACTERISTICS ANALYSIS FOR EFFECT FACTORS INFLUENCING FIRE-RESISTANCE

In order to evaluate the influence of the change in each factor on FRde/FRexp (Figure 1, Figure 4, Figure 7, Figure 10) with the actual values obtained from the experiment of CFT columns making the fire-resisting time drawn from design equations nondimensional, we analyzed the normal distribution (Figure 2, Figure 5, Figure 8, Figure 11) of the probability density after verifying the normality of each distribution within and beyond the scope of the application.

3.1 Influence of the change in axial load ratio (N/Nc)

With the actual values obtained from the experiment of CFT columns making the fire-resisting time drawn from design equations nondimensional, the influence of the change in axial load ratio on fire-resisting time, FRde/FRexp, was evaluated. Figure 1 shows the case within and beyond the scope of the application of the fire-resisting design equations. Also, the normality of FRde/FRexp distribution at each axial load was verified in order to find the influence of the change in axial load ratio in the

fire-resisting design equations. Figure 2 and Figure 3 show the normal distribution of probability density and comparison of the equations, respectively. Also, Table 3 shows the mean and standard deviation for the equations. The AISC equation's estimation of fire-resisting time within the scope of application was almost identical with that obtained from the experiment. At axial load ratio of 0.7 beyond the scope of application, fire-resisting time estimated by the AISC equation was 2.582, which was more than twice as much as that obtained from the experiment and standard deviation was 2.051. Within the scope of application, the larger axial load ratio got, the higher safety factors were applied to fire-resisting time in the AIJ equation, while the safety factor within the constant range of 0.7~0.86 was applied in the equation in Korea. Beyond the scope of application, the mean and standard deviation for the AIJ equation and Korea's equation were 0.22 and 0.04243 and 0.375 and 0.07778, respectively, presenting that higher safety factors were considered. Figure 3 shows definitely the influence of the change in axial load ratio in the design equations.

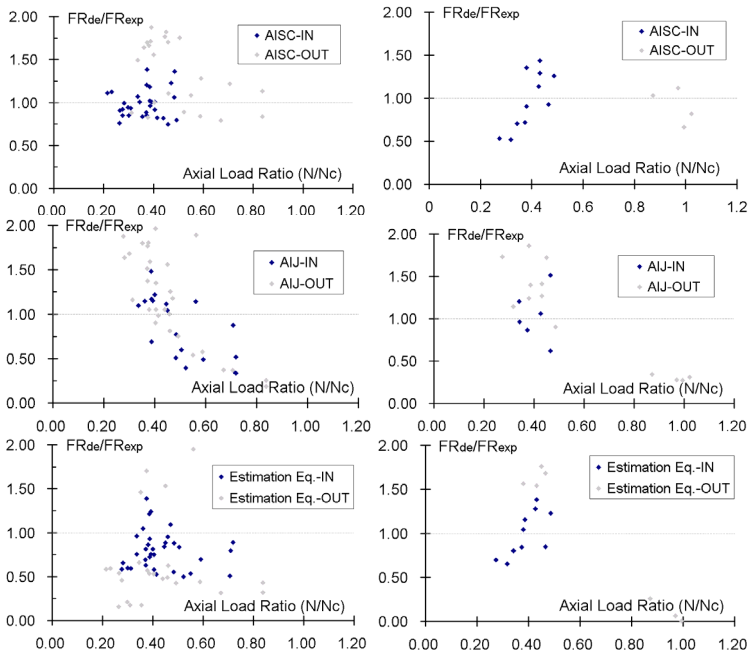

(a) Circular CFT columns (b) Square CFT columns

Fig. 1 – Axial load ratio (N/N_c) vs. Fire-resisting time (FR_{de}/FR_{exp}).

Table. 3 – Influence of the change in axial load ratio

Axial load ratio (N/Nc)	AISC		AIJ		Estimation equation in Korea	
	Mean	Standard deviation (COV)	Mean	Standard deviation (COV)	Mean	Standard deviation (COV)
0.3	0.9567	0.1097	1.1000	0.0000	0.6900	0.1467
0.4	0.9938	0.1736	1.1420	0.2853	0.8647	0.2540
0.5	1.0700	0.2519	0.7971	0.3057	0.8160	0.2174
0.6	1.0600	0.3111	0.4900	0.0000	0.7000	0.0000
0.7	2.5820	2.0510	0.5867	0.2663	0.7333	0.1986
0.8	0.9850	0.2051	0.2200	0.0424	0.3750	0.0778

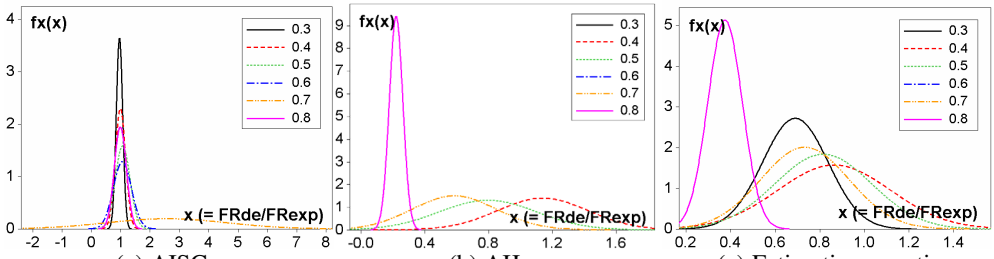

(a) AISC (b) AIJ (c) Estimation equation

Fig. 2 – Normal distribution for the change in axial load ratio.

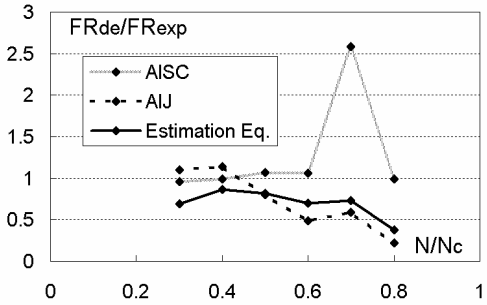

Fig. 3 – Comparison of 3 equations.

3.2 Influence of the change in sectional dimension (D)

As shown in Table 4, the fire-resisting time estimated by the AISC was almost identical with the value obtained from the experiment up to sectional dimension of 318.5mm, whereas its estimation with the mean of 1.113 and standard deviation of 0.2248 beyond the dimension was longer than that from experiment. Figure 5 and Figure 6 show the normal distribution of probability density and comparison of the equations, respectively. Estimating fire-resisting time within the scope of application shorter than actual values, the AIJ design equation and Korea's equation would yield conservative design falling into safe side. Although the AIJ design equation estimated rapidly-increasing fire-resisting time as sectional dimension changed beyond the scope of application, the estimated values were very widely distributed. On the contrary, Korea's equation estimated fire-resistance with higher safety factors taken into consideration as sectional dimension changed beyond the scope of application and standard deviation was not large, presenting that it would be more conservative than the AIJ equation.

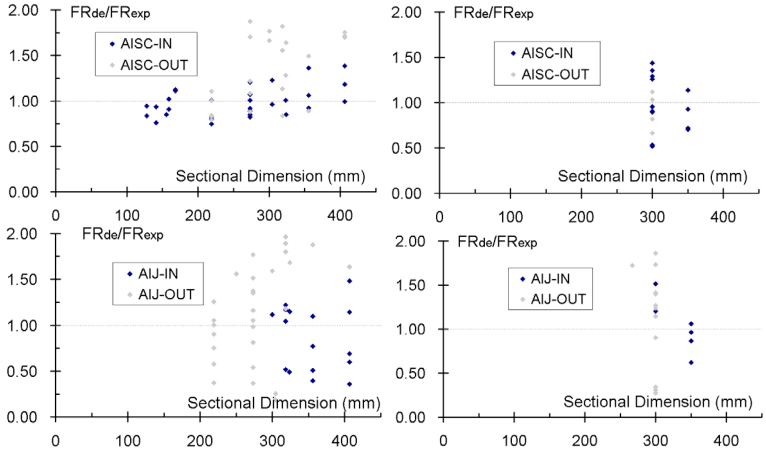

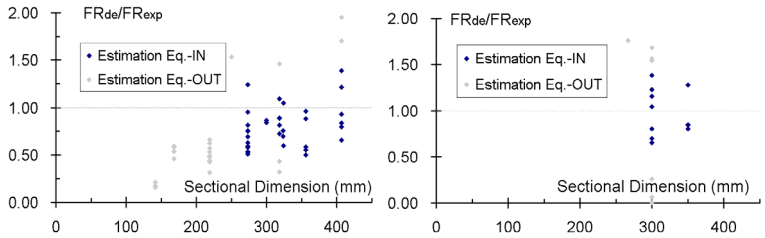

(a) Circular CFT columns (b) Square CFT columns

Fig. 4 – Sectional dimension (D) vs. Fire-resisting time (FR_{de}/FR_{exp}).

Table. 4 – Influence of the change in sectional dimension

D (mm)	AISC		AIJ		Estimation equation in Korea	
	Mean	Standard deviation (COV)	Mean	Standard deviation (COV)	Mean	Standard deviation (COV)
141.3	0.8725	0.0900	6.0750	1.5620	0.1825	0.0206
168.3	1.0020	0.1199	8.6800	4.4180	0.5440	0.0532
219.1	0.8425	0.1167	3.8480	6.2550	1.3960	1.6880
273.1	0.9671	0.1384	1.3050	0.5800	0.7150	0.2117
318.5	1.0560	0.1691	0.9825	0.2991	0.8583	0.1565
355.6	1.1130	0.2248	0.6950	0.3114	0.6940	0.2102
406.4	1.1870	0.2001	0.8540	0.4498	0.9700	0.2758

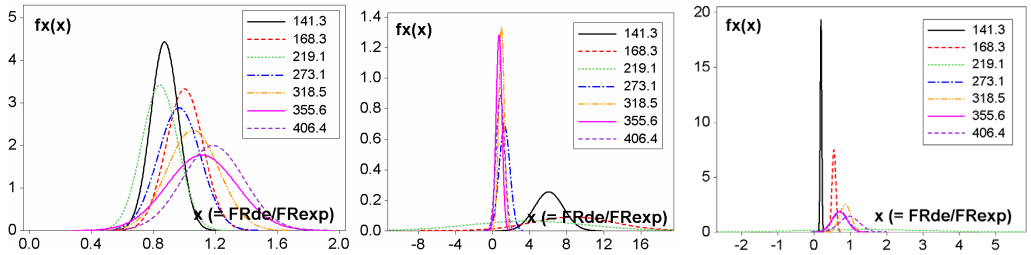

(a) AISC (b) AIJ (c) Estimation equation

Fig. 5 – Normal distribution for the change in sectional dimension.

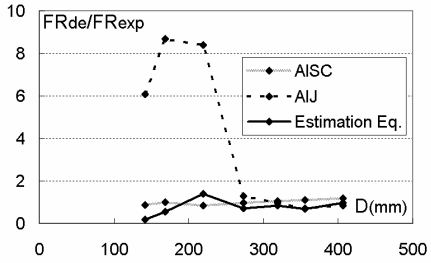

Fig. 6 – Comparison of 3 equations.

3.3 Influence of the change in concrete strength (f_{ck})

Existing studies (V.K.R. Kodur; 1998, LH Han; 2003) have confirmed that concrete strength does not exert a significant influence on the fire-resistance of CFT columns. As shown in Figure 8 and Figure 9, the estimation of fire-resisting time drawn from the AISC, AIJ and Korea's equations also confirmed it. Taking higher factors into consideration, Korea's equation estimated fire-resisting time shorter than the value obtained from experiment.

In all the 3 equations, estimated fire-resisting time beyond the scope of application (concrete strength of 50MPa) increased rapidly by 2~9 times as much as actual values. Among these, with the mean of 2.22 and standard deviation of 0.760, Korea's estimation equation showed the smallest increase, as shown in Table 5.

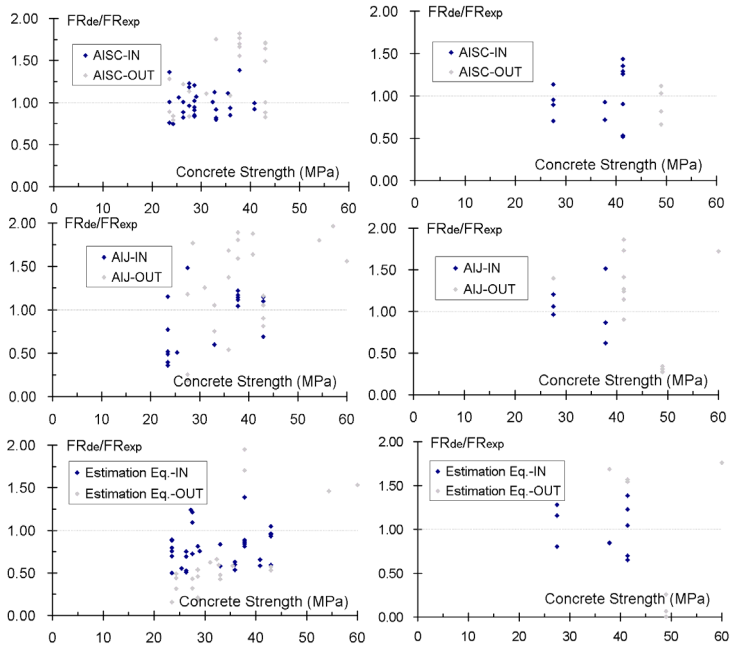

(a) Circular CFT columns (b) Square CFT columns

Fig. 7 – Concrete strength (f_{ck}) vs. Fire-resisting time (FR_{de}/FR_{exp}).

Table. 5 – Influence of the change in concrete strength

fck (MPa)	AISC		AIJ		Estimation equation in Korea	
	Mean	Standard deviation (COV)	Mean	Standard deviation (COV)	Mean	Standard deviation (COV)
25	0.9563	0.2028	0.6000	0.2756	0.6873	0.1451
30	1.0380	0.1447	1.3250	0.2192	0.9886	0.2200
35	0.9263	0.1256	0.6000	0.0000	0.6360	0.1133
40	1.1000	0.2536	1.0430	0.1743	0.8758	0.2199
55	4.7800	0.6081	8.8800	10.0100	2.2200	1.0750
60	4.9400	2.7860	1.7650	0.2899	1.8400	0.4384

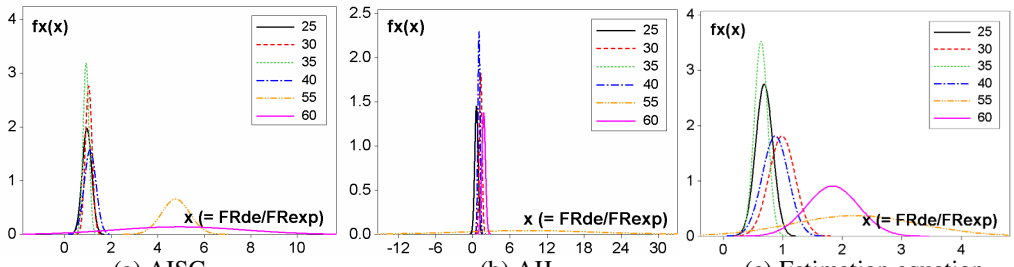

(a) AISC (b) AIJ (c) Estimation equation

Fig. 8 – Normal distribution for the change in concrete strength.

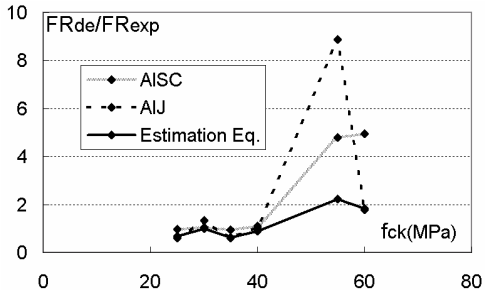

Fig. 9 – Comparison of 3 equations.

3.4 Influence of the change in width-length ratio (KL/D)

As shown in Table 6 and Figure 11, for the change in width-length ratio within the scope of application, the AISC design equation estimated fire-resisting time most precisely. But, Korea's equation taking safety factors of 0.78~0.9 into consideration would yield more stable design. Beyond the scope of application, fire-resisting time estimated by the AIJ design equation increased rapidly as much as 17 times as width-length ratio increased, while Korea's equation considered higher safety factors as width-length ratio increased beyond the scope of application, as shown in Figure 12.

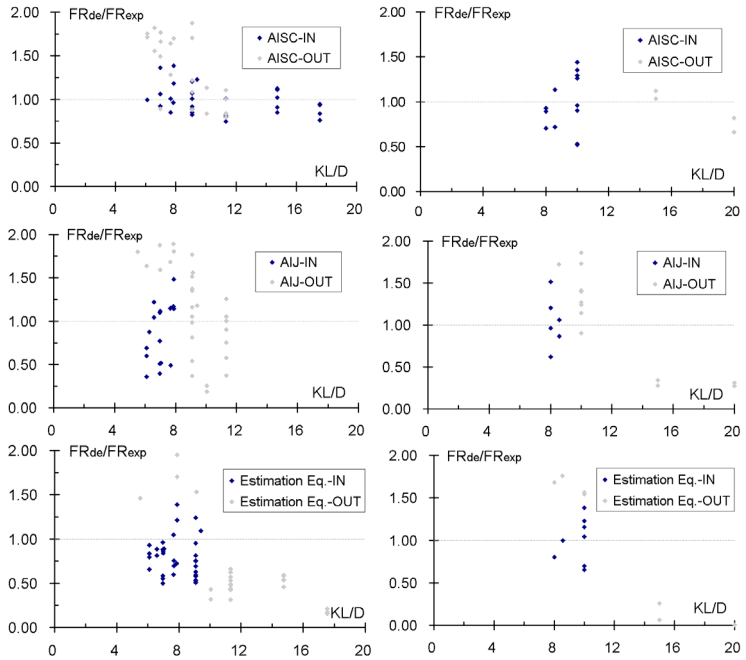

(a) Circular CFT columns (b) Square CFT columns

Fig. 10 – Width-length ratio (KL/D) vs. Fire-resisting time (FR_{de}/FR_{exp}).

Table. 6 – Influence of the change in width-length ratio

Width-length ratio (KL/D)	AISC		AISC		Estimation equation in Korea	
	Mean	Standard deviation (COV)	Mean	Standard deviation (COV)	Mean	Standard deviation (COV)
6.5	1.0830	0.1936	0.7675	0.2999	0.7843	0.1489

8.0	1.0780	0.2111	1.0970	0.3249	0.9186	0.2995
9.0	1.0260	0.1667	1.2880	0.5387	0.7686	0.2376
11.0	0.8425	0.1167	2.1530	4.3900	0.6867	0.7300
15.0	1.0020	0.1199	16.9600	18.8700	1.7110	2.0200
18.0	0.8725	0.0900	6.0750	1.5620	0.1825	0.0206

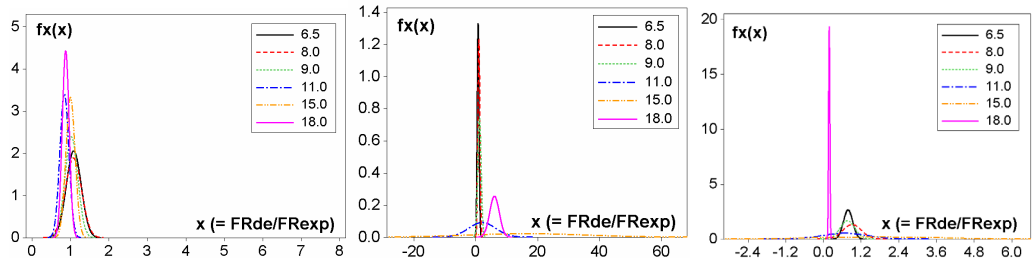

(a) AISC (b) AIJ (c) Estimation equation

Fig. 11 – Normal distribution for the change in width-length ratio.

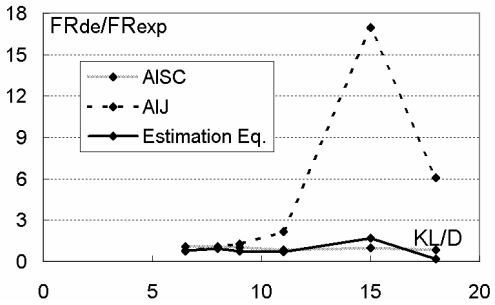

Fig. 12 – Comparison of 3 equations.

4. CONCLUSION

Within the scope of application, the ratio (FR_{de}/FR_{exp}) of fire-resisting time drawn from the AISC design equation to that obtained from experiment under the influence of various factors was approximately 1.0, while it was 0.7~0.8 in Korea's equation, presenting that it would yield safe side. The AIJ equation showed larger standard deviations ranging from 0.6 to 1.0 depending on influential factor.

Beyond the scope of application, fire-resisting time estimated by the AISC equation increased 1.06~2.58 times as long as the value obtained from experiment as width-length ratio increased, whereas the AIJ and Korea's equations produced more conservative estimation of 0.22 and 0.38, respectively. Deviation from experiment increased significantly in the AIJ equation as sectional dimension and width-length ratio changed, while Korea's equation estimated fire-resisting time more conservatively. All the 3 equations estimated longer fire-resisting time than experiment as concrete strength increased.

5. ACKNOWLEDGEMENT

This study was conducted with the support of "Development of fire-resistance design technology for CFT structures" (06 Construction Key D07), a construction technology innovation project in 2006 financed by the Ministry of Construction & Transportation and deputed by the Korea

Institute of Construction & Technology Evaluation & Planning and "Development of highly-efficient production & disaster-prevention technology for skyscrapers", a Brain Korea 21 stage II project of the Korea Research Foundation. The writers of this study would like to express our heartfelt thanks for their support.

6. REFERENCES

[1] American Institute of Steel Construction, (2003), Steel Design Guide 19 - Fire Resistance of Structural Steel Framing.
[2] A. M. Al-Khaleefi, M. J. Terro, A. P. Alex, Y. Wang, (2002), Prediction of fire resistance of concrete filled tubular steel columns using neural networks, Fire Safety J. 37, pp.339-352.
[3] C. Renaud, J.M. Aribert, (2003), Advanced numerical model for the fire behaviour of composite columns with hollow steel section, Steel and Composite Structures, 3(2), pp.75-95.
[4] I. Yasuo, S. Hiroyuki, K. Kazuo, H. Hiromi, U. Hiroki, Y. Takao, (2001), Fire resistance of circular steel tube columns infilled with reinforced concrete, J.Struct. Constr. Eng., AIJ, pp.167-174.
[5] K. Akio, (1995), Fire resistance of concrete-filled steel tubular columns with concrete reinforcement, AIJ, pp.99-100.
[6] K. Kazuo, T. Keiichi, H. Hiromi, (1995), Study on fire resistance of reinforced concrete-filled steel tubular columns, AIJ, pp.101-102.
[7] L.H. Han, X.L. Zhao, Y.F. Yang, and J.B. Feng, (2003), Experimental Study and Calculation of Fire Resistance of Concrete-Filled Hollow Steel Columns, J. Struct. Eng., 129(3), pp.346 ~ 356.
[8] L.H. Han, Y.F. Yang, Lei Xu, (2003), An experimental study and calculation on the fire resistance of concrete-filled SHS and RHS columns, J. Constr. Steel Research 59, pp.427-452.
[9] M. Hideo, F. Mituhiro, U. Hiroki, O. Teturo, W. Nobuo, H. Hiromi, I. Yasuo, (1996), A study on fire resistance efficiency of concrete filled tubular columns without fire resistive covering, AIJ, pp. 39-40.
[10] S. Hideto, I. Kenichi, (2001), Fire resistance of concrete-filled steel tube column with inner reinforcement, J.Struct. Constr. Eng.(AIJ), pp.151-157.
[11] V.K.R. Kodur, (1998), Design Equations for Evaluating Fire Resistance of SFRC-filled HSS columns, J. Struct. Eng., 35(3), pp.81 ~ 93.
[12] V.K.R. Kodur, D.H. Mackinnon, (2000), Design of concrete-filled hollow structural steel columns for fire endurance, Eng. J. 37(1), pp.13-24.
[13] V.K.R. Kodur, (2005), Achieving Fire Resistance through Steel- Concrete Composite Construction.
[14] New Urban Housing Association, Design recommendations for concrete-filled steel tube structures, Japan, (1997).
[15] New Urban Housing Association, Recommendation for Fire resistance Design of CFT structures, Japan, (2004).
[16] D.K. Kim, S.M. Choi, J.H. Kim, K.S. Chung, S.H. Park, Experimental study on fire resistance of concrete-filled steel tube column under constant axial loads, International Journal of Steel Structures, No.5, pp.305-313, 2005.
[17] K.S. Chung, S.M. Choi and D.K. Kim, (2000), Suggestion of an estimation formula on the maximum capacity for CFST columns under fire and axial load, Journal of AIK(Architectural Institute of Korea), Vol.16, No.6, pp.13-20.
[18] S.H. Park, J.Y. Ryoo, K.S. Chung and S.M. Choi, (2007), An evaluation for the fire resistance of concrete-filled steel tube columns under constant axial loads, Journal of KSSC(Korean Society of Steel Construction), Vol.19, No.6, pp.703-714.

EFFECT OF TRANSIENT THERMAL STRAIN ON THE BUCKLING OF SLENDER CONCRETE AND CONCRETE-FILLED COLUMNS IN FIRE

SHAN-SHAN HUANG[1] IAN BURGESS [2] ZHAO-HUI HUANG [3] and ROGER PLANK [4]

ABSTRACT

Pre-compressed concrete has been observed to acquire a large amount of irreversible strain (called Transient Thermal Strain or Load-Induced Thermal Strain) when it is heated. This effect appears not to occur when heating precedes the application of compressive stress. The objective of the research reported in this paper is to assess how this phenomenon affects the buckling resistance of slender concrete and concrete-filled hollow-section columns in fire. Preliminary analyses presented in the paper lead to the conclusion that TTS does have an adverse effect on the buckling temperatures of uniformly heated slender concrete columns.

1. INTRODUTION

Slender concrete and concrete-filled columns have recently been increasingly used, especially in non-seismic regions such as the UK (Fig. 1). Concrete, the main material of such columns, has a relatively newly-found property at high temperatures, defined either as Transient Thermal Strain (TTS) or as Load-Induced Thermal Strain (LITS) [1-6]. Both of these definitions describe the same phenomenon, in which pre-compressed concrete experiences a much larger compressive strain after heating than when it is loaded after being pre-heated, as shown in Fig. 2. This additional strain is large in magnitude and is not recoverable. However,

[1] Dorothy Hodgkin Scholar, University of Sheffield, United Kingdom
email: s.s.huang@shef.ac.uk
[2] Professor, University of Sheffield, United Kingdom
email: ian.burgess@sheffield.ac.uk
[3] Lecturer, University of Sheffield, United Kingdom
email: z.huang@sheffield.ac.uk
[4] Professor, University of Sheffield, United Kingdom
email: r.j.plank@sheffield.ac.uk

it is neither clearly acknowledged in the Eurocodes [7] nor considered in the majority of structural analyses. Since concrete columns which are subjected to an accidental fire are nearly always pre-compressed when they are heated, they are a good example of structural elements which are vulnerable to TTS. The nature of TTS determines its significance. In stocky columns, it causes considerable extra contraction across the whole cross-section, and this has been observed in many tests on short cylinders. However, as the slenderness of the columns increases, such tests become less relevant as the failure mode switches from material crushing to lateral buckling. The way in which TTS affects buckling in such cases forms a gap in current knowledge which needs to be investigated.

Fig. 1 - External application of slender concrete-filled steel columns © *Stahl + Verbundbau*.

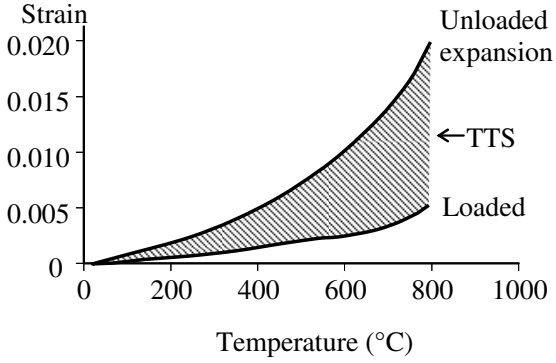

Fig. 2 – TTS, as the difference between total strain of pre-loaded and unloaded concrete, heated for the first time.

The classic simplified model due to F.R. Shanley [8], of a column buckling in its inelastic range, has been extended and its characteristics coded in an initial study of the mechanics of inelastic buckling. High-temperature analysis has also been conducted on this model, and several high-temperature concrete material models involving TTS have been compared. This has been followed by complementary FE analysis, developing the software *Vulcan*. Both analyses show a remarkable reduction of the buckling resistance of uniformly heated concrete columns caused by TTS, revealing the potential dangers of neglecting it in structural analysis and design. The effects of thermal gradients through the cross-sections of columns due to rapid heating, both symmetric and asymmetric, have also been considered.

Parametric studies on both concrete and concrete-filled columns concerning the effects of slenderness ratio, reinforcement and the steel casing are being carried out. The FE analyses using *Vulcan* will then be compared with test results and current design methods. The investigation will later move on to the effect of TTS on columns in continuous structures rather than columns in isolation.

2. SHANLEY-LIKE SIMPLIFIED COLUMN MODEL

In this research, concrete and concrete-filled columns, whose slenderness lies in the 'intermediate' range and so whose global failure mode is inelastic buckling, are of interest. Various inelastic buckling theories have been published since the late 1880s, including the tangent-modulus theory, the reduced-modulus theory and Shanley's theory [8-10]. Although in practice engineers tend to use the over-conservative tangent-modulus theory to obtain simple solutions to inelastic buckling problems, theoretically only Shanley's theory correctly describes the mechanics of inelastic buckling. Shanley demonstrates his theory with a simplified column model consisting of two rigid legs and an elastic-plastic hinge composed of two axial elements [8]. This model has been modified and extended as shown in Fig. 3, and its characteristics coded in this study. It has two degrees of freedom:

- Vertical movement u, which is the mean vertical movement of the springs;
- Rotation θ, which is proportional to the differential displacement of the extreme springs.

Since inelastic buckling is significantly rate-related, two dampers, one vertical and one rotational, are added to the original model. They respectively control the rates of increase of the two degrees of freedom u and θ. By changing the values of the two damping coefficients the extreme situations of inelastic buckling (bifurcation at the tangent-modulus or reduced-modulus buckling loads) can be simulated.

The two-spring Shanley model is extended with multiple springs in order to take into account the material continuity through a cross-section. The axial deformation of each spring is consistent with the usual linear strain-gradient assumption, and hence the mean displacement of each pair of springs at the equivalent locations on opposite sides of the vertical axis is u, and their differential displacement is proportional to θ.

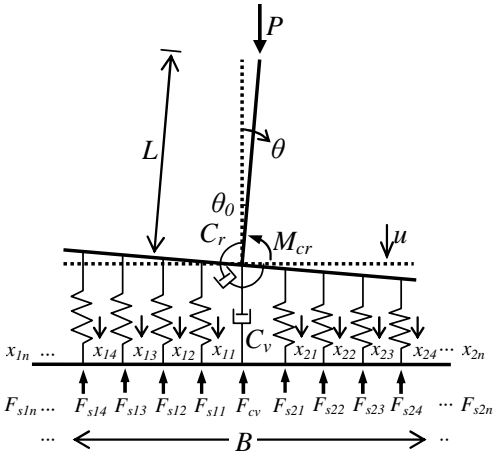

Fig. 3 – Multi-spring model.

2.1 Ambient-temperature analysis on Shanley-like model

A dynamic numerical analysis was conducted on the multi-spring model. Constant loading was imposed on the model. This simulated the application of a weight on top of the column, applied in a single step but very slowly, so that no initial velocity was induced. In the initial time step, the imbalance of the external and internal forces (whose difference is identical to the damping force) induces an acceleration, causing the model to move. The model continues to deform gradually through subsequent time steps until a new static equilibrium is reached, and this equilibrium position is recorded. Fig. 4 shows the development of the deformation of each spring through this dynamic procedure. The same procedure is repeated for successively higher loads until the rotation of the model is seen to diverge, indicating the final loss of stability by buckling. Plotting all the loads against the corresponding rotations θ, recorded at equilibrium, gives the full equilibrium path, as shown in Fig. 5.

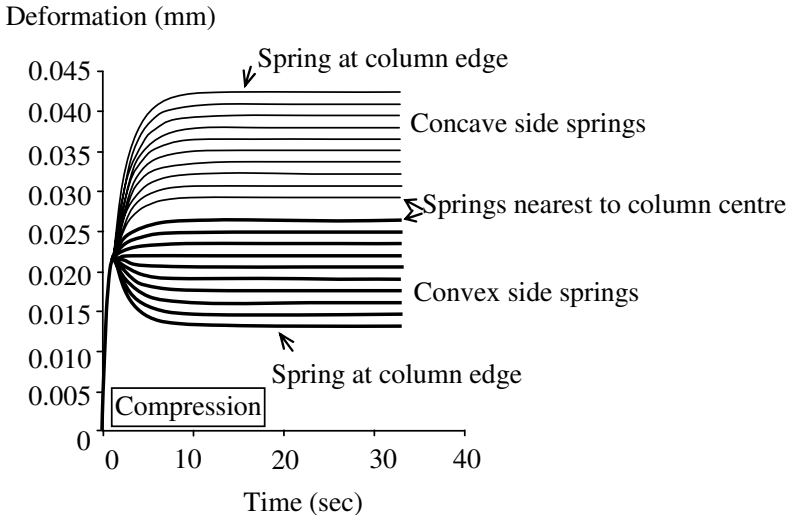

Fig. 4 – Development of the deformation of each spring over time under constant load in reaching equilibrium.

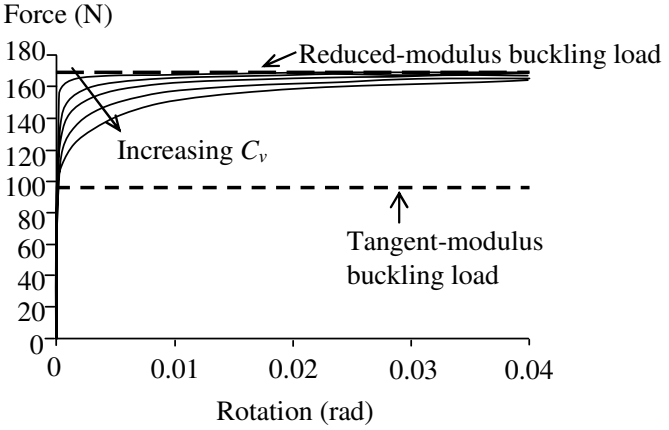

Fig. 5 – Buckling equilibrium load paths of the model with various damping ratios.

The equilibrium load paths of the model with various damping ratios are shown in Fig. 5. The analytical results are compared with the theoretical buckling loads: the tangent-modulus buckling load (the short-dashed straight line) and the reduced-modulus buckling load (the long-dashed straight line). Irrespective of the variation of damping, the rotation always starts to increase significantly at the tangent-modulus buckling load and then continues to increase as the force approaches the reduced-modulus buckling load, but the force never goes beyond this upper bound. This shows the column failing by buckling in the exact manner described by Shanley.

2.2 Elevated-temperature analysis on Shanley-like model

After the program describing the behaviour of the Shanley-like model had been evaluated at ambient temperature, it was then upgraded with Anderberg's [1] mathematical model of the material properties of concrete at elevated temperatures, in which the total strain of uniaxially compressed concrete subjected to elevated temperature consists of four components:

$$\varepsilon = \varepsilon_{th}(T) + \varepsilon_{\sigma}(\sigma) + \varepsilon_{tr}(T,\sigma) + \varepsilon_{cr}(T,\sigma,t) \tag{1}$$

in which ε = total strain; ε_{th} = thermal strain; ε_{σ} = instantaneous stress-induced strain; ε_{cr} = basic creep; ε_{tr} = transient thermal strain; T = temperature; σ = stress and t = time.

Instantaneous stress-induced strain ε_{σ} is the mechanical strain derived from the stress-strain curve. For any given temperature, ε_{σ} is only stress-dependent but the stress-strain curve varies with temperature. Transient thermal strain ε_{tr} is found to be reasonably linear with stress. It is also a nonlinear function of temperature and is approximately proportional to ε_{th}:

$$\varepsilon_{tr} = -k_{tr}\frac{\sigma}{\sigma_{u0}}\varepsilon_{th} \tag{2}$$

where k_{tr} is a constant whose value varies from 1.8 to 2.35, and σ_{u0} is the strength at 20°C.

Uniform temperature distribution across the springs was assumed. The loading procedure was upgraded from the constant loading used in the ambient-temperature analysis to step loading. Both steady-state and transient heating scenarios were applied. In the steady-state heating procedure, the step loading was applied at constant temperature until buckling occurred, and the buckling load of the column at this temperature was assessed. In the transient heating procedure, the column was loaded in steps to a certain load level, and then temperature was applied as a thermal loading, also step by step, until failure occurred. Obviously, the latter process more directly represents the real loading-heating situation of a column subject to an accidental fire, but it requires an instantaneous change of the material properties from a lower temperature to a higher one when the temperature changes, which causes considerable complexity in the numerical analysis. These two approaches were compared in order to assess the necessity of introducing this complexity into the research.

The results of the elevated-temperature analysis on an example model, including 20 springs which all have the same temperature, are briefly presented in Fig. 6. The two solid curves show the ultimate buckling loads of the model at various temperatures, with and without considering transient thermal strain. Comparing these shows that TTS can cause a remarkable reduction of the buckling resistance of slender concrete columns under uniform heating. This result is revealing, because the effect of TTS on buckling has hardly been

considered in structural analysis, although the uniform-temperature assumption is very unrealistic.

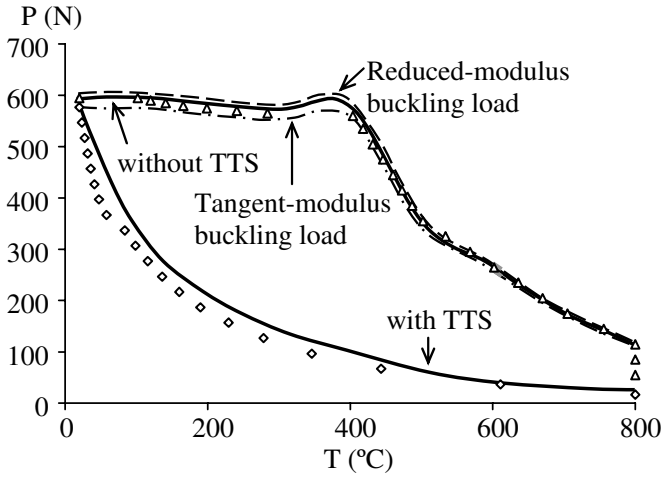

Fig. 6 – Buckling resistance of the model, with and without TTS, compared with theoretical buckling loads at elevated temperatures.

On the other hand, this is less surprising if the stress-dependence of TTS is highlighted. A study of the mechanics of inelastic buckling reveals that, when the column starts to bend, the bending causes differential stresses between the concave and convex sides. At elevated temperatures this difference of compressive stresses will cause differential TTS, which further increases the differential total strain between the two sides, leading to further bending. Due to the rather large magnitude of TTS this interactive effect will be significant.

Fig. 6 also shows that the result of the analysis without TTS lies between the two theoretical buckling loads (the dashed and chain-dot curves), which is consistent with Shanley's theory. The results of the transient heating analysis are shown as the black triangles and diamonds plotting the ultimate buckling temperatures of the model at various load levels, with and without considering transient thermal strain. Their comparison with the results of the steady-state heating analysis indicates little difference between these two heating scenarios, suggesting that the steady-state heating approach is sufficient, at least when the cross-section is uniformly heated, although the influence of the heating scenario is expected to be more significant if a thermal gradient exists through the cross-section. In particular, the magnitude of the additional stresses and strains caused by the thermal gradients should be significantly affected by the stress history.

2.3 Comparisons of high-temperature concrete material models involving TTS

Apart from Anderberg's model, two other mathematical models of the material properties of concrete at high temperature, which involve the transient straining property, have also been applied to the numerical analysis. These two models, which are given by Schneider [6] and Khoury [2] respectively, are briefly noted below.

2.3.1 Schneider's model

In this model, the transient strain ε_{tr} and the basic creep ε_{cr} are combined, and thus there are only three strain components:

$$\varepsilon = \varepsilon_{th} + \varepsilon_{\sigma} + \varepsilon_{tr,cr} \tag{3}$$

$$\varepsilon_{\sigma} = \frac{1+\beta(T,\sigma)}{g(T,\sigma)} \cdot \frac{\sigma}{E} \tag{4}$$

$$\varepsilon_{tr,cr} = \frac{\Phi(T,\sigma)}{g(T,\sigma)} \cdot \frac{\sigma}{E} \tag{5}$$

where β, g and Φ are empirical functions of stress and temperature, and E is the initial tangent modulus of the stress-strain curve at temperature T. The function β is to account for the increase of plasticity of the material as stress level increases, and g takes account of the increase of the initial tangent modulus of the stress-strain curve when pre-stress applies.

2.3.2 Khoury's model

Similarly to Schneider's model, the total strain consists of three components in this model:

$$\varepsilon = \varepsilon_{th} + \varepsilon_{\sigma} + \varepsilon_{tr,cr} \tag{6}$$

$$\varepsilon_{\sigma} = \sigma / E_0 \tag{7}$$

where E_0 is the initial tangent modulus of the concrete material at room temperature.

Distinguishing it from the previous two models, in this model ε_{σ} covers only the linear-elastic range of the instantaneous stress-induced strain derived from the stress-strain curve, ignoring the change of initial tangent-modulus as temperature rises; thus it is called elastic strain. The plastic instantaneous stress-induced strain is combined with the transient thermal strain and the basic creep strain as a single strain component called load-induced thermal strain (LITS). For a stress level equal to $0.3\sigma_{u0}$, LITS is an empirical function of temperature $g(T)$,

$$LITS(T, 0.3\sigma_{u0}) = g(T) \tag{8}$$

For other stress levels, the equation is modified to

$$LITS(T,\sigma) = LITS(T, 0.3\sigma_{u0}) \times \left(0.032 + 3.226 \frac{\sigma}{\sigma_{u0}} \right) \tag{9}$$

where σ_{u0} is the ultimate stress at ambient temperature.

2.3.3 Model comparison

Schneider's and Khoury's models have been implemented into the Shanley-like analysis and compared with Anderberg's model. Since the decomposition of the total strain

varies in these three models, it is not possible to compare each strain component from different models separately, and therefore the comparisons shown in this section are all based on the total strain including the transient straining property.

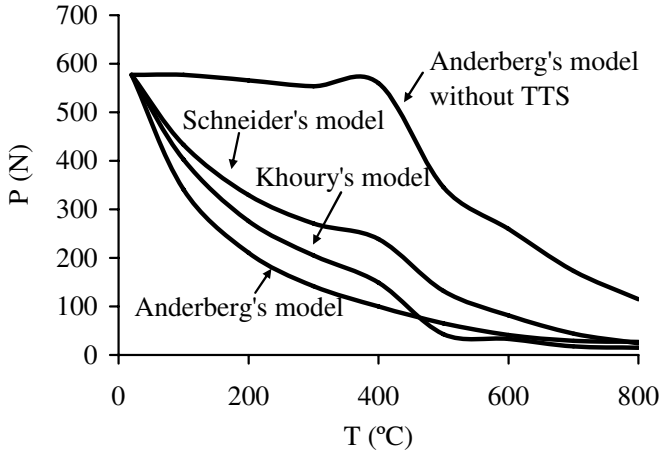

Fig. 7 – Buckling resistance of the multi-spring strut model using various high-temperature concrete material models involving TTS.

Figure 7 shows the ultimate buckling loads of the multi-spring strut over a range of temperatures, applying these three high-temperature concrete material models. It is seen that the three curves are reasonably close to each other at either low or high temperatures whist they split evidently from each other in the temperature range from 200 ºC to 400ºC. Anderberg's model leads to the most conservative prediction of the buckling resistance, except that in the region of 550ºC Khoury's model gives the lowest buckling loads. Although the strain definitions and formulations of the models are completely different from each other, they all show a reduction of the buckling resistance caused by TTS or LITS, compared with the case in which Anderberg's model is applied without the TTS component.

3. FE ANALYSIS WITH *VULCAN*

The analysis on the simplified Shanley-like model was followed by complementary finite element analyses. The FE software *Vulcan* [11], which has been specially developed for structural fire engineering analysis, was further developed to take into account the transient thermal straining property of concrete. The 3-noded beam element of *Vulcan* [11], whose general cross-section consists of a finite number of segments, proved suitable for such development. Each segment is assumed to be fully in contact with adjacent segments, and their relative movements are restricted by the assumption that plane cross-sections remain plane. If the Poisson's ratio of the material is set to zero, these segments should stay reasonably uniaxial, and effectively replace the springs in the Shanley-like model, whilst taking into account the material continuity along the length of the column.

As with the Shanley-like-model, the temperature distribution through the cross-section was assumed to be uniform at this stage, and Anderberg's transient thermal strain model was implemented. A three-metre long, 200mm square, bare concrete column, simply-supported and subject to pure compression under transient heating, was examined. It should be noted that, for a suitable example, the dimensions and material of the column must ensure that the column fails by buckling in the inelastic range, in which case, the tangent-modulus critical

load F_t must be smaller than the compressive strength F_u and larger than the proportional limit F_p of the column. The analysis reveals overall buckling as the major failure mode of the column, and the effect of transient thermal strain on this buckling is illustrated in Fig. 8. This figure shows the failure temperatures of the column at various load levels, both with and without considering transient thermal strain. TTS causes reduction of the buckling resistance of this column as it does to the Shanley-like model. The two curves without TTS in Figures 6 and 8 have different shapes, because different stress-strain curves were used in these two analyses; Anderberg's curve for the former and the EC2 curve for the latter.

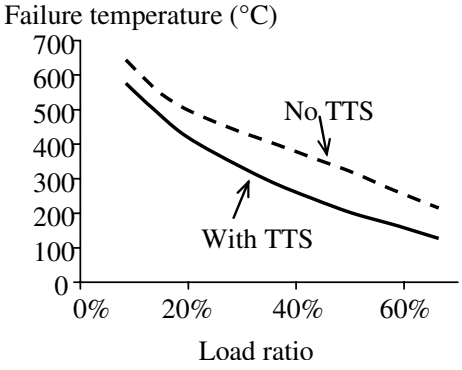

Fig. 8 – Effect of transient thermal strain on the overall buckling of the 3m plain concrete column from *Vulcan* analysis.

This investigation was then extended to reinforced concrete columns. Maintaining the dimensions of the cross-section and the length of the column as for the bare concrete column above, four rebars of 10mm diameter with 25mm cover from the column surface were added. The failure mode of the column is still overall buckling. Fig. 9(a) plots the failure temperatures of this column with or without TTS at various load levels (the dashed curves) which are compared with those of the bare concrete column (the solid curves). The results of the analyses with and without TTS are distinguished by line colours as marked. It is shown that the introduction of TTS causes a reduction of the buckling resistance of the RC column which is similar to that of the bare concrete column.

The decrease of the failure temperature caused by TTS at various load levels for these two types of columns is illustrated in Fig. 9(b). For both types of column, the reduction of the buckling resistance due to TTS is most significant at the intermediate load level when the load ratio (the ratio of the applied load to the cold strength of the column) is around 40%. This may be because the magnitude of TTS depends on the combination of temperature and stress level as implied by Equation (2), and it turns out to be largest when both of these two factors are in the intermediate range. Fig. 9(b) also indicates that, except when the applied load is very low, the reduction of the buckling resistance caused by TTS is more significant for the RC column rather than for the bare concrete column. As demonstrated by the Shanley-like model, such a reduction is very directly related to the amount of lateral deflection occurring, and it is clear that the RC columns have higher bending stiffness than their bare concrete counterparts. This may explain the reason that TTS causes the greater reduction of the buckling resistance to the RC column.

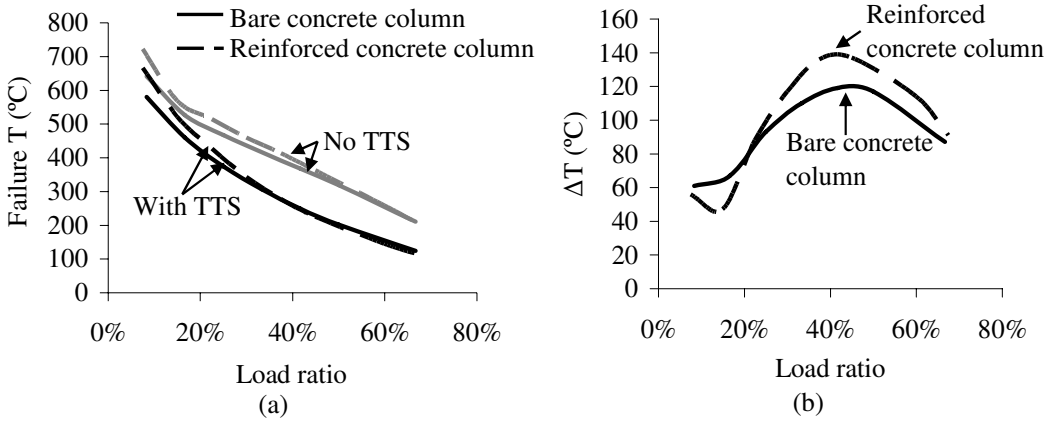

Fig. 9 – Comparison of the effect of transient thermal strain on the overall buckling of the reinforced and bare concrete columns from *Vulcan*.

The effects of the steel casing of concrete-filled columns on the way TTS affects the buckling of such columns at high temperature were also investigated. Two three-metre long concrete-filled columns, made of 10mm and 15mm thick, square steel tubes with a 200 mm square concrete infill, were examined. The effects of TTS on the overall buckling of these columns and bare concrete columns of the same size as their concrete cores were compared, and the results are shown in Fig. 10. TTS still causes a reduction of the buckling resistance of the concrete-filled columns, but this reduction is much smaller than for the concrete and reinforced concrete columns examined previously. It is also shown in Fig. 10(b) that the reduction decreases with increasing thickness of the steel casing. This indicates, logically, that as the thickness-to-width ratio of a concrete-filled column increases, the behaviour of the column is more influenced by the behaviour of the steel tube, and therefore the effect of the transient strain of the concrete infill may not be as significant as for concrete and reinforced concrete columns. However, since the temperature of the concrete core has been overestimated by the simplified assumption that the column is uniformly heated through its cross-section, whilst the effect of TTS is expected to be more significant when a more realistic temperature profile, in which the concrete core is cooler, is applied. Investigation of the effect of the thermal gradient through the cross-section is on-going.

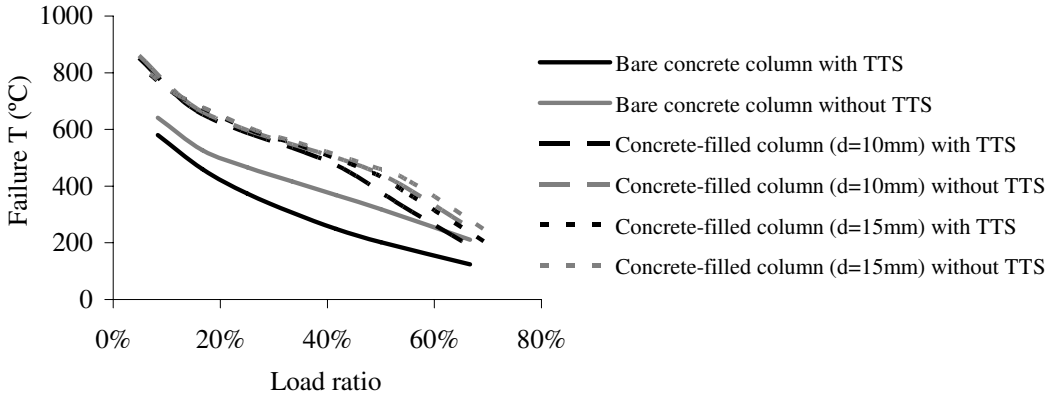

Fig. 10(a) – Comparison of the effect of transient thermal strain on the overall buckling of the concrete-filled and bare concrete columns from *Vulcan*.

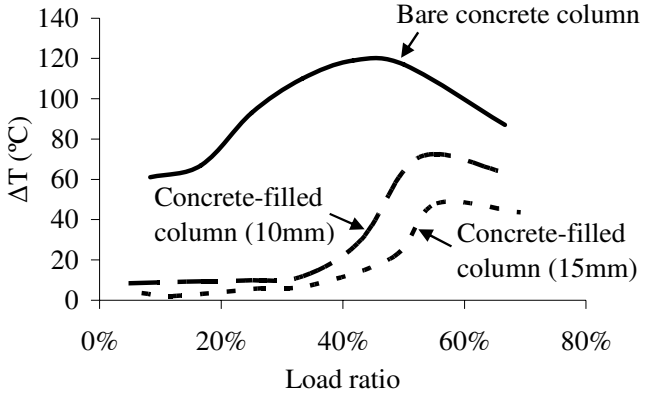

Fig. 10(b) – Comparison of the effect of transient thermal strain on the overall buckling of the reinforced and bare concrete columns from *Vulcan*.

4. CONCLUSIONS & FUTURE WORK

The classic simplified model due to F.R. Shanley, of a column buckling in the material's inelastic range, has been extended and its characteristics programmed in an initial study of the mechanics of inelastic buckling. High-temperature analysis has also been conducted on this model and three high-temperature concrete material models involving TTS have been compared. This has been followed by complementary FE analyses, developing the software *Vulcan*. Both analyses show a remarkable reduction of the buckling resistance of uniformly heated concrete columns caused by TTS, revealing the potential dangers of neglecting this property of concrete in structural analysis and design for fire. Preliminary parametric studies on both concrete and concrete-filled columns concerning the effects of reinforcement and steel casing have been carried out, indicating that the reduction of the buckling resistance caused by TTS is more significant for uniformly heated RC columns compared to bare concrete columns of the same size, and that as the thickness of the steel casing of the concrete-filled columns increases, this reduction decreases.

The effects of thermal gradients through the cross-sections of columns due to rapid heating, both symmetric and asymmetric, are being considered. The FE analyses using *Vulcan* need to be further validated against the Shanley-like model. The analysis will then be compared with test results and current design methods. The investigation will later move on to the effect of TTS on columns in continuous structures rather than single members.

Acknowledgment: *The principal author is grateful for the support of Corus Group Ltd and the Engineering and Physical Sciences Research Council of the United Kingdom, under a Dorothy Hodgkin Scholarship.*

REFERENCES

[1] Anderberg, Y. & Thelanderson, S., *Stress and deformation characteristics of concrete at high temperatures. 2. Experimental investigation and material behaviour model*, Bulletin 54, Lund University, 1976.

[2] Khoury, G. A., *Performance of heated concrete mechanical properties*, Report to the Nuclear Installations Inspectorate of the Health and Safety Executive, London, 1996.

[3] Khoury, G. A., "Strain of heated concrete during two thermal cycles. Part 1: Strain over two cycles, during first heating and at subsequent constant temperature", *Magazine of Concrete Research*, **58** (6), (2006) pp367-385.
[4] Khoury, G. A., Grainger, B. N. & Sullivan, P. J. E., "Transient thermal strain of concrete: literature review, conditions within specimen and behaviour of individual constituents", *Magazine of Concrete Research*, **37** (132), (1985[a]) pp131-144.
[5] Khoury, G. A., Grainger, B. N. & Sullivan, P. J. E., "Strain of concrete during first heating to 600°C under load", *Magazine of Concrete Research*, **37** (133), (1985b) pp95-215.
[6] Schneider, U. & Horvath, J., *Behaviour of ordinary concrete at high temperatures*, Research reports of Vienna University of Technology, Institute of Building Materials, Building Physics and Fire Protection Vol. 9, Vienna, 2003.
[7] European Committee for Standardization *Eurocode 2: Design of concrete structures - Part 1-2: General rules - Structural fire design*. 2004
[8] Shanley, F. R., "Inelastic column theory", *Journal of the Aeronautical Sciences*, **14** (5), (1947) pp261-268.
[9] Bazant, Z. P. & Cedolin, L., *Stability of structures*, Oxford University Press, Oxford, 1991.
[10] Bleich, F., *Buckling strength of metal structures*, McGraw-Hill, New York, 1952.
[11] Huang, Z., Burgess, I.W. & Plank, R.J., *3D Modelling of Beam-Columns with General Cross-Sections in Fire*, Paper S6-5, Third International Workshop on Structures in Fire, Ottawa, Canada, (May 2004) pp 323-334.

APPLICATION OF ADVANCED CALCULATION MODELS FOR FIRE DESIGN IN ROMANIA

RAUL ZAHARIA[1], DAN DUBINA[2], DAN PINTEA[3]

ABSTRACT

Lately, there is a growing demand in Romania for steel structures, especially for industrial and commercial objectives, where erection speed is critical in the choice of the structural solution. The main problem of steel structures is their low fire resistance. Composite steel-concrete solutions have the advantage of increased resistance of the structural element, in the case of fire, as well as in normal conditions. The fire resistance of steel and composite structures may be determined using simplified methods, based on analytical formulas or tables, provided in the corresponding Eurocodes for fire design. For special situations or for complex structures, it may be necessary to perform an advanced analysis, using special purpose programs for the analysis of structures under ambient and elevated temperature conditions.

The paper presents some examples of application of the advanced methods by the authors for some composite steel- concrete buildings in Romania, using the SAFIR computer program. The fire design deals with concrete filled CHS composite cross-sections and cruciform cross sections made of hot rolled profiles, partially encased in reinforced concrete.

1. INTRODUCTION

The basic principle in determining the fire resistance of a structural element is that the elevated temperatures produced by the fire reduce the materials strength and stiffness until possible collapse. When the temperatures on the cross-section of a structural element produce the reduction of the element resistance bellow the level of the effect of actions for fire design situation, it is considered that that element lost its load-bearing function under fire action.

[1] Assoc Professor, University of Timisoara, Department of Steel Structures and Structural Mechanics
email: raul.zaharia@ct.upt.ro.
[2] Professor, University of Timisoara, Department of Steel Structures and Structural Mechanics
email: dan.dubina@ct.upt.ro.
[3] Lecturer, University of Timisoara, Department of Steel Structures and Structural Mechanics
email: dan.pintea@ct.upt.ro.

The fire resistance of composite steel-concrete structures is calculated according to EN1994-1-2[1]. Three methods are available in order to evaluate the fire resistance: the tabulated data method, the simple calculation models and the advanced calculation models.

The tabulated data method is based on observations resulted from experimental study. It is the easiest to apply, but it is limited by the geometrical conditions imposed to the composite cross-section.

The simple calculation models compute the ultimate load of the element by means of formulas or design charts, established on the basis of experimental data.

The advanced calculation models suppose an advanced numerical analysis of the elements, parts of the structure, or of the entire structure under fire, using specialized software for the mechanical analysis of structures under elevated temperatures. For the advanced calculation of the fire resistance of the composite columns presented in this paper, the SAFIR computer program was used[2], which is a special purpose program for the analysis of structures under ambient and elevated temperature conditions. The program, developed at the University of Liege, accommodates various elements for different idealization, calculation procedures and various material models for incorporating stress- strain behaviour under elevated temperatures. The analysis of a structure exposed to fire consists of two steps. The first step involves predicting the temperature distribution inside the structural members, referred to as "thermal analysis". The second part of the analysis, termed the "structural analysis" is carried out to determine the structural response due to static and thermal loading.

The fire is considered an accidental situation which requires, with some exceptions, only verifications against the ultimate limit state. The combinations of actions for accidental design situations are given in the European Standard for basis of structural design EN1990[3], by the following formulas:

$$G_k + P_k + \Psi_{1,1} Q_{k,1} + \sum_{i>1} \Psi_{2,i} Q_{k,i} \text{ or} \tag{1}$$

$$G_k + P_k + \sum_{i\geq 1} \Psi_{2,i} Q_{k,i} \tag{2}$$

in which G_k, P_k, Q_k are the characteristic values of the permanent, variable and prestressing action. According to the European Standard for actions on structures exposed to fire EN1991-1-2[4], the representative value of the variable action Q_1 may be considered as the quasi-permanent value $\Psi_{2,1} Q_{k,1}$, or as an alternative the frequent value $\Psi_{1,1} Q_{k,1}$. The qusi-permanent value is recommended.

A structure, substructure or element in fire situation may be assessed in the time domain, where the failure time must be higher than the required fire resistance time. The failure time is the time for which the resistance of the structure (or substructure, or element, as considered) under elevated temperatures reach the effect of actions for the fire design situation, considering the combination of action in fire situation.

Translation into Romanian of the fire design parts of the Eurocodes is not completely finished. The Eurocodes will be compulsory from January 2010, when all other national building codes will expire. However, the document OM 620/29.04.2005, issued by the Romanian Ministry of Transportation, Civil Works and Tourism, regarding the implementation and use of the structural Eurocodes, states that for the design problems which are not covered by the existing national regulations, Eurocode provisions can be applied, based on CEN approved documents, even before national implementation (this includes fire design as well). On another hand, it has to be underlined that for fire design of steel structures, two normative documents based on ENV1993-1-2 have been already published in Romania since 2000[5,6].

2. CONCRETE FILLED CHS COLUMNS

The first example presents the calculation of the fire resistance for the columns of a three-storey framed building structure for the LINDAB-Romania Company Headquarters, in Bucharest. The office structure has three levels (ground floor, 1st floor, and an attic floor), two spans of 6m each, and 7 bays of 5m, with a total area of 1308 m^2. Taking into account the specific of LINDAB – Romania (systems of steel industrial buildings) the special demand was that the resistance structure must be visible steel, made by circular columns. Because for this type of building, according to Romanian fire regulations, the columns must have 2 hours of fire resistance, the solution of reinforced concrete filled CHS columns was chosen.

A global view of the structure is presented in Figure 1. The office building structural scheme is composed of interior moment-resisting frames and exterior eccentrically braced frames. The lateral force resisting system was considered to be composed of both moment-resisting and eccentrically braced frames, through the diaphragm effect of the r.c. slabs and roof braces. The steelwork is fabricated from European hot-rolled profiles, and partially from built-up sections (steel quality S235). The beams have I cross section, the eccentric braces are RHS sections and the horizontal braces are round bars. Structural elements are joined on site by bolts only, avoiding site welding. Reinforced concrete slabs are fabricated in classical solution, with secondary steel beams and corrugated sheet lost formwork. The columns cross-section is presented in Figure 2. The columns are composed of two sections, with a splice at +6.80 m. Concrete filling is accomplished after erection of each of the column sections, by pumping.

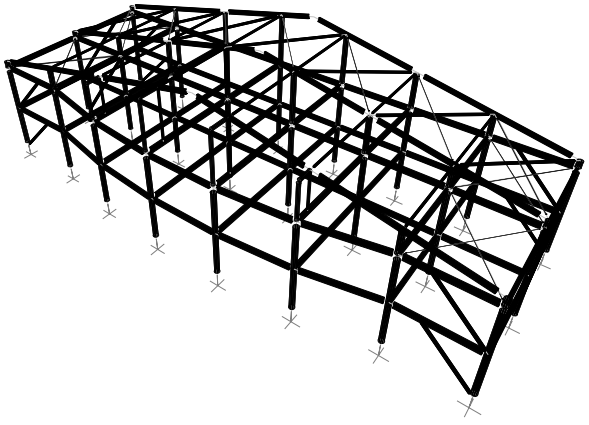

Fig. 1 - Office building structural scheme

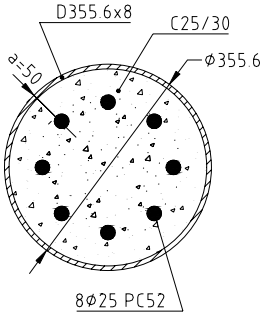

Fig. 2 - Column cross-section

2.1 Tabulated data method

For reinforced concrete filled CHS columns, Table 4.7 of EN1994-1-2[1] is suitable. The load level is 0.148. For fire resistance class R120, corresponding to a load level of 0.3 (the lowest value provided in Table 4.7) the minimum cross-section diameter d, minimum axis distance of reinforcing bars us and minimum percentage of reinforcement p, are:

d_{min} = 260mm < d=355.5 mm

us_{min} = 50mm < us=62.5 mm

p_{min} = 6% > p=4.4%

There is one condition that is not satisfied, the minimum percentage of reinforcement. Meanwhile, the other conditions are satisfied far away from limitations and the value of the load level represents less than 50% of the lowest one provided in the table.

2.2 Simple calculation model

The simple calculation model was applied using the diagrams provided in the CIDECT Design Charts for fire resistance of concrete filled hollow section columns[7]. Using the design chart I15 from this reference, for fire resistance class R120, the ultimate load of a composite column, with the buckling length of 3.4m, made of CHS 355x5.6 profile and filled with C20 concrete with 4% percentage of reinforcement, is:

$N_{fi,\theta,Rd} \cong 150000daN > N_{equ} = 61428daN$

Taking into account the superior characteristics of the column cross-section (8mm for CHS thickness, P=4.4%, C25/30 concrete) the fire resistance class R120 of the column is proved.

2.3 Advanced method using SAFIR program

The verification according to the tabulated data method is not relevant for the case into consideration, because one condition is not fulfilled (percentage of reinforcement). On another hand, in the verification with the CIDECT Design Charts, even if the fire resistance R120 of the column is demonstrated, taking into account the superior characteristics of the studied column in comparison with the data available in the Design Charts, no information about the fire resistance of the column under the imposed load is obtained. Therefore, an advanced analysis was considered. Figure 3 presents the numerical model of the concrete filled CHS column cross-section. Due to obvious reasons of symmetry, only a quarter of the cross-section was represented. Figure 4 shows the temperature distribution after 2 hours of standardized ISO fire. It may be observed that for the CHS profile, the temperatures are superior of 1000°C, so the steel profile exhausted its loading capacity. In the same time, the temperatures of the reinforcing bars are around 500°C and there is an important core of concrete with quite low temperatures.

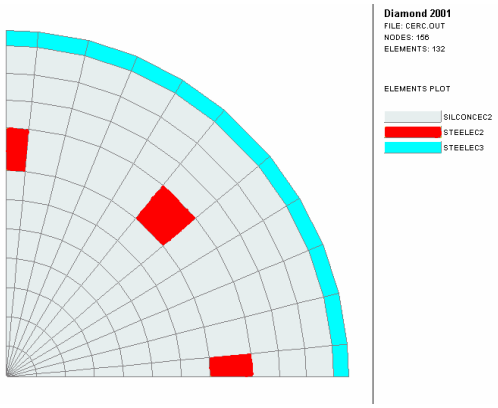

Fig. 3 - Numerical model of the composite cross-section

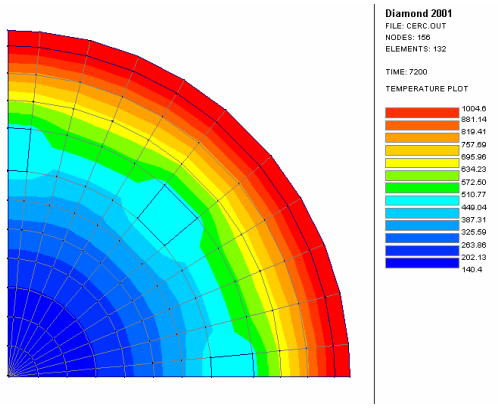

Fig. 4 - Temperature distribution on cross-section after 2h of standardized ISO fire

The column, loaded with the axial force and bending moment, corresponding to the fire situation, was modeled with 2D beam elements. Conservatively, the buckling length of the column was considered as the system length (L_{ei}=1.00L), i.e. the height of the relevant

storey. Equivalent imperfections according to EN1994-1-1[4] were considered. As the characteristic time-displacement demonstrate (Fig. 5) after 2 hours of ISO fire the column is still able to resist to the imposed static loads, due to the bearing capacity reserve provided by the concrete core and the reinforcing bars. The collapse of the column is produced after around 3h of ISO standardized fire.

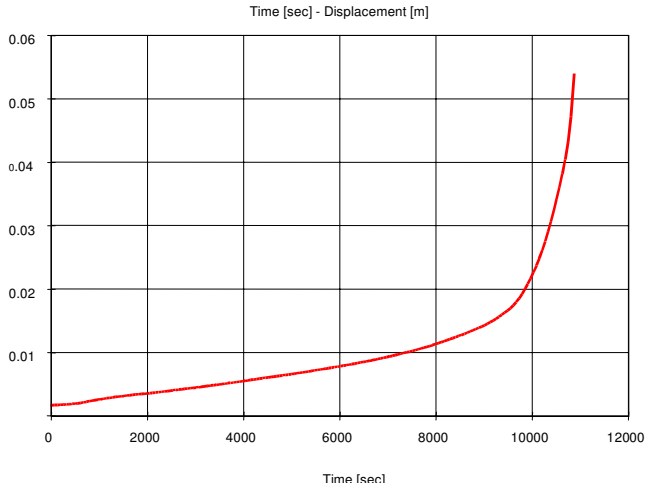

Fig. 5 - Time-displacement characteristic

3. COMPOSITE STEEL-CONCRETE CRUCIFORM COLUMNS

This section presents the calculation of the fire resistance for the composite columns of „Bucharest Tower Centre“ structure, which is the tallest building in Bucharest for the moment (Fig. 6 and 7). The building has 3 basements, one ground floor, 21 floors, 3 technical floors at a total height of 106.3m. The building is 25.5m by 41.5m in plan and has a total construction gross area of approximately 24135m^2.

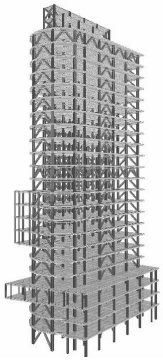

Fig. 6 - General view of the building (3D model)

Fig. 7 - Photo during construction

The building system uses steel braced and unbraced frames (dual structural configuration) (Figs. 8 - 10). The steel structure was designed by Britt Ltd, in cooperation with the “Politehnica” University of Timisoara, CEMSIG Research Centre. The project was

awarded in 2007 with the 1st Prize of the Romanian Association of the Structural Design Engineers AICPS and ECCS Steel Design Award.

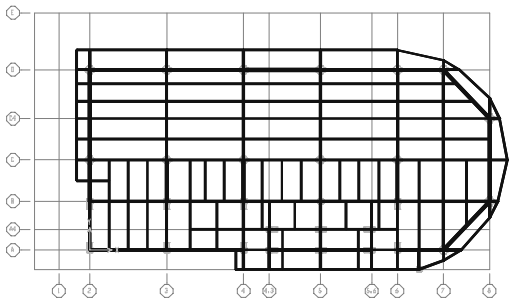

Fig. 8 - Structural system (current floor plan)

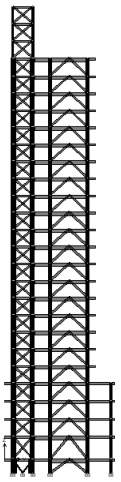

Fig. 9 - Side transversal frame

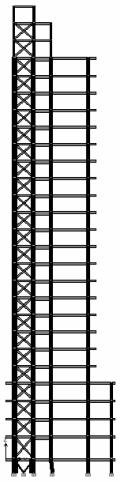

Fig. 10 - Current transversal frame

The columns are made by cruciform cross sections made of hot rolled European profiles, partially encased in reinforced concrete, in order to increase strength, rigidity and fire resistance. According to Romanian fire regulations, considering the specific and particularities of the building, the columns must have 150 minutes of fire resistance. The beams are made of IPE450 to IPE550 sections, except for the coupling beams and the beams connected to inverted V braces, which are HEB800 sections. Secondary beams are made of IPEO300 sections. Headed stud connectors were welded to the top flanges of the beams, to ensure the composite action of beams and concrete slab. In order to allow the development of plastic hinges in the moment resisting frames, no stud connectors were used in the vicinity of beams ends. Centric X braces are made of hot rolled sections, varying from HEB450 in the lower storeys to HEA340 in the upper ones. Similarly, inverted V braces vary from HEB450 to HEA340.

The seismic design was done according to Romanian seismic code P100-1/2006. The design ground acceleration is a_g =0.24g, that corresponds to a reference return period of 100 years. In order to obtain a favourable plastic mechanism and to reduce the over strength requirements on the non dissipative members, S355 steel was generally used for frame members, excepting the braces designed as dissipative members, which use a S235 steel.

Four different cross section types were used for columns, as Figure 11 shows (the values in parathesis represent the maximum load level, i.e. the maximum ratio to the ambient temperature capacity for each set): octagonal sections with identical steel profiles 2HEB500 (0.319), 2HEA800 (0.153), 2HEB800 (0.257), 2HE800x373 (0.303), octagonal sections with different steel profiles HEM800HEM700 (0.310), HEB800HEB700 (0.257), HEA800HEA700 (0.172), double-symmetric rectangular sections HEB1000HEB500 (0.293) and rectangular sections with one axis of symmetry HEB1000HEM500 (0.250), HEB1000 HEB500 (0.201).

The rebars have 25 mm diameter and the concrete is C30/37.

For the purpose of this paper, only the 2HEB500, HEM800HEM700, HEB1000HEB500 and HEB1000HEM500 cross-sections will be presented, as they have the lowest fire resistance under ISO fire from each type of cross section types, respectively.

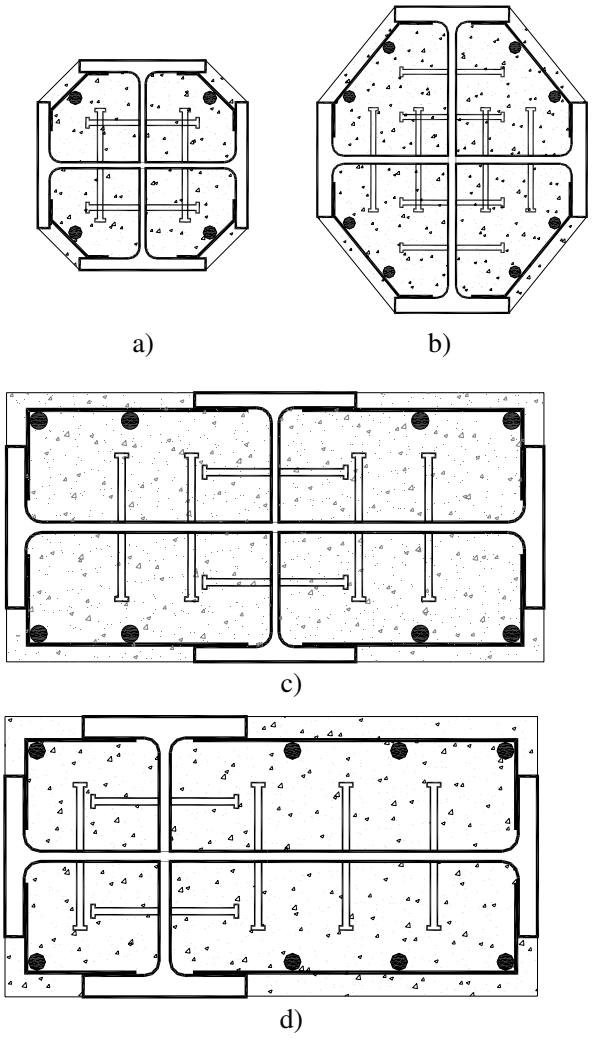

Fig. 11. - Composite cross-sections

Figure 12 shows the temperature distribution on the cross sections of the considered columns, after 150 minutes of ISO fire. Due to symmetry, only a quarter, or half of the cross-sections was modelled. The round reinforcing bars are represented by quadrilateral elements, with equivalent area. For all cross-sections, after 150 minutes of ISO fire, the steel profiles flanges exhausted practically their load capacity, having temperatures greater than 900^{o}C, while the profiles webs and the reinforcing bars have lower temperatures and there is an important core of concrete with quite low temperatures. Consequently, after 150 minutes of ISO fire, the sections have a reserve of load capacity.

The columns, considered as isolated elements, loaded with the axial force and the bending moments on both principal cross-section axes (efforts corresponding to the fire combination of actions), were modelled with 3D beam elements, taking into account that the internal moments have important values in both directions of the principal cross-section axes The buckling length of the columns was considered, conservatively, as the system length. Equivalent imperfections according to EN1994-1-1[8] were imposed on both directions.

The horizontal displacement evolutions at the mid height of the columns of ground floor (which have the highest efforts in fire situation) are presented in figure 13. As the characteristic time-displacement demonstrates, excepting for the columns with rectangular cross-section with one axis of symmetry (d), all other columns of the ground floor does not resist to the 150 minutes of ISO fire under the imposed static loads.

Similar analysis was made for the columns of the upper floors. The fire resistance grows with each floor, as the stress level in the columns decrease on the height of the building. Excepting the columns with octagonal cross section and identical profiles 2HEB500, all columns above the ground floor fulfil the 150 minutes requirement. For the 2HEB500 columns, the R150 fire resistance requirement is fulfilled only from the 11th floor forth.

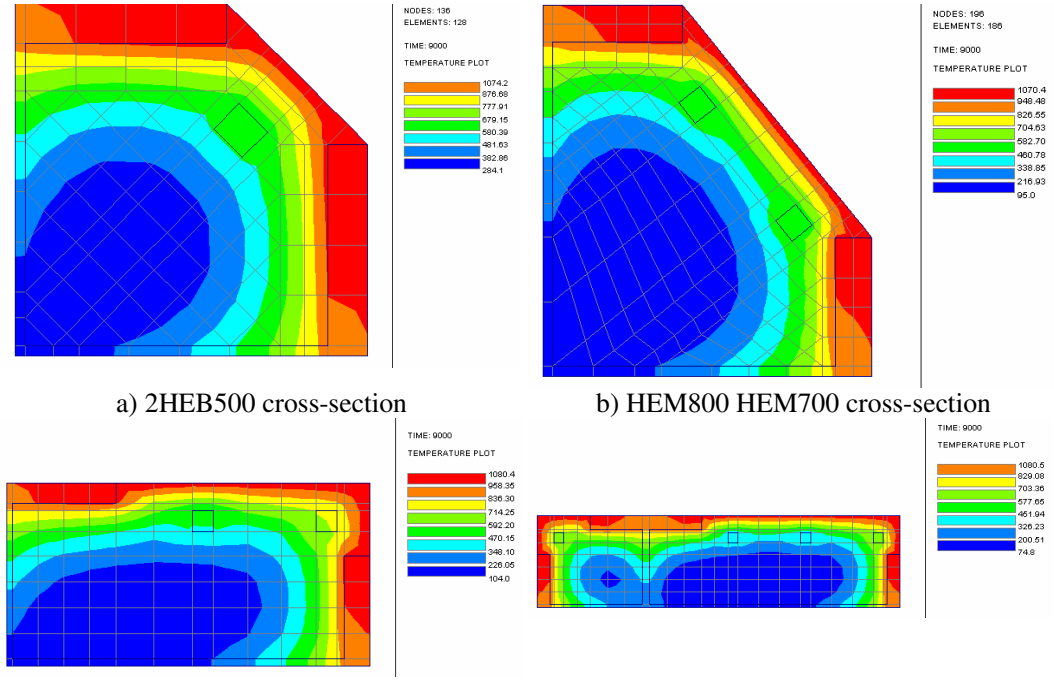

a) 2HEB500 cross-section

b) HEM800 HEM700 cross-section

c) HEB1000 HEB500 cross-section

d) HEB1000 HEM500 cross-section

Fig. 12 - Temperature distribution at 150 minutes of ISO fire

Table 1 gives the corresponding fire resistance times for all considered columns. Fire protection is needed for all the columns on the ground floor, except for the columns with rectangular cross-section with one axis of symmetry, while the 2HEB500 columns need protection up to the 11th floor.

Table 1. Fire resistance times [minutes].

Column	Ground floor	Floors 1-10	Floor 11 - forth
2HEB500	70	100-149	>150
HEM800HEM700	146	>150	>150
HEB1000HEB500	143	>150	>150
HEB1000HEM500	>150	>150	>150

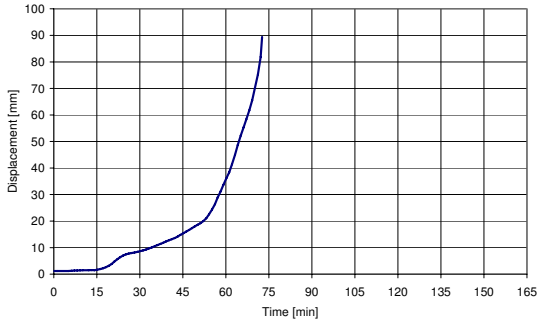

a) 2HEB500 column

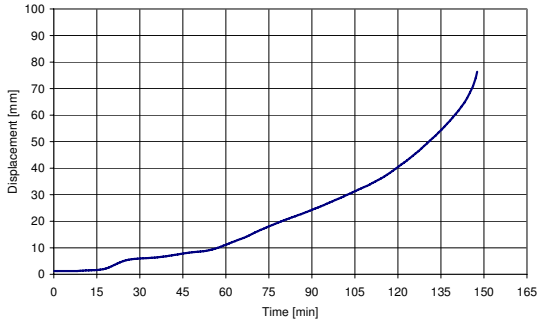

b) HEM800 HEM700 column

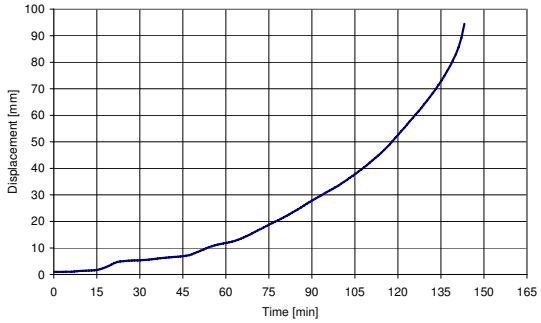

c) HEB1000 HEB500 column

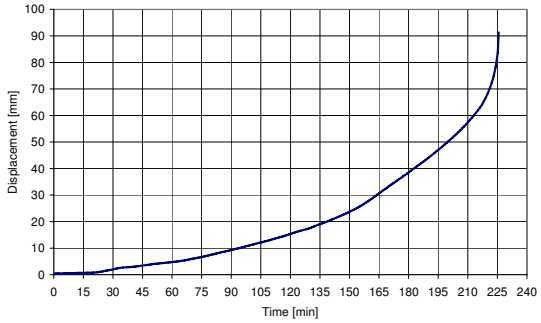

d) HEB1000 HEM500 column

Fig 13 - Displacement evolution under ISO fire.

4. CONCLUSIONS

The outstanding fire resistance obtained for the composite concrete filled circular hollow sections, as well as their increased resistance under usual conditions, confirms the efficiency of this structural solution. The 2 hours fire resistance required for columns in the office building was checked using all the three methods available in the European fire regulations EN1994-1-2. Beside the structural performance of this solution, it should be noted the simpler technology, as compared to the classical reinforced concrete columns. In the case of composite concrete filled circular hollow sections, there is no need for shuttering, leading to important savings in the cost of the structure.

The fire resistance of the composite steel-concrete columns of the „Bucharest Tower Centre“ structure was determined using advanced computation models. The fire analysis considering the ISO fire showed that the fire protection is needed for a limited number of columns of the building, in order to attain the $2^{1/2}$ hours of fire resistance.

REFERENCES

[1] EN1994-1-2: Eurocode 4 - Design of composite steel and concrete structures - Part 1-2: General rules - Structural fire design, 2005, European Committee for Standardization, Brussels.
[2] J. M. Franssen, V. K. R. Kodur, J. Mason, User Manual for SAFIR. A computer program for analysis of structures subbmited to the fire. University of Liege, Department 'Structures du genie civil' Service 'Ponts et charpentes', 2004.
[3] EN1990 Eurocode: Basis of Design, September 2004, European Comittee for Standardisation, Brussels.
[4] EN1991-1-2: Eurocode 1 - Actions on structures - Part 1-2: General actions - Actions on structures exposed to fire, 2005, European Committee for Standardization, Brussels
[5] Normativ pentru verificarea la foc a elementelor structurale ale constructiilor din otel – NP046/ 2000
[6] Ghid pentru verificarea la foc a elementelor structurale ale constructiilor din otel – GP055/ 2000
[7] L. Twilt & all. ‘Guide de dimensionnement – Poteaux en profils creux soumis a l`incendie’ Edite par Comite Internațional pour le Developpement et l`Etude e la Construction Tubulaire – CIDECT, Verlag TUV Rheinland GmbH, Koln, 1994
[8] EN1994-1-1: Eurocode 4 - Design of composite steel and concrete structures - Part 1-1: General rules and rules for buildings, 2005, European Committee for Standardization, Brussels.

Timber Structures

FIRE PERFORMANCE OF GYPSUM PLASTERBOARDS

ANDREA FRANGI[1], VANESSA SCHLEIFER[2], MARIO FONTANA[3], ERIC HUGI[4]

ABSTRACT

A comprehensive research project on the fire behaviour of protective claddings made of gypsum plasterboards and wood-based panels is currently carried out at ETH Zurich. Objective of the research project is the development of a design model for the verification of the separating function (insulation and integrity criteria) of light timber frame wall and floor assemblies. The paper describes the main results of a large number of small-scale fire tests with gypsum plasterboards. Particular attention is given to the FE-modelling of the thermal behaviour of gypsum plasterboards as wells as the comparison between fire tests under ISO-fire and non-standard fire conditions.

1. INTRODUTION

Light timber frame wall and floor assemblies are typical structural elements used in timber engineering. The assemblies consist of solid timber studs or beams with claddings made of gypsum plasterboards, wood-based panels or combinations of these layers. The cavities may be filled with insulation made of rock, glass or wood fibre. Unlike heavy timber structures where the char-layer of fire exposed members performs as an effective protection of the remaining unburned residual cross-section, the fire performance of load bearing and non- load bearing light timber frame assemblies mainly depends on the protection provided by the claddings [1,2,3]. A comprehensive research project on the fire behaviour of protective claddings made of gypsum plasterboards and wood-based panels is currently carried out at

[1] Dr., Institute of Structural Engineering, ETH Zurich, 8093 Zurich, Switzerland,
email: frangi@ibk.baug.ethz.ch
[2] PhD candidate, Institute of Structural Engineering, ETH Zurich, 8093 Zurich, Switzerland,
email: schleifer@ibk.baug.ethz.ch
[3] Prof. Dr., Institute of Structural Engineering, ETH Zurich, 8093 Zurich, Switzerland,
email: fontana@ibk.baug.ethz.ch
[4] Dr., EMPA, 8600 Dübendorf, Switzerland, email: hugi@empa.ch

ETH Zurich in collaboration with the Swiss Federal Laboratories for Materials Testing and Research (EMPA). Objective of the research project is the development of a design model for the verification of the separating function (insulation and integrity criteria) of light timber frame wall and floor assemblies. A large number of fire tests permitted the analysis of different parameters (material, thickness, position and number of the claddings, type and spacing of fasteners used) on the fire performance of fire protective claddings.

The paper describes the main results of the fire tests with fire protective claddings made of gypsum plasterboards. The test results enlarge the experimental background of the fire behaviour of gypsum plasterboards and permit the verification and improvement of calculation models of the fire resistance of gypsum plasterboards. Particular attention is given to the FE-modelling of the thermal behaviour of gypsum plasterboards as wells as the comparison between fire tests under ISO-fire and non-standard fire conditions.

2. FIRE TESTS

A series of 17 small-scale fire tests was performed with non-loaded specimens using claddings made of gypsum or timber subjected to ISO-fire exposure [4]. The fire tests were carried out on the EMPA's small furnace with the inner dimensions of 1.0 x 0.8 m. Gypsum plasterboards of type A and F according to EN 520 [5] as well as gypsum fibreboards from 3 different European manufacturers were studied (see Table 1). Gypsum plasterboards of type A are regular common boards and contain a porous gypsum core with no reinforcement except the paper laminated surface. Gypsum plasterboards of type F have improved core cohesion at high temperatures by adding other materials to the core such as glass fibres and fillers. Gypsum plasterboards of type X commonly used in North America also have improved core cohesion at high temperatures and may be considered similar to gypsum plasterboards of type F. Gypsum fibreboards are manufactured as non-standard boards and have a gypsum core reinforced with paper fibres. Gypsum fibreboards usually have a higher density in comparison to gypsum plasterboards of type A and F (see Table 1) and may show even a better fire performance than gypsum plasterboards of type F [6].

Table 1 – Mean density of the gypsum boards tested under ISO-fir exposure.

Manufacturer	Type	Density [kg/m^3]
Manufacturer 1	Gypsum fibreboard (GF)	1186
Manufacturer 2	Gypsum plasterboard (GP) of type A	908
	Gypsum plasterboard (GP) of type F	853
	Gypsum fibreboard (GF)	1504
Manufacturer 3	Gypsum plasterboard (GP) of type A	810
	Gypsum plasterboard (GP) of type F	889
	Gypsum fibreboard (GF)	1313

In addition to different types of gypsum boards tested, the number, thickness and position of the boards as well as the cavity insulation have been varied. Further also the influence of the type of fasteners used as well as the spacing of the fasteners was analysed. Usually four different claddings were studied in each test (see figure 1). A fire test with four identical gypsum boards showed the same temperature development for each cladding. Therefore the position of the claddings in the furnace did not influence the temperature development. During the tests the temperature at selected locations was measured with thermocouples of type K. For each cladding the thermocouples were placed on the fire unexposed side as well as between cladding and timber frame.

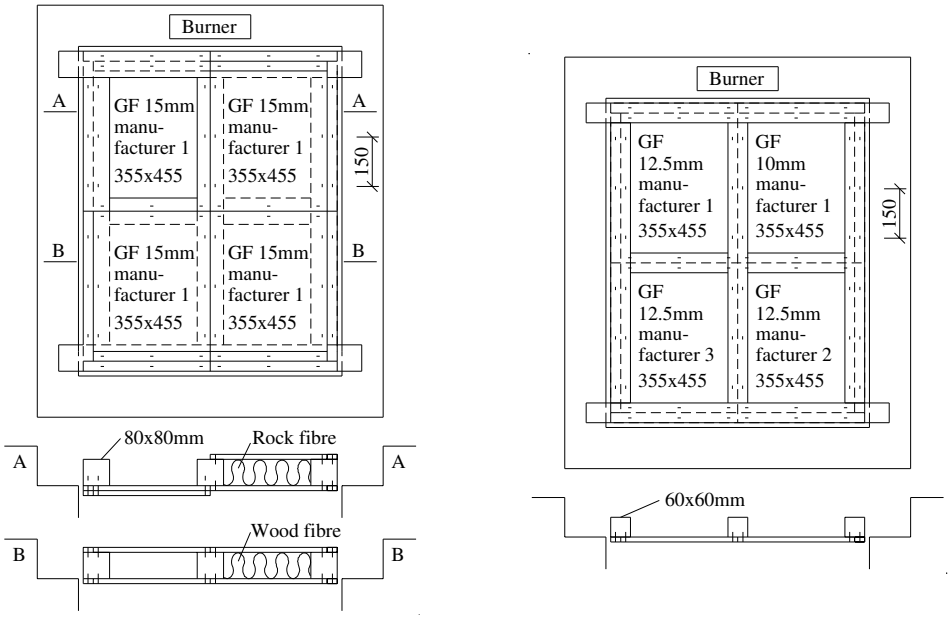

Fig. 1 – Test specimens for the small-scale fire tests: test specimen V4 (left) and V5 (right).

Figure 2 left shows the temperature development on the fire unexposed side of gypsum fibreboards with different thickness. During heating the free and chemically bound water in the gypsum is gradually driven off at temperatures above 100°C. This causes a temperature plateau on the fire unexposed side of the boards that is the main reason for the fire protective function of gypsum boards used as claddings. The duration of this plateau depends on the content of water in the board and therefore on the thickness of the board.

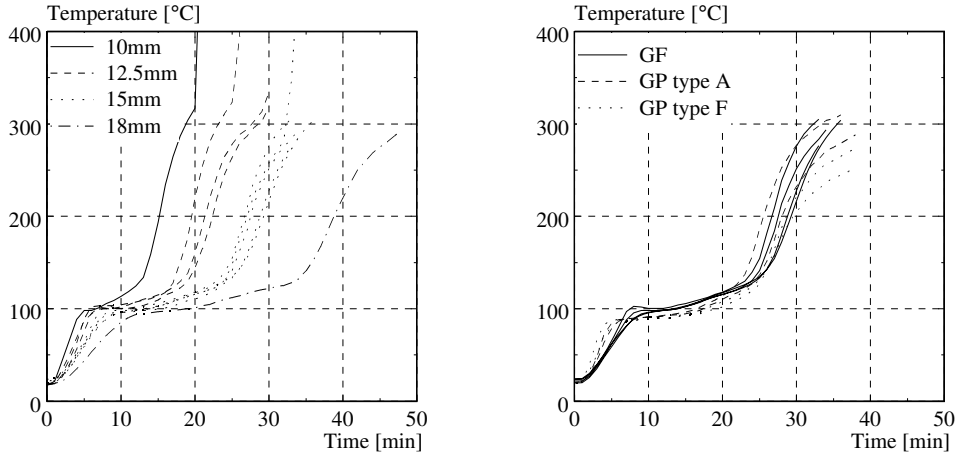

Fig. 2 – Left: temperature development on the fire unexposed side of gypsum fibreboards with different thickness tested as single board; Right: temperature development on the fire unexposed side of different types of 15 mm thick gypsum boards tested as single board

Figure 2 right shows the temperature development on the fire unexposed side for different types of gypsum boards (gypsum plasterboards of type A and F as well as gypsum fibreboards) with the same thickness (15 mm). Even though gypsum boards of different type

and manufacturer (with different density, fibres and fillers) were tested, the duration of the plateau at about 100°C was fairly the same and the overall temperature development measured up to about 200°C was quite similar. Thus, it can be assumed that the content of water and therefore of gypsum for the different boards was about the same. Further, the addition of fibres and fillers to the gypsum core did not change significantly the thermal behaviour of the boards. However, the reinforcement of the gypsum core with fibres and fillers generally improves the stability and the mechanical properties (shrinkage, cracking, ablation, falling off) of the boards after complete dehydration. Remarkable is that density of the gypsum fibreboards was much higher than for the gypsum plasterboards (see table 1), however no significant difference was observed with regard to the thermal behaviour. Thus, the density does not seem to be a relevant parameter to describe the thermal behaviour of gypsum boards. The main parameter is the content of water and therefore the thickness of the board (see fig. 2 left). Fire tests conducted with regular gypsum plasterboards as well as gypsum plasterboards with improved core cohesion from different countries (Sweden, Canada, USA, New Zealand and Japan) and tested as fire protective cladding of a wood member showed similar results [7]. The density of the boards tested varied between 651 and 864 kg/m^3.

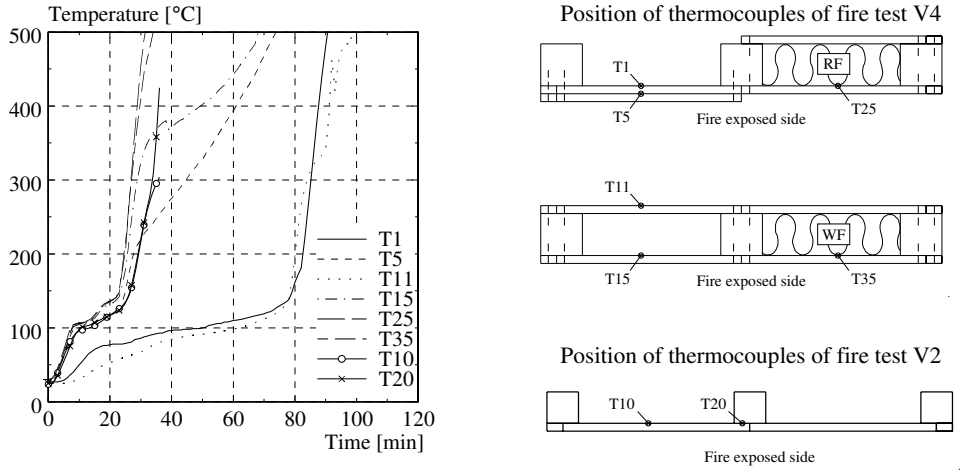

Fig. 3 – Left: temperature development for the small-scale fire test V4 (see figure 1) and V2; Right: position of the thermocouples (RF= rock fibre, WF = wood fibre)

All results shown in figure 2 were obtained testing single gypsum boards directly exposed to fire. In this way the thermal behaviour of the gypsum boards was studied without the influence of additional layers. However, gypsum boards used as cladding of light timber frame assemblies are usually backed by other boards (gypsum, timber), insulation batts (rock, glass or wood fibre) or void cavities. Figure 3 left shows the temperatures measured for the small-scale fire test V4 with 15 mm thick gypsum fibreboards (see figure 1 left) that permitted the analysis of the influence of the void cavity or cavities filled with different insulation (RF= rock fibre, WF = wood fibre) as well as the influence of multiple layers. Further, figure 3 left also gives the temperature development of 15 mm thick gypsum fibreboards tested as single board (fire test V2). It can be seen that the temperatures measured behind the fire exposed gypsum fibreboards for the assemblies with the cavities filled with rock fibre or wood fibre (see thermocouples T25 and T35) were similar and increased faster than for gypsum fibreboards tested as single board (see T10). Additional fire tests with gypsum boards backed with glass fibre showed the same thermal behaviour as for gypsum

boards backed with rock fibre or wood fibre. Thus, insulating batts caused the fire exposed gypsum boards to heat up more rapidly. The temperature development measured behind the fire exposed gypsum fibreboard for the assembly with void cavity (see T15) followed up to 250°C fairly the same development as for gypsum boards backed with rock fibre or wood fibre (see T25 and T35). Subsequently the temperature increase was slower. For the assembly with double layer of 15 mm thick gypsum fibreboards the temperature development measured behind the fire exposed gypsum fibreboard (see T5) followed up to 250°C quite the same development as for gypsum fibreboards tested as single board (see T10). Then the temperature increase was slower. A possible reason may be the effect of some moisture migration from the fire unexposed gypsum board towards the fire exposed gypsum board. Remarkable is that the temperature measured behind the fire unexposed gypsum fibreboard for the assemblies with void cavity and double layer (see T1 and T11) were quite similar. Thus, the void cavity did not influence significantly the temperature development on the fire unexposed side of the assembly.

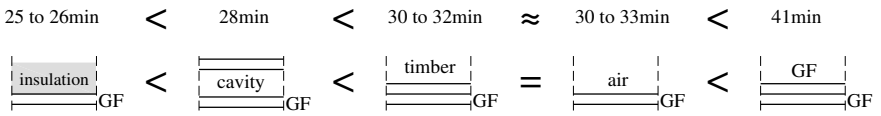

Fig. 4 – Time measured to reach the temperature rise of 250°C (average) and 270°C (at any point) on the fire unexposed side of 15 mm thick gypsum fibreboards tested as single board or backed with different materials.

Table 2 – Measured fire resistance of the small-scale tests V4 and V9 with regard to the insulation criterion (temperature rise criteria: 140°C/180°C at unexposed side of assembly)

Fire test	Test specimen	Insulation time [min]	Figure
V9	3x10 mm gypsum fibreboards	57	10 10 10
V4	15+15 mm gypsum fibreboards with cavity filled with 80 mm thick wood fibre batts (ρ = 178 kg/m^3)	72	15 WF 15
V4	15+15 mm gypsum fibreboards with void cavity	80	15 cavity 15
V4	2x15 mm gypsum fibreboards	83	15 15
V9	2x15 mm gypsum fibreboards with cavity filled with 80 mm thick glass fibre batts (ρ = 27 kg/m^3)	85	15 GF 15
V9	2x15 mm gypsum fibreboards with cavity filled with 40 mm thick rock fibre batts (ρ = 31 kg/m^3)	> 85 (test stopped)	15 RF 31 15
V9	2x15 mm gypsum fibreboards with cavity filled with 40 mm thick rock fibre batts (ρ = 110 kg/m^3)	> 85 (test stopped)	15 RF 110 15
V4	15+15 mm gypsum fibreboards with cavity filled with 80 mm thick rock fibre batts (ρ = 42 kg/m^3)	> 105 (test stopped)	15 RF 42 15

Temperature measurements between gypsum board and timber frame (see for example thermocouple T20 in figure 3) as well as additional results of fire tests with gypsum boards backed by timber boards (OSB, particle boards) showed that the timber had a small influence on the thermal behaviour of the gypsum boards in comparison to gypsum boards tested as single board (see also thermocouples T10 and T20 in figure 3). Figure 4 summarizes the measured time taken to reach the temperature rise of 250°C (average) and 270°C (at any

point) on the fire unexposed side of 15 mm thick gypsum fibreboards tested as single board or backed with different materials.

Table 2 summarizes the measured fire resistance of the small-scale fire tests V4 and V9 with regard to the insulation criterion. According to most standards (e.g. EN 13501-2 [8]) the insulation failure is the time taken for the average temperature on the fire unexposed side of the whole construction to increase by 140°C and at any point by 180°C. It can be seen that assemblies with cavities filled with rock fibre batts showed the highest fire resistance although the thermal behaviour of gypsum boards backed by insulating batts is influenced unfavourable (see figures 3 and 4). The shortest fire resistance was measured for the assembly consisting of 3 layers of gypsum fibreboards, although the total thickness of the gypsum fibreboards was the same as for the other assemblies given in table 2. The main reason is that the 10 mm thick gypsum fibreboards fell off earlier than the 15 mm thick gypsum fibreboards. Remarkable is that the insulation time of the assembly with the cavity filled with 80 mm thick wood fibre batt was lower than for the assembly with void cavity. The reason was that first the wood fibre batt caused the fire exposed gypsum board to heat more rapidly, and secondly the wood fibre batt started to shrink strongly when directly exposed to fire and fell off. Unlike the wood fibre batt rock fibre batt remained in place during the whole time of fire exposure.

3. FE-THERMAL ANALYSIS

For the calculation of the temperature development in gypsum boards subjected to ISO-fire a FE-thermal analysis was conducted using ANSYS 11. The heat transfer to the surface of the member was calculated using temperature-independent constant values according to EN 1991-1-2 [9] for the resultant emissivity by radiation $\varepsilon_{res} = 0.8$ and the coefficient of heat transfer by convection $\alpha_{c,exp} = 25 W/m^2K$ and $\alpha_{c,unexp} = 4 W/m^2K$. Density, thermal conductivity and specific heat capacity of gypsum vary as a function of the temperature. Unfortunately, the thermal properties of gypsum at high temperatures are difficult to measure. Transient effects and the method of measurement can have a significant effect on the test results [10]. Further, the thermal properties are influenced by mass transfer of moisture into or out of the gypsum board as well as cracking and ablation. In order to consider these effects the thermal properties are usually calibrated to results of fire tests. Thus, thermal properties of gypsum used in FE-thermal analyses are often "apparent" values rather than "real" physically correct material properties and explain the large scatter of values used by different authors [11].

For this study the variation of the density with increasing temperature was determined by a thermo gravimetric analysis (TGA) conducted at the Institute for Geotechnical Engineering of ETH Zurich. The analysis was conducted with a heating rate of 20°C/min using a piece of a gypsum board of type A used for the tests. The TGA showed a first mass loss of about 17% between 100 and 170°C and a second mass loss of about 5% between 600 and 750°C and well agreed with results of other studies (see figure 5 left) [12,13,14]. Further, the gases emitted during the TGA were measured. Between 100 and 170°C water vapour (H_2O) was measured and between 600 and 750°C carbon dioxide (CO_2). Figure 5 right compares the temperature-dependent density used for the FE-thermal analysis with values assumed by other authors.

Gypsum boards mainly consist of gypsum, a crystalline form of calcium sulphate combined with water known as calcium sulphate dihydrate ($CaSO_4 \cdot 2H_2O$). When exposed to increasing temperature calcium sulphate dihydrate undergoes two endothermic decomposition reactions in which the chemical bound water is removed leading to calcium sulphate

anhydrite ($CaSO_4$). In addition to calcium sulphate dihydrate gypsum boards contains other materials in various quantities depending on the manufacturer. For example, the results of the TGA in combination with an additional analysis with a Roentgen diffractometer showed that the gypsum board tested consisted of more than 80% of gypsum, about 10% of calcium magnesium carbonate ($CaMg(CO_3)_2$) and the remaining 10% of not well indentified additional materials. A similar composition of a different gypsum board was found in [14].

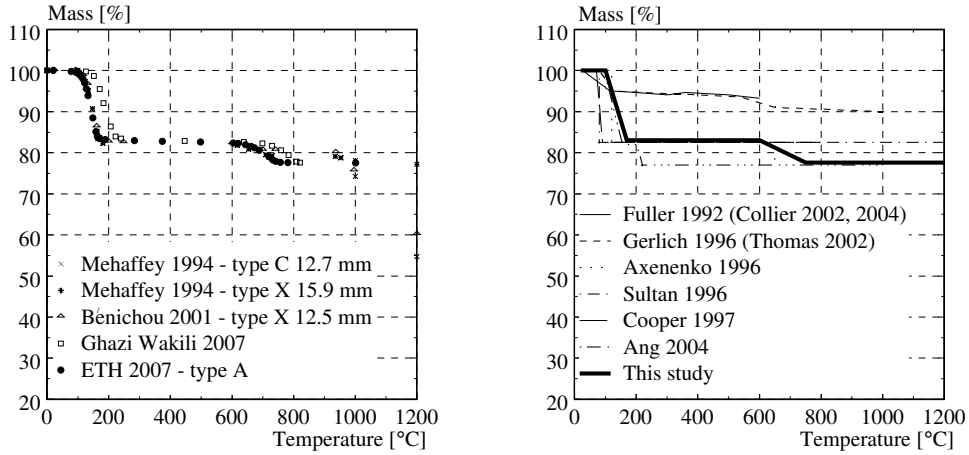

Fig. 5 – Left: Mass loss with increasing temperature measured with thermo gravimetric analysis conducted by different authors; Right: Temperature-dependent density used for the FE-thermal analysis in this study as well in previous studies.

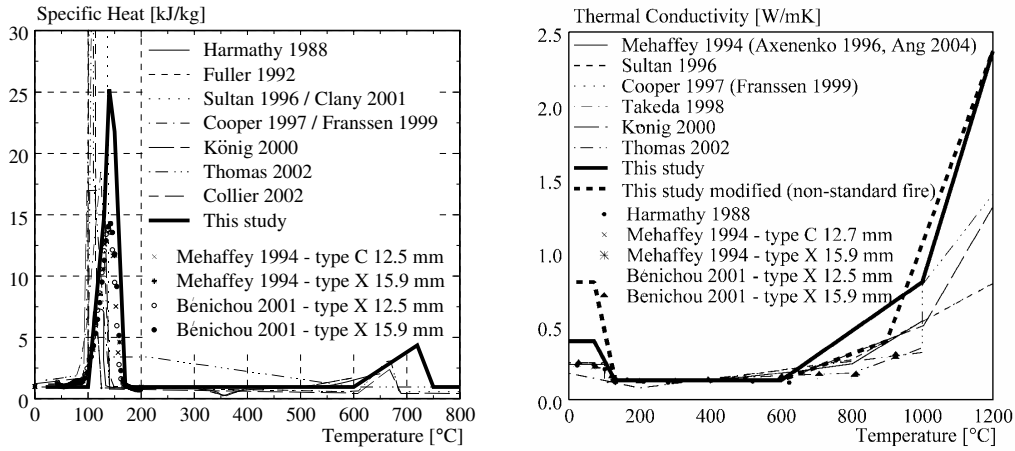

Fig. 6 – Temperature-dependent specific heat (left) and thermal conductivity (right) used for the FE-thermal analysis in this study as well in previous studies. The points given in the figures indicate measured values of the specific heat and thermal conductivity.

Figure 6 left shows the temperature-dependent specific heat used for the FE-thermal analysis. In the figure also values measured and assumed by other authors are given. The variation of the specific heat as a function of the temperature was calculated taking into account the different chemical reactions occurring during the heating of gypsum boards. The first peak in figure 6 left represents the two endothermic reactions of the dehydration of gypsum as mentioned earlier. Based on the TGA results it was assumed that both reactions

occurred between 100 and 170°C. The first peak was assumed by all authors, however the total energy may differ depending on the total amount of free and chemical bound water assumed in the gypsum board or because of model calibration. The second peak represents the decomposition of the calcium magnesium carbonate. Based on the TGA results it was assumed that this reaction occurred between 600 and 750°C. Although the second peak strongly differed from the values assumed by other authors, its influence on the temperature development is not so relevant, as the chemical reaction occurs at elevated temperature and the reaction enthalpy is relative small.

The thermal conductivity was assumed based on measurements found in the literature [12,13,15] and calibrated to results of fire tests with single gypsum plasterboards. The increased thermal conductivity between 20 and 70°C takes into account the increase heat transfer due to mass transfer of moisture. Shrinkage, cracks and ablation of gypsum boards increase the heat flux due to radiation and convection. For simplicity, these effects were modelled by increasing the thermal conductivity starting from 600°C. This approach has already been used by other authors. Figure 6 right shows the temperature-dependent thermal conductivity used for the FE-thermal analysis. In the figure also values measured and assumed by other authors are given.

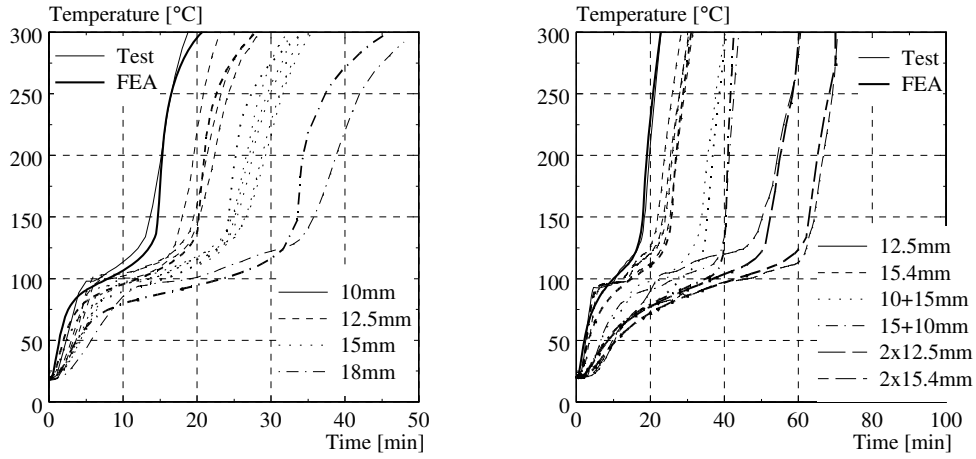

Fig. 7 – Comparison between measured and calculated temperatures for different fire tests.

The results of 10 small-scale fire tests on single gypsum boards were used to calibrate the material properties assumed for the thermal analysis. In this way the thermal behaviour of the gypsum boards was not influenced by other layers. After calibration, the material properties were verified with additional 15 small-scale and large-scale fire tests [16,17,18]. The FE-thermal analysis well predicted the temperature development of gypsum boards. Figure 7 compares some test results with the FE-thermal analysis (FEA).

4. START OF CHARRING AND INSULATION VALUE OF GYPSUM BOARDS

Gypsum plasterboards used as cladding improve the fire resistance of timber structures by protecting the timber surface from fire during a so called protection phase. For example EN 1995-1-2 [19] gives rules for the calculation of the start of charring of timber surfaces protected by fire protective claddings made of wood-based panels or wood panelling as well

as gypsum plasterboards. For claddings consisting of one layer of gypsum plasterboard of type A or F the time of start of charring t_{ch} can be calculated as:

$$t_{ch} = 2.8 \cdot h_p - 14 \quad [\text{min}] \tag{1}$$

where h_p is the thickness in mm of the gypsum plasterboard. EN 1995-1-2 assumes a linear correlation between thickness of the board and start of charring.

Based on a FE-parametric study equation (2) was developed for the calculation of start of charring t_{ch} of timber protected by gypsum boards, where t_{ch} was calculated in analogy to the testing method for fire protective claddings given in EN 13501-2, i.e. considering single gypsum boards backed by a 19 mm thick particleboard. According to EN 1995-1-2 it was assumed that the particleboard protected by the gypsum board started charring when the temperature between gypsum and particleboard reached the temperature of 300°C.

$$t_{ch} = 30 \cdot \left(\frac{h_p}{h_{p,ref}} \right)^{1.2} \quad [\text{min}] \tag{2}$$

where h_p is the thickness in mm of the gypsum board and $h_{p,ref}$ is the thickness of a reference gypsum board ($h_{p,ref}$ = 15mm).

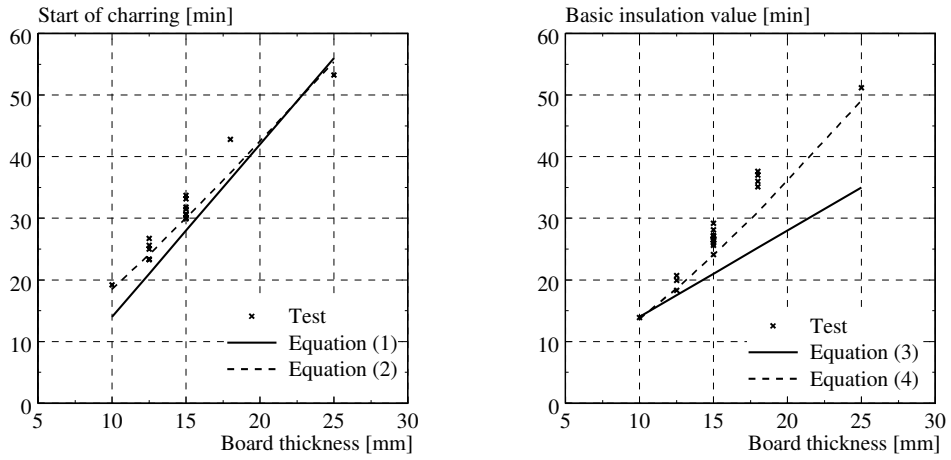

Fig. 8 – Left: Comparison of start of charring measured in the fire tests and calculated according to equation (1) and (2) for all gypsum boards backed by timber board or frame; Right: Comparison of basic insulation value measured in the fire tests and calculated according to equation (3) and (4) for all gypsum boards tested as single board.

Figure 8 left shows the comparison of start of charring measured in the small-scale fire tests and calculated according to equations (1) and (2) for all fire tests with gypsum boards backed by timber board or frame. It can be seen that the difference between equation (1) and (2) is quite small and both well agree with the test results. Unlike EN 1995-1-2 equation (2) assumes a non-linear relationship between thickness of the board and start of charring.

For the verification of the separation function of assemblies, so called component additive methods are common, where the fire resistance of multi-layered constructions is obtained by adding the contribution to the fire resistance of the different layers [20]. For simplification, EN 1995-1-2 calculates the contribution of each layer using a basic insulation value in combination with a position and joint coefficient. The joint coefficient considers the detail of the joints and their influence on the insulation time of layers with joints. The position coefficient considers the position of the layer within the assembly (in direction of the heat flux), because the layers preceding and backing the layer considered have an influence on its

fire behaviour. The basic insulation value $t_{ins,0}$ corresponds to the fire resistance of a single layer without the influence of adjacent materials and depends on the material and the thickness of the layer. According to EN 13501-2 the basic insulation value is the time taken for the average temperature on the fire unexposed side of the whole layer to increase by 140°C and at any point by 180°C. EN 1995-1-2 gives following equation for the calculation of the basic insulation value $t_{ins,0}$ of gypsum plasterboards of type A and F:

$$t_{ins,0} = 1.4 \cdot h_p \quad [\text{min}] \tag{3}$$

where h_p is the thickness in mm of the gypsum plasterboard. Like equation (1) EN 1995-1-2 assumes a linear correlation between thickness of the board and basic insulation value.

A FE-parametric study permitted the development of equation (4) for the calculation of the basic insulation value $t_{ins,0}$ of gypsum boards. The basic insulation value $t_{ins,0}$ was calculated assuming a single gypsum board and considering the criterion of 140°C for the increase of the temperature on the fire unexposed side of the board.

$$t_{ins,0} = 24 \cdot \left(\frac{h_p}{h_{p,ref}} \right)^{1.4} \quad [\text{min}] \tag{4}$$

where h_p is the thickness in mm of the gypsum board and $h_{p,ref}$ is the thickness of a reference gypsum board ($h_{p,ref}$ = 15mm).

Figure 8 right shows the comparison of the basic insulation value measured in the small-scale fire tests and calculated according to equations (3) and (4) for all fire tests with gypsum boards tested as single board. It can be seen that the basic insulation values calculated according to equation (3) (EN 1995-1-2) were in a good agreement only with the results of fire tests with 10 mm thick gypsum boards. By increasing thickness of the board the basic insulation values were underestimated, i.e. the calculation model led to conservative results. Vice versa, the results based on the FE-parametric study (equation 4) agreed better with the test results. Unlike EN 1995-1-2 equation (4) assumes a non-linear relationship between thickness of the board and basic insulation value.

5. FIRE BEHAVIOUR UNDER NON-STANDARD FIRE EXPOSURE

The small-scale fire test V3 performed with one single 15 mm thick gypsum fibreboard was repeated using a non-standard fire exposure. The non-standard fire test was performed activating the furnace burners as extreme as possible. The objective of the fire test was the analysis of the influence on the temperature development of the gypsum fibreboard exposed to a non-standard fire more severe than the ISO-fire exposure.

Figure 9 left shows the temperature development in the furnace as well on the fire unexposed side of the gypsum fibreboard for the ISO-fire and non-standard fire exposure. It can be seen that the gypsum fibreboard was exposed to temperatures about 200°C higher than in comparison to ISO-fire exposure. As a consequence during the non-standard fire test the gypsum fibreboard heated up quicker and finally the gypsum fibreboard failed about than 10 minutes earlier than the gypsum fibreboard tested under ISO-fire exposure. Figure 9 right compares the temperatures measured on the fire unexposed side of the gypsum fibreboard with the results of the FE-thermal analysis for both ISO-fire exposure and non-standard fire exposure. In a first step the FE-thermal analysis for the non-standard fire test was conducted using the same thermal properties assumed for ISO-fire exposure (in the figure 9 right this is indicated as FEA). However, it can be seen that the use of the thermal properties calibrated to ISO-fire exposure did not well predict the temperature development on the fire unexposed side of the gypsum fibreboard for the non-standard fire exposure. A possible reason may be

the strong influence of heat transfer due to mass transfer of moisture that for simplicity in the FE-thermal analysis is considered by using an effective value of the thermal conductivity rather than a physically correct value. It may be expected an increased heat transfer due to mass transfer of moisture for the non-standard fire more severe than the ISO-fire exposure. Thus, in a second step in order to take into account this effect the thermal conductivity was increased between 20 and 70°C and reduced starting from 600°C in comparison to the values assumed for ISO-fire exposure. In the figure 6 right the modified thermal conductivity is indicated with "This study modified (non-standard fire)". With this modification the FE-thermal analysis fairly well predicted the temperature development on the fire unexposed side of the gypsum fibreboard for the non-standard fire exposure (in the figure 9 right this is indicated as FEA modified). The need of calibration of the thermal properties to the fire exposure is a present limitation of common FE-thermal analysis and may be overcome by development of calculation models that take into account phenomena like the heat transfer due to transfer of moisture and cracking.

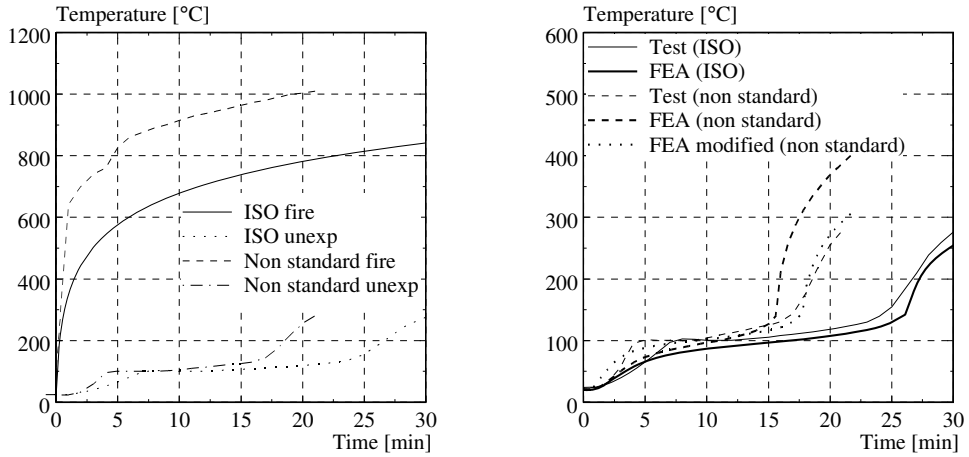

Fig. 9 – Left: temperature development in the furnace as well on the fire unexposed side of the gypsum fibreboard for the ISO-fire and non-standard fire exposure; Right: Comparison between calculated and measured temperatures on the fire unexposed side of the gypsum fibreboard for the ISO-fire and non-standard fire exposure

6. CONCLUSIONS

The fire behaviour of gypsum boards was investigated with a large number of small-scale fire tests. In order to study the thermal behaviour of the gypsum boards without the influence of additional layers some fire tests were performed using single boards. The fire tests showed that the overall thermal behaviour of different types of gypsum boards (with different density, fibres and fillers) was quite similar. Thus, the reinforcement of the gypsum core did not influence significantly the thermal behaviour, however generally improved the mechanical properties (shrinkage, cracking, ablation, falling off) of the boards after complete dehydration. Further, the test results showed that the layer backing the gypsum board may have a strong influence on the thermal behaviour of the gypsum board. Insulating batts caused the fire exposed gypsum boards to heat more rapidly and fail earlier. However, assemblies with cavities filled with insulating batts that remained in place after failure of the cladding showed the highest fire resistance with regard to the insulation criterion. The temperature

development in gypsum boards subjected to ISO-fire exposure was simulated with a FE-thermal analysis. The material properties assumed for the FE-thermal analysis were calibrated to results of several fire tests on single gypsum boards and verified with additional small-scale and large-scale fire tests. A FE-parametric study permitted the development of new equations for the calculation of the basic insulation value of gypsum boards as well as the start of charring of timber protected by gypsum boards. The new equations were in better agreement with fire test results in comparison with the equations given in EN 1995-1-2. A test performed assuming a non-standard fire exposure more severe than ISO-fire showed that the thermal behaviour of the gypsum board was strongly influenced by the fire exposure. Further, the FE-thermal analysis conducted with the material properties assumed for ISO-fire did not well predict the thermal behaviour of the gypsum board. A good agreement between fire test and FE-thermal analysis could be obtained after modifying the apparent thermal conductivity.

7. REFERENCES

[1] Takeda, H. and Mehaffey, JR., "WALL2D: A model for predicting heat transfer through wood-stud walls exposed to fire", Fire and Materials Vol. 22:133–140, 1998.
[2] König, J. and Walleij, L., "Timber frame assemblies exposed to standard and parametric fires, Part 2: A design model for standard fire exposure", Trätek, Report I 0001001, Stockholm, 2000.
[3] Young, S.A. and Clancy, P., "Structural modelling of light-timber framed walls in fire", Fire Safety Journal Vol. 36: 241-268, 2001.
[4] Schleifer, V., Frangi, A. and Fontana, M., „Experimentelle Untersuchungen zum Brandverhalten von Plattenelementen", Institute of Structural Engineering, ETH Zürich, IBK Report No. 302, 2007
[5] EN 520:2004, Gypsum plasterboards, Definitions, requirements and test methods.
[6] Kordina, K. and Meyer-Ottens, C., „Holz Brandschutz Handbuch", 2. Auflage, Deutsche Gesellschaft für Holzforschung e.V., München, Ernst & Sohn Verlag, 1995
[7] Tsantaridis, L.D., Östman, B. and König, J., "Fire Protection of Wood by Different Gypsum Plasterboards", Fire and Materials Vol. 23: 45-48, 1999.
[8] EN 13501-2:2003, Fire classification of construction products and building elements - Part 2: Classification using data from fire resistance tests, excluding ventilation services.
[9] EN 1991-1-2:2002, Eurocode 1: Actions on Structures - Part 1-2: General Actions - Actions on Structures Exposed to Fire.
[10] Thomas, G., "Thermal properties of gypsum plasterboards at high temperatures", Fire and Materials Vol. 26: 37-45, 2002.
[11] Källsner, B and König, J., "Thermal and mechanical properties of timber and some other materials used in light timber frame construction", Proceedings 33th CIB-W18 Meeting, Delft, 2000.
[12] Mehaffey, J.R., Cuerrier, P. and Carisse, G., "A model for predicting heat transfer through gypsum-boards/woos-stud walls exposed to fire", Fire and Materials Vol. 18:297-305, 1994.
[13] Bénichou, N, Sultan, M. A., MacCallum, C. and Hum, J, "Thermal properties of wood, gypsum and insulation at elevated temperatures", NRCC, Internal Report IR-710, Ottawa, 2001.
[14] Wakili, G.K, Hugi, E., Wullschleger, L. and Frank, Th., "Gypsum board in fire - Modeling and experimental validation", Journal of Fire Sciences Vol. 25: 267-282, 2007.

[15] Harmathy T. Z., "Properties of building materials", The SFPE Handbook of Fire Protection Engineering, Society of Fire Protection Engineers / National Fire Protection Association, 2nd Edition, Boston, 1988.
[16] König, J. and Norén J., "Timber frame assemblies exposed to standard and parametric fires -
Part 1: Fire tests", Trätek, Rapport I 9702015, Stockholm, 1997.
[17] König, J. and Walleij L., "One-dimensional charring of timber exposed to standard and parametric fires in initially unprotected and post-protection situation", Trätek, Rapport I 9908029, Stockholm, 1999.
[18] König, J. and Rydholm, D., "Small-scale fire tests of heavy timber components", Trätek, Rapport P 0310036, Stockholm, 2003.
[19] EN 1995-1-2:2004, Eurocode 5, "Design of timber structures, Part 1-2 General rules-Structural fire design".
[20] König, J., Oksanen, T., Towler, K., "A review of component additive methods used for the determination of fire resistance of separating light timber frame construction", Proceedings 33th CIB-W18 Meeting, Delft, 2000.

ON THE DESIGN OF TIMBER BOLTED CONNECTIONS SUBJECTED TO FIRE

PETER MOSS[1], ANDREW BUCHANAN[2], MASSIMO FRAGIACOMO[3] and CARLA AUSTRUY[4]

ABSTRACT

For some years now, Johansen's yield equations have been used in Europe and USA to predict the ultimate strength of bolted (dowelled) connections in timber members under ambient temperatures. More recently, several researchers have begun to investigate the embedment strength of bolted or dowelled connections at elevated temperatures. At the University of Canterbury, research has been carried out to investigate the application of Johansen's yield equations to the prediction of the failure strength of bolted connections in fire conditions. A series of single bolted connections using steel side plates have been heated at constant temperature for several hours, then loaded to failure and used to determine the embedment strength of the joints over a range of temperatures from ambient to 300°C. These temperature-dependent embedment strengths have also been used in Johansen's equations for connections using a central steel plate as well as connections using wood side members. Comparisons have also been made with the results of several similar connections tested in fire conditions and show considerable promise for predicting failure of such joints. A proposal for implementation of an easy-to-use approach for the prediction of the fire resistance of bolted joints has been developed and will be discussed in the paper. The proposal is based on an extension of the Johansen's yield equations to fire conditions, and includes a model for the variation of the embedment strength with the temperature.

[1] Associate Professor, Department of Civil and Natural Resources Engineering, University of Canterbury, Christchurch, New Zealand,
email: peter.moss@canterbury.ac.nz
[2] Professor of Timber Design, Department of Civil and Natural Resources Engineering, University of Canterbury, Christchurch, New Zealand,
email: andy.buchanan@canterbury.ac.nz
[3] Associate Professor, Department of Architecture and Planning, University of Sassari, Alghero, Italy,
email: fragiacomo@uniss.it
[4] Ecole normale superieure de Cachan, France,
email: Carla.Austruy@crans.org

1. INTRODUCTION

Fire is unpredictable and dangerous, especially in residential buildings. The effects of fire on timber structural members are very complex because of the large number of variables involved. Once ignition has occurred, then a layer of char forms as the wood burns. A structural wood member will lose load capacity as the wood is converted to charcoal which has no strength. The thickening char layer protects the remaining wood, resulting in a predictable rate of charring below the surface. The rate of development of this charred layer determines how long the member can continue to carry load before the strength of the remaining unburned wood material is exceeded. A thin layer of heat-affected wood below the char layer will have reduced strength and stiffness.

In recent years, a number of research papers have been published on the influence of temperature on the mechanical properties of wood[1, 2, 3, 4]. Research has also been carried out into the performance of joints in timber members when subjected to fire temperatures[5, 6, 7, 8, 9]. Particular research into the embedment strength of wood at elevated temperatures has also been carried out[10, 11].

Moraes et al[10] carried out embedment tests at temperatures ranging from 20ºC to 240ºC. The 8 mm diameter dowel specimens were heated for 2 hours before testing to a maximum displacement of 5 mm. They found that the embedment strength at 80ºC was 30% lower than at 20ºC but then rose to a peak at 140ºC where it was 15% lower than at 20ºC and then decreased to 40-50% at 240ºC. The tested specimens showed that the moisture content decreases linearly with increase in the test temperature. The specimens had a moisture content of about 5% at 80ºC and were found to be almost oven dry at 140ºC.

For some time now, the European timber code[12] has used formulae based on Johansen's yield equations[13] to predict the strength of timber connections under ambient conditions. Eurocode 5[14] gives some guidance for predicting the strength of connections during fire conditions. Carling[15] defined failure as occurring when the rate of displacement exceeds 10 mm/min, or the total displacement exceeds 15 mm. He also proposed a formula for calculating the time to failure for bolted connections, based on his experimental testing.

This paper describes an experimental investigation to determine the axial tensile strength of a bolted connection that utilised steel or timber splice plates to connect timber members made from LVL (laminated veneer lumber). Single-bolted connections were tested under constant temperature conditions to determine the embedment strength of the LVL over a range of temperatures. The variation of the embedment strength was then used in Johansen's equations (as presented in EC5[12]). The purpose of the research was to investigate the relationship between the embedment strength of LVL timber and the time to failure of the connections when exposed to fire.

2. BACKGROUND TO THE TESTING

The design for the connection tested previously by Lau[16], Chuo[17] and Moss et al.[18] was based on a tensile member in the bottom chord of a floor or roof truss. The timber (LVL) members being joined were 150 × 63 mm. The design properties of the LVL are shown in Table 1. The steel side plates were 6 mm thick. The bolts were 12 mm diameter and were made of Grade 4.6 steel.

The design load on the joint was taken to be 40% of the ultimate tensile strength of the LVL in cold conditions (i.e. a load of 40% of 221 kN = 88 kN) by assuming that other design conditions will be more critical than the tensile strength of the member. With a calculated load factor of 0.33 for fire conditions, this gave an expected fire load of 29 kN. Six bolts were

Table 1 Limit state properties for design with NelsonPine LVL[19].

Elastic Moduli		
Modulus of elasticity	E	10.7 GPa
Modulus of rigidity	G	660 MPa
Characteristic Strength		
Bending	f'_b	42 MPa
Tension parallel to grain	f'_t	22 MPa
Compression parallel to grain	f'_c	35 MPa
Shear in beams	f'_s	6.0 MPa
Compression perpendicular to grain	f'_p	12 MPa

used for the Wood-Wood-Wood (W-W-W) joint, four bolts for the Steel-Wood-Steel (S-W-S) joint, and five bolts for the Wood-Steel-Wood (W-S-W) joint.

The same size timber and steel members were used to fabricate single-bolt joints with 12 mm diameter bolts. The bolts were placed on the member centreline with an end distance of 100 mm, i.e. eight bolt diameters, as shown in Figure 1 for the three different connections.

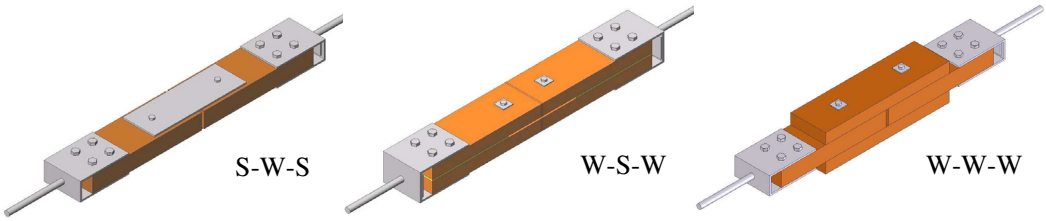

Fig. 1 - The three types of connection tested. Multi-bolted specimens were also used in fire tests.

3. HEATED TESTING

In order to develop a simple method of predicting the load capacity and deformation of connections in timber structures when exposed to known heat flux, a series of tests were carried out at known temperatures in a similar manner to that outlined in previous research[10, 11]. For this testing, a series of single-bolt joints were heated in the furnace for two hours at a constant temperature with no applied load under temperatures ranging from ambient to 280°C.

Fig. 2 - The test frame and furnace used for the heated tests and fire testing.

The test specimens were then quickly loaded to failure in accordance with the loading protocol suggested by ISO 10984-2[20]. The furnace used for both the heated tests and the fire tests is shown in Figure 2.

3.1 Embedment Strength

Since the S-W-S connections were similar to standard embedment test specimens, the results from these tests were used to evaluate a form of embedding strength for the LVL at elevated temperatures. The main differences between the single-bolt joints tested and the testing apparatus as required by ISO 10984-2[20] are outlined in Table 2.

Table 2 Comparison of single-bolt connection and ISO standard embedment test

	Single-bolted SWS connection	ISO Standard Embedment Test[20]
1.	Steel members tightly bolted to timber member (Fig. 1).	No contact between steel members and test specimen.
2.	Two fasteners were used in each test (i.e. one at each member end).	Only one fastener used in test.

The embedment strength was calculated by dividing the critical load by the bearing area (product of bolt diameter and thickness of the member), assuming a mode j/l failure as shown in Figure 6. The "embedment strength" in the ISO standard is based on either the maximum load or the load at 5 mm displacement, depending on which occurs first. As the bolted connection contained two bolts (one at each member end as shown in Figure 1) and the maximum load occurred at a large displacement, the critical load was taken as either the load at 10 mm displacement, or the maximum load. For connections where there was bending of the bolt (mode k in Figure 6), the embedment strength was calculated from the relevant Johansen's yield formula from EC5, including the calculated bending strength of the bolt at elevated temperature.

For connections in ambient conditions, both strength and serviceability are important. Johansen's equations can be used to predict strength, and the use of an embedment strength based on either the maximum load or the load at 5 mm displacement makes some recognition of serviceability. However, in fire situations serviceability is not as important as ensuring that the connection can carry load for some time before collapse occurs. For this reason, it is suggested that the embedment strength should be based on the maximum load regardless of the displacement at which this occurs.

The results for embedment strength versus temperature are shown in Figure 3 where it can be seen that the embedment strength decreases as the temperature increases, reaching a minimum at about 110ºC and then increasing as the temperature increases further to 200ºC, followed by a decrease with further temperature increase. The data points shown by triangles in Figure 3 are the embedment strengths determined using 45 mm thick LVL and 12 mm thick splice plates, where the thinner thickness of LVL fully complies with the thickness to bolt diameter ratio recommended by the ISO standard[20] for embedment strength tests. The approximation 1 of Figure 3 (dashed line) shows the embedment strength based on the maximum load while approximation 2 is the same, except that the embedment strength is now taken as independent of temperature for all temperatures below 20 ºC and above 270 ºC (or minimum strength of 10MPa).

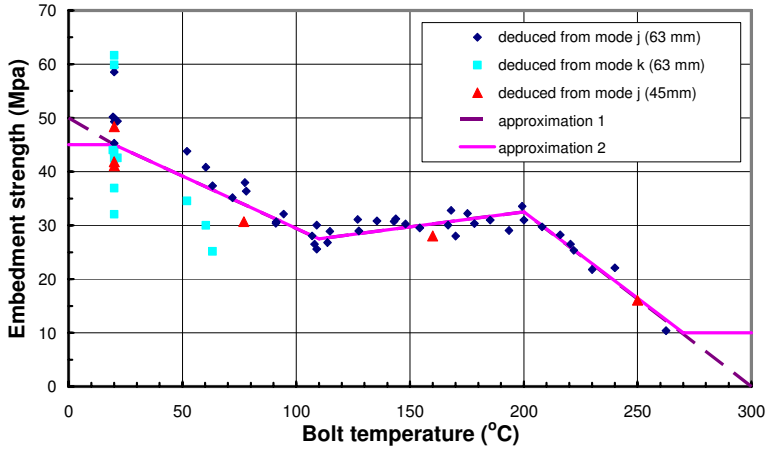

Fig. 3 - LVL embedment strength based on maximum load, and with cut-off below 20°C and above 270°C

3.2 Prediction of fire resistance

The temperatures of the air, the steel plate-wood interfaces, and at several points on the bolts (all measured using thermocouples) are shown in Figure 4 for the S-W-S connection during a typical fire test. It can be seen that the temperatures of the steel side plates and the bolts are effectively the same, with no temperature gradient along the bolt. Figure 5 for the W-W-W connection, on the other hand, shows that it takes longer for the bolt at the centre of the centre member to heat up than it does for the bolt head which is exposed to the fire, with a big temperature gradient along the bolt.

For the S-W-S connections, the experimental failure mode for the bolts at ambient temperatures was mode k whereas for temperatures above 50ºC the failure mode was mode j/l (see Figure 6 for sketches of these failure modes). The comparison between the experimental results and the predicted failure loads using Johansen's equations, and the approximation 1 for the embedment strength shown in Figure 3, are plotted in Figure 6 for modes j/l, k and m, together with the maximum experimental failure loads. It can be seen that, in general, almost all the maximum experimental loads fall on or above the predicted values for failure mode j/l except at 20ºC where the experimental failure loads are scattered about the predicted value for mode k.

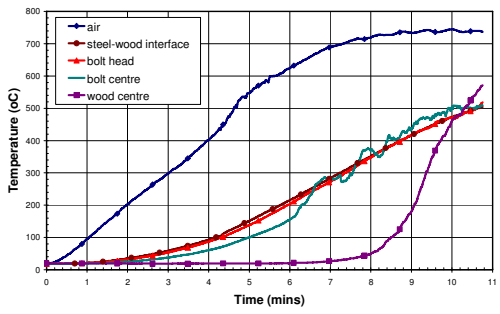

Fig. 4 - Temperatures measured within the S-W-S connection during the fire test.

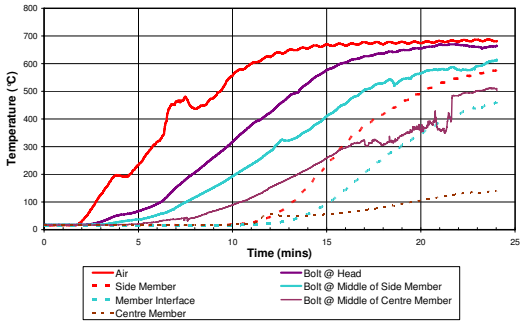

Fig. 5 - Temperatures measured within the W-W-W connection during the fire test.

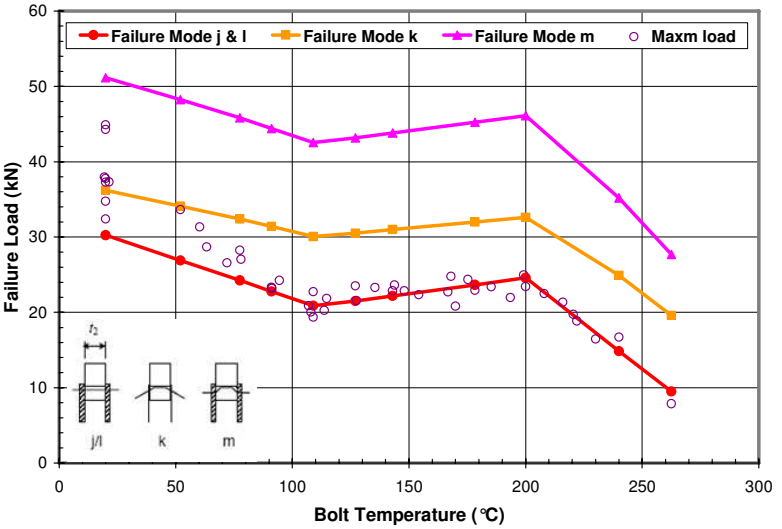

Fig. 6 - Predicted failure loads and maximum experimental loads for single-bolt S-W-S connections tested at constant temperature.

4. FAILURE PREDICTION FOR FIRE TESTED CONNECTIONS

Using the experimental embedment strength calculated from the single bolt S-W-S connection tests, the predicted failure loads in fire for the three connections tested with single bolts are shown in Figures 7-10. The contact thickness between the bolt and the timber members was taken as the original thickness less the thickness of the charred surface as indicated in Equation 1.

$$t_{contact} = t - (n \times D \times \theta) \tag{1}$$

where t = Original timber thickness (mm)
n = Number of charring surfaces (-) (for SWS, n = 2, otherwise n = 1)
D = Experimental charring rate (mm/min)
θ = Charring duration (min)

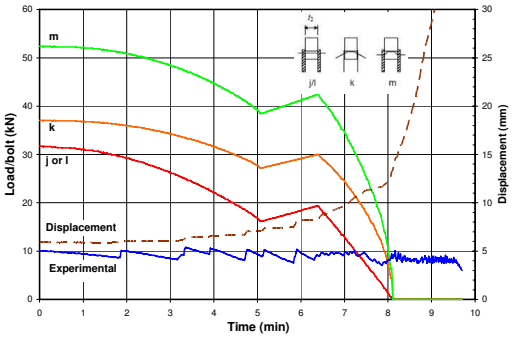

Fig. 7 - Predicted failure loads for a S-W-S connection based on Fig. 3 approximation 1.

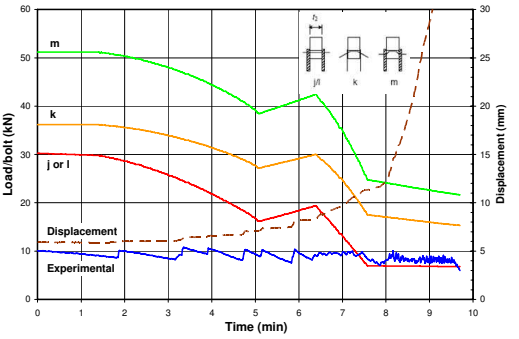

Fig. 8 - Predicted failure loads for a S-W-S connection based on Fig. 3 approximation 2.

In order to derive the curves for the various failure modes shown in Figures 7-10 it is necessary to know the temperature in the bolt over time, T(t), then determine the embedment strength, $f_h(T(t))$ using the approximation depicted in Figure 3 and the yielding moment for the bolt, $M_y(T(t))$. These are then substituted into the Johansen's equations. The reduction of strength during fire exposure is due to the change in embedment strength and the reduction of the contact thickness during the fire.

These calculations were made using the average measured bolt temperatures, assuming uniform temperature along each bolt. Numerical studies are presently under way to predict T=T(t) during a fire, depending on the geometry of the joint, which should enable a future relationship to be established between the fire temperature and the temperature in the bolts.

The prediction of the failure mode and the failure load per bolt for the S-W-S connection using the tri-linear embedment strength curve of approximation 1 of Figure 3 (Figure 7), together with the experimental charring rate and steel strength reduction factor for temperature, were reasonably accurate. The tests were stopped when the total displacement reached 30-40 mm and the rate of displacement was increasing rapidly. However, the estimation of the failure time was too early compared to the experimental failure time; this is because after the LVL has reached its zero embedment strength, the load carrying capacity of the connection is zero, though experimentally it was still able to carry some load. On the other hand, if approximation 2 of Figure 3 is used to determine the failure time (Figure 8), the prediction seems more accurate, allowing for some residual embedment strength in the timber as the bolt cuts its way into slightly cooler timber. Nevertheless, once the LVL reaches its constant embedment strength in Figs 8 to 10, the load carrying capacity of the connection reduces only slightly as the timber chars and therefore the predicted failure time is very sensitive to the load level.

The predicted failure loads for the W-S-W connection using the approximation 2 of Figure 3 are shown in Figure 9. For this particular connection the predicted failure mode is always mode f. While the prediction looks reasonably accurate, it more clearly indicates a range of time over which failure could take place. For the W-W-W connection, Figure 10 shows the predicted failure loads using the approximation 2 of Figure 3 and how they vary throughout the duration of the fire with mode g being the predicted failure mode. Again, the predicted time to failure looks reasonably accurate, but with a very flat curve after constant embedment strength is reached.

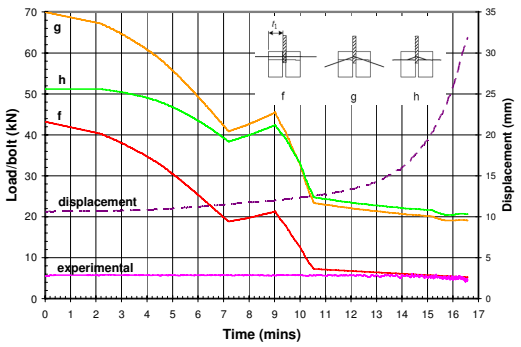

Fig. 9 - Predicted failure loads for W-S-W connection.

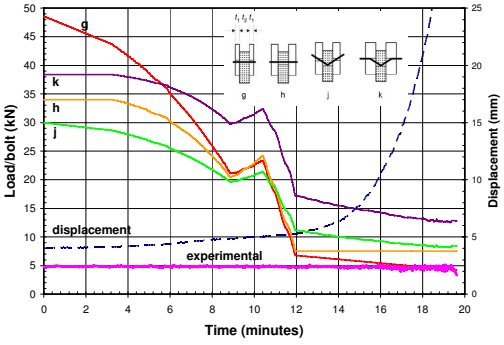

Fig. 10 - Predicted failure loads for W-W-W connection.

5. ANALYTICAL MODELLING

5.1 Determination of thermal properties

In order to augment the limited temperature measurements that it was possible to make on the joints during the testing, Austruy[21] carried out some numerical modelling of the temperature distribution in the S-W-S connection. Unfortunately, there is not much agreement in the literature about the actual values to use for the thermal properties wood[8]. In order to get around this problem, a numerical model of one eighth of the S-W-S connection was made in SAFIR[22] as illustrated in Figure 11 and the numerical results were compared with the experimental results from several of the heated tests. The thermal properties of the wood were adjusted so as to match as nearly as possible the experimental temperatures in the S-W-S connection from four heated tests at 100ºC, 150ºC, 200ºC and 280ºC. The comparisons of the experimental and numerically derived temperatures for a point in the middle of the timber section are shown in Figure 12. In these initial simulations, the thermal parameters were only determined for six different temperatures and it can be seen that while there is reasonable agreement with the experimentally determined temperatures from the 100ºC and 150ºC heated tests. Currently work is underway to increase the number of temperatures at which the thermal parameters are defined in order to get a better fit to the results from the 200ºC and 280ºC heated tests as well. However, there appears to be some difficulty in achieving this as values that work well for the 100ºC and 150ºC heated tests seem to be too low when simulating the 200ºC and 280ºC heated tests.

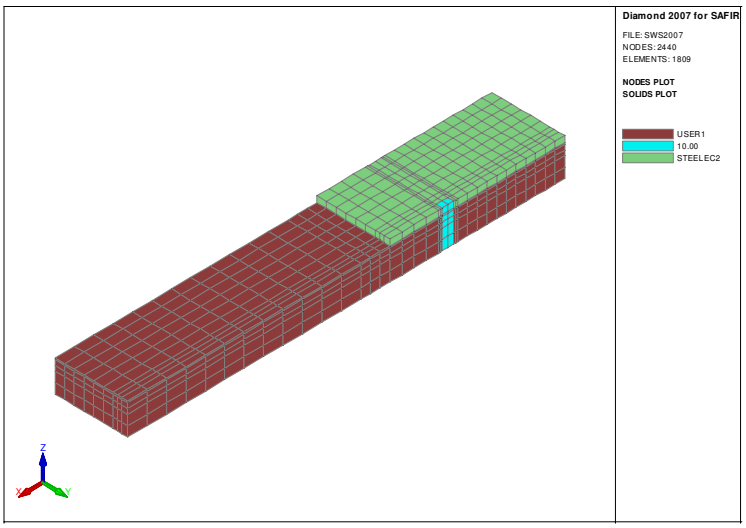

Fig. 11 - The mesh used for the SWS connection

5.2 Prediction of fire resistance

The results of simulating a fire test are shown in Figures 13 and 14. Figure 13 shows the temperature distribution after 12 minutes of fire exposure. Note that the view in Figure 13 has been rotated 90° about the longitudinal axis from the view in Figure 11 so that the bolt is now on the top surface. In Figure 14, the experimental and numerically determined temperatures at the centre of the bolt, and 1 and 2 mm along the member axis from the bolt

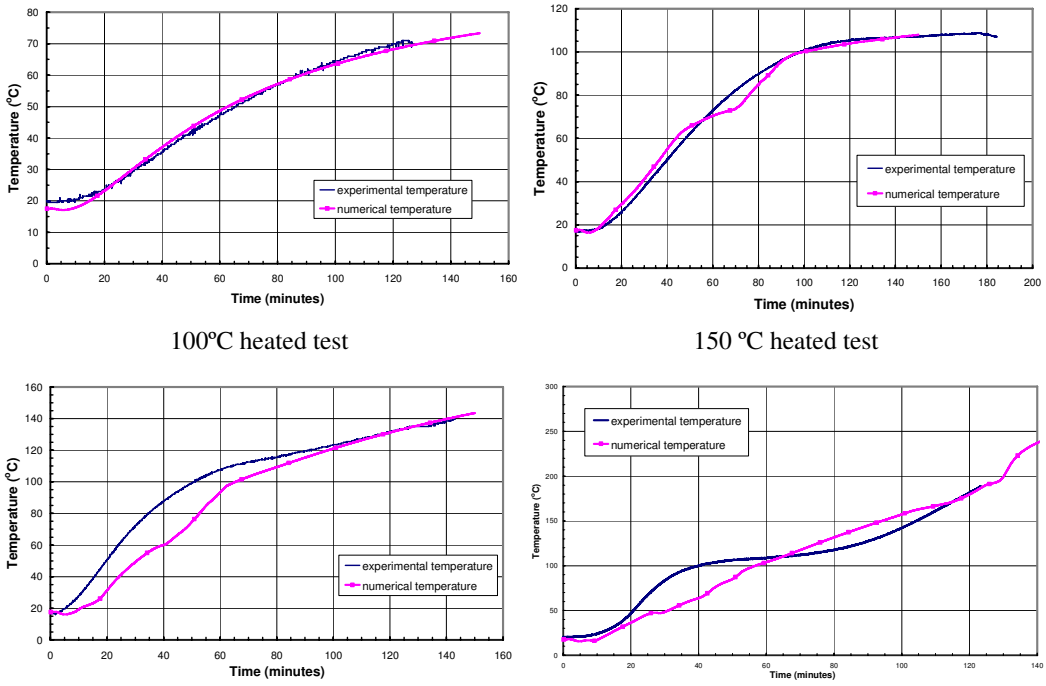

100ºC heated test 150 ºC heated test

200 ºC heated test 280 ºC heated test

Fig. 12 - Comparison of experimental and numerical temperatures

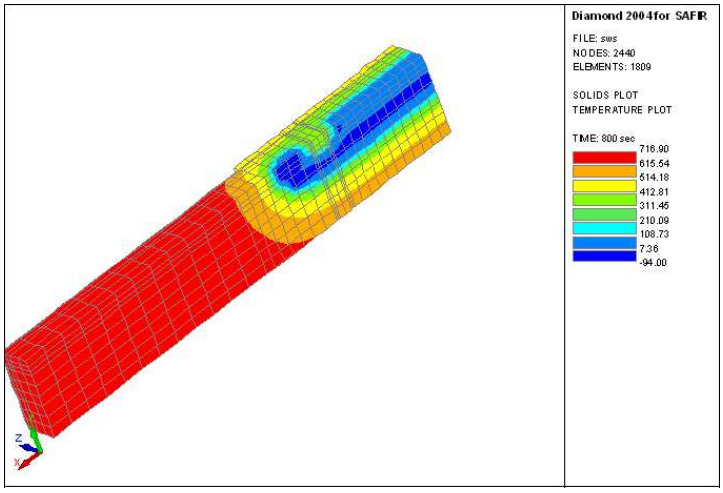

Fig. 13 - Temperature in a SWS connection during a fire test

surface, are compared. It can be seen that the numerically determined bolt temperatures are significantly below the bolt temperatures determined experimentally but do show the same trend. This difference between the experimental and the numerically determined temperatures for a fire test is not surprising since the main calibration of the thermal parameters was carried out using the heated tests for temperatures up to 280°C. The numerical curve of the bolt temperature during a fire, T=T(t), was then used as an input for the prediction of the fire

resistance of the SWS connection. The analytical results are reported in Fig. 15 for a test load of 7.5 kN, which shows a slight underestimation with respect to the experimental failure time of 11.1 minutes for a similar applied load.

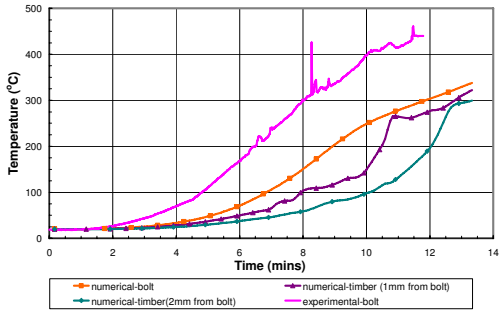

Fig. 14 - Numerical temperatures along the bolt in a SWS connection during a fire test

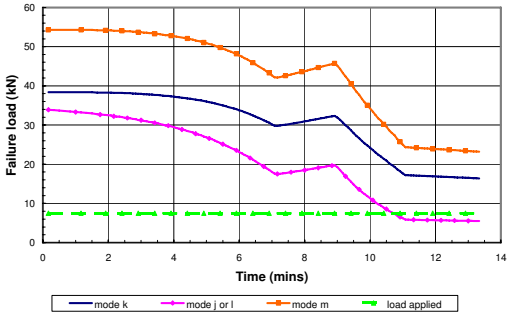

Fig. 15 - Prediction of the failure of a one-bolt SWS connection from SAFIR results

6. DISCUSSION

The decrease of embedment strength from 50ºC to about 110ºC is possibly due to softening of the lignin in the cell walls, while the increase in the range between 110ºC and 200ºC is caused by the timber drying and releasing the bound water from the cells, together with possible rehardening of lignin over this temperature range. The embedment strength results described herein are similar to the results reported by Moraes et al[10], and similar to those reported by Young and Clancy[1] and Jong and Clancy[3] for compression parallel to the grain strength of timber.

Since timber chars at around 300ºC and the char layer has negligible strength, it would seem reasonable for the embedment strength values shown in Figure 3 to reduce to zero at about 300 ºC. However, in a connection that is transferring load, the char layer is displaced as it forms and the bolt continues to heat the wood in contact with it. The result is that the bolt cuts an elongated hole in the wood member; this causes movement in the joint but does not necessarily lead to failure and the joint continues to carry load, as there is a residual embedment strength in the timber as the bolt cuts its way into slightly cooler timber. For this reason, it is suggested that the approximation 2 of Figure 3 should be used instead of that of approximation 1.

If we take failure as occurring when the rate of displacement exceeds 10 mm/min, or the total displacement exceeds 15 mm[15], then Figure 8 for the S-W-S connection gives a good prediction of failure since the rate of deflection increases markedly at about 8 minutes and the total displacement exceeds 15 mm shortly after. However, for the W-S-W (Figure 9) and the W-W-W (Figure 10) connections, there is not the same close agreement between the prediction and the definition of failure based on the displacement and its rate of increase.

7. CONCLUSIONS

The embedment strength of radiata pine LVL can be described by a tri-linear relationship that drops linearly from 45 MPa at 20°C to 25 MPa at 110°C, rises to 27.5 MPa at 200°C, then falls to 10 MPa at 270°C.

This tri-linear embedment strength was used in conjunction with Johansen's yield equations to predict the failure load and the results showed reasonable agreement with the experimental values.

It is difficult to predict the time to failure accurately because the definition of failure is not clearly established, and because there is uncertainly about the actual bolt temperatures and the embedment strength when the bolt temperature exceeds 250°C. The assumption of a lower bound cut-off of embedment strength at 10MPa allowed more accurate predictions of failure time than with the embedment strength dropping to zero.

Further analytical work is needed to provide a more accurate thermal analysis, firstly in the unloaded condition and more importantly in the loaded condition when the hot bolt is cutting through the wood. This then must be extended to multiple bolts and to other dowel-type fasteners such as nails and screws.

8. ACKNOWLEDGEMENTS

Thanks to Nelson Pine for the supply of all the LVL which was tested. Thanks also to David Carshalton for conducting many embedment tests during his summer work experience at the University of Canterbury, and to Bob Wilsea-Smith and Grant Dunlop for laboratory support.

9. REFERENCES

[1] Young S.A., and Clancy P., "Compression mechanical properties of wood at temperatures simulating fire conditions", *Fire and Materials*, Vol. 25, 2001, pp. 83-93.

[2] Reszka P., and Torero J. L., "In depth temperature measurements of timber in fires", *Proc. 4th International Workshop on Structures in Fire*, Aveiro, Portugal, 2006.

[3] Jong F., and Clancy P., "Compression properties of wood as functions of moisture, stress, and temperature", *Proc. 2nd International Workshop on Structures in Fire*, Christchurch, New Zealand, 2002, pp. 223-242.

[4] Janssens M., "Modelling of the thermal degradation of structural wood members exposed to fire", *Proc. 2nd International Workshop on Structures in Fire*, Christchurch, New Zealand, 2002, pp. 211-222.

[5] Frangi A., and Mischler A., "Fire tests on timber connections with dowel type fasteners", *Proc. International Council for Research and Innovation in Building and Construction, Working Commission W18 – Timber Structures, Meeting 37*, Edinburgh, United Kingdom, 2004.

[6] Erchinger C., Frangi A., and Mischler A., "Fire behaviour of multiple shear steel-to-timber connections with dowels", *Proc. International Council for Research and Innovation in Building and Construction – Working Commission W18 – Timber Structure, Meeting 38*, Karlsruhe, Germany, 2005.

[7] Erchinger C., Frangi A., and Mischler A., "Thermal investigations on multiple shear steel-to-timber connections", *Proc. World Conference on Timber Engineering*, Portland, Oregon, USA, 2006.

[8] Racher P., Laplanche K. and Dhima D., "Thermo-mechanical modelling of the timber connection behaviour under fire", *Proc. 4th International Workshop on Structures in Fire (SiF'06)*, 2006, pp. 899-908.

[9] Schabl S., and Turk G., "Coupled heat and moisture transfer in timber beams exposed to fire", *Proc. World Conference on Timber Engineering*, Portland, Oregon, USA, 2006.

[10] Moraes P.D., Rogaume Y., Bocquet J.F., and Triboulot P., "Influence of temperature on the embedding strength", *Holz als Roh- und Werkstoff*, Vol. 63, 2005, pp. 297-302.
[11] Chapuis S., Moraes P.D., Rogaume Y., and Torero J.L., "Evaluation of in-depth temperature distributions and embedding resistance of timber in a fire", *private communication*, 2005.
[12] Eurocode 5 – Part 1-1: *Design of Timber Structures. EN 1995-1-1:2004: General – Common Rules and Rules for Buildings*, European Committee for Standardization, Brussels, Belgium, 2004.
[13] Johansen K.W., "Theory of timber connections", *Int. Assn of Bridge & Struct. Eng.*, Publ. No. 9, 1949, pp. 249-262, Bern, Switzerland.
[14] Eurocode 5 – Part 1-2: *Design of Timber Structures. EN 1995-1-2:2004: General – Structural Fire Design*, European Committee for Standardization, Brussels, Belgium, 2004.
[15] Carling O., "Fire behaviour of metal connectors on wood structures", *Proc. Int. Conf. on Timber Engineering*, London, Vol. 4, 1991, pp. 106-113.
[16] Lau P.H., "Fire resistance of connections in laminated veneer lumber", Fire Engineering Research Report 06/3, 2006, Dept. of Civil Engineering, University of Canterbury, New Zealand, http://www.civil.canterbury.ac.nz/fire/fe_resrch_reps.shtml.
[17] Chuo T.C.B., "Fire performance of connections in LVL structures", Fire Engineering Research Report 07/4, 2007, Dept. of Civil Engineering, University of Canterbury, New Zealand, http://www.civil.canterbury.ac.nz/fire/fe_resrch_reps.shtml.
[18] Moss P.J., Buchanan A.H., Fragiacomo M., Lau P.H., and Chuo, T. "Fire performance of bolted connections in laminated veneer lumber", submitted for publication on *Fire and Materials*, 2007.
[19] NelsonPine NZ LVL10, *Design guides and span tables*, Nelson Pine Industries Ltd, Richmond, Nelson, New Zealand, 2003.
[20] ISO 10984-2, *Timber structures – Dowel-type fasteners – Part 2: Determination of embedding strength and foundation values*, International Standards Organization, Geneva, 1999.
[21] Austruy, C., "Fire resistance of timber connections", Fire Engineering Research Report, 08/2, 2008, Dept. of Civil Engineering, University of Canterbury, New Zealand, http://www.civil.canterbury.ac.nz/fire/fe_resrch_reps.shtml
[22] Franssen, J-M.; Kodur, V.K.R.; and Mason, J., *User's Manual for SAFIR2004: A Computer Program for Analysis of Structures Subjected to Fire*, University of Liège, Belgium, 2004.

FALL-OFF OF GYPSUM PLASTERBOARD IN FIRE

MOHAMED A. SULTAN[1]

ABSTRACT

This paper presents and discusses the results of an attempt that was made to determine the gypsum board fall-off temperature criterion from 80 full-scale fire resistance tests conducted at the National Research Council of Canada in accordance with ULC-S101/ASTM E119 standard fire exposure using floor assemblies constructed with wood joist, wood-I joist, steel C-joist and wood truss; protected with either one or two layers of Type X gypsum board and with and without insulation in the floor cavity. The proposed temperature criterion is based on the sudden temperature rise on the back side of the fire exposed gypsum board that is caused by either the board fall-off or board sagging. Statistical analysis of the gypsum board fall-off temperature is presented. A comparison of the fall-off time based on the temperature criterion and observed board fall-off from fire resistance tests is also presented.

1. INTRODUCTION

With the advent of performance-based codes and performance-based fire safety design options, the development of fire resistance models becomes an important tool to aid their implementation. Currently, major fire safety research efforts are being invested globally into developing numerical models that can be used by designers to facilitate the move to performance-based options. Development of such models faces several challenges such as the availability of reliable thermal and mechanical properties of materials, as well as information on the performance of building materials at elevated temperatures. In lightweight frame construction, one important limitation of the existing models is the prediction of gypsum board fall-off, which significantly impacts the prediction of fire resistance of an assembly. Studies[1,2] showed that the gypsum board provides significant fire resistance protection, owing in major part to its high water content.

[1] Dr. Sultan is a Senior Research Officer and Group Leader of the Fire Resistance and Risk Management Subprogram, Fire Research Program, Institute for Research in Construction, National Research Council of Canada Mohamed.sultan@nrc.gc.ca

Fire resistance models typically consist of a thermal model and a structural model. The thermal model calculates the temperature history of the assembly's components and feeds those temperatures to the structural model for determining the thermal and structural properties at a given time, which are used for calculating the response of the assembly. To calculate the temperature history, it is essential to determine how long the gypsum board ceiling will stay in place to protect the assembly's frame. This can be defined either by the observed time of gypsum board fall-off or, alternatively, by the temperature at which the gypsum board will likely fall-off when exposed to heat. Due to the difficulty in predicting gypsum board fall-off times for assemblies with configurations that have not previously been tested, a time failure criterion is impractical for use in numerical modelling.

The National Research Council's Institute for Research in Construction (NRC-IRC), in collaboration with industry and government partners, has carried out two major experimental research studies (Floors-I[1] and Floors-II[2]) to measure the fire resistance and acoustic performance of full-scale floor assemblies with different framing types. Details on the assemblies' construction and fire resistance results of these studies can be found in References 1 and 2. In these studies, gypsum board fall-off times were determined from test observations and video-recordings of the fire-exposed gypsum board surfaces in a floor furnace operating with premixed flame. Sultan, et al[3], carried out a study on the gypsum board fall-off using 4 different approaches for characterizing the board fall-off when exposed to heat in standard fire tests. The first approach was based on the average temperature recorded at the time of fall-off, during fire resistance tests, of the first piece and at the time of fall-off of the last piece of each gypsum board layer. The second approach used the average of the first and last piece fall-off temperature criteria determined in the first approach. The gypsum board temperature at the time corresponding to the average of the first and last piece fall-off times was used to estimate the average fall-off temperature in the third approach. The last approach dealt with individual temperature histories and looked at the sudden increase in temperature caused by gypsum board fall-off. The purpose of this paper is to present in depth the last and recommended approach and to establish a temperature criterion for the gypsum board fall-off that can be used by the modelers to improve the accuracy of their fire resistance models for lightweight floor assemblies.

2. EXPERIMENTAL INVESTIGATION

Eighty floor assemblies, 4.8 m long by 3.9 m wide, were constructed in accordance with CAN/CSA-A82.31-M91[4] to investigate the effect of different parameters on the fire resistance performance of floor assemblies consisting of solid wood, wood I- joists, steel C- joists and wood trusses. In 72 floor assemblies (see Table 1) resilient channels, spaced either 203 mm o.c. or 406 mm o.c., or 610 mm o.c., were used for sound reduction purposes and attached perpendicular to either the joists or trusses to support the gypsum board ceiling finish. Additional resilient channels were also installed to support gypsum board ends (board short dimension). The resilient channels, 14 mm deep by 58 mm wide, were fabricated from 0.6 mm thick galvanized steel sheets. The channels had a 34 mm wide web, designed to support the gypsum board connection, and one 18 mm wide flattened flange lip connected to the bottom of the joists or trusses. Three types of insulation were used: glass and rock fibre batts, and cellulose fibre insulation either sprayed wet on the underside of the sub-floor and on the side of the joists and allowed to dry to achieve an 11% moisture content or dry blown and supported at the bottom of the joists or trusses with a steel mesh.

Assembly Number	Joist		Ceiling Finish		Sub Floor		Cavity Insulation		Resilient Channels	Fire Resist-ance (min.s)	Gypsum Board Fall-Off (min.sec)			
											Face Layer		Base Layer	
	Type	Spacing (mm)	Layer Number	Thick-ness (mm)	Layer Number	Type	Type	Locat-ion	Spacing (mm)		First Piece	Last Piece	First Piece	Last Piece
FF-01A	WJ	406	1	12.7	1	Ply	***	***	***	30	---	---	24.22	31.20
FF-02A	WJ	406	1	12.7	1	Ply	***	***	406	45	---	---	42.07	47.20
FF-03A	WJ	406	2	12.7	1	Ply	***	***	406	80	49.42	57.30	77.43	82.20
FF-04A	WJ	406	2	12.7	1	Ply	R	B	406	72	48.19	53.15	56.50	63.43
FF-06	WJ	406	2	12.7	1	Ply	G	B	406	67	44.43	48.50	57.30	62.45
FF-07	WJ	406	1	12.7	1	Ply	C1	T	406	59	---	---	34.00	38.22
FF-08	WJ	406	1	12.7	1	Ply	G	B	406	36	---	---	26.14	31.00
FF-09	WJ	406	1	12.7	1	Ply	R	B	406	60	---	---	26.35	32.11
FF-10	WIJ	406	2	12.7	1	Ply	***	***	406	69	47.53	57.59	68.36	70.45
FF-11	WIJ	406	2	12.7	1	Ply	***	***	406	74	49.47	65.15	73.46	76.45
FF-12	WIJ	406	2	12.7	1	Ply	***	***	406	80	54.24	62.43	78.55	82.25
FF-13	WIJ	406	2	12.7	1	Ply	***	***	406	72	56.06	70.00	69.18	74.20
FF-14	WIJ	406	1	12.7	1	Ply	***	***	406	42	---	---	40.53	44.00
FF-15	WIJ	406	2	12.7	1	Ply	G	B	406	64	53.16	59.33	56.50	66.00
FF-16	WIJ	406	1	12.7	1	Ply	R	B	406	46	---	---	36.36	43.07
NRC-02	WIJ	406	2	12.7	1	Ply	R	B	406	77	59.28	66.31	67.04	75.18
FF-17	WIJ	610	2	12.7	1	Ply	G	B	406	75	59.35	69.24	69.04	74.50
FF-18	WIJ	610	2	12.7	1	Ply	G	B	406	74	60.00	65.16	68.16	70.20
FF-19	WIJ	406	1	12.7	1	Ply	C1	T	406	52	---	---	45.10	46.53
FF-20	WIJ	610	2	12.7	1	Ply	G	B	610	65	55.41	60.00	59.38	62.01
FF-22	SJ	406	2	12.7	1	Ply	***	***	406	74.3	66.26	73.19	73.09	74.00
FF-23	SJ	406	2	12.7	1	Ply	G	B	406	68	59.23	64.06	63.26	68.40
FF-24	SJ	610	2	12.7	1	Ply	G	B	406	69	59.48	62.06	65.04	67.23
FF-25	SJ	406	1	12.7	1	Ply	R	B	406	46	---	---	35.50	43.17
FF-26	St\Con	***	2	12.7	1	***	***	***	406	105	52.52	72.14	74.06	81.48
FF-27	SJ	406	2	12.7	1	Ply/Con	G	B	406	60	49.26	55.24	53.22	58.05
FF-28	WJ	406	2	12.7	1	Ply	***	***	406	69	43.49	60.58	67.09	68.55
FF-29	WJ	406	2	12.7	1	Ply	G	B	406	69	45.13	52.54	59.01	62.12
FF- 30	WJ	406	1	12.7	1	Ply	***	***	406	40.49	---	---	40.43	43.00
FF-31	WJ	406	2	12.7	1	Ply	***	***	***	67.10	56.06	61.1	65.32	67.12
FF-32	WJ	406	2	12.7	1	Ply	G	B	406	67.15	53.08	57.08	60.10	62.30
FF- 33	WJ	406	1	12.7	1	Ply	***	***	203	39.55	---	---	39.35	42.00
FF- 34	WJ	406	1	15.9	1	Ply	R	B	203	54.11	---	---	37.19	45.26
FF-35	WJ	406	2	12.7	----	Ply/GC	G	B	406	68.27	53.14	57.50	60.44	64.00
FF- 36	WJ	406	1	15.9	2	Ply	R	B	406	58.49	---	---	31.36	41.34
FF- 37	SJ	406	1	15.9	2	Ply	***	***	406	38.49	---	---	36.30	39.13
FF- 38	SJ	406	1	15.9	2	Ply	R	B	406	53.38	---	---	26.41	38.43
FF-40	SJ	406	2	12.7	----	St/Con	***	***	406	75	60.39	76.55	72.35	79.12
FF-41	WT	406	2	12.7	1	Ply	***	***	406	69.01	57.43	66.46	68.12	71.00
FF-42	WT	406	2	12.7	1	Ply	G	B	406	65.41	53.49	59.35	60.55	65.32
FF-43	SJ	406	2	12.7	----	St/Con	G	B	406	68.25	54.28	59.41	60.10	66.11
FF-44	SJ	406	2	12.7	----	St/Con	G	B	610	61	52.32	54.35	53.30	59.15
FF- 45	WIJ	406	1	15.9	1	OSB	R	B	406	39.31	---	---	29.58	37.58
FF-46	WT	406	2	12.7	1	Ply	G	B	406	67.36	55.19	59.45	61.41	67.40
FF-47	WT	406	2	12.7	----	Ply/Con	G	B	406	72	52.10	57.02	60.02	63.12
FF-48	WT	610	2	12.7	1	Ply	G	B	406	68.18	53.50	59.02	62.23	65.54
FF- 49	WJ	406	1	15.9	2	Ply	C1	T	406	54.13	---	---	37.31	44.18
FF- 50	SJ	406	1	15.9	2	Ply	C1	T	406	63.47	---	---	34.17	45.00
FF-51	SJ	406	2	12.7	1	Ply	***	***	***	65.55	51.16	61.29	66.39	68.45
FF-52	SJ	610	2	12.7	1	Ply	G	B	610	52.3	42.17	49.50	50.14	51.41
FF-53	SJ	406	2	12.7	----	St/Con	R	B	406	70	51.06	57.17	57.46	64.53
FF-54	SJ	610	2	12.7	----	St/Con	***	***	***	66	37.38	56.18	60.37	66.04
FF-55	WIJ	610	2	12.7	1	OSB	G	B	406	60.59	48.36	57.28	56.08	60.00
FF-56	WT	406	2	12.7	1	Ply	***	***	406	65.05	54.35	62.08	61.51	64.24
FF- 57	WIJ	610	1	15.9	2	OSB	R	B	305	50.17	---	---	39.08	43.41
FF-58	WT	406	2	12.7	1	Ply	G	B	406	63.37	48.50	56.19	54.42	63.11
FF-59	WT	610	2	12.7	1	Ply	G	B	610	54.35	40.25	49.02	48.01	52.31
FF-60	WT	406	2	12.7	1	Ply	***	***	***	61.03	43.15	58.45	59.07	60.55
FF-61	WIJ	406	2	12.7	----	Ply/Con	G	B	406	66.58	49.39	56.24	57.14	61.46
FF-62	SJ	610	2	12.7	1	Ply	***	***	***	54.59	46.15	55.31	54.07	56.00
FF-63	WT	406	2	12.7	1	Ply	G	B	406	64.04	51.28	57.23	57.07	62.34
FF-64	WJ	610	2	12.7	1	Ply	***	***	610	58.55	47.08	55.23	54.55	61.30

Table 1: Design Details and Gypsum Board Fall-Off Time

Assembly Number	Joist		Ceiling Finish		Sub Floor		Cavity Insulation		Resilient Channels	Fire Resist-ance (min.s)	Gypsum Board Fall-Off (min.sec)			
											Face Layer		Base Layer	
	Type	Spacing (mm)	Layer Number	Thick-ness (mm)	Layer Number	Type	Type	Locat-ion	Spacing (mm)		First Piece	Last Piece	First Piece	Last Piece
FF-65	SJ	610	2	12.7	1	Ply	C3	T	610	68.55	48.45	52.08	52.39	54.26
FF- 66	WJ	406	1	15.9	1	Ply	R	B	406	50.24	---	---	36.18	43.18
FF-67	WJ	610	2	12.7	1	Ply	G	B	610	57.05	47.29	51.09	51.46	52.39
FF-68	WJ	406	2	12.7	1	Ply	G	B	610	57.27	48.02	53.10	51.58	53.24
FF-69	WJ	610	2	12.7	1	Ply	R	B	610	63.33	49.29	51.51	52.38	56.25
FF-70	WJ	406	2	12.7	1	Ply	C2	---	610	87.2	48.02	52.03	52.03	55.41
FF-71	WT	610	2	12.7	1	Ply	***	***	***	56.16	44.41	51.19	54.28	56.13
FF-72	WT	610	2	12.7	1	Ply	C1	T	610	77.12	49.04	54.09	54.18	57.07
FF-73	WJ	610	2	12.7	2	Ply	G	B	610	58.43	48.19	51.49	51.49	53.20
FF- 74	SJ	610	1	15.9	----	St/Con	C1	T	406	56.20	---	---	31.57	40.15
FF-75	WT	610	2	12.7	----	Ply/Con	G	B	610	60.55	44.12	50.03	50.28	53.07
FF- 76	WIJ	406	1	15.9	2	Ply	C2	---	305	80.19	---	---	38.58	48.32
FF-77	WIJ	406	2	12.7	1	Ply	***	***	***	64.31	52.21	62.02	63.42	63.50
FF- 78	WIJ	406	1	15.9	2	Ply	R	B	305	59.38	---	---	33.00	42.16
FF-79	WT	610	2	12.7	1	Ply	G	B	610	54.35	45.31	51.30	51.27	53.57
FF-80	WT	610	2	12.7	1	Ply	R	B	610	59.34	45.10	50.24	50.24	53.10
FF-81	WIJ	406	2	15.9	2	Ply	R	B	305	90.19	56.41	62.48	65.41	76.03
FF-82	WT	406	2	15.9	2	Ply	C2	---	406	99.14	50.50	63.13	61.33	68.40

Ply-Plywood
Con-Concrete
GC-Gypsum-Concrete
OSB-Oriented strandboard

G-Glass fibre batts insulation
R-Rock fibre batts insulation
B-Bottom
T-Top

WJ-Wood joist
WIJ-Wood-I-joist
WT-Wood truss

C1- Cellulose Fibre Insulation, Wet Sprayed
C2- Cellulose Fibre Insulation, Dry Blown
C3- Cellulose Fibre Insulation, Wet Sprayed with Adhesive

Table 1: Design Details and Gypsum Board Fall-Off Time (continue)

The glass, rock and cellulose insulation satisfied CSA A101-M83[5], CAN/ULC S702-M97[6] and CGSB 51.60-M90[7], respectively. The sub-floor types used in the assemblies were either Canadian Softwood Plywood (CSP) or steel deck with concrete topping. The ceiling finish used in the assemblies was Type X gypsum board, 12.7 mm and 15.9 mm thick, and had Firecode C designation and met the requirements of Type X gypsum board[8,9]. The gypsum boards had an average surface density of 9.85 kg/m^2 for a nominal 12.7 mm thick board and 10.5 kg/m^2 for a nominal 15.9 mm thick board. They were attached perpendicular either to resilient channels in 72 assemblies or directly to the framing in 8 assemblies. Table 1 summarizes the main variable parameters of the assemblies studied. Complete construction details can be found in References 1 and 2.

2.1 Instrumentation and Test Conditions

In addition to the standard instrumentation specified in CAN/ULC-S101-M89[10], numerous thermocouples (over 100) were placed within each floor assembly in order to obtain temperature histories at various locations during fire tests for further use beyond the scope of the above-mentioned studies. Type K (20 gauge) chromel-alumel thermocouples, with a thickness of 0.91 mm, were used for measuring the temperatures of the sub-floor surface and gypsum board surface facing the floor cavity as well as the interface surface between the gypsum board for assemblies with two layers of gypsum board and between the gypsum board and insulation at the floor cavity side. Temperature readings were recorded every minute across the floor assemblies. Details on the locations of the thermocouples can be found in References 1 and 2. All floor assemblies were tested with a superimposed load depending on the components of the assembly. Assemblies FF-01A to FF-09 were tested using a restricted load of 75% of maximum

design load; while assemblies FF-10 to FF-82 were tested on a maximum design load. Two video cameras were used to record the fire-exposed gypsum board performance.

The assembly's gypsum board ceiling finish was exposed to heat in a propane-fired horizontal furnace in accordance with CAN/ULC-S101-M89[10], "Standard Methods of Fire Endurance Tests of Building Construction and Materials". The furnace temperature was measured by nine (20 gauge) shielded thermocouples and the average of these thermocouples was used to control the furnace temperature in such a way that it followed, as closely as possible, the CAN/ULC-S101-M89 standard temperature-time curve. Subsequently, the time of fall-off of the first and last pieces of each gypsum board layer for all assemblies was determined from test observations and through viewing of the video recordings of the experiments.

3. RESULTS AND DISCUSSION

The results of the 80 full-scale fire resistance floor tests, including the time of fall-off of gypsum board layers, are summarised in Table 1 above. The temperature rise on the back face of gypsum board layers (six for each layer) was recorded for all experiments. As an example for the reader, a set of these temperature histories, from floor assembly FF-01A, is provided in Figure 1. An important characteristic identified in these temperature history graphs was a sudden and significant increase in temperature over a period of a few minutes only (often an increase of more than 300°C over a period of a minute). The sudden temperature rises observed seem to correspond to the increase in temperature caused by the fall-off of the gypsum board layer at the location of the thermocouple; the fallen board piece allowing heat to penetrate rapidly into the next layer of the assembly. Some graphs did not display this expected sudden increase in temperature. A variety of factors can explain this phenomenon. An important one to consider is a malfunction of the thermocouple studied. Another factor could be that only cracking or a partial gypsum board fall-off occurred at the location of the thermocouple, which would cause the temperature to increase over a longer period of time. Finally, it is possible that the gypsum board did not fall-off at that thermocouple location.

It is interesting to note that, for assembly FF-01A, no sudden increase in temperature is seen for thermocouple #26, which recorded a maximum temperature of 430°C before the recording instrument was turned off due to the termination of the test. All other thermocouples registered temperatures over 800°C after the 24th minute. This observation suggests that gypsum board remained in place at the location of thermocouple #26, protecting the latter from a rapid temperature increase until data recording was ended.

The temperature at which gypsum board falls off for each thermocouple was thus established as the last temperature recorded before the sudden temperature rise in the layer. Circles were drawn around the selected values in Figure 1 for more clarity. In cases where the step in temperature was not as clearly defined as the ones seen in Figure 1, the average of the two recordings bracketing the base of this sudden temperature rise was taken as the fall-off temperature. Temperature histories with no such sudden temperature increase or multiple temperature steps of the same magnitude were ignored when fall-off temperatures were calculated. The fall-off temperature of each gypsum board layer was then computed as the average of the fall-off temperatures found for each layer. Certain subjectivity was used at this stage to ignore data points that seemed erroneous, most probably due to a dysfunction of the thermocouple.

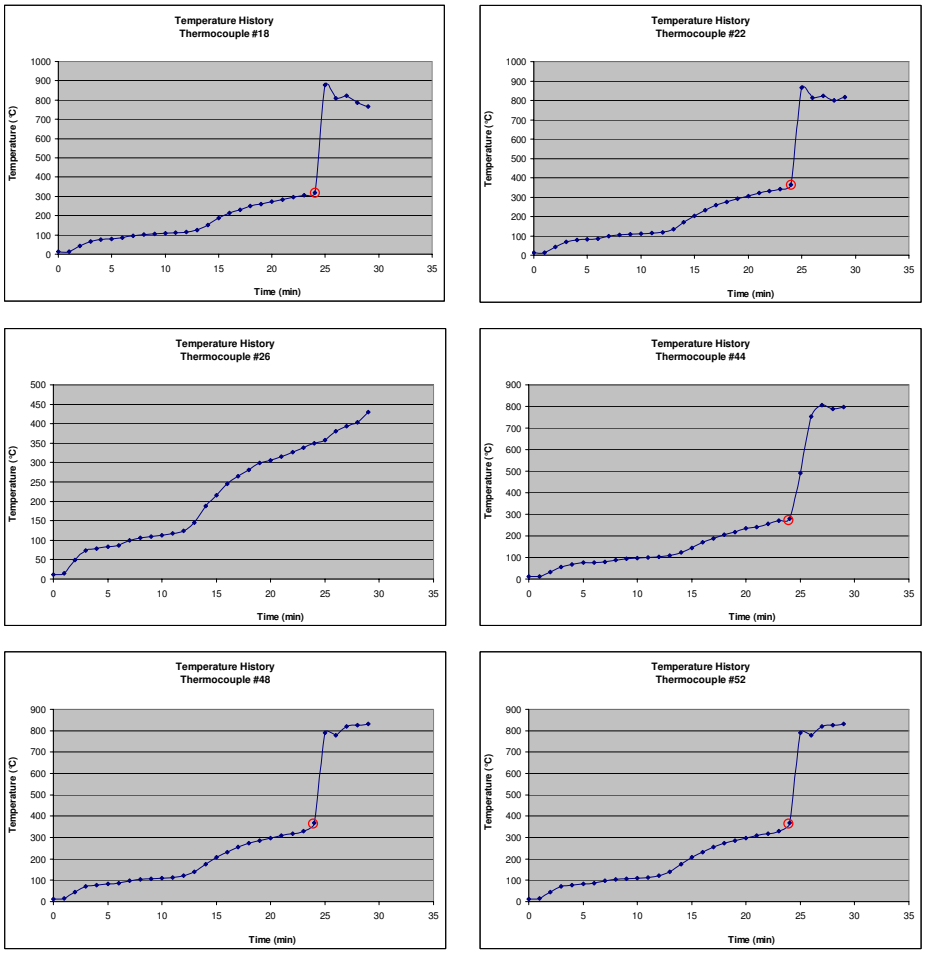

Figure 1 Temperature Histories at the Unexposed Face of the Gypsum Board Layer (Assembly FF-01A)

To ensure that this method gave results that were consistent with observations made during the experiments, the time corresponding to the temperature of fall-off selected was recorded for each thermocouple. Those times were then compared to the fall-off times reported in Table 2. It was seen that temperature increases often occurred up to a minute before the first piece of fall-off was reported. This could be due to cracking in the gypsum board leading to gypsum board fall-off within a short period of time. The time range for fall-off was thus extended by a minute before the first piece of fall-off. Temperatures from the thermocouples with fall-off times outside the expanded time range were discarded. Only 21 points out of 822 temperatures were disregarded due to this reason, which corresponds to 2.6% of the readings. The mean values of fall-off times corresponding to the temperatures selected with this approach are reported in Table 2 for comparison with the fall-off times observed during fire tests. The fall-off temperatures were determined using the procedure described above to ensure that the

temperature increase caused by the fall-off of a piece would not be accounted for in the determination of the temperature causing the piece to fall off.

Figures 2 through 4 show the statistical analysis of the fall-off temperatures found for single layer assemblies without insulation, with glass or rock fibre insulation at the bottom of the cavity and with cellulose fibre insulation and at the top of the cavity and framing sides using resilient channels (RC) spaced at 406 mm o.c., respectively. An important temperature difference is seen between non-insulated and insulated assemblies. This could be due to the added thermal resistance caused by the insulation installation in the floor cavity. The highest temperature is found for assemblies with insulation at the bottom of the cavity above the gypsum board and the lowest is for non-insulated assemblies.

Figures 5 to 14 show the statistical analysis of temperatures found with this method for double gypsum board layer assemblies. Figures 5 through 8 (assemblies with no insulation in the floor cavity) and 9 through 12 (assemblies with insulation in the floor cavity) show the impact of resilient channels spacing (i.e. lower the spacing the more screws) on both face and base layer. Once again, gypsum board fall-off temperatures are highest in assemblies insulated at the bottom of the cavity and lowest in non-insulated assemblies. The base layer fall-off temperatures are found to be significantly lower than face layer fall-off temperatures. Reasons that could explain this phenomenon will be proposed in a later section. As in previous cases, fall-off temperatures are lower with assemblies using wider resilient channels pacing (less number of screws). This difference seems to be more significant for base layer temperatures. This method shows the largest difference in temperature from one category to another or between base and face layers. On the other hand, all standard deviations reported for double layer assemblies, excluding Figures 5 and 6, are below 50°C.

This approach accounts for the fact that the gypsum board layers fall in separate pieces at unevenly distributed intervals to determine the temperature of fall-off. By considering each thermocouple separately, this ensures that the temperature selected represents gypsum board fall-off as closely as the temperatures recorded allow it. The temperature obtained is thus really the temperature at the time of gypsum board fall-off, not the temperature of the gypsum board at the location of the thermocouple at the time of fall-off of a piece of gypsum of a different location.

The only principal drawback of this method of determining temperature criteria for gypsum board is its subjectivity and limited number of thermocouples. Indeed, the location of the sudden temperature rise on the temperature history graphs was not always clearly defined and a fair amount of subjectivity was necessary to select the appropriate temperature. Also, when determining the fall-off temperature of each assembly, data points that did not follow the trend established by other points were sometimes ignored.

The temperature histories studied for this analysis not only present what seems to be the most realistic estimate of the Type X gypsum board fall-off temperatures, but also provides precious information that is key for understanding the behaviour of the different components comprised in floor assemblies.

Interesting observations were derived from the results of the previous analyses. Firstly, the presence and the location of the insulation within the floor assembly were identified as the major factors influencing the temperature of fall-off of gypsum board layers.

It was observed that fall-off temperatures were lowest for non-insulated assemblies, and highest when the insulation was applied directly against the gypsum board layers. This suggests

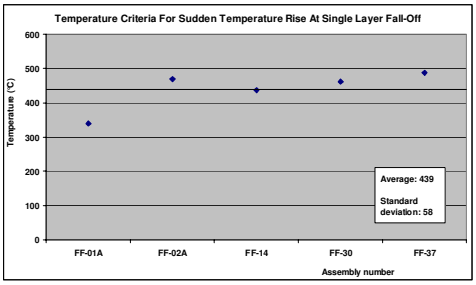

Figure 2 Assembly with single layer of Gypsum Board and no Insulation in Floor Cavity

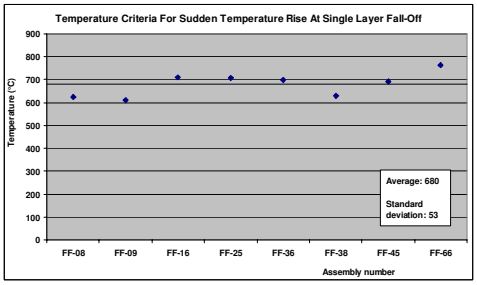

Figure 3 Assembly with single layer of Gypsum Board and Glass or Rock Fibre Insulation in Floor Cavity

Assembly number	Time for Gypsum-Board Fall-off Observations (min.sec)				Time for Gypsum-Board Fall-off Temperature History (min)	
	Face Layer		Base layer			
	1st	last	1st	last	Face Layer	Base layer
FF-01A	***	***	24.22	31.20	***	24
FF-02A	***	***	42.07	47.20	***	42
FF-03A	49.42	57.30	77.43	82.20	49	78
FF-04A	48.19	53.15	56.50	63.43	49	58
FF-06	44.43	48.50	57.30	62.45	48	59
FF-07	***	***	34.00	38.22	***	34
FF-08	***	***	26.14	31.00	***	26
FF-09	***	***	26.35	32.11	***	27
FF-10	47.53	57.59	68.36	70.45	48	***
FF-11	49.47	65.15	73.46	76.45	54	74
FF-12	54.24	62.43	78.55	82.25	55	78
FF-13	56.06	70.00	69.18	74.20	59	***
FF-14	***	***	40.53	44.00	***	40
FF-15	53.16	59.33	56.50	66.00	56	58
FF-16	***	***	36.36	43.07	***	36
NRC-02	59.28	66.31	67.04	75.18	63	69
FF-17	59.35	69.24	69.04	74.50	63	70
FF-18	60.00	65.16	68.16	70.20	63	68
FF-19	***	***	45.10	46.53	***	45
FF-20	55.41	60.00	59.38	62.01	58	60
FF-22	66.26	73.19	73.09	74.00	67	73
FF-23	59.23	64.06	63.26	68.40	61	63
FF-24	59.48	62.06	65.04	67.23	61	66
FF-25	***	***	35.50	43.17	***	35
FF-26	52.52	72.14	74.06	81.48	50	74
FF-27	49.26	55.24	53.22	58.05	50	54
FF-28	43.49	60.58	67.09	68.55	48	67
FF-29	45.13	52.54	59.01	62.12	46	58
FF-30	***	***	40.43	43.00	***	40
FF-31	56.06	61.10	65.32	67.12	56	65
FF-32	53.08	57.08	60.10	62.30	54	61
FF-33	***	***	39.35	42.00	***	39
FF-34	***	***	37.19	45.26	***	38
FF-35	53.14	57.50	60.44	64.00	55	61
FF-36	***	***	31.36	41.34	***	32
FF-37	***	***	36.30	39.13	***	36
FF-38	***	***	26.41	38.43	***	29
FF-40	60.39	76.55	72.35	79.12	67	68
FF-41	57.43	66.46	68.12	71.00	67	71
FF-42	53.49	59.35	60.55	65.32	56	61

Assembly number	Time for Gypsum-Board Fall-off Observations (min.sec)				Time for Gypsum-Board Fall-off Temperature History (min)	
	Face Layer		Base layer			
	1st	last	1st	last	Face Layer	Base layer
FF-43	54.28	59.41	60.10	66.11	57	60
FF-44	52.32	54.35	53.30	59.15	53	54
FF-45	***	***	29.58	37.58	***	30
FF-46	55.19	59.45	61.41	67.40	58	62
FF-47	52.10	57.02	60.02	63.12	54	60
FF-48	53.50	59.02	62.23	65.54	56	62
FF-49	***	***	37.31	44.18	***	38
FF-50	***	***	34.17	45.00	***	35
FF-51	51.16	61.29	66.39	68.45	55	***
FF-52	42.17	49.50	50.14	51.41	44	50
FF-53	51.06	57.17	57.46	64.53	54	58
FF-54	37.38	56.18	60.37	66.04	44	60
FF-55	48.36	57.28	56.08	60.00	51	57
FF-56	54.35	62.08	61.51	64.24	57	61
FF-57	***	***	39.08	43.41	***	***
FF-58	48.50	56.19	54.42	63.11	53	57
FF-59	40.25	49.02	48.01	52.31	44	49
FF-60	43.15	58.45	59.07	60.55	48	59
FF-61	49.39	56.24	57.14	61.46	53	57
FF-62	46.15	55.31	54.07	56.00	46	54
FF-63	51.28	57.23	57.07	62.34	53	59
FF-64	47.08	55.23	54.55	61.30	51	55
FF-65	48.45	52.08	52.39	54.26	49	52
FF-66	***	***	36.18	43.18	***	36
FF-67	47.29	51.09	51.46	52.39	48	51
FF-68	48.02	53.10	51.58	53.24	49	52
FF-69	49.29	51.51	52.38	56.25	50	52
FF-70	48.02	52.03	52.03	55.41	48	52
FF-71	44.41	51.19	54.28	56.13	45	54
FF-72	49.04	54.09	54.18	57.07	51	54
FF-73	48.19	51.49	51.49	53.20	49	51
FF-74	***	***	31.57	40.15	***	32
FF-75	44.12	50.03	50.28	53.07	46	50
FF-76	***	***	38.58	48.32	***	40
FF-77	52.21	62.02	63.42	63.50	53	63
FF-78	***	***	33.00	42.16	***	34
FF-79	45.31	51.30	51.27	53.57	48	52
FF-80	45.10	50.24	50.24	53.10	49	51
FF-81	56.41	62.48	65.41	76.03	56	66
FF-82	50.50	63.13	61.33	68.40	56	62

Table 2 Comparison of Observed Fall-Off and Time of Sudden Temperature Rise

that gypsum fall-off temperature depends on the rate at which heat accumulates in the board. Severity of fire exposure using time and temperature relationships could potentially provide more generic fall-off criteria for numerical modelling. This would require calculating the cumulative board temperature between the beginning of the fire test and the time of fall-off of the assembly.

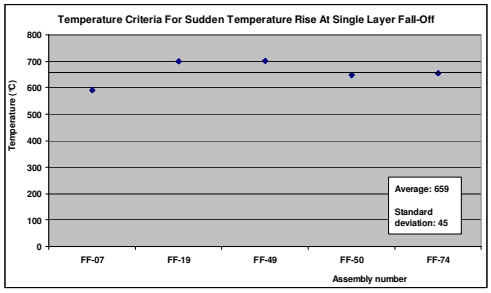

Figure 4 Assembly with single layer of Gypsum Board And Cellulose Spray-on Fibre Insulation

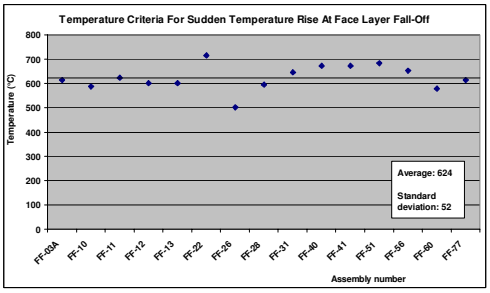

Figure 5 Assembly with Two layers (Face Layer) of Gypsum Board and no Insulation and RC at 406 mm o.c.

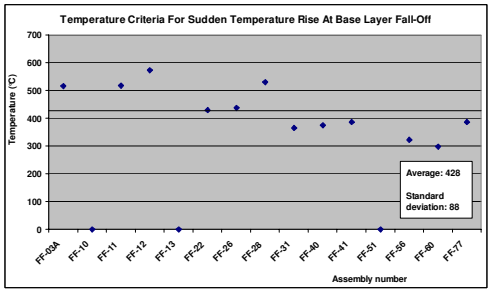

Figure 6 Assembly with Two layers (Base Layer) of Gypsum Board, Cellulose and RC at 406 mm o.c.

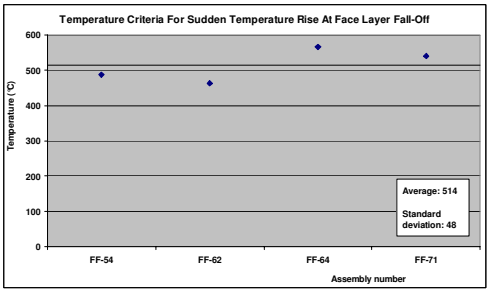

Figure 7 Assembly with Two layers (Face Layer) of Gypsum Board, no Insulation and RC at 610 mm o.c.

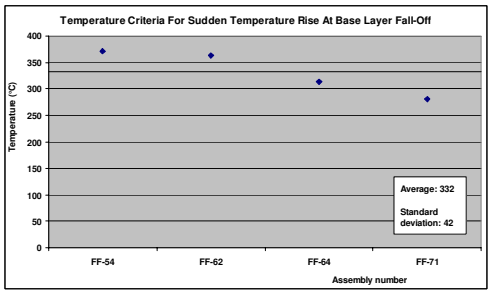

Figure 8 Assembly with Two layers (Base Layer) of Gypsum Board, no Insulation and RC at 610 mm o.c.

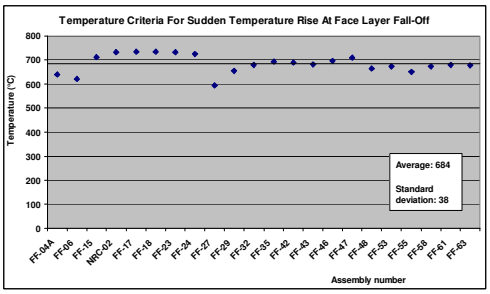

Figure 9 Assembly with Two layers (Face Layer) of Gypsum Board, Glass or Rock Insulation and RC at 406 mm o.c.

Resilient channels spacing dictates the number of screws and spacing used in the attachment of the gypsum board, and thus the loading on each screw. Screw spacing, i.e. loading per screw on a gypsum board sheet, appears to influence the temperature of fall-off of gypsum board. The temperature of fall-off was noted to be lower for assemblies with wider screw spacing. The larger loading per screw on assemblies with wider screw spacing causes larger stresses in the board at the screw locations. This could reduce the capacity of the board to sustain additional stress and cracking could also be induced more quickly at points under high stress in the board. These factors combined would explain why gypsum board falls off at a lower temperature for assemblies using wider resilient channels spacing. It was also seen that, in the

case of double layer gypsum board assemblies, the fall-off temperature of the face layer of gypsum board tends to be higher than the fall-off temperature of single gypsum board layer assemblies, while the base layer fall-off temperatures are usually significantly lower than face layer fall-off temperatures. Face layer temperatures are expected to be higher in double layer gypsum board assemblies than in single layer assemblies, since the second gypsum layer acts as an additional insulation layer. The low temperatures associated with the fall-off of gypsum board base layer, on the other hand, are most likely caused by thermal shock as the result of sudden fall-off of the face gypsum board layer which could lead to cracking and eventually fall off of the base layer faster.

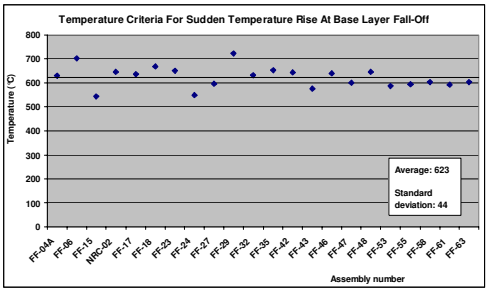

Figure 10 Assembly with Two layers (Base) of Gypsum Board, Glass or Rock Insulation and RC at 406 mm o.c.

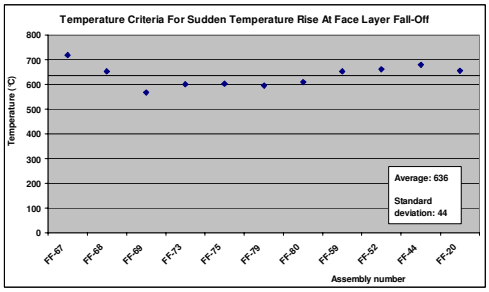

Figure 11 Assembly with Two layers (Face Layer) of Gypsum Board, Glass or Rock Insulation and RC at 610 mm o.c.

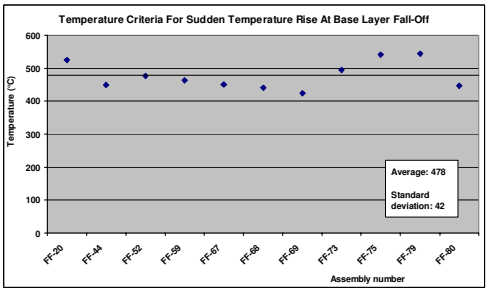

Figure 12 Assembly with Two layers (Base) of Gypsum Board, Glass or Rock Insulation and RC at 610 mm o.c.

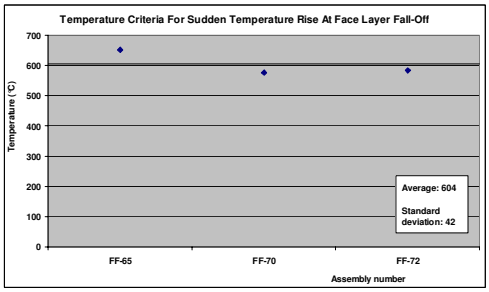

Figure 13 Assembly with Two layers (Face Layer) of Gypsum Board Board and Cellulose Insulation and RC at 610 mm o.c.

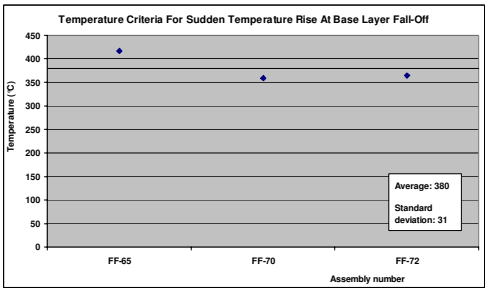

Figure 14 Assembly with Two layers (Base Layer) of Gypsum Board, Cellulose Insulation and RC at 610 mm o.c.

4. TEMPERATURE CRITERIA

The sudden rise in temperature criteria is based on the fact that the fall-off temperatures are determined in a manner that ensures the temperature increase caused by the fall-off of a gypsum piece is not accounted for in the determination of the temperature causing gypsum board to fall off. Table 3 shows the gypsum board fall-off temperature criteria. The values found in this table are taken at the back face of each gypsum board and are based on assemblies constructed with resilient channels. The installation of resilient channels in double layer floor assemblies did not impact the fall-off temperature of gypsum board face layers, which do not come directly in contact with them. In contrast, the recorded fall-off temperatures for base layers, as well as gypsum boards in single layer assemblies, were significantly reduced (by approximately 100°C) in assemblies built without resilient channels. The temperatures found in Table 3 are intended for use with, 12.7 mm thick, Type X gypsum boards. On average, the temperatures were found to be higher for thicker gypsum boards, but it was not possible to establish a clear relationship between board thickness and fall-off temperature due to the limited number of assemblies built with 15.9 mm thick Type X gypsum boards. No single gypsum board layer assembly with 610 mm screw spacing was tested. Only one double layer assembly with sprayed-on insulation and screw spacing at 406 mm was tested and experimental results were not sufficiently consistent for a judgment to be made on the fall-off temperature to use.

Assembly Characteristics		**Fall-Off Temperature ± Standard Deviation (°C)**		
Insulation	**Screw Spacing (mm)**	**Single Layer Assembly**	**Double Layer Assembly**	
			Face Layer	**Base Layer**
No Insulation	*406*	460 ± 20	620 ± 50	430 ± 90
	610	***	510 ± 50	330 ± 40
Insulation against Gypsum Board Layers	*406*	680 ± 50	680 ± 40	620 ± 40
	610	***	640 ± 40	480 ± 40
Sprayed-on Insulation	*406*	670 ± 40	***	***
	610	***	600 ± 40	380 ± 30

Table 3 Type X Gypsum Board Fall-off Temperature Criteria

5. SUMMARY

In this paper, an attempt was made to establish temperature failure criteria for gypsum board. Key findings are as follows:

1. The installation of insulation within the floor assembly was identified as the major factors influencing the temperature of fall-off of gypsum board layers.

2. Fall-off temperatures were lowest for non-insulated assemblies, and highest when the insulation was applied directly against the gypsum board layers.
3. The temperature of fall-off was lower for assemblies with wider resilient channels spacing (less number of screws).
4. A second layer of gypsum board increased the fall-off time for the gypsum board layer exposed to the fire (face layer) compared to an assembly with only one layer of gypsum board, even though the base layer fell off relatively quickly compared to the face layer due to a thermal shock caused by board exposure to heat once the face layer had dropped off.

6. REFERENCES

1. Sultan, M.A., Séguin,Y.P., Leroux, "Results of Fire Resistance Tests on Full-Scale Floor Assemblies", Internal Report No. 764, Institute for Research in Construction, National Research Council of Canada, Ottawa, ON, 1998.
2. Sultan, M.A, Latour, J.C., Leroux, P., Monette, R.C., Séguin, Y.P. and Henrie, J. "Results of Fire Resistance Tests on Full-scale Floor Assemblies – Phase II", Research Report 184, Institute for Research in Construction, National Research Council Canada, Ottawa, Ontario, 2005.
3. Sultan, M.A. and Roy-Poirier "Gypsum board fall-off temperature in floor assemblies exposed to standard fires," Interflam 2007, Proceedings of the 11th International Conference on Fire Science and Engineering (London, UK, September 03, 2007), pp. 979-991, September 03, 2007
4. " CAN/CSA-A82.31-M91, Gypsum Board Application, Canadian Standards Association, Rexdale, ON, 1991.
5. CSA A101-M83, Thermal Insulation, Canadian Standards Association, Rexdale, Ontario, 1983.
6. CAN/ULC-S702-M97, Standard for Mineral Fibre Thermal Insulation for Buildings, Underwriters' Laboratories of Canada, Scarborough, Ontario, 1997.
7. CAN/CGSB 51.60-M90, Cellulose Fibre Loose Fill Thermal Insulation, Canadian Standards Board, Ottawa, Ontario, 1990.
8. CAN/CSA-82.27-M91, Gypsum Board, Canadian Standards Association, Etobicoke, Ontario, Canada, 1991.
9. ASTM C36-97, Standard Specification for Gypsum Wallboard, American Society for Testing and Materials, West Conshohocken, PA, June 1997.
10. CAN/ULC-S101-M89, Standard Methods of Fire Endurance Tests of Building Construction and Materials. Underwriters' Laboratories of Canada, Scarborough, ON, 1989.

MEASUREMENT OF THERMAL PROPERTIES OF GYPSUM BOARD AT ELEVATED TEMPERATURES

SAMUEL L. MANZELLO[#], SUEL-HYUN PARK[°], TENSEI MIZUKAMI[*], DALE P. BENTZ[+]

ABSTRACT

The thermal conductivity, specific heat, mass loss, and linear contraction for gypsum board types widely used in the USA and Japan were measured both at room temperature and elevated temperatures. The gypsum board types tested include Type X and Type C from the USA and Type R and Type F from Japan. Results indicate that the difference in thermal properties of all gypsum board samples tested in the present study is not significant, particularly at elevated temperatures. A large difference in linear contraction among gypsum board samples was observed at elevated temperatures, implying a significant difference in mechanical behavior at fire temperatures. The experimental data set provides valuable information that can be used to model the behavior of gypsum board at elevated temperatures.

1. INTRODUCTION

For a performance-based design approach, it is important to know when wall assemblies collapse and when their effectiveness as a smoke and flame barrier is compromised due to gypsum board shrinkage and cracking. Limited or no experimental data on the performance and failure mechanisms of gypsum board wall assemblies under realistic fire loadings are available; this greatly hampers the application of performance-based design approaches[1-3]. Furthermore, to be able to model the behavior of gypsum board wall assemblies, thermal property data are needed as a function of temperature[1-4]. For gypsum board, critical data is either not available as a function of temperature or large uncertainties

[#] PhD, Mechanical Engineer, Building and Fire Research Laboratory, National Institute of Standards and Technology, Gaithersburg, MD 20899 USA, email: samuelm@nist.gov
[°] PhD, Guest Researcher, Building and Fire Research Laboratory, National Institute of Standards and Technology, Gaithersburg, MD 20899 USA, email: seulpark@nist.gov
[*] MS, Engineer, The Center for Better Living, Tsukuba, Ibaraki, Japan, email: mizukami@tbtl.org
[+] MS, Chemical Engineer, Building and Fire Research Laboratory, National Institute of Standards and Technology, Gaithersburg, MD 20899 USA, email: dale.bentz@nist.gov

exist in regard to the quality of the data reported. Properties of interest include specific heat and thermal conductivity as a function of temperature. In addition to these, the linear contraction and mass loss should be measured as a function of temperature for gypsum board. Furthermore, all of the aforementioned properties are needed for various gypsum board types.

These properties have been determined for common gypsum board types used in Japan and the USA. These include Type X and Type C in the USA; Type R and Type F in Japan. The collaboration between the National Institute of Standards and Technology (NIST) and the Center for Better Living is part of an international effort to assess the performance and failure mechanisms of gypsum wall assemblies under real fires/furnace conditions and to compile an experimental database necessary to validate models that could be used to predict their performance and ultimate failure under various design fires. Property determination is one important aspect of the data collection needed to be able to model the performance/failure of such assemblies; the results presented are part of a NIST effort to quantify gypsum board properties for various gypsum board types. The basic premise is to generate a database of these properties using a suite of in house metrology methods. This methodology will afford a uniform and consistent database for the needed properties necessary to model gypsum board assembly performance under a fire load.

To this end, the Hot Disk Thermal Constants Analyzer® (TPS 2500)[@] was used to determine the room temperature thermal conductivity and specific heat of representative gypsum board samples, whereas the slug calorimeter and differential scanning calorimetry (DSC) were used to determine the thermal conductivity and specific heat as a function of temperature For the mass loss and linear contraction measurements, a simultaneous measurement technique was developed with aid of digital image processing software. Details of each measurement and the results are discussed and presented below.

2. EXPERIMENTAL DESCRIPTION

2.1 Thermal Conductivity and Specific Heat Measurements

The thermal properties of different types of gypsum board (Type X and Type C in the USA; Type R and Type F in Japan) were characterized both at room temperature and elevated temperatures. All of the gypsum board samples were of the same nominal thickness; 15.9 mm. The Hot Disk Thermal Constants Analyzer® (TPS 2500) was used to determine the room temperature thermal conductivity and specific heat of representative samples of gypsum board. The Hot Disk determines thermal transport properties such as thermal conductivity and thermal diffusivity using the transient plane source technique (TPS). Briefly, a nickel wire spiral probe with a radius of about 15 mm was placed between two gypsum board samples, each with dimensions of 152 mm by 152 mm. A constant current applied to the spiral probe creates resistance and thus increases the temperature of the spiral probe. The probe serves as the temperature sensor as well as the continuous plane heat source during the measurement. Since temperature changes in the probe are strongly dependent on sample composition, it is possible to evaluate the thermal transport properties of materials surrounding the probe. Based upon two calculated thermal transport properties, *i.e.*, thermal conductivity and thermal diffusivity, heat capacity can be determined. As the Hot Disk measurement provides the volumetric heat capacity, the room temperature density was used to determine the specific heat on a mass basis.

[@] Certain commercial equipment are identified to accurately identify the methods used; this in no way implies endorsement from NIST.

To determine the specific heat as a function of temperature, differential scanning calorimetry (DSC) was used. DSC specific heat measurements were taken following the procedure outlined in ASTM E 1269-2001[5]. The gypsum board samples used were 6-10 mg in initial mass. To accommodate the gas generation incurred from dehydration, the sample, reference and standard measurements utilized aluminum pans that were sealed except for a 50 μm pinhole in the lid. Measurements were performed with a heating rate of 20 ^{o}C /min under a constant nitrogen gas flow. In addition, the specific heat of powdered sapphire Al_2O_3, as a correction material, was measured under the same operating condition used for the gypsum samples in order to obtain a correction factor. Details on this correction procedure are summarized in the ASTM E 1269-2001[5].

The thermal conductivity as a function of temperature was determined using the slug calorimeter[6]. The slug calorimeter is comprised of a square central stainless steel plate (152 mm by 152 mm by 12.7 mm). A set of 152 mm by 152 mm gypsum board samples (with their paper carefully removed) was installed in a 'sandwich' configuration (*i.e.* steel slug in the center); this provided an adiabatic boundary condition at the central axis of the slug plate. This entire configuration was then placed at the bottom of an electrically heated box furnace and the temperatures of the metal slug and exterior gypsum board surfaces were recorded during multiple heating and cooling cycles. Figure 1 displays a schematic of the slug calorimeter experimental setup. The steel plate has a mass of 2.3 kg and the heat capacity of stainless steel as a function of temperature was taken from the literature[7]. With knowledge of these properties and measured temperatures with time, an apparent thermal conductivity of the gypsum sample can be calculated using the following equation[6]:

$$k = \frac{Fl(M_s C_{p.s} + M_g C_{p.g})}{2A\Delta T} \tag{1}$$

where k is the apparent thermal conductivity, F is the temperature increase rate of the steel slug, l is the gypsum sample thickness, M_s and M_g are the masses of stainless steel and gypsum sample, respectively, $C_{p.s}$ and $C_{p.g}$ are the heat capacity of stainless steel and gypsum sample, respectively, A is the gypsum sample area, and ΔT is the temperature difference across the gypsum sample. In equation 1, $C_{p.g}$ was assumed to be constant with temperature and determined using the Hot Disk measurement.

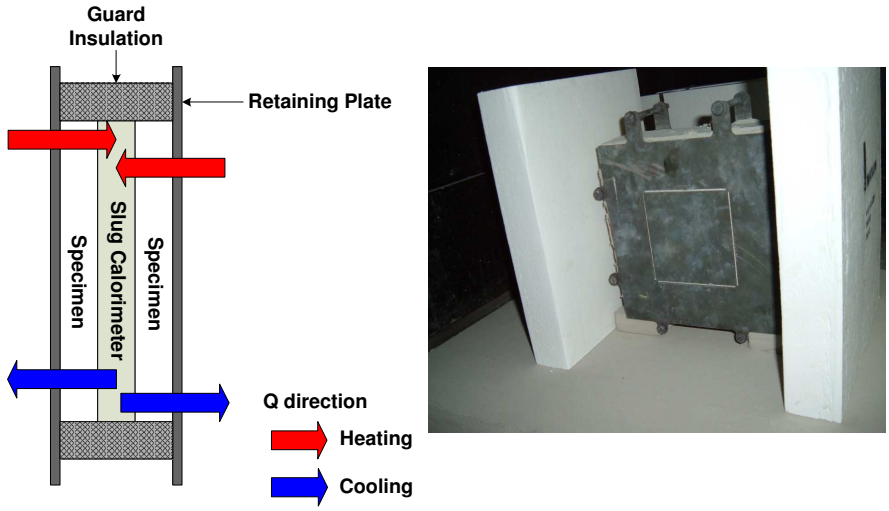

Fig. 1 Schematic and picture of slug calorimeter

2.2 Mass loss and LINEAR contraction measurements

To gain further insights into the physical behavior of gypsum board at elevated temperatures, the mass loss and linear contraction were measured as a function of temperature for the gypsum board samples. Triplicate samples of 15.9 mm thickness gypsum board were cut into rectangles of 152 mm by 50 mm from single sheets of each type and then placed into an oven. Fresh samples were heated up to 900 ^{o}C for 3 h. Similar to prior work, it was observed that the additional mass loss beyond three hours in the oven at a selected temperature was not significant[3]. This was verified by measuring the mass loss as a function of time (up to 24 hours) at a given temperature. Consequently, after a three hour heat-up at a selected temperature, samples were taken out to measure their mass loss and linear contraction. To aid in these measurements, a simultaneous measurement technique was developed. In this technique, the mass of each sample was simultaneously measured using a load cell with 0.01 g accuracy, while a high resolution CCD camera imaged each sample placed on the scale. Figure 2 shows a schematic of the experimental setup for the simultaneous measurement. Each gypsum sample was recorded using a mini-DV recorder and the mass of each sample was saved using a user-developed lab view program before and after the heating procedure. This technique was different from prior work[3] and newly developed as part of this study.

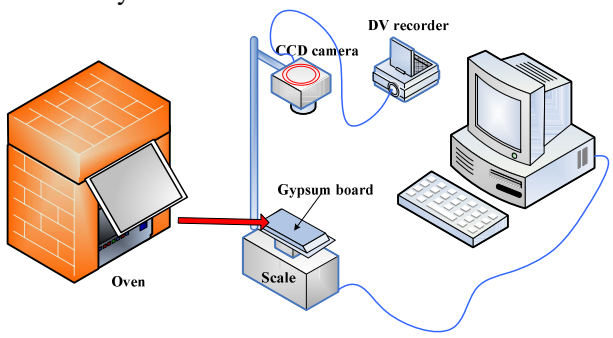

Fig. 2 Schematic of experimental setup for mass loss and linear contraction measurements

The recorded gypsum sample images were digitized and analyzed using digital image processing software (Matrox, Inspector® 8.1). In addition, an analysis algorithm was developed and implemented to consistently interpret the digitized image of gypsum samples. In this algorithm, the background noise was first reduced using a 3 by 3 averaging filter and an edge-enhanced filter was applied to accentuate the edge features of each gypsum board sample. The image of the gypsum board samples were then extracted from the background by setting an appropriate threshold value. Eventually, the extracted images of each gypsum board sample were compared before and after the heating procedure to determine the linear contraction in the longitudinal direction.

3. GYSPUM BOARD PROPERTY CHARACTERIZATION

The thermal properties of four different gypsum boards types were characterized and compared (Type X and Type C in the USA; Type R and Type F in Japan). Table 1 displays the thermal properties of each gypsum sample obtained from the Hot Disk measurements at room temperature. These measurements were performed with the paper in place and with the paper removed from the gypsum board samples. Initially, for the Type X (USA) and Type C (USA) gypsum board samples, the paper was peeled off manually. As this technique was

very laborious, an improved method was conducted for the Type F (Japan) and Type R (Japan) gypsum board samples. For these samples, the paper was removed by placing the gypsum board samples on a mill; this technique resulted in a reduction in thickness of 0.5 mm from each side of the gypsum board samples. The uncertainty in the measurement was found to be ± 10 %. As summarized in Table 1, the specific heat for all gypsum samples with the paper in place in the present study ranged from 891 J/(kg K) to 1017 J/(kg K); thermal conductivity varied from 0.254 W/(m K) to 0.314 W/(m K). The room temperature measurements were subsequently repeated with the paper removed. The removal of the paper influenced the C_p values. In addition, the room temperature density was determined for the gypsum board samples used. Including the paper, these values are: 711 kg/m^3 (Type X-USA); 752 kg/m^3 (Type C-USA); 743 kg/m^3 (Type F-Japan); 805 kg/m^3 (Type R-Japan). The uncertainty in density measurement was found to be ± 10 %.

Table 1 Thermal properties of gypsum samples at room temperature (virgin material)

	With paper on		With paper off	
	C_p [J/kg K]	k [W/m K]	C_p [J/kg K]	k [W/m K]
Type C (USA)	1017	0.276	852	0.276
Type X (USA)	1089	0.258	947	0.252
Type F (Japan)	963	0.254	1,034	0.238
Type R (Japan)	891	0.314	977	0.292

The thermal conductivity as a function of temperature was determined using the slug calorimeter[6] and the results are displayed in Figure 3. During the first heating cycle, the gypsum dehydrated, absorbed some of the energy, and delayed the temperature rise of the slug. As a result, the thermal conductivity was determined based upon the second heating/(natural) cooling cycle. For Type X (USA) and Type C (USA) gypsum board, the thermal conductivity steadily increased with temperature; similar behavior has been observed in thermal conductivity measurements for other gypsum board types[4]. There is a slight difference in thermal conductivity at low temperatures among the gypsum samples investigated. However, at elevated temperatures, the differences were minimal as shown in the figure. Bénichou and Sultan[4] measured thermal conductivity as a function of temperature for 15.9 mm Type X gypsum board; Type C board was not considered. In their work, a thermal conductivity meter was used. For comparison, at temperatures of 300 °C and 700 °C, they reported values of 0.14 W/(m k) and 0.18 W/(m k) for Type X gypsum board, respectively. These values are slightly lower than the present measurements.

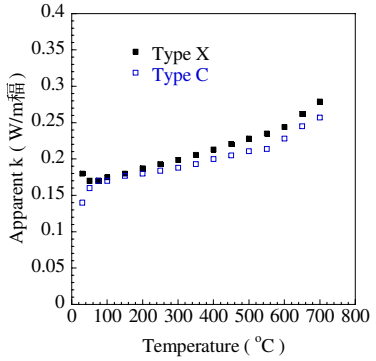

Fig. 3 Thermal conductivity vs. temperature (previously heated) -Type X (USA) and Type C (USA)

The thermal conductivity of the Type F (Japan) and Type R (Japan) gypsum board was not reported due to the large degree of cracking observed after the first heating and cooling cycle in the slug calorimeter for these materials. Figure 4 displays the steel slug temperatures measured during the first heating and cooling cycle. As can be seen, in contrast to the Type X (USA) and Type C (USA) gypsum board, during the first cooling cycle the temperature of the steel slug varied widely for the Japanese gypsum board measurements. The difference in temperature was caused by the severe cracking for Type R (Japan) and Type F (Japan) gypsum board. This prevented an accurate measurement of thermal conductivity due to poor coverage of the slug by the gypsum board. Based on the steel slug temperatures measured during the first heating phase, it is apparent that the thermal conductivity is similar for all four gypsum board types. These results demonstrate that the use of the slug calorimeter for thermal conductivity measurements is limited for materials that crack severely during cooling.

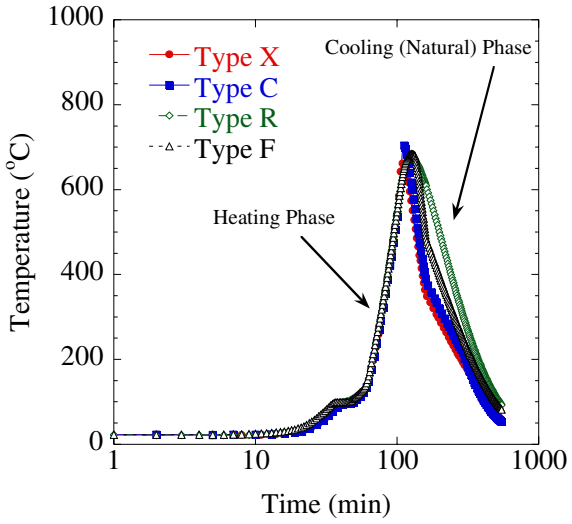

Fig. 4 Average steel (slug) temperature as a function of time; three thermocouples were embedded inside the stainless steel slug

Figure 5a-b displays the results of the DSC measurements for the Japanese and USA gypsum board samples. The DSC traces demonstrate two significant reactions are completed by the time that all samples reached 250 °C. The core material of gypsum board is a porous solid composed primarily of calcium sulfate dihydrate ($CaSO_4\ 2H_2O$), a naturally occurring mineral. The presence of the water molecules is a key feature in establishing the fire resistance properties of gypsum. When heated, crystalline gypsum dehydrates and water is liberated, typically in two separate, reversible chemical reactions[8]:

$$CaSO_4\ 2H_2O + Q \leftrightarrow CaSO_4\ (1/2)H_2O + (3/2)H_2O \quad (2)$$

$$CaSO_4\ (1/2)H_2O + Q \leftrightarrow CaSO_4 + (1/2)H_2O \quad (3)$$

Both of these dehydration reactions are endothermic and generally occur at temperatures between 125 °C and 225 °C. At a temperature of around 400 °C, a third, exothermic reaction occurs, in which the molecular structure of the soluble crystal reorganizes itself into a lower insoluble energy state (hexagonal to orthorhombic):

$$CaSO_4\ (sol) \rightarrow CaSO_4\ (insol) + Q \qquad (4)$$

As displayed in the figures, Type X gypsum board (USA) and Type R gypsum board (Japan) have C_p peaks of similar magnitude, which indicates the energy needed for dehydration (heat of reaction) was quite similar. In addition, the magnitudes of C_p peaks for Type C gypsum board (USA) were comparable to those of the C_p peaks for Type F gypsum board (Japan). The authors are not aware of specific heat data as a function of temperature for Type F (Japan) and Type R (Japan) gypsum board. For Type X 15.9 mm gypsum board, Bénichou and Sultan[4] reported specific heat measurements as a function of temperature using DSC methods. In those measurements, only the first dehydration reaction was observed; namely the reaction described in equation (2) was not observed. With regard to the magnitude of the C_p peak, Bénichou and Sultan[4] reported a C_p value of 28,000 J/{kg K} at a temperature of 125 °C. This is slightly higher than the reported values in the present study (see Fig. 5a).

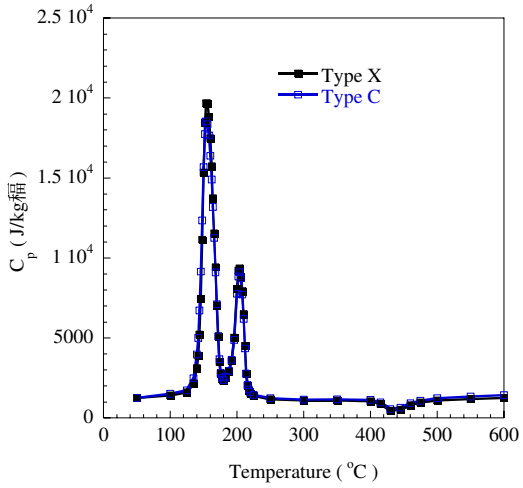

Fig. 5a Specific heat vs. temperature-Type X (USA) and Type C (USA)

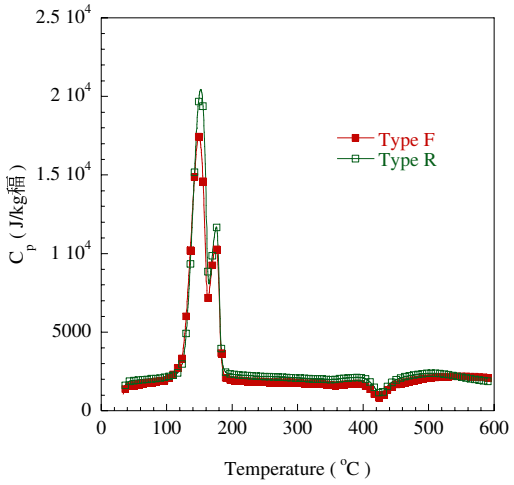

Fig. 5b Specific heat vs. temperature-Type F (Japan) and Type R (Japan)

The mass loss was measured for all gypsum board samples and is plotted as a function of temperature in Figures 6a and 6b, respectively. At each temperature, each data point represents the average of three replicate measurements. As can be seen in Figure 6a, a significant amount of mass loss was observed for all gypsum board samples for temperatures up to 400 °C. This result is expected since the dehydration reactions are completed at temperatures above 250 °C. The Type C gypsum board (USA) and Type F gypsum board (Japan) were similar in terms of the temporal variation in mass loss. The temporal variation in mass loss behavior was also similar for Type X gypsum board (USA) and Type R gypsum board (Japan). Differences in the mass loss observed between two groups may be due to the composition of the materials of each gypsum type which are added for fire resistance characteristics.

The linear contraction of all gypsum board samples is displayed in Figure 7. At each temperature, each data point represents the average of three replicate measurements. The contraction of each gypsum board sample was negligible at temperatures up to 300 °C. On the other hand, differences in the contraction of each gypsum type were found to be considerably significant at higher temperatures. These results suggest that the mass loss due to the dehydration reactions has little effect on contraction of each gypsum sample. Data is available in the open literature for the linear contraction of 12.7 mm Type X gypsum board. Takada[9] measured the linear contraction of 50 mm by 200 mm by 12.7 mm thick Type X gypsum board and reported that the contraction increased as a function of temperature; 1.7 % at a temperature of 700 °C. While the contraction measured by Takada is lower than the reported values for Type X board here, the thickness of the board is different which should influence the results.

Clearly, the linear contraction of the gypsum board is strongly dependent on the composition of the additives. Common additives used to mitigate contraction of the boards include vermiculite. The present results suggest that Type C (USA board) contains the highest degree of additives as compared to the other board types tested. In addition to this, NIST is currently determining mechanical properties of the various gypsum board types as a function of temperature; this work will be the subject of future publications.

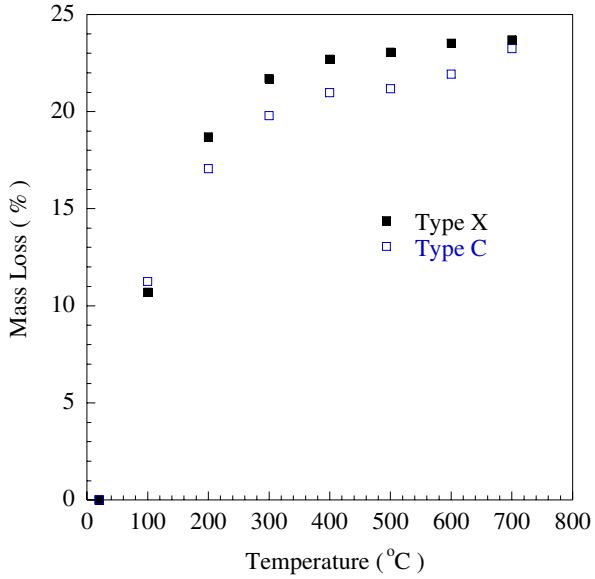

Fig. 6a Mass loss vs. temperature-Type X (USA) and Type C (USA)

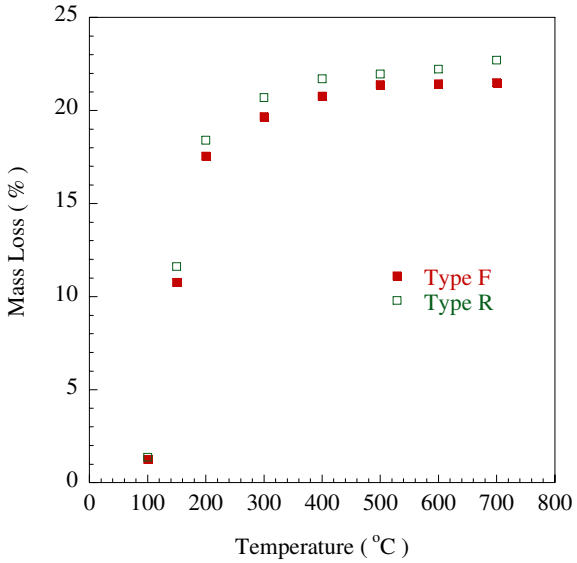

Fig. 6b Mass loss vs. temperature-Type F (Japan) and Type R (Japan)

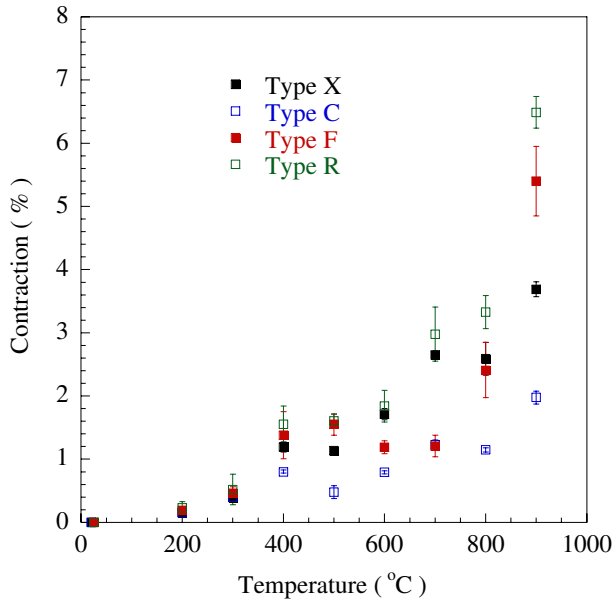

Fig. 7 Linear contraction vs. temperature-Type X (USA), Type C (USA), Type F (Japan) and Type R (Japan)

4. CONCLUSIONS

To be able to model the behavior of gypsum board wall assemblies, thermal property data are needed as a function of temperature. For gypsum board, critical data is either not available as a function of temperature or large uncertainties exist in regard to the quality of

the data reported. Properties of interest include specific heat, density, and thermal conductivity as a function of temperature. The results presented are part of a NIST effort to quantify gypsum board properties for various gypsum board types.

The thermal conductivity, specific heat, mass loss, and linear contraction for gypsum board types widely used in the USA and Japan were measured both at room temperature and elevated temperatures. Results indicate that the difference in specific heat of all gypsum board samples tested in the present study is not significant, particularly at elevated temperatures. A large difference in linear contraction among gypsum samples was observed at elevated temperatures. The experimental data set provides valuable information that can be used to model the behavior of gypsum board at elevated temperatures. As part of the database for gypsum board, NIST is currently determining mechanical properties of various gypsum board types; such work will be the subject of future publications. Finally, it is desired to characterize other gypsum board types in addition to those used in Japan and the USA.

5. ACKNOWLEDGMENTS

Dr. William L. Grosshandler of the Building and Fire Research Laboratory (BFRL)-NIST is the program manager for this effort.

6. REFERENCES

1. Nyman, J.F., "Equivalent Fire Resistance Ratings of Construction Elements Exposed to Realistic Fires," MS Thesis, University of Canterbury, 2002.
2. Gerlich, H., Barnett, C.R., McLellan, D.L., Buchanan, A.H., Predicting the Performance of Drywall Construction Exposed to Design Fires," *Proceedings of the 10th International Fire Science and Engineering Conference* (INTERFLAM), pp. 257-267, Interscience Communications, 2004.
3. Manzello, S.L., Gann, R.G., Kukuck, S.R., and Lenhert, D.B., "Influence of Gypsum Board Type (X or C) on Real Fire Performance of Partition Assemblies," *Fire and Materials*, 31:425-442, 2007.
4. Bénichou, N., Sultan. M., "Thermal Properties of Lightweight-Framed Construction Components at Elevated Temperatures," *Fire and Materials*, 29:165 179, 2005.
5. ASTM E 1269-01: "Standard Method for Determining Specific Heat Capacity by Differential Scanning Calorimetry," ASTM International, West Conshohocken, PA, 2001.
6. Bentz, D.P., Flynn, D.R., Kim, J.H., Zarr, R.R., "A Slug Calorimeter for Evaluating the Thermal Performance of Fire Resistive Materials," *Fire and Materials* 30:257-270, 2006.
7. ASTM E2584-07: "Standard Practice for Thermal Conductivity of Materials Using a Thermal Capacitance (Slug) Calorimeter," ASTM International, West Conshohocken, PA, 2007.
8. Ramachandran, V.S., Paroli, R.M., Beaudoin, J.J., Delgado, A.H., *Handbook of Thermal analysis of Construction Materials*. Noyes Publication, William Andrew Publishing. Norwich, NY 2003.
9. Takada, H., "A Model to Predict the Fire Resistance of Non-Load Bearing Wood Stud Walls", *Fire and Materials*, 27:19-39, 2003.

EXPERIMENTAL AND NUMERICAL INVESTIGATION OF BEHAVIOUR OF TROPICAL WOOD IN FIRE: FROM WOODEN BEAMS TO TIMBER STRUCTURAL ELEMENTS

ERICH HUGI[1], REGINA WEBER[2] and SERGEY SHEPEL[3]

ABSTRACT

Currently, there is a significant lack of information on fire resistance properties of building elements made of tropical wood and with separating function. This presents difficulties for the use of these sorts of wood in production of timber structural elements in the context of fire safety. The object of this investigation is the extrapolation of experimental data obtained using relatively small beams of wood (1 x 0.09 x 0.045 m) to timber structural elements of larger size like fire doors (2.3 x 1.15 x 0.047 m). A series of measurements is carried out for tropical and European species of wood, latter for the purpose of comparison. The values of beam deflections and charring rates as well as the fire resistance time of doors are measured in standard fire (ISO 834-1). A new technique is introduced to measure the oxygen permeability index (OPI) of wood which appears to show a strong correlation with the charring rate. In order to generalize the obtained results, a phenomenological numerical model of beam bending in fire is constructed and validated. However, there is no correlation between the results of the large scale tests using the door leafs and the small scale tests using the small wooden beams.

1. INTRODUCTION

Tropical hardwood species are increasingly used for structural and separating elements in building applications. Therefore, it is important to take into consideration the behaviour of tropical wood in fire. The present study concentrates on fire doors and shutter assemblies where a rather thin layer of wood is installed as room closure.

[1] PhD, Empa Swiss Federal Laboratories for Materials Testing and Research, 8600 Duebendorf, Switzerland, email: erich.hugi@empa.ch
[2] MSc, Empa Swiss Federal Laboratories for Materials Testing and Research, 8600 Duebendorf, Switzerland, email: regina.w@bluewin.ch
[3] PhD, Empa Swiss Federal Laboratories for Materials Testing and Research, 8600 Duebendorf, Switzerland, email: sergey.shepel@empa.ch

In contrast to load bearing heavy timber constructions,[1] door frames and door leaves are of filigree shape, and for this reason their fire resistance depends not only on the charring rate, but also on the deflection due to dehumidification. Fast combustion and unfavourable deflection can cause early loss of integrity as defined in the harmonised European standards EN 1363-1[2] and EN 1634-1[3]. These standards allow manufactures to use any type of wood which satisfies the fire resistance tests, but they do not allow an interchange of parts produced out of different types of wood without additional testing. Door manufacturers working with timber from sustained cultivated tropical forests face a problem of limited availability of certified wood that necessitates a search for an alternative source of supply. Very often, the new source cannot supply the same wood type, or it is located in a different climate region that affects strongly the physical and chemical properties of wood. Unfortunately, testing the alternative wood is costly due to the necessity of using of large scale experimental facilities. Consequently, the question arises whether a few and easy to measure parameters obtained by testing small scale probes can characterize reliably the large scale behavior of fire doors with respect to fire resistance.

The density is one parameter, which can be easily determined, and which is used often to characterize the fire resistance of wood. However, a common conclusion of many investigations involving different sorts of wood is that the wood density does not correlate with the charring rate consistently[4]. Furthermore, it has been demonstrated that the charring rate is strongly affected by the anatomical structure of wood which ultimately controls the transport of gaseous substances through the material[5]. Besides, the performance of wood in fire is also influenced by the chemical impact of components of fire gases on the anatomical structure.

The anatomical structure of wood can be easily and well characterized in terms of the gas permeability[6], since this particular parameter determines the rate of a fluid passing through porous medium. Thus, the gas permeability can be considered as an appropriate parameter characterizing the charring behaviour of wood. In addition to that, the knowledge of the gas permeability is also important from the point of view of characterizing the wood dehumidification in front of the pyrolysis zone. This is crucial for the developing of moisture gradient[7] which causes shrinkage of the material and ultimately the deflection of the specimen.

At Empa, a quantitative investigation of oxygen permeability on fire behaviour of wood was carried out. The oxygen permeability index (OPI) was measured using a technique normally employed for concrete specimens[8]. As a result, a correlation between the OPI and charring rate was found[9]. In addition, in a separate series of tests the deflections of wood specimens in fire were measured. The prime target here was to link the oxygen permeability, charring rate, deflection, Young's modulus and density measured using small scale probes with the large scale behaviour of fire doors with respect to fire resistance. For comparison reasons, some European wood species were also employed in the investigation. Finally, to generalize the obtained results a phenomenological numerical model of wood deflections in fire was built and validated using the experimental data.

2 EXPERIMENTAL PROCEDURE

2.1 Investigation of Wooden Beams at Small Scale

The beam shaped specimens had the dimensions of 1000 x 90 x 45 mm. These dimensions correspond approximately to the size of door frames and door grids (the doors are typically required to have the fire resistance time of 30 min). The beams were air-dried to

equilibrium moisture content. Table 1 lists the wood species employed in the experiment. All the measurements were performed using three specimens of each wood species, except Abachi, Abura and Meranti Red Light. The latter three wood species were studied using only two specimens of each wood.

First, the Young's modulus was measured using the four point bending procedure and the test machine Zwick 1474. These tests were performed according to the standard EN 408[10]. The equilibrium moisture content of the specimens was measured using the moisture measuring device Bollmann H-D-3.10 at 5 and 15 mm depth on two sides of each specimen. The four values obtained for each beam were averaged. Each specimen was weighed and the density calculated.

Table 1: Structural properties of the tested wood species[11].

Wood species	**Scientific name**	**Hardwood/ Softwood**	**Vessel rate**	**Vessel size**	**Vessel grouping**
Abachi	*Triplochiton scleroxylon*	hardwood	Ca. 72%	large	diffuse-porous
Abura	*Hallea ciliata/stipulosa Leroy*	hardwood	Ca. 65%	small-medium size	diffuse-porous
Bibosi	*Ficus glabrata*	hardwood	-	large	diffuse-porous
Cambarà Rojo	*Erisma spp.*	hardwood	Ca. 72%	very large	diffuse-porous
Cambarà Mixto	*Erisma spp.*	hardwood	Ca. 72%	very large	diffuse-porous
Mara Macho	*Cedrelinga catenaeformis Ducke*	hardwood	-	very large	diffuse-porous
Meranti Red Light	*Shorea hypochra Hance*	hardwood	Ca. 55%	very large	diffuse-porous
Roble	*Amburana Cearensis*	hardwood	-	large	diffuse-porous
Palomaria	*Calophyllum brasiliense*	hardwood	-	medium size-large	diffuse-porous
Maple	*Acer pseudoplatanus*	hardwood	Ca. 61%	very small	diffuse-porous
Spruce	*Picea Abies*	softwood	-	-	no pores
Oak	*Quercus robur/petraea*	hardwood	Ca. 39%	very large (early wood) small (late wood)	ring-porous

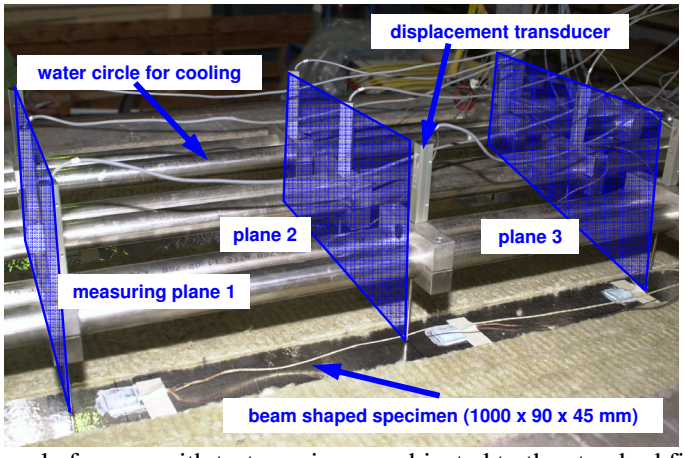

Fig. 1 - Small scale furnace with test specimens subjected to the standard fire ISO 834-1.

In a next step, the charring rate measurements were carried out using the Empa oil-fired horizontal furnace shown in Figure 1. The specimens were exposed to fire on one side

according to the standardized temperature-time curve ISO 834-1[12]. The samples were arranged in a special frame, in which each sample was equipped with three displacement transducers on the side not exposed to fire with the purpose of measuring the deflections. After being exposed to the fire for 25 min, the samples were removed from the furnace and cut into slices with the purpose of calculating the charring rate. Accordingly, three slices of 5 mm thickness were made for each specimen at the locations shown in Figure 1 (measuring planes 1, 2 and 3). The remaining uncharred thickness d_{rem} was determined by averaging over 9 sites for each specimen. The charring rate, β, was determined as follows

$$\beta = \frac{d_{init} - d_{rem}}{t} \tag{1}$$

where d_{init} is the initial thickness of the specimen, and t is the duration of the test.

The permeability of wood was measured at room temperature using a technique which was originally developed for concrete[8] and later adapted to wood by Hugi *et al*[8]. According to this technique, a 25-mm thick slice of a 68-mm diameter core of wood is placed in a tight sample holder on the aperture of the closed cylinder. An initial gas pressure (oxygen in this case) in the cylinder is increased up to 100 kPa. Then, the pressure decay of oxygen due to penetration into the slice of wood is measured for eight hours. The coefficient of permeability is calculated based on the pressure decay and constants that do not depend on the tested material:

$$k = \frac{\omega \cdot V \cdot g \cdot d}{R \cdot A \cdot \theta \cdot t} \times \ln \frac{P0}{P(t)} \tag{2}$$

where k is the coefficient of permeability (m/s), ω is the molar mass of gaseous oxygen (32 g/mol), V is the volume of the pressure cylinder, g the gravitational acceleration, R the universal gas constant (8.313 Nm/Kmol), A the sample cross section, d the sample thickness, θ the absolute temperature, t is time, P_0 the initial pressure in the cylinder and $P(t)$ the pressure at time t.

The oxygen permeability index (OPI) is defined as the negative logarithm of the coefficient of permeability as follows

$$\text{OPI} = -\log_{10}(k) \tag{3}$$

Accordingly, a high OPI value corresponds to a low oxygen permeability. Two measurements of one sample of each wood species were carried out.

2.2 Investigation of Fire Doors at Large Scale

The fire experiments were carried out according to the European standards EN 1363-1[2] and EN 1634-1[3]. All fire doors were of identical design and had the dimensions of 2300 x 1150 x 47 mm (Figure 2). Only the grid of the door leafs and door frames were built out of the same wood as the wooden beams used in the small scale furnace tests. The chosen door construction should manifest the effects of deflection and charring rate as it is of importance for separating elements of filigree shape. The observed failure mode was in all performed large scale fire experiments related to the loss of integrity. Sustained flaming occurred in the upper corner on the side of the door lock and spread along the upper edge of the door leaf towards the side of the door hinges.

Large scale test specimen: Door leaf dimensions 2300 x 1150 x 47 mm.

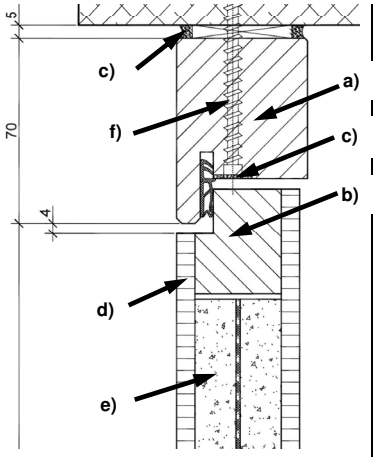

Cut A-A:
a): door frame made of hardwood
b): door leaf grid made of hardwood
c): sealing; d): HDF; e): LDF; f): frame fixing.

Loss of integrity due to deflection of door leaf and charring of door grid and door frame respectively

Detail B: Deflection of door leaf relative to the frame (approx. fire exposure time of 23 minutes).

Fig. 2 - Large scale furnace with test specimens subjected to the standard fire ISO 834-1.

3. RESULTS

3.1 Results of Investigation with Wooden Beams

Table 2 shows a summary of the obtained data for the density, Young's modulus, charring rate, OPI and moisture content for each wood type.

Table 2: Results for the 12 investigated wood species.

Wood species	Beam Nr.	Density [kg/m^3]	Young's modulus [kN/mm$^{2]}$	Charring rate [mm/min]	OPI [-]	Moisture content [%]
Cambarà Rojo	1	604	12.4	0.587	10.67	10.25
	2	609.1	12.7	0.61	10.77	9.65
	3	597.9	11.3	0.593		10
Roble	1	698.3	9.9	0.499	10.78	7.9
	2	674.1	12.3	0.526	10.95	9.75
	3	653.8	11.7	0.533		8.45
Palomaria	1	609.8	13.5	0.603	10.85	7.4
	2	625.5	12.2	0.577	11.04	7.7
	3	598.4	11.4	0.618		7.6
Mara Macho	1	613.2	10.2	0.636	10.38	5.8
	2	603.4	10.8	0.618	10.7	6.1
	3	590.5	10.6	0.548		5.7
Abura	1	558.9	13.5	0.799	10.05	9.15
	2	522	11.3	0.895	10.05	8.9
Cambarà Mixto	1	534.4	9.8	0.746	9.8	9.7
	2	532.7	9.5	0.764	9.84	9.8
	3	528.3	9.2	0.73		9.85
Bibosi	1	465.7	9.0	0.784	9.42	10.8
	2	437.3	8.7	0.764	9.56	10.1
	3	458.5	9.6	0.864		10.35

Abachi	1	383.7	7.4	0.88	9.72	8.15
	2	409	8.4	0.851	9.72	8.5
Meranti RL	1	432.1	12.7	0.677	10.6	8.55
	2	438.5	12.6	0.692	10.6	8.6
Oak	1	625.6	11.3	0.648	11.2	10.95
	2	617.1	11.2	0.644	11.72	12.45
	3	678.3	13.9	0.633		10.85
Spruce	1	421.3	11.3	0.709	10.37	9.25
	2	405.8	10.9	0.727	10.45	10.1
	3	408.2	9.8	0.729		8.4
Maple	1	624.8	9.5	0.748	9.81	7.35
	2	585	9.2	0.82	9.82	6.6
	3	538.9	9.5	0.81		7.25

Figure 3 shows the charring rates of all wood samples versus the deflection values. The deflection was determined by averaging the measured values at the measuring planes shown in Figure 1. As deflections are primarily induced by loss of moisture, the shrinkage causes deflection of the specimens concavely off the fire. Correspondingly, the centre displacement transducer (measuring plane 2) showed the maximum deflection.

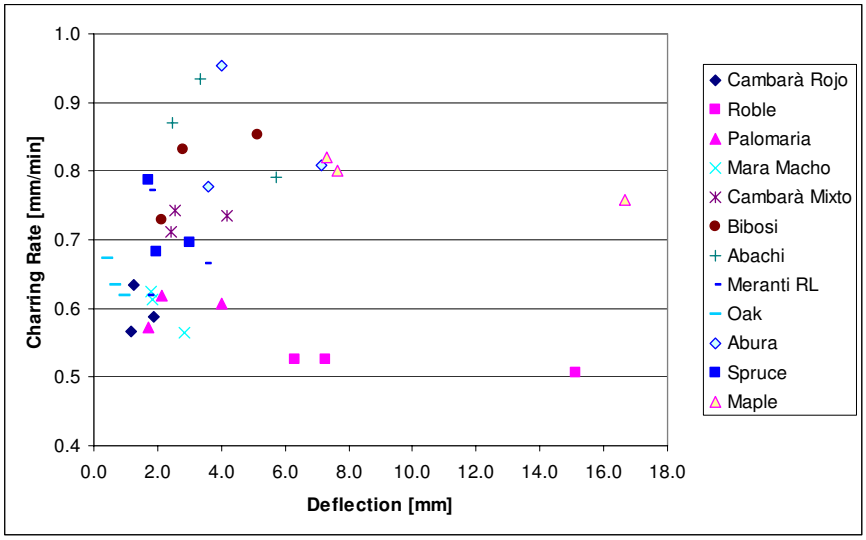

Fig. 3 - Charring rate versus deflection.

The measured charring rates, β, of all wood samples versus the OPI values are shown in Figure 4, with every point showing the average value for each wood species. The resulting relation between β and OPI can be represented using a linear correlation. The parameters of the correlation are given in the figure.

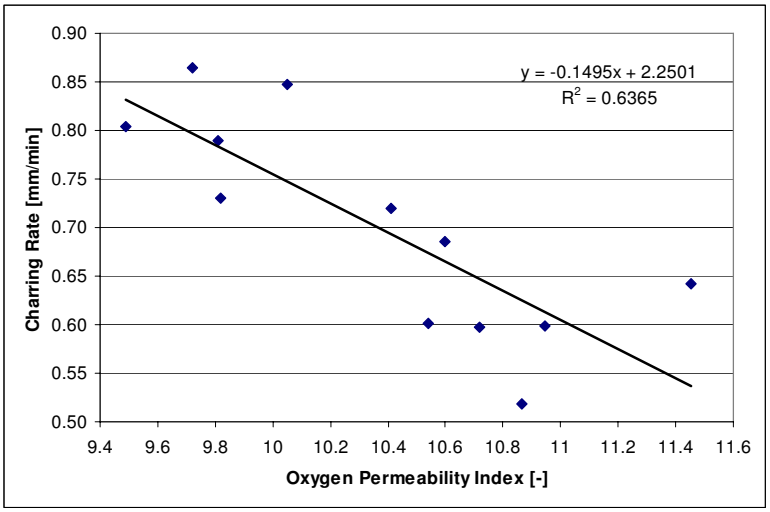

Fig. 4 - Charring rate versus OPI.

3.2 Results of Investigation with Fire Doors

As one can see in Figure 3, in small scale experiments with the wooden beams the oak displayed the lowest deflection of all tested wood species. In contrast, the Roble beams had the highest deflections, despite the fact that the charring rate of Roble was the lowest (see Table 2). The choice of Roble should demonstrate this impact in fire doors on fire resistance time: Higher deflections should effect a reduction of fire resistance time and a lower charring rate should offset this reduction. The choice of Palomaria was based on the same idea. Abachi had moderate deflections on small scale but the highest charring rate of all tested wood species. Spruce and Maple have been chosen for the purpose of comparison.

Overall, seven fire experiments with doors were carried out. The oak was chosen as a reference wood species and, therefore, tested twice. Figure 5 shows the results of the fire resistance experiments: the maximum measured deflection of the door leafs as a function of time. All experiments were stopped when integrity was not fulfilled anymore.

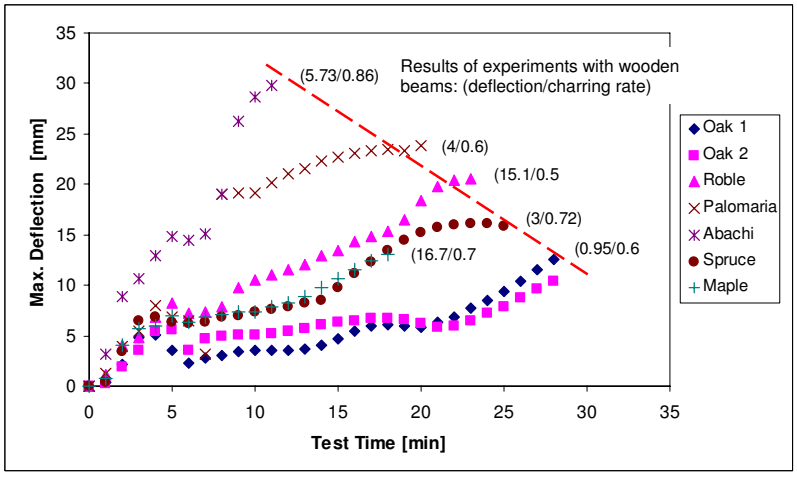

Fig. 5 - Max. deflection of door leaf as a function of testing time

3.3 Results of Finite Element Modelling

Bending of wooden beams in fire was modelled using an assumption of perfect elastic properties of the material. One of the consequences of representing the wood as an elastic material is that the values of deflections caused by shrinkage do not depend on the Young's modulus. Clearly, neglecting the non-linear phenomena such as cracking and mechano-sorptive effect results in overestimation of the predicted stresses and strains. However, this assumption should allow one to get easily a quick estimate of the upper limit on the deflections which can be useful information in the context of scaling-up filigree separating elements beyond the tested size.

To further simplify the model, the heat and mass transfer processes in the wood are not modelled. The wood is assumed to bend solely due to shrinkage caused by the moisture loss in front of the pyrolysis zone[13], whereas the moisture gradients in this region were measured experimentally for each sort of wood employed in the present study. The char region is assumed to have no influence on deflection of the beam. Consequently, the thickness of the beam in simulations is set to $(d_{\text{init}} - \beta t)$,where d_{init} is the initial thickness of the beam. The strain due to loss of moisture, ε_M , is modelled as $\varepsilon_M = \alpha \Delta C$, where α is the shrinkage coefficient, and C is the moisture concentration. It is important to note that the moisture measurements were carried out not *in situ*, but after the combustion tests, so that the characteristic local increase in the moisture content in front of the pyrolysis zone was not observed[7]. The obtained moisture profiles are shown in Figure 6. Thus, the numerical model employed here is phenomenological, as it is based on the experimental observations.

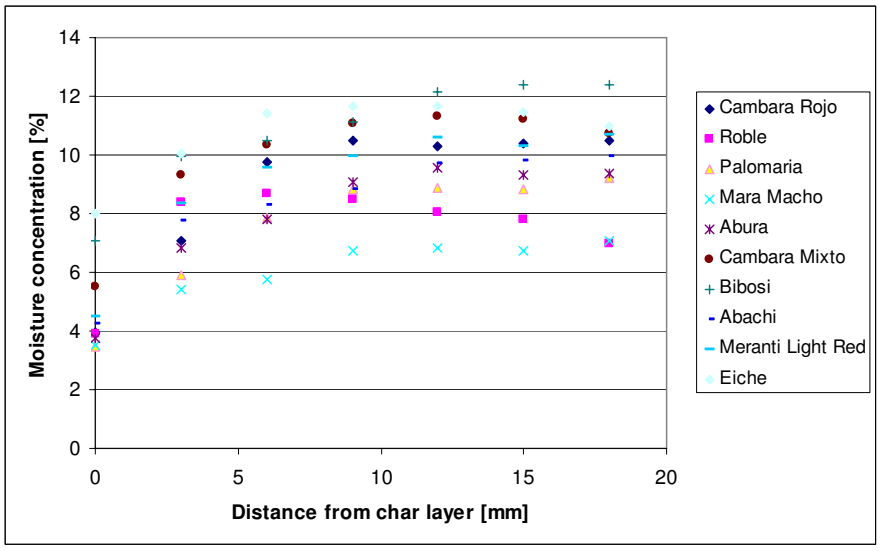

Fig. 6 - Moisture profiles in front of the pyrolysis zone.

The shrinkage coefficients, α , are taken from the open literature[14]. It should be noted that the shrinkage coefficient of wood is not an isotropic quantity: wood shrinks the most in the tangential direction, somewhat less in the radial direction, and the least in the longitudinal direction. The rule-of-thumb states that the shrinkage factors in the longitudinal direction are normally an order of magnitude less than those in the tangential and radial directions. Unfortunately, in timber produced commercially the edges are normally not aligned with directions of year rings, and besides the wood shows large variability of its properties (up to

15%)[14]. These aspects bring considerable uncertainty in evaluation of shrinkage deformation using the shrinkage coefficients reported in the literature, and this needs to be taken into account when analyzing the results of simulations.

The beam is modelled using the plane stress model (i.e. see Timoshenko and Goodier[15]). The equations of equilibrium are solved using the finite element commercial code Comsol[16]. The results are given in Table 3.

Table 3: Deflection in the middle of the wooden beams (the experimental values are the average of the data obtained).

Deflection (mm)	Cambara Rojo	Roble	Palomaria	Mara Macho	Abura	Cambara Mixto	Bibosi	Abachi	Meranti	Oak
Experiment	1.9	15.1	4.0	2.8	7.1	4.2	5.2	5.7	3.5	1.0
Model	1.3	0.50	1.3	1.4	2.2	1.6	3.3	2.5	2.0	1.4

4. DISCUSSION

The fire resistance of door frames and door leaves is characterized normally using two parameters: (1) the charring rate of the material and (2) the maximum deflections of the structure. As the oxygen permeability index (OPI) is an important characteristic of wood structure, one of the purposes of the present study was to find the relation between the OPI value and fire resistance of the material. Experimentally, using nine sorts of tropical wood we found an explicit correlation between the charring rates and the OPI values. However, in a series of combustion tests using wooden beams and a furnace of small scale (the beams were exposed to fire from one side) we failed to find any correlation between the observed deflections of the beams and their charring rates. This implies that the deflections of wooden structures in fire cannot be predicted based only on the knowledge of the charring rate of the material, or equivalently the OPI value. Besides, we found no explicit correlation of the deflections of the beams with either the density of the wood or the Young's modulus. Thus, the fire resistance of the door and door frames cannot be described satisfactorily using any single parameter studied in this work, in particular the OPI value, charring rate, density and Young's modulus.

As one can see from Figure 5, which shows the maximum deflections of the door leaf under fire attack as a function of time, the main failure mode of doors to fire is the deflection of the door leaf out of plane. Unfortunately, there is no correlation between the results of the large scale tests using the door leafs and the small scale tests using the small wooden beams. Apparently, the performance of doors in fire is influenced strongly by their constructive design. However, it is clear that the fire resistance time of the fire door depends on the combination of both deflections and charring rate of the door leaf and the door frame. It remains unanswered though to which extent a lower charring rate compensates an increased deflection and vise versa.

As far as the numerical modelling is concerned, nine of the ten values of deflections of wooden beams predicted numerically are lower than those observed experimentally (Table 3). The worst agreement was obtained for Roble. We assume that one of the most important factors that resulted in the disagreement between the numerical and experimental data is the inaccuracy of the shrinkage coefficients employed in the model. Indeed, the simulations were carried out using the values of the shrinkage coefficients reported in the open literature, which can be significantly lower that the shrinkage coefficients of the commercially produced timber. For instance, Roble beams used in the combustion tests had a clearly twisted internal structure, which obviously caused shrinkage higher than the expected. The other factor that could strongly underestimate the deflections predicted numerically is the data for the moisture

gradients in the pyrolysis zone. We measured the moisture gradients in the wood after the experiments, not *in situ*, that could have resulted in their underestimation.

To sum up, the results obtained in the present study stress the importance of large scale fire resistance tests, which apparently cannot be replaced solely by investigating specimens of simpler shape on a small scale level. However, development of modelling tools and acquisition of data in small scale tests still appears to be a promising way to reduce the costs involved in repetitive large scale testing. This requires further investigation.

ACKNOWLEDGEMNTS

The authors are grateful for the financial support from the Swiss Foundation for Development and International Cooperation (IC) and the Swiss Association of Door Manufacturers (VST).

REFERENCES

[1] Buchanan AH, "Structural design for fire safety", John Wiley & Sons, LTD (2001): 273.
[2] European standard EN 1363-1: 1999, "Fire resistance tests - Part 1: General requirements", CEN Central secretariat, Brussels.
[3] European standard EN 1634-1: 2000, "Fire resistance tests for doors and shutter assemblies - Part 1: Fire doors and shutters", CEN Central secretariat, Brussels.
[4] Babrauskas V, "Charring rate of wood as a tool for fire investigations", Fire safety journal 40 (2005): 528-554.
[5] Lingens A, Windeisen E, Wegener G, "Investigating the combustion behaviour of various wood species via their fire gases", Wood science technology (2005) 39: 49-61.
[6] Resch H, Ecklund BA, "Permeability of wood", Forest products journals (1964) May: 199-206.
[7] White RH, Schaffer EL, "Transient moisture gradient in fire-exposed wood slab", Wood and Fiber 13(1) (1981): 17-38.
[8] Beushausen HD, Alexander MG, Mackechnie J, "Concrete durability specifications in an international context", BFT Concrete Plant + Precast Technology 7 (2003): 22-32.
[9] Hugi E, Wuersch M, et al, "Correlation between charring rate and oxygen permeability for 12 different wood species"; Journal of Wood Sciences (2007) 53: 71-75.
[10] European standard EN 408: 2003, „Holzbauwerke - Bauholz für tragende Zwecke und Brettschichtholz - Bestimmung einiger physikalischer und mechanischer Eigenschaften", CEN Central secretariat, Brussels.
[11] Wagenführ R, "Holzatlas", Fachbuchverlag Leipzig im Carl Hanser Verlag (2007): 816.
[12] International standard ISO 834-1: 1999, "Fire-resistance tests - Elements of building construction - Part 1: General requirements", International Organization for Standardization, Geneva.
[13] Drysdale D. "An introduction to fire dynamics", John Wiley & Sons, LTD (2003): 186.
[14] Rijsdijk JF, Laming PB, "Physical and related properties of 145 timbers", Kluwer Academic Publishers, (1994).
[15] Timoshenko SP, Goodier JN, "Theory of elasticity", McGraw-Hill Book CO, (1988): 15
[16] Comsol Multiphysics 3.2, Comsol AB, (2005).

ASSESSMENT OF EUROCODE 5 CHARRING RATE CALCULATION METHODS

PAULO B. CACHIM[1] and JEAN-MARC FRANSSEN[2]

ABSTRACT

The basic hypothesis for the assessment of fire resistance of wood structures is that for temperatures above 300 ºC, wood is no longer able to sustain any load. Consequently, the determination of the location of the 300 ºC isotherm, the charring depth, is decisive for the result of fire resistance calculation methods. Charring rate of wood is dependent of numerous factors, such as wood species (density, permeability or composition), moisture or direction of burning (along or across the grain).

Eurocode 5, Part 1-2, presents several methods for the calculation of fire resistance of timber structures that are divided into simplified and advanced. In this paper simplified and advanced methods are compared regarding the calculation of the charring depth. Finite element simulations have been performed, using the proposed wood properties of Eurocode 5 using finite element code SAFIR. The influence of parameters such as wood density, moisture or anisotropy has been investigated. The results obtained with finite element calculations were then compared with Eurocode 5 simplified models. Some inconsistencies between methods have been observed. This paper presents proposals to overcome some of the inconsistencies as well as to extend the applicability of the models.

1. INTRODUTION

Fire resistance of wooden members or structures is strongly dependent of the rate at which wood burns. Therefore, codes of practice such as Eurocode 5 Part 1-2 [1], named in this paper as EC5, specify models for the calculation of the amount of charred wood after a certain period of time.

[1] Professor, University of Aveiro, Department of Civil Engineering, Aveiro, Portugal, email: pcachim@ua.pt.
[2] Professor, University of Liege, Department of Structural Engineering, Liege, Belgium, email: JM.Franssen@ulg.ac.be.

Charred wood is bounded by the transition between the pyrolysis layer, the zone where thermal degradation of wood and char formation are actually occurring and the char layer, a zone of cracked charcoal that has no relevant strength or stiffness properties. This transition is usually considered to be located at the 300 ºC isotherm, named the char-line. Charring depth is the distance between the outer surface of the original member and the position of the char-line. The speed at which charring depth advances in the material is called the charring rate and is an essential parameter for fire resistance of wooden structures because it allows the determination of the size of the residual section of wood. Charring rate of wood is dependent of numerous factors, such as wood species, density, moisture, permeability, composition, or direction of burning (along or across the grain). However, only some of these factors can be actually considered in practical applications.

EC5 allows the use of simplified and advanced methods for the calculation of the amount of charred wood. Simplified methods use the charring rate model that is based in the fact that, even if the evolution of charring depth with time is non-linear, in practice, due to its limited non-linearity, it can be considered as linear. This means that the charring rate can be considered independent of time. Advanced methods, use more sophisticated analysis and design procedures that supposedly lead to more accurate predictions of the fire behaviour of structures. The method proposed in EC5 is a conductive model based on thermal properties of wood that uses heat transfer equations for the determination of distribution of temperature within structural sections; this thermal calculation is then normally followed by a structural calculation taking into account the progressive degradation of mechanical properties for the evaluation of the behaviour of the structure.

The aim of the present work is to assess the results obtained by the charring rate and the conductive models of EC5. The study was carried out based on numerical finite element simulations using the finite element code SAFIR [2], which is a special purpose finite element code, developed at University of Liege for studying structures subjected to fire. Influence of moisture and density was investigated. Some proposals for improvement the consistency between the different models of EC5 are also presented.

2. EUROCODE 5 MODELS FOR CHARRING RATE AND THERMAL ANALYSIS

EC5 allows the use of a conductive model based on the resolution, transient, heat transfer differential equation, incorporating thermal properties that vary with temperature for the calculation of thermal fields within structural elements. However, effects such as mass transfer within the elements or structure, reaction energy released inside the wood due to pyrolysis or degradation of material, cracking of charcoal, which increases the heat transfer in the char layer, are not accounted for. EC5 presents conductivity values for the char layer that are apparent in order to take into account increased heat transfer due to shrinkage cracks above about 500 °C that increase heat transfer due to convection and radiation. In addition, specific heat capacity values include the energy necessary to evaporate the water, which explains the presence of the peak between 99 and 120 °C.

Charring rate models use the charring rate concept to calculate the residual section of a wooden cross-section after a certain exposure to fire. EC5 allows the use of two different charring rates: the one-dimensional design charring rate under standard fire exposure, β_0, and the notional charring rate, β_n. When using the one-dimensional charring rate, calculation of cross-sectional properties should be based on the actual charring depth including corner roundings. The use of the notional charring rate allows considering rectangular residual cross sections. In the current work the one-dimensional charring, β_0, rate will be considered and

compared with the conductive model because this eliminates unnecessary complications linked to geometrical considerations and allows concentrating purely on the thermal models.

The charring rate values given in EC5 for softwoods and hardwoods are presented in Table 1. Charring rate values presented in EC5 are independent of density for softwoods with densities above 290 kg/m^3 and for hardwoods with densities above 450 kg/m^3. For hardwoods the charring rate varies linearly for densities between 290 and 450 kg/m^3.

Table 1. Charring rate of wood for simple models of EC5.

Wood type		β_0
Softwood and beech	Glued laminated timber with a characteristic density of ≥ 290 kg/m^3	0.65
	Solid timber with a characteristic density of ≥ 290 kg/m^3	0.65
Hardwood	Solid or glued laminated hardwood with a characteristic density of 290 kg/m^3	0.65
	Solid or glued laminated hardwood with a characteristic density ≥ 450 kg/m^3	0.50

3. INFLUENCE OF DENSITY

The fact that the charring rate changes with wood density has been demonstrated by several authors from several countries [3-6]. However, this dependency is only marginally considered in the charring rate models of EC5 as shown in Table 1. Australian Standard AS 1720.4 [7] explicitly considers the effect of density on the charring rate and is consequently used here for comparison purposes. The dependence of charring rate with density is given in the Australian Standard by:

$$\beta = 0.4 + \left(\frac{280}{\rho_{12}} \right)^2 \tag{1}$$

For calculations of charring depth using the conductive model, the coefficient of heat transfer by convection was considered as 9 W/m^{2}K on unexposed surfaces and 25 W/m^{2}K on surfaces heated with the standard time-temperature curve, according to Eurocode 1, Part 1-2 [8]. The surface emissivity of wood was taken as 0.8. Thermal conductivity, specific heat capacity and density ratio were used with values defined in EC5. Moisture content of wood, w, was considered equal to 0.12. Densities of 200, 290, 450, 600, 800 and 1000 kg/m^3 were investigated. The evolution of charring depth with time for the different densities is shown in Fig. 1, where it is apparent that significant differences exist for different densities.

The curves showing the evolution of the charring depth with time present a slight convexity. The charring rate is the first derivative of the curves. Because of the nearly linear character of the curves average charring rates were calculated for 30 and 60 minutes (taken as the secant value from the origin). From here, the secant charring rate used for comparison purposes is the secant charring rate at 60 minutes.

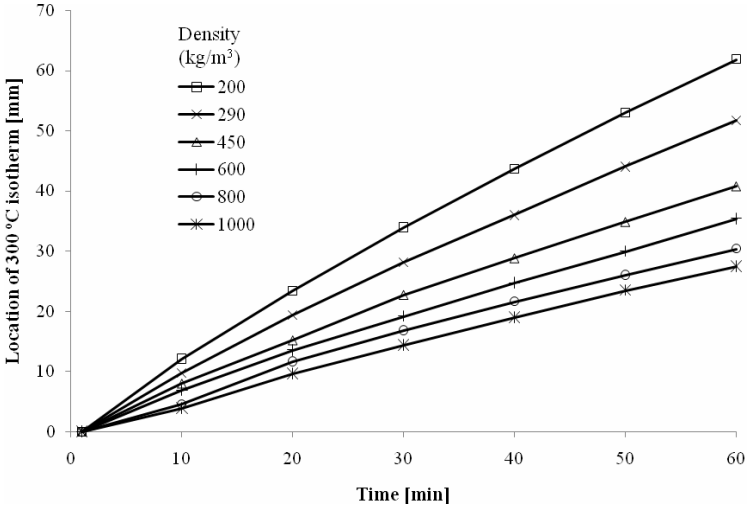

Fig. 1 – Evolution of charring depth with time for several densities.

Charring rate values calculated from Fig. 1 (see Table 2) are compared with the EC5 charring rate model for softwoods (EC5-SW) and hardwoods (EC5-HW), as well as with the Australian Standard, AS. Comparisons of the models show that for densities above 700 kg/m^3, typical of hardwoods, the Australian Standard, EC5-HW and conductive models give relative similar results. Below 600 kg/m^3, the models show significant differences, with the AS model being the one with highest charring rates. EC5-SW and conductive models show good agreement for 450 kg/m^3.

Table 2. Charring rates calculated with the EC5 conductive model (mm/min).

	Density [kg/m^3]					
	200	290	450	600	800	1000
Charring rates at 60 min	1.032	0.876	0.682	0.600	0.512	0.461

The potential regression curve that fits to the results of the conductive model reads:

$$\beta_\rho = 14.28\rho_{12}^{-0.49} \tag{2}$$

with a coefficient $r^2 = 0.998$. Numerical calculations are in agreement with the theory of heat transfer in materials with constant thermal properties that tells that the thermal propagation speed is proportional to the square root of thermal diffusivity:

$$\beta \propto \sqrt{\frac{\lambda}{c\rho}} \tag{3}$$

The results obtained numerically were further compared with experimental measurements performed previously at the University of Liege for tropical hardwoods [9]. Comparison of the conductive model with experimental data is presented in Fig. 2. EC5 charring rate value for hardwoods is also plotted. It can be observed that numerical results form an upper envelope of the experimental values.

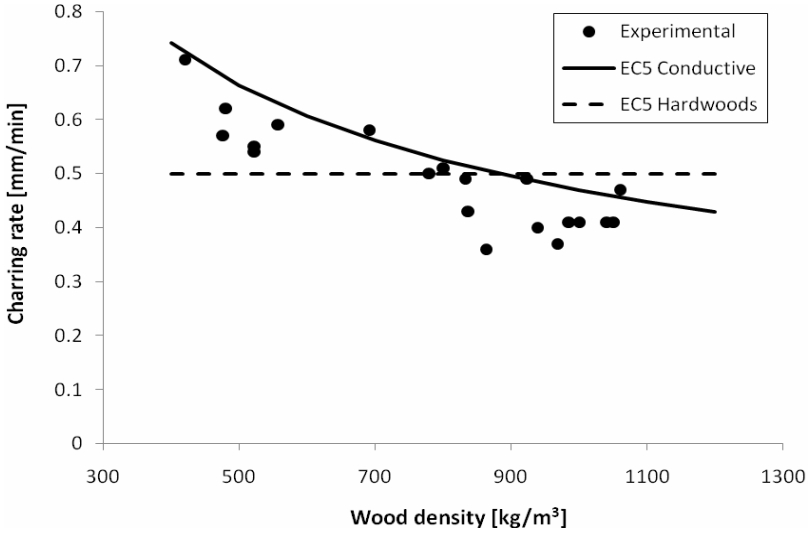

Fig. 2 – Relation between charring rate and water content.

4. INFLUENCE OF MOISTURE

The moisture content of wood has an influence on the thermal behaviour of timber. Heat conductivity of solid wood depends on moisture content as reported by several authors [10-13]. The effects of changes in conductivity of wood below 300 ºC on the charring rate are not significant, but the evaporation of water consumes energy, changing the apparent specific heat curve of the composite wood-water material. Temperature in wood will remain approximately constant at about 100 ºC until all the water has been evaporated. Also density of wood is affected by the moisture content.

The charring rate of wood is proven to be dependent on moisture content as was demonstrated, for example by [3-4, 14-15].

Table 3. Density, moisture content and charring rate in numerical tests with modified conductive model.

Case	Dry density, ρ_0	Water content	Density, ρ_w	Charring rate
	[kg/m^3]	-	[kg/m^3]	[mm/min]
260-0	260	0.00	260	0.881
290-12	260	0.12	290	0.876
320-24	260	0.24	320	0.841
400-0	400	0.00	400	0.702
450-12	400	0.12	450	0.682
500-24	400	0.24	500	0.671
535-0	535	0.00	535	0.609
600-12	535	0.12	600	0.600
665-24	535	0.24	665	0.590
450-0	450	0.00	450	0.662

EC5 specific heat and density ratio curves were defined for service class 1, which means water content around 0.12. However, density ratio is defined in EC5 as a function of the water content indicating that this curve could be used also for water contents different from 0.12. Using this last assumption, calculation of the charring rate was performed for wood with different moisture contents. The base densities considered were 290, 450 and 600 kg/m^3 with 12 % moisture. Thus, dry density of wood is 260, 400 and 535 kg/m^3, respectively. Water contents are equal to 0.0, 0.12 and 0.24 (see Table 3). In addition, in order to compare two situations with the same overall density but with two different moisture contents, wood with dry density of 450 kg/m^3 was also considered (see Table 3). The calculated average charring rates after 60 minutes are presented in Table 3. There is no significant difference between the results (differences in charring rate are less than 3 %) indicating that the conductive model proposed in EC5 is not really able to model the variations of the charring rate with moisture that have been reported in the literature.

5. INFLUENCE OF ORTHOTROPY

Wood is an anisotropic material with most of its properties substantially different when considered along the grain or across the grain. However, since the majority of the thermal calculations performed to evaluate the fire resistance of linear members are related to the transversal directions, little information regarding the longitudinal thermal properties of wood is available. However, there are situations, such as when 3D modelling of connections are performed, where along the grain thermal behaviour of wood is required.

Conductivity of wood along the grain has been reported to be in the range 1.5 to 2.8 times the conductivity across the grain, with the average value being around 2 [15, 16].

Charring rate of wood along the grain is higher than across the grain [15, 17] with ratio between them ranging from 1.3 [17] to 2.0 [15].

Using the above considerations, modified conductive laws for wood have been tested. It must be reminded that the properties of the char layer are those that mainly control the evolution of the charring rate (more than the properties of intact wood located ahead of the charring front). Two different approaches have been tried: (i) multiplication of the conductivity of the char layer above 500 ºC, by a constant factor k_1; and (ii) multiplication of the whole conductivity curve by a constant factor k_2, thus affecting the conductivity of wood and of the char layer. When referring to both parameters, the term *k* parameter is used. Using the k parameter allows consideration of the conductivity across the grain proposed by EC5 to be modified to obtain a specific charring rate along the grain.

Table 4. Charring rate and conductivity normalised charring rate.

		Multiplied values, k_1 or k_2					
		0.5	1.0	2.0	3.0	4.0	5.0
Charring rate [mm/min]	k_1	0.502	0.682	0.981	1.182	1.351	1.512
	k_2	0.551	0.682	0.909	1.071	1.191	1.313
Conductivity normalised charring rate	k_1	0.797	1.000	1.319	1.551	1.725	1.899
	k_2	0.725	1.000	1.420	1.710	1.957	2.188

Wood with density of 450 kg/m^3 and 0.12 moisture was considered in the simulations. Values of the average charring rate at 60 minutes are shown for several values of the k parameter in Table 4.

Conductivity normalised charring rate, $\beta_{z,\lambda}$, was defined in this study as the ratio between the charring rate at a specific k, and the charring rate obtained with EC5 conductivity (k = 1). The conductivity normalised charring rate is the ratio between along and across the grain charring rate. The conductivity normalised charring rate values are shown in Table 4. The results are relatively close, which shows that, as expected, conductivity of wood (below 300 ºC) has little influence for the determination of the charring rate.

An exponential curve was fitted to the results, and the relation between $\beta_{z\lambda}$ and k_1 can be expressed by the regression equation:

$$\beta_{z,\lambda} = k_1^{0.4} \tag{4}$$

while the relation between k_2 and calculated $\beta_{z,\lambda}$, is given by the regression equation:

$$\beta_{z,\lambda} = k_2^{0.47} \tag{5}$$

There is no information in EC5 related to the charring rate or conductivity along the grain. Because the conductivity of wood at room temperature is also dependent on grain direction it seems logical to multiply the whole conductivity curve of wood defined in EC5. Modelling orthotropic behaviour of wood at high temperatures can be carried out by multiplying the conductivity across the grain by a factor k_λ, defined by:

$$k_\lambda = \left(\beta_{//} / \beta_\perp\right)^2 \tag{6}$$

where $\beta_{//}$ is the along the grain required charring rate and $\beta_\perp$ is the usual across the grain charring rate.

6. POSSIBLE MODEL IMPROVEMENTS

6.1. Conductive model

The effect of moisture when using the conductive model can be taken into account using a modified heat capacity curve that depends of moisture. The modified conductive model changes the proposed values for specific heat capacity based on the assumption that the heat capacity of wood with a water content w, c_w, is given by equation (10) [16], in which the effect due to wood–water bond was neglected, and the liquid water specific heat capacity is 4190 J/kgK. It was further considered that specific heat values proposed by EC5 (see column 3 in Table 5) include 12 % water. Equation (10) was then used to calculate the heat capacity of dry wood, c_0 (see column 4 in Table 5).

$$c_w = \frac{c_0 + 4190w}{1+w} \text{ [J/kgK]} \tag{10}$$

The new expression for the moisture dependent specific heat (see column 5 in Table 5), was based on the following considerations: (i) from 20 to 99°C, equation (10) is used as such, with the appropriate value for the dry wood c_0; (ii) from 120°C and beyond, it is assumed that the heat capacity given by EC5 is of dry wood; and (iii) from 99 to 120°C, the term that multiplies w was adapted in order to make the contribution linked to evaporation proportional to the water content. The factor that multiplies the water content in column 5 of Table 5, for temperatures between 99 and 120°C, can be approximately obtained by summing, on one hand, the specific heat capacity of liquid water with, on the other hand, the energy consumed in water evaporation (2250 kJ/kg) divided by the temperature interval (21 °C). The modified specific heat curve multiplied by the density ratio for 0, 12 and 24 % moisture can be observed in Fig. 3.

Table 5. Modified thermal parameters to account for the effect of water content

Temperature	Density ratio, G	Specific heat capacity of wood (EC5)	Specific heat capacity of dry wood, c_0	Specific heat capacity of wood with water, c_w
ºC	-	[J/kgK]	[J/kgK]	[J/kgK]
(1)	(2)	(3)	(4)	(5)
20	1+w	1530	1210	$(1210+4190w)/G$
99	1+w	1770	1480	$(1480+4190w)/G$
99	1+w	13600	1480	$(1480+114600w)/G$
120	1.00	13580	2120	$(2120+95500w)/G$
120	1.00	2120	2120	$2120/G$
200	1.00	2000	2000	$2000/G$

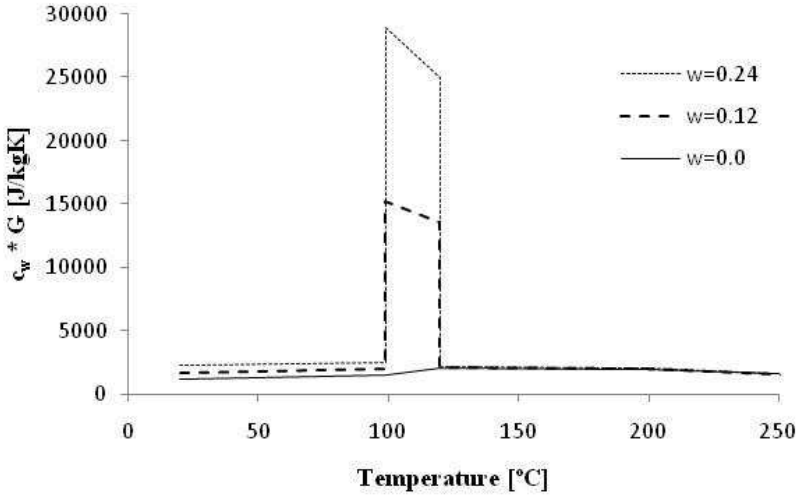

Fig. 3 – Modified specific heat capacity multiplied by G for different water contents.

The influence of the water content on the charring rate of wood was recalculated for the same densities and moisture as previously analysed using the conductive model with the modified properties. The relation between charring rate and moisture for all cases is shown in Fig. 4.

The differences between the different charring rates are now much bigger: 11 to 14 % reduction of the charring rate is observed when the moisture changes from 12 to 24 %, and 22 to 26 % increase if the moisture changes from 12 to 0 %. It can also be observed that the change of the water content (from case 400-0 to 450-12) produces a bigger variation of the charring rate than the corresponding change in density (from case 400-0 to 450-0).

A moisture normalised charring rate, $\beta_{z,w}$, is defined here as the ratio between the charring rate at a specific water content and the charring rate at w=0.12, for the same dry wood density. The relation between the moisture normalised charring rate and the water content was obtained by regression analysis as being

$$\beta_{z,w} = \left(\frac{1.12}{1+w}\right)^{1.5} \tag{11}$$

With the moisture normalised charring rate it is possible to obtain the charring rate at any water content, in the range 0 to 0.24, from the charring rate of wood with w=0.12, independently of wood density.

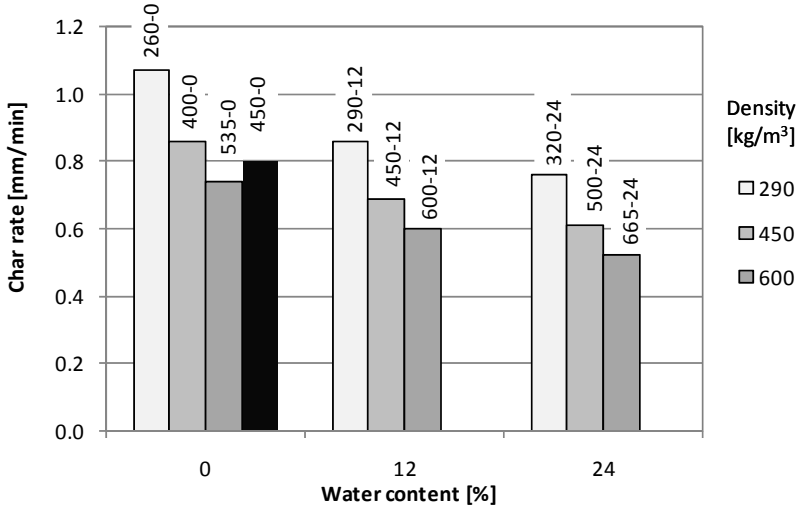

Fig. 4 – Relation between charring rate and water content.

6.2. Charring rate model

The charring rate values proposed by EC5 are independent of density for softwoods and show only a small dependence of density for hardwoods with low densities. Additionally, the charring rate values don't show any dependence of moisture. Therefore, there is some inconsistency between the results of the charring rate model and that of the conductive model. To reduce the differences between the charring rate and the conductive models of EC5 a modified charring rate model is proposed. The proposal consists in modify the basic charring rate calculated for wood with 0.12 moisture and density of 450 kg/m^3, $\beta_{450,12}$, by multiplying it by two factors: one that depends of wood density and other that depends of moisture.

The density term is derived from the results obtained from the numerical analysis. In fact, this correction term already exists in EC5 for panels and a similar expression also existed pre-standard version of EC5 for softwood densities below 290 kg/m^3.

For moisture, results of the modified conductive model, see Equation (11), were used to calculate the modification factor.

The charring rate, $\beta_{\rho,w}$, for wood with moisture content, w, and density at 12% moisture, ρ_{12}, can thus be obtained from $\beta_{450,12}$ as:

$$\beta_{\rho,w} = k_\rho k_w \beta_{450,12} \tag{7}$$

$$k_\rho = \sqrt{\frac{450}{\rho_{12}}} \tag{8}$$

$$k_w = \left(\frac{1.12}{1+w}\right)^{1.5} \tag{9}$$

6.3. Comparison of conductive and charring rate models

The results obtained with the possible improvement of both models are presented in Fig. 5. The evolution of the charring rate with wood density is plotted for water contents of 0, 12 and 24 %, for both the charring rate (CR) and conductive (CO) models. With suggested improvements more coherent charring rate values are obtained together with increased consistency between conductive and charring rate models.

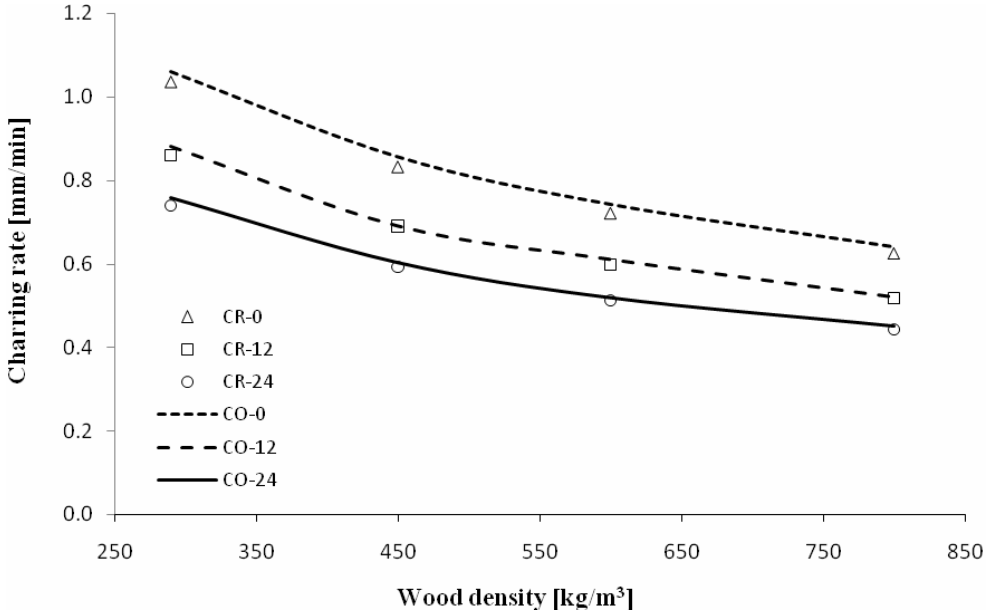

Fig. 5 – Comparison of proposed modified models.

7. CONCLUSIONS

A charring rate and a conductive model are presented in EC5 to calculate fire resistance of structures. Both models have some limitations, but most important, they have some inconsistencies. This paper presents proposals to overcome some of the inconsistencies as well as to extend the applicability of the models.

Material thermal properties presented in EC5 are extended to model orthotropic behaviour with a specified longitudinal charring rate by changing the wood conductivity. In addition, different moisture contents can also be considered by using a modified specific heat capacity curve.

An expression to calculate the charring rate as a function of density and moisture content has been proposed for the charring rate model that is compatible with the conductive model.

8. REFERENCES

[1] EN 1995-1-2:2004. Eurocode 5: Design of timber structures - Part 1-2: General - Structural fire design. CEN, 2004.

[2] Franssen J-M. SAFIR. A Thermal/Structural Program Modelling Structures under Fire, Engineering Journal, A.I.S.C., 2005: 42 (3), pp. 143-158.
[3] White RH, Erik V, Nordheim EV. Charring rate of wood for ASTM E 119 fire exposure. Fire Technology. 1992: 28 (1), pp. 5-30.
[4] White RH, Tran HC. Charring Rate of Wood Exposed to a Constant Heat Flux. Slovak Republic, s.n. Wood & Fire Safety - 3rd Int.l Scientific Conference, 1996, pp. 175-183.
[5] Njankouo JM, Dotreppe J-C, Franssen J-M. Experimental study of the charring rate of tropical hardwoods. Fire and Materials, 2004: 28, pp. 15-24, DOI: 10.1002/fam.831.
[6] König J, Walleij L. One-dimensional charring of timber exposed to standard and parametric fires in initially unprotected and postprotection situations. Swed Inst Wood Technol Res. 1999. Rapport I 9908029.
[7] Australia, Standards. AS 1720.4. Timber structures Part 4: fire resistance of structural timber members. North Sydney, Australia : Standards Australia, 1990.
[8] EN 1991-1-2:2002. Eurocode 1: Actions on structures - Part 1-2: General actions - Actions on structures exposed to fire. CEN, 2002.
[9] Njankouo JM, Dotreppe J-C, Franssen, J-M. Fire resistance of timbers from tropical countries and comparison of experimental charring rates with various models. Construction and Building Materials. 2005: 19 (5), pp. 376-386.
[10] Gu H, Hunt JF. Two-dimensional finite element heat transfer model of softwood. Part III. Effect of misture content on thermal conductivity. [ed.] Society of Wood Science and Technology. Wood and Fiber Science. 2007: 39, pp. 159-166.
[11] FPL. Thermal conductive properties of wood, green or dry, from -40° TO +100° C: A literature review. Madison, Wyscosin, USA : Forest Products Lab., 1977. Report FPL-9.
[12] Parker WJ. Development of a model for the heat release rate of wood - a status report. U.S. Dep. Commerce. 1985. Report NBSIR 85-3163.
[13] Ragland KW, Aerts DJ. Properties of Wood for Combustion Analysis. Bioresource Technology. 1991: 37, pp. 161-168.
[14] Schaffer EL. Charring rate of selected woods transverse to grain. Forest Products Laboratory. Madison, wiscosin, USA : s.n., 1967. Research paper FPL 69.
[15] Hietaniemi J. A Probabilistic Approach to Wood Charring Rate. VTT Building and Transport. Finland : VTT Information Service, 2005. VTT Working Papers 31.
[16] FPL. Wood handbook. Wood as an engineered material. Madison, Wisconsin, USA : Forest Products Laboratory, 1999.
[17] Spearpoint MJ, Quintiere JG. Predicting the piloted ignition of wood in the cone calorimeter using an integral model - effect of species, grain orientation and heat flux. Fire Safety Journal. 2001: 36, pp. 391-415.
[18] Maciulaitis R, Lipinskas D, Lukosius K. Singularity and importance of determination of wood charring rate in fire investigation. Materials Science (MEDŽIAGOTYRA). 2006: 12, pp. 42-47.

FURNACE TESTING OF FULL-SCALE GYPSUM STEEL STUD NON-LOAD BEARING WALL ASSEMBLIES: RESULTS OF MULTI-LABORATORY TESTING IN CANADA, JAPAN, AND USA

SAMUEL L. MANZELLO[*], WILLIAM L. GROSSHANDLER[#], TENSEI MIZUKAMI[°]

ABSTRACT

The present paper discusses the results of a multiple laboratory test program aimed at determining the consistency of large scale furnace testing. The North American Fire Testing Laboratories Consortium (NAFTL) organized a multiple laboratory test program for ASTM E119-00 using a common structural element: a 1-h rated gypsum/steel-stud non-load bearing wall assembly. Walls were tested by six different organizations employing ten different furnace facilities following the guidance provided in ASTM E119-00. In addition to NAFTL members conducting the tests, the program was expanded to include four testing laboratories in Japan; the Center for Better Living served as the organizer for the Japanese testing. Results obtained from these experiments are discussed.

1. INTRODUCTION

Traditional fire resistance testing in the United States has been based upon ASTM standard E119, "Standard Test Methods for Fire Tests of Building Construction and Materials"[1]. The similar international standard is ISO 834[2]. In these tests, building components are subjected to a constantly increasing furnace temperature intended to represent a standard fire. The components are then rated, with units of time, on their ability to withstand the exposure up to a criterion that is defined as a failure point. This criterion may be either based on the temperature rise of the unexposed face of the partition assembly or the efflux of hot gases or flames. It is expected that a 2-h rated wall would resist failure in a real fire for a longer period of time than a similarly functioning 1-h rated wall, and this is invariably the case. What can not be expected, however, is that a 2-h rated wall would

[*] PhD, Mechanical Engineer, Building and Fire Research Laboratory, National Institute of Standards and Technology, Gaithersburg, MD 20899 USA, email: samuelm@nist.gov
[#] PhD, Deputy Director, Building and Fire Research Laboratory, National Institute of Standards and Technology, Gaithersburg, MD 20899 USA, email: wgrosshandler@nist.gov
[°] MS, Engineer, The Center for Better Living, Tsukuba, Ibaraki, Japan, email: mizukami@tbtl.org

necessarily withstand an actual fire in a building for two hours, or that the wall would necessarily fail after two hours. The inability of the fire resistance rating to act as an absolute predictor of performance in an actual fire was recognized from the beginning when the forerunner of ASTM E119 was published in 1918. The reference to fire resistance ratings in common time units has become erroneously interpreted to relate closely (or at least conservatively) to the actual time that a wall would be expected to resist a fire.

Clearly, there are additional limitations to this approach in providing a known degree of fire safety. The test is concluded when the first failure criterion is met. For wall, floors, and ceiling assemblies, this is almost always an excessive temperature on the unexposed face. The more serious fire hazard is the passage of smoke and flames through the partition, and the time to this failure is rarely measured. In addition, there is no method available to relate the response of the partition under this standard exposure to its response in a different (more realistic) design fire. Most realistic fires do not heat a partition uniformly[3]. Real fires can recede, allowing the partition to cool while still in the presence of smoke and flames. In spite of severe shortcomings, these test methods continue to be used throughout the world because (i) a massive data base has been established and is in continual use, (ii) history suggests that the test methods are conservative, and (iii) alternative methods have not been developed yet that are acceptable to the major parties involved.

In any event, designing structures to withstand the hazard posed by an unconfined building fire requires that current (and future) standard fire resistance tests be reliable and consistent, independent of the laboratory performing the test. To this end, the North American Fire Testing Laboratories (NAFTL) consortium was formed in 2004 to provide a forum for the exchange of technical information, to conduct studies, and to develop industry consensus positions relating to the full range of fire tests. Current members include Southwest Research Institute (SwRI), Underwriters Laboratories (UL), FM Approvals, Intertek, NGC Testing, and Western Fire Center. The National Institute of Standards and Technology (NIST), the National Research Council of Canada (NRC-C), and the Fire Testing Laboratory of the Bureau of Alcohol, Tobacco, and Firearms (ATF) are non-voting associate members of NAFTL. The organization is open to any North American-based independent commercial laboratory engaged in fire testing or research.

As a means to overcome the shortcomings previously enumerated, NAFTL organized a multiple laboratory test program for ASTM E119-00[1] using a common structural element: a 1-h rated gypsum/steel-stud non-load bearing wall assembly. Walls were tested by six different organizations employing ten different furnace facilities following the guidance provided in ASTM E119-00[1]. In addition to NAFTL members conducting the tests, the program was expanded to include four testing laboratories in Japan; the Center for Better Living served as the organizer for the Japanese testing. The collaboration between NIST and the Center for Better Living is part of an international effort to assess the performance and failure mechanisms of gypsum wall assemblies under real fires/furnace conditions and to collect data that are necessary to validate models that could be used to predict their performance and ultimate failure under various design fires.

NIST was the qualified independent party responsible for analyzing and reporting the data for the NAFTL and Japanese Laboratory testing[4]. The present study expands on a recently released NIST internal report[4] to include further characterization of the gypsum board used in the tests, reporting the findings of the multiple laboratory testing program using the International System of units (SI), and comparing probes used to characterize furnace temperatures.

2. WALL ASSEMBLY CONSTRUCTED FOR TESTING

A non-load bearing wall consisting of gypsum panels attached to steel studs was constructed for fire testing. Figure 1 displays a detailed drawing of the assembly construction. Steel studs (width: 92 mm, thickness: 25 gauge) were spaced at 406 mm, and type X gypsum panels (USG[i]) with a thickness of 15.9 mm were attached vertically to the studs using type S drywall screws spaced at 305 mm. All of the gypsum board used in this study was provided by USG from a single production run to ensure uniformity. The seams were staggered on the exposed and unexposed face. The partitions were constructed under ASTM guidelines for non-load bearing wall assemblies[5-8]. Following ASTM-E119-00[1], temperatures of the unexposed face were measured using thermocouples placed under insulating pads. In addition to this, temperatures were measured inside the cavity of the constructed assemblies. The location of the temperature measurements are shown in Figure 1.

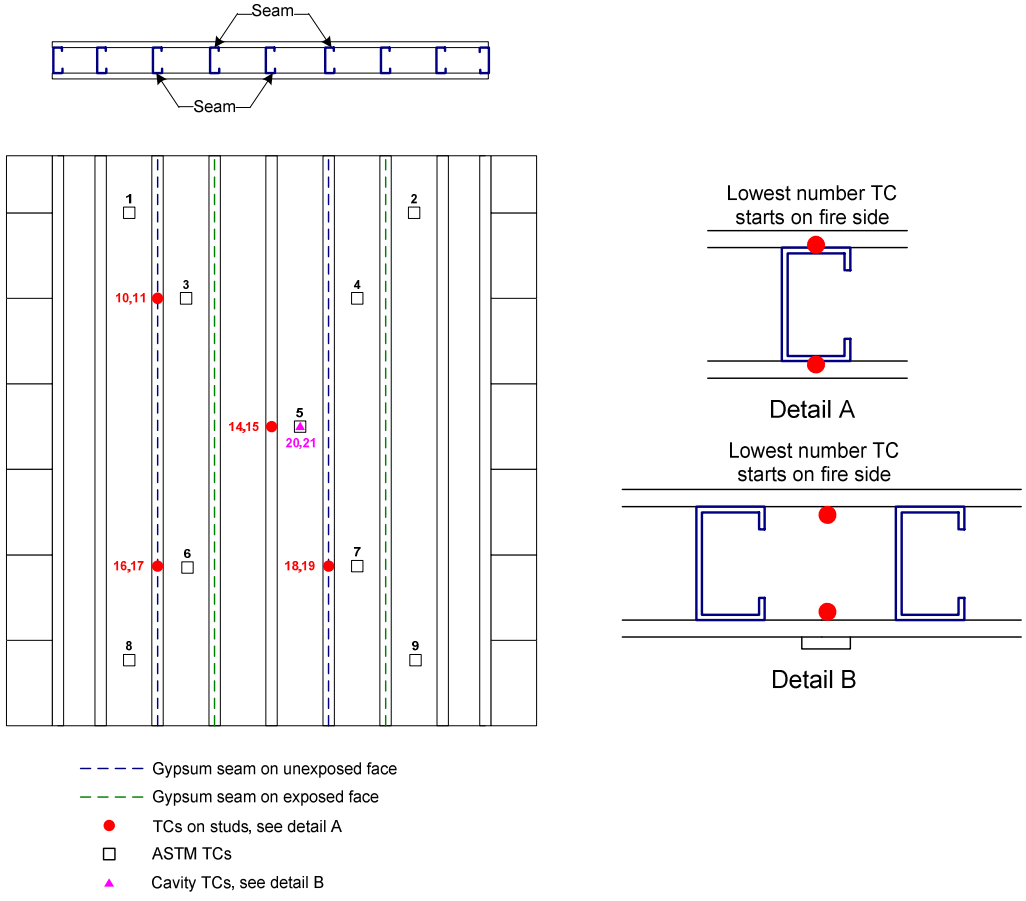

Fig. 1 Drawing of assembly used for testing by all laboratories

[i] Certain commercial products are identified to adequately describe the experimental procedure; this in no way implies endorsement from NIST.

3. GYSPUM BOARD THERMAL PROPERTY CHARACTERIZATION

The thermal properties of the gypsum board used for these experiments were characterized. Thermal properties are required to model the performance of gypsum assemblies used as part of this test series. In addition to this, it was desired to compare the properties of the gypsum board provided for this test series to those of off-the-shelf Type X gypsum board (15.9 mm). The thermal conductivity and specific heat were determined as a function of temperature for representative gypsum board samples. The thermal conductivity as a function of temperature was determined using the Slug Calorimeter[9]. The slug calorimeter is comprised of a square central stainless steel plate (152 mm by 152 mm by 12.7 mm). A set of 152 mm by 152 mm gypsum board samples (with paper carefully removed) was installed in a 'sandwich' configuration (i.e. steel slug in the center); this provided an adiabatic boundary condition at the central axis of the slug plate. This entire configuration was then placed at the bottom of an electrically heated box furnace and the temperatures of the metal slug and exterior gypsum board surfaces were recorded during multiple heating and cooling cycles. The effective thermal conductivity was estimated knowing the heat capacities and densities of the steel slug and gypsum board samples (determined for the gypsum board using the Hot Disk Thermal Constants Analyzer)[4,9].

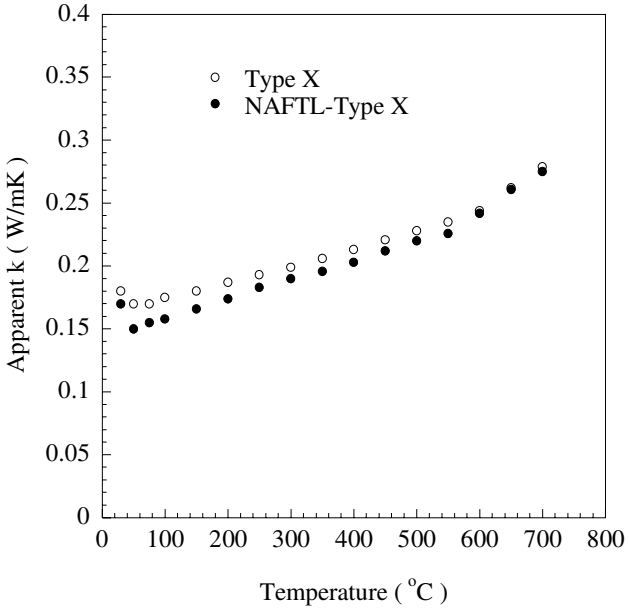

Fig. 2 Thermal conductivity as a function of temperature

During the first heating cycle, the gypsum dehydrated, absorbed some of the energy, and delayed the temperature rise of the slug. The thermal conductivity was determined based upon the second heating/(natural) cooling cycle and is displayed in Fig. 2. The gypsum board used for this test series is denoted as NAFTL-Type X. The thermal conductivity exhibits a slight decrease with temperature then steadily increases with temperature; similar behavior has been observed by Bénichou and Sultan[10] for thermal conductivity measurements for other gypsum board types. The NAFTL-Type X gypsum board used as part of the test series resulted in a slightly lower thermal conductivity as compared to off-the-shelf Type X gypsum board up to temperature of 500 °C. Above these temperatures, little difference was observed between the two gypsum samples.

To determine the specific heat as a function of temperature, Differential Scanning Calorimetry (DSC) was used. DSC specific heat measurements were taken following the procedure outlined in ASTM E 1269-2001[11] at a scanning rate of 20 °C/min. The gypsum board samples used were 10 mg in initial mass. To accommodate the gas generation incurred from dehydration, the sample, reference and standard measurements utilized pans that were sealed except for a 50 μm pinhole in the lid. Figure 3a-b displays the results of these measurements for the NAFTL-Type X board and off-the-shelf Type X board. As can be seen, three reactions are observed for both gypsum board types. Details of these reactions have been described elsewhere[3]. Slight differences were observed in the magnitude of the specific heat for the first dehydration reaction; these differences are within the uncertainty of the measurement.

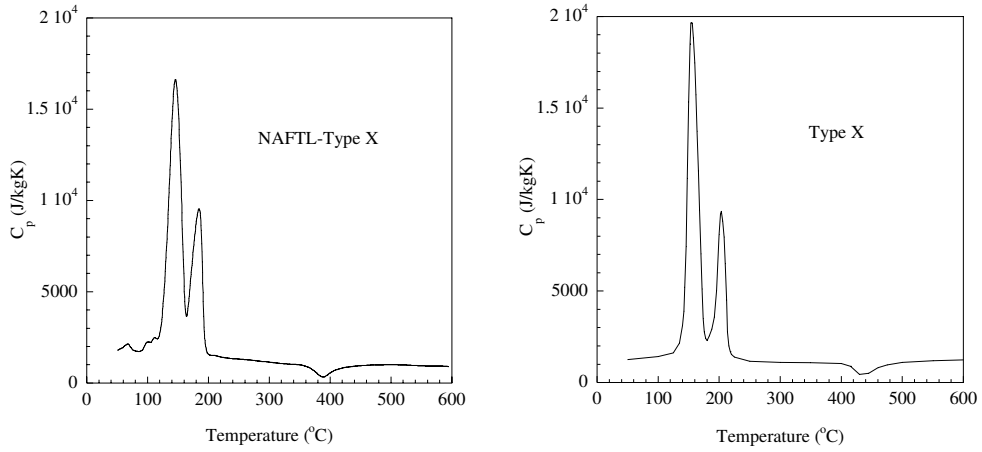

(a) (b)

Fig. 3 (a) Specific heat as a function of temperature for NAFTL-Type X gypsum board (b) Specific heat as a function of temperature for off the shelf Type X board

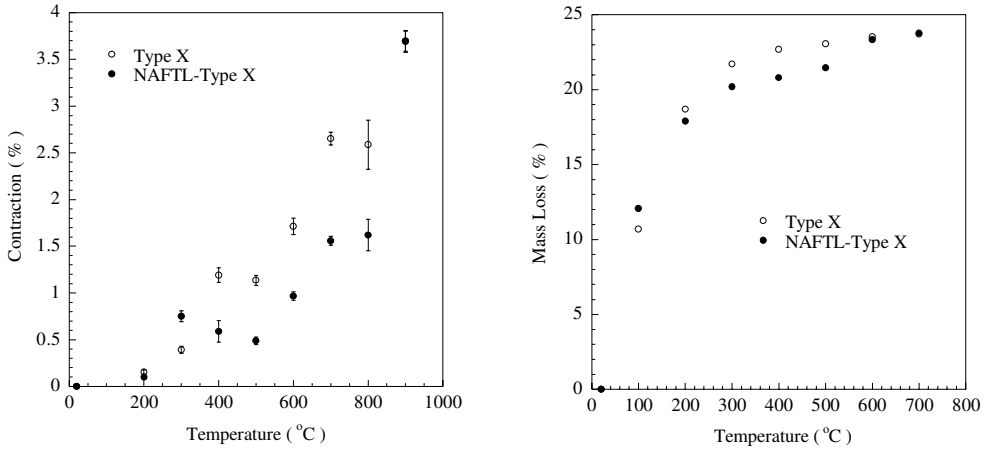

(a) (b)

Figure 4 (a) Gypsum board contraction as a function of temperature (b) Gypsum board mass loss as a function of temperature; each data point is the average of three repeat measurements

The mass loss and linear contraction were measured for the NAFTL-Type X gypsum board and off-the-shelf Type X gypsum board. Samples were cut into 50 mm by 152 mm

rectangles from single sheets of each type of board and inserted into an oven. At each temperature tested, the mass loss was measured as function of time. For a given temperature, the gypsum board samples were inserted into an oven for up to 24 hours. For each temperature tested, no change is mass loss or contraction was observed after the samples were allowed to equilibrate in the oven after three hours of heating. The results of these measurements are displayed in Fig. 4a-b. The contraction of the NAFTL-Type X gypsum board was considerably less at higher temperatures compared to off-the-shelf gypsum board.

Finally, the density at room temperature was determined from 152 mm by 152 mm samples. Based on these measurements, the density was higher for NAFTL-Type X board (760 kg/m^3 ± 0.01 kg/m^3; mean ± standard deviation) as compared to off-the-shelf Type X board (711 kg/m^3 ± 0.02 kg/m^3; mean ± standard deviation).

In summary, the linear contraction as well as the density was higher for the NAFTL Type-X gypsum board as compared to off-the-shelf Type X gypsum board. These results suggest a higher content of additives were present in the NAFTL Type-X gypsum board. Core additives are known to be added to enhance gypsum board performance.

4. FULL-SCALE TEST RESULTS

According to ASTM E119-00[1] specifications, the temperature of the furnace is determined from the average of multiple shielded, slow time-response thermocouples located within the furnace cavity. Each laboratory that participated in the testing mounted the test assembly in their vertical furnace. The temperatures of the North American laboratory furnace tests, designated NA-1 through NA-10, are plotted in Fig. 5a. The temperatures of the Japanese laboratory furnace tests, designated J-1 through J-6, are plotted in Fig. 5b. The dotted line represents the time-temperature curve specified in the ASTM E119-00[1] standard. As can be seen, furnace J-1 failed at approximately 20 minutes into the test. The furnace was subsequently brought on-line again within three minutes of the failure; the cause of failure was due to the activation of a seismic sensor.

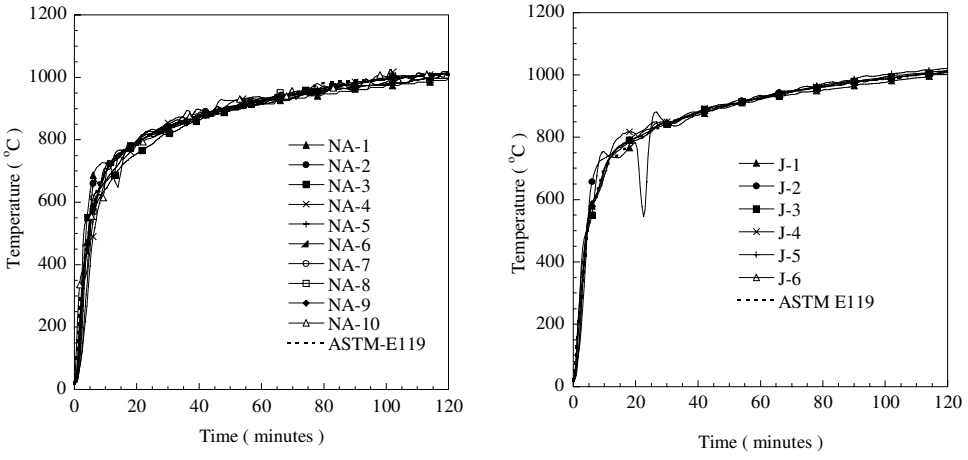

(a) (b)

Fig. 5 (a) Furnace temperature for North American Laboratories (b) Furnace temperature for Japanese Laboratories

Fig. 6a-b displays how closely the furnace temperatures follow the standard temperature curve. One can see that during warm-up, the test furnaces in North America and

Japan deviate by as much as 150 °C from the ASTM E119-00[1] temperature, and are most often on the low side. Due to failure of furnace J-1, a large discrepancy was observed between the E119-00 temperature and furnace J-1.

The average temperature increase on the unexposed wall for each North American and Japanese furnace test is shown in Fig. 7a-b. Note that the ambient temperature has been subtracted from the average temperatures. As mentioned earlier, one of the criteria for rating the fire resistance of a wall assembly is the time when the average temperature of the thermocouples on the unexposed side of the specimen reaches 139 °C above its initial average temperature. This limit is shown as the dotted red line in the figures. Similar to the North American furnaces, the temperature profiles are closely grouped for the first 60 minutes and then begin to diverge. None of the average temperature increases exceed the threshold before 60 minutes, and all have exceeded the threshold by 70 minutes.

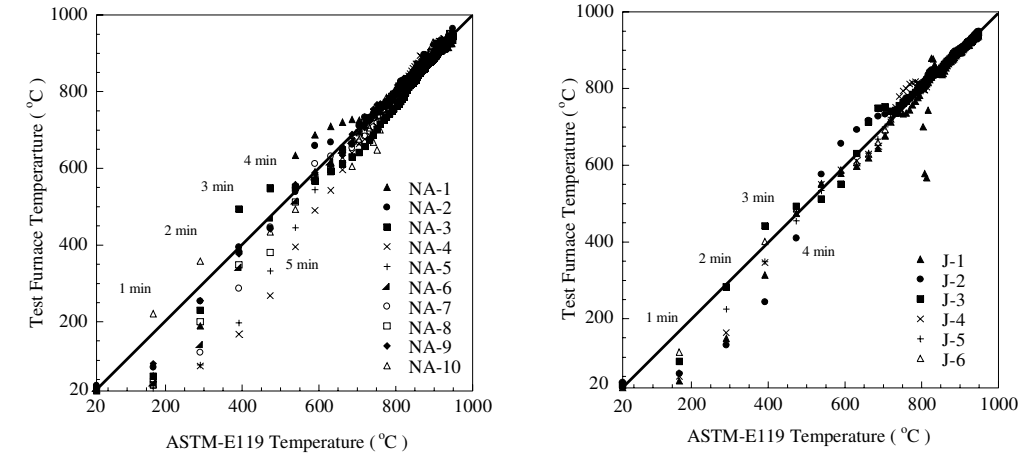

(a) (b)

Fig. 6 (a) Individual furnace temperatures vs. prescribed furnace temperatures-North American Laboratories (b) Individual furnace temperatures vs. prescribed furnace temperatures-Japanese Laboratories

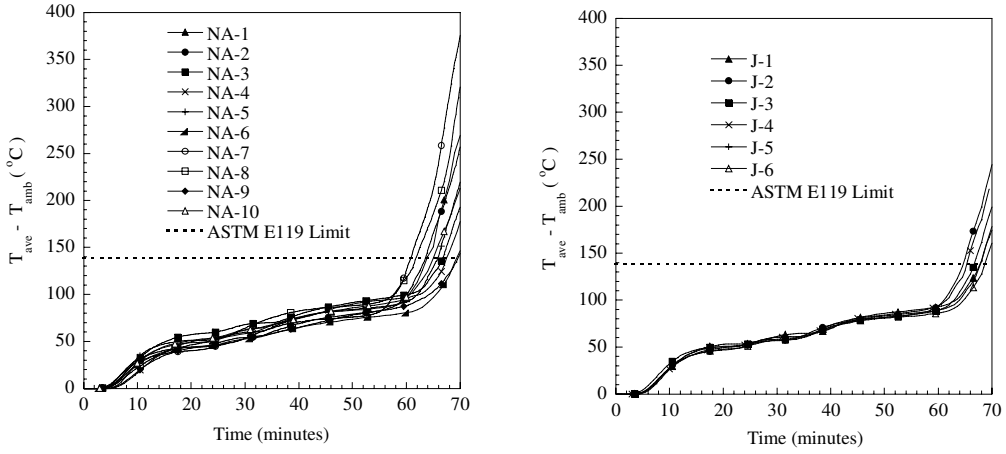

(a) (b)

Fig. 7 (a) Average unexposed face temperatures-North American Laboratories (b) Average unexposed face temperatures-Japanese Laboratories

Furnace pressures were recorded for the North American Laboratories and the Japanese Laboratories. These data are presented elsewhere[4]. A complication with this data was that the location of pressure probe was not the same between each test. As a result, comparing the furnace pressure among laboratories was not useful.

Fig. 8a-b is a plot of the average temperature increase on the unexposed wall for the individual specimen versus the mean value for the temperature increase of all of the tests. The spread in temperatures among the six Japanese Laboratories begins at around 77 ^{o}C, which was very similar to the North American tests. Above these temperatures, the deviation among furnaces is quite large; more than 93 ^{o}C at later times for both the North American and Japanese Laboratories.

The key finding of the ASTM E119-00[1] is the fire resistance rating (see Table 1 and Table 2). For one of the Japanese furnaces, the failure time was based upon the average temperature increase on the unexposed face exceeding 139 ^{o}C. The maximum allowed individual temperature on the backside of the wall (181 ^{o}C) was the failure limit for four Japanese furnaces; one furnace exceeded both criteria simultaneously (within the limit of their data rate). In no case was the wall breached in less than 70 minutes. The wall was not designed to be loaded; hence, the failure to maintain a load was not examined.

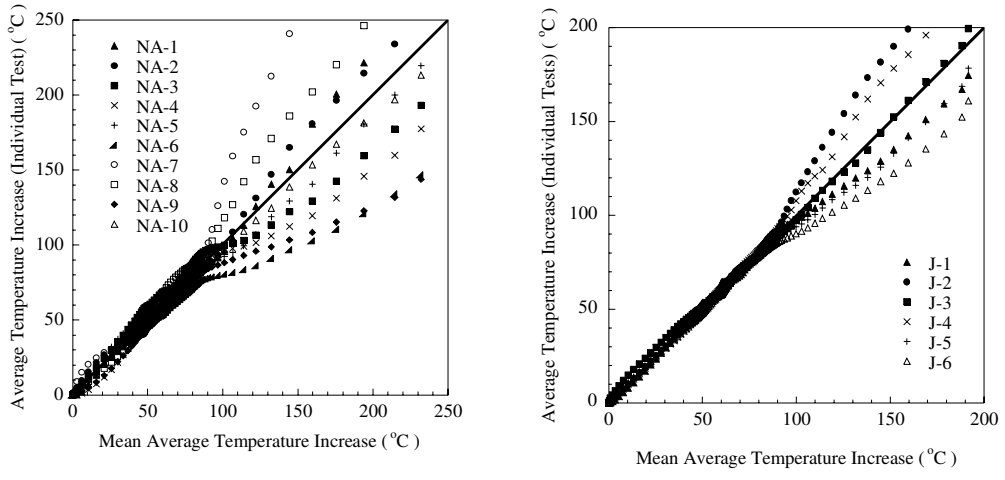

(a) (b)

Fig. 8 (a) Individual test unexposed surface average vs. mean of all ten tests-North American Laboratories (b) Individual test unexposed surface average vs. mean of all six tests-Japanese Laboratories

For five of the North American furnaces, the failure time was based upon the average temperature increase on the unexposed face exceeding 139 ^{o}C. The maximum allowed individual temperature on the backside of the wall (181 ^{o}C) was the failure limit for four North American furnaces, and one North American furnace exceeded both criteria simultaneously (within the limit of their data rate).

In summary, for the Japanese furnaces the overall average time to failure was 67.1 minutes, with a standard deviation of 1.1 minutes. For comparison (see Table 1 and Table 2), the North American furnaces resulted in an overall average time to failure was 65.0 minutes, with a standard deviation of 2.8 minutes. Similar to the North American furnace tests, the fire resistance rating, shown in the second column, is the same for all six Japanese furnaces: 1-h.

4.1 COMPARISON OF FURNACE THERMOCOUPLES

Differences exist between ASTM E119-00[1], ISO 834[2], and Japanese protocols for fire resistance testing of partition assemblies; the measuring probe for monitoring and controlling the furnace temperature is one difference. While both ASTM E119-00[1] and Japanese testing protocol continue to use thermocouples to control the furnace temperature, the ISO 834[2] testing protocol was modified to use the plate thermometer.

Table 1 Summary of Failure Criteria for Japanese Laboratories; all of the Japanese Laboratories arrived at the same Fire Resistance Rating

Laboratory	Fire Resistance Rating	Time to First Failure, minutes	Failed Thermocouple Reading	Other TC's Failing within 1 minute
NA-1	1 hour	64	average	TC3, 5, 7
NA-2	1 hour	62.8	TC3	average
NA-3	1 hour	66.8	average	TC4, 6, 8
NA-4	1 hour	67.5	average	TC3, 6, 8
NA-5	1 hour	65.8	average	TC6
NA-6	1 hour	70	TC3	TC4, 5, 6, 7, average
NA-7	1 hour	60.6	TC7	TC3, 5, 6, average
NA-8	1 hour	61.9	average	TC3, 4, 6
NA-9	1 hour	65.8	TC5	none
NA-10	1 hour	65	average, TC5	TC4, 6, 7
average	1 hour	65.0 +/- 2.8	average	--

Table 2 Summary of Failure Criteria for North American Laboratories

Laboratory	Fire Resistance Rating	Time to First Failure, minutes	Failed Thermocouple Reading	Other TC's Failing within 1 minute
J-1	1 hour	67.7	TC7	Ave., TC6
J-2	1 hour	67.3	TC7	Ave., TC6
J-3	1 hour	66.0	TC6	Ave.
J-4	1 hour	65.5	Ave.	TC3, TC4, TC5, TC6, TC7
J-5	1 hour	68.0	Ave., TC6	TC4, TC5, TC7
J-6	1 hour	68.0	TC7	Ave.
average	1 hour	67.1 ± 1.1	TC7, TC6, Ave	--

For consistency, as part of the full scale testing, all laboratories (NA-1 through NA-10; J-1 through J-6) followed the ASTM E119-00[1] testing method; ASTM thermocouples were selected to control the furnace temperature. For comparison purposes, some of the Japanese laboratories decided to insert all three measuring probes inside the furnace to monitor the furnace temperature. These results obtained from this exercise are displayed in Fig. 9. At the inception of the test, the ASTM thermocouples lagged behind the ASTM-E119-00[1] time-temperature curve. After 10 minutes, there was essentially no difference between the three furnace probes designs. Similar results have been presented by Sultan for a comparison of ASTM shield thermocouples to plate thermometers[12]. For gypsum board partition assemblies, such differences may not be important. However, for assemblies constructed of other materials, such variations may be important. This subject, however, is beyond the scope of the present study.

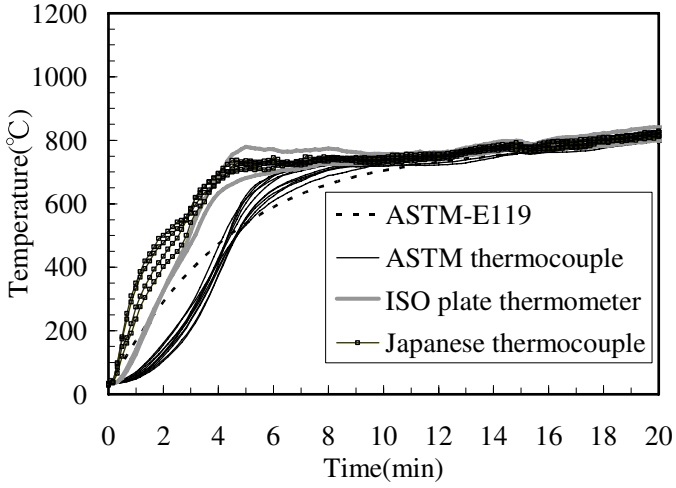

Fig. 9 Furnace temperature recorded by ASTM thermocouples, ISO plate thermometer, and Japanese thermocouples. Japanese bare-bead thermocouple with open protection tube, ISO plate thermometer, and ASTM thermocouple with closed protection tube

5. CONCLUSIONS

The North American Fire Testing Laboratories Consortium (NAFTL) organized a multiple laboratory test program for ASTM E119-00 using a common structural element: a 1-h rated gypsum/steel-stud non-load bearing wall assembly. Walls were tested by six different organizations employing ten different furnace facilities following the guidance provided in ASTM E119-00. In addition to NAFTL members conducting the tests, the program was expanded to include four testing laboratories in Japan; the Center for Better Living served as the organizer for the Japanese testing. NIST was the qualified independent party responsible for analyzing and reporting the data for the NAFTL and Japanese Laboratory testing. The present study expanded on a recently released NIST internal report to include further characterization of the gypsum board used in the tests as well as reporting the findings of the multiple laboratory testing program using the International System of units (SI).

The thermal properties of the gypsum board used for these experiments were characterized and compared to off-the-shelf Type X gypsum board. It was observed that the thermal conductivity and specific heat was not significantly different between the NAFTL-

Type X gypsum board and off-the-shelf Type X gypsum board. The linear contraction as well as the density was higher for the NAFTL-Type X gypsum board as compared to off-the-shelf Type X gypsum board. These results suggest a higher content of additives were present in the NAFTL Type-X gypsum board.

With regard to the full scale assembly tests, for five of the North American furnaces, the failure time was based upon the average temperature increase on the unexposed face exceeding 139 ^{o}C. The maximum allowed individual temperature on the backside of the wall (181 ^{o}C) was the failure limit for four North American furnaces, and one North American furnace exceeded both criteria simultaneously (within the limit of their data rate).

For the Japanese furnaces the overall average time to failure was 67.1 minutes, with a standard deviation of 1.1 minutes. For comparison, the North American furnaces resulted in an overall average time to failure was 65.0 minutes, with a standard deviation of 2.8 minutes. Similar to the North American furnace tests, the fire resistance rating was the same for all six Japanese furnaces: 1-h. The effort described in this paper was the largest ever conducted for fire resistance testing. A similar effort is now underway for load-bearing partition assemblies.

6. AKNOWLEDGEMENTS

The authors acknowledge contributions made by each of the North American laboratories who conducted the fire resistance tests for the wall assembly. The authors would also like to acknowledge the participating Japanese laboratories. U.S. Gypsum supplied 100 % of the gypsum board, created in a special factory run to ensure tight quality control. Western Fire Center is acknowledged for handling and shipping the gypsum board to the different laboratories, including to the participants in Japan. The assistance of the American Council of Independent Laboratories (ACIL) was essential to maintain the anonymity of the test results. Mr. Dale Bentz of NIST assisted with the thermal property measurements and Mr. Alexander Maranghides is acknowledged for helpful discussions.

7. REFERENCES

1. Test Method for Fire Resistance Tests of Building Construction and Materials, ASTM E119-00a, ASTM International, West Conshohocken, PA.
2. Fire Resistance Tests – Elements of Building Construction, ISO 834 Parts 1 through 9, International Organization for Standardization, Geneva Switzerland.
3. S.L. Manzello, R.G. Gann, S.R. Kukuck, and D.B. Lenhert, Influence of Gypsum Board Type (X or C) on Real Fire Performance of Partition Assemblies, *Fire and Materials*, 31:425-442, 2007.
4. W.L. Grosshandler, S.L. Manzello, A. Maranghides, A., and T. Mizukami, Analysis of Inter-laboratory Testing of Non-loadbearing Gypsum/Steel-Stud Wall Assemblies, NISTIR 7471, National Institute of Standards and Technology, Gaithersburg, MD
5. Standard Specification for Installation of Steel Framing Members to Receive Screw-Attached Gypsum Panel Products, ASTM C754-00, ASTM International, West Conshohocken, PA.
6. Standard Specification for Application of Finishing of Gypsum Board, ASTM C840-03, ASTM International, West Conshohocken, PA.
7. Standard Specification for Nonstructural Steel Framing Members, ASTM C645-00, ASTM International, West Conshohocken, PA.

8. Standard Specification for Steel-Piercing Tapping Screws for the Application of Gypsum Panel Products or Metal Plaster Bases to Wood or Steel Studs, ASTM C1002-01, ASTM International, West Conshohocken, PA.
9. D.P Bentz, D.R Flynn, D.R, J.H. Kim, and R.R. Zarr, "A Slug Calorimeter for Evaluating the Thermal Performance of Fire Resistive Materials," *Fire andMaterials* 30:257-270, 2006.
10. N. Bénichou and M. Sultan, "Thermal Properties of Lightweight-Framed Construction Components at Elevated Temperatures," *Fire and Materials*, 29:165-179, 2005.
11. ASTM E 1269-01: "Standard Method for Determining Specific Heat Capacity by Differential Scanning Calorimetry," ASTM International, West Conshohoken, PA, 2001.
12. M. Sultan, "Fire Resistance Furnace Temperature Measurements: Plate Thermometer vs. Shields Thermocouples", *Fire Technology*, 42: 253-267, 2006.

A REVIEW OF MODELS FOR CALCULATION OF THE CHARRING RATE OF SOLID WOOD STRUCTURAL ELEMENTS AND GLUE-LAMINATED BEAMS/COLUMNS

KATHINKA LEIKANGER FRIQUIN[1]

ABSTRACT

Calculation models for charring rate of solid, nail- and glue-laminated wood members for use in fire design of wooden structures have been compared with test results from the literature. The applicability to solid, nail- and glue-laminated wood members, and the accuracy of the models, have been evaluated based on which parameters influencing the charring rate they include, i.e. species, density, moisture content, grain orientation, char contraction factor, external heat flux, thermal conductivity, oxygen concentration and opening factor. The models evaluated in this article are applicable to one- or two-dimensional charring under standard fire exposure.

1. INTRODUCTION

The use of solid wood elements and glue-laminated beams and columns in buildings and structures is gaining popularity in the Nordic countries, and these types of structural members have already been widely used around the world. In countries where timber is a readily available resource, it is a natural choice for construction material. The fire resistance of solid wood slabs and glue-laminated structural members is important when used in buildings, and in many cases, the fire safety of a building with these wooden elements can match or even succeed that of other structural materials. To design a fire safe wooden building the thermal properties of the material, the thermal conditions in the fire compartment and the charring rate of the material must be known. When wood is exposed to elevated temperatures, several factors regarding the material, the conditions in the room and the heat source affect the charring rate. Several attempts have been made to develop models to describe the charring rate of wood and how different factors influence on the charring, but few of them include more than two of these factors.

[1] PhD Student, Norwegian University of Science and Technology, Department of Civil and Transport Engineering, Trondheim, Norway
e-mail: kathinka.friquin@ntnu.no or kathinka.friquin@sintef.no

Large wooden elements are not oven-dry like many test specimens, they have a smaller exposed surface to volume-ratio, and the mass and heat transfer in large cross sections is different from the small test pieces that are commonly used in experiments. Multi-storey wooden structures, with the requirement of maintaining their load bearing abilities through a natural fire, will be exposed to a varying heat flux, and there are several other parameters that will affect the charring rate. There are many thorough reviews of pyrolysis models for wood, but few of them, if any, emphasize on the charring rate of solid wood or glue-laminated structural elements, nor the importance of including the density, moisture content, chemical composition and other factors in the models.

In this paper, several models for calculating the charring rate of solid wood or glue-laminated structural members from the literature are evaluated in regards to which parameters influencing the charring rate they include, i.e. species, density, moisture content, grain orientation, char contraction factor, external heat flux, thermal conductivity, oxygen concentration and opening factor. The reliability and fitness for use of the models are examined based on the parameters included in the model, and the possibility to adjust the material properties and thermal conditions with variations in the species, room or exposure conditions. The models most suited for calculation of charring depths of solid wood elements and glue-laminated timber beams and columns are determined. The charring rate for a few solid, nail- and glue-laminated cross sections have been calculated and compared with experimental results found in the literature. The current study is limited to unprotected solid wood elements and nail- or glue-laminated beams and columns exposed to standard fire. Only wood species commonly used in Europe and North-America are included. The project is part of the Strategic University Programme “Wood as a building material” funded by the Research Council of Norway, and the European WoodWisdom-Net project “FireInTimber – Fire resistance of innovative timber structures”.

2. CALCULATION MODELS FOR CHARRING

Several charring rate models for structural wooden slabs and members have been found in the literature and evaluated here. The models are separated into two groups in Table 1; one-dimensional charring models and two-dimensional charring models. The one-dimensional charring models do not include corner rounding, while the two-dimensional models do (See Fig. 1). Charring models are developed for various types of fire exposure, and in the current research focus is set on ISO 834[1] (ISO) and ASTM E119[2] (ASTM) standard fire exposure. Models for parametric fire exposure are not included in this article. This is because these models require that the opening factors and heat exposure for the experiments are known in order to compare them with each other.

EN 1995-1-2:2004[3] gives two ways of calculating the cross-sectional properties, either by using the actual charring depth including corner rounding, or by calculating a notional cross-section without corner rounding based on the notional charring rate. The position of the char front should be taken as the position of the 300-degree isotherm. Design charring rates for solid hardwoods, except beech, with characteristic densities between 290 and 450 kg/m³, may be obtained by interpolation between the values in Table 2.

Table 1. Separation of models for charring of wood into a group for one-dimensional charring and a group for two-dimensional charring

		Fire exposure			Factors included
Reference	Year	ISO	ASTM	Other	
One-dimensional					
Eurocode 5a[3]	2004	X			Softwood/hardwood, density, solid or laminated
Schaffer[4]	1967		X		Dry density, moisture content, species
Babrauskas[5]	2005	X	X		Density, oxygen concentration, heat flux, duration of fire
Yang et al.[6]	2008			X	Density, time-increasing heat flux rate.
Two-dimensional					
Eurocode 5b[3]	2004	X			Softwood/hardwood, density, solid or laminated, cross-section
AWC[7]	2003		X		Duration of fire

Table 2. Design charring rates β_0 and β_n of timber[3]

	β_0 mm/min	β_n mm/min
a) Softwood and beech		
Glue-laminated timber with characteristic density of ≥ 290 kg/m³	0.65	0.7
Solid timber with a characteristic density of ≥ 290 kg/m³ (incl. beech)	0.65	0.8
b) Hardwood		
Solid/glue-laminated hardwood, characteristic density of 290 kg/m³	0.65	0.7
Solid/glue-laminated hardwood, characteristic density of ≥ 450 kg/m³	0.50	0.55

Table 3. Determination of k_0 for unprotected surfaces with t in minutes[3]

	k_0
t < 20 minutes	t/20
t ≥ 20 minutes	1.0

May 15, 2004 18:57 Research Publishing: Trim Size: 7 x 10 Proceedings sif08:SS603

Table 4. Models for charring rate of wood

References, comments and limitations	Equation
One-dimensional – ISO 834	
Eurocode 5a[3] König[8] argues that because EN 1995-1-2 gives the corner radius as $r = d_{char,0}$ the minimum width $b_{\min}$ should for $d_{char,0} > 40mm$ be changed to: $b_{\min} = 4d_{char,0}$ König[8] also suggests that the notional charring rate for solid timber (see Table 2) is used for nail-laminated timber slabs with normal gap widths to achieve conservative results.	Design charring depth: $d_{char,0} = \beta_0 t$ (1) where the charring rate β_0 is taken from Table 2. Effective charring depth: $d_{ef} = d_{char,0} + 7k_0$ (2) where k_0 is found in Table 3.
One-dimensional – ASTM E119	
Schaffer[4] Charring rate converted to (mm/min) by: $\beta = 25.4/\tilde{\beta}$.	Charring rate: Douglas fir $\tilde{\beta} = 2\left[(28.726 + 0.578\omega)\rho_{dry} + 4.187\right]$ (3) Southern pine $\tilde{\beta} = 2\left[(5.832 + 0.120\omega)\rho_{dry} + 12.862\right]$ (4) White oak $\tilde{\beta} = 2\left[(20.036 + 0.403\omega)\rho_{dry} + 7.519\right]$ (5)
Babrauskas[5] He argued that this equation is applicable to both ISO 834 fire and ASTM E119 fire.	Charring rate: $\beta = 113 k_{O2} \frac{(\bar{q}'')^{0.5}}{\rho t^{0.3}}$ (6) where $k_{O2} = 1.0$ for charring in high oxygen concentration, $k_{O2} = 0.8$ for charring in 8-10%, and $k_{O2} = 0.55$ for charring in 4% oxygen concentration.
One-dimensional – Others	
Yang et al.[6] For time-increasing heat flux. The increasing rate of heat flux for ASTM E119 is approximately 0.07 kW/m²s, and is used in Table 7.	Charring rate: $\beta_\gamma = 136\gamma^{0.51} \cdot \rho^{-0.76}$ (7)

Table 5. Models for charring rate of wood (contd.)

References, comments and limitations	Equation
Two-dimensional – ISO 834	
Eurocode 5b[3]	Notional charring depth: $$d_{char,n} = \beta_n t \quad (8)$$ where the notional charring rate β_n (mm/min) is taken from Table 2. Effective charring depth: $$d_{ef} = d_{char,n} + 7k_0 \quad (9)$$ where k_0 is found in Table 3.
Two-dimensional –ASTM E119	
AWC[7]	Effective charring rate: $$\beta_{eff} = \frac{2.58\beta_n}{t^{0.187}} \quad (10)$$ where β_n is assumed to be 0.64 mm/min.

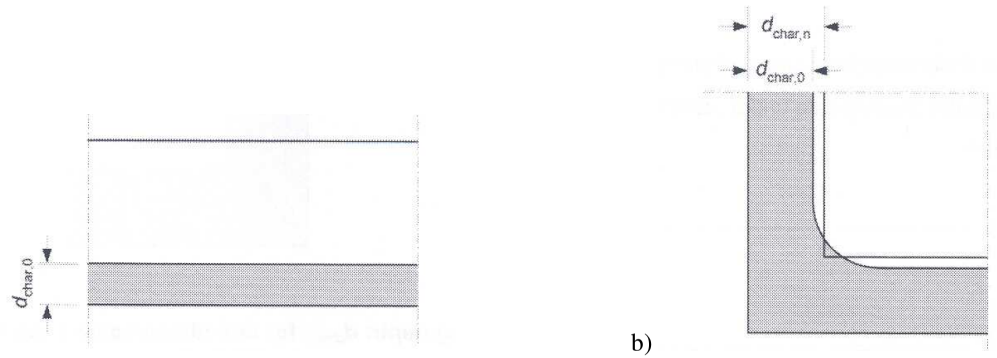

a) b)

Fig. 1. a) One-dimensional charring of wide cross-section with fire exposure on one side. b) Charring depth $d_{char,0}$ for one-dimensional charring and notional charring depth, $d_{char,n}$[3]

3. CALCULATED CHARRING RATES COMPARED WITH TEST RESULTS

The calculation models listed in Table 4 have been compared with charring rate results from test experiments from various laboratories. A short description of the experiments referred to in this article is given in Table 6.

Table 6. Experiments referred to in Table 7 and Table 8

Author	Species	Test apparatus / Fire exposure / Orientation / Exposed sides and time	Specimen size (mm x mm)
White[9]	*Softwood*: Engelmann spruce, Western cedar, Southern pine, Redwood *Hardwood*: Hard maple, Yellow poplar, Red oak, Basswood	Small gas-fired furnace ASTM E119 Vertical One side, 60 minutes	Glue-laminated slabs 63 x 230, 510 mm long, 38 or 46 mm thick laminates
Cedering [10,11]	*Softwood:* Norway spruce	Gas-fired furnace ISO 834 Vertical One side, 60 minutes	Nail-laminated 40 x 140, 1000 mm long Samples nailed together to form a wall of 55-60 planks
König[12]	*Softwood:* Spruce	Small gas-fired furnace ISO 834 Horizontal One side, 30-60minutes	Nail-laminated slabs 315 x 1500, 95 mm thick, 7 laminates of 45 mm thickness nailed together
Landrø[13]	*Softwood:* Spruce	Gas-fired furnace ISO 834 Horizontal One side, 30 minutes	Cross-layered glue-laminated slab 4800 x 3600, 160 mm thick. Loaded with 3 kN/m².
Frangi and Fontana[14]	*Softwood:* Spruce	ISO 834 Beams; three sides Slabs; one side 30-110 minutes	Glue-laminated timber beams, and slabs made of nailed planks, 120 mm thick
Landrø[15]	*Softwood:* Spruce	Gas-fired furnace ISO 834 Beams; three sides Columns; four sides 30 minutes	Glue-laminated timber beams and columns 90 x 300, 1400 mm long 1300 mm long

In Eurocode 5[3], 7 mm is added to the charring depth. The charring rates given in Table 2 have therefore, in the tables below, been increased with 0.12, 0.08 and 0.06 mm/min for 60, 90 and 120 minutes respectively, to include these 7 mm. Test results for dry density wood have only been compared with models using dry density in the equation, and models using

wet density have only been compared with test results for wet density wood. The only exception is calculation results for EN 1995-1-2[3] which normally are valid for wet density wood, but is also applicable to dry density wood where the wet density can be assumed based on the dry density. This is because the charring rate is the same for densities above 290 kg/m³ for softwoods, and for hardwoods the charring rate is the same for wood densities at 290 kg/m³ and for densities above 450 kg/m³. Babrauskas[5] found the average heat flux in the ceiling during ASTM E119 fire to be approximately 92 kW/m². This heat flux is therefore used in the calculations, together with 8-10% oxygen.

3.1. One-dimensional charring

In Table 7 below, one-dimensional charring rate results from the experiments listed in Table 6 have been compared with calculated results using the one-dimensional models from Table 4.

Table 7. Calculated charring rates (mm/min) compared with test results from the literature, for one-dimensional charring of nail- and glue-laminated wood

Species	Ref	Density (kg/m³)	Test results Moisture (%)		Calculation results				
							Exposure time (min)		
			10-12	16-18	Model	Eq. No	60	90	120
Nail-laminated									
Spruce	[10,11]	370	0.71	0.64	EC 5a	β_0(+7)	0.77	0.73	0.71
		370			König [8]	β_n	0.80	0.80	0.80
	[14]	425	0.70		EC 5a	β_0(+7)	0.77	0.73	0.71
	[12]	425	0.70		König [8]	β_n	0.80	0.80	0.80
		370			Babrauskas	(6)	0.69	0.61	0.56
		425					0.60	0.53	0.49
		370			Yang et al	(7)	0.39	0.39	0.39
		425					0.35	0.35	0.35
Glue-laminated									
Spruce	[9]	400*	0.59	0.52	EC 5a	β_0(+7)	0.77	0.73	0.71
(Douglas fir)		400*	x	x	Schaffer	(3)	0.69	0.69	0.69
							0.64	0.64	0.64
	[13]	475	0.64		EC 5a	β_0(+7)	0.77	0.73	0.71
		475			Babrauskas	(6)	0.54	0.47	0.44
		475			Yang et al	(7)	0.32	0.32	0.32
Cedar	[9]	285*	0.75	0.73	EC 5a	β_0(+7)	0.77	0.73	0.71
Pine	[9]	485*	0.76	0.83	EC 5a	β_0(+7)	0.77	0.73	0.71
Redwood	[9]	324*	0.76	0.62	EC 5a	β_0(+7)	0.77	0.73	0.71

Maple	[9]	650*	0.66	0.64	EC 5a	β_0(+7)	0.62	0.58	0.56
Yellow poplar	[9]	482*	0.68	0.68	EC 5a	β_0(+7)	0.62	0.58	0.56
Oak	[9]	635*	0.57	0.56	EC 5a	β_0(+7)	0.62	0.58	0.56
		635*	x		Schaffer	(5)	0.55	0.55	0.55
				x			0.51	0.51	0.51
Basswood	[9]	385*	0.87	0.70	EC 5a**	β_0(+7)	0.74	0.70	0.68

EC 5 = Eurocode 5 * Dry density **Interpolated 0.62 mm/min

3.2. Two-dimensional charring

In Table 8 below, two-dimensional charring rate results from the experiments listed in Table 6 have been compared with calculated results using the two-dimensional models from Table 4. The charring rates have been calculated using the same density and moisture content as the tested samples.

Table 8. Calculated charring rates (mm/min) compared with test results from the literature, for two-dimensional charring of solid and glue-laminated wood

Species	Ref	Density (kg/m³)	Test results Moisture (%)		Calculation results		Exposure time (min)		
			10-12	16-18	Model	Eq. No.	60	90	120
Solid									
Spruce	[14]	378	0.67		EC 5b	β_n(+7)	0.92	0.88	0.86
		378			AWC	(10)	0.77	0.71	0.68
Glue-laminated									
Spruce	[14]	453	0.70		EC 5b	β_n(+7)	0.82	0.78	0.76
		453			AWC	(10)	0.77	0.71	0.68
Spruce	[15]	450		0.67	EC 5b	β_n(+7)	0.82	0.78	0.76
		450			AWC	(10)	0.77	0.71	0.68

EC 5 = Eurocode 5 * Dry density **Interpolated

4. DISCUSSION: APPLICATION OF MODELS ON GLUE-LAMINATED WOODEN ELEMENTS

Many factors influence the charring rate of wood, and researchers have different opinions and experimental results on how they affect the charring. Factors like density, moisture content, species, heat exposure, opening factor etc influence the charring rate in different ways and some are more significant than others. The factors are included in various forms and combinations in the char calculation models described in this report, and are important for the results the models give. The user of the models must know which factors are included and which are neglected, so that the results can be evaluated correctly.

All except one of the models evaluated in this article include the density of the wood, one model varies between different species, two models differs between hardwoods and softwoods, and solid or glue-laminated cross-section, the moisture content is included in one model, another includes the oxygen concentration in the fire compartment, two models include the duration of the fire, and two models include the imposed heat flux.

Comparing the charring rates for nail-laminated cross-sections of *spruce* exposed to one-dimensional fire, the test results for densities between 370-425 kg/m² are equal at about 0.70 mm/min. The calculated charring rates, however, differ widely from 0.35-0.80 mm/min (60 min). The largest values (EC 5a and König[8]) are conservative, while the lowest values (Eq. 7) seem unlikely to achieve. For a 60 minutes exposure, Babrauskas' model (Eq. 6) compares well with the test results.

For glue-laminated cross-sections exposed to one-dimensional fire (Schaffer's model (Eq. 3) for Douglas fir has here been used for spruce), the charring rate test results for *spruce* with densities between 400 kg/m³ (dry density) and 475 kg/m³ varies between 0.59-0.64 mm/min (60 min). The calculated results vary between 0.32-0.77 mm/min, and Schaffer's and Babrauskas' results are closest to the test results. The results from the model in EN 1995-1-2[3] are as much as 30% higher than the test results. The lowest charring rates (Eq. 7) are also here very unlikely.

For *oak* with a dry density of 635 kg/m³ the experiment shows a charring rate of 0.56-0.57 mm/min, while the calculations results in rates between 0.51-0.62 mm/min. Schaffer's model (Eq. 5) for White oak with moisture content 12% compares best with the experiment.

Test results for the other species have only been compared with EN 1995-1-2[3] because the test reports only give the dry density. For the softwoods *cedar*, *pine* and *redwood*, the calculation results at 60 minutes match well the test results for wood with 10-12% moisture content. The calculated charring rates for the hardwoods *maple*, *yellow poplar* and *basswood*, however, do not compare well. The results for maple are closest, while for basswood the results are very different.

The calculated charring rates for solid and glue-laminated *spruce* with a density of 378-453 kg/m³ exposed to two-dimensional fire are much larger than the test results. The results from the model in EN 1995-1-2[3] are as much as 37% higher than the test results.

5. CONCLUSIONS

A few test results have in this article been compared with calculation models for the charring rate of wood found in the literature. The experiments differ widely in species tested, moisture content, cross-section sizes, heat flux, oxygen content etc. and are therefore difficult to compare. Detailed guidelines and methods for testing of charring rates of wood must be developed, where the moisture content, oxygen concentration, sample size and orientation, heat exposure, etc are described for various types of end uses of the test results. This will enable researchers all over the world to compare their test results with each other, and the reproducibility of the tests would be better.

There is a need for more comprehensive charring rate experiments on the most commonly used wood species for building construction. The test results can be used to develop more accurate charring rate models, incorporating several of the influencing factors., like; density, moisture content, species, heat flux, time, opening factor, etc.

Amongst the calculation models evaluated in this article, Schaffer's (Eq. 3, 4 and 5) and Babrauskas' (Eq. 6) models for one-dimensional fire exposure for both nail- and glue-laminated members gave the most accurate charring rates compared with the test results. The model in EN 1995-1-2[3], and the suggestion from König[8] for nail-laminated slabs, were very

conservative. For two-dimensional fire exposure, both the model in EN 1995-1-2[3] and the AWC model (Eq. 10) are very conservative.

The comparisons of the models with test results show that the models including more factors give more accurate results, and the variations between species are large. Schaffer's model includes both dry density and moisture content, and differs between species. Unfortunately, Schaffer only developed variations of the model for three species (Eq. 3, 4 and 5), but variations for more species can be developed. Babrauskas' model (Eq. 6) includes density, oxygen concentration, heat flux and fire duration. Other models also include density, heat flux or fire duration, but none of them differ between species, or include both heat flux and fire duration at the same time.

The wide spread of test results and calculated results for the charring rate shows the obvious need for more research on charring rates for various wood species and fire exposures, and for redevelopment of charring rate models for use in fire safety design of wooden buildings.

NOMENCLATURE

Latin upper case letters

A_i	Area of vertical opening "i" (m²)
A_t	Total area of floors, walls and ceilings enclosing the fire compartment (m²)
A_v	Total area of openings in vertical boundaries of compartment (windows etc.) (m²)
F	Design opening factor ($m^{0.5}$)
O	Opening factor ($m^{0.5}$)
Q	Sum of the products of density and lower calorific value of materials found in the fire compartment (MJ)

Latin lower case letters

b	Absorptivity for the total enclosure
c	Specific heat of the boundary of the compartment (J/kgK)
$d_{char,0}$	Charring depth for one-dimensional charring (mm)
$d_{char,a}$	Charring depth for wide surface (mm)
$d_{char,b}$	Charring depth for narrow surface (mm)
$d_{char,n}$	Notional charring depth (mm)
d_{ef}	Effective charring depth (mm)
f	Coefficient to account for horizontal openings
f_c	Char contraction factor
h_{eq}	Weighted average of heights of all openings (windows etc) (m)
h_i	Height of vertical opening "i" (m)
k	Transfer coefficient of bounding structure
k_0	Coefficient
k_{O2}	Coefficient for oxygen concentration
m	Reciprocal charring rate (min/mm)
q_F	Design fire load related to design opening factor F (MJ/m²)
$\bar{q}''$	Test-average total heat flux (kW/m²)
r	Corner radius (mm)

t Time of fire exposure (min or hrs)

t_0 Time period with a constant charring rate (min)

Greek upper case letters

Γ Factor accounting for the thermal properties of the boundaries of the compartment,

Greek lower case letters

β Charring rate (mm/min)

β_0 Design charring rate for one-dimensional charring under standard fire exposure; Initial rate of charring (mm/min)

β_{eff} Effective charring rate (in/hr)

β_H Charring rate (m/s)

β_n Design notional charring rate under standard fire exposure (mm/min); Nominal charring rate based on one hour exposure (in/hr)

β_{par} Design notional charring rate under standard fire exposure (mm/min)

$\tilde{\beta}$ Charring rate (min/inch)

β_γ Charring rate for time-increasing heat flux (mm/min)

γ Time-increasing rate of heat flux (kW/m²s)

λ Thermal conductivity; Thermal conductivity of the boundary of the compartment (W/mK)

θ Time at which maximum charring is reached for the values used for F and q_F (min)

ρ Density; Density of the boundary of the compartment (kg/m³)

ρ_{dry} Dry specific gravity (kg/m³)

ω Moisture content (%)

REFERENCES

[1] ISO 834-1. *Fire-resistance* tests -- *Elements of building construction -- Part 1: General requirements.*

[2] ASTM E119. *Standard Test Methods for Fire Tests of Building Construction and Materials.*

[3] EN 1995-1-2:2005. *Eurocode 5: Design of timber structures, Part 1-2: General - Structural fire design.*

[4] Schaffer EL. *Charring rate of selected woods - transverse to grain*. FPL Research Paper 69, Forest Products Laboratory: Madison, Wisconsin, USA, Apr. 1967.

[5] Babrauskas V. Charring rate of wood as a tool for fire investigations. *Fire Safety Journal* Sept. 2005; **40**: 528-554.

[6] Yang L-H, Zhou Y, Wang Y, and Guo Z. Predicting charring rate of woods exposed to time-increasing and constant heat fluxes. *Journal of Analytical and Applied Pyrolysis* 2008; **In Press, Corrected Proof**: 10.1016/j.jaap.2007.06.006.

[7] American Wood Council (AWC). *Calculating the Fire Resistance of Exposed Wood Members*. Technical Report 10, American Forest & Paper Association, 2003.

[8] König J. Notional versus one-dimensional charring rates of timber. *8th World Conference on Timber Engineering, Lahti, Finland, 2004.* Lahti, Finland. 2004; 1001-1004.

[9] White RH. *Charring rates of different wood species*. PhD, University of Wisconsin-Madison: 1988.

[10] Cedering M. *Effect of the charring rate of Norway spruce from changes in the oxygen content*. Department of Structural Engineering and Mechanics, Steel and Timber structures, Chalmers University of Technology: Gothenburg, Sweden: 2004.
[11] Cedering M. Effect on the charring rate of wood in fire due to oxygen content, moisture content and wood density. *Fourth International Workshop Structures in Fire.* Aveiro, Portugal. 2006; pp. 8-
[12] König J. *Small-scale fire tests of heavy timber components*. SP Report 0310036, SP Wood Technology: Borås, Sweden, 2003.
[13] Landrø H. *Brannteknisk prøvning av bærende massivtredekke (Fire testing of load bearing glue-laminated timber slabs)*. Tresenteret i Trondheim, Aug. 2006.
[14] Frangi A and Fontana M. Charring rates and temperature profiles of wood sections. *Fire and Materials* Mar. 2003; **27**: 91-102.
[15] Landrø H. *Verification of the fire resistance of construction elements and structures*. PhD, The Norwegian Institute of Technology: SINTEF NBL as, Trondheim, Norway, 1983.

Fire Safety Engineering and Fire Protection

PREDICTION OF INTUMESCENT COATING PERFORMANCE UNDER CONE CALORIMETER-A MATHEMATICAL APPROACH TO PERFORMANCE BASED DESIGN

J.F. YUAN Y C. WANG[1]

ABTRACT

The aim of this research is to build a mathematical model to calculate temperatures in intumescent coating protected steel under different fire conditions. The mathematical model considers mass and volume variations due to chemical decomposition in intumescent coating. The dynamic aspects of the intumescence process and the nonlinearity of thermal properties have been included in this model. This model has been demonstrated to be able to capture the essential characteristics of intumescent coating behaviour under different fire conditions, but requires suitable input data for a large number of material properties. The results of a previous sensitivity study have identified the most important material parameters and this paper presents a method of determining these parameters from a small number of tests. The ultimate aim of this research is to develop a test protocol that would enable the essential material properties of intumescent coating to be determined for applications under different fire conditions. To test the feasibility of this approach, a number of cone-calorimeter tests have been carried out with different coating thicknesses, steel substrate thicknesses, and external heat fluxes. The key material parameters of the tested intumescent coating were determined from a small number of tests. These material parameters were then used in the mathematical model to predict steel temperatures recorded in the other tests. The results indicate that the key variables that have been extracted from a small number of small scale fire tests may be used to predict other fire tests under different fire conditions.

[1] Reader in Engineering, The University of Manchester, School of Mechanical, Aerospace, and Civil Engineering, Manchester, M60 1QD, UK
Email: Yong.Wang@manchester.ac.uk

1. INTRODUCTION

Intumescent coating is now the dominant material used to protect steel structures from fire attack. However the mechanisms determining the fire-resistant properties of intumescent coating are not well understood yet, due to their highly complex physical and chemical natures. This hampers the application of intumescent coating in performance-based fire engineering. At present, building fire resistance design is largely based on the "standard fire condition", and the thermal properties of an intumescent coating are obtained under the standard temperature-time relationship[1]. However, in a natural building fire condition, fire development varies depending upon such factors as the amount of combustible materials, ventilation, and construction lining materials. For conventional fire protection materials, their thermal properties can be pre-determined because their performance is temperature-dependent only. Unlike the conventional fire protection materials, intumescent coating will behave differently according to the applied fire condition, coating thickness, and protected structures. Because intumescent coating is a reactive material whose decomposition processes are extremely dynamic, the temperature-thermal properties relationship of an intumescent coating may be entirely different under different realistic fire conditions and any set of temperature-thermal properties relationship may only be applicable to a very narrow range of fire conditions. A key to widen the applicability of any predictive method is to ensure that it captures the essential features of intumescent coating that govern its behaviour in fire.

A main objective of this research is to establish a reliable predictive-method by using mathematical models to investigate the fire protection performance of intumescent coatings. So far a number of researchers have developed predictive models with different degrees of complexity. At the simplest level, intumescent coating is treated the same as the more conventional non-reactive fire protection materials and different effective thermal conductivity values of intumescent coating are used for different conditions. This is clearly not satisfactory because it will not be possible to extrapolate the results to different applications. At the most complex level, a few researchers[2] have attempted to model the intumescence process at the microscopic level, with detailed consideration of hydrodynamics, heat transfer and chemical reactions related to individual bubble nucleation, production, movement, and burst. This method of simulation is computationally prohibitive, requiring a large amount of input data. So far, it has had limited success, being used only to demonstrate the intumescence process during the very early stage of heating. An alternative third method would be to only consider the essential features of global chemical decomposition and physical behaviour of intumescent coating. This has been followed by a number of researchers with different assumptions[3,4].This paper adopts the third approach and the framework of Di Blasi and Branca[4] but with a few revised assumptions which will be pointed out later in the paper. According to DiBlasi and Branca[4], intumescent coating decomposition is modelled in three global steps and their reaction rates are governed by Arrhenius equation. The intumescence process is simply represented by expansion of the intumescent thickness. In the mathematical model, the governing equations are based on energy and mass conservation, and the model is solved by using the Finite Difference Method (FDM).

As will be shown, even though the model adopted in this study may be considered simple, it still requires a large number of input data for the intumescent coating. It may

be difficult and inefficient to obtain all of these input data precisely. Therefore, the authors carried out a sensitivity study to identify the key input parameters that will have significant influence on the calculated steel temperatures[5]. The main aim of this paper is to present a method of extracting these key input parameters from a small number of fire tests, which would be suitable for application under different test conditions. At this stage, the tests were conducted under Cone calorimeter. Research is on-going to extend this method to more realistic fire conditions.

2. MODEL

Yuan and Wang[5] have presented details of the mathematical model. For understanding the main issues of modelling intumescent coating behaviour, a brief description of the key components and assumptions of the model is provided in this section. For a steel plate protected by intumescent coating exposed to fire, it is acceptable to model the assembly as a one dimensional entity. By discretizing the intumescent coating into a number of layers, such as that shown in Figure 1, Finite Difference Method (FDM) can be used to solve the corresponding equations. From energy conservation, the change in heat flow conducted through a discretized layer of intumescent coating is equal to the change in internal energy of the coating, giving:

$$\frac{\partial}{\partial x}(\lambda\frac{\partial T}{\partial x}) = (m_s C_s + m_g C_g)\frac{\partial T}{\partial t} + C_g T\frac{\partial(\varepsilon x \rho_g)}{\partial t} + C_s T\frac{\partial m_s}{\partial t} + \frac{\partial(\dot{g}T)}{\partial x}C_g + \Delta h(\frac{\partial m_r}{\partial t}) \quad (1)$$

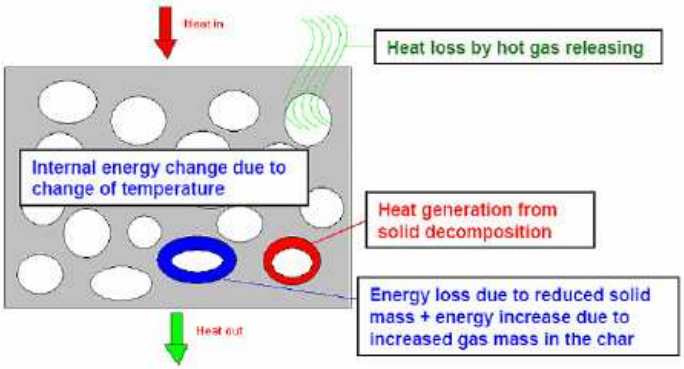

Figure 1 Illustration of energy conservation within an infinitesimal layer of intumescent coating

Where x is coordinate along the coating thickness, m the remaining mass, λ the thermal conductivity,ε the porosity, and subscript r the reactive component, s and g denote solid and gas respectively. The left hand of equation (1) is the conducted heat to

intumescent coating; the 1st term on the right hand side (RHS) is the heat increase due to change in coating temperature; the 2nd and 3rd terms on RHS are heat increases due to change in gas and solid masses respectively; the 4th term on RHS describes convective heat loss due to gas movement and the last term on RHS is heat release from the coating. The equation theoretically applies to the whole intumescent char; however, it is practically solved within discretized layers as aforementioned due to non-linearity of coating properties throughout the thickness. To enable quantification of equation (1), it is necessary to derive the various mass change terms, which are determined by the decomposition process. Arrhenius law is used to describe decomposition process, giving reaction rate constant K:

$$K_j = A_j \exp(-\frac{E_j}{\Re T}), j = 1,2,3 \qquad (2)$$

Where it is assumed that the intumescent coating consists of three basic components, namely: inorganic acid source, blowing agent and charring material. The above subscripts 1, 2 and 3 represent these three materials respectively. It should be noticed here that the 3nd component is a combination of charring agent and organic binding material, according to Cagliostro[6]. It is possible to further refine the model to include more components for more realistic modelling. It is also assumed that individual components degrade independently, although the reactions are in the following time-order: acid release, blowing, and charring. This is considered acceptable in the current stage of this research, as the kinetic values can represent the overall intumescent coating performance as far as the main objectives of the study (i.e. reliable prediction of protected steel temperatures under different fire conditions) are concerned.

The transient solid mass changing rate can be described as:

$$\frac{\partial m_j}{\partial t} = m_j K_j \alpha^n \qquad (3)$$

Where α is the degree of conversion and n is the reaction order.

It is assumed that only product of the blowing agent is responsible for bubble formation and swelling:

$$\frac{\partial x}{\partial t} = \frac{1}{\rho_g}\frac{\partial m_2}{\partial t} \qquad \left(x \le E_{\max} x_0\right) \qquad (4)$$

The gas density may be obtained from the ideal gas law. It is assumed in this study that bubble expansion occurs fast enough so that the pressure inside the char is in balance with the atmospheric pressure. It is also assumed that only the gas generated in each layer of the coating will contribute to swelling of this specific layer. Once a layer has reached its maximum expansion, it is assumed that the bubble volume in this layer does not change any more. Any excessive gaseous product will leave this layer to

maintain atmospheric pressure. This excessive gas will flow through other layers but will not contribute to their expansion.

It is necessary to quantify the porosity ε, which will influence both heat capacity and thermal conductivity of the intumescent coating. If movement of the solid mass is neglected, then:

$$x_s = x_0(1-\varepsilon_0)\frac{m_s}{m_0} \tag{5}$$

The total porosity, ε, is:

$$\varepsilon = \frac{x - x_s}{x} \tag{6}$$

The maximum expansion ratio E_{max} is probably the most important parameter in this predictive mathematical model. It determines the effectiveness of insulation of the intumescent coating. Parallel research is now being conducted to establish a reliable model to estimate this quantity. At present, the maximum expansion ratio is provided as an input value from experimental observation.

With the aforementioned assumptions, volume change of a specific elementary layer is only related to the amount of gas generated within the layer. The net loss of solid mass comes from chemical decomposition of the material and solid product from the reaction. A total mass continuity equation for gas transportation is used to decribe mass flow rate:

$$\frac{\partial \dot{g}}{\partial x} = -\frac{\partial m_s}{\partial t} - \frac{\partial\left(\varepsilon x \rho_g\right)}{\partial t} \tag{7}$$

The formation of a multi-cellular char leads to a significantly reduced thermal conductivity. Rather than using the simplest parallel and serial models as in Di Blasi and Branca[4], a model employing theory closer to reality has been introduced into this study. For a porous material, Russell[7] estimated the thermal conductivity as:

$$\lambda = \lambda_s \frac{\frac{\lambda_g}{\lambda_s}\varepsilon^{\frac{2}{3}} + 1 - \varepsilon^{\frac{2}{3}}}{\frac{\lambda_g}{\lambda_s}(\varepsilon^{\frac{2}{3}} - \varepsilon) + 1 - \varepsilon^{\frac{2}{3}} + \varepsilon} \tag{8}$$

Radiative heat transfer cannot be neglected at high temperatures. Although the opaque solid material does not allow radiation, it takes place within the void in the coating. Separating the total heat conduction coefficient of a gas into that of pure conduction and that due to radiation, one has:

$$\lambda_{rad} = \frac{2}{3} \times 4de\sigma T^3 \tag{10}$$

Where d is the pore diameter. Equation 10 clearly shows the importance of bubble diameter on radiative thermal conductivity of the charred coating structures. In intumescence process, it is assumed that bubble growth is governed by two mechanisms:

initial formation during blowing stage and gradual growth during the charring stage. Bubbles nucleate and grow rapidly during the expanding period, and the growth is considered to have linear relationship with expansion, as the 1st term on right hand side in equation (11).

$$d = d_b \frac{x}{x_0} \frac{1}{E_{\max}} + (d_f - d_b)(1 - \frac{m_3}{m_{30}}) \qquad (11)$$

Once charring process begins, bubbles start to burst and unite. Bubbles grow slowly but the bubble diameter will increase significantly compared with that during expansion. It is assumed that the bubble growth in this stage is linear to depletion of the charring material.

Although the modelling approach adopted in this research may be considered simplistic, it is possible to capture the complex physical and chemical processes of intumescent coating decomposition and their effects on temperature developments in the protected plate and fulfil the engineering requirements. In a previous paper[5], the authors provided a validating example of the modelling approach used in this paper.

The brief description of the model indicates that a large number of material parameters of intumescent coating are required as input data. Table 1 summarises these material properties. It would be difficult to obtain accurate data for all the required properties of intumescent coating in engineering applications. Therefore, the authors[5] have carried out a sensitivity study to identify the key parameters that have the most influence on modelling intumescent coating behaviour and that require accurate information. These key parameters are: E_2, E_3, E_{max} and d_f.

Table 1: A summary of material parameters required as input data

A_1	Pre-exponential factor of acid release	C_g	specific heat capacity of gas
E_1	Activation energy of acid release	λ_c	Thermal conductivity of the coating
A_2	Pre-exponential factor for bubbling	λ_s	Thermal conductivity of steel
E_2	Activation energy of bubbling	ρ_c	Density of initial coating
A_3	Pre-exponential factor for charring	ρ_s	Density of steel
E_3	Activation energy of charring	e_c	Emissivity at coating surface
Δh_1	Heat of pyrolysis of inorganic acid source	d_b	Initial stage bubble size
Δh_2	Heat of pyrolysis of bubbling agent	d_f	Final stage bubble size
Δh_3	Heat of pyrolysis of charring material	E_{max}	Maximum expansion coefficient
v_{10}	Initial mass fraction of inorganic acid source	W_g	Gas mean molecular weight
v_{20}	Initial mass fraction of bubbling agent	h	Convection heat transfer coefficient
v_{30}	Initial mass fraction of charring material	Q	External heat flux
C_c	specific heat capacity of the coating	x_{c0}	Initial coating thickness
C_s	specific heat capacity of steel	x_{st}	Dimension of steel structure

3. EXPERIMENTAL SET-UP

To extract the aforementioned key material properties, it is inevitable that experiments should be conducted. However, it is important that the material parameters extracted from the experiments do not restrict themselves to the specific test conditions, which is the main shortcoming of the procedure embedded in BS EN 13381-4. The desired method of extracting material parameters should enable general applications under different conditions. The aim of the authors' research is to explore the feasibility of developing such a method. Ideally, the fire experiments should be conducted involving realistic fire conditions. Due to time and cost restraints on this project, the experiments used in this paper were conducted under cone calorimeter. Different radiant heat fluxes of 35KW, 50KW, and 65KW were applied. To simulate different structures, various coating and steel plate thicknesses were tested. More detailed information on the cone calorimeter tests is provided in previous work[1]. Whereas the results show the approach has certain capability of modeling coating thermal dynamic behavior, it still requires a couple of empirical values due to its current inability to model the effect of intumescence (final expansion thickness, and bubble size).

A commercially available waterborne intumescent coating (KBS Char21) was investigated. Sample preparation was performed by applying the liquid coating material directly with a brush. Test samples were 100mm wide square steel plates (Three thicknesses: 5mm, 10mm and 20mm). The samples were painted with the intumescent coating of 0.4mm, 0.8mm and 1.2mm in thickness (Dried Film Thickness, DFT). The samples were exposed to thermal radiation in the cone calorimeter using heat fluxes 35kW/m^2, 50kW/m^2 and 65kW/m^2.

The back of the steel plate was attached to a layer of 40 mm thick mineral wool to minimize heat loss to the surrounding environment. To help quantify the inevitable loss of heat from the back of the steel plate, temperatures in the mineral wool were measured by a thermocouple at 20 mm below the steel plate.

At the exposed coating surface, the boundary condition is:

$$\lambda \frac{\partial T}{\partial x} = eQ_{cone} - e\sigma(T^4 - T_0^4) - h_{conv}(T - T_0) \tag{12}$$

Where Q_{cone} is incident heat flux from cone heater, T is coating surface temperature, T_0 is the ambient temperature which is normally taken as 20°C, e is the surface emissivity of the coating surface, σ is Stefan-Bolzmann constant, h_{conv} is convective heat transfer coefficient. In this study, h_{conv} has a constant value 20W/(m^2·K) and e for intumescent coating is 0.92.

The backface of mineral wool was exposed to the air so the boundary condition is:

$$Q_{loss} = e\sigma(T^4 - T_0^4) + h_{conv}(T - T_0) \tag{13}$$

4. RESULTS

As discussed in previous sections, key parameters are required to give reliable predictions. Thermogravimetric Analysis (TGA) would normally be used to obtain the reaction kinetics. Unfortunately, TGA tests were not carried out during these Cone

Calorimeter tests, so an alternative method was used in this study. Among a number of tests, test B_{12} was randomly chosen for extracting the key variables. In this test, steel plate was 10mm and the coating was 0.4mm in thickness, the test specimen was exposed to radiant heat flux 50KW.

E_2 value governs intumescent coating expansion process, therefore determines substrate temperature before full expansion. To estimate this E_2 value, substrate temperature was investigated. It was observed that the intumescent coating reached its maximum expansion at around 900s after the radiation started in test B_{12}. Therefore, the results pre-900s were used to back estimate E_2 value. Standard error of estimate, ('21(*YYSnY*−=$\sum$ is used to measure the predictive error, the deviation of the predicted values and the actual values *Y,* "*n*" stands for number of data collection points), was used to extract E·Y_2. With the aim of fire protection, this research concentrates more on the coating's performance at relatively elevated temperature, at which point the coating has fully expanded. Therefore, it is helpful to ensure that the estimated value can predict better at full expansion. In addition to standard error applied to the whole 900s period, predictive deviation ('*YYDY*−=) at the end of the 900s test has been used to help determination. Table 2 presents simulation results by using different values of E_2. It indicates that the prediction has the best fitting with experimental test when E_2=115kJ/mol.

Table 2 Trial and error results for estimating E_2

Value of E_2 (kJ/mol)	**105**	**110**	**115**	**120**	**125**
Average predictive error during 900s	5.11%	3.21%	3.35%	6.22%	9.02%
Predictive deviation at the end of 900s	-8.16%	-4.40%	-0.6%	3.21%	7.10%

Maximum expansion coefficient (E_{max}=62.5) was used as empirical input value in the simulation. Previous work[1] on estimating thermal conductivity of KBS Char21 coating has indicated that the thermal conductivity of the coating in this B_{12} test was around 0.28Kw/mK at the end of the test. This was used to estimate the bubble size "*d*", which was approximately 300 m after expansion and 3.5mm at the end of the experiment after charring.

To estimate E_3 value, temperatures of the steel substrate were studied between 900s and 2400s, after the maximum expansion has been achieved. Table 3 shows that best fitting for test B_{12} appears when E_3=55kJ/mol. It should be pointed out that with TGA data, E_3 would be obtained first and the bubble size would be obtained by trial and error. Using the aforementioned key material parameters, steel temperatures were calculated and Figure 2 compares the experimental and calculation results. It needs to be noticed, all temperature calculations were carried out in absolute temperature system in order to keep consistency with chemical reaction modelling.

Table 3 Trial and error results for estimating E_3

Value of E_3 (kJ/mol)	45	50	55	60	65
Average predictive error 900s-2400s	4.28%	2.95%	0.50%	4.41%	6.55%

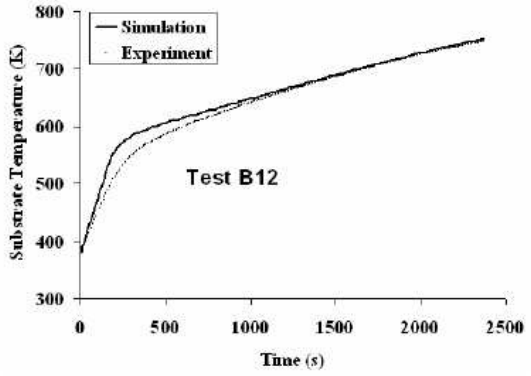

Figure 2 Agreement between simulation and experiment for test B_{12}.

Using the key properties extracted based on test B_{12}, simulations were carried out for the other tests under different cone radiative power, steel thickness and intumescent coating thickness. Table 4 presents simulation results for 21 tests over around 3000s heating period. Again average predictive error and predictive deviation have been used to evaluate the prediction performance. These results indicate the feasibility of using the same set of key parameters for different tests. Average predictive errors during the entire heating period indicate good agreements with the tests with most errors under 5%. It may be noticed that the model has larger errors for coatings with thicker DFTs, and under higher radiative heat fluxes. For the 50kW/m^2 tests, prediction for B_1 has error of 6.63% and prediction for C_4 has error of 13.86%. For the 65kW/m^2 tests, prediction for B_{14} has error of 8.58% and prediction for B_{7B} has error of 7.44%. All these tests used 1.2mm DFT. It may be explained that the thicker the coating is, the more non-linearity the coating will have during the initial fast decomposition process, which the current model was not able to model. On the other hand, higher radiative heat flux induces sharper temperature increase, which in turn favours decomposition dynamics, therefore results in difficulty of prediction. In contrast, B_8 and B_{11} have been simulated with acceptable errors of 2.72% and 3.78% respectively, in the 35kW/m^2 tests. Examples are shown in Figure 3, 4, and 5, to demonstrate predictions under different heating condition and with different initial coating thickness. To further analyse the simulation results, deviations at different points of substrate temperatures have been studied during the heating to assess the model's accuracy at different stages. Predictive deviations at steel temperatures of 200℃, 300℃, and 400℃ were collected in most tests. For tests under higher heat flux (65kW/m^2), deviation at steel temperature of 550℃ was also collected. It can be seen that larger errors mainly appear at the beginning stage before maximum expansion where the steel temperatures were generally low (where for different heating condition,

maximum expansion can be achieved at around 250-350℃). The model accuracy is improved at the later stage when the steel temperature was in the relevant range for practical applications of fire resistant design.

Table 4 Experimental set-up and simulation errors (Average predictive error during the entire heating period and predictive deviations at different steel substrate temperatures)

Cone Radiation (kW/m^2)	Test	Steel Thickness (mm)	DFT (mm)	Average Predictive Error (%)	Deviation at 200℃ (%)	Deviation at 300℃ (%)	Deviation at 400℃ (%)	Deviation at 550℃ (%)
50	A6	20	0.4	2.65	2.98	0.02	-3.65	
	A3	20	0.8	4.44	3.83	-0.96		
	A4	20	1.2	3.81	2.97	-2.23		
	B12	10	0.4	1.85	7.36	3.64	-0.57	
	B13	10	0.8	2.93	5.60	0.57	-2.87	
	B1	10	1.2	6.63	9.81	2.96		
	C11	5	0.4	5.70	11.87	7.18	2.33	
	C8	5	0.8	4.98	10.99	4.35	6.58	
	C4	5	1.2	13.86	10.70	13.97		
65	B1B	10	0.4	3.73	5.19	3.84	-2.40	-2.07
	B2	10	0.4	4.69	2.80	2.99	-4.19	-3.63
	B12B	10	0.8	4.93	8.20	2.26	-3.61	-3.94
	B3B	10	0.8	5.84	6.79	1.56	-5.37	-6.58
	B14	10	1.2	8.58	4.30	-0.98	-8.31	-10.70
	B7B	10	1.2	7.44	5.60	-0.69	-7.91	-9.82
35	B10B	10	0.4	4.50	4.32	2.38	-4.99	
	B16	10	0.4	3.09	2.95	2.61	-3.43	
	B9B	10	0.8	3.39	10.03	1.95	-0.02	
	B4	10	0.8	3.10	4.00	0.92	-4.19	
	B8	10	1.2	2.72	6.80	-0.47	-1.57	
	B11	10	1.2	3.78	8.08	-0.03	0.55	

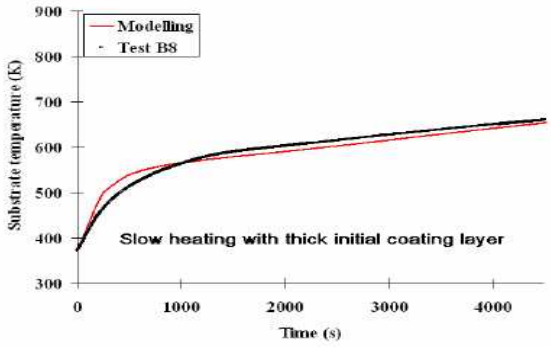

Figure 3 Prediction on experiment under cone heat flux 35kW/m^2, DFT 1.2mm

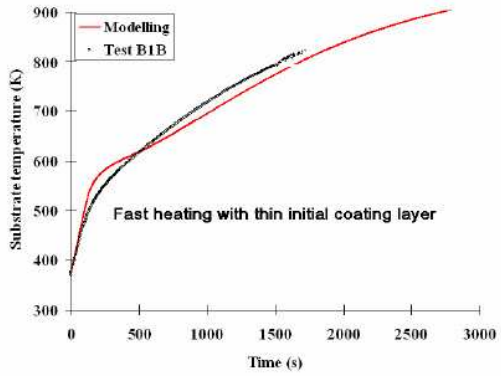

Figure 4 Prediction on experiment under cone heat flux 65kW/m^2, DFT 0.4mm

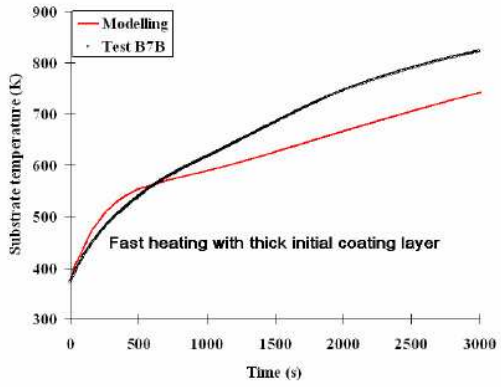

Figure 5 Prediction on experiment under cone heat flux 65kW/m^2, DFT 1.2mm

5. CONCLUSION

A mathematical model has been constructed in this study to model intumescent coating behaviour. Activation energies of the blowing agent and the charring material, the maximum expansion coefficient and bubble size are among the key parameters. Cone calorimeter tests have been conducted to explore the feasibility of obtaining these essential material properties for general application under different fire conditions. It has been successful to use key variables extracted from one test to predict other tests, which indicates the potential to use this mathematical model to predict intumescent coating behaviour under different fire conditions once these key parameters have been quantified from a small set of fire tests.

REFERENCES

[1] Wang Y.C., Goransson U., Holmstedt, G and Omrane A., "A model for prediction of temperatures in steel structures protected by intumescent coating, based on tests in the Cone Calorimeter", Proceedings of the 8th International Symposium on Fire Safety Science, Beijing, China, pp. 235-246(2005)
[2] Butler L, Baum H R and Kashiwagi T, "Three-Dimensional Modelling of Intumescent Behaviour in Fires," Fire Safety Science, Proc. 5th Int. Symp. 523 (1997)
[3] Mamleev V. S., Bekturov, E. A., Gibov, K. M., "Dynamics of Intumescence of Fire-Retardant Polymeric Materials", J. of Applied Polymer Science, 70, 1523 (1998)
[4] Di Blasi, C., Branca, C., "Mathematical Model for the Nonsteady Decomposition of Intumescent Coatings" AIChE J. 47:2359 (2001)
[5] Yuan J.F., Wang Y.C. "Efficient Modelling of Temperatures in Steel Plates Protected by Intumescent Coating in Fire" as a chapter in the book entitled Fire Retardancy of Polymers: New Strategies and Mechanisms, the Royal Society of Chemistry, U.K. (2008)
[6] Cagliostro, D. E., S. R. Riccitello, K. L. Clark, and A. B. Shimizu, ''Intumescent Coating Modelling,'' J. of Fire & Flammability, 6: 205(1975)
[7] Russell, H.W., "Principles of Heat Flow in Porous Insulators," J. of Am Ceram Soc 18:1(1935)
[8] Tsederberg, N.V., Thermal Conductivity of Gases and Liquids, THE M.I.T. PRESS(1965)
[9] Loeb, A.L., "A Theory of Thermal Conductivity of Porous Materials" J. of Am Ceram. Soc. 37:96 (1954)

THE PRACTICAL APPLICATION OF STRUCTURAL FIRE ENGINEERING ON A RETAIL DEVELOPMENT IN THE UK

FLORIAN BLOCK[1], CHAOMING YU[2] and NEAL BUTTERWORTH[3]

ABSTRACT

The British Building Regulations allow the application of performance based design methods to ensure the fire resistance of buildings. This has led to significant amounts of research and testing on the fire performance of structures. This research generated the understanding that steel framed buildings have an inherent fire resistance, which has in turn resulted in the development of specialist numerical calculation tools as well as simplified design methods for the fire design of steel-framed structures.

The paper describes the practical application of these structural fire engineering methods on the example of large retail and cinema complex in the UK. The finite element software Vulcan has been used to analyse the behaviour of large parts of this multi-storey building during a number of likely design fire scenarios in order to optimise the amount of applied passive fire protection to the structure. The building is constructed as a steel composite structure with normal down-stand composite beams supporting a composite floor on trapezoidal metal deck. This type of structure is ideal to utilise the benefits of tensile membrane action during a fire which can be used to omit fire protection from off grid secondary beams. Due to the size and the multiple usage and changing floor construction of the buildings five different sub-frames haven been analysed.

In the UK a number of simplified methods are currently applied to justify partially protected steel structures. These methods are based on individual bays only and therefore do not consider the effects of the surrounding structure. In order to investigate the differences further, the behaviour of the large sub-frame models has been compared with the results of individual bay analysis methods.

[1] PhD Engineer, Buro Happold Ltd, 2 Brewery Place, Brewery Wharf, Leeds LS10 1NE, United Kingdom
email: florian.block@burohappold.com
[2] PhD Graduate Engineer, Buro Happold Ltd, 2 Brewery Place, Brewery Wharf, Leeds LS10 1NE, United Kingdom
[3] MPhil Associate Director, Buro Happold Ltd, 2 Brewery Place, Brewery Wharf, Leeds LS10 1NE, United Kingdom

1. INTRODUCTION

This paper describes how a performance based approach has been adopted to optimise the structural / fire protection solution on a composite-steel framed structure in the United Kingdom (UK). The adopted solution involves designing the structure such that fire protection can be omitted from selected beams. There are several methods and design tools that are available to engineers. The mechanics and methodologies are not new, but this paper explains how finite element analysis has been adopted on a real project and examines the differences between four design methods (Vulcan[3], VulcanLite[3], TSLAB[4] and SCI P288[4]) when applied to a real structure.

2. REGULATORY FRAMEWORK

In the United Kingdom (UK), all buildings are required to comply with the requirements of the Building Regulations. Part B of the Building Regulations[1] relates to fire. In 1984 a new Building Act was passed and in 1985 the Building Regulations were revised. Since 1985, all versions of Part B of the Building Regulations have stipulated functional requirements that have to be achieved by a building. For structural stability in fire, the Building Regulation requirement is that, "The building shall be designed and constructed so that, in the event of fire, its stability will be maintained for a reasonable period". Designers and engineers are able to demonstrate compliance with these functional requirements by a variety of methods. The most simple and common approach is to follow the prescriptive recommendations of guidance documents and codes of standards. For structural fire resistance, the prescriptive standards recommended that elements of structure be tested in accordance with a standard fire test and that they achieve a certain standard depending on the purpose group and height of the building in question. However, as described above, alternative methods can be used to demonstrate compliance with the building regulations. Typically, where non-prescriptive methods are adopted, they will either demonstrate that the proposed solution achieves a standard that is at least as good as that which would be achieved by adopting a prescriptive solution ("equivalency"), or a performance based approach will be adopted to demonstrate that the proposed solution will achieve a suitable performance. In terms of structural fire resistance, a typical performance-based approach will be to demonstrate that the structure can maintain its stability for the entire duration of a realistic, worst-case fire.

3. METHODOLOGY

The paper explains the five steps which were followed to justify the omission of passive fire protection on selected beams:

Agree methodology with Stakeholders: At the outset, it is important to agree the approach with the relevant stakeholders, which are likely to include the client, the insurers, the design team and the controlling authorities. It is necessary to ensure that there is value to be gained from conducting a performance based approach, that the proposed approach does not increase the life-safety or insurance risk, that sufficient information and time will be available, and that the controlling authorities are likely to grant approval. Doing this before embarking on the analysis raises any issues at an early stage and reduces the project risk.

Develop design fires (including cooling): The temperature rise within the different structural elements of a fully protected structure will be similar for a given fire exposure. As

the structure gets hotter, deflections will increase and the load bearing capacity will reduce. Therefore, when comparing the relative performance of different fully protected structures, it is possible to use a standard fire curve. However, in a partially protected structure, the unprotected beams will heat up and cool down significantly quicker than the protected elements. This differential heating can have a significant impact on the performance of the structure and its survival period. Therefore, in the design of such structures, it is very important to consider different fire scenarios and heating regimes. For example, short hot fires can result in large differential expansion between protected and unprotected beams, which in turn leads to large differential deflections and high connection forces, but a long duration fire can have a bigger effect on the overall load bearing capacity of the system.

Develop assessment criteria: It is good practice to agree the assessment criteria prior to conducting the analyses. The selection of appropriate assessment criteria should consider the functional requirements of the structure at fire limit state. For example, some floors are required to be compartment floors, but others are not. If a floor is a compartment floor, it is required to maintain overall stability, prevent smoke and flames passing from the fire side to the non-fire side (integrity), and prevent excessive temperature rise on the unexposed surface (insulation). If a floor is not a compartment floor, it is only required to maintain its overall stability. Similarly, in some instances it is necessary for a structure to meet a particular assessment criterion for the entire duration of the fire, but in others it might only be for the heating phase or for the evacuation period.

Build geometry of the sub-frames and analyse for different fires: When assessing the performance of the structure at fire limit state, it is necessary to determine how much of the structure should be analysed to be representative. Simple design methods, such BS5950: Part 8[2], only consider individual elements. Others, such as VulcanLite[3], TSLAB[4] and SCI P288[4] consider individual bays. When adopting finite element analysis, it is often beneficial, or more realistic to consider large portions of the structure. The extent of the sub-frame adopted for finite element analysis is often a compromise between absolute accuracy and time available: it is typically impossible to analyse a complete structure, so a representative sub-frame will be selected and appropriate boundary conditions will be applied.

Assess connection forces: The differential heating that occurs in a partially protected floor system can result in high connection forces. Therefore, it is important to assess these connection forces and design appropriately. The connections can be designed to resist the forces, ductile connections can be used to reduce the forces, or the structure can be designed such that if the connections fail, overall stability will be maintained.

4. BUILDING DESCRIPTION

The example used in this paper to show the practical application of structural fire engineering methods is a large retail, leisure and cinema complex in north-west England. It occupies a triangular site and the building footprint is approximately 150m x 85m in plan and comprises 2 storeys plus a mezzanine floor. For design purposes the building can be considered to act as two separate structures due to the placement of a movement joint running north to south through the building. On the ground floor level the space is sub-divided into entrance, circulation and retail spaces. A service yard occupies the centre of the site splitting the building on ground floor level. The mezzanine level follows similar use to the ground floor but with the addition of leisure facilities along the southern edge of the site. Above mezzanine level the usage of the building is primarily leisure facilities. Double height bowling and cinema spaces are separated by a concourse area with the cinema spanning across the service yard located below.

The building is constructed as a steel composite structure with normal down-stand composite beams supporting an in-situ composite floor on metal deck. This type of structure is ideal to utilise the benefits of tensile membrane action during a fire which can be used to omit fire protection from off grid secondary beams. Due to the size and the multiple usage and changing floor construction of the buildings five different sub-frames haven been analysed. According to the Approved Document B[5], the fire resistance periods of the building is 60 minutes based on the height of the top occupied floors above ground.

5. DESIGN FIRES

Normal buildings should be designed for post-flashover, compartment fires. These are traditionally described by a compartment temperature with respect to time. However in any given building, there are an infinite number of time-temperature histories that could occur depending on the fire load and compartment characteristics. Clearly it is not possible to assess the impact of all possible fires; therefore an important step of a structural fire engineering assessment is to determine and agree the appropriate design fires. As mentioned above, partially protected structures should be exposed to a number of fires with different duration and temperatures including the cooling phase. The parametric fire curves, as given in EN1991 Part 1.2[6], have been used with different ventilation condition and are shown in Figure 1 below.

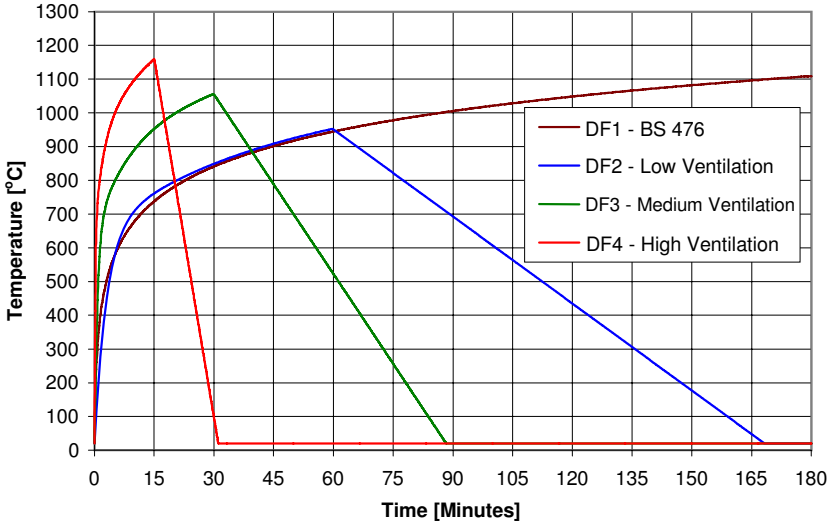

Figure 1: Design Fires

6. ACCEPTANCE CRITERIA

Fire resistance is generally defined by three criteria: Stability, Integrity and Insulation. Therefore, each of these parameters have to be assessed.

Stability: In order to ensure overall stability, it is necessary to ensure that protected beams will continue to perform as required. Limiting the deflection of protected beams to the same limits that are imposed in the Standard Fire Tests ensures that the protection on protected beams will continue to perform as required. Therefore, the deflection of protected

beams will be limited to span/20. In post-flashover fires, unprotected beams become hot, lose strength and ultimately contribute very little to overall stability of the structure. Therefore, it is not necessary to impose a deflection limitation on the unprotected beams. The overall performance of the structure (in terms of overall stability) does not rely on the performance of the slab as the slab will still act as diaphragm if deformed. Providing the performance of the stability members (protected beams and column) can be ensured, overall stability will be maintained. Failure of the slab will only lead to local failure. However, in the Cardington fire tests, deflections of approximately span/10 were experienced and there was no loss of local load carrying capacity. Therefore, if deflections are limited to span/10, not only will the overall stability be maintained, but it is also unlikely that any local collapse will occur.

Integrity: The requirement for integrity is achieved by ensuring that large cracks do not develop in the floor slab. Like most other finite element programs, Vulcan is unable to predict integrity failures; therefore, when it is necessary to maintain the integrity of the floor slab, checks should be put in place to ensure that integrity failures do not occur. This is most commonly achieved by limiting deflections as the deflection of the slab is an indication of its curvature (and the strain that is induced in hogging over protected beams), and if the curvature is too great, the reinforcement may fracture over the protected beams. Furthermore, excessive deflections within the slab could lead to a tension crack forming in the middle of the slab. In either of these scenarios integrity failures of the slab might occur. In reality, the curvature is a function of the differential deflection across the slab; therefore the differential deflection between the slab and protected beams should be assessed. Sufficient research and testing has not been conducted to allow specific guidance on deflection limitations to be developed. Therefore, typically, deflections are limited to those which have been demonstrated to be acceptable in tests. The BS476 Standard Furnace test[7] limits deflections to span/20. Therefore, it is likely that limiting deflections to span/20 would ensure that integrity failures do not occur.

Insulation is not affected by deflections (even if it cracks or spalls, the concrete material will be retained by the metal decking), and integrity failures in the slab will occur before insulation is lost. Therefore, the requirements for insulation will be ensured by complying with the prescriptive requirements for slab thickness.

7. FINITE ELEMENT ANALYSES

The software used to analyse the building is Vulcan, a three-dimensional frame analysis program, which has been developed mainly to model the behaviour of skeletal steel and composite frames, including the floor slabs, under fire conditions. The first step in the analysis process is to determine the relevant sub-frames.

7.1 Geometrical Modelling

An initial scoping study on individual bays using VulcanLite has been carried out in order to determine the required reinforcement mesh type as well as to conduct a cost-benefit analysis showing the economical viability of the project. Subsequently, a detailed assessment has been conducted on four representative sub-frames for the different parts of the building. The building geometry, the proposed fire protection regime and the location of the sub-frames are shown in Figure 2 below.

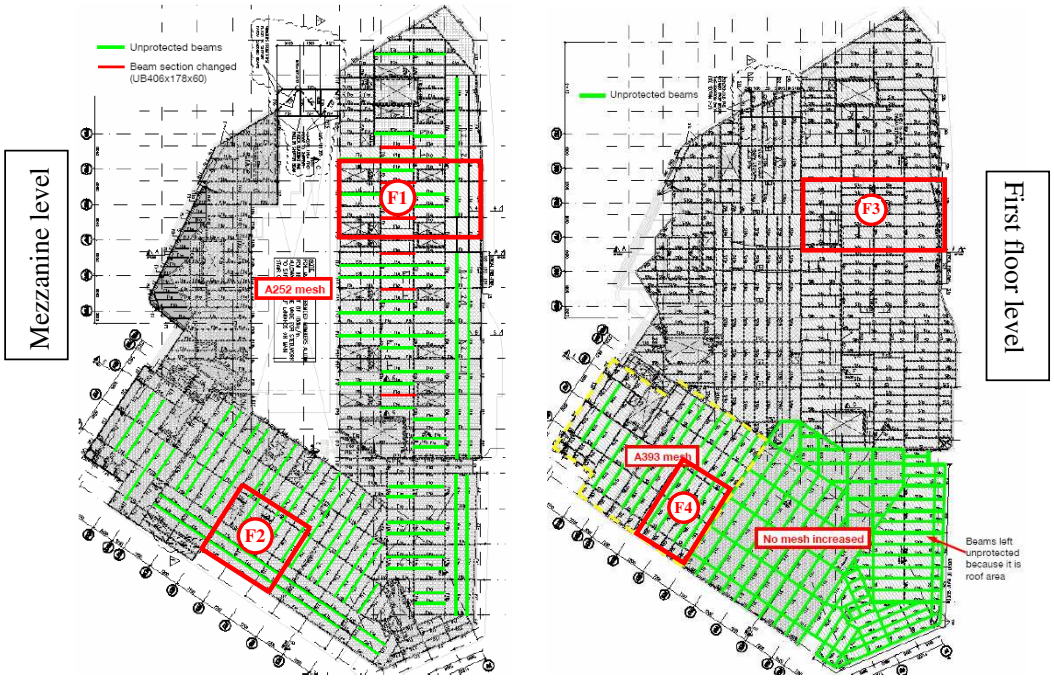

Figure 2: Geometry, proposed fire protection regime and the location of the sub-frames

Due to the constraints of this paper only model F2 and F3 will be discussed in here. The main characteristics of the models are described below.

Concrete Slabs: In the area of F2 the slab is a 150mm thick composite slab cast on Ribdeck E60 trapezoidal deck. As a result from the Stage 1 analyses, A252 is proposed to be the mesh size of the mezzanine floor. In the area of F3 the floor slab is a 200mm thick composite slab cast on a Holorib re-entrant deck. The analyses in Stage 1 suggested that an A393 mesh would be required to reduce the slab deflection in the compartment floor. Grade 35 normal weight concrete is used. According to BS5950: Part 8, a material strength factor 1.10 needs to be applied to the calculations of concrete at elevated temperatures. Therefore, in the numerical analyses, the concrete strength is 32 N/mm^2. As in F2 a trapezoidal deck is used only the continuous part of the slab is modelled in order to capture the worst case temperature distribution of the reinforcement. In F3 however, the full depth of the slab was used considering different stiffness parallel and perpendicular to the ribs, as a re-entrant deck heats up more uniformly.

Boundary Conditions: Where possible the advantage of symmetry in the structure was used in order to reducing computing time. On the symmetric lines, the translations perpendicular to the lines and the rotations along the lines were restrained. This is to account for the adjacent structure which has not been modelled, but would provide lateral restraint to the structure.

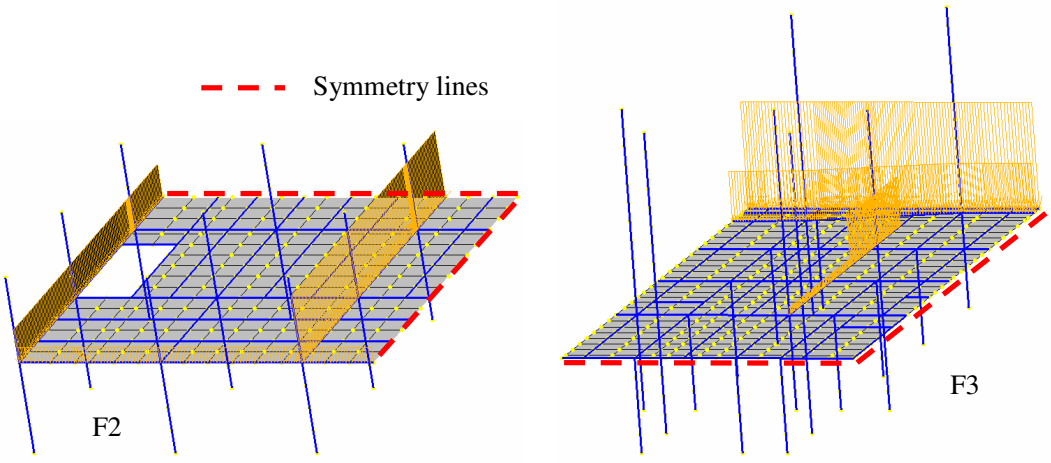

Figure 3: Vulcan models F2 and F3

Loadings: Characteristic design loads were provided, and the Fire Limit State loads were calculated in accordance with BS5950: Part 8, using partial safety factors of 1.0 for Dead Load and Permanent Imposed Load, and 0.8 for Non-permanent Imposed Load. The two Vulcan models are shown in Figure 3 above. The line loads and the applied boundary conditions are also shown. The loads introduced by the super-structure were represented by point loads at the top of the columns.

7.2 Material Temperatures

In order to determine the fire protection level for the protected elements it was assumed that a temperature of 620C and 550C was reached after 60 minutes in the beams and columns respectively. A heat transfer analysis of the beams and the columns has then been undertaken in accordance with EN1993 Part 1.2 [8]. In order to include the effects of thermal curvature, the web and each flange has been analysed separately. For the concrete slabs a 1D heat transfer calculation has been conducted including the effects of moisture in the concrete. For the three parametric fires the resulting temperature histories for protected and unprotected typical steel elements as well as for the slabs are shown in Figure 4.

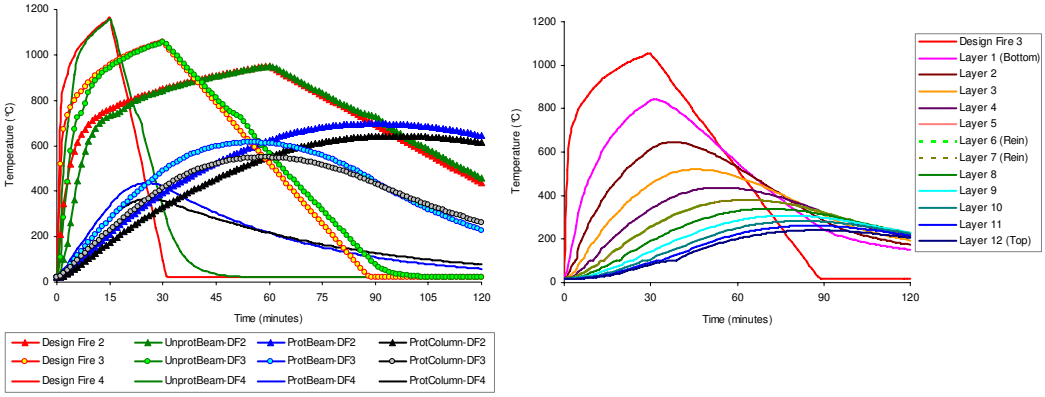

Figure 4: Material temperatures

It can be seen from Figure 4 that the slow fire (Design Fire 2) is critical for both protected beams and columns. The fast fire (Design Fire 4) causes the largest temperature differences between protected and un-protected beams as well as the hottest temperatures of the unprotected beams.

7.3 Results of the Numerical Analyses

After the non-linear analyses have been conducted the deflected shapes, deflections and forces can be examined and compared with the assessment criteria. The deflected shapes of the two models are shown in Figure 5 below.

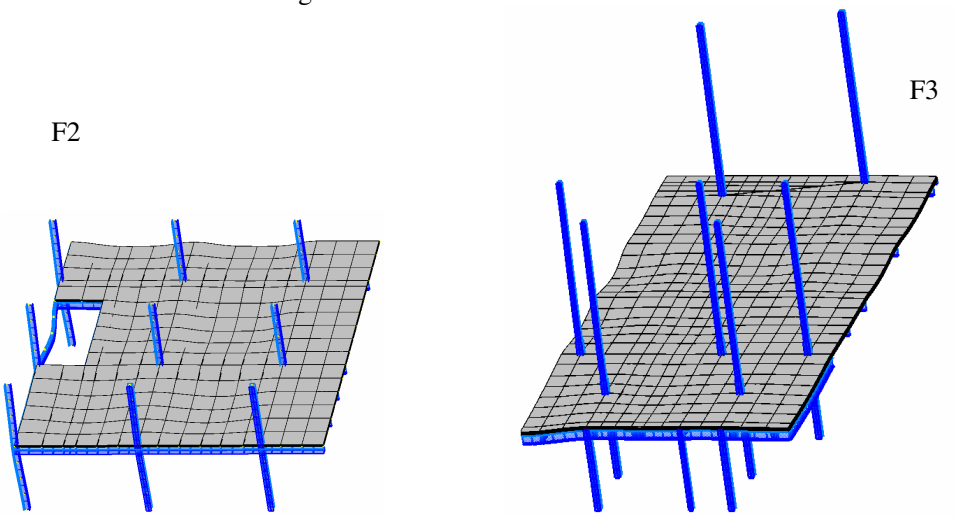

Figure 5: **Maximum deflections of the two Vulcan models**

Furthermore, the vertical deflections for the protected beams and the slab are shown and discussed below.

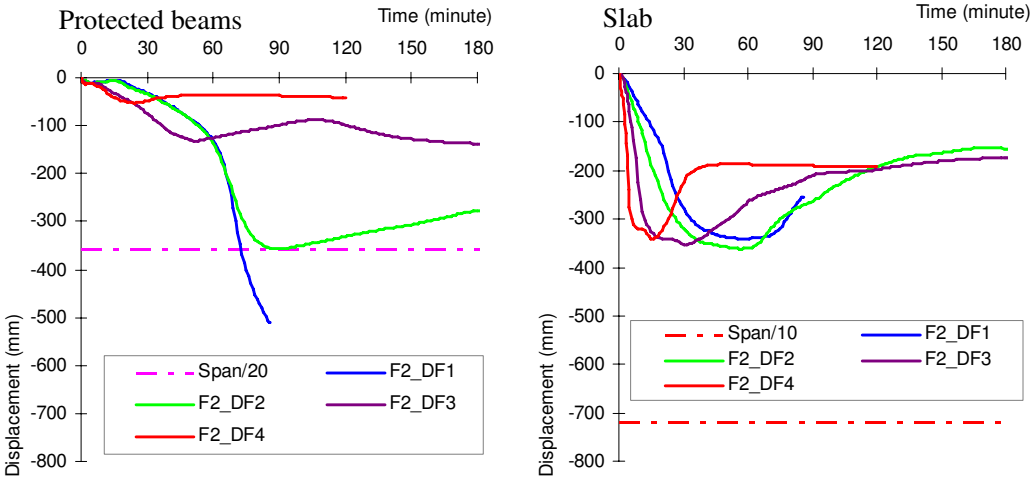

Figure 6 **Vertical deflections of the protected beams and the slab in F2**

From Figure 6 above it can be seen that the deflection of the protected beams and the floor slab remains above the relevant deflection limit in the parametric fire. The protected

beams exceed this limit in the ISO fire (DF1) but well after the prescriptively required fire resistance period of 60 minutes. Therefore, it can be said that the omitting of fire protection to the off-grid secondary beams is acceptable.

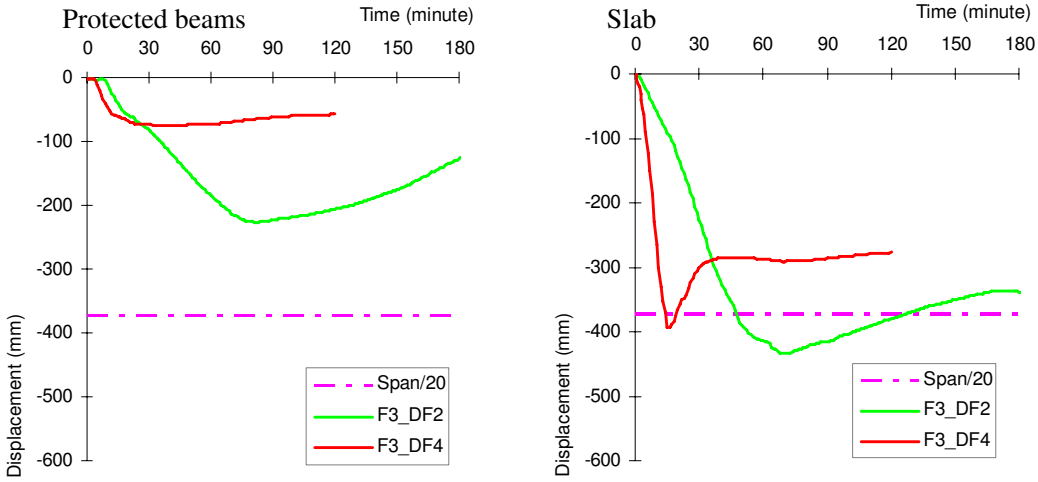

Figure 7 **Vertical deflections of the slab and the protected beams in F2**

The analyses on the model F3 in Design Fire 2 and Design Fire 4 were carried out. As F3 is on a compartment floor, span/20 should be taken as the deflection limits for both the slab and protected beams. It can be observed that the maximum differential deflections of slab in two design fires are both larger than span/20 in 60 minutes. Since the deflections of protected beams are still much less than span/20, the floor deflections should be introduced by the unprotected beams. It is indicated that increasing the section size of protected beams will not help to reduce the deflection of the slab. Therefore, on the first cinema floor, all the beams and columns should be protected in order to maintain the compartmentation.

8. CONNECTIONS

Generally, connection forces in partially protected structures are dominated by the differential thermal movements between the protected and the unprotected beams as well as the restrained of thermal expansion by the columns. As thermal stresses depend on the level of restrained the forces in the structure reduce with increasing flexibility exist between floor slab and beams as well as in the connections. The commercial version of Vulcan currently does not include the local behaviour of connections or the effects of local buckling of the beams. Therefore, any connection forces directly extracted from the software will be high and unrealistic as the structure is modelled as rigidly connected. However, the software can give a correct trend of the forces during the course of a fire. For the fast fire such a typical curve is shown in Figure 8.

It can be seen that in the first few minutes of the fire a peak in tensile forces in the protected beams and compressive forces in the unprotected beams is developed. This peak is caused by the quick heating and therefore thermal expansion of the unprotected beams. It is very likely that this peak will cause local buckling in the bottom flange of the unprotected beams as it could be seen for the full scale fire tests in Cardington. The buckling will release a lot of thermal forces in the whole system. The next occurrence of high connection forces will be during the cooling phase of the fire and is cause by the shortening of the plastically

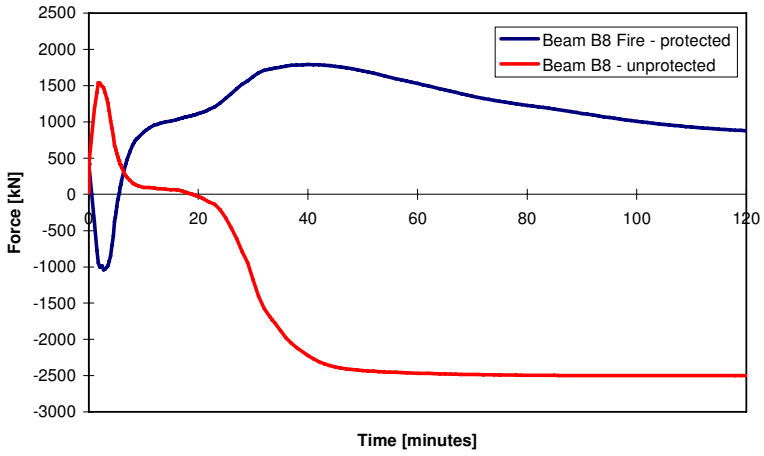

Figure 8: **Typical connection forces in the fast design fire**

deformed unprotected beams. It is this phase of a fire in which connection failure is most likely. One example of this could be seen during the fire tests in Cardington in which the fin-plate connections failed by bolt shearing. In order to prevent such a failure affecting larger parts of the structure three options can be given.

Firstly, the connections can be designed to resist the applied forces.

Secondly, sufficient ductility can be provided in the beam-to-beam connections to allow the thermal movements of the unprotected beams without breaking. Tests at the University of Sheffield [9] have shown that this can be delivered by double web cleat or partial depth endplate connections. These connections would only have to maintain their vertical shear capacity during and after the fire as they are ductile enough to follow the thermal movements without breaking.

Finally, it can be ensured that the unprotected beams can be supported after the connections have failed. For example, the bottom flange of the primary beam could be designed to support the shear loading transferred by the unprotected beam in the fire limit state by overlapping the unprotected secondary beam and the bottom flange of the primary beam. For this option the tying resistance of the connections should be reduced to the structurally allowable minimum to minimise the forces introduced into the structure before the connection fails.

For the connections between protected beams and columns in bays with unprotected beams, endplate connections should be provided. This type of connection has good fire performance as well and is particularly good at transferring compression forces due to the full contact between the endplate and the column flange whilst being ductile enough to deal with the initial tension forces until the unprotected beams have buckled.

9. SIMPLIFIED METHODS

In the UK simplified methods are currently applied to justify partially protected steel structures. Each of these methods has its advantages and disadvantages.

SCI P288 contains design tables that can be used to determine whether the partially protected structure will have sufficient load bearing capacity at fire limit state. The method is applied to a single bay of structure and the tables are quick to use. The method is restricted to rectangular geometries, certain bay sizes and a maximum fire resistance period of 60 minutes. It is not possible to assess likely deflections or connection forces. The tables only consider exposures to the BS476 Standard Fire Curve and as such do not consider the impact of the

differential heating between protected and unprotected elements. Therefore, it is the authors' opinion that SCI P288 cannot be used in isolation to justify partially protected structures.

TSLAB is a software program which implements the Bailey method. It is similar in scope and approach to SCI P288 but has additional features. It can be used for any rectangular geometry. It can adopt both standard and parametric fires but is limited to fire resistance periods of up to 120 minutes. The methodology considers individual bays. It assumes that there is no continuity over protected beams, which is a conservative assumption, but it also assumes that the protected beam do not deflect, which is a non-conservative assumption. Evidence suggests that within a practical range these assumptions compensate to give acceptable solutions, but there is no means of knowing whether this is true for all conditions. This is particularly true for edge or corner bays where there is no continuity over some of the projected beams anyway. Therefore, it is the authors' opinion that TSLAB should only be used for structures that fall within a certain range (the definition of this range is unclear and it is not the subject of this paper) and that it should be used with great care.

VulcanLite is a bespoke interface for Vulcan that uses a "wizard" to generate models for single bays of composite steel-framed structures. Modelling a single bay is sufficient for most buildings where the objective of the analysis is to omit fire protection from beams that do not frame into columns. VulcanLite is not limited to rectangular bays or uniformly distributed loads. It models standard or parametric fires and is not limited to any fire resistance period. Importantly, VulcanLite is based on fundamental mechanics and predicts actual structural performance in fire conditions, including deflections and forces. With the appropriate use of boundary conditions it can model the effects of continuity over the protected beams. As such, it can be used to deliver economic, safe and reliable solutions.

10. COMPARISON BETWEEN VULCAN AND SIMPLIFIED METHODS

As part of the study, the behaviour of the large sub-frame models has been compared with the results of individual bay analyse methods. The tables in SCI P288 could not be used for the study building as the tables are based on a partial safety factor for imposed load of 0.5 rather than the 0.8 which is recommend for all buildings other than offices.

As a comparison two different typical bays have been analysed within the models F2 and F3 analysed above. The results of this comparison are given in Table 1 below.

Table 1: **Comparison of different analysis approaches**

Model	Criterion	T-Slab	VulcanLite	Vulcan
F2	Slab	Pass (A393)	Pass (A252)	Pass (A252)
	Perimeter beams	Failed	Failed	Pass
F3	Slab	Pass (A393)	Pass (A393)	Pass (A393)
	Perimeter beams	Pass	Pass	Pass

One can see the benefit in running more advanced analyses. Although the original perimeter beams in model F2 failed in both simplified methods, it would be possible to increase the perimeter beam size and then justify a reduced mesh thickness using VulcanLite. However, if more of the structure is analysed, the columns and the surrounding structure provide sufficient longitudinal restraint to the perimeter beams to enable them to maintain their stability. For model F3, all approaches show that the chosen mesh size and the original perimeter beams are sufficient to withstand the loads at FLS under all design fires. It should

however, as described in Section 7.0, the final solution for F3 was fully protected as the cinema seating, which is supported on this floor, introduces significant point loads on most intermediate beams causing failure of the floor slab.

What could not be shown in this comparison was that in model F1 a number of beams between columns had to be increased in size due to the additional axial load and P-Δ effects. This could only be picked up by the Vulcan analyses and shows the benefit of including columns in the model. However, if one only wants to conduct an initial study or has to analyse a very simple building, VulcanLite would be sufficient. In addition, it the authors' opinion that VulcanLite is preferred over T-slab. This is primarily due to the fact that it predicts actual performance using fundamental mechanics, but also due to its ability to apply different boundary conditions, to include point loads, to model non-regular geometries, and to assess real deflections and forces.

11. CONCLUSION

This paper summarises the structural fire engineering assessment of a large retail and leisure development in the UK. After discussing the regulatory background in the UK, the methodology of a performance base assessment is described. As an important part of this methodology, assessment criteria have been specified to ensure that the requirements of the Building Regulations are fulfilled after omitting fire protection on selected beams. Furthermore, the importance to analyse a partially protected structure exposed to a series of design fires with different ventilation conditions including the cooling phase is highlighted.

On the example of two large sub-frame models it was shown how Vulcan can be used to calculate the temperatures, determine the structural response and process the results. The behaviour of connections in partial protected structures is discussed and three different options are given to ensure that local connection behaviour has no negative effect on the overall performance during and after the fire.

Finally, a comparison is made between the various available simplified methods to justify partially protected steel composite frames. In this instance, it was concluded that best value could be attained by analysing a large sub-frame using finite element analysis, but that using TSLAB or VulcanLite would result in a conservative design. Attention was drawn to some of the deficiencies of the simple methods and VulcanLite was identified as a viable compromise between approximate methods and finite element analysis of whole sub-frames.

REFERENCES

[1] Department of the Environment, Transport and Regions and Welsh Office, "The Building Regulations - Part B", HMSO, 2000.

[2] British Standards Institution, "BS5950 Structural use of steelwork in buildings – Part 8: Code of practice for fire resistant design", British Standards Institution, London, 2003.

[3] www.vulcan-solutions.com

[4] Newman, G. M., Robinson, J. T., Bailey, C. G., "Fire Safe Design: A New Approach to Multi-storey Steel Framed Buildings", SCI Publication 288, 2nd Edition. Steel Construction Institute, Ascot, UK, 2006.

[5] NBS, "Approved Document B - Fire safety, Volume 2 - Buildings other than Dwellinghouses", The Building Regulations 2000, UK, 2007.

[6] European Committee for Standardisation, "BSEN 1991 – Eurocode 1 – Basis of design and action on structures: Part 1.2: Action on structures exposed to fire",
[7] British Standards Institution, "BS 476: Fire Tests on building materials and structures: Part 20, Method for determination of the fire resistance of elements of construction (general principles)", British Standards Institution, London, 1987.
[8] British Standards Institution, BSEN1993-1-2: 2005, "Eurocode 3: Design of Steel Structures: Part 1-2: General Rule – Structural Fire Design", European Committee for Standardisation.
[9] Yu, H, Burgess, I.W., Davison, J.B., Plank, R.J, "Experimental Investigation of the Tying Capacity of Web Cleat Connections in Fire", EUROSTEEL 2008, Graz, Austria, 2008.

EXPERIMENTAL BEHAVIOUR OF STEEL COLUMNS WITH PARTIAL DAMAGE OF FIRE RETARDANT COATING IN FIRE

GUO-QIANG LI [1] and WEI-YONG WANG [2]

ABSTRACT

Two experimental studies are performed in furnace to investigate the fire behaviour of steel columns with partial loss of fire retardant coating. The specimens are 2.7m long columns fabricated with H shaped structural steel and the cross section of which is H140×100×6×6. The steel columns are connected by flush end-plates at the two ends and the axial load keeps constant with the load ratio of 0.55 subjected the elevation of temperatures in a furnace. The specimens are protected with 20mm depth of fire retardant coating. At the two ends of the steel columns, partial fire retardant coating is damaged artificially in order to investigate the behaviour of steel columns with partial loss of fire retardant coating in fire. The damage length of fire retardant coating is 7% of the complete length of the column for one specimen and 14% fore another one, which are approximately 19mm and 38mm long respectively. The temperature of atmosphere around the specimens is assumed to follow the ISO834 standard temperature. The temperatures of the furnace and specimens and the displacements of axial and lateral of steel columns are measured in the experiment. The temperature distribution along the steel column is also modeled by employing software package ANSYS and is compared with the measured results. The experimental results showed that the fire resistance of steel columns with partial damage of fire retardant coating is reduced. The damage length of fire retardant coating has a great effect on the fire resistance of steel columns. The failure of the specimens is manly resulted by the buckling at the portion where the fire retardant coating is damaged.

[1] Professor, Tongji University, Department of Building Engineering, Shanghai, China
email:gqli@mail.tongji.edu.cn
[2] PhD student, Department of Building Engineering, Tongji University, Shanghai, China
email:wwyong200@yahoo.com.cn

1. INTRODUCTION

It is known that unprotected steel structures do not have the desirable fire-resistance because the temperature of unprotected steel components increases rapidly in fire due to the high thermal conductivity of steel. Spray-on fire retardant coating (FRC) are widely used to protect steel structures against fire because spray-on protective materials can efficiently slow down heat transfer from fire to steel components, and hence lower the rate of temperature increase in steel components. However, spray-on materials are often rather fragile, and they may be easily damaged by mechanical actions, such as impacts, earthquakes and explosions, resulting in a possible fire resistance reduction for the steel components originally protected. The tragic events in New York on September 11, 2001 have dramatically shown that mechanical accidental actions followed by a fire can cause local structural failure and even progressive collapse of tall buildings. Thus, it is essential to understand the effect of partial protection damage caused by mechanical actions on the fire resistance of steel columns.

A few numerical studies have been carried out to investigate the effect of partial spray-on protection damage. Wang Jia et al[1] conducted finite element analysis to predict the temperature distribution of steel columns with partial fire protection loss and found that the length and location of fire protection loss has little impact on the model of temperature distribution over the length of steel components.

Wang Wei-yong et al[2] proposed a method to predict the capacity for stability of restrained steel columns according to principle of stationary potential energy. LI Guo-qiang et al[3] presented a simple approach for predicting the behavior of steel columns in fire with partial damage of FRC based on differential equation of equilibrium.

Tomecek and Milke[4] carried out a two-dimensional finite element study to investigate the effect of spray-on protection loss on the fire resistance of steel columns, and showed that a 4 percent loss of protection resulted in a 15 percent reduction in the time to reach the thermal endpoint criteria for a one-hour rated W10X49 column and a 40 percent reduction in the time for a two-hour rated W10X49 column. An important observation was that the reduction in time was not as severe for a massive column as for a non-massive column. For instance, a W14X233 column showed only a 15 percent reduction in time with the loss of 4 percent of protection during a two-hour exposure. This is appreciably less than that experienced with the W10X49 column. Thus, the massiveness of the column appears to be an important factor in assessing the temperature rise of the column for missing protection as well as for a completely protected column. Ryder et al.[5] also conducted investigation on the same subject by three-dimensional finite element analyses and showed that the fire resistance of a steel column protected with a spray on fire resistant material can be severely diminished if even a small portion of the protection is removed. YU KANG et al[6] carried out a numerical study to investigate the fire resistance reduction of protected steel beams caused by partial loss of spray-on fire protection and found that partial loss of spray-on fire protection can cause a significant moment capacity reduction for protected steel beams exposed to fire. The effect of fire protection loss on the cross-section moment capacity reduction is strongly dependent on the area of protection loss. Besides, the cross-section moment capacity reduction is also affected by several other factors, such as damage shape, damage location, damage penetration and the weight of steel section.

The results of a heat-transfer analysis of steel columns with partial loss of fire protection using the finite element method were also presented by Milke et al[7]. The results indicated that for a given exposure the area of the missing protection and the size of the column are found to have an appreciable effect upon the thermal response of the column regardless of the protection thickness and the area of the missing protection seems to be the primary factor in the temperature rise of the column. Mario Fontana[8] and Markus Knobloch[9] studied the fire behaviour using a three-dimensional finite element heat transfer and structural model, taking into account geometrical nonlinearities, local temperature distributions, thermal strains, and temperature dependent material properties. The results confirmed that local damage of fire protection is a decisive factor for the fire resistance of steel columns and it is important to avoid FRC damaged by periodical repairs or using robust fire protection systems. Stephen PESSIKI[10] performed an analysis to examine the behaviour of steel H columns in fire with damaged spray-applied fire resistive material subjected to concentric axial compression. The conclusions declared that the removal of even relatively small amounts of fire resistance material from the column flange causes dramatic decreases in column axial load capacity for fire resistance duration in excess of 30 minutes. A simplified approach in the temperature domain using the temperature endpoint criteria for steel columns was used in ASTEM E119[11] to calculate the fire resistance of steel columns with partially missing fire protection.

It seems that finite element method have been employed by nearly all the previous researchers to study the temperature distribution and fire resistance of steel members with partial loss of sprayed-on fire insulation material. Although the FEM is powerful, it is not straightforward for understanding the failure mechanism of steel members in fire with partial loss of FRC. In this paper, two experimental studies are performed in furnace to investigate the fire behaviour of steel columns with partial loss of fire retardant coating, the results of which may be used as the date-base for calibrating the analytical approach including FEM.

2. EXPERIMENTAL STUDY

2.1 Test arrangement and instrumentation

Tests were performed in a furnace. The sketch of the experimental set up is shown in Fig.1. The temperature-time curve of the furnace follows the ISO834 standard. The instrumentations include displacement transducers for measuring axial and lateral displacements of the steel columns, load transducer for measuring load and thermocouples for measuring the temperature of the furnace as well as the specimens. Four displacement transducers were employed in the experiments. One of which is used to measure the axial displacement and the others for measuring the lateral displacement of the specimens. Nine thermocouples are utilized to measure the temperature of the specimens, three for measuring the temperature on the portion of FRC damaged and the others for the portion with integrated FRC. The axial load, simulating the internal force in the columns, was introduced by a hydraulic jack attached to a reaction frame and loaded lever and powered by a pressure-controlled pump, which kept constant as the specimen expanded and buckling due to

increasing temperature. Both FRC and aluminium silicate blanket are used to protect the steel portion of the reaction frame in the furnace from the fire. The arrangement of the thermocouples and displacement transducer over the specimen is shown in Fig.2.

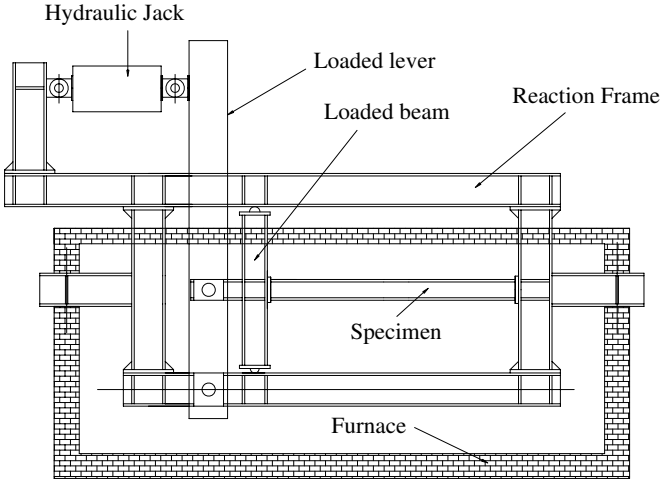

Fig 1 -Sketch of the test set-up

The testing procedure comprises three steps. Firstly, the specimen is loaded axially up to a pre-determined load level. Then start fire in the furnace and maintain the load constant on the specimen. Finally, stop fire in the furnace when failure occurs on the specimens. Temperatures and displacements were recorded at different time in constant-load tests.

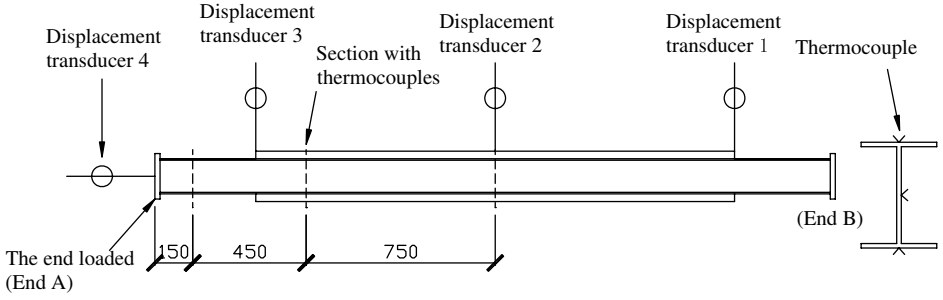

Fig 2 -Thermocouples and displacement transducer arrangement

2.2 Specimen details

The specimens are 2.7m long columns fabricated with H shaped structural steel and the cross section of which is H140×100×6×6. The steel columns are connected by flush end-plates at the two ends and the axial load keeps constant with the load ratio of 0.55 subjected the elevation of temperatures in a furnace. The load ration is defined as a ration of the load on the steel column to column buckling resistance at the normal temperature.

The specimens are protected with 20mm depth of fire retardant coating. At the two ends of the steel columns, partial fire retardant coating is damaged artificially in order to investigate the behaviour of steel columns with partial loss of fire retardant coating in fire. The damage length of fire retardant coating is 7% of the column length for one specimen and

14% fore another one, which is approximately 19mm and 38mm long respectively. The specimen detail is shown in Fig 3.

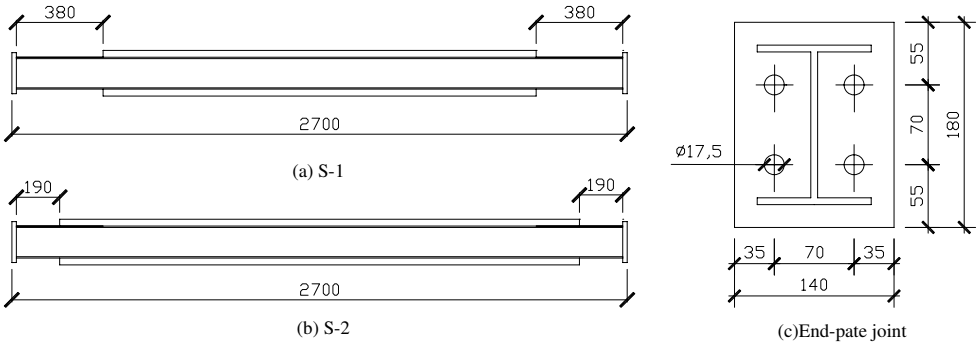

Fig 3 -Specimen details

2.3 Temperature distribution

Fig. 4 and Fig. 5 show typical variations against time of the temperatures of the furnace atmosphere, the portion of the steel columns on the damaged FRC, the portion on the integrated FRC during the heating and cooling phases. The temperature of the fire could be controlled to closely follow the ISO834 standard fire temperature curve except the beginning. Due to the fire protection on the portion with integrated FRC its temperature initially rose much more slowly than the rest of the column. The difference between the temperatures of the portion with damaged FRC and integrated FRC increased to almost 500 °C after about 25 min. After the fire stops, as the rate of rise in fire temperature reduced, the rate of rise of temperatures in the portion with damaged FRC also reduced as a result of the lower radiation increase. However, conduction of heat into the portion with integrated FRC continued.

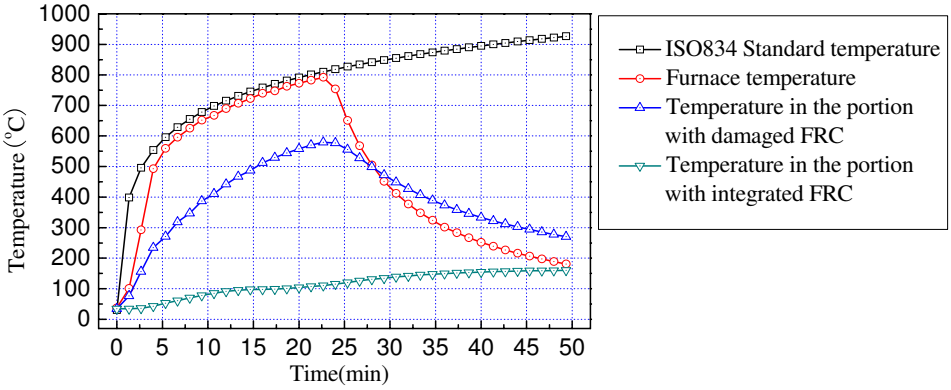

Fig 4 -Temperature-time curve of Specimen S-1

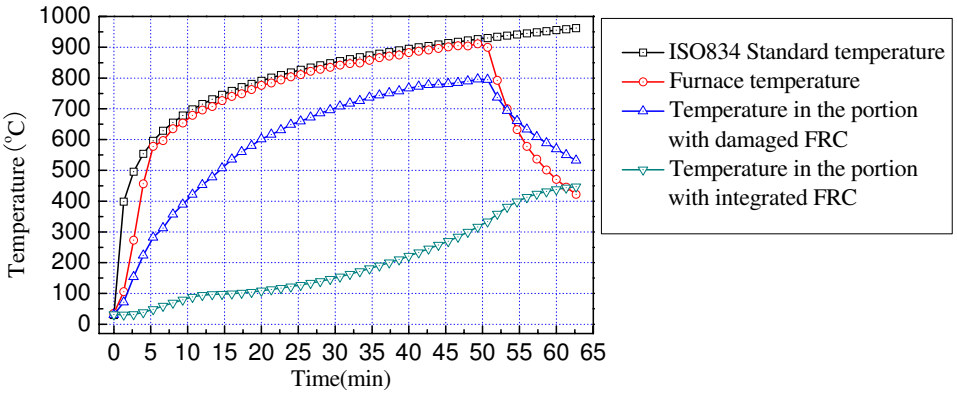

Fig 5 -Temperature-time curve of Specimen S-2

2.4 Axial displacement and failure temperatures

Fig. 6 shows the time–axial displacement curves for columns with partial FRC damage. For specimen S-1, after the specimen is exposed to fire for 15 minutes, the axial displacement increases rapidly and the buckling occur. However, for specimen S-2, the time exposed to fire can last 40 minutes due to the length of the column subjected to fire is short. Fig 7 shows the temperature-axial displacement curves for specimens. The load bearing capacity of steel columns will be reduced with the elevation of temperature and the steel columns will fail when the load bearing capacity reaches ultimate bearing capacity in fire. When failure occurs, great displacement along axial will appear.

With the elevation of temperature of steel columns, the load bearing capacity will decrease and failure occurs when buckling, and the axial displacement of the column will increase rapidly. Based on the experiment results, critical temperature of steel columns with partial FRC damage is defined here as the temperature at which the axial displacement increase abruptly. As can be seen from Fig 7, the critical temperatures of the specimen S-1 and S-2 are 500 and 750 respectively.

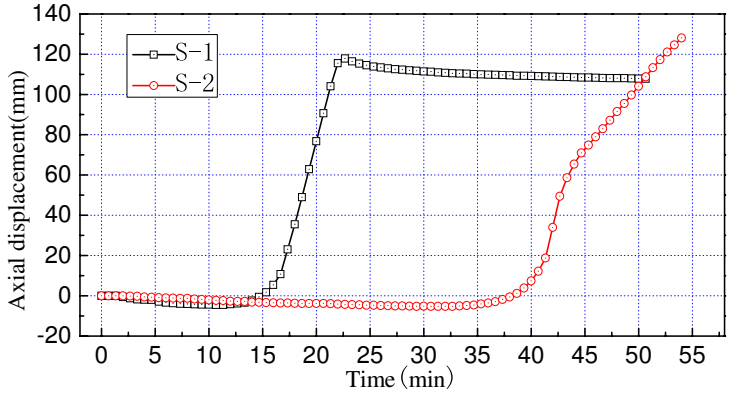

Fig 6 -Axial displacement-time curve of the specimens

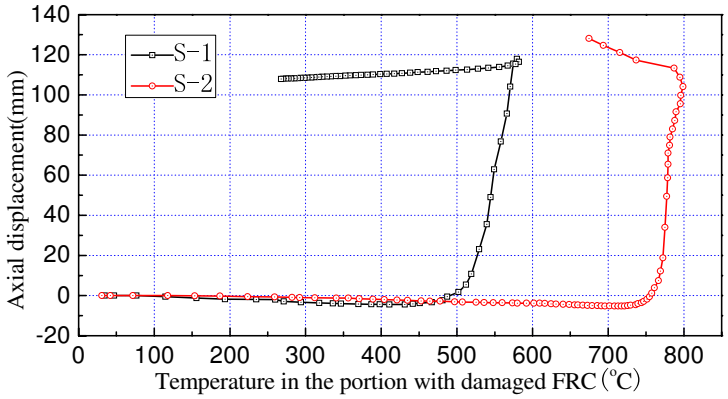

Fig 7 -Axial displacement-temperature curve of the specimens

2.5 Failure of specimens

Fig 8 and Fig 9 show the failure of the two specimens. For specimen S-1, the buckling only occurs around the weak axis on the portion with damaged FRC near to the load applied. For specimen S-2, buckling occurs on the two parts of the column with damaged FRC. The buckling at the portion near the end of load applied is more serious than the other portion which can be seen clearly form the Fig 11.

(a) end A (b) end B

Fig 8 -Failure of Specimen S-1

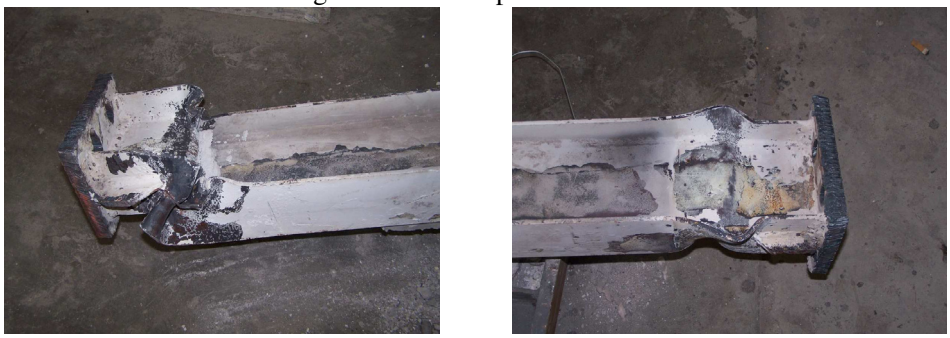

(a) end A (b) end B

Fig 9 -Failure of Specimen S-2

3. HEAT TRANSFER ANALYSES

The heat transfer mechanisms included in the heat transfer analyses are conduction, convection and radiation. Solid70 elements were used to model both steel columns and fire retardant coating. These elements are three-dimensional eight-node linear heat transfer elements. Fig 10 shows the finite element model of S-1 and S-2. Thermal conductivity of the steel as a function of temperature was specified as given in the Eurcode 3[12]. Similarly, the specific heat of the steel as a function of temperature was specified as given in the Eurcode 3[12]. Convection and radiation boundary conditions were specified where member surfaces were exposed to fire. The thermal conductivity and specific heat of the FRC are 0.05 and 1100 respectively, which were given by the coating manufacture company. The density of the coating is 350 Kg/m3.

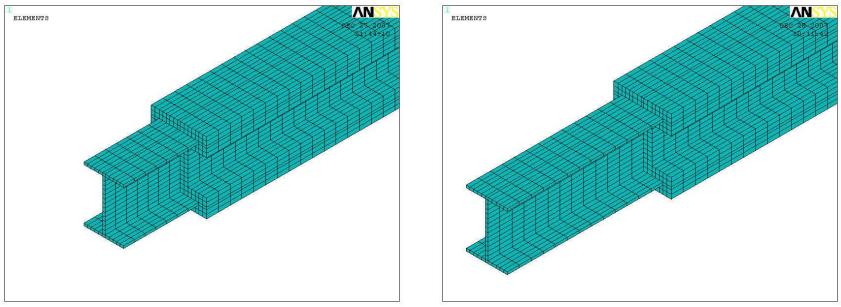

Fig 10 -Finite element model of S-1 and S-2

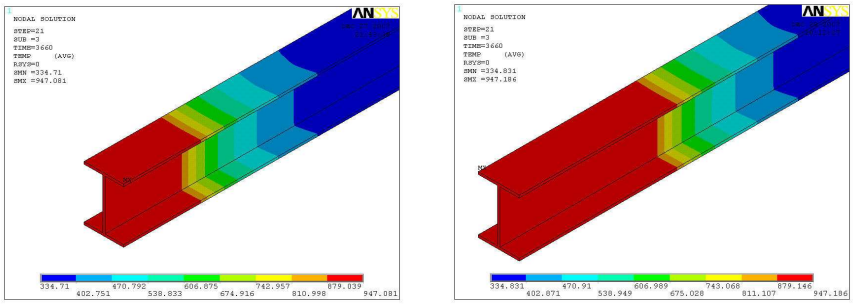

Fig 11 -Temperature distribution of S-1 and S-2 (vertical)

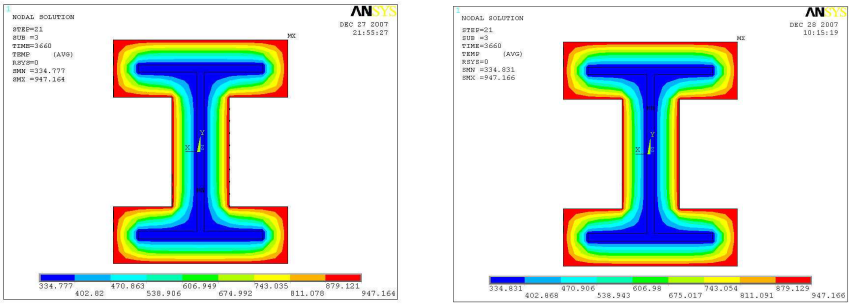

Fig 12 -Temperature distribution of S-1 and S-2 (transverse)

The results of the heat transfer analyses are shown in Fig 11 and Fig 12. Fig 11 shows

the temperature distribution of the steel along the vertical direction and Fig 12 shows the transfer direction. As can be seen from the figs, the temperature is high at the portion without FRC and the temperature is low at the portion with FRC. There is a temperature transition between the two portions. On the section of steel columns, the temperature is symmetrical. Fig 13 and Fig 14 show the comparison of results between analysis and experiment. The result in Fig 13 and 14 shows that the temperature of the steel of both specimens with FRC obtained with analytical prediction and experimental measurement agrees with each other well, but as for the temperature at the portion without FRC, there is some difference between the two results, which may be due to the boundary condition in the analyses is different to the experiment. In the experiment, there is a loaded beam connected to the specimens.

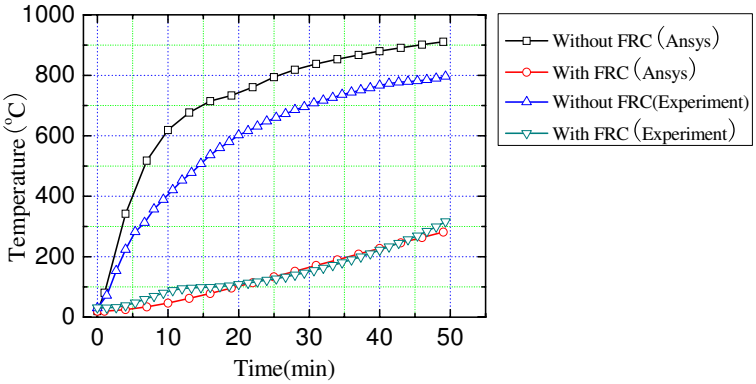

Fig 13 Temperature comparison of S-1 between ANSYS and experiment

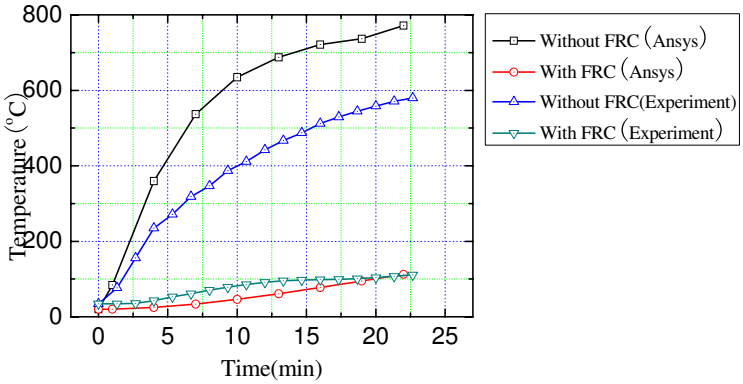

Fig 14 Temperature comparison of S-1 between ANSYS and experiment

4. CONCLUDING REMARKS

Through the experimental study on the fire-resistance of steel columns with partial fire retardant coating damage, the following concluding remarks may be drawn:

1) The failure of the columns with partial damaged FRC in fire happens at the part of FRC damage;

2) Damage length of the FRC has a significant influence on the fire resistance of the steel columns; the shorter the damage length of the FRC, the higher the critical temperature of

the steel columns, at which the columns fail;

3) The failure mode of the steel columns with damaged FRC is buckling at the part of FRC damage.

ACKNOWLEDGEMENT

The support of the Natural Science Foundation of China for Innovative Research Groups (Grant No.50621062) and Key Project (Grant No. 50738005) on the study reported in this paper is gratefully acknowledged.

REFERENCES

[1] WANG Jia, LI Guo-qiang. Effect of Local Damage of Fire Insulation on Temperature Distribution of Steel Members Subjected to Fire. *Structural Engineers*. 2005; 21(5):30-35.

[2] WANG Wei-yong，LI Guo-qiang，WANG Pei-Jun. Stable bearing capacity for Restrained Steel Column after Damage of Fire Retardant Coating in Fire，*Chinese Quarterly of Mechanics*，(In press).

[3] LI Guo-qiang, WANG Wei-yong, CHEN Su-wen. Ultimate Bearing Capacity for Steel Columns after Damage of Fire Retardant Coating in Fire. *Engineering Mechanics*. (In press).

[4] Tomecek DV, Milke JA. A Study of the Effect of Partial Loss of Protection on the Fire Resistance of Steel Columns. *Fire Technology*. 1993; 29(1): 4-21.

[5] Ryder NL, Wolin SD, Milke JA. An Investigation of the Reduction in Fire Resistance of Steel Columns Caused by Loss of Spray-Applied Fire protection, *Journal of Fire Protection Engineering.* 2002; 12(1): 31-44.

[6] Kang Y, Hadjisophocleous GV, Khoo HA. The effect of partial fire protection loss on the fire resistance reduction of steel beams. In: Fourth international workshop Structures in fire, Aveiro. Portugal. May 2006. pp: 63-74.

[7] Milke JA. Analyses of the Impact of Loss of Spray-Applied Fire Protection on the Fire Resistance of Steel Columns. In: Davies D. Evans (Ed.), Fire Safety Science–Proceedings of the Seventh International Symposium, Worcester, USA, 2003.

[8] Fontana M, Knobloch M. Fire resistance of steel columns with partial loss of fire protection. In：Proceedings of the IABSE Symposium Shanghai 2004，Metropolitan Habitats and Infrastructure, IABSE Report Vol. 88, Shanghai, China, ISBN 3-85748-110-2, 2004, pp. 352f.

[9] Knobloch M, Raveglia E, Fontana M. Partial loss of fire protection and structural collapse of high-rise buildings. In: International Congress Fire safety in tall buildings, University of Cantabria, Santander, Spain. October 2006.

[10] Stephen PESSIKI, Kihyon KWON, Byoung-Jun LEE. Fire load behavior of steel building columns with damaged spray-applied fire resistive material. In: Fourth international workshop Structures in fire, Aveiro, Portugal. May 2006. pp: 235-245.

[11] American Society of Testing and Materials, ASTM E-119 00a, Standard Test Method for Fire Tests of Building Constructions and Materials, ASTM Philadelphia, 2000.

[12] Eurcode 3: Design of Steel Structures-Part 1.2: General Actions-Structure Fire Design, British Standards Institution, DD ENV 1993-1-2001, September 2001. London, 66p.

POST-EARTHQUAKE PERFORMANCE OF PASSIVE FIRE PROTECTION SYSTEMS

P.C.R. COLLIER[1]

ABSTRACT

This project has shown that the post-earthquake performance of passive fire protection systems is definitely reduced when subjected to a design level earthquake. The amount of reduction in fire resistance of a 60 minute plasterboard lined wall can be as much as 50%. This is important given that active fire protection systems such as sprinklers may have also been rendered inoperable in the earthquake event. This is a dual problem in that a reduction in the fire resistance requirements of up to 50% may have been permitted because sprinklers were included as part of the fire design. The problem may be further compounded by the increased likelihood of fire outbreak due to disruption of building activities and services. Furthermore, Fire Service attendance cannot be relied upon due to the likelihood of multiple call-outs and possible impediment/blockage of road access. Finally, egress from buildings may be restricted by blocked exit-ways and injuries to people increasing the escape times.

1. INTRODUCTION

The damage caused to passive fire protection systems by earthquake is highly variable and, as a consequence, the reduction in their fire resistance is similarly uncertain. This project[1] endeavoured to quantify the reduction in the fire resistance of a series of plasterboard lined lightweight timber and steel-framed walls after being subjected to simulated earthquake racking to a range of drift ratios extending above and below (+/-) the code limit. The resultant earthquake damage was shown to be a primary cause of the reduction in fire resistance when the walls were subjected to a

[1] Senior Fire Engineer BRANZ Ltd, Private Bag 50 908, Porirua City New Zealand
Email: PeterCollier@branz.co.nz

fire resistance test. The predominant cause of the reduced fire resistance was due to flaming from gaps caused by detachment of the wall linings in isolated locations resulting in Integrity failures, rather than Insulation failures, and as a result of more general failure of the exposed lining. The Integrity failures, in general, occurred around the perimeter of the wall specimens where the majority of the damage occurred and the detachment of the lining was directly attributable to the security of the edge detail in the simulated earthquake racking. The Insulation fire resistance was also shown to be adversely affected by the racking damage but not to the same extent as the Integrity fire resistance and, as a consequence, was not the initial failure recorded in the trials conducted. A subjective judgement of the likely reduction in fire resistance can be made by assessing the damage resulting from the racking process. The amount of reduction in fire resistance of a 60 minute plasterboard lined wall can be as high as 50% in a design level displacement cycle.

2. BACKGROUND

The role of passive fire protection (PFP) systems[2] includes protecting the means of escape from a building in the event of fire, and the control of internal and external fire and smoke spread. Also, previous research[3] has highlighted some of the implications of current fire safety design philosophies based on Fire Service response times, fire-fighting water supplies, and active fire suppression systems (especially sprinklers), which may not be viable following a major earthquake. The likelihood of fires starting is also significantly increased by earthquake and the Fire Service is unlikely to be able to respond quickly.[4 5 6 7 8]

The magnitude of the simulated earthquakes applied to the test walls was based on the characteristics of a moderate earthquake of MM8 intensity (Modified **Mercalli** Intensity Scale) on intermediate soils.[9] In Wellington, New Zealand such an event is considered to be represented by a magnitude 6.0 to 6.5 (Richter scale) earthquake (these earthquakes have a return period of approximately 140 years with a 30% probability in 50 years). The maximum likely inter-storey drift of a 13 storey moment resisting frame building is 1.0 to 1.5%.[10] This is considered a moderate earthquake likely to cause structural damage to a number of buildings of this type, in addition to extensive non-structural damage.

The effectiveness of passive fire protection can be easily compromised where, for instance, in one study over 24% of doors were either removed or wedged open.[11] Another study indicated that only 0.4% drift would result in visible damage and allow smoke spread, and that fire spread would occur at 0.85% when plasterboard is likely to separate from framing.[12] Japanese recommendations[13] suggest a 50% effective reduction in fire resistance for partitions subject to a transient drift of 0.33%. The quality of the workmanship may have an effect on the fire resistance in the absence of any damage caused by earthquake,[14 15] where for poorly constructed plasterboard systems the failure to the Insulation criteria was found to occur 5 minutes earlier on average compared with standard construction walls.

At present new buildings in New Zealand between 30 and 58 m in height typically require 45-60 minutes FRR.[2] However, these buildings are also required to be sprinklered, which makes the situation worse should the sprinkler system be rendered inoperable in an earthquake. Failure rates[3] of sprinklers in buildings in earthquakes show a wide variation, depending on the data source, and whether it is the water supply which is under consideration or reticulation within a building. The range

of data for the reliability analysis suggests that without redundancy systems installed for the water supply and adequate seismic restraint on the sprinkler pipework within a building, the reliability could be as low as 0%. So the fire protection that remains might only be passive, depending on how that survives.

Some PFP systems, such as gypsum plasterboard walls, are very vulnerable to earthquake damage.[16] This can lead to a reduction in fire resistance ratings, thereby threatening the fire safety of the occupants, particularly for walls protecting escape routes. Experimental testing of timber-framed walls under lateral earthquake load indicated that the damage sustained by the wall system became significant at a drift level of 0.6%. This is where considerable deformation of the plasterboard around the nails began to occur. Such deformation would be significant enough to allow the fire cell to be compromised. The additional damage caused by further cycling with drift ratios to 1.3% may result in the loss of the majority of the fire resistance. Lightweight timber partitions are vulnerable to losing their fire resistant capability and this is especially important if the wall is protecting an escape path such as a stairwell. Following an earthquake in a building greater than about 10 storeys, in which sprinklers do not operate and the walls are damaged, the occupants may be unsafe because the expected escape time is greater than the expected failure time of the fire-rated walls surrounding the escape route.

A further study of urban fire spread post-earthquake[5] concludes that if passive fire resistance fails comprehensively, then the risk of fire spreading through buildings and onto neighbouring buildings is increased.

3. EARTHQUAKE RACKING TESTING

Loading frame and instrumentation

A diagrammatic representation of the racking apparatus used to simulate the earthquake exposure is shown in Figure 1. The walls for testing were constructed in a 3000 x 3000 mm fire testing frame leaving a gap around the sides and top of the wall. Gaps of 45 to 90 mm were left at each end to accommodate the 1.5 to 3% maximum drift anticipated, and a gap of 140 mm on the top edge to attach a loading frame connected to a hydraulic ram to apply the racking force. Load skates were positioned at each top corner to minimise uplift and rocking of the wall. A load cell was attached to the hydraulic loading jack to monitor the load. The wall deflection was measured by a main deflection potentiometer on the top plate and six other potentiometers were used to apply corrections for:

- uplift at top corners
- horizontal movement of the bottom edge of the wall
- loading frame attachment to the top plate
- distortion of the fire resistance test frame.

All data was recorded in a data logger and corrections applied for the distortion of the outer frame and sliding movement of the test specimen etc. A typical hysteresis graph is plotted in Figure 2, and the racking results are summarised in Table 1.

Seven racking trials with timber and steel-framed specimens were performed.[1] An energy-based methodology[17] was adopted for simulating the earthquakes. This permitted the application of the loading cycle at a much slower frequency compatible with the jacking equipment. The objective was to simulate as realistically as possible

the number of cycles, displacement and energy dissipation that would be common in an earthquake to that deliverable in a laboratory situation as an experiment. In other words, the specimen wall was subjected to cyclic loading to cause similar damage to that which would result from an earthquake by cycling and building up to oscillations causing an equivalent amount of damage

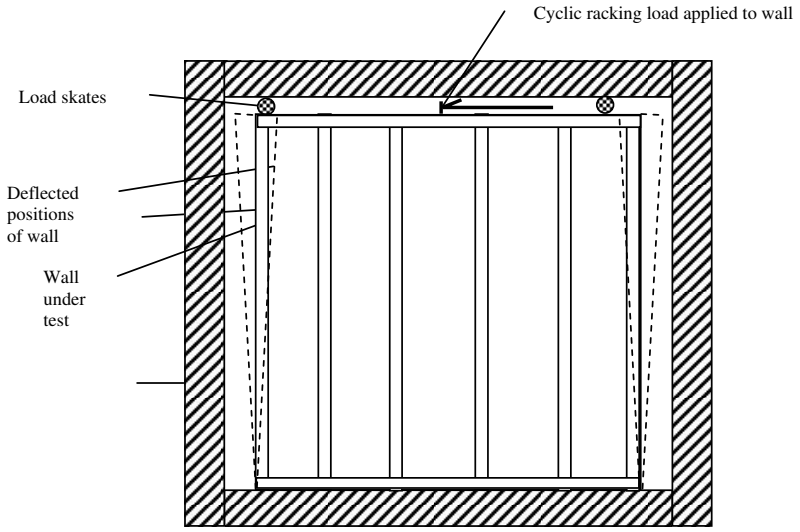

Figure 1: Racking of walls

A typical force-deflection hysteresis graph after correction for frame and restraint movement is shown in Figure 2. The force required for the initial deflection of 8 mm is 16 kN (this is a maximum), and thereafter the force required for the greater deflections actually reduces. This drop-off of the required force is typical once the fixity of the plasterboard to the wall frame has been broken.

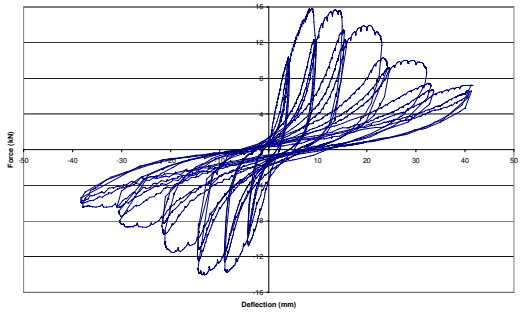

Figure 2: Typical force-deflection hysteresis graph (corrected)

Earthquake simulation by racking

Details of the racking tests are summarised in Table 1, and a typical hysteresis plot generated from the racking of a wall through the full range of cycles is shown in Figure 2.

Table 1: Summary of racking tests Phase 1

	FR3362A	FR3362B	FR3362C	FR3362D	FR3362E	FR3362F	FR3362G
% drift	-1.04, 0.95	-1.32, 1.43	-1.07, 0.84	-1.6, 1.34	-1.9, 2.5	- 1.35, 1.12	-1.35, 1.19
Lining fixing details	(1)	(2)	(3)	(3)	(3)	(4)	(4)
Framing material	Timber	Timber	Timber	Timber	Timber	Steel	Steel
Special features				L-shaped side studs	Double side studs		Included timber door
Lining detachment area mm x mm	3000 (w) x 600 (h) mm top	3000 (w) x 600 (h) mm bottom	Lining was relatively intact on framing	3000 (w) x 600 (h) mm bottom and in particular the corners	Hardly detached at all, but deformed on all 4 corners on both sides	Detached 3000 (w) x 2200 (h) at top. Bottom 800 remained attached	Detached 3000 (w) x 2200 (h) top
Lining to frame gap	7-8 mm	6 mm	~1 mm	7-8 mm	<1mm	5-10 mm	0-10 mm
Peak displacements after corrections, mm	-30.1, 27.6	-38.3, 41.5	-31.08, 24.2	-46.3, 38.8	-55.4, 77.9	-39.3, 35	-39, 34.4
Peak loads, kN -/+	-24.8, 26.8	-14, 15.8	-39.94, 34.5	-47, 50.3	-47.6, 44.6	-20.5, 18.3	-15.8, 12.9
Energy in rack, kJ -/+	2.1	2.1	7.0	10.3	12.9	6.6	2.5
Other features					Fire tested at 1.5% (45 mm) drift		

Lining fixing details:

(1) lining to edge of frame and fastened with nails 40 x 6 g at 300 mm centres etc
(2) 10 mm gap around perimeter
(3) simulated edge detail
(4) steel frame fixing details, studs are floating in channels top and bottom and the lining is only fixed to the studs.

A key indicator of the earthquake resistance of the wall would be obtained by enclosing the outer perimeter of the plot in an envelope to show the extremities of deflections and forces required. The envelopes for the timber-framed and steel-framed walls are plotted in Figure 3 and the area contained within and extremities of the profiles match the degree of constraint imposed by the lining edges. The locations of the absolute maximum forces (maxima and minima) indicate the point at which the resistance to racking is broken and the deflections required to do so. The magnitude of the forces is an indication of the edge restraint as described above.

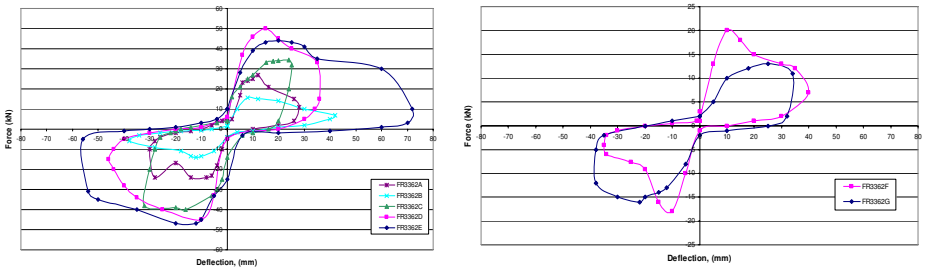

Figure 3: Deflection-force envelopes for timber-framed and steel-framed walls

The hysteresis envelope for the steel-framed walls, where the only difference in the construction between the two walls is the presence of a door, the flexibility imparted by the door and frame is apparent by a lower force being required for the initial deflections. In FR3362F, for the wall only, a break point is clearly indicated at about 20 kN and 10 mm drift and a rapid reduction beyond. In contrast, for FR3362G the maximum load is 13-16 kN at a drift of about 25 mm without a marked reduction at greater deflections. So there is a greater tolerance for drift before the break point is reached on the wall with the door.

Summary of racking tests

In all of the walls subjected to racking some damage to the lining resulted. The location and severity of the damage was dependent on how the lining was fixed to the frame and the restraint around the perimeter by taping and stopping, such as corner details where they were included. Once the region of weakest restraint had failed locally, generally by the lining tearing around the fixings, this relieved the load and the resistance to racking reduced significantly. The wall could then be considered broken and only minimal additional damage to the lining occurred at any other locations. Joints in the lining that had been taped and stopped performed at least equivalent to the continuous lining in the racking process. The presence of an opening, such as a door, did not result in any significant additional damage to the wall. In fact the door assembly added a degree of flexibility to the wall as the door leaf moved within the frame, and this had the effect of spreading the load and resulting damage more evenly over the wall assembly.

In general the racking resulted in damage characterised by loosened plasterboard at the top or bottom of the wall, depending on restraints around the perimeter. It was this damage that was principally responsible for the failure in the subsequent fire resistance test.

4. FIRE RESISTANCE TESTING

After the earthquake racking, the damaged walls were subjected to a fire resistance test in accordance with AS1530.4: 1997 to determine the degradation in fire resistance compared with a baseline test on an undamaged specimen. Preparation of the racked wall specimens for fire resistance testing required that the wall be secured and that the gap between the wall and the test frame at the sides and top were filled with blocking timber and ceramic fibre. It was important that any damage sustained in the racking process was preserved and that any fire preparations did not in any way repair that damage such that a better fire resistance performance was achieved. However, materials to patch expected Integrity failures resulting in flaming were available so that a fire test could be continued and other failures recorded to extract as much data as possible on the performance. The results of the fire tests are summarised in Table 2.

Table 2: Fire resistance tests on racked walls

Test no.	FR3362A	FR3362B	FR3362C	FR3362D	FR3362E	FR3362F	FR3362G
Nominal FR, mins	60	60	60	60	60	60	60
Framing	Timber	Timber	Timber	Timber	Timber	Steel	Steel with door
Racking, % drift	-1.04, 0.95**	-1.32, 1.43	-1.07, 0.84	-1.6, 1.34	-1.9, 2.5	- 1.35, 1.12	-1.35, 1.19
Onset of char, mins	23.5	22.75	24	23	23.5	23.5	23.73
Exp lining fall off, mins	46	62	65	65.5-70	59.25	47.5	55.5
Failure, mins							
Structural	NF	NF	NF	NF	NF	NF	NF
Integrity	30	34	71NF	55	20 then 44	40	36
Insulation	47	62NF*	67	64.75	59NF	51	54
Test stopped	53	62.5	69	69.5	59	54	58
Other features	Failed Integrity at top, Insulation failure linked to the initial Integrity failure	Failed Integrity at bottom	Perimeter secure no Integrity failure	Failed Integrity at bottom right hand corner. Lower portions 600 to 800 mm of studs burnt away at test end	Failed Integrity at top LH corner 20 min, then top RH corner at 44:30 min	Insulation failure at 51 min indicated by scorched paper face	Door failed Integrity at 51+ min, no Insulation failure of door
Construction details, lining fixing	Lining unbounded at top and sides but in contact with sill	Lining unbounded with 10 mm gap around perimeter	Corner detail simulated at ceiling/wall, wall/wall and floor with skirting board	Corner detail simulated at ceiling/wall, wall/wall and floor with skirting board	Corner detail simulated at ceiling/wall, wall/wall and floor with skirting board	The floating top and bottom channels and outer studs were bounded by a rigid …	... (cont) timber frame effectively pin jointed and free to rotate at all 4 corners

* Insulation failure predicted to occur at 66 minutes by extrapolation.

** Drift ratio was intended to be 1.5%, but additional stiffness of the wall and movement within the frame reduced actual drift to about 1%.

Note: baseline test (unracked) failed at 69/69/69, onset of char 24 minutes, and test stopped at 69 minutes. The exposed lining remained attached to the framing at the end of the test.

Analysis and discussion of fire test results

Analysis of the fire test results (by comparing the reduction in the fire resistance against the % drift from racking that each wall was subjected to) does not reveal a consistent reduction with increasing drift as could be expected. One significant reason for the irregularity is that the edge detail was modified in the course of the five timber tests in the series as summarised in Table 2. Generally the initial failure was an Integrity failure, and this was directly attributable to the detachment in the lining at a particular location due to the earthquake racking. Only in one case did a wall fail first due to Insulation (FR3362C) and there was no failure due to Integrity. Significantly in this case, there was no observed detachment of the lining after the racking.

Comparison of Integrity and Insulation failures

The detrimental effect of earthquake racking is more marked on the Integrity than the Insulation fire resistance. Considering the tests with the confined edges (FR3362C, D and E) there appears to be a threshold beyond 1% drift that the lining is essentially broken, potentially resulting in a marked reduction in the Integrity fire resistance. This is consistent with the drop-off in the racking force required at greater displacements (shown in some of the racking graphs). The Insulation fire resistance does not appear to be affected to the same extent.

Comparing the relative downward slope of fire resistance for the steel-framed tests FR3362F and FR3362G in Figure 4 with the timber specimens, the loss of fire resistance is not significantly different for timber or steel-framed walls.

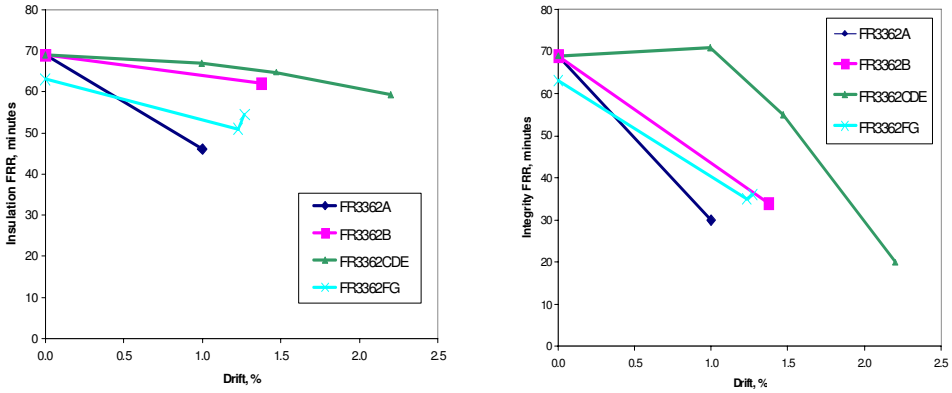

Figure 4: Comparing Insulation and Integrity fire resistance of walls

The presence of the door did not seem to significantly affect the fire performance of the wall; while the door leaf itself is very rigid, the gap between the leaf and the frame introduces flexibility to the system as a whole such that the racking damage was about the same. It is also significant that, in general, throughout all tests conducted the damage to the lining was greater around the perimeter due to the greater relative movement between the lining and the frame. Therefore a door frame in the middle region of a wall is unlikely to be subjected to the same level of movement. This is a likely explanation for the absence of damage to the door and frame and the similarity in performance of the wall/door test to the previous combinations.

Predictors of fire resistance reduction

To assess the mechanism of how the perceived damage to the lining of the wall may have affected the outcome of the fire resistance tests, the temperature recordings of the exposed and non-exposed linings were compared to determine whether there were trends indicating some degradation of the lining, and hence overall system performance other than the recorded end result failures.

The temperature of the exposed lining measured on the cavity side is graphed in Figure 5. These temperatures are usually recorded to give an indication when the studs in a timber-framed wall begin to char, and that is taken as when the temperature exceeds 300^{o}C on the stud. For the 13 mm thick fire-rated lining used in all seven tests conducted, there did not appear to be any detrimental effect at the 300^{o}C milestone which occurred around 23 minutes. However, beyond that time there is some divergence of varying degrees indicating a degraded performance, perhaps attributable to the racking damage. The most significant indicator is when the temperature spikes up several hundred ^{o}C (00's ^{o}C) coinciding with the loss of the lining by falling off in parts or over the majority of the wall surface. It is feasible to expect that such loss of the lining was in part caused by the racking damage, and since all racked tests lost some exposed lining before the baseline test (which hadn't lost any at 69 minutes) this hypothesis is supported.

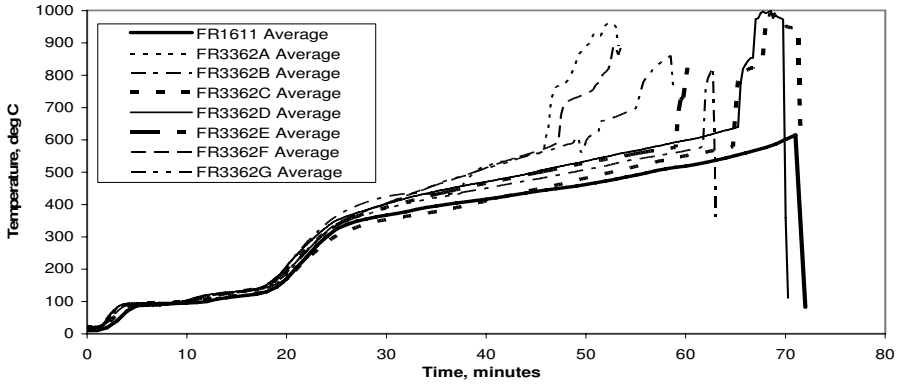

Figure 5: Temperature of exposed linings on cavity side

However, in all tests the loss of some exposed lining followed the initial Integrity failure rather than preceded it so it can be dismissed as a direct cause of the failure, but it is influenced by the racking as indicated in Table 3.

Table 3: Relationship of exposed lining loss to Integrity and Insulation failures

Test	Baseline	FR3362A	FR3362B	FR3362C	FR3362D	FR3362E	FR3362F	FR3362G
Mean drift ratio, %	0	1.0	1.4	0.9	1.5	2.2	1.2	1.3
Loss of exp lining	69NF	46	62	65	60	59	47	50
Integrity	69	30	34	71NF	55	20*	35	36
Insulation	69	47	62NF	67	64	60NF	51	54

* Tested at 1.5% drift.

There also appears to be a relationship between the loss of the exposed lining and Insulation failure. Comparing Figure 5 with Figure 6, a rapid increase in the exposed lining temperature is followed by a slower increase in the rate of rise of the non-exposed lining, but this did not always result in an Insulation failure before the test was stopped.

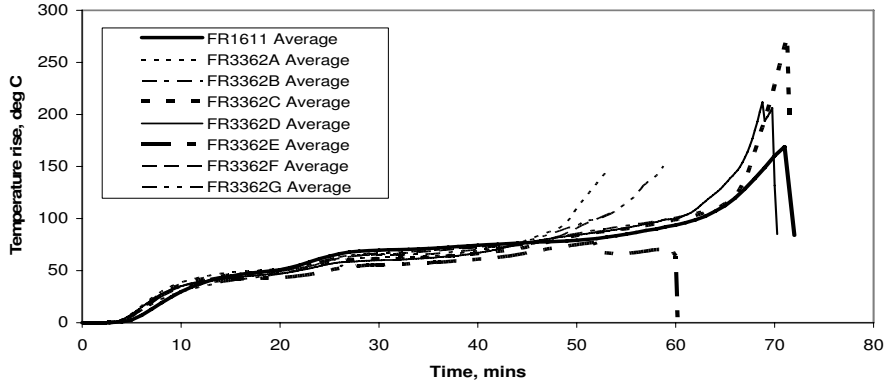

Figure 6: Insulation criterion temperature on non-exposed face of walls

5. CONCLUSIONS

The fire resistance of the seven plasterboard lined walls tested was shown to be reduced by the simulated earthquake racking. While the amount of the reduction in the fire resistance was shown to be generally related to the magnitude of the racking, other features of the attachment of the lining, in particular the finishing of the edges, determined the degree of detachment of the lining. This degree of detachment of the lining was shown to have the greatest impact on the reduction in fire resistance.

In some of the tests the walls were pushed well beyond the code limit (drift of 1.5%) without significantly more damage occurring. The treatment of the lining perimeter had a significant effect on the resistance to racking. Once the initial resistance had been overcome by increased racking displacement, the resistance decreased with very little additional damage being caused. The damage sustained at that breakthrough resistance had a direct effect on the fire resistance, particularly the Integrity.

Consequent to the simulated earthquake damage, various mechanisms were shown to lead to earlier fire resistance failure. The most significant deleterious effects were the localised ones, such as gaps between the lining and the frame leading to Integrity failures. Damage was often confined to a localised detachment of the linings or over an area that was a weakness in the structure. It is less likely that the linings are uniformly damaged by racking as the weakest link in the system yielded first and damage was largely located in that region.

If the wall was fire tested in a deformed state, rather than being restored to zero displacement, this had an influence on the fire resistance. When the wall remained in a displaced position equivalent to 1.5% drift, the gaps between the lining and the frame remained more open on one side than the other and it was this open gap where the first Integrity failure occurred.

The significant factors determining the reduction in fire resistance are summarised as:

- the fire resistance is reduced as a result of damage caused by earthquake racking
- detachment of the lining from the frame and the resulting gaps are a critical factor in the initiation of Integrity failures
- the edge or corner detail of the lining is a critical factor in the magnitude of the reduction of fire resistance as a result of racking
- there is a critical point in the racking displacement in the region of 1.0-1.5% drift when the most significant damage to the lining occurs, and beyond that point only marginally more damage is inflicted
- if the wall remains in a deformed state, and there remains a greater lining to frame gap on one top corner compared to other corners, then it is likely to be an earlier failure at that location than if the wall had been restored to zero displacement
- with the steel-framed wall there was less resistance to racking, but the reduction in fire resistance is about the same for the same displacement of a timber framed wall
- the addition of a door in the steel framed wall resulted in some tearing of the lining around the top corners of the door frame, but this was less severe than

the damage caused at the corners of the wall, where it failed Integrity first followed by an Integrity failure at the top of the door leaf some time later

- for timber and steel-framed walls, plasterboard detachment around the perimeter is the common factor
- the racking process in some cases resulted in some weakening of the lining inboard from the edges, but any resultant premature loss of the exposed lining (compared with unracked lining) was not significant enough to cause an Insulation failure that preceded the Integrity failure for that wall.

This project has shown that the post-earthquake performance of passive fire protection systems is definitely reduced when subjected to a design level earthquake. The amount of reduction in fire resistance of a 60 minute plasterboard lined wall can be as much as 50%. This is important given that active fire protection systems, such as sprinklers, may have also been rendered inoperable in the earthquake event. This is a dual problem in that a reduction in the fire resistance requirements of up to 50% may have been permitted because sprinklers were included as part of the fire design. The problem may be further compounded by the increased likelihood of fire outbreak due to disruption of building activities and services. Furthermore, Fire Service attendance cannot be relied upon due to the likelihood of multiple call-outs and possible impediment/blockage of road access. Finally, egress from buildings may be restricted by blocked exit-ways and injuries to people increasing the escape times.

While this project has identified the magnitude of the problem in relation to the fire resistance of walls, similar reductions in the performance of other PFP systems will exacerbate the problems in limiting the spread of post-earthquake fires that have been identified. So there is an ongoing need to investigate and confirm whether or not earthquake damage to other passive fire resistance systems follows the same trend. If this is shown to be the case, then the risk of fire spread through buildings will be greatly increased in the event of a design level earthquake.

6. REFERENCES

1 Collier, P.C.R. 2005. *Post-earthquake performance of passive fire protection systems.* BRANZ Study Report 147, Judgeford, New Zealand. http://www.branz.co.nz/main.php?page=Free%20Publications&pagenumber=7

2 Department of Building and Housing. 2005. *Compliance Document for New Zealand Building Code: Clauses C1, C2, C3, C4*. ISBN 0-477-01606-5. Wellington, New Zealand.

3 Taylor, J.M. 2003. *Post-earthquake fire in tall buildings and the New Zealand Building Code.* Department of Civil Engineering, University of Canterbury, Christchurch, New Zealand.

4 Robertson, J.N. and Mehaffey, J.R. 2000. *Accounting for fire earthquakes in the development of performance-based codes.* 12th World Conference on Earthquake Engineering. city, country?

5 Cousins, W.J, Heron, D.W, Mazzoni, S., Thomas, G.C. and Lloyd, D. 2003. *Modelling the spread of post-earthquake fire.* Pacific Conference on Earthquake Engineering. city, country?

6 Sharp, G.S. 2003. *Earthquake damage to passive fire protection systems in tall buildings and its impact on fire safety.* Department of Civil Engineering, University of Canterbury, Christchurch, New Zealand.

7 Cameron, C. and James, C. 1998. *The 1923 Great Kanto earthquake and fire.* National Information Service for Earthquake Engineering (NISEE), University of California, Berkeley, USA. Internet Resource: http://nisee.berkeley.edu/kanto/yokohama.html
8 Botting, R. 1998. *The impact of post-earthquake fire on the urban environment.* Fire Engineering Research Report 98/1. University of Canterbury, Christchurch, New Zealand.

9 Brundson, D. and Clark, W. 1993. *Modern multi-storey buildings and moderate earthquakes.* Business Continuance Planning Ltd, report for Earthquake Commission: www.eqc.govt.nz/research/researchpapers/p_304.aspx

10 NZS 4203:1992 Vol 1 and 2. *General structural design and design loadings for buildings.* Standards New Zealand, Wellington, New Zealand.

11 Barnes, G.J. 1997. *Sprinkler trade-offs in the approved documents.* Fire Engineering Research Report 97/1. University of Canterbury, Christchurch, New Zealand.
12 Porter, K.A., Kiremidjian, A.S. and Le Grue, J.S. 2001. 'Assembly-based vulnerability of buildings and its use in performance evaluation'. *Earthquake Spectra* 17(2): 291-312.
13 Sekizawa, A., Ebihara, M. and Notake, H. 2000. *Development of seismic-induced fire risk assessment method for a building.* Proceedings 15th Meeting of the UJNR Panel and Fire Research and Safety (San Antonio), March 1-7, pp145-152 (NISTIR 6588).

14 Nyman, J.F. 2002. *Equivalent fire resistance ratings of construction elements exposed to realistic fires.* Department of Civil Engineering, University of Canterbury, Christchurch, New Zealand.
15 Blackmore, J., Brescianini, C., Collins, G., Delichatsios, M.A., Everingham, G., Hooke, J., Ralph, R., Thomas, I. and Beever, P. 1999. *Fire Code Reform Centre, Project 3: Fire resistance and non-combustibility, Part 3: Room and furnace tests of fire-rated construction, July 1999.* Fire Code Reform Centre Ltd/CSIRO Division of Building, Construction and Engineering, NSW, Australia.
16 Sharp, G.S. and Buchanan, A.H. 2004. *Earthquake damage to passive fire protection systems in tall buildings.* New Zealand Society for Earthquake Engineering Conference. Rotorua, New Zealand
17 Dutta, A. and Maunder, J.B. 2001. 'Energy-based methodology for ductile design of concrete columns'. *Journal of Structural Engineering* 127(12): 1374-1381.

THE RELIABILITY OF STRUCTURES IN FIRE

DAVID LANGE[1], ASIF USMANI[2], and JOSE TORERO[3]

ABSTRACT

Structural fire engineering has been benefiting for some time from a growing understanding of the fundamental mechanics that govern the behaviour of structures under thermal effects. As the field of fire engineering moves from a prescriptive to a performance based approach, this understanding is being used with growing confidence by engineers to develop new design solutions for structures and to justify the implementation of rational fire safe designs with reduced reliance on passive fire protection. However, unlike ambient, or static, design situations, the application of these methods is made without consideration of the reliability of the resulting solution. More often than not, a fire-engineered solution is a deterministic application of fundamental mechanics to a specific thermal and static loading combination, consisting of a 'design fire' and some factored mechanical loading. As a result, safety of the final design can only be guaranteed via the implementation of intentionally conservative assumptions that result in some undetermined and unknown safety factor in the system. These solutions are applied in an ad-hoc manner to areas of perceived high risk.

By taking account of alternative, thermally enhanced load carrying mechanisms, and using stochastic methods to model fire scenarios this paper addresses the application of reliability methods to structural fire engineering, for both protected and unprotected components. A solution is provided that allows for a performance based approach to structural fire engineering that can be calibrated to conform with current and future Eurocode reliability targets, irrespective of the methods which are used to model either the fire or the structure.

[1] MEng, Research Associate, BRE Centre for Fire Safety Engineering, email: david.lange@ed.ac.uk
[2] Professor of Structural Engineering, BRE Centre for Fire Safety Engineering, The University of Edinburgh, School of Engineering and Electronics, email: asif.usmani@ed.ac.uk
[3] BRE/RAE Professor of Fire Safety Engineering, BRE Centre for Fire Safety Engineering, The University of Edinburgh, School of Engineering and Electronics, email: j.torero@ed.ac.uk

1 INTRODUCTION

The current Eurocodes present a design framework which is based upon the First Order Reliability Method, or FORM. The targets of the Eurocodes are based upon indices of Safety or Reliability. The reliability of a system (or component) is a measure of the probability that the load on the system will be less than the systems resistance. This concept is the basis for the partial safety factors which are prevalent throughout design codes worldwide, and it therefore seems only natural to apply it to structural fire safety design.

Current thinking tends to employ annual return periods of fires of given severities, similar to the way in which earthquake probability is defined. In [1], Lin uses a Poisson process to model the probability of fires based upon numbers of annual fire occurrences and floor area. This is similar in approach to work by Ramachandran [2], where the risk from a fire is defined as the product of the probability of fire occurrence and the floor area damaged. While potentially viable from an insurer's perspective, these methods are unsuitable for structural design since fire is often man made and not a natural phenomenon, and probabilities derived from fire statistics suffer from a relatively small sample size.

It follows that for the design of buildings for fire, the following points have to be considered:

1. For Structural design, a building has to be designed under the assumption that a meaningful fire will occur, i.e. P(fire occurring)=1.
2. The quantification of the probability of a particular fire event occurring in a building cannot be simply described as a probability over a return period. This is at odds with existing frameworks for exceptional and accidental loading and suggests that other design frameworks cannot simply have their wording changed to address fire loading.
3. It is unscientific to use historical data to derive statistics for use within a design process and draw probability distributions of fire duration or temperatures for use in a risk assessment.
4. The perceived risk should be associated with real and possible fires in the building being designed and the subjective consequence of these fires on the structure. This data should be based upon information about the individual construction project and its proposed usage.

The second, third and fourth points above are addressed in work by Hostikka and Keski-Rahkonnen [3], where the probability of the fire and the associated consequences are directly related to assumed probability distributions of the variables associated with the fire model and system being designed. Although this work was not focussed on the risk as a result of fire, it did model the probabilities of a number of fire events occurring as a product of a number of assumed distributions of input variables.

2 PROBABILISTIC FIRE MODELS

The list of variables which affect the development and spread of a fire in a compartment is potentially endless, and the more complicated the model used, the higher the number of variables which need to be defined. From the most simple nominal standard fire curve; where the duration of the fire has to be declared, all the way to the most high resolution field model; where the

equations for mass, energy and momentum have to be solved in every field, add to that energy loss through the boundaries and radiative heat transfer and the number of variables can become unmanageable. A balance has to be struck between the quality and complexity of the model, bearing in mind the constraints of the application.

The variables which affect the temperature in a compartment fire can broadly be separated into two groups: deterministic and non- deterministic variables. The deterministic variables are those which are not changing on a day to day basis; e.g. variables such as construction materials, compartment geometry, compartment boundaries and occupancy. Variables which are non-deterministic are those which can change throughout not just the life of the building but from day to day use of the building; e.g. fuel load, fuel distribution (compartment configuration), and ventilation conditions. Generally those variables which are constant within the compartment have some uncertainty about them but this is accounted for in design and analysis by use of a conservative characteristic value. Those other, non-constant, variables are those which cannot be foreseen during the design process and only a range of values with indefinable probabilities can be determined.

According to Knight [4], there are three types of probability relevant to decision making:

1. "a priori probability", which applies where there is "absolute homogeneous classification of instances, completely identical except for really indeterminate factors";
2. "statistical probability", namely, "empirical evaluation of the frequency of association between predicates"; and
3. "estimates", which "must be radically distinguished from probability or chance of either type"

Evidently, "a priori" probability and "statistical" probability are not suited to the study of fire since in the first case there is no homogeneity between events, and in the second case the number of samples is not large enough for there to be a useful informativeness in the frequencies obtained (the informativeness of a number, N, of events tends to 0 as N tends to 0).

The goal in defining a sample set of fires for rational structural design for fire safety is to satisfy the points listed above, i.e.: P(that a meaningful fire will occur)=1; the probability of a fire event occurring in a building cannot be described as a probability over a return period; since historical data cannot be used to derive statistics for use within a design process and it is not possible to draw meaningful probability distributions of fire duration or temperatures from fire statistics we turn to estimates as a best alternative, for which there is a precedent in literature.

3 ACTIVE MECHANISMS

Since the Cardington tests, there has been a great deal of research into the mechanisms which govern structural response in fire[5-10], and also into the identification and analysis of active mechanisms of horizontal [11-14] and more recently vertical structural elements [15-18].

The horizontal mechanisms identified focus on a thermally enhanced membrane mechanism. Upon initiation of growing deflections in fire a floor slab adopts a deflected shape which permits it to adopt a tensile membrane mechanism as opposed to a flexural mechanism. In this case the active mechanism varies with the fire, and the ability of the floor system to sustain the static load to which it is subjected depends upon the evolution of the response of the floor

system over the duration of the fire. The actual load which is applied, however, is only dependant upon the occupancy of the building although common practice is to design a building for a load which has been reduced by an appropriate factor to account for the relatively low probability of a fire occurring at the same time as the building is subject to its maximum design load[19].

Vertical mechanisms of load resistance in fire focus on the ability of a column to sustain the large forces which result from an exposed floor system in either a push-out stage or a pull-in stage, and with a fire on one or more floors. In this case, the active mechanism is bending of the column, and assuming that the column is appropriately encased and that it retains its bending stiffness for the duration of a fire attack, it is the load on the column which varies according to the current state of the floor systems which are supported by it.

4 RELIABILITY THEORY

To summarise the concept of reliability theory, the standard stress-strength model is shown in Figure 1. The load on the system is represented by normally distributed random variable Q, and the resistance of the system is represented by normally distributed random variable R. The probability of failure of the system is the probability that the resistance will be less than the load, i.e.

$$P_f = P(R < Q) \tag{1}$$

For some characteristic value, Q^*, of Q, this is:

$$P_f = P(R < Q^*) = \int_{Q^*}^{\infty} RdLoad \tag{2}$$

or, where Q is also unknown:

$$P_f = P(R < Q) = \int_{-\infty}^{\infty}\int_{Q}^{\infty} RQd^2Load\ . \tag{3}$$

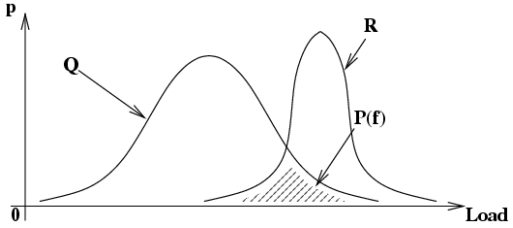

Figure1 Standard stress-strength model

The reliability of a system, S_R, is the probability that the strength is greater than the stress on the system, i.e. $S_R=P(Q<R)$ [20].

$$S_R = P(Q < R^*) = \int_{-\infty}^{R^*} QdLoad \tag{4}$$

$$S_R = P(Q < R) = \int_{-\infty}^{\infty}\int_{-\infty}^{R} QRd^2Load \tag{5}$$

4.1. Margin of Safety and Reliability Index

The margin of safety is the margin between the load and the resistance of the system. For characteristic values of these, Figure 2, this is:

$$M = R^* - Q^* \tag{6}$$

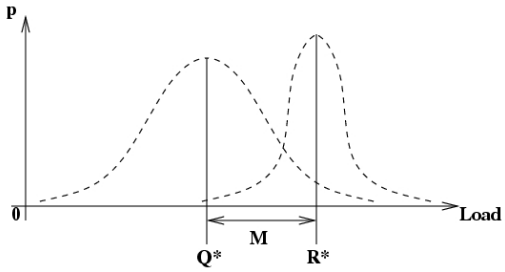

Figure 2 margin of safety is the margin between the characteristic resistance and the characteristic load

For normally distributed values of Q and R, the margin of safety is also normally distributed [21] and has mean and variance:

$$\mu_M = \mu_R - \mu_Q \tag{7}$$

$$Var(M) = \sigma_M^2 = \sigma_R^2 + \sigma_Q^2 \tag{8}$$

The reliability factor, β, is the number of standard deviations of the margin of safety between its mean and 0, Figure 3:

$$\beta = \frac{\mu_M}{\sigma_M} \tag{9}$$

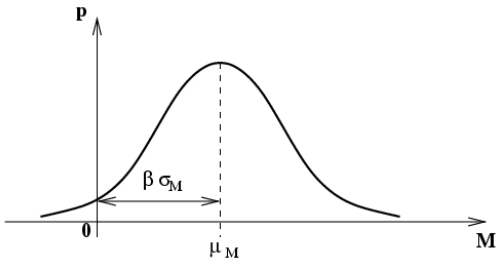

Figure 3 β is the number of standard deviations between the mean of the margin of safety and 0

5 PRACTICAL APPLICATION

A number of sources suggest that the concept of reliability should be applied to structures in fire. The SFPE hand book describes the concept of reliability as a tool for measuring the failure rate of a system [22], and also for estimating physical responses of material and components in fire [23]. Alternative sources describe the concepts of reliability within the derivation of a performance based framework for structural design [20, 21].

The relationship between the reliability of a component or a series of components and the features of the building in which it is contained is not one that is normally addressed as part of a reliability calculation. Yet because of the interaction between the features of a compartment and the effect that this has upon the potential fire load in a building this is of primary importance in the determination of structural reliability in fire and the acceptance or otherwise of a design as part of a performance based design framework.

5.1. Performance Function

A complex system, *Z*, of load and resistance is described by the performance function of the variables which describe the system, *X,* [24]:

$$Z = Z\left(X_1, X_2, ..., X_n\right) = \text{Resistance} - \text{Load} \tag{10}$$

Where each of these variables has some distribution either random or deterministic, the reliability of the system is given by:

$$S_R = 1 - P_f = 1 - \int ... \int f_{X_1, X_2, ..., X_n}\left(x_1, x_2, ..., x_n\right) dx_1 dx_2 ... dx_n \tag{11}$$

The system of variables which represent the performance equation vary depending upon the mechanism being designed for, and the structure providing the mechanism, as well as the occupancy and architectural features of the building being designed.

The use of the performance function must consider the effects of fire at each stage of the design process. At the initial statement of the problem the active mechanism should be considered, whether it is a thermally enhanced one, or changing with the exposure. The actual

analysis of the structure should consider all loads; dead loads, live loads and any additional thermo-mechanical loads:

$$Q = f\left\{\begin{array}{c}\text{Dead Loads}\\ \text{Live Loads}\\ \text{Thermo-mechanical Loads}\end{array}\right\}, R \propto \text{Active Mechanism}$$

The actual integration of the performance function and the determination of the reliability of a structure, system or component is an onerous one which becomes more an more complicated with increasing complexity of both the structural model and the model which is used to describe the fire. Since the number of variables becomes increasingly difficult to manage, alternative methods for the integration of the performance function are required

5.2. Monte Carlo Analysis

Monte Carlo analysis is a random sampling technique which draws on a library of variables and their distributions to generate *N* random events. As with statistical probability, the informativeness of the resulting distribution increases with the number of events, *N*.

$$S_R = 1 - \frac{N_f}{N} \tag{12}$$

6 EXAMPLE

To illustrate the calculation of the reliability of a structure in fire, a Monte Carlo analysis is performed on a composite floor slab. The mechanism is assumed to be a tensile membrane mechanism, as described by Cameron and Usmani[11, 12]. Secondary beams are assumed to provide no additional capacity to the slab at this stage. The fire model used is a Eurocode parametric fire model [25].

6.1. Input Variables

The input variables required for the Monte Carlo analysis can be divided into two broad categories: structural and architectural. Structural variables are largely deterministic and describe the component which is under evaluation. Architectural variables describe the fire, and are in this case limited by the variables required for a parametric fire curve. The architectural variables are also largely deterministic, although there are a number of unknowns and their distributions are estimated here based upon assumed variability of the compartment. The variables are listed in Table 1.

Table 1 Input variables for Monte Carlo analysis

Variable	mean	variance	distribution
slab thickness	150 mm	-	deterministic
length	7 m	-	deterministic
breadth	7 m	-	deterministic
$A_{s,x}$	142 mm^2/m	-	deterministic
$A_{s,y}$	142 mm^2/m	-	deterministic
t_{lim}	900 – 1500 s	-	linear
$b = \sqrt{(\rho c \lambda)}$	1800 $J/m^2s^{1/2}K$	-	deterministic
O	0.15	0.01	normal
$q_{f,d}$	800	200	normal

6.2. Reliability Calculation

The loading on the slab is assumed to be $5kN/m^2$, slightly larger than the load on the Cardington building. The slab should be expected to sustain the load indefinitely through a reasonable fire, therefore the reliability factor is calculated based upon the number of floor slabs which are unable to support the load at the end of the analysis. As expected, the ratio of analyses resulting in failure to those which do not changes according to the number of analyses carried out. A small sample provides little, if any, estimation of a rate of failure and is of poor informativeness, whereas a sample of increasing size provides an increasingly informative estimate of the rate of failure.

Evolution of the mean and standard deviation of the margin of safety with increasing numbers of analyses is shown in figures 4 and 5.

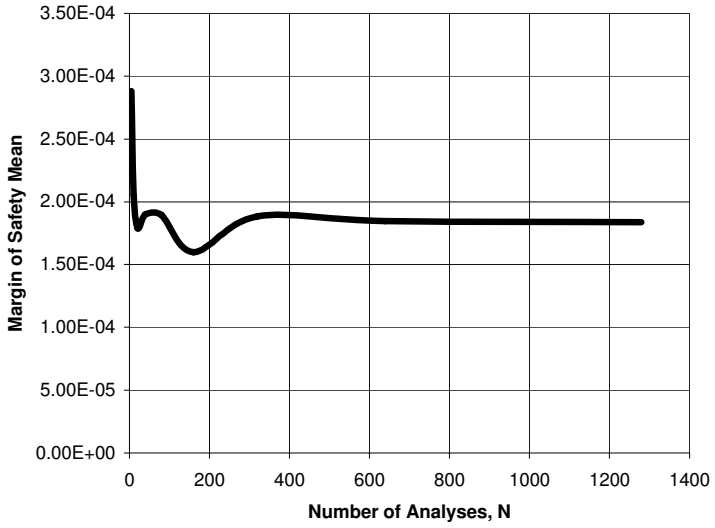

Figure 4 $_M$ variation with number of analyses

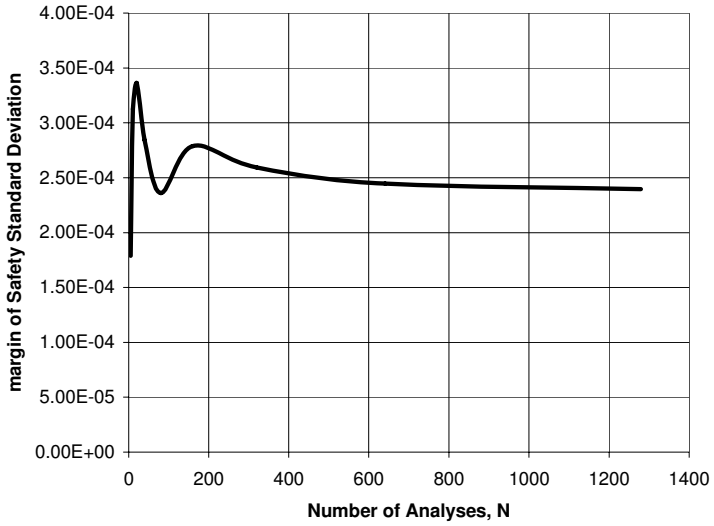

Figure 5 σ_M variation with number of analyses

The evolution of the reliability factor with increasing number of analyses is shown in figure 6.

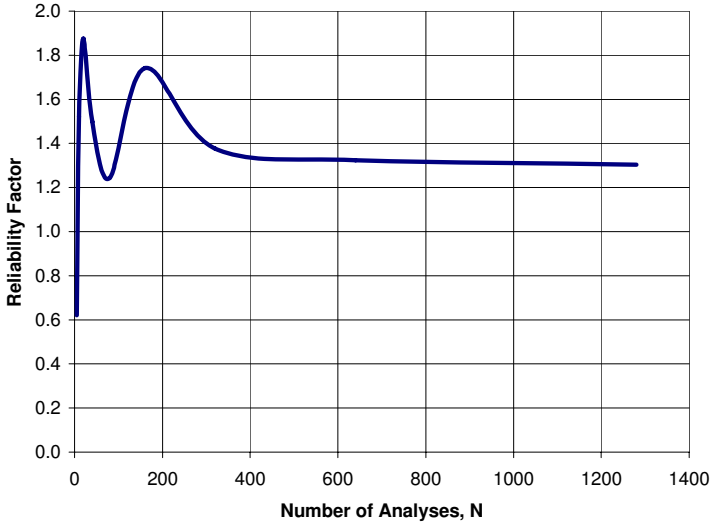

Figure 6 β variation with number of analyses

The reliability factor shown in figure 6 appears to be converging to approximately 1.3. This is relatively low when compared with the reliability goals as defined by the Eurocodes, which range from 3.1 to 4.7, depending upon the classification of the building and the event[26].

Using only the means of the variables used to define the set of sample fires, a single deterministic calculation shows the slab to be able to carry the load. This is as opposed to a relatively large number of failures observed (the number of failures is slightly more than one in a hundred) by using only a relatively simple variation of the fire to which the model is exposed.

7 CONCLUSIONS

This paper describes and attempts simply to address the problems which limit the applicability of reliability theory to structural fire engineering. Whilst the solution posed by estimates of the non-deterministic input variables for a reliability calculation may seem arbitrary and at first of little increased value over the current ad-hoc style of structural fire engineering, the admission and inclusion of the uncertainty of a specific design fire allows for a more diligent approach to fire safety design than that currently imposed by the Eurocodes.

When compared with the results of an analysis carried out using a single parametric fire model, the apparent advantages of adopting a probabilistic approach over a deterministic approach are apparent. Relatively small variations in the thermal loading can have a very positive or negative effect on the ability of a structure to sustain the combination of loads imposed upon it during a fire.

As a part of an inherently modular performance based design framework, the methods and rationales described above are intended to illustrate the possible application of reliability theory to structural fire engineering through reasonable and informed estimates of the structure being designed. The inclusion of the Eurocode parametric fire curve in the example is intended to illustrate the system of estimation and its suitability. The nominal curve used as well as the simple structural models can easily, and arguably more suitably, be replaced by more complicated or robust methods of simulation and assessment, although this will result in a corresponding increase in the number of variables used for the analysis and also the number of analyses required to achieve a solution.

8 REFERENCES

[1] Lin, Y.-S., *Estimations of the probability of fire occurrences in buildings.* Fire Safety Journal. 40(2005): p. 728-735.
[2] Ramachandran, G., *The Economics of Fire Protection*. 1998, London: E & FN SPON.
[3] Hostikka, S., and Keski-Rahkonen, O., *Probabilistic Simulation of Fire Scenarios.* Nuclear Engineering and Design. 224(2003): p. 301-311.
[4] Cheung, T., *A note on Knights concepts of "Risk" and "Uncertainty".*
[5] Usmani, A.S., J.M. Rotter, S. Lamont, A.M. Sanad and M. Gillie, *Fundamental principles of structural behaviour under thermal effects.* Fire Safety Journal. 2001(36): p. 721-744.
[6] Lamont, S., Usmani, A.S., and, Gillie, M., *Behaviour of a small composite steel frame structure in a "long-cool" and a "short-hot" fire.* Fire Safety Journal, 2004. 39(2004): p. 327-357.
[7] Lamont, S., *Behaviour of steel framed structures in fire*. 1997, The University of Edinburgh.

[8] Gillie, M., *The behaviour of steel framed composite structures in fire comditions*. 2001, The University of Edinburgh.
[9] Gillie, M., Usmani, A., and Rotter, M., *A structural analysis of the Cardington British Steel Corner test.* Journal of Constructional Steel Research, 2002. 2002(58): p. 427-442.
[10] Gillie, M., Usmani, A., and Rotter, M., *A structural analysis of the first Cardington test.* Journal of Constructional Steel Research, 2001. 2001(57): p. 581-601.
[11] Cameron, N.J.K., and usmani, A.S., *A new design method to determine the membrane capacity of laterally restrained composite floor slabs in fire Part 1: Theory and method.* The Structural Engineer, 2005. 83(19): p. 28-33.
[12] Cameron, N.J.K., and usmani, A.S., *A new design method to determine the membrane capacity of laterally restrained composite floor slabs in fire part 2: Validation.* The Structural Engineer, 2005. 83(19): p. 34-39.
[13] Bailey, C.G., and Moore, D.B., *The structural behaviour of steel frames with composite floor slabs sunject to fire: Part 1: Theory.* The Structural Engineer, 2000. 78/11(2000): p. 19-27.
[14] Bailey, C.G., and Moore, D.B., *The structural behaviour of steel frames with composite slabs subject to fire: Part 2: Design.* The Structural Engineer, 2000. 78/11(2000): p. 28-33.
[15] David Lange, C.R., A. Usmani, *Tall Building collapse mechanisms initiated by fire: Part 2, Design Method.* The Structural Engineer, 2008(Under Review).
[16] Charlotte Röben, A.U., G. Flint, A. Jowsey, and D. Lange, *Tall building collapse mechanisms initiated by fire: Part 1, Mechanisms Explained.* The Structural Engineer, 2008(Under Review).
[17] Quiel, S.E., and Garlock, M.E.M., *A performance-based design approach for steel perimeter columns subject to fire*, in *Fourth International Workshop Structures in Fire*. 2006: Aveiro.
[18] Garlock, M.E.M., and Quiel, S.E., *Combined axial load and moment capacity of fire-exposed beam-columns with thermal gradients*, in *Fourth INternational Workshop Structures in Fire*. 2006: Aveiro.
[19] *EN 1990:2002 Eurocode - Basis of structural design.*
[20] Rasbash, D.J., Ramachandran, G., Kandola, B., Watts, J.M., and Law, M., Evaluation of Fire Safety. 2004, Chichester: John Wiley & Sons, Ltd.
[21] Performance Based Design of Steel Structures in Fire, work in progress 1st draft. in Structural Engineering for Fire Resistance, Short course at Tianjin University of Technology. 2002.
[22] Van Bowen Jr., J., Reliability, in The SFPE Handbook fo Fire Protection Engineering. 1988, SFPE. p. 4-34 - 4-42.
[23] Berlin, G.N., Probability Models in Fire Protection Engineering, in The SFPE Handbook of Fire Protection Engineering. 1988, SFOE. p. 4-43 - 4-52.
[24] Ayyub, B.M., Uncertainty modelling and analysis in civil engineering. 1998: CRC Press LLC.
[25] EN 1991-1-2:2002 Eurocode 1: Actions on structures - Part 1-2: General actions - Actions on structures exposed to fire.
[26] Diamantidis, D., Risk acceptance criteria: A review. Note prepared for the Joint Committee on Structural Safety, 2004.

THE EFFECTS OF NON-UNIFORM FIRES ON STRUCTURAL BEHAVIOUR

MARTIN GILLIE[1], CHARLOTTE RÖBEN[2], ADAM IRVINE[3] AND SANDY KIRKPATRICK[3]

ABSTRACT

Performance-based fire design codes require the ability to predict structural behaviour during a fire. To date, the assumption of a uniformly distributed fire has most commonly been used for predictions of the behaviour of heated structures. In reality, fires may travel within compartments. This paper examines the fundamental mechanics of beams subject to horizontally travelling fires. Finite element analysis is used to determine the likely response of a heated beam to a simplified version of the sort of temperature loading that experimental results and theoretical predictions suggest will occur in structural members in real compartment fires.

The stress state in the beam resulting from a travelling fire is shown to be more complex than when it is subjected to a uniform fire. Previous work has shown that cooling may be the most critical part of the structural response to fire loading. It is found that during travelling fires a combination of tensile and compressive forces are developed as heating and cooling occur simultaneously. It is concluded that assuming a uniform fire may not necessarily lead to a conservative analysis.

Keywords: travelling fire, fire, cooling, heating, finite element, performance-based design, beams.

[1] Lecturer, University of Edinburgh, BRE Centre for Fire Safety Engineering, Edinburgh, UK, email: mgillie@ed.ac.uk
[2] PhD student, University of Edinburgh, BRE Centre for Fire Safety Engineering, Edinburgh, UK, email: charlotte.roben@ed.ac.uk
[3] MEng Student, University of Edinburgh, BRE Centre for Fire Safety Engineering, Edinburgh, UK

1. INTRODUCTION

Many structural design codes now allow for performance-based design for fire resistance. This approach to fire safety allows engineers to use calculations to predict the behaviour of structures in fire rather than rely on results from fire tests on isolated structural elements, as in prescriptive design. The advantages of performance-based design are well documented and include a more rational consideration of fire loading and the freedom to use innovative structures not covered by prescriptive based codes. However, to be used with confidence, performance-based design requires designers to be able to predict accurately how a structure will respond to fire. To date almost all work on structural behaviour in fire has assumed that temperatures within a fire compartment are uniform at any level. Recent experimental results and observations from real buildings fires, together with computer simulations of real fires, show that the assumption is not valid and that even in relatively small fire compartments there will be significant variations in both gas temperature and heat flux at different locations. It has also been noted that the location of peak gas temperatures does not remain constant with time but moves, depending on the fuel location and oxygen supply. It is thus entirely possible that in a large compartment, the structure will be heating at one location and cooling at another. To date the effects of such of a situation on structural behaviour have not been considered.

This paper is an initial attempt to understand the effects travelling fire may have on structural behaviour and to identify the main consequences for design and safety. It builds upon work by Bailey (1996), and more recently Röben and Gillie (2007) who considered the behaviour of beams and simple structures subject to cooling after a fire, and also on work by Rein *et al.* (2007) who developed an approach for characterising non-uniform fires in a simple manner.

2. RELEVANT FIRE DYNAMICS

Structural fire safety design using prescriptive methods almost always relies on some variant of the Standard Fire Test (BS 476). The gas temperature in this well-known test follows a logarithmic curve and increases without limit over time in a manner that is clearly unrepresentative of real compartment fires. Further, the temperature-time curve is designed for use with relatively small experimental furnaces and so does allow for any variation of temperature in space. Although perhaps suitable for fire rating purposes, using structural temperatures derived from a Standard Fire Test in a performance-based design is difficult to justify. As a consequence, when using performance-based design, it is currently common to use some form of "Natural Fire" to estimate structural temperatures. This approach was developed in by Petterrson *et al.* (1976) who, by considering the energy balance within a fire compartment, were able to produce intrinsic equations for the variation of gas temperature with time for given ventilation, fuel and compartment details. Eurocode 1 (EN1991, 2002) developed this approach by introducing an explicit equation for estimating gas temperatures in fire compartments.

Underlying both the Pettersson and Eurocode approaches to calculating gas temperatures is an assumption that the gases are well mixed and consequently that compartment temperatures are uniform. In turn this implies that structural elements are assumed to be heated uniformly along their lengths, or over their areas. This assumption is not

valid for large fire compartments where the seat of a fire will move in a manner governed by the available ventilation and fuel. However, it has previously been assumed to be reasonable for small fire compartments - up to 500m^2 plan area in the case of the Eurocode. Experimental evidence increasingly suggests even in these situations the assumption of uniform heating is not valid. Cooke (1998) undertook a number of fire tests with uniform fire loads and showed there was a clear progression of peak temperature through compartments as the seat of the fire moved according to the available ventilation. The effect of non-uniform gas temperatures on structural temperatures has been shown to be significant in recent work by Gillie and Stratford (2007) who reported on temperatures in a concrete slab above a fire compartment. Lower surface concrete temperatures varied by as much as 400°C despite a compartment size of only 3.5m by 4.5m.

The fact that even in small compartments significant spatial temperature variations are likely is only beginning to be captured by simple fire models. Rein *et al.*(2007) proposed a model consisting of "near-field" and "far-field" temperatures where the far-field temperatures result from hot gases and near-field temperatures from direct impingement of a flame. They proposed that the duration of exposure to near-field temperatures in well a ventilated fire is governed by the available fuel load and that for office fires will be of the order of 15 minutes. Exposure to far-field temperatures was found to be around 10 times longer and dependent on the size of the fire (itself governed by the ventilation conditions) and geometry of the compartment. It was suggested that gas temperatures could be taken to decay roughly linearly away from the seat of the fire.

It is thus the case that in general compartment fires will "travel" to a greater or lesser extent. To date the implications of this for structural behaviour have not been considered in a systematic manner. The remainder of this paper considers the implications of travelling fires for simple beam structures.

3. STRUCTURAL MODELS

To examine the effects of a travelling fire on a beam, finite element models were used. For conducting parametric studies, a 1-d model consisting of 50 linear beam elements was constructed using ABAQUS. The cross-section of the beam was taken to be a typical I-section (Fig. 1). Material behaviour was taken to be elasto-plastic and typical of a mild steel with a yield strength of 355MPa. Stress-strain relationships were taken from Eurocode 3 (EN1993, 2005).

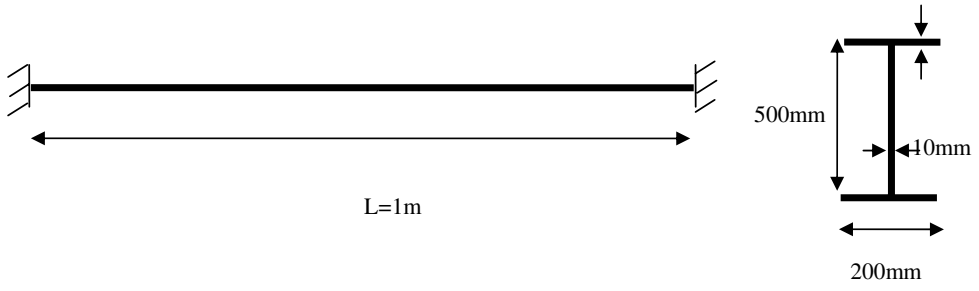

Figure 1. Model geometry

As the manner in which travelling fires should be characterized is still being developed, it was decided to apply simple, representative forms of temperature loading to the beam. This approach also had the advantage of allowing the underlying mechanics to be readily identified. Two kinds of loading were considered (Fig. 2). The first form of loading consisted of a triangular patch of temperature which was defined by two parameters: the patch length and its peak temperature. A triangular form of loading was chosen as this modelled the approximate linear decay of temperature with distance from the centre of the fire suggested by Rein *et al.* (2007). In each case the peak temperature was taken as 1000°C while a variety of patch lengths were considered. No other loads were applied to the beam. The second form of loading was similar to the first but the temperature within the beam now included a thermal gradient such that the lower surface reached a temperature of 1000°C while the upper surface remained at ambient temperature. Most steel beams in fire would be subject to loading somewhere between these two extremes of thermal gradient.

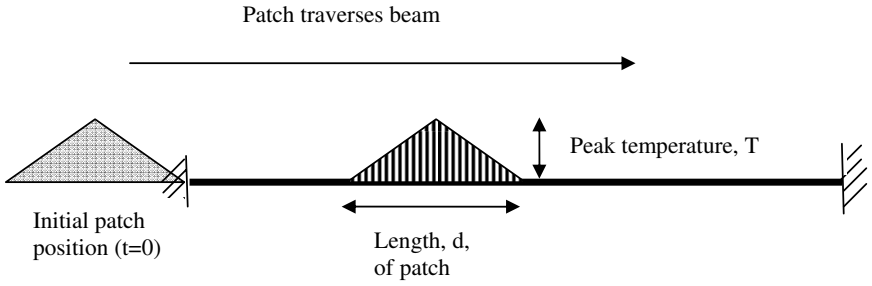

Figure 2. Definition of patch loading.

4. RESULTS

Figure 3 shows results for the case of a fixed-end beam subject to a travelling triangular temperature patch load (Fig. 2). Axial force in the beam, which must be constant along its length, is plotted against pseudo-time. As there are no time dependent phenomena in the model, the time axis is simply a proxy for the location of the temperature patch. At t=0 the beam is at ambient temperature immediately prior to heating, while at t=1 the temperature patch has traversed the entire beam with each section having been heated and then cooled. The figure shows results for a number of different patch lengths varying from 20% of the beam length to 60% of the beam length. The response of the beam when subject to uniform heating and cooling is also shown. It should be noted that as the thermal gradient is zero, no deflections or moments are produced.

The response of the beam can be divided into a number of distinct parts. Initially, as the temperature patch starts to heat the end of the beam, thermal expansion results in compressive forces developing. As expected, the magnitude of these axial forces is greater for longer temperature patches as they result in a greater length of heated beam and hence a

larger

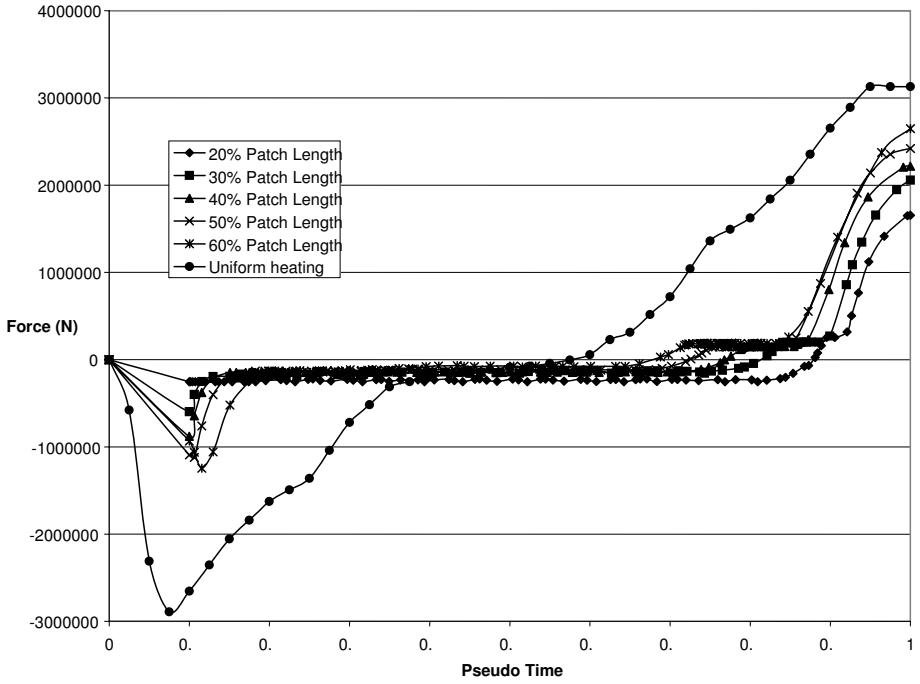

Figure 3. Axial force in the beam when subject to a travelling fire with no thermal gradient.

thermal strain along the beam's length. The peak in axial force occurs at a similar time for each patch length. This is due to the travel times of the patches. The larger patches have a longer total length to cover (the length of the beam and the patch length) in the pseudo time of 1 and thus travel faster. After the initial sharp increase, the axial forces reduce as the material strength decreases with a continuing increase of temperature. As the larger patches travel faster yet have a lower temperature gradient along the patch length, the loss of material strength and thus a reduction in the axial force, occurs at a similar time. The second stage of the response occurs once the cooling portion of the temperature patch is located within the length of the beam. As each portion of the beam is heated, it plastifies in axial compression and so becomes permanently lengthened. Contraction of the plastified sections upon cooling produces tensile strains that largely counteract the compressive strains produced in the heated portion of the beam. This produces a lengthy period when the axial forces are stable as the temperature patch traverses the central portion of the beam. The final stage of the response occurs when the temperature patch traverses off the end of the beam and the full length returns to ambient temperature. At this point there is no thermal expansion to counteract the contraction of the plastified section and so large tensile forces result. This result is in line with earlier findings of Röben and Gillie (2007) who consider the effects of cooling after uniform heating. The effect of varying the length of the temperature patch is surprisingly small while the fire is in progress. Any increases in thermal strains caused by heating are largely offset by a corresponding increase in contraction of the cooling part of the beam. However, upon final cooling the longer patches result in significantly great tensile forces being produced. The limiting case of a uniform heating followed by uniform cooling shows a sufficiently large tensile force being developed for the beam to yield.

Figure 4 shows the axial forces from of the second form of loading where a temperature gradient is applied. This produces significantly different results with tensile forces resulting from early stages of the loading. This is due to the upper portions of the section not being subject to compression.

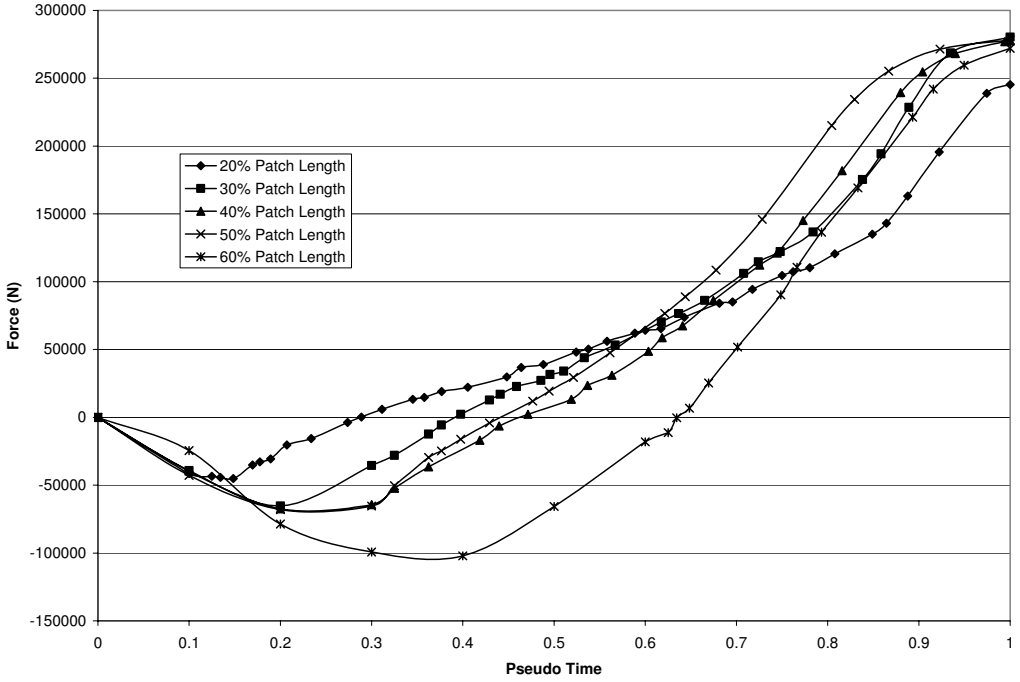

Figure 4. Axial force in the beam when subject to a travelling fire with a temperature gradient

5. CONCLUSIONS

The effects of travelling and localized fires on the behaviour of structures have until recently been ignored. Recent experimental and theoretical work has shown that assuming uniform temperatures in structural elements is not realistic, even for small compartments. Results in this paper indicate that the development of forces produced by travelling fires may be significantly different to those produced by uniform fires and that this should be taken into account in design. In particular beams will likely be subject to both tensile and compressive forces within the duration of a realistic compartment fire, any performance-based design should take account of this. The effects of temperature gradients within the depth of a beam subject to a travelling fire may be significant and lead to tensile forces early in the fire development.

6. REFERENCES

Bailey CG, Burgess IW, Plank RJ (1996), *Analyses of the effects of cooling and fire spread on steel-framed buildings*. Fire Safety Journal 26(273-293).

BS 476 (1987 Fire tests on buildings and structures. Part21: Method of determination of the fire resistance of load-bearing elements of construction. British Standards Institution.
Cooke, G.M.E. (1998) "Tests to determine the behaviour of fully developed natural fires in a large compartment", Fire Note 4, Fire Research Station, Building Research Establishment
Röben C, Gillie M, (2007) *Fundamental mechanics of structures cooling after fire loading* In Proc. 5th International Conference of Advances in Steel Structures. Eds. Liew and Choo. pp700-705
Rein G, Zhang X, Williams P, Hume B, Heise A, Jowsey A, Lane B, and Torero JL (2007), *Multi-story fire analysis for high-rise buildings*. 11th Interflam, London, September.
EN1991 (2002) Eurocode 1: Actions of Structures Part 1-2 Actions of Structures Exposed to Fire, CEN, Brussels
EN1993 (2005) Eurocode 3: Design of Steel Structures Part 1-2 Structural Fire Design, CEN, Brussels.
Pettersson O, Magnuson SE and Thor J (1976) *Fire engineering design of structures* Swedish Institute of Steel Construction, Publication 50.

Author Index